2022 IBIC International Beam Instrumentation Conference

11 – 15 SEPTEMBER 2022
KRAKOW, POLAND

Topics

Beam Charge and Current Monitors
Beam Loss Monitors and Machine Protection
Beam Position Monitors
Transverse Profile and Emittance Monitors
Longitudinal Diagnostics and Synchronization
Feedback Systems and Beam Stability
Data Acquisition and Processing Platforms
Machine Parameter Measurements
Overview and Commissioning

Scientific Programme Committee

Chair
Peter **Forck,** GSI, Germany

Members
Tonia Batten, CLS, Canada
Willem Blockland, SNS, USA
Lorraine Bobb, DLS, UK
Alessandro Cianchi, University Rome, Italy
Alessandro Curcio, CLPU, Spain
Friederike Ewald, ESRF, France
David Gassner, BNL, USA
Nicolas Hubert, SOLEIL, France
Ubaldo Iriso ALBA, Spain
Kevin Jordan, JLAB, USA
Changbum Kim, PAL, Korea
Prapong Klysubun, SLRI, Thailand
Patrick Krejcik, SLAC, USA
Gero Kube, DESY, Germany
Thibaut Lefevre, CERN, Switzerland
Yongbin Leng, SSRF, China
Hirokazu Maesaka, Spring-8, Japan
Daniel Tavares, LNLS, Brasil
Junhui Yue, IHEP, China
Kenichirou Satou, J-PARC, Japan
Victor Scarpine, Fermilab, USA
Volker Schlott, PSI, Switzerland
Adriana Wawrzyniak, SOLARIS, Poland
Kay Wittenburg, DESY, Germany

IBIC2022 — Proceedings

Local Organising Committee

Conference Chair
Adriana **Wawrzyniak,** SOLARIS, Poland

Conference support
Mirosław Burzyński, SOLARIS, Poland
Bogumił Harnik, SOLARIS, Poland
Ireneusz Zadworny, SOLARIS, Poland
Tomasz Zbylut, SOLARIS, Poland
Michał Żurek, SOLARIS, Poland

Scientific Secretary & Webmaster
Agnieszka **Cudek,** SOLARIS, Poland

Graphic Designer
Joanna Kowalik SOLARIS, Poland

Posters
Roman Panaś, SOLARIS, Poland

JACoW Editorial Team
Grzegorz **Kowalski,** SOLARIS, Poland – Editor in Chief
Michael Bree, CLS, Canada
Wojciech Grabowski, NCBJ, Poland
Jaeyu Lee, PAL, Korea
Christine Petit-Jean-Genaz, CERN, Switzerland
Volker RW **Schaa,** GSI, Germany - Technical Editor
Ana Štajminger, ELI, Czech Republic

Exhibitors & Sponsors
Alicja Surowiec, GSI, Germany
Beata Walasek-Höhne, GSI, Germany
Piotr Andryszczak, SOLARIS, Poland

WWW.IBIC2022.ORG

Organizers

Honorary patronage: Jacek Majchrowski Mayor of the City of Krakow

Media patronage

Conference's Partner

Sponsors

11th International Beam Instrumentation Conference
IBIC2020 — SOLARIS & GSI, Auditorium Maximum

Jagiellonian University in Kraków, Poland ★ 11–15 September 2022



Foreword to IBIC2022

The 11th International Beam Instrumentation Conference 2022, IBIC 2022, was held in Kraków, Poland, between September 11th and 15th, 2022. It was hosted by the SOLARIS National Synchrotron Radiation Centre, Jagiellonian University in Krakow, Poland, in collaboration with the GSI Helmholtzzentrum für Schwerionenforschung, Darmstadt, Germany. IBIC is a fruitful and successful gathering of the world's beam instrumentation community, and it is dedicated exploring the physics and engineering challenges of beam diagnostic and measurement techniques for particle accelerators.

The IBIC2022 conference included 38 invited and contributed talks, 2 tutorials, 118 posters, and a 3-day long vendor exhibition with 21 exhibitors that could be visited during the conference. All oral sessions were recorded and posted on YouTube.

IBIC2022 was organized as an in-person event, the first one after two years of online IBIC meetings related to the worldwide COVID crisis. In total, 243 participants from 19 countries got together during the conference; this includes 11 scholarships for PhD students. Unluckily, the COVID travel restrictions prevented the participation of Chinese delegates. Due to the attack against Ukraine, delegates from Russian and Belarusian institutes were excluded from the conference.

The Organizing Committee warmly thank all participants for their participation and enthusiastic contributions to IBIC2022 and the discussion about novelties in the innovative field of accelerator beam diagnostics.

It was great seeing you all again after the long period of travel restrictions!

Adriana Wawrzyniak, IBIC'22 – Conference Chair

Peter Forck, IBIC'22 – Scientific Chair

Scientific Program Committee (SPC)

Peter Forck	**SPC Chair**	GSI	Germany
Tonia Batten		CLS	Canada
Willem Blokland		SNS	USA
Lorraine Bobb		Diamond	Great Britain
Alessandro Cianchi		University Rome	Italy
Alessandro Curcio		CLPU	Spain
Friederike Ewald		ESRF	France
David Gassner		BNL	USA
Nicolas Hubert		Soleil	France
Ubaldo Iriso		ALBA	Spain
Kevin Jordan		JLab	USA
Changbum Kim		PAL	South Korea
Prapong Klysubun		SLRI	Thailand
Patrick Krejcik		SLAC	USA
Gero Kube		DESY	Germany
Thibaut Lefevre		CERN	Switzerland
Yongbin Leng		SSRF/SARI	China
Hirokazu Maesaka		Spring-8	Japan
Kenichirou Satou		J-PARK/KEK	Japan
Victor Scarpine		FNAL	USA
Volker Schlott		PSI	Switzerland
Daniel Tavares		LNLS	Brazil
Adriana Wawrzyniak		SOLARIS	Poland
Kay Wittenburg		DESY	Germany
Junhui Yue		IHEP	China

Local Organizing Committee (LOC)

Adriana Wawrzyniak	**Conference Chair**	SOLARIS	Poland
Conference Support			
Mirosław Burzyński		SOLARIS	Poland
Bogumił Harnik		SOLARIS	Poland
Ireneusz Zadworny		SOLARIS	Poland
Tomasz Zbylut		SOLARIS	Poland
Michał Żurek		SOLARIS	Poland
Webmaster & Scientific Secretary			
Agnieszka Cudek		SOLARIS	Poland
Graphic Designer			
Joanna Kowalik		SOLARIS	Poland
Poster Session Manager			
Roman Panaś		SOLARIS	Poland
Industrial Exhibit & Sponsorship			
Alicja Surowiec		GSI	Germany
Beata Walasek-Hoehne		GSI	Germany
Piotr Andryszczak		SOLARIS	Poland

JACoW Editorial Team (JET)

Grzegorz Kowalski	**Editor-in-Chief**	SOLARIS	Poland
Michael Bree		CLS	Canada
Wojciech Grabowski		NCBJ	Poland
Jaeyu Lee		PAL	South Korea
Christine Petit-Jean-Genaz		CERN	Switzerland
Volker RW Schaa	**Technical Editor**	GSI	Germany
Ana Štajminger		ELI	Czech Republic



Contents

Preface i
Foreword . . . iii
Committees . . . v
Contents . . . vii

Papers 1
MO1C3 – Development of a 6D Electron Beam Diagnostics Suite for Novel Acceleration Experiments at FEBE on CLARA . . . 1
MO2C2 – Beam Tuning Studies in the ESS MEBT . . . 6
MO2I4 – Statistical Properties of Undulator Radiation . . . 11
MOP01 – SLS 2.0 – Status of the Diagnostics . . . 15
MOP02 – An Optical Diagnostic Beamline for the Bessy II Booster . . . 19
MOP03 – Status Overview of the HESR Beam Instrumentation . . . 23
MOP05 – Fiber Bragg Grating Sensors as Beam-Induced Heating Monitor for the Central Beam Pipe of CMS . . . 28
MOP07 – Beam Instrumentation Performance During Commissioning of the ESS RFQ, MEBT and DTL 32
MOP08 – Development of a Waveguide BPM System . . . 37
MOP09 – Towards Higher Stability in Large Scale Cavity BPM Systems . . . 40
MOP10 – Removing Noise in BPM Measurements with Variational Autoencoders . . . 43
MOP12 – Production of Cavity Beam Position Monitors for the ARES Accelerator at DESY . . . 47
MOP13 – Test and Measurements Results of the Pilot Tone Front End Industrialization for Elettra 2.0 . 51
MOP14 – Design and Implementation of an FPGA-Based Digital Processor for BPM Applications . . . 55
MOP15 – Development of Non-Invasive Calibration Software for Front End X-Ray Beam Position Monitors at Diamond Light Source, Oxfordshire, UK . . . 59
MOP16 – Time Resolved Dynamics of Transverse Resonance Island Buckets at SPEAR3 . . . 62
MOP17 – Development of a Scintillation Fibre Transverse Profile Monitor for Low-Intensity Ion Beams at HIT . . . 67
MOP18 – X-Ray Pinhole Camera Spatial Resolution Using High Aspect Ratio LIGA Pinhole Apertures . . 71
MOP19 – Commissioning of the Renewed Long Radial Probe in PSI Ring Cyclotron . . . 76
MOP21 – First Results of PEPITES, A New Transparent Profiler Based on Secondary Electrons Emission for Charged Particle Beams . . . 80
MOP22 – Development of New Beam Position Detectors for the NA61/SHINE Experiment . . . 84
MOP23 – Recent LHC SR Interferometer Simulations and Experimental Results . . . 88
MOP24 – Test of a Prototype for Modular Profile and Position Monitors in the Shielding of the 590 MeV Beam Line at HIPA . . . 92
MOP26 – Bunch Length Measurement Systems at S-DALINAC* . . . 96
MOP27 – Design Considerations of the Corrugated Structures in a Vacuum Chamber for Impedance Studies at KARA . . . 100
MOP28 – Improvements in Longitudinal Phase Space Tomography at PITZ . . . 105
MOP29 – Low Gain Avalanche Detector Application for Beam Monitoring . . . 109
MOP31 – Automatic Adjustment and Measurement of the Electron Beam Current at the Metrology Light Source (MLS) . . . 113
MOP32 – Analog Front End for Measuring 1 to 250 pC Bunch Charge at CLARA . . . 117
MOP33 – Beam Current Measurements at the Nano-Ampere Level Using a Current Transformer . . . 121
MOP34 – New X-Rays Diagnostics at ESRF: The X-BPMs and the Halo-Monitor . . . 125
MOP35 – New Measurements Using Libera-Spark Electronics at ESRF: The High Quality Phase-Monitor and the Single-Electron . . . 129
MOP36 – Novel Beam Excitation System Based on Software-Defined Radio . . . 133
MOP37 – Beam Polarization Measurements with the Revised Compton Polarimeter at ELSA . . . 137
MOP38 – Beam Profile Monitoring and Distributed Analysis Using the RabbitMQ Message Broker . . . 140
MOP39 – Development of Compact Radio Frequency Sources . . . 144
MOP40 – Synchronous Data Service at the European Spallation Source . . . 148
MOP42 – KINGFISHER: A Framework for Fast Machine Learning Inference for Autonomous Accelerator Systems . . . 151
MOP43 – Web-Based Application for Cable Simulation Models . . . 156

MOP44 – Novel Photoemission Type X-Ray Beam Position Monitor for the "White" Undulator Radiation 159
MOP45 – A New Luminosity Monitor for the LHC Run 3 . . . 163
MO3C2 – Diamond-II Electron Beam Position Monitor Development . . . 168
MO3C3 – Pulse-by-Pulse Photon Beam Position Measurements at the SPring-8 Undulator Beamline . . . 173
MO3C4 – Beam Position Monitoring of Multi-bunch Electron Beams at the FLASH Free Electron Laser . 177
TU1I1 – Electro-Optical BPM Development for High Luminosity LHC . . . 181
TU1I2 – Diagnostics with Quadrupole Pick-Ups at SIS18 . . . 186
TU1C3 – Beam-Based Calibration of Sextupole Magnet Displacement with Betatron Tune Shift . . . 192
TU2T1 – Collimation and Machine Protection for Low Emittance Rings . . . 196
TU2C2 – The Diamond Beam Loss Monitoring System at CERN LHC and SPS . . . 202
TU2C3 – Commissioning Beam-Loss Monitors for the Superconducting Upgrade to LCLS . . . 207
TUP01 – Commissioning of the Libera Beam Loss Monitoring System at SPEAR3 . . . 211
TUP02 – Design of High Dynamic Range Preamplifiers for a Diamond-Based Radiation Monitor System . 216
TUP03 – The Beam Loss Monitoring System after the LHC Long Shutdown 2 at CERN . . . 220
TUP04 – Beam Loss Monitor for Polish Free Electron Laser (PolFEL): Design and Tests . . . 225
TUP05 – Experience with Machine Protection Systems at PIP2IT . . . 229
TUP09 – Design of the Beam Position Monitor for SOLEIL II . . . 233
TUP10 – Development of a New Measurement System for Beam Position Pickups in the LINAC and Beam Energy Measurement (Time of Flight) in the MEBT for Medaustron . . . 238
TUP11 – A Cryogenic RF Cavity BPM for the Superconducting Undulator at LCLS . . . 241
TUP12 – First Application of a Multiprocessing System-on-Chip BPM Electronics Platform at SwissFEL 245
TUP13 – Standard Button BPMs for PETRA IV . . . 249
TUP15 – New Gas Target Design for the HL-LHC Beam Gas Vertex Profile Monitor . . . 252
TUP16 – FOCUS: Fast Monte-CarlO Approach to Coherence of Undulator Sources . . . 257
TUP17 – HL-LHC Beam Gas Fluorescence Studies for Transverse Profile Measurement . . . 261
TUP18 – High-Resolution Interferometric Beam-Size Monitor For Low-Intensity Beams . . . 265
TUP19 – Visible Range Polarized Imaging for High Resolution Transverse Beam Size Measurement at SOLEIL . . . 269
TUP20 – Correction for Systematic Errors in Transverse Phase Space Measurements at PITZ . . . 273
TUP21 – Scintillator Nonproportionality Studies at PITZ . . . 277
TUP23 – Commissioning of the Timing System at ESS . . . 281
TUP25 – Simulation and Measurements of the Fast Faraday Cups at GSI UNILAC . . . 286
TUP28 – Coherent Difraction Radiation for Longitudinal Electron Beam Characteristics . . . 291
TUP29 – ZnO(In) Scintillation Light Spectra Investigation for Heavy Ion Detector Application . . . 294
TUP30 – Beam Intensity Measurement in ELENA Using Orbit Pick-Ups . . . 296
TUP31 – The Cryogenic Current Comparator at CRYRING@ESR . . . 300
TUP32 – Differential Current Transformer for Beam Charge Monitoring in Noisy Environments . . . 304
TUP34 – LHC Schottky Spectrum from Macro-Particle Simulations . . . 308
TUP35 – First RF Phase Scans at the European Spallation Source . . . 313
TUP36 – Beam Characterization of Slow Extraction Measurement at GSI-SIS18 for Transverse Emittance Exchange Experiments . . . 318
TUP38 – Deep Neural Network for Beam Profile Classification in Synchrotron . . . 323
TUP39 – Neural Network Inverse Models for Implicit Optics Tuning in the AGS to RHIC Transfer Line . 327
TUP40 – Photon Polarization Switch at ALBA . . . 331
TUP41 – Multi-Dimensional Feedforward Controller at MAX IV . . . 335
TUP42 – Fast Orbit Feedback Upgrade at SOLEIL . . . 339
TUP43 – Requirements and Design for the PETRA IV Fast Orbit Feedback System . . . 343
TU3I1 – Investigating the Transverse Dynamics of Electron Bunches in Laser-Plasma Accelerators . . . 348
TU3C2 – Angular-Resolved Thomson Parabola Spectrometer for Laser-Driven Ion Accelerators . . . 352
TU3C3 – LINAC4 Laser Profile and Emittance Meter Commissioning . . . 357
TU3C4 – A High Performance Scintillator Ion Beam Monitoring System . . . 362
WE1C2 – An X-Ray Beam Property Analyzer Based on Dispersive Crystal Diffraction . . . 366
WE2C2 – Beam Stability in the MAX IV 3 GeV Storage Ring . . . 370
WE2I3 – Adaptive Feedforward Control of Closed Orbit Distortion Caused by Fast Helicity-Switching Undulators . . . 374
WE2C4 – RF System-on-Chip for Multi-Bunch and Filling-Pattern Feedbacks . . . 379

WEP04 – Dual channel FMC High-Voltage Supply . . . 383
WEP06 – An LHC Protection System Based on Fast Beam Intensity Drops . . . 387
WEP07 – Influence of the Beam Induced Irradiation on the Critical Current Phenomena in Superconducting Elements . . . 391
WEP08 – Upgrade of the BPM Long Term Drift Stabilization Scheme Based on External Crossbar Switching at PETRA III . . . 395
WEP09 – Preliminary Evaluation of the MTCA.4 BPM Electronics Prototype for the PETRA IV Project 399
WEP10 – Detection of a DC Electric Field Using Electro-Optical Crystals . . . 403
WEP12 – HL-LHC BPM System Development Status . . . 408
WEP14 – Cavity BPM Electronics for SINBAD at DESY . . . 413
WEP15 – XFEL Photon Pulse Measurement Using an All-Carbon Diamond Detector . . . 416
WEP16 – PSF Characterization of the ALBA X-Ray Pinholes . . . 421
WEP17 – Electron Emission (SEM) Grids for the FAIR Proton Linac . . . 426
WEP20 – Emittance Diagnostics at PETRA IV . . . 430
WEP21 – Merits of Pulse Mode Operation of Residual Gas Ionization Profile Monitor for J-PARC Main Ring . . . 434
WEP22 – Experimental Investigation of Gold Coated Tungsten Wires Emissivity for Applications in Particle Accelerators . . . 438
WEP23 – Assessing the Performance of the New Beam Wire Scanners for the CERN LHC Injectors . . . 443
WEP24 – Modeling and Experimental Evaluation of a Bunch Arrival-Time Monitor with Rod-Shaped Pickups and a Low-Pi-Voltage Ultra-Wideband Traveling Wave Electro-Optic Modulator for X-Ray Free-Electron Lasers . . . 447
WEP25 – Installation and Commissioning of the Pulsed Optical Timing System Extension . . . 451
WEP26 – Status of a Monitor Design for Single-Shot Electro-Optical Bunch Profile Measurements at FCC-ee 455
WEP28 – Studies on Radially Coupled Fast Faraday Cups to Minimize Field Dilution and Secondary Electron Emission at Low Intensities of Heavy Ions . . . 460
WEP29 – Optimization Study of Beam Position and Angular Jitter Independent Bunch Length Monitor for Awake Run 2 . . . 465
WEP30 – Creation of the First High-Inductance Sensor of the New CCC-Sm Series . . . 469
WEP31 – Booster Fillpattern Monitor . . . 473
WEP32 – Secondary Emission Monitor Simulation, Measurements and Machine Learning Application Studies for CERN Fixed Target Beamlines . . . 476
WEP33 – Operational and Beam Study Results of Measurements with the Transverse Feedback System at the Canadian Light Source . . . 481
WEP34 – Orbit Correction Upgrade at the Canadian Light Source . . . 485
WEP36 – Conceptual Design of the Transverse Multi-Bunch Feedback for the Synchrotron Radiation Source PETRA IV . . . 488
WEP37 – Measurements for Emittance Feedback based on Resonant Excitation at Diamond Light Source 492
WEP38 – Control System Suite for Beam Position Monitors at MAX IV . . . 496
WEP40 – A Modern Ethernet Data Acquisition Architecture for Fermilab Beam Instrumentation . . . 500
WEP41 – ENeXAr: An EPICS-Based Tool for User-Controlled Data Archiving . . . 504
WEP42 – Application of Machine Learning towards Particle Counting and Identification . . . 508
WEP43 – Control Systems of DC Accelerators at KAHVELab . . . 512
WE3I1 – Novel Fast Radiation-Hard Scintillation Detectors for Ion Beam Diagnostics . . . 515
WE3C2 – Time-Resolved Proton Beam Dosimetry for Ultra-High Dose-Rate Cancer Therapy (FLASH) . 519
WE3C3 – Fast Spill Monitor Studies for the SPS Fixed Target Beams . . . 522
WE3C4 – Simulated Behavior of CNT Wires Irradiated in the HiRadMat Experimental Line at CERN . . 527
TH1I1 – First Measurement of Longitudinal Profile of High-Power and Low-Energy H Beam by Using Bunch Shape Monitor with Graphite Target . . . 532
TH1C3 – Single-Shot Electro-Optic Detection of Bunch Shapes and THz Pulses: Fundamental Temporal Resolution Limitations and Cures Using the DEOS Strategy . . . 536
TH2C2 – Upgraded CMS Fast Beam Condition Monitor for LHC Run 3 Online Luminosity and Beam Induced Background Measurements . . . 540

Appendices **545**
List of Authors . . . 545
List of Institutes . . . 553

ISBN: 978-3-95450-241-7 ISSN: 2673-5350 doi:10.18429/JACoW-IBIC2022-MO1C3

DEVELOPMENT OF A 6D ELECTRON BEAM DIAGNOSTICS SUITE FOR NOVEL ACCELERATION EXPERIMENTS AT FEBE ON CLARA

T. H. Pacey*,[1], D. Angal-Kalinin[1], A. R. Bainbridge[1], J. R. Henderson[1], J. K. Jones[1], N. Joshi[1], S. Mathisen[1], A.E. Pollard[1], Y. M. Saveliev[1], E.W. Snedden[1], C. Tollervey[1], D. A. Walsh[1]
STFC, Daresbury Laboratory, Warrington, UK
T. J. Overton[1], University of Manchester, Manchester, UK
J. Wolfenden[1], C. Swain, University of Liverpool, Liverpool, UK
[1]also at Cockcroft Institute, Sci-Tech Daresbury, Warrington, UK

Abstract

The FEBE beamline at the CLARA facility will combine a 250 MeV FEL quality electron beam with a 100 TW class laser. One area of research FEBE will support is novel acceleration schemes; both structure and plasma based. There are stringent diagnostic requirements for measuring the input electron beam and challenges in characterisation of the accelerated beams produced by these novel schemes. Several of these challenges include measurement of: micrometer scale transverse profiles, 10 fs scale bunch lengths, single shot emittance, broadband energy spectra at high resolution, and laser-electron time of arrival jitter. Furthermore, novel shot-by-shot non-invasive diagnostics are required for machine learning driven optimisation and feedback systems. This paper presents an overview of R&D activities in support of developing a 6D diagnostics suite to meet these challenges.

INTRODUCTION

The Compact Linear Accelerator for Research and Applications (CLARA) is an ultra-bright electron beam test facility being developed at STFC Daresbury Laboratory. CLARA has been designed to test advanced Free Electron Laser (FEL) schemes that could be later implemented on existing and future short wavelength FELs. CLARA is being constructed in phases. Phase 1 was commissioned in 2018, completing the CLARA Front-End, which consists of a S-band photo-injector gun and linac. Phase 1 produced electron bunches at 10 Hz, up to 250 pC in charge and with energy of 50 MeV. A comprehensive review of results from commissioning CLARA Phase 1 can be found in [1]. Phase 1 was used for two periods of competitively allocated beam exploitation, taking place in 2018/19 and 2021/22. A broad range of experiments were performed in these periods, including multiple experiments on novel acceleration techniques: dielectric wakefield acceleration, THz driven acceleration, and plasma wakefield acceleration. These novel acceleration experiments were performed in the CLARA Beam Area 1 (BA1) user hutch where a 100 mJ class laser system was available for exploitation with the electron beam [2].

Phase 2 of CLARA is currently under construction, comprising of an upgrade to the photo-injector gun and installation of 3 further linacs. This will produces bunches at 100 Hz, 250 pC with final energy of 250 MeV. Included in Phase 2 is the installation of the Full Energy Beam Exploitation (FEBE) hutch. The FEBE hutch represents a step change in experimental capability over BA1, benefiting from both the uplift in electron beam parameters and inclusion of a 100 TW class laser system. The FEBE beamline and hutch will be used for a broad range of experiments, and not exclusively novel acceleration applications. However, it is these novel experiments that pose the greatest challenge for machine performance in terms of beam parameters and subsequent instrumentation.

Phase 3 of CLARA is tied to the R&D requirements for a future UK-XFEL and is not yet funded.

FEBE BEAMLINE

The FEBE beamline is shown in Fig. 1 and comprises of a 4 cell FODO arc, transporting the beam to a shielded hutch with approximately 10×5 m^2 floor space. The room which houses the 100 TW laser system is on the roof directly above the hutch. A detailed discussion of the design of the FEBE beamline can be found in [3]. There are 4 chambers in the FEBE hutch: FMBOX1 for coupling and focusing the laser beam co-linearly with the electron beam, FEC1 ($\approx$ 2 m length) for the primary interaction point (IP) with the focus of both electron and laser beams, FMBOX2 for the dumping and diagnostics of the laser beam, and FEC2 as a secondary electron beam interaction point and for housing a suite of diagnostics. The FEBE beamline has an array of well developed or commercially available diagnostic systems including: Ce:YAG screens, stripline beam position monitors (BPMs), integrating current transformers (ICTs), and Faraday cups (F-cups).

The input electron beam parameters for FEBE are shown in Table 1. Beam parameters which are expected to be achieved following initial commissioning are shown, along with potential future parameters which could be achieved following dedicated machine development. Two charge modes are shown, a maximum charge of 250 pC and a low charge of 5 pC; which is the lowest the current BPM electronics will resolve. These parameters are not exhaustive or prescriptive and FEBE will offer very flexible beam setups to users, significantly improved over that provided to users of BA1. Table 1 also indicates those future parameters which will require diagnostics R&D to experimentally validate.

* thomas.pacey@stfc.ac.uk

Content from this work may be used under the terms of the CC BY 4.0 licence (© 2022). Any distribution of this work must maintain attribution to the author(s), title of the work, publisher, and DOI

ISBN: 978-3-95450-241-7 ISSN: 2673-5350 doi:10.18429/JACoW-IBIC2022-MO1C3

Content from this work may be used under the terms of the CC BY 4.0 licence (© 2022). Any distribution of this work must maintain attribution to the author(s), title of the work, publisher, and DOI

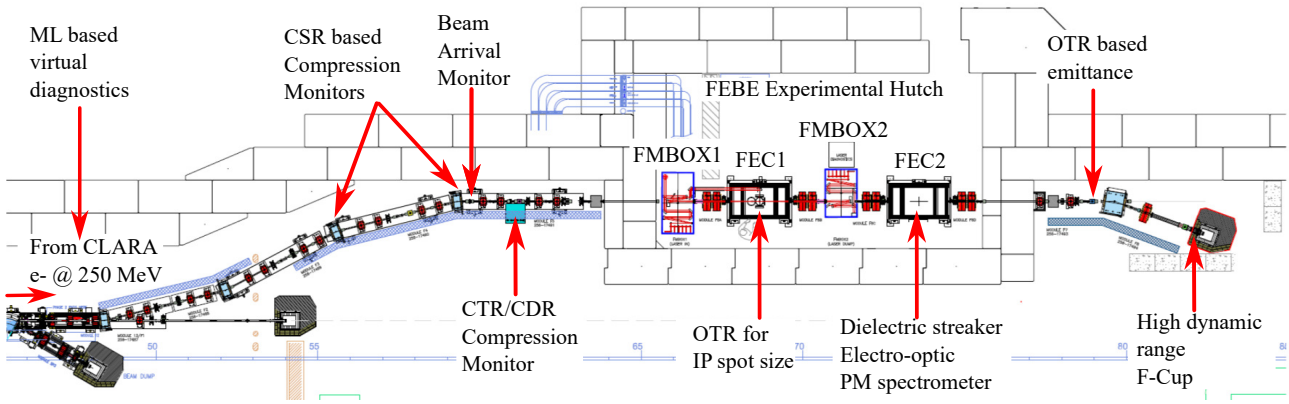


Figure 1: Engineering diagram of FEBE beamline, highlighting areas with diagnostic systems undergoing R&D. These areas are supported by diagnostic systems including Ce:YAG screens, beam position monitors and ICTs.

Table 1: Initial and future input FEBE beam parameters at the primary IP in FEC1. All parameters are for beam energy 250 MeV. Symbol σ_i indicates RMS value, $\epsilon_{N,i}$ indicates normalised RMS emittance. Parameters marked with † will require diagnostic R&D to validate.

Parameter	Initial		Future	
Charge (pC)	250	5	250	$< 5^{\dagger}$
σ_t (fs)	100	$50^{\dagger}$	50 †	$< 50^{\dagger}$
σ_x (µm)	100	20	50	$\sim 1^{\dagger}$
σ_y (µm)	100	20	50	$\sim 1^{\dagger}$
$\epsilon_{N,x}$ (µm)	5	2	< 5	1
$\epsilon_{N,y}$ (µm)	5	2	$< 1^{\dagger}$	$< 1^{\dagger}$

R&D activities supporting making these measurements are highlighted in Fig. 1.

Beams accelerated within FEC1/2 of up to 600 MeV can be transported through the FEBE hutch to the final dipole and spectrometer line. Beams with energy in excess of 600 MeV and less than 2 GeV must be diagnosed and safely dumped in the hutch in FEC2.

6D DIAGNOSTICS R&D

There are several diagnostic systems under development to support measuring future beam parameters in FEBE and meet some of the unique challenges posed by beams from novel acceleration experiments, including: beams with high energy spread, unstable transverse and longitudinal properties, and exacting IP parameters which cannot drift during the experiment. This requires development of single shot diagnostics to monitor and feedback on machine drifts and instabilities in post IP accelerated beams, precise measurements of small focal spot sizes and arrival times, and systems capable of dealing with a large range of beam energies. A non-exhaustive list of current R&D activities at CLARA to meet these requirements is provided below.

PM Dipole Spectrometer

A permanent magnet (PM) dipole spectrometer has been designed for use in FEC2. This spectrometer will be able to measure beam energies in the broad range of 0.05 - 2 GeV, and will support measurement of beams with high energy spread and/or energy instability. The dipole is comprised of NdFeB blocks with a Ni-Cu-Ni coating (for vacuum compatibility) with a gap of 20 mm and a peak field of 0.72 T. It has a modular design, comprising of a total of 5 sections, such that the length of magnet installed can match the expected maximum beam energy. The physical extent of the full magnet, along with electron trajectories across its operating energy range, is shown in Fig. 2. A scintillating screen of 1 m in length and corresponding imaging system would be required to measure beams across the full range.

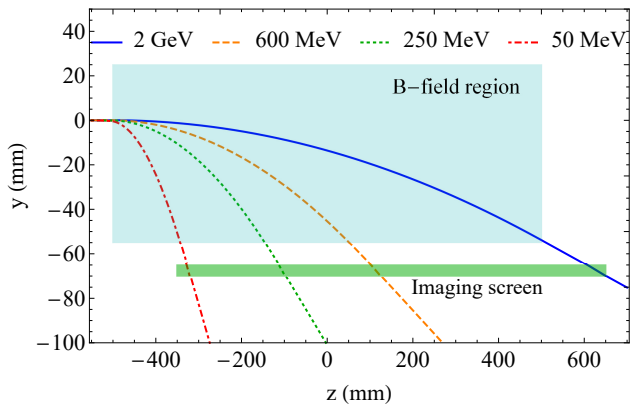


Figure 2: The physical extent of the full PM dipole system for use in FEC2, along with imaging screen. Electron trajectories for the full operating range are shown.

Dielectric Wakefield Streaker

A passive streaker based on a dielectric wakefield accelerator (DWA) structure has been designed to make bunch length measurements across the range of ~ 50 fs to > 1 ps. The streaker works through exciting dipole wakefields when the electron beam propagates off axis in a planar dielectric

ISBN: 978-3-95450-241-7 ISSN: 2673-5350 doi:10.18429/JACoW-IBIC2022-MO1C3

waveguide. Such passive wakefield devices have been shown to make accurate bunch length measurements at operational FEL facilities whilst costing a fraction of that of a RF transverse deflecting cavity (TDC) [4]. Recent studies of the properties of transverse wakefields in DWA structures which were performed in CLARA BA1 are reported in [5]. Along with dipole wakefields, higher order quadrupole-like modes are excited, which cause a non-linear variation in streaking force transversely across the bunch, resulting in reduced resolution of the bunch length measurement. The effect of these higher order wakefields can be negated through use of a second DWA structure orthogonally orientated to the first which increases the average resolution of the measurement across the bunch by a factor of ~ 3, this is shown through simulations in Fig. 3. It should be noted that the DWA streaker resolution does not scale favourably with reducing beam charge, and will not be able to resolve the bunch lengths at low charges.

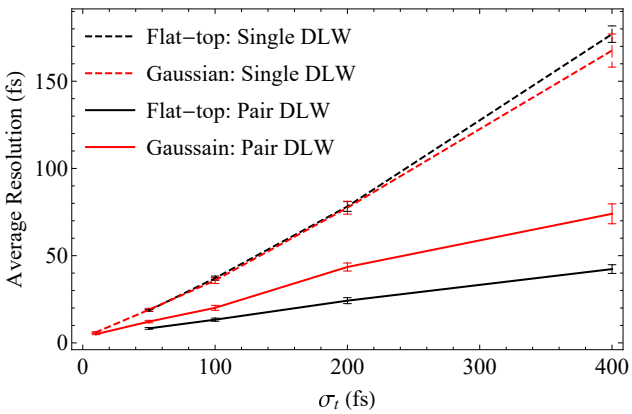


Figure 3: Simulated average resolution of a DWA streaking measurement in FEC2 for varying bunch length σ_t for both Gaussian and flat-top profiles (where flat-top has total length $4\sigma_t$), for charge of 250 pC. The improvement in resolution from using a pair of orthogonally orientated structures to cancel higher order wakefields is shown.

Electro-Optic Bunch Length Reconstruction

A system for bunch length reconstruction based on electro-optic spectral interferometry (EOSI) has been developed with proof of concept experiments performed in CLARA BA1. This non-invasive system used an optical non-linear crystal (gallium phosphide) to imprint the Coulomb field of the electron bunch onto the spectrum of a chirped laser pulse. The EOSI technique for retrieving the bunch profile from the spectrum was shown to have improved temporal resolution over the more conventional spectral decoding (SD) technique. Single shot bunch length measurements were made with bunch charges from 2 pC to 150 pC and down to $\sigma_t = 300$ fs. Measurements were possible with a transverse distance of 1 cm between the beam trajectory and the EO crystal at 100 pC. Future work will focus on development of a more robust fibre coupled system.

Coherent Radiation Bunch Compression Monitors

A coherent transition radiation (CTR) based bunch compression monitor (BCM) was installed and commissioned to support user exploitation in BA1 [1, 2]. This robust BCM was found to be valuable for machine tuning and reproducibility. An upgraded CTR BCM will be installed on FEBE, employing high and low pass filters in order to act as a rudimentary spectrometer, as is shown in Fig. 4. This system, combined with accurate measurements upstream in CLARA using a TDC, will ensure maximally compressed beams can be delivered to FEBE for novel acceleration experiments. In addition to the solid CTR target, a non-invasive coherent diffraction radiation (CDR) target - with a hole in the middle - can also be used to provide shot-to-shot compression jitter measurements. The detector is a bespoke pyroelectric based system, employing variable gain, active noise cancellation, and Winston cones for radiation capture. This detector will also be employed on the FEBE arc for measurement of coherent synchrotron radiation (CSR).

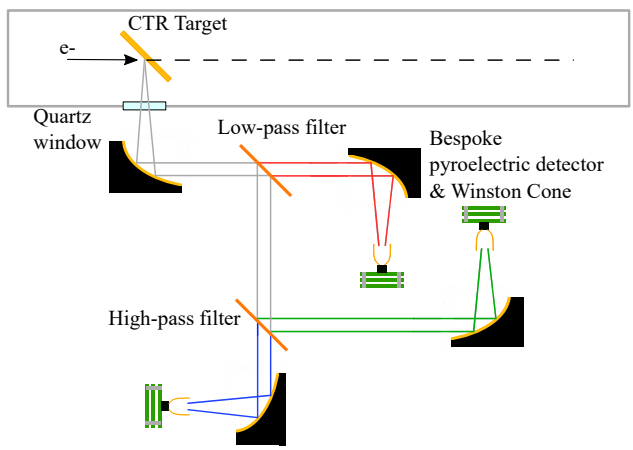


Figure 4: Schematic diagram of the BCM spectrometer system to be installed at end of FEBE arc as indicated in Fig. 1.

Beam Arrival Monitor and Laser Synchronisation

Measurement and reduction of time of arrival (TOA) jitter between the FEBE laser and the electron beam will be vital for laser driven acceleration experiments. The FEBE laser will be optically synchronised to the CLARA optical clock. Design and testing has been completed for producing a stabilised (<10 fs drift over 24 hours) in-fibre clock distribution system and testing is underway for providing two-colour laser locking. A new beam arrival monitor (BAM) is being developed with removable pick-ups in a similar design to [6]. The initial performance target is 10 fs resolution TOA measurement at a minimum of 20 pC, with a future goal of operation at < 5 pC with upgraded BAM pick-ups.

Development work is also progressing on a THz driven electron beam streaker. The THz source would be produced from optical rectification of the FEBE laser in a non-linear crystal, before mode shaping and coupling into a dielectric

Content from this work may be used under the terms of the CC BY 4.0 licence (© 2022). Any distribution of this work must maintain attribution to the author(s), title of the work, publisher, and DOI

ISBN: 978-3-95450-241-7 ISSN: 2673-5350 doi:10.18429/JACoW-IBIC2022-MO1C3

Content from this work may be used under the terms of the CC BY 4.0 licence (© 2022). Any distribution of this work must maintain attribution to the author(s), title of the work, publisher, and DOI

lined waveguide, as in [7]. This laser based streaker system would provide both precise TOA jitter measurements and bunch length measurements for the short, low charge beams shown in Table 1.

OTR Based Emittance Measurements

Imaging of optical transition radiation (OTR) is a well established technique for measuring transverse beam sizes and beam divergences. As both spatial and angular information from the electron beam is encoded in OTR, direct measurement of beam emittance is possible. This requires localising divergence measurements to discrete regions of the spatial OTR image; analogous to making an emittance measurement using a mechanical slit or "pepper-pot". Two techniques are under investigation to produce an OTR based "optical pepper-pot": optical masking using a digital micromirror device (DMD) [8], and imaging with a micro-lens array (MLA) [9]. Current effort is focused on development of bench-top prototype systems and improving accuracy of simulations performed in Zemax. Single shot emittance diagnostics have the potential to be highly impactful for novel acceleration experiments, as conventional multi-shot techniques (e.g. quadrupole scan) are not appropriate for unstable beams. An OTR based pepper-pot also scales favourably with increasing beam energy, in contrast to a mechanical mask.

Virtual Diagnostics

Machine learning (ML) based algorithms can be used to predict beam parameters at a given location from a set of input machine parameters the ML model has been trained on; this is referred to as a virtual diagnostic. Initial simulation studies for FEBE have shown accurate and precise prediction of the IP beam size from an image of a beam either up- or downstream of the IP, for a variety of lattice settings [10]. Prediction of the IP beam size will be vital for experiments where precise transverse diagnostics cannot be installed at the IP due to spatial or mechanical constraints. Future activities will seek to build on the results presented in [11] for longitudinal phase space prediction, and incorporate (simulated) measurements from the CSR/CTR BCM systems.

High Dynamic Range Charge Measurements

The flexible beam delivery of FEBE will require both accurate and precise measurement of charges from < 5 pC to 250 pC. Low charge machine setups will be important for the initial phases of some novel acceleration experiments, as the transverse spot sizes and bunch lengths will be significantly lower than at high charge, as shown in Table 1. A new electronics front end has been developed for the F-cups on CLARA which will maintain accuracy and a high signal-to-noise ratio across this charge range. Further details can be found in [12].

CONCLUSION

The FEBE beamline has a large number of diagnostics dedicated to making beam measurements across the full 6D parameter space. This large number of conventional and novel diagnostics will support both the initial commissioning of FEBE and reaching of its future potential for users. The active R&D efforts in both precision and single-shot diagnostics will benefit future novel acceleration experiments and support this community's efforts in delivering compact accelerators with high beam quality.

ACKNOWLEDGEMENTS

The authors would like to thank the FEBE design team and the wider CLARA team for their work on this project.

REFERENCES

[1] D. Angal-Kalinin *et al.*, "Design, specifications, and first beam measurements of the compact linear accelerator for research and applications front end," *Phys. Rev. Accel. Beams*, vol. 23, p. 044 801, 2020. doi:10.1103/PhysRevAccelBeams.23.044801

[2] D. Angal-Kalinin *et al.*, "Status of CLARA at Daresbury Laboratory," presented at LINAC'22, Liverpool, UK, Aug.-Sep. 2022, paper THPOJO09, to be published.

[3] A. R. Bainbridge, D. Angal-Kalinin, J. K. Jones, T. H. Pacey, Y. M. Saveliev, and E. W. Snedden, "The Design of the Full Energy Beam Exploitation (FEBE) Beamline on CLARA," in *Proc. IPAC'22*, Bangkok, Thailand, 2022, pp. 2594–2597. doi:10.18429/JACoW-IPAC2022-THPOPT015

[4] P. Dijkstal *et al.*, "Self-synchronized and cost-effective time-resolved measurements at x-ray free-electron lasers with femtosecond resolution," *Phys. Rev. Res.*, vol. 4, p. 013 017, 2022. doi:10.1103/PhysRevResearch.4.013017

[5] Y. Saveliev *et al.*, "Experimental study of transverse effects in planar dielectric wakefield accelerating structures with elliptical beams," *Phys. Rev. Accel. Beams*, vol. 25, p. 081 302, 2022. doi:10.1103/PhysRevAccelBeams.25.081302

[6] A. Angelovski *et al.*, "Evaluation of the cone-shaped pickup performance for low charge sub-10 fs arrival-time measurements at free electron laser facilities," *Phys. Rev. ST Accel. Beams*, vol. 18, p. 012 801, 2015. doi:10.1103/PhysRevSTAB.18.012801

[7] M. T. Hibberd *et al.*, "Acceleration of relativistic beams using laser-generated terahertz pulses," *Nat. Photonics*, vol. 14, no. 12, pp. 755–759, 2020. doi:10.1038/s41566-020-0674-1

[8] G. P. Le Sage, T. E. Cowan, R. B. Fiorito, and D. W. Rule, "Transverse phase space mapping of relativistic electron beams using optical transition radiation," *Phys. Rev. ST Accel. Beams*, vol. 2, p. 122 802, 1999. doi:10.1103/PhysRevSTAB.2.122802

[9] F. Bisesto *et al.*, "Recent studies on single-shot diagnostics for plasma accelerators at sparc-lab," *Nucl. Instrum. Methods Phys. Res., Sect. A*, vol. 909, pp. 364–368, 2018. doi:10.1016/j.nima.2018.02.059

ISBN: 978-3-95450-241-7 ISSN: 2673-5350 doi:10.18429/JACoW-IBIC2022-MO1C3

[10] J. Wolfenden *et al.*, "Application of Virtual Diagnostics in the FEBE Clara User Area," presented at LINAC'22, Liverpool, UK, Aug.-Sep. 2022, paper MOPORI05, to be published.

[11] M. Maheshwari, D. J. Dunning, J. K. Jones, M. P. King, H. R. Kockelbergh, and A. E. Pollard, "Prediction and Clustering of Longitudinal Phase Space Images and Machine Parameters Using Neural Networks and K-Means Algorithm," in *Proc. IPAC'21*, Campinas, Brazil, May 2021, pp. 3417–3420. doi:10.18429/JACoW-IPAC2021-WEPAB318

[12] S. Mathisen, T. Pacey, and R. Smith, "Analog Front End for measuring 1 to 250 pC Bunch Charge at CLARA," presented at IBIC'22, Krakow, Poland, Sep. 2022, paper MOP32, this conference.

Content from this work may be used under the terms of the CC BY 4.0 licence (© 2022). Any distribution of this work must maintain attribution to the author(s), title of the work, publisher, and DOI

ISBN: 978-3-95450-241-7 ISSN: 2673-5350 doi:10.18429/JACoW-IBIC2022-MO2C2

BEAM TUNING STUDIES IN THE ESS MEBT

N. Milas*, M. Akhyani, R. A. Baron, C. S. Derrez, M. Eshraqi, Y. Levinsen,
R. Miyamoto, D. Noll, R. Tarkeshian, I. Vojskovic, R. Zeng
European Spallation Source ERIC, Lund, Sweden

Abstract

The European Spallation Source (ESS), currently under construction and initial commissioning in Lund, Sweden, will be the brightest spallation neutron source in the world once its driving proton linac achieves the design power of 5 MW at 2 GeV. Such a high power requires production, efficient acceleration, and almost loss-free transport of a high current beam, thus making the design and beam commissioning of this machine challenging. During the commissioning period in 2022 a campaign for a full characterization of the ESS Medium Energy Beam Transport session (MEBT) was carried out. Both transverse optics and longitudinal parameters were measured and compared to simulations, among them: buncher cavity tuning, transverse emittance, and initial Twiss parameters. In this paper, we present the results and future plans.

INTRODUCTION

The European Spallation Source (ESS), currently shifting from construction to testing and initial beam commissioning in Lund, Sweden, will be a spallation neutron source driven by a long pulse proton linac [1]. The linac consists of normal-conducting (NC) accelerating structures and three sections of superconducting cavities, as well as three transferlines. The NC accelerating structures include an ion source (ISrc), a radio frequency quadrupole (RFQ), and a drift tube linac (DTL). The beam commissioning of the ESS linac is being conducted in stages [2–4]. Commissioning of the first stage, for the ISrc and LEBT, started in September 2018 and continued until early July 2019. The beam was transported through the RFQ and part of the MEBT in 2021. In the first half of 2022 beam was transported to the end of the first DTL tank (DTL1), reaching an energy of 21 MeV. Schedules of the completed commissioning steps are listed in Table 1.

This paper will highlight the studies in the Medium Energy Beam Transport section (MEBT), which follows the RFQ, performed in 2021 and 2022. The main results is an attempt of estimating the input Twiss parameters to the MEBT in all 3 planes, using the Wire Scanners and the sum signals of BPMs. A measurement of the RFQ output energy and beam based calibration of the buncher cavity amplitude will also be presented.

COMMISSIONING HIGHLIGHTS

The first part of the MEBT commissioning started in 2021 (Step 2A in Table 1), and, during this first period, the main focus was on beam transmission through the RFQ and less on the MEBT characterization. During this period, a cautious approach was taken before sending the beam to the RFQ and ramping up beam parameters. Time was spent verifying the systems critical for machine protection, such as the Beam Current Monitors (BCMs), the LEBT chopper, timing configuration [5], and machine protection systems [6]. Nevertheless, within the allocated period of five weeks, the beam was successfully accelerated with the RFQ and a stable beam with 6 mA, 50 µs, and 1 Hz was established up to the MEBT Faraday cup (FC), without any accident. The output energy of the RFQ was verified to be 3.6 ± 0.1 MeV with time-of-flight measurements (Fig. 1). In the very end of this first commissioning round some of the Wire Scanners became available for testing and preliminary measurements [7].

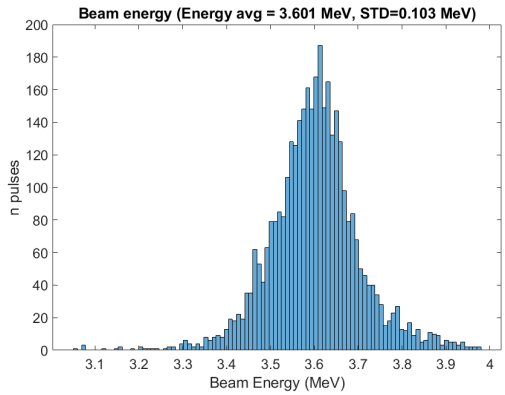


Figure 1: Histogram of the measured RFQ energy with time-of-flight.

In 2022, two additional commissioning periods with approximately nine weeks in total took place (Steps 2B and 2C in Table 1). A stable beam with the nominal 62.5 mA current was established up to the MEBT FC, with an excellent RFQ transmission of ~95%. Testing of the closed-loop operation of the low-level RF (LLRF) of the RFQ also made good progress during these periods, and the RFQ ran with both

Table 1: NC Linac Commissioning Schedule (Two additional periods were allocated for the second step.)

Step	Destination	Start	End
1	Tank after LEBT	2018-09-19	2019-07-03
2A	MEBT	2021-11-10	2021-12-17
2B	MEBT	2022-02-23	2022-03-12
2C	MEBT	2022-04-06	2022-05-23
3	DTL1	2022-05-30	2022-07-13

* natalia.milas@ess.eu

Content from this work may be used under the terms of the CC BY 4.0 licence (© 2022). Any distribution of this work must maintain attribution to the author(s), title of the work, publisher, and DOI

ISBN: 978-3-95450-241-7 ISSN: 2673-5350 doi:10.18429/JACoW-IBIC2022-MO2C2

the feedback and adaptive feed-forward during the following commissioning step (Step 3 in Table 1). During the first period in 2022 (Step 2B in Table 1) a series of measurements with the Wire Scanners was performed and BPMs were tested in the MEBT. The buncher cavities in the MEBT were not available until the second additional period (Step 2C in Table 1). During this period a series of phase scans and cavity tuning studies were carried out first time for the buncher cavities. The emittance measurement units (EMUs) in the MEBT, a pair of slit and grid systems, became available in the last two weeks of the commissioning step for the DTL (Step 3 in Table 1), and a few measurements were made. Unfortunately, the availability of the Wire Scanners during this second period was not stable, and we could not perform new measurements with the design optics fully set nor repeat the Wire Scanners measurements simultaneously with emittance scans.

Transport through the DTL1 was achieved in June 2022 and transport of a beam with the nominal current of 62.5 mA was first attempted on 1st of July, 2022 and established within a few hours.

THE ESS MEBT

The nominal beam parameters of the ESS linac are a peak current of 62.5 mA and pulse length of 2.86 ms at a 14 Hz repetition rate. The MEBT, designed for a beam of 3.62 MeV, is approximately 4 m long and houses a wide range of equipment needed for transverse and longitudinal beam transport and characterization. A set of 11 quadrupoles is used to match the beam in the transverse plane, and three RF buncher cavities are used to counteract debunching and to match the beam in the longitudinal plane to the entrance of the DTL1. A fast chopper, with a rise time of less than 10 ns, is also installed in the MEBT and can be used to clean up the head and tail of the beam pulse. For beam characterization a complete set of diagnostics is foreseen: 3 Wire Scanners, a pair of EMU, 7 Beam Position Monitors (BPMs), a bunch shape monitor (BSM) and a suite of current measurement devices, including one FC and two types of BCMs. Figure 2 is a schematic of the MEBT showing the positions of all diagnostics foreseen for the MEBT.

During the commissioning in 2021 (Step 2A in Table 1), the only diagnostics available in the MEBT throughout commissioning were the BPMs and the beam current monitors (FC and BCMs). The buncher cavities were installed but remained without RF power until the second commissioning period in 2022 (Step 2C in Table 1) [8], during which most of the equipment was running. Currently, the only diagnostics not yet installed in the MEBT is the BSM. The Wire Scanners and the EMUs were available and a more complete characterization of the beam was possible [7].

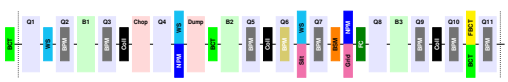


Figure 2: ESS MEBT layout.

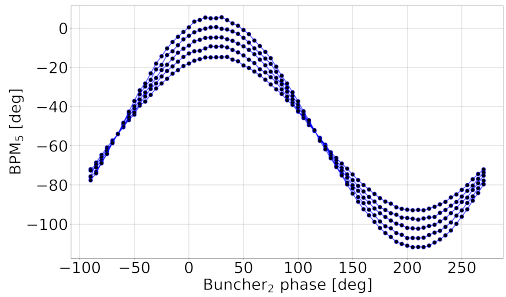


Figure 3: Example of data used for the amplitude calibration of the MEBT bunchers.

MEBT CHARACTERIZATION AND TUNING

Longitudinal Characterization and Tuning

During the commissioning of 2021 (Step 2A in Table 1) a precise measurement of the RFQ output beam energy was performed. Phase signals from two MEBT BPM were compared in the time domain and gave 3.6 ± 0.1 MeV, with meticulous calibration of cable distances and delays performed in advance [4].

All bunchers have pickups that measure the field inside but the values measured by the pickups are often less accurate than those determined by the phase scan. Figure 3 shows an example data of the phase scan of the second buncher. With the knowledge of the energy, it is possible to acquire the ratio $\chi = A_{cav}/A_{beam}$ between the cavity amplitude from the pickup measurement A_{cav} and one from the phase scan A_{beam}, which is a more direct measurement of the field experienced by the proton beam. Table 2 summarizes this calibration factor for all three bunchers. The listed values are results from many phase scans performed over several days, in order to verify stability and repeatability. Details to determine this calibration factor is described in detail in [9].

In addition to the phase and position, the BPMs also provide the amplitude signal. Once the bunchers' settings are known, the amplitude signal can provide information of the longitudinal bunch length through the following expression [10]:

$$u(\omega, \sigma) = Q f(\omega) \exp(-\sigma^2 \omega^2/2) \quad (1)$$

where Q is the bunch charge, the function f is a factor related to the BPM geometry and calibration, ω is the frequency at which the BPMs perform their measurements (in the case of the MEBT BPM, it is 704.42 MHz, twice the RF frequency) and σ is the bunch length at the BPM location. Assuming

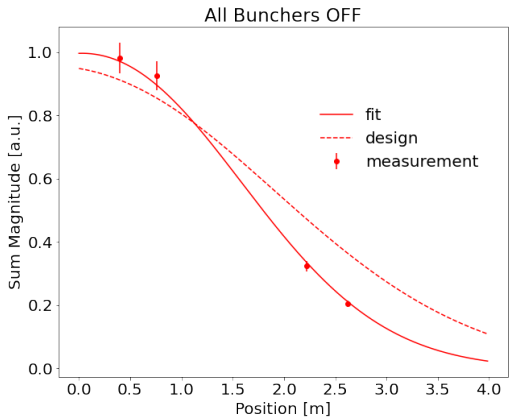
Table 2: MEBT Bunchers Amplitude Calibration Factors

Cavity	χ
Buncher 1	0.96 ± 0.02
Buncher 2	0.98 ± 0.01
Buncher 3	0.89 ± 0.01

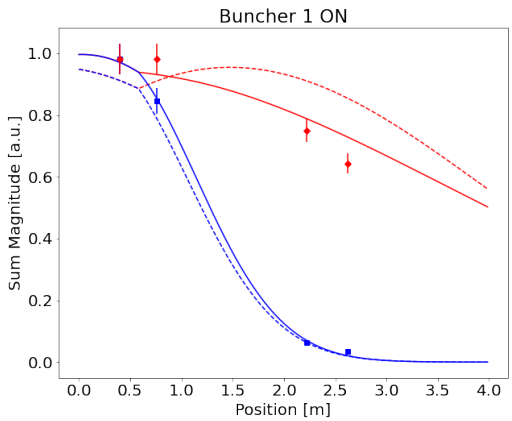
Content from this work may be used under the terms of the CC BY 4.0 licence (© 2022). Any distribution of this work must maintain attribution to the author(s), title of the work, publisher, and DOI

ISBN: 978-3-95450-241-7 ISSN: 2673-5350 doi:10.18429/JACoW-IBIC2022-MO2C2

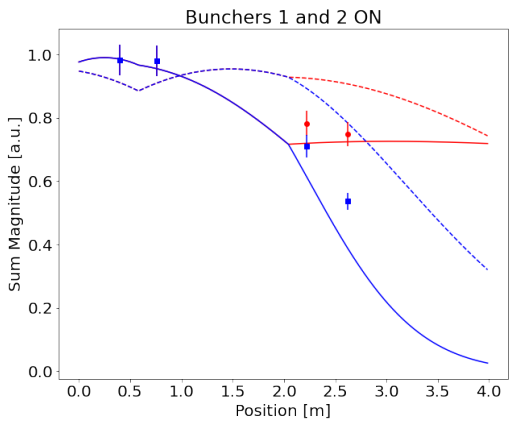
Content from this work may be used under the terms of the CC BY 4.0 licence (© 2022). Any distribution of this work must maintain attribution to the author(s), title of the work, publisher, and DOI



(a) All bunchers detuned and off



(b) Buncher 1 set to bunching (red) and debunching (blue) phases.



(c) Buncher 1 in bunching phase and Buncher 2 in bunching (red) and debunching (blue) phases.

Figure 4: BPMs amplitude signals compared to simulation. The envelope simulations use the twiss parameters listed in Table 3 as input values, full lines are the fitted results and dashed are design.

that all MEBT BPMs have a similar value for the f function, the only dependency on the amplitude signal variation lies on the bunch length.

In order to estimate the input longitudinal Twiss parameters to the MEBT, we measured the sum signals of the first four BPMs when all bunchers are turned off. In this case, the bunch length varies a lot through the MEBT, due to debunching. It was possible to estimate the values of the initial longitudinal Twiss and emittance using the amplitude signal of the first four BPMs (U_{BPM}) and to minimize its simulated value using the calculated bunch length at the BPM position from Eq. (1), according to:

$$S = \sum_{i=1}^{n} [U_{BPM,n} - u(\omega, \sigma_{sim})]^2 \qquad (2)$$

A comparison of the fitted and the design values of the Twiss parameters at the MEBT injection are listed in Table 3. Figure 4(a) shows the measurement data, used for the fitting, and two curves from simulations, where the solid curve uses the Twiss from the fits as input whereas the dashed curve uses the design values as input. Figure 4(b) shows the data and simulations for the case when Buncher 1 was turned on with the design Amplitude value and set to the bunching (red) and debunching (blue) phases. Similarly, in Fig. 4(c), Buncher 1 was on and set to default design values for amplitude and phase, while Buncher 2 was set with the design amplitude and both bunching (red) and debunching (blue) phases. For the simulation curves of Figs. 4(b) and 4(c), the same set of the input Twiss as Fig. 4(a) was used.

Table 3: Longitudinal Parameters at the RFQ-MEBT Interface for a Low Current Beam

Parameter	Design	Fit
$\varepsilon_{N,z}$ (π mm mrad)	0.287	0.18 ± 0.04
α_z	−0.255	0.2 ± 0.4
β_z (m)	0.496	0.2 ± 0.1

Transverse Emittance and Twiss

This section presents a result from 3 Wire Scanner measurements conducting during the commissioning step in 2021 (Step 2A in Table 1) as a part of extensive tests and studies of the Wire Scanners. During this measurement only the first 3 quadrupoles in the MEBT were turned on and none of the bunchers was powered. This special optics was needed to assure that the beam spot on the FC is not damaging the MEBT FC. A set of the 3 profile measurements were taken at 57 mA, close to the MEBT nominal current, and a Gaussian was fitted to each profile. The standard deviation for all profiles measured is plotted in Fig. 5. Using a simple minimizer function and an envelope model, the transverse Twiss parameters at the entrance of the MEBT were calculated and are shown in Table 4. For this fit the longitudinal twiss parameters were frozen to the values already presented in Table 3.

ISBN: 978-3-95450-241-7 ISSN: 2673-5350 doi:10.18429/JACoW-IBIC2022-MO2C2

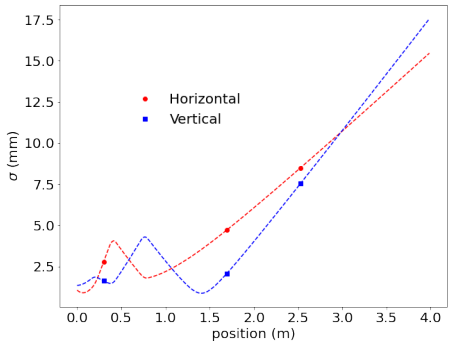


Figure 5: Measurement using all Wire Scanners in the MEBT. Bunchers are not powered and only the first 3 quads are turned on. This was a special optics setup to protect the MEBT FC. The measurements are for a beam current of 57 mA.

Table 4: MEBT Initial Transverse Twiss

Parameters	Design	Fit
$\varepsilon_{N,x}$ (π mm mrad)	0.139	0.53 ± 0.01
α_x	−0.052	0.76 ± 0.02
β_x (m)	0.281	0.26 ± 0.07
$\varepsilon_{N,y}$ (π mm mrad)	0.138	0.3 ± 0.1
α_y	−0.430	−1.0 ± 1.0
β_y (m)	0.498	0.7 ± 0.2

We also performed measurements using the EMU for both planes at the nominal current.The normalized emittance in this case for the vertical and horizontal planes are 0.23 and 0.44 π mm mrad, respectively. The values for the emittance are in agreement with the ones obtained for the Wire Scanner fit.

DISCUSSION AND OUTLOOK

Using different techniques we were able to infer the input Twiss parameters for the MEBT, given the machine configuration we used during Step 2B (see Table 1). For all the planes values were very different than ones expected from the design. For the longitudinal plane the limitation could be shortcoming from the envelope model and the fact that both the BPM sum signal or the model can describe the core of the beam but are not able to define the tails, which can have some influence, specially on the emittance value.

For the transverse plane we encountered an additional issue, during the 2021 commissioning we found out the source repeller was disconnected [4] and thus all emittance measurements from the LEBT performed in 2018-2019 period do not correspond to what we have now. Similarly the source and LEBT configuration established in that commissioning period is not also trustworthy. Unfortunately the LEBT EMUs were not operational during 2021 and 2022 and thus we had no way of optimizing the injection into the RFQ. This could be one of the reasons why the beam Twiss and emittance in the MEBT are so different. In the next commissioning period, in the second quarter of 2023, we expect to be able to re-characterize the LEBT and have a better understanding of the beam that is transported to the MEBT section.

The measurement for the EMU and wire were also never performed for the same beam conditions. The EMU results are very preliminary and require more work on both technical issues, relating to the hardware and motion control, and from the beam physics side, making sure the beam we are sending is stable enough. On particular reason that could explain the high emittances measured, specially in the horizontal plane, is that we observed during the commissioning runs that the beam position throughout the pulse is changing, which can smear the beam in both wires and EMUs measurements and result in bigger emittance values. This effect should be bigger for wires since we use longer pulses, of 20 µs, in comparison to the 5 µs pulse length using for EMU measurements.

CONCLUSION

In 2022 an extensive set of measurements in the MEBT was performed and were combined with results from the 2021 commissioning run in order to get a complete characterization of the MEBT. Estimations of the beam parameter in the RFQ-MEBT interface for all planes were presented and differed substantially from the design values. Some of the differences in the values measured and expected could be due to limitation in the envelope model, other shortcoming could come from assuming Gaussian distributions and not taking into account the beam tails, which can have a big impact on the calculation of the rms values. A new set of measurements and characterization is planned for the next commissioning run when we can perform measurement for transverse and longitudinal in parallel as well and have more control over the beam quality during the measurements, since most of the systems that were in test or commissioning stage in 2022 will be available from the beginning for the next commissioning run.

ACKNOWLEDGEMENT

The authors would like to thank the Operation and Linac teams which were heavily involved in the ESS Linac operation, hardware and beam commissioning for their continuous support and input.

REFERENCES

[1] R. Garoby *et al.*, "The European Spallation Source Design," *Phys. Scr.*, vol. 93, no. 1, p. 014 001, 2017. doi:10.1088/1402-4896/aa9bff

[2] R. Miyamoto, M. Eshraqi, and M. Munoz, "ESS Linac Plans for Commissioning and Initial Operations," in *Proc. HB'16*, Malmö, Sweden, Jul. 2016, pp. 342–347. doi:10.18429/JACoW-HB2016-TUPM5Y01

Content from this work may be used under the terms of the CC BY 4.0 licence (© 2022). Any distribution of this work must maintain attribution to the author(s), title of the work, publisher, and DOI

ISBN: 978-3-95450-241-7 ISSN: 2673-5350 doi:10.18429/JACoW-IBIC2022-MO2C2

[3] D. C. Plostinar *et al.*, "Status of the Normal Conducting Linac at the European Spallation Source," in *Proc. IPAC'22*, Bangkok, Thailand, 2022, pp. 2019–2022. doi:10.18429/JACoW-IPAC2022-WEPOTK001

[4] R. Miyamoto *et al.*, "Beam Commissioning of Normal Conducting Part and Status of ESS Project," presented at LINAC'22, Liverpool, UK, Aug.-Sep. 2022, paper MO1PA02, to be published.

[5] N. Milas, A. A. Gorzawski, and J. J. Jamroz, "Commissioning of the Timing System at ESS," presented at IBIC'22, Krakow, Poland, Sep. 2022, paper TUP23, this conference.

[6] S. Gabourin, M. Carroll, S. K. de Carvalho, A. Nordt, S. Pavinato, and K. Rosquist, "The ESS Fast Beam Interlock System: First Experience of Operating With Proton Beam," presented at LINAC'22, Liverpool, UK, Aug.-Sep. 2022, paper MOPORI17, to be published.

[7] C. S. Derrez *et al.*, "Wire Scanner Systems at the European Spallation Source (ESS): Tests and First Beam Commissioning Results," presented at LINAC'22, Liverpool, UK, Aug.-Sep. 2022, paper TUPOJO13, to be published.

[8] R. Zeng *et al.*, "RFQ Performance During RF Conditioning and Beam Commissioning at ESS," presented at LINAC'22, Liverpool, UK, Aug.-Sep. 2022, paper TUPOPA05, to be published.

[9] Y. Levinsen *et al.*, "First RF Phase Scans in the European Spallation Source," presented at IBIC'22, Krakow, Poland, Sep. 2022, paper TUP35, this conference.

[10] A. Shishlo and A. Aleksandrov, "Noninterceptive method to measure longitudinal Twiss parameters of a beam in a hadron linear accelerator using beam position monitors," *Phys. Rev. ST Accel. Beams*, vol. 16, p. 062 801, 2013. doi:10.1103/PhysRevSTAB.16.062801

Content from this work may be used under the terms of the CC BY 4.0 licence (© 2022). Any distribution of this work must maintain attribution to the author(s), title of the work, publisher, and DOI

ISBN: 978-3-95450-241-7 ISSN: 2673-5350 doi:10.18429/JACoW-IBIC2022-MO2I4

STATISTICAL PROPERTIES OF UNDULATOR RADIATION*

I. Lobach†, Argonne National Laboratory, Lemont, IL, USA
S. Nagaitsev[1], A. Romanov, A. Shemyakin, G. Stancari, Fermilab, Batavia, IL, USA
[1]also at The University of Chicago, Chicago, IL, USA

Abstract

Two experiments were carried out to study the statistical properties of undulator radiation in the Integrable Optics Test Accelerator (IOTA) storage ring at Fermilab. The first experiment studied the turn-to-turn fluctuations in the power of the radiation generated by an electron bunch. The magnitude of these fluctuations depends on the 6D phase-space distribution of the electron bunch. In IOTA, we demonstrated that this effect can be used to measure some electron bunch parameters, small transverse emittances in particular. In the second experiment, a single electron was stored in the ring, emitting a photon only once per several hundred turns. In this regime, any classical interference-related collective effects were eliminated, and the quantum fluctuations could be studied in detail to search for possible deviations from the expected Poissonian photon statistics. In addition, the photocount arrival times were used to track the longitudinal motion of a single electron and to compare it with simulations. This allowed us to determine several dynamical parameters of the storage ring such as the rf cavity phase jitter and the dependence of the synchrotron motion period on amplitude.

INTRODUCTION

In our previous experiments [1–4] with an electron bunch we showed that turn-to-turn fluctuations $\mathrm{var}(\mathcal{N})$ of the number of detected undulator radiation photons per turn $\mathcal{N}$ have two contributions: (1) a Poissonian contribution equal to $\langle\mathcal{N}\rangle$, due to the discrete quantum nature of light, and (2) a collective contribution $\propto \langle\mathcal{N}\rangle^2$, related to the interference between the fields generated by the electrons in the bunch. In this paper, we get rid of the collective contribution by considering a single electron circulating in the Integrable Optics Test Accelerator (IOTA) storage ring at Fermilab in order to thoroughly study the quantum fluctuations and verify that they follow the Poissonian photostatistics $\mathrm{var}(\mathcal{N}) = \langle\mathcal{N}\rangle$, predicted by [5–8]. This research is motivated by the surprising observation of sub-Poissonian photostatistics ($\mathrm{var}(\mathcal{N}) < \langle\mathcal{N}\rangle$) in synchrotron radiation reported in Ref. [9] in a similar experiment setting. In addition, we will use the recorded detection times to study the synchrotron motion of a single electron in IOTA [10], similar to previous experiments in Novosibirsk [11, 12].

* The work is supported by the U.S. Department of Energy, Office of Science, Office of Basic Energy Sciences, under Contract No. DE-AC02-06CH11357.
† ilobach@anl.gov

APPARATUS

In our experiment, a single electron circulated in IOTA with a revolution period of 133 ns and an energy of 96.4 MeV. The undulator parameter is $K_\mathrm{u} = 1.0$ with the number of periods $N_\mathrm{u} = 10.5$ and the period length $\lambda_\mathrm{u} = 5.5$ cm. The wavelength of the fundamental was $\lambda_1 = \lambda_\mathrm{u}(1 + K_\mathrm{u}^2/2)/(2\gamma^2) = 1.16\,\mu$m, where $\gamma = 188.6$ is the Lorentz factor. The second harmonic was in the visible wavelength range. We used a Single Photon Avalanche Diode (SPAD) [13] as a detector, which was mostly sensitive to the visible light with detection efficiency of up to 65%. Two edge-pass filters were used to only collect the radiation between 550 nm and 800 nm. The radiation was focused on the sensitive area of the detector ($\varnothing 180\,\mu$m) by a single focusing lens with a focal distance of 180 mm, see Figs. 1(a),(b). The radiation was collected in a large angle $> 1/\gamma$. The SPAD detector produced a 10-ns-long TTL pulse at each detection event. Its dead time (20 ns) was shorter than the IOTA revolution period (133 ns). Our data acquisition system [Fig. 1(c)] allowed us to record the revolution number and the arrival time relative to the IOTA revolution marker for each detection event for as long as 1 minute at a time.

PHOTOSTATISTICS MEASUREMENTS

In the optimal focusing, the measured photocount rate was 24.7 kHz, or one photocount per 304 revolutions in IOTA (on average). The dark count rate of the SPAD detector was 108 Hz. In addition, we used a 5-ns-long gate around the expected detection arrival time, which allowed us to reduce the effective dark count rate to 4.0 Hz.

Before any analysis of the photostatistics, it was important to realize that the SPAD detector is binary. It produces the same type of pulses (TTL, 10-ns-long) no matter how many photons are detected per one pass. The collected turn-by-turn data can be represented as a sequence of zeros and ones only. Therefore, we had to alter our original expectation of Poissonian photostatistics to a sequence of Bernoulli trials, i.e., there is a probability p of a detection at every revolution, and a probability $(1 - p)$ of no detection. In our case, $p = (3.29 \pm 0.02) \times 10^{-3}$. Figure 2 illustrates the comparison between the expectation (for a sequence of Bernoulli trials) and the measurement for (a) the distribution of interarrival times and for (b) the distribution of the number of photocounts in a certain time window. In both cases, the χ^2 goodness-of-fit test [14, p. 637] results in a P-value [14, p. 140] above the conventional 0.05 threshold. This means that the null hypothesis (exponential or binomial distribution, respectively) cannot be rejected.

Content from this work may be used under the terms of the CC BY 4.0 licence (© 2022). Any distribution of this work must maintain attribution to the author(s), title of the work, publisher, and DOI

ISBN: 978-3-95450-241-7 ISSN: 2673-5350 doi:10.18429/JACoW-IBIC2022-MO2I4

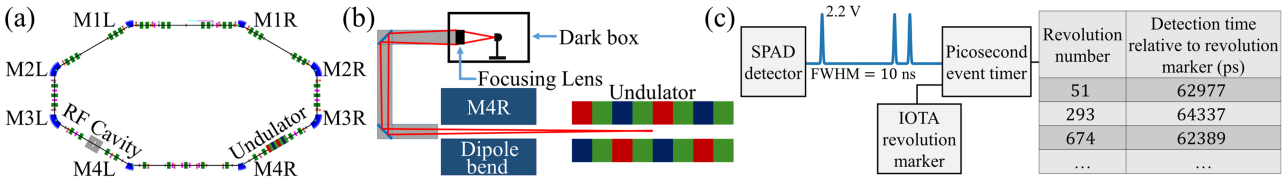


Figure 1: (a) Layout of IOTA, electrons circulate clockwise. (b) Light path from the undulator to the detector (not to scale). (c) Block diagram of the data acquisition system.

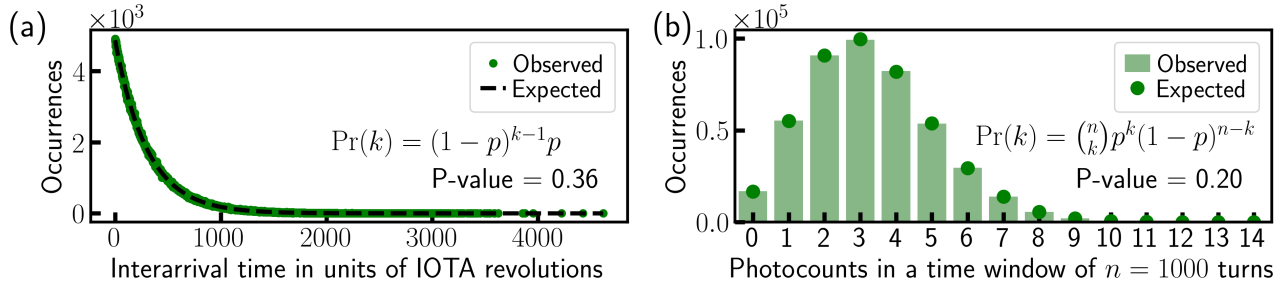


Figure 2: (a) The measured distribution of interarrival times between the photocounts and a fit by a geometric distribution. (b) The measured distribution of the number of photocounts in a time window equal to $n = 1000$ IOTA revolutions and a fit by a binomial distribution.

Some measurements were carried out with an upgraded setup consisting of two SPAD detectors separated by a beam splitter [15]. In this case, the photon number resolution was improved, since there were three possible outcomes for each pass: 0, 1, or 2 detection events. Still, so far we have not observed anything unusual. There was no statistically significant correlation or anticorrelation in the two detectors.

SYNCHROTRON MOTION STUDIES

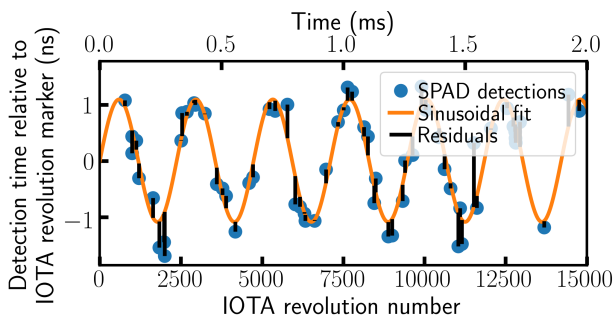


Figure 3: Illustration of the fitting procedure for determination of the synchrotron motion period and amplitude.

Figure 3 illustrates the detection time relative to the IOTA revolution marker as a function of the IOTA revolution number. The observed sinusoidal motion is, in fact, the synchrotron motion of a single electron. The deviations from the sinusoidal fit are due to the time resolution of the SPAD detector (about 0.4 ns rms). On a larger time scale, the amplitude of the synchrotron motion grows and decreases randomly due to the quantum excitation and radiation damping.

We decided to compare the measured arrival times with a simulation of the synchrotron motion. In our simulation [16] we use the following transformation of the relative energy deviation δ_i and the rf phase ϕ_i of a single electron from turn i to turn $i+1$,

$$\delta_{i+1} = \delta_i + \frac{eV_0}{E_0}(\sin\phi_i - \sin\phi_s) - \frac{\langle U\rangle \mathcal{J}_E}{E_0}\delta_i - \frac{U_i - \langle U\rangle}{\beta^2 E_0}, \quad (1)$$

$$\phi_{i+1} = \phi_i - 2\pi q \eta_s \delta_{i+1} + \xi_i, \quad (2)$$

where e is the electron charge, $E_0 = \gamma m_e c^2 = 96.4\,\mathrm{MeV}$, m_e is the electron mass, c is the speed of light, $\beta = \sqrt{1-1/\gamma^2}$ is the relativistic velocity parameter, $V_0 = 380\,\mathrm{V}$ is the rf voltage amplitude, $q = 4$ is the rf harmonic number, $\eta_s = \alpha_c - 1/\gamma^2 = 0.070\,83$ is the phase slip factor (variation of η due to variation of γ is negligible), $\alpha_c = 0.070\,86$ is the momentum compaction factor, $\mathcal{J}_E = 2.64$ is the longitudinal damping partition number [17, p. 445], U_i is the radiation energy loss at ith turn, ξ_i is the rf cavity phase jitter at the ith turn. We model ξ_i as a random variable following a normal distribution with a standard deviation σ_ξ. We refer the reader to [17, Eq. (3.28)] for the symplectic part of the transformation. The derivation of the synchrotron damping term, $-\langle U\rangle \mathcal{J}_E \delta_i / E_0$, is described in [17, pp. 438–445]. The quantum excitation term, $-(U_i - \langle U\rangle)/(\beta^2 E_0)$, is considered in [18]. The energy kick at the synchronous phase ϕ_s compensates for the average energy loss due to the synchrotron radiation, i.e., $eV_0 \sin\phi_s = \langle U\rangle$. The average emitted energy per turn in an isomagnetic ring is [17, pp. 434–435] $\langle U\rangle = 8\pi\alpha\gamma u_c/9 = 10.9\,\mathrm{eV}$, where α is the fine-structure constant, $u_c = 3\hbar c\gamma^3/(2\rho) = 2.8\,\mathrm{eV}$ is the critical energy [18, Eq. (11)], $\rho = 70\,\mathrm{cm}$ is the electron trajectory radius in the dipole magnets, $\hbar$ is the reduced Plank constant. The isomagnetic ring approximation works well in IOTA, the radiation in the undulator is negligible

Content from this work may be used under the terms of the CC BY 4.0 licence (© 2022). Any distribution of this work must maintain attribution to the author(s), title of the work, publisher, and DOI

ISBN: 978-3-95450-241-7 ISSN: 2673-5350 doi:10.18429/JACoW-IBIC2022-MO2I4

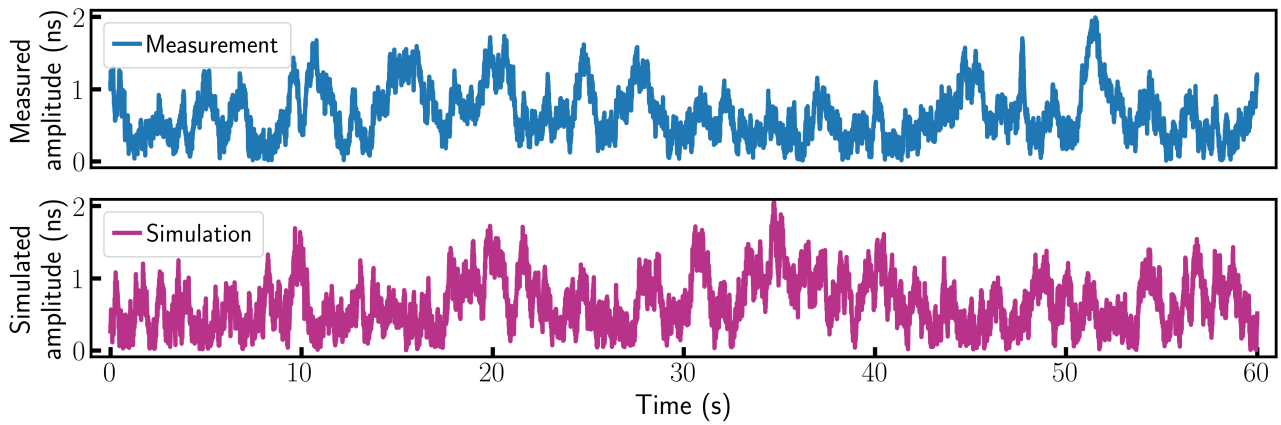


Figure 4: Amplitude of the synchrotron motion of a single electron as a function of time. In the simulation, the rms rf phase jitter is $\sigma_\xi = 6.0 \times 10^{-5}$ rad.

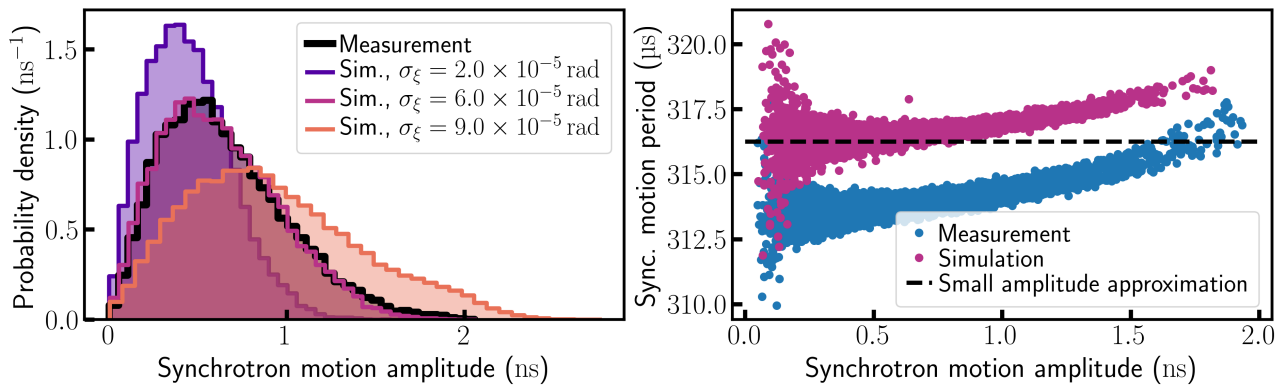


Figure 5: Panel (a) shows the comparison of the measured and simulated distributions of the synchrotron motion amplitude. The best agreement is achieved at the rms rf phase jitter $\sigma_\xi = 6.0 \times 10^{-5}$ rad. Panel (b) shows the synchrotron motion period as a function of the synchrotron motion amplitude.

compared to the bending magnets. The average number of photons emitted per turn in an isomagnetic ring is [18] $\langle \mathcal{N} \rangle = 5\pi\alpha\gamma/\sqrt{3} = 12.5$. To simulate the number of emitted photons at ith revolution, we use a Poisson random number generator with the expectation value $\langle \mathcal{N} \rangle = 12.5$. To simulate the energies of these photons, we use the Monte Carlo generator described in Ref. [18]. The sum of these energies gives U_i.

Using our computer code we can generate the data points as in Fig. 3 for a long interval of time, e.g., 1 minute. By fitting the data with short pieces of sinusoidal curves (as in Fig. 3) one can plot the synchrotron motion amplitude as a function of time, see Fig. 4. We cannot compare the measurement and the simulation in this way directly, because it is a stochastic process. However, we can compare the distributions of the synchrotron motion amplitudes. Figure 5(a) illustrates such a comparison, where the simulation results are presented at three different values of the rms rf phase jitter σ_ξ. We can conclude that in IOTA $\sigma_\xi \approx 6.0 \times 10^{-5}$ rad. We considered more values of σ_ξ than illustrated in Fig. 5(a). Further, using the same piecewise sinusoidal fit we can plot the synchrotron motion period as a function of the synchrotron motion amplitude, see Fig. 5(b). Every point in Fig. 5(b) is calculated from a 25-ms-long interval of time. The measured and the simulated synchrotron motion periods agree rather well, which shows that we understand the parameters of the IOTA ring well.

CONCLUSION

To conclude, in our experiment with a single electron and a binary photon detector, we have not yet observed any deviations of the undulator radiation photostatistics from a memoryless Bernoulli process. Our measurements with two SPAD detectors did not reveal any correlation or anticorrelation in the detected photon pairs. Currently, the next phase of experiments is under preparation, namely, the Mach-Zehnder interferometry of undulator radiation [15]. The detection arrival times can be used to study the synchrotron motion of a single electron and to infer some dynamical parameters of the storage ring, such as the rms rf cavity phase jitter and the synchrotron motion period as a function of amplitude. This diagnostics of the longitudinal motion can complement the diagnostics of the transverse motion [19, 20] and facilitate a complete 3D tracking of a single electron in a ring.

Content from this work may be used under the terms of the CC BY 4.0 licence (© 2022). Any distribution of this work must maintain attribution to the author(s), title of the work, publisher, and DOI

ISBN: 978-3-95450-241-7 ISSN: 2673-5350 doi:10.18429/JACoW-IBIC2022-MO2I4

Content from this work may be used under the terms of the CC BY 4.0 licence (© 2022). Any distribution of this work must maintain attribution to the author(s), title of the work, publisher, and DOI

REFERENCES

[1] I. Lobach *et al.*, "Transverse beam emittance measurement by undulator radiation power noise," *Phys. Rev. Lett.*, vol. 126, p. 134 802, 2021. doi:10.1103/PhysRevLett.126.134802

[2] I. Lobach *et al.*, "Measurements of undulator radiation power noise and comparison with ab initio calculations," *Phys. Rev. Accel. Beams*, vol. 24, p. 040 701, 2021. doi:10.1103/PhysRevAccelBeams.24.040701

[3] I. Lobach *et al.*, "Statistical properties of spontaneous synchrotron radiation with arbitrary degree of coherence," *Phys. Rev. Accel. Beams*, vol. 23, p. 090 703, 2020. doi:10.1103/PhysRevAccelBeams.23.090703

[4] I. Lobach *et al.*, "Transverse Beam Emittance Measurement by Undulator Radiation Power Noise," in *Proc. IBIC'21*, Pohang, Rep. of Korea, 2021, paper TUOA03, pp. 167–167. doi:10.18429/JACoW-IBIC2021-TUOA03

[5] R. J. Glauber, "Some notes on multiple-boson processes," *Phys. Rev.*, vol. 84, no. 3, p. 395, 1951. doi:10.1103/PhysRev.84.395

[6] R. J. Glauber, "Coherent and incoherent states of the radiation field," *Phys. Rev.*, vol. 131, no. 6, p. 2766, 1963. doi:10.1103/PhysRev.131.2766

[7] R. J. Glauber, "The quantum theory of optical coherence," *Phys. Rev.*, vol. 130, no. 6, p. 2529, 1963. doi:10.1103/PhysRev.130.2529

[8] J.-W. Park, "An investigation of possible non-standard photon statistics in a free-electron laser," Ph.D. dissertation, University of Hawaii at Manoa, 2019. http://hdl.handle.net/10125/66233

[9] T. Chen and J. M. Madey, "Observation of sub-Poisson fluctuations in the intensity of the seventh coherent spontaneous harmonic emitted by a RF linac free-electron laser," *Phys. Rev. Lett.*, vol. 86, no. 26, p. 5906, 2001. doi:10.1103/PhysRevLett.86.5906

[10] I. Lobach, S. Nagaitsev, A. Romanov, and G. Stancari, "Single electron in a storage ring: A probe into the fundamental properties of synchrotron radiation and a powerful diagnostic tool," *J.Instrum.*, vol. 17, no. 02, P02014, 2022. doi:10.1088/1748-0221/17/02/p02014

[11] A. Aleshaev *et al.*, "A study of the influence of synchrotron radiation quantum fluctuations on the synchrotron oscillations of a single electron using undulator radiation," *Nucl. Instrum. Methods Phys. Res., Sect. A*, vol. 359, no. 1, pp. 80–84, 1995. doi:10.1016/0168-9002(96)88028-4

[12] I. Pinayev, V. Popik, T. Shaftan, A. Sokolov, N. Vinokurov, and P. Vorobyov, "Experiments with undulator radiation of a single electron," *Nucl. Instrum. Methods Phys. Res., Sect. A*, vol. 341, no. 1, pp. 17–20, 1994. doi:10.1016/0168-9002(94)90308-5

[13] *SPCM-AQRH Single-Photon Counting Module*, https://www.excelitas.com/product/spcm-aqrh, Accessed: 2021-5-4.

[14] R. Freund, W. Wilson, and D. Mohr, *Statistical Methods*. Burlington, MA, USA: Academic Press, 2010.

[15] I. Lobach, "Statistical properties of undulator radiation: Classical and quantum effects," Ph.D. dissertation, The University of Chicago, 2021. https://inspirehep.net/literature/1949955

[16] I. Lobach, *The source code for simulation of the longitudinal motion of a single electron in a storage ring*, https://github.com/IharLobach/ursse.

[17] S.-Y. Lee, *Accelerator physics*. World Scientific Publishing, 2018.

[18] H. Burkhardt, *Monte Carlo generation of the energy spectrum of synchrotron radiation*, http://cds.cern.ch/record/1038899/files/open-2007-018.pdf.

[19] A. Romanov, J. Santucci, G. Stancari, A. Valishev, and N. Kuklev, "Experimental 3-dimensional tracking of the dynamics of a single electron in the fermilab integrable optics test accelerator (IOTA)," *J. Instrum.*, vol. 16, no. 12, P12009, 2021. doi:10.1088/1748-0221/16/12/p12009

[20] A. Romanov *et al.*, "3D Tracking of a Single Electron in IOTA," in *Proc. IPAC'21*, Campinas, SP, Brazil, 2021, paper THXB01, pp. 3708–3713. doi:10.18429/JACoW-IPAC2021-THXB01

ISBN: 978-3-95450-241-7 ISSN: 2673-5350 doi:10.18429/JACoW-IBIC2022-MOP01

SLS 2.0 – STATUS OF THE DIAGNOSTICS

C. Ozkan Loch†, A. Bonnin, J. Vila-Comamala, N. Samadi, A. M. M. Stampfli, R. Ischebeck
Paul Scherrer Institut (PSI), Villigen PSI, Switzerland

Abstract

In this contribution we give an overview of the diagnostics development for SLS 2.0, focusing on the beam size monitors in the storage ring, the screen monitors for the booster-to-ring transfer line, and beam loss monitors for the storage ring. Test results carried out at the SLS will also be presented. Diagnostics that will only receive a DAQ system upgrade will not be discussed here.

INTRODUCTION

The Swiss Light Source (SLS) synchrotron storage ring will be upgraded to a new diffraction-limited lattice [1], and its booster-to-ring transfer line (BRTL) will also be improved accordingly [2]. The current monitor for the storage ring and charge monitor in the BRTL will be re-used with new DAQ systems but same functionalities [2]. Hence, these systems will not be discussed here.

Up until recently, in the SLS there were beam loss monitors only at the exit of insertion devices. The distributed loss monitor system based on a CMOS camera readout [3] was developed for locating losses around the storage ring. The first prototype monitor was used to locate losses due to a beam dump, to survey possible losses in the first three arcs, and look for changes with respect to undulator gap changes. As a result, the loss detection scintillators were improved. An update on the status of these loss monitors will be discussed later in this proceeding.

Beam size monitoring at the SLS depends on the π-polarization [4] technique, using the visible light at 364 nm from a bend magnet. However, this technique only provides the vertical source size. In order to measure both dimensions of the small source size at SLS 2.0 (< 8 μm), X ray imaging optics based on zone plates will be used. This monitor is based on [5, 6]. The source size will also be monitored in two locations in order to determine the energy spread of the storage ring.

The present screen monitors in the BRTL use a 200 μm Ce:YAG scintillator at 45° angle to visualize the beam. The optical resolution is 30 μm. One of the screen monitors was modified to house a 100 μm Ce:YAG scintillator normal to the beam with a mirror at 45° angle to couple out the scintillation light. The imaging camera and objective were changed and a spatial resolution of 19 μm was achieved. This will be further improved for the new BRTL. The requirements and details are discussed in the next section.

SCREEN MONITORS

The booster-to-ring transfer line (BRTL) will provide nominal injection into the SLS 2.0 storage ring. It also allows performing beam parameter measurements during set up and commissioning. The purpose of the BRTL screen monitors is to determine the beam profiles, transverse emittance and energy spread. The BRTL optics design and layout with the location of all diagnostics components can be found in the SLS 2.0 technical design report [2].

Apart from beam profile measurements in the nominal BTR injection mode, the first BRTL screen will be used for emittance measurements by scanning the upstream quadrupoles, and the second screen will be used for determination of the energy spread. The last screen will be used for the adjustment of the transverse beam size (matching) at the "thick" storage ring injection septum.

Table 1: Screen Monitor Requirements Based on Expected Smallest Beam Size, Required Resolution and Field of View

	Emittance	Energy spread	Thick septum
Beam size	<20 μm	700 μm	<20 μm
Screen resolution	<10 μm	10 μm for precision of 3%	10 μm
FOV dia.	20 mm	20 mm	20 mm

A scintillator crystal (Ce:YAG) will be inserted in the electron beam path by means of linear UHV-feedthroughs and pneumatic controls. To view the entire range of beam motion, the scintillator screen will be normal to the beam with a mirror at 45° angle behind it to couple out the scintillation light (Fig. 1a).

An OTR screen will also be installed at 45° angle with respect to the beam and the camera will be mounted in the Scheimpflug [7, 8] geometry to correct the focal plane. To measure the emittance an iris and focus control of the camera objective is necessary. In order to facilitate simple switching between Ce:YAG and OTR measurements, an optical setup per screen will be installed at the emittance measuring screen monitor (Fig. 1b).

DISTRIBUTED BEAM LOSS MONITOR

It was initially planned to use beam loss detectors based on organic fiber scintillators in the storage ring and BRTL to locate losses and monitor the loss pattern during injection (storage ring filling and top-up operation). Similar to the SwissFEL [9], 2-meter long fiber scintillators were coupled to plastic optical fibers (POF) that guide the scintillator light to the detection system. A CMOS camera was used to image the light from 28 fibers simultaneously.

A system was built and tested at SLS. Injection losses were detected during top-up. The location of the fiber scintillator that gives the highest signals during beam dump supports the radiation measurement results concerning the

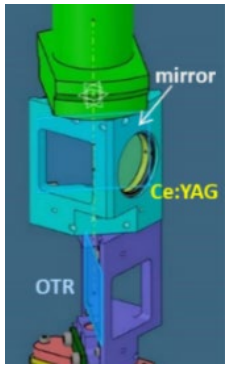
† cigdem.ozkan@psi.ch

Content from this work may be used under the terms of the CC BY 4.0 licence (© 2022). Any distribution of this work must maintain attribution to the author(s), title of the work, publisher, and DOI

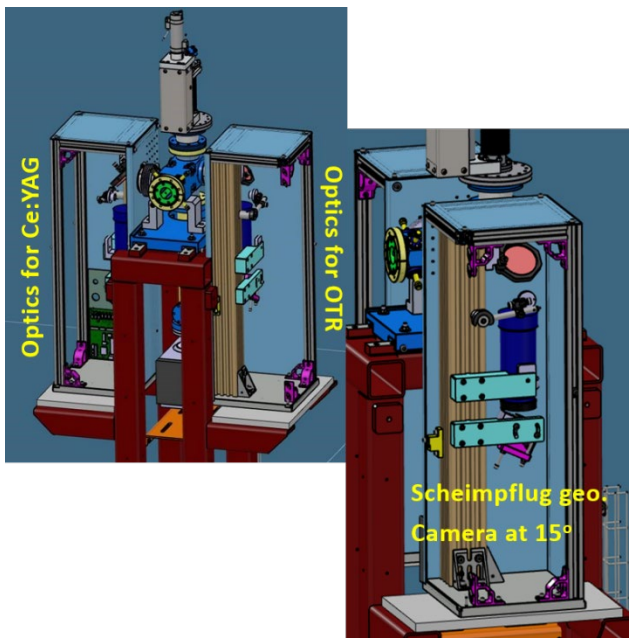
ISBN: 978-3-95450-241-7 ISSN: 2673-5350 doi:10.18429/JACoW-IBIC2022-MOP01

Content from this work may be used under the terms of the CC BY 4.0 licence (© 2022). Any distribution of this work must maintain attribution to the author(s), title of the work, publisher, and DOI

radiation hotspot. Details of the system and the test results can be found in [3].



(a)



(b)

Figure 1: (a) 3D drawing of the screen holder. The top holder is for the scintillator and mirror, and the second holder is for the OTR screen. (b) Two optical setups are used for the emittance measurement screen: one for imaging the scintillator and the second for the OTR screen. The second is in the Scheimpflug condition.

To test the system sensitivity, we also placed a fiber scintillator at the exit of an undulator and scanned the gap. Although the behaviour matched to an existing loss monitor at the location, the signal difference from one gap setting to the next was too small compared to the existing loss monitor (Fig. 2).

For this reason, a new type of scintillator was used. A plate of EJ-204 [10] was used as the scintillator and the emitted blue light was shifted to green using a wavelength shifting fiber, BCF-92 [11]. An image of this plate scintillator assembly can be found in Fig. 3

For comparison purposes, both scintillators were placed at the same location, at the end of the injection straight. The current of the injection septum was varied to create losses. One POF per scintillator was used to guide the scintillation light from the tunnel to the CMOS camera outside. To account for the difference between the POF fibers, their transmission was measured using an LED and the CMOS camera, and normalized to each other. The behaviour of the two scintillators with varying losses are plotted in Fig. 4. Brightness is the sum of the pixel values in the fiber areas as seen by the camera.



Figure 2: Loss versus Undulator gap setting. Orange is the fiber scintillator readout with the CMOS camera, red is the existing loss monitor, green is the gap reading and blue is the lifetime.



Figure 3: Plate scintillator assembley based on the EJ-204 scintillator and the BCF-92 wavelength shifting fiber, wrapped in foil.

For comparison purposes, both scintillators were placed at the same location, at the end of the injection straight. The current of the injection septum was varied to create losses. One POF per scintillator was used to guide the scintillation light from the tunnel to the CMOS camera outside. To account for the difference between the POF fibers, their transmission was measured using an LED and the CMOS camera, and normalized to each other. The behaviour of the two scintillators with varying losses are plotted in Fig. 4. Brightness is the sum of the pixel values in the fiber areas as seen by the camera.

The new scintillator output is four to five times larger than that of the fiber scintillator. After this measurement, only the new plate scintillators were installed at SLS.

BEAM SIZE MONITOR

Similar to the SLS, the storage ring emittances will be derived from measured source sizes using synchrotron radiation from a bend magnet. However, at SLS 2.0, extrac-

ISBN: 978-3-95450-241-7 ISSN: 2673-5350 doi:10.18429/JACoW-IBIC2022-MOP01

tion of visible light is restricted by the mechanical constraints from the neighbouring magnets. Light coupled out from a narrow opening angle requires the use of X-rays.

A vertical emittance of 10 pm and a horizontal emittance of 158 pm are expected for 6.3% emittance coupling. The optimal, dispersion-dominated, source size is 8.6 µm x 6.8 µm.

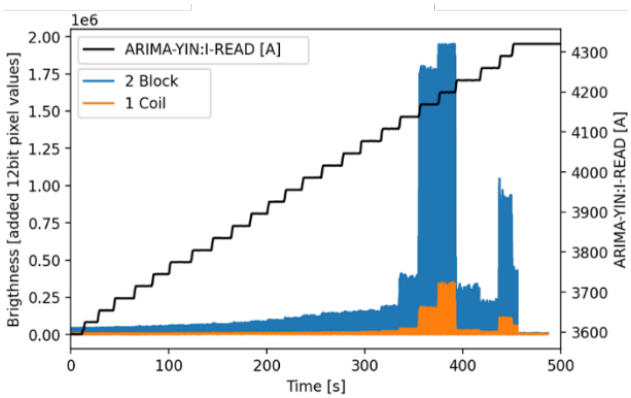


Figure 4: Comparison between the fiber and new scintillators. Orange indicates the behavior of the plastic scintillating fiber, blue indicates the behavior of the plate scintillator, with changing injector magnet current.

tion of visible light is restricted by the mechanical constraints from the neighbouring magnets. Light coupled out from a narrow opening angle requires the use of X-rays.

A vertical emittance of 10 pm and a horizontal emittance of 158 pm are expected for 6.3% emittance coupling. The optimal, dispersion-dominated, source size is 8.6 µm × 6.8 µm.

During machine commissioning, with specified misalignments, a coupling of only 1-2% is expected, which translates to emittance 2-3 pm. With nominal horizontal emittance at full current and open IDs, the vertical emittance will be adjusted to 10 pm to provide sufficient beam lifetime. The range of interest of the vertical emittance to be measured during nominal operation is 8-12 pm. Based on these numbers and the resolution needed to measure an emittance change of 1 pm vertically corresponds to a beam size change of ~400 nm. X-ray optics imaging setup based on Fresnel Zone Plates (FZP) will be used. FZPs allow imaging the beam in 2D and thus, provide size and tilt information simultaneously.

FZPs in transmission geometry are preferred due to their diffraction efficiency reducing photon beam flux and lateral space limitations inside the storage ring tunnel. The first possibility is to use a single zone plate to image the source in the dipole.

We also explore the possibility of using a transmission X-ray microscope (TXM) using two FZPs to shape the image using a condenser zone plate (CZP) [12] and a magnifying zone plate (MZP). This would relax the resolution requirements on the detector. A sketch of the two setups is shown in Fig. 5.

The source size was measured at the TOMCAT beamline at the SLS, with monochromator set to 11.5 keV. The focus of the single zone plate setup was found by varying detector to CZP distance. A plot of the source size with respect to detector location is given in Fig. 6. For the detector, a 5 µm thick LSO:Tb scintillator with 20x microscope objective and a pco.edge camera (pixel size: 6.5 µm) was used. The primary beam was suppressed by placing a central stop (CS) in front of the CZP. The minimum vertical source size was measured as 18.3 µm (rms) and at that detector location the horizontal source size is 78.7 µm (rms).

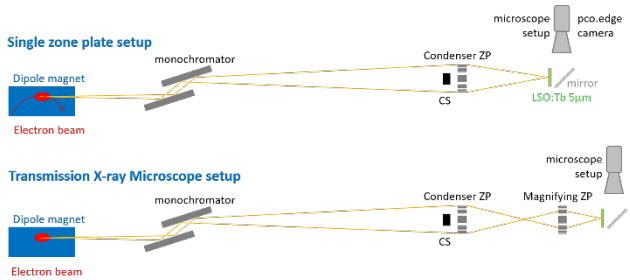


Figure 5: Sketch of the single zone plate setup (top) and the X-ray transmission microscope setup (bottom).

The vertical beam size depends on the day's machine settings and is reasonable. The horizontal beam size is a robust value. It is influenced by the beta beat. Assuming a large beta beat of 10% the variations in source size are ~3% due to this beat. The design beam in the center of the TOMCAT superbend is 55.9 µm (rms) [13].

The minimum horizontal image size could not be achieved since the horizontal and vertical foci are at different detector locations. It is suspected that the thermal bump on the first crystal of the monochromator has a lensing effect on the monochromator and the measured beam size. An excellent explanation of this effect can be found in [14].

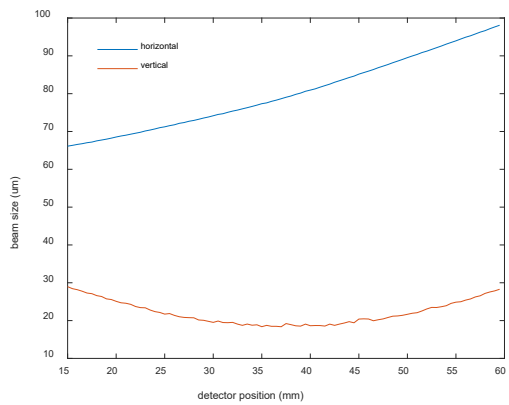


Figure 6: Vertical (red) and horizontal (blue) beam sizes, measured with single zone plate, with respect to detector position. The horizontal focus is at a different location from the vertical focus.

At TOMCAT, with the TXM setup, we achieved a total magnification of 1.01 and measured a vertical beam size of 17.3 µm (rms). In comparison to the single zone plate measurement, this is not surprising since the spot size on the scintillator due to the CZP is expected to be < 4 µm (rms), which is smaller than the scintillator thickness. At 11.5 keV, additional scintillation from the thickness will

Content from this work may be used under the terms of the CC BY 4.0 licence (© 2022). Any distribution of this work must maintain attribution to the author(s), title of the work, publisher, and DOI

ISBN: 978-3-95450-241-7 ISSN: 2673-5350 doi:10.18429/JACoW-IBIC2022-MOP01

Content from this work may be used under the terms of the CC BY 4.0 licence (© 2022). Any distribution of this work must maintain attribution to the author(s), title of the work, publisher, and DOI

blur the image. Figure 7 shows an image of the beam spot with the detector at the vertical focus of the MZP. Unfortunately, the horizontal focus location was out of the detector's range of motion.

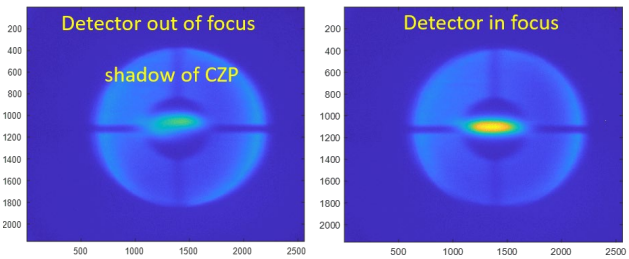


Figure 7: Image of beam focused on the detector with TXM. The vertical source size was measured as 17.3 µm rms. Horizontal minimum is out of the detector's motion range.

In the future, a larger central stop will be used so that the image of the source is completely inside the dark region of the shadow of the central stop, thus avoiding overlap with the direct X-ray beam.

CONCLUSION

For SLS 2.0, new FZP parameters will be calculated to fit the available space, photon beam wavelength, expected photon beam size at FZP location, and desired total magnification. It is also planned to use a filter before the monochromator to reduce the heat load on the monochromator crystal and consequently, the lensing effect of the thermal bump.

The new plate scintillators for the distributed loss monitors seem to be very promising. There are now 35 scintillators distributed around the storage ring for the surveillance of losses and one at the injection straight. A total of 4 loss monitor systems based on a CMOS camera readout are in operation for testing with the SLS beam. These systems will be also installed in SLS 2.0. About 100 scintillators will be distributed around the new storage ring.

ACKNOWLEDGMENTS

This work is possible with the collaboration of A. Stark, F. Barchetti, B. Zimmerli, V. Van de Vijfeijken, M. Baldinger, A. Jaggi, U. Flechsig, C. David, M. Stampanoni, K. Bitterli, R. Krempaska, G. Kotrle, E. Japichino, V. Schlott, A. Streun, M. Aiba, M. Boege, and J. Kallestrup.

REFERENCES

[1] A. Streun *et al.*, "SLS-2 Conceptual Design Report", PSI Bericht, Paul Scherrer Institut, Report no. 17-03, 2017. https://www.dora.lib4ri.ch/psi/islandora/object/psi:34977

[2] H. Braun *et. al.*, "SLS 2.0 storage ring. Technical design report", PSI Bericht, Paul Scherrer Institut, Report no. 21-02, pp. 130-134, 2021. https://www.dora.lib4ri.ch/psi/islandora/object/psi:39635

[3] C. Loch Ozkan, R. Ischebeck, and A. M. M. Stampfli, "CMOS Based Beam Loss Monitor at the SLS", in *Proc. IBIC'21*, Pohang, Rep. of Korea, May 2021, pp. 186-188. doi:10.18429/JACoW-IBIC2021-TUOB02

[4] A. Saa Hernandez, N. Milas, M. Rohrer, V. Schlott, A. Streun, Å. Andersson,, and J. Breunlin, "The new SLS beam size monitor, first results", in *Proc. IPAC13*, Shanghai, China, May 2013, paper MOPWA041, pp. 759-761.

[5] C. David, V. Schlott, and A. Jaggi, "A zone plate based beam monitor for the Swiss Light Source", in *Proc. DIPAC'01,* ESRF, Grenoble, France, 2001, paper PS13, pp. 133-135.

[6] H. Sakai *et al.*, "Improvement of Fresnel zone plate beam-profile monitor and application to ultralow emittance beam profile measurements", *Phys. Rev. ST Accel. Beams,* vol. 10, p. 042801. 2007. doi:10.1103/PhysRevSTAB.10.042801

[7] T. Scheimpflug, "Improved method and apparatus for the systematic alteration or distortion of plane pictures and images by means of lenses and mirrors for photography and for other purposes", GB Patent no. 1196, 1904.

[8] R. Ischebeck, E. Prat, V. Thominet, and C. Ozkan Loch, "Transverse profile imager for ultrabright electron beams", *Phys. Rev. ST Accel. Beams*, vol. 18, p. 082802, 2015. doi:10.1103/PhysRevSTAB.18.082802

[9] C. Ozkan Loch, D. Llorente Sancho, E. Divall, E. Ebner, P. Pollet, R. Ischebeck, and F. Loehl, "Loss monitoring for undulator protection at SwissFEL", *Phys. Rev. Accel. Beams*, vol. 23, p. 102804, 2020. doi:10.1103/PhysRevAccelBeams.23.102804

[10] EJ-204, Eljen Technology, https://eljentechnology.com/products/plastic-scintillators/ej-200-ej-204-ej-208-ej-212

[11] BCF-92, Saint Gobain – Scintillating Fibers, https://www.crystals.saint-gobain.com/radiation-detection-scintillators/fibers#

[12] K. Jefimovs, J. Vila-Comamala, M. Stampanoni, B. Kaulich, and C. David, "Beam-shaping condenser lenses for full-field transmission X-ray microscopy", *J. Synchrotron Radiat.*, vol. 15, pp. 106–108, 2008. doi:10.1107/S090904950704771

[13] Boege, M., Private Communication, 23 December 2021.

[14] M. Antimonov, A. Khounsary, A. Sandy, S. Narayanan, G. Navrotski, "On the influence of monochromator thermal deformations on X-ray focusing", *Nucl. Instrum. Methods Phys. Res., Sect. A,* vol. 820, pp. 164-171. doi:10.1016/j.nima.2016.02.103

ISBN: 978-3-95450-241-7 ISSN: 2673-5350 doi:10.18429/JACoW-IBIC2022-MOP02

AN OPTICAL DIAGNOSTIC BEAMLINE FOR THE BESSY II BOOSTER

T. Atkinson*, Ji-Gwang Hwang, G. Rehm, M. Ries, G. Schiwietz, S. Wiese
Helmholtz-Zentrum Berlin für Materialien und Energie, Berlin, Germany

Abstract

As part of the global refurbishment of the injector at BESSY II, a new optical beamline has been installed in the booster. This paper covers the conceptual design: incorporating the beamline into an operational facility without downtime, the simulation and expectations of the optical transport line, mechanical installation and commissioning with beam. These first results with the present beam delivery system have already achieved source-point imaging and bunch length measurements using a fast diode. With the additional PETRA cavity installed for this booster upgrade and connection to acquire RF power in the 2022 summer shutdown planned, the bunch length diagnostics are critical. The beamline will also undergo a final mechanical upgrade and then see the installation of a streak camera.

MOTIVATION

In a familiar fashion that characterized 3rd generation light sources across the world, injection into the BESSY II storage ring is from a low energy linac followed by a full energy booster synchrotron.

The present injection scheme is highly reliable [1], but a global upgrade was necessary for the BESSY VSR project [2]. The most prominent aspect with respect to the injector is the evidence that the bunch length on injection into the VSR-storage ring needs to be reduced from its present value, by at least a factor of two in order to keep the high injection efficiencies.

The preferred method to produce shorter bunches from the booster is an upgrade of the existing 500 MHz RF system. An additional 5-cell PETRA cavity driven by a 40 kW transmitter has been installed. In terms of beam commissioning, slowly increasing the total RF gradient is a subtle way to actively control and diagnose the beam in all dimensions.

DESIGN CRITERIA

The design criteria was to keep the optical beamline as short and as simple as possible: use established in-house components and install everything over four shutdowns without any dark-time of the high level source-point diagnostics. In order to minimize the beamline transport length, the output port in the booster was moved in 2020 to a more convenient straight section. This modification to the booster hardware was part of a global reshuffle to accommodate the additional cavities, bunch-by-bunch feedback [3] and redundancy for TopUp current measurement. For beam transport, a total of 7 mirrors each 2 inch in diameter are mounted in the standard HZB holders used throughout the facility, see Fig. 1. Motorized 2-point tilt adjustment is possible.

* terry.atkinson@helmholtz-berlin.de

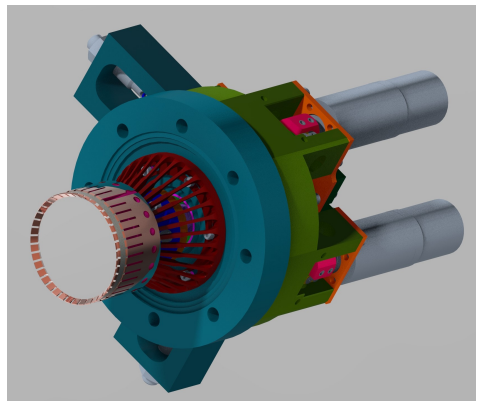


Figure 1: Standard HZB [4] motorized holder for a 2 inch diameter mirror.

The mirrors in the transport line have a surface flatness of lambda/20 to achieve high precision in terms of phase [5]. This allows the source imaging system to measure a spot size close to its diffraction limit.

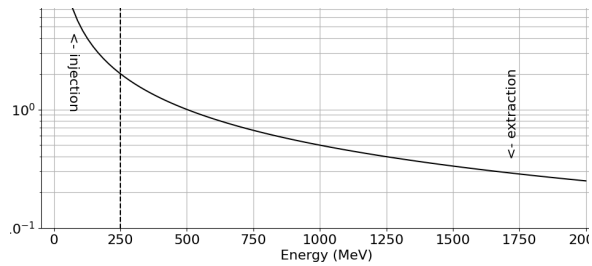


Figure 2: Critical angle of emitted light over the energy ramp of the booster. Without refractive optic, visible light will be outside the angular acceptance for energies < 250 MeV.

From the source, the divergence of the emitted light is corrected using refractive optics, then collimated beam is transported though beamline using the remaining mirrors. There is a 2 degree angle at the output port from the bending magnet.

Noticeably installed is a Intermediate Viewing Point (IVP) consisting of a motorized linear stage and CCD camera at the halfway stage to help align the components. Here both the photon beam and alignment laser were simultaneously observed. Next the beam is transported through the labyrinth out to the optical table. Due to building constraints, a further 20 degree angle is introduced in the labyrinth.

The entire beamline is under vacuum, contains presently one UHV wedged window at the booster output port. This window protects the vacuum in the accelerator and the wedged angle helps to separate spatially unwanted reflection. A second wedged window will be installed next year to com-

Content from this work may be used under the terms of the CC BY 4.0 licence (© 2022). Any distribution of this work must maintain attribution to the author(s), title of the work, publisher, and DOI

ISBN: 978-3-95450-241-7 ISSN: 2673-5350 doi:10.18429/JACoW-IBIC2022-MOP02

Content from this work may be used under the terms of the CC BY 4.0 licence (© 2022). Any distribution of this work must maintain attribution to the author(s), title of the work, publisher, and DOI

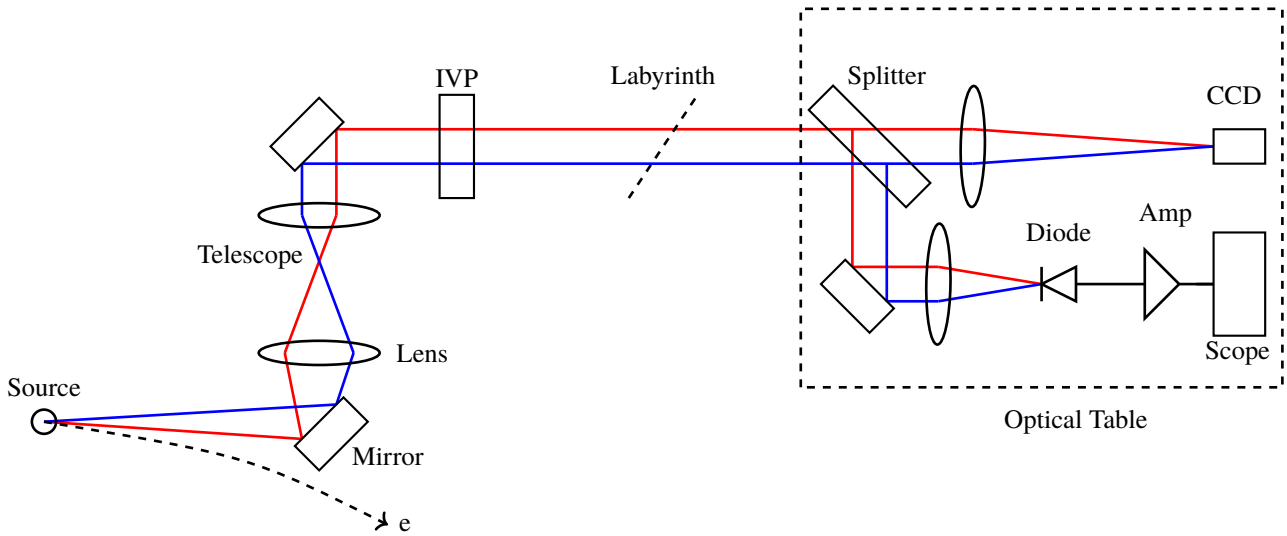


Figure 3: Schematic of the beamline and the present experimental setup on the optical table.

pensate the dispersion effects that may restrict the resolution of beam size diagnostics.

A case study was undertaken to make best use of the fixed distance between the first two mirrors. Here the positions of the lens within the telescope and the resultant chromatic effects for several different lens focus length and type were simulated.

As a guide line, one can estimate that the critical angle: $\theta_c \approx 1/\gamma$ at injection from the 50 MeV linac to be $\theta_c \approx 10$ mrad. With even a larger angular threshold for visible light [6].

Given 10 m from source to final 2 inch (50 mm) diameter mirror, without refractive optics, the light emitted around injection (below 250 MeV, see Fig. 2) will be suppressed below the detection limit. Transmission of the beamline for the same geometric acceptance is improved dramatically when using the telescope.

The design schematic in Fig. 3, highlights the dependence on plain mirrors for beam transport over the 13 m to the optical table. A substantial start-to-end CAD of the whole beamline was developed, see corresponding poster.

By the end of the shutdown in 2021, all fundamental components were installed with the exception of the telescope optic due to delivery problems. The beamline was brought successfully into operation and a single lens was used to generate an image on a CCD camera for the high level diagnostics.

SOURCE-POINT IMAGING

A full characterization of the beamline was not envisaged in this initial set up stage. Emphasis was on stable operation and a beam spot for the high-level diagnostic. Once alignment was achieved, again here the IVP played a vital role, a single 1 m focusing lens some 13 m from the source defined the optic (without telescope and only plane mirrors). The beam diameter at the lens was approximately 20 mm so the half the angular acceptance $\theta_a = 10\,\text{mm} / 13\,\text{m} = 0.77$ mrad. The Abbe limit @600nm $\approx \lambda/(2n \sin\theta_a) = 243\,\mu$m.

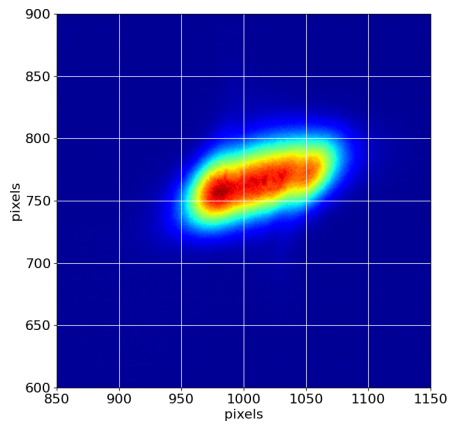


Figure 4: Typical beam image on CCD during machine commissioning whereby alignment optimization and full source-point imaging is ongoing.

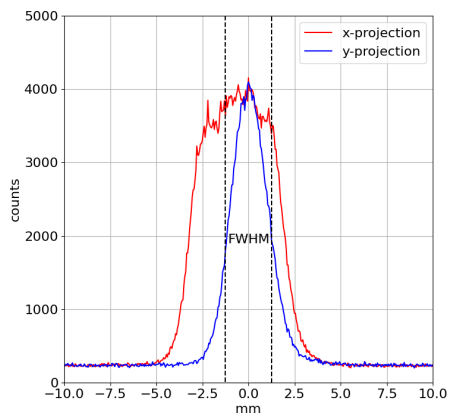


Figure 5: Control system integrated image analysis.

ISBN: 978-3-95450-241-7 ISSN: 2673-5350 doi:10.18429/JACoW-IBIC2022-MOP02

Figure 4 shows a typical beam spot image of the high-level diagnostic (not optimized or at full-focus). The rotation of the profile originated from the angle of the arm in the beamline is compensated by "software". Presently installed is a GT series Allied Vision scientific CCD camera which is designed for imaging in extreme temperatures (from -20 °C up to 65 °C) and fluctuating lighting conditions. In addition, this CDD has good linearity and a pixel size of 4.54 µm. The minimum exposure time is 10 µs, this constitutes to circa 30 turns in the booster.

The Gaussian fit of the vertical projection shown in Fig. 5 suggests $\sigma_y \approx 450\,\mu m$. In this example the beam in the horizontal plane is non-Gaussian and heavily distorted. This was typical during the beamline optimization process and will be addressed again if still apparent after the inclusion of refractive optics and the 2nd wedged window.

The Twiss parameters in the booster at the source can be used to justify some of these early results: Given $\beta_x = 8\,m$, $\beta_y = 3\,m$, $\eta_x = 0.7\,m$ and $\epsilon_{x/y} = 60\,nm$ then $\sigma_x \approx 700\,\mu m$ and $\sigma_y \approx 300\,\mu m$.

BUNCH LENGTH MEASUREMENTS

The installation of a commercial (MSM Metal-Semiconductor-Metal) fast diode from Hamamatsu is a convenient and simple way to measure bunch lengths in the 25 ps regime. Here the diode is powered via a Bias-Tee, the SMA output is connected to a mini-circuit amplifier and the signal is observed on a wideband real-time scope.

Figure 6 shows how the raw data from the scope (black line) is analyzed. In this example, a Gaussian fit of the falling edge of the pulse is taken (red line). This method results in a measured bunch length of 26 ps. Evaluating the rising edge could lead to larger values for the bunch length.

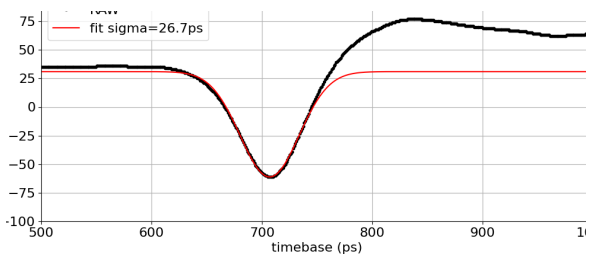


Figure 6: Measurement of pulse on real-time scope. RF cavity voltage cira 604 kV.

The characteristics of the raw data in Fig. 6 are typical for such a system. The overshoot is independent of the amplifier and is a manifestation of the Bias-Tee. The distortions are not caused directly by the inductive resonant circuit $\omega_0 = 1/\sqrt{LC}$ of the Bias-Tee depicted in Fig. 7. The inductance L and capacitance C were measured to be approximately 800 µH and 200 nF respectively which results in a resonant frequency of only 12 kHz. Therefore the very short pulse will not be directly distorted by the operational voltage across the diode via the Bias-Tee. Measurements in the frequency domain such as those described in Ref. [7] to map the insertion loss at high frequencies are still pending. As the light intensity improves through better global alignment and the telescope installation, the amplifier should become redundant and the dedicated studies into this overshoot will continue.

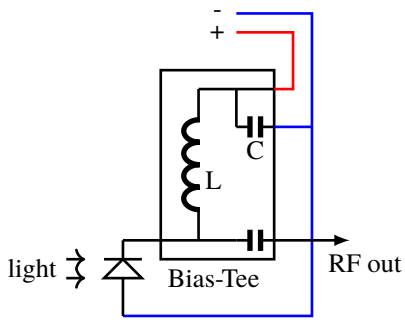


Figure 7: Schematic of fast diode and Bias-Tee [8] circuit diagram.

The specification of the rise-time of the diode is 50 ps. This could be varied using the setup. The rms bunch length at 20 ms in the booster cycle was measured to be $\sigma_t = 26\,ps$ using the scope. Using the Gaussian frequency response notation in Ref. [9] the rise-time is given by:

$$\Delta t_{10-90} = \left(\sqrt{2\ln\frac{1}{0.1}} - \sqrt{2\ln\frac{1}{0.9}}\right)\sigma_t = 1.69\sigma_t = 43\,ps$$

The bandwidth of the diode can be estimated using $BW_{-3dB} * \sigma_t = 0.32$ to be $BW_{diode} = 0.32/\Delta t_{10-90}$.

The bandwidth from the whole system can be approximated using:

$$\frac{1}{\left(BW_{sys}\right)^2} = \frac{1}{\left(BW_{diode}\right)^2} + \frac{1}{\left(BW_{amp}\right)^2} + \frac{1}{\left(BW_{scope}\right)^2} + \ldots$$

where BW_{amp} and BW_{scope} are both 12 GHz. Although the system is bandwidth limited due to the diode, we have the tools to make a Gaussian bandwidth correction to find the 'real' from the 'measured' bunch length on the scope [10].

$$\sigma_{real} = \frac{1}{1.69}\sqrt{(1.69\sigma_t)^2 - \left(\frac{0.32}{BW_{sys}}\right)^2}$$

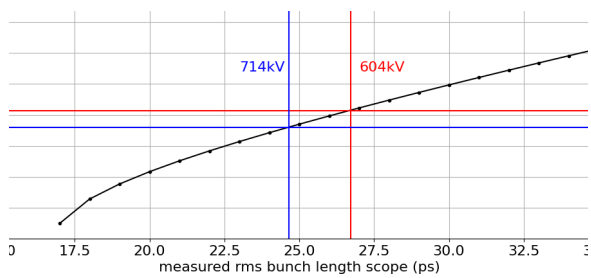


Figure 8: Gaussian bandwidth correction (black line) of measured to real bunch length values at two cavity voltages.

Content from this work may be used under the terms of the CC BY 4.0 licence (© 2022). Any distribution of this work must maintain attribution to the author(s), title of the work, publisher, and DOI

ISBN: 978-3-95450-241-7 ISSN: 2673-5350 doi:10.18429/JACoW-IBIC2022-MOP02

Content from this work may be used under the terms of the CC BY 4.0 licence (© 2022). Any distribution of this work must maintain attribution to the author(s), title of the work, publisher, and DOI

The correction equation is depicted in Fig. 8. Also shown is the experimental data of measured bunch lengths for two different RF voltages in the cavities. In this case the bunch length scales with the voltage given by $\sigma_t \approx 1/\sqrt{V'_{\mathrm{RF}}}$ as expected.

The fast diode is sufficient at this stage in the early operation of the beamline to measure the average bunch lengths at certain points in the booster cycle. The comparison with previous studies [11] is still to be addressed. In this sense, when the cavities are fully commissioned, the further reduction of the bunch length and the non-linear beam dynamics at injection/extraction are better studied using the streak camera, from which the fast diode can be calibrated.

OUTLOOK

The beamline was brought into operation through careful planning without any dark time. Recently the refractive optic was installed and alignment is ongoing. A full characterization of the source-point imaging will be part of a future BSc. project. The adjustments to accommodate for the streak camera will continue in parallel.

REFERENCES

[1] T. Atkinson, P. Goslawski, J. G. Hwang, M. Ries, T. Flisgen, and T. Mertens, "VSR Injector Upgrade at BESSY II", in *Proc. IPAC'18*, Vancouver, Canada, Apr.-May 2018, pp. 4110–4113. doi:10.18429/JACoW-IPAC2018-THPMF030

[2] A. Jankowiak *et al.*, "The BESSY Vsr Project for Short X-Ray Pulse Production", in *Proc. IPAC'16*, Busan, Korea, May 2016, pp. 2833–2836. doi:10.18429/JACoW-IPAC2016-WEPOW009

[3] T. Atkinson *et al.*, "A Longitudinal Kicker Cavity for the BESSY II Booster", in *Proc. IBIC'19*, Malmö, Sweden, Sep. 2019, pp. 150–153. doi:10.18429/JACoW-IBIC2019-MOPP026

[4] FMB Berlin, www.fmb-berlin.de

[5] G. Schiwietz *et al.*, "Bunch-resolved diagnostics for a future electron-storage ring", *Nucl. Instrum. Methods Phys. Res., Sect. A*, vol. 990, p. 164992, 2021. doi:10.1016/j.nima.2020.164992

[6] J. D. Jackson, Chapter 14 in *Classical Electrodynamics*, 1st Edition, Wiley, 1962.

[7] W. J. Song *et al.*, "Development of an On-Line Bunch Length Monitoring System at PLS-II Using an Ultrafast Photodiode", in *Proc. IBIC'21*, Pohang, Korea, Sep. 2021, pp. 384–387. doi:10.18429/JACoW-IBIC2021-WEPP10

[8] ZX85-12G-S+ Mini-Circuits Bias-Tee datasheet, https://www.minicircuits.com/pdfs/ZX85-12G-S+.pdf

[9] S. Bottacchi, *Gigabit Transmission over Multimode Optical Fibre*, pp. 105–106, Wiley, 2006.

[10] J.-G. Hwang *et al.*, "Photodiode Setup for measuring short photon pulses", presented at ARD-ST3 Annual Workshop, 2017, unpublished.

[11] D. Malyutin, T. Atkinson, P. Goslawski, A. Jankowiak, A. N. Matveenko, and M. Ries, "Injection and Bunch Length Studies at the BESSY II Storage Ring", in *Proc. IBIC'17*, Grand Rapids, MI, USA, Aug. 2017, pp. 161–163. doi:10.18429/JACoW-IBIC2017-TUPCC06

ISBN: 978-3-95450-241-7 ISSN: 2673-5350 doi:10.18429/JACoW-IBIC2022-MOP03

STATUS OVERVIEW OF THE HESR BEAM INSTRUMENTATION

C. Böhme, V. Kamerdzhiev[1], Forschungszentrum Jülich, Germany
A. Halama, G.Rupsch, GSI Helmholtzzentrum für Schwerionenforschung, Darmstadt, Germany
[1]also at GSI Helmholtzzentrum für Schwerionenforschung, Darmstadt, Germany

Abstract

The High Energy Storage Ring (HESR), within the FAIR project, will according to current planning provide antiproton beams for PANDA and heavy ion beams for a.o. SPARC. With the beam instrumentation devices envisaged in larger quantities, e.g. BPM and BLM, testing is well underway. Other beam instrumentation instruments like Viewer are in late production stage, Scraper is being tested and for the IPM the 1st of series production has started. An overview of the status of the work package beam instrumentation will be presented as well as test bench results of already produced instruments.

INTRODUCTION

The HESR, part of the FAIR project in Darmstadt, Germany, is dedicated to the field of antiproton and heavy ion physics. The envisaged energy range is 0.8 GeV to 14 GeV for antiprotons and 0.17 GeV/a to 5 GeV/a for heavy ions [1]. The ring will be 574 m long in a racetrack shape. The foreseen beam instrumentation within the modularized start version is:

64	Diagonally Cut Beam Position Monitors (BPM)
118	Beam Loss Monitors (BLM)
2	Beam Current Transformers (BCT)
2	Ionization Beam Profile Monitor (IPM)
1	In-gap particle measurement
1	Schottky Pick-up
1	Phase Pick-up
1	Dynamical Tune-meter
5	Viewer
2	Scraper

BPM SYSTEM

The pick-up design is based upon the COSY BPMs [2], which is a diagonally cut pick-up design. The design was shown in detail in [3]. While 63 BPMs will have the inner diameter of 89 mm, one is designated to be located closely after the injection septum, where the beam pipe has a diameter of 150 mm. Therefore, to not limit the aperture at this place, one BPM has to have a larger diameter. This one is still to be designed.

BPM Testing

Of the 64 envisaged BPMs, 44 have been tested, with an additional 11 recently received from production to be tested in the near future. Every BPM is tested using a wire test bench to check general electrical functionality and determine the linear coefficients and electrical offsets per plane. The test bench is fitted with µ-meter precision linear drives and optical micrometers for moving the wire and determining the precise position. In every BPM two highly precise measured reference markers are added during manufacturing, which are functioning as reference for the wire positioning. The signals are amplified by head amplifiers and the AMPLIFIER 110, before being digitized by a Spectrum 16-bit 250 MHz ADC card. The whole measurement process, including the positioning of the wire, control of the gain of the AMPLIFIER 110, the ADC signal readout, and writing the measured values to a file is done with LabView.

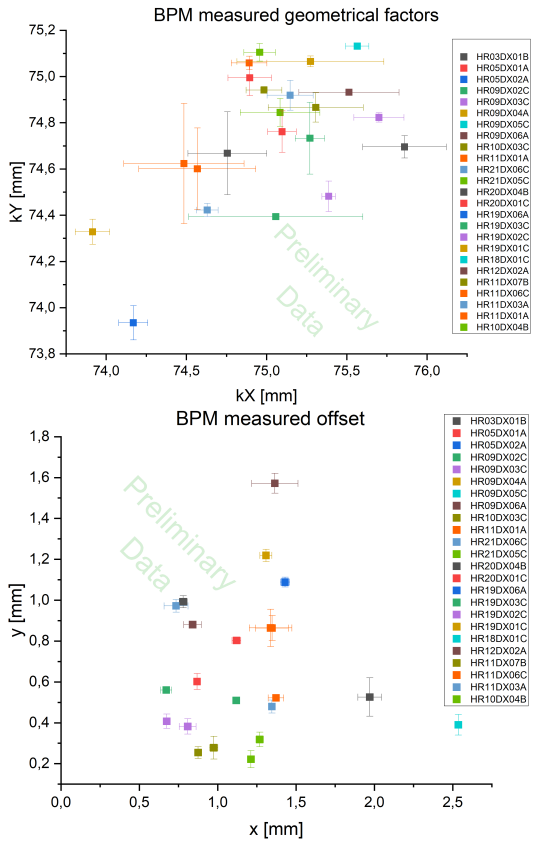


Figure 1: Measured properties of the first 25 BPMs. On the top picture the geometrical factors and the lower picture the electrical offsets compared to the mechanical middle position.

Figure 1 shows the preliminary results of the first 25 tested BPMs for the measurements of the geometrical factors (upper figure) and the electrical center in regards to the mechanical center (lower figure). While the mechanical tolerances for the parts of the BPM directly involved in the measurement process, like the pick-up electrodes, have been specified

Content from this work may be used under the terms of the CC BY 4.0 licence (© 2022). Any distribution of this work must maintain attribution to the author(s), title of the work, publisher, and DOI

ISBN: 978-3-95450-241-7 ISSN: 2673-5350 doi:10.18429/JACoW-IBIC2022-MOP03

Content from this work may be used under the terms of the CC BY 4.0 licence (© 2022). Any distribution of this work must maintain attribution to the author(s), title of the work, publisher, and DOI

with tolerances lower than 0.02 mm, the mechanical deviations have an impact on both, the electrical zero position in regards to the mechanical zero position, and the geometrical factors used for the calculation of the position of the particle beam. The expected values for the BPMs have been presented in [4]. There simulations resulted in k=73.52 and for the offset to 0.7 mm.

With further evaluation of the measured data the statistical errors should be reduced. During the measurement process in some cases the wire, simulating the beam within the test stand, does not move to the foreseen position. Therefore a wrong measurement is recorded leading to an increased statistical error. These cases are not identified reliably by the automated data analysis algorithm, therefore a manual check has to be performed. This is still ongoing.

Signal Amplification

Fixed Gain Head Amplifiers Due to low amplitudes the HESR BPM signals require additional boosting prior to transmission over cables. In order to achieve a better signal to noise ratio head amplifiers with a high impedance low noise input were developed, with the high impedance also flattens the frequency response, especially at low frequencies. At the HESR the expected radiation levels are low enough so that an active solution could be implemented. The amplifier is shown in Figure 2.

The specification of this amplifier is:

Amplification:	20 dB
Noise:	6 µV at 50 pF input capacitance and 10 MHz bandwidth
Bandwidth:	10 MHz default, configurable up to 70 MHz
Input Impedance:	500 kΩ
Power supply:	+8 V and -8 V
Output range:	± 1.5 V at 50 Ω



Figure 2: Picture of the head amplifier developed for the HESR BPM system. The N-type plug is main signal input, calibration ports and signal output ports are facilitated via SMA connectors. The power is connected through the D-Sub plug.

Hadron Pre-Amplifier (AMPLIFIER 110) Within the FAIR project the decision was made early that a common amplifier solution should be developed for all accelerator structures. Therefore the AMPLIFIER 110 (A110) was developed [5] in cooperation of the GSI and Instrumentation Technologies d. d., Slovenia. The A110 is now commercial available.

The A110 has a gain range of +60 dB to -60 dB and is equipped with an overload protection which has been seen necessary especially for the SIS100. It is equipped with a 50 Ω input.

For the above listed arguments the HESR deviated from this concept by introducing active head amplifiers instead of the passive impedance transformer. Still the A110 remains part of the signal chain, as the head amplifier will have a fixed gain. An adjustable gain amplifier is seen necessary to adapt for different beam properties.

The electric power needed for the head amplifiers will be supplied from the A110, as the necessary voltages are available within the A110 and therefore additional power supplies and cables from the power supply rooms are not needed. The necessary modifications to the A110 are designed to be minimal, only one additional card has to be installed within the A110 into a pre-existing empty slot, which can be removed easily if the device would have to be installed at a different location. For signal and power distribution to and from the 4 head amplifiers an additional 1 RU module was designed and has to be installed in addition to the A110 per BPM. Another feature of the distribution unit is the precise splitting of a test signal generated by the A110 to the 4 head amplifiers, which can be used for a relative calibration of the 4 head amplifiers towards each other.

The design is to be adopted by other machines within FAIR, that face low signals levels. The total amount of systems foreseen, consisting of one distribution unit with 4 head amplifiers, is 64 for the HESR, 20 for the collector ring (CR), 10 for the HEBT, and additional 10 for the CRYRING, totalling in 104 units. The production will be done for all systems at once.

Beam Processor

For the readout and calculation of the beam position. the LIBERA Hadron was chosen for all FAIR BPMs. It features an extension for orbit control, which has been adapted to the FAIR magnet control units (ACU). As an extension to the original plan, the orbit control extension units have been ordered for the HESR as well.

BEAM LOSS MONITOR

For machine commissioning, routine operation and further beam optimization detailed beam loss data is very valuable. Unlike other accelerators, the HESR BLM data will not be used for an automated machine protection, as the stored total beam energy will not be high enough to damage the machine. Along the ring 118 BLMs will be used, of which 20 have been so far delivered by GSI, mainly for testing purposes with the FESA test system.

The BLM consists of a BC-400 plastic scintillator and a Hamamatsu photomultiplier (PMT). This solution is favored over e.g. an ion chamber type loss monitor because of the low expected loss rates. The design was presented in detail at [6]. It was developed by GSI and will be used in other

ISBN: 978-3-95450-241-7 ISSN: 2673-5350 doi:10.18429/JACoW-IBIC2022-MOP03

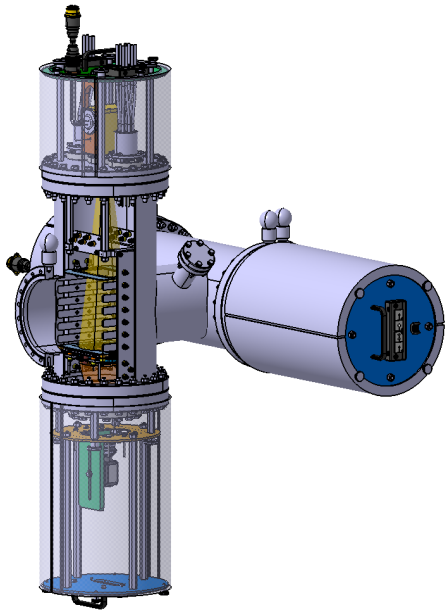


Figure 3: Drawing of the 1st of series IPM [7]. On top a UV lamp is installed in order to perform a relative calibration of the microchannel plates (MCPs), with the simulated light path depicted in yellow. The signals generated by the beam ions ionizing the residual gas, and therefore representing the profile, are amplified utilizing two MCPs and then transformed to a light signal utilizing a phosphor screen. This signal can be transported out of the vacuum vessel through a standard vacuum window and is detected by a standard CCD camera, located in the bottom in the picture. Two identical setups, rotated by 90°, are installed to measure the vertical and horizontal profile.

parts of FAIR as well, e.g. the High Energy Beam Transport (HEBT).

For the readout of the BLMs a µTCA system will be used utilizing scaler SIS8800 and counter SIS8980 from Struck Innovative Systeme GmbH. Both cards are connected to each other via the µTCA backplane and provide 16 channels per card. The BLM PMTs will be powered individually utilizing a multichannel HV system in order to be able to compensate for the properties of the individual BLM detector and the individual location.

FESA Control System Test System

In order to have a FESA control system operational for development and testing, a stripped down test system was installed by Cosylab d. d. at COSY. As a functioning system the control and readout of the BLM system was implemented and can be used in addition to the COSY BLM system with additional BLMs. Besides this test setup, the system is also designed as a reference for further FESA development and testing.

IONIZATION BEAM PROFILE MONITOR

An Ionization Beam Profile Monitor (IPM) was built and tested in cooperation with the GSI in 2007 [8]. Since then it became a very valuable instrument in beam diagnostics at COSY and GSI [9]. Based on both experiences a similar device is under development for the HESR. Depicted in Figure 3, it is being designed in a size that would not only fit the HESR but also in the HEBT. Because of the delicate nature of the microchannel plates and the importance of the system, 2 systems will be installed, providing one backup system in case of failure. Within the HESR and high energy beam transport (HEBT) an amount of 17 devices are foreseen, although some of them only for one plane.

The first of series device is right now being build at the Reserach Center Jülich and it is planned to be ready by the end of this year. Extensive testing of the device is planned to be performed within the COSY synchrotron. Once the testing is completed, which is foreseen to be mid 2023, mass production will be started. Although the vacuum chambers for HESR and HEBT will be different and therefore produced separately, the actual IPM parts, e.g. the parts inside the vacuum chamber or the mounting of the UV lamp and camera, are planned to be produced together. First parts, like a metal mesh to, on one side let through the UV light but have a flat E-field within the E-field cage, and on the other side to protect the MCPs, are already under production at the Research Center Jülich, also for the IPMs in other FAIR machines using a different design, like in SIS100.

VIEWER

There will be 5 viewers installed in the HESR. One at the beginning and end of each telescope and an additional one directly after the injection septum magnet. As shown in Figure 4, the viewer consists of a scintillation screen mounted at 45° and will be moved by a pneumatic drive. As a speciality at the HESR, if the viewer is not used an RF cage will be moved into its place. This is done in order to minimize the overall impedance of the ring. If the RF cage is in its operational position, a second pneumatic drive will move RF fingers in their position to ensure an optimal electrical conduction. Before moving the RF cage out, these springs will be pulled back. The first of series is already tested, the remaining 4 devices are right now being produced.

SCRAPER

The scraper system is shown in Figure 5. There will be 2 scraper systems installed in the HESR. Each system consists of 2 vertical and 2 horizontal jaws. Each jaw of 10 copper rods which are placed in an alternating manner and are each 25 mm in diameter. This layout assures a particle will be slowed down by at least 50 mm of material while the structure will have a minimal effect on the RF impedance while being on its out position. Each jaw can move in farther than the middle of the beam pipe. As a safety measurement the jaws are therefore placed not directly facing

Content from this work may be used under the terms of the CC BY 4.0 licence (© 2022). Any distribution of this work must maintain attribution to the author(s), title of the work, publisher, and DOI

ISBN: 978-3-95450-241-7 ISSN: 2673-5350 doi:10.18429/JACoW-IBIC2022-MOP03

Content from this work may be used under the terms of the CC BY 4.0 licence (© 2022). Any distribution of this work must maintain attribution to the author(s), title of the work, publisher, and DOI

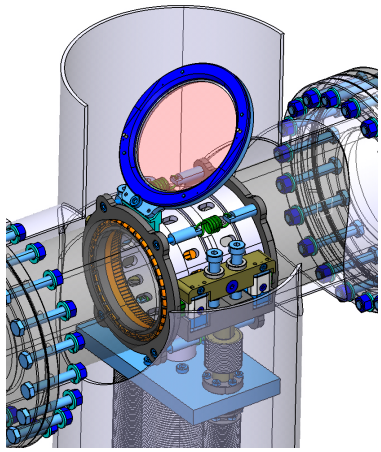


Figure 4: Drawing of the viewer. A scintillator screen is moved into the beam with 45°. While being moved out, a RF cage will be moved into it's position.

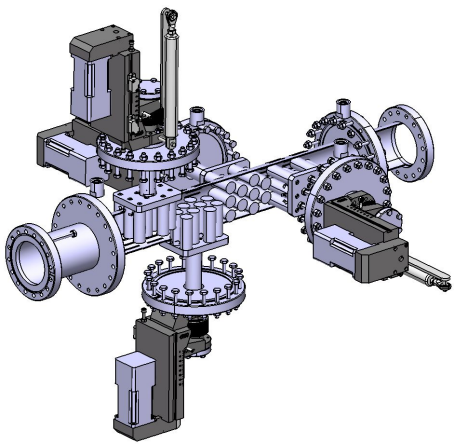


Figure 5: Drawing of the scraper [7]. On each side of each plane the scraper consists of 10 rods of 25 mm diameter. The scraper can move in further than the middle of the beam pipe. To avoid damage, rods for one plane are physically located behind each other.

each other but longitudinally behind one another. If both jaws are moved in fully they will not touch each other and so not being damaged. The mechanical construction of this system is finished, tests of the stepper motor control within the control system are underway.

PHASE PICK-UP

The in-vacuum part of the Phase Pick-Up will be one non-split BPM. This is derived from the construction layout of the regular BPMs and will be manufactured directly after all regular BPMs are manufactured. The readout of the Phase Pick-Up still has to be defined.

IN-GAP PARTICLE MEASUREMENT

The injection scheme of the HESR is planned in a way, that by the use of a barrier bucket RF-mode the circulating beam will be squeezed in about half of the longitudinal space [10]. The so generated cleared region will be used to inject the next bunch of antiprotons into the HESR. For the seamless injection, as few as possible particles should remain in the cleared region, as they will be lost during injection of the next bunch. In order to adjust the RF mode, the amount, or percentage, of remaining particles within the cleared region should be measured. Initially a wall current monitor (WCM) was requested for this task. During the detailed specification it was found the WCM is not capable of performing such measurement.

Further investigations let to a modified design of an IPM, in which the camera was replaced by a photomultiplier and the replacement of a phosphor screen with another form of scintillation screen was discussed. After calculating the particle yield of the residual gas interaction, the yield was found to be in the region of only few particles per second, and therefore within the expected noise background.

Therefore further investigations towards a suitable measurement method are required.

OUTLOOK

At this point in time the production and delivery of the BPM pick-ups are almost completed. The measurement of the BPMs on the designed test stand is also well underway, As well as the calculation of the individual geometrical factors and offsets. The beam current transformers and the scrapers are completely manufactured, while testing is still ongoing. The viewers are in production, with the first of series already tested. For the IPM the design phase is finished, with the first of series right now under construction. Other systems are still in the design phase, like the Schottky Pick-up, or the Beam In-Gap measurement.

REFERENCES

[1] J. Hetzel, "The High Energy Storage Ring (HESR) at FAIR", Presented at Extreme Storage Ring Workshop (ESRW22), Geneva, Switzerland, Jan.-Feb. 2022.

[2] R. Maier *et al.*, "Non-Beam Disturbing Diagnostics at COSY-Jülich", in *Proc. EPAC'90*, Nice, France, June 1990, p. 800–803.

[3] C. Böhme *et al.*, "Status Overview of the HESR Beam Instrumentation", in *Proc. IBIC'18*, Shanghai, China, Sep. 2018, pp. 26–28. doi:10.18429/JACoW-IBIC2018-MOPA01

[4] A.J. Halama *et al.*, "Numerical Comparative Study of BPM Designs for the HESR at FAIR", in *Proc. IBIC'16*, Barcelona, Spain, Sep. 2016, pp. 609–612. doi:10.18429/JACoW-IBIC2016-WEPG01

[5] M. Schwickert *et al.*, "Status of Beam Diagnostics for SIS100", in *Proc. IPAC'17*, Copenhagen, Denmark, 2017, pp. 156–159. doi:10.18429/JACoW-IPAC2017-MOPAB035

[6] P. Boutachkov *et al.*, "Commissioning of the Beam Loss Monitoring System for the HADES Beam-Line at GSI", in *Proc. IBIC'19*, Malmö, Sweden, Sep. 2019, pp. 74–77. doi:10.18429/JACoW-IBIC2019-MOPP006

[7] M. Maubach, GSI, private communication

ISBN: 978-3-95450-241-7 ISSN: 2673-5350 doi:10.18429/JACoW-IBIC2022-MOP03

[8] T. Giacomini *et al.*, "Ionization Profile Monitors - IPM @ GSI", in *Proc. DIPAC'11*, Hamburg, Germany, May 2011, pp. 419–421. https://jacow.org/DIPAC2011/papers/TUPD51.pdf

[9] V. Kamerdzhiev *et al.*, "Results of Electron Cooling Beam Studies at COSY", in *Proc. RuPAC 2010*, Protvino, Russia, Sep.-Oct. 2010, pp. 156–160. https://jacow.org/r10/papers/wechz04.pdf

[10] T. Katayama *et al.,* "Beam Accumulation with Barrier Voltage and Stochastic Cooling", in *Proc. IPAC'10*, Kyoto, Japan, May 2010, pp. 837–839. https://jacow.org/IPAC10/papers/MOPD065.pdf

Content from this work may be used under the terms of the CC BY 4.0 licence (© 2022). Any distribution of this work must maintain attribution to the author(s), title of the work, publisher, and DOI

ISBN: 978-3-95450-241-7 ISSN: 2673-5350 doi:10.18429/JACoW-IBIC2022-MOP05

FIBER BRAGG GRATING SENSORS AS BEAM-INDUCED HEATING MONITOR FOR THE CENTRAL BEAM PIPE OF CMS

F. Fienga[1,*], L. Sito[1], V. R. Marrazzo[1], A. Irace, and G. Breglio[1]
Univeristy of Naples Federico II, Naples, Italy
F. Carra, F. Giordano, and B. Salvant,
European Organization for Nuclear Research (CERN), Geneva, Switzerland
N. Beni[1], and Z. Szillasi[1],
Institute for Nuclear Research of Eötvös Loránd Research Network, Debrecen, Hungary
S. Buontempo[1], National Institute for Nuclear Physics (INFN), Naples, Italy
[1]also at European Organization for Nuclear Research (CERN), Geneva, Switzerland

Abstract

The passage of a high-intensity particle beam inside accelerator components generates heating, potentially leading to degradation of the accelerator performance or damage to the component itself. It is therefore essential to monitor such beam-induced heating in accelerators. This paper showcases the capabilities of iPipe, which is a set of Fiber Bragg Grating sensors stuck on the inner beam pipe of the Compact Muon Solenoid (CMS) experiment installed in the CERN Large Hadron Collider (LHC). In this study, the wavelength shift, linked directly to the temperature shift, is measured and is compared with the computed dissipated power for a set of LHC fills. Electromagnetic and thermal simulations were also coupled to predict the beam-induced temperature increase along the beam pipe. These results further validate the sensing system and the methods used to design accelerator components to mitigate beam-induced heating.

INTRODUCTION

An increase in energy and intensity of the beams is expected as part of the CERN's Large Hadron Collider (LHC) High Luminosity (HL) upgrade [1]. One of the major potential limitations for this upgrade [2] is the heating of accelerator components produced by the presence of the beam itself. This is called beam-induced heating (BIH).

The beam-induced heat load is deposited on the device primarily in three ways: (i) synchrotron radiation [3], (ii) electron cloud [4], and (iii) heating due to impedance [5].

These phenomena can lead to several issues (delays, beam dumps, and even component damage) like, for instance, what occurred in June 2011 during the first Run of LHC [6]. Therefore, it is essential that the components' design phase is able to appropriately account for heating. Additionally, it is necessary to have suitable monitoring systems to regularly monitor temperature-related parameters.

One sensing solution that has spread in the last decade in the High Energy Physics domain is Fiber Optic Sensing (FOS). This work focuses on iPipe, an innovative measuring system based on Fiber Bragg Gratings (FBGs), mounted in the CMS experiment and in acquisition since 2015 [7]. The iPipe system is monitoring CMS's vacuum chamber, the Central Beam Pipe (CBP). Since the CBP is located at one of the interaction points, it is hosting both beams simultaneously to allow them to collide. This two counter-rotating beams situation causes interference phenomena that can lead to an anomalous dissipated power distribution [5].

The possibility to infer various beam parameters using data logged by the iPipe system has already been demonstrated [8]. This work aims to go further, comparing the temperature excursion acquired by the iPipe system during machine operation with a temperature map produced using coupled electromagnetic and thermal simulations. The main goal is to demonstrate the capability of the iPipe system to measure directly the BIH. Moreover, this benchmark enables to further validate the analytical model (with regards to the two counter-rotating beams case in particular) and simulation methodologies that are typically used at CERN.

MEASUREMENTS

FBGs are periodic changes in the refractive index of the optical fiber's core. Such a structure behaves as a stop band filter: it reflects light centered at a specific wavelength, that is called Bragg wavelength (λ_B), and that depends on the effective refractive index of the core (n_{eff}) and the spatial periodicity of the grating (Λ). These dependencies are described in Eq. (1).

$$\lambda_B = 2n_{eff}\Lambda. \quad (1)$$

This structure is intrinsically a sensor since any change either in the refractive index of the core or in the grating period results in a change of the Bragg wavelength. A temperature difference (ΔT) and/or an applied strain (ε) may cause these changes and, as described by Eq. (2), it is possible to correlate the superposition of the two physical effects with the Bragg wavelength variation that they induce [9].

$$\Delta\lambda_B(T,\varepsilon) = \lambda_B \cdot [(1-\rho_e)\cdot\varepsilon + (\alpha_\Lambda + \alpha_n)\cdot\Delta T], \quad (2)$$

where ρ_e is the photo-elastic effect coefficient, α_Λ is the thermal expansion coefficient, and α_n is the thermo-optic effect coefficient.

* francesco.fienga@unina.it

Content from this work may be used under the terms of the CC BY 4.0 licence (© 2022). Any distribution of this work must maintain attribution to the author(s), title of the work, publisher, and DOI

ISBN: 978-3-95450-241-7 ISSN: 2673-5350 doi:10.18429/JACoW-IBIC2022-MOP05

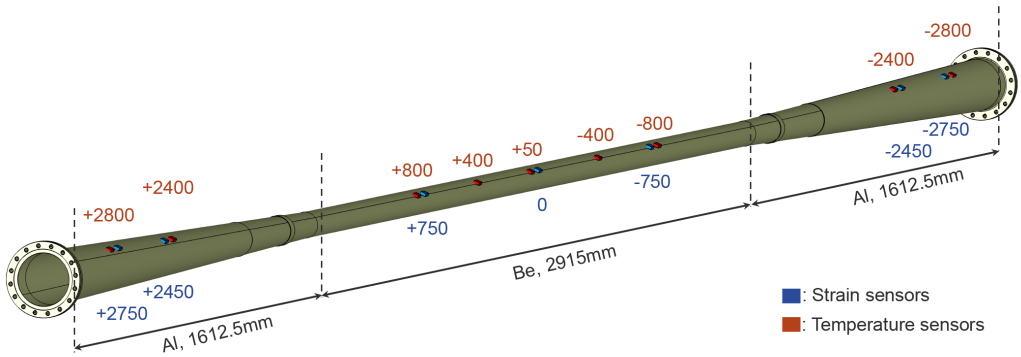


Figure 1: 3D CAD model of the CBP during Run2 (2015-2018). The probes' names refer to their distance from the IP in mm.

Placing the probe only in thermal contact with the structure, thus applying ideally no strain on the fiber, allows to measure the temperature alone. However, during the mounting phase, a certain amount of strain will always be induced. It is then more practical to talk about a wavelength variation, directly linked to a temperature variation, to filter out the initially induced strain.

This approach of relative measurements can be advantageous also in terms or radiation hardening of the FBGs. An ionizing radiation could affect the FBG with a radiation-induced Bragg wavelength shift (RI-BWS). In the case of iPipe, the FBGs employed are femtosecond laser inscribed (fFBG) and this guarantees already a suitable radiation hardening of the probes for the considered environment [10]. Moreover, the dose rate in LHC is such that impact of radiation on the measurements is completely negligible when considering the difference in wavelength.

The case study is the beam pipe of CMS. During the Run2 of LHC (2015-2018) it was made of a central cylindrical section of beryllium, with an external diameter of 45 mm, a thickness of 0.8 mm and a length of almost 3 m. Two conical aluminium sections are then sealing the central region. A 3D CAD model of the structure, with a schematic representation of the probes' position, can be seen in Fig. 1.

The iPipe system is composed of 4 arrays (i.e. 4 optical fibers; only one array is shown in Fig. 1) each with 16 FBG sensors: 7 are glued to the structure to measure strain, 9 are only in thermal contact with the surface to measure temperature variations [7]. In this work the strain probes will not be considered. Moreover, only the central cylindrical section is considered for simplicity. All the results presented in this proceeding are referring to the sensor named P50, that is placed at 50 mm from the beams' collision point, also called Interaction Point (IP).

In Fig. 2, the Bragg wavelength - measured by interrogating the iPipe probe (green curve) - is reported in its evolution in time during the LHC fill 6675 (12-13 May 2018). Moreover, the intensities of the two beams (red and blue curves are respectively beam 1 and beam 2 intensities) are reported. One can observe that the wavelength shift is correlated to the intensity curve with an initial delay. Furthermore, it is interesting to notice the change in concavity of the curve at the end of the intensity ramp. After further investigations it was possible to conclude that the second temperature increase, is due to additional heating coming from the silicon trackers placed all around the CBP that are being turned on.

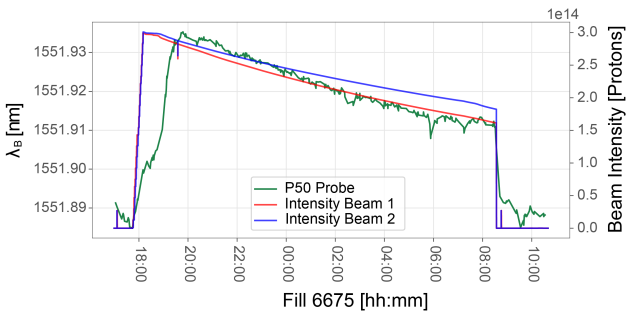


Figure 2: Evolution of the Bragg wavelength measured by the P50 probe during the fill 6675 (green curve). Evolution of the intensity of beam 1 (red) and beam 2 (blue).

This is a showcase of the capabilities of the sensing system that has proven to be an effective solution to monitor the temperature variations continuously at multiple locations along the CMS beam pipe. In particular some peculiarities make it more attractive than other solutions for the CMS environment: (i) multiplexing capabilities and easiness of installation due to the reduced cabling, (ii) immunity to electromagnetic interference (EMI), (iii) robustness to ionizing radiation, and (iv) reduced probability of interacting with generated sub-particles due to the small diameter of the fiber (200 µm).

SIMULATIONS

To effectively produce a temperature map, the approach considered consists of two phases: (i) computing the dissipated power distribution due to the passage of the beam into the component, then (ii) using the power distribution, together with the appropriate thermal boundary conditions and symmetries of the problem, as input for a thermal solver.

Content from this work may be used under the terms of the CC BY 4.0 licence (© 2022). Any distribution of this work must maintain attribution to the author(s), title of the work, publisher, and DOI

ISBN: 978-3-95450-241-7 ISSN: 2673-5350 doi:10.18429/JACoW-IBIC2022-MOP05

Content from this work may be used under the terms of the CC BY 4.0 licence (© 2022). Any distribution of this work must maintain attribution to the author(s), title of the work, publisher, and DOI

Electromagnetic Simulations

In the considered case, two counter-rotating beams are circulating in the component at the same time. This leads to interference phenomena and to a dissipated power distribution that depends on the distance from the IP. The analytical relation of the dissipated power in the two beams case, for a symmetrical beam chamber, is reported in [5]. The actual relation that was employed, after having applied the appropriate simplifications, is presented in Eq. (3).

$$\Delta W(s) = (2 f_0 e N_{beam})^2 \sum_{p=0}^{\infty} |\Lambda(p\omega_0)|^2 \cdot \cdot Re[Z(p\omega_0)] \cdot (1 - cos(p\omega_0 \tau_s)) , \quad (3)$$

where, $f_0 = \frac{\omega_0}{2\pi}$ is the revolution frequency of the beam, e is the charge of the particle, N_{beam} is the number of particles in the beam, Λ is the normalized beam spectrum, Z is the longitudinal beam coupling impedance, and $\tau_s = \frac{2s}{c}$ is the phase shift, with s the distance from the IP and c the speed of light in vacuum.

To effectively implement the equation, the procedure shown in Fig. 3 was used. It is a completely general procedure, that enables to study the dissipated power in a given accelerator component. Starting from the geometry of the device and its material, it is possible to compute the longitudinal beam-coupling impedance.

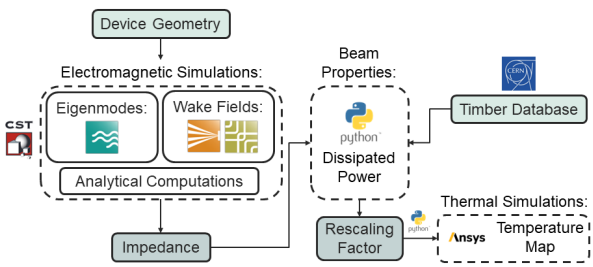


Figure 3: Schematic description of the procedure adopted for electromagnetic simulations.

A python tool was developed to access the CERN's database Timber to extract the parameters of the beams during a certain fill of LHC. This information allows computing the dissipated power density distribution along the structure, as shown in Fig. 4. The dissipated power density distribution (violet curve) is reported as a function of the phase shift (i.e. the distance from the IP) for fill 6675. In addition, the single beam power loss density is shown to underline the overshoot due to the two-beam interactions. Finally, on top of the graph, one half of the CBP is shown with the IP and the positions of the probes highlighted.

Thermal Simulation

Once the dissipated power distribution along the beam pipe has been calculated, it is possible to use it as excitation for a thermal simulation in ANSYS. In addition, to perform the simulation, it is necessary to model the thermal

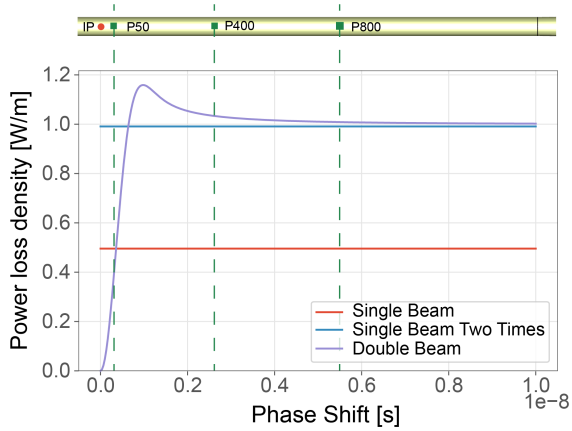


Figure 4: Dissipated power distribution along one half of the CBP for two beams case (violet), single beam case (red), and two times the single beam case (blue).

boundary conditions of the problem accurately. The CBP is surrounded by particle trackers: the closest are the Barrel Pixel Tracker (BPIX) and the Forward Pixel Tracker (FPIX). These trackers are operating at a nominal temperature of $-22\,°C$ therefore, they are contained in two service cylinders that bring electrical connections and cooling system. Moreover, to avoid air condensation, a dry air inlet of 3 m^3/h is provided through a series of holes on top of the BPIX. This whole system described is isolated from the remaining cavern with a thermal jacket [11]. The problem was simplified to obtain the film coefficients along the beam pipe through the use of empirical relations. The value of the analytically calculated coefficients is then reduced in the last portion of the central pipe to take into account: (i) the degradation of the heat exchange mechanism, (ii) the dissipated power coming from the conical sections. The film coefficients applied to the structure are summarized in Table 1.

Table 1: Film coefficient profile along the CBP. The reference point is the IP.

Longitudinal position	Local Film Coeff.
0 –274.4 mm	0.655 W/m^{2}K
274.4 –515 mm	3.34 W/m^{2}K
515 –1500 mm	1.20 W/m^{2}K

RESULTS

Results from the electromagnetic simulation alone will be presented first and then, the result of the final thermal benchmark will be discussed.

For each fill of 2018, thanks to the procedure shown in the electromagnetic simulations section, it was possible to compute the local dissipated power density at 50 mm from the IP and compare it with the temperature excursion registered by the iPipe P50 probe. To get a more significant result, the 2018 fills were filtered to keep only the ones with:

ISBN: 978-3-95450-241-7 ISSN: 2673-5350 doi:10.18429/JACoW-IBIC2022-MOP05

(i) declared stable beam phase, (ii) total duration longer than 6 hr, and (iii) number of bunches greater than 300. After this process, of all the fills of 2018, in Fig. 5, 89 are shown. In addition, a color-map is present as an indication of the maximum intensity of the fill.

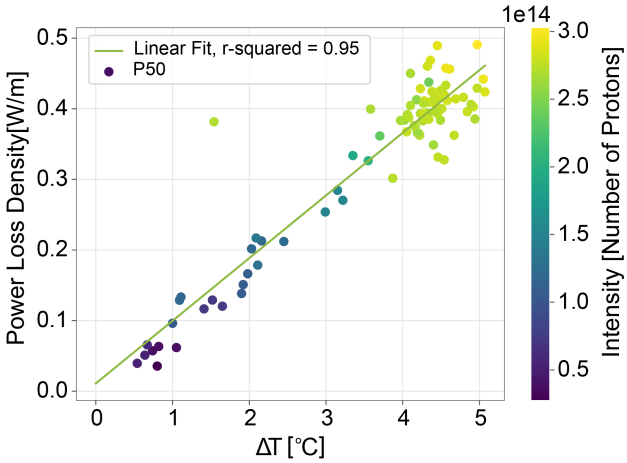


Figure 5: Simulated local dissipated Power against measured temperature excursion.

The data were fitted showing an excellent linearity, with an r-squared of 0.95. This represents an important result that demonstrates the possibility of directly assessing BIH with optical fiber temperature measurements.

A further validation comes from a thermal simulation performed on a subset of 10 fills. The selected fills occurred between April and May 2018 and represent extremely controlled situations. Having computed the dissipated power distribution along the CBP, with the assumption of distributing radially the local dissipated power, the heat source can be considered known. After applying the appropriate symmetries and boundary conditions of the problem, it was possible to obtain a temperature map with ANSYS. For these 10 fills, the thermal excursion registered by the iPipe sensors is compared with the thermal excursion obtained by simulation. The results are shown in Fig. 6 and the agreement is excellent considering the complexity of the problem and the number of approximations made.

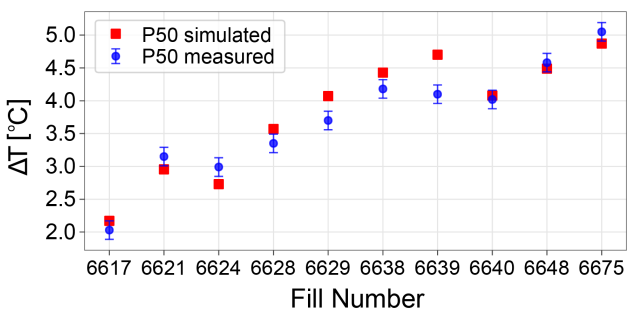


Figure 6: Comparison of simulated and measured temperature excursions.

CONCLUSION

The major purpose of this study has been to validate further the usage of FOS sensing, and more specifically the FBG technology, for monitoring particle accelerator components. It was shown that the iPipe system enables to measure directly the dissipated power due to the passage of the beam. Moreover, a further validation of both the sensing technology and the accelerator component design methodologies was given thanks to a coupled electromagnetic and thermal simulation.

ACKNOWLEDGEMENTS

The authors would like to thank N. Bacchetta, A. Filenius, J. Guardia Valenzuela, M. Masci, G. Rumolo, C. Zannini, and W. Zeuner for their contribution.

REFERENCES

[1] G. Apollinari, O. Brüning, T. Nakamoto, and L. Rossi, "High Luminosity Large Hadron Collider HL-LHC", 2015. doi:10.5170/CERN-2015-005.1

[2] G. Arduini *et al.*, "High Luminosity LHC: challenges and plans", *J. Instrum.*, vol. 11, p. C12081, 2016. doi:10.1088/1748-0221/11/12/C12081

[3] A. A. Sokolov and I. M. Ternov, *Synchrotron radiation*. Akademie-Verlag Berlin, Germany; Pergamon Press, Oxford and cop. 1968.

[4] G. Rumolo *et al.*, "Electron cloud effects on beam evolution in a circular accelerator", *Phys. Rev. ST Accel. Beams*, vol. 6, p. 081002, 2003. doi:10.1103/PhysRevSTAB.6.081002

[5] C. Zannini, G. Iadarola, and G. Rumolo, "Power Loss Calculation in Separated and Common Beam Chambers of the LHC", in *Proc. IPAC'14*, Dresden, Germany, Jun. 2014, pp. 1711–1713. doi:10.18429/JACoW-IPAC2014-TUPRI061

[6] B. Salvant *et al.*, "Update on Beam Induced RF Heating in the LHC", in *Proc. IPAC'13*, Shanghai, China, May 2013, paper TUPME032, pp. 1646–1648.

[7] F. Fienga *et al.*, "A fiber optic sensors monitoring system for the central beam pipe of the CMS experiment", *Opt. Laser Technol.*, vol. 120, p. 105650, 2019. doi:10.1016/j.optlastec.2019.105650

[8] F. Fienga *et al.*, "Fiber Bragg Grating Sensors as Innovative Monitoring Tool for Beam Induced RF Heating on LHC Beam Pipe", *J. Lightwave Technol.*, vol. 39, pp. 4145–4150, 2021. doi:10.1109/JLT.2021.3062458

[9] K. O. Hill and G. Meltz, "Fiber Bragg grating technology fundamentals and overview", *J. Lightwave Technol.*, vol. 15, pp. 1263–1276, 1997. doi:10.1109/50.618320

[10] A. Gusarov and S. K. Hoeffgen, "Radiation Effects on Fiber Gratings", *IEEE Trans. Nucl. Sci.*, vol. 60, pp. 2037–2053, 2013. doi:10.1109/TNS.2013.2252366

[11] CMS Collaboration *et al.*, "The CMS experiment at the CERN LHC", *J. Instrum.*, vol. 3, 2008. doi:10.1088/1748-0221/3/08/S08004

Content from this work may be used under the terms of the CC BY 4.0 licence (© 2022). Any distribution of this work must maintain attribution to the author(s), title of the work, publisher, and DOI

ISBN: 978-3-95450-241-7 ISSN: 2673-5350 doi:10.18429/JACoW-IBIC2022-MOP07

BEAM INSTRUMENTATION PERFORMANCE DURING COMMISSIONING OF THE ESS RFQ, MEBT, AND DTL

T. J. Shea, R. A. Baron, C. S. Derrez, E. M. Donegani, V. Grishin, H. Hassanzadegan, I. Dolenc Kittelmann, H. Kocevar, N. Milas, D. Noll, H. A. Silva, R. Tarkeshian, C. Thomas, European Spallation Source ERIC, Lund, Sweden
T. Papaevangelou, L. Segui, CEA-IRFU, Gif-sur-Yvette, France
I. Bustinduy, ESS Bilbao, Zamudio, Spain
M. Ferianis, Elettra-Sincrotrone Trieste S.C.p.A., Basovizza, Italy

Abstract

In late 2021 through mid 2022, the first protons were accelerated and transported through the European Spallation Source (ESS) Radio Frequency Quadrupole and Medium Energy Transport line at 3.6 MeV, and finally through the first Drift Tube Linac tank at 21 MeV. To enable these achievements, the following beam instrumentation systems were deployed: Ion Source power supply monitors, beam chopping systems, Faraday Cups, Beam Current Monitors (BCM) and Beam Position Monitors (BPM) that also measured phase. Additional systems were deployed for dedicated studies, including Wire Scanners, a slit and grid Emittance Measurement Unit, neutron Beam Loss Monitors and fast BCM and BPM systems. The instrumentation deployment is the culmination of efforts by a partnership of the ESS beam diagnostics section, multiple ESS groups and institutes across the globe. This paper summarizes the beam tests that characterized the performance of the instrumentation systems and verified the achievement of commissioning goals.

INTRODUCTION

Five weeks at the end of 2021 and several more weeks in early 2022 were dedicated to commissioning of the ESS Radio Frequency Quadrupole (RFQ) and Medium Energy Beam Transport line (MEBT) up to a Faraday Cup (FC) located in MEBT. After chopping in the Low Energy Beam Transport line (LEBT) and successful acceleration in the RFQ, the proton beam energy was 3.6 MeV. During June and July of 2022, several more weeks were dedicated to commissioning through the first Drift Tube Linac (DTL) tank with 21 MeV protons transported to a shielded FC. To support commissioning, the instrumentation systems were deployed in each linac section as depicted in Fig. 1. Most were designed to measure beam pulses pulses 5 to 50 µs long with peak current ranging from 6 to 80 mA. This paper focuses on the instrumentation performance that underlies the commissioning results reported in overview papers [1–3].

The ESS beam instrumentation suite includes a wide variety of systems [4] deployed in a staged approach. Systems that are critical for meeting commissioning goals are verified in the laboratory prior to deployment, tested again with other systems in the accelerator environment and then formally verified with beam to achieve operational status. The Faraday Cup (FC), Beam Current Monitor (BCM), Beam Position Monitor (BPM) and Chopper systems have all gone through this workflow. In addition, several other systems were verified for diagnostic beam studies with intent of gaining early experience with beam, sometimes at an intermediate stage of system development. For the recent commissioning runs, the neutron Beam Loss Monitors (nBLM), Wire Scanners (WS) and Emittance Measurement Unit (EMU) were deployed at this level and provided valuable data for the dual purposes of system development and beam characterization.

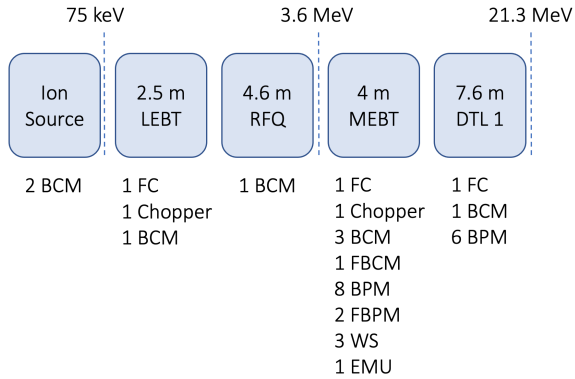


Figure 1: Layout of the linac sections and the beam instrumentation used during the 2021 and 2022 commissioning runs.

BEAM ACCOUNTING

Current Measurements

Six BCMs and three FCs measured the peak beak current that ranged from below 1 mA to beyond the nominal current of 62.5 mA. Figure 2 shows the proton current measured by the BCMs in each of the linac sections, as well as by the FC which was the beam destination at the end of the DTL1. An additional BCM channel also measured the 6 ms pulse extracted from the ion source and this is shown in the inner plot of Fig. 2. The few mA difference between the DTL1 BCM and the DTL1 FC flat top current are due to at least three reasons. Firstly, the DTL1 FC has an entrance foil that filters protons below the nominal energy; secondly, the electron repeller of the DTL1 FC was off; thirdly, the beam is expanded while travelling through the one meter long pipe connecting the DTL1 tank to the shielded beam

Content from this work may be used under the terms of the CC BY 4.0 licence (© 2022). Any distribution of this work must maintain attribution to the author(s), title of the work, publisher, and DOI

ISBN: 978-3-95450-241-7 ISSN: 2673-5350 doi:10.18429/JACoW-IBIC2022-MOP07

destination. The different starting times (shorter than 1 µs) between the rising edges of waveforms reflects the time of flight of the beam and the response time of the electronics. The ringing in the DTL1 FC waveform results from the combined frequency response of the FC electronics and the 40 meter signal cable.

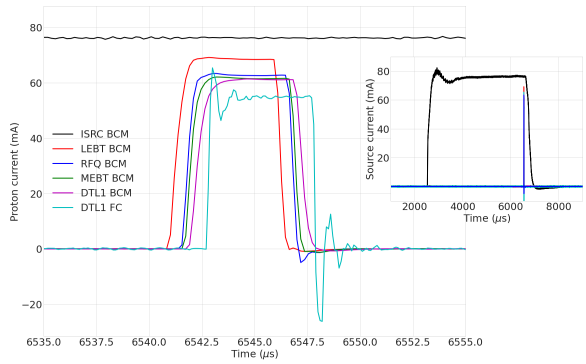


Figure 2: **Main plot:** The 5 µs long proton pulses measured by the BCMs and the DTL1 FC. **Inner plot:** zoom out showing the ms long proton pulse produced by the Ion Source, together with the 5 µs chopped pulse propagated along the accelerator.

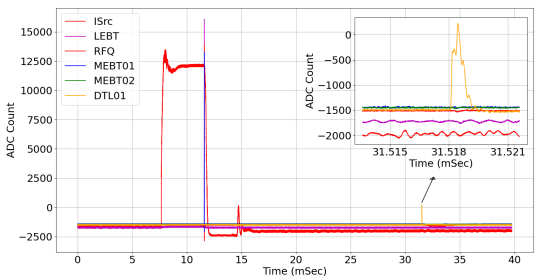


Figure 3: DTL BCM postmortem data showing a spike 20 ms after the beam pulse. The upper right plot shows the spike in more detail.

Machine Protection Functions

The BCM system also provides functions that protect the accelerator from beam-induced damage [5]. To assure the integrity of these functions as well as that of the normal beam characterization functions, the system was verified and calibrated to an accuracy better than the required ±0.8 mA. The system has also demonstrated 0.01 mA precision and 0.1% linearity [6]. Implemented in a field-programmable gate array, the protection functions continuously monitor the current signal and via an interlock system will suppress beam production within 10 µs after detecting an errant condition. Errant conditions include beam detected above a current limit or outside a time window. After verification with beam, these protection functions were relied upon throughout commissioning. Due to the varying conditions during commissioning as well as parallel activities such as radio-frequency (RF) conditioning of the DTL, additional signals challenged the protection functions and led to false trips. An example is shown in Fig. 3. In the DTL BCM, a short spike of current is measured outside the desired time window, an errant condition that led to an interlock. The spike was detected after the DTL when the destination was the MEBT FC, and hence no beam was transported through the DTL. During this time, the DTL tank was being conditioned, so electrons or ions resulting from this process are suspected to be the source of the spike.

Neutron Measurements

The neutron beam loss monitor system [7] was deployed for studies and successfully measured the first neutrons produced as a result of intentional beam loss. In the study, 20 µs proton pulses with an energy of 3.6 MeV and a peak current of about 60 mA were steered onto a chopper dump made of the molybdenum alloy TZM. The sub-µs time structure displayed in Fig. 4 illustrates the fast nBLM detector's intra-pulse measurement capability.

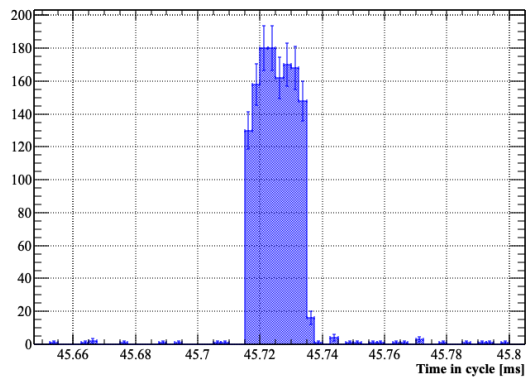


Figure 4: Neutrons detected by the fast nBLM.

CENTROID MEASUREMENTS

The BPMs in the MEBT and DTL measure the transverse position and the phase of the bunch centroids. The MEBT section has been designed with 7 stripline BPMs and an additional BPM to perform time domain characterization of the beam. In the first DTL tank, 6 shorted stripline BPMs are embedded in drift tubes. [8]

In the MEBT only, a so-called fast BPM system performs wide bandwidth characterization of the beam. This system uses regular BPM stripline sensors serviced by a separate 5 GHz bandwidth, 20 GSa/s acquisition system. Calibrated RF chains tap the signals from 2 BPMs spaced 30.1 cm apart. To minimize the measurement error, cables, RF couplers and RF amplifiers have been trimmed to have less than tens of picoseconds propagation delay difference. This system has measured the RFQ output energy, LEBT Chopper vs MEBT Chopper timing alignment, and the beam's general bunching structure. The signal acquisition bandwidth is currently limited by the response of the stripline sensors to the low-velocity protons.

Content from this work may be used under the terms of the CC BY 4.0 licence (© 2022). Any distribution of this work must maintain attribution to the author(s), title of the work, publisher, and DOI

ISBN: 978-3-95450-241-7 ISSN: 2673-5350 doi:10.18429/JACoW-IBIC2022-MOP07

Content from this work may be used under the terms of the CC BY 4.0 licence (© 2022). Any distribution of this work must maintain attribution to the author(s), title of the work, publisher, and DOI

Beam Position

BPMs were typically used during commissioning to perform lattice characterization. Raw waveforms, decimated waveforms and scaler data (1 point per pulse) are available for characterization of the machine and its beam properties. Figure 5 demonstrates a typical example of a beam steering study. In this sequence of waveforms, the ability to measure position variation within the short pulse is evident.

The beam position fluctuations versus beam current have been measured by acquiring position data in the MEBT while varying the iris aperture in the LEBT. Figure 6 shows the the evolution of the beam current and standard deviation of the position measurement during this scan.

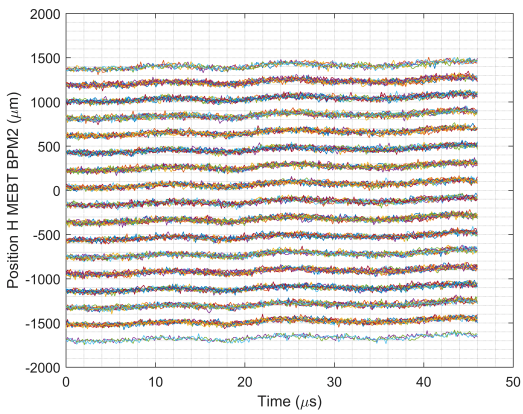


Figure 5: Typical intra-pulse position measurements for a 50 µs pulse and 6 mA beam during a beam steering characterization. Each waveform on the plot corresponds to a pulse acquisition for a specific beam position, adjusted by the MEBT correctors.

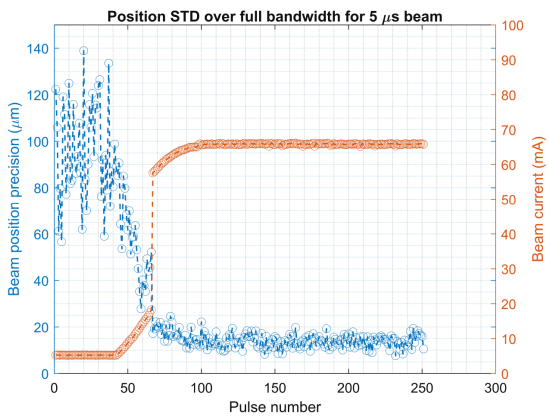


Figure 6: Beam position resolution vs. the beam current for a 5 µs pulse. The plot demonstrates the position measurements standard deviation, which in this case is dominated by the beam fluctuations.

Beam Phase

Phase scans were the primary technique used to tune the MEBT bunchers and the DTL tank. During these scans, the amplitude and phase difference between BPMs are monitored. To avoid interference from the fundamental RF frequency, MEBT and DTL BPMs are tuned to the second harmonic of the beam, making them particularly sensitive to bunch length variations which then results in a strong signature of the optimal RF phase setpoint. A typical plot showing the amplitude and phase difference is presented in Fig. 7.

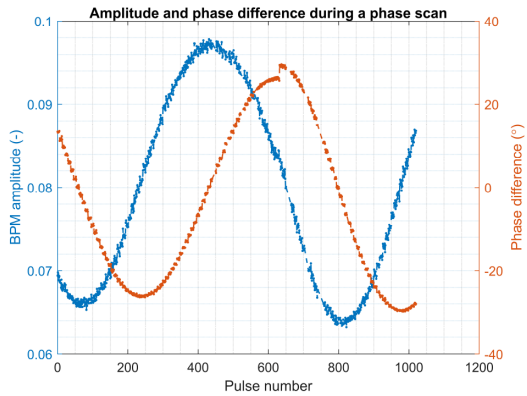


Figure 7: Typical phase scan data from the BPM for a 5 µs pulse length and 5.2 mA beam current. BPM 3 amplitude and phase difference between BPM 3 and 5 are shown on this plot.

Absolute beam energy measurements were performed with the fast BPM system by measuring the absolute time of flight between the two BPM sensors. The measurements over approximately one hour are shown in Fig. 8. Time domain measurements and the distribution are also presented.

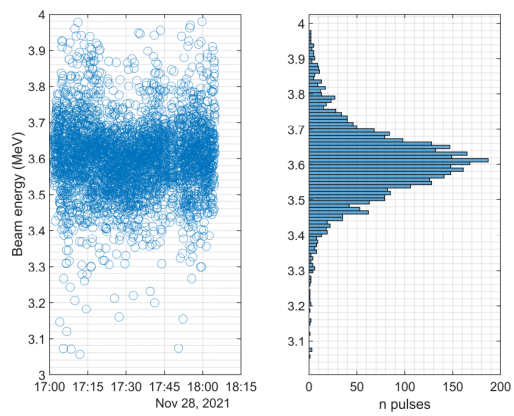


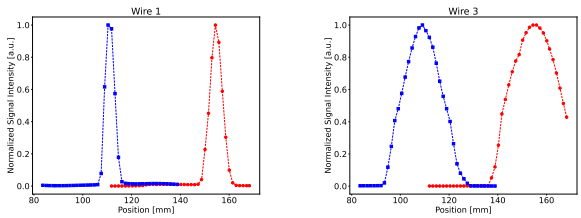
Figure 8: Time domain and energy distribution measurements over approximately one hour of machine operation as measured by the fast BPM.

ISBN: 978-3-95450-241-7 ISSN: 2673-5350 doi:10.18429/JACoW-IBIC2022-MOP07

DISTRIBUTION MEASUREMENTS

Wire Scans

The three MEBT WS stations on the beam line are a delivery from ESS Bilbao, while the full acquisition chain is an in-kind contribution from Elettra Sincrotrone Trieste in Italy. Secondary emission electrons provide the signal from 33 micron carbon wires. Horizontal and vertical wires are mounted on a single actuator that scans at a 45 degree angle from horizontal. Key specifications of the system include a time resolution of 1 µs, an accuracy of 0.1 mm and a dynamic range of 10^3. The system performance can be assessed after running through the verification process that includes a check of wire integrity, optimization of the bias voltage, and setting of the acquisition and motion parameters including scanning speeds, modes, gains and ranges [9]. Once these initial performance assessments were completed, the systems were further tested using high level data evaluation tools. Typical scan results with beam are depicted in Fig. 9.



(a) (b)

Figure 9: Raw scan results for the first (a) and last (b) wire scanners upstream of the MEBT Faraday Cup.

Emittance Scans

Developed as a collaboration between ESS in Lund and ESS Bilbao, the MEBT EMU consists of a slit with a 0.1 mm aperture followed by a wire grid 368 mm downstream. The wires in the grid are 35 microns in diameter and spaced 0.5 mm apart. Additional bias wires control the field seen by the secondary emission electrons, and during initial beam studies, the bias voltage was increased until it stopped affecting the signal. Following configurable gain stages, 5 MSa/s digitizers simultaneously acquire all 24 grid signals. Early in the beam tests, noise from the grid motor drivers was observed on these signals, so the scan software was modified to de-energize the drivers during signal acquisition. This enabled a measurement precision of about ±2 nA in a 200 kHz bandwidth.

After setting up the bias and the signal acquisition parameters, the focus turned to optimization of the scanning parameters. Figure 10 shows a typical scanning result, combining 8 separate scans of the slit. At each grid position, the slit position was scanned in steps of 0.5 mm. The angular resolution of the measurement was improved by taking multiple measurements at grid positions displaced by a fraction of the wire pitch. The angular range was increased by taking multiple sets of measurements with the grid displaced by its total size.

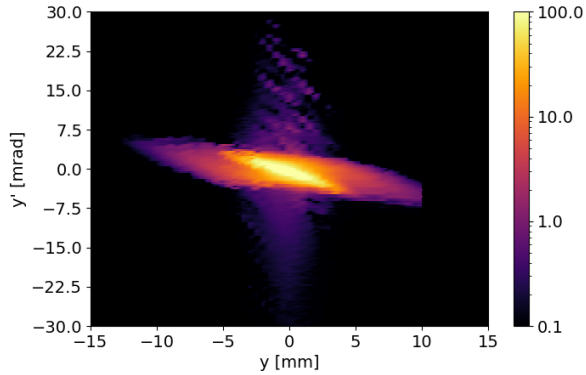


Figure 10: Phase-space measurement using the slit grid emittance scanner. The vertical phase space distribution is shown with a logarithmic intensity scale.

A specific, special beam optic was used for the EMU measurement with the goal of producing a large and divergent beam. The measurement shows a strong beam core with ±5 mm size surrounded by a halo of yet-to-be-determined origin. The low-level signal at |y'|>7.5 mrad around the beam core is assumed to be an artifact of the measurement – all signals disappear when the grid is moved to a position where the core of the beam misses the grid entirely. This data is being further analyzed for better understanding of the performance of the device and the beam optics.

OUTLOOK

All systems required for commissioning were verified and available for first protons. High level performance requirements were met and with some limitations, all of these systems were declared operational. In addition, several instruments were prepared for studies and acquired beam data for the first time. Operational experience revealed the need for some improvements that are underway in preparation for the next commissioning run. This upcoming run, currently scheduled for Spring/Summer of 2023 will take beam through the first 4 of 5 DTL tanks to about 70 MeV.

ACKNOWLEDGEMENTS

The authors appreciate the critical efforts of the many diagnostics and controls team members that brought these instrumentation systems to life. We also thank the operations and commissioning teams that devoted extended hours to beam tuning, studies and data acquisition.

REFERENCES

[1] R. Miyamoto *et al.*, "Beam Commissioning of Normal Conducting Part and Status of ESS Project," presented at LINAC'22, Liverpool, UK, Aug.-Sep. 2022, paper MO1PA02, to be published.

Content from this work may be used under the terms of the CC BY 4.0 licence (© 2022). Any distribution of this work must maintain attribution to the author(s), title of the work, publisher, and DOI

ISBN: 978-3-95450-241-7 ISSN: 2673-5350 doi:10.18429/JACoW-IBIC2022-MOP07

[2] N. Milas, M. Eshraqi, Y. Levinsen, R. Miyamoto, and D. Noll, "Beam Tuning Studies in the ESS MEBT," presented at IBIC'22, Krakow, Poland, Sep. 2022, paper MO2C2, this conferece.

[3] Y. Levinsen *et al.*, "First RF Phase Scans in the European Spallation Source," presented at IBIC'22, Krakow, Poland, Sep. 2022, paper TUP35, this conferece.

[4] T. J. Shea *et al.*, "Overview and Status of Diagnostics for the ESS Project," in *Proc. IBIC'17*, Grand Rapids, MI, USA, Aug. 2017, pp. 8–15. doi:10.18429/JACoW-IBIC2017-MO2AB2

[5] H. Hassanzadegan *et al.*, "Machine Protection Features of the ESS Beam Current Monitor System," in *Proc. IPAC'18*, Vancouver, Canada, Apr.-May 2018, pp. 2058–2060. doi:10.18429/JACoW-IPAC2018-WEPAF088

[6] H. Hassanzadegan *et al.*, "Beam Current Monitor System of the European Spallation Source," in *Proc. LINAC'14*, Geneva, Switzerland, Aug.-Sep. 2014, 526–528. https://jacow.org/LINAC2014/papers/TUPP041.pdf

[7] I. Dolenc Kittelmann *et al.*, "Neutron sensitive beam loss monitoring system for the European Spallation Source linac," *Phys. Rev. Accel. Beams*, vol. 25, p. 022 802, 2022. doi:10.1103/PhysRevAccelBeams.25.022802

[8] R. A. Baron *et al.*, "ESS Beam Position and Phase Monitor System," in *Proc. IBIC'19*, Malmö, Sweden, Sep. 2019, pp. 543–547. doi:10.18429/JACoW-IBIC2019-WEPP015

[9] C. S. Derrez *et al.*, "Wire Scanner Systems at the European Spallation Source (ESS): Tests and First Beam Commissioning Results," presented at LINAC'22, Liverpool, UK, Aug.-Sep. 2022, paper TUPOJO13, unpublished, 2022.

Content from this work may be used under the terms of the CC BY 4.0 licence (© 2022). Any distribution of this work must maintain attribution to the author(s), title of the work, publisher, and DOI

ISBN: 978-3-95450-241-7 ISSN: 2673-5350 doi:10.18429/JACoW-IBIC2022-MOP08

DEVELOPMENT OF A WAVEGUIDE BPM SYSTEM*

A. Lyapin†, W. Shields
John Adams Institute at Royal Holloway, University of London, Egham, UK

Abstract

A mode-selective waveguide beam position monitor (BPM) is under development. It is aimed primarily at electron linacs, although with its low impedance and wide bandwidth it could find alternative applications. In this paper we go over the design of the waveguide BPM system including the sensor and analog electronics, consider requirements to the digital processing and present some simulated results.

INTRODUCTION

Back in 2011, we reported on an idea of a mode-selective waveguide BPM, please, refer to [1] for full details and references to previous work. In a nutshell, we realised that waveguides can be made to selectively couple to the difference mode of the field travelling together with the beam by a special arrangement of coupling slots within the beampipe. At the same time, they suppress the common mode in a way similar to how selective coupling works in cavity BPMs and wakefield suppressing couplers in some accelerating structures. In this proceeding we report on a short project we ran recently that concentrated on advancing this idea towards a design of a complete BPM system. We also discuss the next steps towards a proof-of-principle test.

BENCH MEASUREMENTS

Previously a prototype waveguide BPM had been built for bench testing, Fig. 1. One of the tests carried out with this prototype since the last report was a linearity test. It was done by inserting an antenna into the beampipe to radiate a signal imitating the beam and measuring the transmission from the antenna to the outputs of the waveguide couplers. The aim was to demonstrate the linearity of the device by scanning the antenna position and looking at the corresponding change in the transmission from the antenna to the output port.

The result of this test is shown in Fig. 2. The plot presents the measured transmission coefficient on the complex plane. One can see that all the points lie on a straight line, so the position signal always comes in a certain phase, just like it is the case with cavity BPMs. This allows to separate the position signal from angle and reduce the out-of-phase noise and interference using a phase reference. The measured points corresponding to equal position steps are equidistant, which confirms the device's position linearity.

SENSOR DESIGN

With the encouraging results from bench testing we were able to start designing a prototype for beam measurements. As a starting point, we chose a beam aperture of 8 mm as

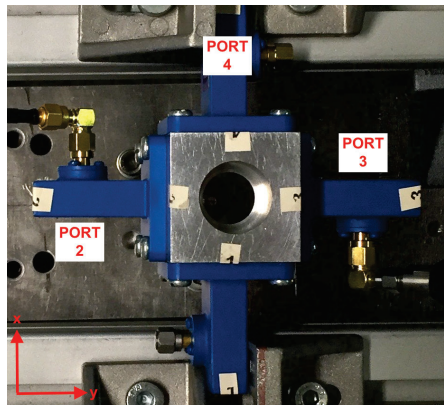


Figure 1: Prototype sensor on a test bench.

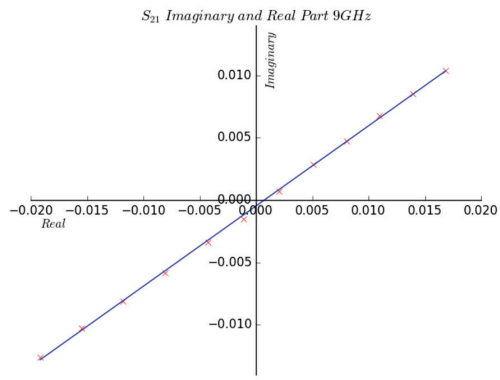


Figure 2: Port transmission measured with a moving antenna.

with little or no modification this would be a fitting design for most undulator beamlines of Free Electron Lasers (FEL). It is also compatible with such a major accelerator project as the Compact Linear Collider (CLIC) and its former test facility now CERN Linear Electron Accelerator for Research (CLEAR), which makes CLEAR a perfect location for future beam tests. We decided to choose 15 GHz as the nominal processing frequency as it was compatible with the selected beampipe diameter. Also, at 15 GHz the waveguide BPM processing can share some parts with the complementary cavity BPM programme running at CLEAR.

The design had thus been optimised for 15 GHz, which is roughly the middle of the chosen WR62 waveguide's passband. Using a Finite Difference Time Domain code GdfidL [2] we tuned the transmission of the difference mode of the beampipe into the output waveguide of the sensor. The resulting transmission curve is shown in Fig. 3. Depending on the chosen processing scheme, a wider or narrower part of the available bandwidth can be used, but up to 10 GHz bandwidth is available.

* Work supported by STFC Follow On Fund grant number ST/T003413/1
† alexey.lyapin@rhul.ac.uk

Content from this work may be used under the terms of the CC BY 4.0 licence (© 2022). Any distribution of this work must maintain attribution to the author(s), title of the work, publisher, and DOI

ISBN: 978-3-95450-241-7 ISSN: 2673-5350 doi:10.18429/JACoW-IBIC2022-MOP08

Content from this work may be used under the terms of the CC BY 4.0 licence (© 2022). Any distribution of this work must maintain attribution to the author(s), title of the work, publisher, and DOI

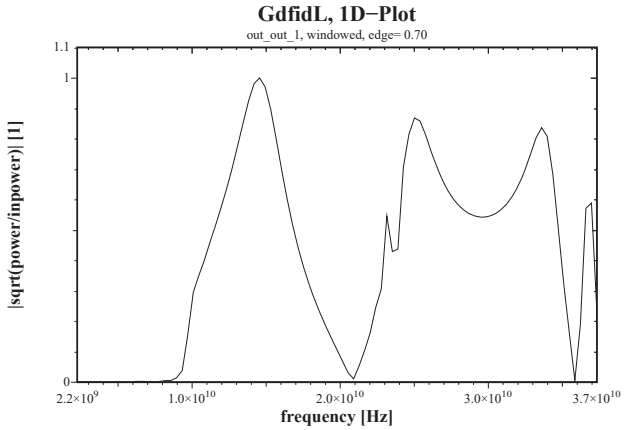


Figure 3: Coupling between the difference mode of the beam pipe and the output waveguide vs frequency.

The wide bandwidth of the waveguide sensor allows for it to be used with closely spaced bunches. One does not get any real boost in signal output (in contrast to cavity BPMs), but a long burst of pulses, such as the one computed for 100 bunches at CLEAR shown in Fig. 4, will produce distinct spectral lines, containing information on the average beam position and intra-beam offsets.

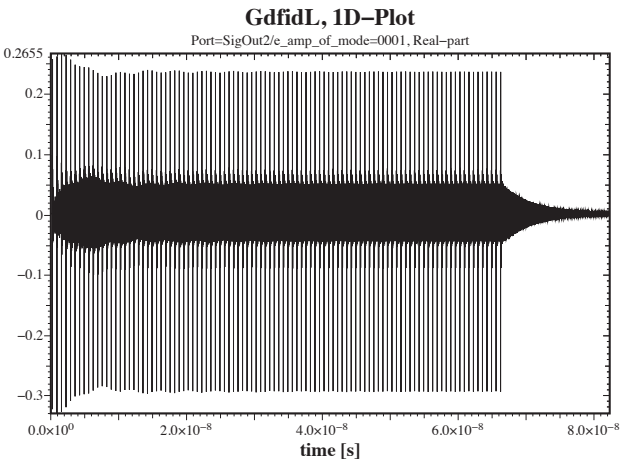


Figure 4: A burst of pulses generated by a long train of bunches.

VACUUM PROTOTYPE

The design of a vacuum prototype is reaching its final stages and is based around the application of radio frequency (RF) compatible vacuum seals [3]. The majority of machining can be done using conventional milling, although spark erosion may be required for the precision cuts of the coupling slots. A 3D view of the main block hosting the waveguide sensors is shown in Fig. 5. As in the figure, the beam would travel through a beampipe going in the vertical direction with output couplers on the sides of the block. Figure 6 shows a cross-section of the block revealing the arrangement of the coupling slot.

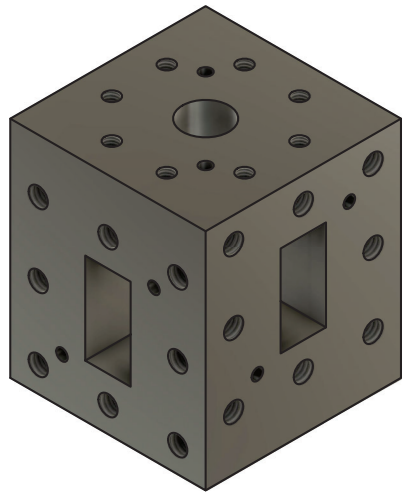


Figure 5: 3D view of the sensor block.

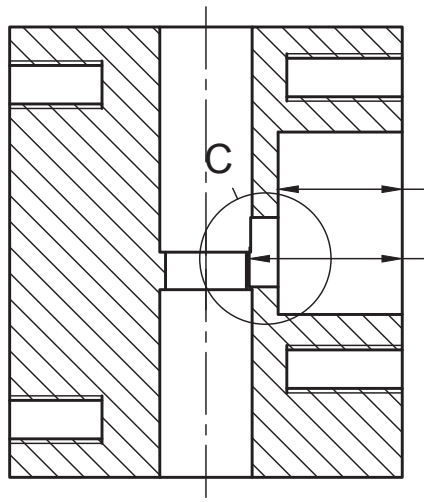


Figure 6: Cross-section of the sensor block showing the coupling slot opening into a section of the waveguide.

SIGNAL PROCESSING

Analogue Electronics

Analogue processing is fairly primitive at the moment and designed for flexibility and linearity rather than high sensitivity, Fig. 7. The chain includes a downconverting mixer followed by a wideband lowpass filter to suppress the high frequency components, primarily local oscillator signal leakage and up-converted input signal. Next there is an amplifier to boost the signal and curb the noise figure from further growth. A final bandpass filter is added to avoid aliasing of harmonics that may be produced by the mixer and amplifier during analogue to digital conversion. Cavity filters can be added to the input to suppress the image signal which may present a real issue with this broadband

ISBN: 978-3-95450-241-7 ISSN: 2673-5350 doi:10.18429/JACoW-IBIC2022-MOP08

sensor. The electronics have been assembled in a modular format, Fig. 8, so that changes can be easily introduced and the bandwidth of the system modified during experiments.

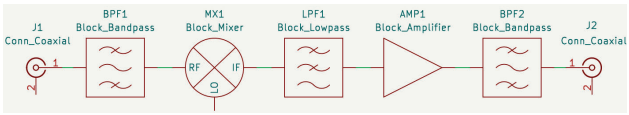


Figure 7: Block diagram of the processing electronics.

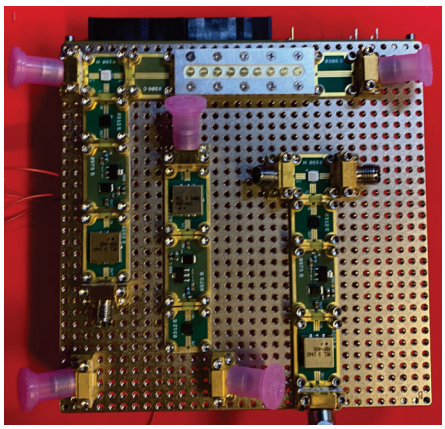


Figure 8: Modular signal processing electronics during the assembly.

Analogue to Digital Converter

The analogue to digital conversion is based on the Analog Devices' AD6676 [4] tunable bandpass $\Sigma - \Delta$ analog-to-digital converter (ADC) with up to 3.2 GSPS ADC clock rate. The interesting feature of this device is that it serves both as an ADC and an In-phase/Quadrature (I/Q) down-converter. Its output is decimated (up to 266 MSPS, 16 bit) complex data describing the amplitude and phase of the input signal. Traditionally, I/Q processing would be realised in an analogue circuit preceding the ADC. More recently, with the advances of high speed ADCs, this last stage would often follow the analogue to digital conversion. This novel converter removes the necessity of additional such processing altogether, which is beneficial to measurement systems, especially to those in which both the amplitude and phase of the signal need to be measured. At present, we are carrying out tests with an evaluation board built around the chip.

CONCLUSION

System design for a prototype waveguide BPM system is primarily complete, a prototype is underway and the subsystems are undergoing bench testing. Simulations show a promising performance in terms of sensitivity and bandwidth. This paper may be vague on detail, this is because the intellectual property (IP) rights have not yet been reserved, so we can not yet disclose the full details of the design. The next steps will involve finishing the prototype system and moving onto beam testing (which is subject to availability of further funding). Once the sensor is confirmed operational, we will start transferring the IP rights to a suitable partner for commercialisation. We are also considering an IP strategy in which the design would be open sourced. In this scenario, accelerator labs would be able to produce their own sensors with possibly a small licensing fee attached and kits for building the devices could be made available from the industrial partner alongside complete devices. Whether this will be possible will depend on various conditions including the funding source and industrial partnerships.

REFERENCES

[1] A. Lyapin, "Mode Selective Waveguide BPM", in *Proc. DIPAC'11*, Hamburg, Germany, May 2011, paper MOPD13, pp. 65–67.

[2] The GdfidL Electromagnetic Field Simulator, http://www.gdfidl.de/.

[3] VATSEAL vacuum RF seal technology from VATVALVE, https://www.vatvalve.com

[4] Analog Devices, AD6676 Wideband IF Receiver Subsystem, https://www.analog.com/en/products/ad6676.html

Content from this work may be used under the terms of the CC BY 4.0 licence (© 2022). Any distribution of this work must maintain attribution to the author(s), title of the work, publisher, and DOI

ISBN: 978-3-95450-241-7 ISSN: 2673-5350 doi:10.18429/JACoW-IBIC2022-MOP09

TOWARDS HIGHER STABILITY IN LARGE SCALE CAVITY BPM SYSTEMS*

A. Lyapin†, M. S. McCallum
John Adams Institute at Royal Holloway, University of London, Egham, UK
A. Aryshev, K. Kruchinin, High Energy Accelerator Research Organisation (KEK), Ibaraki, Japan

Abstract

In this contribution we consider a possible solution to long-term stability issues common in cavity BPM systems. The method will see a wider use active in-situ calibration systems injecting a tone into the measurement channel. We plan to compensate the bulk of the beam generated signal and so potentially extend the dynamic range of the electronics, reduce the amount of wakefield seen by the beam. The signal matching the real beam can then be used for mimicking the beam and calibrating out any drifts of the whole sensing and processing chain. We present the concept, give some simulated results and consider possible hardware solutions.

INTRODUCTION

In a large accelerator such as a Free Electron Laser (FEL) or a Collider, it is critical to ensure a stable and reproducible beam orbit. Therefore, beam position monitors (BPM) need to provide reliable readings during start-up and operation.

Most FELs employ cavity BPMs to achieve sub-μm resolution at low beam charge. Due to overall high stability requirements their machine tunnel is often kept at a very stable temperature, which reduces any drifts in cavity BPMs and allows them to achieve high stability [1]. This is not likely a plausible scenario for a Collider: it may be unreasonable to expect the same level of stability from a 30 km long facility. Therefore, a different solution may be required.

At KEK (Japan), ATF2 is a model of a collider beam delivery system which relies on cavity BPMs [2]. The facility typically operates over the workdays restarting on a Monday. Cavity BPMs are re-calibrated once a stable beam is available. For operational reasons, calibrations may take about 6-8 hours. While within a week cavity BPMs do not experience substantial drifts, calibrations are rarely transferable to the next week due to changing conditions. The cavity BPM system there is equipped with a subsystem generating a test tone, currently injected directly into the processing electronics. While this system demonstrated that the electronics are responsible for a small fraction of the observed drifts, with modifications it can inject a signal directly into the cavities. In this paper we discuss how the injected pulse can be utilised and how such a system could reduce operational and construction costs in a linear collider.

* Work supported by Royal Society International Exchanges IEC313050 and JAI institutional grant STFC ST/V001620/1
† alexey.lyapin@rhul.ac.uk

SYSTEM CONSIDERATIONS

Cavity BPM

Most cavity BPMs deployed at ATF2 use selective waveguide coupling and operate at 6424 MHz (C-band), Fig. 1. Two types of cavities are in use: position sensitive cavities operating the first dipole mode and smaller reference cavities with the first monopole mode tuned to the same frequency $f_{ref} = f_{pos}$ for phase and charge normalisation (Fig. 2). Using the pillbox approximation, the radii of the two types of cavities are then locked by the equality of their frequencies:

$$\frac{j_{01}}{R_{ref}} = \frac{j_{11}}{R_{pos}}, \tag{1}$$

where j_{nm} are Bessel function zeros. This would also mean that in the same environment for both cavities for a change of temperature ΔT the change in diameter is $\Delta R = \alpha \Delta T R$ and the two cavities experience the same frequency offset for a given change in temperature:

$$\frac{\Delta f_{ref}}{\Delta f_{pos}} = \frac{j_{01}}{R_{ref}(1-\alpha\Delta T)} \frac{R_{pos}(1-\alpha\Delta T)}{j_{11}} = 1. \tag{2}$$

However, this closed-cavity model does not take into account the effect of the beampipe, which usually has the same or a very similar diameter in both cavities. Moreover, the cavities always have a small frequency mismatch in the order of 2-3 MHz, varying from cavity to cavity. Together with changes in beam trigger timing these can result in significant phase drifts.

Let us estimate the frequency drifts numerically, again, using a simple model consisting of a cylindrical cavity with only a beampipe attached using the dimensions of ATF2 C-band cavities. The thermal expansion coefficient $\alpha = 17 \cdot 10^{-6}$ for copper. A one degree temperature change would result in the radii of the cavity and beam pipe to expand by 0.91 and 0.34 μm in the position cavity and by 0.65 and 0.27 μm in the reference cavity respectively. In terms of frequency, these changes would result in 39 + 17 = 56 kHz for the position and 251 − 36 = 215 kHz for the reference. Note that for the reference cavity the change in beampipe diameter even has the opposite sign as the perturbation introduced by the beampipe depends on the mode structure. While this actually helps reducing the reference's higher temperature sensitivity, it is still four times that of the position cavity. The temperature sensitivity does not appear so dramatic until it is expressed in terms of the phase advance it produces. These numbers result in about 19 and 72 degree

Content from this work may be used under the terms of the CC BY 4.0 licence (© 2022). Any distribution of this work must maintain attribution to the author(s), title of the work, publisher, and DOI

ISBN: 978-3-95450-241-7 ISSN: 2673-5350 doi:10.18429/JACoW-IBIC2022-MOP09

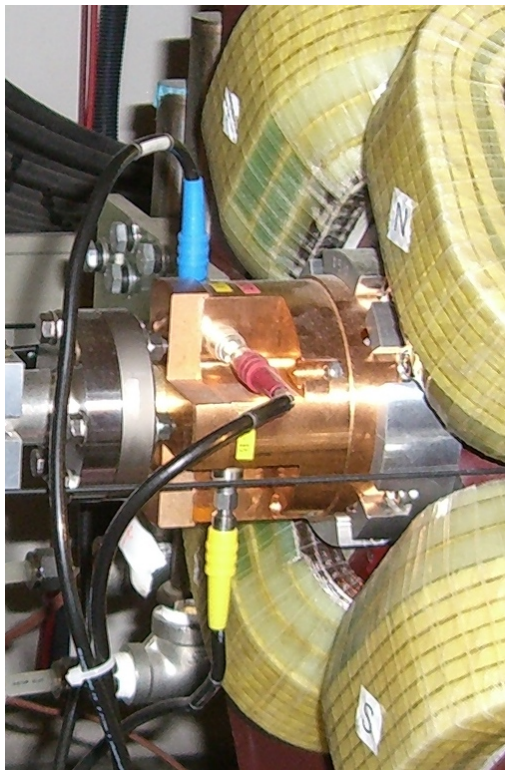


Figure 1: A C-band cavity BPM mounted in a quadrupole magnet in the ATF2 beamline at KEK.

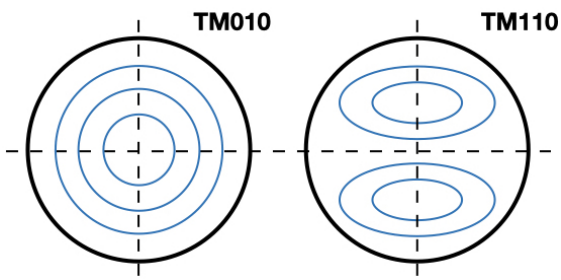


Figure 2: Magnetic field lines in a cylindrical cavity for the monopole (left) and dipole (right) modes.

changes for a quality factor of 6000! The difference is then 53 degrees, which results in a complete mix of the position and angle signals, with the measured position jitter contribution reduced to around 60%. Due to the operational cycle, the temperature in the ATF2 tunnel can change by several degrees, which completely demystifies week-to-week phase jumps observed throughout the operation [3].

Test Pulse

Ideally the test pulse would be equivalent to the electromagnetic pulse produced by the beam, several ps in duration and some 10's of kV in amplitude. This would then be filtered out by the different modes of oscillation possible in the resonating cavity and produce a beam-like signal. In practice, it is not efficient to try generating such a pulse using expensive specialised equipment and just waste most of its energy as it is distributed in a wide spectrum. Furthermore, feeding such a broadband pulse into a cavity presents a problem: most cavity BPMs use waveguide adapters with a bandwidth of 100's of MHz, so a (possibly dangerous) fraction of the pulse would have been reflected even before reaching the cavity.

There are two other possibilities: a continuous wave (CW) tone or a burst of radio-frequency (RF) oscillations. CW is the easiest option, but it does not satisfy the requirement that the system be calibrated with no beam present, it is preferable to have a time-evolving signal so that no assumptions have to be made. A short burst of RF, about a ns in duration, is still about 3 orders of magnitude longer than a beam pulse, but even for a state-or-the-art data acquisition (DAQ) system it is likely to be much shorter or comparable with the sampling time. Thus, the initial transient it may cause will not be noticeable for the system, hence this option appears to be the best one.

Following this discussion, we can summarise the approximate requirements for a test tone source: nanosecond level RF pulse duration, μW power. The shortest pulse duration available with standard laboratory pulse generators does not normally go below 5-10 ns. However, suitable off-the-shelf high speed pulse generators that can provide up to 5 V with 0.2-4 ns pulse duration are available [4].

MODELLING

A very simple model has been used to test the interaction of the beam pulses and RF bursts in a cavity. The cavity is represented by a single-pole filter with a centre frequency of 6424 MHz and a quality factor of 6000. As the beam excitation is instantaneous compared to the RF burst, a single sample in the simulated waveform is set in that case. The RF burst is a Gaussian-modulated sinewave with the same frequency and a σ = 1 ns. The results of the simulation are presented in Fig. 3.

Even this primitive simulation made us realise that the optimum timing for the test pulse is to reach half of its amplitude when the beam arrives. This way, the maximum amplitude the signal can reach is halved, and only for a short transient lasting for only half of the duration of the test pulse. With the correct timing, any static offsets can be significantly reduced and the dynamic range of the system used more efficiently.

Why is this important? Many cavity BPMs at ATF2 operate with static offsets between 0.5 and 1 mm. Due to mechanical limitations, it is not plausible to solve this problem by re-alignment. In the context of a linear collider, one would similarly want to minimise the requirements for re-alignment. The resolution typically degrades with increasing amplitudes due to non-linearities. The range for ATF2 cavities typically does not exceed 1 mm. Keeping the signals low improves the position resolution and allows for the full dynamic range of the electronics to be used for measuring the dynamic changes rather than static offsets. Another possible consequence of injecting a test pulse for compensation of static offsets is a significant reduction of

Content from this work may be used under the terms of the CC BY 4.0 licence (© 2022). Any distribution of this work must maintain attribution to the author(s), title of the work, publisher, and DOI

ISBN: 978-3-95450-241-7 ISSN: 2673-5350 doi:10.18429/JACoW-IBIC2022-MOP09

Content from this work may be used under the terms of the CC BY 4.0 licence (© 2022). Any distribution of this work must maintain attribution to the author(s), title of the work, publisher, and DOI

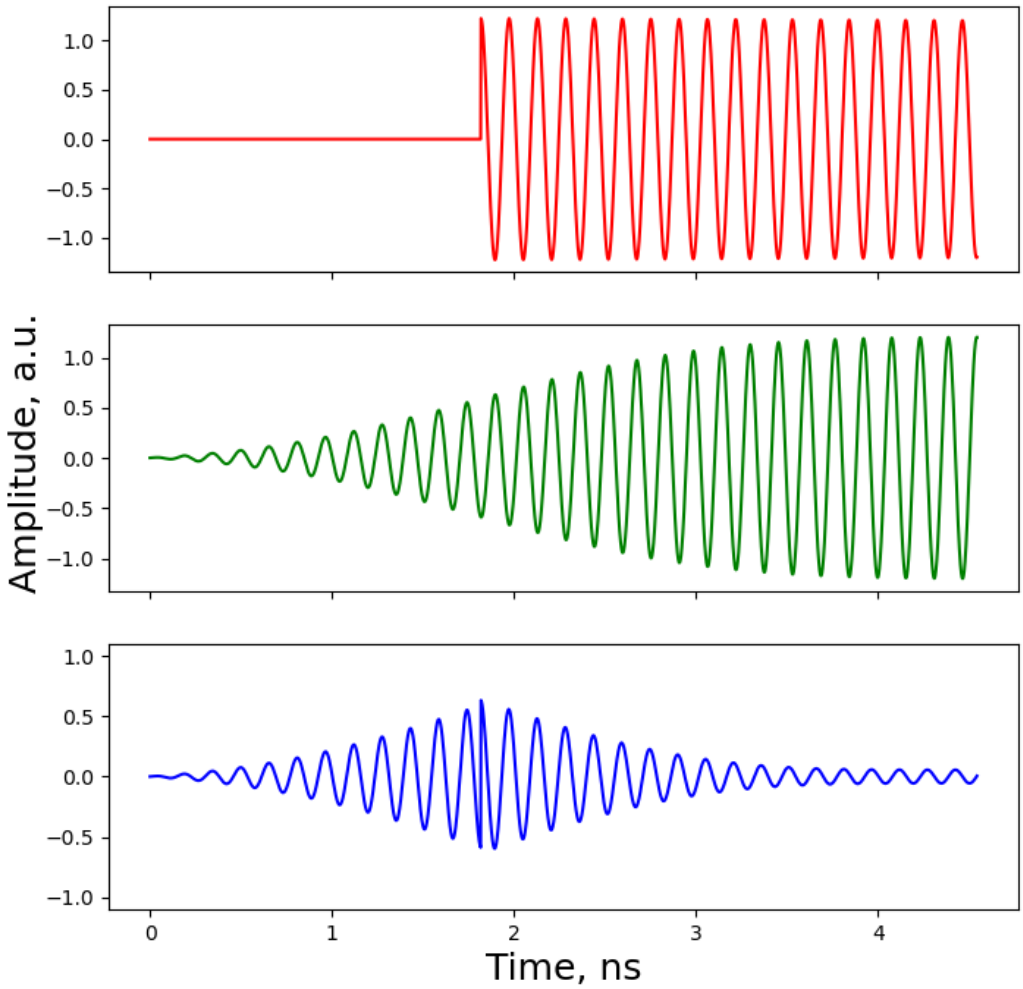


Figure 3: A set of simulated waveforms demonstrating the compensation scheme: beam signal (top), test tone (middle) and the resulting sum signal (bottom).

the wakefields acting back on the bunch. While unlikely to be a huge problem for short bunches in linear colliders, for ATF2 with its typical bunch length of about 7 mm, wakefields result in "banana" shaped bunches, which produce abnormally large projections in transverse directions. This effect complicates the transverse beam size measurements. Reducing the wakefields for cavity BPMs has been a hot discussion topic since they became a suspect in affecting the beam size measurements.

CONCLUSION

This paper lays ground to prototyping an active calibration and compensation system injecting a pulse of RF oscillations into cavity BPM sensors instead or together with the beam signal respectively. Using a very simplistic representation of a microwave cavity we have demonstrated how such a system may operate. However, its practical application will require some carefully judged design decisions to minimise any effect of the drifts in the test tone system itself on the calibration and measurements.

Further work will focus on testing this approach on a single cavity BPM using laboratory test equipment with and without beam. Once a suitable configuration is found, a dedicated set of hardware will be designed and tested.

REFERENCES

[1] D. Lipka, Performance and Plan for 2022 BPM System of the European XFEL, Report, https://confluence.desy.de/download/attachments/236820620/XFEL_BPM_plans_and_status_2021_version20201201.pptx?version=1&modificationDate=1639063854709&api=v2

[2] Y. I. Kim *et al.*, "Cavity beam position monitor system for the Accelerator Test Facility 2", *Phys. Rev. ST Accel. Beams*, vol. 15, p. 042801, 2012. doi:10.1103/PhysRevSTAB.15.042801

[3] A. Lyapin *et al.*, "Cavity BPM System for ATF2", in *Proc. DIPAC'11*, Hamburg, Germany, May 2011, paper MOOC02, pp. 23–25.

[4] AVTECH high speed pulse generators, https://www.avtechpulse.com/speed/.

ISBN: 978-3-95450-241-7 ISSN: 2673-5350 doi:10.18429/JACoW-IBIC2022-MOP10

REMOVING NOISE IN BPM MEASUREMENTS WITH VARIATIONAL AUTOENCODERS

J. P. Edelen, M. J. Henderson, J. Einstein-Curtis, C. C. Hall, RadiaSoft LLC, CO, USA
A. L. Romanov, Fermilab, IL, USA

Abstract

Noise in beam measurements is an ever-present challenge in accelerator operations. In addition to the challenges presented by hardware and signal processing, new operational regimes, such as ultra-short bunches, create additional difficulties in routine beam measurements. Techniques in machine learning have been successfully applied in other domains to overcome challenges inherent in noisy data. Variational autoencoders (VAEs) are shown to be capable of removing significant leevels of noise. A VAE can be used as a pre-processing tool for noise removal before the de-noised data is analyzed via other methods, or the VAE can be directly used to make beam dynamics measurements. Here we present the use of VAEs as a tool for addressing noise in BPM measurements.

INTRODUCTION

In recent years machine learning (ML) has been identified as having the potential for significant impact on the modeling, operation, and control of particle accelerators (e.g. see [1, 2]). Specifically, in the diagnostics space, there have been many efforts focused on improving measurement capabilities and detecting faulty instruments. Relatively recently, ML methods have been utilized to improve optics measurements from beam position monitor data [3]. Additionally, machine learning has been used to identify and remove malfunctioning beam position monitors in the Large Hadron Collider (LHC), prior to application of standard optics correction algorithms [4]. However, noise in BPM measurements remains an issue for processing in even functioning BPMs. The ability to remove noise from these measurements would greatly improve our ability to extract meaningful information from these instruments.

Variational autoencoders (VAEs) are a well established tool for noise reduction due to the enforcement of a smoothness condition in the latent-space representation. This feature of VAEs has been applied to gravitational wave research [5, 6] and geophysical data [7], for example. Recurrent autoencoders have the added advantage of being well suited to work with data sequences. In this paper we explore the use of Variational Recurrent Autoencoders (VRAEs) to remove different power law spectra (colors) of noise from simulated BPM data in a ring. We begin with a review of our data generation model, we then analyze the noise reduction capabilities for Gaussian noise. Finally we test our method using additive noise with different power law spectra.

DATA GENERATION

To simplify exploration of this noise removal technique in this work, we only consider data generated from a simplified model of a circular (periodic) accelerator with analytic solutions [8] . Rather than composing the accelerator of discrete focusing magnets we consider a uniform focusing channel with coupled optics. This reduces the problem to that of a coupled oscillator. We are only considering motion in the transverse plane, such that the equations of motion will be:

$$\begin{aligned} \frac{d^2x}{d\theta} + \nu_x x + Cy = 0 \\ \frac{d^2y}{d\theta} + \nu_y y + Cx = 0. \end{aligned} \tag{1}$$

Where C is the coupling strength and $\theta = 2\pi f t$ is the fractional revolution period in radians. The solutions to the coupled equations of motion will then be:

$$\begin{aligned} x(\theta) = A_x \cos(\nu_+\theta) + B_x \cos(\nu_-\theta) \\ y(\theta) = A_y \cos(\nu_+\theta) + B_y \cos(\nu_-\theta), \end{aligned} \tag{2}$$

with the coupled oscillation frequency given by:

$$\nu_\pm^2 = \frac{1}{2}\left(\nu_x^2 + \nu_y^2 \pm \sqrt{\left(\nu_x^2 + \nu_y^2\right)^2 + 4C^2}\right). \tag{3}$$

The principal goal of the analysis tools developed in this paper will be to extract correct, independent frequencies from noisy, periodic measurements of x and y. These are referred to as the tunes, ν_x and ν_y, in Eq. (1). The amplitude coefficients may be uniquely determined from the initial x and y positions, but are not included here as we do not use them in analyzing performance of the methods presented. Out dataset was generated with tune values ranging from 0.05 to 1.6 and a coupling parameter of 0.1. Figure 1 shows an example of this generated data.

To create test and training data x and y, position data is sampled as if from M BPMs placed around a ring so that BPM m will have a phase offset of $\varphi = 2\pi\nu m/M$. Noise in the measurements at each turn N is sampled from a normal distribution $\mathcal{N}(0, \sigma_M)$, where the variance σ_M, representing the noisiness of each BPM, has been set by sampling from a normal distribution $\mathcal{N}(0, \sigma_{noise})$.

The Variational Recurrent Autoencoder Model

For the VAE model, since we are analyzing time series data, we use a recurrent network architecture for the encoder and decoder, which we will refer to as a VRAE. The implementation of the VRAE architecture is based on [9] and uses Long Short-Term Memory (LSTM) units for both the

Content from this work may be used under the terms of the CC BY 4.0 licence (© 2022). Any distribution of this work must maintain attribution to the author(s), title of the work, publisher, and DOI

ISBN: 978-3-95450-241-7 ISSN: 2673-5350 doi:10.18429/JACoW-IBIC2022-MOP10

Content from this work may be used under the terms of the CC BY 4.0 licence (© 2022). Any distribution of this work must maintain attribution to the author(s), title of the work, publisher, and DOI

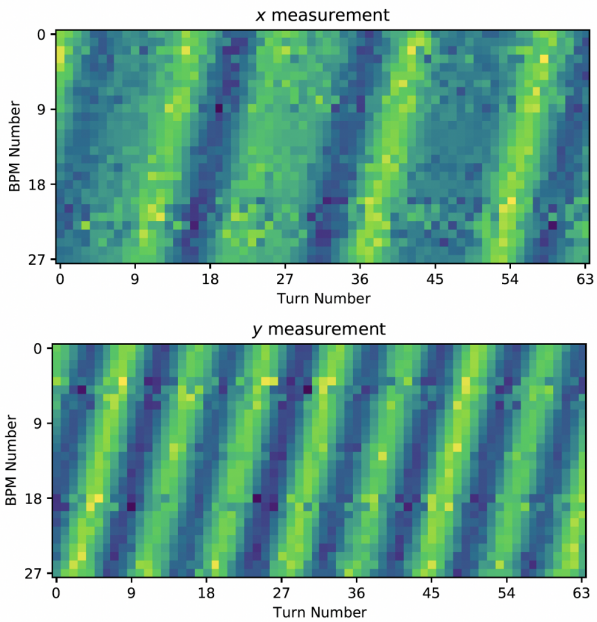


Figure 1: Example of data produced from discrete sampling of Eq. (2) to simulate BPM placement around a ring. Data was created with a Gaussian noise of $\sigma_{noise} = 0.25$ applied.

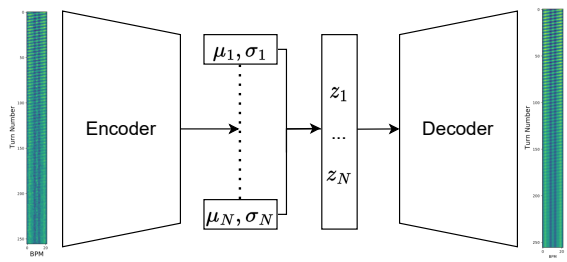


Figure 2: Structure of the VRAE showing encoder and decoder with latent layer parameterized in terms of mean μ_i and variance σ_i for the latent space distribution of dimension i.

encoder and decoder. A schematic of the VRAE is shown in Fig. 2. Both encoder and decoder contain 1 hidden layer of size 90. The latent space dimension was varied from 2 to 6. Linear layers are used to transform from the LSTM output to the distribution parameterization for sampling the latent space. The loss function is composed of two terms: the Kullback–Leibler divergence [10] — which acts as a regularization term — and the reconstruction loss. For the reconstruction loss, mean squared error between the encoder input and decoder output is used.

The VRAE was trained on generated data with a sequence length of 28 turns and with 56 features (28 BPM measurements of x and 28 measurements of y). Training data amplitude was initially normalized, however, this seemed to result in over-fitting and the model would show poor performance when applied to datasets with noise levels or periods that differed from the training set. Training with a dataset

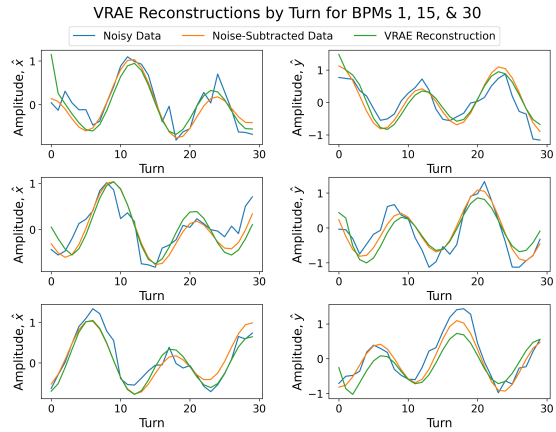


Figure 3: Comparison of autoencoder outputs and inputs without noise for several different BPMs.

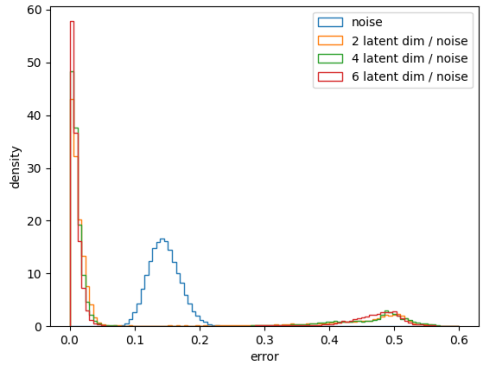


Figure 4: Histogram of the prediction error between the autoencoder output and the noise-subtracted signal for an autoencoder trained both with and without noise. Here we explore the sensitivity of the noise reduction capabilities to size of the latent space. The noise distribution is shown in blue for reference.

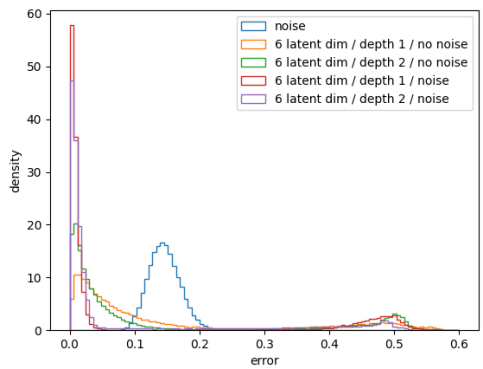


Figure 5: Histogram of the prediction error between the autoencoder output and the noise subtracted signal for an autoencoder trained both with and without noise. Here we explore the sensitivity of the noise reduction capabilities to the network depth. The noise distribution is shown in blue for reference.

ISBN: 978-3-95450-241-7 ISSN: 2673-5350 doi:10.18429/JACoW-IBIC2022-MOP10

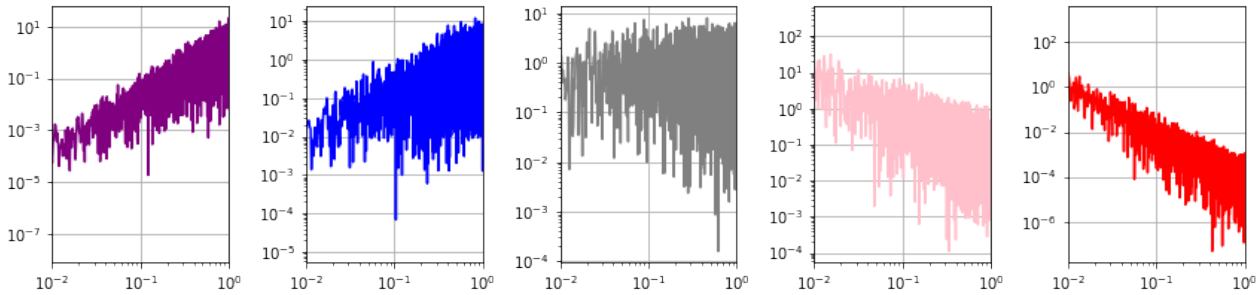


Figure 6: Power spectral densities for different colors of noise, with densities proportional to $1/f^{\beta}$. The factor β for each color of noise, from left to right, is two (violet), one (blue), zero (white), negative one (pink), and negative two (red).

of random initial amplitudes significantly improved overall performance.

Training for both types of autoencoders was performed in the RadiaSoft Sirepo computing platform on NVIDIA Tesla V100 GPUs. Datasets of 50 000 samples were generated from an analytic accelerator model with varying levels of noise, depending on testing to be run. From each dataset, 90% was used for training and 10% for validation.

GAUSSIAN NOISE REDUCTION

Before considering colored noise, we look at random Gaussian noise. Random Gaussian noise has a power spectrum identical to gray or white noise. We trained the autoencoder using data with random noise and compared the reconstruction to the input data with noise subtracted. We explored a wide range of configurations for training and testing, including different model structures. We trained on different noise levels, including on data without noise, to better understand the VRAE's noise reduction capabilities. First we considered training on 20% additive Gaussian Noise. Figure 3 shows a comparison of the autoencoder reconstruction, the noise subtracted data, and the noisy data, for the horizontal and vertical positions of three BPMs in our dataset. Here we see that the VRAE does a very good job of removing noise from the BPM data.

One way to quantify the level of noise is to compute the mean squared error for each BPM and then compute the mean squared error of the errors for all BPMs. Here the error is defined as the difference between the reconstruction and the input data with the noise subtracted. We computed the histograms of these errors over a number of trials and compared the results for several different test cases. Figure 4 shows the noise reduction capabilities of an autoencoder trained and tested on data with noise. Here we also vary the number of latent dimensions. Not only do we see a significant increase in the noise reduction capabilities of this network, but we also see an increase in the noise reduction effectiveness as we increase the number of latent dimensions. This test case is also more representative of operational data where one will not be able to remove the noise prior to training, and would instead be relying on the autoencoder to provide noise reduction.

Figure 5 compares the denoising ability of an autoencoder trained with and without noise, but while varying the number of latent layers of the network. Here the increased depth does appear to improve the noise reduction capabilities, but by far the largest effect is training with noisy data. In all cases there is a peak in the error around 0.5 — these are cases where the autoencoder does not do a good job of reconstructing the original signal.

COLORED NOISE

Our work thus far has been focused on Gaussian random noise, which has no amplitude dependence on frequency, making it white noise (gray in Fig. 6). In electronic systems operated under different environmental conditions, it is possible to have many different kinds of noise. To better understand how well this technique will generalize to real BPM systems, we explore the removal of different colors of noise. Colored noise referrers to power spectrum noise where the intensity of the noise varies with the frequency of the signal. White or gray noise has a uniform intensity with frequency. Pink noise is noise where the intensity is inversely proportional to the frequency in a $1/f$ relationship. For our study we explored denoisinig for four different types of power law noise. Figure 6 shows different spectra of power law noise with their color designations.

Figures 7 and 8 show the results for noise reduction on both Red and Violet noise, respectively, the spectral densities of which have the strongest dependence on frequency. In both cases the VRAE does a good job removing the noise and the results are fairly similar. There are subtle differences between the performance on the two different types of noise, but overall the VRAE is not sensitive to either noise type.

CONCLUSIONS

We have generated a test dataset using a linear optics model and used this dataset to evaluate the ability of VRAEs to remove different types of noise. We explored the effect of different VRAE architectures in conjunction with different noise types, thus demonstrating the efficacy of this technique under a variety of circumstances. Additional work is needed to better understand cases where the VRAE does a poor job of reconstructing signals, leading to an increase in effective

Content from this work may be used under the terms of the CC BY 4.0 licence (© 2022). Any distribution of this work must maintain attribution to the author(s), title of the work, publisher, and DOI

ISBN: 978-3-95450-241-7 ISSN: 2673-5350 doi:10.18429/JACoW-IBIC2022-MOP10

noise. Careful consideration for these edge cases will be important when implementing the method on operational data.

ACKNOWELDGEMENTS

This material is based upon work supported by the U.S. Department of Energy, Office of Science, Office of High Energy Physics under Award Number DE-SC0021699.

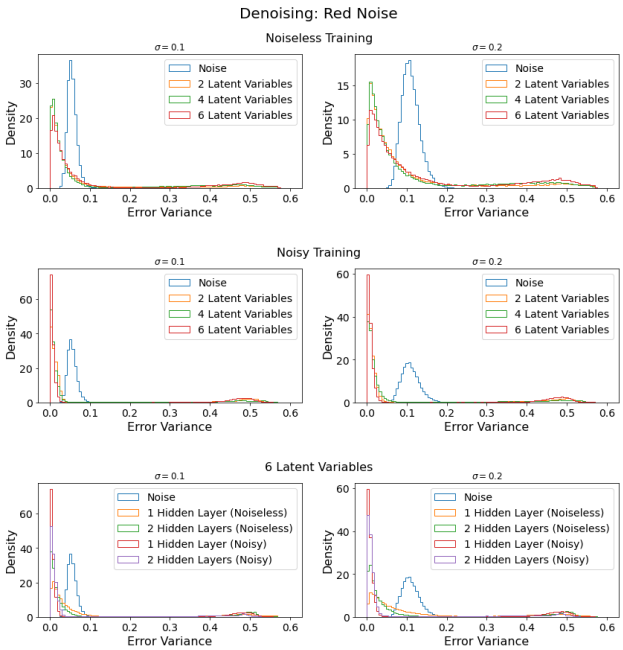


Figure 7: Noise reduction study for Red noise showing effective reduction of the noise spectrum.

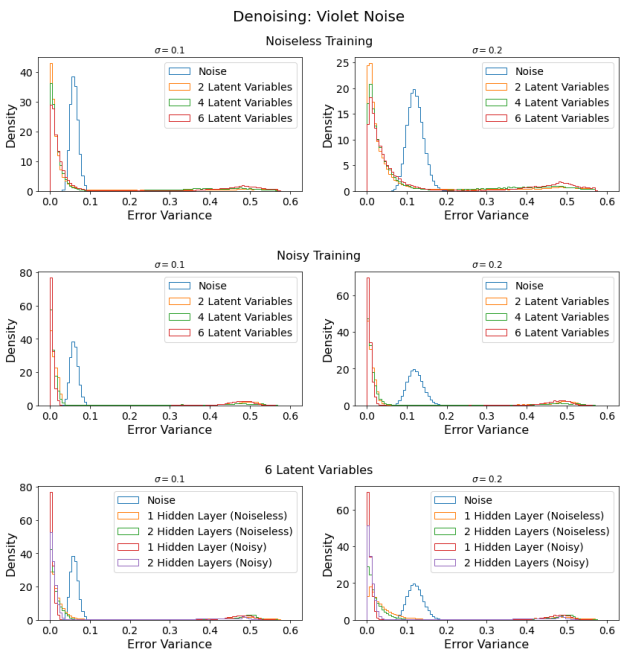


Figure 8: Noise reduction study for Violet noise showing effective reduction of the noise spectrum.

REFERENCES

[1] A. L. Edelen, S. G. Biedron, B. E. Chase, D. Edstrom, S. V. Milton, and P. Stabile, "Neural networks for modeling and control of particle accelerators," *IEEE Trans. Nucl. Sci.*, vol. 63, no. 2, pp. 878–897, 2016. doi:10.1109/TNS.2016.2543203

[2] A. Edelen *et al.*, "Opportunities in machine learning for particle accelerators," 2018. doi:10.48550/arXiv.1811.03172

[3] E. Fol, F. S. Carlier, J. M. C. de Portugal, A. Garcia-Tabares, and R. Tomas, "Machine Learning Methods for Optics Measurements and Corrections at LHC," in *Proc. IPAC'18*, Vancouver, Canada, Apr.-May 2018, pp. 1967–1970. doi:10.18429/JACoW-IPAC2018-WEPAF062

[4] E. Fol, J. M. C. de Portugal, and R. Tomás, "Unsupervised Machine Learning for Detection of Faulty Beam Position Monitors," in *Proc. IPAC'19*, Melbourne, Australia, May 2019, pp. 2668–2671. doi:10.18429/JACoW-IPAC2019-WEPGW081

[5] R. Ormiston, T. Nguyen, M. Coughlin, R. X. Adhikari, and E. Katsavounidis, "Noise reduction in gravitational-wave data via deep learning," *Phys. Rev. Res.*, vol. 2, p. 033 066, 2020. doi:10.1103/PhysRevResearch.2.033066

[6] G. Vajente *et al.*, "Machine-learning nonstationary noise out of gravitational-wave detectors," *Phys. Rev. D: Part. Fields*, vol. 101, p. 042 003, 2020. doi:10.1103/PhysRevD.101.042003

[7] D. Bhowick, D. K. Gupta, S. Maiti, and U. Shankar, "Stacked autoencoders based machine learning for noise reduction and signal reconstruction in geophysical data," 2019. doi:10.48550/arXiv.1907.03278

[8] X. Huang, S. Y. Lee, E. Prebys, and R. Tomlin, "Application of independent component analysis to fermilab booster," *Phys. Rev. ST Accel. Beams*, vol. 8, p. 064 001, 2005. doi:10.1103/PhysRevSTAB.8.064001

[9] O. Fabius and J. R. van Amersfoort, "Variational recurrent auto-encoders," 2015. doi:10.48550/arXiv.1412.6581

[10] D. P. Kingma and M. Welling, "Auto-encoding variational bayes," 2014. doi:10.48550/arXiv.1312.6114

Content from this work may be used under the terms of the CC BY 4.0 licence (© 2022). Any distribution of this work must maintain attribution to the author(s), title of the work, publisher, and DOI

ISBN: 978-3-95450-241-7 ISSN: 2673-5350 doi:10.18429/JACoW-IBIC2022-MOP12

PRODUCTION OF CAVITY BEAM POSITION MONITORS FOR THE ARES ACCELERATOR AT DESY

D. Lipka*, M. Holz, S. Vilcins
Deutsches Elektronen-Synchrotron DESY, Hamburg, Germany

Abstract

The SINBAD facility (Short and INnovative Bunches and Accelerators at DESY) hosts various experiments in the field of production of ultra-short electron bunches and novel high gradient acceleration techniques. The SINBAD facility, also called ARES (Accelerator Research Experiment at SINBAD), is a conventional S-band linear RF accelerator allowing the production of low charge ultra-short electron bunches within a range between 0.5 pC and 1000 pC. The positions of the low charge bunches will be detected by cavity beam position monitors. The principal design is based on the experience from the Eu-XFEL cavity beam position monitors. It consists of a 316 LN stainless steel body with a design loaded quality factor of 70, a resonance frequency of 3.3 GHz and a relative wide gap of 15 mm to reach a high peak position sensitivity of 4.25 V/(nC · mm). This poster covered, the manufacture of the individual mechanical parts, as well as presents the special features in the manufacture of customer designed UHV feedthroughs.

MOTIVATION

SINBAD is a dedicated accelerator R&D facility at DESY, Hamburg, and hosts the ARES linac (Accelerator Research Experiment at SINBAD). It consists of a normal conducting photo-injector and a 100 MeV S-band linear accelerator with beam repetition rates between 10 and 50 Hz for the production of low charge beams (0.5-30 pC) with (sub-) fs duration and excellent arrival time stability [1–4]. For dedicated user experiments bunch charges up to 1000 pC are foreseen. To observe the beam transverse position with highest precision the requirements include a resolution of 5 µm for a beam charge between 5 and 100 pC. To achieve this requirement a cavity beam position monitor (CBPM) is developed.

DESIGN

The CBPM consist of 3 stainless steel discs brazed together which forms the dipole and reference resonators. The dipole mode of the dipole resonator is coupled with 4 symmetric slots to reduce the influence of the monopole mode of the same dipole resonator [5]. The distance of both resonators is chosen to reduce the influence of the reference resonator monopole mode below −100 dB in the dipole resonator mode because both have the same frequency and would add a beam offset, this value corresponds to a maximum of 0.1 µm position offset. The antennas are coupled to the magnetic field of the resonance with multi-contact springs in the body which results in a connection in the body and therefore can not be used for tuning. In general the design is optimized to avoid any tuning in frequency and quality factors by defining all mechanical tolerances small enough to be prepared for mass production. The feedthroughs are connected to the body with flanges to be able to exchange them in case of failure, see Fig. 1. The design values are shown in Table 1.

Table 1: CBPM Design Properties [6]

	Dipole	**Reference**
f_L	3300.0 MHz	
Q_L	69.9	68.9
Q_0	1264	514
Q_{ext}	74.1	79.6
S	4.25 V/(nCmm)	44.5 V/nC

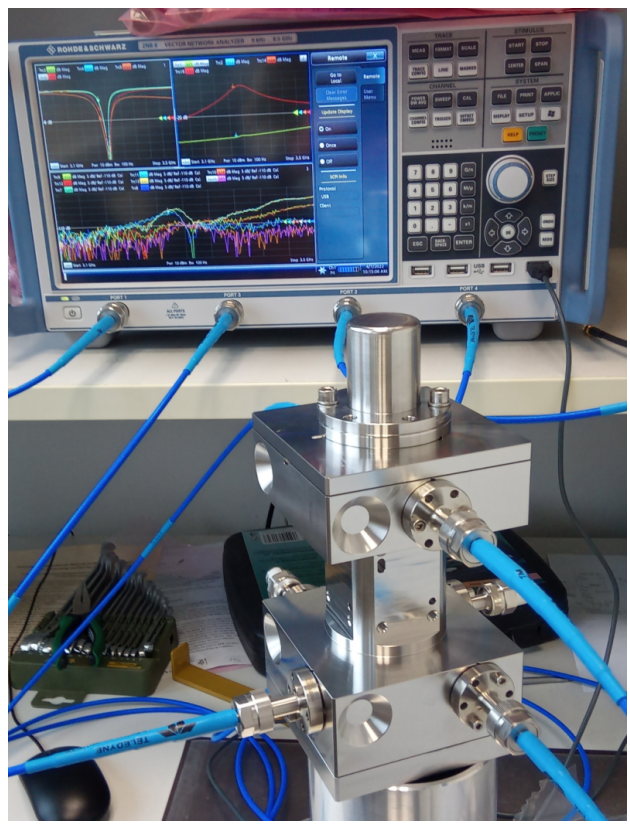


Figure 1: Photo of the CBPM in the laboratory during NWA measurement.

The design is similar to the one for the Eu-XFEL where a low quality factor is required for single bunch measurement with bunch repetition rate of up to 4.5 MHz [7]. The basis

* dirk.lipka@desy.de

Content from this work may be used under the terms of the CC BY 4.0 licence (© 2022). Any distribution of this work must maintain attribution to the author(s), title of the work, publisher, and DOI

ISBN: 978-3-95450-241-7 ISSN: 2673-5350 doi:10.18429/JACoW-IBIC2022-MOP12

Content from this work may be used under the terms of the CC BY 4.0 licence (© 2022). Any distribution of this work must maintain attribution to the author(s), title of the work, publisher, and DOI

is the design for SACLA [8]. The resonance frequency of 3.3 GHz is chosen because of the relative large beam tube of 34 mm such that the cut-off frequency is still higher. These design properties are similar to other already designed CBPMs at DESY for synergy reasons.

INFLUENCE OF FEEDTHROUGH

The RF design does not consider any influence of the feedthroughs. But during laboratory measurements an influence to the external quality factor was observed. Therefore the design of the feedthroughs are investigated with respect to the resonators of the CBPM. In Fig. 2 the dipole and the reference resonator external quality factors are simulated with the Computer Simulation Technology Studio Suite [9]. The feedthroughs are connected on the body with real distances and the permittivity of the isolator is varied. This results in a certain reflection which changes the external quality factor. In this simulation the permittivity is assumed to be the reason of the reflection but other reasons cause this reflection as well e.g. asymmetry of pin to the feedthrough body or different steps of the isolator and so on. The problem

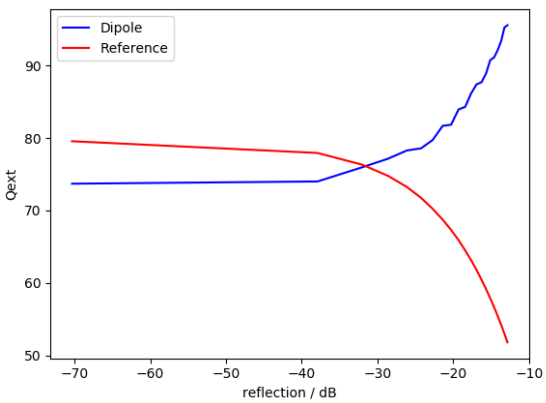


Figure 2: External quality factor as a function of feedthrough reflection for both resonators at 3.3 GHz.

of feedthrough reflection for the external quality factor is visible in Fig. 2 that with reflections above −40 dB the values diverge and causes larger differences in the loaded quality factor for both resonances. This means the dipole signal will gain a longer and the reference signal has a shorter decay time and the sensitivity for peak measurements is affected. The resonance frequency of both resonators are influenced too, see Fig. 3. Fortunately both frequencies are affected in the same manner and the difference of both resonance frequencies are small. The electronics could cover the change of frequency.

To compensate the influence of higher reflection one could change the distance of the feedthrough to the resonator; but this implies additional flanges and inner pin length which is difficult to realize and the influence of the connector and cable could add another change of the quality factor. Another possibility is to decrease the inner diameter of the

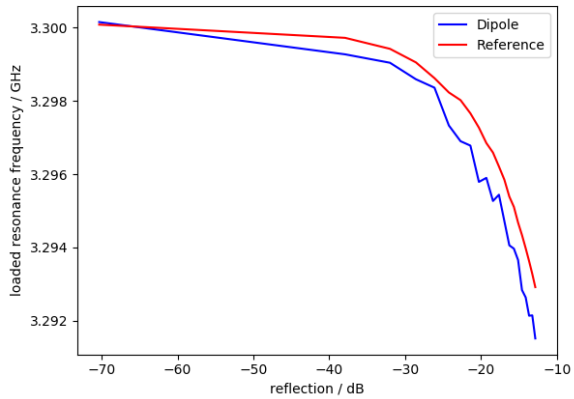


Figure 3: Resonance frequency as a function of feedthrough reflection for both resonators at 3.3 GHz.

gasket such that the reflected signals are compensated. But in simulation the compensation of reflections goes together with reduction of the sensitivity. Therefore feedthroughs with low reflections at the resonance frequency is required of <−30 dB. Still this will change the resonator properties but can be accepted and feedthrough companies should be able to produce them.

FEEDTHROUGH RESULTS

To verify the reflection of feedthroughs one needs a test-setup to avoid reflections at the open end. A possibility to measure the reflection is to mount two feedthroughs together with a certain gasket and pin to minimize the gap in between, see Fig. 4. This increases the reflection of this system



Figure 4: Photo of setup to measure reflection of two feedthroughs.

from a single feedthrough but can be compared with simulation of both together. We used feedthroughs which were developed together with the company BC-Tech in Switzerland [10]. The results of the reflection of a production in 2020 is shown in Fig. 5. The reflection at the resonance frequency of 3.3 GHz is larger compared to the simulation. In addition we investigated the homogeneity of the feedthrough isolator and found enclosed air volume within the isolator which is an indication of non-tightness. Measurements on the feedthroughs verified that few of them was not tight. The reflection of the system is about −20 dB which results that the single feedthroughs end up with about −25 dB. New production in 2022 where the design has been adapted to avoid enclosed air volume in the isolator and results in smaller

ISBN: 978-3-95450-241-7 ISSN: 2673-5350 doi:10.18429/JACoW-IBIC2022-MOP12

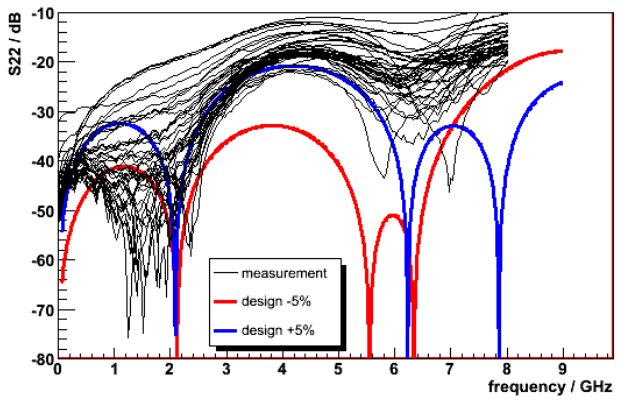


Figure 5: Reflection of two feedthroughs production at 2020 with expected reflections of the system by varying the permittivity by ±5%.

reflections, see Fig. 6. The production in 2022 show again higher reflection than simulated but is better compared to the production in 2020. For measurement of the CBPM mostly the feedthroughs with high reflection from 2020 are used until we observed a significant change of the external quality factor. Afterwards we used feedthroughs with lower reflection from the production of 2022.

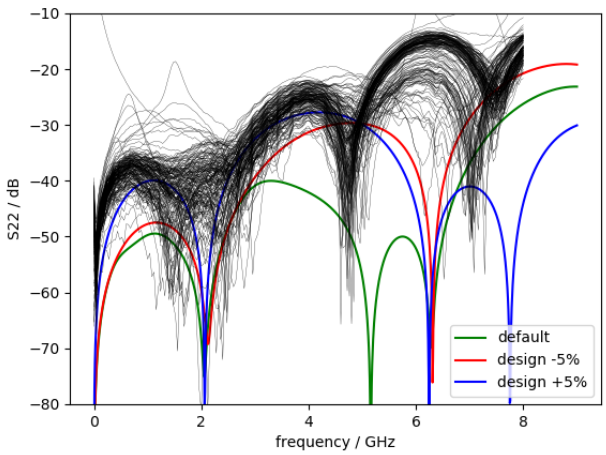


Figure 6: Reflection of two feedthroughs production at 2022 with expected reflections of the system by varying the permittivity by ±5%.

BODY MANUFACTURING AND MATERIAL

For this project, 25 CBPMs were fabricated from forged 316 LN ESR material at three different manufacturers. The raw material came from two different batches and was provided by DESY. The design was developed at DESY and all necessary technical documentation was also provided. The CBPM have CF flanges integrated directly into the body of the components. The aim is thus to obtain a compact design with the smallest possible dimensions.

If these components are then exposed to temperatures required for brazing, 316 LN ESR may loose some hardness. An example for this is shown in Fig. 7 where the hardness of a 316 LN ESR flange was measured before and after a heat treadment of 1110 °C (same procedure than for brazing). Thus, there are two challenges to overcome on these components, the first are the very tight tolerances and the second is compliance with ultra-high vacuum conditions of these parts better than 1×10^{-10} mbar leak rate.

197,5	------>	146,4
195,3	------>	144,5
199,8	------>	145,9
203,2	------>	146,4



Figure 7: Hardness measurements of 316 LN ESR before and after heat treatment with 1110 °C at four different position on the flange. The values are in Brinell Hardness (HB).

All three manufacturers have supplied components within specifications, but there are always discrepancies. These include component cleanliness (smaller threads and deep holes), surface finish, fits, and the manufacture of milled CF knife edges. The latter presents challenges for any manufacturer. The results of which very strongly influence the quality of the CF sealing area. The loss of hardness is a critical device criterion. Therefore a new material for the production of such devices is under development. First tests with the material 1.3964 (ESU) showed superior hardness properties. Further test with detailed heat treatment are foreseen in the future.

CBPM RESULTS

The resonance frequencies and quality factors of the CBPMs are measured in the laboratory before brazing the discs together, after brazing and after final mounting. These steps are chosen to identify problems as earliest as possible to be able to react on discrepancies. The measurements are

Content from this work may be used under the terms of the CC BY 4.0 licence (© 2022). Any distribution of this work must maintain attribution to the author(s), title of the work, publisher, and DOI

ISBN: 978-3-95450-241-7 ISSN: 2673-5350 doi:10.18429/JACoW-IBIC2022-MOP12

Content from this work may be used under the terms of the CC BY 4.0 licence (© 2022). Any distribution of this work must maintain attribution to the author(s), title of the work, publisher, and DOI

Table 2: Resonance Frequency in MHz

	Dipole	Reference
before brazing	3291.4 ± 1.6	3294.7 ± 6.4
after brazing	3293.1 ± 2.5	3294.3 ± 5.4
final assembly	3290.5 ± 1.2	3294.9 ± 1.4

done with a 4-port network analyzer and the reflected data are analyzed according [8].

In Table 2 the resonance frequency results are listed of all produced CBPMs according the mentioned steps. Not all CBPMs are already brazed and finally assembled: 25 CBPMs are measured before brazing, 11 after brazing and 8 after final assembling. Therefore the results presents different amount of CBPMs. The dipole resonance frequency is lower compared to the reference resonator which is according to the simulation result shown in Fig. 3. But the used feedthroughs for final assembling was with low reflection therefore a higher resonance frequency was expected from simulation. In Table 3, the loaded quality factor results are shown. Note that with low reflected feedthrough after final assembling the dipole quality factor becomes near to the design value; still the reference quality factor is lower than required. Fortunately the expected electronics will cover the difference [11]. The sensitivity of all 8 final assembled CBPMs are (4.482 ± 0.056) V/(nC · mm) for the dipole resonator and (48.1 ± 0.9) V/nC which is already larger than expected from simulations.

Table 3: Loaded Quality Factor

	Dipole	Reference
before brazing	85.2 ± 11.2	56.9 ± 3.7
after brazing	80.2 ± 7.8	63.0 ± 4.7
final assembly	73.6 ± 1.6	59.6 ± 1.9

SUMMARY

We produced some CBPMs for ARES. During production we observed an influence of the feedthrough to the dominating external quality factor. Therefore feedthroughs with low reflections are required which are produced, improved and re-produced. The stainless steel needs attention to keep the hardness during the brazing process.

REFERENCES

[1] U. Dorda *et al.*, "The Dedicated Accelerator R&D Facility Sinbad at DESY", in *Proc. IPAC'17*, Copenhagen, Denmark, May 2017, pp. 869–872. doi:10.18429/JACoW-IPAC2017-MOPVA012

[2] B. Marchetti *et al.*, "Status Update of the SINBAD-ARES Linac Under Construction at DESY", in *Proc. IPAC'17*, Copenhagen, Denmark, May 2017, pp. 1412–1414. doi:10.18429/JACoW-IPAC2017-TUPAB040

[3] E. Panofski *et al.*, "Status Report of the SINBAD-ARES RF Photoinjector and LINAC Commissioning", in *Proc. IPAC'19*, Melbourne, Australia, May 2019, pp. 906–909. doi:10.18429/JACoW-IPAC2019-MOPTS026

[4] F. Burkart *et al.*, "The Experimental Area at the ARES LINAC", in *Proc. IPAC'19*, Melbourne, Australia, May 2019, pp. 867–870. doi:10.18429/JACoW-IPAC2019-MOPTS014

[5] V. Balakin *et al.*, "Experimental results from a microwave cavity beam position monitor", in *Proc. PAC'99*, New York, USA, March 1999, pp. 461–464. doi:10.1109/PAC.1999.795732

[6] D. Lipka, M. Dohlus, M. Marx, S. Vilcins, and M. Werner, "Design of a Cavity Beam Position Monitor for the ARES Accelerator at DESY", in *Proc. IBIC'18*, Shanghai, China, Sep. 2018, pp. 269–272. doi:10.18429/JACoW-IBIC2018-TUPB05

[7] D. Lipka, D. Nölle, M. Siemens, and S. Vilcins, "Development of Cavity BPM for the European XFEL", in *Proc. LINAC'10*, Tsukuba, Japan, Sep. 2010, paper TUP094, pp. 629–631.

[8] H. Maesaka *et al.*, "Sub-micron resolution rf cavity beam position monitor system at the SACLA XFEL facility", *Nucl. Instrum. Methods Phys. Res., Sect. A*, vol. 696, pp. 66-74, 2012. doi:10.1016/j.nima.2012.08.088

[9] Computer Simulation Technology, http://www.cst.com

[10] BC-Tech AG company, https://bctech.ch/.

[11] B. Lorbeer *et al.*, "Cavity BPM Electronics for SINBAD at DESY", presented at IBIC'22, Krakow, Poland, Sep. 2022, paper WEP14, this conference.

ISBN: 978-3-95450-241-7 ISSN: 2673-5350 doi:10.18429/JACoW-IBIC2022-MOP13

TEST AND MEASUREMENTS RESULTS OF THE PILOT TONE FRONT END INDUSTRIALIZATION FOR ELETTRA 2.0

G. Brajnik*, R. De Monte, Elettra Sincrotrone Trieste, Trieste, Italy
M. Cargnelutti, U. Dragonja, P. Leban, P. Paglovec, B. Repič, A. Vigali
Instrumentation Technologies, Solkan, Slovenia

Abstract

Elettra 2.0 will be the low-emittance upgrade of the present machine, a third-generation lightsource based in Trieste, Italy. The new machine, foreseen to be completed in 2025-2026, will be equipped with 168 beam position readout systems divided into 12 cells. The BPM electronics will be based on the prototypes developed by the laboratory, relying on the pilot-tone compensation technique for assuring the required resolution and long-term stability. The industrialization and production of the BPM electronics system are being carried out in partnership with Instrumentation Technologies, a company that has experience with BPM readout systems within the accelerator field. This paper will present the results of the industrialization of one of BPM system's key component: the Pilot Tone Front End, focusing on its improvements introduced on electronic and mechanical sides, giving not only a significant performance gain with respect to the previous prototype but also improving robustness and reliability. An overview of the testing procedures that will assure the performance repeatability of the series will also be provided.

INTRODUCTION

In previous conferences we already presented the overall development of the new electron beam position monitoring system for Elettra 2.0, the low-emittance upgrade of the Italian synchrotron, from the early pilot tone proof of concept [1] to the integration of the complete prototype system in Elettra's global orbit feedback [2]. The partnership signed with Instrumentation Technologies has accelerated the process towards the final industrialized system, foreseen to be installed in 168 locations of the new machine in 2025-2026. In particular, thanks to the modular approach, we firstly focused on the improvement of the pilot tone front end (PTFE) [3] before moving to the digital acquisition unit. In this paper we present the industrialization results of the former, a mature product ready to be produced in series.

MECHANICAL AND ELECTRONIC IMPROVEMENTS

In Ref. [3] we listed the foreseen improvements, such as the possibility of changing the bandpass filter, the extra gain stage, the single board design, the integrated power over ethernet feature. After implementing them, further modifications have been made for increasing reliability and performance.



Figure 1: Pilot Tone Front end.

Shielding and heat management: a large-area aluminium heatsink has been applied over the PCB, with mounting holes for future installation on girders: this allows for an homogeneous heat distribution and adequate dissipation (see Fig. 1). The heatsink serves also as an EMI shield, covering all the RF traces. In addition, another aluminium block completely covers the filters section, reducing external temperature influence.

Amplifiers matching: input and output matching of RF amplifiers that are inside the front end was improved, in order to reduce as much as possible signal reflections and standing waves, with a trade-off between topology of matching circuit, number and value of its components and performance and repeatability of the design. Still, the obtained gain with respect to the original prototype is significant: S_{11} parameter went from −14 dB to −31 dB and S_{22} parameter from −14 dB to −26 dB, measured at 500 MHz.

Ethernet controller: the Ethernet to UART communication chip has been changed from Lantronix to Wiznet, due to PoE compatibility of the latter. The new design is about ten times cheaper, with benefits in term of lower EMI, lower generated heat and power consumption.

Pilot tone generation: accuracy and phase noise of the internal pilot tone generator have been improved: the former has been increased with carefully tuning of crystal's load capacitors, the latter reduced with a new implementation of PLL's loop filter. In addition, the user can choose an external source for supplying the pilot signal.

* gabriele.brajnik@elettra.eu

Content from this work may be used under the terms of the CC BY 4.0 licence (© 2022). Any distribution of this work must maintain attribution to the author(s), title of the work, publisher, and DOI

ISBN: 978-3-95450-241-7 ISSN: 2673-5350 doi:10.18429/JACoW-IBIC2022-MOP13

Content from this work may be used under the terms of the CC BY 4.0 licence (© 2022). Any distribution of this work must maintain attribution to the author(s), title of the work, publisher, and DOI

Power management: the power tree has completely rearranged. Now the overall load is evenly distributed among the voltage regulators, and their dropout voltage has been lowered in order to reduce the dissipated power.

PERFORMANCE RESULTS

A dedicated setup in two climatic chambers has been prepared to evaluate the effectiveness of the compensation on cables (see Fig. 2): all the active devices (generator, PTFE and readout electronics) were held at constant temperature and humidity, while a temperature profile was applied in the chamber containing only one cable (LMR-195, 20 metres). It has to be noted that this is a worst case scenario, since in real environments the temperature variation will affect all the four cables more or less in the same way, reducing the produced drift on the calculated position. Three temperature profiles have been applied, a step from 25 to 15 °C, a slow ramp from 15 to 35 °C and another step from 35 to 25 °C.

Results are quite the same for the various profiles, and are shown in Table 1, where the previous PTFE prototype has been compared with the new industrialized version. A reduction of about 4 times of the temperature dependence on the compensated position has been obtained, proving benefits from the improvements made.

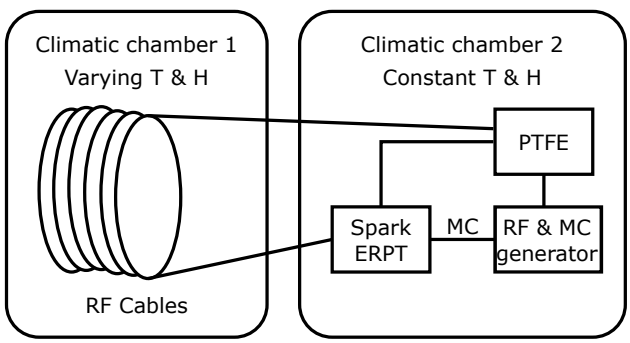


Figure 2: Climatic chamber setup.

Table 1: Compensation Effectiveness

	X/T (non comp.) [µm/K]	XC/T (comp.) [µm/K]
25 °C-15 °C step		
Prototype	-8.2	-3.7
PTFE	-6.5	0.9
15 °C-35 °C ramp		
Prototype	-7.8	-3.65
PTFE	-6.3	1.0
35 °C-25 °C step		
Prototype	-7.9	-3.6
PTFE	-6.2	1.0

Tests at Elettra

In addition to measurements performed in controlled environment, tests have been made also in a real scenario, where temperature and humidity can change.

So, we put the PTFE in Elettra service area: its outputs were connected with high-quality short cables to an in-house developed digitizer already presented in Ref. [4]: the processing chain is described in Ref. [5]. Position calculation is expressed in nanometers, with a scale factor of 20 mm, and an equivalent bandwidth of 10 Hz. As a source, we used the signal coming from a single Elettra storage ring pickup splitted in four, in order to emulate a stable beam.

Figure 3 shows the results of a long-term measurement in a 12-hour time window. Machine was running at 2 GeV, with 310 mA of current (top-up mode) and a standard multibunch filling pattern (80%). Digitizer was locked to machine clock and RF frequency was 499.654 MHz.

Standard deviation on calculated positions were 32 nm for the horizontal plane and 51 nm for the vertical plane. In both planes, position remained within ±150 nm peak-to-peak.

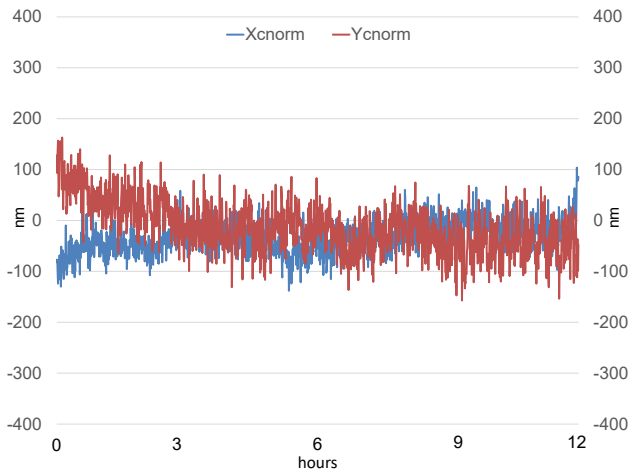


Figure 3: Long-term measurement with short cables in a 12-hour window.

Subsequently, we decided to change connection cables from PTFE to digitizer with longer ones (LMR-195, 20 metres), in order to simulate a common situation in beam diagnostics (PTFE in machine tunnel and digitizer in service area). The source was changed to an RF generator that emulates the beam with the same filling pattern, due to scheduled maintenance of the accelerator. The time window was extended to 24 hours. Results are reported in Fig. 4.

Standard deviation on calculated positions increased to 62 nm for the horizontal plane and 120 nm for the vertical plane. In both planes, position remained within ±300 nm peak-to-peak. Performance worsening is due to cable losses and to temperature and humidity variation during the measurement (see Fig. 5).

ISBN: 978-3-95450-241-7 ISSN: 2673-5350 doi:10.18429/JACoW-IBIC2022-MOP13

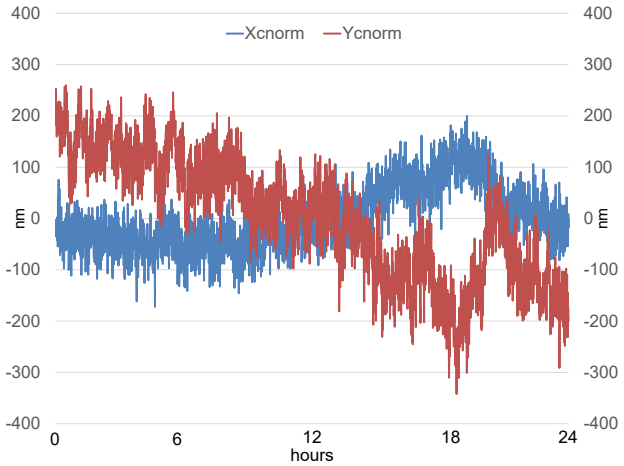


Figure 4: Long-term measurement with long cables in a 24-hour window.

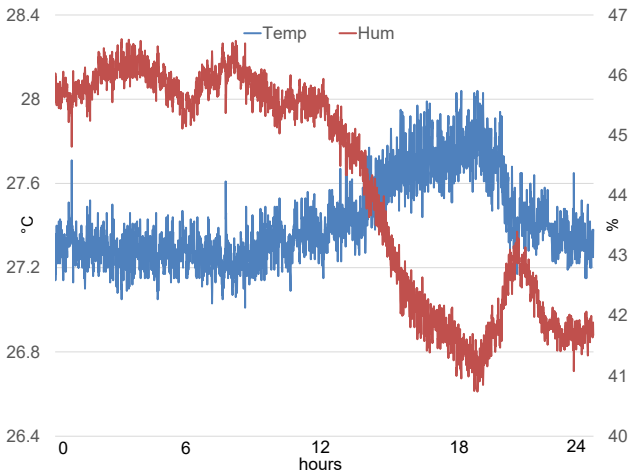


Figure 5: Temperature and humidity variation during 24-hour long-term measurement.

FAT PROCEDURE

Rigorous testing is performed to ensure similar and within-spec operation of all mass-produced units. With every new product rolling off the production line, it is important to set up effective factory acceptance tests (FAT) early in the product's lifespan. Here lies another balancing act of specifying pass-fails early enough to automate the process but also to specify them on enough samples, so that they are effective in detecting defects and don't detect many false positives (test sensitivity and specificity). FATs are also a good opportunity to collect additional statistics about the system while lengthening the whole FAT for only a couple of percent. This can be used later to define better pass-fails or better understand the system. FATs are divided in three categories:

Checking Basic Functionalities

With visual inspection we confirm that all visible components are at their designated place and the lack of physical damage to the unit indicates that it went through a correct assembly process. Status LEDs are toggled to confirm that all visual interfaces are in good working condition.

Next, a connection to the PTFE is established over telnet to check power supply voltages and currents and compare them to pre-defined pass-fails. Normal working temperature is also checked after initial warmup. Optic latch is visually checked for light pulses when changing attenuators.

RF Signal Chain

Every component along the RF signal chain is included in at least one test case, to ensure correct operation. Testing setup is presented in Figs. 6 and 7. A R&S SMB100A signal generator is used for the RF signal and to provide the reference clock to the AWG, spectrum analyzer and indirectly also the machine clock for a Libera Spark ERPT, used as readout electronics.

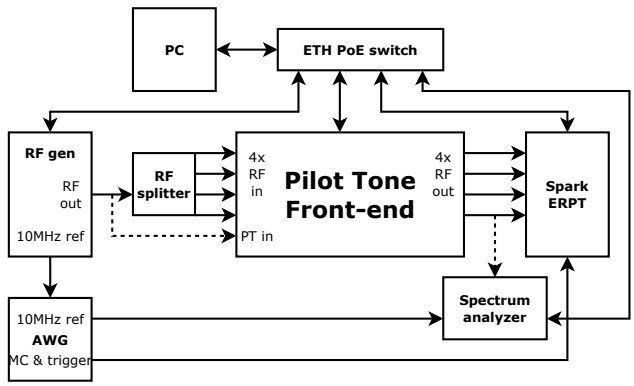


Figure 6: Test setup diagram.

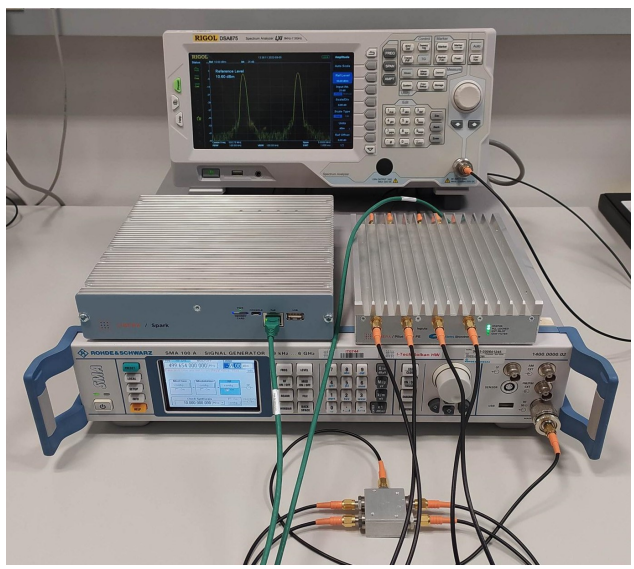


Figure 7: FAT testbench.

With the spectrum analyzer we determine the accuracy of the pilot tone frequency and amplitude and the RF signal amplitude on PTFE inputs and outputs. The latter ensures

Content from this work may be used under the terms of the CC BY 4.0 licence (© 2022). Any distribution of this work must maintain attribution to the author(s), title of the work, publisher, and DOI

ISBN: 978-3-95450-241-7 ISSN: 2673-5350 doi:10.18429/JACoW-IBIC2022-MOP13

Content from this work may be used under the terms of the CC BY 4.0 licence (© 2022). Any distribution of this work must maintain attribution to the author(s), title of the work, publisher, and DOI

same power levels regardless of the cables used. The internal pilot tone generator is checked to verify that the PLL remains locked with various frequency settings and that it outputs a signal with consistent power. A frequency sweep is performed on both band-pass filters on all four channels.

For the following tests, an internal Libera Spark ERPT is used to evaluate the compensation effectiveness and to quickly assess all four signal paths of the PTFE. We measure signal-to-noise of each channel with following signal combinations: only RF signal present, only PT from internal generator, only PT from external generator and both RF and PT combined. Signal-to-Noise ratio is defined as $20\log_{10}(\mu/\sigma)$ of 10k samples of fast 10 kHz data. All measurements are done for multiple different attenuator settings on the PTFE. RF generator output is varied so that we have a constant power on the Libera Spark and measure just the properties of the PTFE. With this we also check that all attenuators and amplifiers (three gain stages in total) are in working order. Short example measurement results in Fig. 8.

Crosstalk is measured between all channel combinations and a minimum of 50 dB isolation is guaranteed.

RF generator + Internal PT						Signal-to-Noise				
Power [dBm]	pt_att [dB]	att_1 [dB]	att_2 [dB]	att_3 [dB]	max adc	A [dB]	B [dB]	C [dB]	D [dB]	Limit [dB]
-20	0	0	20	30	5461	84,0	84,1	83,9	84,0	80
-25	5	0	15	30	5464	83,8	84,0	83,9	83,8	80
-30	10	0	10	30	5504	82,3	82,5	82,3	82,4	80

Figure 8: FAT result example.

Long-term Measurements

The above-mentioned tests are performed on every unit, and since they are all automated, they take less than half an hour to be performed. To balance rigor and effectiveness, one unit out of 10 is tested for a longer period (typically 14 hours), to re-verify long-term behaviour and to root out any systematic defects. Either from components being from different batches, or some other unpredictable factor. In this case, the instrument is left on in the test setup over night with both RF and internal PT signals present and compensated data at 10 Hz rate is logged. A slow and monotonous temperature change is expected overnight and from that the temperature coefficient of position is calculated, with the pass-fail set to 4 µm/K in both directions.

CONCLUSION

The industrialization phase of the Pilot Tone Front End has been concluded: several improvements increased its overall quality, both in terms of performance and reliability. A dedicated quality control procedure has been developed in order to assure that all produced units will satisfy the requirements.

However, the worldwide shortage of electronic components remain a critical issue, currently faced with continuous monitoring of delivery dates and availability, weekly meetings to keep the parties informed and constant iterations to find acceptable solutions (e.g. equivalent parts from different suppliers, wise PCB design for mounting different alternatives, etc).

REFERENCES

[1] G. Brajnik, S. Bassanese, S. Carrato, G. Cautero, and R. De Monte, "A Novel Electron-BPM Front End With Sub-Micron Resolution Based on Pilot-Tone Compensation: Test Results With Beam", in *Proc. IBIC'16*, Barcelona, Spain, Sep. 2016, pp. 308–311. doi:10.18429/JACoW-IBIC2016-TUPG02

[2] G. Brajnik, S. Bassanese, G. Cautero, S. Cleva, and R. De Monte, "Integration of a Pilot-Tone Based BPM System Within the Global Orbit Feedback Environment of Elettra", in *Proc. IBIC'18*, Shanghai, China, Sep. 2018, pp. 190–195. doi:10.18429/JACoW-IBIC2018-TUOC01

[3] G. Brajnik, M. Cargnelutti, R. De Monte, P. Leban, P. Paglovec, and B. Repič, "Current Status of Elettra 2.0 eBPM System", in *Proc. IBIC'21*, Pohang, Rep. of Korea, May 2021, pp. 71–74. doi:10.18429/JACoW-IBIC2021-MOPP16

[4] G. Brajnik, S. Cleva, R. De Monte, and D. Giuressi, "A Common Diagnostic Platform for Elettra 2.0 and FERMI", in *Proc. IBIC'19*, Malmö, Sweden, Sep. 2019, pp. 280–282. doi:10.18429/JACoW-IBIC2019-TUPP003

[5] M. Colja, S. Carrato, G. Brajnik and R. De Monte, "Design and Implementation of an FPGA-Based Digital Processor for BPM Applications", presented at IBIC'22, Krakow, Poland, September 2022, paper MOP14, this conference.

ISBN: 978-3-95450-241-7 ISSN: 2673-5350 doi:10.18429/JACoW-IBIC2022-MOP14

DESIGN AND IMPLEMENTATION OF AN FPGA-BASED DIGITAL PROCESSOR FOR BPM APPLICATIONS

M. Colja*, S. Carrato, University of Trieste, Trieste, Italy
G. Brajnik, R. De Monte, Elettra-Sincrotrone Trieste, Trieste, Italy

Abstract

Digital processing systems have been proven to often outperform analog elaboration. Indeed, thanks to high-density DSPs and FPGAs, operations in digital domain give results that are impossible to achieve in other ways. On the other side, dealing with this great performance and flexibility is not always straightforward: the processing chain needs to be accurately planned to reach the desired goals, avoiding erratic behaviours in the digital domain. In this paper, we focus on the design and implementation of an FPGA-based digital processor that will be used in the electron beam position monitors of Elettra 2.0. After digitizing the 500 MHz beam signals from the pickups, the system executes a digital down conversion, followed by several filtering and demodulating stages, in order to have a selectable data rate that is suitable for both diagnostics and feedback. The position calculation is also performed in FPGA as well, with the well-known difference-over-sum algorithm. According to results provided by a fixed-point simulation, the overall system has been implemented in an Intel Arria 10 FPGA, demonstrating the correct design functionality that meets the specified requirements.

INTRODUCTION

Digital signal processing has become a standard approach for realizing beam position monitor systems (BPM), thanks to the availability of high-speed, high-performance ADCs and FPGAs [1]. In synchrotrons, it is well known that information about beam position lies in the amplitude of the signal detected by the pickups: due to the typical beam fill patterns used in those machines and after a mandatory analog signal conditioning, it can be seen as a sine with a frequency equal to RF frequency of the accelerator. So, to extract its amplitude after digitization, there is the need for a digital receiver and demodulator that can do it properly for extracting its amplitude after digitization. Then, position calculation algorithm like difference-over-sum can be applied on demodulated amplitudes, converting them into a real beam position, related to vacuum chamber dimensions using a suitable scale factor.

This architecture will be used for the new eBPM system of Elettra 2.0, the low-emittance upgrade of the current machine. The overall modular system and some of its components (e.g. the pilot tone front end) have been already presented [2]; but in this paper we will focus on simulation and FPGA implementation of the complete digital processing chain, from ADC data to calculated position.

* matija.colja@elettra.eu

DIGITAL PLATFORM AND A/D CONVERSION

The digital platform (Fig. 1) has already been presented in previous papers [2,3]: analog signals from the front end are digitized by an FMC card with four LTC2107, 16-bit ADCs running at 150.38 MS/s, that is 130 times the revolution frequency and phase-locked with it.

Thanks to bandpass sampling technique [4] there is no need for an analog downconversion stage: the 499.654 MHz signal is seen by the ADCs as a 48.514 MHz sine, since it is folded back in the Nyquist zone corresponding to three times the sampling frequency. Obviously, this approach needs a high-performance, low-jitter clocking stage and an analog bandpass filter to reduce out-of-band noise.

Then, ADC data are processed by an Intel Arria 10 GX FPGA: the high amount of logic gates and DSP resources render it possible to realize in digital the complete processing chain. Connections with external devices are assured by internal transceivers attached to SFP+ modules capable to go at a speed up to 10 Gb/s.



Figure 1: Digital platform.

Content from this work may be used under the terms of the CC BY 4.0 licence (© 2022). Any distribution of this work must maintain attribution to the author(s), title of the work, publisher, and DOI

ISBN: 978-3-95450-241-7 ISSN: 2673-5350 doi:10.18429/JACoW-IBIC2022-MOP14

Content from this work may be used under the terms of the CC BY 4.0 licence (© 2022). Any distribution of this work must maintain attribution to the author(s), title of the work, publisher, and DOI

DIGITAL RECEIVER

Moving to the digital domain, we chose a direct conversion digital receiver (or digital down converter, DDC) paired with a quadrature amplitude demodulator. The input signal from the ADCs is shifted to the baseband by mixing (multiplying) it with a sine and a cosine generated by a numerical controlled oscillator (NCO). A low-pass CIC decimator filter [5] suppresses the high frequency components and reduces the data rate to turn-by-turn (TbT, 1.156 MHz) frequency. Since CIC filters have a magnitude response that causes a droop in the passband region, a compensation FIR corrects it. To avoid dealing with complex numbers, there are separate I and Q paths so that it is possible to reuse the same filters for both components.

Then, amplitude demodulation is performed by squaring I and Q, summing them and taking the square root of the result. Another CIC decimator reduces data rate to 10 kHz for global feedback (FA data output): compensation is not required since after amplitude demodulation, signal is DC-centred. User can choose to retrieve amplitudes of the four channels at TbT or FA data rate.

All the processing is done using integers in place of floating point numbers. More details on the implementation are listed below, looking at Fig. 2, where only one channel is depicted for sake of simplicity:

1. ADC 16-bit signed data (two's complement) running at 150.38 MHz;
2. multipliers: digital version of mixers. They perform frequency translation of the input signal near to the DC and are implemented using 18x18 bit hardware multipliers in DSP cells [6];
3. NCO (digital version of local oscillator): it generates a sine and cosine for I and Q processing with sufficient precision (18 bit), higher than ADC data and running at sampling frequency. It is implemented using Intel IP core [7];
4. CIC decimator filter: it suppresses the high frequency component generated by multiplication and reduces data rate to TbT frequency. The rate change factor is 130, the number of stages is 6 and the differential delay is equal to 1. It is implemented using Intel IP core [8], input and output are 32-bit wide. Bits are reduced using Hogenauer pruning;
5. FIR compensator: it corrects CIC magnitude response, and has been generated with a MATLAB appropriate routine. The 19 coefficients are symmetrical, with a length of 17 bits. It is implemented with Intel IP core [9], input and output are 32-bit wide;
6. square operation: it is implemented directly in DSP cells, with 32-bit input and 64-bit output;
7. sum of I and Q squares: it consists in a simple 64-bit adder;
8. square root: it is implemented using Intel IP integer arithmetic core [10], 64-bit input, 32-bit output;
9. second CIC decimator for changing data rate to 10 kHz as required by feedback. The rate change factor is 116 with 6 stages, input and output are 32-bit wide.

After writing all the code in Verilog language, the design has been successfully compiled in Quartus Prime. Table 1 reports FPGA resource usage after synthesis and fitting in terms of Adaptive Logic Modules (ALMs), dedicated logic registers (REGs), 20 kbits memory blocks (M20K), block memory bits (BMBs), DSP blocks (DSP) for every Verilog entity: IQ-amp includes squares, summing and square root stages.

Table 1: FPGA Resource Usage

Entity	ALMs	REGs	M20k	BMB	DSP
Mult-18x18	0	0	0	0	1
NCO	64	224	2	27648	2
CIC-130	358	907	3	1092	0
FIR	244	360	2	8192	2
IQ-amp	600	1117	0	0	6
CIC-116	357	943	3	1092	0

It has to be noted that for the complete digital receiver (4 channels), we need 8 multipliers, 8 CICs (TbT rate), one NCO, one FIR (can be reused for all channels and IQ components thanks to time domain multiplexing) and 4 IQ-amp entities. Additional 4 CICs (FA rate) are included for the 10 kHz data stream.

Pilot-tone compensation feature [11] can be enabled implementing a second digital receiver with a dedicated NCO tuned to pilot frequency, doubling the amount of resources needed. However, this topic is beyond the scope of this paper.

POSITION CALCULATION

After demodulating the four amplitudes, the position is calculated with the well-known difference-over-sum (DoS) algorithm, widely used in BPM applications:

$$x = K_x \frac{(A+D)-(B+C)}{A+B+C+D}, \quad y = K_y \frac{(A+B)-(C+D)}{A+B+C+D} \tag{1}$$

where K_x and K_y are the scale factors related to vacuum chamber dimensions (20 mm for Elettra), and A, B, C, D are the demodulated amplitudes. Calculations inside FPGA are done scaling accordingly the coefficients in order to avoid a non-integer quotient and for obtaining x and y as 32-bit signed integers expressed in nanometers (LSB is 1 nm), mainly for backward compatibility with the existing Elettra control system.

For an effective debug, user can choose data source and data rate nearly at every processing stage. High amount of samples can be stored in 8 GB an external DDR3 RAM memory, otherwise real-time data stream at 10 kHz (FA) or

ISBN: 978-3-95450-241-7 ISSN: 2673-5350 doi:10.18429/JACoW-IBIC2022-MOP14

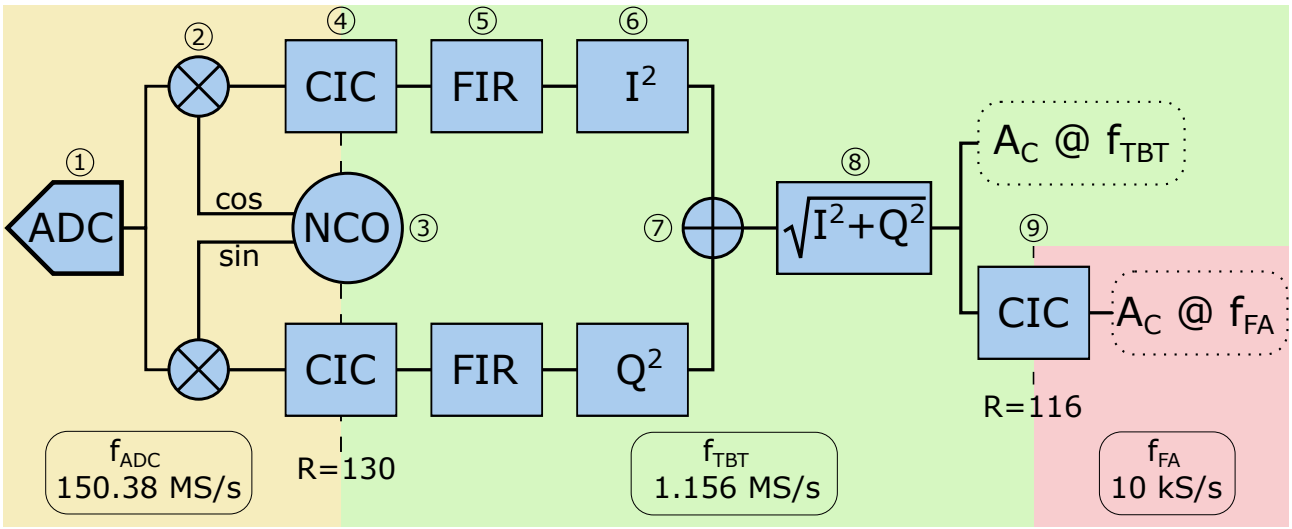


Figure 2: Block diagram of digital receiver: only channel A is shown.

at TbT data rate can be sent to external systems through multiple Ethernet connections (1 Gb/s or 10 Gb/s). The overall simplified FPGA block diagram can be seen in Fig. 3.

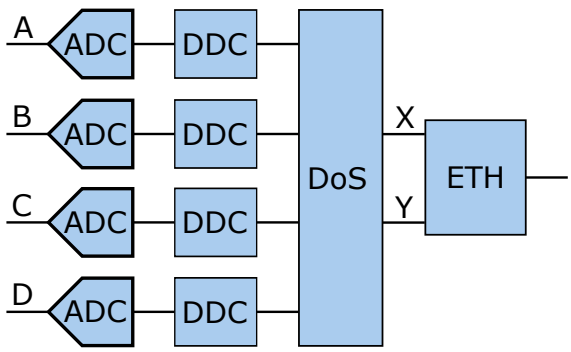


Figure 3: Simplified block diagram of whole processing chain.

SIMULATION AND RESULTS

In order to validate the design, the entire processing chain has been simulated in MATLAB using the fixed-point designer toolbox, thus having the same behaviour of FPGA logic. Every step of the chain has been compared with theoretical results, based mainly on signal-to-noise ratio (SNR) measurements. Decimation and filtering increases SNR since bandwidth is reduced, so we can express the quantity called decimation gain in decibels:

$$\mathrm{DG_{dB}} = 10\log_{10}(R), \tag{2}$$

where R is the rate change factor. In this way, the process gain obtained at TbT data rate is about 21 dB ($R = 130$), while at FA data rate is about 42 dB ($R = 130 \cdot 116$).

Nevertheless, there is a relation between SNR of demodulated amplitudes and standard deviation of calculated positions [12]:

$$\sigma_x = \frac{K_x}{2} \cdot \left(\sqrt{\mathrm{SNR}}\right)^{-1}, \quad \sigma_y = \frac{K_y}{2} \cdot \left(\sqrt{\mathrm{SNR}}\right)^{-1}. \tag{3}$$

These expressions allow us to have a direct relation between the SNR at ADCs inputs and the resulting noise on positions:

$$\sigma_x = \frac{K_x}{2} \cdot \left(\sqrt{10^{\frac{\mathrm{SNR_{dB}}}{10}}}\right)^{-1}, \quad \sigma_y = \frac{K_y}{2} \cdot \left(\sqrt{10^{\frac{\mathrm{SNR_{dB}}}{10}}}\right)^{-1}, \tag{4}$$

where $\mathrm{SNR_{dB}}$ is the sum of input SNR and processing gain ($\mathrm{SNR_{in,dB}} + \mathrm{DG_{dB}}$).

Simulations

First of all, we decided to check the entire MATLAB chain, generating a sinusoidal signal with an additive white gaussian noise (different realizations of the statistic process for every channel) to emulate a stable and centred beam. Checks on effective and expected SNR are performed at every stage of the simulation, to understand if quantization or processing errors could corrupt it. Varying input SNR, resulting noise on position follows in a good way Eq. (3), meaning that the entire processing does not limit the resolution up to wanted specifications, at least 200 nm at 10 kHz data rate for Elettra 2.0 for 60 dB of input SNR (Fig. 4).

Then, as an intermediate step, we moved to real data: a 499.654 MHz signal from a RF generator, splitted in four and fed to ADCs, has been used to emulate a stable beam. Raw data from ADCs have been acquired and used in MATLAB simulation. Standard deviation on position saturates at about 90 nm, even if SNR is increased (Fig. 5). This means that there is a noise contribution that increases with signal amplitude and dominates thermal noise after a break even point (located at about 9000 ADC bins, corresponding to −3 dBm at ADC input). ADC full scale is about at +3 dBm, so there is a range of 11 dB where there is no improvement. Since

Content from this work may be used under the terms of the CC BY 4.0 licence (© 2022). Any distribution of this work must maintain attribution to the author(s), title of the work, publisher, and DOI

ISBN: 978-3-95450-241-7 ISSN: 2673-5350 doi:10.18429/JACoW-IBIC2022-MOP14

Content from this work may be used under the terms of the CC BY 4.0 licence (© 2022). Any distribution of this work must maintain attribution to the author(s), title of the work, publisher, and DOI

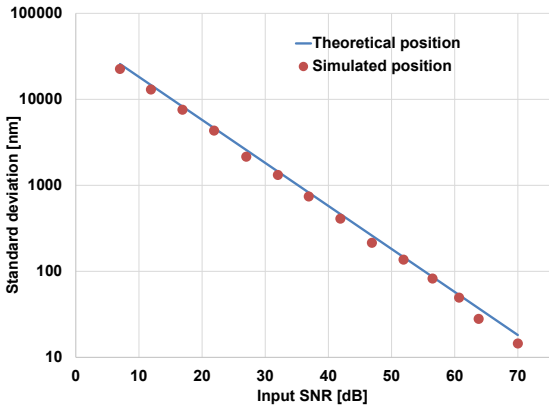


Figure 4: Standard deviation versus input SNR at 10 kHz data rate of theoretical and simulated positions.

raw data are involved, ADCs are the most likely suspects for causing this: further investigations are ongoing, mainly related to jitter of ADC sample-and-hold stage; the absolute jitter of sampling clock is not involved because, by simultaneously affecting all four amplitudes, can be compensated by the difference-over-sum algorithm, while the observed effect is related to a difference between the channels.

The same behaviour is observed moving to full FPGA processing: in that case all the calculations are done inside the unit, logging only the positions, which confirms the correct operation of the overall processing chain.

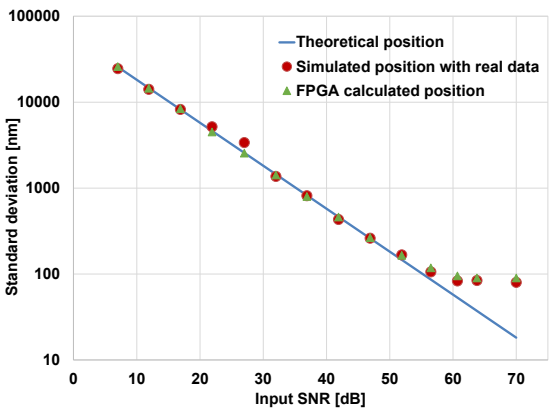


Figure 5: Standard deviation versus input SNR at 10 kHz data rate of theoretical and positions from real data.

CONCLUSION

A complete digital eBPM processor has been successfully implemented in an FPGA: both simulations and experimental data confirm the validity of all processing stages with good agreement with theoretical results. Using real data from ADCs sets a limit on higher achievable resolution: this is most probably due to jitter issues on ADC's sample-and-hold stage, since this effect is correlated with amplitude of input signal. Tests are underway to further investigate this behaviour and to propose some solutions.

REFERENCES

[1] M. Wendt, "BPM Systems: A brief Introduction to Beam Position Monitoring", in *Proc. CAS Beam Instrumentation 2018*, Tuusula, Finland, Jun. 2018, pp. 355-393. doi:10.48550/arXiv.2005.14081

[2] G. Brajnik, S. Cleva, R. De Monte, and D. Giuressi, "A Common Diagnostic Platform for Elettra 2.0 and FERMI", in *Proc. IBIC'19*, Malmö, Sweden, Sep. 2019, pp. 280–282. doi:10.18429/JACoW-IBIC2019-TUPP003

[3] G. Brajnik, M. Cargnelutti, R. De Monte, P. Leban, P. Paglovec, and B. Repič, "Current Status of Elettra 2.0 eBPM System", in *Proc. IBIC'21*, Pohang, Rep. of Korea, May 2021, pp. 71–74. doi:10.18429/JACoW-IBIC2021-MOPP16

[4] R. G. Vaughan, N. L. Scott and D. R. White, "The theory of bandpass sampling", *IEEE Trans. Signal Process.*, vol. 39, no. 9, pp. 1973-1984, Sep. 1991. doi:10.1109/78.134430

[5] E. Hogenauer, "An economical class of digital filters for decimation and interpolation", *IEEE Trans. Acoust. Speech Signal Process.*, vol. 29, no.2, pp. 155–162, Apr. 1981. doi:10.1109/TASSP.1981.1163535

[6] Intel Arria 10 Native Fixed Point DSP IP Core User Guide, https://www.intel.com/content/www/us/en/docs/programmable/683583/current/intel-arria-native-fixed-point-dsp-ip.html

[7] Intel NCO IP Core: User Guide, https://www.intel.com/content/www/us/en/docs/programmable/683406/17-1/about-the-nco-ip-core.html

[8] CIC Intel FPGA IP: User Guide, https://www.intel.com/content/www/us/en/docs/programmable/683246/19-3-19-3/about-the-cic.html

[9] Intel FIR II IP Core: User Guide, https://www.intel.com/content/www/us/en/docs/programmable/683208/17-1/about-the-fir-ii-ip-core.html

[10] Intel FPGA Integer Arithmetic IP Cores User Guide, https://www.intel.com/content/www/us/en/docs/programmable/683490/20-3/altsqrt-integer-square-root-ip-core.html

[11] G. Brajnik, S. Bassanese, G. Cautero, S. Cleva, and R. De Monte, "Integration of a Pilot-Tone Based BPM System Within the Global Orbit Feedback Environment of Elettra", in *Proc. IBIC'18*, Shanghai, China, Sep. 2018, pp. 190–195. doi:10.18429/JACoW-IBIC2018-TUOC01

[12] G. Brajnik, S. Carrato, S. Bassanese, G. Cautero, and R. De Monte, "Pilot tone as a key to improving the spatial resolution of eBPMs", *AIP Conf. Proc.*, vol. 1741, p. 020013, 2016. doi:10.1063/1.4952792

ISBN: 978-3-95450-241-7 ISSN: 2673-5350 doi:10.18429/JACoW-IBIC2022-MOP15

DEVELOPMENT OF NON-INVASIVE CALIBRATION SOFTWARE FOR FRONT END X-RAY BEAM POSITION MONITORS AT DIAMOND LIGHT SOURCE

C. Houghton*, C. Bloomer, L. Bobb, Diamond Light Source Ltd, United Kingdom

Abstract

Tungsten blade based photoemission X-ray Beam Position Monitors (XBPMs) are widely used as white beam diagnostics at synchrotrons. Traditionally, the scale factors are determined by stepper motor movements of the XBPM, or by controlled electron beam displacements, and measuring the response. These measurements must be repeated for each ID gap to produce a complete set of scale factors for all operational conditions. This calibration procedure takes time and cannot be done while users are acquiring data. In addition, the scale factors can vary over time due to changes to the storage ring. It is possible for these scale factors to become inaccurate, reducing the accuracy of the beam position measured by the XBPMs. By using the intrinsic kHz electron beam movements and correlating the signals from electron beam position monitors and XBPMs it is possible to have real-time calculation of the scale factors without the need to disturb user operation. Presented in this paper is a method to non-invasively calculate scale factors during normal user operation. A comparison of the precision of this method versus the traditional stepper motor method is presented.

INTRODUCTION

To monitor and improve the stability of the photon beam Diamond Light Source utilises two X-ray beam position monitor (XBPMs) on most insertion device (ID) front ends. Each XBPM is mounted on stepper motors to enable precise alignment of the XBPM with the incident X-ray beam. Traditionally, the XBPM calibration factors, or 'scale factors' are obtained by measuring the position response of the XBPM whilst a known stepper motor offset is applied, to simulate real X-ray beam movements. Alternatively, the beam movements can be generated using an electron beam bump. Corrector magnets are used to induce a known angular offset through the ID. This in turn produces a fixed offset of the X-ray beam at the XBPM. A scale factor, K, can be calculated by comparing the measured response of the four XBPM blades to the known applied beam offset. The response of the XBPM is defined by

$$(\Delta/\Sigma)_x = \frac{(I_A + I_D) - (I_C + I_B)}{I_A + I_B + I_C + I_D} \quad (1a)$$

$$(\Delta/\Sigma)_y = \frac{(I_A + I_B) - (I_C + I_D)}{I_A + I_B + I_C + I_D} \quad (1b)$$

where Δ/Σ is a dimensionless position and $I_{(A,B,C,D)}$ are the currents from the four XBPM blades (A = top-left; B = top-right; C = bottom-right; D = bottom-left) when viewed from the X-ray source. The calculation of the XBPM scale factors using these methods has several limitations. Firstly, both these methods require specific machine development time and cannot be done during user operation. Secondly, the XBPM scale factor is dependent on the ID settings particularly the ID gap. As the ID gap varies there are changes to the XBPM sensitivities due to the change in the photon beam distribution [1, 2]. Currently, the scale factors, K_x and K_y, are calculated for a selection of ID gaps and can be used to convert the dimensionless position, Δ/Σ, to a horizontal and vertical position in millimeters. Current methods for calibration use interpolation in order to populate lookup tables for all possible ID gaps.

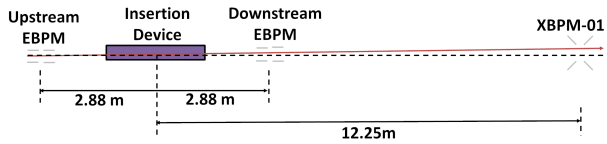


Figure 1: Schematic of the EBPM and XBPM locations for a typical Diamond Light Source Insertion Device straight.

Presented in this paper is a method for utilising the intrinsic electron beam movements and fast electronics in order to calculate XBPM scale factors passively during user operation.

SET-UP

Diamond Light Source has a Fast Acquisition network which can synchronously capture the position data from electron beam position monitors (EBPMs) and XBPMs at a rate of 10 kHz [3]. This data stream allows for the comparison of the electron beam trajectory through the ID with the X-ray beam position at the XBPM. For the duration of one user run at Diamond Light Source, 1 s of the 10 kHz position data was collected from the EBPMs and XBPMs at intervals of 10 seconds from the I14 insertion device beamline. The 'projected' position of the X-ray beam at the XBPM is determined from a geometric projection of the EBPM measurements from either side of the insertion device out to the distance of the XBPM. Figure 1 shows a schematic of the system and distance to these components.

The projected and measured X-ray beam positions are analysed by calculating the Singular Value Decomposition (SVD); finding the major axis between the two data sets returns the scale factor between the XBPM response and the EBPM projections [4]. Figure 2 shows the correlation between the measured and the projected XBPM measurement.

* claire.houghton@diamond.ac.uk

Content from this work may be used under the terms of the CC BY 4.0 licence (© 2022). Any distribution of this work must maintain attribution to the author(s), title of the work, publisher, and DOI

ISBN: 978-3-95450-241-7 ISSN: 2673-5350 doi:10.18429/JACoW-IBIC2022-MOP15

Content from this work may be used under the terms of the CC BY 4.0 licence (© 2022). Any distribution of this work must maintain attribution to the author(s), title of the work, publisher, and DOI

A time series plot, Fig. 3, shows the projection of the EBPM measurement in good agreement with the measured XBPM position both horizontally and vertically. The standard deviation of the residual error between the two measurements once the scale factor was applied was 0.29 µm horizontally and 0.30 µm vertically.

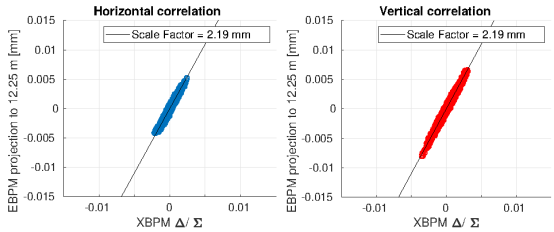


Figure 2: Graphs showing the horizontal (left) and vertical (right) correlation between the projected and measured XBPM position. The scale factor shown here is calculated from the SVD of the correlation.

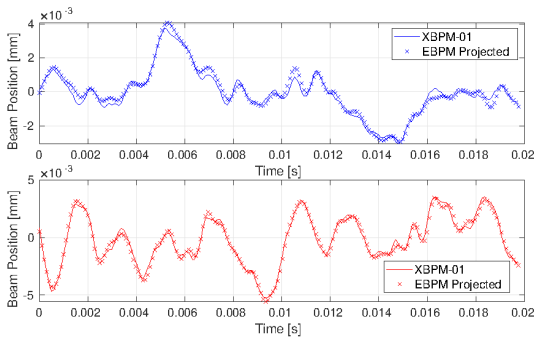


Figure 3: The horizontal (top) and vertical (bottom) beam position over 200 microseconds for the projected EBPM and the measured XBPM with measured scale factor applied.

RESULTS

The scale factors for the XBPM-01 on Diamond Light Source's I14 beamline were measured over a range of ID gaps using the three methods described above. The stepper motor and EBPM angular bump data were collected on the same day and show good agreement with each other over a range of ID gaps as seen in Fig. 4. The non-invasive calibration data shown is the median measured scale factor for each gap acquired using the 1 s long 10 kHz acquisitions collected over a 7-day period. The error bars represent the standard deviation from the measured median. The median of the data was taken in order to minimise the impact of possible outliers on the result (for example particularly noisy measurements acquired immediately after top-up injections; or measurements acquired immediately after an ID gap movement). All three methods show good quantitative agreement over the 5.0 - 9.0 mm range of ID gaps used by the beamline. There is a slightly better correlation in the vertical axis than in the horizontal axis. The reasons for this are not yet fully understood.

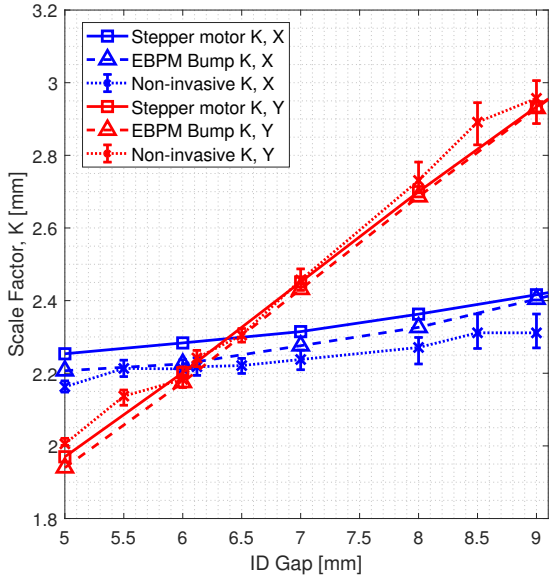


Figure 4: Graph showing the measured scale factors by three calibration methods over a range of ID gaps.

Over the course of a run there are multiple things that can impact the scale factor. These include the machine parameters such as ID gap, as seen in Fig. 4, and environmental factors such as temperature and humidity. Data collected over a 5 week period of user operation has been analysed. Sorting the data by the ID gap, to within 0.5 mm, and taking the median over different time scales it is possible to see how long term machine drifts impact the scale factor. Figure 5 shows the median scale factor for a constant ID gap, 6 mm, over different timescales: 1 week, 24 hours and 1 hour. The error bars represent the standard deviation of the data from the median value at a given ID gap. Over the course of the week both the 24 hour and 1 hour median data shows broadly the same trend for the horizontal and vertical scale factors. The error bars on the three data sets are nominally the same, suggesting that taking the median over a week does not reduce the accuracy in the calibration by a significant amount.

In Fig. 6 the full 5 weeks of measured scale factors is shown, with the median taken over 1 hour periods. The importance of obtaining accurate scale factors at multiple different ID gaps is illustrated by how much the scale factors vary under each of the beamline's different operating conditions and gaps over this period. For example, when the beamline steps the ID gap from 7.0 mm to 8.5 mm increasing K_y by 19%. In addition, similar drifts to those seen in Fig. 5 are present with an increase in K_y on day 20 before returning to the nominal level a few hours later. This change is independent of the ID parameters and would not have been observed using previous methods. Although the mechanism behind this variation in K_y is not understood, it is nonethe-

ISBN: 978-3-95450-241-7 ISSN: 2673-5350 doi:10.18429/JACoW-IBIC2022-MOP15

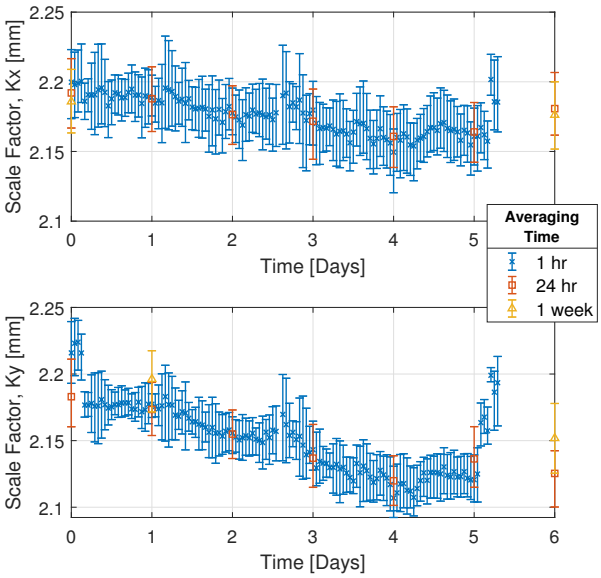


Figure 5: The median scale factor measured over 6 days of data collection using different time-scales for ID gap of 6 mm. The error bars represent the standard deviation from the median. (Top) horizontal K_x, (Bottom) vertical K_y.

less useful information and can help identify potential issues either with the synchrotron or with the XBPMs themselves. The variation in K_y implies that the X-ray beam size may be varying, which could impact the beamline.

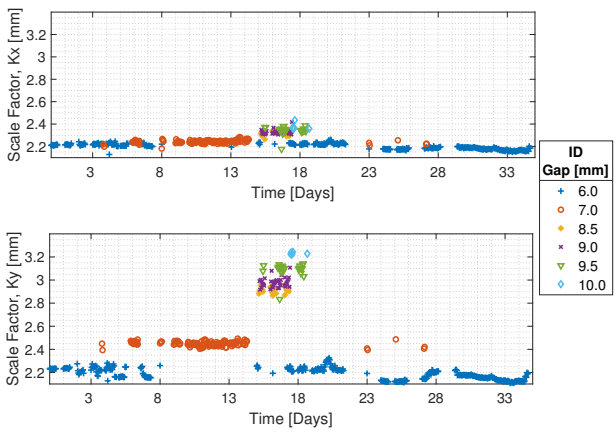


Figure 6: The median scale factors measured over 24 hour periods across 5 weeks of data collection. A range of ID gaps used by the beamline are plotted. (Top) horizontal K_x, (Bottom) vertical K_y.

CONCLUSION

The good agreement between the non-invasive method for calculating calibration factors with previously understood methods, the stepper motor movements and EBPM angular bump, suggest it can be used in place of or alongside those existing methods. There are some discrepancies with the non-invasive method but results show K_x and K_y are equal of previous methods to within 5% and 3% respectively. The reduced time required for collecting data and the ability to obtain more accurate results for the most used gaps could mean the scale factors are more representative of the needs of the users.

By analysing the long term drift of the scale factors the impact of machine drifts can be seen. Currently these calculations are being done offline at the end of the week allowing for corrections to be made in line with machine and environmental drifts. In future these scale factors could be done in real-time and be available as an on-line diagnostic.

FUTURE WORK

Currently the system has been used for data collection and analysis. Applying the measured scale factors and assessing the residual drift is the next step [5]. The causes of the long term drifts seen in Figs. 5 and 6 are not fully understood. The direct comparison between the drifts and measured humidity do not show a clear correlation, suggesting there are other mechanisms involved. Further work is also needed to understand the cause for the discrepancy between the three methods for scale factor calculation described. This method also has a use for calibrating the XBPMs observing beam from Elliptically Polarising Undulators where the beam size and shape can vary significantly depending on the operating mode. Building up calibration tables using stepper motor movements can be time consuming as there are so many potential combinations of ID gap and phase. The technique presented in this paper would enable on-line lookup tables to be generated during normal user operation.

REFERENCES

[1] O. Singh and G. Decker, "Operational Experience with X-ray Beam Position Monitors at the Advanced Photon Source (Invited)", in *Proc. PAC'01*, Chicago, IL, USA, Jun. 2001, paper ROAB008, pp. 539–543. https://jacow.org/p01/papers/ROAB008.pdf

[2] T. Warwick, N. Andresen, G. Portmann and A. Jackson, "Performance of photon position monitors and stability of undulator beams at the advanced light source", *Rev. Sci. Instrum.*, vol. 66, pp. 1984–1986, doi:10.1063/1.1145777

[3] M. G. Abbott, G. Rehm, and I. Uzun, "A New Fast Data Logger and Viewer at Diamond: the FA Archiver", in *Proc. ICALEPCS'11*, Grenoble, France, Oct. 2011, paper THCHMUST03, pp. 1244–1247.

[4] C. Bloomer and G. Rehm, "Real-time Calculation of Scale Factors of X-ray Beam Position Monitors during User Operation", in *Proc. IBIC'12*, Tsukuba, Japan, Oct. 2012, paper MOPA13, pp. 79–82.

[5] D. Shu *et al.*, "Smart X-ray beam position monitor system using artificial-intelligence methods for the Advanced Photon Source insertion-device beamlines", *J. Synchrotron Radiat.*, vol. 5, no. 3, pp. 632–635, May 1998. doi:10.1107/S0909049597017056

Content from this work may be used under the terms of the CC BY 4.0 licence (© 2022). Any distribution of this work must maintain attribution to the author(s), title of the work, publisher, and DOI

ISBN: 978-3-95450-241-7 ISSN: 2673-5350 doi:10.18429/JACoW-IBIC2022-MOP16

TIME RESOLVED DYNAMICS OF TRANSVERSE RESONANCE ISLAND BUCKETS AT SPEAR3*

K. Tian†, J. Corbett, J. Kim, J. Safranek
SLAC National Accelerator Laboratory, CA, USA

Abstract

Transverse Resonance Island Buckets have been studied at SPEAR3 as an option for timing experiment mode operation. In this mode, with proper lattice optics settings, the electron beam populates to island orbits with the excitation from a kicker. In this paper, we will report the experimental observation of beam dynamics with turn by turn beam position monitors and a fast gated camera.

INTRODUCTION

The SPEAR3 3-GeV, high-brightness third-generation storage ring, upgraded in 2004, operates at 500 mA in top-off mode, with high reliability and low emittance. Recently, there is growing interest in conducting time-resolved experiments from the user community. To enhance the timing mode experimental capability of SPEAR3 and fulfill the requirements of timing users and high-brightness users simultaneously, efforts have been devoted to develop new operation modes in SPEAR3.

Beam resonances in a storage ring are generally considered as limiting factors for the beam performance. Therefore, operational betatron tunes are chosen to avoid harmful resonance lines such as those of integer tunes and half-integer tunes. However, when a potential-well is formed around certain high-order resonances, a bunch can be trapped inside the potential-well and become stable. This so-called Transverse Resonance Island Bucket (TRIBs) mode has been studied and demonstrated at BESSY II [1] and MAX-IV [2]. Operating in this mode, it is possible to select and populate part of the bunch train on a different closed orbit from the main bunch. At the interested beamline, the unwanted X-ray from the main bunch train can be blocked to improve the signal-to-noise ratio of the timing experiment. The under-development 6 nm lattice of SPEAR3, has a designed ν_x of 15.32, which can be successfully exploited for the TRIBs studies. The TRIBs mode can be activated by either the SPEAR3 transverse multi-bunch feed back (TMFB) kicker [3] or one of the three injection kickers, K1, under slightly different lattice settings.

SPEAR3 TRIBs MODE

Tracking Simulations

Prior to our experimental studies, tracking simulations were first conducted with the 6 nm lattice to confirm the possibility for running TRIBs mode in this lattice. Using ELEGANT [4], single particles with variable initial offsets were tracked in a lattice obtained from optics fitting with LOCO [5]. The distribution of three resonance islands is visualized in the top plot of Fig. 1 as three potential wells when $\nu_x = 0.3333$. Once the electron beam is trapped in one of these islands, the new orbit (x, x'), passing through the centers of the 3 islands as shown in the bottom plot of Fig. 1, is closed every 3 turns.

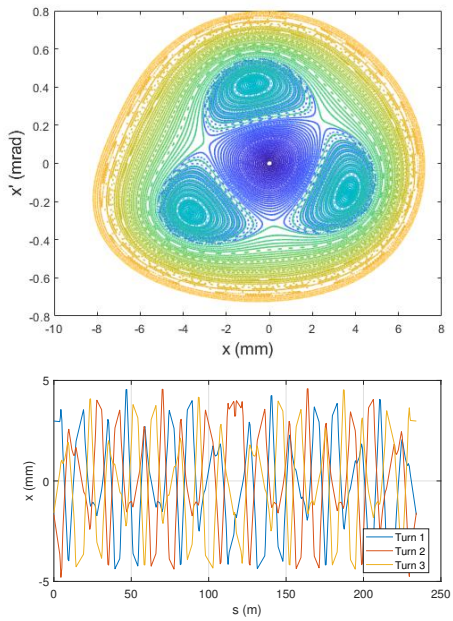


Figure 1: Closed orbit for SPEAR3 TRIBs optics.

TRIBs Excitation

The nominal chromaticity of the 6-nm lattice is +2 for both the horizontal and the vertical planes. During our TRIBs study, the horizontal chromaticity, ξ_x, was reduced to nearly 0 using a chromaticity response matrix. $\xi_x = 0$ helps to avoid tune shifts caused by momentum deviation when driving the beam horizontally. Experimentally, it was found that the TRIBs mode could be better excited when ξ_x was slightly larger than zero. We were able to drive the TRIBs mode either with the TMFB kicker or the injection kicker, K1. With the TMFB kicker, ν_x was increased to 0.3297 from the design value of 0.32 due to the relatively weak strength of the kicker. In addition, the kicker needed to be set up with a frequency sweep within a short period of time. On the other hand, the K1 kicker strength was strong enough to move the beam to the TRIBs islands with a single pulse. Because the excitation from the K1 kicker was relatively

* Work supported by U.S. Department of Energy under Contract No. DE-AC02-76SF00515
† ktian@slac.stanford.edu

Content from this work may be used under the terms of the CC BY 4.0 licence (© 2022). Any distribution of this work must maintain attribution to the author(s), title of the work, publisher, and DOI

ISBN: 978-3-95450-241-7 ISSN: 2673-5350 doi:10.18429/JACoW-IBIC2022-MOP16

straightforward, it has been the main way being used for the TRIBs study at SPEAR3.

SPEAR3 has 3 injection kickers (K1, K2, K3), normally used for the closed orbit bump during off-axis injection. The K1 kicker has a calibration factor about 1.21 mrad/kV. By manipulating the kicker timing and the control software, we were able to drive the kicker in a single shot mode on demand. During the experiment, a single bunch of about 18 mA was filled initially and the K1 strength was swept in steps for TRIBs excitation, while the bunch current was decaying.

Diagnostics Tools

The TRIBs excitation in steady state can be observed by an x-ray pinhole camera or a TbT BPM. SPEAR3 is equipped with one pinhole camera and two SPARK TbT BPMs [6]. However, due to the relatively low beam current, the X-ray intensity was low and the exposure time of the pinhole camera needed to be as long as 1.5 second for good signals. The visible diagnostic beam line (Synchrotron Light Monitor, or SLM) at SPEAR3 has a fast gated, image-intensified PiMax camera. With a minimum gating time of 2 ns, the PiMax camera can image the single bunch in SPEAR3 on a single-pass basis. Along with the two TbT SPARK BPMs, they are effective tools to probe TRIBs dynamics. In Table 1, we list the twiss parameters at the injection kicker K1, the source point of the pinhole camera, the source point of SLM, and the two TbT BPMs.

Table 1: Twiss Parameters at Selected Locations

	β_x(m)	α_x	β_y(m)	α_y
K1	9.72	-0.07	4.52	-0.17
pinhole	0.55	-0.18	15.57	-0.28
SLM	1.55	1.56	14.16	-2.47
TbT1	2.79	2.38	12.30	-3.04
TbT2	8.34	-7.32	10.56	6.30

Experimental Observations

The TRIBs orbit separation was observed for a wide range of K1 settings from 0.3 kV to 0.55 kV with various bunch currents. In Fig. 2, we show an example of such observations. As mentioned earlier, the synchrotron radiation intensity was low, as a result, the exposure time of the x-ray camera was increased to 1.5 second in order to capture the beam image. Though the separation of the TRIBs orbits are larger than the field of view of the camera sensor, it was still clear that, after a single kick from K1, the beam was moved from the core, i.e. the default orbit before the kick, to three island orbits. This is also illustrated by the projection of the beam images to the horizontal axis in Fig. 2. The data from the TbT BPM1 shows three parallel lines, through which the turn-by-turn orbit cycles. The TbT BPM measures the centroid obit of the whole beam, which concurs with the TRIBs closed orbit only when all particles are in the same island. Tracking simulations results in the bottom right figure show that the island separation distance agrees well with the orbit data measured by the TbT BPM1. This implies that all particles in the bunch were kicked into one island rather than being distributed to three islands. This was further verified by the measurement with the fast gated camera as shown in Fig. 3.

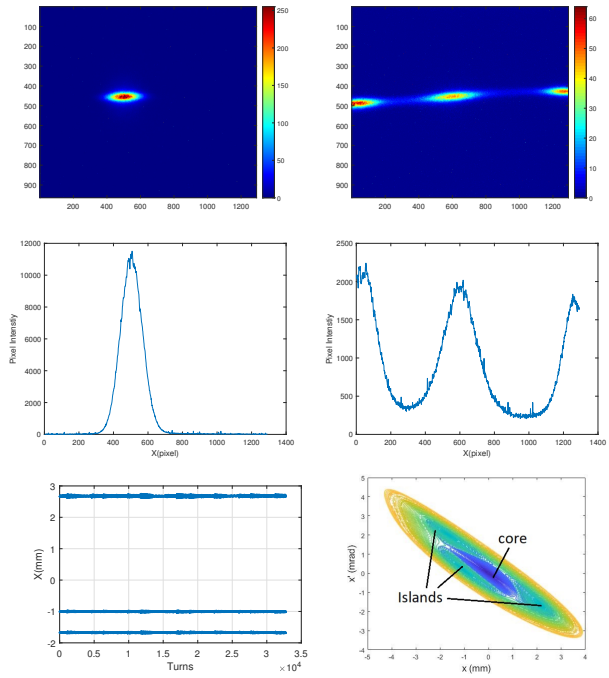


Figure 2: Experimental observations of TRIBs with a single bunch of 17 mA: x-ray pinhole images before (top left) and after (top right) the K1 kick; the projection of the pinhole images to the horizontal axis (middle); TbT BPM1 data for 32,760 turns or 25.6 ms, after the K1 kick (bottom left); island distribution at the location of TbT BPM1.

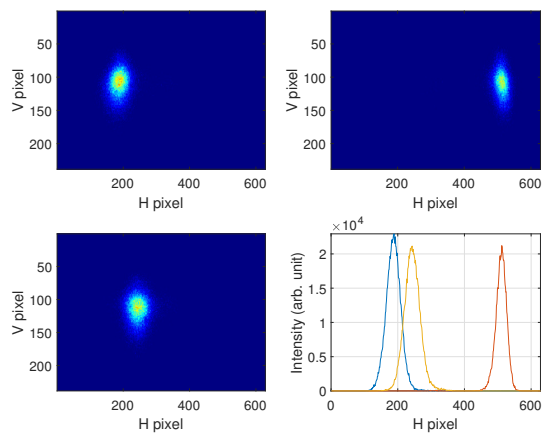


Figure 3: Single turn imaging of the TRIBs beam at 12 mA with the intesity projection to the horizontal axis.

The exposure time of the PiMax camera was set to 100 ns for single turn imaging and we took multiple images of the

Content from this work may be used under the terms of the CC BY 4.0 licence (© 2022). Any distribution of this work must maintain attribution to the author(s), title of the work, publisher, and DOI

ISBN: 978-3-95450-241-7 ISSN: 2673-5350 doi:10.18429/JACoW-IBIC2022-MOP16

Content from this work may be used under the terms of the CC BY 4.0 licence (© 2022). Any distribution of this work must maintain attribution to the author(s), title of the work, publisher, and DOI

beam after the 12 mA single bunch was excited to the stable TRIBs orbit. All the images indicated that the whole bunch was moving through 3 closed orbit position as shown in Fig. 3. One should note that the visually large vertical beam size in the PiMax images was due to the diffraction-limited visible SR beam and instrumentation distortion.

It is worth noting that the beam stayed in the TRIBs orbit for as long as 20 minutes without any sign of damping down to the core orbit. In order to damp the beam back to the core, we needed to fire the K1 kicker again. This was consistent for TRIBs excitation when the single bunch current was high, e.g. larger than 6 mA. However, for lower bunch current, e.g. below 3 mA, the results were less consistent and the beam tended to damp down to the core obit within 60 seconds or less without an additional kicking.

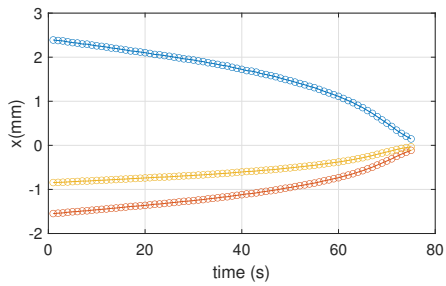


Figure 4: Orbit displacement of the single bunch 3.25 mA beam decreases over time.

In Fig. 4, we show the measured centroid orbit separation reduced over 75 seconds for a single bunch 3.25 mA beam after it was excited to the TRIBs orbit. The data were obtained from the average island orbit of the TbT BPM1 data taken at the rate of once a second. To understand the current dependent effects for the TRIBs excitation, we were motivated to measure the transient dynamics during the excitation.

TIME RESOLVED TRIBS DYNAMICS

Timing Setup

In order to better understand the beam dynamics of the TRIBs excitation, particularly the bunch current dependent effects in our study, we conducted a series of experimental measurements to probe the transient dynamics of TRIBs excitation. For these measurements, we needed the capability to capture both the transverse profiles of the beam and the beam position with turn-by-turn resolution for a single bunch in SPEAR3. This required us to synchronize the data acquisition of the fast gated PiMax camera and the TbT BPMs with the single-shot excitation from K1.

The timing set up to synchronize each different diagnostics is summarized in Fig 5. Because the trigger units for each diagnostic tool were located in different physical locations, multiple SRS Delay Generators were used for the timing setup. An SLM-DG645 was set up in the SLM with the 1.28 MHz ring revolution clock as the input trigger but decimated it to 10 Hz before sending to the B117-DG535

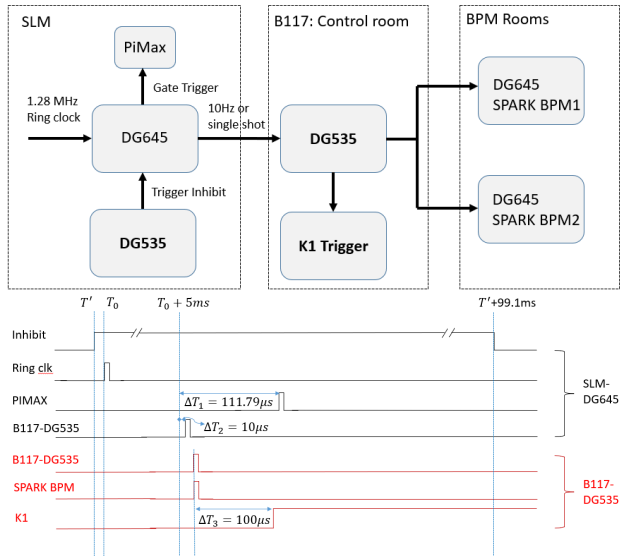


Figure 5: Timing setup and timing diagram.

in the control room as an input trigger. The reason for decimation to 10 Hz is to avoid over-driving the 10 Hz K1 kicker. The B117-DG535 produced the trigger signals for the TbT BPMs in two BPM rooms and the K1 trigger in the control room. By adjusting B117-DG535 to delay the K1 trigger by 100 s with respect to the TbT BPM triggers, we ensured the TbT BPMs capture the data when the K1 fired. The SLM-DG645 also provided the trigger signal for the PiMax camera. Therefore, by adjusting the delay of the output trigger signals to the PiMax Camera, ΔT_1, and the B117-DG535, ΔT_2, we can adjust the timing between the K1 kicker and the PiMax camera. The empirical settings were ΔT_1=111.79 µs and ΔT_2=10 µs to capture the first turn images after the kicker was fired. To capture other turns, a delay in multiples of the 781 ns revolution time can simply be added to ΔT_1. Finally, to drive the K1 kicker, TbT BPMs, and the PiMax camera with a single synchronous shot, we utilized the inhibit function of the SLM-DG645.

Time Resolved Imaging Results

For the synchronous time-resolved measurements, a 2 mA single bunch was filled in the storage ring and was driven to the TRIBs orbits by the K1 kicker with different pulse voltages: 0.4 kV, 0.45 kV, and 0.55 kV. For each case, we configured the PiMax to take 50 images with 2 second intervals starting right after the kick was fired (t=0). This provided samples of the transverse profiles of the TRIBs excitation over a 98-second period. After examining all the beam images, it was found that for all cases, the beam damped to the core orbit within 98 seconds, a similar process shown in Fig. 4. However, with different driving strengths from K1, we did find some differences in the time resolved images.

In Fig. 6, we compared the three cases by showing the images for the first 54 seconds in intervals of 6 seconds. With the 0.45 kV kick the TIRBs orbit lasted longer than the other two cases. In addition, unlike the case for the high

ISBN: 978-3-95450-241-7 ISSN: 2673-5350 doi:10.18429/JACoW-IBIC2022-MOP16

current beam, there were always some particles remaining in the core orbit not being populated into the island orbits after the K1 kick.

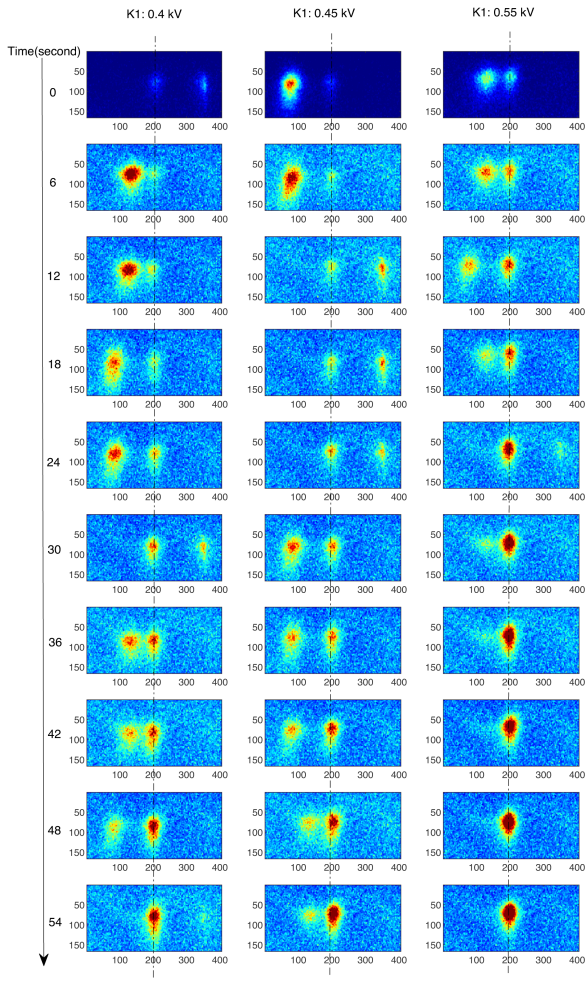


Figure 6: Time resolved TRIBs imaging for a 2 mA single bunch with K1 set to 0.4 kV, 0.45 kV, and 0.55 kV, respectively. The dash-dot lines indicate the location of the core orbit.

TbT BPM Data

The synchronized TbT BPM1 data is shown in Fig. 7 for both high and low current beam with different K1 kick amplitude. At a lower K1 voltage of 0.32 kV for a 14 mA bunch, the orbits of the high current beam slowly converged to the TRIBs orbits. The process was longer than 26 ms, but once the beam settled in the island orbits, it would stay for an extended period of time. This process was shorter when the K1 votage was increased to 0.58 kV, for which it took about 26 ms for the beam to settle in the island orbit. On the other hand, at K1 voltage of 0.35 kV for the 2 mA beam, the charge centroid orbit separation as measured from the TbT BPM never reached the full TRIBs orbit, because, as we learned from the PiMax data shown in Fig. 6, part of the beam was still in the core orbit. In the 2 mA case, without an external driving source to the TRIBs orbits, the particles would damp down to the core on the order of tens of seconds. It appears that, at 0.45 kV, the 2 mA beam was placed right to the TRIBs potential well. This is consist with the results at t=0 second in Fig. 6, which shows most of particles are on the TRIBs orbit.

In Fig. 8, the centroids of the TRIBs orbits for the 2 mA single bunch are plotted for various K1 voltages. The maximum separation of the TRIBs orbit occurs at 0.45 kV and drops significantly for 0.55 kV and 0.35 kV. This suggests that for low current bunch, the range of K1 voltage to populate all beam to the TRIBs islands is small. In Contrast, the K1 voltage requirement for the high current bunch to be driven to the TRIBs is more relaxed as shown in the data presented earlier.

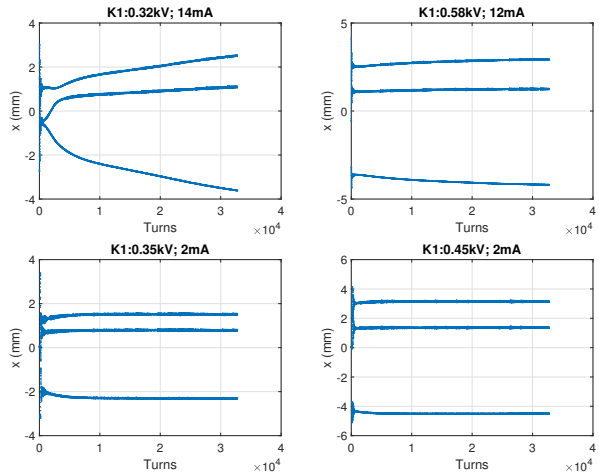


Figure 7: TbT BPM data for TRIBs excitation with different beam currents and K1 votage.

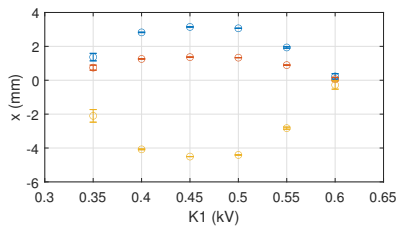


Figure 8: Measured charge centroid separation of the 2 mA single bunch changes with K1 voltage.

SUMMARY

Synchronous experimental studies on the TRIBs dynamics have been carried out in SPEAR3. We observed the current dependent effect in driving a single bunch to TRIBs using one of the injection kickers. The underlying physics is still unknown, but further studies, both experimental and theoretical, are under the way.

ACKNOWLEDGEMENTS

We would like to acknowledge P. Goslawski for useful discussions. We want to thank the SPEAR3 operation and technical teams for supporting the work.

Content from this work may be used under the terms of the CC BY 4.0 licence (© 2022). Any distribution of this work must maintain attribution to the author(s), title of the work, publisher, and DOI

ISBN: 978-3-95450-241-7 ISSN: 2673-5350 doi:10.18429/JACoW-IBIC2022-MOP16

Content from this work may be used under the terms of the CC BY 4.0 licence (© 2022). Any distribution of this work must maintain attribution to the author(s), title of the work, publisher, and DOI

REFERENCES

[1] P. Goslawski, A. Jankowiak, F. Kramer, M. Ries, M. Ruprecht, and G. Wuestefeld, "Transverse Resonance Island Buckets as Bunch Separation Scheme", in *Proc. IPAC'17*, Copenhagen, Denmark, May 2017, pp. 3059–3062. doi:10.18429/JACoW-IPAC2017-WEPIK057

[2] D. K. Olsson *et al.*, "Studies on transverse resonance island buckets in third and fourth generation synchrotron light sources", *Nucl. Instrum. Methods Phys. Res., Sect. A*, vol. 1017, p. 165802, 2021. doi:10.1016/j.nima.2021.165802

[3] K. Tian *et al.*, "Commission of the Transverse Bunch-by-Bunch Feedback at SPEAR3", in *Proc. IPAC'19*, Melbourne, Australia, May 2019, pp. 4081–4084. doi:10.18429/JACoW-IPAC2019-THPRB112

[4] M. Borland, "ELEGANT: A flexible SDDS-compliant code for accelerator simulation", Argonne National Lab., IL, USA, LS-287, 2000. doi:10.2172/761286

[5] J. Safranek, "Experimental determination of storage ring optics using orbit response measurements", *Nucl. Instrum. Methods Phys. Res., Sect. A*, vol. 388, pp. 27–36, 1997. doi:10.1016/S0168-9002(97)00309-4

[6] F. Toufexis, S. Condamoor, W. J. Corbett, L. W. Lai, and P. Leban, "BPM Processor Upgrades at SPEAR3", in *Proc. NAPAC'19*, Lansing, MI, USA, Sep. 2019, pp. 591–594. doi:10.18429/JACoW-NAPAC2019-TUPLE15

ISBN: 978-3-95450-241-7 ISSN: 2673-5350 doi:10.18429/JACoW-IBIC2022-MOP17

DEVELOPMENT OF A SCINTILLATION FIBRE TRANSVERSE PROFILE MONITOR FOR LOW-INTENSITY ION BEAMS AT HIT*

R. Hermann†, [1,2], T. Haberer[2], A. Peters[2], T. Gehrke[1,3,4], B. Leverington[5] and M. Galonska[2]
[1]Heidelberg University Hospital, Department of Radiation Oncology, Heidelberg, Germany
[2]Heidelberg Ion-Beam Therapy Center (HIT), Department of Radiation Oncology, Heidelberg University Hospital, Heidelberg, Germany
[3]German Cancer Research Centre (DKFZ), Department of Medical Physics in Radiation Oncology, Heidelberg, Germany
[4]National Center for Radiation Research in Oncology (NCRO), Heidelberg Institute for Radiation Oncology (HIRO), Heidelberg, Germany
[5]Physikalisches Institut, Ruprecht-Karls-Universität Heidelberg, Heidelberg, Germany

Abstract

The Heidelberg Ion-Beam Therapy Center (HIT) provides proton, helium, and carbon-ion beams with different energies and intensities for cancer treatment and oxygen-ion beams for experimentation. The accelerator is able to provide ion beam intensities below the range used for therapies by manually degrading the beam. The beam monitoring system instrumentation currently installed is unable to measure the beam profile at these intensities. A secondary system that could cover this low intensity range is therefor of interest. The principle of operation is based on scintillating fibres, particularly those with enhanced radiation hardness. The fibres transform the deposited energy of a traversing ion into photons, which are then converted and amplified via silicon photomultipliers (SiPMs) into electric pulses. These pulses are recorded and processed by a novel and dedicated readout electronics: the front-end readout system (FERS) A5200 by CAEN. A prototype set-up consisting of all the above-mentioned parts was tested in beam and has proven to record the transverse beam profile successfully from intensities of 1E7 ions/s down to 1E2 ions/s.

INTRODUCTION

The HIT facility provides proton, carbon, and helium ion pencil beams for cancer treatment and research, and oxygen ion beams for experiments, all with various energies, beam spot sizes and intensities. HIT uses the method of intensity-controlled raster scanning of pencil beams as a dose delivery system.

The beam position and width (focus) in the horizontal and vertical plane are constantly monitored by two multiwire proportional chambers (MWPC) and the intensity by three ionization chambers (IC). Their signals are used for position and intensity control via a feedback system. As this built-in setup is specifically designed for tumour treatments it does not need to be, and is not, sensitive to low-intensity ion beams, i.e. below 1E5 ions/s. This detector reported in this contribution closes this gap.

Low intensity beams are of interest for experiments, but also for a new imaging modality with potential of treatment verification: helium-beam radiography [1]. The presented work is part of this project. Only low intensities may be used as radiation dose in the patient has to be limited to the lowest amount possible and ion tracking based on sing ion imaging is desirable. For an optimized performance, the low-intensity ion beam needs to be provided in a controlled way.

Out of three possible detector technologies (gas, semiconductor, and scintillating fibre based) the scintillating fibre was chosen because of its advantages in terms of permanent use and placement within the beamline of an accelerator: the relatively low cost of the fibres while covering a larger active area, no need of attached subsystems like cooling, gas or vacuum and electronics remain in a safe distance from the beam. This idea follows techniques used in high energy physics, coupling scintillating fibres to silicon photomultipliers for single particle tracking [2]. The Super Proton Synchrotron has developed a similar system, although with different readout electronics and beam conditions [3].

A novel specialized commercial front-end readout electronic board came into use: the FERS A5202 by CAEN, which was for instance successfully implemented in a dual readout calorimeter by the team of R. Santoro [4]. Due to the commercial character, there was no need for an own development in electronics or software. Thus, one can concentrate on specific data evaluation routines. Also scaling up the detector to the desired size of 25 x 25 cm² with a sub-millimetre resolution is feasible to implement due to the scalability of the readout system.

MATERIALS AND METHODS

Ion Beam Characteristics

Adopted to the dose delivery system, the HIT accelerator provides ion beams for cancer treatment by a slow extraction scheme, i.e. the ions are extracted over several seconds (“Spill length”, here: 5 s). The energy/intensity range is given in Table 1. The beam spot sizes range from about 3 to 30 mm defined a s full -width half-maximum (FWHM), depending on the ion type and energy. For reaching low

* Work funded by the German Research Foundation (Deutsche Forschungsgemeinschaft, DFG), project number 426970603.
† richard.hermann@med.uni-heidelberg.de

Content from this work may be used under the terms of the CC BY 4.0 licence (© 2022). Any distribution of this work must maintain attribution to the author(s), title of the work, publisher, and DOI

ISBN: 978-3-95450-241-7 ISSN: 2673-5350 doi:10.18429/JACoW-IBIC2022-MOP17

Content from this work may be used under the terms of the CC BY 4.0 licence (© 2022). Any distribution of this work must maintain attribution to the author(s), title of the work, publisher, and DOI

intensities, particle loss is forced by detuning the bending magnet right behind the ion sources.

Table 1: Therapeutically Ion Beam Specifications Provided by the HIT Accelerator

Ion	Energy [MeV/u]	Intensity [ions/s]
Proton	48.12 – 221.06	8.0e+7 – 3.2e+9
Helium	50.57 – 220.51	2.0e+7 – 8.0e+8
Carbon	88.83 – 430.10	2.0e+6 – 8.0e+7
Oxygen	103.77 – 430.32	1.0e+6 – 4.0e+7

Prototype Setup and Working Principle

The detection method of the prototype setup is as follows: The ions from the ion beam pass through the scintillating fibres, where part of their energy is lost through ionisation and re-emitted as photons through fluorescence. A small percentage (< 5.3%) of them is trapped in the fibres via total internal reflection at the core-cladding interfaces and guided to silicon photomultipliers (SiPMs), which create an electronic signal for every detected photon. These signals are processed by a front-end readout system (FERS) and transmitted to a computer via USB or Ethernet.

A 3D printed structure composed of black polyacid (PLA) is used to arrange and mount the fibres in a single plane, and then couple them to the SiPMs. A schema of the complete arrangement is shown in Fig. 1. This whole arrangement is covered with a box blocking external light, which may superimpose the signal, create unwanted noise and could lead to destructive currents. For the latter, the electronics have an overcurrent security turn off.

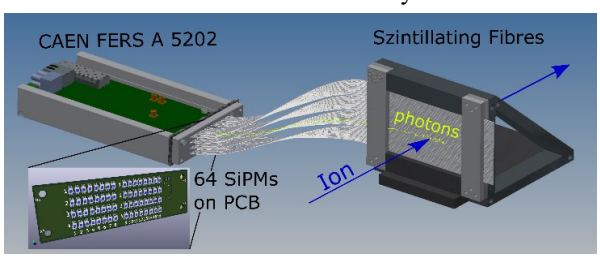


Figure 1: Experimental setup: scintillating fibres in frame, 64x SiPMs soldered on a printed circuit board (PCB), electric signal processing in FERS A5202.

Scintillating Fibres

The scintillation process describes the conversion of energy absorbed (e.g. deposited by ions which pass through the scintillating material, described by the Bethe-Bloch-formula) into photons in or close to the visible range. In the described setup organic plastic fibre scintillators with a 1 mm diameter are used. These fibres absorb and emit the energy via weakly bound orbital electrons, typically in benzene rings. A wavelength shifter (Stokes shift) is added to the scintillator to prevent the re-absorption of photons within the material and for tuning the output wavelength to the desired one.

To figure out if the more radiation hard green emitting fibres have a significantly lower light output or signal-to-noise ratio compared to the more common blue ones the two fibre types have been installed next to each other in this first test setup, as shown in Fig. 2.

Radiation damage is unavoidable when interfering with the ion beam. In scintillating fibres, the damage shows as losses in short wavelengths, i.e. the blue parts of the spectrum. The two fibres tested in the prototype setup were: (a) Kuraray SCSF-78 with the blue colour output (peak at $\lambda = 450$ nm), a fast decay time of 2.8 ns, and a long attenuation length of over 4 m and (b) Kuraray SCSF-3HF (3-hydroxyflavone) with a green output (peak at $\lambda = 530$ nm) and therefore higher radiation hardness, with a similar attenuation length, but a slower decay of 7 ns [5].

One additional advantage of scintillating fibres, in general, is their insensitivity to the magnetic field. This is of interest in the upcoming project of beamline integrated Magnet Resonance Imagers (MRIs).



Figure 2: The two fibre types glued into 3D prints. The scintillating fibre area consists of (a) 32 blue fibres (channel 0 – 31) and (b) 32 green fibres (channel 32 – 63).

The fibres have single or multi-cladding, which describes one or two thin layers around the fibres (thickness of a layer is 2% of the fibre diameter) with lower refractive indices. This increases the fraction of light, which is trapped inside the fibre. The scintillating core is polystyrene with a refractive index of n0 = 1.59. A single layer of Polymethylmethacrylate (PMMA, n0 = 1.49) raises the trapping efficiency to at least 3.1 %, and with a second layer of the fluorinated polymer (FP, n0 = 1.42) it reaches 5.4 % [5].

Silicon Photomultipliers (SiPMs)

The silicon photomultiplier S13360-1350PE by Hamamatsu is a set of 667 single avalanche photodiodes (APDs) which together form an active area of 1.3 x 1.3 mm². The APDs are operated in Geiger mode, which means their output is independent of the number of photons [6].

These SiPMs were chosen for their fitting photon detection efficiency (PDE) spectrum shown in Fig. 3. The refractive index of 1.55 in the window material fits the one of the scintillating fibres so that no photons are reflected at the interface.

Even in the case of an airgap, still small enough that all non-reflected photons hit the SiPM, an upper limit estimation of the loss would only be 11.8%. (Calculated with Fresnel equations and based on the worst condition which still transmits light: an incidence angle of 26.7° [5] at the interface from the fibre (n0 = 1.59) to air (n0 = 1) and subsequently from air to the SiPM window (n0 = 1.55).

The signal amplification (gain) of the SiPMs creates 1.7E6 electrons for each detected photon. The pulse of a 1 mm² pixel pitch, consisting of 50 µm pixels (APDs), recovers within 50 ns (20 MHz) [6]. If several photons hit within the recharging phase the recovery may not be completed. This may lead to uncounted hits.

ISBN: 978-3-95450-241-7 ISSN: 2673-5350 doi:10.18429/JACoW-IBIC2022-MOP17

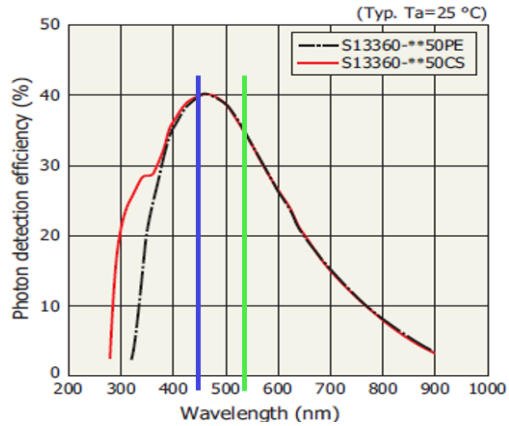


Figure 3: PDE of the Hamamatsu S13360-130PE. The blue (λ = 450 nm) and green (λ = 530 nm) lines indicate the output wavelength of the SCSF-78 and the SCSF-3HF scintillating fibres.

Front End Readout System (FERS)A5202

The FERS A5202 is specifically designed to read out SiPMs in large detector arrays [7]. The standalone boards are capable of reading out 64 channels and can be connected in series (daisy chain) via a concentrator board to up to 8192 channels. Different acquisition modes are available of which the Counting and Timing Mode are the ones of interest here. In Counting mode, a time window is set in which the counts per channel are summed up. The count caps at 20 Mcps, which is exactly the limit for pulse level recovery of the used SiPMs (20 MHz). In Timing mode, the exact timestamp of each firing SiPM is saved. Due to more detailed information, the timing mode is limited by how data is packed and transmitted in the links to a lower number of ions per second (~5E4 ions/s) compared to the Counting mode (~1E7 ions/s). The estimations were evaluated in experiments at HIT and could be improved via adjustments. Detailed information about the data structure, the description of the different measure modes (Counting, Timing, timestamped spectroscopy and pulse height analysis) and the used built-in electronics (e.g. Citiroc, FPGA) are found in the associated manuals CAEN provides [7].

EXPERIMENTAL RESULTS

The purpose of the detector is to measure the position, beam width, and the intensity of the beam at low intensities (<1E5 ions/s). This was successfully tested in the range of 1E2 – 1E7 ions/s.

The low end of the intensity spectrum (1E2 pps) is set due to lacking data for reliable position measurement. Purely by statistical probability, the beam position determined by a fit could vary with these few counts in the order of millimetres, which is worse than the position accuracy of the detector of at least 1 mm. A measurement close to this lower limit in intensity has been successfully achieved with a helium ion beam with the maximal available energy of 220 MeV/u, shown in Fig. 4.

Figure 4 also shows noise. This noise is mainly thermal, which shows up as so-called dark counts. The dark count rate (DCR) while having no beam can be brought below the value of 50 Hz by correct settings. One is the threshold setting of the SiPMs, where a signal is only counted if at least 5 APDs (“pixels”) of a SiPM fire simultaneously. This takes out crosstalk events within the SiPMs. In between the SiPMs a light shielding blocks this crosstalk.

Having beam there is crosstalk, which happens in between the fibres and limits the SNR to a factor of 50 – 100. More details about the crosstalk between the fibres can be found in [3].

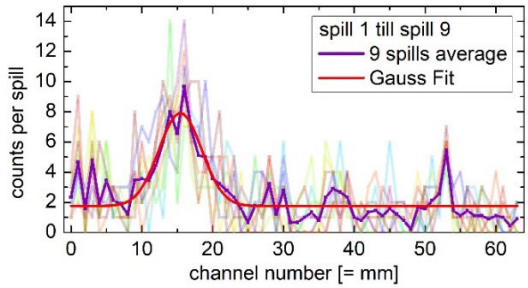


Figure 4: Proof of concept measurement of a low-intensity helium beam with ca. 8 ions/s (recorded by TimePix [1]). An average over several spills is needed as the non-feedbacked low-intensity spills vary in intensity.

The upper end of the possible spectrum is 1E7 ions/s, shown in Fig. 5. It also shows 1D beam profiles of the four different ion types provided at HIT. As the intensity range is different for each ion type a setting at the low end of the therapeutic range was chosen. Noticeable are the non-smooth profiles of helium and proton, where the intensities are above 1E7 pps. At this point, some counts are missed and the gaussian form gets lost. The reason for the missed counts is the SiPM recharge duration of 50ns, as photons incoming within that time will not be detected.

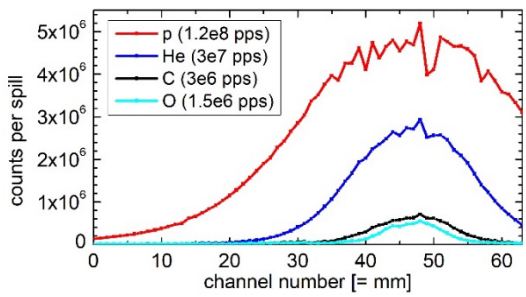


Figure 5: 1D beam profiles of all 4 ion types at HIT with different intensities. The beam energy is irrelevant, as a count is independent of the number of photons created.

In a context like a therapy accelerator, radiation damage to in-beam-line detectors is a major issue. Over time a high amount of dose (ions depositing energy) is delivered, damaging the detector. This means a regular refurbishing or replacement of the scintillating fibres.

There are more radiation hard scintillating fibres, but SiPMs have a higher PDE for the blue spectra, see Fig. 3. Therefore, the 3HF green and the “standard” blue fibres have been set up for comparison. Contradicting the expectation set by the better PDE for the blue spectra, measurements at HIT show that the green 3HF have a higher output and SNR, as Fig. 6 indicates.

Content from this work may be used under the terms of the CC BY 4.0 licence (© 2022). Any distribution of this work must maintain attribution to the author(s), title of the work, publisher, and DOI

ISBN: 978-3-95450-241-7 ISSN: 2673-5350 doi:10.18429/JACoW-IBIC2022-MOP17

Content from this work may be used under the terms of the CC BY 4.0 licence (© 2022). Any distribution of this work must maintain attribution to the author(s), title of the work, publisher, and DOI

Besides beam position and beam width also intensity can be measured with the presented setup. Two 5 s long low-intensity carbon ion spills with 430 MeV/u have been compared, and are shown in Fig. 7. A comparison with the internal in-beamline integrated and calibrated scintillator shows that the spill shapes are matching (intensity variation due to non-feedbacked beam). Also, a comparison of two feedback-controlled spills with different energy levels but the same intensity showed a difference in intensity of only 1%.

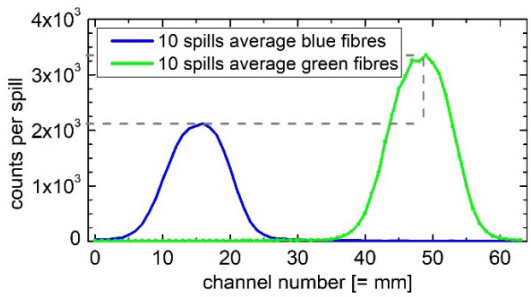


Figure 6: Ion counts averaged over 10 spills: Kuraray SCSF-78 (blue, 450 nm) and Kuraray SCSF-3HF (green, 530 nm).

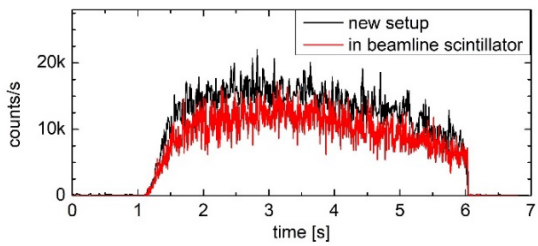


Figure 7: Intensity vs. time measurement of a 5 s spill (time bin 5 ms): presented detector (black), in-beamline integrated and calibrated detector (red).

CONCLUSION

The scintillating fibre profile monitor has been successfully tested with the proton, helium, carbon and oxygen ion beams provided at the HIT facility. The energies varied from 50 – 430 MeV/u with intensities from 1E2 up to 1E7 pps. The lower limit is only due to too low signals for fitting, while the upper limit is due to the speed of the electronics (SiPMs and FERS A5202). Testing two different fibre types showed that the general-purpose fibres with a 450 nm output are inferior in terms of SNR compared to the desired more radiation hard 3HF fibres with a 530 nm output.

In conclusion, the described setup is a reliable and fully functional beam position, width, and intensity monitor for the yet unmonitored low-intensity ion beams at HIT. With that applications based on controlled low-intensity beams, like ion radiography, become feasible.

OUTLOOK

For a controlled low-intensity ion beam at HIT, the measurement data of the presented setup needs to be transferred in real-time to the intensity control system. The integration into the feedback system is one main future development.

A simpler and closer next step will be the second fibre layer orthogonal to the first one to make a simultaneous horizontal and vertical measurement possible, preferably done with square instead of round fibres for a more evenly distributed in-beam material.

Provided that a perfect synchronization to other detectors can be established this monitor could work as a single ion front tracker, which is a highly desired option for the purpose of the underlying DFG project, the ion radiography detector.

As a final step, this setup will either be itself extended to a full 256 x 256 mm² plane or more likely combined with the scintillating fibre planes of [2]. This would allow monitoring of single ions up to the highest intensities (proton, 3.2E9 ions/s) with one set of scintillating fibre mats, greatly decreasing the necessary in-beam material.

ACKNOWLEDGEMENTS

Many thanks to the HIT team to be always helpful and providing such a great experimental environment. Special thanks to Patrick Busch, Stephan Brons, Eike Feldmeier, Christian Schömers and Andreas Gaffron.

To Romualdo Santoro and his team from INFN working on a Dual Readout Calorimeter with the same front-end readout [4]: thanks for the helpful discussions and also for the design of the SiPM-PCB.

REFERENCES

[1] T. Gehrke, M. Martišíková, *et al.*, "Experimental helium-beam radiography with a high-energy beam: Water-equivalent thickness calibration and first image-quality results", *Med. Phys.*, vol. 49, pp. 5347-5362, 2022. doi:10.1002/mp.15795

[2] B.D. Leverington *et al.*, "A prototype scintillating fibre beam profile monitor for Ion Therapy beams", *J. Instrum.,* vol. 13, p. 05030, 2018. doi:10.1088/1748-0221/13/05/P05030

[3] I. Ortega Ruiz *et al.*, "A Multipurpose Scintillating Fibre Beam Monitor for the Measurement of Secondary Beams at CERN", in *Proc. IBIC2018,* Shanghai, China, Sep. 2018, pp. 468-471. doi:10.18429/JACOW-IBIC2018-WEPB15

[4] M. Antonello *et al.*, "Dual-readout calorimetry: Present status and perspective", *Int. J. Mod. Phys. A,* vol. 36, p. 2142017, 2021. doi:10.1142/S0217751X21420173

[5] Kuraray Co., Ltd., "Plastic Scintillating Fibres", https://www.kuraray.com/uploads/5a717515df6f5/PR0150_psf01.pdf (checked last 03.08.2022)

[6] Hamamatsu Photonics K.K., "MPPC Technical note", https://www.hamamatsu.com/content/dam/hamamatsu-photonics/sites/documents/99_SALES_LIBRARY/ssd/mppc_kapd9008e.pdf (checked last 03.08.2022)

[7] CAEN S.p.A., "FERS-5200 Front-End Readout System Datasheet DS7218", https://www.caen.it/products/a5202/ (checked last 03.08.2022)

ISBN: 978-3-95450-241-7 ISSN: 2673-5350 doi:10.18429/JACoW-IBIC2022-MOP18

X-RAY PINHOLE CAMERA SPATIAL RESOLUTION USING HIGH ASPECT RATIO LIGA PINHOLE APERTURES

N. Vitoratou*, L. Bobb, Diamond Light Source, Oxfordshire, UK
G. Rehm, Helmholtz-Zentrum für Materialien und Energie, Berlin, Germany
A. Last, Karlsruhe Institute of Technology, Karlsruhe, Germany

Abstract

X-ray pinhole cameras are employed to provide the transverse profile of the electron beam from which the emittance, coupling and energy spread are calculated in the storage ring of Diamond Light Source. Tungsten blades separated by shims are commonly used to form the pinhole aperture. However, this approach introduces uncertainties regarding the aperture size. X-ray lithography, electroplating and moulding, known as LIGA, has been used to provide thin screens with well-defined and high aspect ratio pinhole apertures. Thus, the optimal aperture size given the beam spectrum can be used to improve the spatial resolution of the pinhole camera. Experimental results using a LIGA screen of different aperture sizes have been compared to SRW-Python simulations over the 15 – 35 keV photon energy range. Good agreement has been demonstrated between the experimental and the simulation data. Challenges and considerations for this method are also presented.

INTRODUCTION

X-ray pinhole cameras (XPCs) are a well-established diagnostic tool for measurement of the 2D transverse beam profile of the electron beam in the storage ring [1]. From the acquired beam size measurement, combined with knowledge of the lattice parameters, the emittance and coupling are calculated. The expected beam sizes in Diamond-II will be smaller than the nominal operation of Diamond, particularly for emittance measurement of the squeezed beam after correction of the lattice using the linear optics from closed orbits (LOCO) method [2].

The Point Spread Function (PSF) of the imaging system should be minimised to improve the spatial resolution. The overall PSF is represented by the contributions of the scintillator screen, the lens, the camera sensor and the pinhole aperture itself which is a fundamental component in the pinhole camera. Reduction of the PSF can be achieved by using the optimal pinhole aperture size for the given photon beam energy of the synchrotron radiation [1]. For sufficient contrast at photon energies in the 15 – 60 keV range, the pinhole aperture must be formed using a material with a high atomic number.

High Z-number materials are often difficult to machine, especially to form high aspect ratio structures, e.g. a rectilinear square aperture of 10 µm × 10 µm with a thickness of 250 µm to 1 mm. Due to this, the pinhole aperture is often formed by stacking two orthogonal sets of tungsten blades separated by precisely machined shims. The thickness of the shims between the tungsten blades sets the aperture size [3]. Although the blades have surfaces that are easy to polish and the shims can be manufactured to the specified thickness, there are drawbacks to this stacked design. Firstly the pinhole aperture, which from theory should be an infinitesimally thin screen is a 10 mm long tunnel, making simulation challenging. Secondly, the effective aperture size is typically larger than the shim thickness. And thirdly, the absolute measurement of the effective aperture size in this geometry is not trivial.

LIGA (X-ray lithography) technology [4] enables the fabrication of high-aspect ratio structures using high-Z materials such that the pinhole aperture size is known and controllable. Furthermore, the tunnel-like geometry of the aperture is removed to provide better agreement with theoretical models. At the Karlsruhe Institute of Technology, unique LIGA screens are produced. These are made from gold with a thickness up to 250 µm. Thus, allowing the comparison between simulations of the pinhole camera with real acquired data on the accelerator. This could enable simulation of the PSF of the pinhole camera instead of PSF measurement using Touschek calibration with beam which is time-consuming [5].

In this paper, simulations and measured pinhole camera images from a bending magnet sourcepoint using a LIGA screen are compared.

EXPERIMENTAL SETUP

Pinhole camera 3 is installed on the Diagnostics X-ray beamline inside the storage ring tunnel for the purpose of R&D. A schematic of the setup is shown in Fig. 1. The pinhole-to-scintillator distance is 9.72 m, the source-to-

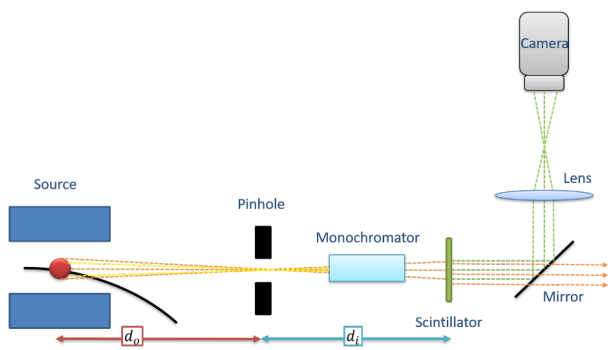


Figure 1: Schematic of an X-ray pinhole camera from a bending magnet sourcepoint.

* niki.vitoratou@diamond.ac.uk

Content from this work may be used under the terms of the CC BY 4.0 licence (© 2022). Any distribution of this work must maintain attribution to the author(s), title of the work, publisher, and DOI

ISBN: 978-3-95450-241-7 ISSN: 2673-5350 doi:10.18429/JACoW-IBIC2022-MOP18

Content from this work may be used under the terms of the CC BY 4.0 licence (© 2022). Any distribution of this work must maintain attribution to the author(s), title of the work, publisher, and DOI

pinhole magnification was measured as 2.54, the source-to-pinhole distance is 3.82 m and the scintillator-to-camera magnification was measured as 1.02. Approximately 1 m upstream of the scintillator is a multilayer monochromator. The bandwidth of the Mo/Si multilayer monochromator is < 1 keV [6]. The parameters of the multilayer monochromator are summarised in Table 1.

Table 1: Multilayer Monochromator Parameters

Parameter	Value
Mirror dimensions	300 mm × 50 mm
d-spacing	4.8 nm
Coating	Mo/Si
Substrate	Float glass
Number of layer-pairs	100

A side effect of multilayer monochromator on micro-imaging applications is the stripe pattern induced in the image [6]. On the Diagnostics X-ray beamline the monochromator reflects in the horizontal plane to ensure that the vertical dimension of the imaged beam profile is not distorted by this well-known banding effect. The single bounce monochromator means it is necessary to track the reflected beam with a camera mounted on translation stages. At 12 keV, the Bragg angle is ≈ 0.67 degree, which gives a beam-deflection of ≈ 23 mm at a distance of 1 m.

Figure 2 shows the design for the LIGA pinhole screen. The screen features square apertures with sizes ranging from 10 µm to 50 µm. For each aperture size there is a 3×3 grid of apertures. The apertures are separated to ensure independent images are obtained from each pinhole. A 400 µm aperture is included for initial alignment. Each pinhole aperture size was checked using a scanning electron microscope (SEM) to verify the size. Differences in the range of few microns were revealed between the measurement and the specification. This was taken into account for the comparison studies between experiment and simulation.

SIMULATION

The Synchrotron Radiation Workshop in Python (SRW-Python) [7, 8] was used to simulate the image of the photon beam at the scintillator screen. The simulation settings were defined according to the experimental setup. Firstly, the SR emitted from a single electron sourcepoint propagated through a square pinhole aperture was simulated for a fixed photon energy. This was then extended using the partially coherent wavefront propagation for 2000 individual electrons with a Gaussian distribution representing the electron beam profile.

The procedure was repeated for a set of energies from 15 – 35 keV for each pinhole aperture size. The simulation assumes X-rays propagate in vacuum, therefore the 1 mm aluminium window from vacuum-to-air and 10 m air are omitted. The monochromator was also omitted from the simulation since the photon energy is specified.

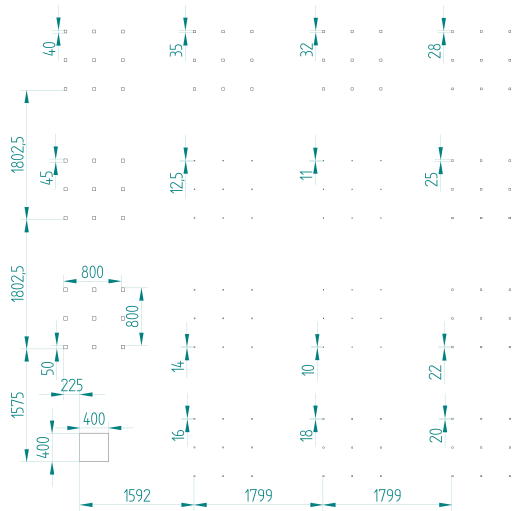


Figure 2: Pinhole screen design of 3x3 arrays of square holes.

The simulated beam intensity data from SRW was used to construct the 2D image of the beam on the scintillator screen. The image was convolved with the scintillator screen PSF which was measured experimentally using the knife edge method. The vertical projection of the beam on the scintillator screen was fitted with a 1D Gaussian fit and the sigma provided the vertical beam size on the scintillator screen.

PINHOLE APERTURE MEASUREMENTS

Figure 3 shows an image acquired using the LIGA screen with the monochromator retracted (i.e., with white beam). Some leakage is seen of the SR fan through the ≈ 250 µm thick LIGA screen. Images were then acquired for a range of

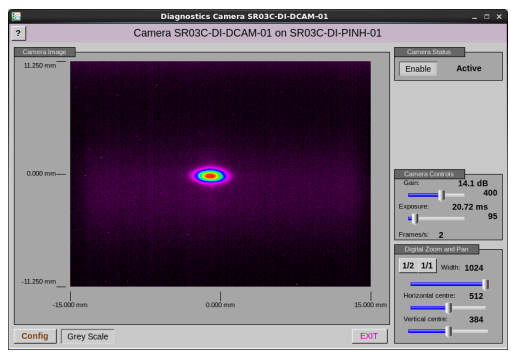


Figure 3: White beam image using the LIGA screen.

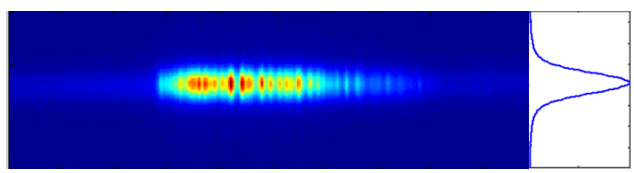
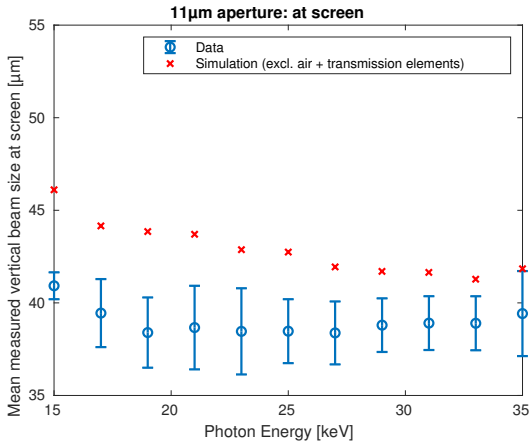
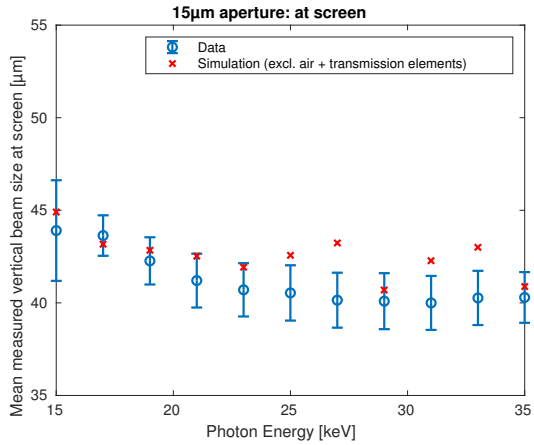


Figure 4: Image from the pinhole camera at 23 keV using a 25 µm aperture.

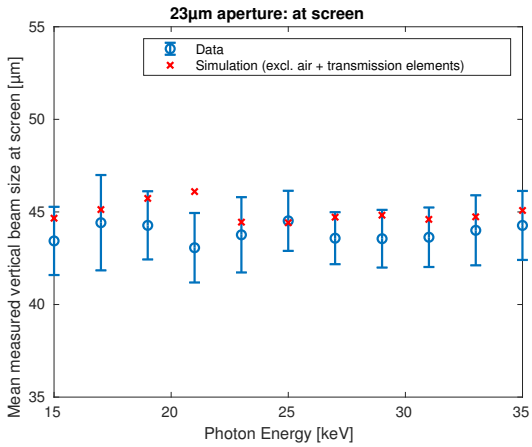
ISBN: 978-3-95450-241-7 ISSN: 2673-5350 doi:10.18429/JACoW-IBIC2022-MOP18



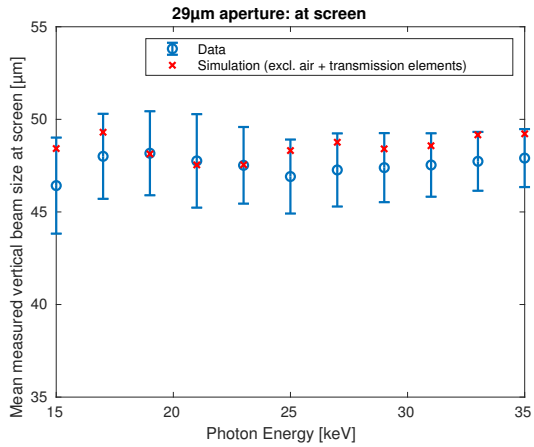
(a) 11 µm aperture.



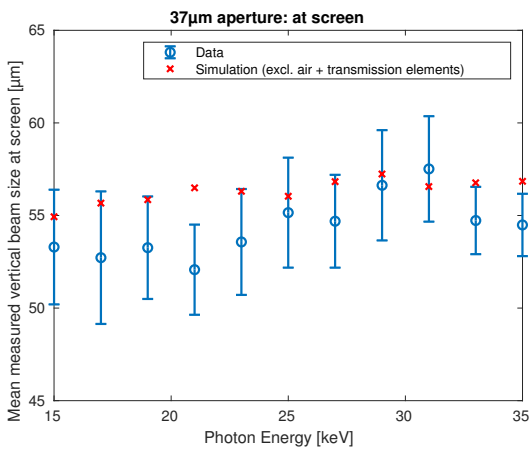
(b) 15 µm aperture.



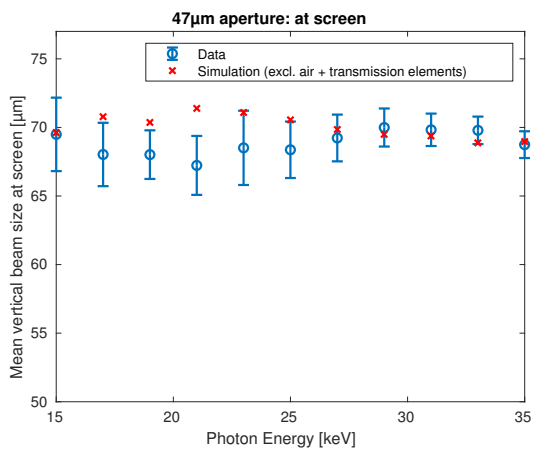
(c) 23 µm aperture



(d) 29 µm aperture



(e) 37 µm aperture



(f) 47 µm aperture

Figure 5: Comparison of simulation and experimental data for different LIGA pinhole aperture sizes and photon energies.

photon energies using different aperture sizes. A typical image is shown in Fig. 4. The expected stripe pattern from the multilayer monochromator is observed, however the vertical profile of the beam is preserved in the image.

The vertical beam size was measured by stacking five images from the pinhole camera. Hot pixels were removed using a median filter. Due to the stripe pattern, each column of the stacked image was fitted with a 1D double Gaussian profile, where one of the Gaussian curves represents the beam profile while the second Gaussian describes the background.

To ensure reasonable fits, a signal-to-noise threshold was applied to only include columns where the Gaussian peak that represents the beam profile was 20 times greater than

Content from this work may be used under the terms of the CC BY 4.0 licence (© 2022). Any distribution of this work must maintain attribution to the author(s), title of the work, publisher, and DOI

ISBN: 978-3-95450-241-7 ISSN: 2673-5350 doi:10.18429/JACoW-IBIC2022-MOP18

Content from this work may be used under the terms of the CC BY 4.0 licence (© 2022). Any distribution of this work must maintain attribution to the author(s), title of the work, publisher, and DOI

the average background. The average background was taken from a corner of the image where the SR fan intensity was significantly reduced. The background in the region of the image is significantly greater than the obtained average background, thus a threshold factor of 20 was found to be most appropriate.

The experimental data for a range of aperture sizes is shown in Fig. 5. For each data point the average measured vertical beam size is presented with an error bar of the standard deviation from the Gaussian fits of the columns of the image. The vertical beam size at the scintillator screen is compared over a range of photon energies from 15 – 35 keV. The standard deviations range from a few per cent up to 10% with respect to the average measured beam size at each photon energy.

EXPERIMENT AND SIMULATION COMPARISON

The experiment and simulation data comparison was conducted for different aperture sizes from 11 to 47 µm as shown in Fig. 5. The aperture size used as the label in the plots is according to the SEM measurements and not the specification.

The relative difference between the simulated and experimentally measured beam sizes over a range of photon energies for each aperture is summarised in Fig. 6. For most cases, the mean value of the relative difference across the energy range for each aperture size is below 5% with the highest value being 8%, excluding the 11 µm dataset.

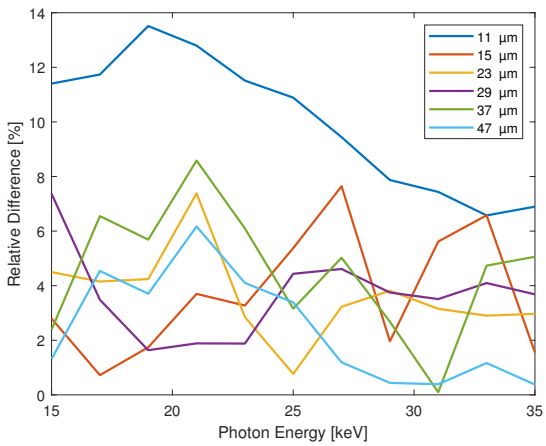


Figure 6: Relative difference between the simulated and measured beam sizes over a range of photon energies for each aperture size.

It should be noted that a small degree of disagreement was expected since the simulation uses a bare lattice and assumes perfectly monochromatic light, whereas the data was acquired from the synchrotron with insertion devices at gaps for nominal user beam and the multilayer monochromator has finite bandwidth. Also, the photon absorption in the aluminium window from vacuum-to-air and the 10 m air were not included in the simulation.

For the 11 µm aperture the relative difference between the simulated and measured beam sizes is much higher in comparison to the other apertures. This discrepancy may arise from the quality of the 11 µm apertures, which were observed to be visually poorer under the SEM, since these apertures approach the aspect ratio limit of the LIGA fabrication process.

CONCLUSIONS

LIGA offered the possibility to control the pinhole aperture size and to compare the simulations with the experiment. SEM measurements were important to validate the accuracy of the specified aperture size and eventually to achieve a good agreement between the experiment and the simulation.

The smallest vertical beam sizes were obtained from pinhole apertures in the range of 11 – 23 µm. However, the monochromatic photon flux at the image plane was low and five images had to be acquired to improve the signal to noise ratio. As the aperture size increases, the flux increases whilst the spatial resolution of the pinhole camera decreases.

The experimental data shows a good agreement ($\lesssim 8\%$) with the simulation for the 15 – 47 µm aperture sizes and implies that the pinhole camera system performs as described in the simulation. The remaining discrepancy between simulation and aperture size may be further reduced through optimisation of the simulation and data analysis. Therefore this work could be extended to simulate the broadband PSF for white beam given the known aperture size, thereby removing the need for time-consuming beam measurements of PSF.

Excluding the 11 µm dataset from these measurements and given the white beam spectrum peaks at 23 keV, the optimal aperture size from simulation and experiment for this pinhole camera is approximately 15 µm.

ACKNOWLEDGEMENTS

The authors acknowledge the support of the Karlsruhe Nano Micro Facility (KNMFi) and the KARA synchrotron light source facility at the Karlsruhe Institute of Technology (KIT).

REFERENCES

[1] C. Thomas, G. Rehm, I. Martin, and R. Bartolini, "X-ray pinhole camera resolution and emittance measurement," *Phys. Rev. ST Accel. Beams*, vol. 13, no. 2, p. 022 805, 2010. doi:10.1103/PhysRevSTAB.13.022805

[2] R. Tomás, M. Aiba, A. Franchi, and U. Iriso, "Review of linear optics measurement and correction for charged particle accelerators," *Phys. Rev. Accel. Beams*, vol. 20, p. 054 801, 2017. doi:10.1103/PhysRevAccelBeams.20.054801

[3] P. Elleaume, C. Fortgang, C. Penel, and E. Tarazona, "Measuring beam sizes and ultra-small electron emittances using an X-ray pinhole camera," *J. Synchrotron Radiat.*, vol. 2, no. 5, pp. 209–214, 1995. doi:10.1107/S0909049595008685

ISBN: 978-3-95450-241-7 ISSN: 2673-5350 doi:10.18429/JACoW-IBIC2022-MOP18

[4] E. W. Becker, W. Ehrfeld, P. Hagmann, A. Maner, and D. Münchmeyer, "Fabrication of microstructures with high aspect ratios and great structural heights by synchrotron radiation lithography, galvanoforming, and plastic moulding (LIGA process)," *Microelectron. Eng.*, vol. 4, no. 1, pp. 35–56, 1986. doi:10.1016/0167-9317(86)90004-3

[5] L. M. Bobb, A. F. D. Morgan, and G. Rehm, "Performance Evaluation of Molybdenum Blades in an X-ray Pinhole Camera," in *Proc. IBIC'16*, Barcelona, Spain, Sep. 2016, pp. 795–798. doi:10.18429/JACoW-IBIC2016-WEPG63

[6] A. Rack *et al.*, "Comparative study of multilayers used in monochromators for synchrotron-based coherent hard X-ray imaging," *J. Synchrotron Radiat.*, vol. 17, no. 4, pp. 496–510, 2010. doi:10.1107/S0909049510011623

[7] O. Chubar *et al.*, *Synchrotron radiation workshop.* https://github.com/ochubar/SRW

[8] O. Chubar *et al.*, "Main functions, recent updates, and applications of Synchrotron Radiation Workshop code," in *Advances in Computational Methods for X-Ray Optics IV*, International Society for Optics and Photonics, vol. 10388, 2017, pp. 13–27. doi:10.1117/12.2274285

Content from this work may be used under the terms of the CC BY 4.0 licence (© 2022). Any distribution of this work must maintain attribution to the author(s), title of the work, publisher, and DOI

ISBN: 978-3-95450-241-7 ISSN: 2673-5350 doi:10.18429/JACoW-IBIC2022-MOP19

COMMISSIONING OF THE RENEWED LONG RADIAL PROBE IN PSI's RING CYCLOTRON

M. Sapinski*, R. Dölling, M. Rohrer, Paul Scherrer Institut, Villigen, Switzerland

Abstract

PSI's Ring cyclotron is a high intensity proton cyclotron producing a CW proton beam of 2 mA. The beam is accelerated over about 180 turns from 72 MeV to 590 MeV. The Long Radial Probe, called RRL scans the beam along a machine radius over the whole range of turns, i.e. from 2048 mm to 4480 mm. A replacement for the RRL has been developed in the last years. The recently installed new probe drives three carbon fibers with 30 μm diameter through the turns and measures secondary electron emission (SE) currents, providing information on horizontal and vertical beam shape and position. Additional drives are available for a later extension of measurement capabilities. The main challenges are the coupling of the device elements to RF fields leaking from the accelerating cavities, plasma interfering with the measured signal, and the performance of the carbon fibers in a harsh environment with a high-intensity beam and RF heating. We report on the commissioning of the probe with RF and beam and discuss measurement results.

INSTRUMENT DESIGN

The RRL drives three carbon fibers stretched between the upper and bottom trolley, along the radius of PSI's Main Ring cyclotron [1, 2]. The trolleys, powered by the same stepper motor, move synchronously with a speed of 29.7 mm/s. The fibres are oriented vertically and tilted -45° and +45° seen in the beam direction. The setup is visualized in Fig. 2 of [3].

The vertical wire (0°) crosses all orbits in the cyclotron, the -45° wire misses the first orbit and the +45° wire misses the first four orbits. Each scan is performed in two directions: from the parking position at a radius of 4480 mm to the most inner position at 2048 mm (scan *in*) and back (scan *out*).

Between the upper and bottom parts of the main structure of the probe there is a 40 mm clearance for the beam. The structure is milled out of an aluminum alloy (EN AW-5083) and its overall weight is around 100 kg. It contains cables, cable trays, metallic perforated transmission belts used to move the trolleys, and thermocouples to measure the main probe structure temperature. It is grounded at the top and bottom of the vacuum chamber by 20 roller contacts each (Fig. 1). The contacts are installed in pairs, spaced by 25 cm. Four shields are installed on both sides to protect fibres from RF fields and plasma.

Measurement of trolley vibrations performed with PCB-356B18 triaxial accelerometer revealed that the highest vibration amplitude is in the direction of the scan (Fig. 2). The frequency spectrum is broad and drops above 400 Hz, however, it is not yet clear how it affects the signal quality.

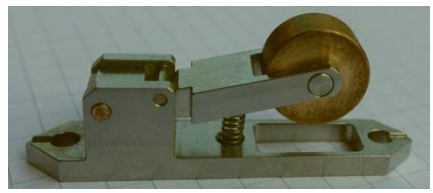


Figure 1: Roller contact for grounding probe structure.

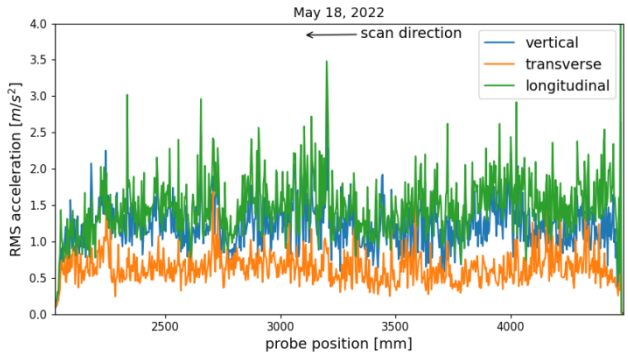


Figure 2: The RMS acceleration measured on the trolley during the scan.

The RRL is installed in the intermediate sector chamber #2, an area of the cyclotron in between two dipole magnets and not equipped with a RF cavity (see Fig. 3 of [2]). This sector contains the electrostatic injection septum EIC and is on the outside equipped with three air-filled ionization chambers called MRI2 at the low radius, MRI9 at the high radius, and MRI9B in the middle.

The signals from the carbon fibers are digitized by MESON logarithmic amplifier modules [4] outside of the bunker, which also control the movement of the trolleys.

COMMISSIONING WITHOUT BEAM

One of the main concerns was the coupling of the RRL structure and the carbon wires to the RF fields leaking out of the cyclotron RF cavities. Therefore, numerous RRL measurements were performed during the RF-conditioning period in March and April 2022.

Observation of RF Heating

Fast detection of eventual strong temperature changes of RRL elements is not possible with the thermocouples due to the large thermal inertia of the main structure. Hence, a FLIR AX8 camera with infrared and visible light sensors has been installed at the height of the machine midplane (Fig. 3). The viewport with a ZnSe IR-transparent window was mounted on a specially-designed flange with an angle allowing for optimal coverage of the probe structure. This flange was equipped with RF shields due to concerns about

* e-mail address: mariusz.sapinski@psi.ch

Content from this work may be used under the terms of the CC BY 4.0 licence (© 2022). Any distribution of this work must maintain attribution to the author(s), title of the work, publisher, and DOI

ISBN: 978-3-95450-241-7 ISSN: 2673-5350 doi:10.18429/JACoW-IBIC2022-MOP19

RF field influence on the camera. Finally, no such influence has been observed during the succeeding measurements. In the course of the RF conditioning, the FLIR camera was set up to register images every few seconds. An example is shown in Fig. 4. An additional camera, SONY SNC-RX570P, was mounted on a second viewport. It provided additional imaging and remotely-controlled illumination, as IR imaging has been done in dark, with all bunker lights off.

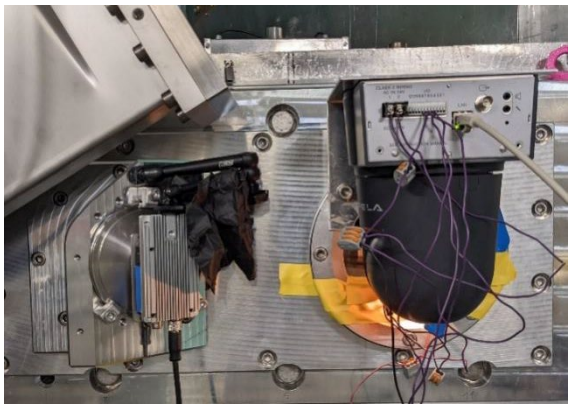


Figure 3: FLIR camera (left) and Sony camera. The RRL is on the left, outside of the frame. (A fragment of the vacuum valve, separating the RRL probe chamber from the machine vacuum, is visible in the upper left corner.)

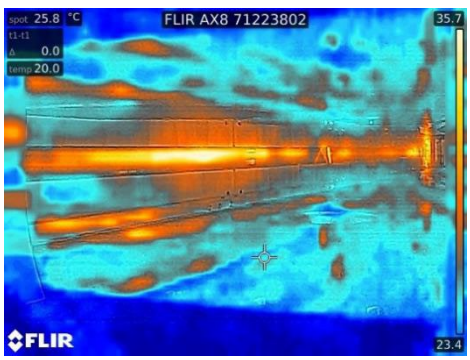


Figure 4: Image produced by the FLIR camera in mixed mode, where both, IR sensor and visible spectrum image are overlapped. The temperature scale is not corrected for viewport transmission. The three wires /\| are apparent.

No fast temperature changes of structure parts have been observed during commissioning. At regular RF operation the main probe structure stayed below 40 °C. However, with one of the 50 MHz RF cavities (#3) accidentally switched off, the thermocouples indicated heating of the main probe structure at a rate of 12 °C/hour. Uninterrupted, this may result in temperatures above 100 °C and hence we will interlock this.

The carbon fibers are glowing due to heating by the RF coupling to it. The temperature could not be measured by the IR sensor because of its limited spatial resolution. However, the glowing was also apparent in visible light as seen in Fig. 5. The vertical wire exhibits the strongest glow. This wire broke at a scan done with RF cavity #3 switched off, i.e. at stronger RF input. At replacement of this wire, the readback cable was disconnected at the wire mount. The decreased capacitance already resulted in a weaker glowing. In addition, we will install isolators with lower permittivity in the wire mounts. Measurement of the -45° wire resistance during the scan shows a decrease from 4.4 kΩ at the parking position down to 3.4 kΩ in the middle of the scan. The temperature estimated from the drop of resistivity is reaching 1130 K (Fig. 6).



Figure 5: Carbon fibres glowing in visible spectrum due to excitation by RF field leaking from RF cavities.

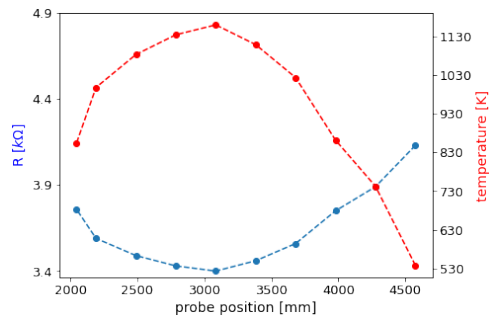


Figure 6: Wire resistance in various probe positions. Estimation of wire temperature based on resistance temperature coefficient $-5 \cdot 10^{-4}$ [1/K] and active wire length 56 mm.

Interaction with Electrostatic Injection Septum

The RRL is measuring the very first beam orbit, right after the EIC, which operates with a static voltage of 140 kV. No effect of the presence of the RRL on the HV and dark current of EIC has been observed.

However, when later scanning high-intensity beams, an increased number of beam interlocks due to EIC HV trips have been noticed. Interestingly those interlocks take place mainly during the scan out. Possibly dust particles from the bottom of the chamber are transported towards the EIC, provoking sparks.

COMMISSIONING WITH BEAM

The first measurements with the beam took place on April 27th, 2022. The IR camera, which survived weeks of operation in the presence of RF fields and gamma rays from multipacting electrons, suffered radiation damage and stopped working after receiving an approximate flux of about $2.5*10^5$ neutrons/cm^2. However, no dead pixels were

Content from this work may be used under the terms of the CC BY 4.0 licence (© 2022). Any distribution of this work must maintain attribution to the author(s), title of the work, publisher, and DOI

ISBN: 978-3-95450-241-7 ISSN: 2673-5350 doi:10.18429/JACoW-IBIC2022-MOP19

observed and the radiation damage most likely occurred in camera electronics.

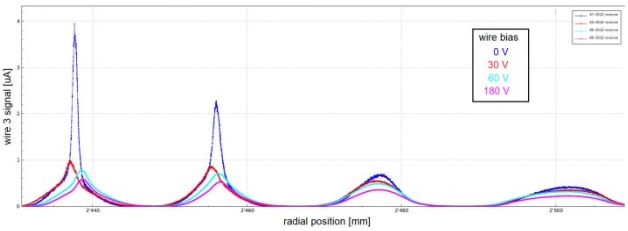


Figure 7: Effect of wire biasing. The four turns seen by the +45° wire are differently affected by TE due to the different beam current densities caused by different horizontal and vertical beam sizes. As always, wire positions at midplane height are corrected for the relative wire positions in the probe head.

The high power density input by the beam in addition to the RF-heating leads to the occurrence of a strong thermionic emission (TE) when the wire crosses the beam. At full beam current, the TE signal can be several times higher than the SE signal at a wire potential of 0 V. A bias voltage of 30 V, applied to the wires, suppresses the TE to a high degree, while the SE is much less affected. At higher bias voltages the TE and SE are further suppressed, but comparatively strong (Fig. 7). The difference at lower bias voltage may be explained by the counteracting effect of the bunch space-charge potential which is present at the creation of all SE but only of a low percentage of TE [5].

An example of a profile registered by the vertical wire at a test beam with reduced intensity is depicted in Fig. 8. At larger machine radii, orbits overlap leading to difficulties in the determination of the peaks. This is especially challenging at high beam intensity. Turn separation is an important parameter of a cyclotron. It is shown in Fig. 9. Figures 7 and 8 have been obtained at special injection settings, which should result in reduction of vertical beam oscillations. This centered beam setting can only be used with reduced beam intensity, because of high relative beam losses.

Figure 10 zooms on the profiles registered by all three wires at inner machine radii. The relative position of the peaks measured by vertical and tilted wires can be used to compute the vertical positions of the turns [6], as shown in Fig. 11. The oscillations of the vertical beam position from orbit to orbit are expected [7], however a large bump at low energies up to about 130 MeV is still being investigated.

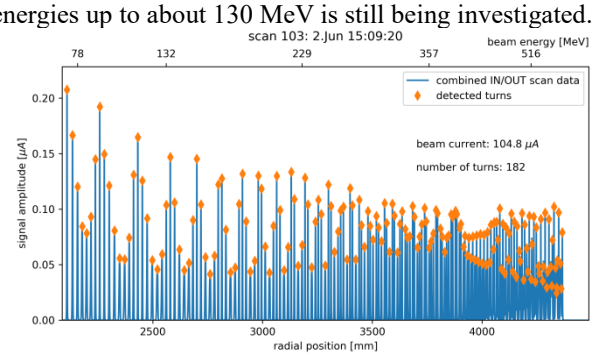


Figure 8: Profile from 0° wire performed at special injection settings (centred beam) with wire bias 60 V.

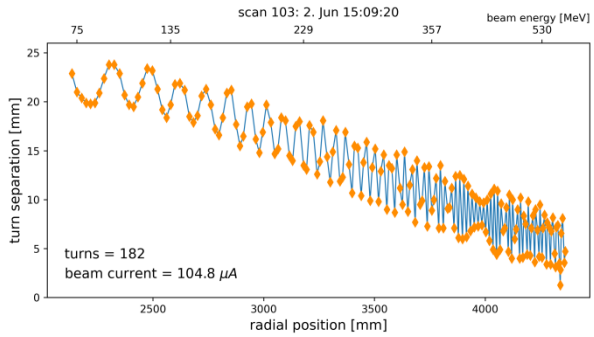


Figure 9: Turn separation derived from 0° wire peak positions as a function of machine radius (The peak finding algorithm has a problem at large radii). The blue line is a guide for the eye.

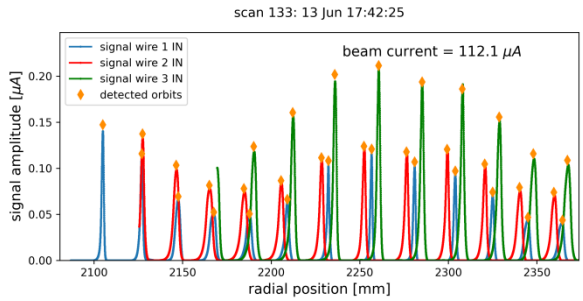


Figure 10: Signals of 0°, -45°, +45° wires. (Wire bias 60 V.)

The position of this bump (r=2500 mm) approximately coincides with an activation hot spot of the probe structure of about 1 mSv/h, discovered after about one month of RRL presence inside the cyclotron. The Monte-Carlo simulations using MNCP [8] revealed that the observed activation could be generated by a loss of the primary beam of the order of 5 nA per meter of machine radius. However, the loss could be generated on a carbon collimator upstream with a narrower gap. The simulation indicates that the activation will not increase in the long term if the probe structure stays in the sector chamber only for the monthly beam development shifts. Motorization of the probe insertion is underway to provide this. However, also the beam loss mechanisms in the Ring cyclotron and the role of the carbon collimators have to be better understood to lower the beam losses in the cyclotron in general.

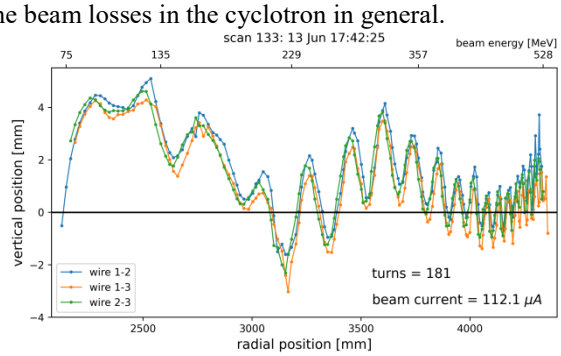


Figure 11: Vertical position of the beam obtained from comparison of wire signals. Due to uncertainties in the vertical position of the probe, the absolute values of measured beam position may be offset or tilted.

Content from this work may be used under the terms of the CC BY 4.0 licence (© 2022). Any distribution of this work must maintain attribution to the author(s), title of the work, publisher, and DOI

ISBN: 978-3-95450-241-7 ISSN: 2673-5350 doi:10.18429/JACoW-IBIC2022-MOP19

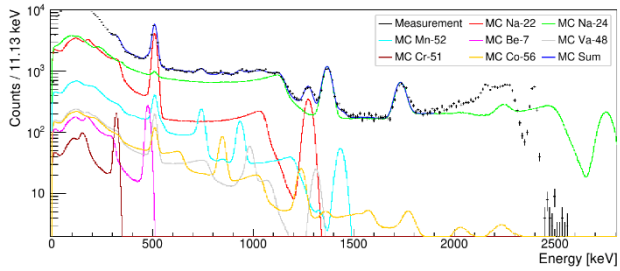


Figure 12: Gamma-ray spectrum at the hot spot [9].

Figure 12 shows the gamma spectrum measured in the location of the hot spot using portable spectrometer BRAD and fitted using contributions from expected radioisotopes. The measured spectrum is closest to the simulated contributions from various radioisotopes assuming proton energy in the range 60-80 MeV, what suggests that the activation is caused by scattered beam.

The vertical oscillations are affected by the injection angle and trim coils. Measurements of the vertical oscillations have been performed changing injection angle and trim coils. A correlation between the amplitude of the vertical bump at r=2500 mm and the signal in the MRI2 chamber has been found. This indicates that the presence of the vertical bump leads to increased beam losses, however, the increased loss does not have to be due to RRL presence.

The vertical and the +45° wire broke at a later point, surprisingly without significant thermal load. These events will be studied by analyzing the wires' remnants with electron microscope to maximize wire reliability.

CONCLUSIONS

The main Ring Cyclotron long radial probe has been renewed and the 3-wire scan brought to operation. It already provided valuable measurements, but there are still issues that have to be addressed. Besides activation and TE, these issues are the increased number of EIC trips during the scan, survival of the carbon fibers exposed to strong RF fields and vibrations, and signal noise. Therefore the ongoing developments include, e.g., further study of the configuration of the RF shields, internal cable quality, lower wire diameters and improved wire mounting. In parallel, the extension of measurement capabilities by equipping the additional drives with, e.g., loss monitors and phase probes will be pursued.

ACKNOWLEDGEMENTS

The authors would like to thank R. Senn and S. Lindner for assembling the probe, R. Senn for contributing to the design of the drag chain support, J. Bachmann for flange design, J. Snuverink for adapting the probe driving software, I. Besana for MNCP calculations, X. Wang and P. Hottinger for performing the noise measurement, M. Hauenstein for activation measurements, E. Hohmann for providing the gamma-ray spectrometer, D. Werthmüller for Gamma-ray spectrum evaluation, E. Yukihara and L. Bossin for precise dosimetry, R. Kan for providing the Sony camera and organizing bunker works, H. Zhang and C. Baumgarten for discussions, beam dynamics simulations and setting up beam centred beam used to obtain Figs. 8 and 9.

REFERENCES

[1] M. Seidel *et al.*, "Production of a 1.3 MW proton beam at PSI", in *Proc. IPAC'10*, Kyoto, Japan, May 2010, paper TUYRA03, pp. 1309-1313.

[2] R. Dölling *et al,* "Development of a replacement for the Long Radial Probe in the Ring Cyclotron", in *Proc. Cyclotrons'19*, Cape Town, South Africa, Sep. 2019, pp. 86-89. doi:10.18429/JACoW-Cyclotrons2019-MOP024

[3] R. Dölling, E. Johansen, M. Roggli and M. Rohrer, "Progress of Profile Measurement Refurbishment Activities at HIPA", in *Proc. IBIC'20,* Santos, Brazil, Sep. 2020, pp. 179-183. doi:10.18429/JACoW-IBIC2020-WEPP33

[4] E. Johansen, "VME Meson design specification", PSI, Villigen, Switzerland, Jun. 2010, unpublished.

[5] R. Dölling, "Bunch-shape measurements at PSI's high-power cyclotrons and proton beam lines", in *Proc. Cyclotrons'13*, Vancouver, Canada, Sep. 2013, paper TU3PB01, pp. 257-261.

[6] L. Rezzonico *et al.*, "Diagnostics for high intensity beams", in *Proc. BIW'94,* Vancouver, Canada, Oct. 1994, *AIP Conf. Proc.,* vol. 333, pp. 398-494, 1995. doi:0.1063/1.48013

[7] C. Baumgarten, H. Zhang, private communication, Jun. 2022.

[8] M. I. Besana and J. Snuverink, "Activity simulations for long probe RRL", unpublished report, Aug. 2022.

[9] D. Werthmüller, private communication, Jul. 2022

Content from this work may be used under the terms of the CC BY 4.0 licence (© 2022). Any distribution of this work must maintain attribution to the author(s), title of the work, publisher, and DOI

ISBN: 978-3-95450-241-7 ISSN: 2673-5350 doi:10.18429/JACoW-IBIC2022-MOP21

Content from this work may be used under the terms of the CC BY 4.0 licence (© 2022). Any distribution of this work must maintain attribution to the author(s), title of the work, publisher, and DOI

FIRST RESULTS OF PEPITES A NEW TRANSPARENT PROFILER BASED ON SECONDARY ELECTRON EMISSION FOR CHARGED PARTICLE BEAMS

C. Thiebaux†, L. Bernardi, F. Gastaldi, Y. Geerebaert, R. Guillaumat, F. Magniette, P. Manigot, M. Verderi, Laboratoire Leprince-Ringuet, CNRS-Ecole polytechnique, Institut Polytechnique de Paris, Palaiseau, France
E. Delagnes, F. Gebreyohannes, O. Gevin, CEA-IRFU, Université Paris-Saclay, Saclay, France
F. Haddad[1], C Koumeir, F. Poirier, GIP ARRONAX, Saint-Herblain, France
[1]also at Laboratoire SUBATECH, Nantes, France
N. Servagent, Laboratoire SUBATECH, IMT Atlantique, Nantes, France

Abstract

The PEPITES project* consists of a brand new operational prototype of an ultra-thin and radiation-resistant profiler capable of continuous operation on mid-energy (O(100 MeV)) charged particle accelerators in the vacuum of the beamline. Secondary Electron Emission (SEE) is chosen for the signal because it requires a small amount of material and is very linear. The monitor is made of segmented electrodes (strips), generating the SEE signal when crossed by the beam. Signals from the strips are carried outside the beamline and are read by a dedicated low-noise and high-dynamic electronic. A demonstrator is installed at ARRONAX and has been successfully operated on a wide dynamic. Its permanent installation will allow a long-term feedback.

INTRODUCTION

Protontherapy dose delivery requires a continuous and accurate measurement of beam properties, intensity, position and profile during patient treatment. The beam monitors must be thin enough to limit the effects of scattering to a submillimeter lateral spread of the beam at the patient. For monitors located a few meters upstream of the patient, this translates into a material budget of less than 15 µm water equivalent thickness (WET). Good resistance to radiation is also necessary, as the long exposure time results in integrated doses of some 10^6 to 10^8 Gy per year.

To fulfil these requirements, PEPITES [1,2], a new type of transparent beam profiler (< 10 µm WET) has been developed. It equips the beam line of the ARRONAX cyclotron [3] and will be used daily to monitor the beam during radiobiological and preclinical experiments [4]. The profiler will measure the lateral beam shape in a broad range of energy (15 – 70 MeV) and a wide range of intensity (100 fA – 10 nA), for alpha, proton and deuteron particles.

* Work supported by Agence Nationale de la Recherche ANR-17-CE31-0015, ANR-11-EQPX-0004
† thiebaux@llr.in2p3.fr

PRINCIPLES

PEPITES uses secondary electron emission (SEE) for the signal as it requires only a minimal thickness of material (~10 nm); very linear, it also offers a great dynamic.

The SEE yield is proportional to the dE/dx of the beam particles [5,6] and is independent of the beam intensity up to current far beyond expected needs both for medical use and radiobiology needs. The lateral beam profile is sampled using segmented electrodes, constructed by thin film methods. Gold strips, as thin as the electrical conductivity allows (50 nm), are deposited on an as thin as possible insulating substrate which, in contrast with conventional systems like ionization chambers, are free from mechanical constraints and can be as thin as achievable. Polyimides (PI), such as Kapton® or CP1™, are chosen as polymer substrates because of their insulating properties and the presence of aromatic cycles in their structure that make them extremely resistant to radiation [7]. When crossing the gold, the beam ejects the electrons by SEE, the current thus formed in each strip allows the sampling.

The thinness of the monitor disturbs very little the incident beam, which can then be delivered to the patient while keeping the profiler in the line, ensuring continuous monitoring. Also, it makes the energy deposit very small allowing the monitor to tolerate higher currents than existing systems without suffering from overheating problems. Besides, the absence of mechanical efforts on the membranes makes radiation damages of less consequence than with classical systems like ionization chambers allowing to extend the operation duration of the system.

Detector Layout

The layout of the prototype is shown in Fig. 1. It consists of four electrodes: two segmented cathodes each facing an anode (with a 15 mm gap) biased at 100 V to ensure the collection of secondary electrons emitted by the strips. The four electrodes are made of 50 nm thick gold deposited by chemical vapor phase on polymer membranes: 32 strips for cathodes and fully metallized anodes. The membranes are made of 1.5 µm thick CP1™, a colorless polyimide produced by the NeXolve company[1]. Initially developed for

[1]https://www.nexolvematerials.com/

ISBN: 978-3-95450-241-7 ISSN: 2673-5350 doi:10.18429/JACoW-IBIC2022-MOP21

solar sails, its availability in very small thickness make it a key aspect to meet the 10 µm WET budget.

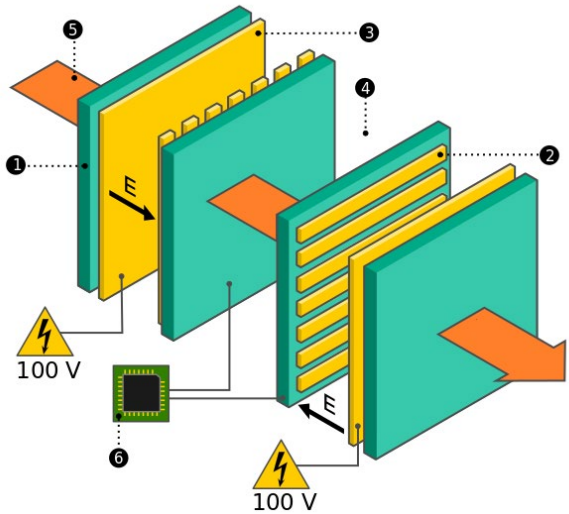


Figure 1: Schematic layout of PEPITES prototype. CP1™ membranes (1) sustain 50 nm thick gold strips (2) or are fully metallized (3). They stand in vacuum (4) where the beam (5) crosses the strips and produces secondary electrons. The signals coming from each strip are read by a dedicated readout chip (6). The actual prototype is made of 32 strips cathodes (2).

The profiler is divided into two mechanically independent blocks for the measurements of the beam position and lateral shape in the two directions (X and Y). The signals from the strips can be rather low as resulting from SEE (about 10% yield) and spreading of the beam over several strips. A dedicated low-noise and high dynamic Application Specific Integrated Circuit (ASIC) has been developed at CEA. One ASIC per block reads each strip individually. The whole system operates in the vacuum of the beamline and can be put on and off the beam path by a translation movement device.

PROTOTYPE

Figure 2 shows the realization of the project. The sensitive area (golden part) is mounted on an arm, itself bound to a flange that ensures the vacuum-air interface. The strip plans are 70×70 mm, with 32 strips, as simulation shows this ensures an at least 1 mm precision on beam position and width. High quality thin connectors (2×32 cables) carry the signal from the strips through the flange, up to a connector, on the air side of the flange. On this picture, the BNC cables, for voltage application to the anodes, are also visible.

The SEE rate depends on the Z of the material. We chose to use gold as we targeted proton beam currents down to a fraction of pA. Gold is in addition easy to handle and does not oxidize (which would result in an alteration of SEE rate). To have strips and anodes conductive, the deposit must be at least 30 nm thick so that the metallic structure materializes; this is thick enough for the SEE. A 50 nm deposit is made for safety, which represents ~0.5 µm WET. The 1.5 µm CP1™ corresponds to ~2.1 µm WET.



Figure 2: PEPITES sensitive area (gold) mounted on its support tool (see text).

The radiation tolerance of the system results from two sources: the intrinsic tolerance of the materials and the minimal mechanical stress applied to them. As a polyimide the CP1™ has an excellent radiation tolerance compared to other thermoplastics such as Mylar or PEEK. Since no mechanical stress is applied to the films that are in the vacuum of the beamline, damage is of lesser consequence than in a stressful case, which is favorable with respect to detector lifetime.

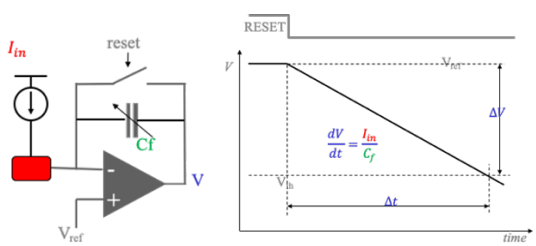


Figure 3: Current measurement principle used in the dedicated ASIC and based on a current to time conversion. Details are provided in the text.

The ASIC current measurement principle is illustrated on Fig. 3. The continuous signal current I_{in} charges the capacitance C_f making the output tension V to evolve at the rate $dV/dt = I_{in}/C_f$. The time Δt needed to range the predefined tension interval ΔV is then proportional to I_{in} -which provides the measurement- and inversely proportional to C_f

Content from this work may be used under the terms of the CC BY 4.0 licence (© 2022). Any distribution of this work must maintain attribution to the author(s), title of the work, publisher, and DOI

ISBN: 978-3-95450-241-7 ISSN: 2673-5350 doi:10.18429/JACoW-IBIC2022-MOP21

Content from this work may be used under the terms of the CC BY 4.0 licence (© 2022). Any distribution of this work must maintain attribution to the author(s), title of the work, publisher, and DOI

-which is used to define several gains of the system using a programmable capacitance.

The complete system is installed on site, the beam line AX3, at ARRONAX (Fig. 4). A vacuum chamber is mounted on the beamline and a translation system allows the sensitive area to be moved in or out the beam path. On this picture, PEPITES is in the "in beam" position. The sensitive area (Fig. 2) is visible through the vacuum chamber porthole. At the top of the flange, the readout system is visible as a metal box.



Figure 4: Complete system on AX3 beamline in ARRONAX.

Studies of the material tolerance to radiation and associated damage have been carried out to anticipate the detector lifetime and identify possible weaknesses: with gammas from ^{137}Cs and 68 MeV protons at ARRONAX [8], 2 MeV and 160 keV protons at CSNSM ("Centre de Sciences Nucléaires et de Sciences de la Matière", IJCLab, Orsay, France), and 2 MeV electrons at LSI ("Laboratoire des Solides Irradiés", Ecole polytechnique, Palaiseau, France). None of them showed significant defects of the sensitive parts of the detector and could not call into question the principle of operation of the PEPITES detector in the long term [1,8].

A more stringent test for CP1™ was performed on samples with gold strips, irradiated in air at ARRONAX with a 300 nA and 68 MeV proton beam for ~2.5 h. Around a 10^{16} H^+/cm^2 fluence, the CP1™ became fragile (samples were not destroyed but became sensitive to direct contacts). The estimated dose in CP1™ was 2×10^7 Gy. It is interesting to note that similar strip plans tolerated much larger doses with 2 MeV electrons at LSI (up to 10^8 Gy with no effect, and 10^9 Gy with CP1™ becoming fragile) and 2 MeV and 160 keV proton at CSNSM (10^8 Gy, with no effect), with the irradiations done with the samples in vacuum. There could be two possible interpretations (which are not mutually exclusive): one concerns the presence of nuclear interactions formed in the 68 MeV proton irradiations, generating fragments with high LET, and the other the damage increased by chemical reactions in the air.

Finally, a study of irradiation on material aging was carried out. In order to mimic the standard operating conditions of the detector, a sample was mounted on a Faraday cup (in the vacuum of the beam line) and moved in and out of the beam. The sample received O(10^{17}) protons for a dose of O(10^8) Gy, including a high intensity period of ~45 s at O(6 µA), and no noticeable degradations was observed.

RESULTS

The prototype has measured its firsts beams at the end of May 2022 and has been able to operate smoothly the monitor with proton beams from 1 pA to 20 nA. Beam spots can be seen on Fig. 5, where the measured signal current peaks at 35 fA for the 1 pA beam.

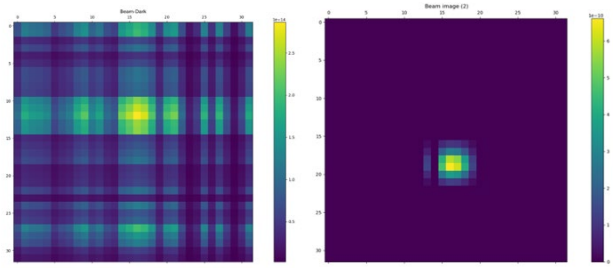


Figure 5: Profile current 1 pA (left) and 20 pA (right).

Taking advantage of the vertical translation capability we made repetitive measurements of the same beam (I_{beam} ~500 pA), shifting the detector vertically with a step equal to the width of one strip (1.95 mm) each time. All spectra were identical on vertical strips (Fig. 6, right), demonstrating the uniformity of signal emission, and identical modulo the displacement on the horizontal strips (Fig. 6, left), as it should be.

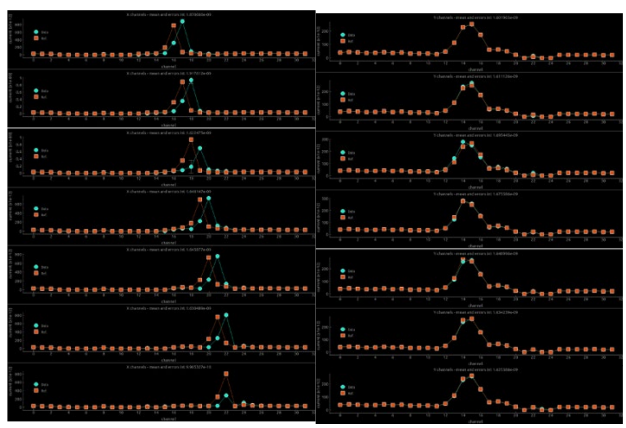


Figure 6: Horizontal strips (left) and vertical strips (right) current during vertical scan. The difference between two consecutive lines corresponds to a vertical movement of PEPITES with regard to the beam axis, with a step equal to

ISBN: 978-3-95450-241-7 ISSN: 2673-5350 doi:10.18429/JACoW-IBIC2022-MOP21

the strip width. On each line are also displayed the measured current (green) and the current at the position before this measurement (red).

We verified the detector WET by two means. In the first one, we measured in air the energy loss of 5.593 MeV alpha particles from a ^{238}Pu source flying through one or two metallized planes. The water equivalent loss is estimated using SRIM and is found to be 1.6 – 1.9 µm per plan (the uncertainty being related to the imprecision on the air segment lengths travelled by alphas on the setup). This is lower than then expected thickness, ~2.5 µm WET, obtained by calculation. A second, more preliminary measurement shows that the proton beam width at the beamline exit (~60 cm from PEPITES) increases by 0.13 mm when inserting PEPITES in the beam path.

CONCLUSIONS

We built and installed at ARRONAX a new type of beam profiler, PEPITES, using secondary electron emission. Built with thin film techniques and using very thin materials, the detector has a WET of less than 10 µm. The radioresistance of the materials has been investigated by several means and show that the detector should withstand several years of operation at ARRONAX as well as in medical protontherapy centers, if the monitor is adopted there. First measurements occurred with 68 MeV proton under various beam conditions. The prototype ran smoothly with 1 pA to 20 nA beams and has shown excellent behavior. The project is now entering a feedback phase which will be acquired at ARRONAX with frequent use of the system.

REFERENCES

[1] C. Thiebaux *et al*., "Development of transparent profiler based on secondary electrons emission for charged particle beams", in *Proc. Cyclotrons'19,* Cape Town, South Africa, 2019, pp. 302-304. doi:10.18429/JACoW-Cyclotrons2019-THB04

[2] D. Bernard, B. Boyer, P. Manigot, C. Thiebaux, and M. Verderi, "Systeme de caracterisation d'un faisceau de particules chargees et machine de production d'un faisceau de particules chargees comprenant un tel systeme", European Patent Office, EP3749981A1, Dec. 16, 2020.

[3] F. Poirier *et al.*, "Studies and upgrades on the C70 Cyclotron Arronax", in *Proc. Cyclotrons'16*, Zurich, Switzerland, 2016, pp. 235-237. doi:10.18429/JACOW-CYCLOTRONS2016-TUD02

[4] C. Koumeir *et al*., "The Radiobiological Platform at Arronax", *Radiat. Prot. Dosim.*, vol. 183, pp. 270-273, 2019. doi:10.1093/rpd/ncy301

[5] E. J. Sternglass, "Theory of secondary electron emission by high-speed ions", *Phys. Rev.*, vol. 108, pp. 1-12, 1957. doi:10.1103/PhysRev.108.1

[6] J. Schou, "Transport theory for kinetic emission of secondary electrons from solids by electron and ion bombardment", *Nucl. Instrum. Methods*, vol. 170, pp. 317-320, 1980. doi:10.1016/0029-554X(80)91032-0

[7] E. A. Plis *et al*., "Review of Radiation-Induced Effects in Polyimide", *Appl. Sci.*, vol. 9, p. 1999, May 2019. doi:10.3390/app9101999

[8] S. Elidrissi-Moubtassim *et al*., "Exploring radiation hardness of PEPITES, a new transparent charged particle beam profiler", *Nucl. Instrum. Methods Phys. Res., Sect. B*, vol. 466, pp. 8-11, 2020. doi: 10.1016/j.nimb.2020.01.003

Content from this work may be used under the terms of the CC BY 4.0 licence (© 2022). Any distribution of this work must maintain attribution to the author(s), title of the work, publisher, and DOI

ISBN: 978-3-95450-241-7 ISSN: 2673-5350 doi:10.18429/JACoW-IBIC2022-MOP22

DEVELOPMENT OF NEW BEAM POSITION DETECTORS FOR THE NA61/SHINE EXPERIMENT

M. Urbaniak*, Y. Balkova, S. Kowalski, S. Puławski, K. Wójcik
University of Silesia, Institute of Physics, Chorzów, Poland

Abstract

NA61/SHINE is a fixed-target experiment located at the CERN Super Proton Synchrotron (SPS). The development of new beam position detectors is part of the upgrade of the detector system. Two types of detectors have been manufactured and tested. The first one is a scintillating fibers detector with a photomultiplier as a readout. The scintillating fibers detector consists of two ribbons, which are arranged perpendicularly to each other. Each ribbon is made of two layers of 250 µm diameter fibers. The grouping method was used, which allows using of a single multichannel photomultiplier for one detector. The second type of detector is based on the single-sided silicon strip detector (SSD). In this project, Si strips produced by Hamamatsu (S13804) were used, where the pitch has a width equal to 190 µm. The developed detectors must meet several requirements: they should work efficiently with proton and lead beams with beam intensity on the level of 100 kHz, the detector's material on the beamline should be minimized, and the detectors should be able to determine the position of X and Y hit of each beam particle with maximum possible accuracy.

INTRODUCTION

NA61/SHINE is a fixed-target experiment located in the North Area of the CERN Super Proton Synchrotron (SPS) [1]. Developing a new Beam Position Detector (BPD) is part of the upgrade of the detection system of the experiment during the Long Shutdown 2 (LS2) upgrade. Two alternative BPD designs are described in the paper.

The NA61/SHINE detector system includes Time Projection Chambers (TPCs), Time of Flight detectors (ToF), and Vertex Detector (VD) downstream of the target. The system's primary goal is to measure the particles produced in the interaction of the beam particles with the target. Additionally, upstream of the target is located a set of beam detectors that provides the identification, timing references, and beam position measurements. The schematic layout of the detector system is shown in Fig. 1.

Beam Position Detectors are used to calculate the trajectory of the incoming beam particle based on its measurement in X and Y planes along the beamline. The new beam position detectors should allow for the measurement of the trajectory of each proton or lead beam particle separately with intensities on the level of 100 kHz with maximum possible accuracy. Additionally, the detector should operate in a vacuum. Two types of detector have been designed and manufactured and are currently being tested: a scintillating fibers detector and a single-sided silicon strip detector.

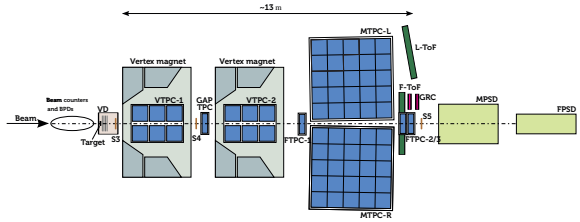


Figure 1: Schematic layout of the NA61/SHINE experiment after the LS2 upgrade.

SCINTILLATING FIBERS DETECTOR

The scintillating fibers detector consists of two ribbons placed perpendicularly to each other. Such construction allows measuring the position of the particle passage in the XY plane. Each ribbon is made of two layers of scintillating fibers. Saint-Gobain, round shape, double cladding scintillating fibers (BCF-60) with 250 µm diameter were chosen [2]. The BCF-60 has an extra 3HF formulation which increases its radiation hardness. Layers are shifted relative to each other by a distance equal to the radius of a single fiber, which minimizes the detector's dead area. The end of each ribbon is connected to the 256-channel multianode Hamamatsu photomultiplier (H9500). The photo of the prototype detector is presented in Fig. 2.

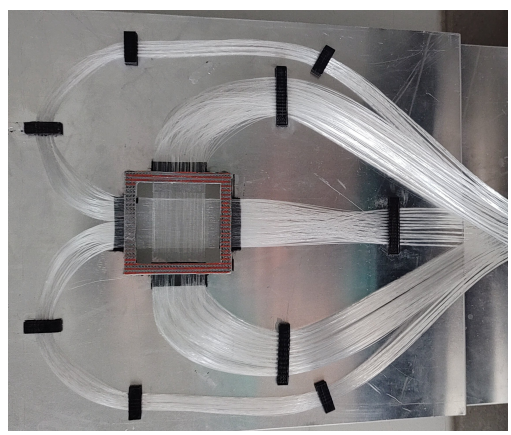


Figure 2: Photo of the scintillating fibers detector.

Finally, grouping of the fibers was implemented to reduce the number of readout channels from 480 to 88. Instead of connecting each fiber to one photomultiplier pixel, ten or twelve fibers are connected into groups and applied to a single pixel. The grouping is as follows: the fiber ends

* marta.urbaniak@us.edu.pl

Content from this work may be used under the terms of the CC BY 4.0 licence (© 2022). Any distribution of this work must maintain attribution to the author(s), title of the work, publisher, and DOI

ISBN: 978-3-95450-241-7 ISSN: 2673-5350 doi:10.18429/JACoW-IBIC2022-MOP22

from one side are grouped into 12 groups of contiguous fibers. The other ends of the fibers are grouped based on their position in the first grouping: all first fibers build one group, the second next, etc. Grouping is carried out separately for each layer of the ribbon. After the beam particle passes the ribbon, it generates a signal at both ends of the fiber, which allows for precise position measurement. More details of the grouping method may be found in Ref. [3]. A special matrix has been designed to accurately apply the grouped fibers to the corresponding pixel of the photomultiplier. The matrix is shown in Fig. 3.

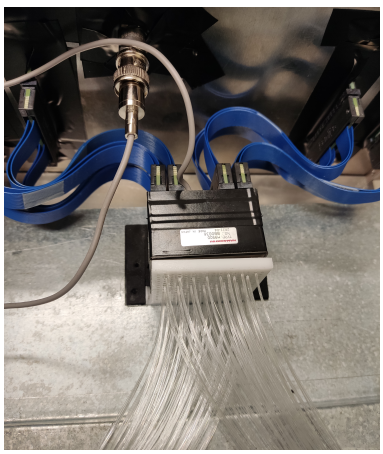


Figure 3: Matrix for combining grouped fibers with photomultiplier pixels.

The use of proton and lead beams requires optimizing the detector and its readout for two extreme scenarios. The studies show that only approximately 100 photons will reach the end of the fiber after the passage of the proton beam particle. On the other hand, for the lead nuclei, about 7,000 times more photons will be registered. Results are shown in Fig. 4 for protons and in Fig. 5 for lead nuclei. Additionally, the optical cross-talk between the fibers was studied. Analysis was performed for protons and lead nuclei in the energy range from 10 to 150 GeV per nucleon. The simulation showed that for protons, optical cross-talk is negligible. For lead nuclei, the amount of light leaked to the nearest fibers is, at maximum, on the level of 1% of the light recorded in the struck fiber.

SILICON STRIP DETECTOR

The second manufactured detector is based on the Hamamatsu S13804 Silicon Strip Matrix [4]. It is a silicon wafer with p-n junctions arranged in a stripe formation. The active area is 97x97 mm^2 in size. The detector has 1024 stripes arranged in two rows. The pitch between the strips is 190 µm. In the final design, two detectors are placed in the 6-way vacuum fitting. One of them determines the position in the X-plane, and the other one, rotated by 90°, determines the position in the Y-plane. The schematic layout of the detector placed in the vacuum fitting is shown in Fig. 6. Detectors are placed on aluminum plates, which stabilize them and

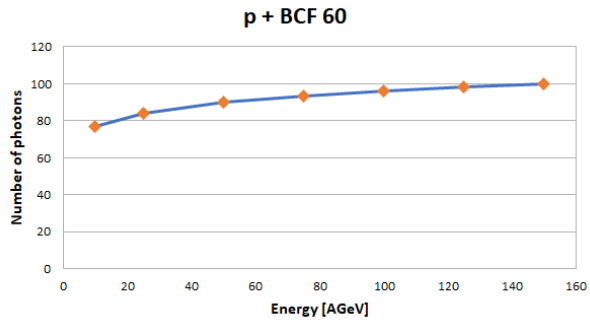


Figure 4: Amount of light at the end of the fiber after the passage of proton.

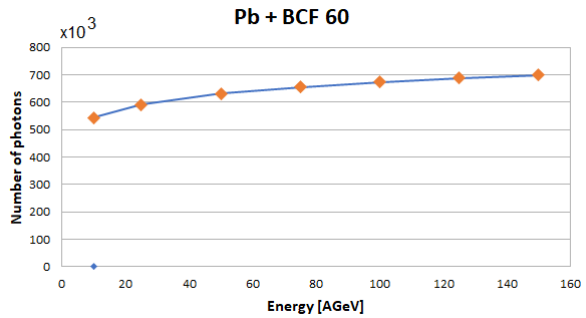


Figure 5: Amount of light at the end of the fiber after the passage of lead nucleus.

ensure that they are in the correct position for the beam. The signal is extracted through ISO-K vacuum flanges with two high-density vacuum feedthrough connectors connected to the detectors by flexible PCB. The photo of the detector is presented in Fig. 7.

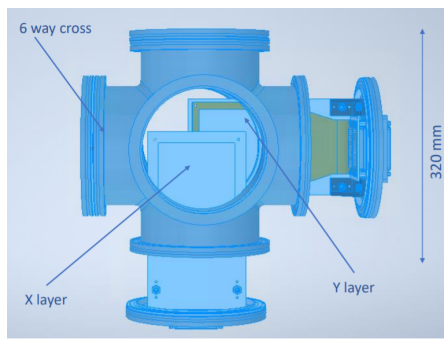


Figure 6: Silicon strip detector in 6-way vacuum fitting.

A dedicated charge amplifier has been manufactured for the detector and is placed outside the vacuum fitting. It consists of a fast and charge-sensitive amplifier, an intermediate amplifier, and an output buffer. Since it was equipped with an electronically-controlled scale-changing feature, the same board is usable for protons and lead nuclei beams. The detector mounted on the beamline is shown in Fig. 8.

Content from this work may be used under the terms of the CC BY 4.0 licence (© 2022). Any distribution of this work must maintain attribution to the author(s), title of the work, publisher, and DOI

ISBN: 978-3-95450-241-7 ISSN: 2673-5350 doi:10.18429/JACoW-IBIC2022-MOP22

Content from this work may be used under the terms of the CC BY 4.0 licence (© 2022). Any distribution of this work must maintain attribution to the author(s), title of the work, publisher, and DOI



Figure 7: Photo of the silicon strip detector.



Figure 8: Silicon strip detector mounted on the beamline.

TEST RESULTS

Both detectors were tested on a 30 GeV/c proton beam. Tests have shown that the scintillating fibers detector must be tested on a heavy ion beam or a proton beam, with energy that is not near minimum ionization energy. Tests of the strip detector have shown that we can measure the position of passing protons and we can determine the beam profile. However, due to the low signal-to-noise ratio, some signals are lost in the noise, which significantly reduces the detector's performance. An example of a signal from a proton can be seen in Fig. 9. The algorithm for finding the signal and reconstructing the beam position is based on three main parameters: the signal-to-noise ratio, signal appearance time, and signal rise time. The values of the rise time cut used in the algorithm were selected based on the distribution, which is shown in Fig. 10. Additionally, Fig. 11 shows the distribution of the signal width. An example of a beam profile in the Y position can be seen in Fig. 12.

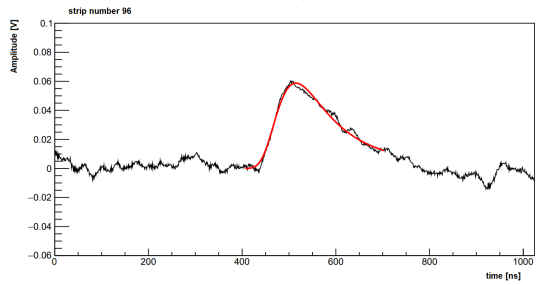


Figure 9: Example of a signal from 30 GeV/c proton, measured by silicon strip detector.

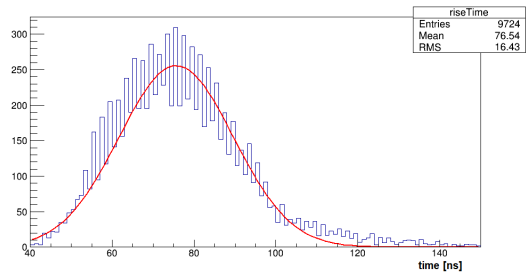


Figure 10: Distribution of the measured signals rise time, by silicon strip detector.

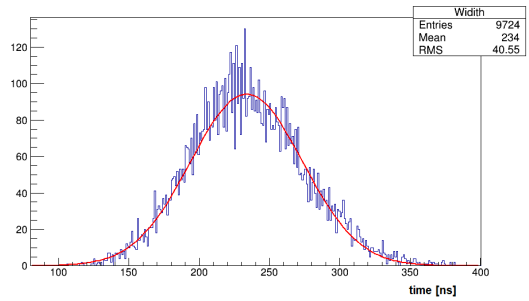


Figure 11: Distribution of the measured signals width, by silicon strip detector.

Currently, the work is ongoing to modify the amplifier to obtain a better signal-to-noise ratio and thus to be able to determine the position of the proton beam with the accuracy assumed during detector construction.

CONCLUSION

In conclusion, two types of beam position detectors for the NA61/SHINE experiment have been manufactured and

ISBN: 978-3-95450-241-7 ISSN: 2673-5350 doi:10.18429/JACoW-IBIC2022-MOP22

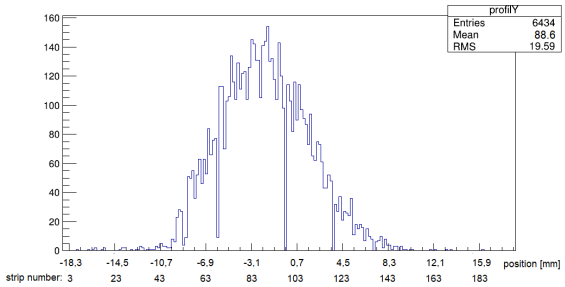


Figure 12: 30 GeV/c protons beam profile in Y position.

are currently being tested. It is planned that both detectors will be used depending on the type of measurement. The estimated positional resolution for silicon strip detector is equal to 190 µm, and for scintillating fiber detector is equal to 125 µm.

The first test results show that the scintillating fiber detector is inefficient for the proton beam with energy near minimum ionization energy. Therefore it will be used for measurements with heavy-ions beams. In addition, tests on protons with energy in the order of several dozen MeV, which, due to higher energy losses in the material, should significantly affect the value of the signal-to-noise ratio, are planed.

Silicon strip detector test results show that we are able to measure the position of the beam particles, but due to the low signal-to-noise ratio, many signals are lost which reduces the detector performance and requires changes to the amplifier.

ACKNOWLEDGEMENTS

This work is supported by: National Science Center, Poland Grant No. 2018/31/G/ST2/03910 - BEETHOVEN CLASSIC 3, the Research Excellence Initiative of the University of Silesia in Katowice and Norwegian Financial Mechanism 2014-2021 (grant 2019/34/H/ST2/00585).

REFERENCES

[1] N. Abgrall *et al.*, “NA61/SHINE facility at the CERN SPS: beams and detector system”, *J. Instrum.*, vol. 9, no. 6, p. P06006, 2014. doi:10.1088/1748-0221/9/06/p06005

[2] Saint-Gobain, Plastic Fiber, https://www.crystals.saint-gobain.com/radiation-detection-scintillators/fibers

[3] D. Lo Presti *et al.*, “Development of a scintillation-fiber detector for real-time particle tracking”, *J. Instrum.*, vol. 8 no. 4, p. P04015, 2013. doi:101088/1748-0221/8/04/P04015

[4] Hamamatsu, "Single-sided SSD for high energy particle position detection", https://www.hamamatsu.com/eu/en/product/type/S13804/index.html

Content from this work may be used under the terms of the CC BY 4.0 licence (© 2022). Any distribution of this work must maintain attribution to the author(s), title of the work, publisher, and DOI

ISBN: 978-3-95450-241-7 ISSN: 2673-5350 doi:10.18429/JACoW-IBIC2022-MOP23

RECENT LHC SR INTERFEROMETER SIMULATIONS AND EXPERIMENTAL RESULTS

D. Butti*,[1], E. Bravin, G. Trad, CERN, Geneva, Switzerland
S. Gibson, Royal Holloway, University of London, Egham, United Kingdom
[1]also at Royal Holloway, University of London, Egham, United Kingdom

Abstract

At the CERN Large Hadron Collider (LHC), among the different systems exploiting Synchrotron Radiation (SR) for beam diagnostics, interferometry is under study as a non-invasive technique for measuring absolute transverse beam sizes. Extensive numerical simulations, recently completed for characterising the spatial coherence of the LHC SR source, facilitated the optimisation of the LHC interferometer design and the existing prototype system tested in the past has been refurbished to include the new simulation findings. This contribution will describe the simulation specificity and then focus on the first measurements performed in a very tight schedule during the LHC Run 3 test run in October 2021. Such experiments allowed to obtain a first validation of the expected system performance at the injection energy of 450 GeV. A complete benchmark of the simulations will be carried out in 2022 as soon as the LHC will reach its top energy of 6.8 TeV.

INTRODUCTION

The transverse beam diagnostics at the Large Hadron Collider (LHC) is currently performed with two families of operational instruments [1]. Wire scanners (WS) provide an absolute size measurement but their usage is limited below a certain beam intensity due to damage to the wire caused by beam-wire interactions. A second instrument, the Beam Synchrotron Radiation Telescope (BSRT), exploits synchrotron radiation imaging for the continuous monitoring of the beam size. At present the BSRT cannot provide an absolute measurement and so a cross-calibration with the WS is required.

Synchrotron radiation interferometry is an optical technique, alternative to imaging, that can provide a non-invasive and absolute measurement of the transverse size of a luminous source [2]. This technique has been proposed for beam diagnostics [3] and it is currently exploited at the LHC to complement the operational instrumentation with a redundant and independent system [4].

The Beam Synchrotron Radiation Interferometer (BSRI) installed at the LHC is a classical Young's double slit interferometer. The visible synchrotron radiation (SR) emitted by the beam is sampled by two slits. The wavelets propagate through an optical system that produces the SR interferogram onto an intensified camera. The technique is based on a fundamental result of classical optics, the Van Citter and Zernike theorem (VCZ). This theorem states that the spatial coherence $|\gamma_{12}|$ of the points sampled by the slits coincides with the Fourier transform of the source transverse profile [5]. For Gaussian sources, the coherence as a function of the slit separation D is still a Gaussian

$$|\gamma_{12}| = \exp^{-\frac{D^2}{2\sigma_{coh}^2}}. \quad (1)$$

The standard deviation $\sigma_{coh} = (\lambda L_0)/(2\pi\sigma)$ defines the coherence area of the radiation, where λ is the wavelength, L_0 the source distance and σ the source size.

Experimentally, the spatial coherence is measurable though the visibility of the radiation interferogram

$$V = \frac{2\sqrt{I_1 I_2}}{I_1 + I_2}|\gamma_{12}|, \quad (2)$$

being I_1 and I_2 the total light transmitted through each aperture whose effect is to reduce the expected visibility if the slits are unevenly illuminated, i.e. $I_1 \neq I_2$.

The VCZ theorem strictly applies to thermal sources which consist of many point-like independent emitters radiating an isotropic wavefront. In case of non-thermal sources, such as SR radiated by relativistic beams, the theorem has to be validated on a case-by-case basis [6, 7].

In this paper, the unique features of the LHC SR source are presented and the results of the VCZ validation by means of SR simulations are discussed.

THE LHC SYNCHROTRON RADIATION SOURCE

The radiation source used for beam diagnostics at the LHC consists of two types of magnetic devices [8]. At injection energy, visible light is emitted by a superconducting undulator. As the beam energy increases, the undulator spectrum drifts towards the soft X-rays region. Above 2 TeV, the main source of visible light becomes the $D3_R$, a D3-type dipole located just downstream of the undulator. The undulator and the $D3_R$ are the main devices of the LHC SR source. A second D3-type dipole, the $D3_L$, contributes to the SR emitted at high beam energy. This dipole is located approximately 100 m upstream of the undulator, on the opposite side of the RF cavity section. After the source, the SR propagates for ~ 25 m inside the beam chamber until it is intercepted and extracted by an in-vacuum mirror that sends the light towards the BSRI slits. Figure 1 shows a layout of the source devices and the extraction system.

The contribution from the $D3_L$ has been recently detected with the SR interferometer [9]. The presence of this dipole is in fact negligible for the BSRT as it is far away from the

* daniele.butti@cern.ch

Content from this work may be used under the terms of the CC BY 4.0 licence (© 2022). Any distribution of this work must maintain attribution to the author(s), title of the work, publisher, and DOI

ISBN: 978-3-95450-241-7 ISSN: 2673-5350 doi:10.18429/JACoW-IBIC2022-MOP23

Table 1: Summary of the LHC Source Parameters Relevant to SR Interferometry, Comma Separated Values Refer to the Horizontal and Vertical Direction Respectively

Parameter	Injection	Flat-top	Unit
Device	Und	$D3_R$ (and $D3_L$)	-
Source dist. L_0	29.5	~ 26.7	m
Beta β	205, 287	200, 300	m
Beam size σ	1030, 1220	270, 330	µm
Coh. area σ_{coh}	2.5, 2.2	8.8, 7.2	mm
SR spot size	50, 50	10, 12	mm
Emittance ε_n	2.5		µm
Wavelength λ	400 - 560		nm

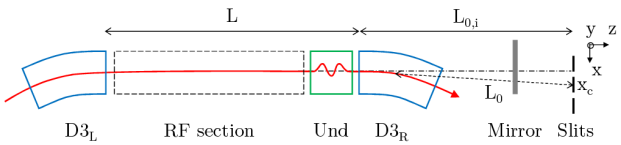


Figure 1: LHC synchrotron radiation source.

main $D3_R$ source and its light is completely out of focus at the final image. The interferometer does not focus light from any specific device. Although the $D3_R$ remains the main source of light at flat-top, the $D3_L$ light interferes with the $D3_R$ radiation and affects the wavefront arriving at the interferometer slits. SR from the two dipoles arrive at the slit plane with a phase delay $\Delta\varphi$ that can be written as

$$\Delta\varphi = \frac{2\pi}{\lambda}\left(\frac{L}{2\gamma^2} + \frac{r^2}{2L_{0,i}}\frac{L}{L+L_{0,i}}\right), \qquad (3)$$

being γ the beam relativistic factor, L the $D3_L$ to $D3_R$ distance, L_0 the $D3_R$ to slit distance and $r^2 = x^2 + y^2$ the transverse radial coordinate at the slit plane. The first term of Eq. (3) represents the phase slippage between protons and light travelling between the dipoles. This gives a constant delay which does not create any modulation of the SR intensity distribution. The second term is purely geometrical and stems from the different curvatures of the two wavefronts at the slit plane. The r^2 factor gives rise to an interference pattern characterised by concentric fringes. Figure 2 shows an example of the synchrotron radiation arriving at the BSRI. The concentric rings created by the dipole interference are clearly visible in both the simulated and experimental intensity distributions.

SYNCHROTRON RADIATION SIMULATIONS

Extensive simulations have been carried out to investigate the applicability of the VCZ theorem to the case of the LHC SR source. The objective of the simulations is to verify that the model of Eqs. (1) and (2) allows to retrieve the beam size from the interferogram visibility within an accuracy of ± 2.5%. This tolerance is compatible with the ± 5% emittance uncertainty desired by the LHC operation.

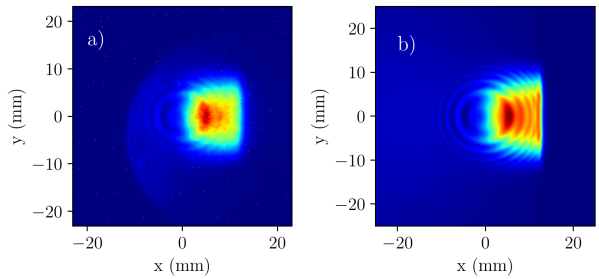


Figure 2: Experimental (a) and simulated (b) SR spatial distribution arriving at the slit plane at 6.8 TeV. The observation wavelength is 400 nm. The main lobe of the light is the SR emitted by the $D3_R$, modulated by the interference with the $D3_L$. The vertical cut at $x = 12$ mm is the edge of the extraction mirror. The circular cut in the background of (a) is created by the finite aperture of a filter wheel installed upstream of the observation screen.

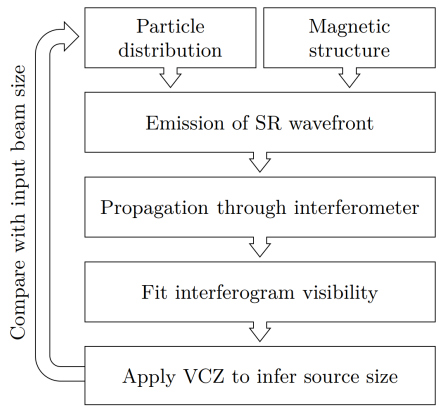


Figure 3: Simulation workflow.

Simulations are performed with a code based on Synchrotron Radiation Workshop (SRW), a standard tool for physical optics simulations of SR [10, 11]. The simulation strategy is outlined in Fig. 3. The code computes the wavefront emitted by a single particle sampled out of the beam distribution. The field is then propagated through the series of apertures and lenses of the interferometer to produce the single particle interferogram. The procedure is repeated and the beam interferogram is computed as the incoherent sum of the single particle ones. The resulting pattern is fitted to obtain the fringe visibility. The corresponding source size is computed using the VCZ relations and the result is compared to the one given as an input for the particle distribution.

Simulations confirm the VCZ theorem at injection energy along both the horizontal and vertical directions. This result is expected from the source parameters summarised in Table 1. The spatial distribution of the undulator radiation is much larger than its typical coherence area. This means that the light is almost uniform within its coherence area. The VCZ model is thus applicable in its canonical form.

Content from this work may be used under the terms of the CC BY 4.0 licence (© 2022). Any distribution of this work must maintain attribution to the author(s), title of the work, publisher, and DOI

ISBN: 978-3-95450-241-7 ISSN: 2673-5350 doi:10.18429/JACoW-IBIC2022-MOP23

Content from this work may be used under the terms of the CC BY 4.0 licence (© 2022). Any distribution of this work must maintain attribution to the author(s), title of the work, publisher, and DOI

The situation is more critical at 6.8 TeV. A typical flat-top beam size of 300 µm produces SR with a coherence area in the order of 8 mm. This value is comparable to the size of the available light spot. As a consequence, the emitted light cannot be considered as uniform within the coherence area, both because of its finite extent and the presence of the dipole interference effects. Another issue with the VCZ theorem at flat-top is the longitudinal position of the source, needed to define the source distance L_0. SR at flat-top is emitted along a beam trajectory that spans almost 4 m inside the $D3_R$ dipole so that a value for L_0 cannot be defined a priori. Both these issues hinder the applicability of the VCZ model in its standard formulation. Equation (1) provides nonetheless a compact and practical expression to retrieve the source size from the measured radiation coherence. The simulation campaign at flat-top aims to overcome these limitations. The goal is to search for configurations of the SR interferometer for which the VCZ equations provide an approximate estimation of the real source size, accurate within the required limits. For this purpose, the slit position and size have been optimised to minimise the effects of the nonuniform light distribution. On the other hand, the parameter L_0 has been defined as the distance between the slit centre x_c and the beam, measured along the tangent to the trajectory impinging on x_c, as illustrated in Fig. 1. For small beam deflections, this distance can be approximated as

$$L_0 \approx L_{0,i}\sqrt{1-\frac{2\rho x_c}{L_{0,i}^2}}, \qquad (4)$$

being $\rho = 6013$ m the dipole bending radius and $L_{0,i} \approx 30$ m the longitudinal distance between the start of the magnet and the slit plane. It is important to stress that Eq. (4) does not identify an exact longitudinal position of the source at flat-top, whose longitudinal extension is an intrinsic feature of dipole radiation. The expression is a practical result that preserves the VCZ equations by just re-defining the source distance parameter.

An example of interferometry simulations at flat-top is reported, for the vertical direction, in Fig. 4. The coherence simulated with two point-like apertures (solid lines) is affected by the two dipole interference. By using properly extended slits (dashed lines), the dipole interference fringes are averaged and the oscillations of the coherence are damped. The coherence obtained with the optimised slit shape is in good agreement with the VCZ prediction, evaluated with the source distance definition of Eq. (4). In particular, any slit position with $x_c > 6$ mm features a discrepancy between simulations and analytical estimation within the required tolerance. This result proves that the VCZ formula is still valid to infer the beam size. The method relies only on the adoption of some specific slit configurations and a proper definition of the source distance. It is therefore suitable to be deployed in an operational instrument.

Similar considerations apply to the horizontal direction at flat-top. The main difference is the narrower region of slit positions where the VCZ formulas are applicable. This difference stems from the asymmetry of the dipole radiation in the horizontal direction, which leaves less margin for optimisation.

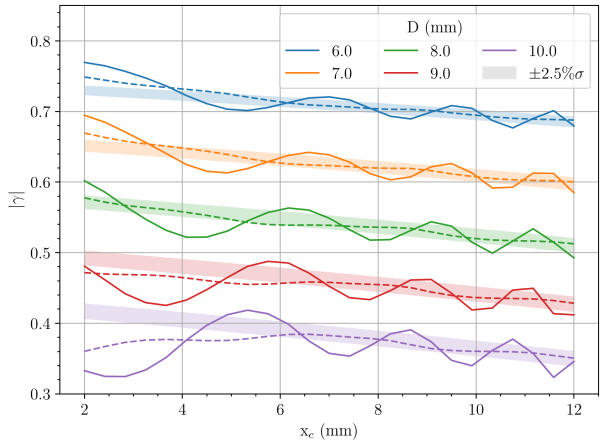


Figure 4: Simulations of the validity of the VCZ theorem along the vertical direction at 6.8 TeV and 560 nm observation wavelength. For several slit separations, the spatial coherence obtained by the simulated interferograms using Eq. (2) is plotted as a function of the horizontal slit centre. The results with standard square apertures of 0.5 mm × 0.5 mm (solid lines) are compared to an optimised configuration of rectangular slits of 0.5 mm × 4 mm (dashed lines). Color bands represent the VCZ prediction with a 2.5% tolerance.

HIGHLIGHTS FROM RUN 3 COMMISSIONING

The LHC SR interferometer has been refurbished for LHC Run 3 that started in spring 2022 and the upgraded setup is now being commissioned.

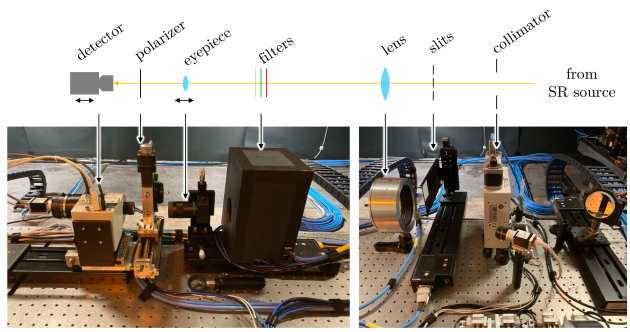


Figure 5: SR interferometer setup for LHC Run 3.

Figure 5 shows the hardware installed on the same table as the other LHC SR monitors. The whole setup is remotely controlled from a Python GUI which also provides a real-time processing of the acquired interferogram.

The instrument performance has been already validated by measuring nominal bunches at injection energy. Figure 6 reports an example of beam size monitoring. This measurement has been performed during two consecutive stable

ISBN: 978-3-95450-241-7 ISSN: 2673-5350 doi:10.18429/JACoW-IBIC2022-MOP23

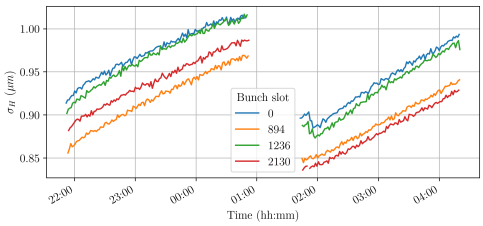


Figure 6: Horizontal beam size evolution during two stable beam fills with four bunches colliding at injection energy. The gap in the measurements corresponds to the time interval between the dump of the first fill and the injection of the second one.

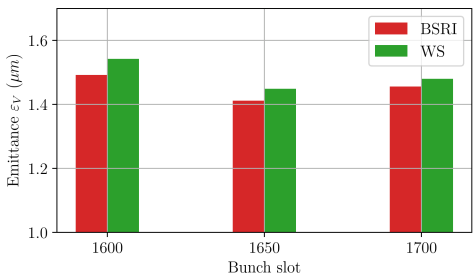


Figure 7: Comparison between the BSRI and WS measurements of the vertical emittance of three nominal bunches at injection energy.

beam fills at injection energy. The SR interferometer is able to resolve, with a precision better than 2%, the different sizes of the four circulating bunches. The beam size growth induced by the collisions is clearly visible throughout each fill.

The absolute measurement at injection energy is also compatible with the reference values provided by the wire scanner. A comparison of the vertical emittance measurement for three bunches is displayed in Fig. 7. The emittance measured by the two instruments agrees within 3%. The BSRI performance along the horizontal direction is similar, thanks to the axial symmetry of the undulator radiation.

Some discrepancies are present at 6.8 TeV. Although a relative measurement is still achievable, the absolute value of the emittance is systematically higher than the reference one provided by the WS. This means that the acquired interferograms have a lower visibility than the expected one. Investigations are ongoing to identify the origin of this discrepancy. Some common causes of visibility loss, for example mechanical vibrations in the setup, have been already excluded as possible causes. Tests are currently ongoing to identify whether some specific component of the hardware is responsible for the loss of visibility. In parallel to the investigations on the setup, data analysis aims at searching for some general correction that would allow to compensate for this effect in a self-consistent way.

CONCLUSION

The status of SR interferometry at the LHC has been presented in this contribution. Despite the challenging scenario given by the LHC SR source, simulations show that the technique is theoretically exploitable for absolute beam size measurements. The VCZ theorem can be used to infer the beam size from the measured interferogram visibility. At injection energy, the theorem is valid in its canonical form. The complexity of the SR source at flat-top affects the VCZ model. Simulations allow to optimise the slit configurations and provide a specific definition of the source distance so that the analytical result offered by the VCZ theorem can still be used to retrieve the beam size.

The benchmarking of such simulations is ongoing. Preliminary results confirmed the scenario at injection energy while some discrepancies are still present at 6.8 TeV, where the measured visibility is systematically lower than the expected one. Investigations are ongoing to identify the sources of the visibility loss or to find a self-consistent way to compensate for it.

REFERENCES

[1] G. Trad *et al.*, "Status of the beam instrumentation at the LHC", in *Proc. 7th Evian Workshop on LHC beam operation*, Evian Les Bains, France, Dec. 2016, pp.185–192.

[2] J. Goodman, *Introduction to Fourier Optics, 4th Edition*, NY, USA: W. H. Freeman, 2017.

[3] T. Mitsuhashi, "Beam profile and size measurement by SR interferometers", in *Beam measurement*, World Scientific, 1999, pp. 399–427. doi:10.1142/9789812818003_0018

[4] G. Trad, "Development and optimisation of the sps and lhc beam diagnostics based on synchrotron radiation monitors", Ph.D. thesis, Université Grenoble Alpes, Saint-Martin-d'Hères, France, 2015.

[5] F. Zernike, "The concept of degree of coherence and its application to optical problems", *Physica*, vol. 5, pp. 785–795, 1938. doi:10.1016/S0031-8914(38)80203-2

[6] G. Geloni, E. Saldin, E. Schneidmiller, and M. Yurkov, "Transverse coherence properties of x-ray beams in thirdgeneration synchrotron radiation sources", *Nucl. Instrum. Methods Phys. Res., Sect. A*, vol. 588, pp. 463–493, 2008. doi:10.1016/j.nima.2008.01.089

[7] Y. Takayama and S. Kamada, "Spatial coherence of bending magnet radiation and application limit of the van Cittert–Zernike theorem", *Phys. Rev. E*, vol. 59, p. 7128, 1999. doi:10.1103/PhysRevE.59.7128

[8] L. Ponce, R. Jung, and F. Méot, "LHC proton beam diagnostics using synchrotron radiation", CERN, Geneva, Switzerland, Rep. CERN-2004-007, 2004. doi:10.5170/CERN-2004-007

[9] D. Butti, "Synchrotron radiation interferometry for beam size measurement at the Large Hadron Collider", M.S. thesis, Politecnico di Milano, Milan, Italy, 2019.

[10] O. Chubar, http://github.com/ochubar/SRW

[11] O. Chubar and P. Elleaume, "Accurate and efficient computation of synchrotron radiation in the near field region", in *Proc. EPAC'98*, Stockholm, Sweden, Jun. 1998, pp. 1177–1179.

Content from this work may be used under the terms of the CC BY 4.0 licence (© 2022). Any distribution of this work must maintain attribution to the author(s), title of the work, publisher, and DOI

ISBN: 978-3-95450-241-7 ISSN: 2673-5350 doi:10.18429/JACoW-IBIC2022-MOP24

TEST OF A PROTOTYPE FOR MODULAR PROFILE AND POSITION MONITORS IN THE SHIELDING OF THE 590 MeV BEAM LINE AT HIPA

R. Dölling†, M. Sapinski, F. Marcellini, Paul Scherrer Institut, Villigen, Switzerland

Abstract

A new generation of monitor plugs is under development as spares for the ageing wire profile monitors and beam position monitors inserted into massive shielding in the target regions of the 590 MeV proton beam line at HIPA. A prototype was installed recently in the beam line to the ultra-cold neutron source UCN, to test the performance of wire monitor, BPM and modular mechanical design in a low-radiation environment. We report on first measurements with beam.

INTRODUCTION

The design of the prototype [1, 2] and its vacuum chamber closely resembles the one foreseen in the target region, just the intermediate section with the shielding is subtracted. Beam to UCN is provided either continuously as a splitted beam of a few µA or as the full deflected 1800 µA beam for 8 s, repeated every 300 s.

WIRE MONITOR

At the location of the prototype, the vertical width of the beam is narrow, resulting in the highest thermal load to a wire monitor in the 590 MeV beam lines. The load is higher at the horizontally moving wires MBPT1 than at the vertically moving wires MBPT2. In addition, the wire speed of the prototype is actually only 0.06 m/s, four times lower than that of most in-shielding monitors. This is due to the maximum rate of full steps of 2 kHz, which can be provided by the actual MESON modules [3] driving the stepper motor and reading the signal currents from the wires. The speed will be increased at a later step, when the new driver electronics, based on an extension of the read-out electronics [2] under development, is available. To compensate for the low speed, we reduced the diameter of the molybdenum wires from 48 µm to 25 µm in a first step. In a second step we reduced the diameter to 13 µm and the number of wires per monitor from two to one. In each scan the wires of horizontal and vertical monitor synchronously pass the beam with a forward and a backward motion, 'meeting' at the beam axis twice. Each scan is documented by the control software.

Wire Performance

Secondary emission (SE) as well as thermionic emission (TE) can contribute to the wire signal. Unlike [4], we did not bias the wires to a positive potential for suppressing TE. With the 25 µm wires we observed an evolution of TE over a few passes with higher beam current applied (Figs. 1-4).

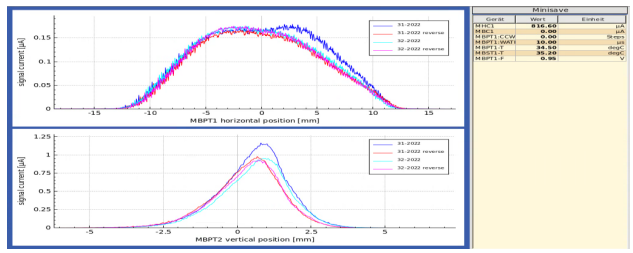


Figure 1: Two scans at a beam current of 820 µA (first time above 100 µA). In the first pass, a TE contribution is visible at MBPT1, but in the following three passes not. (The beam current was stable during this time.) A single pass at 820 µA seems sufficient to 'condition' the surface for lower TE.

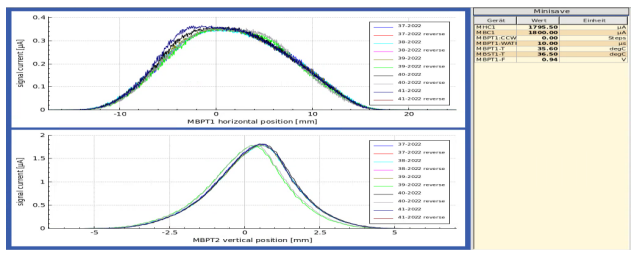


Figure 2: After five further scans with beam current increased to 1800 µA, first signs of TE appeared at MBPT1.

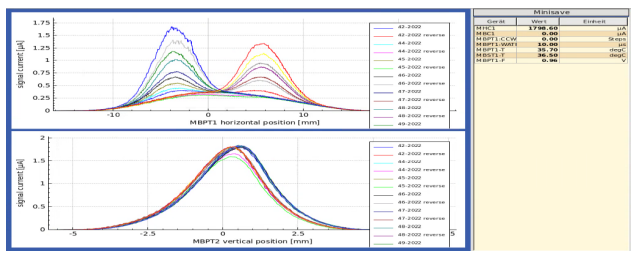


Figure 3: In the following 9 runs at 1800 µA, TE reappeared strongly at MBPT1 in the second half of the passes, where the wire has already heated up. However, the signal without TE, visible in the first half of the passes, does not change much. This indicates that the wire diameter is not reduced due to evaporation.

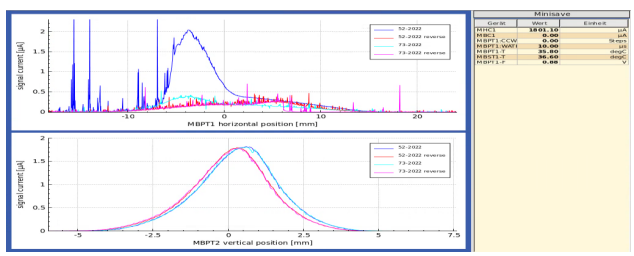


Figure 4: In the next scan, the 21st with beam current above 800 µA, the first of the horizontally moving wires (MBPT1) broke. This resulted in increased noise from the dangling wire ends. In the 39th scan, the second horizontally moving wire also broke.

† doelling@protonmail.com

Content from this work may be used under the terms of the CC BY 4.0 licence (© 2022). Any distribution of this work must maintain attribution to the author(s), title of the work, publisher, and DOI

ISBN: 978-3-95450-241-7 ISSN: 2673-5350 doi:10.18429/JACoW-IBIC2022-MOP24

At the presence of TE at MBPT1, also a small increase of signal at MBPT2 is visible (Figs. 1-3), however nearly independent of the amount of TE at MBPT1.

The increase of TE over the series of scans may be caused by a change of work function or by a lower emissivity leading to higher maximum temperatures. The latter is more likely, since the wire breakage hints to the presence of higher temperatures. A simulation of the heating (Fig. 5) indicates that at full beam current evaporation of wire material should be significant. A lifetime of 29 scans is predicted by that. This is contradicting the conclusion from Fig. 3 and the microscopic observation of the wire end (Fig. 6). Further studies are needed to get a better understanding.

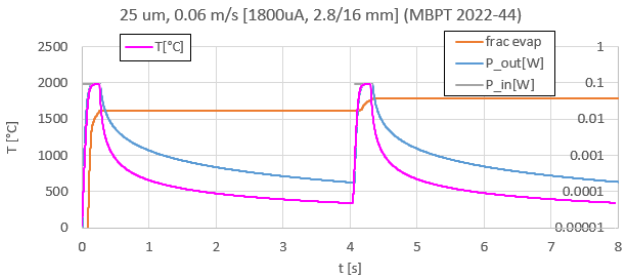


Figure 5: Rough simulation of 25 µm wire heating in the beam center at 1800 µA beam current. Wire temperature, fraction of evaporated material, input and output power are calculated assuming a homogeneous rectangular beam with width double the fwhm measured, stopping power @590 MeV, specific heat @1000°C and temperature dependent emissivity and evaporation rate given by [5]. Thermal equilibrium is reached after the first half of the pass.

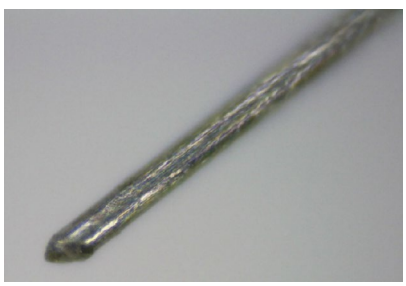


Figure 6: End of broken wire at a magnification of ~800. No thinning is visible.

With the single 13 µm wire, the signal is lower in accordance with the reduced sum of wire circumferences. Signal to noise ratio in the beam core is comparable. A very minor TE contribution appeared only at the first scan at 200 µA beam. However the application of beam currents of up to 2000 µA caused a relative decrease of signal at later scans at low beam current. We still have to accumulate a larger number of scans to see a development. A simulation analogous to Fig. 5 predicts ~450°C lower temperatures for the thinner wire and an evaporation-related lifetime of 20000 scans. Thermal equilibrium is still reached and a wire speed above 0.24 m/s would be required to lower temperatures. According to simulation, the 48 µm wires of the other 590 MeV monitors survive only due to lower beam current densities in that locations.

Force Sensor

A force sensor allows to observe the force applied to the feedthrough and in-vacuum mechanics. It performs well in spite of a long cable length of ~30 m (Fig. 7).

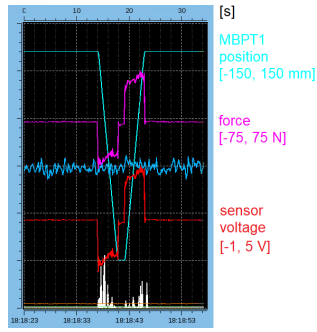


Figure 7: Force sensor reading at full scan. The force at rest corresponds to the weight of the moved parts.

BPM

The capacitive pickup variant (Ref. [2] Fig. 6, modified for horizontal beam) has been implemented in the prototype. The signals of the four pickups are transferred via a short radiation hard (metal, ceramics) cable module and a short PE cable with removed mantle to the feedthrough, and further via ~30 m of 1/4"-Cellflex SCF14-50JFN cable with a damping of ~1.8 dB to a LeCroy 640zi scope or an Rhode&Schwarz FSV spectrum analyser. Different from the standard BPM, no preamplifier is used in the bunker.

Higher-Order Modes of the Monitor

With the large diameter and short length of the BPM, and with profile monitor parts nearby, higher-order modes (HOM) excited by the beam are more prominent than in our standard BPMs. In the measured signal spectrum (Fig. 8), this is visible as an increased 'underground' at around 300 MHz and above 700 MHz, besides the harmonics of the bunch repetition frequency f_{RF} = 50.63 MHz.

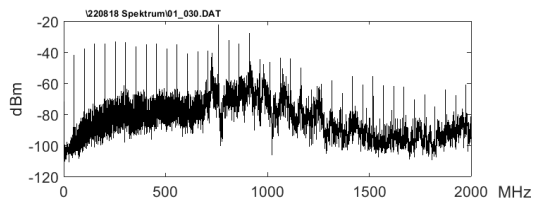


Figure 8: Spectrum of a single pickup at a beam of 1800 µA taken with the spectrum analyser at a bandwidth of 20 kHz.

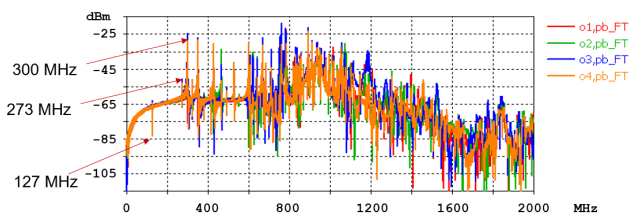


Figure 9: HOM spectrum according to a CST simulation. Excitation by a single bunch of 1800 µC and 58 mm r.m.s. length.

Content from this work may be used under the terms of the CC BY 4.0 licence (© 2022). Any distribution of this work must maintain attribution to the author(s), title of the work, publisher, and DOI

ISBN: 978-3-95450-241-7 ISSN: 2673-5350 doi:10.18429/JACoW-IBIC2022-MOP24

Content from this work may be used under the terms of the CC BY 4.0 licence (© 2022). Any distribution of this work must maintain attribution to the author(s), title of the work, publisher, and DOI

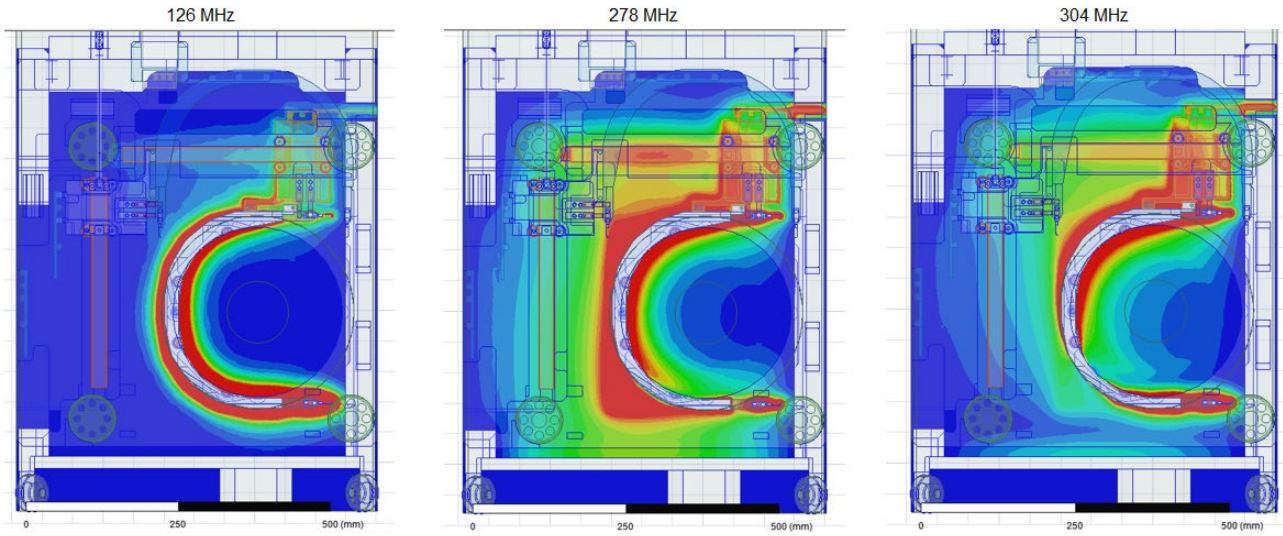


Figure 10: Distribution of electric field of the first three HOM. Structure grounded at chamber bottom and top.

This relates to a detailed CST simulation of the monitor structure (Figs. 9 and 10). The HOM spectra of measurement and simulation compare reasonably. The fork of the horizontally moving MBPT1, which in the parking position is close to the beam, is involved in all three modes. A grounding of the fork's free end in the parking position would shift these HOM to much higher frequencies. However, it is difficult to provide this reliably.

Position Determination

To measure the signals of all four pickups the 4-channel scope was used. Fig. 11 gives an example.

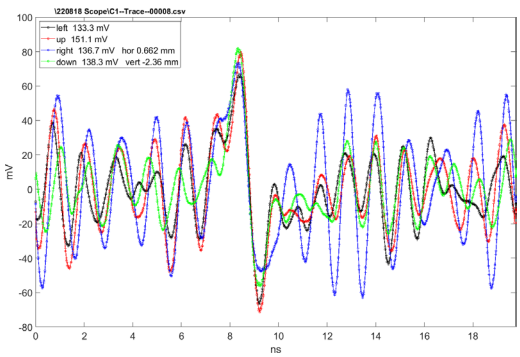


Figure 11: The four pickup signals averaged over 5063 periods of f_{RF}. Sampling rate 20 GS/s. (The legend gives the peak-to-peak height and the position derived from this by using Eq. (1) with zero offset.)

From a FFT of the pickup signals, the intensities of the first 12 harmonics of f_{RF} were determined by adding all channels in a peak above 3 per mille of the maximum. This was done for several vertically shifted beams of known vertical position y_{ref}. The relation

$$y_{BPM}[\text{mm}] = r_{eff}[\text{mm}]\frac{U_{down} - U_{up}}{U_{down} + U_{up}} + y_{offset} \qquad (1)$$

could be established with r_{eff} = 53 mm and significant offsets y_{offset}, depending on the used harmonic, which are caused by the presence of HOM (Fig. 12). The CST simulation predicted $r_{eff} \sim 55$ mm in good agreement. (The physical radius of the BPM is 100 mm.) Just for harmonic 2, which is used at our standard BPM, the offset is here close to 0 mm. However, the BPM should be calibrated with the profile monitor. We still have to determine if these offsets depend on beam current.

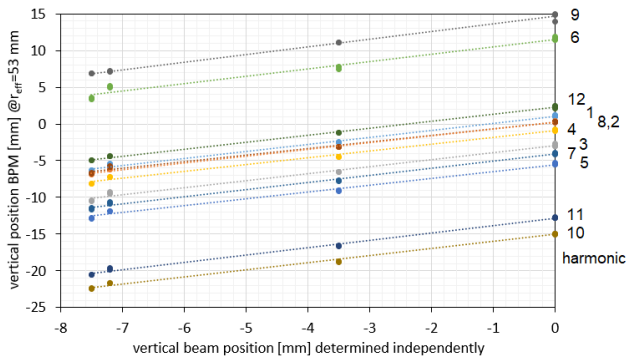


Figure 12: Correlation between vertical beam position measured by MBPT2 and neighbouring BPM with the beam position determined by the BPM prototype. Beam current 1800 µA.

Subharmonics

Interestingly, subharmonics at multiples of $f_{RF}/10$ appear in all measured spectra over a broad range (Fig. 13).This frequency is not natural to the RF amplifiers or RF cavities or resonators of both upstream cyclotrons or bunchers. However, in the far upstream Injector 2 cyclotron with a harmonic number of 10, $f_{RF}/10$ corresponds to the time of a turn revolution, i.e. to the time difference between bunches moving in the same radial 'spoke' of bunches, but at radially neighbouring turns.

Somehow 'information' must be transferred from a bunch in a turn to a bunch in a neighbouring turn, being then 'displaced' by the time of a turn revolution. It is likely that beam current noise at frequencies in the kHz and low MHz range, which is overlaid to the bunch pattern and generated mainly by the ion source, plays a role here. (e.g., a measurement of the number of turns in the cyclotron [6] is based on this.)

ISBN: 978-3-95450-241-7 ISSN: 2673-5350 doi:10.18429/JACoW-IBIC2022-MOP24

A candidate for the transfer of protons may be the beam extraction. The last turns are separated to a high degree at the electrostatic septum, but a small overlap remains. Hence, a small fraction of protons from the second last turn is also extracted. Beam dynamics considerations must clarify if these protons 'survive' up to the much downstream location of the BPM.

A candidate for the transfer of information on bunch charge are the strong space charge forces in the Injector 2, which also affect radially neighbouring bunches. There is no indication of the presence of $f_{RF}/6$ subharmonics corresponding to the Ring cyclotrons harmonic number. However, the space charges forces are lower there.

It would be interesting to clarify the underlying mechanism, since such measurements may possibly deliver information on the quality of extraction, the space charge forces or other parameters.

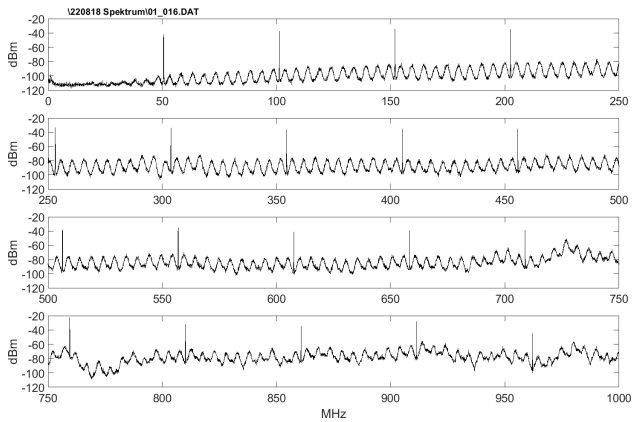


Figure 13: Spectrum of a single pickup at a beam of 1800 µA taken with the spectrum analyser at a bandwidth of 2 kHz.

ACKNOWLEDGEMENTS

The authors would like to thank R. Widmer and S. Lindner for assembling the monitor, T. Rauber and P. Simon for providing vacuum chamber and lifting gear and organizing bunker works, J. Snuvering for adapting the profile monitor driving software, H. Lutz, G. Gamma and K. Bitterli for electronics and controls integration, J.-Y. Raguin for additional RF simulations, B. Keil, A. Dietrich, M. Rizzi, M. Schneider and D. Treyer for discussions.

AUTHOR CONTRIBUTIONS

RD and MS provided the wire monitor chapter. RD provided the BPM chapter with exception of the CST simulations which were done by FM.

REFERENCES

[1] R. Dölling, D. Berisha, J. Germanovic, D. C. Kiselev, F. Marcellini, and K. M. Zehnder, "Development of Modular Spare Parts for the Profile and Position Monitors of the 590 MeV Beam Line at HIPA", in *Proc. IBIC'19*, Malmö, Sweden, Sept. 2019, pp. 402-406. doi:10.18429/JACoW-IBIC2019-TUPP035

[2] R. Dölling, E. Johansen, M. Roggli, and M. Rohrer, "Progress of Profile Measurement Refurbishment Activities at HIPA", in *Proc. IBIC'20*, Santos, Brazil, Sep. 2020, pp. 179-183. doi:10.18429/JACoW-IBIC2020-WEPP33

[3] E. Johansen, "VME Meson design specification", PSI, Villigen, Switzerland, June 2010, unpublished.

[4] M. Sapinski, R. Dölling, M. Rohrer, "Commissioning of the renewed long radial probe in PSI's Ring Cyclotron", presented at IBIC'22, Krakow, Poland, Sept. 2022, poster MOP19, this conference.

[5] https://www.plansee.com/de/werkstoffe/molybdaen.html

[6] P. A. Duperrex and A. Facchetti, "Number of turn measurements on the HIPA cyclotrons at PSI", in *Proc. IPAC'18*, Vancouver, Canada, Apr.-May 2018, pp. 2334-2336, doi:10.18429/JACoW-IPAC2018-WEPAL067

Content from this work may be used under the terms of the CC BY 4.0 licence (© 2022). Any distribution of this work must maintain attribution to the author(s), title of the work, publisher, and DOI

ISBN: 978-3-95450-241-7 ISSN: 2673-5350 doi:10.18429/JACoW-IBIC2022-MOP26

BUNCH LENGTH MEASUREMENT SYSTEMS AT S-DALINAC*

A. Brauch†, M. Arnold, J. Enders, L. E. Jürgensen, N. Pietralla, S. Weih
Technische Universität Darmstadt, Institute for Nuclear Physics, Darmstadt, Germany

Abstract

A high-quality beam is necessary for electron scattering experiments at the superconducting Darmstadt electron linear accelerator S-DALINAC. An optimisation of the bunch length to typical values of < 2 ps is performed to reach a high energy resolution of 10^{-4}. Currently, this is accomplished by inducing a linear momentum spread on the bunch in one of the accelerating cavities. The bunch length can then be measured with a target downstream. This method is time consuming and provides only an upper limit of the bunch length. Two new setups for bunch length measurements will improve the optimisation process significantly. On the one hand, a new diagnostic beam line is set up in the low energy beam area. It includes a deflecting copper cavity used for measuring the bunch length by shearing the bunch and projecting its length on a target. On the other hand, a streak camera placed at different positions downstream the injector and the main linac will be used to measure the bunch length. Optical transition radiation from an aluminium coated kapton target is used to perform this measurement. The present layout of both systems and their current status will be presented in this contribution.

INTRODUCTION

Since 1991 the institute operates the S-DALINAC for high-resolution electron scattering experiments [1]. It is a thrice-recirculating linear electron accelerator that produces a continuous-wave electron beam at a frequency of 2.997 GHz. The accelerator is designed to reach its maximum energy resolution of 10^{-4} with bunch lengths < 2 ps [2]. Currently, this property of the electron bunches is checked with a method involving the last cavities of injector and linac as well as a dispersion calibrated target. By operating these cavities 90° off-crest the length of the passing bunches is changed and made visible on the beam target. As a result, an estimate for the bunch length can be extracted. Although the method works and provides a useful result for accelerator diagnostics, it causes some difficulties:

- Because of the intrinsic transversal beam size of the bunch and broadening caused by the used targets, the bunch length measured is only an upper estimate.
- The bunch length is only determined at the position of the last cavities of injector and linac and must be extrapolated for other locations.
- The method does not allow for an evaluation of the bunch length when all cavities are operated as intended.

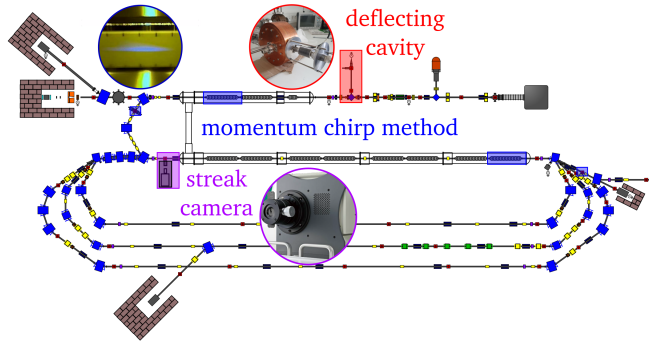


Figure 1: Floorplan of the S-DALINAC. The positions for the current method for bunch length measurements (picture from [3]) are highlighted in blue. The new methods using a deflecting cavity and a streak camera (picture from [4]) are planned to be used at the locations in red and purple.

To tackle these issues, two new devices for bunch length measurements are planned to be used at the S-DALINAC. One of these is a deflecting copper RF cavity that is placed in an upward diagnostic beam line (see Fig. 1). It will enable a bunch length measurement in the normal-conducting beam line area in front of the injector. While it is possible to do a bunch length measurement with the prebuncher this method also only provides an upper estimate of the bunch length [3]. Instead, the deflecting cavity will allow for a direct measurement of the bunch length. The width broadening caused by the target is planned to be eliminated by replacing the target with a wire scanner. The simulated properties of the diagnostic beam line and its current status will be presented in the following section. The other device is a streak camera used for the high energy areas of the accelerator. Therefore, the planned setup and its parameters will be presented here.

SETUP FOR BUNCH LENGTH MEASUREMENTS IN FRONT OF THE INJECTOR

A sketch of the setup for bunch length measurements with the deflecting cavity is shown in Fig. 2. A dipole magnet, which can be used to lead the beam into the upward diagnostic section, is situated downstream a chopper prebuncher system. The magnet is broadening the beam in one transversal dimension. The energy resolution of the bunch can be estimated by measuring the width on the target. A deflecting copper cavity with its TM_{110} mode imposes a shear on the bunch for the bunch length measurement.

* Work supported by DFG (GRK 2128) and the State of Hesse within the Research Cluster ELEMENTS (Project ID 500/10.006).
† abrauch@ikp.tu-darmstadt.de

Content from this work may be used under the terms of the CC BY 4.0 licence (© 2022). Any distribution of this work must maintain attribution to the author(s), title of the work, publisher, and DOI

ISBN: 978-3-95450-241-7 ISSN: 2673-5350 doi:10.18429/JACoW-IBIC2022-MOP26

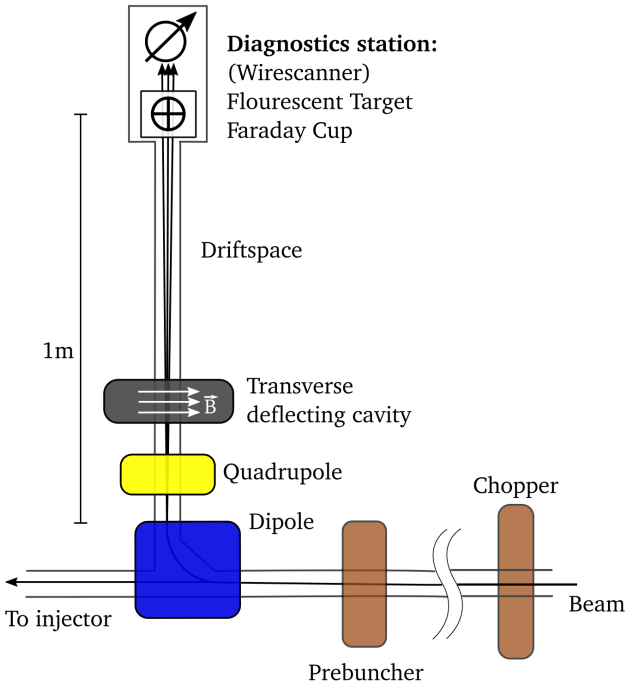


Figure 2: Sketch of the planned setup for bunch length measurements in front of the injector of the S-DALINAC (following [3]).

Likewise, the increased width in the other transversal dimension caused by the cavity is related to the bunch length. A quadrupole magnet is placed between the dipole magnet and deflecting cavity to improve the accuracy of the bunch length measurement (for details see below).

Simulation of Diagnostic Setup

Using the particle tracking code ASTRA [5] (and elegant [6] for the dipole) the setup was simulated with various bunch configurations. The width and length of normal distributed electrons in a bunch can be given in terms of standard deviations. Here the bunch length is defined as σ_{z_0} and the bunch width in one transversal dimension is given as σ_x (here assumed as the x-dimension, for simplicity). The total width on the target at the end of the diagnostic setup is given by:

$$\sigma_x = \sqrt{\sigma_{x,0}^2 + \sigma_{x,TDC}^2} = \sqrt{\sigma_{x,0}^2 + \left(\frac{2\pi}{\beta\lambda}\frac{d\langle x\rangle}{d\varphi}\sigma_{z_0}\right)^2}. \quad (1)$$

$\sigma_{x,0}$ is the width of the bunch without the influence of the deflecting cavity. $\sigma_{x,TDC}$ is the width increase by shearing the bunch when it passes the deflecting cavity. Rearranging Eq. (1) for the bunch length yields:

$$\sigma_{z_0} = \frac{\beta\lambda}{2\pi}\frac{\sqrt{\sigma_x^2 - \sigma_{x,0}^2}}{\frac{d\langle x\rangle}{d\varphi}}. \quad (2)$$

This formula requires two measured values before the bunch length can be extracted. One of these is a derivative of the mean beam position as a function of the phase of the cavity that obeys the following relation:

$$\frac{d\langle x\rangle}{d\varphi} = l\frac{p_{x,0}}{p_z}. \quad (3)$$

$p_{x,0}$ is the deflecting momentum caused by the cavity. It depends on the phase φ at which the deflecting cavity is operated. p_z is the longitudinal momentum of the bunch in beam direction and l is the length of the path between the target and the centre of the cavity. Instead of measuring the values on the right hand side of Eq. (3), the mean value in the deflected dimension of the projected bunch distribution $\langle x\rangle$ is measured. This is done for various values of φ around the set point for the bunch length measurement. A linear fit is applied to the measured values and the slope of this fit is equal to the right hand side of Eq. (3). The derivative is determined easily during operation in this manner and this has to be done only once (unless the momenta are changed). The other value to be measured for using Eq. (2) is the intrinsic width of the bunch in the deflecting dimension $\sigma_{x,0}$. By switching off the deflecting cavity this value is evaluated on the target screen.

The simulations had the goal to check whether the proposed measurement setup can be realised under the conditions of the beam in this location. This was achieved by multiple simulations with increasingly complex bunch distributions with a particle size of 5000. The first tests used a Gaussian bunch with a point like transversal beam size (essentially the electrons are aligned like pearls on a necklace). For the final runs the whole area from thermionic gun to the target of the diagnostic section was simulated using a realistic bunch. Space charge effects were not considered due to the small charge of the S-DALINACs bunches (33 aC – 6.7 fC).

The simulations were performed with bunch lengths of 3.57 ps, 9.94 ps and 16.54 ps that cover the range of the expected bunch lengths at this setup. It was found that the intrinsic width of the bunches $\sigma_{x,0}$ is too large for an accurate measurement (at least a relative uncertainty of 10%). A good accuracy can only be obtained when $\sigma_{x,TDC} \gg \sigma_{x,0}$ according to other works [7]. As a result, a quadrupole magnet was added to the setup. Also the chopper in front of the diagnostic section is causing a initial shear on the bunches. This shear can either increase σ_x or reduce it depending on the direction the deflecting cavity is shearing the bunch. The shear direction of the deflecting cavity is fixed by one of two possible set points of φ. The increased σ_x will be called $\sigma_{x,+}$ and the reduced σ_x will be called $\sigma_{x,-}$ from now on. The initial shear of the chopper is compensated by measuring $\sigma_{x,+}$ as well as $\sigma_{x,-}$ and use their mean value to calculate the bunch length [8]. Finally, the simulated beam images have a size that is barely fitting into the installed beam pipe in the diagnostic section. Since the radiation caused by the electrons hitting the beam pipe with an energy of 250 keV is not inhibiting the measurement, the beam pipe diameter will not be increased. The low currents in the µA-range used for the measurement will also lead to only minor amounts of radiation.

Content from this work may be used under the terms of the CC BY 4.0 licence (© 2022). Any distribution of this work must maintain attribution to the author(s), title of the work, publisher, and DOI

ISBN: 978-3-95450-241-7 ISSN: 2673-5350 doi:10.18429/JACoW-IBIC2022-MOP26

Content from this work may be used under the terms of the CC BY 4.0 licence (© 2022). Any distribution of this work must maintain attribution to the author(s), title of the work, publisher, and DOI

The extracted bunch length measurements from the images are summarised in Table 1. The simulated bunch distributions on the target screen are given in Fig. 3.

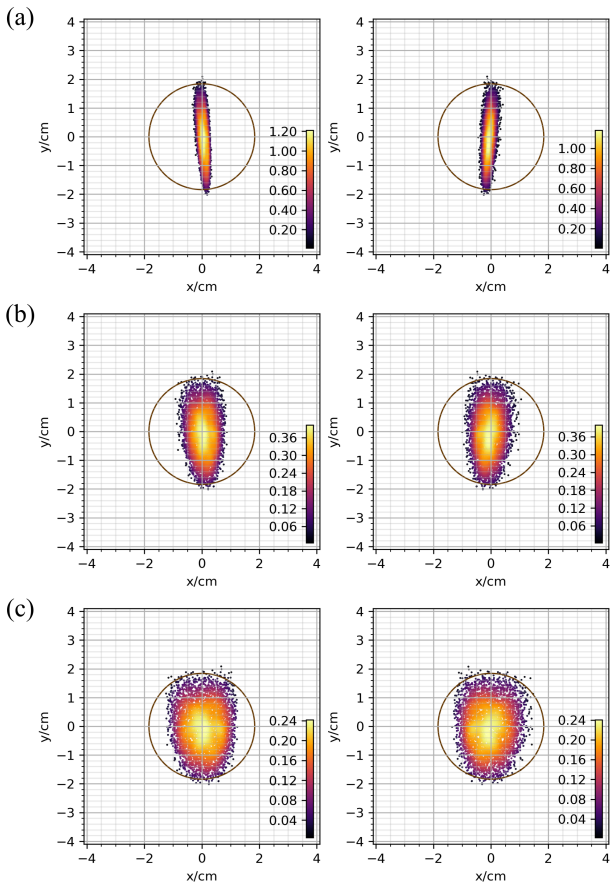


Figure 3: Distribution of the electrons hitting the target at the end of the diagnostic section. Cases (a)-(c) are identical to the cases shown in Table 1. The left side shows the set point of φ leading to the larger width $\sigma_{x,+}$ on the screen. The right side shows the set point of φ leading to the smaller width $\sigma_{x,-}$ on the screen. The brown circle shows the beam pipe currently installed in the diagnostic section. The normalised relative density is shown in the colours of the dots and has arbitrary units. The simulation results for these figures can be found in Table 1.

Table 1: Simulation results from the images in Fig. 3. The tested bunch lengths $\sigma_{z_0,\mathrm{code}}$ do not deviate more than 2% from the measured bunch lengths extracted from the images $\sigma_{z_0,\mathrm{screen}}$. $\sigma_{x,+}$ and $\sigma_{x,-}$ are the image widths on the beam target for each set point of φ that are used to calculate $\sigma_{z_0,\mathrm{screen}}$.

cases	(a)	(b)	(c)
$\sigma_{z_0,\mathrm{code}}$	3.57 ps	9.94 ps	16.54 ps
$\sigma_{z_0,\mathrm{screen}}$	3.57 ps	10.01 ps	16.88 ps
$\sigma_{x,+}$	4.50 ps	11.84 ps	18.71 ps
$\sigma_{x,-}$	4.07 ps	11.34 ps	18.11 ps

SETUP FOR BUNCH LENGTH MEASUREMENTS BEHIND THE INJECTOR UP TO 10 MeV

Because of the high energies behind the injector a different setup at this position is planned to be used for bunch length diagnostics. This setup involves the use of a streak camera that transforms light pulses with a photocathode into low energy electron bunches. These bunches are deflected with a pair of electrodes and hit a phosphor screen where the bunch length can be read out. Figure 4 shows a sketch of the streak camera.

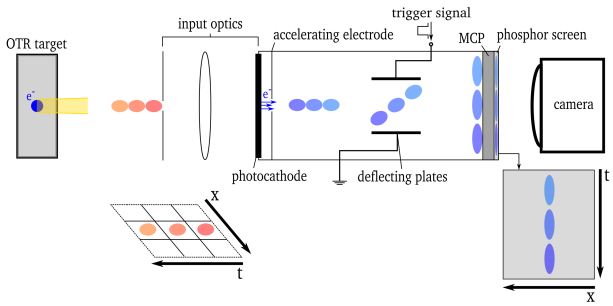


Figure 4: Sketch of a streak camera and its internal setup. Photoelectrons are created and deflected with a pair of electrodes to enable the measurement of the bunch length on a phosphor screen (following [4]).

Because of the camera being only receptive to visible light the electron bunches behind the injector must be transformed to light pulses. This will be achieved by using optical transition radiation (OTR) targets. They conserve the temporal structure of the bunch and are implemented in S-DALINAC already for emittance measurements. This light must be transported to the slit in front of the streak camera via a telescope and periscope. The former reduces the transversal size of the light pulse and improves the accuracy of the measurement just like the quadrupole magnet does for the deflecting cavity. The latter is used to prevent a direct line of sight between camera and target. This prevents radiation from the direction of the target from causing damage to the device. Covering the camera beneath a massive lead shielding prevents radiation from any other direction from entering the camera. The last mirror of the periscope will be an off axis parabolic mirror focusing the light pulse directly on the slit of the camera.

To be able to measure the typical bunch lengths of the accelerator, a resolution of ≤ 1 ps is required. Multiple factors contribute to the resolution of a streak camera, but the most important factor is the slit size in front of the camera. This resolution factor R_{slit} can be estimated by multiplying the whole slit width b_{slit} with the velocity v_{streak} the camera deflects the bunches over its screen at the end of the device.

$$R_{\mathrm{slit}} = b_{\mathrm{slit}} v_{\mathrm{streak}} \tag{4}$$

ISBN: 978-3-95450-241-7 ISSN: 2673-5350 doi:10.18429/JACoW-IBIC2022-MOP26

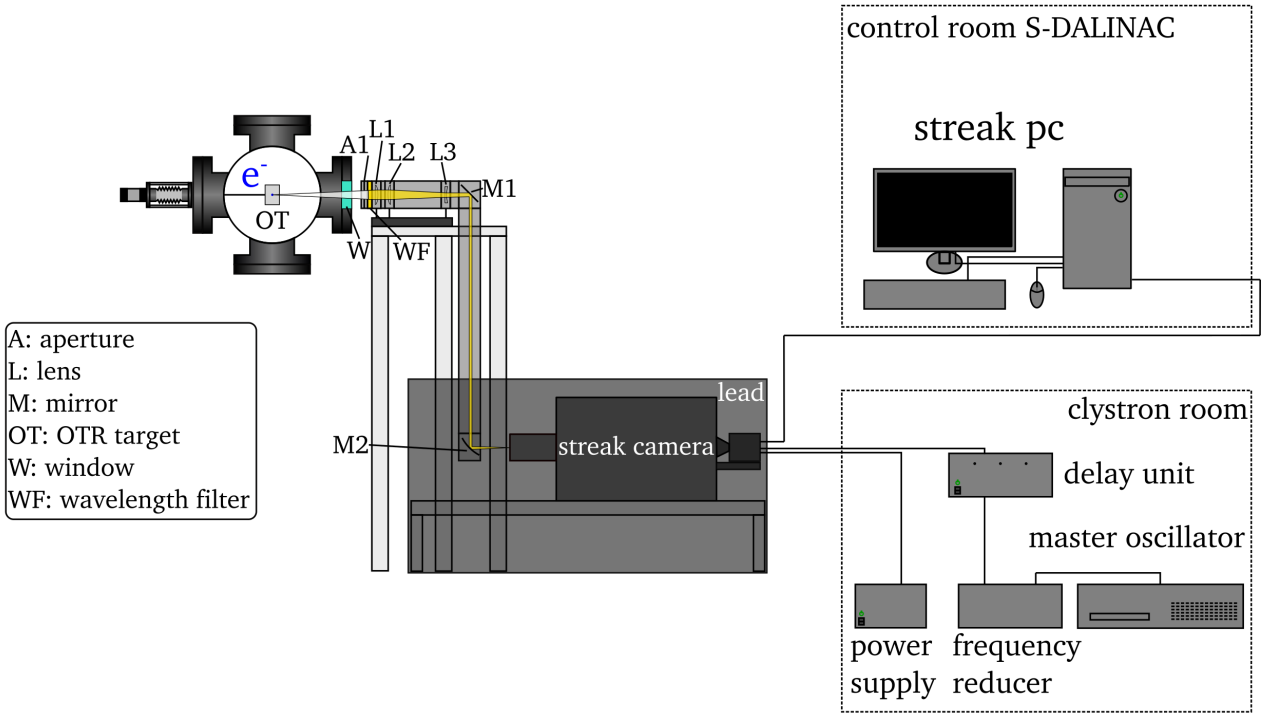


Figure 5: Proposed setup for a streak setup to measure bunch lengths via OTR targets. The created light pulses enter a telescope followed by a periscope leading the light to the streak camera close to the floor. The last mirror in the periscope is concave so that the light is focused on the small entrance slit of the camera.

Using v_{streak} of the proposed device (C10910 by Hamamatsu) and a resolution value of 1 ps one would require a slit width of 94.4 µm. This highlights the necessity of the optics setup in front of the camera. Figure 5 shows the proposed setup for the streak camera.

CONCLUSION

For a high-quality beam at the experimental sites of the S-DALINAC the bunch length must be optimised to a value of < 2 ps. In front of the injector a diagnostic section with a deflecting cavity will enable measurements of the bunch length. Simulations of this section revealed the necessity of a quadrupole magnet because of the large beam width decreasing the accuracy of the measured bunch lengths. For the superconducting areas of the accelerator a setup involving a streak camera is planned to be used. Because of the required resolution and the vulnerability of the camera a telescope-periscope setup is intended for the device.

REFERENCES

[1] N. Pietralla, "The Institute of Nuclear Physics at the TU Darmstadt", *Nucl. Phys. News*, vol. 28, no. 2, pp. 4–11, 2018. doi:10.1080/10619127.2018.1463013

[2] F. Hug, "Erhöhung der Energieschärfe des Elektronenstrahls am S-DALINAC durch nicht-isochrones Rezirkulieren", Ph.D. thesis, Technische Universität Darmstadt D17, Darmstadt, Germany, 2013.

[3] S. Weih, "Injector Optimization at the Superconducting Darmstadt Linear Electron Accelerator S-DALINAC", Ph.D. thesis, Technische Universität Darmstadt D17, Darmstadt, Germany, 2022.

[4] Hamamatsu Photonics K.K., Universal streak camera C10910 series, https://www.hamamatsu.com/content/dam/hamamatsu-photonics/sites/documents/99_SALES_LIBRARY/sys/SHSS0016E_C10910s.pdf

[5] S. M. Lidia, K. Floettmann, and P. Piot, "Recent Improvements to the ASTRA Particle Tracking Code", in *Proc. PAC'03*, Portland, OR, USA, May 2003, paper FPAG015, pp. 3500–3502.

[6] M. Borland, "ELEGANT: A flexible SDDS-compliant code for accelerator simulation", Argonne National Lab., IL, USA, LS-287, 2000. doi:10.2172/761286

[7] D. Marx *et al.*, "Lattice considerations for the use of an x-band transverse deflecting structure (TDS) at SINBAD, DESY", *J. Phys.: Conf. Ser.*, vol. 874, p. 012078, 2017. doi:10.1088/1742-6596/874/1/012078

[8] D. X. Wang *et al.*, "Measurement of femtosecond electron bunches using a rf zero-phasing method", *Phys. Rev. E*, vol. 57, pp. 2283–2286, 1998. doi:10.1103/PhysRevE.57.2283

Content from this work may be used under the terms of the CC BY 4.0 licence (© 2022). Any distribution of this work must maintain attribution to the author(s), title of the work, publisher, and DOI

ISBN: 978-3-95450-241-7 ISSN: 2673-5350 doi:10.18429/JACoW-IBIC2022-MOP27

DESIGN CONSIDERATIONS OF THE CORRUGATED STRUCTURES IN A VACUUM CHAMBER FOR IMPEDANCE STUDIES AT KARA

S. Maier*, M. Brosi†, H. J. Cha, A. Mochihashi, M. J. Nasse, P. Schreiber, M. Schwarz, A.-S. Müller
Karlsruhe Institute of Technology, Karlsruhe, Germany

Abstract

Two parallel, corrugated plates will be installed at the KIT storage ring KARA (KArlsruhe Research Accelerator). This impedance manipulation structure can be used to study and eventually control the electron beam dynamics and the emitted coherent synchrotron radiation (CSR) at KARA. In this contribution, we present the design of the impedance manipulation structure with corrugated plates, simulation results showing the influence of different corrugation parameters on its impedance, and the impact of this additional impedance source on the temporal changes in the emitted CSR in the presence of the microbunching instability.

INTRODUCTION

Unlike the incoherent synchrotron radiation, the coherent synchrotron radiation (CSR) does not scale linearly but quadratically with the number of emitting particles, so consequently the emitted photon flux can be enhanced by multiple orders of magnitude, for typical electron synchrotron radiation facilities. This makes it attractive to use the CSR for various kinds of applications. However, the emitted radiation is only coherent when its wavelength is longer than the emitting structure. Therefore, very short bunches and thus a high particle density is required to extend the CSR to a higher frequency range and to increase the total radiation intensities. In such a short-bunch regime, collective phenomena occur due to an interaction of an electron bunch with its own self-emitted CSR, which can lead to bunch deformations and dynamic instabilities like the so-called microbunching instability [1]. Especially, the microbunching instability leads to dynamically changing substructures and thereby intermittent regions of increased longitudinal charge density causing intense bursts of CSR in the THz frequency range.

A versatile impedance manipulation chamber is in development and will be installed into the KIT storage ring, KARA. The purpose of this chamber is to study the effect on the microbunching instability by manipulating the longitudinal impedance and thereby affecting the longitudinal beam dynamics of the electron bunches. The additional impedance is generated by a pair of horizontal, parallel plates with periodic, rectangular corrugations. Figure 1 shows a schematic drawing with the parameters corrugation depth h, corrugation width g, periodic length L, and plate distance $2b$. A cylindrical corrugated pipe has been tested in a linear accelerator by Bane *et al.* [2, 3], where they produced narrow-banded THz pulses of Smith-Purcell radiation [4], which is not examined in the KARA project. To our knowledge, such a structure has not yet been tested in a storage ring, where the wakefields in the corrugated structure can affect frequently the bunch profile and the resulting CSR due to the passing of the structure with a revolution frequency of 2.7 MHz (for KARA).

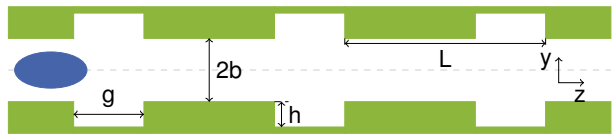


Figure 1: The corrugated pipe in cross section with the relevant geometric parameters corrugation depth h, corrugation width g, periodic length L, and plate distance $2b$ is shown. The electron bunch is indicated in blue.

The longitudinal impedance $Z^{\parallel}$ of a cylindrical, corrugated pipe has been theoretically described in Ng *et al.* [5] with the validity range $L \lesssim h \ll b$, as

$$\frac{Z^{\parallel}}{L} = \frac{Z_{\mathrm{vac}}}{\pi b^2}\left[\pi k_{\mathrm{res}}\delta\left(k^2 - k_{\mathrm{res}}^2\right) + i \cdot \mathrm{P.V.}\left(\frac{k}{k^2 - k_{\mathrm{res}}^2}\right)\right] \quad (1)$$

with the resonance wave number $k_{\mathrm{res}} = \sqrt{\frac{2L}{bgh}}$, the wave number $k = \frac{\omega}{c}$, the vacuum impedance $Z_{\mathrm{vac}} \simeq 377\,\Omega$, the δ-distribution, and the principal value $\mathrm{P.V.}(x)$ [6].

At KARA, the CSR impedance is the dominant longitudinal impedance source in the short-bunch operation mode at 1.3 GeV. In the frequency range below 200 GHz, the parallel plate impedance gives for the impedance per revolution the highest contribution with up to 10 kΩ and thus an additional impedance of 1 kΩ, which can be generated by the corrugated structure, could significantly contribute to the total impedance. For now, the parameter values of the corrugations in Table 1 were chosen so that the theoretical resonance frequency $f_{\mathrm{res}} = \frac{c}{2\pi}k_{\mathrm{res}}$ lies between 50 GHz and 200 GHz. The simulated impedance can be described by an effective resonator model [7] that is characterized by the resonance frequency f_{res}, the shunt impedance Z_0, and the quality factor Q.

Table 1: Parameter Values Used for the Simulations

Parameter	Variable	Range
Periodic length	L	50 µm to 200 µm
Corrugation depth	h	50 µm to 300 µm
Corrugation width	g	12.5 µm to 150 µm

* sebastian.maier@kit.edu
† Now at MAX IV Laboratory, Lund, Sweden

Content from this work may be used under the terms of the CC BY 4.0 licence (© 2022). Any distribution of this work must maintain attribution to the author(s), title of the work, publisher, and DOI

ISBN: 978-3-95450-241-7 ISSN: 2673-5350 doi:10.18429/JACoW-IBIC2022-MOP27

To determine the smallest possible plate distance for experiments, a set of two vertical scrapers were moved towards the beam from the top and the bottom. This experiment, in the short-bunch operation mode, showed a drastic reduction of the beam lifetime due to a significant loss of electrons for a vertical opening of $b_{\mathrm{Scraper}} \leq 3\,\mathrm{mm}$. Based on this and taking into account the different value of the vertical beta-function at the position of the scraper and the planned chamber, $b = 5\,\mathrm{mm}$ was chosen as the smallest plate distance for the simulations. In the following, if not explicitly stated otherwise, the duty-cycle of the corrugations is taken to be 50% or rather $L/g = 2$. At KARA, a limited space of around 48 cm is available in the ring for the entire chamber including taper sections and vacuum pumps. Therefore, the length of the corrugated structure is limited to 20-25 cm, but in this paper a length of $s = 10\,\mathrm{cm}$ was chosen to reduce the simulation time. In contrast to Ref. [8], design considerations of the corrugated plates will now also be discussed in this contribution.

IMPEDANCE SIMULATION

To simulate the impedance of the corrugated structures, the Wakefield solver of the CST Particle Studio [9] was used. Its numerical code computes the wakefields in the time domain and calculates the impedance from the Fourier transformation of the longitudinal wake potential and the Fourier transformed charge distribution of the bunch. The simulated structure consists of two corrugated plates of stainless steel and vacuum between them. A more detailed description of the settings for the impedance simulations is given in Ref. [10].

Plate Distance

The impact of the plate distance $2b$ on the impedance is of great importance for the chamber design because of the need to be able to remove the additional impedance for the normal KARA machine operation. Furthermore it is a tuning knob during the experiments as the parameters of the corrugation structures are typically fixed. The variation of the real part of the longitudinal impedance of a corrugated structure with the half plate distance b is shown in Fig. 2. The increase of the plate distance results in a distinct reduction of the magnitude of the impedance, as expected from Eq. (1).

Figure 3 shows the shunt impedance Z_0 for different b, fixed $h = 200\,\mu\mathrm{m}$ and $L = 100\,\mu\mathrm{m}$. From Eq. (1) we would expect a $1/b^{5/2}$ dependency based on the pre-factors of the δ-function. From the fit, however, we find a $1/b^{\gamma}$ with $\gamma = 2.23 \pm 0.02$ behavior with an exponent smaller than predicted for a cylindrical corrugated pipe in the equation. The deviation might be explained by the different geometric shape of the structure (parallel corrugation plates). Furthermore, the simulation results showed that the exponent was not constant for different corrugation parameters and increased with both L and h.

Figure 2 also shows that f_{res} is not nearly as strongly affected by plate distance as Z_0, but is rather determined by

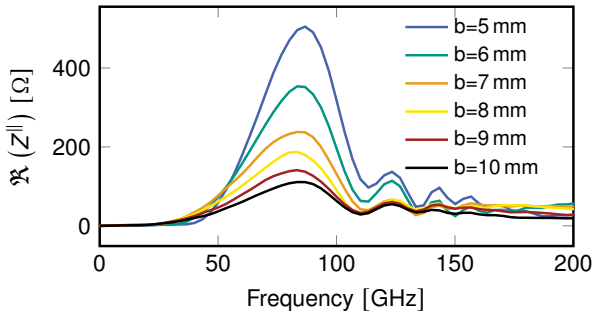


Figure 2: Real part of the longitudinal impedance $Z^{\parallel}$ for different half plate distances b and a fixed corrugation depth $h = 200\,\mu\mathrm{m}$ and periodic length $L = 100\,\mu\mathrm{m}$, respectively.

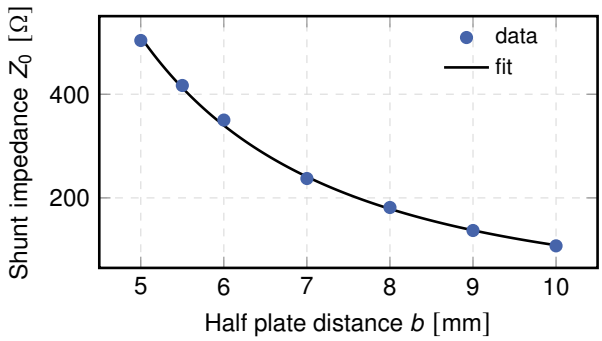


Figure 3: Shunt impedance Z_0 in dependence of the half plate distance b. The parameters of the corrugations are the same as in Fig. 2. The fit validates the $1/b^{\gamma}$ behaviour with $\gamma = 2.23 \pm 0.02$.

the corrugation parameters [10]. This gives the possibility to manipulate the strength of the influence of an additional impedance without significantly affecting other characteristics of the impedance.

Plate Width

In the case of a narrow transverse width of the corrugated plate, the side edges could affect the impedance. To determine the required width, to avoid effects of the lateral edges of the corrugated plate on the impedance, simulations as a function of the plate width x_0 of the corrugated structure were done. The real part of the longitudinal impedance for a corrugated structure with the parameters $h = 200\,\mu\mathrm{m}$ and $L = 100\,\mu\mathrm{m}$ for different plate widths x_0 is shown in Fig. 4. It can clearly be seen that for narrower corrugated plates not only the strength of the impedance is suppressed but also f_{res} is shifted. Above a width of x_0 =16 mm, it seems that the impedance characteristics remain nearly unchanged. In Fig. 5 the impedance parameters Z_0 and f_{res} - determined by fit - are shown in dependency of the plate width. In the case of $x_0 \leq 10\,\mathrm{mm}$, the shunt impedance increases roughly linearly with x_0 before it seems to approach a level of saturation to an asymptotic limit, which is assumed to be reached at $x_0 \geq 16\,\mathrm{mm}$. Moreover, the resonance frequency reaches the asymptotic limit for the same width x_0 of the corrugated structure, so this could be defined as the minimum necessary width.

Content from this work may be used under the terms of the CC BY 4.0 licence (© 2022). Any distribution of this work must maintain attribution to the author(s), title of the work, publisher, and DOI

ISBN: 978-3-95450-241-7 ISSN: 2673-5350 doi:10.18429/JACoW-IBIC2022-MOP27

Content from this work may be used under the terms of the CC BY 4.0 licence (© 2022). Any distribution of this work must maintain attribution to the author(s), title of the work, publisher, and DOI

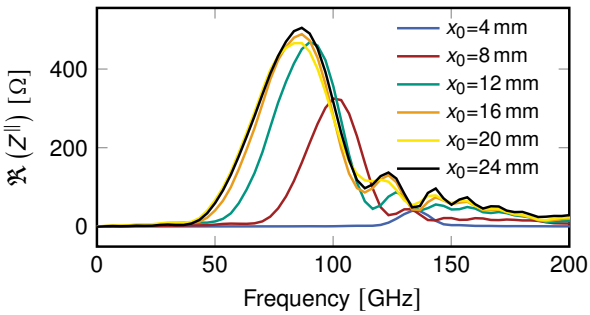


Figure 4: Real part of the longitudinal impedance $Z^{\parallel}$ for a different width x_0 of the corrugated plate with a fixed corrugation depth $h = 200\,\mu\text{m}$ and periodic length $L = 100\,\mu\text{m}$, respectively.

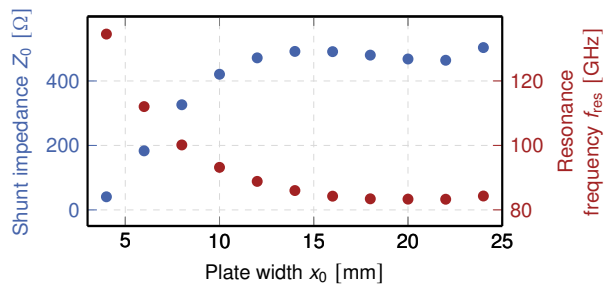


Figure 5: Shunt impedance Z_0 (blue) and resonance frequency f_{res} (red) in dependence of the width x_0 of the corrugated plate for a fixed corrugation depth $h = 200\,\mu\text{m}$ and periodic length $L = 100\,\mu\text{m}$, respectively.

However, the horizontal dimension of the bunch ($\sigma_x \approx 0.5$ mm) as well as the horizontal orbit in the section of the impedance chamber need to be taken into account. Therefore we chose $x_0 = 20$ mm as the realistic width. This relatively narrow width compared to the normal KARA vacuum chamber width of $x_{\text{KARA}} = 70$ mm makes it possible to mount three independent strips with different corrugation parameters next to each other. This allows switching between different corrugations without breaking the vacuum in the chamber. By moving the corrugation plates with the three strips horizontally, the active strip interacting with the electron bunch can be chosen by centering the strip over the bunch orbit. However, since one strip is required as a reference strip without any corrugations, only two strips with different corrugations can be installed. By moving the corrugated plates vertically far enough apart ($2b = 32$ mm) the normal KARA beam pipe cross section can be imitated, practically disabling the additional corrugation impedance.

To find the structure parameters and the resulting impedance that efficiently affect the microbunching instability, beam dynamic simulations have been performed, which are described in the following section.

BEAM DYNAMICS SIMULATION

The beam dynamics simulations were done with the in-house developed Vlasov-Fokker-Planck solver, Inovesa [11], which can reproduce the longitudinal beam dynamics during the microbunching instability observed at KARA [12]. For the studies presented here, settings that match the short-bunch operation mode at KARA with a synchrotron frequency $f_{\text{sync}} = 9.44$ kHz, the acceleration voltage $V_{\text{RF}} = 1.048$ MV, and the zero-current bunch length $\sigma_{z,0} = 4.1$ ps at a beam energy of $E = 1.3$ GeV were used for Inovesa. The total impedance is defined as a sum of the dominant CSR parallel plate impedance [13] and the additional impedance of the corrugated plates. The former was shown to drive the microbunching instability [12, 14] at KARA. The corrugated plate impedance is described and given by the resonator model and its parameters f_{res}, Z_0, and Q.

Threshold Current & Bursting Frequency

The CST impedance simulations have shown that for a plate distance of $b = 5$ mm and a structure length of 20 cm the impedance parameters $Q = 3$ and $Z_0 = 1\,\text{k}\Omega$ can be realized. In Ref. [8] we have already presented the results of Inovesa beam dynamics simulations directly above and below the unperturbed microbunching bursting threshold current I_{thr} with additional corrugated plate impedances, with varying f_{res}. The bursting threshold current is the limit, above which the first fluctuations in the intensity of the CSR occur. Below the threshold current, the fluctuation power at the bursting frequency, which is the dominant frequency of the intensity fluctuation of the CSR caused by microbunching, is drastically reduced in amplitude [15]. So this parameter can be used to determine the bursting threshold current.

Preliminary studies showed that impedances with $f_{\text{res}} = 110$ GHz and $f_{\text{res}} = 180$ GHz affect the fluctuation power of the emitted CSR particularly for the used typical KARA parameters. Hence, we simulated the beam dynamics for these two settings in detail by calculating so-called spectrograms with Inovesa. The results for these two cases, together with the case without additional impedance as reference are shown in Fig. 6. A spectrogram is the Fourier transform of the emitted CSR time-domain signal as function of bunch current showing the fluctuation frequency of the emitted radiation intensity. It indicates the dominant frequencies caused by microbunching. For the current range directly above the threshold this results in a finger-like structure, that is characteristic of the microbunching-induced beam dynamics directly above the threshold current [14, 16].

It can be seen that the general "shape" of this finger is not changed significantly by an additional corrugated plate impedance with $Z_0 = 1\,\text{k}\Omega$. However, the two different impedances affect the characteristic parameters of the finger, namely the threshold current I_{thr} and the bursting frequency at the threshold f_{burst}. This shows that the longitudinal beam dynamics is modified by the additional impedance in comparison to the pure CSR impedance case.

For the $f_{\text{res}} = 110$ GHz impedance the threshold current is reduced significantly by 16 µA (7.1%), whereas the bursting frequency at the threshold is not changed. In contrast,

ISBN: 978-3-95450-241-7 ISSN: 2673-5350 doi:10.18429/JACoW-IBIC2022-MOP27

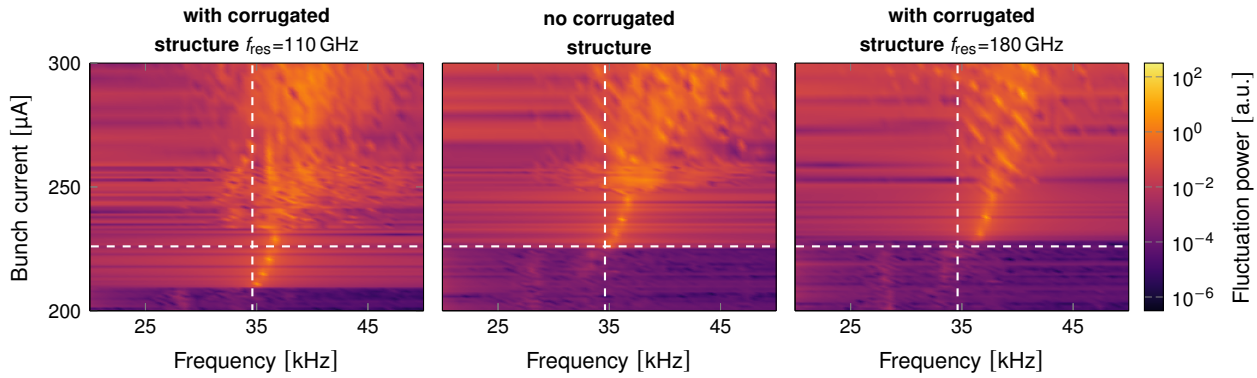


Figure 6: Color-coded power of the emission fluctuations as a function of the fluctuation frequency around the bursting frequency f_{burst} as a scan over the bunch current with and without additional corrugation impedances for two resonance frequencies f_{res}.The shunt impedance and quality factor were fixed at $Z_0 = 1\,\mathrm{k\Omega}$ and $Q = 3$, respectively. The white dashed lines mark the onset of the fluctuations due to the microbunching and the corresponding bursting frequency in the case without the corrugated structure (center).

for a corrugation impedance with $f_{\mathrm{res}} = 180\,\mathrm{GHz}$ the threshold current is increased slightly by 3 μA, so that the CSR outbursts and the emission of intense THz radiation are suppressed for a somewhat larger current range. Additionally, in this case the bursting frequency increased by 1.9 kHz.

Figure 7 illustrates how both threshold parameters develop for the two impedance configurations in dependence on the shunt impedance. This shows that depending on the chosen f_{res} of the additional impedance, one threshold parameter changes significantly and almost linearly with increasing shunt impedance, whereas the other parameter remains nearly unchanged.

SUMMARY & OUTLOOK

It is planned to install a chamber with two horizontal, parallel plates with corrugated structures into the KARA storage ring to study and manipulate the microbunching instability. The impedance simulations showed that the possibility of changing the distance between the plates and the electron beam offers a tuning knob to change the shunt impedance during operation. Furthermore, it is planned to mount three strips with a width of $x_0 = 20\,\mathrm{mm}$ nearby each other on a plate so that different structures can be tested without breaking the vacuum. The current plan is, that two strips will have corrugations producing an impedance with a resonance frequency of $f_{\mathrm{res}} = 110\,\mathrm{GHz}$ and $f_{\mathrm{res}} = 180\,\mathrm{GHz}$, respectively. The remaining strip will not have any corrugations to separate the influence of the corrugated structure from the change of the geometric aperture of the beam pipe.

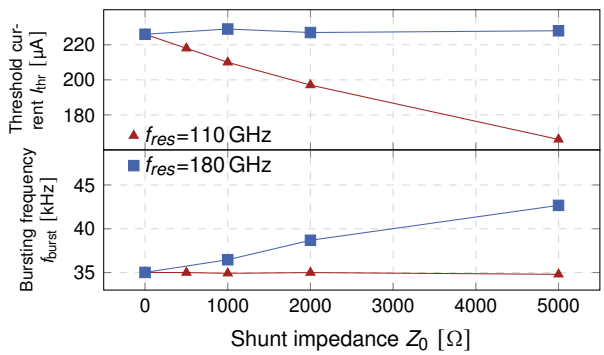


Figure 7: Bursting threshold and frequency for different shunt impedances Z_0. An additional impedance with a resonance frequency $f_{\mathrm{res}} = 180\,\mathrm{GHz}$ (blue) affects the bursting frequency, whereas $f_{\mathrm{res}} = 110\,\mathrm{GHz}$ (red) changes the threshold current.

Beam dynamics studies with the Vlasov-Fokker-Planck solver Inovesa, indicate that the resonance frequency is the crucial parameter of the additional impedance, which decides in what way the microbunching instability is influenced. This parameter decides whether the bursting threshold is reduced (and thus intensive THz radiation is emitted at even lower currents), or the dominant fluctuation frequency in the emitted CSR intensity is changed.

As a next step, the corrugated plate will be manufactured and the chamber details will be determined. A key challenge is to design a short taper section that allows both vertical and horizontal movement of the corrugated plates.

ACKNOWLEDGEMENTS

This work is supported by the DFG project 431704792 in the ANR-DFG collaboration project ULTRASYNC.

S. Maier and P. Schreiber acknowledge the support by the Doctoral School „Karlsruhe School of Elementary and Astroparticle Physics: Science and Technology“ (KSETA).

REFERENCES

[1] A.-S. Müller *et al.*, “Far Infrared Coherent Synchrotron Edge Radiation at ANKA”, in *Proc. PAC'05*, Knoxville, TN, USA, May 2005, paper RPAE038, pp. 2518-2520. https://jacow.org/p05/papers/rpae038.pdf

[2] K. L. F. Bane and G. Stupakov, “Terahertz radiation from a pipe with small corrugations”, *Nucl. Instrum. Methods Phys. Res., Sect. A*, vol. 677, pp.67-73, 2012. doi:10.1016/j.nima.2012.02.028

Content from this work may be used under the terms of the CC BY 4.0 licence (© 2022). Any distribution of this work must maintain attribution to the author(s), title of the work, publisher, and DOI

ISBN: 978-3-95450-241-7 ISSN: 2673-5350 doi:10.18429/JACoW-IBIC2022-MOP27

Content from this work may be used under the terms of the CC BY 4.0 licence (© 2022). Any distribution of this work must maintain attribution to the author(s), title of the work, publisher, and DOI

[3] K. L. F. Bane *et al.*, "Measurement of terahertz radiation generated using a metallic, corrugated pipe", *Nucl. Instrum. Methods Phys. Res., Sect. A*, vol. 844, pp.121-128, 2017. doi:10.1016/j.nima.2016.11.041

[4] S. J. Smith and E. M. Purcell, "Visible Light from Localized Surface Charges Moving across a Grating", *Phys. Rev.*, vol. 92, no. 4, 1953. doi:10.1103/PhysRev.92.1069

[5] K. Y. Ng *et al.*, "Explicit expressions of impedances and wake functions", Fermi National Accelerator Lab. (FNAL), Batavia, IL, USA, 2010.

[6] V. S. Vladimirov, *Equations of Mathematical Physics*, New York, NY, USA: M. Dekker, 1971, p.75

[7] K. Y. Ng, "Impedances of bellow corrugations", Fermi National Accelerator Lab. (FNAL), Batavia, IL, USA, 1987.

[8] S. Maier *et al.*, "Simulation of the Effect of Corrugated Structures on the Longitudinal Beam Dynamics at KARA", in *Proc. IPAC'22*, Bangkok, Thailand, June 2022, pp. 2241-2244. doi:10.18439/JACoW-IPAC2022-WEPOMS006

[9] CST Studio Suite, Dassault Systèmes, https://www.cst.com

[10] S. Maier *et al.*, "Impedance Studies of a Corrugated Pipe for KARA", in *Proc. IPAC'21*, Campinas, Brazil, May 2021, pp. 2039-2042. doi:10.18429/JACoW-IPAC2021-TUPAB251

[11] Inovesa, https://github.com/Inovesa

[12] P. Schönfeldt *et al.*, "Parallelized Vlasov-Fokker-Planck solver for desktop personal computers", *Phys. Rev. Accel. Beams*, vol. 20, p. 030704, 2017. doi:10.1103/PhysRevAccelBeams.20.030704

[13] J. B. Murphy, R. L. Gluckstern, and S. Krinsky, "Longitudinal wakefield for an electron moving on a circular orbit", in *Part. Accel.*, vol. 57, 1997. https://cds.cern.ch/record/1120287/

[14] M. Brosi *et al.*, "Fast Mapping of Terahertz Bursting Threshold and Characteristics at Synchrotron Light Sources", *Phys. Rev. Accel. Beams*, vol. 19, p. 110701, 2016. doi:10.1103/PhysRevAccelBeams.19.110701

[15] M. Brosi *et al.*, "Studies of the Micro-Bunching Instability in Multi-Bunch Operation at the KARA Storage Ring", in *Proc. IPAC'17*, Copenhagen, Denmark, May 2017, pp. 3645–3648. doi:10.18429/JACoW-IPAC2017-THOBA1

[16] M. Brosi, "In-Depth Analysis of the Micro-Bunching Characteristics in Single and Multi-Bunch Operation at KARA", PhD thesis, Institut für Beschleunigerphysik und Technologie, KIT, 2020. doi:10.5445/IR/1000120018

ISBN: 978-3-95450-241-7 ISSN: 2673-5350 doi:10.18429/JACoW-IBIC2022-MOP28

IMPROVEMENTS IN LONGITUDINAL PHASE SPACE TOMOGRAPHY AT PITZ

N. Aftab*, Z. Aboulbanine, P. Boonpornprasert, G. Georgiev, J. Good, M. Gross, A. Hoffmann, M. Krasilnikov, X.-K. Li, A. Lueangaramwong, R. Niemczyk, A. Oppelt, H. Qian, C. Richard, F. Stephan, G. Vashchenko, Deutsches Elektronen-Synchrotron DESY, Zeuthen, Germany
W. Hillert, University of Hamburg, Institute for Experimental Physics, Hamburg, Germany
A. J. Reader, School of Biomedical Engineering and Imaging Sciences, King's College London, UK

Abstract

Methodical studies to improve the longitudinal phase space (LPS) tomography of space-charge dominated electron beams were carried out at the Photo Injector Test facility at DESY in Zeuthen (PITZ). An analytical model was developed to quantify mean momentum, RMS energy spread, bunch length and phase advance. Phase advance analysis determined the booster phase scan range and step size to be used for obtaining momentum projections. A slit was introduced before the booster to truncate the beam in transverse plane to strongly reduce the space charge effects. The signal resolution of this truncated beam was improved by careful beta function control at the reference screen of the momentum measurements. The reconstruction algorithm was changed from Algebraic Reconstruction Technique (ART) to Image Space Reconstruction Algorithm (ISRA) owing to its assurance of non-negative solutions. In addition, the initial physically justified assumption of LPS, based on low-energy section measurements, was established to clear out noise-like artefacts. This paper will highlight the improvements made in the LPS tomography and compare the simulated and experimental results.

INTRODUCTION

Free-electron Lasers (FELs) require high-brightness electron beams to generate coherent radiation with short wavelength and high intensity. The Photo Injector Test facility at DESY in Zeuthen (PITZ) was established as a test stand of high-brightness electron sources for the European XFEL and FLASH [1]. The PITZ beamline consists of a normal conducting L-band 1.6-cell copper gun cavity with a Cs_2Te photocathode that produces ~6.5 MeV electron bunches with variable bunch lengths and up to several nC charge. The electron beam is further accelerated by a cut-disc type accelerating structure called booster, to an energy of up to ~20 MeV. Downstream the booster, the beamline consists of different diagnostics for detailed measurements of the electron beam properties. The transverse phase space characterization of the beam is done using a slit scan technique [2]. The longitudinal phase space (LPS) characterization is done using a transverse deflecting structure [3]. To determine LPS of the beam before the booster, a tomographic reconstruction technique is applied [4]. Figure 1 shows the PITZ beamline till the high energy spectrometer.

* namra.aftab@desy.de

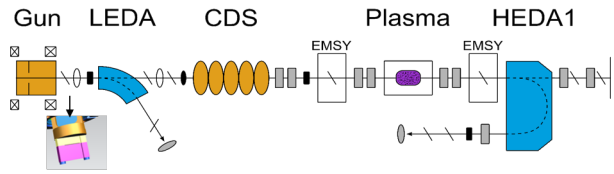


Figure 1: PITZ beamline till the high energy spectrometer with a slit shown at the first screen station after the gun.

The results of tomography obtained by the existing method has many artefacts and hence overestimates the longitudinal emittance. A hard charge cut is applied on the reconstructed LPS to give correct values. Also, the reconstruction results are more accurate for low-charge beams ~10 pC since space-charge forces are not catered for the algorithm. Typically, 250 pC beams are characterized at PITZ since this is the working point of the European XFEL.

In this paper, the procedure adopted in the experiment for obtaining the momentum projections for 250 pC beam will be explained. The optimized projections are fed to an Image Space Reconstruction Algorithm (ISRA) [5]. The algorithm will be described as well as the formulation of the initial estimate for the iterations. This initial estimate is built from the low energy section and plays a vital role for reliable reconstruction. An analytical model to understand the longitudinal phase advance of the beam is also described. The paper discusses the improvements made in the LPS tomography and compares the simulated and experimental results.

LPS MODELLING

The particle motion can be characterized in LPS by the momentum p_z of the particle corresponding to the phase of the booster. This can be used to understand and quantify the quality of an electron beam for accelerator design and phase space manipulations. To derive an analytical model for such a beam, the distribution of the particles can be approximated by an ellipse with some correlation as shown in Fig. 2.

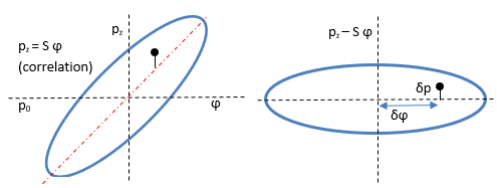


Figure 2: LPS with correlation (left) w/o correlation (right).

Content from this work may be used under the terms of the CC BY 4.0 licence (© 2022). Any distribution of this work must maintain attribution to the author(s), title of the work, publisher, and DOI

ISBN: 978-3-95450-241-7 ISSN: 2673-5350 doi:10.18429/JACoW-IBIC2022-MOP28

Content from this work may be used under the terms of the CC BY 4.0 licence (© 2022). Any distribution of this work must maintain attribution to the author(s), title of the work, publisher, and DOI

If we consider a particle with an initial momentum from the electron gun p_z^{gun} is being accelerated by the booster, then the final momentum of the particle p_z^{boo} can be calculated by Eq. (1):

$$p_z^{boo} = p_z^{gun} + S\delta\varphi + \delta p + V\cos(\varphi + \delta\varphi), \quad (1)$$

where, S is the LPS linear chirp that defines the correlation, V is the momentum gain by the booster, φ is the phase of the booster w.r.t. maximum mean momentum gain phase and the (x, y) co-ordinates of the particle in the phase space ellipse are shown by $(\delta\varphi, \delta p)$. The average beam momentum after the booster can be found by integrating all the particles in the phase space ellipse. After a few mathematical steps, we derive Eq. (2):

$$\langle p_z^{boo} \rangle = p_z^{gun} + V\cos\varphi(1 - \sigma_\varphi^2/2). \quad (2)$$

The RMS momentum spread can be found by subtracting the mean momentum from the momentum distribution. It is expressed in Eq. (3) as:

$$\sigma_p^2 = \sigma_{p_{min}}^2 + V^2(\sin\varphi - \sin(\varphi_{\sigma_{p_{min}}})^2\sigma_\varphi^2. \quad (3)$$

From Eq. (2) and (3), we can derive Eq. (4) that gives bunch length:

$$\sigma_\varphi = \sigma_p/|V\sin\varphi|. \quad (4)$$

The phase advance Φ of the phase space ellipse can be calculated by using the bunch length and the minimum RMS energy spread. The formula is shown in Eq. (5):

$$\Phi = \tan^{-1}(S\sigma_\varphi/\sigma_{p_{min}}), \quad (5)$$

where S is the slope of the LPS. In experiment, we can use the modelled energy spread as slope and find the beam phase advance. As the booster phase varies, the beam phase advance is significant around the minimum energy spread phase and decreases gradually as the energy spread increases. This trend can be seen by plotting RMS energy spread relative to its minimum against phase advance. Note that this model does not take space charge effects into account.

EXPERIMENT OPTIMIZATION

The experiment was conducted for a 250 pC beam produced by ~6.6 ps FWHM laser and accelerated up to 16.95 MeV. The measurement procedure consists of the following steps:

- Low energy dispersive arm (LEDA) section was used to scan the gun phase and find the corresponding mean momentum and momentum spread as shown in Fig. 3.
- Since the beam is space-charge dominated, it was chopped transversely by inserting a 200 µm-wide slit after the gun to strongly reduce the space charge effects. Figure 1 shows the location of the slit.
- A solenoid scan was done to obtain approximately 10 pC after the slit.
- A steerer was used to vertically center the beam on the reference screen for the momentum measurements.

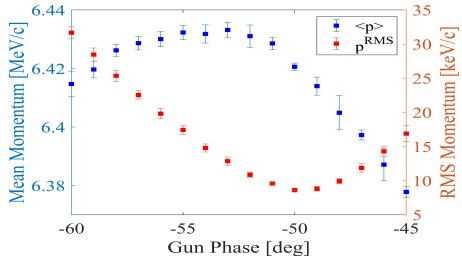


Figure 3: Low energy momentum scan.

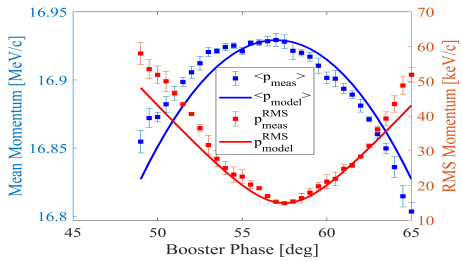


Figure 4: High energy momentum scan and the fitted model.

- High energy dispersive arm (HEDA1) was used to do a rough scan of the booster phase to find the optimum phase range and step size for reconstruction.
- The booster phase scan was repeated and the corresponding momentum projections were saved after focusing the beam on the reference screen for improved resolution.

Figure 4 shows the mean momentum and momentum spread corresponding to each booster phase.

The model fits well to the measured data around the maximum mean momentum and the minimum energy spread but there is some discrepancy at the off-centre phases. This is due to the deviation of the beam trajectories in the dipole for the off-crest phases causing systematic error in the measurement. This error can be removed by centring the beam on the momentum measurement screen by adjusting the dipole current for every booster phase.

Figure 5 shows the relative momentum spread corresponding to the phase advance. The phases advance varies significantly around 70° until 1.5 keV and then until 3 keV the change is gradual ~10°. After 3 keV the phase advance is almost negligible. The momentum projections for tomography should correspond the to booster phase range which covers the whole LPS phase advance and the step size should be optimized in order to produce a smooth curve.

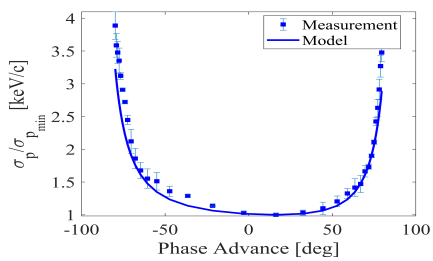


Figure 5: Phase advance from measurement and fitted model.

ISBN: 978-3-95450-241-7 ISSN: 2673-5350 doi:10.18429/JACoW-IBIC2022-MOP28

RECONSTRUCTION ALGORITHM

A variety of techniques have been developed to reconstruct higher dimensional distributions from lower dimensional projections, commonly known as tomography [6]. Tomography often involves an image (or object representation) reconstruction technique that utilizes projections of the object from different viewing angles and then uses iterative equation solving methods e.g. maximum entropy technique (MENT) [7] or algebraic reconstruction technique (ART) [8] to reconstruct the original distribution.

Image Space Reconstruction Algorithm (ISRA)

ISRA is a non-negative multiplicative least squares algorithm and is derivable from a least squares objective function [9]. The equation for ISRA is expressed as:

$$x^{k+1} = x^k \frac{A^T m}{A^T A x^k}, \tag{6}$$

where x^k is a vector containing the current estimate of reconstructed phase space and x^{k+1} is the next update, m is a vector that contains projections corresponding to all booster phases also known as sinogram as shown in Fig. 6, and A is a weight matrix built from the LPS model. The weights are distributed in the neighboring pixels by bilinear interpolation to model the signal analogue to discretization conversion effects.

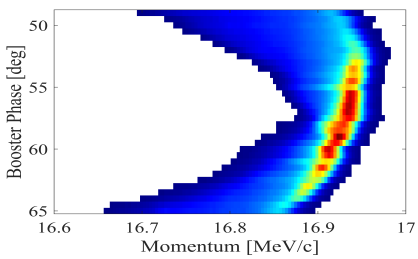


Figure 6: Sinogram.

ISRA takes a current estimate and forward projects it to form a vector Ax^k. This vector is back projected to form a predicted back projected vector. Similarly, the measured projections are also back projected using the system matrix. The ratio of these back projections provides a correction factor to update the current estimate. The initial estimate x^1 vector can be taken as a vector of uniform values (e.g. 1). The iterations are carried out until the root mean square error (RMSE) between measured sinogram and predicted sinogram falls below the tolerance level i.e. 0.5%.

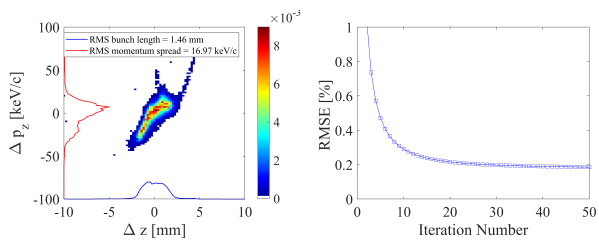


Figure 7: LPS after 50 iterations when $x^1 = 1$ (left) RMSE (right).

Figure 7 shows the reconstructed LPS after 50 iterations. The colorscale shows it is normalized to 1. After ~30 iterations, RMSE is already well below the tolerence level (~0.2%) and there are only a few noise artefacts. This can be further improved by using an initial estimate from low energy momentum measurement.

Initial Estimate from LEDA

An initial educated guess of LPS from LEDA was established to further improve the reconstruction results. Basically, the momentum profile at an off-crest phase $\rho_n(p_z)$ was used to select the range of phase from LEDA scan to be used as an initial matrix. Once we had the range, a Gaussian was fit on each of the mean momentum points as shown in Fig. 8. The amplitude of the Gaussians was taken from the weights of off-crest phase momentum profile normalized to 1. The expression for initial guess for LPS can be written mathematically by Eq. (7).

$$LPS(z, p_z) = \sum_{n=1}^{N} G_n(p_z)\Delta_n(z), \tag{7}$$

where $G_n(p_z)$ is the p_z- distribution for the n^{th} longitudinal slice within the bunch scanned by the step function $\Delta_n(z)$. Equations 8 and 9 show their formulas:

$$G_n(p_z) = \rho_n/(\sqrt{2\pi}\sigma_{pn}) \exp^{[-(p_z - p_{z_n})^2/(2\sigma_{pn}^2)]} \tag{8}$$

$$\Delta_n(z) = 1/\Delta z, |z - z_n| \leq \Delta z\ /\ 2. \tag{9}$$

The reconstructed LPS after 50 iterations starting from a well-defined initial estimate is shown in Fig. 9. The artefacts are almost removed and the overall structure is similar to the uniform initial estimate case. The initial estimate from LEDA not only removes the noise but also impacts the overall distribution of particles in phase space. One can compare the RMS bunch length and energy spread values of reconstructed LPS to note this effect.

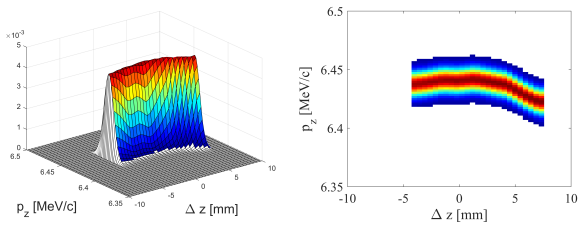


Figure 8: weighted Gaussian p_z-distributions along the bunch at selected LEDA phase range (left) shown as initial estimate (right).

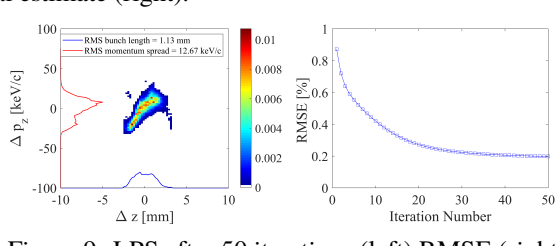


Figure 9: LPS after 50 iterations (left) RMSE (right).

Content from this work may be used under the terms of the CC BY 4.0 licence (© 2022). Any distribution of this work must maintain attribution to the author(s), title of the work, publisher, and DOI

ISBN: 978-3-95450-241-7 ISSN: 2673-5350 doi:10.18429/JACoW-IBIC2022-MOP28

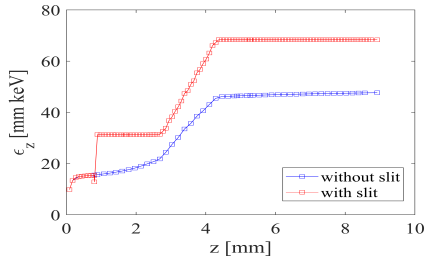


Figure 10: ϵ_z without and with the slit along the beamline. Booster starts at 2.675 m and ends at 4.385 m.

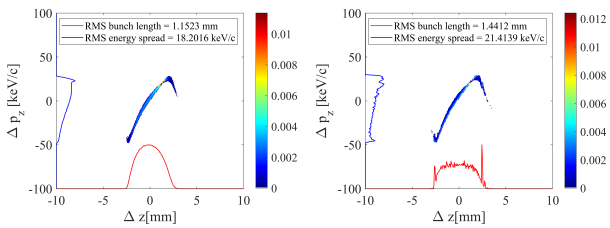


Figure 11: LPS before slit at 0.8 m (left) and after slit at 1.7 m (right).

Comparison with Simulated LPS

A Space Charge Tracking Algorithm (ASTRA) [10] was used to simulate the beam with similar parameters with and without the slit at 0.8 m. It was observed that after inserting the slit, the beam energy and bunch length increased slightly causing increase in the longitudinal emittance along the beamline. Figure 10 shows the plot of the ϵ_z starting from the gun to the high energy section. Figure 11 shows the beam and its projections before the slit at 0.8 m and after the slit at 1.7 m. The weights along the momentum profiles are changed by the introduction of the slit which was used to remove transverse space charge effects. As a result, there is a systematic error introduced because of correlation in p_z and radial plane [11].

Figures 7 and 9 show the reconstructed LPS with bunch length and momentum profiles and corresponding RMS values. The ϵ_z after 50 iterations for uniform initial matrix case is 24.85 mm · keV and for the case with the pre-defined initial matrix from low energy sections is 14.29 mm · keV. The increase in bunch length and energy spread caused by the insertion of the slit is compensated by using the initial estimate from LEDA.

CONCLUSION AND OUTLOOK

Methodical studies for LPS reconstruction via tomography were done that included better signal resolution with careful beta function control with the help of a slit and phase advance analysis during booster phase scan. Another important step accomplished was artefact-free and improved reconstruction results by using ISRA and an initial estimate from LEDA. A combination of improved experimental conditions and optimized reconstruction algorithm yielded reliable LPS tomography results. The next step would be minimizing the systematic error by centering the beam on the momentum measurement screen for all booster phases as well as using better noise compensation for improved SNR. This would not only decrease the RMSE but also the required number of iterations for convergence.

REFERENCES

[1] E. J. Jaeschke *et al.*, *Synchrotron Light Sources and Free-Electron Lasers*, Springer Cham, 2016, p. 155. doi:10.1007/978-3-319-14394-1

[2] M. Krasilnikov *et al.*, "Experimentally minimized beam emittance from an L-band photoinjector", *Phys. Rev. ST Accel. Beams*, vol. 15, p. 100701, 2012. doi:10.1103/PhysRevSTAB.15.100701

[3] L. V. Kravchuk *et al.*, "Layout of the PITZ Transverse Deflecting System for Longitudinal Phase Space and Slice Emittance Measurements", in *Proc. LINAC'10*, Tsukuba, Japan, Sep. 2010, paper TUP011, pp. 416–418.

[4] D. Malyutin, "Time resolved transverse and longitudinal phase space measurements at the high brightness photo injector PITZ", Ph.D. dissertation, Universität Hamburg, Germany, 2014.

[5] M. E. Daube-Witherspoon and G. Muehllehner, "An Iterative Image Space Reconstruction Algorithm Suitable for Volume ECT", *IEEE Trans. Med. Imaging*, vol. 5, pp. 61–66, 1986. doi:10.1109/TMI.1986.4307748

[6] A. C. Kak, M. Slaney, *Principles of Computerized Tomographic Imaging*, IEEE Press, 1979.

[7] S. F. Gull and T. J. Newton, "Maximum entropy tomography", *Appl. Opt.*, vol. 25, pp. 156–160, 1986. doi:10.1364/AO.25.000156

[8] H. Loos *et al.*, "Longitudinal phase space tomography at the SLAC Gun Test Facility and the BNL DUV FEL", *Nucl. Instrum. Methods Phys. Res., Sect. A*, vol. 528, p. 189, 2004. doi:10.1016/j.nima.2004.04.044

[9] A. R. De Pierro, "On the Convergence of the Iterative Image Space Reconstruction Algorithm for Volume ECT", *IEEE Trans. Med. Imaging*, vol. 6, pp. 174–175, 1987. doi:10.1109/TMI.1987.4307819

[10] K. Floettmann, A space charge tracking code - ASTRA, http://desy.de/~mpyflo

[11] H. Qian, *et al.*, "Slice energy spread measurement in the low energy photoinjector", *Phys. Rev. Accel. Beams*, vol. 25, 2022. doi:10.1103/PhysRevAccelBeams.25.083401

Content from this work may be used under the terms of the CC BY 4.0 licence (© 2022). Any distribution of this work must maintain attribution to the author(s), title of the work, publisher, and DOI

ISBN: 978-3-95450-241-7 ISSN: 2673-5350 doi:10.18429/JACoW-IBIC2022-MOP29

LOW GAIN AVALANCHE DETECTOR APPLICATION FOR BEAM MONITORING

V. Kedych*, T. Galatyuk[1], W. Krüger
Institut für Kernphysik, Technische Universität Darmstadt, Darmstadt, Germany
S. Linev, J. Pietraszko, C. J. Schmidt, M. Träger, M. Traxler, F. Ulrich-Pur
GSI Helmholtzzentrum für Schwerionenforschung GmbH, Darmstadt, Germany
J. Michel, Goethe-Universität, Frankfurt, Germany
A. Rost, FAIR GmbH, Darmstadt, Germany
V. Svintozelskyi, Taras Shevchenko National University of Kyiv, Kyiv, Ukraine
[1]also at GSI Helmholtzzentrum für Schwerionenforschung GmbH, Darmstadt, Germany

Abstract

The Superconducting DArmstadt LINear ACcelerator (S-DALINAC) was constructed as a twice-recirculating electron accelerator. During the upgrade in 2015/2016 a third recirculation line as well as the option to operate the S-DALINAC in Energy recovery LINAC (ERL) mode were added. In order to optimize the beam during operation in ERL mode, it is important to provide a dedicated non-destructive beam monitoring system. A promising detector technology for this task is the low gain avalanche diode (LGAD), which is a novel silicon detector optimized for 4D-tracking, i.e. the simulataneous measurement of the particle's position and time with high spatial (< 100 µm) and timing (> = 30 ps) precision. In this contribution we present the results of a first proof-of-principle measurement utilizing LGAD technology for beam time structure monitoring at the S-DALINAC at the Technical University of Darmstadt, Germany, in the normal (non ERL) operation mode.

INTRODUCTION

Energy recovery LINAC (ERL) is a novel technique in electron beam acceleration [1]. In contrast to the normal operation mode, where the major part of the beam energy remains unused, the beam in ERL mode can be sent back to the accelerator with a phase shift of 180° resulting in a negative energy gain. Consequently, energy is put back into a radio frequency (RF) field of the accelerating cavity, which can be used for the acceleration of the next beam. Thus, ERL reduces the required RF power for the acceleration and allows to accelerate high current beams with higher energy in comparison to traditional LINACs.

The S-DALINAC [2] (Fig. 1) is a superconductive linear electron accelerator at TU Darmstadt, Germany. It was constructed as a twice-recirculating accelerator in continuous wave (cw) operation at 3 GHz. Since an upgrade with a third recirculating beam line in 2015/2016, it is possible to operate S-DALINAC as an ERL [1]. A one circulation ERL mode was successfully demonstrated in 2017 with efficiency $92.1^{+3.7}_{-13.9}$ % [1]. In August 2021 S-DALINAC was successfully operated in twice recirculated ERL mode [3]. In this mode both once decelerated and once accelerated beams

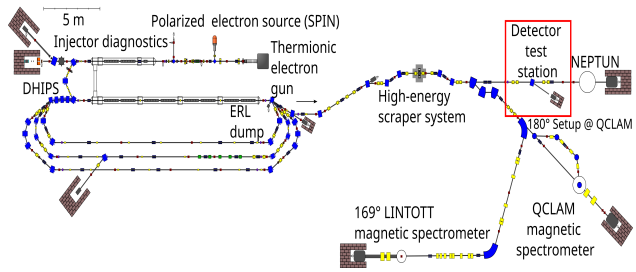


Figure 1: Layout of the S-DALINAC including experimental areas. The red rectangle represent the position of the experimental setup.

share the same beam line but have a different orbit, leading to a repetitive bunch rate of 6 GHz. In order to measure both beams simultaneously and to optimize the acceleration and deceleration process, a non-destructive beam monitoring system able to resolve this 6 GHz time structure, corresponding to 166 ps between the bunches, is required [4]. A promising detector technology that could potentially fulfil this task is the low gain avalanche diode (LGAD), which is a novel silicon detector optimized for 4D-tracking applications [5]. The high spatial granularity (< 100 µm) and excellent time resolution (< 50 ps [6]) of LGADs make an LGAD-based detector a promising candidate for beam time monitoring tool at the S-DALINAC.

In October 2021, the first proof of principle measurement of an LGAD-based beam monitoring system was performed at the S-DALINAC. The main goal of this experiment was to resolve the beam time structure of an 85 MeV electron beam using an LGAD strip sensor. For this purpose, a simplified setup was prepared and placed in a dedicated test beam area (marked by the red square in Fig. 1) outside the recirculating beam lines. Since placing the detector outside the accelerator made it impossible to simultaneously monitor the accelerated and decelerated beams, the measurement was done in the S-DALINAC normal operation mode, which, in contrast to its ERL mode, features a beam time structure of 3 GHz. Although the overall goal is to eventually use an LGAD-based setup as a monitoring tool during the ERL operation of the S-DALINAC, measuring the S-DALINAC in its normal operation mode still allowed to show the proof-

* v.kedych@gsi.de

Content from this work may be used under the terms of the CC BY 4.0 licence (© 2022). Any distribution of this work must maintain attribution to the author(s), title of the work, publisher, and DOI

ISBN: 978-3-95450-241-7 ISSN: 2673-5350 doi:10.18429/JACoW-IBIC2022-MOP29

Content from this work may be used under the terms of the CC BY 4.0 licence (© 2022). Any distribution of this work must maintain attribution to the author(s), title of the work, publisher, and DOI

of-concept of the proposed beam monitoring system. The preliminary results of this experiment were presented at the Vienna Conference of Instrumentation in February 2022 as a part of the LGAD application overview talk [7]. In this contribution, however, we present a more detailed analysis and discussion.

SETUP

For the first measurement, a prototype setup based on an LGAD multi-strip sensor was prepared. The sensor was produced at Fondazione Bruno Kassler (FBK) with a size of 0.5 × 1 cm^2, a thickness of 200 µm and a sensor pitch of 50 µm. As shown in Fig. 2, the readout pads of the LGAD were bonded to a Printed Circuit Board (PCB). The signals from the LGAD were processed by a

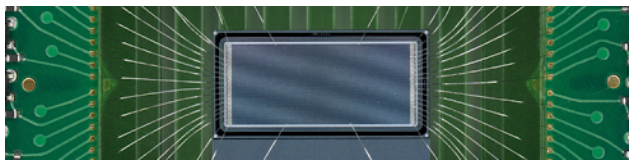


Figure 2: Photograph of the LGAD sensor mounted on the PCB.

PaDiWa [8] leading edge discrimination board connected to Field Programmable Gate Array (FPGA) based Time-to-Digital (TDC) converter [9]. The full experimental setup is shown in Fig. 3.

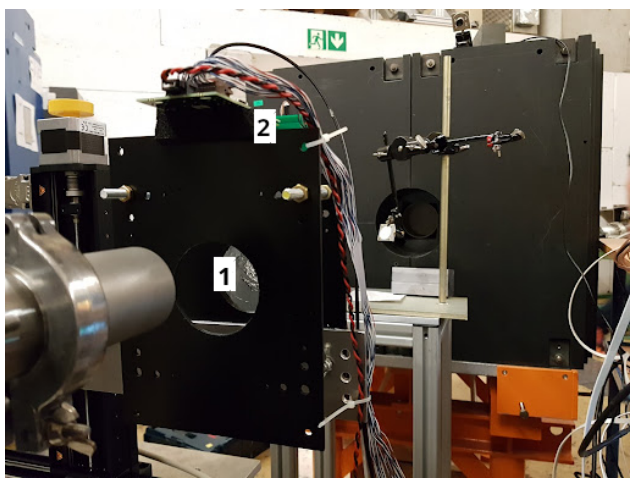


Figure 3: Photograph of the setup at S-DALINAC. LGAD sensor marked as (1), PaDiWa board - as (2).

RESULTS

The Time of Arrival (ToA) and Time over Threshold (ToT) of electrons passing through the sensor were measured and the difference between the ToAs of two hits registered inside the same strip was calculated. Figure 4 demonstrates a dependence of the difference of ToA between two registered hits as a function of ToT. The absence of data in the time difference region below 50 ps represents the dead time of

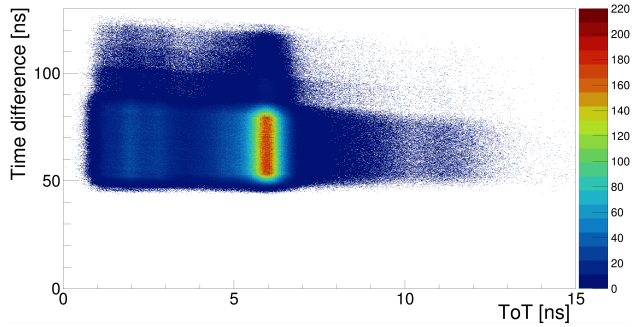


Figure 4: ToA time difference as a function of reference hit ToT for two hits inside the same strip.

the system. Because of the leading edge discriminator board used in the system, an additional calibration was performed to remove the dependence of the ToA of the signal based on its corresponding ToT (i.e. time walk effect). First, a narrow cut of 100 ps on partner signal ToT was introduced to focus on a signal that comes from a real particle passing through the LGAD sensor. Figure 5 demonstrates raw data

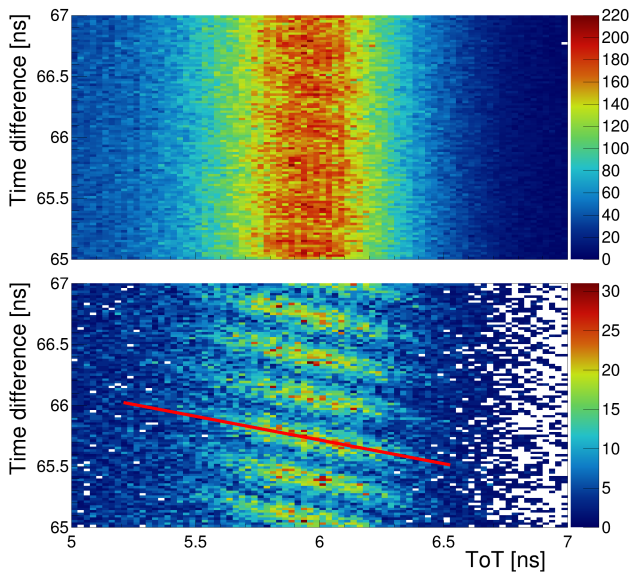


Figure 5: Raw data without (upper) and with (bottom) narrow ToT cut. Red line on the bottom plot represent time walk calibration parameters.

for small time difference and ToT ranges without (top) and with (bottom) the narrow ToT cut. Also, the bottom plot of Fig. 5 exhibits so-called time walk effect. To compensate for this time walk and, therefore, remove any systematic dependence of the ToA difference based on the ToT, a time walk calibration was performed. To calculate the calibration parameters, one of the peaks in Fig. 5 was fitted with a linear function. The calibration parameters were then applied on an event-by-event basis by correcting the individual ToAs based on their corresponding ToTs. The results of this calibration are shown in Fig. 6. Additionally, a cut on ToT lower that 4 ns was applied to remove signals that originates from

ISBN: 978-3-95450-241-7 ISSN: 2673-5350 doi:10.18429/JACoW-IBIC2022-MOP29

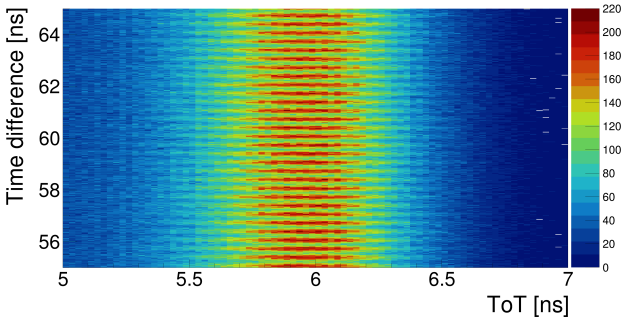


Figure 6: Time walk calibrated data.

capacitive coupling. Detailed discussion on this topic was given in [6]. After applying the calibration, the next step was to identify all peaks in the time spectrum and fit them with a sum of Gaussian and constant to estimate the background. The fits were done by making a projection onto the Y axis of the histogram shown in Fig. 4. The outcome of this procedure is depicted in Fig. 7. In the last step, the time

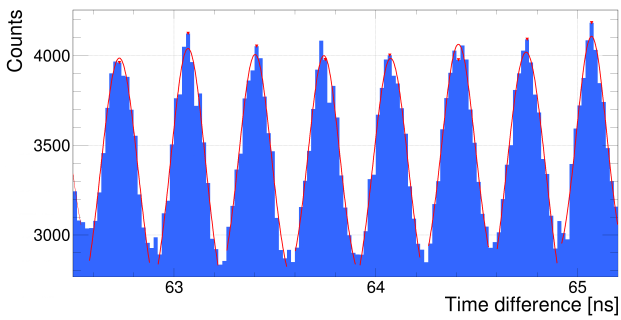


Figure 7: Projection on time difference axis of the histogram shown in Fig. 4 in small range. Red triangles represent position of each identified peak, red lines - fit function.

difference between each of the consecutive peaks was calculated and the one-dimensional histogram was fitted with the Gaussian function. The result is shown in Fig. 8. The mean time difference between two consecutive peaks, obtained from the fit, is 333.4 ps which corresponds to the 3 GHz operating frequency of the S-DALINAC. This indicates that the beam time structure was successfully resolved during normal operation mode.

FUTURE UPGRADE

A new telescope setup, based on 2 LGADs, is being prepared for the upcoming beam time. Each sensor has a form factor of 1 cm × 1 cm with 100 µm pitch and 200 µm thickness (thinned sensor to minimize multiple scattering inside the sensor) with 86 channels per sensor. The telescope setup will allow the measurement of the same electron twice, which increases the time resolution. In addition, it will be possible to remove the signal propagation time inside the strip and remove the signals that come from capacitive coupling. Also, the front end electronics will be upgraded with 8 DiRICH5s1 [8] boards, which is an amplification and

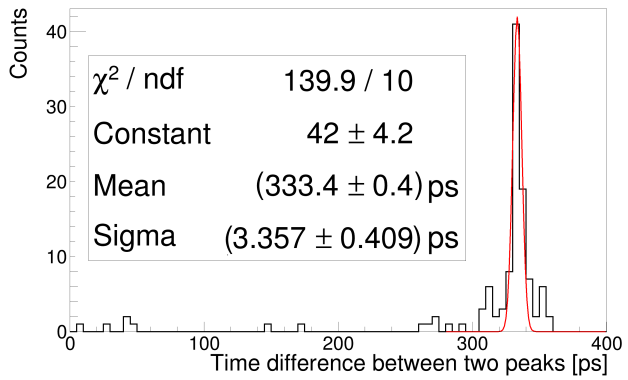


Figure 8: Gaussian fit of the time difference between two consecutive peaks from the data presented in Fig. 7.

leading edge discriminator board that features 32 read-out channels with an FPGA based TDC on board.

SUMMARY

For the twice recirculating ERL mode of the S-DALINAC, a monitoring system capable of measuring of two beams passing the same beam line with the bunch rate of 6 GHz is needed. An LGAD-based detector is a promising candidate for such kind of monitoring because of its excellent timing resolution. The setup for beam timing monitoring based on LGAD was prepared and installed at the dedicated experimental hall at the S-DALINAC. Due to the placement of the setup simultaneous measurement of two beams in the same beam line was not possible. Nevertheless, the first proof-of-principle measurements was successful, showing that the 3 GHz beam time structure of the S-DALINAC operated in its normal mode could be resolved with the LGAD strip sensor.

ACKNOWLEDGEMENTS

This work has been supported by DFG under GRK 2128.

REFERENCES

[1] M. Arnold *et al.*, "First ERL Operation of S-DALINAC and Commissioning of a Path Length Adjustment System", in *Proc. IPAC'18*, Vancouver, Canada, Apr.-May 2018, pp. 4859–4862. doi:10.18429/JACoW-IPAC2018-THPML087

[2] N. Pietralla, "The Institute of Nuclear Physics at the TU Darmstadt", *Nucl. Phys. News*, vol. 28, no. 2, pp. 4–11, 2018. doi:10.1080/10619127.2018.1463013

[3] F. Schließmann *et al.*, "Realization of a multi-turn energy-recovery accelerator", submitted for publication.

[4] M. Dutine *et al.*, "Concept of a Beam Diagnostics System for the Multi-Turn ERL Operation at the S-DALINAC", in *Proc. IPAC'22*, Bangkok, Thailand, Jun. 2022, pp. 254–256. doi:10.18429/JACoW-IPAC2022-MOPOPT012

[5] N. Cartiglia *et al.*, "Design optimization of ultra-fast silicon detectors", *Nucl. Instrum. Methods Phys. Res., Sect. A*, vol. 796, pp. 141–148, 2015. doi:10.1016/j.nima.2015.04.025

Content from this work may be used under the terms of the CC BY 4.0 licence (© 2022). Any distribution of this work must maintain attribution to the author(s), title of the work, publisher, and DOI

ISBN: 978-3-95450-241-7 ISSN: 2673-5350 doi:10.18429/JACoW-IBIC2022-MOP29

[6] J. Pietraszko *et al.*, "Low Gain Avalanche Detectors for the HADES reaction time (T_0) detector upgrade", *Eur. Phys. J. A*, vol. 56, no. 7, p. 183, 2020. doi:10.1140/epja/s10050-020-00186-w

[7] W. Krüger *et al.*, "LGAD technology for HADES, accelerator and medical applications", *Nucl. Instrum. Methods Phys. Res., Sect. A*, vol. 1039, p. 167046, 2022. doi:10.1016/j.nima.2022.167046

[8] The TRB collaboration, http://trb.gsi.de

[9] A. Neiser *et al.*, "TRB3: a 264 channel high precision TDC platform and its applications", *J. Instrum.*, vol. 8, p. C12043, 2013. doi:10.1088/1748-0221/8/12/c12043

Content from this work may be used under the terms of the CC BY 4.0 licence (© 2022). Any distribution of this work must maintain attribution to the author(s), title of the work, publisher, and DOI

ISBN: 978-3-95450-241-7 ISSN: 2673-5350 doi:10.18429/JACoW-IBIC2022-MOP31

AUTOMATIC ADJUSTMENT AND MEASUREMENT OF THE ELECTRON BEAM CURRENT AT THE METROLOGY LIGHT SOURCE (MLS)

Y. Petenev, J. Feikes, J. Li
Helmholtz-Zentrum Berlin für Materialien und Energie (HZB), Berlin, Germany
R. Klein, M. Müller, A. Barboutis
Physikalisch-Technische Bundesanstalt (PTB), Berlin, Germany

Abstract

The electron storage ring MLS (Metrology Light Source) is used by the Physikalisch-Technische Bundesanstalt (PTB), the German metrology institute, as a primary source standard of calculable synchrotron radiation in the ultraviolet and vacuum ultraviolet spectral range. For this, all storage ring parameters have to be appropriately set and measured with low uncertainty. E.g., the electron beam current can be varied by more than 11 orders. This adjustment of the electron beam current, and thus the spectral radiant intensity of the synchrotron radiation, for the specific calibration task is conveniently performed fully automatic by a computer program.

INTRODUCTION

The PTB, the German metrology institute, utilizes the electron storage ring Metrology Light Source (MLS) [1] in Berlin - Adlershof for the realization of the radiometric units in the near infrared, visible, ultraviolet and vacuum ultraviolet spectral range. For this purpose, the MLS is operated as a primary source standard, i.e., the spectral radiant intensity of the synchrotron radiation (SR) is calculated by means of the Schwinger equation [2]. Adapting this to electron storage rings, where the electron revolves, the Schwinger equation has to be multiplied with the revolution frequency n, yielding the spectral radiant intensity for one stored electron. If N electrons are stored, which is equivalent to a stored electron beam current I of

$$I = N \, \mathrm{e} \, \mathrm{n}, \tag{1}$$

then the spectral radiant intensity of synchrotron radiation from electron storage rings is directly proportional to the stored electron beam current, i.e., the number of stored electrons [3]. With the necessary equipment installed to measure and control the electron beam current over a wide dynamic range, the radiant intensity of the synchrotron radiation can be adjusted accordingly. It should be mentioned that the stated direct proportionality between N and the spectral radiant power is only valid for wavelengths that are shorter than the length of the stored electron bunches, typically being in the mm range, and therefore no coherence effects are present in the near IR, VIS, VUV and soft X-ray spectral range.

The variation of the electron beam current does not change the spectral characteristics of the synchrotron radiation. The spectral characteristics, on the other hand, can be changed by adjustment of the electron energy. At the MLS, e.g., the electron beam energy can be chosen to be between 105 MeV and 630 MeV, which changes the characteristic wavelength between 735 nm and 3.4 nm, respectively. This allows creating a tailor-made spectral shape for specific applications and avoiding unwanted high-energy parts of the spectrum, which could lead to instabilities due to thermal load, optics degradation, higher diffraction orders or increased stray light, but this is not the focus of this paper.

In this paper we focus on the variation of the electron beam current over more than 11 decades. The adjustment of the electron beam current is widely used for the calibration of wavelength-dispersive spectrographs or for the calibration of counting detectors, with very low electron beam currents, even single photon detectors can be calibrated. To facilitate these calibrations, a fully automated program was developed for the adjustment of the electron beam current to the desired value and its accurate measurement.

INSTRUMENTATION

At the MLS, the stored electron beam current can be varied by more than 11 decades, that means from a maximum current of approx. 200 mA down to a single stored electron (1 pA). As a matter of course, the equipment for a controlled adjustment of the electron beam current must be installed at the storage ring in order to utilize this potential. This is implemented only at a few other facilities worldwide, since most electron storage rings are operated as large-scale synchrotron radiation user facilities, which do not have the flexibility of changing the operational parameters such as electron beam current or electron beam energy. At the MLS, equipment is also installed to monitor the beam size over the whole possible range of electron beam current.

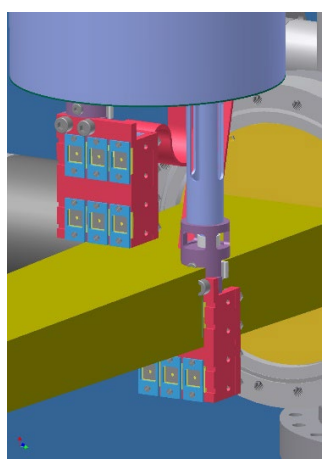


Figure 1: Schematics of the photo diodes assembly (red) as illuminated by the synchrotron radiation (green).

Content from this work may be used under the terms of the CC BY 4.0 licence (© 2022). Any distribution of this work must maintain attribution to the author(s), title of the work, publisher, and DOI

ISBN: 978-3-95450-241-7 ISSN: 2673-5350 doi:10.18429/JACoW-IBIC2022-MOP31

Content from this work may be used under the terms of the CC BY 4.0 licence (© 2022). Any distribution of this work must maintain attribution to the author(s), title of the work, publisher, and DOI

Currents in the upper range, i.e., above some mA, are measured with two commercially available DC parametric current transformers (PCT) [4], which are traceably calibrated on a regular basis. For an absolute determination of the electron beam current, the offset signal of these monitors have to be carefully measured and taken into account; this offset signal is dependent on the electron energy, i.e., the magnetic induction of the surrounding bending magnets [3] and also seems to slightly depend on the stored current itself, most probably due to some thermal effects. The relative uncertainty of the electron beam current measurement by the PCT is given by the uncertainty in the calibration factor and the non-linearity. The relative uncertainty of each of these contributions is $1 \cdot 10^{-4}$. A further uncertainty is given by the oscillating drift of the offset current, which is typically some µA.

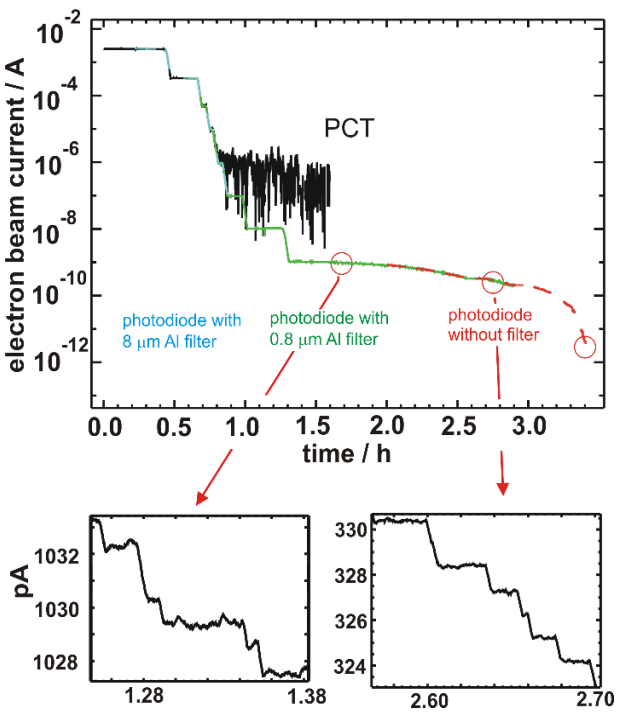


Figure 2: Illustration of the electron beam measurement over more than 11 decades.

For the measurement of electron beam current below approximately 1 mA, LN_2-cooled windowless Si photodiodes [5] with linear response are used that are irradiated by the direct synchrotron radiation covering the full spectral range from the vacuum UV to the IR. In a special UHV front end section inside the storage ring housing these photodiodes can be moved into the orbital plane of the synchrotron radiation by means of computer-controlled stepper motors from above. Two individual blocks each with 6 photo diodes are in usage right now, as is illustrated in Fig. 1. On one block, the photo diodes in the lower row are covered with Al filters with 8 µm in thickness (thick filtered diodes), photo diodes in the upper row are unfiltered. The second block differs from the first only in the fact, that the lower photo diodes are covered with 0.8 µm thick Al filters (thin filtered diodes). The filtered photodiodes are connected by long low-noise cables to electrometers [6] that are placed outside of the storage ring housing. The unfiltered photo diodes are connected to I/U transformers [7] that are mounted close by in the storage ring housing and the voltage signal is measured by DVM that are located outside the ring. Normally only one photo diode of each kind is used.

For the reduction of the electron beam current a vertical scraper is used, that is placed close to the stored beam and thus greatly reduces the beam lifetime.

BASIC MEASUREMENT PROCEDURE

The calibration factor k_{D1}, which relates the photocurrent I_{D1} to the electron beam current I_{MLS} by

$$I_{MLS} = k_{D1} \cdot I_{D1} \quad (2)$$

is determined for the thick filtered photodiode by comparison with the electron beam current measured by the PCTs first. This is done for electron beam currents in the range from 10 mA to 0.1 mA. This so calibrated photodiode is than used for the beam current measurement down to the µA region. In the µA region the thin filtered diodes are inserted and the measured photo current is compared to the one from the thick filtered diode, giving the calibration factor k_{D2} This photo diode is then used for the beam current measurement down to the nA region.

The relative uncertainty in this intermediate electron beam current range is dominated by the non-linearity of the photodiodes and drifts and is estimated to be well below 2%.

It should be mentioned that the calibration factors depend on the electron energy. For 630 MeV electron beam energy, the calibration factors are roughly 34 mA/mA for the 8 µm Al filtered photo diode and 2.8 mA/mA for the 0.8 µm Al filtered diode, respectively.

Electron currents in the range of some nA, are determined by counting the number of stored electrons, first developed at the Tantalus electron storage ring [8] and also utilized at the SURF electron storage ring [9]. To do this, the electrons are gradually kicked out of the storage ring by a mechanical scraper that can be placed closely to the electron beam, while measuring the step-like drop of the synchrotron radiation power by the cooled, unfiltered photodiodes. The electron beam current is then given by the product of electron number, electron charge and revolution frequency (Eq. (1)). Once the number of stored electrons has unambiguously been determined, the relative uncertainty in the electron beam current measurement is dominated by the relative uncertainty in the measurement of the revolution frequency, which is about $1 \cdot 10^{-7}$.

Figure 2 illustrates the measurement of the electron beam current over the entire range. Because the measurement is rather time consuming, a computer program based on the python language was developed to do this task fully automated as is described in the next section.

ISBN: 978-3-95450-241-7 ISSN: 2673-5350 doi:10.18429/JACoW-IBIC2022-MOP31

AUTOMATED PROGRAM

Basically, the program performs the measurement sequence as described above: It controls the position of the feed-throughs with the photo diodes and the position of the scraper used to reduce the electron beam current. It automatically determines the calibration factors for the photo diodes. In the range below some nA, the program also performs the electron counting. To give an impression, the top panel of the program is shown in Fig. 3.



Figure 3: Top panel of electron beam current control program.

Once a target beam current value is given, the program automatically sets the electron beam current to this value. The program records all tasks, so that also later an offline check or re-evaluation of the recorded data can be performed. First, the program determines the calibration factor that relates the photo current of the thick filtered photo diode to the PCT -measured electron beam current. Therefore, the program, by successive placement of the scraper close to the electron beam, reduces the current to approx. 10 mA first, thereafter to 1 mA and 0.1 mA. At these values the electron beam current measurement are performed for some 100 s by the PCT and the photo diode. Figure 4 shows as example such a calibration measurement. Then, a linear fit is performed for the three measurement points at 10 mA, 1 mA and 0.1 mA, yielding the calibration factor and the PCT offset value, see Fig 5 for an example. Thereafter, the program sets the electron beam current to the preselected value by repeated placement of the scraper close to the beam.

Since it was observed that the measured photo current slightly depends on the measurement range of the electrometer, the program can be optionally used in a special mode which controls the measurement range of the electrometer and corrects possible deviation. For this, the photo current is measured for about 100 s in the respective upper measurement range of the electrometer. Then the electrometer is switch to the next lower range by the program and the photo current is measured in this range for another 100 s. A possible deviation is than corrected by an additional factor. Moreover, for each measurement range offset values, that have to be determined separately before, can be subtracted before matching the measurement in the two adjacent measurement ranges. These offset values can result from poorly balanced input amplifiers of the electrometer and can be in the range of several tens of µA. Figure 6 shows an example of this feature.

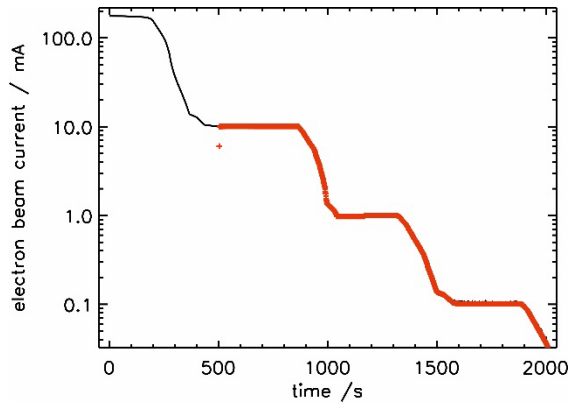


Figure 4: Black: measured electron beam current with the PCT; Red: Measured photo current of the 8 µm filtered photo diode multiplied with the calibration factor.

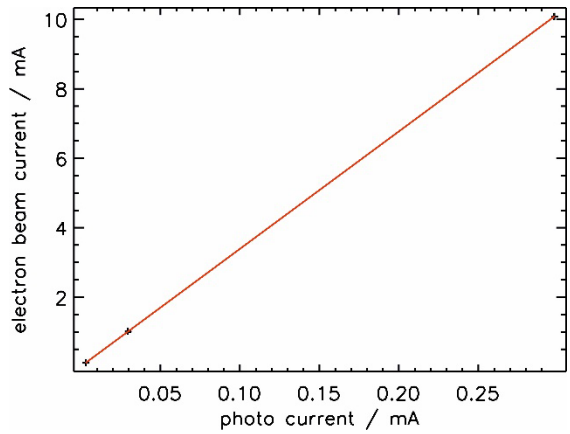


Figure 5: Example of the determination of the calibration factor for the 8 µm filtered photo diode.

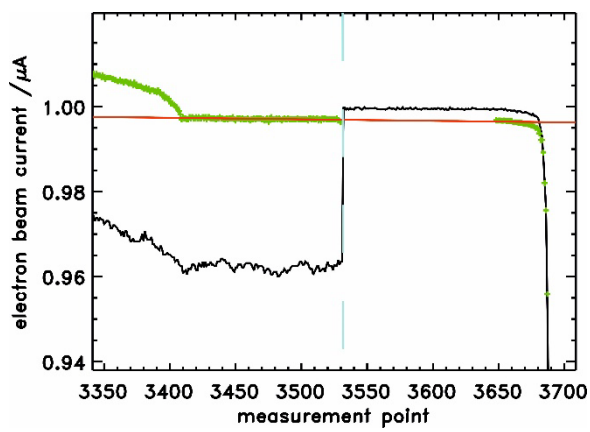


Figure 6: Example for the adjustment at a range switch of the electrometer: black: beam current measurement with the thick filtered diode; vertical dashed line indicates the range switch, green curve: calculated electron beam current keeping track of the previous range switches, red line: fit to the plateau values.

Content from this work may be used under the terms of the CC BY 4.0 licence (© 2022). Any distribution of this work must maintain attribution to the author(s), title of the work, publisher, and DOI

ISBN: 978-3-95450-241-7 ISSN: 2673-5350 doi:10.18429/JACoW-IBIC2022-MOP31

Content from this work may be used under the terms of the CC BY 4.0 licence (© 2022). Any distribution of this work must maintain attribution to the author(s), title of the work, publisher, and DOI

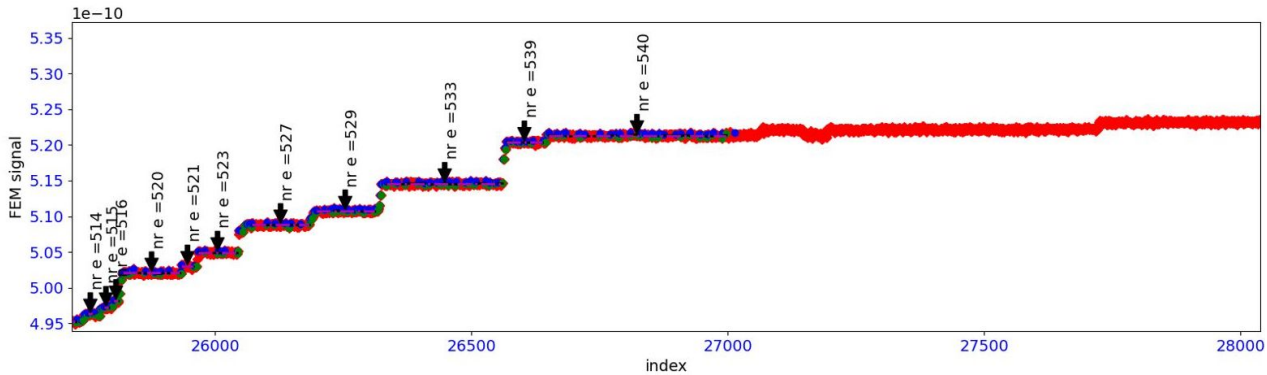


Figure 7: Example of electron counting in the range of 500 electrons (500 pA).

Electron currents below approx. 1 nA can be measured by counting the electrons when they are kicked out by the scraper. One electron is equivalent to an electron beam current of 1 pA. Figures 7 and 8 show examples from the electron counting by the program.

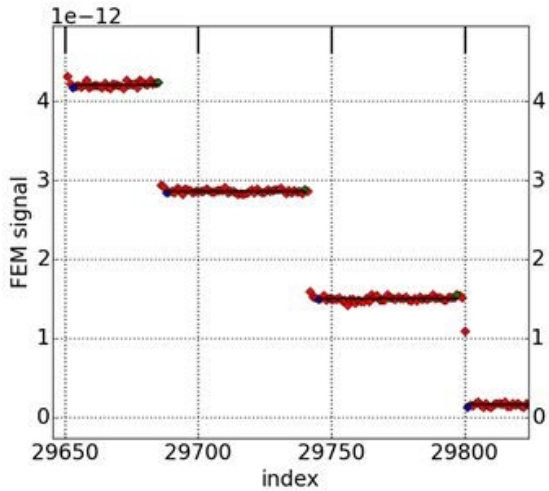


Figure 8: Example for counting of last three electrons.

The program adjusts and measures the target value normally in the range of several µA or nA. The special calibration tasks are then performed with this selected stored electron beam current, e.g. the calibration of an energy dispersive detector. After the calibration has been performed, the program can thereafter be used to reduce the beam current further into the counting rang.

Doing this allows for a stringent test of the measured beam current in the nA range: The values given by the photo current measurement, that ultimately relates to the PCT current measurement, and the beam current value obtained by counting the electron can be compared. From the degree of agreement, an uncertainty of the beam current measurement in the intermediate range, i.e., the beam current rage between the PCT measurement and electron counting range can be estimated.

This has up to now only been performed once: The electron counting resulted in a value of 541 pA, which is regarded as the true value. The current measured with the thick filtered diode was 539 pA, that of the thin filtered diode 536 pA. This is very promising but, has to be confirmed by further measurements. Using the option to control the measurement range of the electrometer resulted in a slightly worse result of 527 pA, showing that most probably the offset values for the measurement ranges are not predefined correctly.

SUMMARY

An automated program to control and measure the electron beam current at the MLS over a range of more than 11 decades has been developed. This program will highly facilitate the setting of the appropriate beam current needed for a calibration task. The program basically works as planned. A first comparison of the measurement of the mean current by photo diodes calibrated with the PCT current measurement to that resulting from electron counting is very promising but, has to be proven by further measurements.

REFERENCES

[1] R. Klein *et al.,* "Operation of the Metrology Light Source as a primary radiation source standard", *Phys. Rev. ST Accel. Beams*, vol. 11, p. 110701, 2008. doi:10.1103/PhysRevSTAB.11.110701

[2] J. Schwinger, "On the Classical Radiation of Accelerated Electrons", *Phys. Rev.,* vol. 75, p. 1912, 1949. doi:10.1103/PhysRev.75.1912

[3] R. Klein *et al.,* "Accurate Measurement of the MLS Electron Storage Ring Parameters", in *Proc. IBIC'16,* Barcelona, Spain, Sep. 2016, pp. 600-603. doi:10.18429/JACoW-IBIC2016-WECL02

[4] K. Unser, "The parametric current transformer, a beam current monitor developed for LEP", CERN SL/91-42, 1991.

[5] IRD AXUV 100, Opto Diode Corp., Newburg Park, CA, USA.

[6] Keithley electrometer 617, Cleveland, Ohio, USA.

[7] Femto Messtechnik GmbH, Berlin.

[8] E. Fairchild, *New Techniques in Space Astronomy*, Dordrecht, NL: Springer, 1971.

[9] U. Arp *et al.,* "SURF III-an improved storage ring for radiometry", *Metrologia*, vol. 37, p. 357, 2000. doi:10.1088/0026-1394/37/5/2

ISBN: 978-3-95450-241-7 ISSN: 2673-5350 doi:10.18429/JACoW-IBIC2022-MOP32

ANALOG FRONT END FOR MEASURING 1 TO 250 pC BUNCH CHARGE AT CLARA

S. L. Mathisen[1, *], T. H. Pacey[1], R. J. Smith[1], UKRI STFC, Sci-Tech Daresbury, Warrington, UK
[1]also at Cockcroft Institute, Sci-Tech Daresbury, Warrington, UK

Abstract

As part of the development of the CLARA electron accelerator at Daresbury Laboratory, a new analog front end for bunch charge measurement has been developed to provide accurate measurements across a wide range of operating charges with repetition rates of up to 400 Hz. The qualification tests of the front end are presented. These include tests of the online calibration system, compared to a bench Faraday cup test setup; online beam test data with a Faraday cup from 1 to 200 pC; online beam test data with a wall current monitor from 1 to 200 pC, and tests using signal processing such as singular value decomposition. This is demonstrated to enable the measurement of bunch charges in the order of 100 fC using both Faraday Cups and Wall Current Monitors.

INTRODUCTION

The CLARA front-end is the first phase of the CLARA 250 MeV Free Electron Laser (FEL) test facility, based at Daresbury Laboratory. The front-end has been used to provide high energy electrons for experiments during two experimental runs in 2018/19 [1] and 2021/22 [2]. The combined CLARA/VELA facility currently incorporates two Wall Current Monitors (WCMs), four Faraday Cups (FCs) and one Integrated Current Transformer (ICT) for bunch charge diagnostics, and plans for the full CLARA facility, due to be commissioned in 2024, will include further charge devices.

The existing charge diagnostics system installed on the CLARA/VELA FCs and WCMs is based on an *LC* integrator circuit with a resonance frequency of 30 MHz [3]. This system has many problems: It relies on out-of-production components, it requires interpolation after being digitized to accurately measure charge, each front-end requires two multi-core cables run through the radiation shielding and it lacks important features, such as automatic calibration or multiple sensitivity settings to better support low charge operations.

This paper presents results from the final production version of an upgraded front end for charge detection, based on an earlier presented prototype [4]. This final system is substantially improved over both the older *LC* integrator circuit and the previously presented prototype in many ways. First an overview of the front end will be presented briefly, followed by bench tests to verify the system's operation and quantify measurement uncertainty. Finally tests conducted as part of the CLARA 2021/22 experimental run are presented, including online measurement of ultra low charges.

* storm.mathisen@stfc.ac.uk

SYSTEM DESIGN

The system design is presented in three sections: The analog signal chain that converts signals from charge devices into an output pulse with an amplitude proportional to charge, the charge injection circuit for onboard calibration of the analog signal chain; and the digital control circuitry to enable operators to adjust the settings of the front end. Figure 1 shows a functional diagram of the circuit.

Analog Signal Chain

The analog signal chain is divided into three sections: Input filter and buffer, charge integration circuitry and output buffer. The input filter consists of a 100 MHz cut-off low-pass filter which enables the front end to be agnostic about the bandwidth of the charge device it is connected to. The bandwidth of an FC is controlled through the impedance it is discharged through, but a WCM can have a bandwidth up to several GHz. The filter is a simple *RC* filter. Following the input filter is an analog switch that select any of three inputs: Charge device input with the input filter, an unfiltered input for front end testing, and the onboard charge injection circuitry. The input is buffered by a unity gain FET op-amp, and is enclosed within an RF shield to limit the effect of external noise sources.

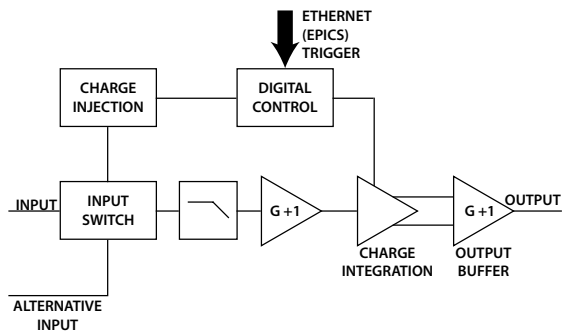


Figure 1: Block diagram of the presented front-end.

The charge integration circuit relies on an ADA4350 Analog Front End integrated circuit [5]. This circuit features a FET input amplifier with six switchable feedback paths, a differential output buffer and control via a serial interface. Five of the feedback paths are used for different integrator sensitivity settings, and the last one to amplify the signal without integration. The values of the components used in the feedback network were selected to ensure that each feedback path has the same frequency response. One goal of the new front end was to enable shot-by-shot measurement of both bunch charge and dark current simultaneously, a

Content from this work may be used under the terms of the CC BY 4.0 licence (© 2022). Any distribution of this work must maintain attribution to the author(s), title of the work, publisher, and DOI

ISBN: 978-3-95450-241-7 ISSN: 2673-5350 doi:10.18429/JACoW-IBIC2022-MOP32

Content from this work may be used under the terms of the CC BY 4.0 licence (© 2022). Any distribution of this work must maintain attribution to the author(s), title of the work, publisher, and DOI

significant improvement over the previous system, which can only measure one or the other. As the charge integrator only integrates signals that are above the cutoff frequency, the cutoff frequency is selected such that dark current has a bandwidth below this cutoff and bunch charge has a bandwidth above it. Figure 2 shows the frequency response of each feedback setting, normalized by their DC gain for comparison purposes. The sensitivities and their expected range from simulations are listed in Table 1.

Table 1: Front End Sensitivity Settings and Their Design Operating Range

Sensitivity	Capacitance	Operating range
Highest	2 pF	0 – 10 pC
High	15 pF	2 – 20 pC
Medium	51 pF	2 – 40 pC
Low	300 pF	10 – 150 pC
Lowest	1 nF	10 – 250 pC

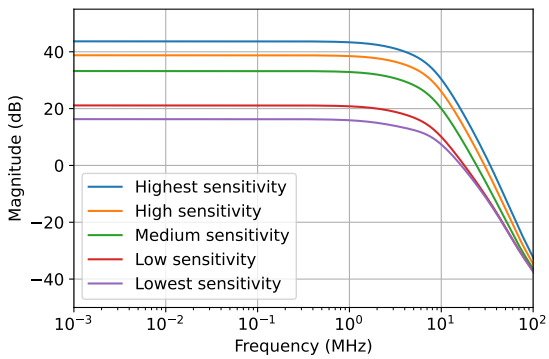


Figure 2: Simulated frequency response of each sensitivity setting. The front end integrates above 10 MHz.

Charge Injection Circuit

The charge injection circuit enables a range of known charges to be injected into the circuit as a calibration signal. The circuit charges a capacitor of a known capacitance C to a known voltage V and, by shorting the charging voltage to ground through an analog switch, discharges the stored charge into the front end's analog signal chain. The stored charge is given by $q = VC$. To provide a wide range of charges for calibration, four high precision voltage references, ranging from 500 mV to 4096 mV, and uses an 8-bit digital potentiometer are used to control the charging voltage. The available calibration charges ranges from 0 – 51 pC in 200 fC steps up to 0 – 418 pC in 1.64 pC steps. An external board with a similar circuit, charged from a higher resolution DAC and powered by a battery was used for the uncertainty quantification. This external calibration circuit has a range of 0 – 255 pC with a resolution of 4 fC.

Digital Control

CLARA uses EPICS as its control system, and the front end is designed to be controlled via Ethernet using EPICS. Ethernet connectivity is provided by a Raspberry Pi Compute Module 4 (CM4), a credit card-sized embedded computer running Linux. During the tests presented in this paper, the CM4 was running a simple server responding to bytes sent via TCP from a soft EPICS IOC, but in the future it is planned that the CM4 will run an IOC itself. The CM4 does not control the board directly, it instead sends commands to a microcontroller which then controls the board. This is mainly due to the deterministic timing available on the microcontroller, which is synchronized to the machine timing system via a trigger, simplifying signal processing. This ensures that settings are only changed outside the sampling window of the ADCs. As the serial interface clocks only run during transmission, this reduces cross-talk between the digital and analog sections. It also ensures that no spurious data during setting changes causes trips due to high instantaneous bunch charge.

RESULTS

Bench Testing

The front end was first bench tested using an external charge injection circuit connected to a calibrated 12-bit resolution oscilloscope. The charge injection circuit's output is discharged into a Faraday cup, which is connected to the front end. The oscilloscope stores the output of the front end, the reference voltage of the charge injection circuit's DAC and the output voltage of the DAC. The sensitivity of each setting was measured at ten points spaced out across the expected range of the setting using the external charge injection circuit. 100 samples were taken at each point. The results are presented in Fig. 3, showing that all sensitivity settings are linear across their operating ranges.

To determine the uncertainty of the bunch charge measurement, 1000 shots were recorded from an external charge injection circuit set to roughly the center of the operating range for each sensitivity setting. The results are shown in Table 2. The uncertainty for each sensitivity is around 1% of the injected charge, which is consistent with the results in Fig. 3.

Table 2: Uncertainty for Each of the Ranges

Sensitivity	Charge	Uncertainty ($\pm 2\sigma$)
Highest	5 pC	101.2 fC
High	10 pC	196.8 fC
Medium	20 pC	379.9 fC
Low	75 pC	1.38 pC
Lowest	150 pC	2.77 pC

Beam Testing

Tests with beam were carried out in three distinct setups. First the front-end was connected to a Faraday cup and

ISBN: 978-3-95450-241-7 ISSN: 2673-5350 doi:10.18429/JACoW-IBIC2022-MOP32

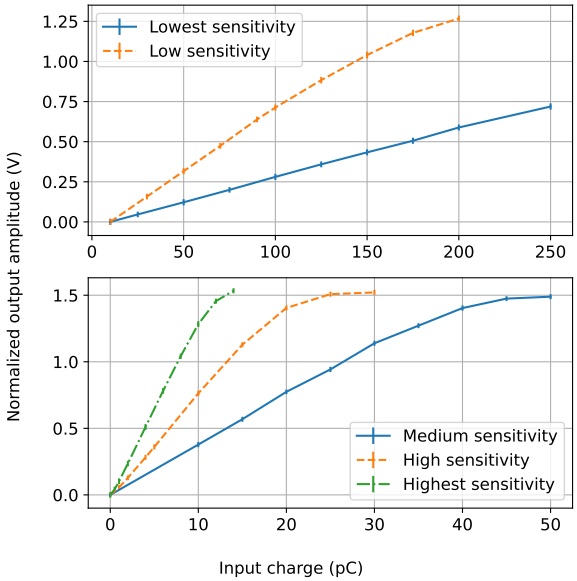


Figure 3: Calibration curves for each sensitivity setting, measured using an external charge injection circuit.

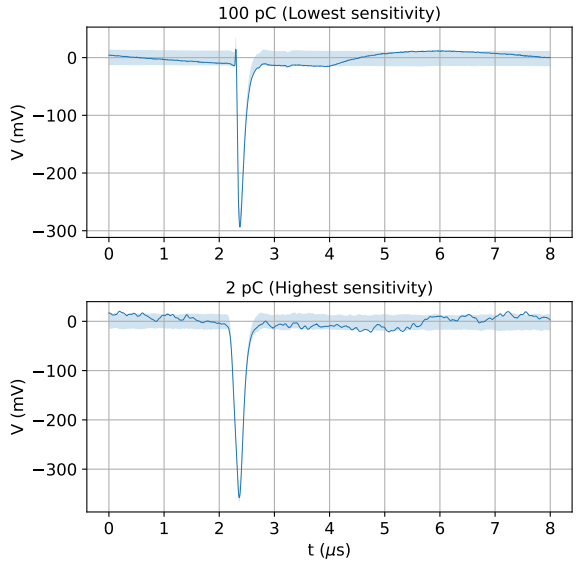


Figure 4: Measured output of the new front end when connected to a Faraday Cup at 100 pC, measured with the lowest sensitivity setting, and 2 pC, measured at the highest sensitivity setting. The shaded areas are $\pm 2\sigma$ per sample.

tests were run across the normal operating bunch charges of CLARA (2 – 100 pC). To verify the simultaneous measurement of bunch charge and dark current, the front end was then connected to the WCM installed at the exit from the CLARA gun. Finally, as part of one of the user experiments carried out on CLARA in 2022 the front end was used to measure ultra low charges < 500 fC.

Figure 4 shows the measured output of the front end when it is connected to a Faraday Cup. The bunch charge is proportional to the peak value of the output signal. At the highest sensitivity setting a bunch charge of 2 pC can be measured with roughly the same Signal-to-Noise Ratio (SNR) as with 100 pC on the lowest sensitivity setting. Previously the noise floor of CLARA's charge diagnostics was between 1 and 5 pC.

Figure 5 shows the output of the front end when connected to a WCM. These measurements were all taken at the highest sensitivity setting, due to the very low signal developed by the WCM. The signal is of the opposite polarity due to the WCM measuring the image current of the electron beam. The SNR for 100 pC and 20 pC bunch charges is shown to be well within detectable limits. A 2 pC bunch charge gives a much lower SNR, but is still detectable. Figure 6 shows how the bunch charge is determined when there is dark current present. When fully integrated into the control system, adjustable averaging windows for the base and top of the bunch charge pulse will be implemented.

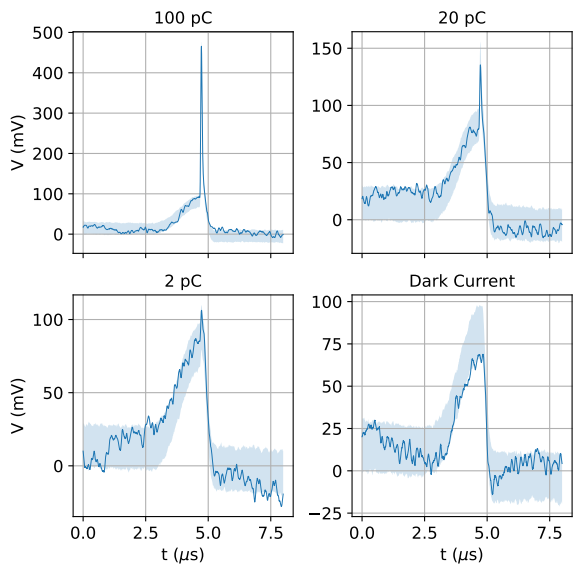


Figure 5: Measured output of the new front end when connected to a WCM at 100 pC, 20 pC and 2 pC, as well as with only dark current. The shaded areas are $\pm 2\sigma$ per sample.

Ultra Low Bunch Charges

While the main intended operating range of the front end is above 2 pC, during the recent CLARA experimental run some users requested very low charges. Using the highest sensitivity setting, an in-air Faraday cup and Singular Value Decomposition (SVD), which has previously been used to remove noise from ICTs [6], charges as low as 150 fC were measured shot-to-shot. This measurement was not done online, and was instead done by buffering 100 shots of data and then performing SVD on that buffer. Figure 7 shows a comparison between the single shot raw data, a simple 100 shot average and a single shot after SVD.

Content from this work may be used under the terms of the CC BY 4.0 licence (© 2022). Any distribution of this work must maintain attribution to the author(s), title of the work, publisher, and DOI

ISBN: 978-3-95450-241-7 ISSN: 2673-5350 doi:10.18429/JACoW-IBIC2022-MOP32

Content from this work may be used under the terms of the CC BY 4.0 licence (© 2022). Any distribution of this work must maintain attribution to the author(s), title of the work, publisher, and DOI

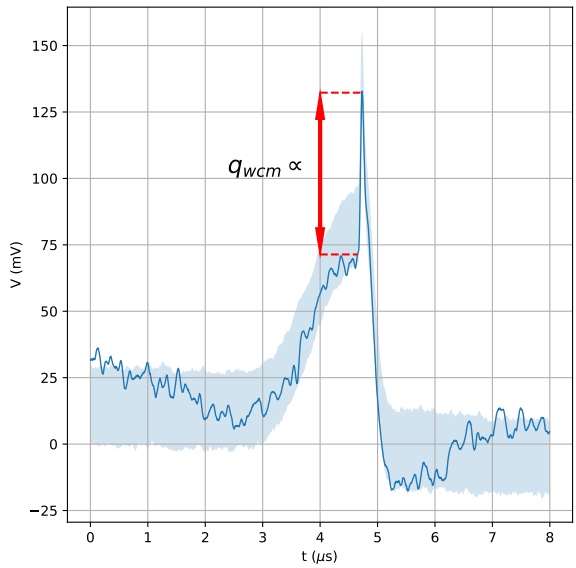


Figure 6: Illustration of how to measure the bunch charge (q_{wcm}) with dark current. The shaded areas are $\pm 2\sigma$ per sample.

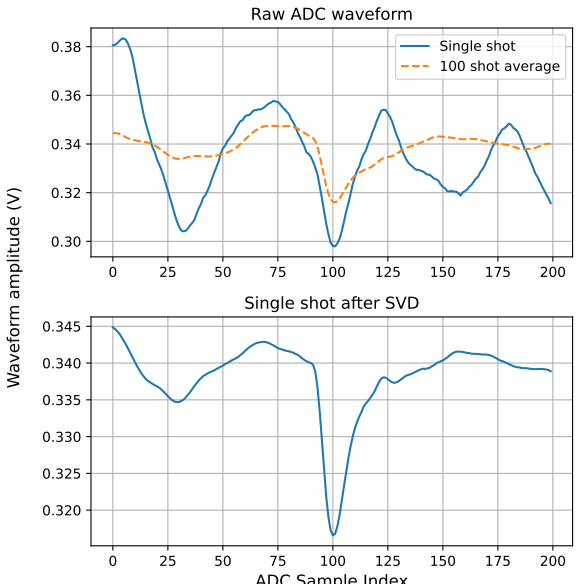


Figure 7: Output of the front end when connected to a Faraday cup exposed to 150 fC, compared to a 100 shot average and a single shot after SVD.

CONCLUSION

A new front end for charge devices, such as WCMs and FCs, has been demonstrated. The front end has multiple sensitivity settings, a charge injection circuit for calibration and is designed to operate across the 2 – 250 pC design specification for CLARA. Bench tests have confirmed that the sensitivity settings have linear outputs in their operating windows and that the uncertainty of the system's measurement is around 1%. Tests with beam have confirmed that the front end works as expected with FCs and WCMs, including simultaneous shot-by-shot dark current and bunch charge measurements. Finally, measurement of Ultra Low Bunch Charges (< 500 fC) using SVD has been demonstrated using offline data post-processing. The front end will be deployed as part of the CLARA Phase 2 upgrade, due to be commissioned in 2024.

REFERENCES

[1] D. Angal-Kalinin *et al.*, "Status of Clara Front End Commissioning and First User Experiments", in *Proc. IPAC'19*, Melbourne, Australia, May 2019, pp. 1851–1854. doi:10.18429/JACoW-IPAC2019-TUPRB083

[2] D. Angal-Kalinin *et al.*, "Status of CLARA at Daresbury Laboratory", presented at the LINAC'22, Liverpool, UK, Aug.-Sep. 2022, paper THPOJO09, unpublished.

[3] A. Kalinin, "Precise Instruments for Bunch Charge Measurement", in *Proc. IPAC'14*, Dresden, Germany, Jun. 2014, pp. 3703–3705. doi:10.18429/JACoW-IPAC2014-THPME182

[4] S. L. Mathisen, Y. M. Saveliev, and R. J. Smith, "Charge Detection System for the CLARA/VELA Facility", in *Proc. IBIC'19*, Malmö, Sweden, Sep. 2019, pp. 111–114. doi:10.18429/JACoW-IBIC2019-MOPP015

[5] Analog Devices ADA3450 Datasheet, https://www.analog.com/media/en/technical-documentation/data-sheets/ada4350.pdf

[6] J. Chen, Y. B. Leng, L. Y. Yu, and N. Zhang, "The Removal of Interference Noise of ICT using the PCA Method", in *Proc. IBIC'18*, Shanghai, China, Sep. 2018, pp. 22–25. doi:10.18429/JACoW-IBIC2018-MOOC03

ISBN: 978-3-95450-241-7 ISSN: 2673-5350 doi:10.18429/JACoW-IBIC2022-MOP33

BEAM CURRENT MEASUREMENTS AT THE NANO-AMPERE LEVEL USING A CURRENT TRANSFORMER

M. Xiao†, M. J. van Goethem, S. Brandenburg
PARTREC UMCG, University of Groningen, Groningen, Netherlands
T. Delaviere, L. Dupuy, F. Stulle, Bergoz Instrumentation, Saint-Genis-Pouilly, France

Abstract

In conventional proton therapy (PT) typical beam currents are of the order of 0.1 nA. At these currents dose monitoring is reliably achieved with an ionization chamber. However, at the very high dose rates used in FLASH irradiations (employing beam currents >100 nA) ionization chambers will exhibit large intensity dependent recombination effects and cannot be used. A possible solution is a current transformer. Here we report on the performance of the LC-CWCT (Bergoz Instrumentation, France) which has been developed to push noise floor of such non-destructive current measurement systems into the nano-ampere range. We present first beam current measurements at the PARTREC cyclotron (Netherlands). Beam currents measured by the LC-CWCT and a Faraday Cup were shown to linearly correlate up to the maximum intensity of 400 nA used in the measurements. For pulsed beams, charge measured by the LC-CWCT linearly correlated with pulse length over the measurement range from 50 to 1000 µs. Measurement noise as low as 2.8 nA was achieved. The results confirm that the LC-CWCT has the potential to be applied in FLASH PT for accurate determination of beam current and macro pulse charge.

INTRODUCTION

FLASH PT aims to use ultra-high dose rate (>40 Gy/s) beams for cancer treatment, which has been proven in pre-clinical studies to spare doses for healthy tissues while maintaining the treatment effects on some specific tumour models [1-3] compared to conventional PT. The beam current extracted for FLASH PT is around 1000 times higher than for clinical PT (~0.1 nA), which leads to a challenge for beam extraction in clinical cyclotrons.

Some studies also show that the beam time structure causes a variation of the FLASH effect [4]. Further studies need to be done to examine conditions and beam parameters, i.e. current, pulse width, energy, frequency, triggering the FLASH effect in clinical practices. Thus, it is of great significance to have a flexible test bench capable of providing varying beam parameters for FLASH PT studies.

The PARTREC cyclotron is expected to provide ultra-high dose rates for FLASH pre-clinical studies over the next few years. Because the PARTREC facility is not in clinical use it is more flexible and modifications to beam intensity and time structure can be implemented more easily than at a clinical facility.

However, the beam monitor and control system designed for use at clinical dose rates, which is based on ionization chambers (ICs), faces a challenge in delivering precise doses at beam currents used to achieve FLASH beam dose rates. Specifically, the response of plane-parallel ICs [5-7] shows a dependence on dose rate which can become unacceptably large at ultra-high beam currents due to volume recombination effects; an effect which can be neglected in clinical settings. For FLASH PT studies, it is essential to improve the beam monitoring system for high currents (i.e. a few 100 nA to µA). Tests have shown that the ion collection efficiency of a plane-parallel IC designed at PARTREC is around 83% with a peak current of 543 nA (at 150 MeV beam energy).

A Faraday cup was applied in previous experiments to control the delivered proton fluence and to deduce IC efficiency, assuming the Faraday cup is dose rate independent. For FLASH dose rates, a current transformer, which is non-destructive to the beam, can provide the necessary redundancy in dose delivery by measuring beam currents for both CW and pulsed beams.

For the present study we tested a specially developed current transformer, the LC-CWCT, with a 150 MeV proton beam at the PARTREC cyclotron. Macro-pulse length and average current were varied during the measurements. A Faraday cup was installed at the end of the beamline to give a reference value for the input beam current. The aim of this work was to verify the noise levels of the LC-CWCT output signals of different bandwidths (100 Hz, 10 kHz and 350 kHz) in a real beam environment, and the potential of using an LC-CWCT in FLASH PT for real-time beam monitoring and control under complicate beam conditions.

LC-CWCT AND BCM-CW-E

The CWCT and the corresponding BCM-CW-E electronics [8] have been successfully used to measure micro-ampere beam currents with sub-microampere resolution [9]. By applying a fast sample-and-hold measurement the BCM-CW-E deduces level of the CWCT output signal between any two consecutive beam pulses. From these signal levels average input currents can be deduced. The only necessary condition is that input beam bunches are well separated. For convenience the output signal is provided with three different bandwidths: 350 kHz, 10 kHz and 100 Hz.

The CWCT can be considered a noise free current source. All noise is either coming from the signal processing on the BCM-CW-E electronics, or from environmental noise, for example, captured by the coaxial cables connecting CWCT and BCM-CW-E.

In such a situation a very effective way of boosting the signal-to-noise ratio is to amplify the signal directly at the source. That means, by adding a low noise amplifier directly at the CWCT output the measurement range can be

† m.xiao@umcg.nl

Content from this work may be used under the terms of the CC BY 4.0 licence (© 2022). Any distribution of this work must maintain attribution to the author(s), title of the work, publisher, and DOI

ISBN: 978-3-95450-241-7 ISSN: 2673-5350 doi:10.18429/JACoW-IBIC2022-MOP33

Content from this work may be used under the terms of the CC BY 4.0 licence (© 2022). Any distribution of this work must maintain attribution to the author(s), title of the work, publisher, and DOI

shifted to lower currents. The low current limit is given only by the noise introduced by this amplifier. To distinguish from the normal CWCT, the combination of CWCT and low noise amplifier is called LC-CWCT.

Performance of the LC-CWCT was first measured on a test bench. The noise floor was determined to $\sigma_{350kHz} = 300$ nA, $\sigma_{10kHz} = 36$ nA, $\sigma_{100Hz} = 7$ nA for the three available output signals of different bandwidth. Such low noise levels render the LC-CWCT interesting for many ion accelerators which produce beam currents <1 µA, thus requiring non-destructive beam instrumentation with nano-ampere resolution.

However, these values were determined in a rather low noise electronics lab. Since particle accelerators tend to be an environment with plenty of electromagnetic noise, it was decided to verify LC-CWCT performance in a particle accelerator.

MEASUREMENT SETUP

A proton beam was accelerated to 150 MeV with a bunch repetition frequency of 55 MHz. During the experiments, the average beam current could be varied up to 400 - 500 nA. Time structure of the proton beam could be controlled to have macro-pulse lengths varying from 50 µs to 1000 µs, i.e. from short pulse mode to near CW mode. The beam spot size of around 3.5 mm (FWHM) passed entirely though the LC-CWCT aperture of 96 mm.

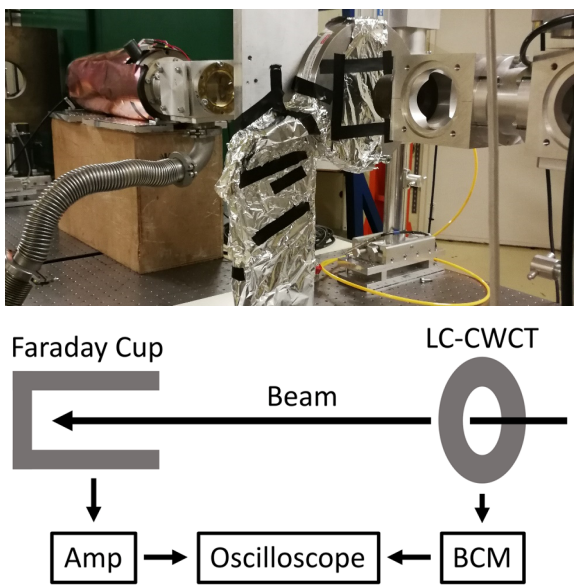


Figure 1: Photograph of the experimental setup with LC-CWCT (wrapped in aluminium foil to reduce noise) and Fcup (top). Schematic drawing of experimental setup and electronics readout system (bottom).

Figure 1 (top) shows a photograph of the experimental setup with the LC-CWCT and the Faraday cup (Fcup). The LC-CWCT was installed behind a beam window close to the end of an experimental beamline of the PARTREC cyclotron. About 1 m further the beam was collected by a Fcup. First tests with beam showed that indeed some non-negligible noise was picked up. Completely wrapping the LC-CWCT in aluminium foil resolved this issue. Note that the proton beam passed the aluminium foil without noticeable degradation.

A schematic drawing of the experimental setup is shown in Fig. 1 (bottom), including the electronics readout system. The LC-CWCT output signal was processed by the BCM-CW-E electronics module. The current signal from the Fcup was converted to a voltage signal by an amplifier (FEMTO, DLPCA-200). All output signals were recorded by an oscilloscope (Rohde&Schwarz RTH1004). The digitized data was stored for off-line analysis.

The Fcup works as an absolute dosimeter in this experiment controlling the total delivered proton fluence, since it is dose rate independent. Its inhouse design allows to reduce vacuum pressure to around 10^{-3} to 10^{-4} mbar. The Fcup setup also has an electron suppression electrode that prevents secondary electrons from escaping the Fcup It was previously calibrated with a current generator connected to the same amplifier (gain = 10^7, bandwidth = 50 kHz), so that the output voltage signal shows a linear response as a function of the input current.

Noise and Accuracy Evaluation

To evaluate the noise and accuracy of the LC-CWCT, we applied a low beam current (around 24 nA) with a macro-pulse length of 900 µs and a repetition frequency of 1 kHz. The beam was kept on for 1.5 s, corresponding to a total of 1500 input pulses. BCM-CW-E 100 Hz output signal was recorded on the oscilloscope. Other ports of the oscilloscope were connected to the Fcup and the input pulse timing trigger.

For a second test, beam current was increased stepwise to around 500 nA with a macro-pulse length of 1000 µs and a macro-pulse repetition frequency of 10 Hz. This time 10 kHz and 350 kHz BCM-CW-E output signals were recorded. The above two cases were repeated 25 times for each beam setup. The digitized data was saved with the oscilloscope for off-line analysis.

Linearity Evaluation

The other critical functionality we were interested in was proportionality with beam current, which was expected to be linear over a wide current range.

The input beam pulse length was 900 µs with a beam current ranging from around 20 nA to 400 nA. BCM-CW-E 10 kHz output was recorded on the oscilloscope. The electronics connection of other channels (i.e. Fcup and timing trigger) was the same as for the noise and accuracy evaluation. For the linearity test, average signals of 128 macro-pulses were digitized and saved by the oscilloscope.

For a second test, beam current remained unchanged. Macro-pulse length was varied from 50 µs to 1000 µs. Oscilloscope connections were as before, averaging was set to one. By integrating on the oscilloscope macro-pulse charges were obtained and saved. For each macro-pulse length setting 25 values were saved.

ISBN: 978-3-95450-241-7 ISSN: 2673-5350 doi:10.18429/JACoW-IBIC2022-MOP33

RESULTS AND DISCUSSIONS

Noise Evaluation

The main objective of the noise measurements was to determine whether measurement noise in the accelerator is comparable to the noise obtained during lab measurements. A typical macro-pulse measurement is shown in Fig. 2 (top). Noise of the 350 kHz bandwidth output is about 210 nA and noise of the 10 kHz filtered output is around 28 nA. The noise obtained from a series of datasets is plotted in Fig. 2 (bottom). All of the values measured in the accelerator are below the noise obtained in test bench measurements (i.e. $\sigma_{350kHz} = 300$ nA, $\sigma_{10kHz} = 36$ nA). The lower noise is due to a shorter measurement time which does not permit to capture low frequency noise.

For much lower beam currents, these high bandwidth BCM-CW-E outputs are still too noisy to obtain useful current information. Figure 3 shows the measured current (~24 nA) from the 100 Hz bandwidth output for 1500 macro-pulses of 900 µs length repeated at 1 kHz. The obtained noise level is around 2.8 nA, which is lower than that tested in the lab (i.e. $\sigma_{100Hz} = 7$ nA).

High bandwidth outputs work well for high beam currents, but their noise level is unacceptable when the beam current is below a few 10 nA. On the contrary, the 100 Hz bandwidth output works well for lower beam currents with long macro-pulse lengths (i.e. nearly CW beams). However, this output will be too slow to process short, pulsed beams (i.e. a few 10 µs), in which case the 10 kHz (or higher) bandwidth output may be preferable.

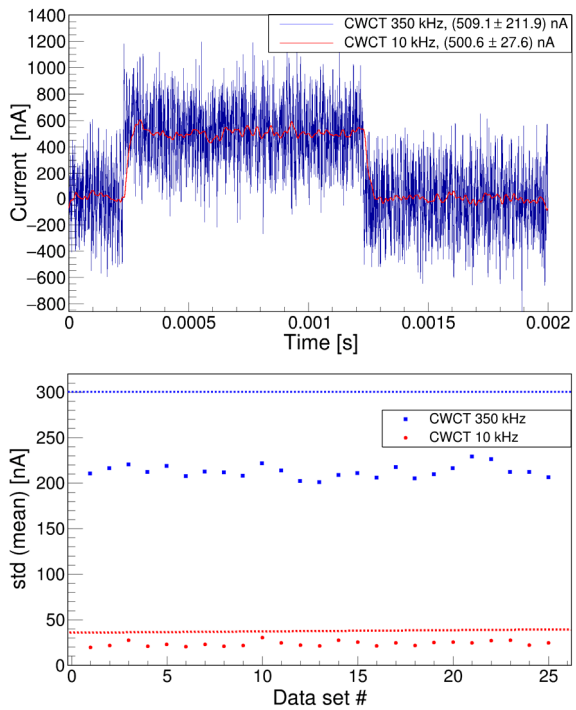


Figure 2: Measured beam currents for macro-pulses of 1000 µs, 10 kHz and 350 kHz BCM-CW-E outputs (top). Noise levels from the two outputs for 25 sequential input macro-pulses, dashed lines indicate noise levels obtained by bench measurements (bottom).

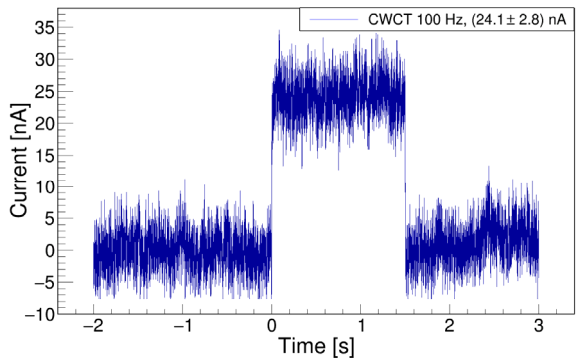


Figure 3: Measured beam current with a low output bandwidth (100 Hz) and long input beam. The beam was kept for 1.5 s with a total of 1500 macro-pulses (900 µs length, 1 kHz repetition rate).

Linearity Evaluation

A range of beam currents was applied to LC-CWCT and Fcup to evaluate linearity of the current transformer. Assuming the Fcup is dose-rate independent, the current measured by the LC-CWCT is linearly proportional to the current collected by the Fcup from 24 to around 400 nA average beam current, as shown in Fig. 4. The error bars are small since averages of 128 macro-pulses were used for these measurements. Noise of the 10 kHz output is around 30 nA, which is unacceptable for a few 10 nA input beam. However, averaging of 128 macro-pulses reduces noise level to just a few nA.

The current measured by the LC-CWCT is almost 25% higher than that collected by the Fcup, as shown in the linear fit equation. There might have been some beam losses in the beamline in between LC-CWCT and Fcup. That means, not all particles which passed through the LC-CWCT were collected by the Fcup. This is a systematic error due to the experimental setup, which does not affect the linearity test of the device. However, due to these experimental conditions a comparison of the absolute measurement accuracy was not possible.

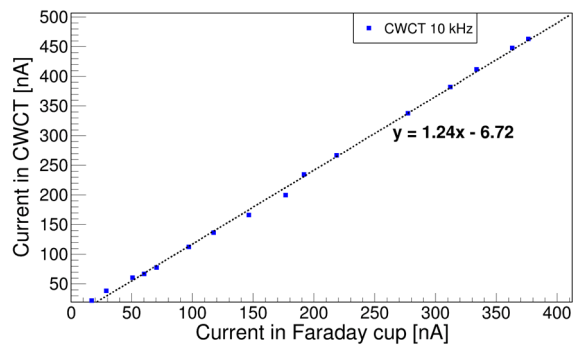


Figure 4: Beam current measured by LC-CWCT (10 kHz output) as a function of current collected by the Fcup. The input macro-pulse length was 900 µs and the output signals (i.e. both LC-CWCT and Fcup) were averaged for a total of 128 pulses (error bars are smaller than the markers).

For very short macro-pulses, the output signal from the 10 kHz bandwidth output cannot reach a plateau as shown in Fig. 5 (top). Its bandwidth corresponds to a rise time of

Content from this work may be used under the terms of the CC BY 4.0 licence (© 2022). Any distribution of this work must maintain attribution to the author(s), title of the work, publisher, and DOI

ISBN: 978-3-95450-241-7 ISSN: 2673-5350 doi:10.18429/JACoW-IBIC2022-MOP33

Content from this work may be used under the terms of the CC BY 4.0 licence (© 2022). Any distribution of this work must maintain attribution to the author(s), title of the work, publisher, and DOI

about 35 µs. This is the reason why for previously discussed current measurements macro-pulses >500 µs were used.

However, it is possible to estimate the charge of short macro-pulses (<100 µs) by performing an integration of the output signals. Figure 5 (bottom) shows the average measured charge for 25 input macro-pulses as a function of the macro-pulse length. Measured charge and macro-pulse length correlate linearly. Thus, even if macro-pulse length is too short for direct current measurements, macro-pulse charge can still be accurately determined by integration of the LC-CWCT output signal.

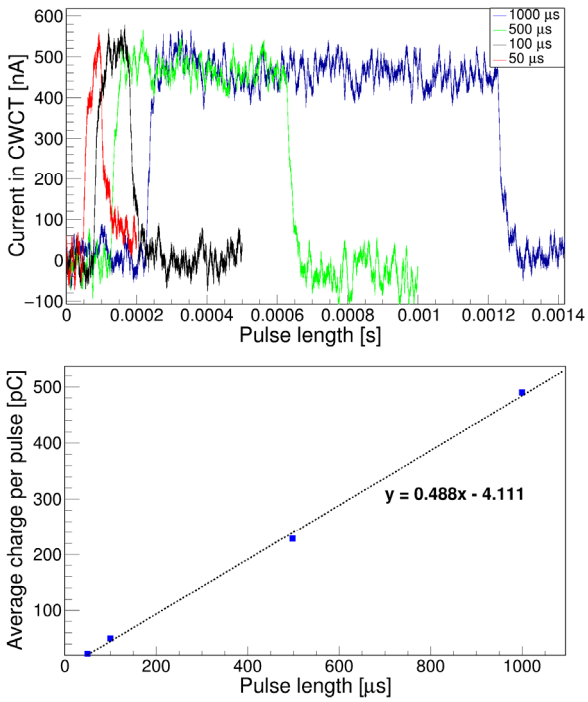


Figure 5: Macro-pulse current measured by LC-CWCT (10 kHz output) depending on macro-pulse length ranging from 50 to 1000 µs (top). Macro-pulse charge obtained by integration of LC-CWCT output signal as a function of macro-pulse length, averages of 25 input macro-pulses (bottom). Error bars are smaller than the marker.

CONCLUSION

In this experiment, we evaluated the performance of a newly developed current transformer LC-CWCT in terms of noise level and linearity in a proton beam environment. The results show that the noise level measured with beam is as low as measured on a test bench. With a noise level of 2.8 nA (100 Hz measurement bandwidth) even beam currents as low as 24 nA could be well resolved.

However, the 100 Hz output bandwidth is too slow for short, pulsed beams. Higher bandwidth outputs with 10 kHz and 350 kHz bandwidth were also tested with a much higher beam current up to around 500 nA. Measured noise levels were around 28 nA and 210 nA, respectively. Also these values showed good reproducibility over time and agreed with results measured on a test bench.

The LC-CWCT 10 kHz output was compared to a Faraday cup. Good linearity over a wide current range up to the maximum measured current of around 460 nA was observed. The measured macro-pulse charge was also found to be linear with pulse lengths ranging from 50 to 1000 µs, at the above current level.

The LC-CWCT provides signals with three bandwidths (100 Hz, 10 kHz, 350 kHz) which allows measuring either low currents with low noise levels or short macro-pulses with fast response time. Since the LC-CWCT is a non-destructive device, it can be installed anywhere along the beamline for online dose monitoring. Our measurements show that it has the potential to be used in FLASH PT studies with varying beam characteristics. Furthermore, LC-CWCT characteristics may be applicable for current and charge measurements in other low-current particle accelerators.

REFERENCES

[1] V. Favaudon *et al.*, "Ultrahigh dose-rate FLASH irradiation increases the differential response between normal and tumor tissue in mice", *Sci. Transl. Med.*, vol. 6, no. 245, p. 245ra93, 2014. doi:10.1126/scitranslmed.3008973

[2] P. Montay-Gruel *et al.*, "Irradiation in a flash: Unique sparing of memory in mice after whole brain irradiation with dose rates above 100 Gy/s", *Radiother. Oncol.*, vol. 124, no. 3, pp. 365-369, 2017. doi:10.1016/j.radonc.2017.05.003

[3] M. C. Vozenin *et al.*, "The Advantage of FLASH Radiotherapy Confirmed in Mini-pig and Cat-cancer Patients The Advantage of Flash Radiotherapy", *Clin. Cancer Res.*, vol. 251, pp. 35-42, 2019. doi:10.1158/1078-0432.CCR-17-3375

[4] J. D. Wilson, E. M. Hammond, G. S. Higgins, and K. Petersson, "Ultra-High Dose Rate (FLASH) Radiotherapy: Silver Bullet or Fool's Gold?", *Front. Oncol.*, vol. 9, p. 1563, 2020. doi:10.3389/fonc.2019.01563

[5] H. Palmans, R. Thomas, and A. Kacperek, "Ion recombination correction in the Clatterbridge Centre of Oncology clinical proton beam", *Phys. Med. Biol.*, vol. 51, no. 4, p. 903, 2006. doi:10.1088/0031-9155/51/4/010

[6] S. Rossomme *et al.*, "Ion recombination correction factor in scanned light-ion beams for absolute dose measurement using plane-parallel ionisation chambers", *Phys. Med. Biol.*, vol. 62, no. 13, p. 5365, 2017. doi:10.1088/ 1361-6560/aa730f

[7] M. Liszka *et al.*, "Ion recombination and polarity correction factors for a plane–parallel ionization chamber in a proton scanning beam", *Med. Phys.*, vol. 45, pp. 391-401, 2018. doi:10.1002/mp.12668

[8] F. Stulle *et al.*, "Beam Loss and Average Beam Current Measurements Using a CWCT", in *Proc. LINAC'18*, Beijing, China, Sep. 2018, pp. 882-885. doi:10.18429/JACoW-LINAC2018-THPO086

[9] F. Stulle *et al.*, "Beam Current Measurements with Sub-Microampere Resolution using CWCT and BCM-CW-E", in *Proc. IBIC'19*, Malmö, Sweden, Sep. 2019, pp. 63-66. doi:10.18429/JACoW-IBIC2019-MOPP003

ISBN: 978-3-95450-241-7 ISSN: 2673-5350 doi:10.18429/JACoW-IBIC2022-MOP34

NEW X-RAYS DIAGNOSTICS AT ESRF: THE X-BPMs AND THE HALO-MONITOR

E. Buratin*, K. Scheidt, European Synchrotron Radiation Facility, Grenoble, France

Abstract

Two new X-ray diagnostics have been installed in the Front-Ends of the Storage Ring of the ESRF's Extremely Brilliant Source (EBS) recently.

Two independent optical X-BPMs at 23 m distance from their bending magnet source-point are giving extremely useful additional information on the vertical beam stability in comparison to the e-BPMs data.

A vertical beam Halo-monitor allows to measure permanently and quantitatively the level the electron density at large distance (1 – 3 mm) from the beam core, in a non-destructive manner.

INTRODUCTION

The Extreme Brilliant Source (EBS) ring at the European Synchrotron Radiation Facility (ESRF) is operational since mid-2020, generating coherent and bright x-rays for the scientific users [1]. The X-rays are generated by an electron beam of 6 GeV and 200 mA, with horizontal and vertical emittances of 120 pm and 10 pm, respectively. EBS can run with different filling schemes, such as 7/8 multibunch with a single bunch up to 8 mA, uniform, 16 bunches and 4 bunches.

A large range of diagnostics are in operation since the commissioning to measure the parameters, characteristics and behaviour of the beam [2].

Since last autumn we have added two new X-rays diagnostics: 1) the X-rays Beam Position Monitor (X-BPM) to check the vertical beam stability and 2) the Halo-monitor to measure the vertical halo at large distance from the beam core. In this paper we present the systems and the first results.

THE X-BPMS

Two optical X-BPMs have been implemented in the Front End (FE) of the beamlines BM8 and BM16 that have 0.85 T bending magnets as their X-ray source. These X-BPMs are of a first version that aimed at satisfying the proof-of-principle of getting a reliable image of the passing X-rays and to use that for verifying the mid- and long-term positional stability of these X-rays. This first version allows, through use of UHV-bellows etc., the sensor to be inserted, and so to measure, but not to serve the beamline, or to be extracted, thereby letting the full X-rays to the beamline. After the here below reported success with this first version we are now installing a 2nd version (in October) that will measure permanently while leaving the X-rays for the beam line users unperturbed.

* elena.buratin@esrf.fr

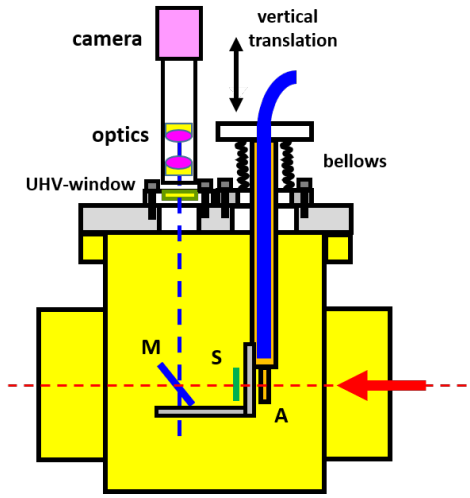


Figure 1: The X-BPM shown in inserted position.

The X-BPM (see Fig. 1) consists of a scintillator (S) behind a cooled copper absorber (A), a 45-degrees mirror (M), an UHV viewport and a camera with a set of achromats. The latter focusses on to the camera array the image that the X-rays emits by passing through the scintillator screen. (see Fig. 2).

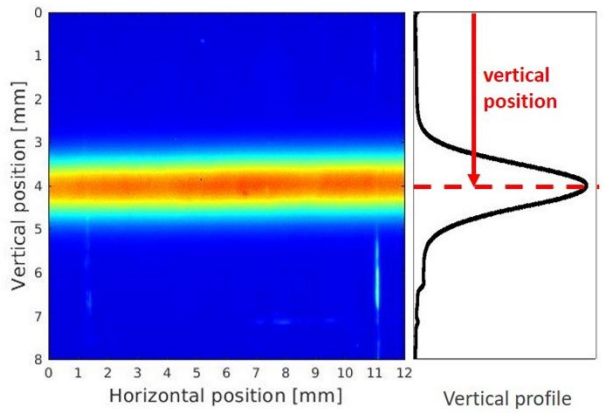


Figure 2: The BM8 X-ray image with 200 mA beam current, 1 ms exposure time, 0 dB gain, 2*2 binning.

The centre of the vertical profile is essentially the vertical X-ray beam position, and the only value of interest to us. It is calculated and stored at 1 Hz and these vertical X-rays positions can then be compared with fully independent readings obtained from a duo of standard electron e-BPMs in the region of the source-points of these BMs. From these 2 e-BPMs both the angle and the position of the electron beam at the BM source-point is obtained, thereby allowing a calculation of the position of the X-ray beam at 23 m distance.

In Fig. 3 is shown the vertical position of the BM8 X-rays as measured by our new X-BPM (purple) and that obtained

Content from this work may be used under the terms of the CC BY 4.0 licence (© 2022). Any distribution of this work must maintain attribution to the author(s), title of the work, publisher, and DOI

ISBN: 978-3-95450-241-7 ISSN: 2673-5350 doi:10.18429/JACoW-IBIC2022-MOP34

Content from this work may be used under the terms of the CC BY 4.0 licence (© 2022). Any distribution of this work must maintain attribution to the author(s), title of the work, publisher, and DOI

from the e-BPMs (blue) over few minutes. Both signals show a sub-µm resolution and are in very good agreement.

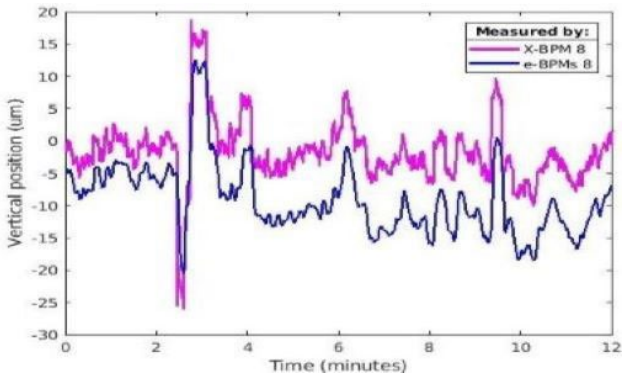


Figure 3: The (BM8) X-rays vertical position measured by the X-BPM and obtained from e-BPMs over few minutes.

In Fig. 4 these same two independent vertical positions of the BM16 X-rays over 15 hours are shown and we can note two issues: (a) the top-up injections (30 min interval) are detected by both devices, but (b) the positions no longer agree and show significant drift.

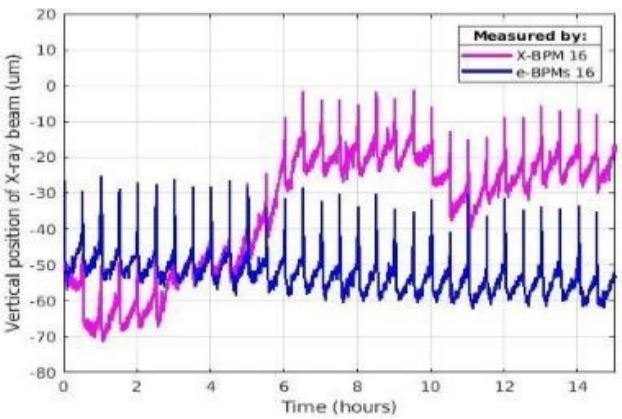


Figure 4: The (BM16) X-rays vertical position measured by the X-BPM and obtained from e-BPMs over 15 hours.

During 2 periods in December and March we could keep the X-BPMs inserted for a full week (the beamline users were exceptionally not taking the X-rays) and this has been very helpful in tracking the origin of these drifts. These are effectively introduced by variations of the temperature of the e-BPM electronics that affect their correct electron beam position readings. These devices being in the orbit control loop means that an angular error (typ. a few µrad) of the beam steering is introduced, which becomes very manifest in the X-BPM being at 23 m distance.

As a consequence, we are now adding a simple but effective temperature stabilization to those cubicles that hold these e-BPM electronics, in particular in those zones that serve the orbit control in bending magnet sources of which the ESRF has 17 in total.

THE HALO MONITOR

The X-rays of a 0.57 T dipole magnet being accessible in the (partial) Front-End module of a non-existing beamline offer us the possibility to install a few simple components to constitute a novice diagnostic that allows to measure the so-called halo population of the electron beam. In this case it concerns the halo in the vertical plane and at a distance of roughly 1 to 3 mm from the central beam-core [3].

Concept and Components

The main components are shown in Fig. 5 in the vertical plane together with the (simplified) trajectory of the X-rays that are emitted from the electrons (at extreme left of the picture) and travel towards the detector (extreme right) which is a two-dimensional X-ray imager read-out by a standard camera. It is important to note that the X-rays from the central beam-core are many orders of magnitude stronger than those emitted from the electrons that make up the weak halo population. The specificity in our concept is to attenuate this powerful X-ray beam by an absorber that is vertically positioned so to intercept that beam.

However, the X-rays of typically 60 keV have a small but not a zero divergence as is supposed in the illustration. In fact, this divergence amplitude is 1E-9 for a divergence angle of 200 µrad. This means that the absorber (at roughly 6 m from the source) needs to positioned at least 1.2 mm below the central axis, so to reduce this unwanted divergence signal to a negligible level compared to the level of the X-rays emitted by the Halo. Consequently, it implies that this system can only detect the halo levels at say 1 to 3 mm distance from the beam-core.

The UHV of the Front-End is separated from the free air further down-stream by a 6 mm Aluminium window. At this point a further (movable) attenuator (1 mm thick Tungsten), provides flexibility in attenuation, and the detector on a two-axis translation stage are situated.

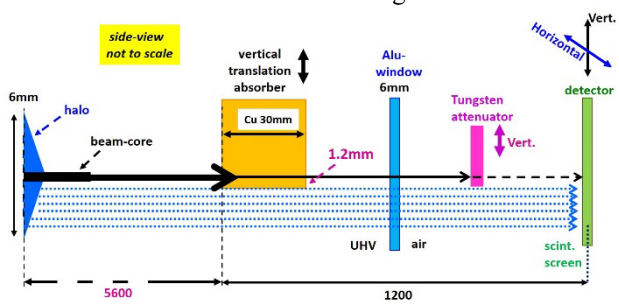


Figure 5: The main components and the paths of the X-rays of both the beam-core and that of the halo population.

The detector is protected by a 5 mm thick lead box, and contains a 2 mm thick LYSO scintillator (15 x 15 mm), a double chicane with 3 mirrors, a set of achromat lenses and a CMOS camera and covers a 8 x 6 mm field of view. The system has given permanent results since its installation in March without any need for repair or maintenance.

Verifications and Calibration

The Fig. 6 shows a typical image (left) and its vertical profile (right). The beam-core signal there is produced by the main beam with its X-rays very strongly attenuated by the 30 mm Copper, the 6 mm Aluminium (although negligible in comparison) and the 1 mm Tungsten. While

ISBN: 978-3-95450-241-7 ISSN: 2673-5350 doi:10.18429/JACoW-IBIC2022-MOP34

for the halo signal beneath, the X-rays are only attenuated by the 6 mm Aluminium window. In the commission period of this device, the edges of the Copper and Tungsten absorber had been correctly positioned vertically, so to satisfy two conditions: a) let the X-rays emitted from the halo signal avoid these absorbers and b) intercept the divergent X-rays emitted from the main central beam so to ensure that these do not create a fake (background) signal in that lower zone where the system is supposed to only measure the genuine halo level. It implies that there is blind zone where the system cannot measure.

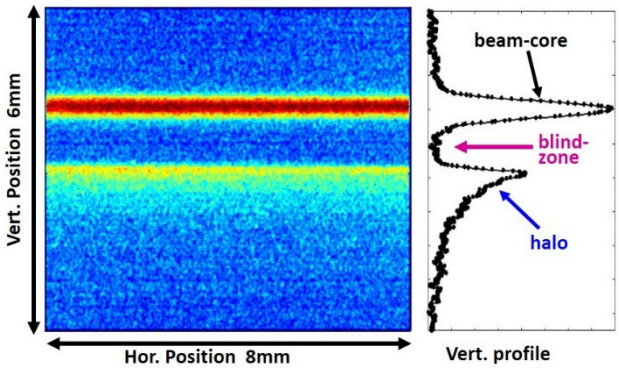


Figure 6: The typical image obtained shows clearly the beam core and the halo (below).

It is important to verify that this signal that we attribute to be the halo is not polluted by some parasitic signal by scattered X-rays, or from an incorrect positioning of the vertical absorber. In our storage ring we can use the vertical scraper to do such verification by positioning this scraper edge very close w.r.t. to the electron beam. By doing this in a relative fast scan, during which the scraper is typically put at distances of 3 to 0.3 mm in steps of 0.1 mm, and by measuring the halo levels at each step with a 1 sec measurement time, we observe the progressive reduction and the final extinction of the halo level in our halo monitor.

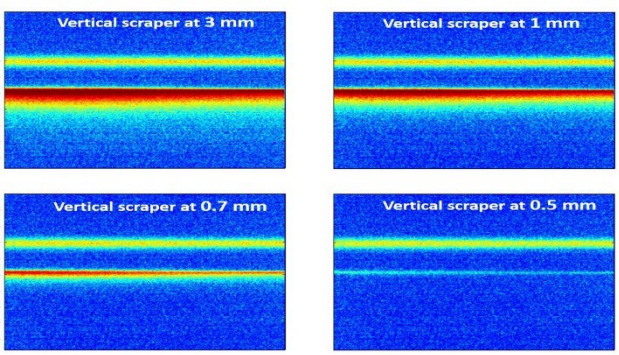


Figure 7: Verification results using the vertical scraper to check that halo signal is not polluted by parasitic signal.

The Fig. 7 (images) and Fig. 8 (profiles) shows the very satisfying results of such verification. At that particular moment and by pure coincidence the UHV vacuum in our ring was strongly impaired which created a strong halo. This explains why the halo signal in this data appears stronger then the beam-core signal.

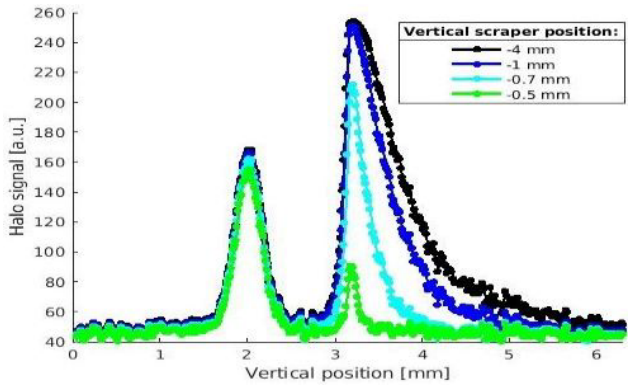


Figure 8: Verification results using the vertical scraper to check that halo signal is not polluted by parasitic signal.

Having the possibility, during dedicated accelerator studies times, to either fully insert, or to fully extract the Cu absorber and W attenuator, allows performing a simple calibration of our detector, by measuring at:
a) low beam current (0.018 mA), the absorber & attenuator withdrawn, and a 2 ms camera's exposure time
b) at nominal (200 mA), the absorber & attenuator inserted, and a 200 ms camera's exposure time.
This yielded an attenuation value of 3E-7 of those X-rays detected from the beam-core w.r.t. those from the halo-population. Applying this calibration to the standard obtained data allows to express the halo-population directly in beam current as shown in Fig. 9.

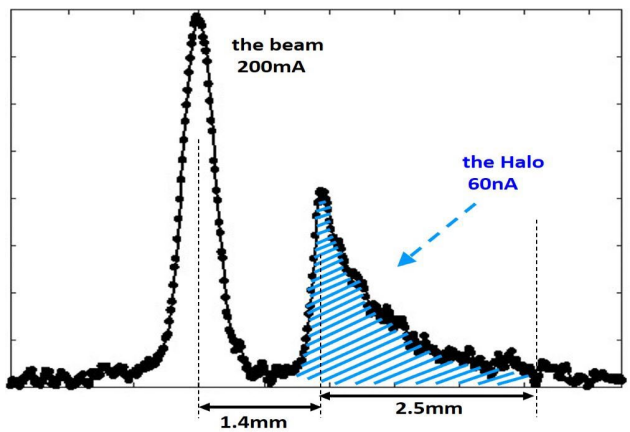


Figure 9: typical results with a calibrated value of halo population expressed in beam current.

Results Under Numerous Beam Conditions

The level of the halo population in an electron ring like our EBS is strongly determined by the scattering rate of which there are two distinct types: a) vacuum scattering due to interaction of the electrons with residual gas molecules and b) Touschek scattering due to the high density in the central beam-core. In Fig. 10 the effect of the latter is shown by operating the beam with 2 different settings of the vertical emittance, i.e. 2 pm·rad and 10 pm·rad. Strictly speaking the Touschek scattering, affecting the electrons essentially in the horizontal plane, show-up on this (vertical plane) halo monitor due to the small but inevitable H-V coupling in the lattice.

Content from this work may be used under the terms of the CC BY 4.0 licence (© 2022). Any distribution of this work must maintain attribution to the author(s), title of the work, publisher, and DOI

ISBN: 978-3-95450-241-7 ISSN: 2673-5350 doi:10.18429/JACoW-IBIC2022-MOP34

Content from this work may be used under the terms of the CC BY 4.0 licence (© 2022). Any distribution of this work must maintain attribution to the author(s), title of the work, publisher, and DOI

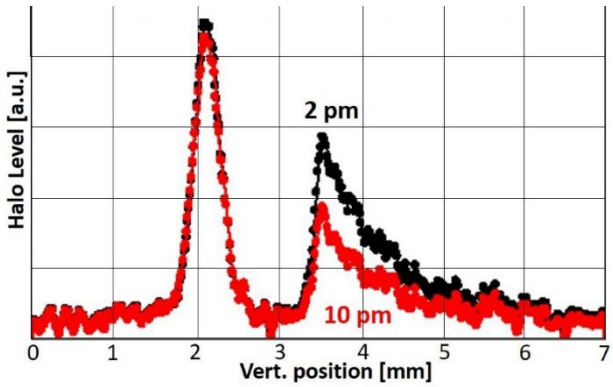


Figure 10: Stronger halo level for lower vertical emittance.

The effect of vacuum quality was assessed very neatly by creating temporarily an impaired local vacuum by switching on one of the titanium sublimators in the ring. The Fig. 11 shows the result of this manipulation.

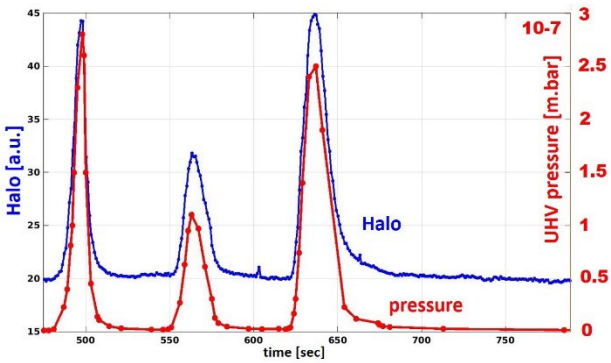


Figure 11: The excellent correlation between the halo level and the vacuum pressure on three specific events.

During normal USM operation the halo signal is conveniently correlated with numerous signals from other diagnostics. An example is shown in Fig. 12.

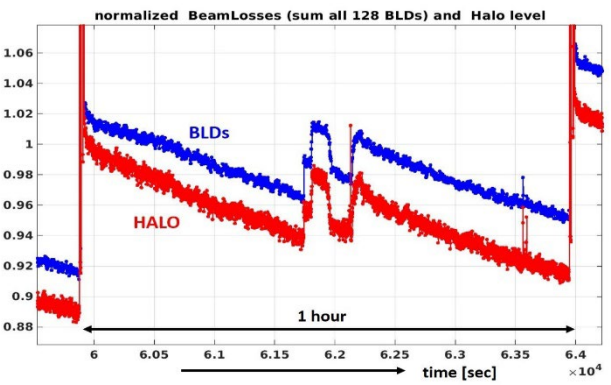


Figure 12: A typical 1 hr recording of the sum of signals of our 128 beamloss detector units and the halo-signal.

CONCLUSION

New X-ray diagnostics were successfully implemented in available Front-Ends: Two optical X-BPMs with µm resolution will be very useful to assess the long-term beam stability. A vertical non-destructive halo-monitor is a novice and very sensitive diagnostics giving additional info on many beam parameters and the vacuum quality.

ACKNOWLEDGMENTS

The authors would like to thank Guillaume Denat, Fouhed Taoutaou and Nicolas Benoist for the design, the support and the maintenance of the two systems. Thanks to the Front End group for the support during installation and the ACU unit for the development of the software applications. Thanks to Hugo Pedroso Marques for the support during the titanium sublimator test. Thanks to the operation group for the MDT time.

REFERENCES

[1] J.-L. Revol *et al.*, "Status of the ESRF-extremely brilliant source project", in *Proc. IPAC'18*, Vancouver, BC, Canada, 2018, pp. 2882–2885. doi:10.18429/JACoW-IPAC2018-THXGBD3

[2] L. Torino *et al.*, "Overview on the Diagnostics for EBS-ESRF", in *Proc. IBIC'19*, Malmö, Sweden, Sep. 2019. doi:10.18429/JACoW-IBIC2019-MOA003

[3] K. B. Scheidt, "Non-Destructive Vertical Halo Monitor on the ESRF's 6GeV Electron Beam", in *Proc. IBIC'14*, Monterey, CA, USA, Sept. 2014, paper MOCYB1, pp. 2-6.

ISBN: 978-3-95450-241-7 ISSN: 2673-5350 doi:10.18429/JACoW-IBIC2022-MOP35

NEW MEASUREMENTS USING LIBERA-SPARK ELECTRONICS AT ESRF: THE HIGH-QUALITY PHASE-MONITOR AND THE SINGLE-ELECTRON

E. Buratin*, P. Borowiec, G. Denat, N. Benoist, J. Jacob, K. Scheidt, F. Taoutaou
European Synchrotron Radiation Facility, Grenoble, France

Abstract

Several new diagnostics have been installed and exploited at the ESRF's new Extremely Brilliant Source (EBS) at the end 2021. A Libera-Spark BPM device has been implemented to measure the phase of Booster and EBS rings, with high resolution and up to turn-by-turn rate. In the Storage Ring we achieved irrefutably the control, injection and measurement of single electron(s) with the use of transfer-line screens, the visible-light extraction system and a low-cost photo-multiplier tube, combined with the commercial Spark Beam Loss Monitor. Further planned developments, like the TCPC technique, on this are on-going and will be essential to verify that our Booster cleaning process reaches a level of zero-electron bunch pollution in EBS.

INTRODUCTION

The Extremely Brilliant Source (EBS) ring is a fourth-generation machine that generates X-rays with a 6-GeV and 200-mA electron beam. The complex chain includes a Linac, a Booster and the EBS ring and it is operational since 2020 at the European Synchrotron Radiation Facility (ESRF) in Grenoble [1].

A large number of diagnostics were used to commission the ring and these devices continue their operation and use for both the User-mode operation (USM) and for studies during the Machine Dedicated Time (MDT) [2, 3].

New diagnostics were implemented recently that exploit to the full the Libera electronics: a beam-phase-monitoring for both the Booster and EBS rings with a Spark-BPM and a single-electron measurement with a Libera Beam Loss Monitor (BLM) [4].

THE PHASE-MONITOR

The measurement of the beam phases of both the Booster and EBS is done by a single Libera Spark, the same model used for the BPMs. With beam phase is defined here the phase relation w.r.t. the ESRF's RF-master source, which is the reference for all cases and results reported here below. This master source is at the heart of both the RF-accelerator system and the distribution of timing signals used for numerous purposes in the ESRF facility.

The principle of using a Spark BPM is similar to a former version that used a Libera-Brilliance-BPM [4]. It uses the so-called I and Q digital signals that are generated on each of the 4 RF input signals. It important to stress that neither the Spark's under-sampling of the rf-frequency (352.2 MHz), nor the internal PLL being a simple software version (quasi-PLL) and therefor wobbly w.r.t. to any external signal to such Spark, does not affect its potential for measuring with high resolution and precision the phase relation between the 4 RF-inputs.

Figure 1 shows the connections of the timing signals and the 4 RF inputs: a) the Booster signal coming from a stripline, b) the EBS-SR signal coming from BPM buttons, and the c) and d) fed by the RF-master-source. For the latter, having 2 identical signals at 2 different inputs allows to assess the resolution of the device.

With an upgraded firmware the Spark now generates directly the phase relations between the 4 RF signal in the SA-stream of 20 Hz.

The I and Q data also being available from triggered buffers, with the turn-by-turn as the fastest rate (355 kHz), also means that the phase information is fully available for studying very fast events.

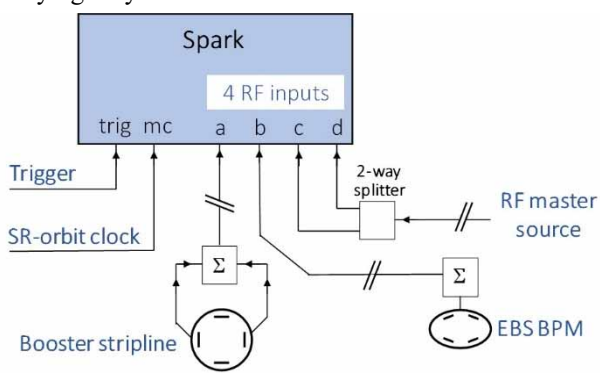


Figure 1: The connections of the phase-monitor.

The Phase Measurement Results, Slow and Fast

The slow (20 Hz) output of the phase monitor is shown in Fig. 2 which shows the phase of the beam under two distinct conditions: the (digital) phase-control-loop in the RF-transmitter system being ON and OFF. This control loop has a (slight) digitization problem that explains the noisy behaviour in the left part of the graph.

The typical resolution with this 20 Hz stream is a few millidegrees.

The device also provides the phase data at the faster rates of 355 kHz and 5.5 kHz (i.e. 2.8 µs and 180 µs sampling time) through triggered buffers. This allows to measure precisely at the injection time and results of this are shown in Figs. 3 and 4.

The green curves in these graphs show the real phase resolution of this measurement monitor, since measured by the device at 2 dedicated channels and in exactly the same manner and at the same time.

* elena.buratin@esrf.fr

Content from this work may be used under the terms of the CC BY 4.0 licence (© 2022). Any distribution of this work must maintain attribution to the author(s), title of the work, publisher, and DOI

ISBN: 978-3-95450-241-7 ISSN: 2673-5350 doi:10.18429/JACoW-IBIC2022-MOP35

Content from this work may be used under the terms of the CC BY 4.0 licence (© 2022). Any distribution of this work must maintain attribution to the author(s), title of the work, publisher, and DOI

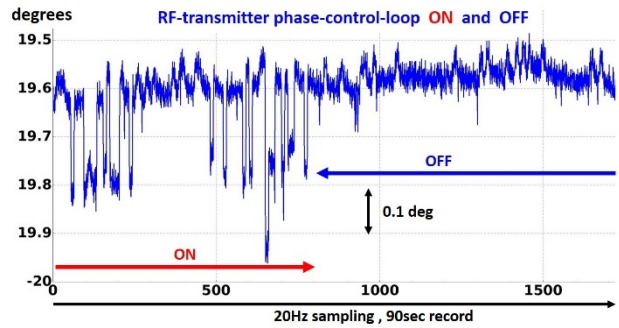


Figure 2: Typical results of the slow phase monitoring.

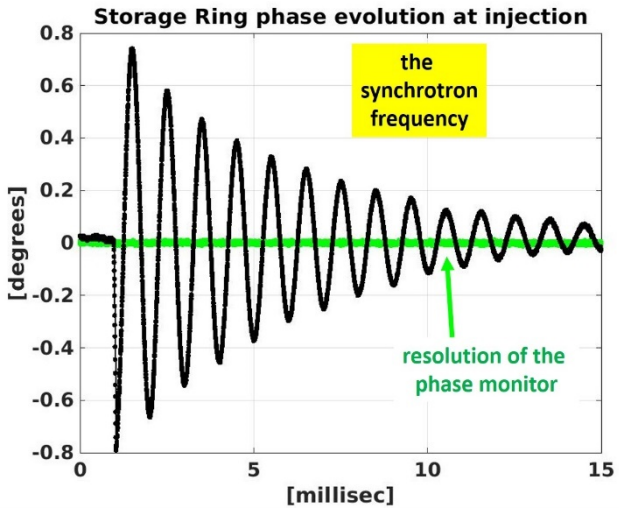


Figure 3: The time-resolved phase at injection.

This data reveals in great details the synchrotron frequency and also the details of our (new) injection scheme with a bump that now starts 50 μs before the injection moment.

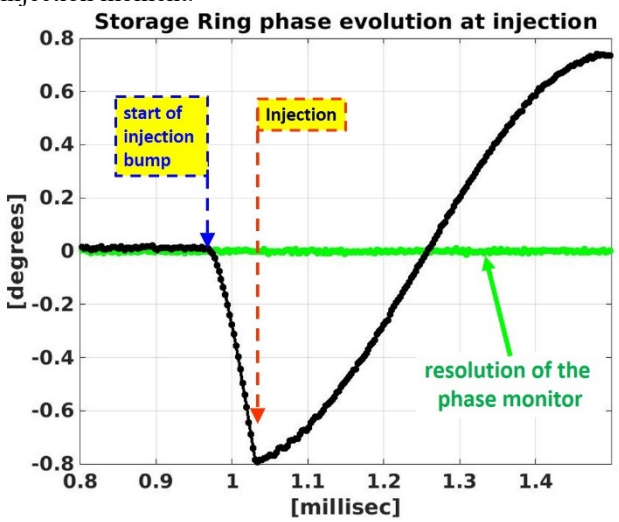


Figure 4: Details of time-resolved phase at injection.

The phase oscillation visible in the time-domain is dominated by the synchrotron frequency. Calculating the frequency spectrum of this yields the red curve shown in Fig. 5.

The exact value of this synchrotron frequency is thus easily and accurately obtained, and it can be measured in dedicated accelerator studies, e.g. as function of the stored beam current, or under different configurations of the RF-cavities. The measurement results of this, together with simulated data is shown in Fig. 6.

To be noted on the black curve in Fig. 5, that is taken a normal decay time, are the spikes at e.g. 100, 150, 300, 600 Hz. These are caused by deficiencies in the power-supply system of some RF klystrons.

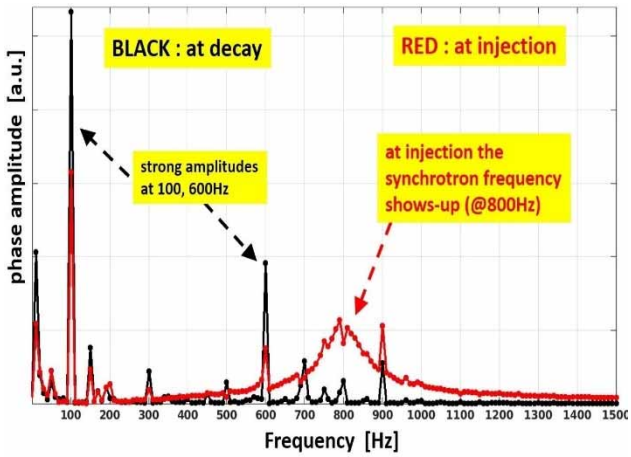


Figure 5: Frequency spectra of the phase, both at injection (red) and during normal decay (black).

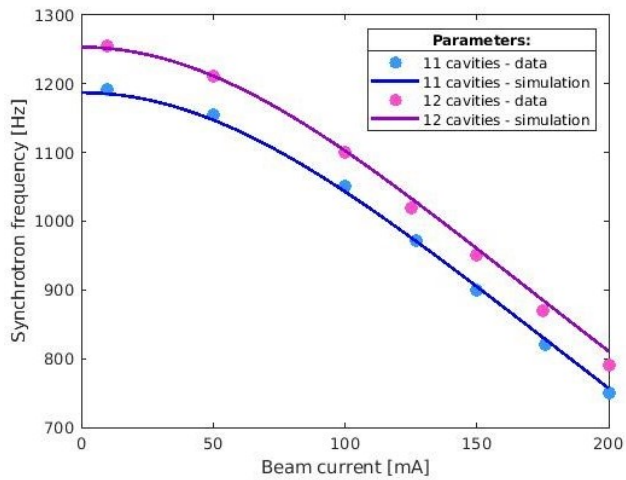


Figure 6: Simulation and measurement results of the synchrotron frequency as a function of beam current.

The Booster Phase Measurement

The same and unique device measures also the time resolved phase of the booster. The 4 Hz Booster has a full cycle of 250 ms, with 135 ms of beam and acceleration time. In Fig. 7 we can observe the high reproducibility of 4 of such consecutive cycles, which shows a swing of about 15 degrees in the middle of the acceleration cycle. These data were taken with 5.5 kHz sampling rate.

In Fig. 8 the details of this are shown, with an oscillatory burst between 80-90 ms after injection. The sampling rate of the monitor here was 355 kHz and this allows to assess that phase oscillation itself with high precision at 13 kHz frequency and 0.5 deg. rms amplitude.

ISBN: 978-3-95450-241-7 ISSN: 2673-5350 doi:10.18429/JACoW-IBIC2022-MOP35

These details are in most cases confirming the theoretical knowledge of the Booster, i.e. the beam dynamics aspects and the functioning of its components like the magnet's ramping power-supplies (RIPS) and the RF-acceleration system.

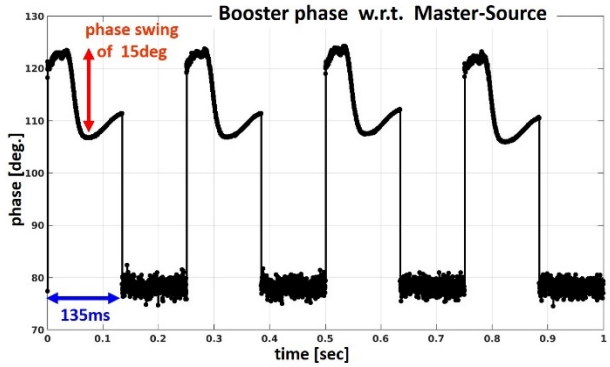


Figure 7: The time-resolved Booster-phase evolution of 4 consecutives injection cycles.

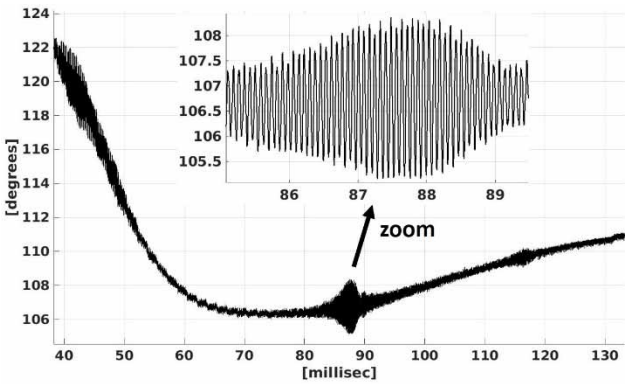


Figure 8: Fine details of the time-resolved Booster-phase.

THE SINGLE-ELECTRON MEASUREMENT

A Libera Beam Loss Monitor (BLM) is used together with a low-cost photomultiplier tube (PMT) and the visible light available in our optics lab for measuring irrefutably a single electron in our EBS storage ring.

The EBS ring has an orbit revolution time of 2.816 µs and it operates with typically 200 mA beam current, which is equivalent to $3.5 \cdot 10^{12}$ electrons. The challenge is considerable to measure the lowest possible beam current which by definition is a single electron. This is obviously far out of range for ordinary current measurement devices.

However, the photon flux produced by synchrotron radiation is huge. This for modern synchrotron light sources in general, and in the visible light spectrum.

The Visible Light Set-Up

In our optics laboratory we have an easy and permanent access to such visible synchrotron light, that is extracted by a system that avoids any major wave-front deformation [5].

The visible light is generated by a 0.62 Tesla dipole magnet and extracted by an in-vacuum water-cooled visible-light mirror that can be completely inserted for low beam currents. That visible light, with roughly 2 mrad of angular divergence extracted in both planes, follows a path through a periscope with 3 mirrors in air, and is conveniently focussed by an achromat (f=3m) onto a compact PMT (model: Hamamatsu 10721-110). The PMT signal is acquired by one channel of the BLM electronics, in integration mode.

The gain of the PMT and the acquisition parameters can be very conveniently controlled by the BLM and thus optimized for this ultra-low level of light detection. In this configuration it can be calculated that, for one single electron stored, the PMT is exposed to about 1500 photons/second, in the 400-700 nm wavelength range.

The Injection and Control of Single Electrons

The production of single electrons in the storage ring is done by operating the injector in a very particular way that is described here below. The injector is comprised of a 200 MeV Linac, a 6 GeV booster synchrotron and 2 transfer-lines. For normal injection this injector delivers about 10^9 electrons at each injection shot, that is working at 4 Hz rate.

For this experiment we need to reduce that to a rate of 1 electron for only every 1000 injections, i.e. 1 electron every 4 minutes. It is to be noted that the above mentioned PMT is a 400 Euros device that is operated in a very ordinary manner, e.g. no cooling etc. Consequently, the noise of this detector is far from ideal and well above the level of 1500 photons/sec. To overcome this, we conveniently operate the BLM with an integration time of several seconds. However, it implies that we need to reduce that single electron injection rate to something significantly slower than that.

This is achieved by operating the our Linac with its gun simply off. In theory this should then never produce any electron at all. However, there is a very small current caused by electrons extracted by the strong electric fields in the Linac acceleration structure. A tiny fraction of these 'parasitic' or 'dark-current' electrons get through into the booster and are then accelerated, extracted and injected into the storage ring. The number of these electrons has been assessed with our device at about 100 electrons per shot. This is still far too much, and in order to reduce this further we use screen monitors in the transfer-line TL2 that simply act like attenuators. The electrons at 6 GeV are not totally affected by these thin screens, and by inserting typically three of such screens we can reduce the injection rate to something like 5 electrons per hour [6].

The Measurement of Single Electrons

The first measurements have been performed in February 2022. The injection chain was continuously injecting at 4 Hz, with Linac gun off, and four TL2-screens were inserted. The PMT was set to 1 MΩ impedance and to 0.7 V gain, and the BLM in integrating mode, with 8-second integration/sampling time to maximize the signal-to-noise ratio.

Figure 9 shows the signal collected over one hour. The five distinctive steps clearly correspond each to the arrival

Content from this work may be used under the terms of the CC BY 4.0 licence (© 2022). Any distribution of this work must maintain attribution to the author(s), title of the work, publisher, and DOI

ISBN: 978-3-95450-241-7 ISSN: 2673-5350 doi:10.18429/JACoW-IBIC2022-MOP35

of an additional electron. Obviously, in the above described method the arrival time of these electrons is subjected to the intrinsic statistical uncertainties and thus totally unpredictable. Some electrons arrived after 4 minutes, some after 15, in this shown record.

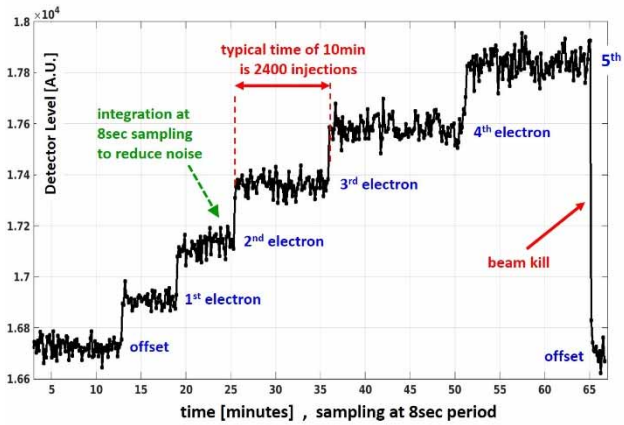


Figure 9: The injection of 1-2-3-4-5 electrons over a time span of 1 hour, measured with 8 sec integration mode.

After one hour we killed the five stored electrons and retrieved the same background level, so temperature effects do not affect this measurement.

The Measurement of Those Undesired Electrons

The above described single-electron set-up has served for some very stringent verifications on the beam filling pattern in the ring. The ESRF has in total 992 RF-buckets for the electrons, but in some particular filling patterns only a few of these are filled (e.g. 16-bunch mode) while all the other buckets should be totally empty.

The above system is limited since it cannot measure if undesired electrons are occupying those buckets that should be empty, if at the same time the good bunches are filled. However, during specific dedicated accelerator studies, we have been able to use it successfully for: (a) the fine-adjustment of some parameters in our dedicated booster bunch-cleaning system and (b) adapting the parameters of the injector's extraction system, like bump amplitude and H-V coupling value, to avoid any untimely extracted electrons to end-up populating buckets that should remain empty.

The above measurement results were confirmed by special detector methods on a user beamline (ID18) that has independent measurement capabilities of detecting close to zero electron pollution levels. In the near future we intend to implement a Time-Correlated-Photon-Counting system so to obtain more flexibility and usefulness in controlling this purity/pollution issue of these undesired electrons.

CONCLUSION

At ESRF, two new Libera-based electronics have been implemented, to constitute two new diagnostics: (1) high performance beam phase measurements with a Spark BPM, and (2) to irrefutably measure beam currents as low as single-electrons using a Spark BLM.

This simple and low-cost high-quality phase-monitor is in permanent operation and very powerful in detecting and studying the slightest phase events, of both slow and fast nature, of the beam in the EBS storage ring.

It has the same functionality and performance for the beam in the Booster.

Extending our capability of beam current measurement down to the challenging single-electron level was successful and has already proven to be useful for some cross-check verifications on the purity issue, which itself is essential for certain specific ESRF user operation modes.

ACKNOWLEDGMENTS

The authors would like to thank the ACU group for the software applications, the Beam-Dynamics and Operation groups for the support during MDT time. Many thanks to the ID18 beamline colleagues for cross-checking the purity levels before and after optimizations.

REFERENCES

[1] J.L. Revol *et al.*, "Status of the ESRF-extremely brilliant source project", in *Proc. 9th Int. Particle Accelerator Conf. (IPAC'18)*, Vancouver, BC, Canada, 2018, pp. 2882–2885. doi:10.18429/JACoW-IPAC2018-THXGBD3

[2] L. Torino *et al.*, "Overview on the Diagnostics for EBS-ESRF", in *Proc. 8th Int. Beam Instrumentation Conf. (IBIC'19)*, Malmö, Sweden, Sep. 2019. doi:10.18429/JACoW-IBIC2019-MOA003

[3] E. Buratin *et al.*, "New applications and studies with the ESRF Beam Loss Monitoring at injection", in *Proc. 10th Int. Beam Instrumentation Conf. (IBIC'21),* Pohang, Rep. of Korea, Sep. 2021, pp. 299–302. doi:10.18429/JACoW-IBIC2021-TUPP35

[4] B. Joly *et al.*, "Upgrade of the beam phase monitors for the injector and the storage ring of the ESRF", in *Proc. 2nd Int. Beam Instrumentation Conf. 2013 (IBIC'13*), Oxford, UK, Sep. 2013, paper WEPC33.

[4] Instrumentation Technologies Libera book, https://www.i-tech.si/wp-content/uploads/2022/06/Libera-Book-2022.pdf

[5] E. Buratin *et al.*, "Results with the Visible Light diagnostics with EBS now in full User-service mode", *DEELS-21*, Jul. 2021, SESAME-Jordan (Indico).

[6] E. Buratin *et al.*, "The SINGLE-electron experiment in the ESRF Storage Ring and future developments to improve bunch pollution measurements", *DEELS-22*, Jun. 2022, HZB Berlin (Indico).

Content from this work may be used under the terms of the CC BY 4.0 licence (© 2022). Any distribution of this work must maintain attribution to the author(s), title of the work, publisher, and DOI

ISBN: 978-3-95450-241-7 ISSN: 2673-5350 doi:10.18429/JACoW-IBIC2022-MOP36

NOVEL BEAM EXCITATION SYSTEM BASED ON SOFTWARE-DEFINED RADIO

P. J. Niedermayer*, R. Singh,
GSI Helmholtzzentrum für Schwerionenforschung, Darmstadt, Germany

Abstract

A signal generator for transverse excitation of stored particle beams is developed and commissioned at GSI SIS18. Thereby a novel approach using a software-defined radio system and the open-source GNU Radio ecosystem is taken. This allows for a low cost yet highly flexible setup for creating customizable and tuneable excitation spectra. Due to its open-source nature, it has the potential for long term maintainability and integrability into the accelerator environment. Furthermore, this opens up the possibility to easily share algorithms for the generation of waveforms across accelerator facilities.

As a first application, the device is used to control the coherence and amplitude of transverse oscillations by excitation in the vicinity of betatron sidebands. It enables measurement of beam parameters like tune and chromaticity. On a longer term, it will be used for more complex tasks such as beam shaping, extraction and automated parameter scans towards these complex processes.

SOFTWARE-DEFINED RADIOS

Software-defined radio (SDR) describes an RF transceiver technology in which signal processing is implemented in software. It is widely used in radio communication systems, but has potential applications in many fields. An SDR typically consists of a frontend with ADCs and DACs, and a backend performing the digital signal processing (DSP). Here, a universal software radio peripheral (USRP) was used as off-the-shelf frontend to generate the RF signals. For implementation of the DSP the open source GNU Radio framework [1] was chosen, which allows to graphically design signal processing flow graphs. The large flexibility and low cost of modification make the device a natural choice not only for prototyping [2], but also for experiments and regular use in the accelerator environment. A general challenge with DSP is the unavoidable processing delay. However, as will be shown in this contribution, modern computer technology and active data flow control enable overcoming this obstacle.

NEW SIGNAL GENERATOR FOR BEAM EXCITATION

For transverse excitation one typically needs two independent signals for the horizontal and vertical plane which are linked to the changing revolution frequency of the accelerated beam. It must also be possible to start the signal by means of a trigger. Figure 1 depicts the working principle of the signal generator meeting these requirements. The USRP digitizes the revolution frequency reference signal (sine with frequency f_{rev}) and receives the trigger (TTL pulse) via the general purpose input/outputs (GPIOs). It streams the data via Gigabit Ethernet to an industrial PC, where GNU Radio performs the DSP. The generated signals are streamed back to the USRP and delivered at the two RF ports.

We use the model N210 and low-frequency daughterboards with parameters listed in Table 1. The DACs provide sampling rates of up to 400 MS/s. In practice, however, this is limited by the data processing rate to about 10 MS/s, allowing to handle and generate frequencies up to 5 MHz.

Table 1: Specification of the USRP N210

Frequency range	0 to 30 MHz
DAC/ADC resolution	16/14 bit (±1 V)
RF ports	2 in- and 2 outputs (50 Ω)
GPIO ports	2 × 16 (TTL)

Minimisation of Signal Delay

The challenge in using an SDR for applications requiring feedback and trigger is to achieve a low signal processing delay. A GNU Radio flow graph consists of blocks performing discrete operations on the signal data stream. The data is processed in chunks and buffered in between these blocks, which improves efficiency but introduces an artificial delay. While GNU Radio is able to optimize buffer usage and data processing to find a trade-off [3], it requires a settling time and is not optimal if a minimal processing delay is crucial. In our application, the data flows from ADC to DAC, which both have a fixed sampling rate. Until the first data sample has been processed by GNU Radio and transmitted back to the USRP, the DAC buffer lacks samples and can not

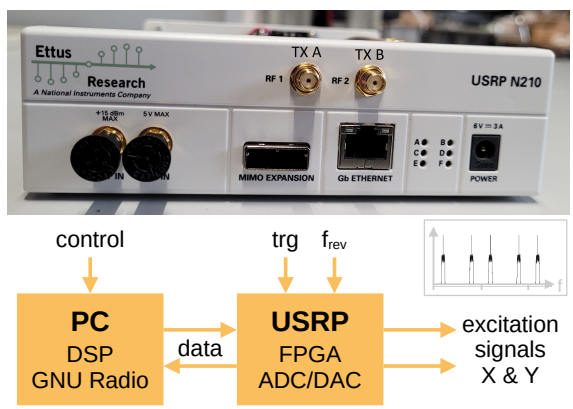


Figure 1: USRP hardware and signal generation scheme.

* p.niedermayer@gsi.de

Content from this work may be used under the terms of the CC BY 4.0 licence (© 2022). Any distribution of this work must maintain attribution to the author(s), title of the work, publisher, and DOI

ISBN: 978-3-95450-241-7 ISSN: 2673-5350 doi:10.18429/JACoW-IBIC2022-MOP36

Content from this work may be used under the terms of the CC BY 4.0 licence (© 2022). Any distribution of this work must maintain attribution to the author(s), title of the work, publisher, and DOI

produce a signal (underrun). While the average processing speed settles to the sampling rate, spikes in the processing time can result in further underruns. Every time this happens, the amount of samples being buffered grows, which, multiplied by the sampling rate, defines the signal delay. Since no samples are ever discarded, their amount never decreases, and the delay can quickly accumulate to several 100 ms without taking action against it.

To reduce the signal delay, two measures were taken: First, the overall processing time of the GNU Radio flow graph was improved by enabling real-time scheduling, generating baseband signals with reduced sampling rate, setting a maximum buffer size and reducing the overall flow graph complexity.

Second, the triggered operation mode allowed to implement active flow control via a novel out-of-tree (OOT) block [4]. Being the last block in the signal processing chain, it can safely discard incoming samples while waiting for a trigger. Thereby, buffers are drained and the amount of buffered samples – and hence the signal delay – is reduced to a minimum. Upon trigger, incoming samples are conveyed to the USRP. To mitigate underruns due to spikes in the processing time, a deterministic number of samples (1 ms) is inserted in front of the actual data stream. In addition, the bursty transmission mode of the USRP is exploited by adding appropriate burst start and end tags to the data stream.

Figure 2 shows how the signal delay between RF in- and output of the USRP was reduced to about 2 ms by implementing these measures. Without modifications to the FPGA image, the trigger level can only be polled, thus introducing the observed jitter which corresponds to the polling rate of 1 kHz. As can be seen by comparing the signal delay at the start and after 5 s, the build-up and accumulation of delay due to underruns is mitigated successfully. There were also no underruns logged by the USRP. The remaining delay is sufficient for the application as described in the next section, but is expected to be improved by using a newer USRP model with support for DSP directly on the FPGA.

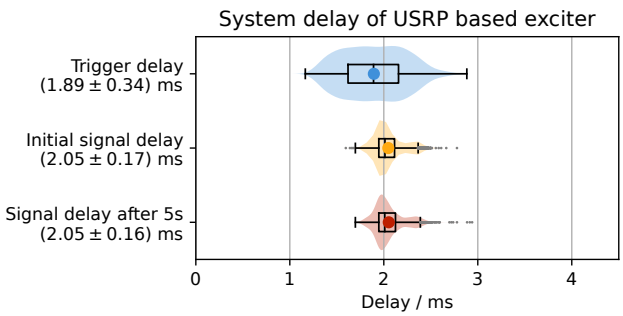


Figure 2: Benchmarking results for triggered signal generation with feedback on an industrial computer (2.1 GHz CPU, 8 cores, 32 GB RAM) running our GNU Radio flow graph at 10 MS/s. Box plots and kernel density estimates are based on 7428 events taken over about 20 hours.

Flow Graph for Signal Synthesis

Several GNU Radio flow graphs have been implemented to generate the excitation signals. The excitation signal of desired type and bandwidth is generated in baseband at a reduced sampling frequency (Fig. 3). Three basic signal types have been implemented (Fig. 4): a binary sequence randomly flipping between ±1 which yields a random binary phase-shift keying (RBPSK) modulation; a band-filtered uniform white noise; and a sinusoidal frequency modulated sine (chirp). The baseband signal is up-sampled and frequency shifted to the desired sidebands of the revolution frequency f_{rev}. The latter is determined from the supplied RF reference signal by means of a phase-locked loop (PLL) to follow the frequency ramp during acceleration, or can alternatively be specified manually by the operator (Fig. 5). Since the excitation bandwidth Δf is constant, the relative width $\Delta q = \Delta f / f_{\mathrm{rev}}$ decreases during acceleration and hence the spectral power density increases. This compensates for the increasing rigidity of the beam.

APPLICATION FOR TUNE AND CHROMATICITY MEASUREMENT

In order to measure the betatron tune using beam position monitors (BPMs), coherence of the betatron oscillations must be established by using transverse excitation [5] at the betatron frequency. Figure 5 shows an excitation flow graph for this purpose, which supports excitation in the vicinity of two distinct betatron sidebands at $(h \pm q) f_{\mathrm{rev}}$ with revolution

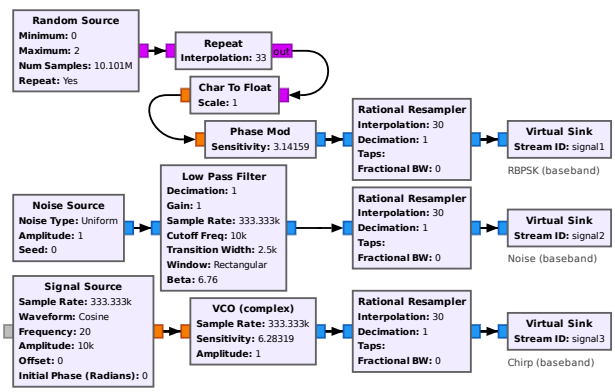


Figure 3: GNU Radio flow graphs for baseband signals.

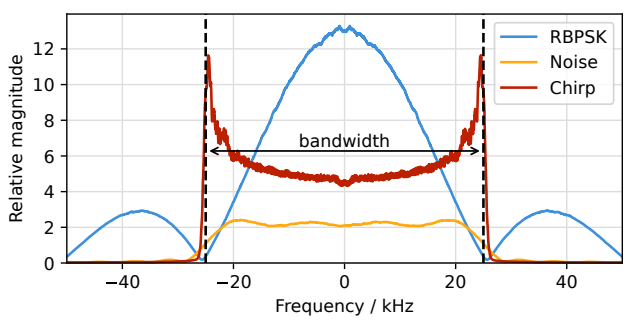


Figure 4: Frequency spectra of baseband signals.

ISBN: 978-3-95450-241-7 ISSN: 2673-5350 doi:10.18429/JACoW-IBIC2022-MOP36

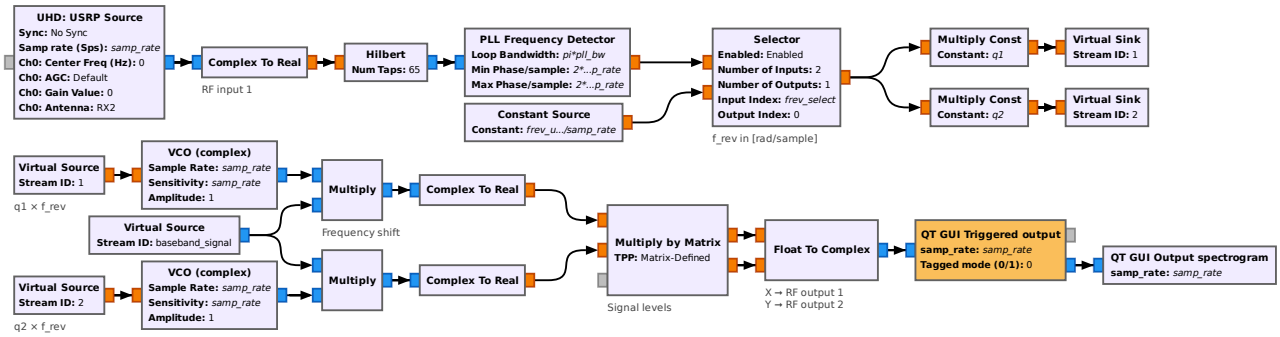


Figure 5: GNU Radio flow graph for excitation of betatron oscillations in both planes. The revolution frequency is recovered from the signal on RF input 1, and the baseband signal is frequency shifted to the respective sidebands corresponding to the tunes q_1 and q_2. The highlighted custom OOT block is used to trigger and deliver the signals to the RF outputs.

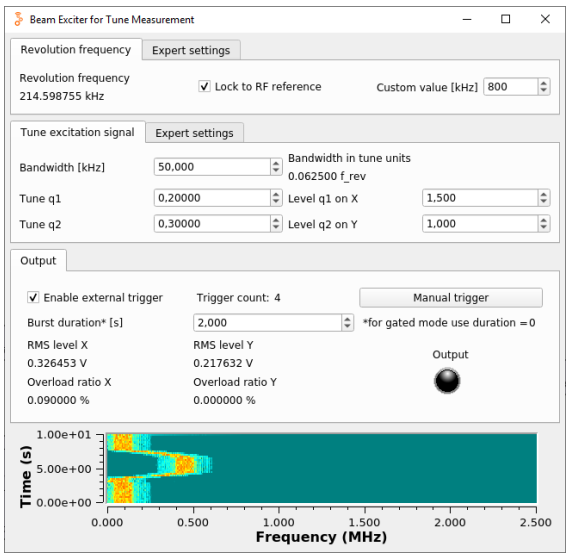


Figure 6: Control interface for tune measurements.

harmonic h and tune q. In the absence of coupling, q_1 and q_2 correspond to the horizontal and vertical tune; but it is also possible to excite a single plane at two distinct frequencies by specifying non-zero crosstalk signal levels. The operator interface built with GNU Radio to run the flow graph and adjust the excitation parameters is depicted in Fig. 6.

For each plane, the generated excitation signal is split by a 180° divider into two signals of opposite polarity, each of which is amplified with a 50 W RF amplifier and transmitted to a stripline unit [6] whose E- and B-fields deflect the beam, their contributions being of the same order of magnitude. In short lens approximation, the resulting angular kick is

$$\Delta x' \approx \frac{E_x}{E\rho} l + \frac{B_y}{B\rho} l \approx \left[\frac{1}{E\rho} \frac{l}{d_x} + \frac{1}{B\rho} \frac{l\mu_0}{\pi R w_x} \arctan\left(\frac{w_x}{d_x}\right) \right] \Delta U$$

where $B\rho = p/q$ and $E\rho = pv/q$ are the magnetic and electric rigidity of the beam, ΔU is the voltage between the electrodes, $l = 37\,\text{cm}$ the electrodes' length, $d_x = 20\,\text{cm}$ or $d_y = 7\,\text{cm}$ their spacing, $w_x = 12\,\text{cm}$ or $w_y = 22\,\text{cm}$ their width before bending and $R = 50\,\Omega$ the impedance.

For the actual measurement of the machine tune, the turn-by-turn beam position is recorded using capacitive shoebox-type pickups and Libera Hadron signal processors [7]. A Fourier analysis then yields the eigenfrequencies of transverse motion normalized to the revolution frequency in the interval $0 < f/f_{\text{rev}} < 0.5$, where the tune is observed as resonance peak. Fractional tunes with $q > 0.5$ are visible at $1 - q$ due to aliasing. Likewise, the tune can be measured as a function of time by using a Short-time Fourier transform (STFT).

The new excitation system was commissioned at the Heavy Ion Synchrotron SIS18 at GSI in May 2022 using a 195.7 MeV/u uranium U^{28+} beam. At this highest rigidity of 18 Tm the maximum deflection angle provided by the excitation system for a sinusoidal signal is $\Delta x' = 0.19\,\mu\text{rad}$ and $\Delta y' = 0.38\,\mu\text{rad}$.

Figure 7 shows the measured tune during injection and acceleration using the new excitation system. The excitation produces a clear response up to the maximum beam rigidity. At 0.25 s the excitation was switched off, resulting in a decay of the tune response as the transverse oscillations are damped and become incoherent. Even for the high ramping

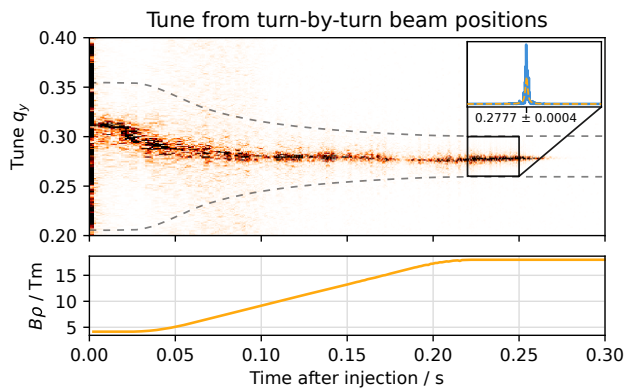


Figure 7: Continuous tune measurement during acceleration using noise excitation with a bandwidth of 16 kHz (dotted lines) and an RMS signal level of 0.088 V (prior to amplification). The bottom plot shows the increasing beam rigidity.

Content from this work may be used under the terms of the CC BY 4.0 licence (© 2022). Any distribution of this work must maintain attribution to the author(s), title of the work, publisher, and DOI

ISBN: 978-3-95450-241-7 ISSN: 2673-5350 doi:10.18429/JACoW-IBIC2022-MOP36

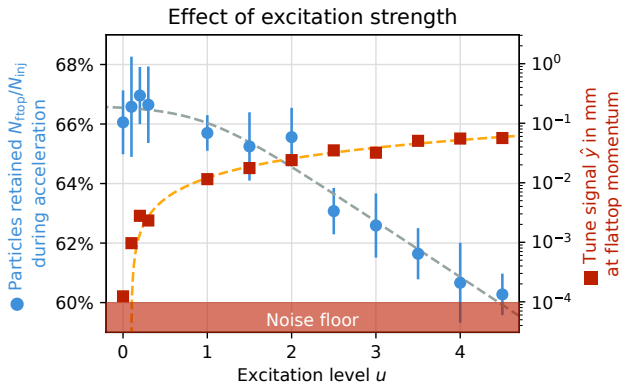


Figure 8: Left: fraction of particles reaching flat-top N_{ftop} versus injected particles $N_{\mathrm{inj}} \approx 2.1 \times 10^{10}$, fitted by a soft-plus function centred at $u_0 = 0.9(4)$. Right: amplitude of betatron oscillation $\hat{y}$ and noise floor $\hat{y}_{\mathrm{noise}} \approx 0.09(1)$ µm, fitted by a linear function with slope $\hat{y}/u = 0.0134(6)$ mm.

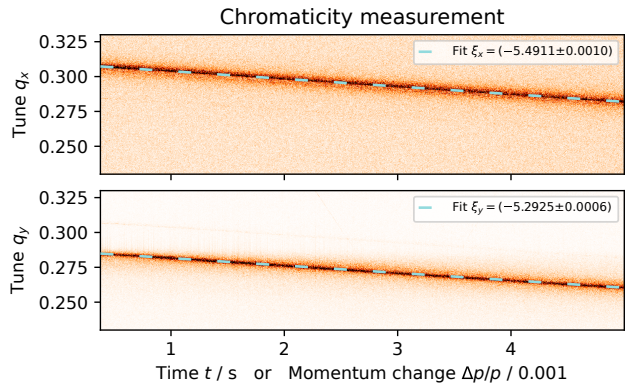


Figure 9: Determination of chromaticity $\xi = \Delta q/(\Delta p/p)$ by continuously measuring the tunes while changing the beam momentum via an RF detuning.

speed of 8 T/s as foreseen for SIS100, the signal delay of 2 ms is non-critical for excitation at the first sidebands: The resulting maximum displacement of the excitation band at the beginning of the ramp was measured to be 0.008 tune units, which is easily compensated by the bandwidth. It was found that excitation at the sideband $0 + q$ also produces the highest signal-to-noise ratio and is therefore preferred for excitation.

Excitation with the RBPSK signal and the bandlimited noise signal showed no systematic difference for the investigated bandwidths; the chirp excitation however was found to be less suitable because of its pulsed response. Compared to the previously used fixed pseudo-random noise generator, the new excitation signal with variable spectral power resulted in a more homogeneous amplitude in the tune spectra throughout the acceleration ramp.

Figure 8 shows the effect of noise excitation strength on the induced beam losses and the achieved tune signal strength. The bunching and acceleration efficiency of the machine as set up for this measurement was about 66 % without excitation. Small excitation levels $u < 0.9$ lead to no additional losses while still producing sufficiently large betatron oscillations for observation of the tune in the spectra. A beam size measurement showed no blow-up beyond the measurement resolution of 2 mm.

The excitation is also used for measurement of the chromaticity $\xi = \Delta q/(\Delta p/p)$. Here, the beam momentum p is changed by detuning the RF cavity frequency with a programmed linear ramp. The resulting tune change is then measured over time as shown in Fig. 9 and the chromaticity is calculated from the linear fits.

FURTHER APPLICATIONS

The new excitation signal generator was also already used successfully for tune measurements at the Experimental Storage Ring ESR of GSI. In addition to tune and chromaticity measurements, the flexibility of the device allows usage for further applications such as Radio Frequency Knock Out (RF-KO) extraction. The feasibility of this approach was first demonstrated at Heidelberg Ion Beam Therapy Center (HIT) [2], and recently also demonstrated at GSI SIS18.

The new developments for usage in feedback systems and triggered applications as described in this article are made available through the repository [4] and can be used and adopted at other facilities. The repository also provides an easy way to share GNU Radio flow graphs for the generation of excitation signals.

ACKNOWLEDGEMENTS

The authors would like to acknowledge Bastian Bloessl and Eike Feldmeier for support with GNU Radio and advice on SDRs. We thank Oleksandr Chorniy for support with Libera Hadron and assistance during beamtimes.

REFERENCES

[1] GNU Radio, https://www.gnuradio.org

[2] E. Feldmeier *et al.*, "Upgrade of the Slow Extraction System of the Heidelberg Ion-Beam Therapy Centre's Synchrotron", in *Proc. IPAC'22*, Bangkok, Thailand, Jun. 2022, pp. 2509–2512. doi:10.18429/JACoW-IPAC2022-THPOST029

[3] B. Bloessl *et al.*, "Benchmarking and Profiling the GNURadio Scheduler", in *Proc. GNU Radio Conference*, Huntsville, AL, USA, Sep. 2019.

[4] Software Radio Beam Exciter, repository available on GSI git, https://git.gsi.de/p.niedermayer/exciter

[5] R. J. Steinhagen, "Tune and chromaticity diagnostics", in *CERN Accelerator School: Course on Beam Diagnostics*, Geneva, 2009. doi:10.5170/CERN-2009-005.317

[6] P. Kowina *et al.*, "Digital base-band tune determination", in *Proc. BIW10*, Santa Fe, NM, USA, May 2010, pp. 341–344.

[7] A. Reiter *et al.*, "Comparison of beam position calculation methods for application in digital acquisition systems", in *Nucl. Instrum. Methods Phys. Res., Sect. A*, vol. 890, pp. 18–27, 2018. doi:10.1016/j.nima.2018.02.046

Content from this work may be used under the terms of the CC BY 4.0 licence (© 2022). Any distribution of this work must maintain attribution to the author(s), title of the work, publisher, and DOI

ISBN: 978-3-95450-241-7 ISSN: 2673-5350 doi:10.18429/JACoW-IBIC2022-MOP37

BEAM POLARIZATION MEASUREMENTS WITH THE REVISED COMPTON POLARIMETER AT ELSA

M. Switka*, K. Desch, D. Elsner, Physikalisches Institut, University of Bonn, Germany
W. Hillert, Institut für Experimentalphysik, University of Hamburg, Germany

Abstract

The Compton Polarimeter at the ELSA 3.2 GeV storage ring has been designed to measure the polarization degree of the stored electron beam by analyzing the profile of the backscattered gamma-beam with a silicon microstrip detector. Utilizing a scattering asymmetry from interaction with circularly polarized laser light, the electron beam polarization is determined from the vertical shift of the gamma-beam's center of gravity in respect to the handedness of the laser light. The installation of a new laser source and silicon strip detector has improved the polarimeter's performance significantly. Additionally, the profile analysis could be enhanced by using a Pearson type peak function fit. The analyzing power was determined through the observation of the Sokolov-Ternov effect and a statistical measurement accuracy of 2% could be obtained within 5 minutes of measurement time. The polarimeter resolves the expected spin dynamical effects occurring in the storage ring and has shown to be a robust and reliable measurement system for operation with the GaAs source for polarized electrons.

INTRODUCTION

Electron beam polarimetry based on the Compton effect has been successfully performed at multiple laboratories operating with spin-polarized beams. However, the approach to determine the beam polarization from a profile analysis of the backscattered photons is to our knowledge unique at ELSA [1]. The backscattered beam profile has a polarization-dependent vertical asymmetry which results in a shift of the profile's center of gravity $\bar{z}$ under photon beam helicity change (left to right-handed or vice-versa):

$$\Delta z = \bar{z}_L - \bar{z}_R = \mathcal{D} \cdot \mathcal{P}_e \cdot S_3 \,, \tag{1}$$

where $\mathcal{D}$ is the analyzing power of the polarimeter, S_3 the degree of circular photon polarization and $\mathcal{P}_e$ the electron polarization degree parallel or anti-parallel to the magnetic bending field. Simulations for ELSA [2] show that $\mathcal{D} \gtrsim 70\,\mu\text{m}$ for a detector 15 m away from the photon-electron interaction point. Hence, we use a silicon microstrip detector with sufficient vertical resolution to measure the backscattered beam profile to obtain the polarization degree of the electron beam.

THE COMPTON POLARIMETER

Optical System and γ-Beam Detector

Circularly polarized laser photons of 532 nm wavelength are focused onto the center of a defocusing quadrupole magnet (compare with Fig. 1), where the transverse electron beam profile has minimum ellipticity $\sigma_z/\sigma_x = 0.69$ to 0.44 between 1.2 GeV to 3.2 GeV.

With an **optical system** [3] the beam waist can be varied from $\omega_0 = 0.66$ mm to 1.6 mm to match the transverse size of the electron beam. As photon source a cw laser with 18 W beam power is used, of which approx. 14 W were measured to be available at the interaction point. The helicity of the photon polarization can be changed through pneumatically driven rotatable $\lambda/4$ waveplates. The degree of circular polarization is measured before the beam dump.

The **detector** [4] for the backscattered photons with up to 328 MeV energy consists of a lead converter target in front of an in-house developed silicon microtrip detector. With 768 vertically distributed 13-bit channels at 50 µm pitch it yields a resolution of $\Delta z_b = 14\,\mu\text{m}$.

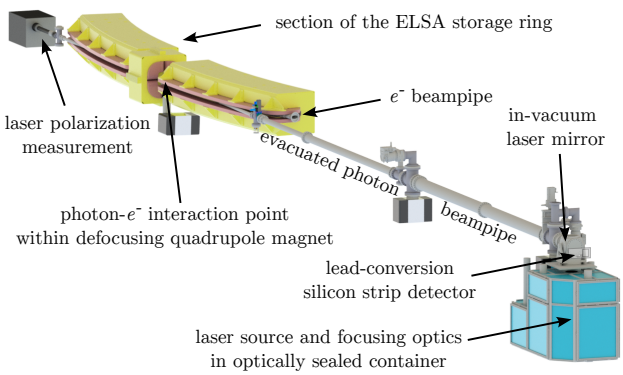


Figure 1: Compton polarimeter at ELSA: A cw laser beam of circularly polarized photons is focused onto the center of a quadrupole magnet. The backscattered γ-photons from head-on collisions with stored electrons are detected by a microstrip detector with vertical resolution.

Backscattered Beam Profile and Function Fit

An exemplary measured vertical photon profile which backscattered off a 1.3 GeV electron beam is shown in Fig. 2. While the measurands $\bar{z}_L$ and $\bar{z}_R$ can be obtained by determining the distribution's mean ("center of gravity"), this approach was found to be prone to the influence of stray radiation and statistical count fluctuation [3]. A more robust method includes a data fit to a conformable function, such as the Pearson type IV distribution:

$$P_{IV}(x) = h \cdot \left[1 + \left(\frac{x - x_0}{s}\right)^2\right]^{-l} \cdot \exp\left[-\nu \cdot \arctan\left(\frac{x - x_0}{s}\right)\right] \tag{2}$$

* switka@physik.uni-bonn.de

Content from this work may be used under the terms of the CC BY 4.0 licence (© 2022). Any distribution of this work must maintain attribution to the author(s), title of the work, publisher, and DOI

ISBN: 978-3-95450-241-7 ISSN: 2673-5350 doi:10.18429/JACoW-IBIC2022-MOP37

Content from this work may be used under the terms of the CC BY 4.0 licence (© 2022). Any distribution of this work must maintain attribution to the author(s), title of the work, publisher, and DOI

For $\nu = 0$ the distribution holds no skewness and it is called Pearson type VII. As indicated by the residuals

$$e(x) = y(x) - f(x)$$

between model $y(x)$ and fit to model data $f(x)$ in Fig. 2 (bottom), the skewness is non-zero and should be accounted for in the model. However, in practice the number of free parameters in Eq. (2) or in a spline fit reduces the robustness of the method and it has shown that a fit to the Pearson type VII distribution determines the measurand most reliably [3].

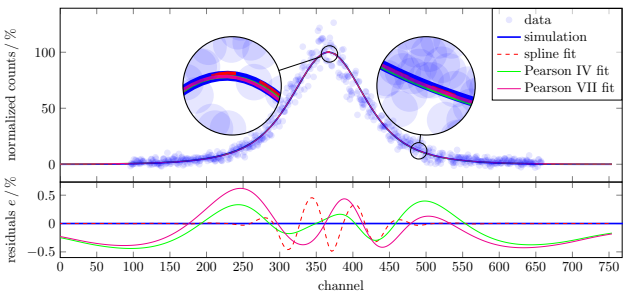


Figure 2: Measurement data compared to simulation data, on which different fit algorithms are applied. Their goodness is here indicated by the magnitude of the residuals.

A measurement with source-polarized 1.32 GeV electrons is shown in Fig. 3. Therein, electrons with alternating helicity are injected into the storage ring for a typical spill cycle interval of approx. 6 s. The photon distribution is analyzed accumulatively and the measurand visualized for the different electron spin helicities ($\Delta z_{e\uparrow}$ and $\Delta z_{e\downarrow}$) as well as the mean of their absolute values

$$\Delta z_{e\downarrow\uparrow} = \left(|\Delta z_{e\uparrow}| + |\Delta z_{e\downarrow}|\right)/2 \,.$$

While $\Delta z_{e\downarrow\uparrow}$ engages the vicinity of its final value within a minute of measuring time, it remains within the decreasing statistical error boundaries, especially when the Pearson VII fit function is chosen. This behavior was observed for the majority of measurements perforemed in the scope of [3], allowing the Compton polarimeter to be used for "quick measurements", when spin-related machine parameters are to be optimized or *scanned*.

Polarimeter Calibration

The analyzing power of Eq. (1) is measurable via the Sokolov-Ternov effect [5] (self-polarization) occurring for stored electron beams:

$$\mathcal{P}_e(t) = \mathcal{P}_\infty \left(1 - e^{-t/\tau}\right) \quad \equiv \quad \Delta z(t) = \Delta z_\infty \left(1 - e^{-t/\tau}\right) \,.$$

A data fit to the exponential increase of beam polarization $\mathcal{P}_e(t)$ determines the time constant τ and equilibrium polarization $\mathcal{P}_\infty$. It is noteworthy that $\mathcal{P}_\infty$ is beam-energy dependent, as depolarizing mechanisms occur at different magnitudes for different spin-tunes (compare e.g. with [3,6]). Calibration measurements are to be carried out where $\mathcal{P}_\infty$ is

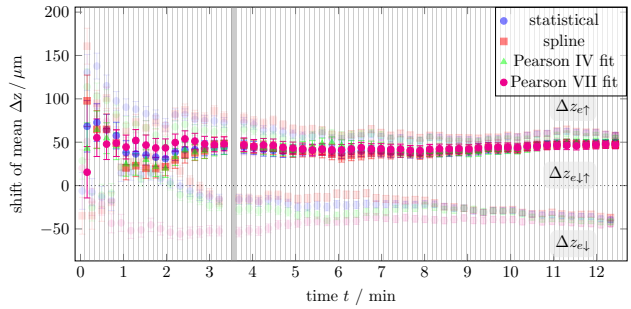


Figure 3: Measurement of the shift in the means Δz of alternatingly polarized 1.32 GeV electrons with different profile analysis methods. The gray background indicates inhibited time intervals which occur during storage ring injection or due to erroneous machine spills.

expected to be $\approx 92.38\%$ and where τ is in the order of minutes (e.g. > 2.2 GeV). The polarimeter's effective analyzing power

$$\mathcal{D} = \frac{\Delta z_\infty}{\mathcal{P}_\infty \cdot \mathcal{P}_\gamma}$$

also includes the finite degree of circular photon polarization $S_3 = \mathcal{P}_\gamma = (98.03 \pm 0.02)\%$ and was determined to amount

$$\mathcal{D}_{\text{eff}} = \mathcal{D} \cdot \mathcal{P}_\gamma = (60.0 \pm 8.8)\,\mu\text{m}/100\% \qquad (3)$$

for a calibration measurement at 2.73 GeV, as shown in Fig. 4. The rather large measurement error is to be reduced in the future by further measurements and therewith systematic studies of the energy-dependency of depolarizing effects.

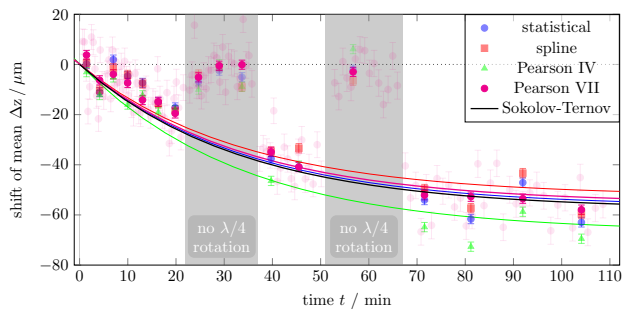


Figure 4: Self-polarization of a stored electron beam (Sokolov-Ternov effect), where the backscattering profile is analyzed through different methods. The solid dots represent time-averaged data of the individual opaque measurement nodes. The polarimeter functionality was verified with halted $\lambda/4$ waveplate rotation (gray background) which resulted in a sufficiently precise null-measurement.

Measurement Error

The polarimeter measurement error is given by

$$\Delta \mathcal{P}_e = \sqrt{\underbrace{\left(\frac{1}{\mathcal{D}_{\text{eff}}}\Delta(\Delta z)\right)^2}_{\text{statistical}} + \underbrace{\left(\frac{\Delta z}{\mathcal{D}_{\text{eff}}^2}\Delta \mathcal{D}_{\text{eff}}\right)^2}_{\text{systematic}} + \dots} \,, \qquad (4)$$

ISBN: 978-3-95450-241-7 ISSN: 2673-5350 doi:10.18429/JACoW-IBIC2022-MOP37

where the systematic error is assumed to be dominated from the calibration procedure (compare with Eq. (3)). The statistical error is depending on the total signal count N, the distribution's standard deviation σ, the strip resolution Δz_b and the distribution's shape, given by the individual detector counts n_i:

$$\Delta\bar{z} = \sqrt{\frac{\sigma^2}{N} + \Delta z_b^2 \cdot \frac{\sum_i n_i^2}{N^2}} \,.$$

The obtainable detector count rate depends on the stored beam current, the available laser power, and on how well the laser beamline is adjusted. Typically it amounts approx. 250 Hz/(W · mA). Therewith, a statistical accuracy of 2% could be achieved within 5 minutes and 1.4% within 15 minutes of measuring time. The scattering rate scales somewhat with beam energy, as shown in Fig. 5.

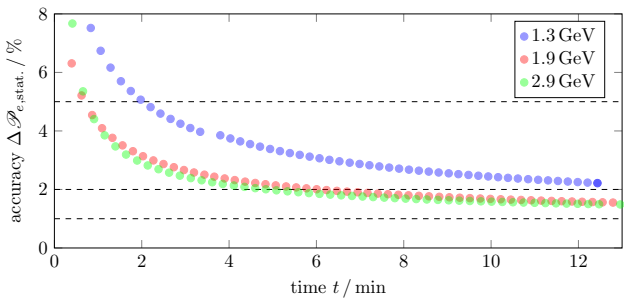


Figure 5: Statistical error in dependence of measuring time for different electron beam energies.

POLARIZATION MEASUREMENTS

The polarimeter performance is well demonstrated by observing the beam polarization degree in dependence of spin-rotating effects. For example, a solenoid field was applied in the transfer beamline between 50 kV polarizing GaAs source [1] and linear accelerator, acting as spin rotator, where complete loss of beam polarization is expected at ±90° (spin precession axis perpendicular to bending field). As shown in Fig. 6, the measureand Δz and its statistical error agrees well with the expected dependancy on the spin rotation angle.

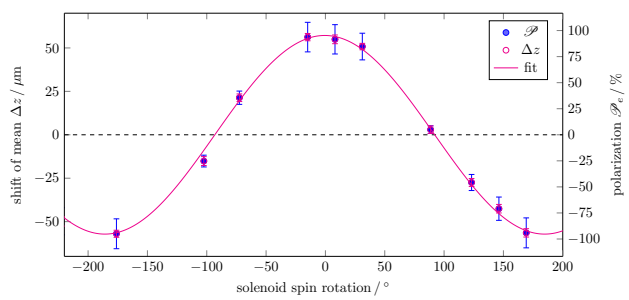


Figure 6: Measured beam polarization in the storage ring (uncalibrated and calibrated) as function of spin rotation angle by application of an additional solenoid field in the transfer beamline behind the polarizing source.

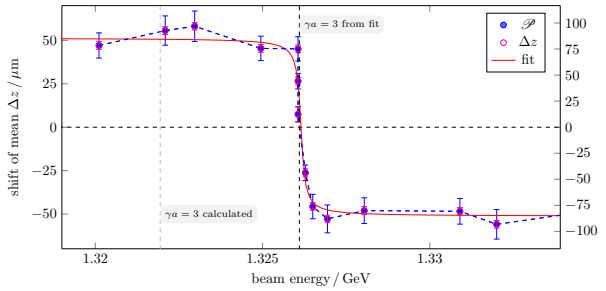


Figure 7: Measured spin-flip around a depolarizing imperfection resonance $\gamma a = 3$. The difference between measured and calculated resonance energy indicates a slight deviance of set and actual electron beam energy.

Polarization measurements were performed in the vicinity of the $\gamma a = 3$ imperfection resonance (a being the anomalous magnetic dipole moment), as shown in Fig. 7. Therein, a spin flip is observable after crossing the resonance, whose impact was artificially increased by applying slight orbit misalignments. The difference between calculated and observed resonance energy suggests a minor deviance of the storage ring's beam energy calibration.

CONCLUSION

We successfully demonstrated the operation of the Compton polarimeter at ELSA. The achievable statistical precision shows that reliable polarization measurements of stored electrons can be performed and spin-dynamical effects are well observable within minutes. The systematic error due to calibration of the analyzing power is expected to be improved with further self-polarization measurements.

REFERENCES

[1] W. Hillert *et al.*, "Beam and spin dynamics in the fast ramping storage ring ELSA", *EPJ Web Conf.*, vol. 134, p. 05002, Jan. 2017. doi:10.1051/epjconf/201713405002

[2] W. Hillert *et al.*, "Compton Polarimetry at ELSA", *AIP Conf. Proc.*, vol. 1149, p. 1160, Aug. 2009. doi:10.1063/1.3215612

[3] M. Switka, "Photon based electron beam analysis at ELSA utilizing synchrotron radiation and Compton scattering", Ph.D. thesis, Phys. Dept., University of Bonn, Bonn, Germany, 2020. https://nbn-resolving.org/urn:nbn:de:hbz:5-60334

[4] R. Zimmermann, W. Hillert, and J. C. Wittschen, "A New Counting Silicon Strip Detector System for Precise Compton Polarimetry", in *Proc. IPAC'11*, San Sebastian, Spain, Sep. 2011, paper TUPC074, pp. 1171–1173.

[5] A. Sokolov and I. Ternov, "Ch. 21.3", in *Radiation from Relativistic Electrons*, C Kilmister, Ed. New York, NY, USA: American Institute of Physics, 1986.

[6] D. Barber *et al.*, "The HERA polarimeter and the first observation of electron spin polarization at HERA", *Nucl. Instrum. Methods Phys. Res., Sect. A*, vol. 329, no. 1, p. 79, 1993. doi:10.1016/0168-9002(93)90924-7

Content from this work may be used under the terms of the CC BY 4.0 licence (© 2022). Any distribution of this work must maintain attribution to the author(s), title of the work, publisher, and DOI

ISBN: 978-3-95450-241-7 ISSN: 2673-5350 doi:10.18429/JACoW-IBIC2022-MOP38

BEAM PROFILE MONITORING AND DISTRIBUTED ANALYSIS USING THE RabbitMQ MESSAGE BROKER

D. Proft*, K. Desch, D. Elsner, F. Frommberger, S. Kronenberg, A. Spreitzer, M. Switka
Physikalisches Institut, University of Bonn, Germany

Abstract

The ELSA facility utilizes several digital cameras for beam profile measurements on luminous screens and synchrotron radiation monitors. Currently a multitude of devices with analog signal output are being replaced in favor of digital outputs, preferably with data transfer via Ethernet. The increased network traffic for streaming, analyzing, and distribution of processed data to control system and machine operators is managed through a supplementary camera network in which distributed computing is performed by the `RabbitMQ` message broker. This allows performant and platform-independent image acquisition from multiple cameras, real time profile analysis, and supports programming interfaces for `C++` and `Python`. The setup and performance of the implementation are presented.

INTRODUCTION

As in most facilities the beam images at ELSA [1] are obtained through several different observation techniques via synchrotron radiation or luminous screens based on fluorescence, intensified phosphorescence or transition radiation. Thereby numerous camera systems from various manufacturers are in use, whose data acquisiation and transfer techniques are based on different interfaces. In practice, this makes it difficult to grant reliable and permanent access to all imaging systems for operators or control system algorithms, especially when hardware from different decades with individual digitizers, software, and software platforms are required. In the following we present an approach of unifying the various image streams to provide more reliable and uniformly accessible beam image data for beam observation, profile analysis, beam parameter measurements, and hence, machine optimization.

IMAGING HARDWARE

Cameras With Analog Output

The prevalent form of imaging has been based on cameras with analog output signals (e.g. *composite video*), which served its purpose for basic adjustment procedures, such as beam alignment. However, the analog signals are usually transmitted over long coaxial lines to distant video multiplexers and digitizers and are prone to interference with a multitude of disturbing signals from the accelerator environment. In those setups the requirements for quantitative beam profile measurements with adequate precision are rarely met due to visual defects from transmission or imperfect exposure settings, as shown in Fig. 1 a). In addition, multiple digitizer cards installed at different work stations suffer from aging and incompatibility with modern operating systems. Some images are not digitized at all and broadcasted to a screen in the control room, lacking the advanced capability for processing by computer vision algorithms.

Cameras with Digital Output

The usage of cameras with digital signal output overcomes the above mentioned issues and the *GigE Vision* communication interface allows for cameras to be conveniently connected through a network of Ethernet switches allowing bi-directional communication between camera and accelerator control system (e.g. to set shutter time or frame rate). In this configuration power can be provided over the Ethernet cable itself (PoE), implying convenient hardware connectivity up to 100 m away from a network switch (compare with Fig. 1 b)). This is especially useful for temporarily installed monitoring cameras, which only require an Ethernet cable (e.g. on a reel) to function. As explicated below, cameras with *GenICam* interface allow good software connectivity.

Some camera systems often operate through enclosed, proprietary software environments running on dedicated computers, such as a streak camera (see Fig. 1 c). Usually, data transfer and device control inferfaces via TCP/IP protocol are availble and the computers can be used as image servers, whose data stream is manageable through prevalent programming environments such as *Python* or *C++*. This way any computer operating digitizer cards (*framegrabber*) can be integrated into the camera network.

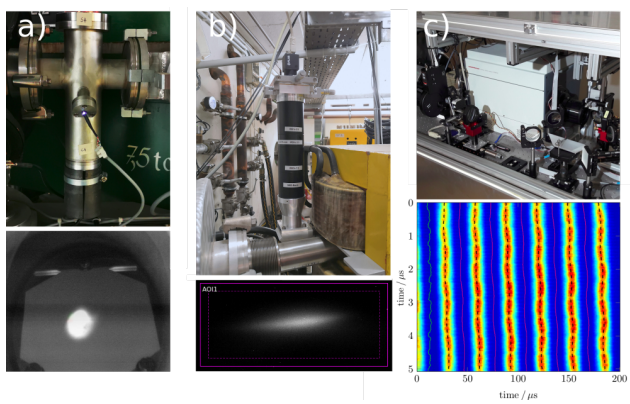


Figure 1: Examplary hardware and corresponding beam images: a) chromox screen monitor with saturated image and visual defects from analog signal, b) synchrotron radiation monitor equipped with Ethernet camera, c) streak camera as bunch train monitor with analyzed image (tune measurement).

* proft@physik.uni-bonn.de

Content from this work may be used under the terms of the CC BY 4.0 licence (© 2022). Any distribution of this work must maintain attribution to the author(s), title of the work, publisher, and DOI

ISBN: 978-3-95450-241-7 ISSN: 2673-5350 doi:10.18429/JACoW-IBIC2022-MOP38

Camera Network

To protect the accelerator control system and its process network from data traffic overload when *GigE Vision* cameras and other devices are connected, a separated network infrastrucuture of multiple gigabit Ethernet switches with power over Ethernet (PoE) capability are installed throughout the facility, where long distances are bridged via switches with fibre transmission capability. The accelerator process network is connected to the camera network through a gateway computer whose outgoing data traffic contains only selected information, such as size- and rate-reduced image streams or numeric fit results.

Magnification Calibration

The individual optical system of a beam monitor determines the image magnification and hence, the calibration ratio of pixel to object size, which can be as simple as a single factor. In the case of luminous screens, which are typically mounted under an observation angle of 45°, in most cases the warped image yields an image magnification as function of one transverse position (compare with Fig. 1 a)). In addition, digitizers may change the resolution of the original broadcast for lines or columns separately.

FGrabbit FRAMEWORK

`FGrabbit` is a distributed image acquisition and analysis framework for beam profile monitoring developed for ELSA. It supersedes the multitude of individually developed solutions — internally called *Framegrabber* — for the different monitoring stations spread around the accelerator facility. The development goal was to build one common software environment for all monitoring stations where only the interface to the corresponding hardware (camera) is device dependent. Emphasis was laid on a *distributed* system for network and CPU load balancing.

Message Broker & Concept

The fundamental building block is the `RabbitMQ`[1] message broker software, that is utilized to distribute *messages* to a number of software tools for further processing. These messages contain either raw or calibrated image data with sizes of up to 10 MiB per frame, or analysis results in the form of e.g. parameters of typically two-dimensional profiles.

Several instances of `RabbitMQ` running on different machines (called *nodes*) form a cluster and allow message distribution between each other. This way, transparent access to camera data is possible from every node. Furthermore, each node takes care of one or more cameras and usually the complete processing chain involved: processing of raw images to calibrated images, preparation of fits to user-selectable profiles and execution of the corresponding fit algorithms. Limiting the processing chain to only one machine reduces the network traffic drastically, as raw image data remains on the same machine. Nevertheless, multiple machines can take part, if e.g. more processing power is required.

The processing scheme for each node is shown in Fig. 2. The different steps are explained in detail in the following.

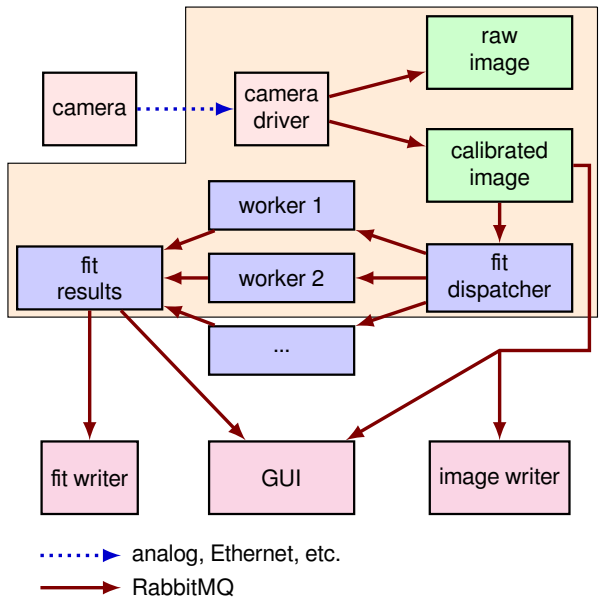


Figure 2: Schematic sketch of processing chain usually taking place on a single node (orange). The chain consists of image acquisition (red), provisioning of raw and calibrated images (green) and fitting (blue). User applications typically access the data from any node (magenta).

Image Acquisition

For the wide variety of cameras and image acquisition systems individual *camera drivers* were implemented. Most of the existing analog video capture cards from many different vendors are incompatible to modern PC hardware. The pre-existing image acquisition software was extended to stream the raw images via a compressed TCP/IP connection to a server application acting as camera driver for these devices. *video4linux* (e.g. USB and HDMI capture devices) and *GigE Vision* devices are natively included in the drivers — the latter also via the *harvesters* `Python` library (see below).

Image Calibration

A distinct calibration needs to be carried out for each of the stations. Hence, a regular checkerboard pattern (with up to 15 × 15 fields) with edge length of up to typically 5 mm is temporarily installed as screen and captured by the imaging system including the specific camera. To account for the tilt angle of 45° that the screen is mounted in relation to the camera (see Fig. 3), one transverse dimension of the calibration pattern is stretched by a factor of $\sqrt{2}$. For the calibration procedure a performant, reliable computer-vision based approach is used, where a sequence of raw camera images is captured, the corresponding positions of the inner edges of the checkerboard pattern are derived, averaged and

[1] Open source message broker: `https://www.rabbitmq.com`

Content from this work may be used under the terms of the CC BY 4.0 licence (© 2022). Any distribution of this work must maintain attribution to the author(s), title of the work, publisher, and DOI

ISBN: 978-3-95450-241-7 ISSN: 2673-5350 doi:10.18429/JACoW-IBIC2022-MOP38

Content from this work may be used under the terms of the CC BY 4.0 licence (© 2022). Any distribution of this work must maintain attribution to the author(s), title of the work, publisher, and DOI

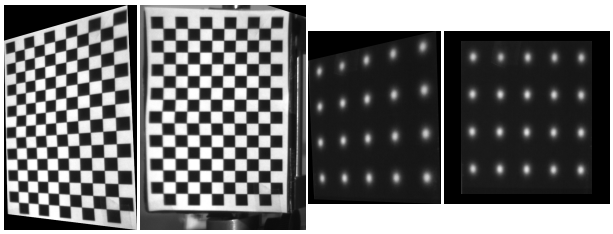


Figure 3: Left two images: Checkerboard pattern used for calibration as raw image from camera (left) and resulting calibrated image (right). Right two images: Test pattern with 5 × 4 Gaussian profiles as raw image (left) and calibrated image (right)

then mapped to the respective real world coordinates. With *openCV*'s 3D reconstruction and camera calibration capabilities [2] the corresponding 3x3 homography transformation matrix M_h and translation matrix T is derived and stored as a calibration data set within FGrabbit's configuration subsystem. Image coordinates $\vec{x}'$ can now be projected to real world coordinates $\vec{x}''$ using

$$\vec{x}'' = T \cdot M_h \cdot \vec{x}' \quad . \tag{1}$$

After applying the calibration, the raw camera images are automatically de-warped (interpolated) into calibrated images and published to RabbitMQ. All further image processing and analysis is carried out using the de-warped images (see Fig. 2).

With a test setup and a very rough calibration, by utilizing a paper printout of a checkerboard, measurements of the beam profile position and beam sizes with a relative deviance below 2% could be achieved. Even better results are expected as soon as the checkerboard pattern is replaced by a thin laser engraved PVC plate with the proper dimensions of the respective screen.

Processing / Fitting

From the de-warped image subimages can be cropped out according to the position and dimensions of *areas of interest* (AOIs), which can be easily defined via the graphical user interface (GUI). A *fit job* is created from the cut out segment and complemented by metadata (e.g. timestamps, see below) describing the original image as well as the function to be fitted to the data. The *fit job* is then dispatched to a *fit queue* from which several *fit workers* consume and eventually fit functions to the image data. The fit results (typically parameters μ_i, σ_i, rotation angle, intensity and background level of a 2D Gaussian profile) are finally published back to a RabbitMQ *exchange*[2].

A GUI displays the (calibrated) images, AOIs and fit results to the user, or dedicated tools can be used to e.g. write fit results to a file or transfer the results to to the accelerators control system.

[2] In the AMQ protocol messages are sent to *exchanges* and then routed to different queues for message delivery.

Configuration Subsystem

All configuration parameters of the cameras (e.g. frame rate, exposure time, external trigger configuration), the calibration data and the fit properties (e.g. AOI position, fit function) are stored in a central key-value database that is accessible via RabbitMQ. With appropriate callback mechanisms being implemented in the *C++* and Python library, parameter updates are broadcasted to the client applications. Remote procedure calls (RPC) allow for communication between the different applications as well as execution of common tasks (e.g. setup of new cameras, update of calibration data sets).

Deployment

All applications and libraries are deployed using a single Docker [3] image. With that approach, new RabbitMQ nodes can be joined into the cluster with ease and run isolated from the operating system. The nodes can either run the whole FGrabbit tool chain including *camera drivers*, *fit dispatcher* and *fit workers* or just run *fit workers* to increase computing power.

Python Interface

In addition to the framework's full-featured C++ interface, a Python interface allows for a quick and easy access to FGrabbit in projects by researchers and students. The Python interface is based on the RabbitMQ client library *Pika*[3]. Divided into different types of *exchanges*, the FGrabbit-features are handled by *exchange*-specific classes with a specialized set of functions. A brief overview of the functional scope is given in the following:

- The **image-data**-class includes functions for publishing images - both raw and calibrated. Each image contains a *header* with camera metadata, a timestamp and a serial number for identification and later assignment in the event of backlogs during time consuming tasks such as *fit jobs*. Likewise it is possible to subscribe to any camera *exchange*. One can choose to receive a raw stream or the already calibrated image.

- The **fit-data**-class allows users to access live fit data for a selected camera and AOI. Up to now *fit jobs* are handled by the reliable C++ fit library presented below. However, the architecture of the FGrabbit-framework enables Python scripts to handle *fit jobs* and publish fit results. This possibility can find use in application-dependent unique image analysis without the need to extend the C++-library.

- The **config-data**-class interfaces with the *configuration subsystem* described above. One essential function of this class is to request a complete key-value set regarding a specified *topic* (e.g. general, camera, calibration data, fit properties). Along with a subscription feature that allows for callback mechanisms upon configuration

[3] Open source AMQP 0-9-1 library: https://github.com/pika/pika

ISBN: 978-3-95450-241-7 ISSN: 2673-5350 doi:10.18429/JACoW-IBIC2022-MOP38

updates, an object can be configured initially and kept up to date. Likewise, an update function implements a way to control devices and set properties for AOIs, fits, etc. Within the config-data-class, additional RPCs can be executed for common tasks (e.g. adding cameras).

- The **log-data**-class attaches to the global programming language independent logging *exchange*. Besides the possibility to send log messages, there is also a subscription method to receive all or filtered log messages. This is used e.g. for a log viewer realized with the `cutelog` [4] GUI to investigate the overall health on the whole system.

With the briefly described features above and following the naming scheme in Fig. 2, `Python` scripts can embody *camera drivers*, *fit writers*, *image writers* and *fit workers*. In particular, the ability to have `Python` *camera drivers* simplifies image acquisition thanks to freely available `Python` libraries like the one described in the following section.

GenICam-Harvesters Library Bi-directional communication with e.g. *GigE Vision* devices can be established via the generic programming interface for computer vision cameras *GenICam* [5]. The *Harvesters*[4] `Python` library aims to simplify the image acquisition process via this interface. It allows both for easy acquisition through *GenTL* producers (the transport layer interface, here hidden for the consumer) and uncomplicated feature node manipulation to remote control devices. During the development of `FGrabbit`, *Harvesters* has proven to ba a reliable and simplified alternative to implementations of the *GenICam* interface by closed source software development kits (SDKs) from various manufactures.

IMPROVEMENT OF FIT PERFORMANCE

In addition to the optimization of the workflow using the new `FGrabbit`, the performance and accuracy of the fit algorithm was also improved. In the scope of [6] a `C++` library for the analysis of beam images at various camera observed beam monitoring stations was developed. The library is based on the *Gnu Scientific Library* [7] and *Ceres* [8]. This library implements two-dimensional fits for several functions suited for profile analysis. Special emphasis was put on the analysis of saturated and rotated profiles. Hence two fit functions were established for this cases. The first implements a Gaussian profile with a saturation compensation (by implementing a flattop into the function and thus neglecting the saturated area). The second implements a rotation angle, which clearly increases the computing effort, but also increases the fit accuracy for slightly rotated profiles noticeably. The performance of the new fit functions and the reached fit accuracy was extensively examined using a generator, which emulates typical images with known profile parameters. 5000 of these images were fitted by the new algorithm and the deviation between simulated and fitted profile parameters for all images were analyzed. The results of this statistical analysis are shown in Table 1. The relative deviation of the widths of the beam spot is in all cases in the order of a tenth of a percent or lower, the relative deviation of the intensity is around 1%. With the usage of the rotated Gaussian fit function relative deviations in the order of these displayed in Table 1 were reached also for rotated profiles.

Table 1: Relative Deviation of the Fit Results from the Simulated Values for 5000 Analyzed Images and The Results Presented as: $\mu \pm \sigma$, Referring to Mean and Standard Deviation of a Laplace Distribution

	Gaussian		Gaussian + *flattop*	
	not-sat.	sat.	not-sat.	sat.
$\Delta I_0/\%$	0.8 ± 0.4	-13.3	0.8 ± 0.4	1.0 ± 0.4
$\Delta\sigma_v/\%$	0.1 ± 0.5	5.9	0.0 ± 0.4	0.1 ± 0.8
$\Delta\sigma_h/\%$	0.1 ± 0.5	7.1	0.0 ± 0.4	0.1 ± 0.3

CONCLUSION

The `FGrabbit` framework, which is being developed at ELSA, provides a solution for processing a multitude of varying camera signals for beam profile analysis and other tasks. An improved library for two-dimensional fits and automated image calibration is included. The image acquisition and data processing work load is distributed over arbitrarily many worker computers in a separated camera network and managed by the `RabbitMQ` message-broker. The unified data can be easily accessed via interfaces in `C++` and `Python`, as well as through the accelerator control system.

REFERENCES

[1] W. Hillert *et al.*, "Beam and spin dynamics in the fast ramping storage ring ELSA", *EPJ Web Conf.*, vol. 134, p. 05002, Jan. 2017. doi:10.1051/epjconf/201713405002

[2] G. Bradski, "The OpenCV Library", Dr. Dobb's Journal of Software Tools, 2000.

[3] D. Merkel, "Docker: lightweight linux containers for consistent development and deployment", *Linux J.*, vol. 2014, no. 239, 2014.

[4] A. Bus, "Cutelog – GUI for logging", 2019, https://github.com/busimus/cutelog

[5] European Machine Vision Association. "GenICam Standard", https://www.emva.org/standards-technology/genicam/

[6] S. Kronenberg, "Entwicklung einer Softwarebibliothek zur automatisierten Analyse von Strahlabbildern an ELSA", Bachelor thesis, University of Bonn, Bonn, Germany, 2020.

[7] M. Galassi *et al.*, GNU Scientific Library Reference Manual (Release 2.7), 2021, http://www.gnu.org/software/gsl

[8] S. Agarwal, K. Mierle & Ceres Solver Team, "Ceres Solver", 2022, https://github.com/ceres-solver/ceres-solver

[4] Developed by the GenICam collaboration: https://github.com/genicam/harvesters

Content from this work may be used under the terms of the CC BY 4.0 licence (© 2022). Any distribution of this work must maintain attribution to the author(s), title of the work, publisher, and DOI

ISBN: 978-3-95450-241-7 ISSN: 2673-5350 doi:10.18429/JACoW-IBIC2022-MOP39

DEVELOPMENT OF COMPACT RADIO FREQUENCY SOURCES

M. S. McCallum*, A. Lyapin
John Adams Institute at Royal Holloway, University of London, Egham, United Kingdom

Abstract

Our group is developing a family of compact radio frequency sources aiming to cover 50 MHz to 20 GHz with several models. The primary goal is to provide an alternative to using expensive laboratory generators in permanent installations. In addition, we work towards providing a higher specification than similar telecommunications devices as this is a typical requirement in accelerator instrumentation. We take a minimalistic approach with only a network interface planned, assuming that such a device operates remotely in a large facility. An interface is in the works for monitoring and control using EPICS (Experimental Physics and Industrial Control System). In this paper, we present the results of rapid prototyping with XMicrowave components. The first measurements show encouraging phase noise performance and spectral purity.

INTRODUCTION

The aim of our project is to achieve the phase noise and spectral purity performance of a mid-range benchtop radio frequency (RF) generator, albeit at the loss of versatility. This loss is deemed acceptable if the only purpose of the source is to generate a stable signal at a fixed frequency, for example in a local oscillator (LO) application. In these proceeding we are looking at the performance of a signal source based on a low cost frequency synthesizer in comparison with commercially available examples of sources in both compact and benchtop formats.

We will thus be looking at 3 sources: a high quality Rohde and Schwarz SMA 100A [1] benchtop generator, an AtlanTecRF ASG-3000 compact signal source [2] aimed at Communications market, and our source developed around the Analog Devices' ADF4355 [3]. For brevity, these will be called SMA 100A, ASG, and ADF4355 respectively.

ADF4355 FREQUENCY SYNTHESIZER

The ADF4355 chip combines a Phase Locked-Loop (PLL) and a Voltage Controlled Oscillator in one package and allows for the implementation of integer-N and fractional-N PLL frequencies. Apart from a reference frequency, it requires only a handful of external components to operate. A series of internal frequency dividers allows for an operating frequency range of 54 MHz to 4.4 GHz. The ADF4355 chip has programmable output power, RF output mute, and can be controlled by a 3 wire Serial Peripheral Interface (SPI). We are currently using the device at the default loop bandwidth of 20 kHz.

Our implementation employs a budget Raspberry Pi 2040 microcontroller, housed on a W5100S-EVB-Pico by WIZnet [4]. Beside the low cost, this device has the advantage of running MicroPython, which shortens the development cycle compared to a classic microcontroller. We chose a board incorporating the Ethernet interface, as this is our preferred way of communicating with the device. ADF4355 along with other variable components following it are controlled using the GPIO pins of the microcontroller via SPI. A custom software stored in the FLASH memory of the board is initialised at the powerup and waits for an external command. Commands are sent via the Ethernet port, which are at the moment limited to changes in output frequency and power. The controller then calculates the required settings for the synthesizer chip and programs its registers accordingly.

Behind the scenes the changes of frequency and power settings trigger additional adjustments to filter banks and variable attenuators aimed at optimising the harmonics content and equalising the signal at different frequencies.

For the first prototype, we used rapid microwave prototyping blocks provided by XMicrowave [5]. A convenience PCB hosts the W5100S-EVB-Pico along with a few ancillary components, and simplifies connections to the RF blocks. A 3D printed enclosure houses all the elements of the prototype, including a high quality reference source.

PERFORMANCE COMPARISON

We compare the performance of the three sources by analysing their Phase Noise Measurements (PNM) at three different "inconvenient" fractional frequencies: 1033.33 MHz, 1879.68 MHz, and 2998.75 MHz. We also look at the spectral purity of each of the three sources. The data for these measurements was taken on a Rohde and Schwarz FSW 50 with a resolution bandwidth (RBW) of 20 kHz and a video bandwidth (VBW) of 30 Hz.

Phase Noise Performance

In Figure 1 we can see the PNM for each of the three sources at an output frequency of 1033.33 MHz. Looking at the phase noise for the ASG, blue line, we can see that the phase noise is relatively high at low frequency offsets. As the frequency offset becomes larger, the PNM decreases and plateaus. Next we can see the appearance of spurs, which increase the phase noise. Finally, the phase noise rolls off to about −105 dBc/Hz.

The black line shows the phase noise performance of the AF4355 frequency synthesizer. There the phase noise starts low at about −80 dBc/Hz, and decreases to about −105 dBc/Hz. Then it increases to about −90 dBc/Hz at the edges of the PLL bandwidth before steeply decreasing to −140 dBc/Hz at a higher frequency offsets.

Lastly, we have the phase noise performance of the SMA 100A in red. This source starts with a low phase noise of

* Contact Email: mark.mccallum@rhul.ac.uk

Content from this work may be used under the terms of the CC BY 4.0 licence (© 2022). Any distribution of this work must maintain attribution to the author(s), title of the work, publisher, and DOI

ISBN: 978-3-95450-241-7 ISSN: 2673-5350 doi:10.18429/JACoW-IBIC2022-MOP39

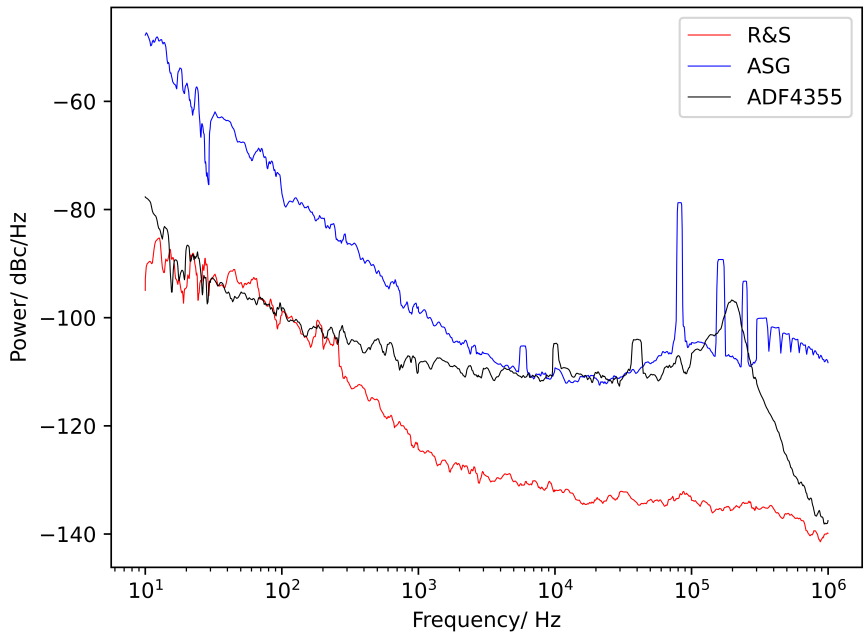


Figure 1: Phase Noise Measurement for the three sources at a frequency output of 1033.33 MHz.

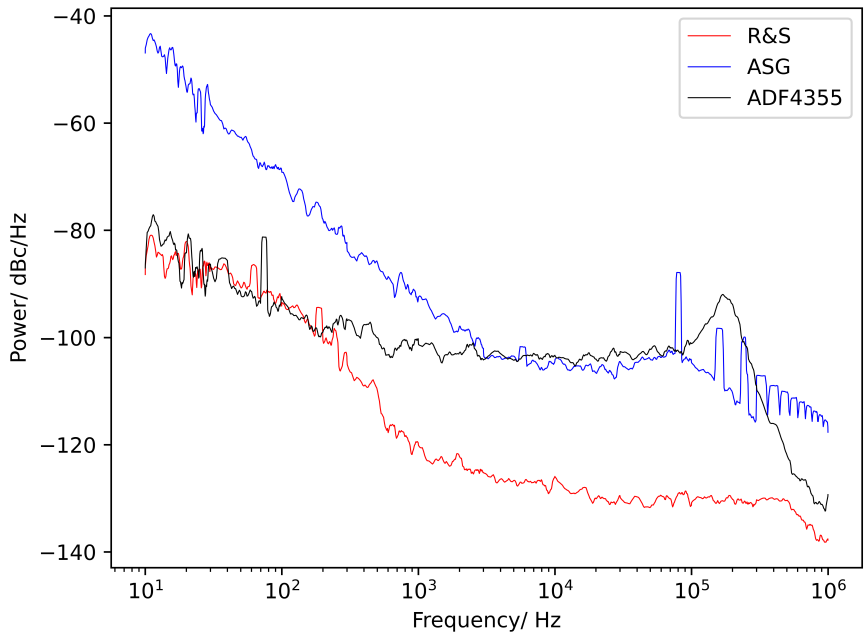


Figure 2: Phase Noise Measurement for the three sources at a frequency output of 1879.75 MHz.

−90 dBc/Hz, which decreases steadily to −140 dBc/Hz at larger offsets.

The pattern repeats for the PNMs taken at the two other chosen frequencies. Figure 2 is the frequency output of 1897.75 MHz and Figure 3 is the frequency output of 2998.68 MHz.

To quantify the phase noise performance of the three sources, we calculated the phase jitter of all three sources based on the measurements at each of the chosen frequencies. Here, in Table 1, we show the phase jitter for a frequency output of 2998.68 MHz. For a frequency output of 1033.33 MHz, the timing jitter for the SMA 100A, ADF4355, ASG is 45.27 fs, 404.4 fs, and 2265 fs respectively. For a frequency output of 1879.75 MHz the timing jitter for the SMA 100A, ADF4355, ASG is 49.69 fs, 394.7 fs, and 1582 fs respectively.

Table 1: RMS Phase Jitter Measurements for a Frequency Output of 2998.68 MHz

Device	**Δt, fs**	**$\Delta\phi$, rad**	**$\Delta\phi$, deg**
SMA 100	39.95	0.752	0.042
ADF4355	303.60	5.72	0.327
ASG	1266	23.85	1.366

Content from this work may be used under the terms of the CC BY 4.0 licence (© 2022). Any distribution of this work must maintain attribution to the author(s), title of the work, publisher, and DOI

ISBN: 978-3-95450-241-7 ISSN: 2673-5350 doi:10.18429/JACoW-IBIC2022-MOP39

Content from this work may be used under the terms of the CC BY 4.0 licence (© 2022). Any distribution of this work must maintain attribution to the author(s), title of the work, publisher, and DOI

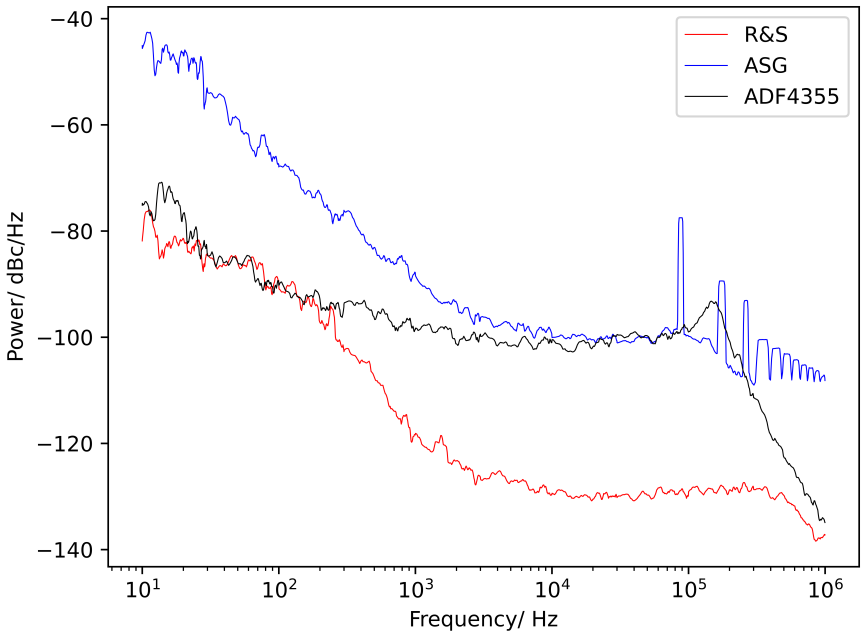


Figure 3: Phase Noise Measurement for the three sources at a frequency output of 2998.68 MHz.

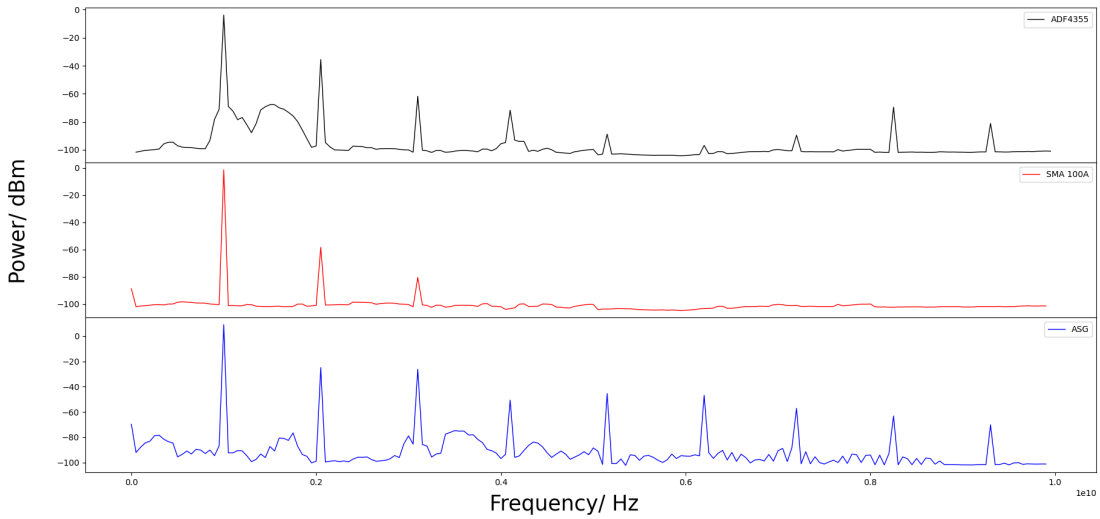


Figure 4: Spectral output of the three sources for a frequency output of 1033.33 MHz.

Clearly, our synthesizer performs well in phase noise measurements sitting firmly between in the targeted niche between the typical representatives of laboratory and compact sources. Further improvements, such as the optimisation of the PLL bandwidth, may still be possible.

Spectral Performance

In Figure 4, one can see the spectrum of the three sources at a frequency output of 1033.33 MHz measured up to 10 GHz. The top plot shows the spectral output of our ADF4355, the middle plot for the SMA 100A, and the last plot shows the spectral output of the ASG. Once again, the spectral output of ADF4355 is superior compared to the compact source presenting a much cleaner spectrum with fewer strong harmonics and boundary spurs. The data for these measurements was taken on a Rohde and Schwarz FSW 50 with a resolution bandwidth (RBW) of 20 kHz and a video bandwidth (VBW) of 30 Hz.

PERFORMANCE CONCLUSION

In phase noise performance our ADF4355 based frequency synthesizer is comparable to the Rohde and Schwarz SMA 100A at lower frequencies off sets (10 Hz – 120 Hz), while SMA 100A clearly outperforms it in a wider range. However, we achieved the goal of reaching a higher specification compared to the ASG signal generator with a 4-5 times lower integrated phase noise. With the present spec, our source can be applied in all but the most demanding local oscillator applications. Our goal is achieving sub-100 fs jitter, this may still be possible with some optimisation of the

ISBN: 978-3-95450-241-7 ISSN: 2673-5350 doi:10.18429/JACoW-IBIC2022-MOP39

PLL. The ADF4355 based source also achieves a reasonable spectral purity with the first harmonic at about −40 dBc and strongly suppressed higher harmonics.

APPLICATIONS

There are number of potential applications for a compact high frequency source within accelerator physics [6]. Providing test or local LO signals for up/down-converters are typical applications. Remote control capability and compact size of our design are important in the busy environment of a particle accelerator.

Outside of particle accelerator labs, beside potential usefulness as a general laboratory or communications equipment, such a source could be useful is in building quantum computing systems [7]. Qubit Control and manipulation is achieved at RF frequencies. RF sources provide excitation and LO signals for the readout. The phase noise requirements are typically higher than for communications systems.

CONCLUSION

Our first prototype of a compact RF source is en route to achieving its goals in terms of high signal quality, outperforming commercially available budget options and in some aspects approaching the specs of expensive benchtop generators. Further improvements may still be possible with minimal changes to the current hardware. In the next stages of this project we will focus on integrating the system towards a pre-production prototype that could be manufactured in larger quantities. Similar models covering different frequency ranges are also in the works.

REFERENCES

[1] Rohde and Schwarz, "R and S SMA100A Signal Generator Specifications", accessed on 7th September 2022, https://scdn.rohde-schwarz.com/ur/pws/dl_downloads/dl_common_library/dl_brochures_and_datasheets/pdf_1/SMA100A_dat-sw_en_5213-6412-22_v0700.pdf

[2] Atlantic Microwave, "Miniature Signal Generators ASG Series", accessed on 7th September 2022, https://www.atlanticmicrowave.com/sites/default/files/products/downloads/Miniature\%20Signal\%20Generators\%20-\%20ASG\%20Series.pdf

[3] Analog Devices, "ADF4355", accessed on 7th September 2022, https://www.analog.com/en/products/adf4355.html

[4] WIZnet W5100S-EVB-Pico, accessed on 7th september https://www.wiznet.io/product-item/w5100s-evb-pico/

[5] XMicrowave, "X-MWblocks", accessed on 7th September 2022, https://www.xmicrowave.com/product-category/x-mwblocks/

[6] S. A. Bogacz *et al.*, "Accelerator Physics", accessed 7th September, https://casa.jlab.org/publications/viewgraphs/USPAS2016/L_6_RF_Acceleration.pdf

[7] J. Raftery *et al.*, "Direct digital synthesis of microwave wave forms for quantum computing", 2017. doi:10.48550/arXiv.1703.00942

Content from this work may be used under the terms of the CC BY 4.0 licence (© 2022). Any distribution of this work must maintain attribution to the author(s), title of the work, publisher, and DOI

ISBN: 978-3-95450-241-7 ISSN: 2673-5350 doi:10.18429/JACoW-IBIC2022-MOP40

SYNCHRONOUS DATA SERVICE AT THE EUROPEAN SPALLATION SOURCE

R. Titmarsh*, ISIS, STFC, Rutherford Appleton Laboratory, Oxfordshire, UK
J. F. Esteban Müller, J. P. S. Martins, European Spallation Source ERIC, Lund, Sweden

Abstract

The Synchronous Data Service (SDS) is a tool to monitor and capture events in the European Spallation Source, building on top of the EPICS control system. Large amounts of data from different input-output controllers are acquired and synchronised at the level of beam pulses. The acquisition can be triggered by beam events through the timing system or manually by a user. Captured data is stored in standardised NeXus files and indexed in a database for easy searching and retrieval.

INTRODUCTION

At ESS, the operation of the proton linac, target, and neutron experiments are controlled using the EPICS [1] control system. EPICS is a distributed control system, and that means that the data produced in different Input/Output Controllers (IOC) is received by clients in a non-deterministic order.

At our facility, EPICS' data is archived by the Archiver Appliance [2]. This tool stores each signal as a time series, so the effort of correlating data from different sources lies with the client side.

In some applications, it is important to obtain a snapshot of the machine status containing several signals from various sources that belong to the same beam pulse. Typical examples are machine tuning and optimization, or troubleshooting of failures (post-mortem).

In order to ensure that the data is synchronized in all relevant devices, a precise timing system capable to generate triggering signals is required. In this paper we describe both the hardware and software implementation under development at ESS that will allow pulse-synchronous data acquisitions and archival, which we refer to as the Synchronous Data Service (SDS).

SOFTWARE ARCHITECTURE

A diagram of the SDS architecture is shown in Fig. 1. The main design goals are scalability and flexibility, and for that reason we followed a microservices pattern.

The service consists of 3 different types of components or microservices: one or more collector services that collect data from EPICS IOCs and produce NeXus [3] files, an indexer service that aggregates metadata from the collectors, and one or more data retriever services that allow users to query for the data in different ways. These components and their prototype implementation are described in more detail below.

* ross.titmarsh@stfc.ac.uk

These microservices rely on a storage backend consisting of an Elasticsearch [4] database that stores the metadata and a CEPH-based [5] distributed file system that contains the NeXus files.

Collector Services

We developed a prototype version of a generic collector service. It is implemented in Python 3 using the asyncio framework. PV Access is supported through the p4p [6] package. Channel Access support was considered not necessary since our control system is fully EPICS7 compliant.

This service creates a set of "collectors" from definitions in a JSON file, each collector listens for a single type of event on a set of EPICS PVs. Each instance of this service has a "collector manager" that listens to the EPICS PVs of the collectors within it, parses the received messages and forwards them to the relevant collector. Multiple instances of the service can be deployed to distribute the load. The collector collects the events into "datasets" by the pulse ID of the triggering pulse. The information about the triggering event must be included by the IOC and it is discussed later.

Using asyncio allows the many collectors to run concurrently, allowing multiple datasets to be constructed at the same time. This means it can handle events arriving out of order or overlapping each other.

The dataset is a virtual HDF5 file that is expanded as events are received. When the dataset is complete (defined as a configurable timeout, default is 2 seconds), it is written to a remote file system for storage and its metadata is sent to the indexer service. Datasets can be submitted with an "expire by" timestamp after which the data can be removed from storage.

Custom collector services can be developed to support other protocols or for different use cases. For instance, a post-mortem event triggered after the machine trips can generate a huge amount of data. In that case some systems may be configured to act as collector services by storing data locally for later transferring it to the central storage and to the indexer service.

Indexer Service

This service receives the collector definitions and the datasets' metadata and stores them in a database to enable fast search and retrieval.

The prototype was developed in Python 3 using the FastAPI [7] framework. It provides a REST interface that can be consumed by the collector services.

The Elasticsearch database was chosen for its capability of handling large volumes of data and for enabling complex

Content from this work may be used under the terms of the CC BY 4.0 licence (© 2022). Any distribution of this work must maintain attribution to the author(s), title of the work, publisher, and DOI

ISBN: 978-3-95450-241-7 ISSN: 2673-5350 doi:10.18429/JACoW-IBIC2022-MOP40

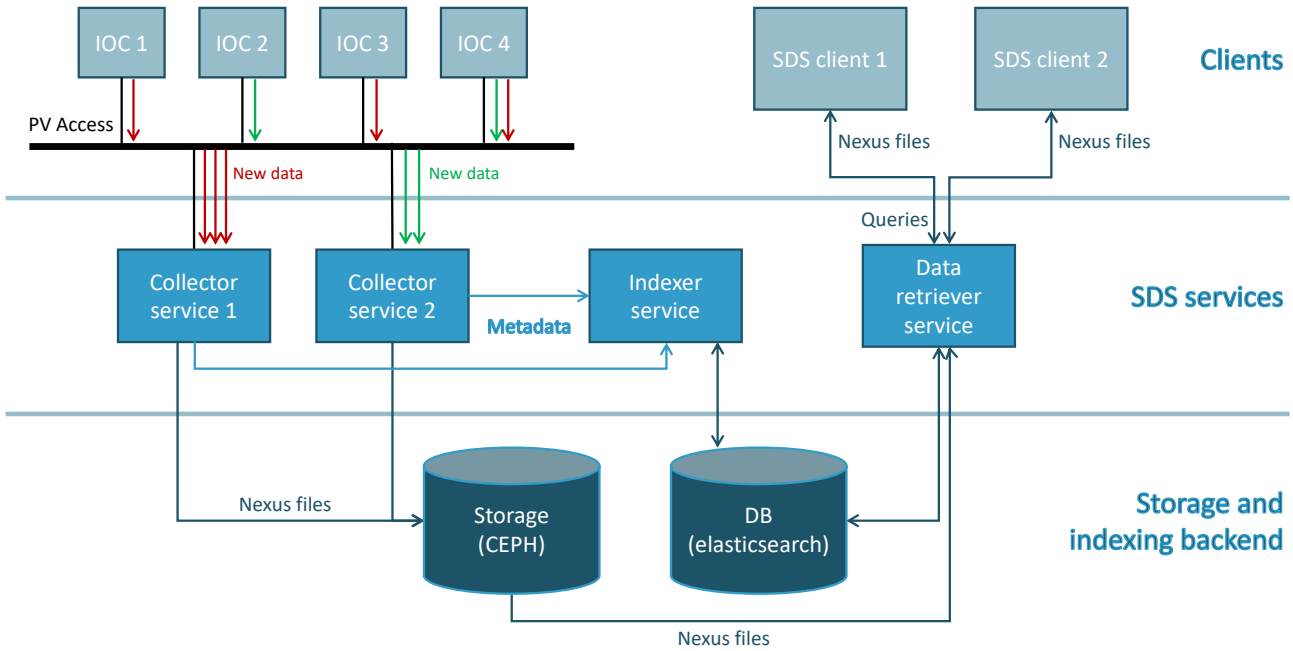


Figure 1: SDS architecture. The clients are shown on the top layer and can be either EPICS IOCs generating new data or SDS clients querying datasets and receiving NeXus files. In the middle layer it is shown the SDS services, including the collector services that collect data from the IOCs and interface with the indexer service that aggregates the metadata, and also the data retriever service that provides a REST interface for users to retrieve data. Finally, the bottom layer shows the storage and indexing backends.

queries with high performance. It is also simple to scale its performance by setting up a cluster.

Data Retriever Service

The data retriever service is the main entry point for users who want to access the data.

The technologies chosen for this prototype are the same as for the indexer service: Python 3 and the FastAPI framework. The retriever provides a REST interface for querying datasets and files. Datasets can be queried by collector, a date range, or a triggering pulse id range. Files can be retrieved using the same queries as for datasets, or directly by specifying a filename or dataset ID.

When a query result spans over several files or a subset of a file, the retriever service generates a new NeXus file that contains only the requested datasets.

The retriever service can also be scaled by deploying several instances and using an HTTP load balancer, e.g., Nginx or Apache.

DEPLOYMENT

A mirror of the code in our internal repository service, Gitlab, runs a continuous integration pipeline that generates a Docker image containing the SDS software. This simplifies the deployment to just pulling the Docker image and setting up a few environment variables.

TIMING SYSTEM

The timing system of the ESS linac is based on the MRF timing system [8]. The MRF system works with deterministic transmission of events from the Event Master (EVM) to the Event Receivers (EVR) via dedicated fibre-optics network. On the EVR side, the arrival of events is used to generate configurable electrical signals that can be used as acquisition or synchronization triggers on various devices. SDS will use dedicated events to trigger acquisitions, either periodically or on-demand. SDS events can be manually triggered by a user or generated after another event (e.g., machine trip).

The MRF timing network can also distribute data packets to all nodes, which are decoded at the EVRs and exported as EPICS PVs. At ESS, this data package is transmitted just before the next machine cycle and contains information about the beam that will be generated in the next round, such as beam mode, beam destination, beam length and the unique ID of the machine cycle. EPICS IOCs that are driven by events and triggers from the timing system can obtain precise timestamps and the pulse ID from the EVRs and add this information to the data structure of the PVs that contain measurement data. This ID is used by the SDS to correlate the data.

SDS can in principle be used together with any other timing system as long as it defines events and pulse IDs in the same way. In practice, one could also implement a custom collector that generates these metadata from other sources.

Content from this work may be used under the terms of the CC BY 4.0 licence (© 2022). Any distribution of this work must maintain attribution to the author(s), title of the work, publisher, and DOI

ISBN: 978-3-95450-241-7 ISSN: 2673-5350 doi:10.18429/JACoW-IBIC2022-MOP40

Content from this work may be used under the terms of the CC BY 4.0 licence (© 2022). Any distribution of this work must maintain attribution to the author(s), title of the work, publisher, and DOI

INPUT/OUTPUT CONTROLLERS

Some design considerations are required for IOCs to be compatible with SDS. The PVs that will be monitored by SDS need to be triggered by an event receiver (EVR) from the timing system. For systems that don't have a physical interface to EVRs, software triggers derived from the specific event counter can be used to synchronize acquisition (with reduced accuracy). For PVs with array data, the preferred structure is the `NTNDArray` format, in which the metadata containing the information about the timing event (event code and name) that triggered the SDS event can be appended to the structure as `NTAttribute` fields. For scalar PVs, a custom Normative Types structure will be used to encapsulate data and metadata. In both cases the pulse ID from the timing event that triggers the data acquisition needs to be copied into the `userTag` field of the PV and the timestamp corresponding to the SDS event should be copied to the `seconds` and `nanosseconds` fields.

In some use cases, the user might be interested in data from several pulses before and/or after the SDS triggering event. For that cases, we implemented a configurable circular buffer that continuously runs in the IOC. When an SDS event is received, it sends all the pulses stored in the buffer and then keeps sending the next few pulses as configured. Each PV update sent by the IOC will be tagged with the corresponding pulse ID, and all updates will share the same metadata.

NEXT STEPS

Now that we have a running prototype of the SDS software, we are planning to deploy it to a test environment for integrated testing with real hardware.

After that, a graphical user interface would be needed. At the moment we are exploring the use of PSI's Databuffer UI [9] as a simple user interface that aggregates data both from SDS and also from the Archiver Appliance instances running at ESS. It displays data from PVs as time series.

Later we would need to develop a dedicated UI that enables users to browse the collectors and datasets, and that more easily displays correlated data for a single pulse.

SUMMARY

The software architecture of the SDS system has been presented and described in detail. A first prototype of the system is ready and tested with emulated IOCs. The system shows high flexibility and the possibility of scaling up for better performance.

The code can be found at `https://github.com/EPICS-SDS/sds`.

ACKNOWLEDGEMENTS

The authors would like to thank Ricardo Fernandes for previous work on collecting system requirements, and together with Lars Johansson for information about databuffer-ui. We are also grateful to Timo Korhonen for his useful input on the system design. Thanks also to Bryan Jones for his support in making possible this collaboration between ISIS and ESS.

REFERENCES

[1] EPICS collaboration, `https://epics-controls.org/`

[2] M. Shankar, The EPICS Archiver Appliance documentation, `https://slacmshankar.github.io/epicsarchiver_docs`

[3] NeXus data format website, `http://www.nexusformat.org/`

[4] Elasticsearch website, `https://www.elastic.co/`

[5] CEPH website, `https://ceph.io/en/`

[6] M. Davidsaver, PVAccess for Python documentation, `https://mdavidsaver.github.io/p4p/`

[7] S. Ramírez, FastAPI documentation, `https://fastapi.tiangolo.com/`

[8] MRF website, `http://www.mrf.fi/`

[9] Databuffer-ui repository, `https://github.com/paulscherrerinstitute/databuffer-ui`

ISBN: 978-3-95450-241-7 ISSN: 2673-5350 doi:10.18429/JACoW-IBIC2022-MOP42

KINGFISHER: A FRAMEWORK FOR FAST MACHINE LEARNING INFERENCE FOR AUTONOMOUS ACCELERATOR SYSTEMS

L. Scomparin*, E. Blomley, T. Boltz†, E. Bründermann, M. Caselle, T. Dritschler, A. Kopmann, A. Mochihashi, A.-S. Müller, A. Santamaria Garcia, P. Schreiber, J. L. Steinmann, M. Weber
Karlsruhe Institute of Technology, Karlsruhe, Germany

Abstract

Modern particle accelerator facilities allow new and exciting beam properties and operation modes. Traditional real-time control systems, albeit powerful, have bandwidth and latency constraints that limit the range of operating conditions currently made available to users. The capability of Reinforcement Learning to perform self-learning control policies by interacting with the accelerator is intriguing. The extreme dynamic conditions require fast real-time feedback throughout the whole control loop from the diagnostic, with novel and intelligent detector systems, all the way to the interaction with the accelerator components. In this contribution, the novel KINGFISHER framework based on the modern Xilinx Versal devices will be presented. Versal combines several computational engines, specifically combining powerful FPGA logic with programmable AI Engines in a single device. Furthermore, this system can be natively integrated with the fastest beam diagnostic tools already available, e.g. KAPTURE and KALYPSO.

INTRODUCTION

Ensuring stable operation of the future particle accelerator facilities will pose a challenging problem, where traditional control systems are expected to not reach the desired performance. An interesting possibility is the use of Machine Learning (ML) techniques. Reinforcement Learning (RL) [1] is a prominent approach, which recently has shown several relevant results [2–5]. The basic idea is to model the control problem as the interaction between an agent and a system. The agent obtains some observable from the system that are expected to carry information about an underlying and often hidden state and chooses an action from an action space. Then, a reward is obtained from the system giving a metric of how good the taken action was. Reinforcement Learning is a series of algorithms allowing to train such an agent by using the rewards given by the system.

One of these challenging problems is the control of micro-bunching instabilities (MBI) [6] in synchrotron light sources, where the interaction of the beam head with the wake field produced by the Synchrotron Radiation (SR) emitted from the tail leads to the development of substructures in the longitudinal phase-space. One successful attempt was already performed at SOLEIL [7], in this case using traditional control techniques based on chaos theory. The underlying idea of this feedback loop is to stabilize the system around pre-existing unstable equilibrium points.

One intriguing capability of RL is its great versatility: by changing the reward function different goals are achievable, even when they might not be characteristic of a given stable condition. For example, the emission of Coherent Synchrotron Radiation (CSR) could be enhanced or suppressed while setting an acceptable level of fluctuation in the emitted power. Moreover, the enhancement of a specific radiation frequency range could be achieved.

MODULAR ARCHITECTURE FOR FAST INFERENCE

One of the issues that can be encountered when implementing RL techniques with accelerators are latency limitations. Namely, the complete feedback loop (comprising beam diagnostic detector readout, feature extraction, observable evaluation with the agent and action taking) needs to be taken in a time frame comparable to the dynamics of the physics that needs to be controlled. In the case of the MBI, this imposes latency constraints in the order of the synchrotron periods, i.e. of a few tens of microseconds.

A fundamental requirement necessary in order to minimise deployment and testing time for different RL algorithms is a modularity oriented model. Such a system can be divided into four main parts. First, a detector readout interface (1) is needed to retrieve data with low-latency and high-throughput. This data stream from the detector is then fed into the feature extraction part (2), which produces higher-level observables that are then fed into the agent module (3) that chooses an action. The action needs then to be applied to the system, in this case the accelerator, through an action taking part (4), that can interface to a part of the machine control system, ideally with a low-latency connection. A schematic view of this system is shown in Fig. 1.

On top of this inference signal path two other systems are needed: a slow-control system and a training system. Both of these are less time-critical compared to the feedback path. The training system needs to keep track of the observables, of the actions taken, and of the rewards, so that this information can be retrieved during training to update the agents's parameters. Meanwhile, the slow-control allows the operator to set different parameters and tune the system based on the needs of the facility.

KINGFISHER

The different modules and signal paths described in the previous section have different computational requirements. For instance, fast but simple operations are required when interfacing with the readout electronics, while the agent

* luca.scomparin@kit.edu
† now at SLAC, Menlo Park, California

Content from this work may be used under the terms of the CC BY 4.0 licence (© 2022). Any distribution of this work must maintain attribution to the author(s), title of the work, publisher, and DOI

ISBN: 978-3-95450-241-7 ISSN: 2673-5350 doi:10.18429/JACoW-IBIC2022-MOP42

Content from this work may be used under the terms of the CC BY 4.0 licence (© 2022). Any distribution of this work must maintain attribution to the author(s), title of the work, publisher, and DOI

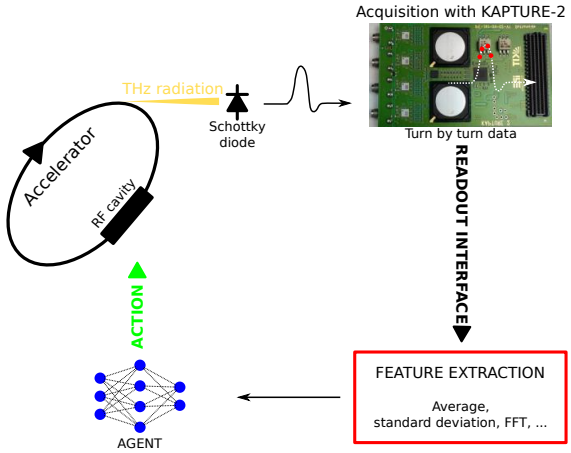


Figure 1: Schematic view of the modular RL feedback system. Changing detector, interface, or agent should minimally impact the remaining blocks of the system.

could be very computationally intensive due to the need of several floating point multiply and accumulate operations. Moreover, in order to employ the several ML frameworks already widely used and available [8, 9] in the training path, high-level operations are needed.

To fulfill all these requirements a heterogeneous platform is necessary. One possible choice is the Xilinx VCK190 evaluation board [10] based on the novel Xilinx Versal XCVC1902 Adaptive Compute Acceleration Platform (ACAP). This novel device combines an FPGA and an ARM processor in the usual System-on-Chip (SoC) configuration with a powerful AI Engine Array allowing fast floating point and integer arithmetic operations. These three components are deeply interconnected with a low-latency, high-throughput Network-on-Chip (NoC) that is also integrated with high speed transceivers, for example a 100 gigabit ethernet interface.

The modular approach described in the previous section is implemented on the VCK190 as the KINGFISHER platform (Fig. 2). The system comprises several interfaces to detector systems (KAPTURE [11], KALYPSO [12], and THERESA [13]), and to the available accelerator longitudinal feedback systems (Low Level RF (LLRF) and Bunch-By-Bunch feedback system (BBB) [14]), all implemented as FPGA blocks. The more computationally heavy operations, namely feature extraction and agent inference, are carried out by the the AI Engines, while the ARM processor has the task to run the slow-control and the training algorithms as Petalinux applications.

Agent

Reinforcement Learning allows great variability on the nature of an agent. For the current problem it was shown that a feed-forward neural network exhibits a sufficient degree of control [3]. In order to evaluate the performance of the system a simple feed-forward neural network (eight input and output neurons, four 64 neurons wide hidden layers) was developed on the AI Engine array, as described in [15]. The latency was shown to be almost four times better (4.5 µs) with respect to the same network deployed on a Zynq Ultrascale+ FPGA [15], while using 32 bit floating point arithmetics compared to 8 bit integers. Moreover, the system is fully reconfigurable from the processor allowing the online updating of weights and biases that are then used for the next computation.

The single precision floating point arithmetic and reconfiguration capabilities are extremely intriguing: the training of the neural networks can be performed on an identical network deployed on the ARM processor, where all widespread ML Python libraries are available, and the new agent coefficients are directly uploaded to the agent network on the AI Engines, without the need of quantization and pruning steps usually necessary when deploying a model on FPGA.

Feature Extraction

Features based on the work in reference [3] were implemented. Namely, a stream of CSR power measurements acquired using the KAPTURE system with a sampling rate equal to the revolution frequency of the accelerator (in this case ≈ 2.7 MHz) were divided in batches that are 1024 samples long. The extracted observables are respectively the mean and variance of the acquired samples, the maximum bin of the Discrete Fourier Transform, the maximum bin squared absolute value normalized to the sum of the remaining bins, and its ratio of imaginary to real part.

Average and standard deviation are computed using the following equations

$$\bar{x} = \frac{1}{N}\sum x_i \tag{1}$$

$$\sigma_x^2 = \frac{1}{N}\sum x_i^2 - \left(\frac{1}{N}\sum x_i\right)^2 \tag{2}$$

this specific expression for the variance is used because it does not require knowledge of the value of the average during computation and thus can be computed on the streaming data, therefore reducing latency.

Regarding the Fourier Transform (FT) some care is necessary: the AI Engine tiles are not able to natively compute sine and cosine functions with floating point precision in an efficient manner. Moreover, there is not enough memory on the engines to store a complete lookup table of the Discrete FT (DFT) samples (32 kB available, even though the neighbouring tiles can share memory bank, allowing a maximum of 160 kB). A possible way to circumvent this issue is to employ an FFT algorithm, for example the Cooley–Tukey algorithm, but this requires to have all the samples before computing the final FFT, thus severely impacting latency. For the sake of computational optimization, the calculation is divided into chunks that are then summed up when a new FT output is needed. In the formula below the summation is divided into M chunks, each one needing a sequence of N/M samples for the update. The final FT bin is composed using the M chunks. The value of M can be chosen arbitrarily, provided it is a divisor of N.

ISBN: 978-3-95450-241-7 ISSN: 2673-5350 doi:10.18429/JACoW-IBIC2022-MOP42

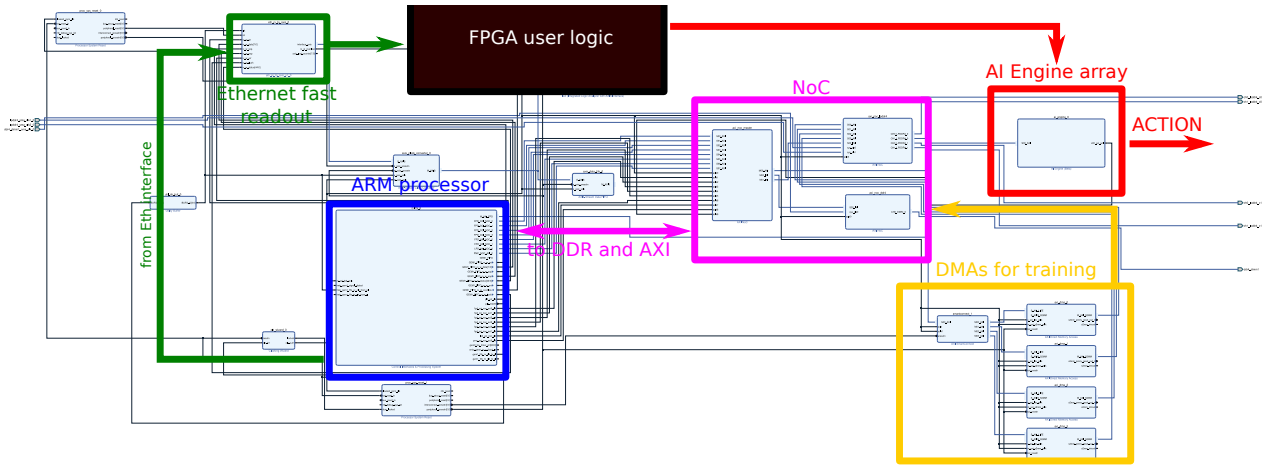


Figure 2: Schematic diagram showing the signal path inside of the KINGFISHER platform.

$$X_k = \sum_{n=0}^{N-1} x_n \, e^{-i\frac{2\pi}{N}kn} = \sum_{m=0}^{M-1} \sum_{j=0}^{N/M-1} x_{\frac{N}{M}m+j} \, e^{-i\frac{2\pi}{N}k(\frac{N}{M}m+j)}$$
$$= \sum_{m=0}^{M-1} e^{-i\frac{2\pi}{M}mk} \sum_{j=0}^{N/M-1} x_{\frac{N}{M}m+j} \, e^{-i\frac{2\pi}{N}kj} \tag{3}$$

This version allows to dramatically reduce the size of the lookup table: each coefficient depends either on m or on j, never both, so instead of using N coefficients per FT bin, only $\frac{N}{M} + M$ are needed.

When computing one 1024 sample FT every 256 input samples the measured latency is in the order of a few tens of microseconds. Such latency is strongly dependent on how the computation is divided among different AI Engine tiles. Additional optimization is ongoing in order to improve latency by more cleverly managing the distribution of workload and communications between tiles.

Training Module

In order to obtain all information necessary for training the agent, an infrastructure composed of several Xilinx Direct Memory Access (DMA) IPs are employed. This part is able to monitor all data streams in the feedback path and store them in one of the two DDR memories of the VCK190. In the current design 8 GB of DDR4 memory are used to run the Petalinux OS, while the remaining 8 GB of LPDDR4 store data from the DMA.

It is then possible to write data to a file for off-line analysis and also use it directly for training employing the widespread ML libraries and then to upload the new set of parameters to the agent.

Pseudo-random Number Generator

Most of RL algorithms need a random source in order to guide the exploration of new policies [1]. A pseudo-random number generator has been developed and implemented on the FPGA in Verilog. This module is based on the Permuted Congruential Generator XOR SHift Random Rotation (PCG-XSH-RR) algorithm [16] with a 64 bit hidden state. This specific implementation works at a maximum clock frequency of 250 MHz and produces a 32 bit random unsigned integer or floating point number every two clock cycles. This algorithm was specifically chosen due to its simple implementation and good quality of random number output.

Actuator

The beamline where the diagnostic instrumentation is located is physically separated from the control system instrumentation employed to apply the feedback operation. To reduce the issues associated with this separation a Xilinx ZCU102 evaluation board [17] was used to implement a system that is controllable via Gigabit Ethernet and allows to select different action types, e.g. generate several sinusoidal analog signals with selectable amplitude and frequency, together with a white noise source (using the random number generator from the previous section) with an output sample rate of ≈ 2.7 MHz, allowing a turn-by-turn controllable beam kick at KARA in single-bunch operation.

The latency of the system was measured by sending a command from KINGFISHER via a two meter long CAT6 Ethernet cable and checking with an oscilloscope the time necessary to apply it to the analog output. The latency measured is of 2.5 µs, e.g. less than 7 full revolutions of the beam at KARA.

KAPTURE Integration

The diagnostic signal used for the current tests is the THz radiation sampled by a Schottky diode readout with the KAPTURE-2 system [11]. KAPTURE-2 allows the sampling of a fast signal on a turn-by-turn basis for all bunches in the accelerator. Compared to the previous versions of the system using the Highflex [18] board, for this integration the new Highflex-2 [15] was used. The firmware was ported to the newer Xilinx Zynq Ultrascale+ architecture and the

Content from this work may be used under the terms of the CC BY 4.0 licence (© 2022). Any distribution of this work must maintain attribution to the author(s), title of the work, publisher, and DOI

ISBN: 978-3-95450-241-7 ISSN: 2673-5350 doi:10.18429/JACoW-IBIC2022-MOP42

Content from this work may be used under the terms of the CC BY 4.0 licence (© 2022). Any distribution of this work must maintain attribution to the author(s), title of the work, publisher, and DOI

embedded Gigabit Ethernet MAC (GEM) was controlled from the FPGA in order to continuously stream data of up to 5 bunches. This interface is then connected to the GEM on the VCK190 board as shown in the picture in Fig. 3. In the future, the system will be improved further allowing the streaming of all data on fast high-data throughput optical data links.

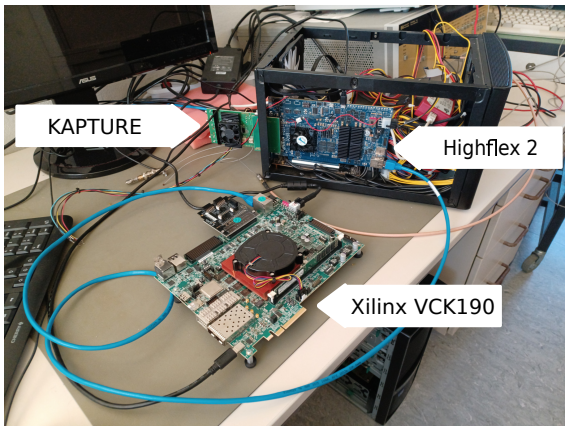


Figure 3: Picture of the VCK190 Evaluation Board connected to the Highflex-2 board where KAPTURE is mounted.

BEAM TESTS

The above KAPTURE and KINGFISHER system has been tested during several beam times at the KIT synchrotron light source KARA storage ring facility at KIT using the 1.3 GeV short-bunch operation mode. All systems were separately tested, although the closed loop tests need to wait for upgrades to the LLRF system in order to apply the required feedback signal. Nonetheless it was possible to perform stable measurements of the THz signal with feature extraction. Small longitudinal kicks where applied by connecting the actuator analog output to the longitudinal BBB feedback system while disabling the internal filters so the signal is directly applied to the beam. This configuration was shown to be working by inducing longitudinal oscillations at specific frequencies, as shown in Fig. 4, where the spectrum of a Beam Position Monitor (BPM) read with the BBB system clearly shows a peak at the excitation frequency. Unfortunately this kind of action is not strong enough in the current longitudinal BBB setup to sufficiently influence the micro-bunching instability.

CONCLUSION

The novel KINGFISHER platform was introduced as a general low-latency inference system for Reinforcement Learning for intelligent control of particle accelerators. The main blocks were discussed, as well as their architecture. First results during beamtime have shown that all blocks work correctly, leaving the addition of a low-latency feedback input to the accelerator control system as the last step before the final testing of the complete feedback loop can be carried out.

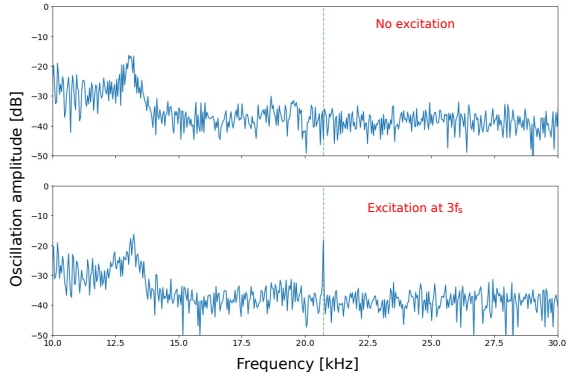


Figure 4: Sinusoidal excitation at three times the synchrotron frequency: top plot shows the BPM spectrum when the excitation is off, bottom plot when the excitation is on. The vertical dashed green line shows the frequency of the applied excitation.

ACKNOWLEDGEMENTS

We would like to thank Y.-L. Mathis and his team for beamtime and support at the KARA IR1 beamline.

The work was in part supported by BMBF ErUM-Pro FKZ 05K19VKC (TiMo) and in part by the Innovationspool Project ACCLAIM.

REFERENCES

[1] R. S. Sutton and A. G. Barto, *Reinforcement Learning, second edition*. Cambridge, MA, USA: MIT Press, 2018.

[2] W. Wang *et al.*, "Accelerated Deep Reinforcement Learning for Fast Feedback of Beam Dynamics at KARA," *IEEE Trans. Nucl. Sci.*, vol. 68, pp. 1794–1800, 2021. doi:10.1109/TNS.2021.3084515

[3] T. Boltz, "Micro-bunching control at electron storage rings with reinforcement learning," Ph.D. dissertation, Karlsruher Institut für Technologie (KIT), Germany, 2021. doi:10.5445/IR/1000140271

[4] J. S. John *et al.*, "Real-time artificial intelligence for accelerator control: A study at the fermilab booster," *Phys. Rev. Accel. Beams*, vol. 24, p. 104 601, 2021. doi:10.1103/PhysRevAccelBeams.24.104601

[5] F. H. O'Shea, N. Bruchon, and G. Gaio, "Policy gradient methods for free-electron laser and terahertz source optimization and stabilization at the fermi free-electron laser at elettra," *Phys. Rev. Accel. Beams*, vol. 23, p. 122 802, 2020. doi:10.1103/PhysRevAccelBeams.23.122802

[6] M. Brosi *et al.*, "Systematic studies of the microbunching instability at very low bunch charges," *Phys. Rev. Accel. Beams*, vol. 22, p. 020 701, 2019. doi:10.1103/PhysRevAccelBeams.22.020701

[7] C. Evain *et al.*, "Stable coherent terahertz synchrotron radiation from controlled relativistic electron bunches," *Nat. Phys.*, vol. 15, pp. 635–639, 2019. doi:10.1038/s41567-019-0488-6

ISBN: 978-3-95450-241-7 ISSN: 2673-5350 doi:10.18429/JACoW-IBIC2022-MOP42

[8] A. Paszke *et al.*, "Pytorch: An imperative style, high-performance deep learning library," in *Proc. Advances in Neural Information Processing Systems*, vol. 32, 2019, pp. 8024–8035.

[9] Martín Abadi *et al.*, *TensorFlow: Large-scale machine learning on heterogeneous systems*, Software available from tensorflow.org, 2015. https://www.tensorflow.org

[10] *Xilinx VCK190 Evaluation Board*. https://www.xilinx.com/products/boards-and-kits/vck190.html

[11] M. Caselle, "KAPTURE-2. a picosecond sampling system for individual THz pulses with high repetition rate," *J. Instrum.*, vol. 12, p. C01040, 2017. doi:10.1088/1748-0221/12/01/c01040

[12] L. Rota *et al.*, "KALYPSO: Linear array detector for high-repetition rate and real-time beam diagnostics," *Nucl. Instrum. Methods Phys. Res., Sect. A*, vol. 936, pp. 10–13, 2019. doi:10.1016/j.nima.2018.10.093

[13] O. Manzhura *et al.*, "Terahertz Sampling Rates with Photonic Time-Stretch for Electron Beam Diagnostics," in *Proc. IPAC'22*, Bangkok, Thailand, 2022, pp. 263–266. doi:10.18429/JACoW-IPAC2022-MOPOPT017

[14] Dimtel, Inc., https://www.dimtel.com

[15] W. Wang, "Towards intelligent data acquisition systems with embedded deep learning on MPSoC," en, Ph.D. dissertation, Karlsruher Institut für Technologie (KIT), Germany, 2021. doi:10.5445/IR/1000133898

[16] M. E. O'Neill, "PCG: A family of simple fast space-efficient statistically good algorithms for random number generation," Harvey Mudd College, Tech. Rep. HMC-CS-2014-0905, 2014.

[17] *Xilinx ZCU102 Evaluation Board*. https://www.xilinx.com/products/boards-and-kits/ek-u1-zcu102-g.html

[18] M. Caselle *et al.*, "A high-speed DAQ framework for future high-level trigger and event building clusters," *J. Instrum.*, vol. 12, p. C03015, 2017. doi:10.1088/1748-0221/12/03/c03015

Content from this work may be used under the terms of the CC BY 4.0 licence (© 2022). Any distribution of this work must maintain attribution to the author(s), title of the work, publisher, and DOI

ISBN: 978-3-95450-241-7 ISSN: 2673-5350 doi:10.18429/JACoW-IBIC2022-MOP43

WEB-BASED APPLICATION FOR CABLE SIMULATION MODELS*

M. C. Paniccia†, S. Clark, D. M. Gassner, R. Hulsart, P. Thieberger
Brookhaven National Laboratory, Upton, USA

Abstract

Signal attenuation in a coaxial cable increases with cable length, and the amount of attenuation and signal distortion is dependent on the signal's spectral frequency content. A model of these variations can help predict a signal's expected loss and distortion. This paper describes a free web-based application developed to provide accurate SPICE models for various coaxial cable types. The user can specify a length, select between different cable types, or upload a cable's attenuation curve, and receive a SPICE model for that cable. These simulation models have been used to assist the design and development of new instrumentation systems for the future Electron-Ion Collider (EIC).

INTRODUCTION

The new Electron-Ion Collider (EIC) will include over a thousand new beam position monitors (BPMs) and many other instrumentation systems spread throughout the complex. Signals generated at the various sensors must traverse cable lengths as great as 250 m. Understanding the signal loss and distortion as they propagate over these distances is a key aspect of the system design process. To assist in the design process, analog circuits are modeled with the Simulation Program with Integrated Circuit Emphasis (SPICE) [1]. The SPICE simulation provides a transient and steady-state response of the system allowing for the first-pass representation of expected performance. Modeling cables in SPICE poses a unique challenge as cable performance changes over distance and frequency content. Since most signals from instrumentation systems have a wide frequency content, it is imperative to accurately capture the frequency-dependent performance of the cabling.

A procedure for developing a SPICE simulation model for frequency-dependent cable loss is described in [2]. The frequency-dependent attenuation performance is simulated by creating a multistage passive filter with poles and zeros mapped along the cable's transfer function. A custom Python script was developed to implement the pole-zero approximation method and several simulation models were generated for different coaxial cables. To test the validity of the models, spare cable assemblies were tested in the lab with narrow pulses, and the SPICE model performance matched closely to the measured data. The Python scripts were integrated into a web application to make the cable simulation process accessible to the entire EIC team and the broader instrumentation community.

* Work supported by the US Department of Energy under contract No. DE-AC02-98CH10886.
† mpaniccia@bnl.gov

SPICE MODEL

The creation of the SPICE model starts with defining the cable's frequency-dependent attenuation characteristic curve. The characteristic curve acts like a filter's transfer function and defines the cable's response in the frequency domain. Cable manufacturers typically provide attenuation values at specific frequencies at a specified length; most often 100 ft or 100 meters. If not provided by the manufacturer, the characteristic curve can be measured using a network analyzer. Once established, the characteristic curve can be defined as an equation that can provide attenuation values for any given frequency. This equation takes the form of Eq. (1).

$$Atten = a_0 \sqrt{MHz} + a_1 \, MHz + a_2. \quad (1)$$

In generating the SPICE model, an equation for each cable type is determined using the least squares approximation of Eq. (1) to the attenuation versus frequency values provided by the manufacturer. The cable's characteristic curve is then scaled by the distance at which it was measured, assuming attenuation is proportional over distance and frequency. A pair of spare cables of different lengths were measured to verify this assumption using a network analyzer. The measurements were compared to the estimated attenuation curve using the proportional approximation and are shown in Fig. 1. For both cables, the proportional approximation proved to be conservative.

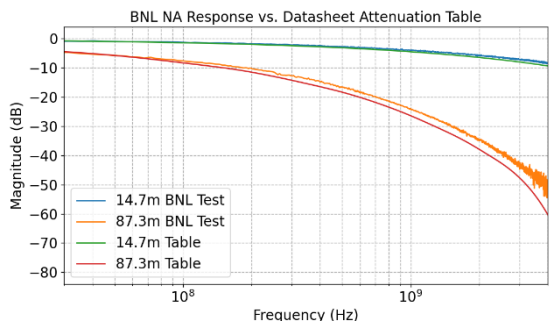


Figure 1: Comparison of LMR240 frequency-dependent attenuation characteristic curve and measured BNL network analyzer data.

The next step in the derivation of the SPICE model is to use the pole-zero approximation process described in [2]. This process recreates the characteristic curve for frequency-dependent attenuation by creating a circuit with a transfer function with a similar slope. The transfer function is created from multiple poles and zeros that are set along the characteristic curve. The poles and zeros are generated using resistors and capacitors configured in a low-pass filter. Multiple stages are connected using the SPICE Voltage

Content from this work may be used under the terms of the CC BY 4.0 licence (© 2022). Any distribution of this work must maintain attribution to the author(s), title of the work, publisher, and DOI

ISBN: 978-3-95450-241-7 ISSN: 2673-5350 doi:10.18429/JACoW-IBIC2022-MOP43

Controlled Source to prevent loading. The multistage poles-zeros transfer function is calculated using a non-linear least squares regression fit provided by the Python SciPy.Optimize library [3]. The results from the fit are translated into resistor and capacitor values for each filter stage. The number of filter stages can vary based on accuracy and runtime performance. In the web application, the stages are set to 6 poles and 5 zeros, and the circuit is shown in Fig. 2.

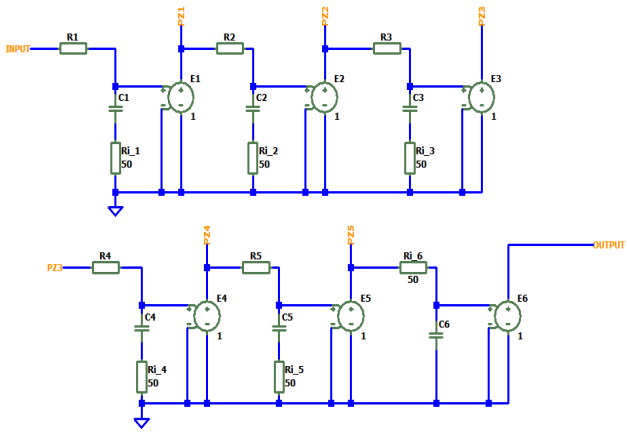


Figure 2: Graphical representation of the SPICE subcircuit. This subcircuit has 6 poles and 5 zeros and uses a 50 Ω impedance.

After the resistor values are calculated from the fit, the values are applied directly to the subcircuit SPICE library file. To do this, a generic library with the predefined netlist for the circuit is stored on the web page server and read into the application as a string. Using the Python string.format method, the resistors, and capacitors are assigned to each stage and the updated string is written to a new library file.

TEST AND VALIDATION

To verify the validity of the simulation models, cable assemblies were tested at various lengths with narrow pulses. The cable assemblies included two LMR240 50 Ω coaxial cables, and two several-meter custom Tefzel 50 Ω semi-rigid coaxial cables. The length of each cable assembly was measured with a Mohr CT100 Time-Domain Reflectometer (TDR). An arbitrary pulse generator was configured to provide unipolar pulses with pulse widths between 200 ps to 10 ns. Each pulse was measured directly on the oscilloscope and was exported into a CSV file. Then each cable assembly was connected to the pulse generator and the responses were again measured on an oscilloscope and exported into a CSV file.

SPICE models were developed for each cable type at the measured lengths. The captured input pulses that were exported from the oscilloscope were loaded into the SPICE simulation file as a piece-wise linear voltage source and connected to the cable SPICE models. The results from the SPICE simulation for both types of cables matched closely to the cable output pulses measured on the oscilloscope, examples are shown in Figs. 3 and 4.

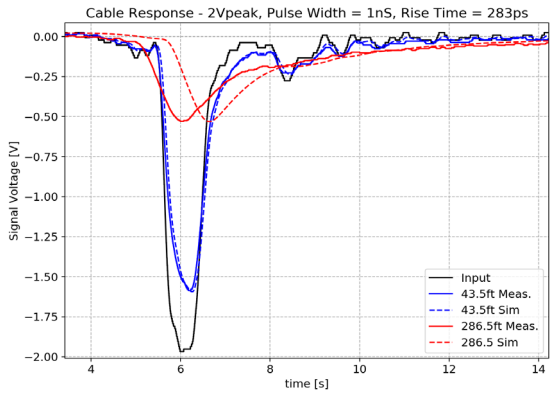


Figure 3: LMR240 50 Ω coaxial cables at 14 and 83 m. The input pulse width is 1 ns FWHM and a rise time of 283 ps.

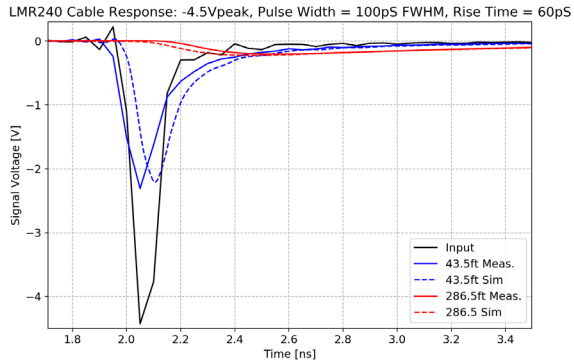


Figure 4: LMR240 50 Ω coaxial cables at 14 and 83 m. The input pulse width is 100 ps FWHM and a rise time of 60 ps.

WEB APPLICATION

The web application acts as an online calculator for generating the SPICE subcircuits for user-specified cables and lengths. Within the application, the user can select SPICE libraries for multiple cable types over a range of common lengths or generate a custom subcircuit model for a specific cable length or upload a new cable profile. The SPICE subcircuits can be added directly to any SPICE simulation system. When selecting a predefined library, an assembly file is included for use with LTSPICE. The subcircuit consists of pole-zero low-pass filter elements and an ideal transmission line that adds a delay based on the cable's velocity of propagation. New uploaded cables use the default velocity of propagation value of 85% unless otherwise specified. The application utilizes HTML and the Python Flask library to build the web page. Flask is a lightweight framework that was easily integrated with the Python scripts used to create the SPICE models.

Predefined Page

The predefined page provides users with libraries for cables previously characterized. The page includes a table with the frequency-dependent attenuation values for several common lengths along with the characteristic curve at 100 m. The corresponding resistor and capacitor values re-

Content from this work may be used under the terms of the CC BY 4.0 licence (© 2022). Any distribution of this work must maintain attribution to the author(s), title of the work, publisher, and DOI

ISBN: 978-3-95450-241-7 ISSN: 2673-5350 doi:10.18429/JACoW-IBIC2022-MOP43

quired to recreate the pole-zero cable model are also included in a separate table. A custom library of SPICE models for several common lengths and an LTSPICE assembly file are available for download at the bottom of the page. The user can create a custom SPICE subcircuit by specifying the desired length in the length text field. After hitting the Calculate button a new SPICE library file will become available for download.

Upload Page

On the Upload Page, the user can add new cables and generate custom SPICE models for them. New cable profiles are uploaded as either a CSV, TXT, or XLS file containing the frequency-dependent attenuation values or manually added directly to a table. A characterization curve is generated for the uploaded data along with the representative function and a SPICE model for download. When uploading the profile, the user can specify the cable impedance and velocity; if left blank they will default to 50 Ω and 85%, respectively. An example of the output from the Upload Page is shown in Fig. 5.

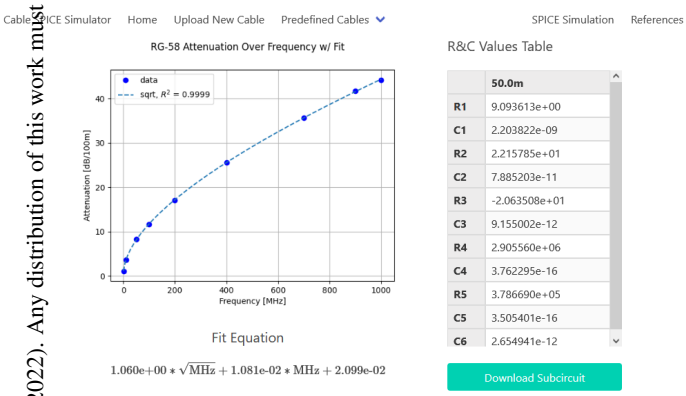


Figure 5: Output from the Upload New Cable section of the Cable SPICE Simulator web application. The SPICE subcircuit modeled is for a 50-meter RG-58 cable.

USE IN EIC BPM DESIGN

Determining the distribution and location of the EIC Beam Position Monitor (BPMs) electronics has been an important focus of the instrumentation preliminary design. In the presently proposed design, none of the BPM electronics will be located inside the tunnel, to reduce potential radiation related problems. Instead, the plan is to utilize external service buildings spread around the ring. As a result, the cable lengths can vary from 100-240 m long. At these relatively large cable lengths, the variation in the level of signal degradation between cables can have a significant impact on the system performance and cost.

To study the performance of the various cable types, BPM responses are generated using CST Studio. The BPM responses are then imported into a SPICE program as a piecewise linear voltage source and connected to the cable model under test. A comparison between several 50 Ω cable types at the maximum distance of 240 m is shown in Fig. 6.

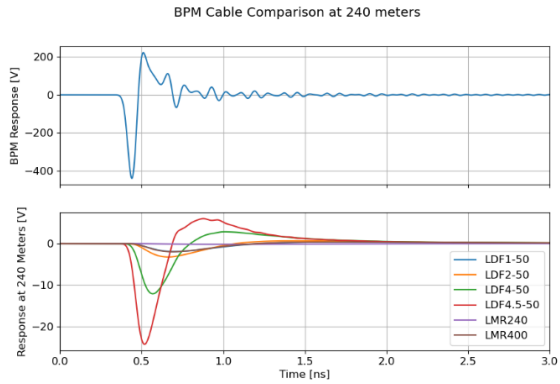


Figure 6: Response to BPM signal across various 50 Ω cables. All cables use SPICE models developed with the procedure discussed herein.

CONCLUSION

Accurate modeling of coaxial cables in SPICE presents a unique challenge. Using the models created with pole/zero approximation, designers can easily test the performance of complex signals over long-distance cables and receive reasonable results.

The models presented in this paper and the ones available on the web application are not a complete representation of the cable performance. These models are not bidirectional and will not model the performance of impedance mismatches nor do they include variations in temperature and humidity. However, the SPICE models derived using the pole-zero approximation provide an accurate simulation of the frequency-dependent attenuation and can assist in understanding the signal loss in complex signals.

REFERENCES

[1] L. W. Nagel and D. O. Pederson, "SPICE (Simulation Program with Integrated Circuit Emphasis)", University of California, Berkeley EECS Department, UCB/ERL M382, Apr. 1973.

[2] B. Hyland., "An Improved and Simple Cable Simulation Model", *EDN*, Jul. 2012, https://www.edn.com/improve-and-simplify-cable-simulation

[3] P. Virtanen, R. Gommers, *et al.*, "SciPy 1.0: fundamental algorithms for scientific computing in Python", *Nat. Methods*, vol. 17, pp. 261-272, 2020. doi:10.1038/s41592-019-0686-2

Content from this work may be used under the terms of the CC BY 4.0 licence (© 2022). Any distribution of this work must maintain attribution to the author(s), title of the work, publisher, and DOI

ISBN: 978-3-95450-241-7 ISSN: 2673-5350 doi:10.18429/JACoW-IBIC2022-MOP44

NOVEL PHOTOEMISSION TYPE OF X-RAY BEAM POSITION MONITOR FOR THE 'WHITE' UNDULATOR RADIATION*

P. Ilinski†, MAX IV Laboratory, Lund University, Lund, Sweden

Abstract

A novel photoemission type of X-ray Beam Position Monitor (XBPM) for the 'white' undulator radiation is proposed. The XBPM employs beamline frontend fixed mask as a source of photocurrent signal. Signal spatial distribution and XBPM response were analyzed for various undulator radiation parameters.

INTRODUCTION

Photoemission blade type X-ray Beam Position Monitors (XBPM) [1] are standard for most synchrotron radiation facilities. The photoemission blade XBPMs are non-invasive and can provide high spatial resolution but encountering some drawbacks affecting their performance. Initially, the frontend (FE) XBPMs were developed as a standalone component, equipped with positioning stages. Signal response of the photoemission blade XBPM is quite vulnerable to the surface condition of the blades. Also, since operating with negative bias applied to the blade, a conductive deposit can be accumulated at insulator surfaces, leading to substantial increase of the dark current [2]. Operating without bias reduces the blade XBPM signal level.

Most of the time, the FE XBPM is located behind the fixed mask, which is a part of the FE and designed to absorb vast amount of the incident undulator radiation. Knowledge of undulator beam position relative to the FE fixed mask (FM) allows to reduce FM exit aperture and to achieve better beam alignment along the frontend. An XBPM, which is part of the FM was developed [3], it is based on detecting x-ray fluorescence from FM surfaces. Spatial calibration of the XBPM, which is fixed in space, can be performed by deflecting the undulator radiation beam [4]. This is a preferable way to spatially calibrate FE XBPM, since it corresponds to actual operation conditions, when the undulator beam is moving relative to the XBPM and not vice versa.

Proposed novel type of photoemission XBPM is part of the FM. It is detecting the photoemission produced at the FM surface under undulator radiation. The Photoemission Mask (PheM) XBPM will allow to combine XBPM and the frontend FM and to overcome some drawbacks of the photoemission blade XBPMs.

LAYOUT

Photoemission Mask XBPM consists of a fixed mask and detection part with four pickup electrodes, which are hidden from undulator radiation (Fig. 1). The electrodes are collecting photoelectrons emitted from the fixed mask when exposed to the undulator radiation. The PheM XBPM can be a combination of upstream and downstream fixed masks with signal pickup part in between. In this case, the photocurrent signal will be collected from both fixed masks. These signals may be separated in case, if two sets of readout electrodes will be installed in between upstream and downstream masks. The PheM XBPM can also be a combination of upstream mask and downstream readout flange with pickup electrodes, such layout may be compatible with frontends already in operation. Since the fixed masks are electrically grounded, the electrodes need to be under positive potential to collect photoelectrons. In this situation the residual ions will not be attracted to the electrodes and therefore no conductive deposit will be developed at the insulator's surfaces.

Calculation of the PheM XBPM signal distribution was performed for the upstream fixed mask with the exit aperture of 11 mm by 11 mm and the downstream fixed mask with the exit aperture of 9 mm by 9 mm. The upstream fixed mask exit aperture dimensions correspond to the dimensions of the MAX-IV CoSAXS frontend upstream fixed mask. The downstream fixed mask dimensions were chosen not to obstruct the configuration of already installed blade type XBPMs at the CoSAXS frontend. Geometrical and electrostatic layouts can be further optimized for dedicated PheM XBPM design.

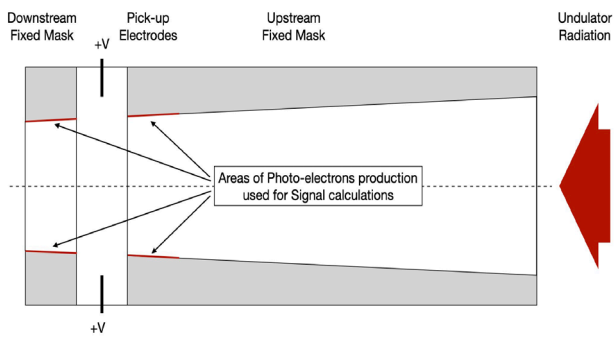


Figure 1: Layout of the Photoemission Mask XBPM.

RADIATION SOURCE

Radiation from planar and elliptical undulator radiation sources was used to calculate the PheM XBPM signal. The flux spectral density of MAX-IV CoSAXS planar undulator for K=1.25 is presented in Fig. 2 for various observation angles. As can be seen, at large observation angles, the PheM XBPM signal is generated mostly by the undulator harmonics with fundamental energies below 1 keV.

The wavelength of fundamental undulator harmonic is proportional to:

*Research conducted at MAX IV is supported by the Swedish Research council (contract 2018-07152), the Swedish Governmental Agency for Innovation Systems (contract 2018-04969), and Formas (contract 2019-02496)
†petr.ilinski@maxiv.lu.se

Content from this work may be used under the terms of the CC BY 4.0 licence (© 2022). Any distribution of this work must maintain attribution to the author(s), title of the work, publisher, and DOI

ISBN: 978-3-95450-241-7 ISSN: 2673-5350 doi:10.18429/JACoW-IBIC2022-MOP44

$$\lambda_n \sim \frac{1}{n}\left(1+\gamma^2\theta^2+\frac{K^2}{2}\right) \quad (1)$$

so, at large observation angles, θ, the wavelength of the fundamental undulator harmonic, λ_n, is dominated by observation angle rather than by undulator K-value. That will make photoelectron signal generated at large angles less dependent to the undulator gap changes.

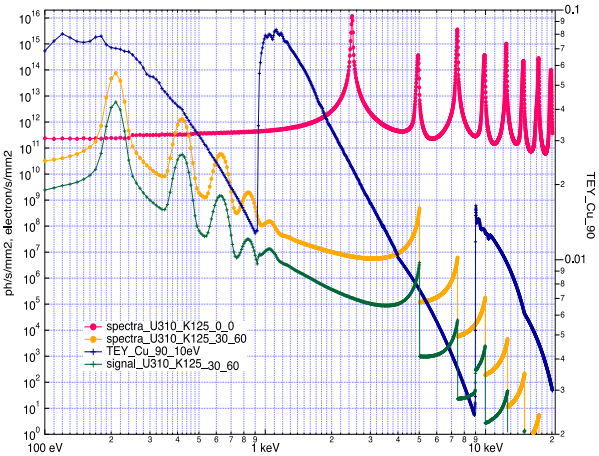


Figure 2: Undulator radiation flux spectral density of MAX-IV CoSAXS planar undulator, K=1.25: on-axis (pink), 0.7 mrad (yellow). Signal spectral density, 0.7 mrad (green). Copper Total Electron Yield (blue).

Bending magnet radiation makes contribution to the total flux and therefore creates a constant background. Modern ultimate storage rings are multi-bent achromats with weak dipoles magnetic field, MAX-IV 3 GeV main dipole has magnetic field of 1.16 T and soft end field of 0.22 T [5]. So, bending magnet radiation will not introduce much of a background signal at MAX-IV 3 GeV storage ring.

SIGNAL

Operation of the PheM XBPM is based on photoemission from the fixed mask under undulator radiation. The resulting photoemission signal is convolution of the undulator spectral density and the total electron yield (TEY) of the FM material, which is mostly copper. Copper TEY data for normal incidence was used [6] in presented signal calculations. The TEY at grazing incidence is higher, so PheM XBPM signal estimations correspond to the lower boundary levels. Signal density spatial distributions were calculated for 300 mA at 10 m for MAX-IV CoSAXS planar undulator for K=1.25 and K=2.0 (Figs. 3-4). Rectangles are indicating photoemission production areas used for signal calculations, outer rectangles correspond to the upstream FM, inner rectangles correspond the downstream FM. Signal density spatial distributions for MAX-IV SoftiMAX APPLE undulator for circular (CP), vertical (VP) and horizontal (HP) polarizations are shown in Figs. 5-7 for K_x=3.35 and K_y=3.35 correspondingly. SRW program was used for undulator radiation calculations [7].

The PheM XBPM signal level is reaching few milli-amperes. The signal levels are higher compared to the blade type XBPM [8] mostly due to the larger area of the photoemission source. Typical area of the XBPM blade is in the order of 1 mm², while photoemission area of the PheM XBPM is ~10 mm². The efficiency of the photocurrent collection by the PheM XBPM will depend on electrostatic field configuration, which can be optimized for required performance.

Sensitivity, linearity and spatial range of XBPM is characterized by the calibration curve. PheM XBPM calibration curves, shown for considered cases in Figs. 8-12, were calculated for vertical direction as (S1-S2)/(S1+S2), where S1 and S2 are signals from the upper and lower fixed masks areas contributing to signal.

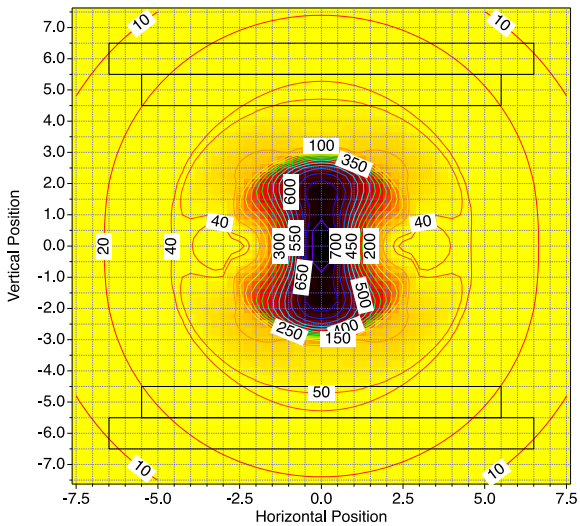


Figure 3: PheM XBPM signal [μA/mm²] spatial distribution at 10 m, MAX-IV CoSAXS planar undulator, K=1.25. Rectangles are indicating photoemission production areas used for signal calculation: upstream FM (outer rectangles), downstream FM (inner rectangles).

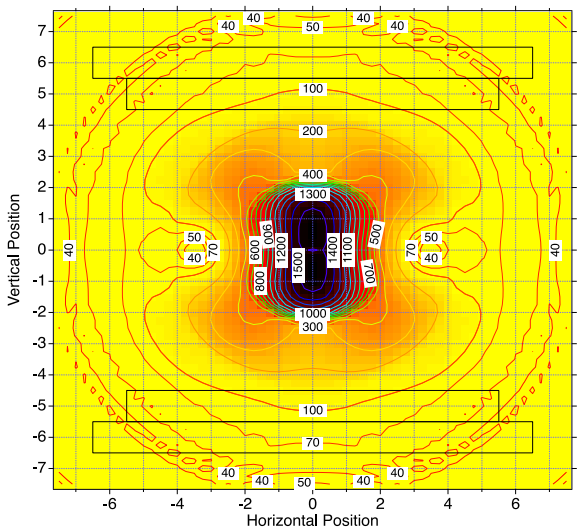


Figure 4: PheM XBPM signal [μA/mm2] spatial distribution at 10 m, MAX-IV CoSAXS planar undulator, K=2.0. Rectangles are indicating photoemission production areas used for signal calculation: upstream FM (outer rectangles), downstream FM (inner rectangles).

Content from this work may be used under the terms of the CC BY 4.0 licence (© 2022). Any distribution of this work must maintain attribution to the author(s), title of the work, publisher, and DOI

ISBN: 978-3-95450-241-7 ISSN: 2673-5350 doi:10.18429/JACoW-IBIC2022-MOP44

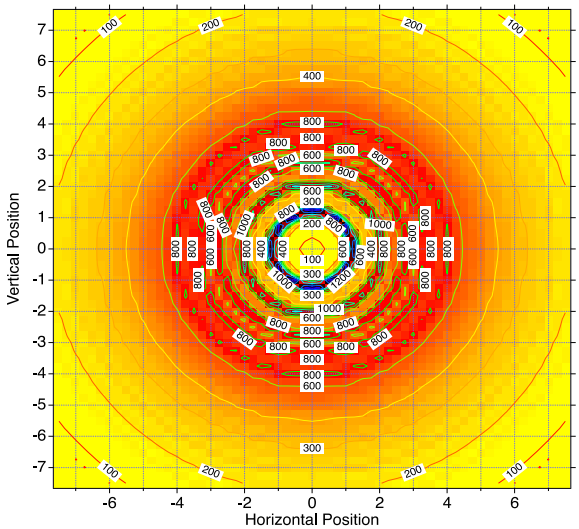


Figure 5: PheM XBPM signal [μA/mm²] spatial distribution at 10 m, MAX-IV SoftiMAX APPLE undulator, circular polarization, K_x=3.35, K_y=3.35.

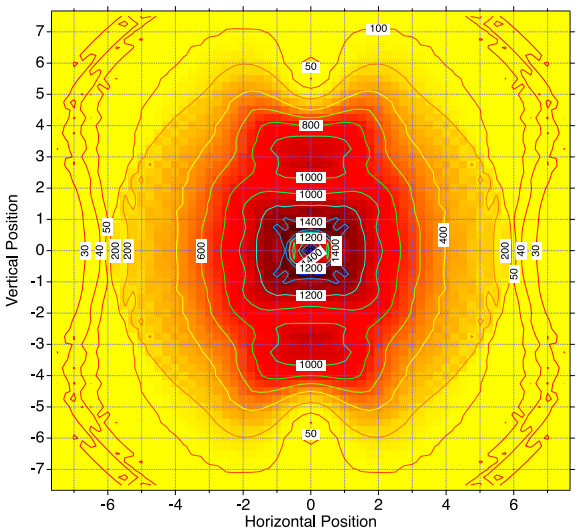


Figure 6: PheM XBPM signal [μA/mm²] spatial distribution at 10 m, MAX-IV SoftiMAX APPLE undulator, vertical polarization, K_y=3.35.

As can be seen, the signal level is higher for the downstream mask (red and blue solid lines) compared to the signal levels from the upstream mask (red and blue dashed lines). Calibration curves were calculated separately for the downstream mask (green solid lines) and for the upstream mask (green dashed lines). In general, signals from both fixed masks, if not separated, will be summed up by the pick-up electrode, the resulting calibration curves are also shown as black solid lines. As can be seen from calibration curves, the PheM XBPM response for considered cases is quite linear up to ~100 urad deviation of the undulator radiation beam. Since there is no high heat load at the detection section, the PheM XBPM spatial range of operation is limited only by the nonlinearity response.

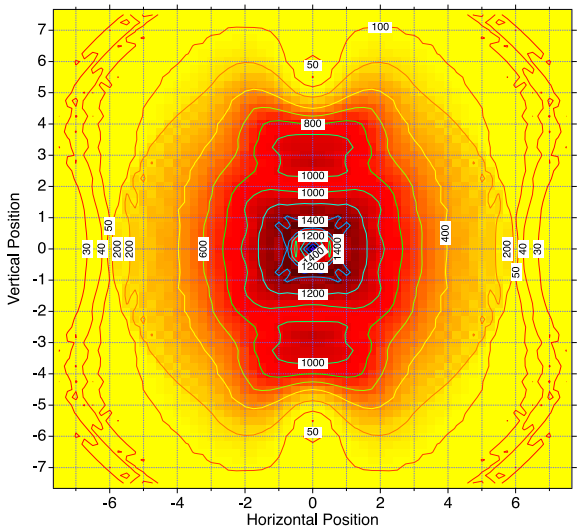


Figure 7: PheM XBPM signal [μA/mm²] spatial distribution at 10 m, MAX-IV SoftiMAX APPLE undulator, horizontal polarization, K_x=3.35.

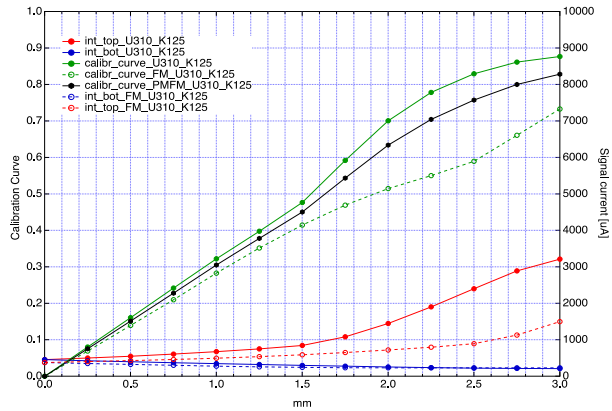


Figure 8: PheM XBPM Signals (red and blue) and Calibration curves (green), total (black), MAX-IV CoSAXS undulator, K=1.25 at 10 m.

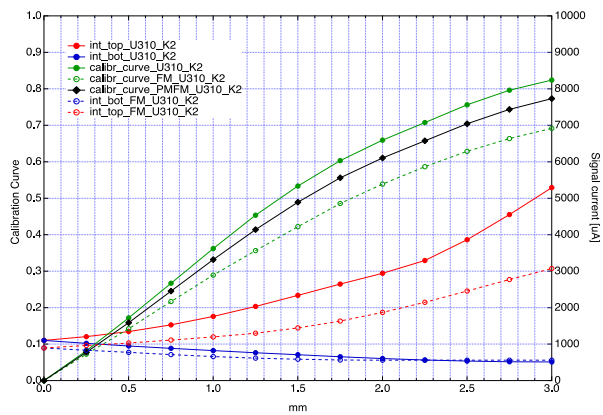


Figure 9: PheM XBPM Signals (red and blue) and Calibration curves (green), total (black), MAX-IV CoSAXS planar undulator, K=2.0 at 10 m.

Content from this work may be used under the terms of the CC BY 4.0 licence (© 2022). Any distribution of this work must maintain attribution to the author(s), title of the work, publisher, and DOI

ISBN: 978-3-95450-241-7 ISSN: 2673-5350 doi:10.18429/JACoW-IBIC2022-MOP44

Content from this work may be used under the terms of the CC BY 4.0 licence (© 2022). Any distribution of this work must maintain attribution to the author(s), title of the work, publisher, and DOI

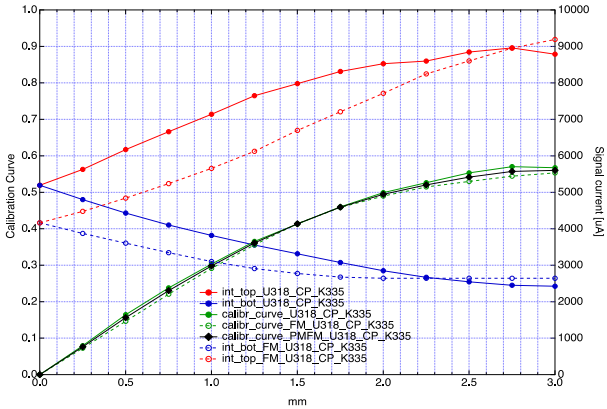


Figure 10: PheM XBPM Signals (red and blue) and Calibration curves (green), total (black), MAX-IV SoftiMAX APPLE undulator, circular polarization, K_x=3.35 K_y=3.35 at 10 m.

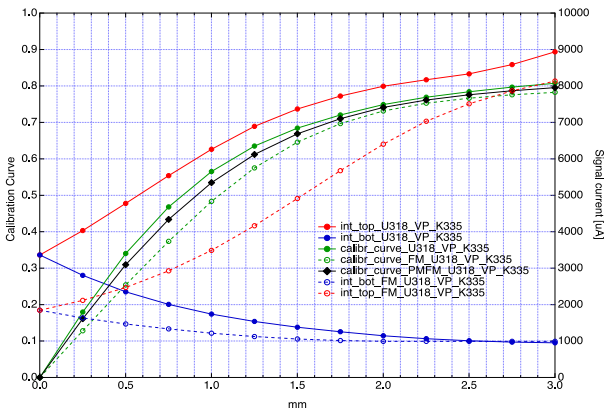


Figure 11: PheM XBPM Signals (red and blue) and Calibration curves (green), total (black), MAX-IV SoftiMAX APPLE undulator, vertical polarization, K_y=3.35, 10 m.

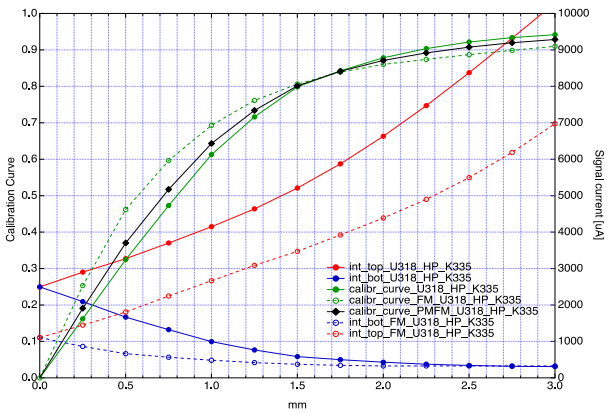


Figure 12: PheM XBPM Signals (red and blue) and Calibration curves (green), total (black), MAX-IV SoftiMAX APPLE undulator, horizontal polarization, K_x=3.35, 10 m.

CONCLUSION

A novel photoemission type of the frontend XBPM for the 'white' undulator radiation is proposed. The PheM XBPM is a part of the frontend fixed mask. Fixed mask is used as a source of photoelectrons, which are collected by positively biased electrodes. Positive bias will eliminate the possibility of building a conductive deposit onto the insulator surfaces around the electrodes. Electrodes are hidden from the undulator radiation, so there is no high heat load at the detection section. The PheM XBPM signal yield are higher compared to the blade type XBPM due to larger area of signal production. Further electrostatic improvements of the PheM XBPM can be consideration of an additional pick-up stage to separate signals from the upstream and the downstream fixed masks, or an additional electrode section in between detection section and the fixed mask to control signals collection.

The PheM XBPM concept will simplify the overall beamline frontend design when directly defining the beam position relative to the frontend fixed mask. Due to the PheM XBPM design simplicity, it can be potentially installed at the existing frontends.

REFERENCES

[1] E. D. Johnson and T. Oversluizen, "Compact flux beam position monitor," *Rev. Sci. Instrum.*, vol. 60, p. 1947. 1989.

[2] C. Bloomer and G. Rehm, "Operation of Diamond Light Source XBPMs with Zero Bias," in *Proc. IBIC2013*, Oxford, UK, Sept. 2013, paper TUPC10, pp. 376-379.

[3] B. X. Yang *et al.*, "Performance Test of the Next Generation X-Ray Beam Position Monitor System for the APS Upgrade", in *Proc. IBIC'16*, Barcelona, Spain, Sep. 2016, pp. 78-81. doi:10.18429/JACoW-IBIC2016-MOPG17

[4] C. Bloomer and G. Rehm, "Real-time Calculation of Scale Factors of X-ray Beam Position Monitors during User Operation", in *Proc. IBIC'12*, Tsukuba, Japan, Oct. 2012, paper MOPA13, pp. 79-82.

[5] H. Tarawneh, L.-J. Lindgren, and B. Anderberg, "Prototype soft end dipole magnet for MAX-IV, fabrication and measurements," *Nucl. Instrum. Methods Phys. Res., Sect. A*, vol. 546, p. 620, 2005.

[6] H. Henneken, F. Scholze, M. Krumrey, and G. Ulm, "Quantum efficiencies of gold and copper photocathodes in the VUV and X-ray range," *Metrologia*, vol. 37, pp. 485-488, 2000.

[7] O. Chubar and P. Elleaume, "Accurate and Efficient Computation of Synchrotron Radiation in the Near Field Region", in *Proc. EPAC1998*, Stockholm, Sweden, June 1998, paper THP01G, p. 1177.

[8] P. Ilinski, "Optimization of NSLS-II Blade X-ray Beam Position Monitors: From Photoemission Type to Diamond Detector", in *Proc. IBIC'13*, Oxford, UK, Sep. 2013, paper MOPC10, pp. 67-70.

ISBN: 978-3-95450-241-7 ISSN: 2673-5350 doi:10.18429/JACoW-IBIC2022-MOP45

A NEW LUMINOSITY MONITOR FOR THE LHC RUN 3

S. Mazzoni*, W. Andreazza, E. Balci, D. Belohrad, E. Bravin, N. Chritin,
J. C. Esteban Felipe, T. Lefevre, M. Martin Nieto, M. Palm[1]
CERN, Geneva, Switzerland
[1]presently at Terapet SA, Satigny, Switzerland

Abstract

The Beam RAte of Neutrals (BRAN) is a monitor that provides a relative luminosity measurement for the four LHC experiments. BRANs are used during operations as a tool to find and optimise collision and to cross-check experiments luminosity monitors. While each LHC experiment is equipped with BRANs, in this contribution we will focus on the new monitors installed for ATLAS and CMS that will replace the ageing gas chambers during LHC run 3. These will also serve as prototypes for the future High Luminosity LHC monitors that will need to sustain an even higher collision rate. A description of the BRAN as well as the first results obtained during the LHC Run 3 start-up will be presented.

INTRODUCTION

The BRANs are luminosity monitors installed on both sides of the four LHC experiments to measure the relative luminosity. The working principle is the detection of electromagnetic showers produced inside a target absorber by neutral particles (neutrons and high-energy photons) from the collisions. The detected signal I is thus proportional to the collision rate, that can be related to the luminosity $\mathcal{L}$ through [1]

$$I \propto N = \sigma \mathcal{L} \ , \qquad (1)$$

where N is the collision rate and σ the relative cross section. Neutral particles propagate in the direction of the colliding particles and can be intercepted at a sufficient distance from the Interaction Point (IP) when the two LHC beams are sufficiently separated by the D1 dipole. In the case of the Interaction Regions (IR) 1 and 5 - Atlas and CMS respectively - the BRANs are inserted inside the Target Absorber of Neutrals (TANs) at approximately 140 metres from the IP, in a position as close as possible to the maximum of the shower produced in the TAN.

BRANs are *relative* bunch by bunch luminosity monitors that are mostly used by LHC operators as a simple and reliable tool to find and optimise collisions and to cross-check the *absolute* luminosity monitors maintained by the LHC experiment that measure the actual instantaneous and integrated luminosities. As mentioned, the absolute calibration of the BRANs is not per se a requirement, the emphasis being on the stability, linearity and resolution. Table 1 contains a summary of the BRAN requirements. During the LHC runs 1 and 2, the BRANs installed in IR 1 and 5 were gas ionisation chambers [2] produced by Lawrence Berkeley

* stefano.mazzoni@cern.ch

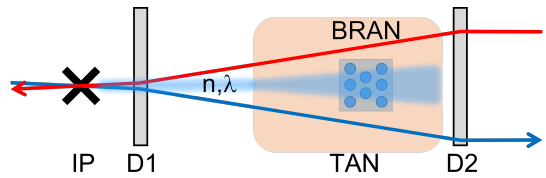


Figure 1: Layout of IR 1 and 5. BRANs are installed in the TANs approximately 140 metres from IP.

National Laboratory. While these detectors worked well through the LHC runs, they have been operating since 2009 in a high radiation environment and suffer from ageing components. In addition, these cannot be operated in the future High Luminosity (HL) run 4 of LHC as new absorbers with different geometry will replace the TANs to cope for the increased collision rate. It was therefore decided to develop new BRANs for IR 1 and 5 with the aim of replacing the gas chambers for LHC run 3 and to serve as a prototype to test materials and detection principles for the HL run 4. Two such detectors have been installed in February 2022 during the LHC year-end technical stop (YETS), at the right of IP1 and left of IP5. The two remaining BRANs are being assembled in view of an installation during the 2022-23 YETS. In this contribution we will describe the instruments and present the very first data available to date from Run 3 commissioning.

INSTRUMENT DESIGN

The principle of the new BRANs is the measurement of Cherenkov radiation produced in fused silica rods that are crossed by the showers produced by the TANs. Eight 603 mm long, 10 mm diameter fused silica rods are hosted in a mixed copper and aluminium enclosure that is inserted in the 100 mm wide TAN slot as shown in Fig. 2a. The rods are made of an ultra-pure, Hydrogen-free synthetic silica with low OH content. This type of material - Suprasil 3302 by Heraeus Quarzglas - was chosen among other types of fused silica that have been irradiated inside the IR1 TAN during the 2nd LHC run as it showed the minimum drop of transmission over the range 160-650 nm, attaining 20% of the transmission of the non-irradiated sample after being exposed to a dose of 0.8 MGy [3]. These results have been confirmed by a post run analysis of the spectral transmission of five rods performed in 2018 at the university of Illinois [4] showing that transmission of Suprasil in the visible range (400-600 nm) is practically unaffected by radiation exposure. As for the UV, all samples show a decrease of transmissivity particularly around 214 and 325 nm where

Content from this work may be used under the terms of the CC BY 4.0 licence (© 2022). Any distribution of this work must maintain attribution to the author(s), title of the work, publisher, and DOI

ISBN: 978-3-95450-241-7 ISSN: 2673-5350 doi:10.18429/JACoW-IBIC2022-MOP45

Table 1: Summary of BRAN Requirements from Ref. [5]

Use case	Resolution [Hz/µb]	Rel. accuracy
Initial beam finding and overlap	10^{-2} (nominal bunch) 10^{-4} (pilot bunch)	±10%
Luminosity maximisation	±1%	±1% nice to have ±5% sufficient

most of the Cherenkov photons are produced. The presence of hydrogen affects the rate at which this process takes place, with hydrogen-free silica degrading almost instantaneously but attaining a stable value, as opposed to hydrogen-rich samples that have a slower decay but exhibit transmission variation over time at steady state. Cherenkov radiation

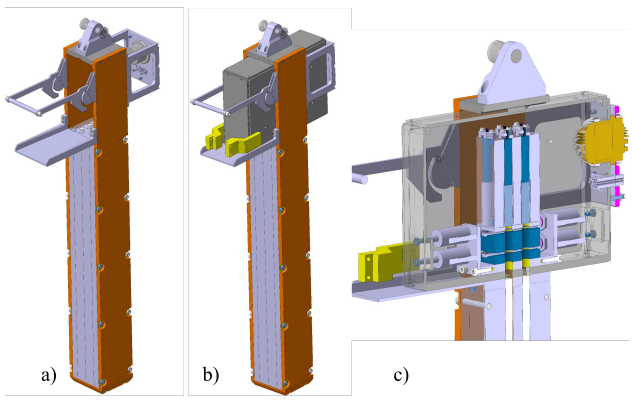


Figure 2: BRAN design: glass rods enclosure (a). The Photo Multiplier (PMT) light-tight enclosure is slid on top (b). Section (c) shows the solenoid-actuated light apertures and the PMTs.

produced in the fused silica bars propagates to its extremities, the top one in contact with a PMT. The type chosen (Hamamatsu R2496) is a fast time response, 8 mm diameter head-on bialkali PMT with a fused silica window that has been used, in its version with borosilicate glass window, in the Run 2 studies of Ref. [3]. Each of the eight PMTs is protected by a magnetic shield case and is hosted inside a light tight enclosure that is slid on top of the silica bars enclosure (see Fig. 2b). The sliding mechanism is equipped with a handle to facilitate the connection/disconnection of the PMT enclosure and to facilitate robotic handling. The amount of Cherenkov radiation impinging on the detectors can be controlled by means of variable aperture that are inserted in front of the PMTs (see Fig. 2c) by means of push solenoids. Three transmission levels of approximately 100%, 10% and 1% can be set independently to the first line of three PMTs closer to the IP (see Fig. 1) to have two sets of channels with different sensitivity to cope with the large instantaneous luminosity range that is achieved during machine commissioning and operation. Solenoids have been chosen against other technologies (e.g. pneumatic actuators) for simplicity and tolerance against the very high dose that is achieved in IR 1 & 5.

SIGNAL PROCESSING

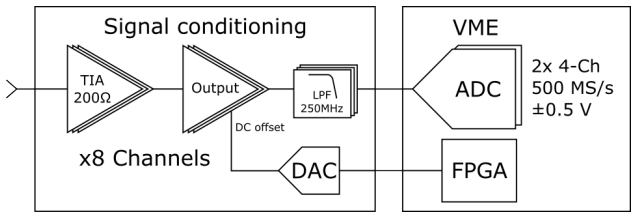


Figure 3: Schematic of the BRAN data acquisition.

The signals from the PMTs are conditioned using custom-made front-ends composed of trans-impedance amplifiers (G=200 V/A) followed by 250 MHz anti-alias filters (see Fig. 3). High radiation dose in the LHC tunnel causes the analogue electronics to fail quickly, so the front-ends cannot be placed close to the PMTs. They are instead installed in the service galleries through 213 and 138 metres-long cables for IR 1 & 5 respectively.

The analogue signals are digitized using digital acquisition systems (DAQ) installed as well in the service galleries. The signals are digitized using two FMC form-factor 4-channel 500 MSPS 14-bit ADCs, each hosted in an in-house built VME FMC Carrier [6], which provides necessary FPGA resources to perform digital signal processing and communication upstream using the VME bus.

Due to cable length, noise is induced by electromagnetic coupling, with significant perturbations in the bandwidth up to ≈ 200 kHz, peaking at 600 Hz, causing as well DC baseline shifts. As such DC displacement can cause saturation of the ADC, it has to be corrected before the signal is converted to the digital stream by injecting an opposite voltage to the amplifier stage using DAC. The DAC stores the default value internally, and can only be re-programmed through the VME interface. The 600 Hz noise component is significantly lower than the LHC revolution frequency of 11.2 kHz, it can be digitally removed.

The digital processing chain is shown in Fig. 4. The entire processing is performed over four 16-bit words ADC frames, a word being composed of 14-bit MSB aligned sample and two zeroed LSBs. With four ADC channels that represents a total of 256 bits per frame running at a frame rate of 8 ns, the sample rate of 500 MSPS is achieved. The two unused LSBs in each word are used to tag in each channel the samples by the turn and bunch marks. The timing information comes from the LHC beam synchronous timing (BST). As the two data sources are asynchronous - ADC running at 500 MHz,

Content from this work may be used under the terms of the CC BY 4.0 licence (© 2022). Any distribution of this work must maintain attribution to the author(s), title of the work, publisher, and DOI

ISBN: 978-3-95450-241-7 ISSN: 2673-5350 doi:10.18429/JACoW-IBIC2022-MOP45

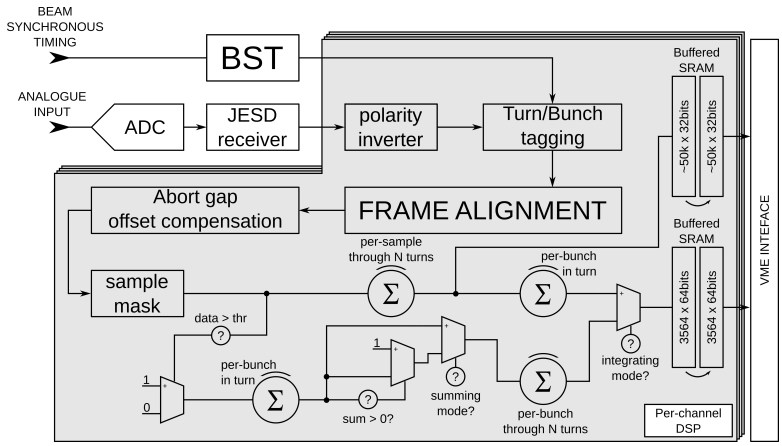


Figure 4: Simplified schematic of the BRAN digital data processing.

BST at 160 MHz, the stream tagging incurs in an uncertainty of 1 ADC sample (2 ns), hence integral of one LHC bunch slot corresponds to a sum of 12 or 13 samples.

As the BRAN is a turn-based measurement instrument, all the words within a single LHC turn must be aligned such that the first word in the turn starts at the boundary of the frame. This simplifies the synchronization of the per-sample and per-bunch accumulators to the turn. The frame aligned data are compensated for the offset by subtracting at each turn a pedestal corresponding to the average signal measured in the LHC abort gap region of the previous turn. A sample mask can be setup to clear individual samples within a bunch slot.

The firmware currently supports three mutually exclusive operating modes, which return a vector of 3564 × 64 bits signed values:

- **Integrating mode** - cumulation of individual samples over N turns followed by their integration per bunch slot
- **Summing mode** - expresses number of samples in the bunch slot exceeding a given threshold when cumulated over N turns
- **Counting mode** - how many times in the given bunch slot there was at least one sample exceeding the threshold when cumulated over N turns

Firmware further exports the raw output of the per-sample accumulator as a vector of 44500 × 64 bits signed values. These data are used to set up correctly the timing relation to the measured beam signal, and serve for debugging as well. Dual-port memory blocks used to store the results are equipped with locking mechanism assuring enough time for the SW layer to load the data. IRQ is triggered when new data arrive to the output buffers.

The memory buffers content is periodically fetched through the VME interface, published and logged through the CERN's Front End Server Architecture (FESA) server running on the VME crate front-end computer.

FIRST DATA FROM LHC RUN 3 COMMISSIONING

Counting Mode for Low-Luminosity Fills

The first collisions at 6.8 TeV took place between May and June 2022. Plotted in Fig. 5 is the very first data from the

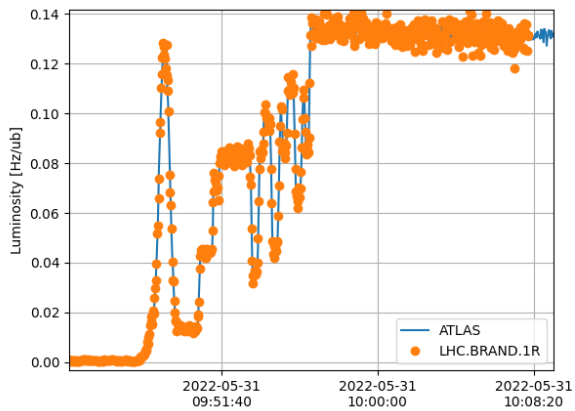


Figure 5: First BRAN data from IR1: low luminosity commissioning run with pilot bunch (orange points). Data are plotted against the reference instantaneous luminosity published by ATLAS.

BRAN detector installed in IR1 right (orange points) against the reference instantaneous luminosity published by the ATLAS experiment. The plot shows the beginning of luminosity scans with one colliding nominal bunch at $\beta^* = 19.2$ m. The BRAN is set-up for low-luminosity fills, that is in counting mode and with 0% attenuation. The BRAN shows a very good agreement with the experiment luminosity data over the entire scan range. Data at 0.14 Hz/µb show a large scattering due to the fact that some parameters (amplifier gain, counting threshold, ...) were not optimised and the overall data processing scheme was still in commissioning. The standard deviation of the noise at $\sigma = 2.3 \times 10^{-4}$ Hz/µb, defines the *initial* per-bunch luminosity resolution. As mentioned earlier, fused silica bars will loose optical transmission due to

Content from this work may be used under the terms of the CC BY 4.0 licence (© 2022). Any distribution of this work must maintain attribution to the author(s), title of the work, publisher, and DOI

ISBN: 978-3-95450-241-7 ISSN: 2673-5350 doi:10.18429/JACoW-IBIC2022-MOP45

Content from this work may be used under the terms of the CC BY 4.0 licence (© 2022). Any distribution of this work must maintain attribution to the author(s), title of the work, publisher, and DOI

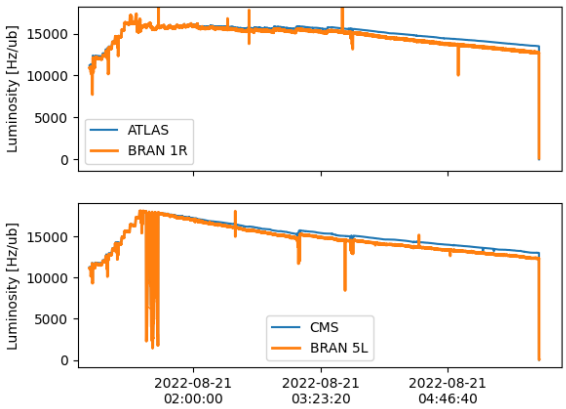


Figure 6: High luminosity fill 8147 with data from IR1 (top) and IR5 (bottom). It can be noticed how the BRAN signal tends to decrease with respect to the respective experiment instantaneous luminosity.

radiation exposure, expecting to level out at approximately 20% of the initial value. As such, the steady-state sensitivity per bunch (i. e. to relative luminosity variations) is expected to be approximately 10^{-3} Hz/µb. This fulfills the requirement for nominal bunches but is some 10 times larger than the one for pilot bunches.

Integrating Mode for Physics Fills

For full physics beams with order of 2500 colliding bunches and $\beta^* = 0.3$ m, the instantaneous luminosity can reach values up to $\mathcal{L} \propto 1.7 \times 10^4$ Hz/µb. The high number of colliding bunches makes it imperative to attenuate Cherenkov light to the maximum value (1% transmission), and for such low β^* integrating mode is preferred over photon counting method that no longer yields the correct relative variation to luminosity per bunch due to the high number of photoelectrons produced per collision event. Figure 6 shows BRAN data from IR1 (top) and IR5 (bottom) for fill 8147 with 2400 colliding bunches. While the agreement between BRAN and experiment luminosity is fair, there can be noticed spike-like data perturbations, and a progressive drop of the BRAN signal that, for this specific fill, reaches 5.9% and 4.8% for IR1 and 5 respectively over a fill duration of approximately 5 hours. Such a behaviour is still under investigation, a possible explanation for the slow signal drop being the progressive loss of transmission of fused silica bars, as discussed earlier. Another possible explanation is a progressive ageing of the PMTs that can happen when exposed to an excessive amount of light, even when the produced anode current is below the maximum rated value (30 µA for R2496 type). The average anode current per PMT however is estimated between 1 and 3 µA. That, according to the manufacturer's guidelines, is a safe level when PMT response stability over time is the priority. Typical resolution for full physics fills is of the order of 50 Hz/µb RMS, so in general better than 1% as required.

Fused Silica Transmission Loss

A progressive loss of transmission in the UV of the fused silica bars affects the overall BRAN light yield. Figure 7 shows the average total luminosity signal from the BRANs during stable beam mode (each point is a physics fill), normalised to the respective experiment absolute luminosity monitor. In accordance with preliminary tests during LHC Run 2, the transmission is expected to drop approximately 80% when at steady state. The decrease in light yield per collision event can be compensated by increasing the aperture from 1 to 10% for high luminosity fills, but will decrease the resolution for the low luminosity use case. The last point of BRAN left of IP5 is significantly lower than expected. This is due to a displacement of the signal baseline that lowers the overall signal intensity. The amplitude of the luminosity signal per bunch however is in line with the previous fill. This effect is still being investigated, but it is unrelated to transmission loss.

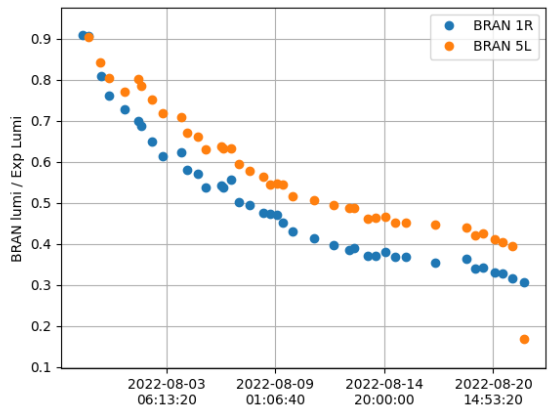


Figure 7: Decay of BRAN vs. Experiment luminosity signal as a function of time during 40 LHC fills in August 2022.

CONCLUSION

We have presented the design and preliminary data of the new BRANs for the LHC High luminosity IRs that will be operated during Run 3. The first two instruments have been installed during the 2021-22 LHC YETS and are being commissioned. Preliminary data show that the BRANs can fulfill most of the requirements for resolution and relative accuracy in both low and high luminosity fills. The relative accuracy is at present around 5% within a fill but a general trend is present probably due to transmission loss of the silica bars. It is expected that at steady state the long-term relative accuracy will be between 5% and 1%. Two additional BRANs will be installed during the 22-23 LHC YETS. The performance and behaviour of the four instruments during Run 3 will be instrumental to the design of the future HL-LHC BRANs that will be operated in the even harsher environment of Run 4, where instantaneous luminosity reach values as high as 6×10^4 Hz/µb and the yearly dose order of 1 GGy.

ISBN: 978-3-95450-241-7 ISSN: 2673-5350 doi:10.18429/JACoW-IBIC2022-MOP45

REFERENCES

[1] E. J. N. Wilson, *An Introduction to Particle Accelerators*, Oxford University Press, 2001.

[2] H. S. Matis, M. Placidi, A. Ratti, W. C. Turner, E. Bravin and R. Miyamoto, "The BRAN luminosity detectors for the LHC", *Nucl. Instrum. Methods Phys. Res., Sect. A*, vol. 848, pp. 114–126, 2017. doi:10.1016/j.nima.2016.12.019

[3] S. Jacobsen, "BRAN C prototype at LHC interaction point 1", CERN internal note, 2016.

[4] S. Yang *et al.*, "Optical Transmission Measurements of Fused Silica Irradiated at the CERN Large Hadron Collider", Fall 2022 Meeting of the APS Division of Nuclear Physics, manuscript in preparation.

[5] R. Assmann *et al.*, "On the measurement of the relative luminosity at the LHC", CERN document LHC-B-ES-0007 rev 1.1, 2004.

[6] A. Boccardi, "Ongoing electronic development in the CERN Beam Instrumentation Group: challenges and solutions for the measurement of particle accelerator beam parameters", *J. Instrum.*, vol. 8, no. 03, p. C03006, 2013. doi:10.1088/1748-0221/8/03/c03006

Content from this work may be used under the terms of the CC BY 4.0 licence (© 2022). Any distribution of this work must maintain attribution to the author(s), title of the work, publisher, and DOI

ISBN: 978-3-95450-241-7 ISSN: 2673-5350 doi:10.18429/JACoW-IBIC2022-MO3C2

DIAMOND-II ELECTRON BEAM POSITION MONITOR DEVELOPMENT

L. T. Stant*, M. G. Abbott, L. Bobb, G. P. Cook, L. Hudson,
A. F. D. Morgan, E. Perez-Juarez, A. J. Rose, A. Tipper
Diamond Light Source, Oxfordshire, United Kingdom

Abstract

The UK national synchrotron facility, Diamond Light Source, is preparing for a major upgrade to the accelerator complex. Improved beam stability requirements necessitate the fast orbit feedback system be driven from beam position monitors with lower noise and drift performance than the existing solution. Short-term beam motion must be less than 2 nm/$\sqrt{\text{Hz}}$ over a period of one second with a data rate of 100 kHz, and long-term peak-to-peak beam motion must be less than 1 µm. A new beam position monitor is under development which utilises the pilot-tone correction method to reduce front-end and cabling perturbations to the button signal; and a MicroTCA platform for digital signal processing to provide the required data streams. This paper discusses the challenges faced during the design of the new system and presents experimental results from testing on the existing machines.

INTRODUCTION

Diamond Light Source is a 3 GeV, 300 mA third-generation synchrotron located in Oxfordshire, UK. User operation began in early 2007 and since then a total complement of 33 beamlines have been commissioned. To further increase capabilities of the facility a new injector and storage ring will replace the existing machine, with the 18-month dark period scheduled for late 2026. This major upgrade, Diamond-II, will increase the energy to 3.5 GeV, reduce the horizontal emittance to 160 pm, and provide twice the number of straights [1].

As part of the Diamond-II upgrade, the storage ring electron beam position monitor (EBPM) processing electronics will be replaced[1]. Several factors influenced this decision:

- Due to the higher closed-loop crossover frequency and lower latency requirements of the fast orbit feedback for Diamond-II, the data rate from the EBPM system must increase from 10 kHz to 100 kHz, which is not supported by the existing systems.
- At the time of the Diamond-II CDR [1], the state-of-the-art multiplex switching solution would have created many harmonics in the measurement data for the required data rate.
- The existing systems will be over 20 years old and most have been repaired at least once.

Table 1 summarises the requirements of the Diamond-II EBPM system.

Table 1: EBPM Requirements for Diamond-II

Parameter	Diamond-II
Number of EBPMs	252 (11/12 per cell)
Geometric factor k	7.3 mm
Short-term motion (<1 s)	
Commissioning (0.3 mA)	<130 nm/$\sqrt{\text{Hz}}$
User beam (300 mA)	<2 nm/$\sqrt{\text{Hz}}$
Long-term motion (<1wk)	<1 µm pk-pk

The increasing adoption of the MicroTCA computing platform in the synchrotron community, combined with suitable technical resource available at Diamond Light Source, led to the choice of an in-house developed solution instead of an off-the-shelf product. The different parts of the EBPM system design will now be discussed.

BUTTON PICKUPS

Similar to Diamond, there will be two types of EBPM: primary EBPMs used for insertion device beam alignment will be located in straights on dedicated thermally stable pillars; and standard EBPMs located in the arcs will be mounted directly to the girders. Whereas the Diamond vessels were significantly wider in the horizontal dimension, the Diamond-II vessels are circular.

The button pickups are of a similar design to those used in the Diamond DDBA cell upgrade [2] and the ESRF design [3]. Due to the challenging manufacturing requirements of the button pickups, ongoing discussions with suppliers and other light sources have been necessary [4].

FRONT-END SYSTEMS

Analogue Front-End

Before digitisation, the signal from the button pickups must be filtered and amplified/attenuated by an analogue front-end. Typically, this unit will also include some form of compensation scheme to continuously correct the gain and phase variations between the EBPM channels. In Diamond, the compensation scheme chosen was multiplex switching located outside the vault. By moving the compensation inside the vault (i.e. closer to the buttons) it is possible to also correct for variations in cable gain and phase which have been shown to vary with temperature and humidity [5]. Due to promising results [6–9] and the avoidance of switching harmonics, the pilot tone compensation scheme was selected for use in the Diamond-II analogue front-end (D2AFE).

The D2AFE module (shown in Fig. 1a) contains four RF channels, each comprising of two stages of filtering, ampli-

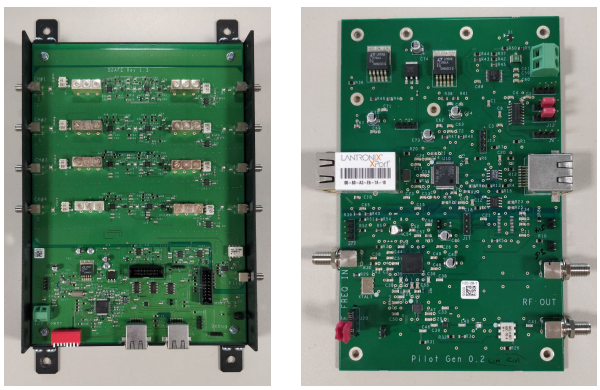
* laurence.stant@diamond.ac.uk

[1] The existing LINAC and booster EBPM systems will be refurbished and upgraded as a future project.

Content from this work may be used under the terms of the CC BY 4.0 licence (© 2022). Any distribution of this work must maintain attribution to the author(s), title of the work, publisher, and DOI

ISBN: 978-3-95450-241-7 ISSN: 2673-5350 doi:10.18429/JACoW-IBIC2022-MO3C2

fication and switched attenuation as shown in Fig. 2. An externally supplied pilot tone is coupled into the channel as early as possible, to compensate for variation in the D2AFE components. Helical filters are used for the bandpass elements. Channel performance of the current prototype is 52 dB maximum gain, >80 dB spurious-free dynamic range, 14 MHz bandwidth and −51 dB adjacent channel crosstalk. An output power measurement is provided via a coupler and log detector, which can trigger a <500 ns trip to engage full attenuation and protect downstream equipment.



(a) D2AFE. (b) PTG.

Figure 1: The PCB assemblies for the front-end systems. The D2AFE board size is 17 cm by 24 cm and the PTG board size is 10 cm by 16 cm.

Control of the switched attenuation and monitoring of power supplies, RF output powers and temperatures is provided per cell via a chained RS485 serial interface over Cat6 cable to the Controls Instrumentation Area (CIA) outside the vault. Power for each cell is provided via dual-redundant 12 V switched-mode supplies in the CIA, individually cabled to each D2AFE where linear regulators provide quiet 5 V and 3.3 V rails.

To validate the decision to locate the D2AFEs on the girder, radiation measurements have been taken over the previous two years. A set of RADFET [10] sensors and D2AFE boards have been located on the side of the girder downstream of the storage ring injection septum and collimators. Table 2 lists the measured doses, with negligible exposure on or close to the floor of the vault. A survey of radiation tolerance of D2AFE parts showed the only concerning items were the linear regulators, which degraded after a 40 Gy dose on a board mounted to the beampipe. The STM32 ARM microcontroller has shown no operational issues up to 170 Gy. The lower girder positions should receive a dose of 40 Gy after only 3.3 years with Diamond-II predicted losses, so instead D2AFEs will be located as close to the floor as possible. Extra noise and drift from the longer cables before pilot injection will be alleviated using passive external pilot injectors mounted on the girder top, connecting to the buttons using semi-rigid cable.

Table 2: Radiation Measurements over Two Years beside Diamond Girder, Downstream of Injection (Highest Dose Area)

Position	Radiation Dose (Gy)
Beampipe	308
100 mm below girder top	7.7
200 mm below girder top	5.4
300 mm below girder top	3.2
400 mm below girder top	4.0
500 mm below girder top	Negligible
Floor of vault	Negligible

Pilot Tone Generator

A single pilot tone is generated per cell by a redundant pair of pilot tone generators (PTG, shown in Fig. 1b) located in the CIA, and is distributed to a maximum of 16 D2AFEs. The tone is generated by a dual-loop PLL locked to a machine RF reference from an event receiver, avoiding the risk of free-running local crystals struggling with the narrow pilot filter in digital processing. The two modules feed an RF hybrid which allows the running PTG to failover to the backup without swapping hardware. Each output routes to one of the two cell girders, where at a patch panel another D2AFE unit is used as a distribution amplifier with controllable attenuation per channel (with pilot input terminated). These outputs are then distributed to the D2AFEs along the girder via local two-way splitters.

The PTG also provides the RS485 to Telnet interface for the D2AFE serial chain, which is available to the MicroTCA EPICS IOC in the same rack. Each end of the RS485 chain connects to a PTG, to provide separate redundancy of both the control interface and pilot tone. The PTG and D2AFE use a similar ARM microcontroller with common libraries for communication and firmware updates.

Firmware Update Method

To update nearly 300 D2AFEs and PTGs using local programming adapters would be very inefficient, so a remote firmware update method was developed using an in-application bootloader. This method can update the entire storage ring in under ten minutes if required, as each cell can run updates in parallel. In case a bad firmware is deployed, a fast handheld programmer with rescue image is being prepared to minimise disruption.

DIGITISATION AND PROCESSING

The EBPM signals from the entire cell are brought to a diagnostics rack in the CIA. A single 12-slot MicroTCA chassis, shown in Fig. 3, contains all of the required AMC cards for EBPMs, x-ray beam position monitors (XBPM), receiving machine events and providing machine protection outputs from beam position interlocks. For Diamond-II the orbit feedback and beamline interlocks will also include XBPM data to improve drift and fault tolerance, so it is

Content from this work may be used under the terms of the CC BY 4.0 licence (© 2022). Any distribution of this work must maintain attribution to the author(s), title of the work, publisher, and DOI

ISBN: 978-3-95450-241-7 ISSN: 2673-5350 doi:10.18429/JACoW-IBIC2022-MO3C2

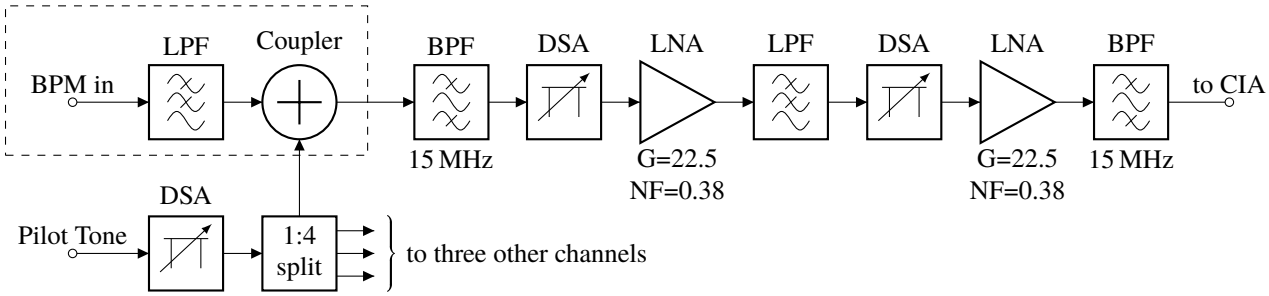


Figure 2: The architecture for one of the four channels in the D2AFE unit, including low-pass filters (LPF), helical band-pass filters (BPF), digital step attenuators (DSA) and low noise amplifiers (LNA). The initial filter and coupler (dotted box) is being developed as an external option.

convenient to locate them together and standardise on the same FMC carrier AMC. Each EBPM digitiser card uses two 8-channel 16-bit 250 Msps ADC FMCs, allowing for four EBPMs per card. This means a maximum provision of 16 EBPMs can be facilitated with only four AMCs. Beam position interlocks can be provided for the machine protection system using a custom RTM connected to one or more of the EBPM AMCs, subject to implementation.

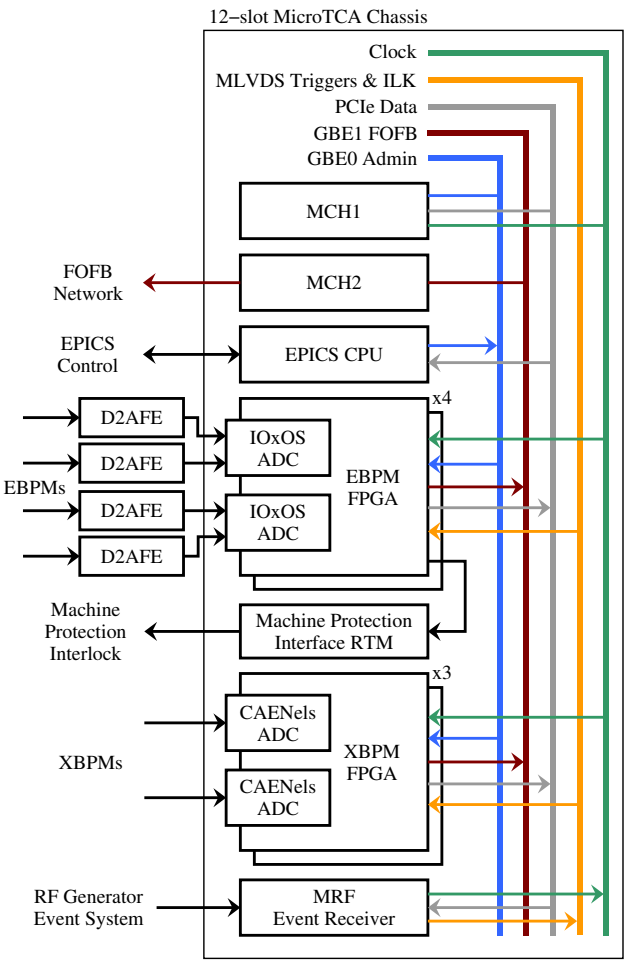


Figure 3: Architecture of a cell diagnostics MicroTCA crate.

The ADC data, acquired at 215 Msps, can be streamed directly to RAM for development and testing, but otherwise is mixed with a 70 MHz reference ($f_{RF} - 2f_{sample}$) before downsampling into standard acquisition streams, as shown in Fig. 4. In addition to the fast and slow acquisition (FA, SA) streams, a medium acquisition (MA) stream is generated for use in fault detection. The pilot signal is extracted as additional FA, MA and SA streams for analysis.

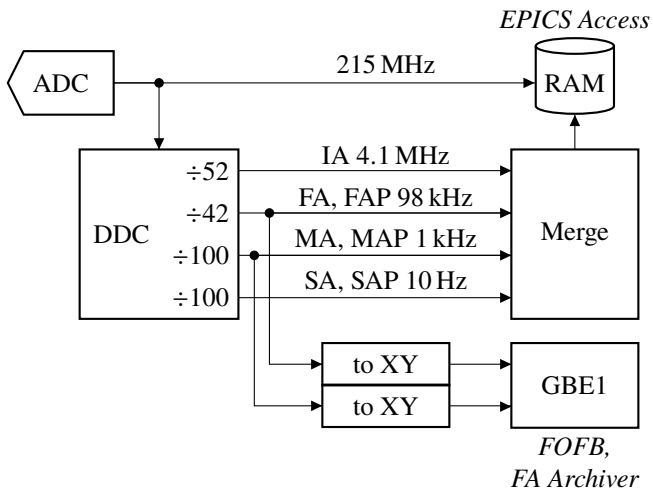


Figure 4: Diamond-II EBPM data streams. The fast, medium and slow acquisition streams also generate respective pilot streams.

SYSTEM MEASUREMENTS

A spare EBPM on the Diamond storage ring has been used for testing the design. The majority of testing so far has been to assess noise and drift performance, using a 1:4 splitter driven by a single button pickup. Figure 5 shows an SA measurement of this setup, which highlights the benefit of a pilot-compensated signal. The line at 1.67 mHz and its decaying harmonics are caused by the 10 minute top-up, and are reduced by increasing the attenuation in the D2AFE to improve the linearity. This is a trade-off with signal-to-noise ratio and is still under investigation. The line at 0.5 Hz is the flash rate of a status LED on the D2AFE modulating the

Content from this work may be used under the terms of the CC BY 4.0 licence (© 2022). Any distribution of this work must maintain attribution to the author(s), title of the work, publisher, and DOI

ISBN: 978-3-95450-241-7 ISSN: 2673-5350 doi:10.18429/JACoW-IBIC2022-MO3C2

power supply, which shows the high system sensitivity. This status LED has now been made steady-state.

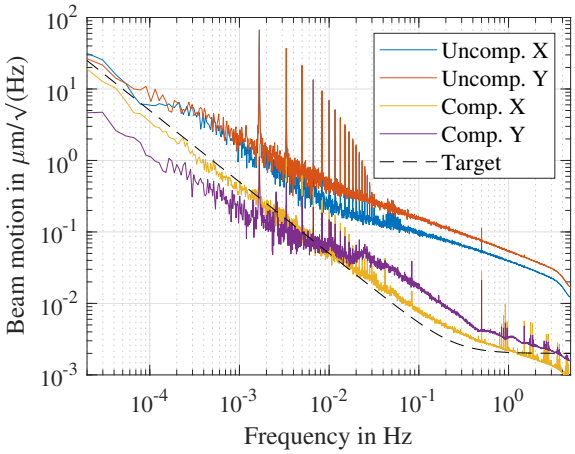


Figure 5: Spectral plot of EBPM motion from SA stream. Target is the <2 nm/$\sqrt{\text{Hz}}$ short-term requirement blended towards the <1 µm pk-pk long-term requirement below 1 Hz.

Increased noise on the Y signal is caused by the FMC ADC arrangement. Each ADC has two channels, so a four-button EBPM will have two groups of two channels with correlated noise, with uncorrelated noise between groups. The ABCD-to-XY transformation means that either X or Y will have improved noise, so the cables will be reconfigured to optimise the vertical Y signal.

Figure 6 shows an equivalent measurement from the FA stream. Although there are some spectral lines still to investigate, the performance is generally well within the requirement.

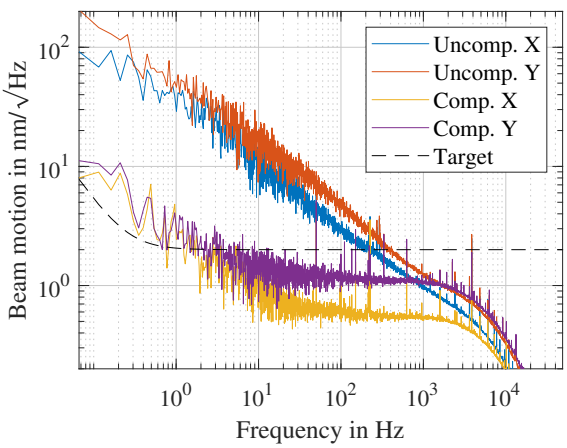


Figure 6: Spectral plot of EBPM motion from FA stream. The target continues as for Fig. 5.

Stability measurements from the SA stream are shown in Figs. 7 and 8. Although the performance of the Y signal is satisfactory, the X signal is drifting significantly, at times exceeding the target. The cause of this is revealed in Fig. 8, where the C and D button signals are shown to be strongly correlated with humidity measured close to the EBPM. Some humidity correlation is also seen in the A and B signals to a lesser extent. The inverse relationship of the drift between the C and D signals suggests that the cause may be from humidity drift of an imbalance inside the 1:4 splitter used for measurement, which is being investigated.

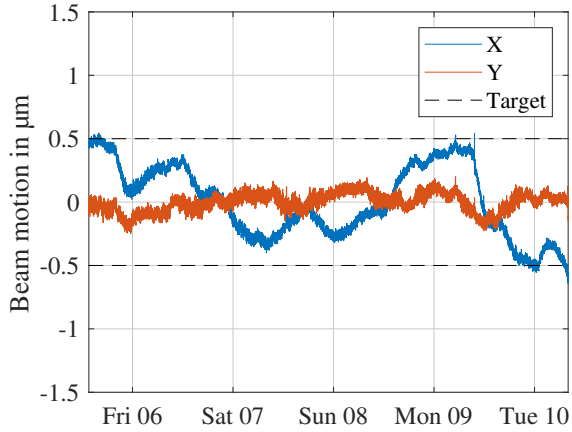


Figure 7: EBPM stability over five days from SA stream data. Target is <1 µm pk-pk long-term requirement.

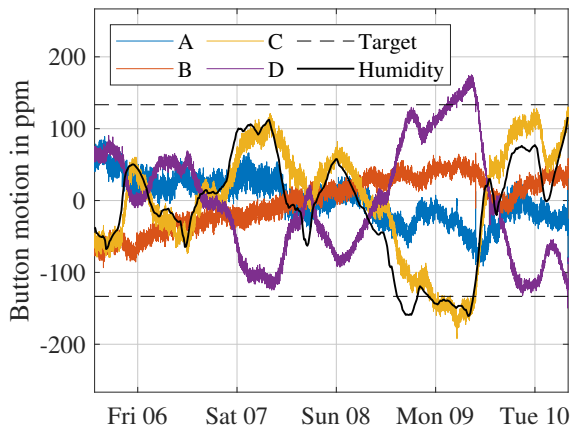


Figure 8: Button signals over five days, showing strong correlation with a local humidity sensor. Humidity is scaled to fit and ranges from 25% to 40% RH. Target is <1 µm pk-pk long-term requirement translated to individual buttons.

CONCLUSION

This paper has presented the new EBPM system for Diamond-II. Although still under development, the current results are encouraging and have validated the design decisions. Next steps include improving long-term stability and investigating software compensation methods for drift.

ACKNOWLEDGEMENTS

The authors wish to thank Dr. Guenther Rehm of Helmholtz-Zentrum Berlin for initial development work on this project.

Content from this work may be used under the terms of the CC BY 4.0 licence (© 2022). Any distribution of this work must maintain attribution to the author(s), title of the work, publisher, and DOI

ISBN: 978-3-95450-241-7 ISSN: 2673-5350 doi:10.18429/JACoW-IBIC2022-MO3C2

Content from this work may be used under the terms of the CC BY 4.0 licence (© 2022). Any distribution of this work must maintain attribution to the author(s), title of the work, publisher, and DOI

REFERENCES

[1] "Diamond-II conceptual design report," Diamond Light Source Ltd., Tech. Rep., 2019. https://www.diamond.ac.uk/dam/jcr:ec67b7e1-fb91-4a65-b1ce-f646490b564d/Diamond-IIConceptualDesignReport.pdf

[2] R. Bartolini *et al.*, "Double-double bend achromat cell upgrade at the Diamond Light Source: From design to commissioning," *Phys. Rev. Accel. Beams*, vol. 21, no. 050701, 2018. doi:10.1103/PhysRevAccelBeams.21.050701

[3] K. B. Scheidt, "Newly developed 6mm buttons for the BPMs in the ESRF Low-Emittance-Ring," in *Proc. IBIC'14*, Monterey, CA, USA, 2014, pp. 346–350. https://jacow.org/IBIC2014/papers/TUPF14.pdf

[4] A. Morgan, "Technological review of beam position button design and manufacture," in *Proc. IBIC'19*, Malmö, Sweden, 2019, pp. 448–452. doi:10.18429/JACOW-IBIC2019-WEAO01

[5] G. Rehm and C. Bloomer, "Impact on relative humidity on EBPM readings," in *Proc. DEELS'15*, Barcelona, Spain, 2015. https://indico.cells.es/event/22/contributions/426/

[6] G. Brajnik, S. Carrato, S. Bassanese, G. Cautero, and R. De Monte, "Pilot tone as a key to improving the spatial resolution of eBPMs," *AIP Conf. Proc.*, vol. 1741, no. 1, p. 020 013, 2016. doi:10.1063/1.4952792

[7] G. Brajnik, S. Bassanese, G. Cautero, R. De Monte, M. Ferianis, and G. Rehm, "Reducing current dependence in position measurements of BPM systems by using pilot tone: Quasi-constant power approach," in *Proc. IBIC'18*, Grand Rapids, MI, USA, 2018, pp. 301–303. doi:10.18429/JACOW-IBIC2017-TUPWC09

[8] M. Cargnelutti *et al.*, "Stability tests with pilot-tone based Elettra BPM RF front end and Libera electronics," in *Proc. IBIC'18*, Shanghai, China, 2018, pp. 289–292. doi:10.18429/JACOW-IBIC2018-TUPB13

[9] G. Kube, "BPM Studies in view of PETRA IV," 15th Libera Workshop, Online at Instrumentation Technologies (Slovenia), 2020. https://bib-pubdb1.desy.de/record/452052

[10] A. Holmes-Siedle and L. Adams, "RADFET: A review of the use of metal-oxide-silicon devices as integrating dosimeters," *Int. J. Radiat. Appl. Instrum. Part C*, vol. 28, no. 2, pp. 235–244, 1986. doi:10.1016/1359-0197(86)90134-7

ISBN: 978-3-95450-241-7 ISSN: 2673-5350 doi:10.18429/JACoW-IBIC2022-MO3C3

PULSE-BY-PULSE PHOTON BEAM POSITION MEASUREMENTS AT THE SPring-8 UNDULATOR BEAMLINE*

H. Aoyagi†, H. Osawa, K. Kobayashi, T. Fujita, S. Takahashi
Japan Synchrotron Radiation Research Institute (JASRI/SPring-8), Hyogo, Japan

Abstract

A pulse-mode X-ray beam position monitor that enables pulse-by-pulse position measurement in the synchrotron radiation beamline of the synchrotron radiation facility was improved, and evaluation tests were performed. The monitor was equipped with blade-shaped detection elements utilizing diamond heatsinks to reduce stray capacitance, and a microstrip transmission line to improve high-frequency characteristics. The detection elements operate as photocathodes and generate single unipolar pulses with a full width at a half-maximum of less than 1 ns. This operation allows pulse-by-pulse measurement of the synchrotron radiation beam. To ensure operations at the undulator beamline in SPring-8, where the synchrotron radiation power is very intense, further improvements were introduced to the detecting elements to enhance heat resistance. The evaluation results of sensitivity and resolution in the pulse-by-pulse photon measurement and observation of beam oscillation during beam injection are discussed herein.

INTRODUCTION

We developed a pulse-mode X-ray beam position monitor (PM-XBPM) that enables pulse-by-pulse position measurements in the synchrotron beamline of SPring-8, a synchrotron radiation facility, and are working on practical applications. To improve the high-frequency characteristics, this monitor is equipped with diamond heatsinks to reduce the blade-shaped detecting elements' stray capacitance and a microstrip transmission line to match the impedance. The detection principle is the same as conventional X-ray beam position monitors (XBPMs), in which four blade-shaped detection elements are arranged vertically and horizontally, with the photon beam axis as the center of symmetry, and the current signal ratio of each detection element is read out as position information. The prototype was installed in a bending-magnet beamline (BM-BL), and evaluation tests were conducted. Thus, a unipolar pulse signal with a pulse length of 0.7 ns FWHM was generated, and a pulse-by-pulse beam position of the synchrotron radiation beam was observed [1].

To ensure the stable operation of the monitor in the insertion device beamline (ID-BL), where the synchrotron radiation power is extremely high, we aimed to enhance the heat resistance by modifying a diamond heatsink and a water-cooling holder [2]. By doubling the size of the diamond heatsink in the beam axis direction to 16 mm compared with the prototype, the contact area with the cooling base was increased to enhance the thermal resistance. This improvement increased the photon-receiving area, which led to an increase in the current signal. Furthermore, the heat-transfer efficiency was enhanced by adopting a wedge-shaped copper plug.

We confirmed the basic performance of the modified pulse-mode XBPM at a BM-BL (BL02B1), which has a maximum power density of 1.5 kW/mrad^2 and an actual irradiation power density of approximately 0.1 W/mm^2). Subsequently, it was transferred to the ID-BL (BL35XU), which has a maximum power density of approximately 500 kW/mrad^2 and an actual irradiation power density of approximately < 25 W/mm^2), and evaluation tests were performed. This paper discusses the position sensitivity, resolution, and observation of the beam oscillation during a top-up injection.

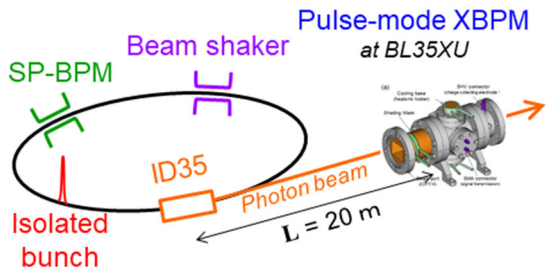


Figure 1: Setup of position sensitivity measurement.

POSITION SENSITIVITY

Perturbation by Beam Shaker and Amplitude Measurement by SP-BPM

Figure 1 illustrates the measurement system used for evaluating position sensitivity. A single isolated bunch was injected into the storage ring, and the bunch current was 0.95 mA. Betatron oscillations were excited horizontally and vertically using the bunch-by-bunch feedback (BBF) kickers at Cell 04 in the horizontal direction and a 0.9-m kicker at Cell 30 in the vertical direction. The perturbation frequency was set to 28.9 kHz (ν_x = 41.1382) in the horizontal direction and 60.0 kHz (ν_y = 19.3257) in the vertical direction. The excitation of the betatron oscillation was locked by a phase-locked loop (PLL) to automatically follow the tuning changes caused by the opening and closing of the ID gap and the bunch current. The perturbation amplitude was adjusted by the Dimtel iGp12 DAC output, and when the amplitude at the BPM of cell 21 reaches 100 μm, the DAC output is called "nominal kick power 100%." The kick angles corresponded to θx = 0.033 μrad and θy = 0.047 μrad under this condition. The stationary perturbation amplitude excited by radio frequency knockout

* Work supported by Japan Society for the Promotion of Science through a Grant-in-Aid for Scientific Research, No.18K11943 and No.21K12530.
† aoyagi@spring8.or.jp

Content from this work may be used under the terms of the CC BY 4.0 licence (© 2022). Any distribution of this work must maintain attribution to the author(s), title of the work, publisher, and DOI

ISBN: 978-3-95450-241-7 ISSN: 2673-5350 doi:10.18429/JACoW-IBIC2022-MO3C3

Content from this work may be used under the terms of the CC BY 4.0 licence (© 2022). Any distribution of this work must maintain attribution to the author(s), title of the work, publisher, and DOI

(RFKO) at any single-pass BPM (SP-BPM) can be converted to the amplitude at the PM-XBPM point. Figure 2 presents the estimated amplitude at the PM-XBPM (BL35XU) position 20.3 m from the source, which is converted from the amplitude observed at the SP-BPM (cell 21). The following values were used as conversion coefficients [2]:

$$\frac{|y_{XBPM}|}{|y_{BPM}|} = \frac{\sqrt{\left(\sqrt{\beta_{ID}} - \frac{\alpha_{ID} L}{\sqrt{\beta_{ID}}}\right)^2 + \frac{L^2}{\beta_{ID}}}}{\sqrt{\beta_{BPM}}} = 3.90 \,/\, 1.90 \text{ (hor. / ver.)},$$

where $\alpha_{ID} = -1.195\times10^{-5}$, $\beta_{ID} = 31.16$ m, $\beta_{BPM} = 31.21$ m in the horizontal direction and $\alpha_{ID} = +4.61\times10^{-6}$, $\beta_{ID} = 5.04$ m, $\beta_{BPM} = 5.73$ m in the vertical direction. The perturbation amplitude was adjusted by the iGp12 DAC output, and "nominal kicker power" was set to 100%, 75%, 50%, 25%, and 0%. The photon beam amplitude is linear to the DAC output value.

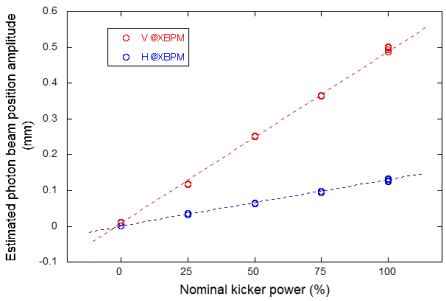


Figure 2: Photon beam position amplitude at PM-XBPM estimated from SP-BPM data.

Amplitude Measurement by PM-XBPM

Each pulse signal from the four detector elements (UL: upper-left, UR: upper-right, LL: lower-left, LR: lower-right) of a PM-XBPM was measured with an oscilloscope (4 GHz b.w., 50 GS/s, High Res. Mode, 12 bit). The horizontal and vertical beam positions were calculated using the integrated waveforms. Figure 3 shows a connecting diagram of PM-XBPM. To protect the oscilloscope, each signal cable was connected to a divider with a terminator of 50 Ω at one end instead of connecting it directly to the oscilloscope.

Figure 4 shows the oscillation during 40 consecutive turns observed by this monitor and the fitting curves of sine waves when the "nominal kick power" is changed. Here, the vertical and horizontal directions exhibit linearity (Fig. 5).

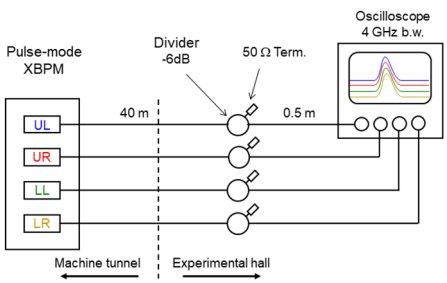
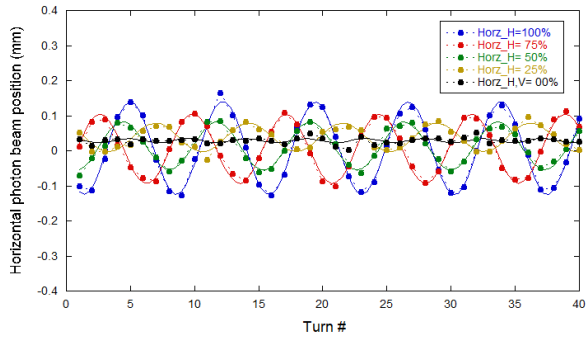
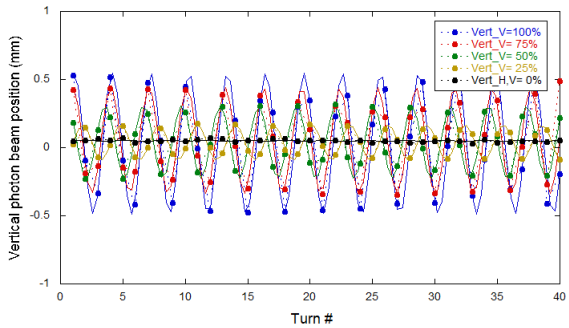


Figure 3: Connecting diagram of PM-XBPM.



(a) Horizontal



(b) Vertical

Figure 4: Photon beam amplitude measured by PM-XBPM.

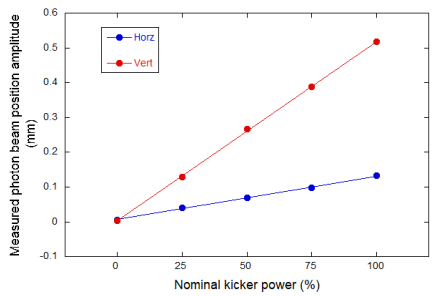
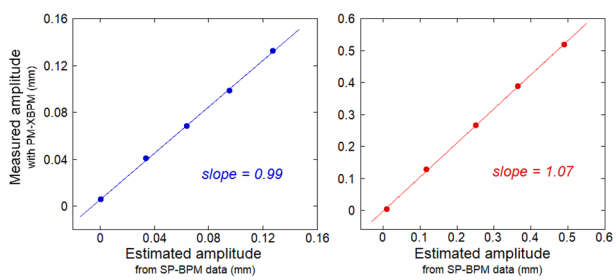


Figure 5: Amplitude of PM-XBPM readouts.

Comparison of SP-BPM and PM-XBPM

Figure 6 shows the correlation between SP-BPM and PM-XBPM data. The horizontal axis represents the amplitude at the PM-XBPM estimated from the amplitude observed by the SP-BPM (Fig. 2), and the vertical axis represents the amplitude measured by the PM-XBPM (Fig. 5). Sufficient linearity for practical uses was confirmed in both horizontal and vertical directions.



(a) Horizontal (b) Vertical

Figure 6: Correlation between XBPM and SP-BPM.

ISBN: 978-3-95450-241-7 ISSN: 2673-5350 doi:10.18429/JACoW-IBIC2022-MO3C3

RESOLUTION

Using the connection diagram described above (Fig. 3), we evaluated the resolution depending on the bunch current. The bunch current was set to 0.5, 1, 2, 3, 4, and 5 mA/bunch, as shown in Fig. 7. To reduce an influence of the pulse tails on the next pulses, a bunch interval was set to 24 buckets (47.2 ns) and low-current bunches were arranged from the front. The bunch current in each bucket was kept constant during this measurement by top-up injection. Figure 8 shows the superimposed waveforms of each bunch.

Figure 9 shows the fluctuations in Diff/Sum from the pulse heights of the four detection elements. The vertical axis in Fig.10 indicates the value (units: mm) obtained by multiplying the standard deviation of Diff/Sum by the correction factor. In both the horizontal and vertical directions, the fluctuation, that is the resolution, is likely to decrease as the bunch current increases. The minimum resolutions were obtained at a bunch current of 5 mA/bunch and were 4.5 μm std horizontally and 4.5 μm std vertically. Figure 10 also shows the fluctuations when the bandwidth is digitally narrowed to 200 MHz using the built-in oscilloscope function. The minimum resolutions were also obtained at a bunch current of 5 mA/bunch and were 1.7 μm std horizontally and 1.2 μm std vertically. Using a low-pass filter extends the pulse length; however, if the bunch interval is wide, the pulse information will be easier to read with a high-speed ADC. The resolution was low at lower bunch currents under these measurement conditions. Still, by optimizing the range of the oscilloscope, we achieved the design goal of a resolution of 10 μm std.

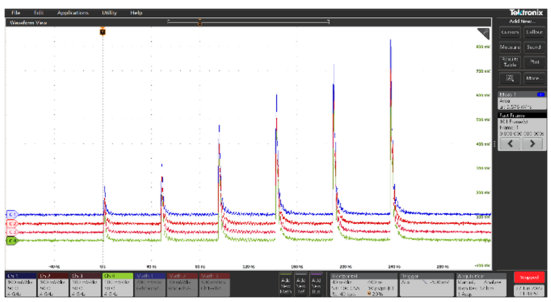


Figure 7: Screen capture of the oscilloscope. Applied voltage of the charge collecting electrodes (HV) is +300 V. ID gap is 6.7 mm.

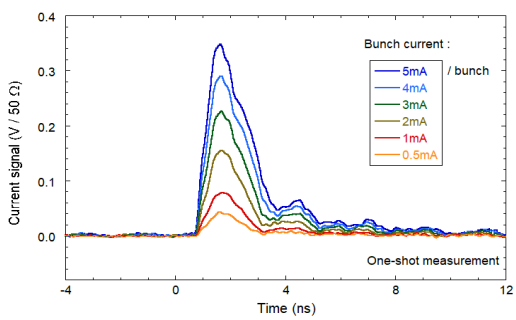


Figure 8: Waveforms of PM-XBPM. HV is +300 V. ID gap is 9.6 mm.

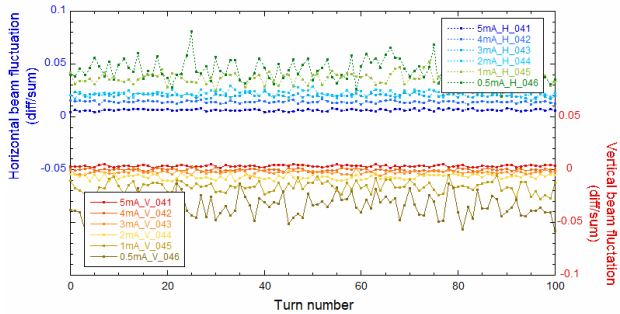


Figure 9: Fluctuation in diff/sum of the PM-XBPM data.

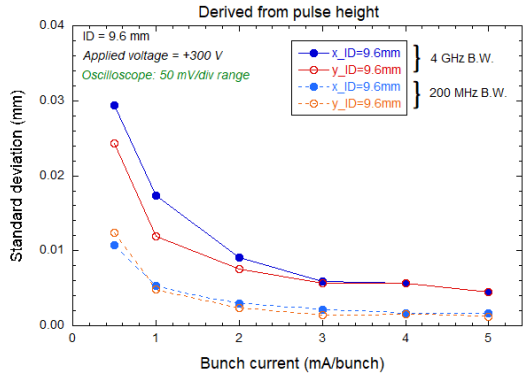


Figure 10: Bunch current dependence of the fluctuations.

BEAM OSCILLATION DURING BEAM INJECTION

A top-up injection is regularly performed during user time to supply stable beams to user experiments at SPring-8. However, the photon beam oscillated briefly during beam injection once every 20–40 s. Therefore, we attempted to observe the pulse-by-pulse behavior of the synchrotron radiation beam using PM-XBPM, synchronizing with the injection timing. Figure 11 shows the connecting diagram. The signal from each detection element was connected to a combiner (labeled "Divider" in the figure) through an attenuator (-10 dB). Therefore, the influence of reflected pulses can be attenuated. To observe the horizontal position, the combined signal from the UR and LR was connected to Channel 1 of the oscilloscope, and the combined signal from the UL and LL was connected to Channel 2. The cables were reconnected when switching to the vertical measurement.

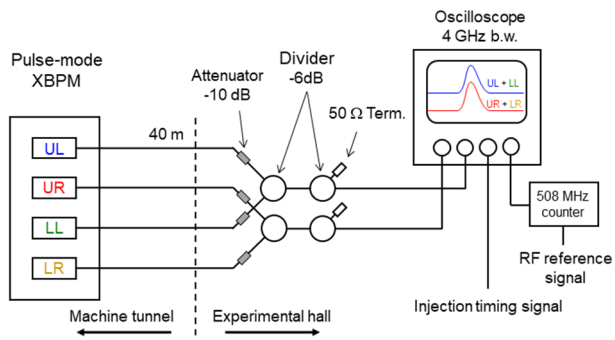


Figure 11: Connection diagram of PM-XBPM.

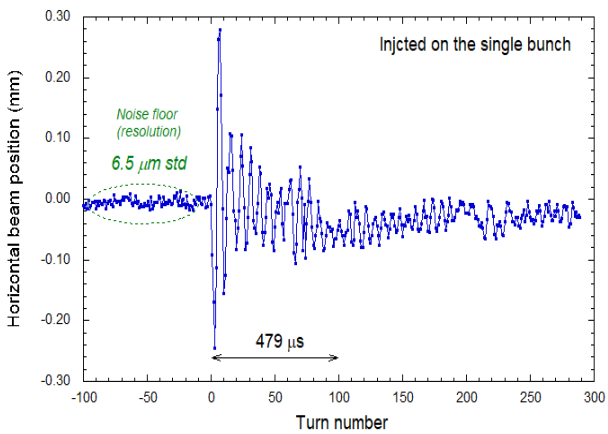
Content from this work may be used under the terms of the CC BY 4.0 licence (© 2022). Any distribution of this work must maintain attribution to the author(s), title of the work, publisher, and DOI

ISBN: 978-3-95450-241-7 ISSN: 2673-5350 doi:10.18429/JACoW-IBIC2022-MO3C3

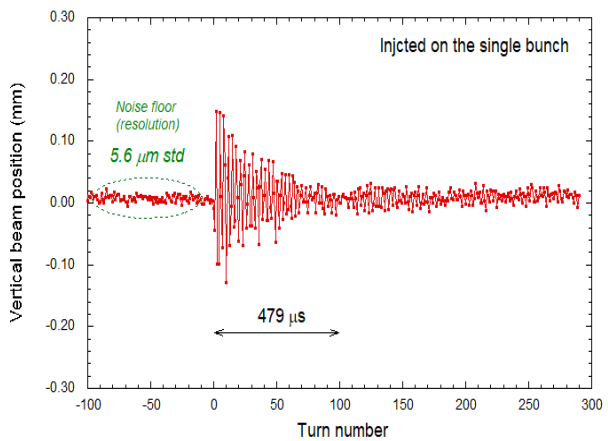
Content from this work may be used under the terms of the CC BY 4.0 licence (© 2022). Any distribution of this work must maintain attribution to the author(s), title of the work, publisher, and DOI

We observed the oscillation of the isolated bunch (5 mA/bunch) during the user time ("11/29-bunches + 1 bunches" mode [3]). As illustrated in Fig. 12, different behaviors were observed in the horizontal and vertical directions, suggesting that the PM-XBPM detects the horizontal and vertical directions independently. Here, the standard deviation of the beam fluctuation before the timing of beam injection can be interpreted as the resolution of this measurement system. Both the horizontal (6.5 μm std) and vertical resolution (5.6 μm std) are lower than the resolutions driven in the previous section. This is because that the pulse-height reduced by an additional divider (-6 dB) as a combiner and an attenuator (-10 dB).

Next, the oscillation of pulses was observed at 23.6 ns intervals during the user time ("203 bunches" mode [3]). Figures 13 (a)–(c) present the horizontal oscillation, while Fig. 13 (d)–(f) illustrate the vertical oscillation. The vertical axes indicate the Diff/Sum of channel 1 and channel 2, which represents the transverse photon beam position. Each pulse with a bunch separation of 23.6 ns could be observed individually. These oscillations during beam injection are diminished after several 100 μs, and they do not affect user experiments.



(a) Horizontal



(b) Vertical

Figure 12: Turn-by-turn oscillation during beam injection. Revolution time of the storage ring is 4.79 μs. HV is +300 V. ID gap is 9.6 mm.

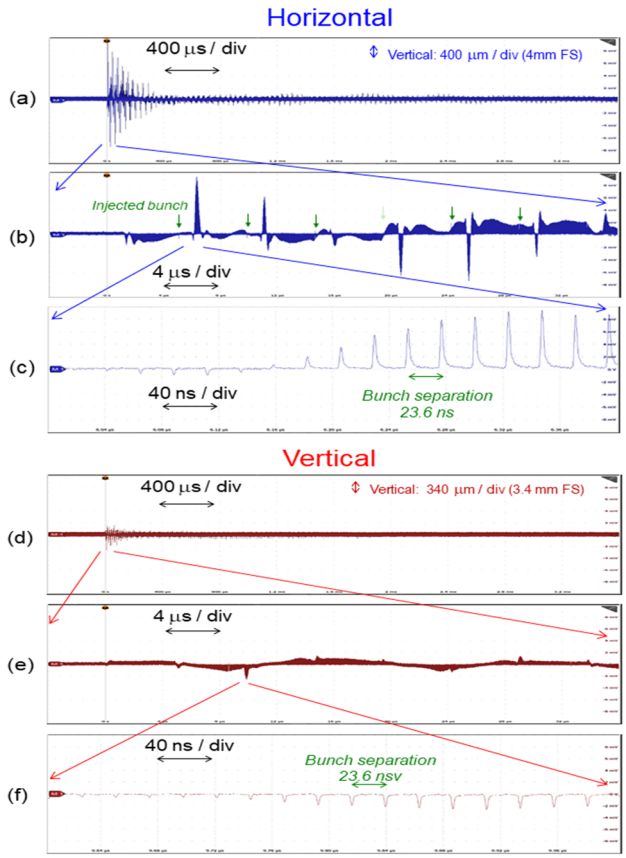


Figure 13: Screen captures of the oscilloscope observing oscillations of pulses with 2.36 ns separation. HV is +300 V. ID gap is 9.6 mm.

CONCLUSION

The evaluation tests of PM-XBPM with enhanced heat resistance were performed in ID-BL at SPring-8. Thus, stable operation in the ID-BL, which has a much higher synchrotron radiation irradiation than the BM-BLs, was verified. Regarding position sensitivity, it was confirmed that the PM-XBPM responds linearly to the perturbation amplitude of the photon beam by applying a stationary perturbation to the electron beam using a beam shaker. Furthermore, we quantified the resolution for different bunch currents and confirmed that a design goal of 10 μm std was achieved. Finally, pulse-by-pulse measurement was demonstrated at the SPring-8 ID-BL by observing the beam oscillation during beam injection. As a next step, introduction of an appropriate fast ADC is required to utilize this monitor in user experiments.

REFERENCES

[1] H. Aoyagi *et al.*, "Pulse-mode x-ray beam position monitor prototype for a synchrotron radiation beam line", *Phys. Rev. Accel. Beams,* vol. 24, p. 032803, 2021. doi:10.1103/PhysRevAccelBeams.24.032803

[2] H. Aoyagi *et al.*, "Toward higher resolution in pulse-mode x-ray beam position monitor", in *Proc. 18th Annual Meeting of Particle Accelerator Society of Japan (PASJ2021),* THP026.

[3] http://www.spring8.or.jp/en/users/operation_status/schedule/bunch_mode/

ISBN: 978-3-95450-241-7 ISSN: 2673-5350 doi:10.18429/JACoW-IBIC2022-MO3C4

BEAM POSITION MONITORING OF MULTI-BUNCH ELECTRON BEAMS AT THE FLASH FREE ELECTRON LASER

N. Baboi*, B. Lorbeer, H.-T. Duhme
Deutsches Elektronen-Synchrotron (DESY), Hamburg, Germany

Abstract

The superconducting FLASH user facility (Free electron LASer in Hamburg) accelerates 10 electron bunch trains per second, which are mostly used to produce high brilliance XUV and soft X-ray pulses. Each train usually contains up to 600 electron bunches with a typical charge between 100 pC and 1 nC and a minimum bunch spacing of 1 µs. Various types of beam position monitors (BPM) are built in three electron beam lines, having a single bunch resolution of 2 – 100 µm rms. This paper presents multi-bunch position measurements for various types of BPMs and built in at various locations. The dependency of the resolution on the beam offset is also shown.

INTRODUCTION

The Free electron LASer in Hamburg (FLASH) produces ultra-short intense XUV and soft X-ray pulses [1-3]. Beam diagnostic [4] is essential in obtaining and maintaining a high quality electron beam necessary for the self-amplified spontaneous emission effect responsible for producing the photon beams.

Beam Position Monitors (BPMs) are an important part of the beam diagnostics in FLASH. Many types of BPMs are built in along the ca. 250 m of the facility, being distributed in 3 electron beam lines. The BPM type at each location depends on the beam pipe and resolution requirements. Some types can detect bunches with a charge between ca. 10 to 1000 pC, and have a single bunch resolution of 2 to 15 µm rms. Others need a higher charge, and have higher values for the resolution, but they are in most cases still in accordance with the local demands.

While the behavior of the BPMs is in general well understood, only the behavior of the first bunch has been so far studied in detail. In this paper we present the analysis of each bunch in long trains. The single bunch behavior for different bunch offsets is also shown.

The FLASH Facility

An overview of the FLASH layout is shown in Fig. 1 [3]. A photoelectric gun produces every 100 ms electron bunch trains with a length of up to 600 µs and a repetition frequency of up to 1 MHz. TESLA superconducting structures accelerate them to an energy of up to 1.25 GeV. Two bunch compressors are used to reduce the bunch length to tens till hundreds of fs. The train is then split to the two undulator beamlines, FLASH1 and FLASH2, where photon pulses are produced. A third beam line splits off of FLASH2 and accommodates a laser-plasma experiment, FLASHForward [5]. Table 1 gives a summary of the main parameters of the electron and photon beams.

Note that currently the facility is at the end of an upgrade and refurbishment shutdown, with the main goals of increasing the energy, installing a laser heater, and a new bunch compressor [6].

Beam Position Monitors in FLASH

The different kinds of BPMs installed in the accelerator are able to measure the transverse position of each bunch within a train. Each type has several designs, depending on the beam pipe, whose diameter ranges from 10 to ca. 100 mm. There are button BPMs (one of the designs is described here [7]) and stripline BPMs [8], both types with electronics developed for FLASH [9]. Also there are cavity BPMs with electronics developed for the European XFEL [10] in the undulator section in FLASH2, as well as "cold" cavity BPMs in the accelerating modules [11].

The single bunch resolution has been evaluated for various charges and beam offsets. The method used for calculation is based on linear regression and is described in [12].

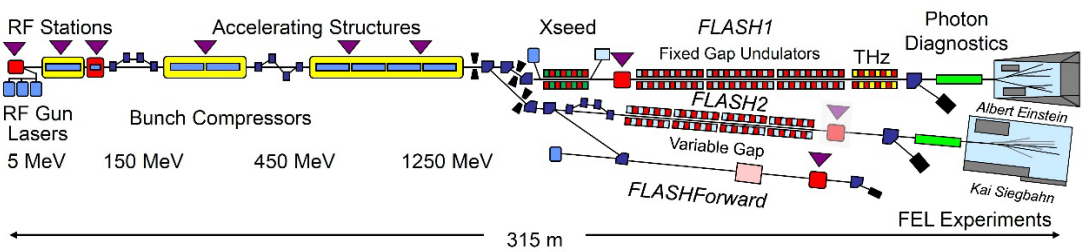


Figure 1: Schematic layout of FLASH [3].

* nicoleta.baboi@desy.de

Content from this work may be used under the terms of the CC BY 4.0 licence (© 2022). Any distribution of this work must maintain attribution to the author(s), title of the work, publisher, and DOI

ISBN: 978-3-95450-241-7 ISSN: 2673-5350 doi:10.18429/JACoW-IBIC2022-MO3C4

Content from this work may be used under the terms of the CC BY 4.0 licence (© 2022). Any distribution of this work must maintain attribution to the author(s), title of the work, publisher, and DOI

Table 1: Operational Parameters of the Electron and Photon Beams [2]

Parameter	FLASH1	FLASH2	Units
Electron beam:			
Beam energy	0.38-1.25	0.38-1.25	GeV
Normalised emittance (rms)	0.5-1	0.5-1	mm mrad
Bunch charge	0.1-1.2	0.02-1	nC
Bunches per second	1-5000	1-5000	
Photon beam:			
Wavelength	51-4.2	90-4	nm
Pulse duration (FWHM)	<30-200	<30-200	fs
Pulse energy	1-500	1-1000	µJ

Figure 2 shows typical resolutions measured for a FLASH1 bunch of charge of 0.4 nC (upper plot) and 0.3 nC for the FLASH2 case. The bunches for both beamlines pass a common beamline until ca. 150 m before being directed towards one of the 2 beamlines. Note that most BPMs have a single bunch resolution well below 10 µm rms, the requirement for these charges being 30 µm for most of them, and 10 µm for the undulator section (ca. 200 – 230 m in FLASH1 and ca. 190 – 230 m in FLASH2).

Most button BPMs (red plus and diamond symbols) have a 34 or 40.5 mm beam pipe diameter (monitor constant of 9, respectively 10.6 mm) and typically have a resolution better than 5 µm. In the FLASH1 beamline there are button BPMs with 10 mm beam pipe diameter and pencil-like antennas (constant 2.5 mm). These achieve similar resolution with additional amplifiers. Large button BPMs have a diameter of ca. 100 mm (monitor constant of 25 mm), as it is the case in the plot for a monitor at ca. 140 m in the common beam line. These show a lower resolution, above 5 µm. Most stripline BPMs have a beam pipe of 34 mm, and a constant around 9 mm, showing a typical resolution below 4 µm rms.

The cold cavity BPMs installed in the accelerating modules in the common part were designed for larger bunch charges, in general having a less reliable performance at charges below 0.4 nC. For higher charges their resolution is usually below 30 µm therefore also satisfying the requirements.

A summary of the typical single bunch resolution, measurement range for the charge and transverse offset is given in Table 2. The dependency of the resolution on the beam charge and offset is given later in this paper.

Table 2: Typical BPM Parameters

BPM-type	Charge [nC]	Offset [% diam.]	Single-bunch resolution [µm rms]
Button	0.02-1	ca. 30%	3-100
Stripline	0.01-1	ca. 30%	2-15
Cavity	0.01-1	ca. 10%	1-3
Cold cavity	0.4-1.5	ca. 20%	20-100

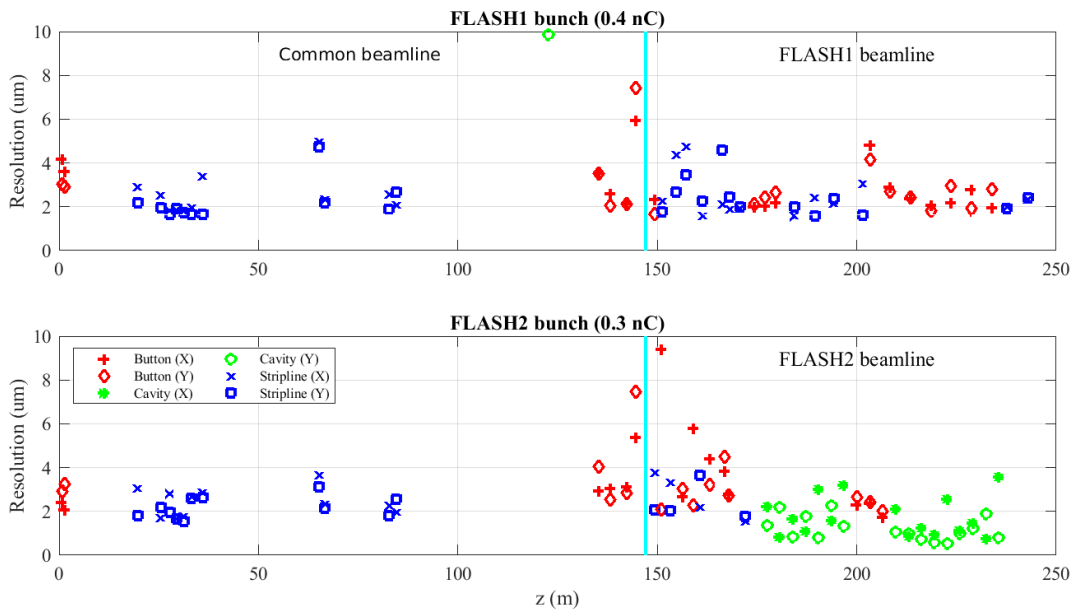


Figure 2: Resolution of the first bunch in the FLASH1 train (upper plot, 0.4 nC) and the FLASH2 one (lower plot, 0.3 nC).

ISBN: 978-3-95450-241-7 ISSN: 2673-5350 doi:10.18429/JACoW-IBIC2022-MO3C4

POSITION RESOLUTION ALONG THE BUNCH TRAIN

In order to check if the performance of the beam position monitoring described in the previous section is maintained along the bunch train, we analysed each bunch in long trains for FLASH1. The method mentioned above for determining the resolution is now used for each bunch. Note that in FLASH1 no cavity BPMs are installed, except in the cryo-modules [11]. Since these are at or below the lower limit of their charge range, are not shown here. Therefore, we give results for button and stripline BPMs. The MTCA-based reading of these two types of BPMs is described in [9].

Data from 200 bunch trains were collected, each with 340 bunches of 0.2 – 0.4 nC charge. The beam energy was ca. 1 GeV. The bunch repetition frequency was varied between 1000 and 50 kHz. Typical results for one button and one stripline BPM are shown in Figs. 3 and 4 respectively. Both BPMs are located after the accelerating section at the beginning of the FLASH1 beamline, at around 150 m.

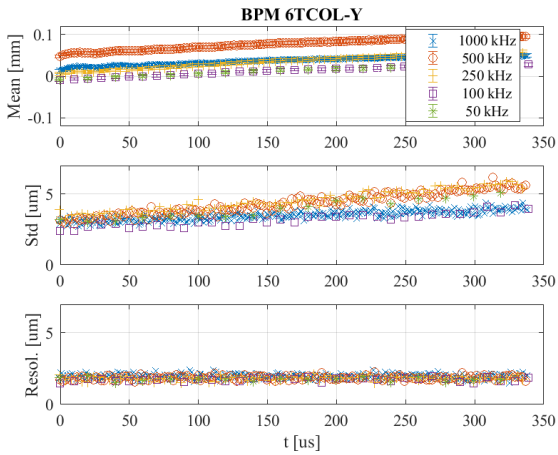


Figure 3: Mean (up), standard deviation (middle) and resolution (down) of the vertical bunch position for each bunch along the pulse train for various bunch repetition frequencies for a button BPM with an inner beam pipe diameter of 34 mm.

In each figure, the upper plot displays the average beam position reading of the 200 pulses and the middle one the standard deviation for each bunch. The lower plot gives the single bunch resolution. The various curves correspond to bunch trains with different bunch frequencies.

One notices in the upper plots in both figures that the offset of a given bunch is different for different frequencies. Already the orbit of the first bunch in the train is different. It turns out that also the charge is different for different bunch frequencies, as seen in the upper plot in Fig. 5. This figure shows the analysis of the charge reading for one toroid in the facility, for each bunch in the train, similar to the analysis made for BPMs. The charge is slightly different for the first few µs, and varies between 0.2 nC for a bunch frequency of 1 MHz to 0.4 nC for 50 kHz.

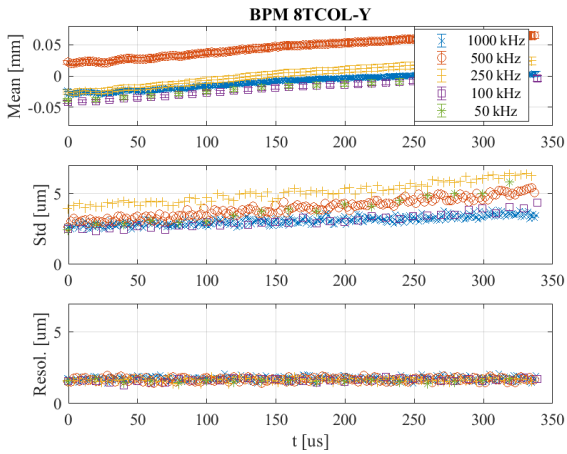


Figure 4: Similar to Fig. 3 for a stripline BPM with an inner beam pipe diameter of 34 mm.

This change in the charge may explain at least in part the difference in the standard deviation for the position as well as the charge reading for a given bunch (middle plots in Figs. 3–5). The difference in the beam position for various bunch frequencies plays a minor role, as it will be seen in the next section.

It is interesting to note in Figs. 3 and 4 that the bunch offset varies along the bunch train. This is already seen for the first BPM after the gun. Moreover, also the standard deviation of the reading changes along the train. The resolution however remains constant for both BPMs.

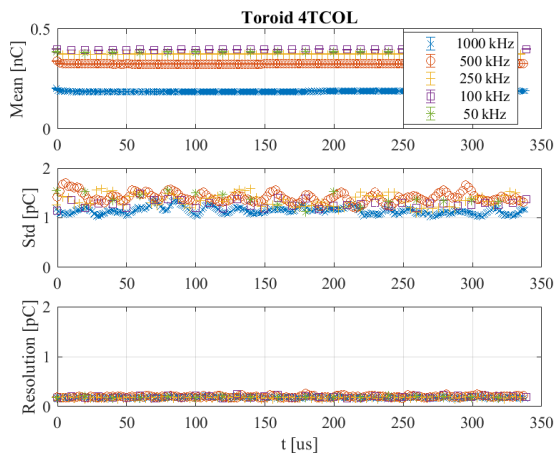


Figure 5: Mean (up), standard deviation (middle) and resolution (down) of the charge reading from one toroid for each bunch along the pulse train for various bunch repetition frequencies.

The question arose, whether there is a pattern in the BPM reading along the train. Figure 6 shows the Fourier transform of each of the plots in Fig. 4 for the stripline BPM. No clear pattern can be recognized for any of the plots.

Content from this work may be used under the terms of the CC BY 4.0 licence (© 2022). Any distribution of this work must maintain attribution to the author(s), title of the work, publisher, and DOI

ISBN: 978-3-95450-241-7 ISSN: 2673-5350 doi:10.18429/JACoW-IBIC2022-MO3C4

Content from this work may be used under the terms of the CC BY 4.0 licence (© 2022). Any distribution of this work must maintain attribution to the author(s), title of the work, publisher, and DOI

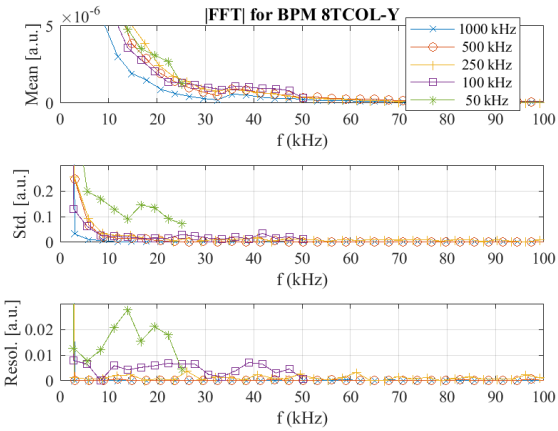


Figure 6: FFT of each plot in Fig. 4.

BPM RESOLUTION VERSUS BUNCH OFFSET

In order to find the dependency of the BPM resolution with the beam offset, single bunch pulses with various offsets at three subsequent stripline BPMs were generated (left plot in Fig. 7). The bunch charge was ca. 0.4 nC. In each case 200 pulses were measured from which the resolution was calculated. The results are shown in the right plot of the same figure.

One observes that the resolution stays below 4 µm rms for a wide range of beam offsets of more than ±4 mm, the beam pipe diameter being 34 mm. For larger offsets the resolution degrades considerably.

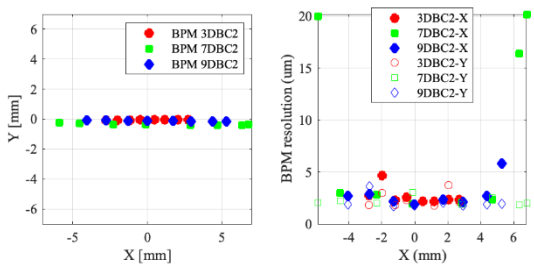


Figure 7: Dependency of the single bunch BPM resolution on the beam position (right) and the corresponding beam position readings (left).

Note that the dependency of the BPM resolution on the beam charge can be found in [9].

SUMMARY

In this paper the dependency of the single bunch resolution for button and stripline BPMs in the FLASH facility at DESY, Hamburg, along bunch trains was studied. Various bunch frequencies were generated during this study. While there is a variation of the beam position as well as of the standard deviation of the position reading along the bunch train, no dependence of the resolution was observed.

Further measurements show that the single bunch resolution stays unchanged within a transverse range of the stripline-BPMs larger that ±4 mm.

REFERENCES

[1] K. Honkavaara et al., "Status of the Free-Electron Laser User Facility FLASH", presented at the FEL2022, Triest, Italy, Aug. 2022, paper MOP37, to be published.

[2] M. Vogt *et al.*, "Status of the Superconducting Soft X-Ray Free-Electron Laser User Facility FLASH", in *Proc. IPAC'22*, Bangkok, Thailand, Jun. 2022, pp. 1006–1009. doi:10.18429/JACoW-IPAC2022-TUPOPT005

[3] Free-electron laser FLASH, https://flash.desy.de/

[4] N. Baboi *et al.*, "Upgrade and status of standard diagnostic-systems at FLASH and FLASHForward", in *Proc. IBIC'18*, 2018, pp. 13–17. doi:10.18429/JACoW-IBIC2018-moob03

[5] R. D'Arcy *et al.*, "FLASHForward: plasma wakefield accelerator science for high-average-power applications", *Philos. Trans. R. Soc. London, Ser. A*, vol. 377, p. 20180392, Aug. 2019. doi:10.1098/rsta.2018.0392

[6] L. Schaper *et al.*, "FLASH2020+ Project Progress: Current installations and future plans", presented at the FEL2022, Triest, Italy, Aug. 2022, paper TUP51, to be published.

[7] D. Lipka, B. Lorbeer, D. Nölle, M. Siemens, and S. Vilcins, "Button BPM Development for the European XFEL", in *Proc. DIPAC'11*, Hamburg, Germany, 2011, paper MOPD19, pp. 83–85.

[8] D. Noelle, G. Priebe, M. Wendt, and M. Werner, "BPMs with precise alignment for TTF2", *AIP Conf. Proc.*, vol. 732, pp. 166–173, 2004. doi:10.1063/1.1831144

[9] B. Lorbeer, H.-T. Duhme, D. Lipka, R. Neumann, and N. Baboi, "High resolution and low charge button and stripline beam position monitor electronics upgrade at FLASH", *J. Phys. Conf. Ser.*, vol. 1067, p. 072011, 2018. doi:10.1088/1742-6596/1067/7/072011

[10] D. Lipka *et al.*, "FLASH undulator BPM commissioning and beam characterization results", in *Proc. IBIC'14*, Monterey, CA, USA, 2014, paper TUPF07, pp. 315–319.

[11] R. Lorenz *et al.*, "First operating experiences of beam position monitors in the TESLA Test Facility Linac", in *Proc. PAC'97*, Vancouver, Canada, May 1997, paper 9P090, pp. 2137–2139.

[12] N. Baboi *et al.*, "Resolution studies at beam position monitors at the FLASH facility at DESY", in *AIP Conf. Proc.*, Batavia, IL, USA, 2006, vol. 868, pp. 227–237. doi:10.1063/1.2401409

ISBN: 978-3-95450-241-7 ISSN: 2673-5350 doi:10.18429/JACoW-IBIC2022-TU1I1

ELECTRO-OPTICAL BPM DEVELOPMENT FOR HIGH LUMINOSITY LHC

A. Arteche*, S. M. Gibson†, John Adams Institute at Royal Holloway, University of London, UK
T. Lefèvre, T. Levens, CERN, Geneva, Switzerland

Abstract

An Electro-Optic Beam Position Monitor (EO-BPM) is being developed as a high-frequency (up to 10 GHz) diagnostic for crabbing and Head-Tail intra-bunch detection at the HL-LHC. Following an earlier prototype at the SPS that demonstrated single-pickup signals, an upgraded design of an interferometric EO-BPM has been beam-tested at the HiRadMat facility for validation and characterisation studies. In the new design, the fibre-coupled Mach-Zehnder interferometer arms are modulated by lithium niobate waveguides integrated in an upgraded opto-mechanical arrangement that has been developed to produce a highly magnified image field replica of the passing Coulomb field. A new detection technique that is directly sensitive to the interferometric optical difference signal from opposite EO buttons has been applied to measure single-shot bunches for the first time. A transverse resolution study over a ±20 mm range at 3 GHz bandwidth produced the first successful electro-optic bunch-by-bunch position measurement at the HiRadMat in-air extraction line. The results of this campaign show promise for an in-vacuum design that is in production for beam tests at the SPS during Run-3 of the LHC.

INTRODUCTION

The Electro-Optic Beam Position Monitor (EO-BPM) has been proposed as a high-frequency diagnostic for the High Luminosity Large Hadron Collider (HL-LHC), with an operational bandwidth that targets up to 6 – 10 GHz [1, 2]. Among the potential applications are the detection of crabbed-bunch rotation and as a higher bandwidth alternative to standard Head-Tail instability monitors [3].

A prototype of a single EO pickup with a lithium niobate (LN) crystal located 66.5 mm away from the beam was installed in the SPS in 2016, delivering the first EO acquisition of a proton-induced signal [4, 5]. The far location, the long bunch length, and the initial pickup design implied the detection of modulating fields below 1 kV/m, which represented a major challenge [6]. To enhance the signal strength, the prototype was replaced during the 2017 SPS run by a modified version that incorporated an electrode to concentrate the modulating field in the LN crystal, proving to be a good strategy [6, 7]. Since then, several improvements of the optical configuration and stability have been incorporated, transitioning towards a more compact and robust phase interferometer model [8, 9]. The culmination is the new opto-mechanical design tested at HiRadMat that, thanks to a refined electrode design, delivers a highly magnified image replica E_z of the propagating Coulomb field E_C within a LN waveguide volume. This hot-spot mechanism enhances the modulating field E_z parallel to n_e by a significant factor, reaching 190 kV/m for a nominal SPS bunch, according to CST numeric simulations [10].

In combination with the upgraded pickup, a new optical detection technique is proposed as shown in Fig. 1. A Common Interferometric Point (IP-C) is generated when two optical paths combine after going through LN waveguides embedded in EO buttons placed on opposite sides of the pipe. Additionally on each side, one path through the crystal pickup combined with a simple bypass generates left and right side interferometers (IP-L & IP-R). While previous experiments at the SPS were based on the latter, this paper presents results from the common mode for first time.

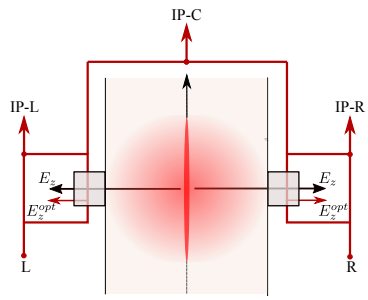


Figure 1: Triple interferometric layout of the EO-BPM.

The optical paths are linearly polarised in z at each LN waveguide, so E_z will activate the linear Pockels effect. This induces a time-profile optical modulation that is a replica of the passing bunch at IP-L & IP-R, and also at IP-C only when the beam is off-centre. Each interferometer has two output fibres from a 2×2 fused-coupler, so that each IP produces two opposite sign modulations: in-phase (+) and anti-phase (-). The IP-C detection allows us to correlate signal strength and transverse position using a single channel, and could also potentially deliver a straight intra-bunch measurement.

In summer 2021, the first interferometric EO-BPM system based on this promising fibre-coupled waveguide model was propitiously installed and tested at the HiRadMat facility. The proton bunch parameters for this SPS extraction line towards a target were similar to those for the nominal LHC bunch, typically $\sim 1.15 \cdot 10^{11}$ protons and $4\sigma \sim 1$ ns long Gaussian bunches. In-air characterisation tests of the transverse resolution were performed for single-shots and the results are presented in this paper. The ultimate goal of this campaign was to validate the common-mode detection technique and the new waveguide-based EO-BPM design under realistic beam conditions.

* alberto.arteche@rhul.ac.uk
† stephen.gibson@rhul.ac.uk

Content from this work may be used under the terms of the CC BY 4.0 licence (© 2022). Any distribution of this work must maintain attribution to the author(s), title of the work, publisher, and DOI

ISBN: 978-3-95450-241-7 ISSN: 2673-5350 doi:10.18429/JACoW-IBIC2022-TU1I1

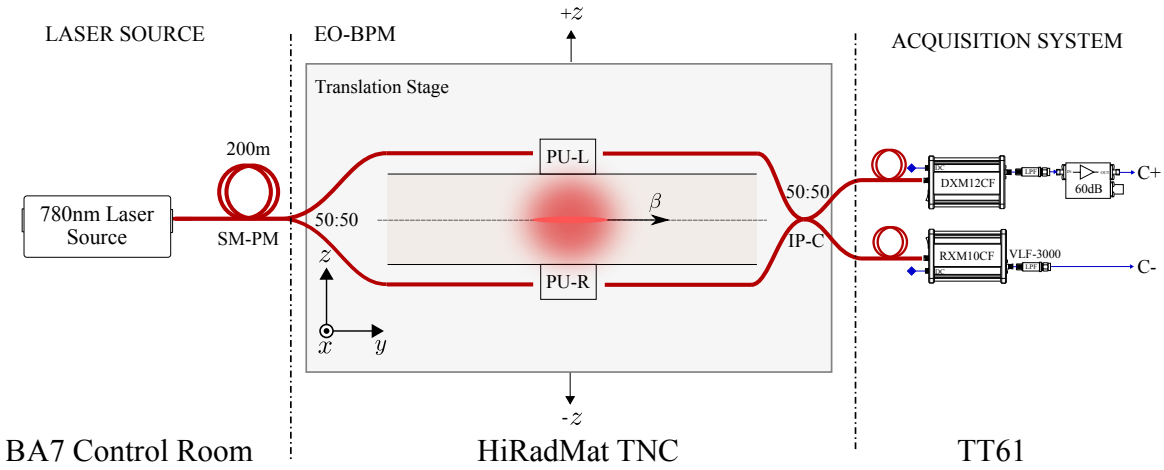


Figure 2: Simplified experimental setup showing locations of the laser source, the common mode Mach-Zehnder interferometer that generates an optical different signal, and the two detectors at the in-phase and anti-phase fibre-coupled outputs.

TRANSVERSE BEAM RESOLUTION TEST

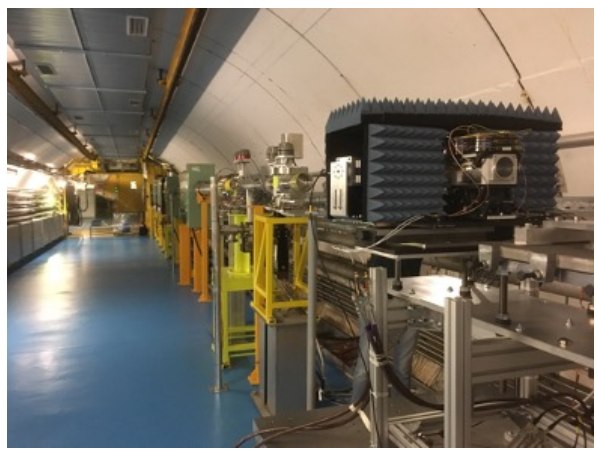
Experimental Setup at HiRadMat

The experimental hardware was implemented in three different locations that were fully fibre-connected as shown in Fig. 2. At the surface level in the BA7 control room, a CW Optical Beam (OB) emerging from a narrow linewidth 780 nm laser source is carried over 200 m of Single Mode Polarisation Maintaining fibre (SM-PM) to the TNC tunnel, where the light is evenly split to feed the EO-BPM installed in a free-space section along the HiRadMat beamline. As explained earlier, both arms go in parallel across the crystal waveguides and are combined at IP-C, trying to keep the distance equal to reduce the interferometric length.

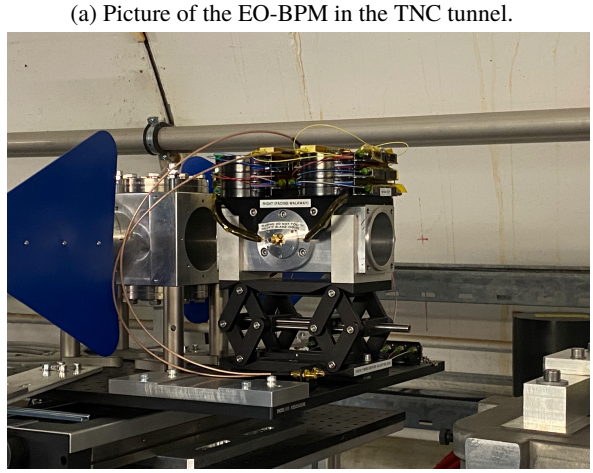
The optical signal was split and then conveyed by 20 m of SM fibre to the acquisition system placed located in the adjacent TT61 tunnel, where two different detection systems measured simultaneously the in-phase (C+) and anti-phase (C-) signals. The split signals permitted us to check the opposite sign modulation and therefore confirm the interferometric nature of the beam signal.

The diagram reveals that C+ was readout by a Thorlabs DXM12CF receiver lacking any pre-amplification connected to a 1 GHz 60 dB amplifier, whereas the photodetector Thorlabs RXM10CF required no further amplification. A 3 GHz Low Pass Filter (LPF) limited the outcome bandwidth of both detectors. The DC optical power reaching the detectors never exceeded 4 mW and the optical modulations were in the order of 1 – 2 mW.

The two EO pickups were installed on opposite sides of a 61 mm diameter pipe in the horizontal plane. As it was an in-air test, the system was assembled on a pipe section resting on a stepping-motor translation stage that allowed transverse movement with respect to the proton beam within a ±20 mm range. Positive offsets ($+z$) indicate the proton beam approaches the right pickup and negative values otherwise. Figure 3 shows the EO-BPM body on the translation stage installed in the HiRadMat beamline.



(a) Picture of the EO-BPM in the TNC tunnel.



(b) Close-up picture of the EO-BPM.

Figure 3: Pictures of the EO-BPM system installed in a free-space section of the HiRadMat beamline in the TNC tunnel.

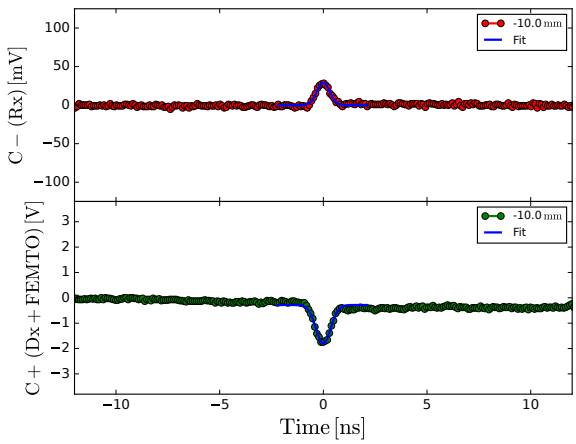
Content from this work may be used under the terms of the CC BY 4.0 licence (© 2022). Any distribution of this work must maintain attribution to the author(s), title of the work, publisher, and DOI

ISBN: 978-3-95450-241-7 ISSN: 2673-5350 doi:10.18429/JACoW-IBIC2022-TU1I1

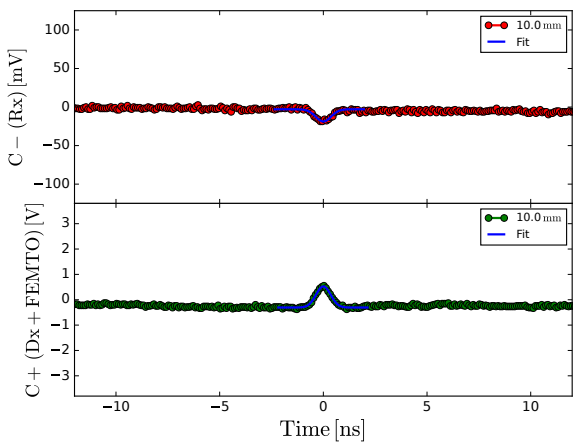
The stability of the interferometric working point was assessed by a wavelength lock-in system based on an in-house etalon. To prevent the laser frequency from drifting, this system provided with a feedback for the laser piezo to compensate accordingly. This is also one of the relevant new features that were integrated in the system with respect to the previous experiments at the SPS. In addition, optical probes were installed to detect possible back reflections and malfunctioning.

Beam Test Results

We present two different sets of single-shot proton bunch measurements, taken parasitically throughout a multi-experiment data-taking campaign at HiRadMat. As those sets were acquired on different dates, the beam intensity was slightly different for each one, particularly, at almost nominal SPS bunch charge ($\sim 1.02 \times 10^{11}$) and at lower charge ($\sim 7 \times 10^{10}$).



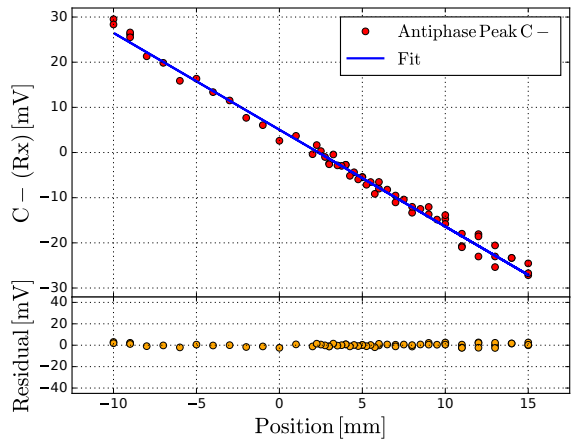
(a) $z = -10.0$ mm



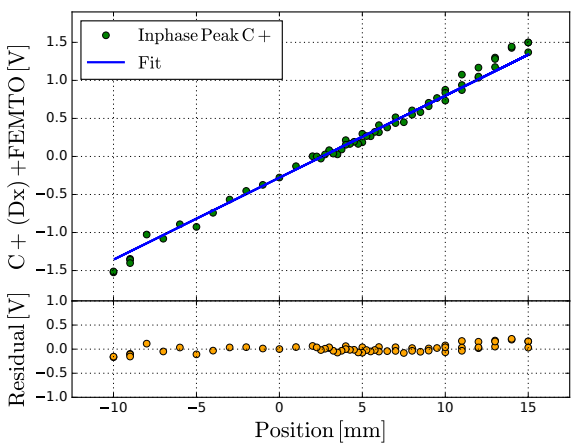
(b) $z = +10.0$ mm

Figure 4: Collection of common mode signals that correspond to in-phase C+ (green) and anti-phase C- (red) optical modulations induced by passing SPS-like proton beams obtained in the HiRadMat extraction line.

Figure 4 is a representative collection of the time-profile single-shot measurements. For each passing beam, a pair of in-phase C+ (green) and anti-phase C- (red) optical modulations were acquired. Despite being a highly radiation environment where most of the electronic equipment exhibited a great deal of distorting noise, the common mode channels C+ & C- delivered a reasonably clean and good quality signal, especially in the pre-amplified channel C-.



(a) Pre-amplified channel C-; +107.8 mV/mm



(b) Amplified channel C+; −2.1 mV/mm

Figure 5: Peak signal modulation against translation stage position z for a set of low intensity single-shot measurements.

Those traces were taken at different transverse positions z by moving remotely the translation stage. Given the diagram depicted in Fig. 2, a larger signal should be expected out of C+ as it includes a 60 dB amplification, i.e. a factor 1000 after the receiver, whereas C- is the signal directly from the pre-amplified detector. Also, the interferometric signals exhibited opposite signs, as foreseen. The acquisition bandwidth was limited by the 1 GHz output of the amplifier in C+, and the LPF at 3 GHz in the pre-amplified channel C-. By implementing an automated feedback to the laser to control the working point on the transfer function, we assured all the

Content from this work may be used under the terms of the CC BY 4.0 licence (© 2022). Any distribution of this work must maintain attribution to the author(s), title of the work, publisher, and DOI

ISBN: 978-3-95450-241-7 ISSN: 2673-5350 doi:10.18429/JACoW-IBIC2022-TU1I1

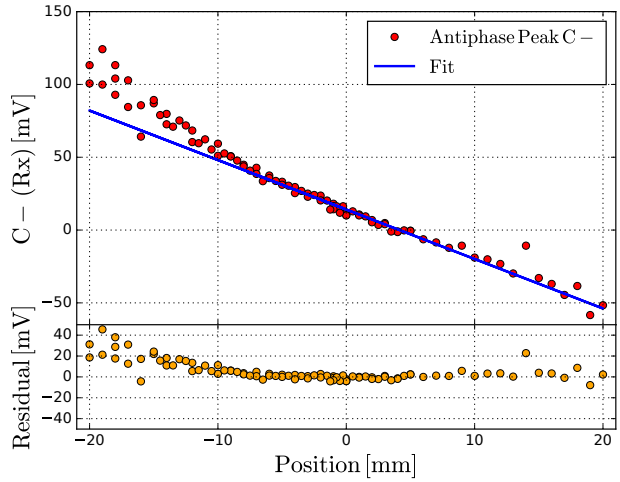
Content from this work may be used under the terms of the CC BY 4.0 licence (© 2022). Any distribution of this work must maintain attribution to the author(s), title of the work, publisher, and DOI

points were obtained at the same conditions of sensitivity so the peak strength variation was driven almost uniquely by the proton bunch parameters.

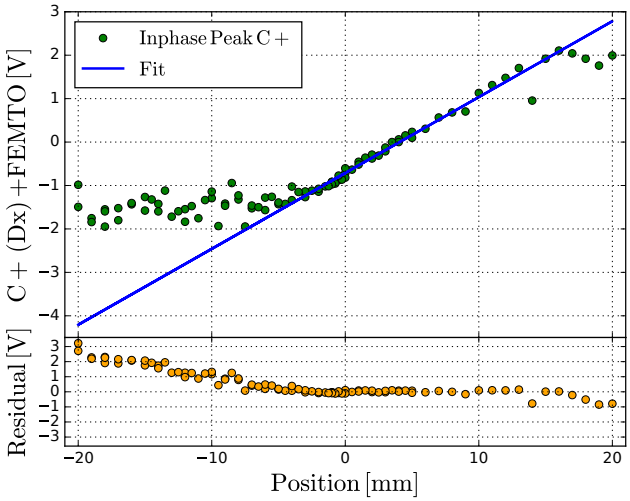
Figures 5 and 6 show the trace peak value extracted from the fit versus the translation stage position z for the low and nominal beam intensities, respectively. The in-phase C+ is represented in green whereas the anti-phase C- is in red. Due to the opposite sign nature, the pre-amplified modulation C- translates into a negative slope whereas the amplified C+ modulation is positive. Ideally, if the pickups were equally responsive, no signal should be expected at $z = 0$. However, one can observe that the distribution of points does not cross the centre, but there is an off-centre offset that implies an non-symmetric response between the prototype pickups. The sign of the offset implies a less than optimal performance of the right pickup, as expected due to small imperfections that were identified during assembly at RHUL prior to shipping to CERN. It is important to note that the 60 dB amplifier had a maximum output voltage of $|V| \sim 2$ V, which is why the cloud of points saturates in Fig. 6 for C+ due to a high beam signal at large displacements compared to the smaller range for the same channel in the low intensity set.

A straight line fit to the data in the non-saturating region was performed for each signal, as indicated by the blue lines in Figs. 5 and 6, which also show the residual difference between the experimental peak value and fitted blue line is shown by lower plots. The measured gradients for the nominal and low intensity data sets, and for each amplifier type are summarised in Table 1. The standard deviation of the residual σ_{residual} was used to estimate an upper limit on the transverse linearity over the full range of the fit, as included in Table 1. The results demonstrate that this direct optical difference signal exhibits good linearity over a wide translation range. The sub-millimetric linearity represents an upper limit on the resolving capability of the EO pickup which is expected fundamentally to be much better, given that the residuals shown here are uncorrected for the effects of bunch charge variations from the HiRadMat single-shot extraction line, laser optical power fluctuations, and include amplifier noise of the prototype acquisition system. These results demonstrate the first single-shot, bunch-by-bunch translation measurements, taken over many hours and on different days, and show there is room for improvement in future, particularly in the detection system.

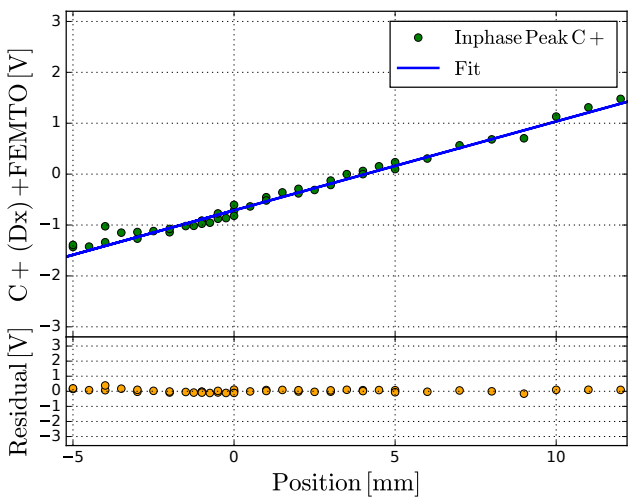
Due to the entirely optical nature of signal generation process, this technology has great potential as a diagnostic tool for high-radiation target beamlines, such as HiRadMat, where back-scattering effects can adversely impact conventional electronics. Even in this system due to the relatively close location of the acquisition system in the adjacent accelerator tunnel, the amplified channel C- exhibited electronic distortion in the time-profile baseline. In a future system design, the acquisition system is sufficiently separated from the beamline or target by a longer length of optical fibre to ensure a clean good-quality signal.



(a) Pre-amplified channel C-; −3.4 mV/mm



(b) Amplified channel C+; +174.7 mV/mm



(c) Zoomed-in amplified channel C+

Figure 6: Peak signal modulation against translation stage position z for a set of nominal intensity single-shot measurements.

ISBN: 978-3-95450-241-7 ISSN: 2673-5350 doi:10.18429/JACoW-IBIC2022-TU1I1

Table 1: Gradient, Standard Deviation of the Residuals and the Linearity Calculated for Each Beam Intensity Case and Channel

Single-shot Set case	Bunch Intensity	Gradient [mV/mm]	σ_{residual} [mV]	Linearity [µm]
Low-Intensity amplified C+	$\sim 7 \times 10^{10}$	107.8	49.2	460
Low-Intensity pre-amplified C-	$\sim 7 \times 10^{10}$	-2.1	1.1	520
High-Intensity amplified C+	$\sim 1.02 \times 10^{11}$	174.7	75.1	430
High-Intensity pre-amplified C-	$\sim 1.02 \times 10^{11}$	-3.4	2.2	650

CONCLUSION

The characterisation studies performed during the HiRadMat campaign that are reported here represent a major milestone in the development of the Electro-Optic Beam Position Monitor. For first time, complete sets of passing single bunches were successfully acquired combining interferometric optical modulations from opposite EO pickups. This approach achieved the first EO transverse beam position measurement. These results confirm that the new EO waveguide design has improved by two orders of magnitude the measured field with respect to the previous design, as predicted by electromagnetic CST simulations. Moreover, the anti-phase channel C- delivered a 3 GHz time-profile traces, achieving a bandwidth comparable with state-of-the-art electromagnetic head-tail monitor alternatives.

This in-air EO-BPM prototype system demonstrates sub-millimetric linearity over a wide translation range at the first attempt. In future, the optical power could be increased, the assembly process improved, and the acquisition system optimised to help approach the fundamental resolution expected from the pickup, and obtain a more symmetric response.

An in-vacuum EO-BPM design is currently in production and is planned to be installed in the SPS and tested during Run-3 of the LHC. This will enable further validation of the EO-BPM concept in an operational accelerator environment, and as a demonstrator ahead of implementation of multiple EO-BPMs for the HL-LHC era.

ACKNOWLEDGEMENTS

Work supported by UK STFC grants ST/N001583/1, ST/P00203X/1, Royal Holloway University of London & CERN. This project has received funding from the European Union's Horizon 2020 Research and Innovation programme under GA No 101004730. We would like to gratefully acknowledge the very useful assistance provided by Pascal Simon and the HiRadMat team.

REFERENCES

[1] S. M. Gibson *et al.*, "High Frequency Electro-Optic Beam Position Monitors for Intra-Bunch Diagnostics at the LHC", in *Proc. IBIC'15*, Melbourne, Australia, Sep. 2015, pp. 606–610. doi:10.18429/JACoW-IBIC2015-WEDLA02

[2] G. Apollinari et al., "High-Luminosity Large Hadron Collider (HL-LHC): Technical Design Report V. 0.1", CERN-2017-007-M, Yellow Report, 2017. doi:10.23731/CYRM-2017-004

[3] T. E. Levens, K. Lasocha and T. Lefevre, "Recent Developments for Instability Monitoring at the LHC", in *Proc. IBIC'16*, Barcelona, Spain, Sep. 2016, pp. 852–855. doi:10.18429/JACoW-IBIC2016-THAL02

[4] A. Arteche *et al.*, "Development of a Prototype Electro-Optic Beam Position Monitor at the CERN SPS", in *Proc. IBIC'16*, Barcelona, Spain, Sep. 2016, pp. 634–637. doi:10.18429/JACoW-IBIC2016-WEPG09

[5] A. Arteche *et al.*, "First Beam Tests at the CERN SPS of an Electro-Optic Beam Position Monitor for the HL-LHC", in *Proc. IBIC'17*, Grand Rapids, MI, USA, Aug. 2017, pp. 270–273. doi:10.18429/JACoW-IBIC2017-TUPCF23

[6] A. Arteche, "Studies of a prototype of an electro-optic beam position monitor at the CERN Super Proton Synchrotron", Ph.D. thesis, Royal Holloway, University of London, CERN-THESIS-2018-316, 2018.

[7] S. M. Gibson, A. Arteche, A. Bosco, S. E. Bashforth, M. Krupa and T. Lefevre, "Enhanced Bunch Monitoring by Interferometric Electro-Optic Methods", in *Proc. IPAC'18*, Vancouver, Canada, Apr.-May 2018, pp. 2353–2356. doi:10.18429/JACoW-IPAC2018-WEPAL073

[8] A. Arteche *et al.*, "Characterisation of Electro-Optic Pickups for High Bandwidth Diagnostics at the High Luminosity LHC", in *Proc. IPAC'19*, Melbourne, Australia, May 2019, pp. 2690–2693. doi:10.18429/JACoW-IPAC2019-WEPGW088

[9] A. Arteche, S. E. Bashforth, A. Bosco, S. M. Gibson, M. Krupa, and T. Lefèvre, "Beam Measurements at the CERN SPS Using Interferometric Electro-Optic Pickups", in *Proc. IBIC'19*, Malmö, Sweden, Sep. 2019, pp. 457–460. doi:10.18429/JACoW-IBIC2019-WEA004

[10] Computer Simulation Technology, https://www.cst.com/

Content from this work may be used under the terms of the CC BY 4.0 licence (© 2022). Any distribution of this work must maintain attribution to the author(s), title of the work, publisher, and DOI

ISBN: 978-3-95450-241-7 ISSN: 2673-5350 doi:10.18429/JACoW-IBIC2022-TU1I2

DIAGNOSTICS WITH QUADRUPOLE PICK-UPS AT SIS18

Adrian Oeftiger*, Rahul Singh
GSI Helmholtzzentrum für Schwerionenforschung GmbH, Darmstadt, Germany

Abstract

The beam quadrupole moment of stored beams can be measured with a four-plate quadrupole pick-up. The frequency spectrum of the quadrupole moment contains not only the usual first-order dipole modes (the betatron tunes) but also the second-order coherent modes, comprising of (1.) (even) normal envelope modes, (2.) odd (skew) envelope modes and (3.) dispersion modes. As a novel diagnostic tool, the measured frequencies and amplitudes provide direct access to transverse space charge strength through the tune shift as well as linear coupling (and mismatch thereof), along with the benefit of a non-invasive beam-based measurement. Technically, quadrupole moment measurements require a pick-up with non-linear position sensitivity function. We discuss recent developments and depict measurements at the GSI SIS18 heavy-ion synchrotron.

INTRODUCTION

Quadrupolar pick-ups (QPU) in a beam line provide information about the coherent transverse second-order moments of a passing bunch of particles. These devices have often been used in studies measuring the beam emittance or injection mismatch of the optics functions [1–3], or the strength of space charge in synchrotrons [4–8]. The advantage is the non-invasive and thus non-destructive nature of measuring the quadrupolar moment S_{QPU} via induced currents in the four symmetrically arranged electrodes, in particular for inferring the transverse RMS emittances in comparison to destructive profile measurement methods like flying wire scans or secondary electron emission (SEM) grids. Typically, *time domain* oriented methods to determine the emittance from a measured quadrupolar moment demand well controlled experimental setups, where differential offsets in the quadrupolar moments need to be understood and controlled precisely while the strong dipole component in the signal needs to be suppressed. These challenges could possibly be the main reason why QPUs are typically not yet used as beam diagnostics in regular operation. A technically less demanding and thus potentially more rewarding approach in a synchrotron is to profit from the *frequency domain* and measure the bunch eigenmodes, where only the frequency content and not the absolute values of S_{QPU} matter.

The quadrupole spectrum of a circulating beam has a rich structure. Most often the two even transverse envelope modes of the oscillating $\sigma_{x,y}(s)$ are studied, most prominently for measuring the strength of space charge by determining the coherent tune shift of the envelope due to space charge defocusing. Past experiments mainly studied coasting beam conditions [4–7].

At the same time, space charge broadened resonances typically become an issue mostly under bunched beam conditions. A truly useful diagnostic tool for direct space charge strength quantification thus should be applicable to bunched beam. A recent study for the first time accomplishes this space charge measurement of bunched beams [8] at the CERN Proton Synchrotron (PS): since the envelope oscillations due to injection mismatch typically decohere very rapidly in bunches, they are much more challenging to measure than in coasting beams. As an alternative, the study establishes the quadrupole beam transfer function (Q-BTF) technique based on a transverse feedback system, which quadrupolarly excites the bunch in a frequency sweep while measuring the beam response in the QPU. Such measured "bands" of coherent envelope modes due to varying defocusing by space charge depending on the longitudinal line charge density are expected to reveal the maximum coherent envelope tune shift at the longitudinal peak line charge density.

Another notable finding from bunched beam Q-BTF measurements in Ref. [8] is the observation of the coherent dispersion mode. In Ref. [9] the connection of this mode to head-tail instabilities has been illuminated, as the dispersion mode locks onto the correlation between transverse displacement and longitudinal momentum. Furthermore, as also mentioned in Ref. [9], the space charge shift of the coherent dispersion mode frequency could in principle be used to quantify space charge as an alternative to envelope mode frequency shifts.

The quadrupole moment spectrum further contains the skew quadrupole resonances [9]. Their mode amplitude indicates injection mismatch with respect to linear coupling, which can be useful for a direct beam-based measurement. This approach again intrinsically includes space charge in contrast to conventional BPM-based methods such as the closest-tune approach $|C^-|$ [10], as dipole-moment-based measurements are insensitive to coupling contributions from space charge.

For bunched beam, the quantitative influence of chromatic detuning on the measured envelope bands has been raised as an open point, given its oscillatory nature due to synchrotron motion. Simulations in Ref. [8] demonstrate the significant widening of the measured envelope band width due to chromaticity. In this contribution we present new measurement results from the GSI SIS18 synchrotron, based on a recently established Q-BTF setup involving a quadrupole kicker and pick-up. While proton beams in CERN PS suffer from head-tail instabilities at intensities where space charge becomes relevant, (heavy-ion) beams in the SIS18 can reach significant space charge strength at lower intensities where head-tail instabilities play no significant role. SIS18 there-

* a.oeftiger@gsi.de

Content from this work may be used under the terms of the CC BY 4.0 licence (© 2022). Any distribution of this work must maintain attribution to the author(s), title of the work, publisher, and DOI

ISBN: 978-3-95450-241-7 ISSN: 2673-5350 doi:10.18429/JACoW-IBIC2022-TU1I2

fore provides stable measurement conditions when switching to zero chromaticity optics. We are hence in the position to compare the width of the envelope band measured both at natural and fully corrected chromaticity.

OVERVIEW

Four electrodes, symmetrically arranged in 90° steps in the transverse plane around the passing beam as indicated in Fig. 1, pick up on the quadrupolar moment of the passing beam by combining their induced voltages as $S_{\mathrm{QPU}} = (U_T + U_B) - (U_L + U_R)$ [11]. This quadratic signal

$$S_{\mathrm{QPU}} \propto \langle y^2 \rangle - \langle x^2 \rangle \tag{1}$$

contains contributions from all collective second-order modes coupling into the transverse plane, where x denotes the horizontal particle offset and y the vertical offset. The notation $\langle \cdot \rangle$ refers to the expectation value summing over all particles in the beam.

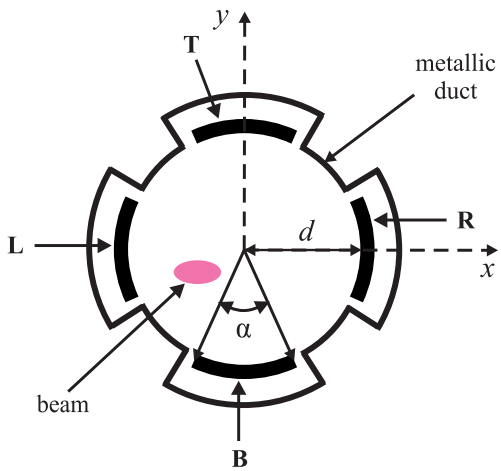


Figure 1: Schematics of four electrodes in quadrupolar pick-up, taken from Ref. [11].

Let us consider betatron motion x_β around a constant equilibrium orbit $\bar{x}$ with overlaid dispersive motion $D_x\delta$ for dimensionless momentum offset $\delta \doteq \frac{\Delta p}{p_0}$. D_x denotes the horizontal dispersion for this particle, $D_x = \partial x / \partial \delta$. The horizontal particle coordinate at the QPU location thus amounts to

$$x = \bar{x} + x_\beta + D_x\delta \,, \tag{2}$$

and likewise for the vertical plane. The collective quadratic signal thus splits up into

$$S_{\mathrm{QPU}} \propto \underbrace{\left(\langle y_\beta^2 \rangle - \langle x_\beta^2 \rangle\right)}_{\left(\sigma_y^2 - \sigma_x^2 + \langle y_\beta \rangle^2 - \langle x_\beta \rangle^2\right)} + 2 \cdot \bar{y} \, \langle y_\beta \rangle - 2 \cdot \bar{x} \, \langle x_\beta \rangle \tag{3}$$
$$+ \left\langle y_\beta \, \delta \right\rangle - \left\langle x_\beta \, \delta \right\rangle + \text{longitudinal } \delta \text{ terms} \,.$$

On top, for skew components in the focusing channel, additional coupling terms appear involving $\sigma_x\sigma_y$ and a skew envelope term σ_{xy}^2 (first discussed by Chernin [12]).

The spectral content of S_{QPU} comprises all the corresponding eigenmodes for these coherent first- and second-order moments. Given the bare betatron tunes $Q_{x,y}$, we thus conceptually expect to see

- $Q_{x,y}$: dipolar transverse motion from $\bar{x} \cdot \langle x \rangle$, $\bar{y} \cdot \langle y \rangle$,
- $2Q_{x,y}$: dipolar transverse motion from $\langle x_\beta \rangle^2$, $\langle y_\beta \rangle^2$,
- $2Q_{x,y} - \Delta Q_{x,y}^{\mathrm{env,SC}}$: horizontal and vertical even envelope modes from $\sigma_{x,y}^2$,
- $Q_{x,y} - \Delta Q_{x,y}^{\mathrm{disp,SC}}$: horizontal and vertical coherent dispersion mode from $\langle x_\beta \, \delta \rangle$, $\langle y_\beta \, \delta \rangle$, and
- $|Q_x - Q_y|, Q_x + Q_y$: odd envelope or Chernin modes from σ_{xy}^2, $\sigma_x\sigma_y$.

Note that this association of the two even envelope modes with a respective transverse degree of freedom is only valid for vanishing coupling. For full coupling, i.e. isotropic focusing $Q_x = Q_y$, the two modes become simultaneous anti-phase and in-phase oscillations of both planes, sometimes called "anti-symmetric" and "breathing" modes.

In general, the second-order modes are affected by coherent tune shifts due to direct space charge defocusing (unlike the first-order modes). This is indicated by $\Delta Q_{x,y}^{\mathrm{env,SC}}$ for the even envelope modes and by $\Delta Q_{x,y}^{\mathrm{disp,SC}}$ for the coherent dispersion mode (for further discussion see e.g. Ref. [13]).

The coherent tune shift of the odd envelope modes does not significantly depend on space charge under typical conditions of synchrotrons, as discussed by Aslaninejad and Hofmann [14], which is why we do not consider a corresponding ΔQ^{SC} term above. The odd envelope tunes coherently shift mainly due to the emittance ratio.

SIS18 SETUP

The GSI heavy-ion synchrotron SIS18 features two dedicated quadrupole electrode setups in section 4 (Fig. 2 in [7]) and section 12. Figure 2 displays the location of

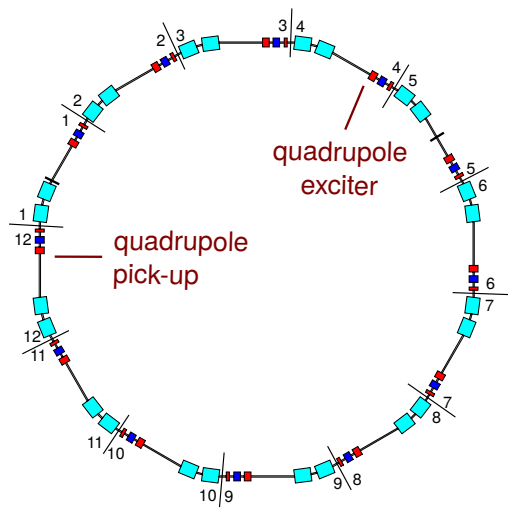


Figure 2: SIS18 survey with exciter and pick-up system to measure the quadrupole beam transfer function.

the quadrupole exciter and the pick-up in sectors 4 and 12,

Content from this work may be used under the terms of the CC BY 4.0 licence (© 2022). Any distribution of this work must maintain attribution to the author(s), title of the work, publisher, and DOI

ISBN: 978-3-95450-241-7 ISSN: 2673-5350 doi:10.18429/JACoW-IBIC2022-TU1I2

Content from this work may be used under the terms of the CC BY 4.0 licence (© 2022). Any distribution of this work must maintain attribution to the author(s), title of the work, publisher, and DOI

respectively. The β-function at the exciter location is exactly four times larger in the horizontal than in the vertical plane as can be seen in Fig. 3. Hence, the energy transfer to the beam is expected to be larger in the horizontal plane. These

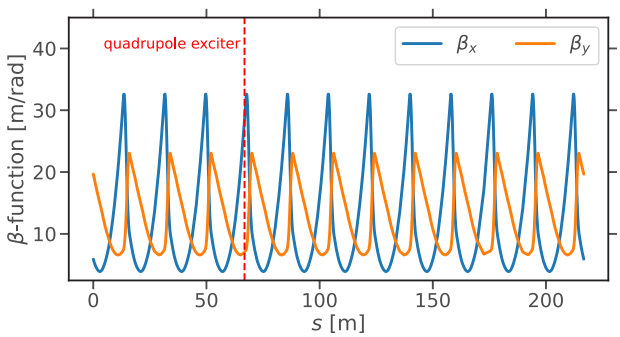


Figure 3: Twiss β-functions around SIS18.

two legacy capacitive pick-ups were utilized for quadrupolar excitation and the quadrupolar signal measurements, respectively. On the excitation side, the pick-up plates in section 4 were connected to a couple of 400 W 55 dB power amplifiers via magnetic-flux-based impedance transformers with a winding ratio of $\frac{n_2}{n_1} = 6$. The transformers are installed directly on the pick-up plates in the SIS18 tunnel and perform matching between the 50 Ω output impedance of the amplifiers to 100 pF capacitive load of the exciter plates. This quadrupole exciter system can provide a maximum power of 400 W which corresponds to a maximum voltage of 3 kVpp with a frequency range of 0.1 to 2 MHz. The frequency response of the excitation pathway is simulated via *spice* as shown in Fig. 4. For a maximum induced voltage of 2 kVpp,

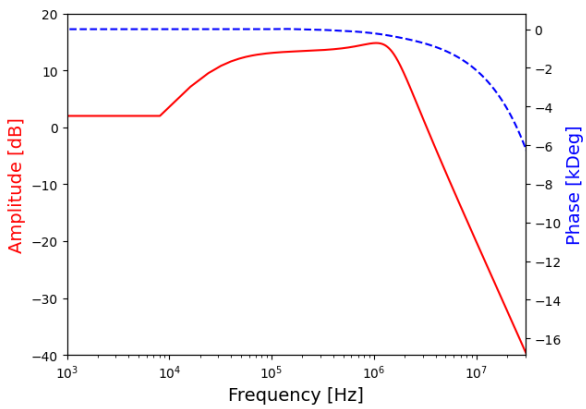


Figure 4: Simulated frequency response for the quadrupolar excitation path. 14 dB corresponds to factor 6 increase in the voltage applied on the plates with respect to the power amplifier output voltage. 3 dB reduction is seen at 100 kHz and 2 MHz defining the bandwidth of excitation system. The right axis depicts the phase response showing a large group delay introduced by the 80 m coaxial cable.

the simulated quadrupole field gradient in the exciter plates in shown in Fig. 5.

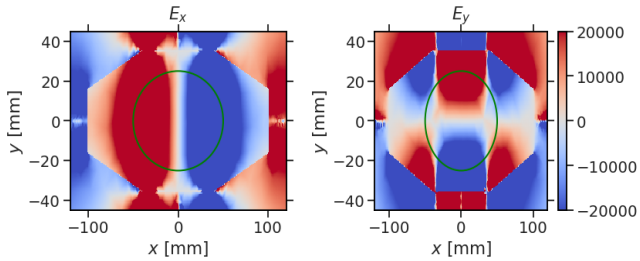


Figure 5: The static electric field components when 1 kV is applied on left and top plates while −1 kV is applied on right and bottom plates. E field units are in V/m.

The quadrupolar field gradient in the pick-up centre is $\approx 1.9\,\mathrm{MV/m^2}$ per plate which is used as input for the beam dynamics simulations. Other auxiliary components in the excitation set-up are a temperature monitor of the transformers and an attenuated signal from the plates for online monitoring.

On the acquisition side, the quadrupole pick-up in section 12 is utilised where each plate signal was digitised after 80 dB amplification by means of a 2 GHz, 250 MSa/s oscilloscope. The quadrupolar and dipolar signal reconstruction was carried out numerically followed by synchronization with the cavity rf signal. For comparison, the heaviest ions U^{238+} feature a revolution frequency of 150 kHz at injection energy.

The measurements have been conducted with lead ions Pb^{65+} at a low flat-top energy of 80 MeV/u equivalent to $B\rho = 4.2$ T m. The transverse geometrical rms emittances were evaluated via beam profiles measured with an ionisation profile monitor, determined as $\epsilon_x = 13$ mm mrad and $\epsilon_y = 11$ mm mrad at excitation start. The rf systems ran at a total of 6.3 kV and a harmonic of $h = 4$, the bunch length was estimated to a full width at half maximum value of 15.3 m. The bunch current amounted to 2 mA such that, at this energy, space-charge detuning becomes negligibly small with $\Delta Q^{KV} \lesssim 10^{-3}$. Doublet optics are employed with model tunes of $Q_x = 4.1$ and $Q_y = 3.22$. The envelope modes are thus expected around fractional tunes of $2q_x = 0.2$ and $2q_y = 0.44$, which sufficiently separates all modes simplifying the analysis of the measured spectra. The exciter rf signal has been swept between fractional tunes of 0.05 to 0.45 (about 25 to 250 kHz in baseband) to capture the beam response across the frequency range of interest. Q-BTF measurements have been recorded for both natural chromaticity ($Q'_x = -6.2$ and $Q'_y = -3.9$) and corrected chromaticity (using the two sextupole families with experimentally confirmed $|Q'_x|, |Q'_y| < 0.1$).

SIMULATION RESULTS

The experiment has been modelled in a particle tracking simulation with a detailed SIS18 lattice and including self-consistent space charge effects, based on the SixTrackLib [15] and PyHEADTAIL [16, 17] libraries. The results for a 10 ms duration of the sweep are shown in Fig. 6 for natural chromaticity and in Fig. 7 for corrected chromaticity.

ISBN: 978-3-95450-241-7 ISSN: 2673-5350 doi:10.18429/JACoW-IBIC2022-TU1I2

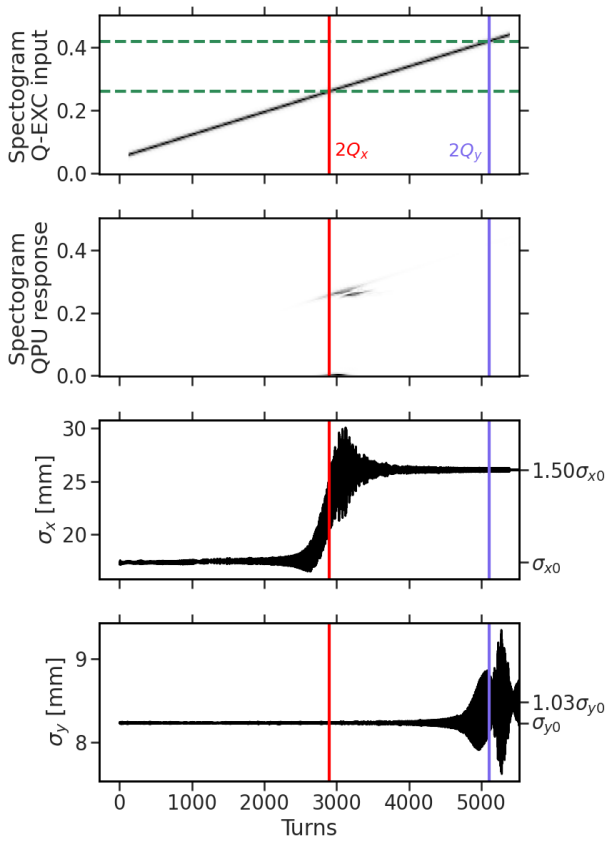


Figure 6: Q-BTF simulation at natural chromaticity.

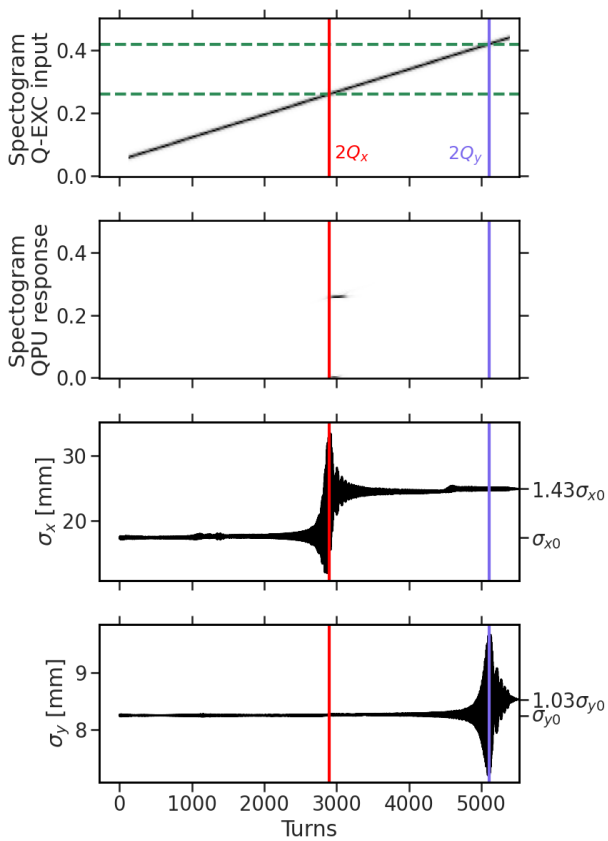


Figure 7: Q-BTF simulation at zero chromaticity.

The upper-most panel shows a spectrogram of the excitation signal, the second panel a spectrogram of the pick-up signal S_{QPU}, and the third and fourth panel the time evolution of the rms beam sizes in the horizontal and vertical plane, respectively.

The beam responds to the excitation signal with a clear oscillation in the horizontal and vertical beam sizes around the respective turns where the excitation frequency reaches $2q_x$ and $2q_y$. The average beam size increases indicating the emittance growth due to the envelope resonance. Irrespective of the chromaticity setting, the final beam size increased by about one and a half times in the horizontal and only marginally in the vertical plane. The QPU signal mainly exhibits the horizontal size oscillation in both displayed cases, the vertical oscillation is much smaller. The stronger effect in the horizontal plane originates in the larger horizontal β-function at the exciter.

A noticeable outcome of the simulations is the much narrower tune response in the corrected-chromaticity scenario. Figure 8 displays a comparison of the FFT-computed frequency spectra of S_{QPU}. The full width at half maximum of the horizontal envelope peak in the natural-chromaticity case is 2.3 times wider in comparison to the corrected-chromaticity case.

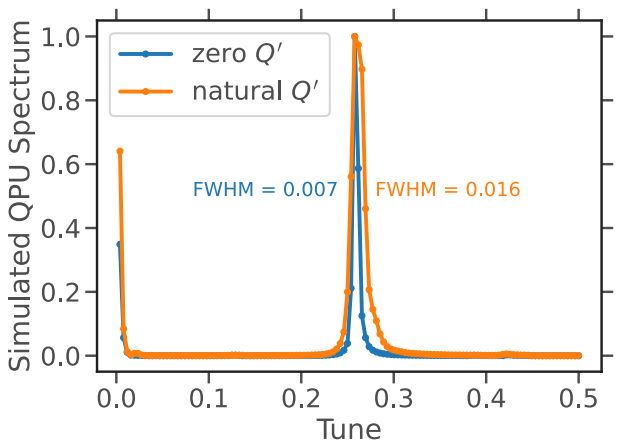


Figure 8: Comparison of simulated envelope resonances.

EXPERIMENTAL RESULTS

The turn-by-turn dipolar S_H, S_V and quadrupolar signals S_{QPU} were then reconstructed digitally using the relations, $S_H = (U_L - U_R)$, $S_V = (U_T - U_B)$ and $S_{\mathrm{QPU}} = (U_T + U_B) - (U_L + U_R)$. Simultaneously, beam current and transverse profiles were measured using a DC current transformer and ionisation profile monitors during the experiment. Figure 9 shows the quadrupolar spectrogram for natural chromaticity settings against a chirp excitation. The horizontal envelope mode excitation is more prominent in comparison to the vertical envelope mode in line with the simulations.

A comparison of the spectra for both chromaticities is shown in Fig. 10. The width of the envelope peak for corrected chromaticity is much narrower as predicted by simulations and points to a negligible chromatic tune spread.

Content from this work may be used under the terms of the CC BY 4.0 licence (© 2022). Any distribution of this work must maintain attribution to the author(s), title of the work, publisher, and DOI

ISBN: 978-3-95450-241-7 ISSN: 2673-5350 doi:10.18429/JACoW-IBIC2022-TU1I2

Content from this work may be used under the terms of the CC BY 4.0 licence (© 2022). Any distribution of this work must maintain attribution to the author(s), title of the work, publisher, and DOI

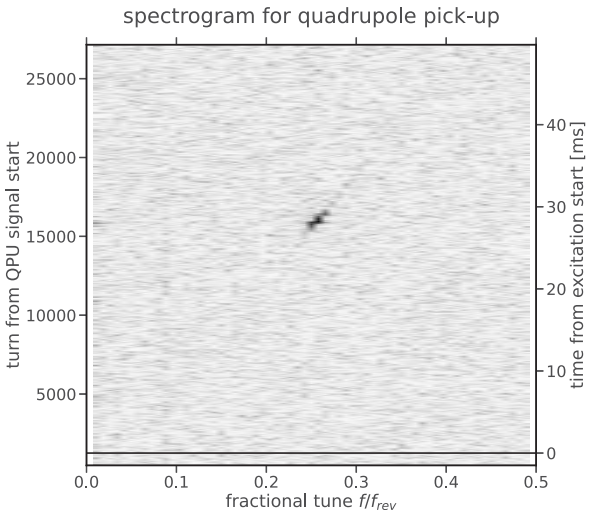


Figure 9: Quadrupolar spectrogram for natural chromaticity.

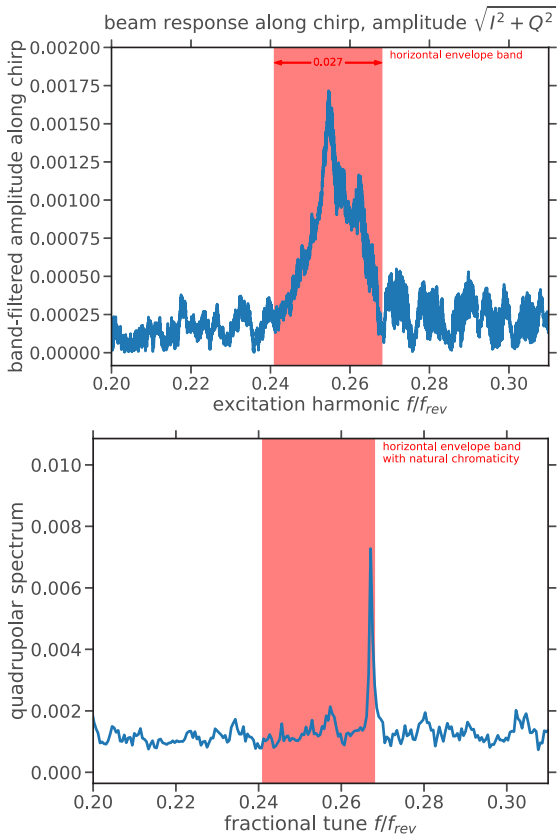


Figure 10: Quadrupolar spectra for natural chromaticity (top panel) and corrected chromaticity (bottom panel). The tune shift in the latter can be attributed to misaligned sextupoles.

The shift of mode frequency toward a larger value for corrected chromaticity can be attributed to uncorrected orbit in the sextupoles, which are powered to correct chromaticity. Figure 11 shows the sum signal of the quadrupolar pick-up.

A blow up in beam profile in both transverse planes as well as beam losses were distinctly observed at the horizontal and vertical envelope resonance excitation, respectively. The simultaneous measurement of the envelope mode frequencies and beam blow up clearly distinguishes between the excitation of second order dipolar modes and the envelope modes.

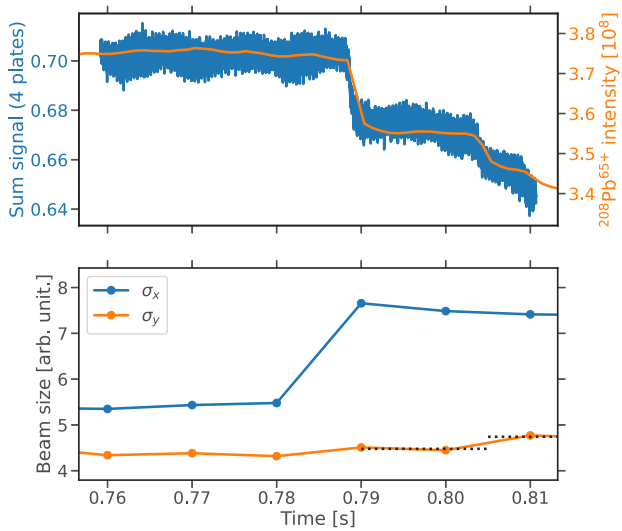


Figure 11: (Top) An overlay of the blue sum signal with the orange DCCT signal, (Bottom) Measured transverse profile widths as a function of time. The transverse blow up and losses coincide with the envelope mode excitation.

CONCLUSION

Following an overview of the expected modes in the quadrupole spectrum of a bunched beam, the quadrupole transfer function setup at GSI SIS18 has been discussed. First experimental results are well in agreement with the beam dynamics simulations of the experiment. The measurements demonstrate, for the first time, the considerable broadening of the envelope resonance width for bunched beams due to chromaticity.

ACKNOWLEDGEMENTS

The authors are grateful for the dedicated setup of the equipment by W. Kaufmann, for the support during the control room activities by O. Chorniy, B. Galnander, D. Rabusov, for technical support by S. Klaproth, C. Krüger, K. Lang, P. Niedermayer, T. Sieber, and to P. Forck and M. Schwickert for enabling this measurement campaign.

REFERENCES

[1] R. H. Miller, J. E. Clendenin, M. B. James, and J. C. Sheppard, "Nonintercepting emittance monitor", Stanford Linear Accelerator Center, Tech. Rep. SLAC-PUB-3186, 1983.

[2] A. Jansson, "Noninvasive single-bunch matching and emittance monitor", *Phys. Rev. ST Accel. Beams*, vol. 5, no. 7, p. 072 803, 2002. doi:10.1103/PhysRevSTAB.5.072803

[3] C.-Y. Tan, "Using the quadrupole moment frequency response of bunched beam to measure its transverse emittance", Fermi National Accelerator Laboratory (FNAL), Batavia, IL, Tech. Rep., 2007. doi:10.2172/919077

ISBN: 978-3-95450-241-7 ISSN: 2673-5350 doi:10.18429/JACoW-IBIC2022-TU1I2

[4] M. Chanel, "Study of Beam Envelope Oscillations by Measuring the Beam Transfer Function with Quadrupolar Pick-up and Kicker", in *Proc. EPAC'96*, Sitges, Spain, Jun. 1996, paper WEP014G, pp. 1015–1017. https://jacow.org/e96/PAPERS/WEPG/WEP014G.PDF

[5] T. Uesugi *et al.*, "Observation of Quadrupole Mode Frequency and its Connection with Beam Loss", in *Proc. PAC'99*, New York, NY, USA, Mar. 1999, paper TUP139, pp. 1821–1823. https://jacow.org/p99/papers/TUP139.pdf

[6] R. C. Bär, "Untersuchung der quadrupolaren BTF-Methode zur Diagnose intensiver Ionenstrahlen", Ph.D. dissertation, Universität Frankfurt, Germany, 2000.

[7] R. Singh *et al.*, "Observations of the Quadrupolar Oscillations at GSI SIS-18", in *Proc. IBIC'14*, Monterey, CA, USA, Sep. 2014, pp. 629–633. https://jacow.org/IBIC2014/papers/WEPD01.pdf

[8] A. Oeftiger, "Requirements and Results for Quadrupole Mode Measurements", in *Proc. HB'18*, Daejeon, Korea, Jun. 2018, pp. 393–398. doi:10.18429/JACoW-HB2018-THA1WE02

[9] A. Oeftiger, "Diagnostics with quadrupolar pick-ups", in *CERN Yellow Rep. Conf. Proc.*, Zermatt, Switzerland, Sep. 2019, vol. 9, pp. 130–136. doi:10.23732/CYRCP-2020-009.130

[10] G. Guignard, "The general theory of all sum and difference resonances in a three-dimensional magnetic field in a synchrotron; part 1", CERN, Tech. Rep., 1975. https://cds.cern.ch/record/323328

[11] J. A. Tsemo Kamga, W. F. O. Müller, and T. Weiland, "Analytical and numerical calculation of the second-order moment of the beam using a capacitive pickup", *Phys. Rev. Accel. Beams*, vol. 19, no. 4, p. 042 801, 2016. doi:10.1103/PhysRevAccelBeams.19.042801

[12] D. Chernin, "Evolution of RMS beam envelopes in transport systems with linear X-Y coupling", *Part. Accel.*, vol. 24, pp. 29–44, 1988. http://cds.cern.ch/record/1053510

[13] Y. S. Yuan, O. Boine-Frankenheim, G. Franchetti, and I. Hofmann, "Dispersion-induced beam instability in circular accelerators", *Phys. Rev. Lett.*, vol. 118, p. 154 801, 15 2017. doi:10.1103/PhysRevLett.118.154801

[14] M. Aslaninejad and I. Hofmann, "Effect of space charge on linear coupling and gradient errors in high-intensity rings", *Phys. Rev. ST Accel. Beams*, vol. 6, p. 124 202, 2003. doi:10.1103/PhysRevSTAB.6.124202

[15] M. Schwinzerl, H. Bartosik, R. D. Maria, G. Iadarola, A. Oeftiger, and K. Paraschou, "Optimising and Extending a Single-Particle Tracking Library for High Parallel Performance", in *Proc. IPAC'21*, Campinas, Brazil, May 2021, pp. 4146–4149. doi:10.18429/JACoW-IPAC2021-THPAB190

[16] A. Oeftiger, "An Overview of PyHEADTAIL", CERN, Tech. Rep. CERN-ACC-NOTE-2019-0013, 2019. https://cds.cern.ch/record/2672381

[17] A. Oeftiger and S. Hegglin, "Space Charge Modules for PyHEADTAIL", in *Proc. HB'16*, Malmö, Sweden, Jul. 2016, pp. 124–129. doi:10.18429/JACoW-HB2016-MOPR025

Content from this work may be used under the terms of the CC BY 4.0 licence (© 2022). Any distribution of this work must maintain attribution to the author(s), title of the work, publisher, and DOI

ISBN: 978-3-95450-241-7 ISSN: 2673-5350 doi:10.18429/JACoW-IBIC2022-TU1C3

BEAM-BASED CALIBRATION OF SEXTUPOLE MAGNET DISPLACEMENT WITH BETATRON TUNE SHIFT

S. Takano†[1], T. Fujita, M, Takao, K. Fukami[1], M, Masaki, T, Watanabe[1], JASRI, Hyogo, Japan
H. Maesaka[2], K. Soutome[2], T. Hiraiwa, H. Tanaka, RIKEN SPring-8 Center, Hyogo, Japan
K. Ueshima, QST, Miyagi, Japan
[1]also at RIKEN SPring-8 Center, Hyogo, Japan
[2]also at JASRI, Hyogo, Japan

Abstract

The alignment of sextupole magnets is one of the critical issues for the upcoming 4th generation light sources and future colliders to ensure enough dynamic aperture for stable operation and minimize deterioration of beam quality. We propose a beam-based calibration (BBC) method for the sextupole magnet displacement by observing the betatron tune shift. The beam position that makes the horizontal and vertical betatron tunes invariant to the sextupole strength marks the magnet center. The key is to increase the betatron coupling so that the vertical displacement of a sextupole from the beam results in a tune shift large enough for the calibration. The feasibility studies at SPring-8 successfully demonstrated the principle for calibrating both horizontal and vertical sextupole displacements in quantitative agreement with the theory.

INTRODUCTION

The alignment of sextupole magnets is one of the critical issues for the upcoming 4th generation light sources and future colliders. The misalignment and the beam offset in sextupoles should be within a few 10 μm to ensure enough dynamic aperture for stable operation and minimize deterioration of beam quality. A sextupole magnet horizontally displaced from the beam exerts a normal quadrupole (Q) field, and a vertically displaced one a skew Q field. We propose a beam-based calibration (BBC) method to measure the displacement of a sextupole magnet by observing the betatron tune shift. The beam position that makes the horizontal and vertical betatron tunes invariant to the sextupole strength marks the magnet center. We studied experimentally the feasibility of the proposed BBC for the sextupole magnet on the SPring-8 storage ring and successfully demonstrated the principle for calibrating both the horizontal and vertical displacements. In this paper, we overview the theoretical background related to the betatron tune-based BBC and elaborate on the results of feasibility studies at SPring-8.

THEORETICAL BACKGROUND

Magnetic Field of a Sextupole

Suppose that a beam passes through a sextupole magnet with offset (x_0, y_0) from the center of the magnetic field. When each particle in the beam moves (Δx, Δy) around this point, the magnetic field at the destination point is expressed in the forms

$$B_x = B''(x_0 + \Delta x)(y_0 + \Delta y), \quad (1)$$

$$B_y = \frac{B''}{2}\{(x_0 + \Delta x)^2 - (y_0 + \Delta y)^2\}, \quad (2)$$

where B" is the gradient of the sextupole magnet. Eqs. (1) and (2) can be rewritten in the forms

$$B_x = B''x_0y_0 + B''x_0\Delta y + B''y_0\Delta x + B''\Delta x\Delta y, \quad (3)$$

$$B_y = \frac{B''}{2}(x_0^2 - y_0^2) + B''x_0\Delta x - B''y_0\Delta y + \frac{B''}{2}((\Delta x)^2 - (\Delta y)^2). \quad (4)$$

The second and third terms in Eqs. (3) and (4) represent the normal and skew Q components in the magnetic field, respectively. Therefore, in a sextupole magnet, the beam passing through with a horizontal offset, $x_0 \neq 0$, undergoes a normal Q magnetic field, and the one passing through with a vertical offset, $y_0 \neq 0$, undergoes a skew Q field. The skew Q field in the sextupole magnet drives the linear coupling of the betatron motion that adds to the indigenous coupling driving term of the whole storage ring.

Betatron Tune Shift by a Displaced Sextupole

For the coupled betatron motion, if we define the difference between the fractional parts of unperturbed betatron tunes ν_x and ν_y as

$$\Delta \equiv \nu_x - \nu_y - q \quad (5)$$

with q an integer, the eigentunes in the normal coordinate ν_u and ν_v, which are observed in actual measurements instead of ν_x and ν_y, can be expressed as

$$\nu_{u,v} = \nu_{x,y} \mp \frac{1}{2}\left(\Delta - \sqrt{\Delta^2 + |c|^2}\right), \quad (6)$$

and

$$\nu_{u,v} = \nu_{x,y} \mp \frac{1}{2}\left(\Delta + \sqrt{\Delta^2 + |c|^2}\right), \quad (7)$$

for $\Delta \geq 0$ and $\Delta < 0$, respectively, where C is the coupling driving term (complex number) for the whole ring [1]. In what follows, we will address the case $\Delta < 0$ as in the studies reported in this paper.

† takano@spring8.or.jp

Content from this work may be used under the terms of the CC BY 4.0 licence (© 2022). Any distribution of this work must maintain attribution to the author(s), title of the work, publisher, and DOI

ISBN: 978-3-95450-241-7 ISSN: 2673-5350 doi:10.18429/JACoW-IBIC2022-TU1C3

Suppose the sextupole gradient is varied by ΔB" as the beam passes at (x_0, y_0) in the sextupole. Then, the change in the horizontal and vertical betatron tunes can be expressed as

$$\Delta\nu_x = +\frac{\beta_x(s)}{4\pi}\frac{\Delta B''L}{[B\rho]}x_0 - \frac{1}{2}\sqrt{\Delta^2+|C_0+\delta C|^2}+\frac{1}{2}\sqrt{\Delta^2+|C_0|^2}, \quad (8)$$

$$\Delta\nu_y = -\frac{\beta_y(s)}{4\pi}\frac{\Delta B''L}{[B\rho]}x_0 + \frac{1}{2}\sqrt{\Delta^2+|C_0+\delta C|^2}-\frac{1}{2}\sqrt{\Delta^2+|C_0|^2}, \quad (9)$$

where C_0 is the initial coupling driving term for the whole ring. The first term in Eqs. (8) and (9) represents the tune shift due to a change in the focusing of the normal Q field of a horizontally displaced sextupole. The second term in Eqs. (8) and (9) is due to a change in the coupling δC brought about by the skew Q field of a vertically displaced sextupole. The additional driving term δC is given by

$$\delta C = \frac{1}{2\pi}\frac{\Delta B''L}{[B\rho]}y_0\sqrt{\beta_x(s)\beta_y(s)}e^{i[\phi_x(s)-\phi_y(s)-2\pi\Delta\cdot s/L_0]} \quad (10)$$

with the ring circumference L_0, and the betatron functions and phase advances at the sextupole β_x, β_y, ϕ_x, and ϕ_y. Eqs. (8), (9), and (10) illustrate that the magnetic center of the sextupole magnet can be marked as the beam position where both the horizontal and vertical tunes are invariant to the sextupole field strength. To lowest order of |δC|, Eqs. (9) and (10) can be rewritten as

$$\Delta\nu_x \fallingdotseq +\frac{\beta_x(s)}{4\pi}\frac{\Delta B''L}{[B\rho]}x_0 - \frac{\sqrt{\beta_x(s)\beta_y(s)}}{4\pi}\frac{\Delta B''L}{[B\rho]}\frac{|C_0|cos(\phi_0-\phi_1)}{\sqrt{\Delta^2+|C_0|^2}}y_0, \quad (11)$$

$$\Delta\nu_y \fallingdotseq -\frac{\beta_y(s)}{4\pi}\frac{\Delta B''L}{[B\rho]}x_0 + \frac{\sqrt{\beta_x(s)\beta_y(s)}}{4\pi}\frac{\Delta B''L}{[B\rho]}\frac{|C_0|cos(\phi_0-\phi_1)}{\sqrt{\Delta^2+|C_0|^2}}y_0, \quad (12)$$

where ϕ_0 and ϕ_1 are arguments of C_0 and δC, respectively.

Betatron Tune Based Sextupole Displacement Calibration

Putting $\Delta\nu_x = \Delta\nu_y = 0$ in Eqs. (8) and (9) or in (11) and (12), two loci of fixing points for ν_x and ν_y can be obtained. If we suppose the horizontal and vertical betatron functions at the target sextupole magnet are different, the two loci intersect at only one point at the sextupole center.

In the small coupling limit, $|C_0| \to 0$, information on the vertical center of the sextupole is missing in the tune shift. In that case, we can find the horizontal center of the sextupole by moving the beam horizontally regardless of the vertical beam offset and by observing either the horizontal or vertical tune. For real rings with a finite coupling, the key is to increase the betatron coupling so that the vertical displacement of a sextupole from the beam results in a tune shift large enough for calibration. In our feasibility studies at SPring-8, we increased the coupling as described below.

FEASIBILITY STUDIES AT SPring-8

We conducted feasibility studies on the betatron tune-based BBC of sextupole magnet displacement on the SPring-8 storage ring, an 8 GeV photon source electron ring with a 1436 m circumference. For the target of the BBC, a sextupole magnet placed in one of the 30-m-long straights of the ring [2] with a beam position monitor (BPM) head nearby was employed. The beam position at the target sextupole was controlled by using local orbit bumps. There were two other sextupoles involved in the orbit bumps that are used in the normal operation of SPring-8. They were switched off temporarily during the experiments.

Beam Monitoring

Equally spaced 21 electron bunches were stored on the storage ring for the BBC study. The BPM nearby the target sextupole was read by a recently developed MicroTCA.4-based electronics [3]. Fast COD data were sampled at 10 kHz with sub-micron resolution [3]. Two out of the stored 21 bunches were subject to real-time tune monitoring, one for the horizontal tune and the other for the vertical one. Two sets of bunch-by-bunch feedback and diagnostics signal processor iGP12 of Dimtel, Inc. [4] were employed. Single bunch phase tracker capability integrated into the processor provided real-time tune monitoring with ~ 10^{-5} precisions at a 5 Hz sampling during the experiments.

Coupling Control with Skew Q Magnets

To obtain effective data sensitive to the vertical displacement of the sextupole magnet relative to the beam, we temporarily increased the betatron coupling by using skew Q magnets integrated into the storage ring. The overall coupling driving term C_T can be expressed as

$$C_T = C_0 + \Delta C_{SkQ} \quad (13)$$

where C_0 is the original coupling driving term for the whole ring and ΔC_{SkQ} is the driving term added by the skew Q magnets. First, we searched the argument ϕ_0 of C_0 by observing the projected beam size σ_y varying the argument ϕ_{SkQ} of ΔC_{SkQ} keeping the magnitude of ΔC_{SkQ} at a constant value. The beam size σ_y can be related to the argument ϕ_{SkQ} by a formula

$$\frac{\sigma_y^2}{\beta_y} = \frac{\frac{1}{2}|C_T|^2}{\Delta^2+|C_T|^2}\varepsilon_0 \approx \frac{\frac{1}{2}\left(|C_0|^2+2|C_0||\Delta C_{SkQ}|\,cos(\phi_{SkQ}-\phi_0)+|\Delta C_{SkQ}|^2\right)}{\Delta^2}\varepsilon_0, \quad (14)$$

Content from this work may be used under the terms of the CC BY 4.0 licence (© 2022). Any distribution of this work must maintain attribution to the author(s), title of the work, publisher, and DOI

ISBN: 978-3-95450-241-7 ISSN: 2673-5350 doi:10.18429/JACoW-IBIC2022-TU1C3

Content from this work may be used under the terms of the CC BY 4.0 licence (© 2022). Any distribution of this work must maintain attribution to the author(s), title of the work, publisher, and DOI

where ε_0 is the beam emittance. The value of ϕ_{SkQ} maximizing the magnitude $|C_T|$ was found to be 27˚ and the argument ϕ_0 was experimentally determined as 27˚ as shown in Fig.1. Hereafter, we fixed the argument ϕ_{SkQ} at 27˚. Second, we observed the projected beam size σ_y varying the magnitude of ΔC_{SkQ} to evaluate the magnitude of C_0. The value of $|\Delta C_{SkQ}|$ minimizing the vertical σ_y was found to be -0.008 and the magnitude $|C_0|$ was experimentally determined to be 0.008 as shown in Fig.2. Finally we set the $|\Delta C_{SkQ}|$ to the maximum available value of 0.05, which lead to a magnitude of the total coupling driving term $|C_T|$ of 0.058.

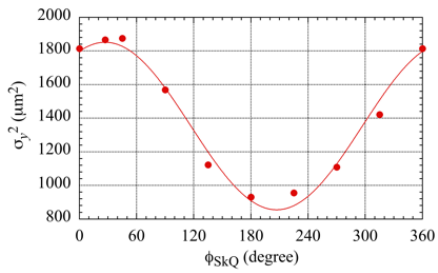


Figure 1: Search for ϕ_{SkQ} maximizing σ_y.

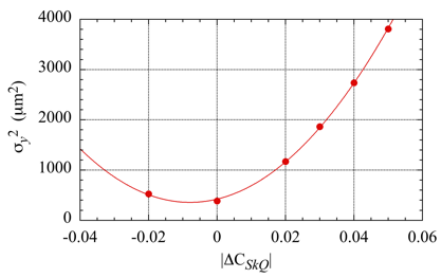


Figure 2: Search for $|\Delta C_{SkQ}|$ minimizing σ_y.

The sensitivity to the vertical displacement of the sextupole magnet relative to the beam is proportional to a factor, $|C_0|/\sqrt{\Delta^2 + |C_0|^2}$, as shown in Eqs. (11) and (12). Besides the coupling control described above, the magnitude of Δ, the difference between the fractional parts of unperturbed betatron tunes ν_x and ν_y, was decreased to obtain extra gain for the sensitivity to the vertical displacement. The original betatron tune (ν_x, ν_y) was (41.14, 19.325). The vertical tune was changed to 19.225 temporarily for the experiments. The enhancement in the factor, $|C_0|/\sqrt{\Delta^2 + |C_0|^2}$, is calculated to be 13. Sensitivity to the vertical offset was improved by a factor of more than 10.

Proof-of-Principle Experiments

The measurement procedures in our proof-of-principle experiments for the sextupole BBC are as follows,

- Step 1: Set a vertical orbit bump.
- Step 2: Sweep the horizontal beam position with a local orbit bump monitoring the beam position and the betatron tune under two conditions: target sextupole magnet OFF and ON.
- Step 3: Set other vertical orbit bumps, and repeat the measurements in Step 2 for each set of the vertical orbit bump.
- Step 4: For each set of the vertical orbit bump, find beam positions (x_1, y_1) and (x_2, y_2) where the horizontal and vertical betatron tunes are invariant, respectively, for the sextupole OFF and ON. The intersection of the loci of (x_1, y_1) and (x_2, y_2) marks the center of the target sextupole magnet

Results

Examples of data obtained in Step 2 of the proof-of-principle experiments for the sextupole BBC are shown in Fig. 3.

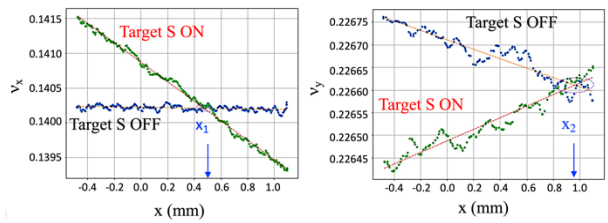


Figure 3: Examples of data obtained in Step 2 of the proof-of-principle experiments for the sextupole BBC corresponding to a vertical orbit bump of +0.1 mm.

The sextupole center is the beam position where both the horizontal and vertical betatron tunes are invariant to the magnet strength as shown in Eqs. (8) and (9). Measured horizontal tune fixing points (x_1, y_1) and vertical tune fixing points (x_2, y_2) are shown in Fig. 4. The

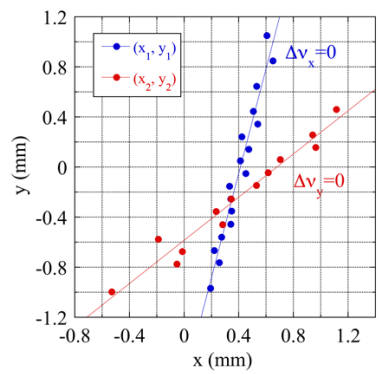


Figure 4: Measured horizontal tune fixing points (x_1, y_1) and vertical tune fixing points (x_2, y_2). The intersection of fitted loci of (x_1, y_1) and (x_2, y_2), respectively, marked the center of the target sextupole magnet.

intersection of fitted loci for (x_1, y_1) and (x_2, y_2), respectively, successfully marked the center of the target sextupole magnet. The beam position (x, y) corresponding to the center of the target sextupole magnet was determined to be $(0.347 \pm 0.014,\ -0.288 \pm 0.034)$ in millimeters where the precisions were evaluated from the residuals of the fit. The specified beam position also figures the BPM offset to the target sextupole.

ISBN: 978-3-95450-241-7 ISSN: 2673-5350 doi:10.18429/JACoW-IBIC2022-TU1C3

To compare the results in Fig. 4 quantitatively with the theory given by Eqs. (8) and (9), the betatron function at the target sextupole was calibrated by using the observed tune shift due to the normal Q field in the target sextupole corresponding to the first term in Eqs. (8) and (9). The horizontal betatron function β_x was $32.16 \pm 0.17\ m$, and the vertical betatron function β_y was $6.41 \pm 0.12\ m$. The measured horizontal tune fixing points (x_1, y_1) and vertical tune fixing points (x_2, y_2) are shown in Fig. 5 after subtracting the BPM offset together with the loci of tune fixing points calculated with the experimentally calibrated betatron function at the target sextupole. The measured fixing points for ν_x and ν_y were in good agreement with that calculated theoretically as shown in Fig. 5.

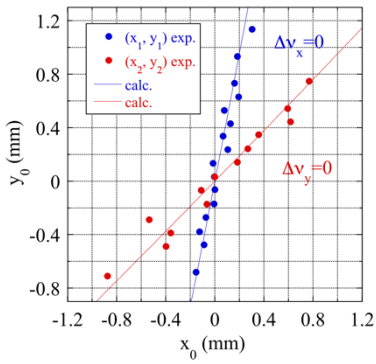


Figure 5: Measured horizontal and vertical tune fixing points (x_1, y_1) and (x_2, y_2), respectively, after subtracting the BPM offset compared with the calculations by Eqs. (8) and (9).

The principle of the betatron tune-based BBC for the sextupole displacement was successfully demonstrated in quantitative agreement with the theory. The precision of the measured sextupole center was a few tens of microns.

ISSUES AND CHALLENGES

We found that the vertical tune unexpectedly changed depending on the horizontal beam position even when the target sextupole was off, as shown in Fig. 3. Influences of the residual field in the sextupoles involved in the orbit bumps and the orbit bump leakages need to be investigated.

While the experimentally evaluated horizontal betatron function β_x of 32.2 m was consistent with the design value of 34.5 m, the experimental β_y of 6.4 m was smaller than the design of 10.5 m. Detailed examinations of the distortions of betatron functions over the storage ring would be necessary.

To apply the betatron tune-based BBC to the entire sextupole magnets in a storage ring for practical use, it is necessary to complete the measurement in a short time. Future studies will be considered employing faster beam orbit manipulation, i.e. by AC exciting the steering magnets and faster betatron tune tracking.

SUMMARY

A beam-based calibration (BBC) method with the betatron tune shift for the sextupole magnet displacement is proposed. The feasibility studies at SPring-8 successfully demonstrated the principle for both horizontal and vertical sextupole displacements in quantitative agreement with the theory. The measurement resolution of 10 μm will be feasible with further improvements. Issues on the observed horizontal position-dependent vertical tune variation for the target sextupole switched off and the vertical betatron function at the target sextupole need to be resolved by future studies. To apply to the entire sextupole magnets in a storage ring for practical use, it is necessary to complete the measurement in a short time. Future studies will be considered employing faster beam orbit manipulation and betatron tune tracking.

REFERENCES

[1] M. Takao, "Linear analysis of Hamilton perturbation theory for coupled betatron motion", *Phys. Rev. ST Accel. Beams*, vol. 9, p. 084002, 2006. doi:10.1103/PhysRevSTAB.9.084002

[2] H. Tanaka *et al.*, "Beam commissioning and achieved performance of SPring-8 storage ring phase-2 lattice with four magnet-free long straight sections", *Nucl. Instrum. Methods Phys. Res., Sect. A,* vol. 486, pp. 521-538, 2002. doi:10.1016/S0168-9002(01)02153-2

[3] H. Maesaka *et al.*, "Development of MicroTCA.4-Based BPM Electronics for SPring-8 Upgrade", in *Proc. IBIC'19*, Malmö, Sweden, Sep. 2019, paper WEBO03, pp. 471-474. doi:10.18429/JACoW-IBIC2019-WEBO03

[4] https://www.dimtel.com

Content from this work may be used under the terms of the CC BY 4.0 licence (© 2022). Any distribution of this work must maintain attribution to the author(s), title of the work, publisher, and DOI

ISBN: 978-3-95450-241-7 ISSN: 2673-5350 doi:10.18429/JACoW-IBIC2022-TU2T1

COLLIMATION AND MACHINE PROTECTION FOR LOW EMITTANCE RINGS*

J. Dooling†, Y. Lee, M. Borland, A. Grannan, C. Graziani, R. Lindberg, G. Navrotski
Argonne National Laboratory, Lemont, IL, USA
N. Cook, RadiaSoft, Boulder, CO, USA
D. Lee, University of California, Santa Cruz, CA, USA

Abstract

The reduced emittance and concomitant increase in electron beam intensity in Fourth Generation Storage Ring (4GSR) light sources lead to the challenging machine protection problem of how to safely dispose of the circulating charge during unplanned whole-beam loss events. Two recent experiments conducted to study the effects of 4GSR whole-beam aborts showed that damage to candidate collimator materials can be severe. This is a paradigm shift for SR light source machine protection. Typically the biggest threat to the machine is from CW synchrotron radiation. The choice of collimator material is important. High-Z, high-density materials such as tungsten may appear effective for stopping the beam in static simulations; however, in reality, short radiation lengths will cause severe destructive hydrodynamic effects. In our experiments, significant damage was observed even in low-Z aluminum. Thus unplanned, whole-beam aborts cannot readily be stopped in a single collimator structure. In this tutorial, alternatives such as multiple collimators and fan-out abort kicker systems will be discussed. Collimator design strategy and foreseen diagnostics for their operation will also be presented.

INTRODUCTION

The ultra-low emittance, high-intensity electron beams in Fourth Generation storage ring (4GSR) machines are capable of causing high-energy-density (HED) interactions on technical surfaces such as collimators or vacuum chamber walls. HED is defined as energy densities exceeding roughly 10^{11}J/m^3 [1]. Dose is defined as absorbed energy per unit mass, $D = E_a/\rho$. HED conditions represent an acute dose of 37 MGy in aluminum, 11.2 MGy in copper, and 5.2 MGy in tungsten. The term "acute" is somewhat ambiguous; here it implies the duration of the deposition is short. A useful rule-of-thumb is to compare the duration with a thermal diffusion time defined from the heat equation as $\tau_D = L^2/\alpha$, where L is a characteristic scale length of the absorbed energy distribution and α is the diffusivity. For systems undergoing rapid temperature or phase changes, α is a complex function of dose and time. For example, diffusivity and thermal conductivity change significantly in aluminum as the material changes from solid to liquid phase [2]. Thermal conductivity falls further if the collimator enters a warm dense matter (WDM) regime [3]. Hence, sophisticated, self-consistent analysis may be required to properly capture material evolution under incident dose.

MACHINE PROTECTION

Third-generation storage ring light sources have typically not focused on protecting accelerator hardware from loss of the circulating electron beam; the effort has been and is still centered on protecting components from x-ray photons. Some measures have been taken such as shielding undulator permanent magnets from accumulated dose caused by high-energy electromagnetic showers; however, this exposure takes place over weeks and months and is not mechanically destructive. Attention to synchrotron photons is warranted given that insertion device beam lines generate kilowatts of beam power with power densities up to 600 kW/mrad^2 [4].

The Advanced Photon Source Upgrade (APS-U) Final Design Report (FDR) [4] states, "The machine protection system (MPS) protects the APS storage ring vacuum system from x-ray beam heating, loss of water cooling, and elevated vacuum levels." On the other hand, documentation for high-energy experimental facilities such as the Electron Ion Collider (EIC) explicitly discuss the need for MPS to protect against beam strikes [5], "...the primary goal of the MPS is to protect the EIC accelerators from the possible damage caused by electron and proton beams."

Two experiments conducted in the APS storage-ring (SR) [6] have led to the understanding that disposal of the electron beam during a whole beam dump—both planned and unplanned—must also be included in the function of the APS-U MPS. This language has been added to the MPS engineering specification document.

In the following subsections, we present a brief overview of MPS realizations at several accelerator facilities including APS-U. The selection is by no means comprehensive.

APS-U, Argonne National Laboratory

A schematic of the APS-U MPS topology is presented in Fig. 1. Twenty local MPS (LMPS) modules distributed around the ring feed the main MPS unit in the Main Control Room (MCR). Block diagrams for the logic paths are presented in Fig. 2. The top schematic depicts the Main logic block and the lower the local logic. Important subsystems to the MPS include the Front End Equipment Protection System (FE-EPS). The hierarchical architecture is common to

* This research used resources of the Advanced Photon Source (APS), one of the five U.S. Department of Energy (DOE) Office of Science user facilities and is based on work supported by Laboratory Directed Research and Development (LDRD) funding from Argonne National Laboratory, provided by the Director, Office of Science, of the U.S. DOE under Contract No. DE-AC02-06CH11357.
† dooling@anl.gov

Content from this work may be used under the terms of the CC BY 4.0 licence (© 2022). Any distribution of this work must maintain attribution to the author(s), title of the work, publisher, and DOI

ISBN: 978-3-95450-241-7 ISSN: 2673-5350 doi:10.18429/JACoW-IBIC2022-TU2T1

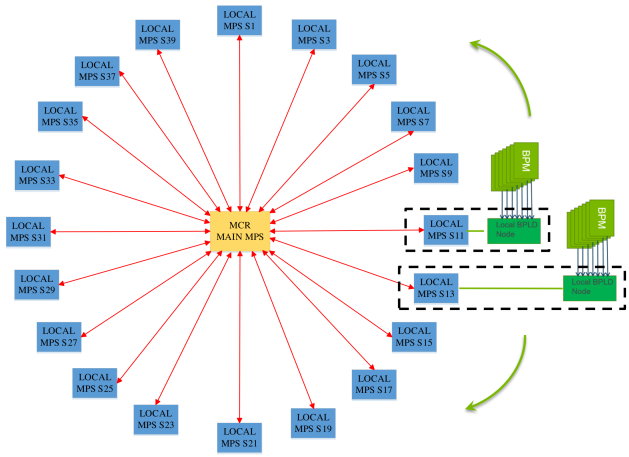


Figure 1: APS-U MPS topology.

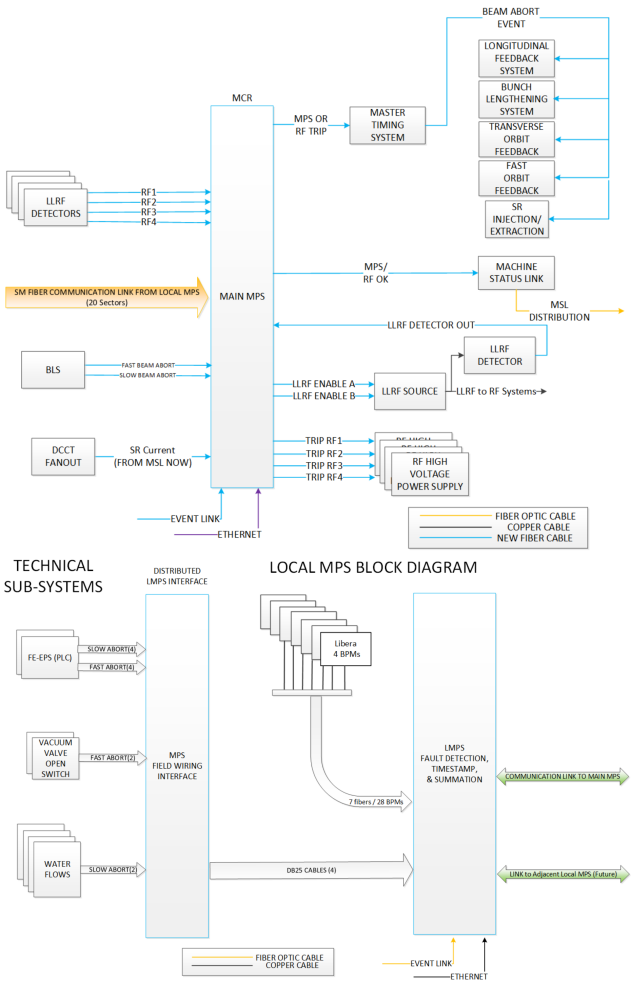


Figure 2: Logic diagrams for the main (top) and local MPS blocks (bottom). BLS stands for the bunch lengthening system.

many MPS configurations at other large laboratories, including those discussed below. For comparative purposes, the stored energy is 4.4 kJ and the average power is 1.2 GW if lost in one turn in the APS-U SR with 200 mA of circulating charge at 6 GeV.

EIC, Brookhaven National Laboratory

The EIC [7] will employ separate dedicated dump lines to terminate both proton and electron beams [5]. For the protons, the existing line for the Relativistic Heavy Ion Collider (RHIC) will be used, whereas a new line is planned for the electrons. The MPS must also protect against synchrotron x-ray photons. For operations at 10 GeV, the 3.834 km circumference electron ring stores 1160 bunches of 27.5 nC. Stored energy for this fill pattern is 320 kJ and average circulating power is 25 GW.

Proton Improvement Plan II, Fermilab

The Proton Improvement Plan II (PIP-II) at Fermilab will operate an 800 MeV superconducting linac at a current of 2 mA [8]. Operations are scheduled to begin in 2028. Four levels of protection are provided by the PIP-II MPS. First, the main level of protection comes from four upstream locations near the ion source utilizing four pairs of current sensitive devices: two pairs of ring pick ups and two pairs of scrapers. The second layer detects local beam losses in the medium energy beam transport (MEBT) line. The third level involves tracking readiness status from various subsystems such as RF, vacuum, and water. Finally, various configurations are considered including beam intensity, fill pattern, and destination [9].

Spallation Neutron Source, Oak Ridge National Laboratory

The Spallation Neutron Source (SNS) is a user facility operating a high-power proton beam. The purpose of the 1.4 MW proton beam is to strike a heavy metal target for neutron production. Similar to the APS, it must operate continuously for days at a time with periodic breaks for maintenance and studies, making reliability and up-time paramount. The SNS MPS has gone through a number of changes since first operations in 2006 [10–12]. Presently, the Fast Protection System (FPS), responsible for terminating beam, is being upgraded in a staged process [13]. The process starts with the Master MPS and Ring to Target Beam Transfer line (RTBT) components. Next, the Medium Energy Beam Transport (MEBT) and the coupled-cavity linac (CCL) systems will be addressed, followed by the injection dump and linac, and finally the Extraction Dump.

STRATEGY FOR PROTECTION OF APS-U CHAMBERS AND COLLIMATORS

The APS-U MPS system includes beam-position-limits detectors (BPLDs) that will abort the beam if the orbit exceeds defined amplitude or slope. The initial motivation for this system was to protect against damage to vacuum chambers from synchrotron radiation, which might bypass a radiation absorber if the orbit is large. In light of damage seen to APS collimators and to materials such as aluminum

Content from this work may be used under the terms of the CC BY 4.0 licence (© 2022). Any distribution of this work must maintain attribution to the author(s), title of the work, publisher, and DOI

ISBN: 978-3-95450-241-7 ISSN: 2673-5350 doi:10.18429/JACoW-IBIC2022-TU2T1

Content from this work may be used under the terms of the CC BY 4.0 licence (© 2022). Any distribution of this work must maintain attribution to the author(s), title of the work, publisher, and DOI

in APS experiments, it was realized that the BPLD system should also be configured to protect components from electron beam strikes. To understand the requirements, computer simulations of beam aborts in the presence of orbit distortion were performed with `elegant` [14, 15]. The simulations include models of the APS-U rf systems and cavities, including beam-loading, which significantly affects the rate of energy loss per turn when the rf systems trip (as they do for a beam abort). We modeled an uncontrolled orbit by ramping up the strength of one or more steering magnets, with the ramping rate determined by the power supply limit for the APS-U fast correctors. This simulates runaway fast orbit feedback. The rf drive was then muted when the orbit distortion at the relevant BPMs exceeded a threshold value. Simulations were performed for various threshold values and evaluated in terms of whether particle losses were seen outside the whole-beam dumps. We found that, in order to prevent such losses, the interlock level should be ± 2 mm in the horizontal plane and ± 1.5 mm in the vertical plane. In both cases, the interlocks can be imposed only at the two BPMs per sector that have the largest beta function. These thresholds are comparable to those needed to protect the chamber from synchrotron radiation.

APS-U incorporates identical beam dumps in five consecutive sectors. Simulations show that, even in the presence of errors, the identical beam dumps reduce the probability of missing the dumps to less than 1%. Since we anticipated that the APS-U whole-beam dumps will be damaged over time, they are designed to be serviced without breaking ring vacuum, thanks to a load-lock system and removable surface pieces. Even so, it is desirable to reduce damage in order to increase the service interval and, more importantly, to reduce the chance that gradual erosion of the dump surfaces would lead to beam strikes in unwanted locations. Toward this end, we are incorporating a fan-out kicker (FOK) into the APS-U. This kicker will be fired when an rf system trips (or is commanded to trip). The FOK pulse duration will be one revolution period, with a half-sinusoidal shape, so that different bunches are kicked by different amounts. The idea is to disperse the bunches across the dump surface vertically and decrease the energy density, to either reduce or eliminate damage. Simulations with `elegant` show that if the kick amplitude does not exceed 200 µrad, there are no losses except at the beam dumps. For this kick amplitude, the maximum dose in aluminum is less than 2 MGy which is well below the damage threshold.

Another advantage of the FOK is that it has the potential to reduce the energy density sufficiently so that using copper for the beam dump surface may become an option. (Copper has a lower damage threshold than aluminum because of its comparatively poor heat capacity.) This is desirable because copper's higher Z (than aluminum) would result in better localization of the losses.

The use of the FOK for machine protection is complicated by the desire to use it for diagnostics purposes, primarily measurement of the vertical-plane dynamic acceptance. Simulations show that, if the orbit is well controlled, use of the FOK as a diagnostic is safe up to 30 mA stored current, in which case the beam hits a whole-beam dump. If the orbit is not well controlled, as might happen in early commissioning before the BPLDs are active and before the lattice is well tuned, the limit is reduced to 3.5 mA since a strike on a copper photon absorber is then a possibility.

APS-U will operate in on-axis swap-out mode [16, 17] at 200 mA with as few as 48 bunches, entailing disposal of single 15.3 nC bunches at the swap-out dump. Unlike the beam striking the whole-beam dumps, a swapped-out bunch is lost in a few hundred picoseconds, meaning that thermal diffusion does not help to diffuse the effect. In the original vertical-plane injection scheme [18], the beam would strike the dump surface at near-normal incidence, resulting in doses sufficient to melt aluminum. To prevent damage to the dump, we incorporated a decoherence kicker (DK) [19], that will be fired at least 200 turns prior to the swap-out event. This kicker will use a fast pulser similar to the pulsers used for injection, so it will only significantly affect the bunch being replaced. We have since switched to a horizontal-plane injection scheme that allows for a very gradual taper on the swap-out dump, so the dose is greatly reduced. However, should an injection/extraction kicker misfire, the bunch may impact other components with a less glancing angle. As a result, the DK is still considered essential. The DK waveform is monitored so that the injection/extraction kickers will not fire if the DK does not fire as required.

COUPLED CODE SIMULATIONS

We have begun to model the damage that unplanned and unprotected beam losses will have on accelerator components and materials in the APS-U SR [20, 21].

Figure 3 presents a dose map composed of multi-turn loss distributions derived from `elegant` simulations and measurements from a 200 mA beam dump described in Ref. [6]. The loss distributions are then used in MARS [22]

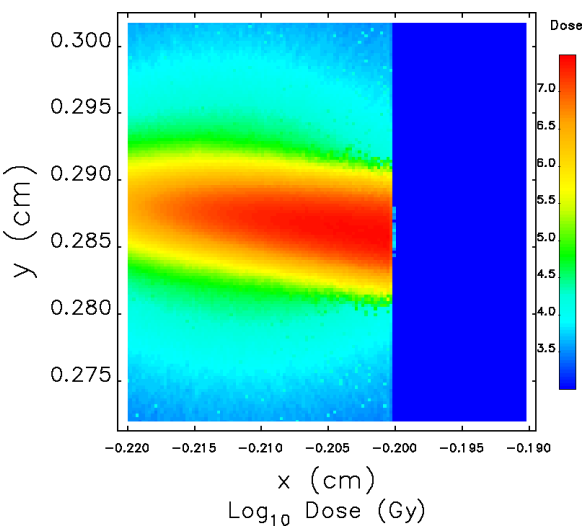


Figure 3: Multi-turn dose map from a 200 mA beam dump. The region $x < 0.2$ cm is aluminum and vacuum otherwise.

ISBN: 978-3-95450-241-7 ISSN: 2673-5350 doi:10.18429/JACoW-IBIC2022-TU2T1

Table 1: Thermal Properties

	c_p (J/(kg-K))	c_l (J/(kg-K))	T_1 (K)	T_m (K)	T_v (K)	ΔH_f (J/kg)	ΔH_v (J/kg)	D_v (J/kg≡Gy)
Aluminum	900	1138	293	933	2743	3.21×10^5	1.14×10^7	1.434×10^7

to generate the dose map. This distribution assumes the collimator surface remains intact during the beam dump. However, we have seen that the assumption is not the case during loss studies.

The MARS-generated dose map is passed to the FLASH code. FLASH [23] is a magnetohydrodynamics (MHD) based multi-physics code with a broad range of user communities among astrophysicists and plasma physicists. We use FLASH to simulate the collimator damage and the plasma evolution due to the beam strikes, making careful numerical assumptions to *emulate* the solid-state material and its phase change, both of which have limited scopes of implementations in FLASH.

FLASH assumes that every material inside the simulation domain is an inviscid compressible fluid. Without considering electromagnetic effects, the hydrodynamics properties are updated by solving the conservative form of Euler equations,

$$\begin{aligned} \frac{\partial \rho}{\partial t} + \nabla\cdot(\rho\mathbf{v}) &= 0, \\ \frac{\partial \rho\mathbf{v}}{\partial t} + \nabla\cdot(\rho\mathbf{v}\mathbf{v}) + \nabla P &= 0, \\ \frac{\partial \rho E}{\partial t} + \nabla\cdot[(\rho E + P)\mathbf{v}] &= 0, \end{aligned} \tag{1}$$

where ρ is the fluid density, $\mathbf{v} = (u, v, w)$ is the fluid velocity, and P is the thermal pressure. The total energy E is the sum of the internal energy and kinetic energy per unit mass,

$$E = \epsilon + \frac{1}{2}|\mathbf{v}|^2. \tag{2}$$

The pressure P and the temperature T are obtained by calculating the equation of states (EOS), where we rely on precalculated tabulated EOS data. FLASH will read the tabulated EOS data with given internal energy and density as,

$$P, T = \mathrm{EOS}(\rho, \epsilon). \tag{3}$$

We utilize FLASH's multi-temperature model that handles pressure, temperature, and internal energy separately for ions and electrons, which are not necessarily equal in high-energy-density plasmas. In other words, FLASH calculates Eqs. (1) and (3) separately for ions ($P_{\mathrm{ion}}, \epsilon_{\mathrm{ion}}, T_{\mathrm{ion}}$) and electrons ($P_{\mathrm{ele}}, \epsilon_{\mathrm{ele}}, T_{\mathrm{ele}}$), and computes the heat exchanges between electrons and ions through collisions.

The input energy dose map from the MARS simulation results will be added to the electron's internal energy (i.e., $\epsilon_{\mathrm{ele}} = \epsilon_{\mathrm{ele}} + E_{\mathrm{MARS}}$). This energy increment will be translated into the temperature rises at the collimator regions. FLASH will perform the thermal diffusion calculations by solving the isotropic diffusion equation as

$$\rho c_v \frac{\partial T}{\partial t} = \nabla\cdot K\nabla T, \tag{4}$$

where c_v is the specific heat at constant volume, and K is the thermal conductivity. Again, the multi-temperature model solves Eq. (4) for both ions and electrons separately, although we use electrons' thermal diffusion only, assuming that the electrons are the primary energy carrier.

FLASH provides several models to calculate the electron's thermal conductivity, K_{ele}, for plasma materials. For example, the Spitzer conductivity model [24] follows

$$K_{\mathrm{ele}} = \left(\frac{8}{\pi}\right)^{3/2} \frac{k_B^{7/2}}{e^4\sqrt{m_{\mathrm{ele}}}} \left(\frac{1}{1+3.3/\bar{z}}\right) \frac{T_{\mathrm{ele}}^{5/2}}{\bar{z}\ln\Lambda_{ei}}, \tag{5}$$

where k_B is the Boltzmann constant, e is the electron charge, m_{ele} is the mass of an electron, $\bar{z}$ is the average ionization level, and $\ln\Lambda_{ei}$ is the Coulomb logarithm associated with electron-ion collisions.

We should note that the model described in Eq. (5) is only valid for an ionized gas. In the case of solid-state matter (i.e., the collimator), we need to use a different approach for calculating the thermal conductivity. Currently, we are using a constant thermal conductivity (e.g., $2.05\times10^2\ \mathrm{Wm^{-1}K^{-1}}$ for aluminum) inside the collimator.

Alongside the different approaches for the thermal conductivity calculations inside the collimator region, we need to take care when updating physical quantities inside the collimator regions, as FLASH considers everything as a compressible fluid. Our strategy to *emulate* a solid-state matter and its phase transition are to utilize the `bdry_var` switch provided in FLASH.

FLASH offers the functionality of immersing a stationary physical boundary within the simulation domain, tagged as `bdry_var`. If a cell is tagged as `bdry_var`, then FLASH omits the hydrodynamics updates (i.e., neglects to solve Eq. (1)) to force the physical quantities at the cell to remain stationary. We initially tag the `bdry_var` of all the cells inside the collimator regions and let FLASH calculate only the thermal diffusion with a constant conductivity, expressed in Eq. (4). With this approach, we expect to see dispersion of the electron beam dose due to thermal conduction. In order to emulate the phase transition, we turn off the `bdry_var` if a cell reaches a threshold temperature. With `bdry_var` turned-off, FLASH will assume the cell is an inviscid compressible gas fluid vaporized from the solid collimator state.

This simplified two-phase model in our simulations introduces two main issues: determining the phase-transition threshold value and simulating the liquid-state matter. One

Content from this work may be used under the terms of the CC BY 4.0 licence (© 2022). Any distribution of this work must maintain attribution to the author(s), title of the work, publisher, and DOI

ISBN: 978-3-95450-241-7 ISSN: 2673-5350 doi:10.18429/JACoW-IBIC2022-TU2T1

Content from this work may be used under the terms of the CC BY 4.0 licence (© 2022). Any distribution of this work must maintain attribution to the author(s), title of the work, publisher, and DOI

possible method to determine the threshold value is to use the boiling temperature for the collimator material. However, this implies that FLASH calculates EOS for the solid-state matter correctly. As our current EOS data is only applicable for plasma, we have to use an arbitrary threshold value by considering it as a hyperparameter. In the case of the aluminum collimator, we configured the threshold value as 4115 K by benchmarking the trench formation patterns observed in the experimental results reported in [6]. It should be noted that the value 4115 K is just an interim value, and we expect a more accurate configuration once we improve the EOS models for the solid-state matter.

We also need to contemplate the liquid state during the phase transition to capture the collimator deformation more correctly. In our recent experiments reported in [6], we observed irregular-shaped collimator deformation, which is not captured in our FLASH simulations. We believe this is due to the lack of liquid state calculations in our current FLASH simulation setups. To help obtain a succinct idea of the liquid state contribution to the trench formation in the collimator, we took a heuristic strategy of performing the simulation by lowering the threshold value at the end of beam loss. This result is displayed in the right panel of Fig. 4. Obviously, a far more detailed analysis of the material properties is required to model the fluid dynamics in this situation properly. We will explore such options in our future study.

A 3-D microscopy view of a section of aluminum struck by a 200 mA, 6 GeV electron beam during collimator irradiation studies mentioned above is presented in Fig. 5. The melt channel is approximately 200 µm wide and 50 µm deep. Presumably a significant melt region lies below the channel surface [25]. Melted, expelled aluminum lines the channel above the collimator surface. We note that not every struck region looks like Fig. 5. Some have sharper, deeper walls similar to the simulation shown in Fig. 4 left.

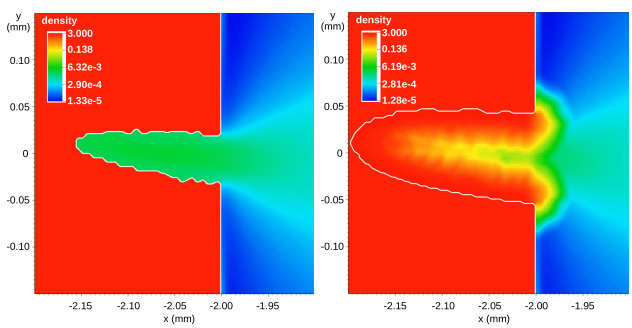


Figure 4: Allowing the release condition to jump from 4115 K to 2743 K at the end of energy deposition. In both frames, the white curve indicates the release boundary. Left: Density prior to the change in the release condition. Right: Density 5 ns after the release temperature threshold jump. The material within the new boundary is now a low-temperature plasma that may emulate a *liquid phase* region.

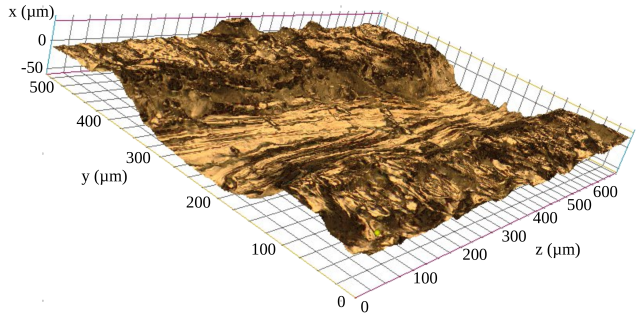


Figure 5: 3-D microscopy image showing the region of an aluminum collimator test piece struck by a 200 mA, 6 GeV beam dump.

DISCUSSION

We can perform a naive calculation of dose to give a general idea of the state of the irradiated material. Ignoring thermal diffusion, complete vaporization should take place for a specific energy or dose, D, if the following is true,

$$D \geq c_p(T_m - T_1) + \Delta H_f + c_l(T_v - T_m) + \Delta H_v, \quad (6)$$

where c_p is the specific heat at constant pressure, c_l the specific heat for liquid, T_m the melting temperature, T_1 the starting temperature, and T_v the vaporization temperature. ΔH_f and ΔH_v are the heat of fusion and heat of vaporization enthalpies. Assigning D_v the equality condition, Table 1 gives these values for aluminum. Thus, complete vaporization requires a dose of 14.34 MGy. The release condition shown in Fig. 4 left, $1.5T_v$ or 4115 K, corresponds to a dose of 4.83 MGy and notionally places material into a mixed-phase regime. The specific energy required to take the material to the fully melted condition without vaporization (ignoring ΔH_v) is 2.94 MGy. Rapid thermal expansion of the material will occur during this process, even without vaporization, which may also contribute to expulsion of material.

SUMMARY

Machine Protection Systems play a key role in assuring the reliability and sustainability of their respective accelerator facilities. In large facilities, MPS is implemented in hierarchical structures. Both hadron and electron beams are capable of mechanically damaging accelerator hardware. Work is underway to model the effects of beam strikes on accelerator hardware by coupling codes that simulate particle dynamics, particle-matter interactions, and hydrodynamic effects. Our initial results show promise when comparing simulations with experimental data.

ACKNOWLEDGEMENTS

For MPS information, special thanks to M. Smith and H. Bui of APS Argonne National Laboratory (ANL), A. Warden of PIP-II Fermilab, A. Drees. of EIC/RHIC Brookhaven National Laboratory, and A. Justice of SNS Oak Ridge National Laboratory. For assistance with analysis scripts, thanks also to R. Soliday and H. Shang of APS ANL.

ISBN: 978-3-95450-241-7 ISSN: 2673-5350 doi:10.18429/JACoW-IBIC2022-TU2T1

REFERENCES

[1] R. P. Drake, *Introduction to High-Energy-Density Physics*. Springer International Publishing, 2018. doi:10.1007/978-3-319-67711-8_1

[2] M. Leitner, T. Leitner, A. Schmon, K. Aziz, and G. Pottlacher, "Thermophysical Properties of Liquid Aluminum," *Metall. Mater. Trans. A*, vol. 48A, pp. 3036–3045, 2017. doi:10.1007/s11661-017-4053-6

[3] A. McKelvey *et al.*, "Thermal conductivity measurements of proton-heated warm dense aluminum," *Sci. Rep.*, vol. 7, no. 7015, pp. 1–10, 2017. doi:10.1038/s41598-017-07173-0

[4] "Advanced Photon Source Upgrade Project Final Design Report," Advanced Photon Source, Argonne National Laboratory, Tech. Rep., 2019. https://publications.anl.gov/anlpubs/2019/07/153666.pdf

[5] S. Seletskiy and A. Drees, "Electron ion collider machine protection system: Requirements for an electron storage ring abort system," Electron-Ion Collider, Brookhaven National Laboratory, Tech. Rep., 2020. https://technotes.bnl.gov/PDF?publicationId=222327

[6] J. Dooling *et al.*, "Collimator irradiation studies in the argonne advanced photon source at energy densities expected in next-generation storage ring light sources," *Phys. Rev. Accel. Beams*, vol. 25, no. 4, p. 043 001, 2022. doi:10.1103/PhysRevAccelBeams.25.043001

[7] C. Montag, "eRHIC - an Electron-Ion Collider at BNL," Collider Accelerator Department, Brookhaven National Laboratory, Tech. Rep., 2018. https://www.osti.gov/servlets/purl/1566296

[8] S. Nagaitsev and V. Lebedev, "A cost-effective upgrade path for the fermilab accelerator complex," Tech. Rep., 2021. doi:10.48550/arXiv.2111.06932

[9] A. Warner *et al.*, "Machine Protection System Research and Development for the Fermilab PIP-II Proton Linac," in *Proc. ICALEPCS'17*, Barcelona, Spain, Oct. 2017, pp. 1643–1645. doi:10.18429/JACoW-ICALEPCS2017-THPHA110

[10] C. S. III, D. J. Armstrong, A. Jones, T. A. Justice, and D. H. Thompson, "The SNS Machine Protection System: Early Commissioning Results and Future Plans," in *Proc. PAC'05*, Knoxville, TN, USA, May 2005. https://jacow.org/p05/papers/RPPE021.pdf

[11] S. W. Lee, J. A. Ball, M. T. Crofford, T. L. Davidson, T. W. Hardek, and S. L. Jones, "Spallation Neutron Source High-Power Protection Module Test Stand," in *Proc. LINAC'10*, Tsukuba, Japan, Sep. 2010, pp. 262–264. https://jacow.org/LINAC2010/papers/MOP089.pdf

[12] A. P. Zhukov, "Experience with the SNS Loss Monitoring and Machine Protection," in *Proc. NAPAC'13*, Pasadena, CA, USA, Sep.-Oct. 2013, pp. 714–718. https://jacow.org/PAC2013/papers/WEYA2.pdf

[13] T. A. Justice, personal communication, 2022.

[14] M. Borland, "elegant: A Flexible SDDS-Compliant Code for Accelerator Simulation," Advanced Photon Source, Tech. Rep. LS-287, 2000. http://www.aps.anl.gov/Science/Publications/lsnotes/ls287.pdf

[15] Y. Wang and M. Borland, "Implementation and Performance of Parallelized Elegant," in *Proc. PAC'07*, Albuquerque, NM, USA, Jun. 2007, pp. 3444–3446. https://jacow.org/p07/papers/THPAN095.pdf

[16] R. Abela, W. Joho, P. Marchand, S. V. Milton, and L. Z. Rivkin, "Design Considerations for a Swiss Light Source (SLS)," in *Proc. EPAC'92*, Berlin, Germany, Mar. 1992, pp. 486–489.

[17] L. Emery and M. Borland, "Upgrade Opportunities at the Advanced Photon Source Made Possible by Top-Up Operations," in *Proc. EPAC'02*, Paris, France, Jun. 2002. https://jacow.org/e02/papers/TUALA003.pdf

[18] A. Xiao and M. Borland, "Transport Line Design and Injection Configuration Optimization for the Advanced Photon Source Upgrade," in *Proc. IPAC'18*, Vancouver, Canada, Apr.-May 2018, pp. 1287–1289. doi:10.18429/JACoW-IPAC2018-TUPMF017

[19] M. Borland, J. C. Dooling, R. R. Lindberg, V. Sajaev, and A. Xiao, "Using Decoherence to Prevent Damage to the Swap-Out Dump for the APS Upgrade," in *Proc. IPAC'18*, Vancouver, Canada, Apr.-May 2018, pp. 1494–1497. doi:10.18429/JACoW-IPAC2018-TUPMK004

[20] J. C. Dooling *et al.*, "Simulations of Beam Strikes on Advanced Photon Source Upgrade Collimators using FLASH, MARS, and elegant," in *Proc. IPAC'21*, Campinas, Brazil, May 2021, pp. 2562–2565. doi:10.18429/JACoW-IPAC2021-WEXC04

[21] J. C. Dooling *et al.*, "Hydrodynamic and Beam Dynamic Simulations of Ultra-Low Emittance Whole Beam Dumps in the Advanced Photon Source Storage Ring," Albuquerque, New Mexico, USA, Aug. 2022, presented at NAPAC'22, Albuquerque, New Mexico, USA, Aug. 2022, paper TUPA21, to be published.

[22] N. V. Mokhov, "The Mars Code System User's Guide," Fermilab, FN 628, 1995.

[23] B. Fryxell *et al.*, "FLASH: An adaptive mesh hydrodynamics code for modeling astrophysical thermonuclear flashes," *Astrophys. J. Suppl. Ser.*, vol. 131, no. 1, pp. 273–334, 2000. doi:10.1086/317361

[24] S. Atzeni and J. Meyer-ter-Vehn, *The physics of inertial fusion: beam plasma interaction, hydrodynamics, hot dense matter*. OUP Oxford, 2004.

[25] J. C. Dooling *et al.*, "Diagnostics for Collimator Irradiation Studies in the Advanced Photon Source Storage Ring," in *Proc. IBIC'20*, Santos, Brazil, Sep. 2020, pp. 26–33. doi:10.18429/JACoW-IBIC2020-TUAO02

Content from this work may be used under the terms of the CC BY 4.0 licence (© 2022). Any distribution of this work must maintain attribution to the author(s), title of the work, publisher, and DOI

ISBN: 978-3-95450-241-7 ISSN: 2673-5350 doi:10.18429/JACoW-IBIC2022-TU2C2

THE DIAMOND BEAM LOSS MONITORING SYSTEM AT CERN LHC AND SPS

E. Calvo*, E. Effinger, M. Gonzalez-Berges, J. Martínez, S. Morales, B. Salvachua, C. Zamantzas
CERN, Geneva, Switzerland
J. Kral, Faculty of Nuclear Sciences and Physical Engineering (FNSPE), Prague, Czechia

Abstract

The Large Hadron Collider (LHC) and the Super Proton Synchrotron (SPS) accelerators are equipped with 17 pCVD diamond based Beam Loss detectors at strategical locations where their nanosecond resolution can provide insights into the loss mechanisms and complement the information of the standard ionization chamber type detectors. They are used at the injection and extraction lines of the LHC and SPS, to analyse the injection or extraction efficiency, and to verify the timing alignment of other elements like kicker magnets. They are used at the betatron collimation region and are being also explored as detectors to analyse slow extractions. The acquisition chain was fully renovated during the second LHC long shutdown period (from December 2018 to July 2022) to provide higher resolution measurements, real-time data processing and data reduction at the source as well as to integrate seamlessly to the controls infrastructure. This paper presents the new hardware platform, the different acquisition modes implemented, the system capabilities and initial results obtained during the commissioning and operation at the beginning of the LHC's Run 3.

INTRODUCTION

The LHC is currently equipped with 12 pCVD diamond beam loss detectors (dBLM), and 5 more are installed at the SPS. Their time response, in the order of a few nanoseconds, complements the information provided by the standard ionisation chambers, which deliver very sensitive but much slower measurements (from 40 µs at LHC to 5 ms at SPS). Since the minimum LHC bunch spacing is 25 ns, pCVD detectors can provide bunch-by-bunch beam loss measurements. This time resolution is of particular interest at the injection and extraction regions, where the presence of unbunched beam or ghost bunches on the abort gap, can induce high and fast losses during the kicker ramps. This is the reason why half of the LHC diamond BLM detectors and most of the SPS detectors are located in those regions. The complete topology of the dBLM detectors can be seen in Fig. 1 where their locations are represented by green dots.

The second area of high interest equipped with three detectors per beam, is the LHC betatron collimation region, in IR7, where the LHC global aperture limit is located. On that area, bunch-by-bunch losses can be monitored along the full proton fill, and the loss distribution along the batches can provide additional information on the loss causes (electron cloud, long-range beam-beam interactions, etc) [1].

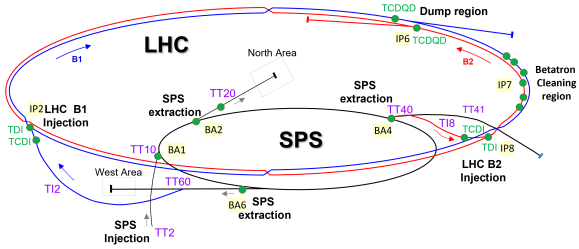


Figure 1: Location of diamond detectors at SPS and LHC.

This paper presents the recent changes that were implemented on the diamond BLM system installed in the CERN accelerator complex as well as some recent measurements to highlight their performances.

DIAMOND BLM HARDWARE

The diamond beam loss monitors consist of pCVD diamond detectors, 10 mm x 10 mm x 0.5 mm in size with gold electrodes of 8 mm x 8 mm on both sides. They are operated with a bias voltage of 500 V, which corresponds to an electric field strength of 1 V/µm. The detectors are connected to a splitter, which provides one DC and two AC outputs. Each of the two AC outputs is either amplified or in some cases attenuated in order to obtain two overlapped operational ranges, thus extending the full dynamic range. Amplifiers consist of either 20 or 40 dB gain, 2 GHz bandwidth, and can withstand up to 1 MGy TID [2].

These three elements are commercial components from CIVIDEC Instrumentation GmbH, and are mounted on a metallic support which positions the detector above or below the beam pipe, downstream of a collimator. Figure 2 shows a typical installation of one of those detectors installed by the end of one the SPS to LHC transfer lines. The acquisition

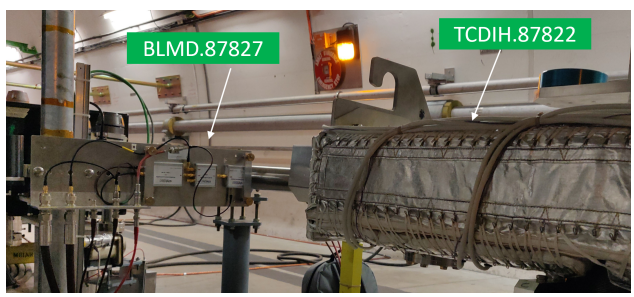


Figure 2: Photo of a dBLM detector installed at the end of the TI8 LHC injection line.

* eva.calvo.giraldo@cern.ch

Content from this work may be used under the terms of the CC BY 4.0 licence (© 2022). Any distribution of this work must maintain attribution to the author(s), title of the work, publisher, and DOI

ISBN: 978-3-95450-241-7 ISSN: 2673-5350 doi:10.18429/JACoW-IBIC2022-TU2C2

electronics are located in the auxiliary galleries at LHC or in the surface buildings at SPS installations, where the expected radiation levels are significantly lower.

In previous runs, those detectors were readout using fast oscilloscopes or CIVIDEC's ROSY DAQ systems. However, during the second LHC long shutdown period, the acquisition system has been migrated to the standard back-end hardware platform used by the CERN Beam Instrumentation group, a 6U VME64x FMC carrier card (VFC-HD) [3]. As shown in Fig. 3, this card has been equipped with a commercial mezzanine from Innovative Integration (FMC-1000), hosting a two-channel 14-bit 1250 MSPS ADC (AD9680) and 16-bit 1250 MSPS DAC (DAC38J82). Unfortunately, the maximum operational sampling frequency is limited to 650 MSPS, due to the ARRIA V GX transceivers of the VFC-HD card [4]. This digitiser is DC coupled and its bandwidth extends from DC to 500 MHz. This migration, has been motivated by the need to homogenize the hardware and software diversity of acquisition systems among CERN beam instrumentation devices, and to reduce the maintenance and integration effort with the different CERN control layers.

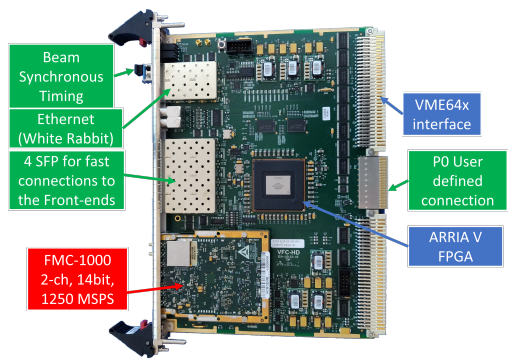


Figure 3: Photo of the VFC-HD card with a FMC-1000 card.

The current hardware platform provides a certain number of advantages, but also some inconveniences. It provides a higher resolution (14 bit instead of 8 bit ADC) and a larger bandwidth (500 MHz vs 250 MHz), but a lower sampling rate (650 MSPS vs 1.25 GSPS) and a reduced input range (±0.45 V vs ±20 V) [5] than previously tested systems. Nevertheless, the most practical advantage is the flexibility to add or adapt new acquisition methods, triggering mechanisms or correction algorithms in-house.

One important feature is that each VFC-HD card receives and decodes the CERN beam synchronous timing (BST) [6] via an optical link, providing turn and bunch clocks, triggers, and other machine information like the energy, beam mode, etc. This is of particular importance since it allows to trigger simultaneously multiple devices in the machine, with minimal skew, as well as tagging the samples as belonging to particular bunches.

ACQUISITION MODES

The FPGA hosted on the VFC-HD card has been programmed to provide several acquisition modes in parallel, from which five buffers publish data continuously and one in a triggered mode. The detectors positioned in transfer or dump lines use the triggered mode as the beam passes only once, while detectors located in rings provide data continuously, typically published and logged by the software layer at 1 Hz. The next paragraph provides a brief description of the different modes implemented:

- **Loss arrival time histogram** This acquisition mode provides the distribution of the losses arrival time along an LHC turn. The digitizers bin each LHC turn in slots of 1.53 ns (corresponding to the 650 MSPS sampling frequency). Each bin, has an associated counter which is increased if in that bin the rising edge of the loss signal crosses a programmable threshold. The counts are accumulated over a programmable time period, generally 1 s. That is, for one LHC turn, 57802 counters with 16-bit depth are used.
- **Bunch loss integral** This acquisition accumulates the digitised samples corresponding to the same bunch, during a programmable number of turns. The resulting array is published and logged by the software every second.
- **Turn loss integral** This mode presents the turn-by-turn losses for a programmable number of turns.
- **Raw distribution** This is an expert mode used to analyse the correct behaviour of the system, in particular the noise and signal distribution levels. It presents a histogram of the measured ADC samples. Histogram counters are accumulated for a programmable number of turns.
- **Bunch integral distribution** Similarly to the previous mode, this mode displays the histogram of the bunch integral losses accumulated within 1 s.
- **Capture** This mode consists on writing continuously the digitised data to the DDR VFC-HD memories, until the reception of a freeze signal, which can be received through the Beam Synchronous Timing (BST), a front-panel connector, a VME command, or can be internally auto-generated based on different waveform recognition patterns. In addition, the data recording can be gated, using a selection of consecutive bunches or some internal counters.

FIRMWARE ARCHITECTURE

Figure 4 shows a simplified functional block with the most important components of the acquisition firmware. The mezzanine contains a two channel 14-bit ADC that streams the digitised data using 4 differential 6.5 Gbps lanes. The FPGA uses an Intel JESD204B receiver IP core to receive this data. The streamed data is decoded, and split in two independent channels, exposing 4 samples/channel at 162.5 MHz (frame clock). In order to relax the FPGA timing requirements, 2 consecutive frames are grouped in a 112-bit parallel bus per

Content from this work may be used under the terms of the CC BY 4.0 licence (© 2022). Any distribution of this work must maintain attribution to the author(s), title of the work, publisher, and DOI

ISBN: 978-3-95450-241-7 ISSN: 2673-5350 doi:10.18429/JACoW-IBIC2022-TU2C2

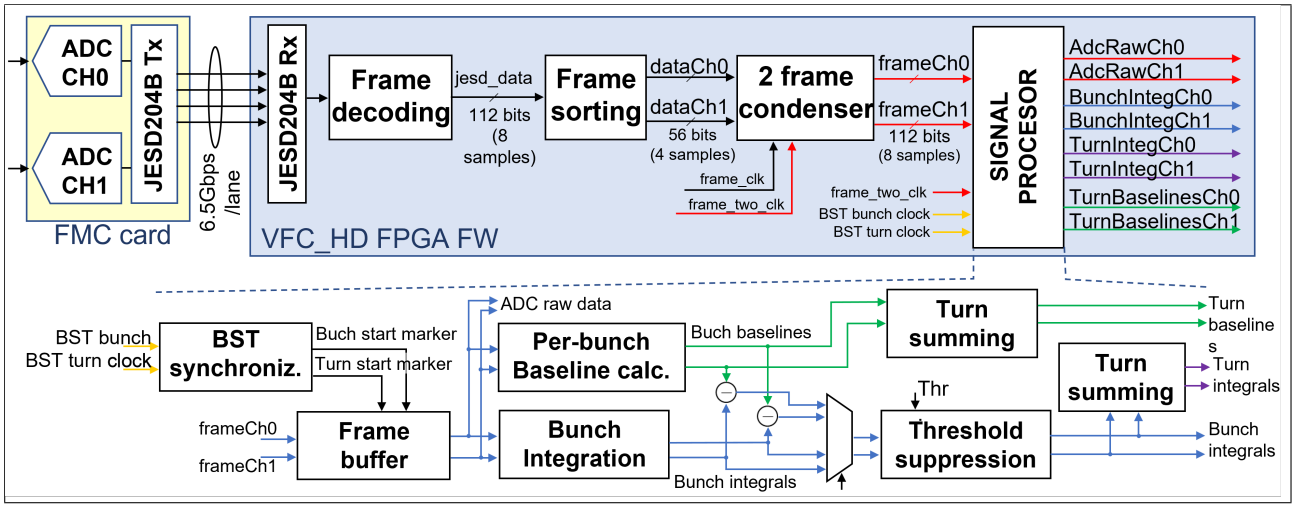


Figure 4: Simplified functional block diagram of the LHC and SPS diamond BLM firmware.

channel, which allows reducing the internal clock from this point to 81.25 MHz.

As mentioned earlier, one of the main functionalities required by the system is to accumulate the losses per bunch. For this, the system is connected to the LHC or SPS BST, which provides bunch and turn beam synchronous clocks. BST bunch and turn start flags are synchronized with the ADC samples by measuring the relative phase of those clocks with respect to the frame clock. A "Frame buffer" allows to manually apply thin delays to compensate for the cable lengths of each detector. After that, ADC samples between two consecutive bunch start flags are accumulated to get the bunch loss integrals on that turn. Unfortunately, the signals from LHC dBLM detectors show long decay tails (as it can be observed in Fig. 5), that overlap with the signals from the following bunches. This produces an error on the bunch-by-bunch loss calculation. In order to reduce this error, a module tries to estimate the baseline of each bunch, which can then be subtracted from the bunch loss integral. Finally, bunch loss integrals obtained between turn start flags are accumulated together to obtain the turn loss integrals. Optionally, one can enable a discriminator that will suppress the bunch loss integrals corresponding to values around the noise level. After this processing, bunch loss integrals are stored on buffers where each position corresponds to a particular bunch slot and are accumulated along consecutive turns for a programmable period of time. The per-bunch baseline interpolation algorithm is currently very basic. It calculates the average value using the first and last ADC samples of each bunch slot.

SYSTEM COMMISSIONING AFTER SECOND LHC LONG SHUTDOWN

The reduced input analogue range of the FMC-1000 card becomes a bottleneck at the LHC injection locations during parts of the commissioning phase, since the amount of losses change significantly between fills. This required the replacement of amplifiers and attenuators on several occasions and might require in the future an upgrade of the front-end acquisition chain to adjust the signal gains remotely.

As mentioned earlier, the calculation of the bunch loss integrals requires the beam loss data to be perfectly in phase with the bunch and turn flags. This required a commissioning step consisting in inducing losses on a particular bunch, and adjusting some fine delays, implemented in the firmware, until the signal appeared perfectly centred between the corresponding bunch flags. This can currently be done through a python application which can detect the beam populated bunch from the fast beam current transformer data and automatically calculate those delays.

Once this is done, the capture acquisition mode can optionally record data only from selected consecutive bunches, allowing longer capture windows with still very thin time resolution. This feature was tested injecting in the LHC a

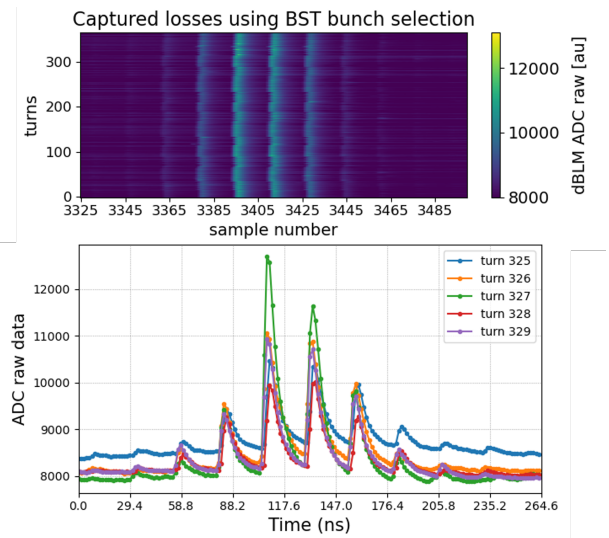


Figure 5: Capture data on selected bunches. Top: reconstruction with 365 turns. Bottom: Zoom on turns 325-329.

Content from this work may be used under the terms of the CC BY 4.0 licence (© 2022). Any distribution of this work must maintain attribution to the author(s), title of the work, publisher, and DOI

ISBN: 978-3-95450-241-7 ISSN: 2673-5350 doi:10.18429/JACoW-IBIC2022-TU2C2

train of 12 nominal bunches (3.3% of an LHC turn), and inducing transversal losses (horizontal or vertical) by adding white noise to the beam with the LHC Transverse damper (ADT) in some bunches at the center of the batch. Figure 5 shows on the top the captured data using this bunch selection feature. The bottom part shows an extraction of 5 turns from the previous figure. As it can be seen, the ADT excitation window length induced measurable losses in only 6 out of the 12 bunches of the train.

USE CASES

The time resolution of the diamond detectors opens the door to the use of loss signals in many use cases. Some examples are explained below.

LHC Injection Quality Checker (IQC)

The dBLM detectors installed at the end of the SPS to LHC transfer lines are one among the several beam instrumentation devices which are integrated into the controls application called Injection Quality Checker. This application is used to analyse the quality of each injection in terms of injection oscillations, losses, beam intensity, etc. Figure 6 shows the dBLM acquisitions from two consecutive injections on LHC B1 (top) and B2 (bottom). In the first injection, consisting of 3 batches of 36 bunches, similar losses were observed. While on the second injection, consisting of 5 batches of 36 bunches each, it can be clearly observed how the losses exponentially grow with each batch. The bottom red line represents the injection kicker strength, and it is used to examine the time relation between the losses and the kicker ramps. In the example shown, losses happened at the kicker flat top area, therefore the operators can clearly distinguish they were not due to a kicker timing misalignment.

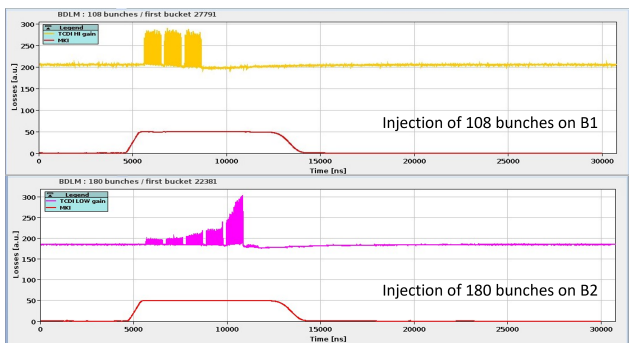


Figure 6: IQC screenshots showing injection data from the dBLM monitors in the LHC injection lines.

SPS North Area Slow Extraction

Two diamond BLM monitors are installed in the SPS extraction region towards a fixed target experimental facility, called SPS North Area. The beam is extracted via a slow extraction process (currently lasting 4.8 s), and it should be delivered to the users, unbunched and with uniform proton-on-target rates. The two detectors were recently tested to monitor the residual presence of the 200 MHz RF component along the extraction phase. Unfortunately, the diamond BLM signals in this case were very weak and polluted with some interference. In order to exploit the detectors signals it was necessary to make several 2 ms recordings using the capture mode on different extractions. These data were converted to frequency and the spectrum averaged. FFTs with and without beam were subtracted, removing thus all systematic interferences. Figure 7 shows the spectrum obtained. By triggering the capture on different moments during the slow extraction process, the evolution of the SPS RF component could be monitored and optimized [7].

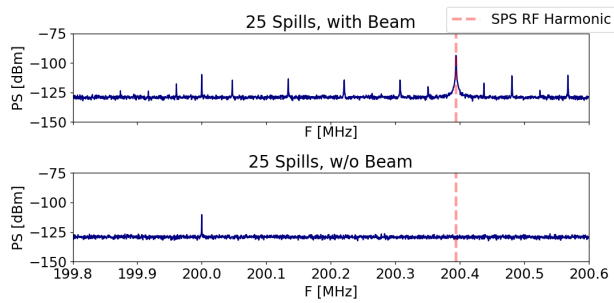


Figure 7: FFT data around the SPS RF nominal frequency as measured by diamond BLM detectors on the TT20 slow extraction line.

CONCLUSION

LHC and SPS have been equipped with BLM diamond detectors since several years. During the last LHC Long Shutdown, new acquisition systems were deployed using VFC-HD carrier modules and FMC digitiser mezzanines. It has allowed the implementation of several acquisition modes and triggering features, but its suffers from some constraints like its reduced input analogue range. The new functionalities, like the bunch-by-bunch integral and the advanced trigger mechanisms have rapidly become essential to monitor injection and extraction efficiency as well as bunch by bunch and turn by turn losses.

ACKNOWLEDGMENTS

We would like to show our gratitude to P. A. Arrutia and F. Roncarolo for sharing their knowledge about the SPS slow extraction diamond measurements.

REFERENCES

[1] B. Salvachua, "Beam Diagnostics for Studying Beam Losses in the LHC," in *Proc. IBIC'19*, Malmö, Sweden, Sep. 2019, pp. 222–228. doi:10.18429/JACoW-IBIC2019-TUA001

[2] E. Griesmayer, B. Dehning, D. Dobos, E. Effinger, and H. Pernegger, "A Fast CVD Diamond Beam Loss Monitor for LHC," in *Proc. DIPAC'11*, Hamburg, Germany, May 2011, pp. 143–145.

Content from this work may be used under the terms of the CC BY 4.0 licence (© 2022). Any distribution of this work must maintain attribution to the author(s), title of the work, publisher, and DOI

ISBN: 978-3-95450-241-7 ISSN: 2673-5350 doi:10.18429/JACoW-IBIC2022-TU2C2

[3] A. Boccardi, M. B. Marin, T. E. Levens, B. Szuk, W. Vigano, and C. Zamantzas, "A Modular Approach to Acquisition Systems for Future CERN Beam Instrumentation Developments," in *Proc. ICALEPCS'15*, Melbourne, Australia, Oct. 2015, pp. 1103–1106. doi:10.18429/JACoW-ICALEPCS2015-THHB2O02

[4] D. Belohrad, D. E. Pereira, J. Kral, and S. B. Pedersen, "Upgrade of the LHC Bunch by Bunch Intensity Measurement Acquisition System," in *Proc. IBIC'16*, Barcelona, Spain, Sep. 2016, pp. 135–138. doi:10.18429/JACoW-IBIC2016-MOPG39

[5] E. Griesmayer and P. Kavrigin, "Rosy diamond readout system," CIVIDEC Instrumentation, Manual PK/055, 2015.

[6] D. Domínguez, J. J. Gras, J. Lewis, J. J. Savioz, J. Serrano, and F. J. Ballester, "An FPGA Based Multiprocessing CPU for Beam Synchronous Timing in CERN's SPS and LHC," in *Proc. ICALEPCS'03*, Gyeongju, Korea, Oct. 2003, pp. 113–115.

[7] F. Roncarolo *et al.*, "Fast spill monitor studies for the SPS fixed target beams," presented at IBIC'22, Krakow, Poland, Sep. 2022, paper WE3C3, this conference.

Content from this work may be used under the terms of the CC BY 4.0 licence (© 2022). Any distribution of this work must maintain attribution to the author(s), title of the work, publisher, and DOI

ISBN: 978-3-95450-241-7 ISSN: 2673-5350 doi:10.18429/JACoW-IBIC2022-TU2C3

COMMISSIONING BEAM-LOSS MONITORS FOR THE SUPERCONDUCTING UPGRADE TO LCLS*

Alan S. Fisher†, G. W. Brown, E. P. Chin, C. I. Clarke, W. G. Cobau, T. Frosio, B. T. Jacobson, R. Kadyrov**, J. A. Mock, Jino Park, E. Rodriguez, P. K. Roy, M. Santana Leitner, J. J. Welch
SLAC National Accelerator Laboratory, Menlo Park, CA, USA

Abstract

Commissioning of the 4-GeV, 120-kW superconducting linac, an upgrade to the LCLS x-ray FEL at SLAC, began in summer 2022, by accelerating a beam through the first cryomodule to 100 MeV. This autumn the beam will accelerate along the full linac, pass through the bypass transport line above the copper linac, and end at a new high-power tune-up dump at the muon shield wall. The first beam through the undulators is expected by early 2023, at a rate well below the full 1 MHz. A new system of beam-loss detectors will provide radiation protection, machine protection, and diagnostics. Radiation-hard optical fibres span the full 4 km from the electron gun to the undulators and their beam dumps. Diamond detectors cover anticipated loss points. These replace ionization chambers previously used with the copper linac, due to concern about ion pile-up at high loss rates. Signals from the new detectors are integrated with a 500-ms time constant and compared to the allowed threshold. If this level is crossed, the beam stops within 0.2 ms. We report on the initial commissioning of this system and on the detection of losses of both photocurrent and of dark current from the gun and cryomodules.

INTRODUCTION

SLAC removed the first km of its 3-km copper electron linac, completely emptying this part of the tunnel and the Klystron Gallery above it for the first time since construction in the 1960s. The LCLS-II Project replaced this with a new superconducting (SC) linac with 35 12-m-long cryomodules operating at f_{RF} = 1.3 GHz and two third-harmonic cryomodules. All have been installed in the first 700 m of this 1-km section of the tunnel (Fig. 1 of [1]).

In addition, two variable-gap undulators, for hard and soft x-rays, replaced the fixed-gap LCLS undulator. Both are in use with beam from the LCLS normal-conducting (NC) copper linac, in the third km. With a complex arrangement of bend magnets and kickers, one linac can share its rate between the two undulators, or the SC beam can go to one undulator and the NC beam to the other.

The SC linac, driven with continuous-wave (CW) RF power, will produce 4-GeV bunches with variable spacing at 1 MHz (f_{RF}/1400). The risk of damaging beam loss grows as the maximum operational beam power jumps from 500 W for the NC linac to 120 kW. A planned energy upgrade (LCLS-II-HE) will install more cryomodules with higher gradients, doubling the beam energy to 8 GeV and so doubling the beam power and the potential for damage.

* SLAC is supported by the U.S. Department of Energy, Office of Science, under contract DE-AC02-76SF00515.
† afisher@slac.stanford.edu
** Present address: Apple Inc., Cupertino, California

The SC photoinjector is driven by CW RF at 186 MHz (f_{RF}/7) with a 1.3-GHz buncher. This source generates 750-keV electron bunches, which enter the first cryomodule (CM01) after 3 m. Each cryomodule has 8 RF cavities and operates at a temperature of 2 K.

At this time (early September 2022), photocurrent at 10 Hz passed through CM01 and reached energies from 80 to 100 MeV. The commissioning path then terminated the beam at collimator CYC01 (56 m from the cathode, Fig. 1), which was locked with its jaws closed. Alternatively, bunches have been kicked into the DIAG0 diagnostic line that can sample the full-rate beam at up to 120 Hz.

In October 2022, we plan to commission the 3.2 km path from the gun to the tune-up dump in the beam switchyard (BSY). Beam may travel through the undulators to their beam dumps for the first time by the start of 2023.

LONG BEAM-LOSS MONITORS

SLAC has depended on ion chambers [1] for loss measurements, to cover extended regions and points of known loss, such as beam stoppers or collimators. Simulations [1] have demonstrated that at high loss rates ions piling up in these devices may blind them to further losses. This consideration and others led to the adoption of new designs using Cherenkov emission in quartz optical fibres as Long Beam-Loss Monitors (LBLMs), and electron-hole pairs in diamond chips as Point Beam-Loss Monitors (PBLMs) [1]. This paper reports only on the LBLM performance during early commissioning through CM01, since most PBLMs are in the high-energy region that has not yet seen beam.

LBLM Design

As an electromagnetic shower from beam loss passes through the radiation-hard quartz optical fibre, it emits Cherenkov light traveling both upstream and downstream. A photomultiplier tube (PMT) is placed at the fibre's downstream end to detect this light, since our tests found 4 times more signal in this direction [1]. The PMT is in a rack-mounted chassis outside the tunnel, to be accessible and near the signal-processing electronics (Fig. 7 of [1]). At the fibre's upstream end, an LED emits weak light modulated at 0.8 Hz. A digital signal processor (DSP) detects this "self-check" or "heartbeat" using a sensitive filter based on a digital lock-in amplifier. This frequency is below any beam rate and is shared through the power line ((60 Hz)/75 = 0.8 Hz) by the LED and DSP. The red-sensitive PMT (Hamamatsu H7422P-40) is housed in a Peltier-cooled module operating at 0°C to limit dark current [1].

Content from this work may be used under the terms of the CC BY 4.0 licence (© 2022). Any distribution of this work must maintain attribution to the author(s), title of the work, publisher, and DOI

ISBN: 978-3-95450-241-7 ISSN: 2673-5350 doi:10.18429/JACoW-IBIC2022-TU2C3

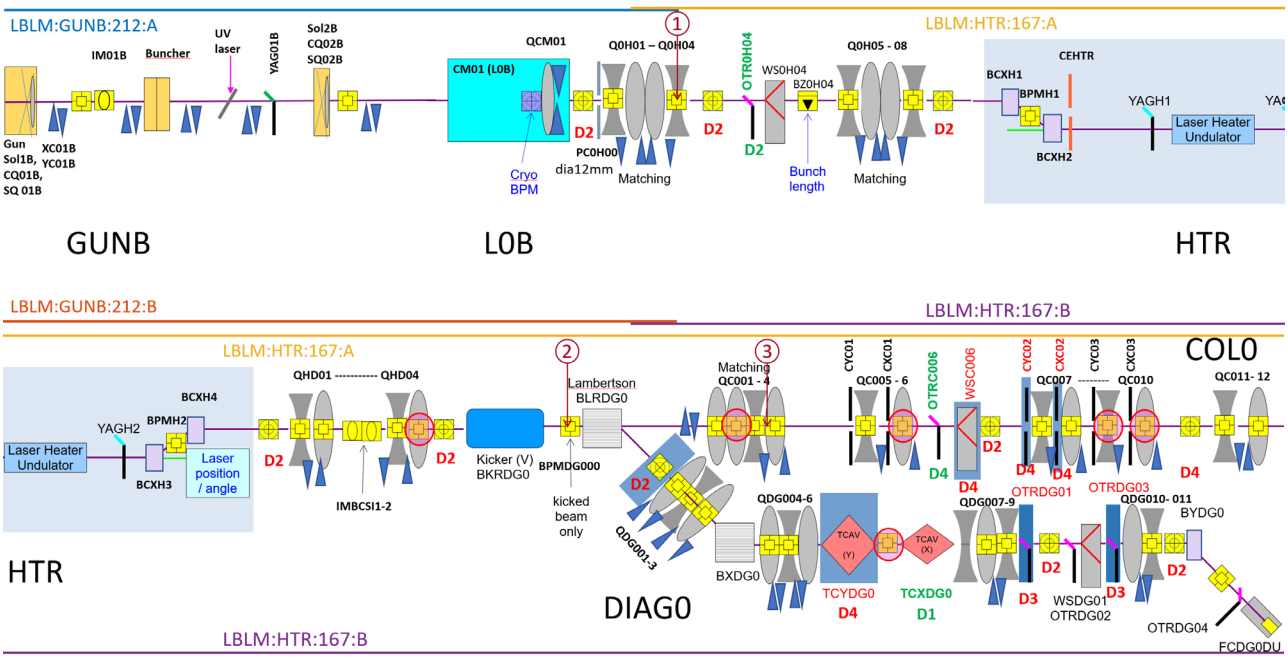


Figure 1: During the initial commissioning period, L0B (CM01, the first cryomodule) accelerated electrons from the 750 keV gun to a maximum of 100 MeV. The beam passed through the laser-heater chicane (without undulator or laser) and entered the first collimation region COL0. Collimator CYC01 was locked closed to stop the beam. Bunches could also be kicked into diagnostic beamline DIAG0, designed to sample a high-rate beam at up to 120 Hz. The three circled numbers show locations where bunch bursts were steered into the beampipe to test the LBLMs. The coverage of the four fibres in this region is shown. The HTR fibres end further downstream.

LBLM Locations

LBLMs cover the full 4-km path from the gun (GUNB) to the undulator beam dumps. The fibre length is typically 200 m, but lengths are adjusted to span a functional zones such as linac L2B (cryomodules between the first and second bunch compressors BC1B and BC2B, where the "B" suffix distinguishes the SC machine from similar sections of the NC machine). To provide redundancy and different viewing angles, all SC linac regions have two fibres on separate shut-off chains. This linac, which runs from west to east, has A-Chain fibres on the north wall at beam height and 90 cm (transversely) from the beam, and B-Chain fibres on the tunnel ceiling toward the south wall, 3 m from the beam (Fig. 2). To compensate for the greater distance, PMTs for B-Chain fibres operate at a higher voltage.



Figure 2: Photo during installation showing the A fibre on the right (north) wall and the B fibre on the ceiling at left. Both are in 6-mm orange "fibre ducts" that allow fibre replacement in a few minutes, without entering the tunnel.

Two fibre pairs span the region just commissioned (Fig. 1). The GUNB pair starts upstream of the gun and continues 8 m past linac L0B (CM01). The HTR fibres cover the laser-heater region. They overlap the GUNB fibres by 4 m and continue for 68 m, past collimator CYC01 that ended the beam path for 100-MeV commissioning.

Dark Current from the Gun

The gun energy, 750 keV, is near the 200-keV Cherenkov threshold in the quartz fibres and is too low to create radiation showers. Consequently, no LBLM signal has been seen from the gun and buncher alone. After acceleration in L0B, beam losses produce strong signals.

Dark current - with the gun, buncher, and L0B all on, but without photocathode laser pulses - can be seen on both the GUNB and HTR fibres, but especially on the HTR pair due to their much longer path after L0B. Adjustments upstream of CM01 have a strong effect. In Fig. 3, a motor moves a "ladder" of collimating apertures upstream of L0B. A Ce:YAG screen on the ladder shows "hot spots" of dark current from the cathode rim imaging to a radius between 10 and 12 mm. A 24-mm aperture passes this dark current

Content from this work may be used under the terms of the CC BY 4.0 licence (© 2022). Any distribution of this work must maintain attribution to the author(s), title of the work, publisher, and DOI

ISBN: 978-3-95450-241-7 ISSN: 2673-5350 doi:10.18429/JACoW-IBIC2022-TU2C3

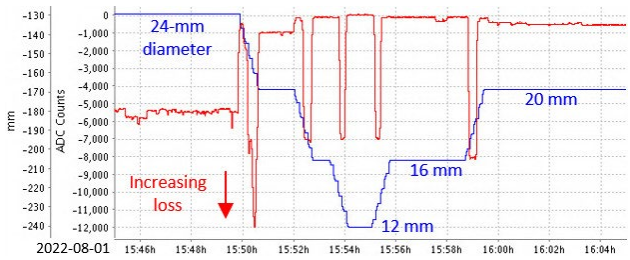


Figure 3: Gun dark current (red) seen by the HTR B fibre as a motor (blue) changes collimating apertures, 1 m before CM01. Loss signals are negative and go downward. Strong loss also appears when the motor is between apertures.

into L0B, creating a strong loss signal. The 20-mm aperture cuts dark current significantly. The 16-mm and 12-mm apertures limit it even more but require tighter focusing of the photocurrent. A small reduction in the field of the focusing solenoid at the gun also raises dark-current losses.

Burst of Photocurrent Bunches

Single bursts of 500 bunches of photocurrent were produced with 2-µs bunch spacing (1 ms burst length), each with 220 pC at 80 MeV (18 mJ each, 8. J total). Corrector magnets directed this beam at grazing incidence onto the beampipe at three locations (Fig. 1) in the 38 m between protection collimator PC0H00 and halo collimator CYC01.

Figure 4 shows the LBLM responses at Location 1. Charge from each bunch accumulates on the integration capacitor and decays with a 500-ms *RC* time constant. The correctors here could make a loss only in the +*x* (north) direction. The forward angle of the loss shower brings it to the ceiling past the end of the B fibre of the GUNB pair, giving this fibre a weak signal. All show a pedestal consisting of an ADC offset for each channel, soon to be measured and subtracted; dark current, which was kept low in this test by using the 20-mm aperture and a sufficiently high solenoid field; and the small 0.8-Hz modulation of the self-check LED.

Figure 5 summarises all locations and loss directions. Locations 2 and 3 are too far downstream for the GUNB fibres to detect their losses. Shielding by local structures is evident in the weaker response at Location 2, especially for the HTR A fibre. Here the loss was on the –*x* (south) side, away from the wall, suggesting a directional effect. At Location 3, the correctors allowed losses in three directions, –*x* and +*y* (up), and –*y*. The response of the ceiling fibre was greater for downward, not upward, loss, which may indicate that the direction of the loss is less important than details of local showering and shielding. The –*x* losses at Locations 2 and 3 show that one fibre in a pair can compensate for a weak signal from the other, demonstrating the value of redundancy with two viewing angles.

A beampipe hit at grazing incidence can present a "thin" target: the resulting electromagnetic shower mostly escapes. We will next test thick targets, such as collimators. In FLUKA simulations, these signals could be as much as 50 times weaker, depending on target shape, but a preliminary look at loss from scraping on PC0H00 showed only a factor of 3. Because this collimator has a central aperture

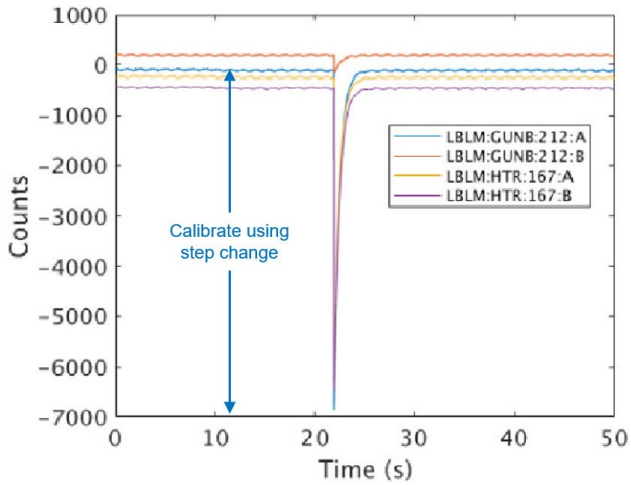


Figure 4: Loss of a 500-pulse burst (8.8 J) at grazing incidence on the beampipe at Location 1. A signal of 1 mV at the digitiser input corresponds to 25.2 ADC counts.

to pass photocurrent, some of the loss seen may have been caused by scraping on the beampipe rather than a pure thick-target loss.

BCS trips were tested at Location 1 with the three fibres that gave strong responses (Fig. 4). Bursts of 500 bunches were fired as the trip level was moved between 90 and 500 mV. Whenever the signal exceeded the trip threshold, trip requests went through the logic to the shut-off control.

Initial Calibration

These measurements provide a preliminary calibration relating the lost beam energy to the loss signal. Figure 5 shows a typical signal level of 75 mV for the loss of 8.8 J in the 1-ms burst. However, if the bunches making this loss arrive uniformly in time, at a steady 17.6 W, then the capacitor charge from earlier bunches will decay with the 500-ms time constant, lowering the peak after 500 ms by the factor $(1-e^{-1})$. The typical signal should be reduced to 47.4 mV, or 2.7 mV/W.

Compare this level to the safety thresholds specified by the Radiation Physics group. In the linac, the Beam Containment System (BCS, which protects both personnel outside the tunnel and radiation-safety components inside)

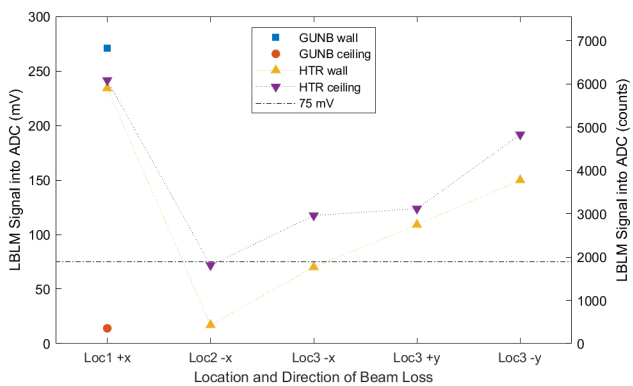


Figure 5: LBLM signals from grazing-incidence beam loss at 3 locations, in the directions indicated. Correctors could make a loss in more than one direction at Location 3 only.

Content from this work may be used under the terms of the CC BY 4.0 licence (© 2022). Any distribution of this work must maintain attribution to the author(s), title of the work, publisher, and DOI

ISBN: 978-3-95450-241-7 ISSN: 2673-5350 doi:10.18429/JACoW-IBIC2022-TU2C3

Content from this work may be used under the terms of the CC BY 4.0 licence (© 2022). Any distribution of this work must maintain attribution to the author(s), title of the work, publisher, and DOI

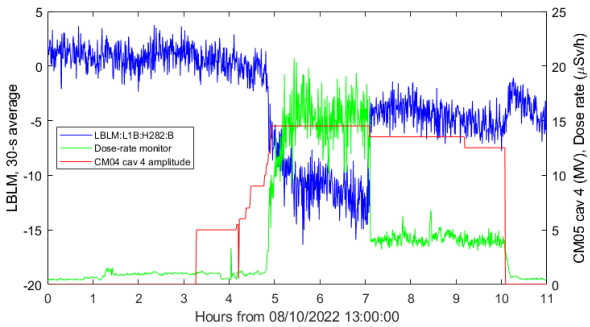


Figure 6: Comparing an LBLM (30-s average) to the RF in cavity 4 of CM05 and to a radiation dose-rate monitor.

must trip (shut off) the beam for losses above 1 kW. A BCS trip shutters the laser but also shuts off RF to L0B, which makes recovery slow. The Machine Protection System (MPS, which protects accelerator hardware) recovers quickly and is intended to trip first, with a threshold that is usually 10 times lower - 100 W in the linac.

The measured signals are strong at levels well below these thresholds. In fact, scaling to the BCS level of 1 kW gives 2.7 V, exceeding the maximum of 2 V in the BCS hardware. However, thick targets will lower this calibration. Ultimately trip levels will be reconsidered with data from tests in which losses are made at frequent intervals throughout the beam path.

Field Emission from Cryomodules

The cryomodule for CM01 was selected for low field emission, since electrons emitted there can closely match the photocurrent in energy and pass through the full linac, leading to damage at high energy. We have not seen field emission from CM01, but it has not been on without gun RF too, and the gun's dark current dominates the signal.

A more revealing test of the sensitivity of the LBLMs to field emission came when all cryomodules (except the harmonic modules) were turned on for several hours and their gradients gradually raised. RF experts noted that cavity 4 of CM05 began emitting above 12 MV (Fig. 6). A radiation monitor measured a dose rate of 20 μSv/h. This small emission was also observed by LBLM:L1B:H282:B, but at a level of 12 counts rather than the thousands from burst losses. Consequently, the signal was averaged in 30-s bins (24 periods of 0.8 Hz) to filter the self-check modulation.

This B fibre is on the ceiling and ends 13.6 m upstream of the cavity. The A fibre of the pair did not see the signal, nor did the next fibre pair, which runs along this cavity. Note that the phases of the cavities were not adjusted for acceleration but were random. This phasing may have promoted backward acceleration toward the end of fibre H282:B. Alternatively, another cavity may also have been emitting during this interval, since many gradients were changed at nearly the same time. A dedicated study of field emission is needed in which the amplitude of a suspect cavity is raised and lowered independently.

Fast Waveform for Diagnostics

In addition to beam containment and machine protection, the LBLMs were designed for a third application. The

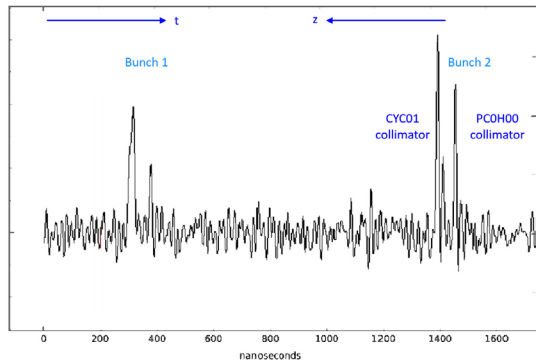


Figure 7: Fast waveform digitizer, showing two bunches 1 μs apart. Each scrapes upstream collimator PC0H00 and ends at collimator CYC01, 38 m downstream. Bunch 2 arrives after bunch 1, but for each the downstream loss reaches the PMT first.

passive filter/splitter that provides *RC* integration of the low frequencies in the signal also sends frequencies above 1 MHz to a fast waveform digitizer. The arrival time of the signal at the PMT then indicates the loss location (Fig. 7).

Electrons travel at speed c along the beamline to the loss point, but the Cherenkov light travels in the fibre at c/n, where n, the refractive index, is 1.45. With the PMT at the downstream end of the fibre, signals from two loss points separated by a distance L arrive separated in time by $\Delta t_d = -(n-1)L/c$. The sign indicates that the upstream loss arrives before the downstream, so that the signs of their linac coordinate z and of arrival time t are opposite. With the PMT at the upstream end, the arrival-time difference, $\Delta t_u = +(n+1)L/c$, is approximately 5 times greater.

Despite lower z resolution, we chose the downstream position to gain the factor of 4 in signal strength noted earlier. Since the PMT itself is fast, with a 1-ns rise time, fast electronics could provide finer resolution, but the digitiser's 350-MSamp/s rate and 80-MHz anti-aliasing filter slow its response. Overshoot is also visible in Fig. 7. Two improvements are under consideration: the sample rate can be raised to 380 MHz (although the anti-aliasing filter may limit the benefit), and we have begun testing a deconvolution of the overshoot. Nevertheless, the figure shows a clear separation of two peaks from collimators 38 m apart.

CONCLUSIONS

The LBLMs have demonstrated a strong and robust response to losses of both photocurrent and gun dark current at 80 MeV. They provide good coverage but with variations from local shielding. The onset of field emission from cryomodules has been observed. Waveforms for beam-loss localization have been seen. Testing will resume with thick targets before continuing through the full linac to 4 GeV.

REFERENCES

[1] A. S. Fisher *et al.*, "Beam-loss detection for the high-rate superconducting upgrade to the SLAC Linac Coherent Light Source", *Phys. Rev. Accel. Beams,* vol. 23, p 082802, 2020. doi: 10.1103/PhysRevAccelBeams.23.082802

ISBN: 978-3-95450-241-7 ISSN: 2673-5350 doi:10.18429/JACoW-IBIC2022-TUP01

COMMISSIONING OF THE LIBERA BEAM LOSS MONITORING SYSTEM AT SPEAR3*

K. Tian†, S. Condamoor, J. Corbett, N. L. Parry, J. J. Sebek, J. Safranek, F. Toufexis
SLAC National Accelerator Laboratory, Menlo Park, CA, USA

Abstract

SPEAR3 is a third generation synchrotron radiation light source, which operates approximately 9 months each year with a very high reliability. The beam loss monitoring system in the storage ring has recently been upgraded to the modern Libera system from the original legacy hardware. During the initial stage of the new beam loss monitoring system deployment, it proved to be useful for a new lower emittance lattice commissioning in SPEAR3. In this paper, we will report progress in the Libera system commissioning in SPEAR3 and present some first results.

INTRODUCTION

In a high brightness synchrotron radiation light source, it is of great importance to monitor and reduce electron beam losses to improve machine performance and machine protection. As a result, besides various radiation detectors, many facilities also equip with a dedicated beam loss monitoring system to characterize the beam losses. The beam loss monitoring system in SPEAR3 was first deployed to conduct a precise measurement of electron beam energy in the storage ring by observing the resonant spin depolarisation of the beam [1]. The beam loss detector (BLD) was a NaI scintillator coupled to a photo-multiplier tube (PMT). The loss events captured by the scintillator were converted to analog signals and counted by a Struck 3820 scaler, which was integrated into the EPCIS control system and provided pulse counts as the loss rate. NaI detectors also proved to be beneficial for other accelerator physics experiments [2]. However, there were several drawbacks to the system. First, only one high voltage power supply (HVPS) delivered voltage to each PMT, which was not ideal because each detector could require different bias voltage for optimal performance. In addition, the data acquisition system relied on legacy NIM hardware for signal processing. They were not reliable and hard to maintain. As a result, we were motivated to upgrade the SPEAR3 BLM with modern technology. Inspired by successful experience from ESRF [3, 4] and SOLEI [5], we chose the commercial solution of Libera BLM system from Instrumentation Technologies [6].

HARDWARE DEPLOYMENT

The Libera beam loss monitoring solution consists of two main components, the BLD and the beam loss monitor (BLM). Similar to the original BLD in SPEAR3, the Libera BLD is a PMT-based detector with a plastic scintillator, EJ-200 [7]. The PMT is from Hamamatsu with a built-in HVPS module. As shown in Fig. 1, the scintillator and the PMT are housed in a compact aluminium enclosure with a lead sleeve to shield the X-rays from the synchrotron radiation during operation. The typical response from the PMT for a loss event of the cosmic background detecting in the lab is also show in Fig. 1 to illustrate the pulse response of the detector. The PMT output signal from the detector has several ns rising time and about 20 ns falling time. The

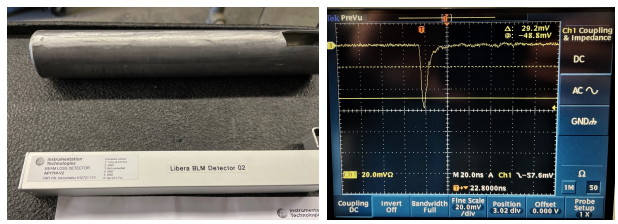


Figure 1: Libera BLD with the lead sleeve (left) and the analog signal for background cosmic ray detection (right).

Libera BLD essentially is a photo multiplier tube (PMT) with a built-in scintillator to convert an individual loss event to a fast analog pulse lasting for about 20 ns. On the other hand, the Libera BLM, each of which can support 4 BLDs, is the digital processing unit for the analog signals from loss events. The ADC of the BLM samples this analog signal at a sampling rate up to 125 MHz or a sampling period of 8 ns. As a result, an isolated beam loss event is converted to a digital peak being formed by about 3 sampling points. The bucket spacing of SPEAR3 is 2.1 ns, therefore, the Libera system is not able to resolve the beam loss with bunch-by-bunch resolution. However, this is still an improvement from the old system, which had a resolution of about 400 ns. Another benefit from the new system compared with the old one is power delivery and gain control from the BLM unit to the BLDs. In SPEAR3, the Libera BLM was integrated into the EPICS control system for easy configuration and control [8].

3 BLMs with 12 BLDs were acquired from the vendor with 9 BLDs installed in SPEAR3. These BLDs are distributed around the storage ring: 1 at the movable scrapers; 1 at a designated Touschek loss point at the center quadrupole at Girder 3 (3G QFC); 1 at the injection septum magnet; 1 at each of the four in vacuum undulators (IVUs); 1 at each of the two elliptical polarized undulators (EPUs). As shown in Fig. 2, the location for the BLD installation in SPEAR3 is limited due to the dense layout of the accelerator components. Most BLDs were installed horizontally in the beam plane so that the scintillator was close to the ring chamber

* Work supported by U.S. Department of Energy under Contract No. DE-AC02-76SF00515
† ktian@slac.stanford.edu

Content from this work may be used under the terms of the CC BY 4.0 licence (© 2022). Any distribution of this work must maintain attribution to the author(s), title of the work, publisher, and DOI

ISBN: 978-3-95450-241-7 ISSN: 2673-5350 doi:10.18429/JACoW-IBIC2022-TUP01

Content from this work may be used under the terms of the CC BY 4.0 licence (© 2022). Any distribution of this work must maintain attribution to the author(s), title of the work, publisher, and DOI

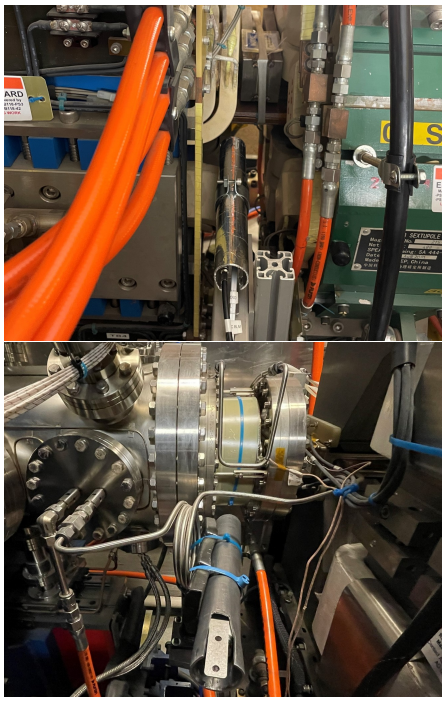


Figure 2: The Libera BLD installed at the 3G QFC (top) and at the ID 12-2 (bottom), one of the SPEAR3 IVUs.

and the electronics in the PMT could have enough distance from the adjacent magnet poles to avoid the interference from the magnetic fringe fields. Nonetheless, it was aware that the installation of the BLDs may not be ideal for beam loss detection especially for comparing the loss events at different locations. Due to limited resources, the BLDs have not yet been calibrated.

BEAM MEASUREMENT

Counting Mode

The BLM software provides two digital processing options for users to choose: triggered data buffers and counter streams. For the triggered data buffers, the sampled input beam loss signals are summed or averaged and stored to the SUM and AVG buffers. In this approach, a phase locked loop (PLL) with input from the ring clock controls the sampling frequency so that the buffered data correlates with the turn-by-turn beam loss. For the counter streams, the ADC data is continuously processed for pulse counting to provide the count rates for the beam loss measurement. This counting mode is particular of our interest because it offers the same function as the old system in SPEAR3. Therefore, we have been focusing on the implementation of the counting mode. Next, we are planning to develop functions to take advantage of the triggered data buffers because they can detect fast beam loss during beam injection or when shutting down the RF.

ADC Protection

The Libera BLM conditions the raw PMT signal from the BLD though a input termination (50 Ω or 1 MΩ), and a programmable attenuation before digitizing the signal with a 14bit ADC. This allows individual sensitivity control for each channel and each BLD. However, during operation, when the injection occurs, the loss events increase significantly and the ADC can be saturated by the input signal. We were particularly concerned about the ADC damage over a long period time in saturation, therefore, before keeping the BLM on line during operation, we developed an auto configuration program to switch the BLM configuration right before each injection. The program monitors an EPICS PV changing status 2 seconds before the start of the injection process to switch the BLM to a preset configuration designated for the injection period. Figure 3 shows an example of the program working during 5 injections. The blue curve represents the maximum ADC count provided by the BLM software. The ADC saturation level is 8191 and would occur during the injection if keeping the BLD configuration unchanged. For this detector, the gain control voltage (red line) was reduced from 0.7 V for measuring the lifetime loss between top off injection to 0.5 V during the injection, which was effective in avoiding the ADC saturation.

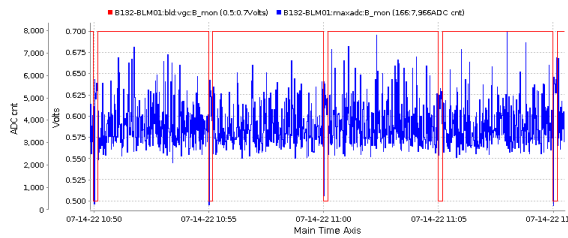


Figure 3: The gain of the BLD was switched from 0.7 V to 0.5 V at injection to avoid ADC saturation.

Lifetime Loss Measurement

To confirm that the loss rates measured in the counting mode represent beam lifetime loss, we conducted beam loss measurements by moving the horizontal scraper to fix the loss point of the ring. During the experiment, 100 mA beam was filled in the ring. As mentioned earlier, the vacuum chamber for the 3G QFC has a reduced horizontal aperture and the location was designed with high nonlinear dispersion bump to capture most of the lifetime loss during operation. As a result, when the horizontal scraper was parked far away from the beam, as shown in Fig. 4, the loss rates were largest at 3G QFC, about 2000 counts/sec. The next two most lossy points are the ID5, at about 500 counts/sec, and the septum, at about 60 counts/sec. This was mostly as expected except that the reading from ID5 was a bit higher than expected.

As shown in Fig. 5, when closing the scraper gradually, the dominated loss point started to shift away from the 3G QFC to the scraper. The scraper position was at -6mm when the loss rates at the two locations were same. We stopped the scraper at −2.6 mm.

ISBN: 978-3-95450-241-7 ISSN: 2673-5350 doi:10.18429/JACoW-IBIC2022-TUP01

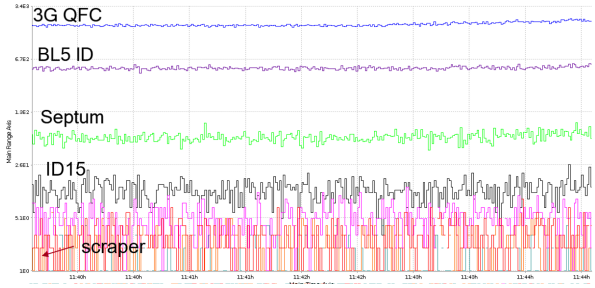


Figure 4: The loss rates in counts/second for different BLDs (in logarithmic scale) with the scrapers were parked.

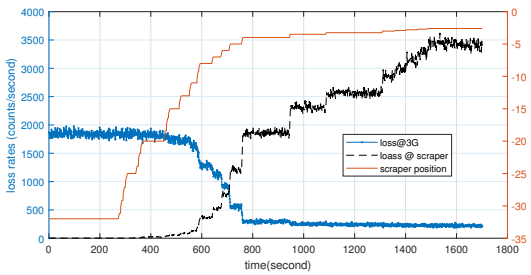


Figure 5: The loss rates in counts/second for different BLDs (logarithmic scale) when the horizontal scraper was scanned.

The Touschek lifetime is determined by the beam current and the 3D beam size. By adjusting the skew quadrupoles, we changed the vertical beam size slightly which in turn changed the lifetime. The loss rates can also be calculated from the time derivative of the stored beam currents (NPCT loss rates). We compared the measured results from the two different methods with the horizontal scraper was parked and closed to −2.6 mm respectively. The results are shown in Fig. 6. When the scraper was parked, the loss rate at 3G QFC was compared with the NPCT loss rate scaled by a factor of 50,000; when the scraper was moved to −2.6 mm, the loss rate at the scraper was used for comparison with the NPCT loss rates scaled by a factor of 25,000. In both cases, the measured loss rates from the two methods agreed well confirming accurate determination of beam lifetime measurements with the BLM system.

Injection Loss

During normal operations, we were able to capture the raw ADC signals in the data buffer of the BLM during beam injection and between the fills. We compared them in Fig. 7. Due to the large amount of loss events during the injection, the PMT signals piled up resulting in long pulses lasting more than 1 turn. Therefore, pulse counting is not useful to characterize the injection loss. On the other hand, for lifetime loss between the fills, the loss events were more isolated leading to the clean impulse response signal of the PMT. This is the reason that the counting mode works well for characterize the lifetime loss. In addition, the signals for injection was more repeatable, but the lifetime loss signal was not due to its stochastic nature.

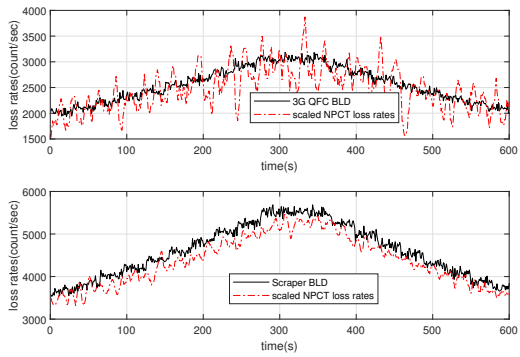


Figure 6: Comparison of the loss rates measured from the BLDs and the current monitor in the storage ring when the scraper was parked (top) and closed (bottom).

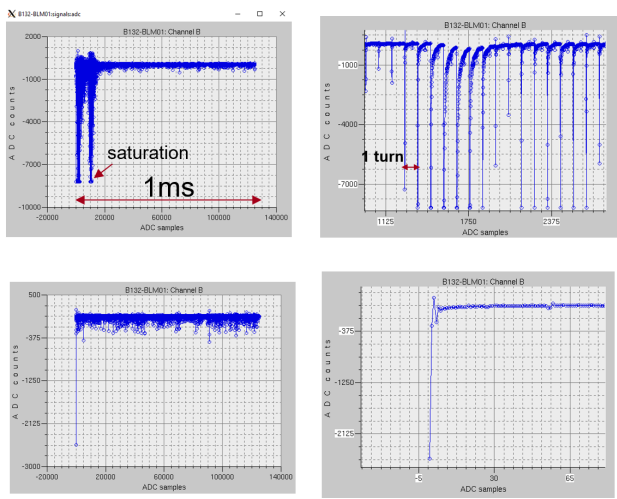


Figure 7: Raw ADC signals of the 3G-BLD for the injection beam loss (top left:the injection loss signal for 1 ms; top right: zoomed in) and the life time beam loss (bottom left: lifetime loss signal for 1 ms; bottom right: zoomed in).

3G DUMP APERTURE CHARACTERIZATION

The Libera BLD was helpful to characterize the designated 3G QFC chamber aperture when the new lower emittance lattice was commissioned in 2021 [9]. Based on the tracking simulations, the operation of the new lattice with reduced emittance of 7 nm required the modification of the 3G QFC chamber half aperture from −32 mm to −15 mm. Otherwise, the lifetime loss would mostly occur at the septum, and the RF beam dump loss would distribute at different insertion devices depending on the magnet gap settings of the in vacuum insertion devices. A new insert was designed and installed in the 3G QFC chamber to reduce the aperture to −15 mm and serve the designated beam dump (3G dump) when shutting off the RF. During beam commissioning of the new lattice, it was critical to confirm the 3G QFC chamber aperture was indeed at or smaller than −15 mm. The normal beam based technique to probe the aperture is to

Content from this work may be used under the terms of the CC BY 4.0 licence (© 2022). Any distribution of this work must maintain attribution to the author(s), title of the work, publisher, and DOI

ISBN: 978-3-95450-241-7 ISSN: 2673-5350 doi:10.18429/JACoW-IBIC2022-TUP01

Content from this work may be used under the terms of the CC BY 4.0 licence (© 2022). Any distribution of this work must maintain attribution to the author(s), title of the work, publisher, and DOI

create local orbit bump till the beam gets lost at the aperture. However, due to the large aperture, the steering magnets are not strong enough to move the beam to the aperture. Alternatively, we conducted beam based aperture scan with both the injection kicker and the steering magnets. The 3G dump aperture was then determined using tracking simulations based on the beam based measurement results. This indirect characterization was later confirmed by the RF beam loss measurement with the libera BLD at 3G QFC.

As described earlier, in the 7 nm lattice, when cutting off the storage ring RF power abruptly, according to the tracking studies, the beam loss will be captured mostly at the 3G dump if its physical aperture in the -x direction is less than 15 mm. However, if a local orbit bump is applied to the beam orbit at the 3G dump in the +x direction, away from the dump, at some point, the RF dump loss can distribute to other locations. This process was simulated in tracking studies by changing the 3G dump aperture. With BLDs installed at the 3G dump and the septum, we were able to perform RF beam dump studies and compare with the tracking results. During the experiment, we filled a single bunch of 4 mA in the 7 nm lattice. The RF was turned off abruptly with different DC bumps at the 3G dump, while the BLDs near the 3G dump and the septum were triggered to acquire the raw ADC data. The measurement data for the BLDs are compared in Fig. 8.

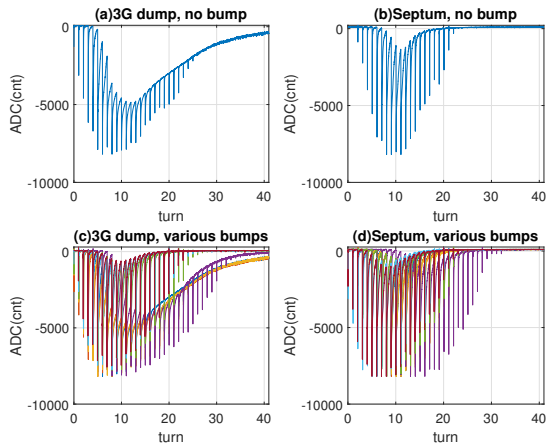


Figure 8: Raw ADC signals of the BLDs at 3G dump and Septum for the RF beam dump measurements.

Due to the large number of electrons lost when cutting off the RF, loss signals pile up and form broader peaks lasting nearly one turn as shown in Fig. 8. These broader peaks were seen in the BLD signals from the 3G dump and the septum. The lower envelope of the signals at the 3G dump appear to have larger amplitude and last longer when comparing the signal profiles in Fig. 8(a) and (b). This can suggest that the 3G dump has much higher loss event rates resulting in more significant signal pile-up. Another observation from the BLD signals is that the beam appears to be gone completely within 30 turns after the RF is cut off. The results with different orbit bumps away from the 3G dump are shown in Fig. 8(c) and (d). They correspond to beam bumps of 0 mm, 1.5 mm, 2 mm, 2.5 mm, 3 mm, 3.5 mm, and 4 mm, respectively, at the 3G dump. The signal profiles at the 3G dump change little when the beam bump is smaller than 3 mm (green line).When the DC bump is larger than 3 mm, the BLD signals have a reduced lower envelope and look similar to the signals from the septum BLD. We believe the integrals of the BLD signals in these measurements have strong correlations to the local beam loss rates, therefore we plot the results in Fig. 9 along with the tracking simulation results with different 3G dump apertures. If we correlate the turning points in the two plots, we conclude that the 3G dump aperture is about −14.25 mm, which agrees well with the result of −14.5 mm from the aperture scan. The measured 3G dump aperture was slightly smaller than the design value of −15 mm, but still met the operational requirements.

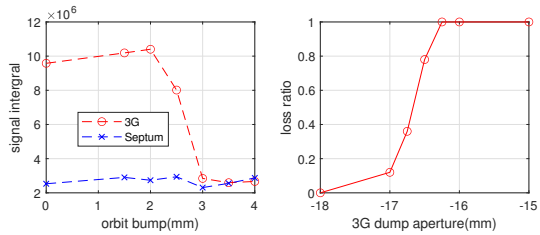


Figure 9: BLD measurments vs tracking simulations.

SUMMARY

The commissioning of the Libera beam loss monitoring system at SPEAR3 is still in progress, but early results are promising and interesting. Next, we will focus on developing the functionality to characterize injection loss around the storage ring.

ACKNOWLEDGEMENTS

We would like to acknowledge E. Buratin, P. Leban, G. Rehm, and L. Torino for useful discussions. We want to thank the SPEAR3 operation and technical teams for supporting the work.

REFERENCES

[1] K. P. Wootton *et al.*, "Resonant Spin Depolarisation Measurements at the SPEAR3 Electron Storage Ring," in *Proc. IPAC'12*, New Orleans, LA, USA, May 2012, pp. 771–773.

[2] K. Tian, J. Safranek, and Y. Yan, "Machine based optimization using genetic algorithms in a storage ring," *Phys. Rev. ST Accel. Beams*, vol. 17, p. 020 703, 2014. doi:10.1103/PhysRevSTAB.17.020703

[3] L. Torino and K. B. Scheidt, "New Beam Loss Detector System for EBS-ESRF," in *Proc. IBIC'18*, Shanghai, China, Sep. 2018, pp. 346–352. doi:10.18429/JACoW-IBIC2018-WEOB01

[4] E. Buratin, N. Benoist, N. Carmignani, F. Ewald, J.-L. Pons, and K. B. Scheidt, "New Applications and Studies with the ESRF Beam Loss Monitoring at Injection," in *Proc. IBIC'21*, Pohang, Korea, 2021, pp. 299–302. doi:10.18429/JACoW-IBIC2021-TUPP35

ISBN: 978-3-95450-241-7 ISSN: 2673-5350 doi:10.18429/JACoW-IBIC2022-TUP01

[5] N. Hubert, M. E. Ajjouri, and D. Pédeau, "New Beam Loss Monitor System at SOLEIL," in *Proc. IBIC'19*, Malmö, Sweden, Sep. 2019, pp. 118–121. doi:10.18429/JACoW-IBIC2019-MOPP017

[6] Instrumentation Technologies. https://www.i-tech.si

[7] Eljen Technology. https://eljentechnology.com

[8] F. Toufexis *et al.*, "Automated Management of Libera SPARK Module IOCs in SPEAR3," in *Proc. IBIC'20*, Santos, Brazil, Sep. 2020, pp. 51–55. doi:10.18429/JACoW-IBIC2020-TUPP12

[9] K. Tian *et al.*, "Commissioning of the Lower Emittance Lattice at SPEAR3," in *Proc. IPAC'22*, Bangkok, Thailand, 2022, pp. 1502–1505. doi:10.18429/JACoW-IPAC2022-TUPOMS036

Content from this work may be used under the terms of the CC BY 4.0 licence (© 2022). Any distribution of this work must maintain attribution to the author(s), title of the work, publisher, and DOI

ISBN: 978-3-95450-241-7 ISSN: 2673-5350 doi:10.18429/JACoW-IBIC2022-TUP02

DESIGN OF HIGH DYNAMIC RANGE PREAMPLIFIERS FOR A DIAMOND-BASED RADIATION MONITOR SYSTEM

M. Marich*, S. Carrato, L. Vitale, University of Trieste, Trieste, Italy
G. Brajnik, G. Cautero, D. Giuressi, Elettra Sincrotrone Trieste, Trieste, Italy
L. Bosisio, A. Gabrielli, Y. Jin, L. Lanceri, INFN-Trieste, Trieste

Abstract

Regardless of the different accelerator types (light sources like FELs or synchrotrons, high energy colliders), diagnostics is an essential element for both personnel and machine protection. With each update, accelerators become more complex and require an appropriate diagnostic system capable of satisfying multiple specifications, that become more stringent as complexity increases. This paper presents prototyping work towards a possible update of the readout electronics of a system based on single-crystal chemical vapor deposition (scCVD) diamond sensors, monitoring the radiation dose-rates in the interaction region of SuperKEKB, an asymmetric-energy electron-positron collider. The present readout units digitize the output signals from the radiation monitors, process them using an FPGA, and alert the accelerator control system if the radiation reaches excessive levels. The proposed updated version introduces a new design for the analog front end that overcomes its predecessor's limits in dynamic range thanks to high-speed switches to introduce a variable gain in transimpedance preamplifiers, controlled by an ad-hoc developed FPGA firmware.

INTRODUCTION

SuperKEKB [1] hosts Belle II, designed for precision measurements of weak interaction parameters for finding New Physics beyond the Standard Model of particle physics [2]. The inner Belle II employs two types of detectors, namely microstrip and pixel sensors, which are silicon based [3]. The main concern is to reduce their performance degradation caused by radiations exceeding 20 Mrad (MGy). Indeed, the absorption, in short time intervals, of significant dose rates from the inner detector parts can cause their irreversible damage [4]. To reduce these risks, continuously monitoring radiation levels throughout the experiment and signalling abort requests is fundamental. The main abort signal is generated by the central control room after receiving abort requests from the local control rooms, indicating abnormal accelerator and/or beam conditions.

DIAMOND CONTROL UNIT

The current monitoring instrument named DCU (Diamond Control Unit) is an FPGA based system capable of handling up to 4 Diamonds Sensors for both electron and positron monitoring. The FPGA (Cyclone V GX 5CGXFC5C6F27C7N) is a high performance device equipped with 77K Programmable Logic Elements, part of the Cyclone V GX Starter Kit. In this kit we can find a plethora of useful hardware components, such as an HSMC connector (to link other peripherals) and a 4 GB LPDDR2 memory. The memory is a key factor of the monitoring system, since, as we will see later on, the acquired data are processed and then saved.

Currently there are 7 DCUs (Diamond Control Unit) with 4 diamonds each, that are monitoring the High Energy Electron Ring (HER) and the Low Energy Positron Ring (LER). Mezzanine boards are used to connect the Cyclone V FPGA to the diamonds, each one developed for a particular task, such as analog to digital conversion, amplification and bias. Figure 1 shows the block diagram of the system and Fig. 2 is a picture of the assembled unit.

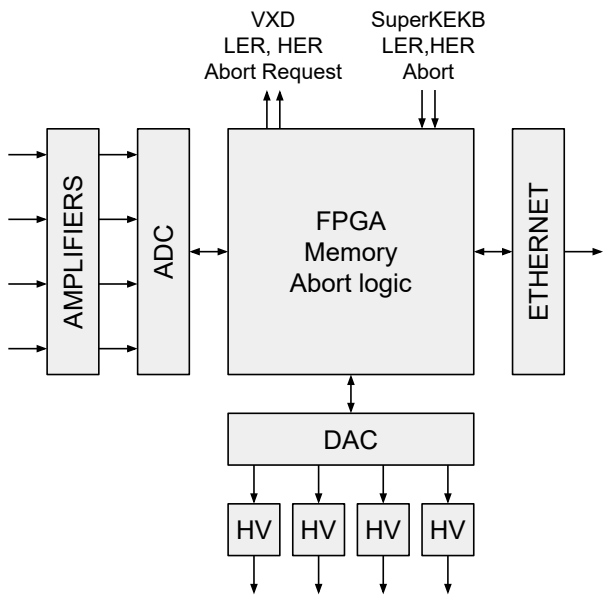


Figure 1: DCU block diagram.

Amplifier Board

It converts the input current in a voltage and filters the signals for each of the 4 channels. One important aspect of the transimpedance stage (TIA) is the variable gain obtained, as shown on the schematic (see Fig. 3), by switching between different feedback networks which are selected by FPGA controlled relays. The TIA's operational amplifier is an LTC6268, a low noise 500 MHz FET input amplifier with low input capacitance and low bias current. The filtering stage is implemented with an OPA211, low power, low noise density precision amplifier. The bandwidth is selected with

* marco.marich@elettra.eu

Content from this work may be used under the terms of the CC BY 4.0 licence (© 2022). Any distribution of this work must maintain attribution to the author(s), title of the work, publisher, and DOI

ISBN: 978-3-95450-241-7 ISSN: 2673-5350 doi:10.18429/JACoW-IBIC2022-TUP02

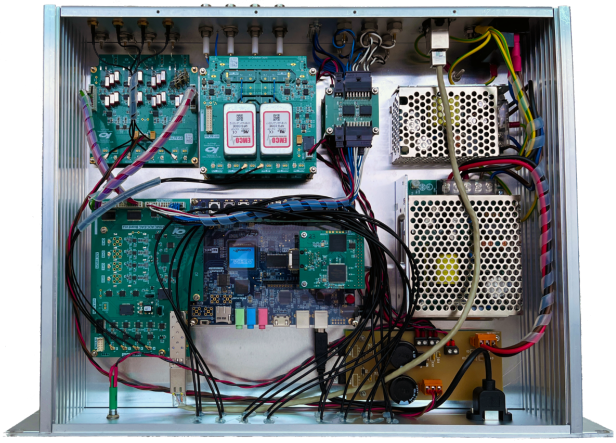


Figure 2: DCU image.

the same technique as gain switching. In Table 1, for each range, the current ranges are shown with the corresponding rms noise values, measured in 100 kHz data (third column) and in 10 kHz data (fifth column). The typical corresponding ranges and rms noise values in dose-rate units can be obtained multiplying these values by the average calibration factor $k = 35\,\mathrm{mrad/s/nA}$. The effective dynamic ranges (DR) expressed in decibel at 100 kHz and 10 kHz are also shown in the fourth and sixth columns.

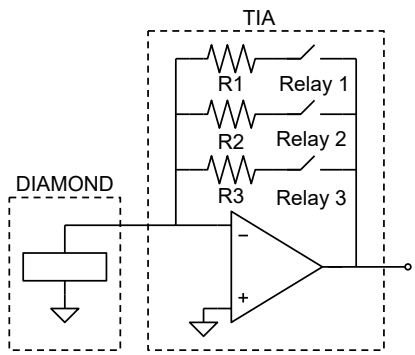


Figure 3: Simplified TIA schematic.

Table 1: TIA Ranges and Noise

Range	Current range	100 kHz Noise	100 kHz DR	10 kHz Noise	10 kHz DR
0	36 nA	0.23 nA	44 dB	0.8 pA	93 dB
1	9 µA	3 nA	70 dB	70 pA	102 dB
2	4.5 mA	0.22 µA	86 dB	40 nA	101 dB

HSMC Board

It acts as an interface between the Cyclone V GX Starter Kit and the other mezzanine boards, and is the connecting link between the analog and digital world. For the analog to digital conversion the AD9653 is used. It is a quad, 16-bit, 125 MSPS ADC with an on-chip sample-and-hold circuit. It is also equipped with an SPI user control interface for different features. To provide an ethernet connection to the DCU a SFP interface was installed. This transceiver supports the Ethernet Gigabit Protocol; with a specific Verilog HDL code, UDP standard was implemented for the exchange of data and commands to and from the DCU. The HV Bias board is responsible for the generation of the 4 voltages necessary to bias the 4 diamonds. The DC-DC converters employed to generate these voltages (~120 V) are 4 EMCO modules. This high voltage converter is characterized by high stability, low ripple and a programmable output voltage ranging from 0 V to 1000 V. The other components on the board are necessary for the correct operation of the converter. The control signals are driven by the DACs, situated on the ADC/DAC board, which are in turn configured by the FPGA.

Working Principle

Assuming a sampling frequency of the current to voltage signal of 50 MHz, the sum of 125 samples is available every 2.5 µs (400 kHz). These sums are defined "400 kHz Data" and are stored in a circular DDR memory. The stored data are further accumulated in groups of 40 000, to obtain the sum of 5 000 000 values defined as "10 Hz Data". In the event that "400 kHz Data" value is greater than a predetermined threshold value for a predetermined duration, "Alarm" signals are generated and the data storing is stopped. These signals are sent to the accelerator central control unit to activate the beam abort procedure. When this happens the control unit generates a proper interrupt signal which is sent to all of the machine systems. "10 Hz Data" can continuously be read at 10 Hz with the possibility of detecting a portion of these with a proper flag [4].

The diamond-based system has been providing useful information on beam losses in the interaction region, used for accelerator tuning (injection, collimators), estimates of beam-induced background composition, and integrated radiation doses in the VXD (Vertex Detector) region. However there are some evident limitations of the system. In this paper we will focus mainly on two of the most important ones: dynamic range and speed of gain switching.

PROPOSED CIRCUIT

The DCU dynamic range (Table 1) is not sufficient to accommodate all of the requirements. In particular:

1. accelerator tuning needs measurements of dose-rates down to the order of 1 mrad/s, with a 10% precision of about 0.1 mrad/s, corresponding on average to about 3 pA;
2. beam losses correlated with aborts can reach or exceed 10-100 krad/s, corresponding to currents of the order of several milli-ampere;
3. in continuous injection mode, the beam-losses peak during short time intervals at values exceeding the average losses by more than two orders of magnitude.

Content from this work may be used under the terms of the CC BY 4.0 licence (© 2022). Any distribution of this work must maintain attribution to the author(s), title of the work, publisher, and DOI

ISBN: 978-3-95450-241-7 ISSN: 2673-5350 doi:10.18429/JACoW-IBIC2022-TUP02

Content from this work may be used under the terms of the CC BY 4.0 licence (© 2022). Any distribution of this work must maintain attribution to the author(s), title of the work, publisher, and DOI

The separation of the functions of 20 detectors (6 DCUs) dedicated to monitoring smaller currents in range 0, and four detectors (one DCU) dedicated to generate beam aborts on large signals in range 2, is a compromise solution, working only to some extent; in particular, injection spikes still saturate range 0. A wider dynamic range is needed.

To satisfy the request an extra range was added, by increasing the number of resistors. As shown in Table 2 the ranges were recalculated to provide a higher dynamic range, reducing both the possibility of front end saturation and the smallest input current detectable.

Table 2: New TIA Ranges

Range	Current	LSB	R feedback
0	10 nA	153 fA	250 MΩ
1	1 µA	15.3 pA	2.5 MΩ
2	100 µA	1.53 nA	25 kΩ
3	10 mA	153 nA	250 Ω

To address the second limitation the analysis of which component contributes mostly to the time necessary to switching gains has been performed. Due to their electromechanical working principle the commutation time for relays is the main cause that contributes to the switching duration. In addition, it is mandatory to take into account the fact that a gain switch requires a two step process known as "make before break" to avoid an open feedback. This process consists in enabling the relay of the desired gain (make) before disabling the relay of the undesired gain (break), increasing the switching time. This means that the times to pass from one range to another are of the order of several milliseconds, which prevents the continuity of following the temporal evolution of the current when it takes place on several ranges. The adopted solution replaced the relays with high-speed analog switches (TS5A 1066). These single-pole single-throw (SPST) switches have a t_{on} of 4.8 ns maximum and a t_{off} of 3 ns maximum. Comparing the switching time between the current and past solution it is evident how much time is saved.

Figures 4 and 5 show the "make" and "break" signal and the corresponding TIA output; the two images differ in the duration of the make-break process. Analyzing the TIA's output some damped oscillations can be detected. This phenomena can be assigned to two main factors: charge injection from the switch and the frequency response of the closed loop system to the make (break) step. These factors contribute to extend the duration of the gain transient to about 1.5 µs, still more than 1 order of magnitude lower than that of the previous solution.

Finally, thanks to the high speed switches, this approach allows to identify (and therefore give an alarm) much more quickly a sudden increase of the current. In fact, when a DCU is monitoring very low currents (pA order), it necessarily works in a very low analog bandwidth configuration (kHz order). In this situation the problem is not given by

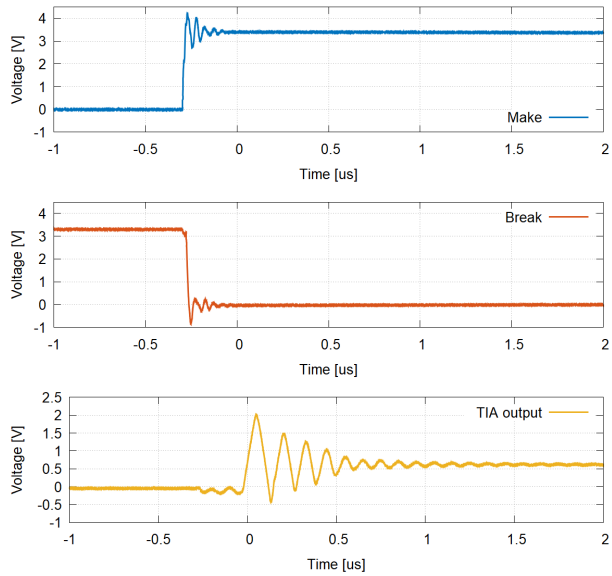


Figure 4: Make (blue), break (red) switch control signals from FPGA with no delay between each other and TIA output (yellow).

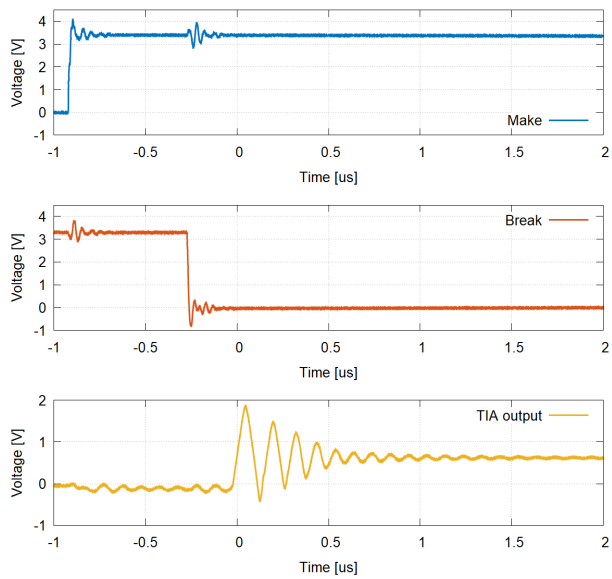


Figure 5: Make (blue), break (red) switch control signals from FPGA with 640 ns delay between each other and TIA output (yellow).

the speed of the switches, but by the limited rise time of the front end: a possible rise in the current would be filtered by the amplifier, so identifying alarming values too late. The architecture proposed here would allow periodical sampling (for example every few tens of us, depending on the maximum expected current rise times) of the current in the least sensitive range (and therefore with the highest analog bandwidth): thus any reading other than 0 pA in that range would indicate a sudden increase in the current, since - given the dynamics of the system - even the values relating

ISBN: 978-3-95450-241-7 ISSN: 2673-5350 doi:10.18429/JACoW-IBIC2022-TUP02

to the least significant bits in the maximum range are several times greater than the full scale of the lower ranges. This periodic reading would only affect the number of accumulated samples ("400 kHz Data") which, once every "N" would be only 50 instead of 125, introducing a small increase in noise on that single sample (being averaged over a lower number of values), however almost negligible. Although the proposed solution is definitely better, it needs further investigation to better characterize the charge injection and its effects on the system.

Furthermore, although this approach does not substantially introduce particular criticalities, it is also true that it introduces periodic dead times, which can be of the order of some percentage of the total time. For this reason, other alternatives will be studied to solve this problem with a different working principle, by rethinking the input stage and adopting the "current integration-charge balancing" approach. Current integration is a promising option since it can obtain high dynamic ranges, without the use of switches [5].

CONCLUSION

Protecting the inner Belle II detectors from excessive radiation is of vital importance to reduce their degradation. The proposed architecture could provide a valid alternative to the present system, since commutation times were reduced more than one order of magnitude. Further development of the system is required, that include Verilog HDL code for a more elaborate control of the switches, memorization of the sampled data and the transmission of the abort signal to the central control room. Simultaneously, the charge integration approach will be investigated.

REFERENCES

[1] Y. Ohnishi *et al.*, "Accelerator design at SuperKEKB", *Prog. Theor. Exp. Phys.*, vol. 2013, no. 3, Mar. 2013. doi:10.1093/ptep/pts083

[2] Belle II experiment, https://www.belle2.org

[3] T. Abe *et al.*, "Belle II Technical Design Report", doi:10.48550/arXiv.1011.0352

[4] S. Bacher *et al.*, "Performance of the diamond-based beam-loss monitor system of Belle II", *Nucl. Instrum. Methods Phys. Res., Sect. A*, vol. 997, May 2021. doi:10.1016/j.nima.2021.165157

[5] P. Horowitz and W. Hill, "Multislope converters", in *The art of electronics* (3rd ed.), Cambrige University Press, 2015.

Content from this work may be used under the terms of the CC BY 4.0 licence (© 2022). Any distribution of this work must maintain attribution to the author(s), title of the work, publisher, and DOI

ISBN: 978-3-95450-241-7 ISSN: 2673-5350 doi:10.18429/JACoW-IBIC2022-TUP03

THE BEAM LOSS MONITORING SYSTEM AFTER LHC LONG SHUTDOWN 2 AT CERN

M. Saccani*, E. Effinger, W. Viganò, C. Zamantzas, CERN, Geneva, Switzerland

Abstract

Most of the LHC systems at CERN were updated during the Long Shutdown 2, from December 2018 to July 2022, to prepare the accelerator for High-Luminosity. The Beam Loss Monitoring system is a key part of the LHC's instrumentation for machine protection and beam optimisation by producing continuous and reliable measurements of beam losses along the accelerator. The BLM system update during LS2 aims at providing better gateware portability to future evolutions, improving significantly the data rate in the back-end processing and the software efficiency, and adding remote command capability for the tunnel electronics. This paper first recalls the Run 1 and Run 2 BLM system achievements, then reviews the main changes brought during LS2, before focusing on the commissioning phase of Run 3 and future expectations.

INTRODUCTION

The Large Hadron Collider (LHC) provided proton-proton collisions at a top energy of 8 TeV in Run 1 (11-2009 to 02-2013) and at 13 TeV during Run 2 (04-2015 to 11-2018). To achieve higher luminosity, the accelerator, as well as its injectors and experiments, underwent a first phase of upgrades during the Long Shutdown 2 (LS2), among which the improvement of cryogenic power, magnet diode, dump absorbers, and collimators. The LHC Run 3 started in July 2022 with a 13.6 TeV top energy and is expected to last 3 or 4 years, before LS3 brings a second phase of upgrades to allow 5x to 7x higher luminosity, as described in the High-Luminosity LHC (HL-LHC) preliminary design report [1].

The Beam Loss Monitoring (BLM) system is used for advanced beam diagnostics to tune beam parameters by characterising loss patterns and locations. It is also a key part of machine protection. The system architecture, presented on Fig. 1, has been proposed in 2007 [2] to meet the LHC specifications [3]. The technical choices resulted in a highly reliable system, to protect the machine against excessive losses. Only a small deposition of the order of 100 mJ/cm^3 out of the 320 MJ beam energy stored in the rings risks to provoke a magnet quench. To ensure safe operation, the beam shall be extracted in less than 3 LHC turns when excessive losses are detected.

The LHC BLM system consists of about 4000 detectors, covering all the critical loss locations around the ring, injection and extraction lines, cold superconducting magnets, collimators, etc. Those Ionisation Chambers (IC) are cylindrical tubes filled with N_2 and hosting electrodes polarized at 1.5 kV. Those electrodes collect the charges generated by the passage of secondary particles created by protons lost from the LHC beams [4]. The electrical current generated is acquired by Current to Frequency Converters (CFC) located in the tunnel. Measurements are digitised and optically transmitted every 40 µs to the surface. The back-end electronics located in 2 racks per LHC Interaction Point (IP) provides one Gy/s value per channel on 12 different time windows, ranging from 40 µs to 83.9 s. If one of theses values exceeds a predefined threshold a beam dump is requested.

BLM PERFORMANCE IN RUN 1 & 2

During the first two LHC runs, the BLM system protected the machine and contributed to the tuning of the beam parameters [5]. This section reviews the system performance during this period and the modifications implemented based on experience and simulation models.

* mathieu.saccani@cern.ch

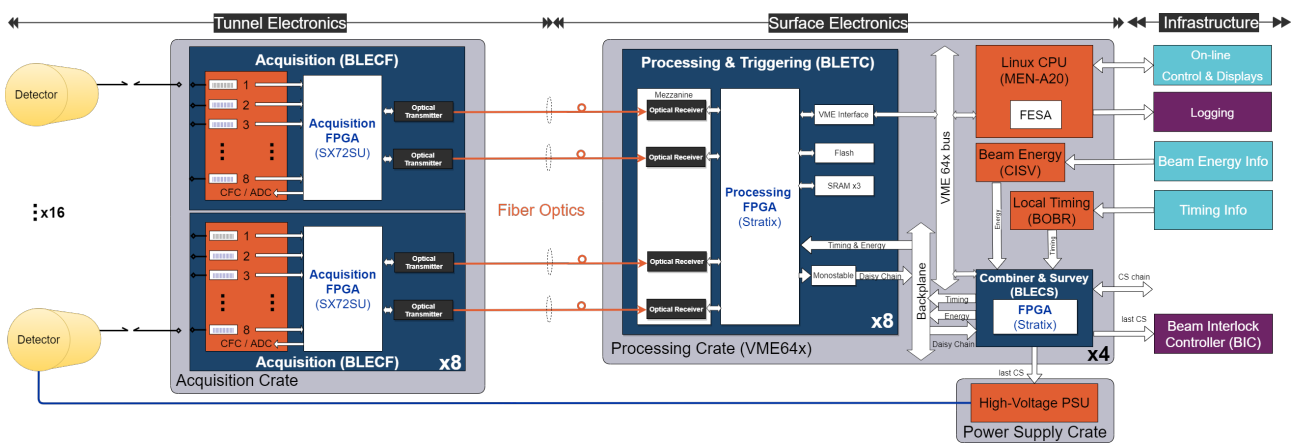


Figure 1: Schematic overview of the BLM system architecture in LHC.

Content from this work may be used under the terms of the CC BY 4.0 licence (© 2022). Any distribution of this work must maintain attribution to the author(s), title of the work, publisher, and DOI

ISBN: 978-3-95450-241-7 ISSN: 2673-5350 doi:10.18429/JACoW-IBIC2022-TUP03

Beam Diagnostics

The BLM system displays and stores data at 1 Hz. In addition, short buffers with 40 µs resolution can save data on dedicated timing event triggers, such as a beam abort request [6]. In both Runs, the BLM system played a key role in the LHC parameter optimisation. The validation of the accelerator settings was done via loss maps at every stage of the cycle with low intensity ($3{\cdot}10^{10}$ protons): injection, start and end of the energy ramp, and for different beta-star and roman pots configurations [7, 8].

The loss values are published in Gy/s, converted from the electric charge measured by ICs with the factor $7.41{\cdot}10^{-4}$ Gy/mA. To obtain an absolute loss value (number of protons from the beam), the system is calibrated using the beam current variations given by the Beam Current Transformers (BCT), when losses are initiated by primary collimators. During Run 2, the calibration process was enhanced by combining the loss measurements of several BLMs initiated at the same location and loss patterns observed on different planes (horizontal, vertical and longitudinal). In addition, the beam lifetime based on BLMs is a parameter operationally implemented and monitored since Run 2. It is obtained by combining BCTs values with the sum of the signals of 4 specific BLM detectors giving similar losses in horizontal and vertical planes [9].

The Run 1 was affected by unexpected millisecond scale losses caused by dust particles, so-called Unidentified Falling Objects (UFOs). They generated 35 protective beam dumps. But as the beam energy doubled in Run 2, 816 monitors were relocated and their thresholds updated [10] to limit beam dumps caused by UFO (139 dumps during Run 2).

Detectors & Electronics

The high sensitivity of the ICs is suitable for machine protection, but limits the flexibility of the BLM system as a beam diagnostic tool. Little Ionisation Chambers (LIC) are shorter ICs, shown on Fig. 2, which connect to the same electronics and remain below saturation for high losses. With a reduced sensitive volume, they are 30x less sensitive than ICs. Secondary Emission Monitors (SEM) further extend the detection dynamic range, by a factor of $7{\cdot}10^{5}$, using a 3-plate electrodes and 10^{-9} mbar internal pressure [11].

From Run 1, 300 SEMs were used for monitoring only. In Run 2, 108 were replaced with LICs, about 50 additional ICs were added for machine protection, and around 300 defective ICs were opened and repaired, diodes were added to distribution boxes to block high-voltage (HV) return, and 6 new cables were installed per IP to separate the different types of detector, and arcs from straight sections.

Around 670 acquisition cards (BLECF) have been placed along the LHC ring below each quadrupole magnet or concentrated in alcoves. They tolerate up to 500 Gy Total Ionizing Dose (TID) in 20 year lifespan. The input dynamic ranging from 10 pA to 1 mA is covered by using a CFC combined with an ADC to obtain such a resolution [12]. To achieve a Safety Integrity Level 3 (SIL), i.e. 10^{-7} to 10^{-8} failure/h,



Figure 2: IC and LIC pair installed on a LHC dipole magnet.

different test modes, status information, protection circuits, and a redundant data transmission are implemented, as well as firmware triplication to protect against Single Event Upsets (SEU). Finally, at the end of Run 1, several RC filters were added to some detectors to avoid saturation on short losses close to injection. The downside effect is a longer time response and delay on dump request [13]. In Run 2, an option to mask the abort request from a few monitors during the injection process was added but never used operationally.

In terms of back-end electronics, 27 crates that house 348 processing boards (BLETC) are distributed among the 8 LHC IPs [14]. During Technical Stops (TS) and LS1, CPUs were upgraded to MEN-A20 (was PowerPC), more electronics were deployed in the injection regions and water-cooled sealed racks were installed to limit optical receiver faults and false dumps. During LS1, the buffers for extraction post-operation check (XPOC) were separated per beam, and 100 Hz refreshed data was provided to help collimator setup.

Machine Protection

As LHC machine protection requires SIL3, achieving high dependability was addressed since Run 1. But increasing reliability often leads to more complex systems which, as a downside, reduces its availability [15]. Compromises were made to meet requirements while generating a minimum of false dumps due to electronics glitches. For example, opting for redundant optical links divides by 2 the failure probability, but doubles the amount of preventive maintenance, components and diagnostics.

The Combiner and Survey module (BLECS) terminates the BLM beam permit daisy-chain. If an error is detected in the electronics or a loss threshold is breached, it immediately requests a beam dump to the Beam Interlock System (BIS). In addition, the BLECS monitors the HV, distributes the beam energy value to BLETCs for the threshold selection, and sends commands to the tunnel electronics. It performs a 20 mn long self-check [16], in particular to test every monitor connection before each LHC refill.

Between the 2 Runs, refined FLUKA simulations led to adjustment of most of the BLM thresholds. In Run 1, thresholds were updated via interactive C++ scripts, then uploaded to the LHC Software Architecture (LSA). To avoid possible human errors, since the number of thresholds is more than $1.2{\cdot}10^{5}$ (12 running-sums and 32 energy levels per monitor), a dedicated tool was designed [17]. A clear predefined threshold management process is occasionally used to update values, agreed by the operation and machine protection teams to match new LHC configurations [18].

Content from this work may be used under the terms of the CC BY 4.0 licence (© 2022). Any distribution of this work must maintain attribution to the author(s), title of the work, publisher, and DOI

ISBN: 978-3-95450-241-7 ISSN: 2673-5350 doi:10.18429/JACoW-IBIC2022-TUP03

Content from this work may be used under the terms of the CC BY 4.0 licence (© 2022). Any distribution of this work must maintain attribution to the author(s), title of the work, publisher, and DOI

OVERVIEW OF THE MODIFICATIONS DURING LS2

The LHC BLM system underwent major upgrades in LS2 (2018-2022) to improve its performance, reliability, and availability. This section gives more details on these changes.

New Hardware

During LS2, 30% of the detectors were re-installed to allow the opening of the magnet interconnections. Ten detectors were added to the new collimators, or moved, e.g. in the absorber (TDIS), the dispersion suppressor (TCLD), or the beam dump regions. The tunnel electronics has also been consolidated: 15 acquisition cards (2%) have been exchanged for repair, barcodes were added to track assets, and WorldFIP (Factory Instrumentation Protocol) fieldbus receivers have been deployed in all racks to provide reliable remote reset capability and reduce the duration and number of interventions. On the back-end side, 44 processing cards (13%) have been exchanged, and an optical receiver mezzanine less sensitive to temperature and low-power was designed and produced. In addition, a firmware overhaul led to a simpler, modular, and high-performance implementation: in terms of data transfer rate, clock and reset trees, optical link stability, sanity checks time, and also reusability. The generic RTL code will facilitate migration to a new platform in the future. This redesign was extensively verified in simulation through state-of-the-art verification methodology and 4 levels of test-benches to reach full code coverage. On the software side, the CPU OS was migrated to 64b CentOS 7 (was SL6), and consequently the real-time software (FESA) and drivers were ported to this new version. Eventually, the whole BLM application suite was redelivered to correct minor bugs and add more checks.

Reliability & Availability

From the beginning of the BLM system design, many efforts have been made to predict reliability using Failure Mode Effects and Criticality Analysis (FMECA) and Fault Trees. During the first two LHC Runs, to reach even higher results, several weak hardware parts were redesigned to reduce their failure rate, such as the back-end mezzanine for optical reception. Preventive maintenance has been carried out through comprehensive diagnostics that automatically generate early warnings, and through fault monitoring since 2012 [19]. Finally the system dependability analysis was periodically updated [20] to help define the future upgrade and maintenance strategy. As a result, the availability and reliability of the BLM should improve significantly in the next Run, and the number of interventions should decrease consequently. In the extract of the CERN Accelerator Fault Tracker (AFT) presented in Fig. 3, the beginning of Run 3 seems to show a sensible decrease in BLM blocking faults compared to the first Runs. Those faults are only the ones preventing LHC operation, and not the faults shadowed by redundancy for instance. It is difficult to extrapolate from the BLM availability the impact on the LHC luminosity. Although correlated, they do not scale proportionally, as this depends on the fault time in the LHC operational scenario [21].

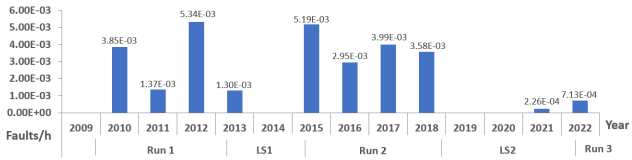


Figure 3: Number of BLM blocking faults per hour of LHC operation (extracted from CERN AFT).

Run 3 Commissioning after LS2

The commissioning of the system for Run 3 followed four consecutive steps at the end of LS2:

1. The Individual System Test (IST), where each channel connection is verified and calibrated by experts.
2. The Dry-Run, in collaboration with LHC operators to validate the connection to the control infrastructure.
3. The Beam Test, with a low-intensity pilot beam, where each location is tested and the connections to the Beam Dump System are verified.
4. The commissioning for Physics, where the beam intensity and energy are increased gradually, and each step is validated by the LHC machine protection committee.

An important parameter of the BLM system performance is the latency, i.e. the time between the passage of particles through the detector and the dump request. A specific test was performed in 2022 during commissioning: for each LHC beam and IP, an arbitrary collimator was closed to generate local losses, and a pilot bunch was injected. The result is presented in Table 1: the LHC BLM system latency was always less 3 LHC turns (267 µs = 3 × 89 µs).

Table 1: BLM Latencies† During Run 3 Commissioning

LHC Interaction Point	Beam 1	Beam 2
IP1 (ATLAS)	46 µs	44 µs
IP2 (ALICE + B1 inj.)	43 µs	41 µs
IP3 (Momentum Cleaning)	61 µs	~ 114 µs††
IP4 (RF) †††	-	-
IP5 (CMS)	30 µs	53 µs
IP6 (B1 & B2 Dump)	35 µs	32 µs
IP7 (Betatron Cleaning)	64 µs	88 µs
IP8 (LHCb + B2 inj.)	56 µs	~ 177 µs††

† Injection kick top to dump request, time of flight corrected.
†† Stretched because of RC filter installed on the detector.
††† No collimator at IP4.

FUTURE CHANGES EXPECTED DURING LS3 & LS4

Despite the consolidation and upgrades in LS2, after more than 14 years of operation, the BLM hardware is ageing, while the number of spare parts is decreasing. Electronics will require replacement within the decade.

ISBN: 978-3-95450-241-7 ISSN: 2673-5350 doi:10.18429/JACoW-IBIC2022-TUP03

New Processing Electronics in LS3

During LS3, the BLM processing electronics will be renewed. As most Beam Instrumentation (BI) systems, the back-end unit is installed in a radiation-free area which allows the use of a standard module [22]. This new board, called VFC-HD, is a high pin count FMC carrier used as a VME-based unit for data concentration and processing. It provides all the common features used in the BI group, as summarised in Fig. 4.

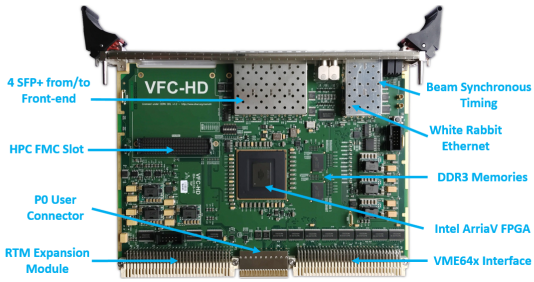


Figure 4: Overview of the VFC-HD features.

For the BLM system, the 4 standard SFP+ transceivers will replace the currently used mezzanine card, and the more recent FPGA will provide additional processing resources to improve efficiency and flexibility, and strengthen critical parts by using redundancy for example. In addition, to maintain a high level of reliability after installation of the VFC-HD modules, extensive testing was carried out after manufacture: destructive, functional, burn-in, validation, and run-in. This testing methodology [23] was implemented on a sophisticated test bench [24] to verify the 1150 assets produced.

New Acquisition Electronics in LS4

A new acquisition electronics is under development to replace the BLM acquisition crate in the SPS in LS3. The plan is to design an architecture that could also be deployed in the LHC in LS4. Another constraint is the need to keep backward compatibility with the current LHC chassis.

The main objectives of this redesign are:

- to reduce the time resolution to 5 µs (was 40 µs)
- to increase radiation tolerance to 1 kGy (was 500 Gy)
- to ensure safety: guarantee SIL3 while protecting against direct HV contacts and improving groundings.
- to improve reliability and availability: less repair time and complexity, more commands and diagnostics.

As illustrated in Fig. 5, this 3U acquisition crate is composed of a special backplane that hosts 8 signal inputs from the detectors, an input power unit with a 230 V_{AC} transformer, a power supply module generating local voltages, a crate controller with a nanoFIP fieldbus connection, and the modernised CFC board (BLECF2) with its 2 optical links to the surface.

BLM ASIC

A new front-end ASIC (Application Specific Integrated Circuit) under development at CERN is depicted in Fig. 6.

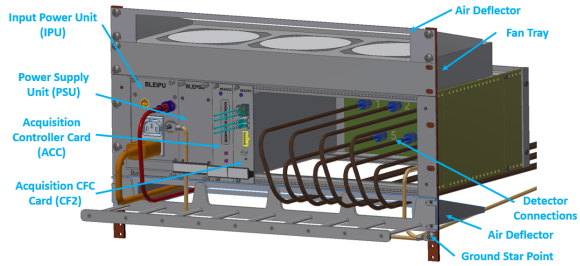


Figure 5: 3D view of the future acquisition crate.

This chip will allow the BLM acquisition system to withstand radiation doses up to 500 kGy (was 500 Gy) resulting from the upcoming HL-LHC upgrade. This will help place electronics closer to the beam and minimise the noise picked up by cables. The chip consists of two independent ADC channels readout by redundant blocks interfaced directly to LPGBT (Low Power GigaBit Transceiver) [25]. Using a CFC combined with a Wilkinson ADC, the ASIC provides a fast 10 µs readout (was 40 µs), which can detect losses and request a beam dump in less than 1 LHC turn.

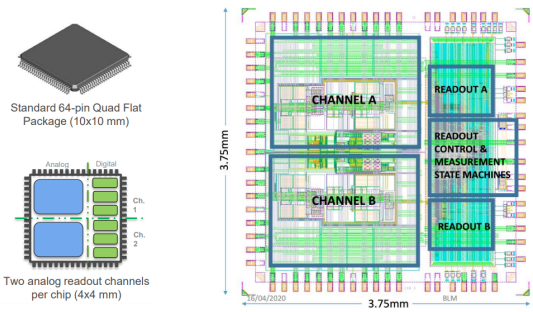


Figure 6: Overview of the BLMASIC chip architecture.

Since BLM protection relies on a reliable detection of a wide range of currents, a strict characterisation and validation of this ASIC is required, including irradiation tests [26]. The test campaigns on prototypes showed that in all cases (SEU, TID, temperature) the device can perform loss measurements down to 1 pA, with an error below 1% in the range [35 µA ; 1 mA].

CONCLUSION

During LS2, the LHC BLM system was significantly updated to solve the issues discovered during Run 1 and 2. The hardware changes are expected to increase reliability and reduce the number of interventions. The firmware and software upgrades aimed at providing more processing time margins, and increasing portability for future hardware replacement. After nearly a year of beam testing and Run 3 operation, the system seems to perform better. Availability and reliability have improved, the number and duration of interventions have dropped, and false dumps have disappeared. Although it is too early and not easy to quantify, this good performance gives hope that the impact of BLM faults on the overall luminosity of the LHC will decrease.

Content from this work may be used under the terms of the CC BY 4.0 licence (© 2022). Any distribution of this work must maintain attribution to the author(s), title of the work, publisher, and DOI

ISBN: 978-3-95450-241-7 ISSN: 2673-5350 doi:10.18429/JACoW-IBIC2022-TUP03

Content from this work may be used under the terms of the CC BY 4.0 licence (© 2022). Any distribution of this work must maintain attribution to the author(s), title of the work, publisher, and DOI

REFERENCES

[1] G. Apollinari, I. Béjar Alonso, O. Brüning, M. Lamont, and L. Rossi, *High-Luminosity Large Hadron Collider (HL-LHC): Preliminary Design Report*. CERN, 2015. doi:10.5170/CERN-2015-005

[2] B. Dehning *et al.*, "The LHC Beam Loss Measurement System," in *Proc. PAC'07*, Albuquerque, NM, USA, Jun. 2007, pp. 4192–4194. https://jacow.org/p07/papers/FRPMN071.pdf

[3] B. Jeanneret and H. Burkhard, "Functional Specification: on the Measurement of the Beam Losses in the LHC Rings," CERN, Geneva, Switzerland, Tech. Rep., 2004. https://ab-div-bdi-bl-blm.web.cern.ch/Specification/LHC-BLM-ES-0001-20-00.pdf

[4] B. Dehning *et al.*, "LHC Beam Loss Detector Design: Simulations and Measurements," in *Proc. PAC'07*, Albuquerque, NM, USA, Jun. 2007, pp. 4198–4200. https://jacow.org/p07/papers/FRPMN072.pdf

[5] B. Dehning, "Beam Loss Monitors at LHC," in *2014 Joint International Accelerator School: Beam Loss and Accelerator Protection*, 2016, pp. 303–318. doi:10.5170/CERN-2016-002.303

[6] B. Dehning *et al.*, "First Experience with the LHC Beam Loss Monitoring System," in *Proc. PAC'09*, Vancouver, Canada, May 2009, pp. 3522–3524.

[7] B. Dehning *et al.*, "Overview of LHC Beam Loss Measurements," in *Proc. IPAC'11*, San Sebastian, Spain, Sep. 2011, pp. 2854–2856. https://jacow.org/IPAC2011/papers/THOAA03.pdf

[8] E. B. Holzer *et al.*, "Commissioning and Optimization of the LHC BLM System," in *Proc. HB'10*, Morschach, Switzerland, Sep.-Oct. 2010, pp. 487–491.

[9] B. Salvachua, "Beam Diagnostics for Studying Beam Losses in the LHC," in *Proc. IBIC'19*, Malmö, Sweden, Sep. 2019, pp. 222–228. doi:10.18429/JACoW-IBIC2019-TUA001

[10] B. Lindstrom *et al.*, "Dynamics of the Interaction of Dust Particles with the LHC Beam," *Phys. Rev. Accel. Beams*, vol. 23, p. 124 501, 2020. doi:10.1103/PhysRevAccelBeams.23.124501

[11] M. Kalliokoski *et al.*, "Performance study of little ionization chambers at the Large Hadron Collider," in *Proc. IEEE NSS/MIC 16*, Strasbourg, France, 2016, p. 8 069 744. doi:10.1109/NSSMIC.2016.8069744

[12] E. Effinger, B. Dehning, J. E. Emery, G. Ferioli, and C. Zamantzas, "Single gain radiation tolerant LHC beam loss acquisition card," in *Proc. DIPAC'07*, Venice, Italy, May 2007, pp. 319–321.

[13] M. Sapinski, "Impact of the RC filters on BLM thresholds," 2010. https://ab-div-bdi-bl-blm.web.cern.ch/Thresholds_WG/2010/RCfilters_v1.pdf

[14] C. Zamantzas, B. Dehning, E. Effinger, J. Emery, and G. Ferioli, "The LHC Beam Loss Monitoring System's Surface Building Installation," in *Proc. 12th Workshop on Electronics for LHC and Future Experiments (LECC 2006)*, 2006, pp. 552–556. https://cds.cern.ch/record/1020105/files/ab-2007-009.pdf

[15] G. Guaglio, B. Dehning, and C. Santoni, "Reliability Considerations on the LHC Beam Loss Monitors System," *AIP Conf. Proc.*, vol. 773, pp. 191–196, 2004. doi:10.1063/1.1949526

[16] J. Emery, B. Dehning, E. Effinger, A. Nordt, M. G. Sapinski, and C. Zamantzas, "First Experiences with the LHC BLM Sanity Checks," *J. Instrum.*, vol. 5, no. 12, p. C12044, 2010. doi:10.1088/1748-0221/5/12/c12044

[17] M. Nemcic, "Calculation of abort thresholds for the Beam Loss Monitoring System of the Large Hadron Collider at CERN," Bachelor thesis, Bristol University, UK, 2012. https://cds.cern.ch/record/1511063/files/CERN-THESIS-2012-233.pdf

[18] M. Kalliokoski *et al.*, "BLM threshold evolution and 2016 proposal," in *Proc. 6th Evian Workshop on LHC beam operation*, 2016, pp. 191–196. https://cds.cern.ch/record/2294668

[19] C. Roderick, L. Burdzanowski, D. M. Anido, S. Pade, and P. Wilk, "Accelerator Fault Tracking at CERN," in *Proc. ICALEPCS'17*, Barcelona, Spain, Oct. 2017, pp. 397–400. doi:10.18429/JACoW-ICALEPCS2017-TUPHA013

[20] V. Schramm, "Dependable System Development Methodology and Case Study for the LHC Beam Loss Monitoring System at CERN," Ph.D. dissertation, University of Stuttgart, Germany, 2021. doi:10.18419/opus-11571

[21] V. Schramm, W. Viganó, and C. Zamantzas, "System's Performances in BI," in *Proc. 8th Evian Workshop on LHC beam operation*, 2019, pp. 59–62. https://cds.cern.ch/record/2813541/files/document.pdf

[22] A. Boccardi, M. B. Marin, T. E. Levens, B. Szuk, W. Vigano, and C. Zamantzas, "A Modular Approach to Acquisition Systems for Future CERN Beam Instrumentation Developments," in *Proc. ICALEPCS'15*, Melbourne, Australia, Oct. 2015, pp. 1103–1106. doi:10.18429/JACoW-ICALEPCS2015-THHB2O02

[23] V. Schramm, M. Saccani, W. Viganò, and B. Bertsche, "Combined Testing And Validation Strategy For The New LHC Blm Processing Module," in *Proc. 65th Annual Reliability & Maintainability Symposium*, 2019, pp. 1–7. doi:10.1109/RAMS.2019.8769268

[24] M. Gonzalez-Berges, J. O. Robinson, M. Saccani, V. Schramm, and M. A. Stachon, "Test-bench Design for New Beam Instrumentation Electronics at CERN," in *Proc. ICALEPCS'19*, New York, NY, USA, Oct. 2019, pp. 323–327. doi:10.18429/JACoW-ICALEPCS2019-MOPHA049

[25] S. Biereigel *et al.*, "The lpGBT PLL and CDR Architecture, Performance and SEE Robustness," in *Proc. TWEPP 2019 Topical Workshop on Electronics for Particle Physics*, Santiago De Compostela, Spain, 2019, p. 034. doi:10.22323/1.370.0034

[26] F. Martina *et al.*, "Methodology, Characterisation and Results from the Prototype Beam Loss Monitoring ASIC at CERN," in *Proc. IBIC'21*, Pohang, Korea, Sep. 2021, pp. 294–298. https://jacow.org/ibic2021/papers/TUPP34.pdf

ISBN: 978-3-95450-241-7 ISSN: 2673-5350 doi:10.18429/JACoW-IBIC2022-TUP04

BEAM LOSS MONITOR FOR POLISH FREE ELECTRON LASER (PolFEL): DESIGN AND TESTS*

R. Kwiatkowski†, D. Zaloga, R. Nietubyc, J. Szewinski
National Centre for Nuclear Research, Otwock, Poland
A. Wawrzyniak, National Synchrotron Radiation Centre SOLARIS, Krakow, Poland

Abstract

The Beam Loss Monitor (BLM) system is primarily used for machine protection and is especially important in the case of high energy density of accelerated beam, when such a beam could cause serious damages due to uncontrolled loss. PolFEL linear accelerator is designed with the beam parameters, which made BLM an essential system for machine protection. The design of BLM system for PolFEL is composed of several scintillation probes placed along and around the accelerator. The paper reports on design and first tests of prototype detector, which is planned to be used for PolFEL project. The prototype was tested in NCBJ and SOLARIS, using radioactive calibration samples and linear electron accelerator as a sources. We also present results of numerical investigation of radiation generated due to interaction of fast electrons with accelerator components.

INTRODUCTION

The motivation for using Beam Loss Monitoring system is the detection of unwanted events of fast charged particles escaping the designated path along the beamline. While not being incorporated directly into the vacuum system and beam instrumentation, the BLM is an important part of the high-energy accelerator, which could generate intense beams of high energies and power. The main role of the BLM is to protect the machine from damages (short- or long-term) caused by energetic particles hitting the vacuum components, and/or escaping vacuum pipe without puncturing them, and damaging sensitive equipment due to excessive radiation. Being important system for large facilities, the working principle of beam loss monitors could also be used for beam controlling and fine-tuning of its position and alignment.

THE PolFEL PROJECT

The PolFEL project, namely the construction of Free Electron Laser in Poland is in the preparation for a few years, and at in the present phase it have main features and components already fixed. It is driven by superconducting linear accelerator, based on TESLA SRF technology, and is designed to operate both in continuous wave (cw) and long pulse (lp) mode. The generation of coherent light is planned in three branches, i.e. in the THz, IR and VUV range. The planned parameters of PolFEL electron beam are listed in Table 1.

Table 1: The Parameters of PolFEL Electron Beam (cw mode) [1-3]

parameter/position	Gun	VUV line	THZ line
Bunch charge [pC]	20-250	<100	250
Repetition rate [kHz]	50	50	50
Bunch length [ps]	2-10	0.1	<10
Beam energy [MeV]	4	<154	<979
Beam current [μA]	12.5	5	12.5
Beam power [W]	-	770	940

BEAM LOSS TYPES

We could highlight two kind of losses, which lead to increased readout in the BLM system, i.e.: regular and irregular ones.

Regular Losses

Regular, controlled, losses are unavoidable part of accelerator operation and, therefore could be used for diagnostics purposes, like injection studies, energy tail measurements, lifetime limitations, etc. They occur usually as an effect of aperture changes or scattering on residual gas.

Irregular Losses

The irregular, uncontrolled, losses are events, which could lead to potentially hazardous situation and damage the equipment or vacuum components. Such losses could resulted from misaligned beam, leaks or obstacles in vacuum system, failures of beam control, or other accelerator parts. The severity of such an event varies from excess irradiation of nearby devices up to puncturing vacuum vessel wall, in case of prolonged exposition to electron beam.

DETECTORS FOR BLMs

Beam Loss Monitor, being in principle a detector of ionizing radiation, could be built using various types of components. The factors, deciding of device selection are, among others: intrinsic sensitivity; calibration procedures; radiation hardness; reliability; dynamic range; time resolution; size limitations; cost; saturation handling.

The BLM used worldwide are constructed using such detectors like: ionization chambers; PIN diodes; secondary emission monitors, scintillation detectors and cherenkov detectors. Each of the detectors have its char-

*The construction of PolFEL received funding from the European Regional Development Fund in the framework of the Smart Growth Operational Programme and Regional Operational Programme for Mazowieckie Voivodeship.
† email: Roch.Kwiatkowski@ncbj.gov.pl

Content from this work may be used under the terms of the CC BY 4.0 licence (© 2022). Any distribution of this work must maintain attribution to the author(s), title of the work, publisher, and DOI

ISBN: 978-3-95450-241-7 ISSN: 2673-5350 doi:10.18429/JACoW-IBIC2022-TUP04

Content from this work may be used under the terms of the CC BY 4.0 licence (© 2022). Any distribution of this work must maintain attribution to the author(s), title of the work, publisher, and DOI

acteristics and differences, which make them proper choice for selected requirements [4, 5].

SELECTION AND DESIGN FOR PolFEL

During the selection process of an optimal BLM detector, we have taken into account the aforementioned features of the detector, and also the experience and know-how of our group in NCBJ. The scintillator BLM detector, coupled with miniature PMT module is characterized by:

- high detection efficiency
- high dynamic range
- range variation by selecting PMT gain
- relatively easy calibration
- custom shape and dimensions of detector
- relatively low price
- additional fail-safe feature using side LED

The prototype, meant to test the principles and operation of BLM was build using H11901 photomultiplier and EJ-232 fast plastic scintillator, which match the requirements mentioned earlier [6, 7]. The motivation behind these choices was to find small size PMT with integrated HV supplier and voltage divider, and scintillator, which is easily accessible, relatively cheap, and has high efficiency, and fast timing. The design is presented in Fig. 1.

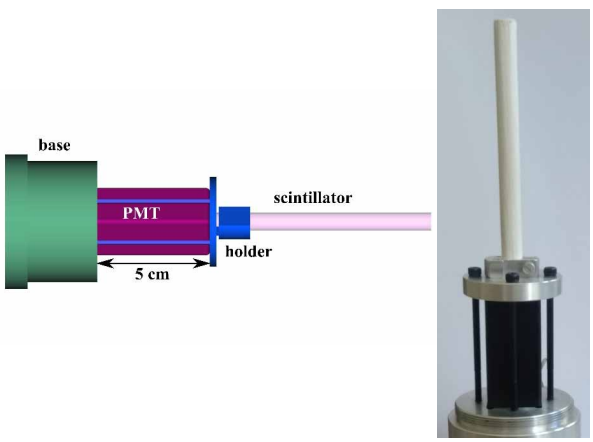


Figure 1: Design of the BLM detector (left) and photo of an actual prototype (right).

The BLM detector consists of scintillator rod (8 mm in diameter, 100 mm in length) coupled with PMT using special holder. Small size of scintillator was chosen on the basis of calculations and maximum electron energy. While in the GeV energy range, 8-millimeter scintillator could have too small efficiency, in the range up to 300 MeV, such detector is sufficiently large. The PMT is then encased in Al, light-proof case. Whole detector is only 6- by 21-centimeters, therefore it could be easily placed nearby various accelerator components.

MONTE CARLO CALCULATIONS

The expected performance and efficiency of BLM design was investigated using Monte Carlo simulations using FLUKA and GEANT4 codes. The calculations were performed in a few steps. The first approximation included cylindrical vacuum pipe and cylindrical scintillator placed at side of the pipe. Next, we added some steel obstacles between beam interaction point and the detector, in order to estimate shielding by accelerator components. The second part of calculations was to reconstruct design of one of the beamline fragments. This was done using GDML readout functionality of GEANT4, which allowed us to relatively easy translate CAD geometry into GEANT4 one. In order to assess the required computing power, the simulations using GEANT4 were performed with increasing similarity to the CAD model. The geometries used during calculations are presented in Fig. 2 [8].

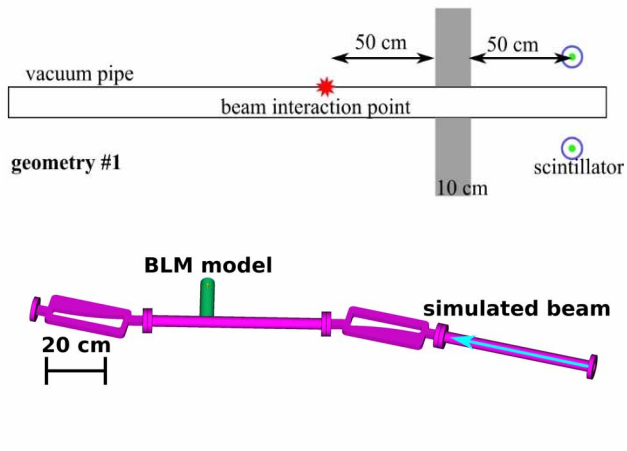


Figure 2: Geometries used during MC calculations: geometry used for preliminary calculations (top), simplified reconstruction of beamline fragment (bottom).

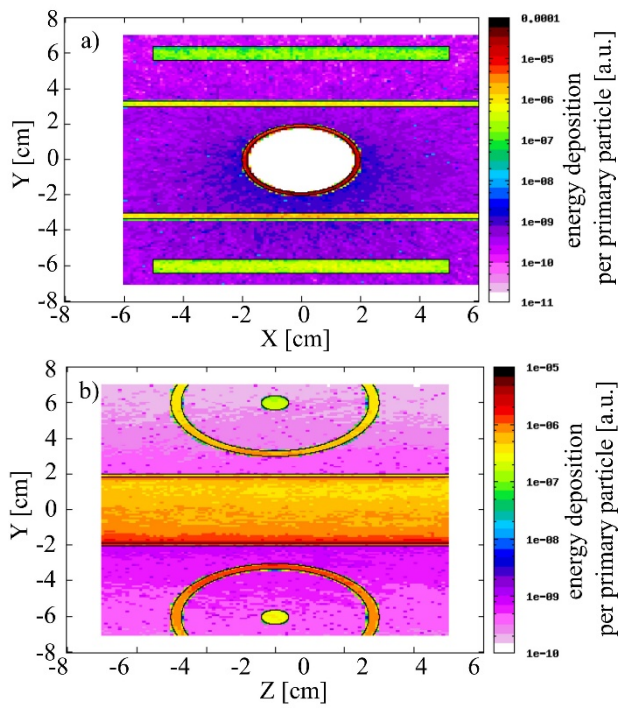


Figure 3: Energy deposition on Cartesian grid: XY plane (top), YZ plane (bottom).

For illustration purposes, and to better understand distribution of radiation generated during “beam loss

ISBN: 978-3-95450-241-7 ISSN: 2673-5350 doi:10.18429/JACoW-IBIC2022-TUP04

event", we plotted energy deposition on Cartesian grid. The XY an YZ projections, calculated for the simplified geometry are shown in Fig. 3.

The tally used during calculations was energy deposition in the scintillator. Results of calculations, in form of histograms of energy deposition events, are presented in Figs. 4-5.

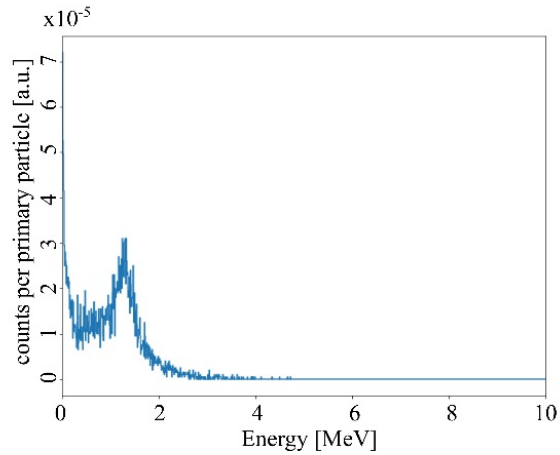


Figure 4: Histogram of energy deposition, calculated for simple geometry using FLUKA code. Electron energies was set to 72 MeV.

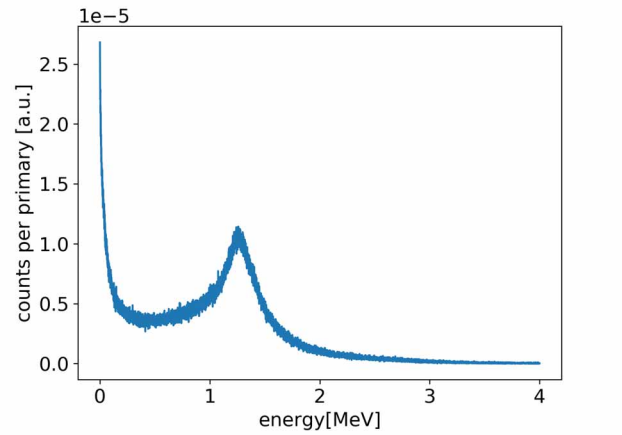


Figure 5: Histogram of energy deposition in scintillator, calculated for simple beamline geometry using GEANT4 workbench. Electron energies was set to 150 MeV.

PROTOTYPE TESTS

The experimental testing of our BLM detector was performed in two phases so far. During the first phase, we have constructed detector using spare parts available in our laboratory. The purpose of such work was to test small plastic scintillator coupled with detector on high-energy linear accelerator. The detector was tested on SOLARIS accelerator, and it showed, that amount of light generated in our system was large enough to further miniaturize the setup.

Based on the preliminary tests and MC simulations, we have decided to design a new setup, which is shown in Fig. 1. The component include small scintillator and PMT photosensitive detector with integrated HV supplier and voltage divider.

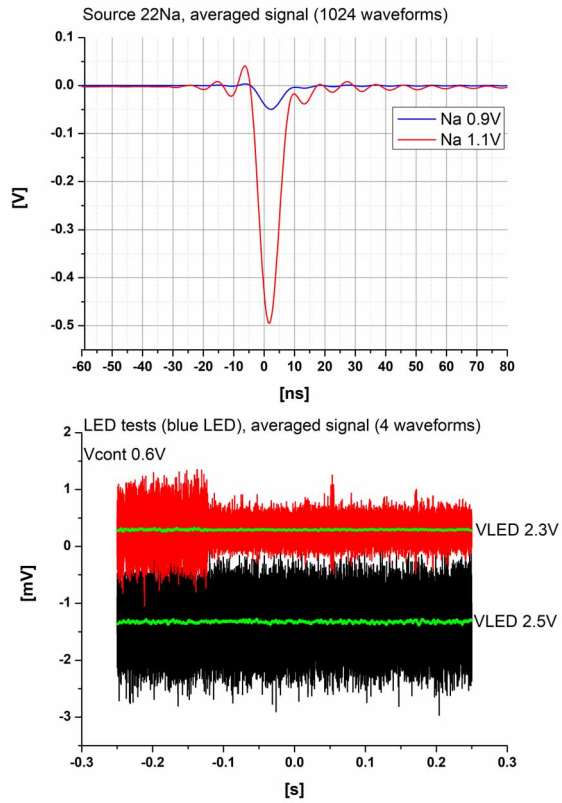


Figure 6: Results of laboratory tests of BLM detector: signals recorded using radioactive 22Na calibration source (top), PMT response to LED placed next to the scintillator (bottom).

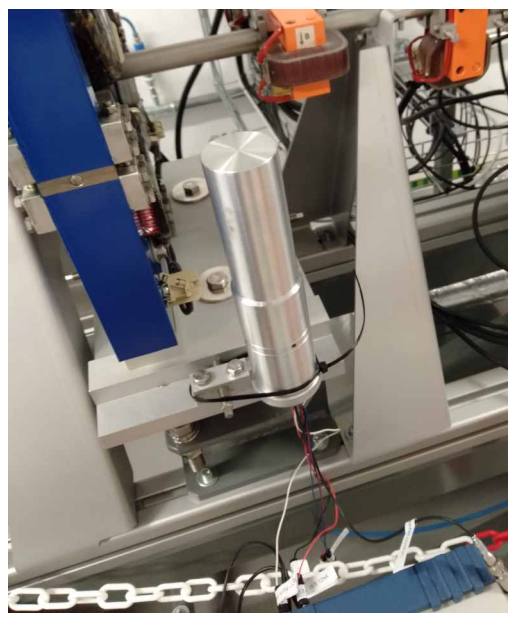


Figure 7: BLM detector placed in the vicinity of SOLARIS linac beamline.

The prototype device was aim to investigate the design behavior in the radiation field of electron accelerator. The first measurements, performed to check the connections

Content from this work may be used under the terms of the CC BY 4.0 licence (© 2022). Any distribution of this work must maintain attribution to the author(s), title of the work, publisher, and DOI

ISBN: 978-3-95450-241-7 ISSN: 2673-5350 doi:10.18429/JACoW-IBIC2022-TUP04

Content from this work may be used under the terms of the CC BY 4.0 licence (© 2022). Any distribution of this work must maintain attribution to the author(s), title of the work, publisher, and DOI

and operation, was made using radioactive sources. We have observed distinct signals and response to built-in test-LED. Results are shown in Fig.6.

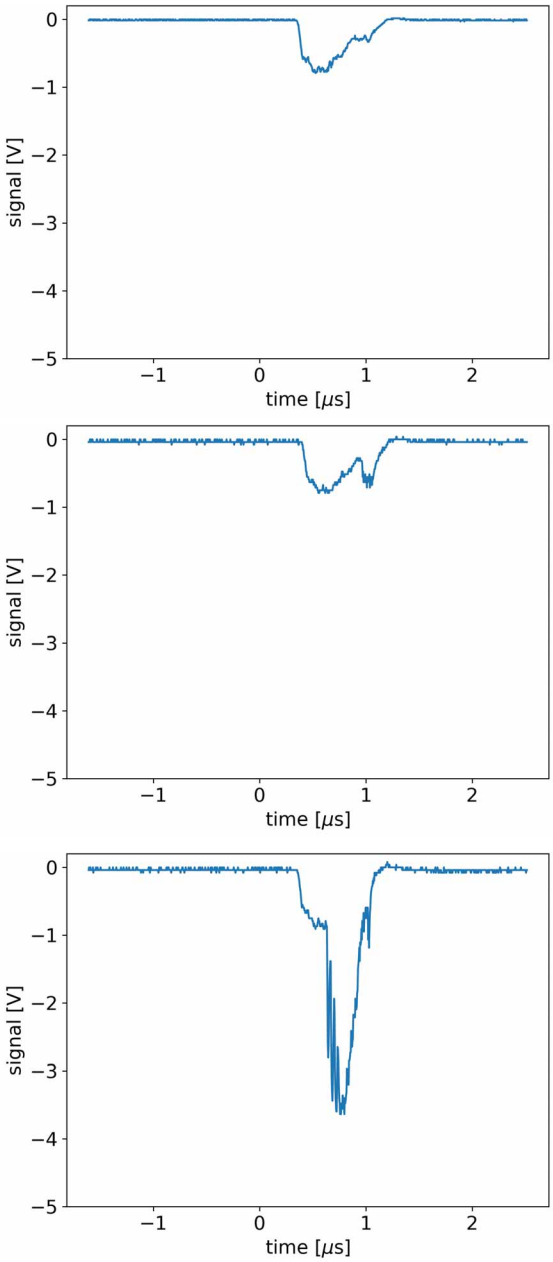


Figure 8: Exemplary signals recorded during tests at SOLARIS accelerator: central beam (top), beam tilted in Y-plane (middle), beam tilted in X-plane (bottom).

Afterward, it was tested on a linear accelerator in SOLARIS facility. During the tests, we have changed position, PMT gain and working conditions of accelerator. The experimental setup is shown in Fig. 7. The results are shown in Fig. 8. Based on the performed prototype tests, we can conclude, that the designed detector could be used for monitoring of beam losses in the electron linear accelerator. The detector, however, needs some additional considerations and testing in order to assess the impact of RF noises and selection of readout electronics.

CONCLUSIONS

The BLM system, which is essential for operation of large-scale facilities, is important also for medium-size ones like PolFEL. While being primary the safety device, BLM could also be used for control and fine-tuning the beam. The beam loss monitor for PolFEL accelerator was designed on the basis of Monte Carlo calculations and preliminary experimental tests. The prototype design was build of small plastic scintillator and miniature PMT module. Both the calculations and measurements showed usability and efficiency of the proposed design. The detector is still under development and numerical, and experimental investigation, to further improve its capabilities.

REFERENCES

[1] J. Sekutowicz, "PolFEL in context of other FEL facilities" ,presented at Wilga 2019 Summer Symposium on Photonics Applications and Web Engineering, Wilga, Poland, May 2019, unpublished.

[2] J. Sekutowicz, P. Czuma, P. Krawczyk, K. Kurek, J. Lorkiewicz, R. Nietubyć, J. Poliński, M. Staszczak, K. Szamota-Leandersson, J. Szewiński, "Polish free electron laser: short technical description", *Proc. SPIE Int. Soc. Opt. Eng., vol.* 1105405, p. 1105405, 2019. doi:10.1117/12.2526756

[3] P. Krawczyk, "PolFEL project: towards the construction of the Polish Thz/IR/VUV Free Electron Laser", presented at TERFEL International Conference on Free Electrons Laser Applications in Infrared and THz Studies of New States of Matter, Warsaw, Poland, Jul. 2022.

[4] K. Wittenburg, "Beam Loss Monitors", presented at CAS - CERN Accelerator School: Beam Instrumentation, Tusula, Finland, June 2018. https://arxiv.org/abs/2005.06522

[5] Robert E. Shafer, "A Tutorial on Beam Loss Monitoring", in *AIP Conf. Proc.*, vol. 648, p. 44, 2002. doi:10.1063/1.1524391

[6] Hamamatsu Photonics K.K., https://www.hamamatsu.com

[7] SCIONIX Holland B.V., https://scionix.nl

[8] R. Kwiatkowski, M. Krakowiak, R. Nietubyc, J. Szewinski, A. Wawrzyniak, "Design and Numerical Investigations of Scintillation Beam Loss Monitor for PolFEL", in *Proc. IBIC'21*, Pohang, Korea, Sep. 2021, pp. 281. doi:10.18429/JACoW-IBIC2021-TUPP31

ISBN: 978-3-95450-241-7 ISSN: 2673-5350 doi:10.18429/JACoW-IBIC2022-TUP05

EXPERIENCE WITH MACHINE PROTECTION SYSTEMS AT PIP2IT *

A. Warner†, M. Austin, L. Carmichael, J.-P. Carneiro, B. Hanna, E. Harms, M. Ibrahim, R. Neswold, L. Prost, R. Rivera, A. Shemyakin, J. Wu, Fermilab, Batavia, IL, USA

Abstract

The PIP-II Injector Test [1] (PIP2IT) facility accelerator was assembled in multiple stages in 2014 – 2021 to test concepts and components of the future PIP-II linac that is being constructed at Fermilab. In its final configuration, PIP2IT accelerated a 0.55 ms x 20 Hz x 2 mA H^- beam to 16 MeV. To protect elements of the beam line, a Machine Protection System (MPS) was implemented and commissioned. The beam was interrupted faster than 10 µs when excessive beam loss was detected. The paper describes the MPS architecture, methods of the loss detection, procedure of the beam interruption, and operational experience at PIP2IT.

INTRODUCTION

PIP2IT is a prototype accelerator assembled as a testbed for developing and testing some of the novel and challenging technologies required to construct the Proton Improvement Plan-II (PIP-II) project at Fermilab [2]. The central element of PIP-II is the 2 mA, 800 MeV H^- linac which comprises a room temperature front end followed by an SRF accelerator. The PIP2IT (Fig. 1) was constructed in two phases. The first phase consisted of the room temperature portion of the machine, or Warm Front-end (WFE), which comprises a H^- ion source, a radio-frequency quadrupole (RFQ) and a transport line for delivering beam to the superconducting section of the accelerator at 2.1 MeV. In the second phase, it was appended by two cryomodules called a Half Wave Resonator (HWR) and a Single Spoke Resonator type1 (pSSR1).

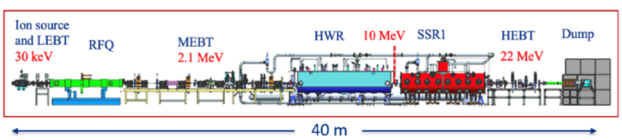


Figure 1: PIP2IT Accelerator Layout.

In the final PIP2IT operational scenario, a 5 mA, 0.55 ms x 20 Hz beam out of the RFQ was scraped transversely in the Medium Energy Beam Transport (MEBT), primarily with scrapers, and then half of the bunches was removed by a bunch-by-bunch chopping system in an aperiodic pattern required for the future injection into the Booster [3]. Then, the beam with 2 mA pulse current was accelerated in the HWR and pSSR1 cryomodules to 8 and 16 MeV, correspondingly, and transported through the High Energy Beam Transport (HEBT) to a beam dump. A machine protection system capable of inhibiting the beam within 10 µs in response to an acute beam loss, protecting machine components from beam damage, and monitoring the machine configuration was developed.

MPS SCHEME

The PIP2IT MPS scheme tested several features that had been envisioned to be used at PIP-II.

- The main layer of protection is beam inhibiting by a small number (four) of devices that were carefully tested and administratively controlled. All of them are upstream of the RFQ.
- The global protection of the linac is performed by comparison of signals from pairs of current-sensitive devices. These devices (4 pairs) are administratively controlled.
- The second layer of protection, the local protection, controlled the beam loss to multiple electrically isolated electrodes in the MEBT.
- The third level was the readiness signals from the subsystems (vacuum, RF etc.).
- Finally, the beam could be operated only at specific combinations of beam intensities and machine configurations defining how far the beam can propagate. Each combination had its own table of the MPS parameters to control.

This hierarchy, on one hand, provided a robust protection, and, on the other hand, a significant flexibility in operation.

PROTECTION SYSTEM DESIGN

The machine protection system at PIP2IT was not a distributed system and was intended as a testbed for demonstrating the methods needed to protect accelerator components, adequately monitor beam current losses, develop the system logic, provide flexibility to beam measurements and to test hardware and tools required to build a larger scale distributed system for the PIP-II project.

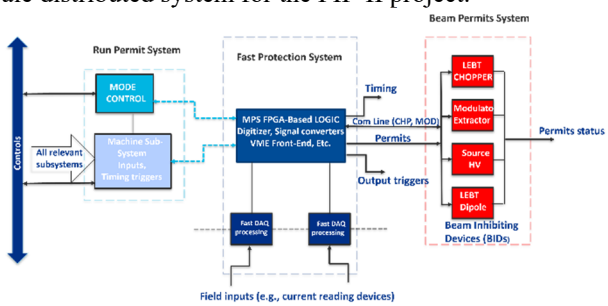


Figure 2: Simplified MPS concept.

The MPS ultimately received Ok/Not-Ok signals from subsystems and managed permits to Beam Inhibiting Devices (BIDs). Figure 2 shows the simplified block diagram. The Low Energy Beam Transport (LEBT) chopper was the primary BID that was cutting the beam off 150 ns after its

* This manuscript has been authored by Fermi Research Alliance, LLC under Contract No. DE-AC02-07CH11359 with the U.S. Department of Energy, Office of Science, Office of High Energy Physics
† warner@fnal.gov

Content from this work may be used under the terms of the CC BY 4.0 licence (© 2022). Any distribution of this work must maintain attribution to the author(s), title of the work, publisher, and DOI

ISBN: 978-3-95450-241-7 ISSN: 2673-5350 doi:10.18429/JACoW-IBIC2022-TUP05

Content from this work may be used under the terms of the CC BY 4.0 licence (© 2022). Any distribution of this work must maintain attribution to the author(s), title of the work, publisher, and DOI

permit went away. The other three BIDs were the ion source extractor voltage and its bias voltage as well as the LEBT bend current. While the extractor reaction time was similar to the chopper's, the bias voltage and the bend current were dropping in sub-second range.

The input signals to the MPS have various formats: relay contacts, LVTTL, toggling square wave and UART-like serial data. Fault detection is designed to these signal formats to ensure accelerator safety. Broken or loose cables in the paths of these signals will be detected and accelerator will not be allowed to operate before fixing the issue. The input signals were processed at the same rate independently on the signals origin, removing the permit from BIDs within 1 µs after receiving the interruption. While an automated beam recovery after intermittent trips has been foreseen, it was not implemented because of the planned continuously changing operational conditions of the test machine.

Reaction of the MPS to the input signals was defined by the tables generated for specific accelerator conditions, described by machine configurations and beam modes.

Machine configurations determined how far beam could propagate along the beamline. The MPS was checking that the devices limiting the beam propagation were activated (e.g., the scrapers were moved in, and the valve downstream closed) and masked the irrelevant downstream sensors. Four implemented machine configurations are shown in Table 1. Implementation of the machine configurations and software to switch between them provided important flexibility in commissioning. At the start, sections of the accelerator could be sequentially commissioned without modification of the MPS. Later, two different commissioning activities could be performed in parallel. For example, with the machine in the MEBT configuration, testing of the MEBT absorber was performed in parallel with RF commissioning of the SRF cavities.

Table 1: PIP2IT MPS Configurations

Configuration	Purpose	Beam to	Restriction
Ion Source (IS)	Condition	No beam	IS valve
LEBT	IS & LEBT tuning	End of LEBT	LEBT scraper
MEBT	MEBT Tuning	MEBT absorber	MEBT scrapers
Full Line	HEBT	Dump	All open

The allowed beam power, controlled by the pulse duration, was defined by two beam modes: a diagnostic mode, with maximum pulse duration of 10 µs for tuning, commissioning, and beam studies, and an Operational mode with a maximum pulse duration up to 0.55 ms consistent with PIP-II beam requirements. In the diagnostic mode, the maximum instantaneous power density was estimated to be below the damage threshold for insertable devices such as scrapers, wires, Allison scanners, and Faraday Cup. In the operational mode with much higher damage potential, the insertable devices were not allowed to be moved in. A so-called Mode Controller program managed the configurations and modes available to the user. It provided a comprehensive overview of the machine status, enforced, and monitored the machine configurations, and set limits on beam parameters (beam modes) for the defined machine configurations.

BEAM LOSS MEASUREMENTS

The complete assortment of beam current sensing devices is shown in Fig. 3. Because the beam damage potential in the ion source, LEBT, and the RFQ was considered to be low, current readings from these areas are not fed into the MPS. Because of the tight space limitations in the MEBT, the devices there are compact electrostatic pickups (RPU, described later). Since part of the beam is removed in the middle of the MEBT by the chopping system, there are two RPU pairs, upstream and downstream of the MEBT absorber. The beam loss in the cryomodules is controlled by comparison of currents read by ACCTs placed at the exit of the MEBT and entrance of the HEBT, and the HEBT loss is calculated by comparison of currents of the ACCT at its entrance and the beam dump.

Measurement of the uncontrolled beam loss in the MEBT is more complicated. First, half of the bunches is removed by the MEBT chopping system onto the MEBT absorber. Therefore, the MPS controls separately the beam loss upstream and downstream of the absorber. Second, the MEBT elements are tightly packed, and inserting two additional ACCTs on both sides of the absorber is difficult. Instead, the control of the loss is made with four electrostatic pickups, so-called Ring Pickups (RPUs). Each RPU is a metal cylinder mounted inside a flange. The RPU electronics analyses the 162.5 MHz component of the capacitive signal from the cylinder and delivers its amplitude to the MPS. Importantly, this signal doesn't depend on the pulse width in the wide range from microseconds to CW. In combination with constant beam properties through the pulse, it allowed beam tuning in the MEBT with 10 µs pulses to calibrate the RPUs. With chopping off, the beam was propagated through the MEBT, and the loss was identified by comparison of ACCTs at the entrance and exit of the MEBT. In this state, the RPU signals were calibrated to take into account the effect of the beam width on the RPU signal. After tuning to scrape the beam as required and to minimize the undesired loss to acceptable levels, comparison of the signals from two RPU pairs (beginning of the MEBT to entrance of the absorber box and downstream of

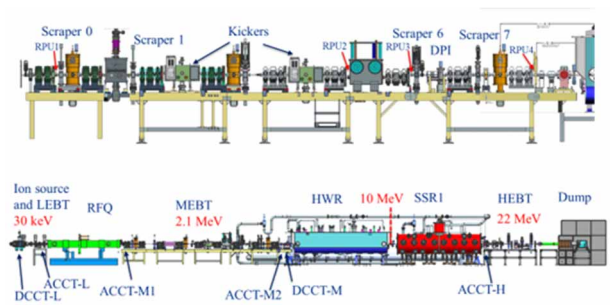


Figure 3: Layout of the Beam-Current channels.

ISBN: 978-3-95450-241-7 ISSN: 2673-5350 doi:10.18429/JACoW-IBIC2022-TUP05

the absorber box to the MEBT exit) was activated in the MPS.

The RPUs were also used by the MPS to monitor the beam pulse length as an additional protection layer in a case of the LEBT chopper failure.

Comparison of currents with ACCTs and RPU provided the global protection of the corresponding sections. To add a protection layer for the elements restricting the beam aperture and, therefore, the most susceptible to the beam damage, these elements were electrically isolated, biased to suppress the secondary electron emission, and their signal, fed into the MPS, and were monitored for extensive beam loss. These channels included:

- 16 channels of horizontal and vertical scrapers, housed in 4 crosses. They were used to scrape the beam and configure the beamline in the MEBT mode.
- 4 Kicker Protection Electrodes (PEs), metal plates placed at both ends of the chopper deflecting structures to protect these structures from primary beam exposure.
- Differential Pumping Insert (DPI), a 200 mm long, 10 mm ID pipe which separated high vacuum and ultra-high vacuum, particle free regions.

The thresholds for current losses at these devices were included into the MPS configuration files.

Beam Loss Protection Integral

The primary MPS tool used to protect the MEBT and the cryomodules at PIP2IT was based on the comparison of readings from the current measuring devices. In the initial implementation, the beam current was read in a 0.25 ms window, and the average values were compared. The bias of each individual device was adjusted based on reading the device during the beam-off time between pulses. In the final implementation, it was found to be advantageous to use an integration method with a limit on the integral moderated by a damping function. The integration improved the stability of the loss detection by decreasing the sensitivity to the measurement noise. In addition, comparison of the threshold could be made continuously instead of waiting for the end of an acquisition window. This method also improved the processing and reaction time to that of the FPGA clock speed and digitizer resolution. This algorithm was applied both to comparison of currents in the global protection and individual current signal in the local protection.

The FPGA based implementation of the algorithm instructed the MPS to drop the beam permit signal if the value $Q(T)$ calculated according to Eq. (1) exceeded a user-specified threshold Q_{th}:

$$Q_{th} < Q(T) = e^{\frac{-T}{\tau}} \int_0^T \Delta I(t) \cdot e^{\frac{t}{\tau}} dt \qquad (1)$$

where T is the time of evaluation. Eq. (1) assumes that the integration starts before actual start of the beam and after the beam-off window for baseline subtraction. $\Delta I(t)$ is the difference between readings of two beam current devices at time t; τ is a time constant.

For a constant beam loss in a short time scale, $T << \tau$, $Q(T) \approx \Delta I \cdot T$. Correspondingly, the threshold Q_{th} should be chosen to ensure that in the case of total beam loss with current I_0, the interruption condition is fulfilled in the time T_{th} safe for the protected section:

$$Q_{th} = I_0 \cdot T_{th} \qquad (2)$$

For a constant beam loss in long time scales, $T >> \tau$, $Q(T) \approx \Delta I \cdot \tau$. The choice of the constant τ is determined by the maximum beam loss sustainable in steady state ΔI_{max}:

$$\tau = {}^{Q_{th}}/_{\Delta I_{max}} \qquad (3)$$

Such an algorithm roughly mimics how the temperature rises in a metal irradiated by a beam, where transition from μs to ms scales corresponds to thermal conductivity playing a significant role. Numerical estimations of various loss scenarios showed that with chosen thresholds the temperature rise in the beam irradiated stays well below 1000 K.

Figure 4 illustrates the concept as applied to the cryomodules. The resolution for losses was ~3% limited by noise.

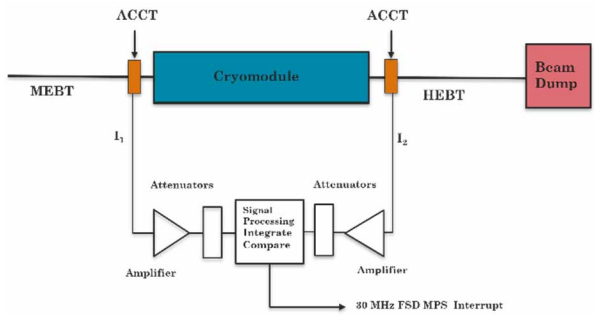


Figure 4: Cryomodule Protection Concept.

Three ACCTs, four RPUs and the beam dump were incorporated into the so-called Differential Beam Current Monitoring (DBCM) system. The discrete form of the integral described was implemented on FPGA based, 125 MHz digitizers on a VME platform. Figure 5 shows the block design for the analog current signals and the VHDL implementation.

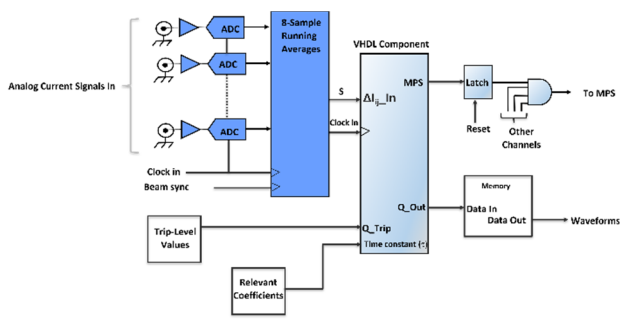


Figure 5: System Digitizer and VHDL Component.

The VHDL component was designed to remove a 30 MHz MPS permit signal which in turn removes a 5 MHz chopper permit if the integration component was interrupted from calculating. The code that did the calculation made the comparisons with the limit values estab-

Content from this work may be used under the terms of the CC BY 4.0 licence (© 2022). Any distribution of this work must maintain attribution to the author(s), title of the work, publisher, and DOI

ISBN: 978-3-95450-241-7 ISSN: 2673-5350 doi:10.18429/JACoW-IBIC2022-TUP05

Content from this work may be used under the terms of the CC BY 4.0 licence (© 2022). Any distribution of this work must maintain attribution to the author(s), title of the work, publisher, and DOI

lished in Table 2. These parameters for the various threshold limits were protected and controlled as part of a larger set of configuration parameters for the MPS. This implementation removes the MPS permit out to the main MPS logic system in 8ns if a threshold is exceeded as measure on the system clock, Fig. 6.

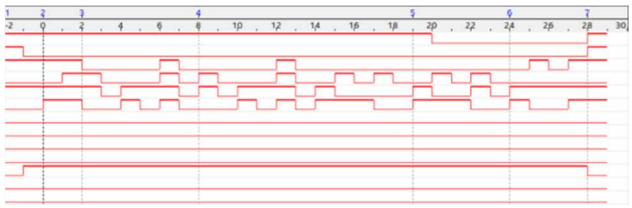


Figure 6: DBCM response time to threshold trips (min clock cycle 8 ns)

Table 2: PIP2IT MPS Protection Parameters

System	Power, W	Q_{th}, mA·µs	τ, µs	Based on
Scrapers	75	100	5000	Scraper current
HWR/p SSR1	20	20	2000	ACCT diffs
PEs	40	100	5000	PE current
DPI	25	2	2000	DPI current

DISTRIBUTED SYSTEM HARDWARE

Part of the MPS development at PIP2IT was focused on designing and testing the hardware necessary to build a distributed MPS for protecting the future PIP-II accelerator and demonstrate methods for integration with the larger accelerator complex at Fermilab. The hardware required to concentrate subsystem signals, manage permits, and beam aborts was tested to verify signal integrities, distribution with optical fibre links, reaction timing etc. These concentrators where specifically used to manage and consolidate the signals derived from the HWR and SSR1 cryomodule Quench Protection Circuits and the RF Protection circuits. Combinations of these units were installed with appropriate cable lengths to mimic a distributed system. The units dropped the local permit within 100 ns of an input going low and sent signals to subsequent concentrator units within 140 ns to 270 ns. The signal is analyzed for integrity and passed along again repeating the sequence. The hardware in Fig. 7 operates in a failsafe manner with active-high TTL logic. Each units have 8 optically isolated permit inputs which are maskable. The units were designed to use single mode or multimode fibre for connection to a fibre abort link. The concentrator units are FPGA based and can be programmed to execute any logic needed. The design demonstrated the flexibility to extend the system and integrate with the larger accelerator complex while achieving the response require for PIP-II.

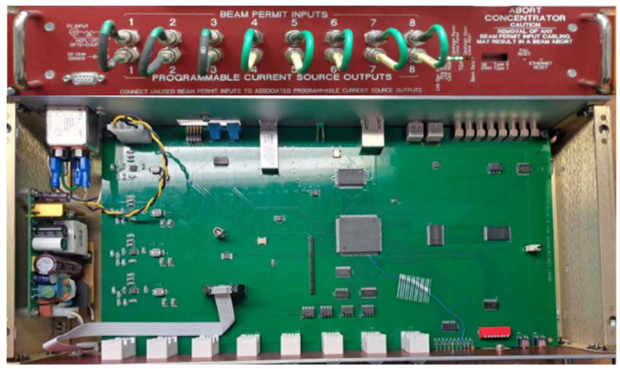


Figure 7: Eight Channel Signal Concentrator box front panel and interior views.

PLANS FOR PIP-II MPS

MPS operational experience at PIP2IT was useful for evaluating some hardware, firmware algorithms, and aspects of the architecture needed for the PIP-II project. The development and subsequent testing of differential beam current monitoring verified the algorithm and the implementation for this system. The method will be reemployed on newer hardware for transmission losses with ACCTs at PIP-II. Ring Pickup electrodes and the methods implemented to monitor chopped beam and losses in the MEBT will be designed into the version. The WFE MPS architecture will be for the most part re-implemented on a modular FPGA platform as part of the larger distributed system. The Concentrator hardware with some minor firmware modification to accommodate the specific of its application will be reused in conjunction with other hardware. The Configuration and Mode control experience gained at PIP2IT will be utilized to develop robust monitoring tools. The final overall architecture of the distributed MPS will be designed on the FPGA based the concentrator experience gained as the response times introduced and measure proved adequate for the needs ahead.

ACKNOWLEDGEMENTS

The authors are thankful to the many people who contributed to building the PIP2IT and those who contributed to its operation and MPS commissioning, these include but are not limited to, D. Crawford, A. Feld, M. Geelhoed, B. Hendrix, K. Koch, A. Prosser, G. Saewert, T. Zuchnik.

REFERENCES

[1] "The Proton Improvement Plan-II (PIP-II) Final Design Report", 2021 (unpublished).

[2] E. Pozdeyev *et al.*, "Beam Commissioning and Integrated Test of the PIP-II Injector Test Facility", presented at LINAC'22, Liverpool, UK, Sep. 2022, paper MO1PA01.

[3] A. Shemyakin *et al.*, "Design of 162-MHz CW bunch-by-bunch chopper and prototype testing results", in *Proc. HB'18*, Daejeon, Korea, Jun. 2018, pp. 428-433. doi:10.18429/JACoW-HB2018-THP1WC03

ISBN: 978-3-95450-241-7 ISSN: 2673-5350 doi:10.18429/JACoW-IBIC2022-TUP09

DESIGN OF THE BEAM POSITION MONITOR FOR SOLEIL II

M. El Ajjouri, N. Hubert, A. Gamelin, F. Alves, Synchrotron SOLEIL, Saint-Aubin, France

Abstract

The Beam Position Monitors (BPM) for the SOLEIL low emittance upgrade project (SOLEIL II) are currently in the design phase. Efforts are put on the minimization of the heat load on the button by optimizing the longitudinal impedance and the BPM materials.

To validate the mechanical design and tolerances, a first prototype has been manufactured and controlled. This paper presents the mechanical design of the BPM, the metrology of the prototype and the lessons learned from this prototyping phase.

INTRODUCTION

SOLEIL is the French third generation light source routinely operated for external users since 2008 with electron beam emittance of 4 nm·rad at an energy of 2.75 GeV and a nominal current of 500 mA (uniform filling pattern). A low emittance upgrade project is currently in the Technical Design Report (TDR) phase. The reference lattice features a natural emittance of 84 pm.rad [1, 2]. It is based of alternating 7 bend and 4 bend achromats to minimize the displacement of the current source point and realignment of the beamlines, keeping the tunnel shielding wall unchanged. Main comparison lattice parameters are listed in Table 1.

Table 1: Main baseline TDR lattice parameters

	SOLEIL	***SOLEIL II***
Circumference (m)	354.1	353.9
Beam energy (GeV)	2.75	2.75
Beam current (mA)	500	500
Lattice Type	DBA	7BA/ 4BA
Straight section number	24	20
Natural emittance (pm·rad)	4000	84
RMS Nat. Bunch length (ps)	15	9
RF Voltage (MV)	2.8	1.8
RF Frequency (MHz)	352.2	352.4
Vacuum chamber size (mm)	70/25	12 round

BPM SPECIFICATIONS

SOLEIL II storage ring will be equipped with 180 BPMs: 7 per 4BA section, 10 per 7BA section and 4 additional BPMs in the two long straight sections (Fig. 1).

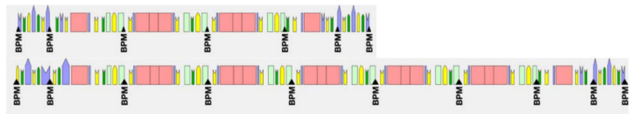


Figure 1: 4 BA cell (up) and 7 BA cell (down), and the beam position monitor location on the SOLEIL II lattice.

The main BPM specifications are listed in Table 2.

Table 2: Main Specification of the Beam Position Monitors

	Time scale/freq.	***Specifications***
Number of BPM		~180
BPM radius		16 mm
BPM resolution	@10 Hz @100 kHz TbT	1 µm@0.1 mA 50 nm@500 mA 100 µm@0.1 mA 1 µm@500 mA
Beam current dependence	0.1-20 mA in a single bunch	10 µm
Stability	One day One week	500 nm 1 µm
Absolute accuracy before BBA		<500 µs

BPM BLOCK MECHANICAL DESIGN

BPM Mechanical Integration

SOLEIL II vacuum chambers will have a drastically small inner diameter of 12 mm to allow high gradients in the quadrupoles and sextupoles. To keep the BPM body in the shadow of the bending magnets synchrotron radiation, their inner diameter will be enlarged to 16 mm. Systematic tapers upstream/downstream each BPM will ensure a smooth transition between the two pipe diameters.

A large part of the bending magnet synchrotron radiation power will be intercepted (and absorbed) by the vacuum chambers. To minimize the mechanical stress induced by the vacuum chambers during the thermalization of the machine, the straight section BPM will be isolated with bellows. In the arcs, due to high component density, only one bellow between two BPMs is foreseen. All the BPMs will be the fixed points of the vacuum chamber with rigid supports connected either to the ground (straight sections) or the girders (in the arcs).

To achieve the long-term stability requirements of 500 nm a day, 1 µm a week, and considering a temperature in the tunnel stabilized at ±0.1 °C, low thermal expansion stands will be considered in the straight sections. Invar is

Content from this work may be used under the terms of the CC BY 4.0 licence (© 2022). Any distribution of this work must maintain attribution to the author(s), title of the work, publisher, and DOI

ISBN: 978-3-95450-241-7 ISSN: 2673-5350 doi:10.18429/JACoW-IBIC2022-TUP09

Content from this work may be used under the terms of the CC BY 4.0 licence (© 2022). Any distribution of this work must maintain attribution to the author(s), title of the work, publisher, and DOI

the best candidate. As shown in Fig. 2, its thermal expansion would remain below 300 nm for a 1.2 m heigh stand.

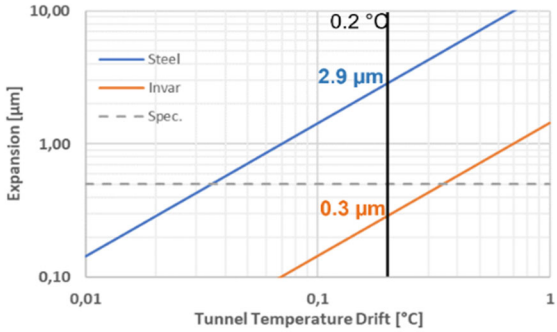


Figure 2: Expansion of 1.2 m heigh stand made of Invar (orange) and steel (blue). Steel stand would not fit our 24h stability requirement below 500 nm.

Button Design Optimization

The heating of the button due to the trapped fields is an important aspect to take care in the design. Optimization of the longitudinal impedance by adapted feedthrough geometry and materials allows to reduce significantly the power deposited on the button. Usual optimisation of the different parts of the feedthrough (button, ceramic and gap dimension) have been studied and published in [3].

Additional possible ways of improving the longitudinal impedance have been investigated for SOLEIL II button BPM. Based on the work carried out on the optimisation of the BPM impedance of Sirius [4], we compared the usual straight button shape (90° angle) with a conical one (65° angle) (Fig. 3).

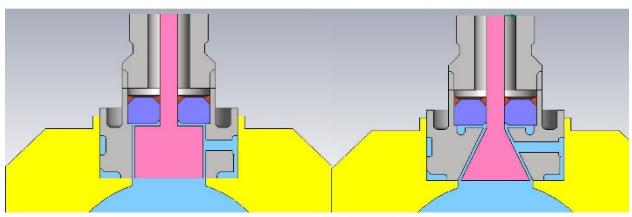


Figure 3: Schematics of two different button geometries: 90° button shape (left) and 65° (conical) button shape (right).

With the conical shape trapped modes are shifted to higher frequencies (Fig. 4).

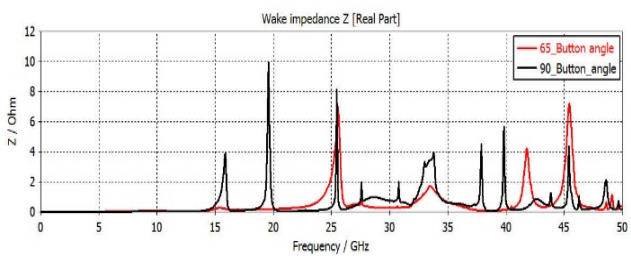


Figure 4: The real part of longitudinal impedance for different button geometry: black 90° button angle, red 65° button angle computed by CST Studio Suite [5].

SOLEIL II main operational mode will be 500 mA distributed uniformly in the 416 bunches. Bunches will be lengthened up to about 30 ps rms using a harmonic RF cavity. In case of a failure of this cavity, the power deposited on the BPM for a bunch length of 10 ps rms has also been studied.

For bunch length of 10 ps rms, the conical shape button will have 37% less power deposited compared to the straight one. For bunch length of 30 ps rms, the conical button is slightly worse than the 90° one but deposited power remains very low (0.15 W on the 4 buttons). (See Table 3).

Table 3: Power Loss Versus Button Shape

Button shape	conical	straight
Pl(mW) @(σ=30 ps rms)	150	100
Pl(mW) @(σ=10 ps rms)	2200	3020

The calculation of the spectral distribution of the power dissipated in the BPM shows that significant peaks are around 15 and 20 GHz for the straight button (Fig. 5), while for the conical button the peak is around 25 GHz. The maximum amplitude of the spectrum is three times greater for straight button than the conical button (0.36 W against 0.12 W).

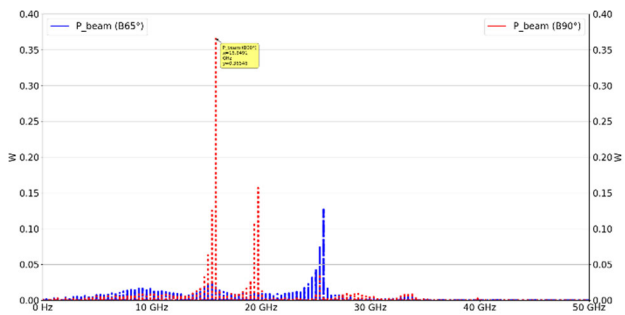


Figure 5: The spectral distribution of the power dissipated in the BPM (blue) for the 65° button and (red) 90° button.

3D simulations of the trapped mode surface current at 25 GHz for 10 ps rms bunch length confirm that the charge circulation at this frequency is well located on the button surface (Fig. 6).

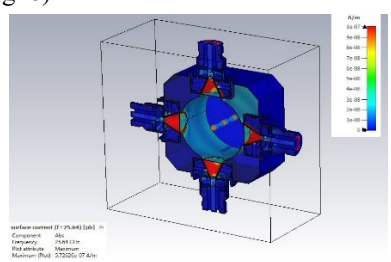


Figure 6: Trapped mode at 25 GHz for 10 ps rms bunch length.

Materials Considerations

When the trapped modes are excited, circulating charges around the button and its housing will heat the materials.

ISBN: 978-3-95450-241-7 ISSN: 2673-5350 doi:10.18429/JACoW-IBIC2022-TUP09

The distribution of deposited power is made accordingly to the conductivity of the materials used for the button and its body. This is proportional to the ratio of the square roots of electrical conductivity [6]: if the materials are identicals, the power is equally distributed, but if the electrical conductivity of the button is higher than the one of the body, the power deposition will be enhanced on the body instead of the button. For example, in the case of molybdenum button and stainless-steel body only 26% of the heating power will go on the button (Table 4). On the contrary a low conductivity material should be avoided for the button.

Table 4: Distribution of Power Deposited in the Button According to the Materials

Body \ Button	Molybdenum	Copper	316LN
Molybdenum	50%	46%	75%
Copper	64%	50%	85%
316LN	26%	15%	50%

Chromium Zirconium Copper (CuCrZr) is foreseen for SOLEIL II vacuum chamber material and eventually also for the BPM blocks. Copper is not adapted for a button housing due to its high electrical conductivity. Nevertheless since the feedthrough design has its own button housing, a different material as stainless steel can be chosen for this part.

The impedance simulation and the power loss in the BPM is much better for the CuCrZr body than the stainless steel. Impedance at low frequency (resistive wall) is much lower in the case of a BPM with the copper body compared to stainless steel (Fig. 7).

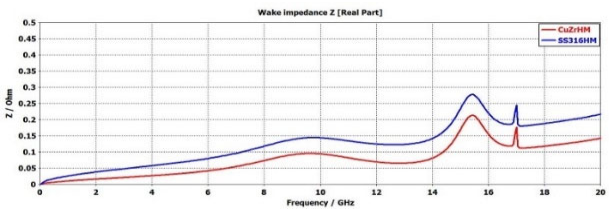


Figure 7: Real part of longitudinal impedance (in blue 316LN and in red CuCrZr).

The calculation of the dissipated power in Table 5 shows a very significant difference between the two materials.

Table 5: Total power loss versus BPM body's materials (button is in molybdenum, and button housing in stainless steel)

Power loss	SS316LN	CuCrZr
σ=30 ps rms (mW)	320	150
σ=10 ps rms (mW)	3000	2200

PROTOTYPING

To validate the mechanical design of the feedthrough and its integration in the BPM body, we have manufactured a batch of twelve buttons based on our design. (Fig. 8).

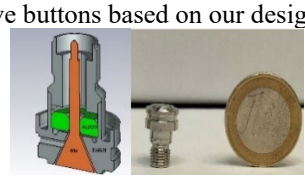


Figure 8: New BPM Feedthrough. The button diameter is 5 mm and the gap between buttons and its housing is 200 µm.

Metrology

Careful metrology has been carried on to check the mechanical tolerances and qualify the mechanical manufacturing. With such small pieces, traditional mechanical metrology tools are not well adapted, and we employed optical methods to measure the different dimensions like the button diameter and flatness, its concentricity and retreat with respect to its housing. Microscope pictures and images analyse software [7] has been used in addition to interferometer measurements (Fig. 9).

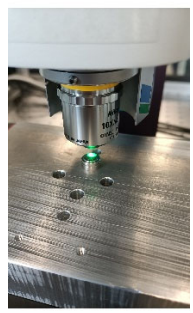


Figure 9: White light Interferometry (WLI) measurement of the button flatness and position.

The measurements show that some buttons present a tilt with respect to the external body (Fig.10).

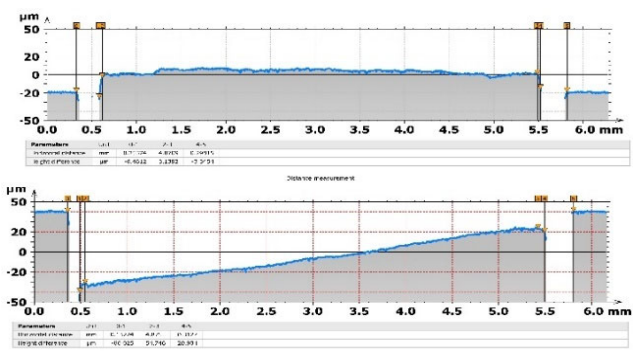


Figure 10: Flatness observed to button up good flatness and down bad flatness.

This tilt directly affects the gap between the button and its body. This variation of the gap is confirmed by microscope observations (Fig. 11). This tilt is due to a mechanical shift of the button during the brazing process. Future

Content from this work may be used under the terms of the CC BY 4.0 licence (© 2022). Any distribution of this work must maintain attribution to the author(s), title of the work, publisher, and DOI

ISBN: 978-3-95450-241-7 ISSN: 2673-5350 doi:10.18429/JACoW-IBIC2022-TUP09

Content from this work may be used under the terms of the CC BY 4.0 licence (© 2022). Any distribution of this work must maintain attribution to the author(s), title of the work, publisher, and DOI

design will be adapted in order to improve the way of maintaining the button at the right position at brazing.

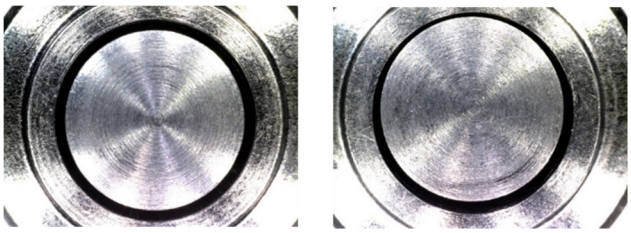


Figure 11: Microscope picture of two buttons, one with a good concentricity (left) and another one with an important concentricity error due to a tilt of the button (right).

Capacitance Measurement

Button capacitance has been measured with a Time Domain Reflectometer (TDR). All buttons shown a similar capacitance (~4 pF) except the one that had the biggest concentricity error for which the capacitance is sensitively different (5.3 pF) (Fig. 12).

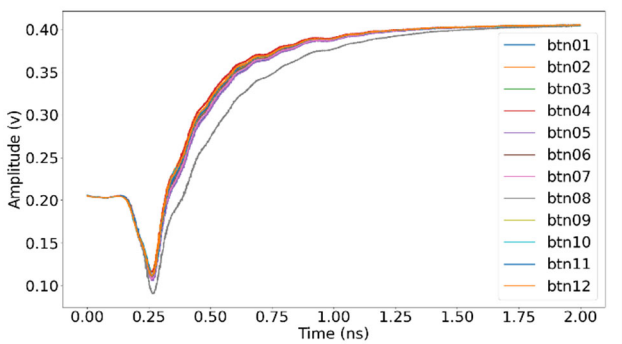


Figure 12: Button capacitance measurement with TDR.

This measure will allow us to relax certain tolerances such as button concentricity, tilt and gap imposed for the future buttons manufacturing.

Button Welding

Two batches of 4 buttons have been selected depending on their metrology measurements. Each batch has been welded on a BPM block manufactured in-house. A dedicated mechanical positioning system prevents any displacement of the button during the welding procedure (Fig. 13).



Figure 13: The welding process(left), the current BPM size and the new BPM (right).

BPM Calibration

The electrical offset of the BPM has been measured with the Lambertson method [8]. This method uses the coupling between buttons/electrodes to determine the gain factors of each electrode. The ratios between gain factors provide the difference between the mechanical and electrical centers. The measurement has been made at 352 MHz with a 4-port Vector Network analyser (Fig. 14). Table 6 summarizes the S-parameter matrix for the BPM prototype 1.

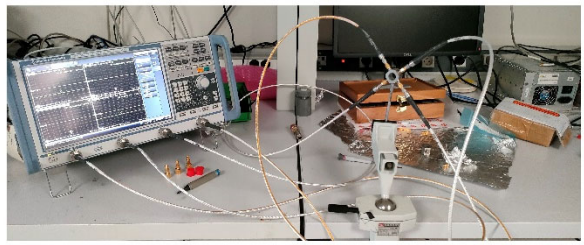


Figure 14: The electrical offset measurement setup.

Table 6: S Parameter Matrix (dB) for BPM Prototype N°1

Port	1	2	3	4
1		-81.6979	-89.1576	-81.5442
2	-81.7720		-81.5876	-89.7595
3	-89.1834	-81.6291		-81.4207
4	-81.5856	-89.7807	-81.4792	

Table 7 resumes the electrical offset obtained for both prototypes.

Table 7: Electrical Offset Calculated from S Parameter Matrix

	Prototype1	Prototype 2
X Offset	20 µm	2 µm
Y Offset	-45 µm	10 µm

Resulting offsets are very small and well within specifications (absolute accuracy of the BPM system <500 µm). There is nevertheless a discrepancy with those expected from the button metrology measurements and their arrangement on the BPM blocks. Investigations are ongoing to understand the reason.

CONCLUSION

The manufacturing of these buttons is a first step in the validation of the conical shape design. Several ways of improvements have already been identified with the manufacturer for a second design version, working on the mechanical but also on the production cost aspects.

In the near future, vacuum flanges will be welded on the BPM block prototypes for vacuum testing, as well as for NEG coating validation.

ACKNOWLEDGMENT

The authors would like to express our very great appreciation to Dr Kubsky and his team for their valuable and constructive suggestions during the button's metrology. We would like also to thank the mechanical and vacuum groups for their participation in the project.

ISBN: 978-3-95450-241-7 ISSN: 2673-5350 doi:10.18429/JACoW-IBIC2022-TUP09

REFERENCES

[1] Synchrotron SOLEIL "Conceptual Design Report", https://www.synchrotron-soleil.fr/en/file/13803/download?token=OUzsp46P

[2] A. Loulergue *et al.*, "TDR Baseline Lattice for the Upgrade of SOLEIL", in *Proc. IPAC'22*, Bangkok, Thailand, Jun. 2022, pp. 1393-1396. doi:10.18429/JACoW-IPAC2022-TUPOMS004

[3] M. El Ajjouri, F. Alves, A. Gamelin, and N. Hubert, "Preliminary Studies for the SOLEIL Upgrade BPM", in *Proc. IBIC'21*, Pohang, Korea, Sep. 2021, paper MOPP31, pp. 128

[4] H. O. C. Duarte, S. R. Marques, and L. Sanfelici, "Design and Impedance Optimization of the SIRIUS BPM Button", in *Proc. IBIC'13*, Oxford, UK, Sep. 2013, paper TUPC07, pp. 365-368.

[5] https://www.3ds.com/products-services/simulia/products/cst-studio-suite/electromagnetic-systems/

[6] I. Pinayev and A. Blednykh, "Evaluation of Heat Dissipation in the BPM Buttons", in *Proc. PAC'09*, Vancouver, Canada, May 2009, paper TH5RFP014, pp. 3471-3472.

[7] https://www.digitalsurf.com/software-solutions/profilometry/

[8] W. X. Cheng, B. Bacha, and O. Singh, "NSLS2 Beam Position Monitor Calibration", in *Proc. BIW'12*, Newport News, VA, USA, Apr. 2012, paper MOPG022, pp. 77-79.

Content from this work may be used under the terms of the CC BY 4.0 licence (© 2022). Any distribution of this work must maintain attribution to the author(s), title of the work, publisher, and DOI

ISBN: 978-3-95450-241-7 ISSN: 2673-5350 doi:10.18429/JACoW-IBIC2022-TUP10

DEVELOPMENT OF A NEW MEASUREMENT SYSTEM FOR BEAM POSITION PICKUPS IN THE LINAC AND BEAM ENERGY MEASUREMENT (TIME OF FLIGHT) IN THE MEBT FOR MedAustron

M. Repovz†, M. Cerv, C. Kurfuerst, G. Muyan, S. Myalski, A. Pozenel, C. Schmitzer, M. Wolf
EBG MedAustron, Wiener Neustadt, Austria
A. Bardorfer, B. Baricevic, P. Paglovec, M. Skabar
Instrumentation Technologies, Solkan, Slovenia

Abstract

The MedAustron Ion Therapy Centre is a synchrotron-based particle therapy facility which delivers proton and carbon beams for clinical treatment. Currently, the facility treats roughly 44 patients per day and is improving its systems and workflows to further increase this number. MedAustron was commissioned and is operational without fully integrated systems for measurements of "time of flight" (beam energy) in the MEBT and beam position in the LINAC. This paper presents the newly developed system for these use cases, which will improve the overall commissioning and QA accuracy. It will unify the hardware used for the cavity regulation in the injector low level radio frequency system LLRF and the synchrotron LLRF. It will furthermore be used for SYNC pickups, Schottky monitors and the RF knock-out exciter. The new system is based on the CotS MicroTCA platform, which is controlled by the MedAustron Control System based on NI-PXIe. Currently it supports fiber-optic links (SFP+), but other links (e.g. EPICS, DOOCS) can be established. The modular implementation allows for integration with other components such as motors, amplifiers, or interlock systems and will increase the robustness and maintainability of the accelerator.

INTRODUCTION

After the Low Energy Beam Transfer (LEBT) line the beam is pulsed (with an electrostatic deflector) and accelerated with an RFQ and an Interdigital H-Mode Drift Tube Linac (IH-DTL) cavity (part of the linear accelerator) followed by the Medium Energy Beam Transfer (MEBT) line. Starting after the IH-tank and continuing along the complete MEBT line the Phase Probes (PHPs) for beam energy measurements are placed (4 locations in total) whilst to determine the beam position a Four-Button Probe is located at the entrance of the IH-tank.

These measurement devices are now integrated into a new system that has been developed in collaboration with Instrumentation Technologies.

The developed system description and operation will be elaborated, followed by the first measurement results and concluded by the advantages and disadvantages of the selected implementation as well some short information about the outlook.

SYSTEM DESCRIPTION

For the readout electronics and data processing an off the shelf piece of hardware has been selected. One of the requirements was the need to use the same electronics for beam position measurement with the pickups in the LINAC, beam energy measurement (Time of Flight) as well as Injector LLRF [1].

The hardware selected is based on the MicroTCA.4 architecture for which Vadatech is the company that provides all the needed components. The crate foreseen to be used for the complete injector system is presented in Fig. 1 with all its connections.

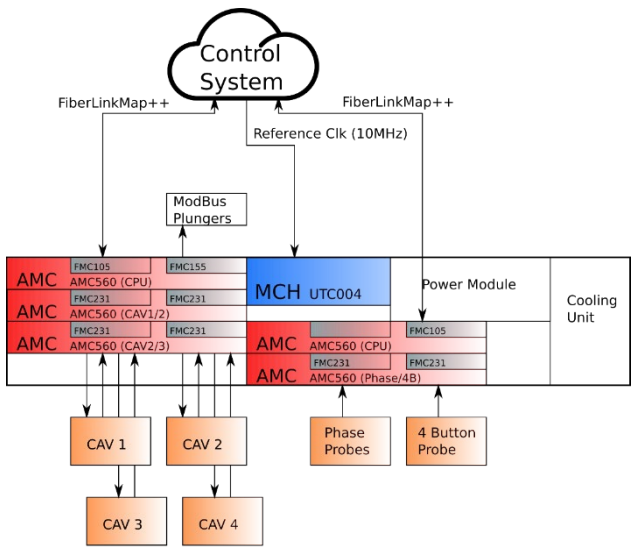


Figure 1: The MicroTCA crate and its connections.

For the four Phase Probes one FMC231 card [2] is needed and for the Four-Button Probe an additional

FMC231 card on the same AMC560 card [3] is required. For communication with the MedAustron control system a proprietary protocol on FiberLinkMap++ is used which goes via SFP+ optical connection on a second AMC560 card equipped with a FMC105 card [4]. The other AMC560 cards with an MC231 and an FMC105 are to be used for the injector low lever RF.

† matjaz.repovz@medaustron.at

Content from this work may be used under the terms of the CC BY 4.0 licence (© 2022). Any distribution of this work must maintain attribution to the author(s), title of the work, publisher, and DOI

ISBN: 978-3-95450-241-7 ISSN: 2673-5350 doi:10.18429/JACoW-IBIC2022-TUP10

OPERATION

In this paragraph operation of the system is presented (Fig. 2).

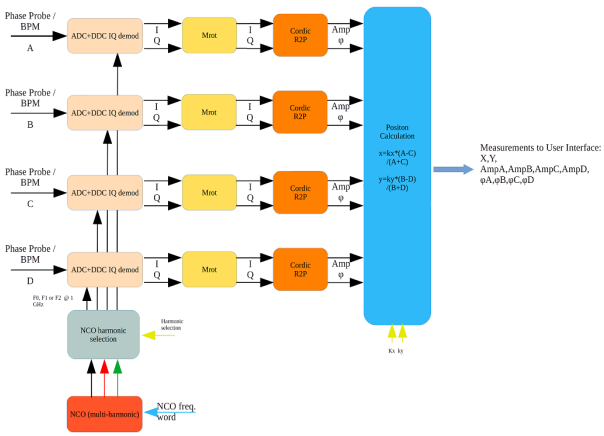


Figure 2: Block Diagram of the Digital Signal Processing scheme used.

With the relatively low Linac frequency of 216.816 MHz, a direct sampling approach is used. The RF signals generated by the Phase Probes and the Four-Button Probe are amplified in close proximity to the probes, sent to the MicroTCA crate and digitized without any specific analog front end. The same group delay for all probes is ensured by using exactly the same cable lengths and amplifiers.

After the direct sampling analog to digital conversion the signals are converted to baseband by downmodulation with a numerically controlled oscillator. The resulting in-phase and -quadrature signals are then filtered in multiple stages and converted to amplitude and phase information individually for each Phase Probe or each button of the Four-Button Probe.

Knowing the distance between the Phase Probes the phase information gathered in the previous steps can be used to calculate the velocity of the particles and from there the energy of the particles.

On the other hand, the amplitudes measured by the Four-Button Probe can be used to calculate the position of the beam inside the beam pipe. The basic assumption for this calculation is that the two opposing buttons generate the same amplitude signal if the beam passes exactly in the center of the beam pipe.

MEASUREMENTS

The Time of Flight measurements shown here were acquired during an amplitude scan of the IH-DTL. The results show a good energy resolution but also multiple issues with the beam, which remain to be investigated. First, the currently used LLRF + amplifiers do not properly regulate either amplitude or phase in the IH-DTL, resulting in a huge energy variation during single pulses. Second, with different energy outputs of the IH-DTL, the phase of the debuncher located between the second and the third phase probe has to be adjusted. As this wasn't done during the amplitude scan, the debuncher changes the energy considerably for some IH output energies.

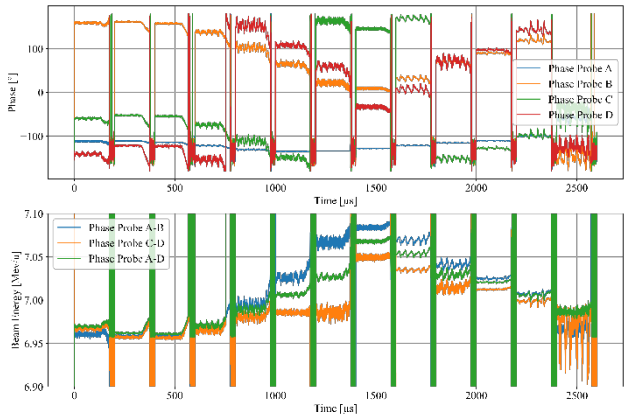


Figure 3: Phase measurements of the 4 Phase Probes available (Top); Calculated Particle Energy (Bottom).

For the position measurements the first results are not as promising as for the ToF measurements. First of all, a lot of crosstalk was seen from the IH-DTL (the Four-Button probe is directly mounted at the entrance of the IH). Therefore the presented measurements were taken at the second harmonic. The second issue found is that the calibration data for the used probe is outdated and questionable. Currently it is unknown if this calibration was never measured or if the data was lost in the last ten years without using this measurement device. Unfortunately without valid calibration data it is unknown which difference between the two opposing probes corresponds to which absolute position offset.

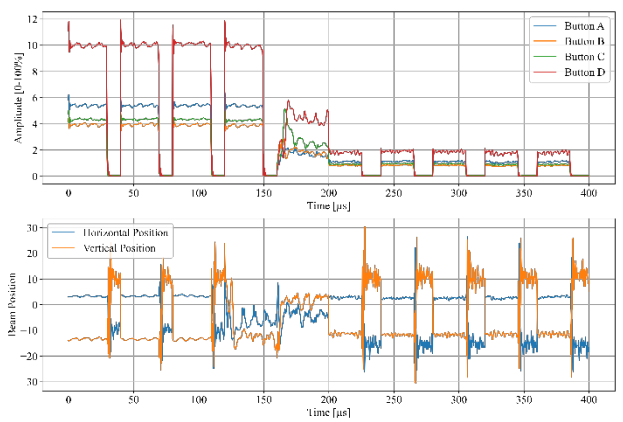


Figure 4: Amplitude Measurements of the 4 Buttons in the BPM measured at the 2nd Harmonic (Top); Beam Position without proper scaling (Bottom); Particle Species changed after 200 µs.

SUMMARY

The system is already in use for beam verification and is being used for Helium beam commissioning [5]. With the first measurements performed some unexpected beam behaviour was observed which needs to be further investigated.

Content from this work may be used under the terms of the CC BY 4.0 licence (© 2022). Any distribution of this work must maintain attribution to the author(s), title of the work, publisher, and DOI

ISBN: 978-3-95450-241-7 ISSN: 2673-5350 doi:10.18429/JACoW-IBIC2022-TUP10

The operation (measurements) is currently only possible via a local web interface (see Fig. 5). To have the system available via the MedAustron Accelerator Control System (MACS) some integration work is needed, which is foreseen as a next step.



Figure 5: Amplitude and TOF measurement with "local" web user interface.

To measure beam position of the IH-DTL and TOF a manual procedure which involved corrections and had errors was used. With the new measurement system this is simplified and makes the four-button probe and phase probes much more usable.

OUTLOOK

The platform selected is also foreseen to be used for measurement of the beam position in the Synchrotron where shoebox pickups are installed. The beam position measurement itself has already been proven, thus (if needed) an adaptation to a new electrical interface will be done. In addition, the same hardware is foreseen to be used also for Schottky pick-up measurements as well as synchrotron low level RF (LLRF) and RF knock-out extraction. A simplified block diagram of the synchrotron LLRF with the position feedback from the shoebox pickups is presented in Fig. 6.

Having the same hardware for all the mentioned systems will bring a reduction of operational costs by having a lower number of different hardware components in use. This will drastically lower the number of different required spare parts as well as number of hours spent on trainings for different components.

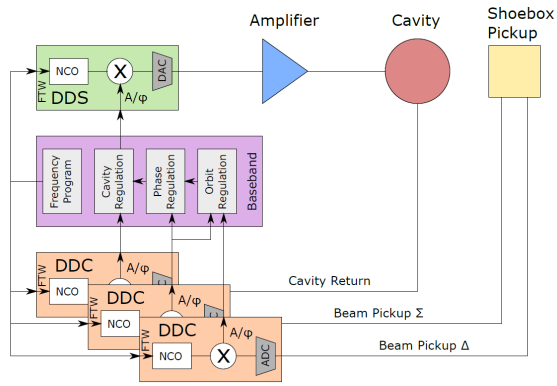


Figure 6: Block diagram of Synchrotron LLRF in connection with Shoebox pickup.

REFERENCES

[1] M. Wolf *et al.*, "Development and integration of a new low-level RF system for MedAustron", presented at the LINAC'22, Liverpool, UK, Aug. 2022, paper THOPA12, to be published.

[2] FMC231 Datasheet, https://www.vadatech.com/media/FMC231_FMC231_Datasheet.pdf

[3] AMC560 Datasheet, https://www.vadatech.com/media/AMC560_AMC560_Datasheet.pdf

[4] FMC105 Datasheet, https://www.vadatech.com/media/FMC105_FMC105%20Datasheet.pdf

[5] N. Gambino *et al.*, "First injector commissioning results with helium beam at MedAustron Ion Therapy Center", *J. Phys.: Conf. Ser.*, vol. 2244, p. 012109, 2021. doi:10.1088/1742-6596/2244/1/012109

Content from this work may be used under the terms of the CC BY 4.0 licence (© 2022). Any distribution of this work must maintain attribution to the author(s), title of the work, publisher, and DOI

ISBN: 978-3-95450-241-7 ISSN: 2673-5350 doi:10.18429/JACoW-IBIC2022-TUP11

A CRYOGENIC RF CAVITY BPM FOR THE SUPERCONDUCTING UNDULATOR AT LCLS*

C. Nantista†, P. Krejcik, A. Haase, SLAC National Accelerator Laboratory, Menlo Park, CA, USA.

Abstract

The new superconducting undulator beamline at LCLS requires the BPMs to be operated at cryogenic temperatures alongside the undulator magnets. They are used for beam-based alignment of the undulator magnets and quadrupole and require submicron resolution to achieve good FEL performance. This is to be achieved with X-band RF cavity BPMs, as is done now on the permanent undulator beamline. However, operating the cavities at cryogenic temperatures introduces significant challenges. We review the changes in RF properties of the cavities that result from cooling and how the design is changed to compensate for this. This includes a novel approach for employing a rectangular cavity with split modes to separately measure the X and Y position without coupling.

INTRODUCTION

A new superconducting undulator (SCU) is being installed on the hard x-ray undulator beamline (HXR) at the LCLS-II free electron laser at SLAC. The first two cryogenic modules will be installed at the end of the existing HXR permanent magnet undulator (PMU) beamline so that the FEL performance of the SCU can be measured and compared.

SCUs have been used extensively in storage rings as insertion devices but this will be the first time such a device is used in the x-ray FEL beamline at SLAC. An SCU has advantages in an FEL because of its tunability, and stronger magnetic fields in shorter period length undulators. These characteristics will generate brighter, shorter wavelength x-rays than a PMU, with a shorter FEL gain-length, resulting in a more compact beamline.

In order to realize these advantages it is necessary to install the SCU together with the other beamline components that integrate it into an FEL, including correction coils, phase shifter, quadrupole and BPM. All these components are considered necessary for the prototype module as well so that its performance can be quantitatively assessed. The BPM, which is the subject of this paper, is particularly important because it allows beam-based alignment (BBA) of the undulator beamline to be performed with sufficient precision to allow optimum FEL performance to be achieved. Submicron BPM resolution is required with bunch charges of 100 pC so that the BBA will result in full overlap of the electron and photon beams within micron tolerances.

The shorter gain length advantage of the SCU can only be exploited if all the beamline components are compactly arranged on the beamline without wasting any space with cold to warm transitions. That means that all components, including the BPM, must be mounted inside the cryomodule and operated at liquid He temperatures, as shown in Fig. 1.

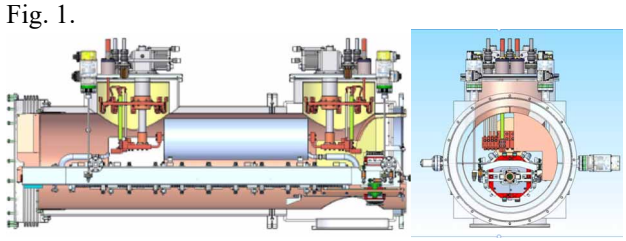
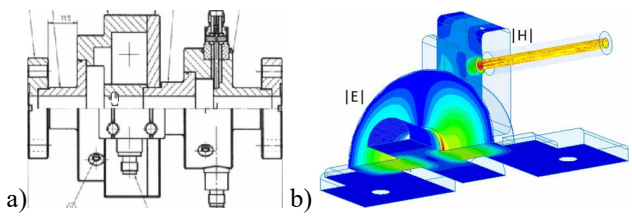


Figure 1: Cutaway and end views of the cryomodule containing the SCU and quadrupole (red) and BPM (copper) at the RH downstream end.

BPM DESIGN CONSIDERATIONS

The LCLS-II free electron laser at SLAC requires monitoring of the beam position with sub-micron level resolution in both x and y. At LCLS we have successfully used X-band RF cavity beam position monitors, or RFBPMs, of a unique configuration, illustrated in Fig. 2, whose design was developed over the last couple of decades [1-3]. It consists of two independent resonant cavities, dipole and reference, with signals coupled out through coaxial vacuum feed-throughs. A distinguishing feature benefiting sensitivity is the magnetic coupling of the dipole cavity fields into side waveguide stubs in a way that shields the pickups from the monopole mode [4].



a) b)

Figure 2: a) cutaway and external view of the LCLS room temperature RFBPM geometry and b) field simulation of dipole cavity coupling [5].

Several factors prevent us taking this RFBPM design and simply mounting it inside the cryomodule. First, the dimensional changes as it is cooled to 40°K produce a large shift in the resonance frequency that must be compensated by machining the cavity to different dimensions at room temperature. Note, that although the SCU coil must operate at 4.2°K, the adjacent components such as the quadrupole and BPM are only cooled to the temperature of the cryomodule thermal shield at 40°K.

The expansion coefficient also decreases exponentially with temperature, as shown in Fig. 3. The coefficient is so small below about 40°K that contraction effectively stops below that temperature, allowing us to accurately predict the machining dimensions at room temperature in order to

* Work supported by U.S. Department of Energy under Contract Numbers DE-AC02-06CH11357.
† nantista@slac.stanford.edu

Content from this work may be used under the terms of the CC BY 4.0 licence (© 2022). Any distribution of this work must maintain attribution to the author(s), title of the work, publisher, and DOI

ISBN: 978-3-95450-241-7 ISSN: 2673-5350 doi:10.18429/JACoW-IBIC2022-TUP11

achieve the correct tuning frequency at cryogenic temperatures.

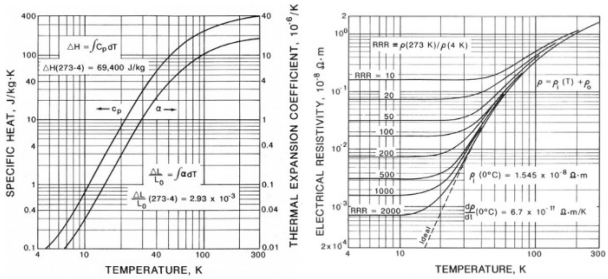


Figure 3: Thermal expansion coefficient (left) and resistivity (right) are shown as a function of temperature for copper.

Secondly, although there is no intention to create a superconducting BPM, the conductivity of the copper decreases significantly at cryogenic temperatures so that the cavity Q factor, and the cavity coupling must be recalculated for the new design so that the loaded Q_L factor is within design requirements. The resistivity of copper is plotted as a function of temperature in Fig. 3, where it is seen to plateau below about 20°K. The residual resistance ratio (RRR) equal to the ratio of its resistivity at 293°K to the resistivity at 4.2°K depends on the composition and purity of the copper used.

The third design consideration is that the RFBPM once mounted in the cryomodule cannot be accessed to adjust the mechanical tuners to adjust either the frequency or cross-coupling of the cavity. For this reason we have developed a design that requires fewer iterations of tuning adjustments to achieve the desired resonant frequency with minimal X-Y coupling. The present LCLS RFBPM evolved from an elegant design concept [4] in which a single, cylindrical dipole cavity is used to measure both the X and Y dipole modes. Separate X and Y coupling slots in this design ensure that only one mode in each plane is coupled to the output port. This concept works perfectly only if the dipole cavity remains perfectly symmetric.

In practice, the LCLS RFBPM has four radial tuning screws that dimple the inner cavity wall so that the X and Y resonant frequencies can be tuned to compensate for machining and brazing imperfections. These adjustments break the symmetry of the cavity and it becomes difficult to simultaneously tune a single cavity to obtain the correct X and Y frequencies as well as minimizing the coupling that gets introduced between X and Y when the frequencies are adjusted. An iterative procedure was developed between SLAC and PAL for using the four tuning screws per dipole cavity, at the 45° positions, that converged in most cases to achieve frequencies and coupling ratios within the specified tolerances [5]. In our new cryogenic design, X-Y signal independence is determined by cavity orthogonality achieved in fabrication and unaffected by cavity tuning. Thus the need for iterative tuning is avoided.

The fourth and final design consideration was motivated by mechanical practicality. The present LCLS RFBPMs are fitted with 6 vacuum, SMA coaxial feedthroughs which are quite fragile and easily developed vacuum leaks during handling. Our preliminary testing of a spare RFBPM on a test stand showed that the feedthroughs are also subject to failure when cryogenically cooled. For this reason, in our new design we will reduce the number of ports from 6 to 3 and we will replace the feedthroughs with more robust waveguide vacuum windows, with commercial waveguide-to-coax adapters on the non-vacuum side.

In addition to halving the vacuum interfaces and minimizing cost and complexity, this reduction from two ports per mode to one also addresses an RF concern. In use, only one port of each pair in the old design is cabled, while the other is terminated with a load to maintain field symmetry. Change in the match of such loads at cryogenic temperature could affect the cavity frequencies and electrical centers.

Double ports were useful (though not required) for Q_L measurement and, with a single dipole cavity, necessary for symmetry and for tuning out cross-coupling.

One final benefit might be added. Though not often a problem, a few units of the two-cavity RFBPM design were found to be unusable due to excessive frequency separation of the X and Y dipole modes, which cannot be tuned out via the 45° tuning pins. Going to three cavities, with dipole modes independently tunable avoids this problem.

DESIGN WITH DISCRETE POSITION CAVITIES

The distinguishing feature of our new design is that we now replace the single, cylindrical dipole-mode cavity with two rectangular dipole-mode cavities to measure the X and Y positions separately. The rectangular shape ensures that the two dipole modes in each cavity are widely separated in frequency, so that only one dipole mode in each plane is at the 11.424 GHz band of the receiver electronics.

The cost to pay is that the RFBPM must now have three cavities instead of two, and the resultant beamline length is somewhat longer, given the requirement of several beampipe diameter cavity separation. The layout of the internal volume of the two dipole-mode cavities and cylindrical monopole-mode reference cavity is shown in Fig. 4.

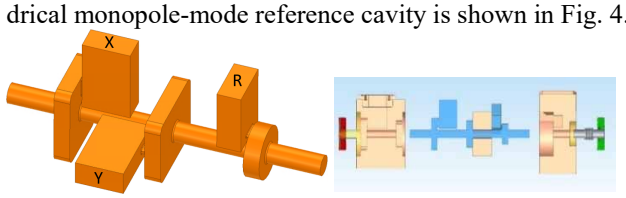


Figure 4: The RF cavity BPM comprises two rectangular X and Y dipole mode cavities and a cylindrical reference cavity.

Cavity RF Designs

Assuming a modest RRR of 50, consistent with the experience of other programs, and an operating temperature of 20 K, the right plot of Fig. 3 predicts a copper resistivity of $\rho = \sim 0.031 \times 10^{-8}\ \Omega$m, compared to a value of $1.71 \times 10^{-8}\ \Omega$m at room temperature, giving a boost in Q_0 ($\propto \rho^{-1/2}$) of ~7.43.

To assure sufficient signal decay between bunches, the cavities of the new cryo RFPBM need to retain roughly the

Content from this work may be used under the terms of the CC BY 4.0 licence (© 2022). Any distribution of this work must maintain attribution to the author(s), title of the work, publisher, and DOI

ISBN: 978-3-95450-241-7 ISSN: 2673-5350 doi:10.18429/JACoW-IBIC2022-TUP11

same loaded quality factor $Q_L = (1/Q_0 + 1/Q_e)^{-1}$ in operation as specified for the old design, specifically 1,900 – 3,000. With the significant increase in Q_0, this means Q_e must be reduced by larger external coupling.

Thus, more of the energy deposited by an electron bunch will flow out of the cavity, and with the elimination of a second port discussed above, all emitted energy will go into the diagnostic signal, rather than half being wasted in a load. This will help compensate the increased losses anticipated in bringing the signal out of the cryostat.

Both new cavity designs retain the 0.25″ length of the old design. The beampipe diameter, however, was dropped from 9 mm to 8 mm to limit required cavity separation.

The reference cavity, used for determining the sign of the position measurements and scaling for bunch charge, retains the basic pillbox geometry, with magnetic coupling to a WR75 waveguide machined to overlap behind it as shown in Fig. 5. A transverse slot near the perimeter of the cavity face couples its azimuthal H field to the transverse H field near the waveguide short.

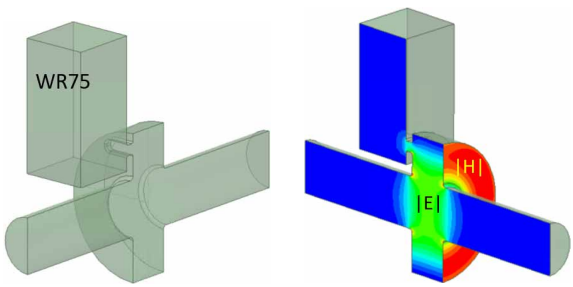


Figure 5: Half views of the reference cavity.

With the resistivity above, simulation of this cavity with Ansoft HFSS yields $Q_0 = 48{,}170$. The coupling slot was adjusted to give simulated $Q_e = 2{,}363$ and $Q_L = 2{,}240$. The cavity diameter was fine tuned to set the TM_{010} resonance at 11.424 GHz.

The new dipole cavities are rectangular with a 1.2 aspect ratio to break the orthogonal polarization degeneracy and rounded corners. A central vertical slot couples the vertical H field of the TM_{210} mode through one face into the side of a WR75 port, as shown in Fig. 6.

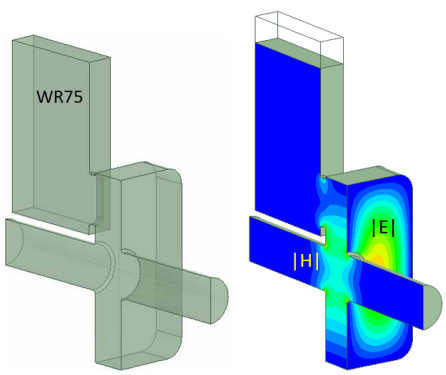


Figure 6: Half views of the dipole cavity.

An unloaded quality value of $Q_0 = 50{,}770$ was calculated with cryogenic resistivity, and the slot then adjusted to give simulated $Q_e = 2{,}332$ and $Q_L = 2{,}227$. The cavity size was adjusted to restore a frequency of 11.424 GHz. The nearest parasitic modes, TM_{120} and TM_{130}, are respectively 1.10 GHz lower and 3.46 GHz higher, and neither one's fields can geometrically couple to the waveguide.

The effective offset $(R/Q)_\perp$ of the new dipole cavity is calculated to be 3.6 Ω/mm², comfortably above the old >2 Ω/mm² specification. The decay time constant for all cavities is $\tau = \sim 62$ ns, satisfactory for the ~1 μs minimum bunch spacing of LCLS-II. With Q_e heavily dominating, anything from 50% cryogenic increase to infinite Q_0 would satisfy the Q_L specification range, so our assumption on the RRR is not crucial.

The couplings at operating temperature of the reference and dipole cavity designs are $\beta = \sim 20.4$ and 21.8, respectively, but at room temperature they will be only ~2.74 and 2.93, facilitating cold test characterization.

Vacuum Window

The vacuum window to be incorporated into each of the three signal waveguides (one per cavity), is a standing wave block window, with thickness adjusted for matched transmission. It is centered in a short section of the WR75 port waveguide stub with thinned walls and rounded corners to facilitate brazing. Figure 7 shows the geometry and the simulated return loss.

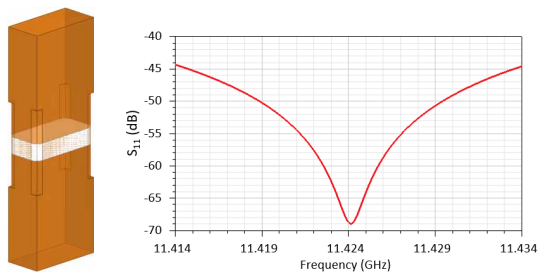


Figure 7: WR75 ceramic waveguide window design with plot of the $|S_{11}|$ match.

Cryogenic RF Test

A spare RFBPM of the old design was installed in an experimental cryostat and brought from room temperature to ~7 K, with coaxial connections to a network analyzer to measure resonant frequency shifts. Results, presented in Fig. 8, agreed well with established thermal expansion data for copper, showing a frequency rise of ~0.33%, flat below 40 K. Our design models will be scaled up in size accordingly for machining. Though its match is fairly broad, the design of the window ceramic will also need to be adjusted to help counter the alumina contraction.

Due to mismatches and lossy cables (stainless rather than copper for thermal conductivity considerations), measurements were not sensitive nor clean enough to experimentally verify the estimated change in Q_0 during this test.

Content from this work may be used under the terms of the CC BY 4.0 licence (© 2022). Any distribution of this work must maintain attribution to the author(s), title of the work, publisher, and DOI

ISBN: 978-3-95450-241-7 ISSN: 2673-5350 doi:10.18429/JACoW-IBIC2022-TUP11

Content from this work may be used under the terms of the CC BY 4.0 licence (© 2022). Any distribution of this work must maintain attribution to the author(s), title of the work, publisher, and DOI

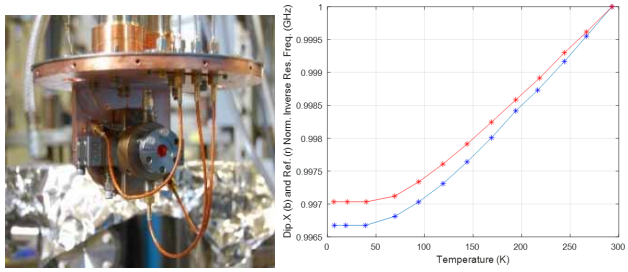


Figure 8: A spare X-band RFBPM mounted for insertion in a cryostat and normalized plots of the inverse measured resonance frequencies of the cavities during cooldown.

Mechanical Design

The cavities will be machined out of blocks of copper, with waveguide coupling slots to the ports where waveguide windows are mounted, as shown in Fig. 9.

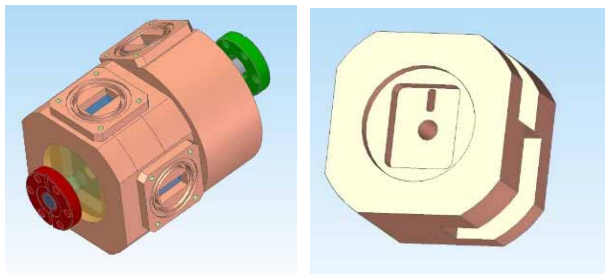


Figure 9: View of the brazed assembly (left), and a detail of the machining of a rectangular cavity with a single waveguide coupling slot.

Each dipole cavity, as well as the reference cavity, now has only one tuning screw (not shown in the preliminary CAD images) to adjust the resonant frequency, since the out-of-plane frequency mode is no longer important and has no effect on X-Y coupling. The tuning procedure is to tune the cavities on a test bench at room temperature to a frequency lower than the nominal 11.424 GHz by an amount Δf which has been calculated beforehand and experimentally confirmed, so that the correct tune is obtained at the cryogenic operating temperature. Our cryogenic testing shows that this frequency shift Δf is very repeatable within our operating tolerance.

The three windows will be fabricated separately and attached, after RF and vacuum testing, via weld flanges (not yet incorporated into Fig. 9). Waveguide-to-coax adaptors will be connected to the instrument-flanged ports, and three coaxial cables will connect the RFBPM to external feedthroughs on the cryomodule.

CONCLUSION

We have developed a new RF cavity BPM design for installation within a superconducting undulator cryomodule. Consideration of thermally induced changes in frequency and conductivity as well as lessons learned and accessibility has led to significant changes from the design successfully employed at room temperature in the LCLS-II undulator beamlines. Most notably, the dipole modes are separated into distinct cavities and fewer, more robust windows are employed. The effort toward producing a prototype is currently underway.

ACKNOWLEDGEMENTS

The authors would like to acknowledge the preliminary design exploration of Changbum Kim, the technical effort of Bobby McKee, the cryogenic test accommodation of Paul Welander and the mechanical design contribution of Stephen Boo.

REFERENCES

[1] R. Johnson *et al.*, “An X-Band Cavity for a High Precision Beam Position Monitor”, in *Proc. DIPAC’03*, Mainz, Germany, May 2003, paper PT13, p. 196.

[2] A. Young *et al.*, “Performance Measurements of the New X-Band Cavity BPM Receiver”, in *Proc. IBIC’13*, Oxford, UK, Sep. 2013, paper WEPC24, pp. 735-738.

[3] S. J. Lee *et al.*, “PAL-XFEL Cavity BPM Prototype Beam Test at ITF”, in *Proc. FEL’15*, Daejeon, Korea, Aug. 2015, pp. 468-470. doi:10.18429/JACoW-FEL2015-TUP043.

[4] Z. Li *et al.*, “Cavity BPM with Dipole-Mode-Selective Coupler”, in *Proc. PAC’03*, Portland, OR, USA, May 2003, paper ROAB004.

[5] C. D. Nantista *et al.*, “Performance of the SLAC-PAL-Vitzrotech X-band Cavity BPMs in the LCLS-II Undulator Beam Lines”, in *Proc. IBIC’21*, Pohang, Korea, Sep. 2021, pp. 136-139. doi:10.18429/JACoW-IBIC2021-MOPP34

ISBN: 978-3-95450-241-7 ISSN: 2673-5350 doi:10.18429/JACoW-IBIC2022-TUP12

FIRST APPLICATION OF A MULTIPROCESSING SYSTEM-ON-CHIP BPM ELECTRONICS PLATFORM AT SwissFEL

B. Keil†, R. Ditter, M. Gloor, G. Marinkovic, J. Purtschert
Paul Scherrer Institute, Villigen, Switzerland

Abstract

We have developed a new BPM electronics platform based on a MultiProcessing System-on-Chip (MPSoC). This contribution introduces the first application of the platform at the Paul Scherrer Institute (PSI), which is the cavity BPM system for the SwissFEL soft X-ray undulator beamline called "Athos", where a larger number of systems are now operational. Measurement results and differences to the predecessor system will also be presented.

INTRODUCTION AND MOTIVATION

PSI has several particle accelerator facilities, including, the High Power Proton Accelerator (HIPA), the Swiss Light Source (SLS), and SwissFEL, a hard X-ray free electron laser. The RF beam position monitors (BPMs) for the proton and electron beams of these accelerators [1-3] as well as the European X-ray FEL BPMs [4] have electronics - developed mainly by PSI - that were so far based on the VME64x form factor, with analog-to-digital converters (ADCs) using parallel data outputs.

However, for the BPMs of the latest SwissFEL undulator line called "Athos" [5] that generates soft X-rays as well as for future upgrades of SLS and HIPA BPMs, we decided to develop a new platform called "DBPM3". It has a form factor tailored to future PSI BPM systems based on MPSoCs and ADCs with multi-gigabit serial interconnect. MPSoCs integrate several performant CPUs, rich FPGA fabric, various external interfaces and high-speed interconnect on a single chip, enabling the design of more compact and cost efficient BPM systems.

Table 1: PSI Accelerators and RF BPM Systems

PSI Facility	BPM Type	Frequency		FPGA/ASIC Type
		Beam	BPM	
HIPA	Coil	50 MHz	100 MHz	2x Virtex-2 Pro & DDC-ASICs
SLS	Button	500 MHz	500 MHz	DDC-ASICs
Swiss-FEL Linac ...	Cavity (Two Resonators)	2-bunch ΔT=28ns 100 Hz	3.3 GHz	2x Artix-7/ 1x Kintex 7
... Aramis Undulators ...		1-bunch 100 Hz	4.9 GHz	
... Athos Undulators				1x Zynq UltraScale+ MPSoC

In the following sections, we describe the hardware, software and firmware architecture of the DBPM3 platform. Measurement results and commissioning experience of the first DBPM3 application, the Athos undulator cavity BPM system, are also presented. Besides Athos, we plan to use the DBPM3 platform also for the SLS 2.0 project [6], which is a major upgrade of SLS with a new low-emittance storage ring. Another application will be the upgrade of the 18 years old HIPA BPM electronics. Due to the smaller number of BPMs in Athos compared to SLS 2.0, Athos enabled us to get experience with the platform before producing larger quantities for SLS 2.0, where first beam is expected in 2025.

DBPM3 PLATFORM

Hardware

A DBPM3 unit has a 3 height unit (HE) 19" wide housing. As shown in Figs. 1 to 3, up to six single-width RF front-ends (RFFEs or "daughterboards") can be inserted from the rear side, or three double width RFFEs (for SLS 2.0), or two with triple-width RFFEs (for Athos). The number of BPMs per DBPM3 unit is four for Athos and three for SLS 2.0.The redundant power supply is also inserted from the rear side.

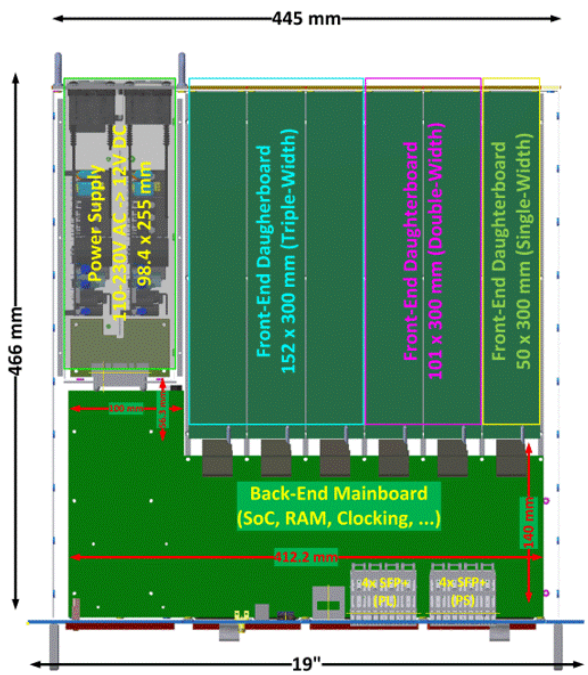


Figure 1: Top view of a DBPM3 unit with cover removed.

The digital back-end mainboard is mounted behind the front panel, having a direct coplanar 120-pin connectors to each daughterboard. The connector is self-centering, and

Content from this work may be used under the terms of the CC BY 4.0 licence (© 2022). Any distribution of this work must maintain attribution to the author(s), title of the work, publisher, and DOI

ISBN: 978-3-95450-241-7 ISSN: 2673-5350 doi:10.18429/JACoW-IBIC2022-TUP12

Content from this work may be used under the terms of the CC BY 4.0 licence (© 2022). Any distribution of this work must maintain attribution to the author(s), title of the work, publisher, and DOI

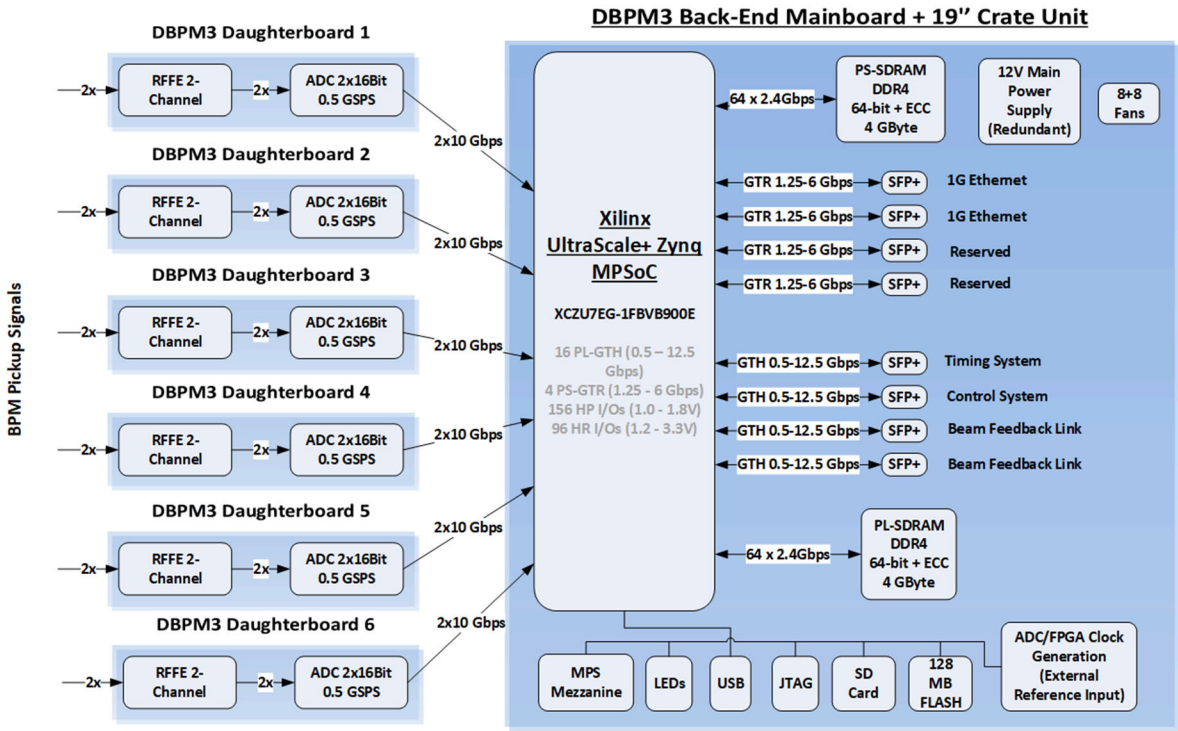


Figure 2: Simplified block schematics the of DBPM3 platform. Up to six front-end electronics modules ("daughterboards") can be plugged into the unit, each connected to the digital back-end mainboard with a 120-pin high-speed connector. The RFFE of the Athos cavity BPMs has two triple-width daughterboards, each serving two BPMs.

supports up to 25 Gbit/s data rate per connector pin pair for differential signals. The back-end has a single MPSoC of type Zynq UltraScale+ ("ZynqU+") from the company Xilinx/AMD. The ZynqU+ integrates on a single chip: A 4-core 64-bit ARM CPU ("APU" = Application Processing Unit), a 2-core 32-bit CPU ("RPU" = Real-time Processing Unit), and an FPGA with programmable logic (PL). Moreover, the MPSoC has various interfaces (Ethernet, I2C, DRAM, multi-gigabit links, USB, SD Card, JTAG, ...), combined with high-bandwidth interconnect structures.

The back-end board has two 64-bit wide DRAMs with 4 GByte size each and 8-bit ECC, 8 SFP+ transceivers at the front panel, and a generic clock synthesis unit supporting external accelerator reference clocks from all PSI accelerators, ranging from 50 to 500 MHz.

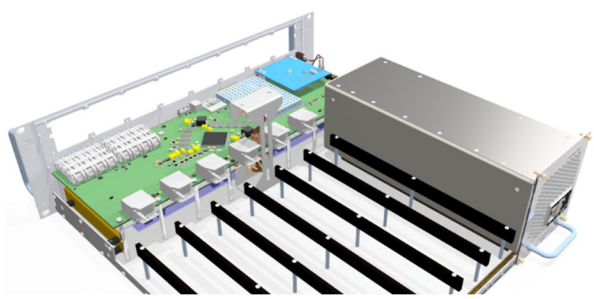


Figure 3: DBPM3 unit, view from rear side with top cover, daughterboards and fan trays removed. The digital back-end mainboard is shown at top left (green PCB). The redundant plugged power supply and guide rails for daughterboards are shown at the right top and bottom side.

In contrast to previous BPM electronics generations based on VME64x, the new Athos DBPM3 electronics has RFFE and ADCs on the same PCB, thus avoiding cable connections between RFFE and ADCs needed for previous systems. The Athos DBPM3 electronics as well as a first SLS 2.0 button BPM electronics prototype both use the same dual-channel ADCs of type ADS54J69 with 16-bits and up to 500 MSamples per second (MS/s). The ADC data is transmitted to the back-end mainboard via the JESD204B standard, using differential multi-gigabit signal lanes working at up to 10 Gbit/s per lane, depending on the adjustable ADC sample rate as well as on the optional on-chip data decimation and filtering supported by the ADC.

Table 2: Comparison of DBPM3 with the Previous MBU Platform

	MBU	DBPM3
ADC Interface	parallel (LVDS)	serial (JESD204B)
RFFE to ADC Connection	differential coaxial cables	PCB traces on common PCB
Integrated Timing Event Receiver	yes	yes
Integrated EPICS IOC	no (but planned)	yes
# Printed Circuit Boards per BPM	3.25	1.33
# FPGAs per BPM	1.75	0.33

Each of the six daughterboard connectors of the DBPM3 back-end supports two multi-gigabit full duplex link pairs, enabling the use of both JESD204 ADCs and DACs on

ISBN: 978-3-95450-241-7 ISSN: 2673-5350 doi:10.18429/JACoW-IBIC2022-TUP12

daughterboards. This makes the DBPM3 platform also suitable for other applications like fast feedbacks. The connector provides clock and synchronisation signals for JESD204B ADCs or local oscillators on the daughterboards, using LMK04828 and LMK01020 clock synthesis chips on the back-end. There are also additional connector signals for fast and slow data, control and synchronization, hot-swap power supply voltages, board serial number and type identification. An EEPROM on the RFFE contains gain and phase calibration tables.

The power supply voltages and currents of back-end and daughterboards are remotely monitored, supporting also remote power cycling. The speed of the fans at the front side of the DBPM3 unit (shown in Fig. 4) can be regulated individually to optimize thermal stability.



Figure 4: DBPM3 front side with two rows of eight fans.

Thanks to new technologies like JESD204B and MPSoC, the hardware complexity, production effort and costs could be significantly reduced compared to previous BPM electronics generations, see Table 2. Due to the smaller number of PCBs and much smaller number of connector pins per BPM and reduced number of cables, we also expect a reduction of the long-term maintenance effort and an even higher MTBF than the present systems.

Cavity BPM RFFE/ADC Hardware

Figure 5 shows the RFFE electronics for the Athos undulator BPMs, with six SMA connectors for BPM input signals. The electronics has symmetric channels for position and charge signals of the cavity BPM pickups, with three dual-channel ADCs close to the mainboard connectors. One ADC is shared by two BPMs, with negligible crosstalk.

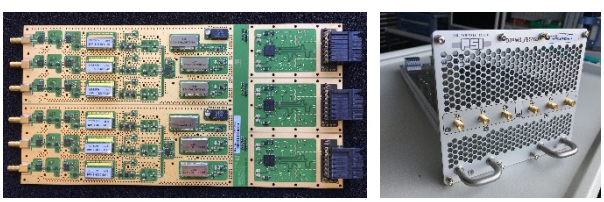


Figure 5: Athos cavity BPM RFFE board for two BPMs. Left: Printed circuit board (PCB). Right: Board with rear panel and metal RF shields mounted on both PCB sides.

The RF input stage of the DBPM3 RFFE for Athos is nearly identical to the previous VME-based electronics platform called MBU (Modular BPM Unit) installed in the SwissFEL linac and hard X-ray undulator line (“Aramis”) [4]. However, the electronics production cost per undulator BPM was reduced about 2.5 times by the new DBPM3 platform (Fig. 6).

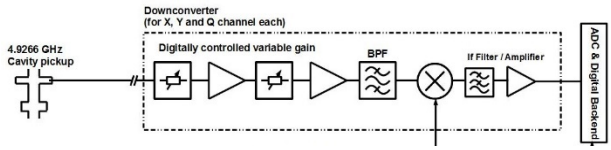


Figure 6: Simplified block diagram of a cavity BPM RFFE input channel. The 4.9266 GHz signal of the two position resonators and the reference resonator of the cavity BPM pickup (loaded quality factor ~1000) are mixed to an intermediate frequency of 134 MHz, digitized, and then mixed digitally to baseband by the PL in the MPSoC.

Software and Firmware

In general, the DPBM3 software and firmware is split into a BPM specific part and a generic part. The latter is used for all DBPM3 applications, including remote management of the DBPM3 unit, health status monitoring, DRAM and ADC interfaces.

The 4-core 64-bit “APU” CPU of the MPSoC is booting Linux at power-up, where the bit stream of the FPGA part of the chip is then loaded in a 2nd step, either from an external SD card, or from an external file server via Ethernet. Loading an EPICS control system IOC on top of EPICS as a 3rd and last step of the booting process enables remote access to various generic and BPM specific settings and measurement data.

The calculation of the beam position from the ADC data is done in FPGA firmware programmed in VHDL, while tasks like automatic range control of the digital step attenuators (DSAs) of the RFFEs are implemented in software on the 2-core 32-bit “RPU” CPU, supporting bare metal C code on one CPU core and FreeRTOS on the other core. The signal processing algorithms for the Athos BPMs are mainly identical to the previous BPM platform “MBU” [4] and will thus not be described again here again. The RFFEs are precalibrated in the lab with an RF generator, and calibration tables are stored in an EEPROM on the RFFE. The tables are used by the MPSoC to digitally correct the attenuation and phase of the channels for each DSA setting, compensating production tolerances of the DSA chips.

The MPSoC also contains a so-called embedded event receiver (EEVR) implemented in firmware that decodes the protocol of the global a timing/event system delivered via fiber optic cables to the DBPM3 units. For SwissFEL, this enables time stamping of the BPM data with a unique global bunch ID directly on the MPSoC, thus making sure the data delivered to the control and archiving system has a correct time stamp and bunch ID.

Content from this work may be used under the terms of the CC BY 4.0 licence (© 2022). Any distribution of this work must maintain attribution to the author(s), title of the work, publisher, and DOI

ISBN: 978-3-95450-241-7 ISSN: 2673-5350 doi:10.18429/JACoW-IBIC2022-TUP12

Content from this work may be used under the terms of the CC BY 4.0 licence (© 2022). Any distribution of this work must maintain attribution to the author(s), title of the work, publisher, and DOI

MEASUREMENT RESULTS

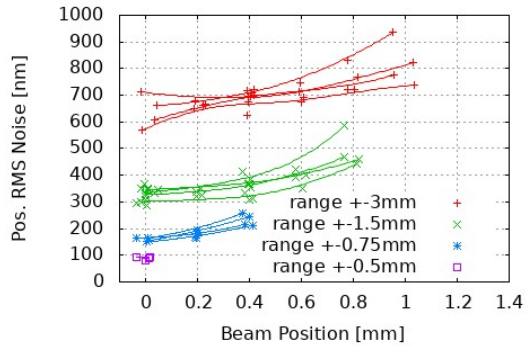


Figure 7: Beam position noise of the Athos DBPM3 BPM electronics vs. beam position offset, measured at ~200pC bunch charge with 25 Hz rep rate, for different position measurement ranges.

Figure 7 shows the RMS noise of the DBPM3 electronics as a function of the beam position offset, for different measurement ranges. The maximum limit of the range is defined as the beam position where the ADC reading reaches the ADC full scale, for a given fixed setting of the digital step attenuators (DSAs). The DSAs of the RFFE are used for position and charge range adjustment with 63 dB range. The beam position at three adjacent Athos undulator BPMs was moved simultaneously in steps of 0.2mm for a given range. Athos was operating with single bunches, 200 pC bunch charge and 25 Hz repetition rate. The position noise was calculated from a 10 second data interval, by correlation of the readings of the three BPMs, assuming that all three have the same electronics noise. The calculation also assumes that all orbit perturbations occur upstream or downstream of the three BPMs, but not in between them. Thus, the values are a pessimistic estimate for the upper limit of the BPM electronics noise.

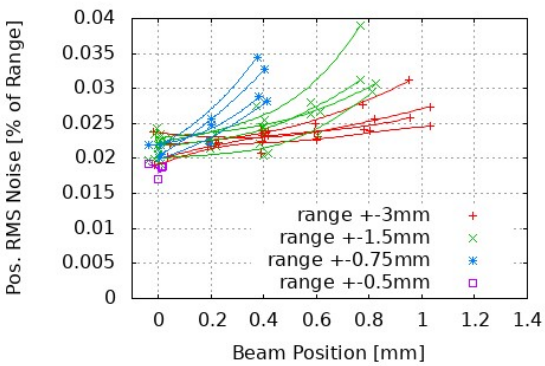


Figure 8: DBPM3 electronics beam position measurement noise in percent of the measurement range.

Figure 8 shows the position noise, normalized to the position range by dividing the absolute noise by 50% of the peak-to-peak range. For small beam position offsets close to 0mm, the dependence of the position on the range is rather small. This shows that the contribution of the thermal noise of the RFFE analog input chain remains smaller than the noise contribution of the ADC during the measurements. The digital step attenuators of the RFFE position cavity signals were varied by 16 dB overall for the ranges shown in the plot.

The inner aperture of the Athos undulator BPM pickups is only 5mm, compared to 8mm for the Aramis hard X-ray undulators of SwissFEL. Therefore the beam offsets during user operation of Athos are usually only reach some 100 µm. Quadrupole magnets and BPMs in the Athos undulators are mounted together on a motorized 2D mover, thus the BPMs and quadrupoles are usually well centered close to the "golden orbit" that provides optimal lasing conditions.

CONCLUSION AND OUTLOOK

A new BPM platform based on RF front-ends with JESD204B ADCs and a digital back-end with a MPSoC has been successfully commissioned at the SwissFEL Athos beamline, being in operation since end 2020. The next DBPM3 application is SLS 2.0, where RFFE prototypes are presently being tested at the SLS. After putting SLS 2.0 in operation in 2025, the next DBPM3 application will be the upgrade of the HIPA proton BPM system, where the present ageing BPM system is operational since 2005 [3]. In addition to BPMs, the DBPM3 unit is also suitable for general beam diagnostics, measurement and feedback systems, where the 3HE unit and large volume available for daughterboards/RFFEs supports also PCBs with larger components, like photomultipliers for beam loss monitors.

ACKNOWLEDGEMENTS

The authors gratefully acknowledge the contributions and support of the following colleagues: Daniel Engeler (digital back-end design), Daniel Treyer and Chris Deutschendorf (DBPM3 clocking circuitry design), Markus Stadler (RFFE prototype design), and Fabio Marcellini (Athos BPM pickup design).

REFERENCES

[1] V. Schlott *et al.*, "Commissioning of the SLS Digital BPM System", *Proc. PAC'01*, Chicago, USA, 2001

[2] B. Keil, P.-A. Duperrex, and M. U. Müller, "Commissioning of a New Digital BPM System for the PSI Proton Accelerators", in *Proc. EPAC'06*, Edinburgh, UK, Jun. 2006, paper TUPCH092.

[3] B. Keil *et al.*, "First Beam Commissioning Experience With The SwissFEL Cavity BPM System", in *Proc. IBIC'17*, Grand Rapids, MI, USA, Aug. 2017, pp. 251-254. doi:10.18429/JACoW-IBIC2017-TUPCF17

[4] B. Keil *et al.*, "The European XFEL Beam Position Monitor System", in Proc. IPAC'10, Kyoto, Japan, May 2010, paper MOPE064, pp. 1125-1127.

[5] R. Ganter *et al.*, "Status of Athos, the Soft X-Ray FEL Line of SwissFEL", in *Proc. FEL'19*, Hamburg, Germany, Aug. 2019, pp. 753-756. doi:10.18429/JACoW-FEL2019-THP085

[6] A. Streun, "SLS 2.0, the Upgrade of the Swiss Light Source", in *Proc. IPAC'22*, Bangkok, Thailand, Jun. 2022, pp. 925-928. doi:10.18429/JACoW-IPAC2022-TUPOST032

ISBN: 978-3-95450-241-7 ISSN: 2673-5350 doi:10.18429/JACoW-IBIC2022-TUP13

STANDARD BUTTON BPMs FOR PETRA IV

S. Strokov, M. Holz, G. Kube, D. Lipka, S. Vilcins
Deutsches Elektronen-Synchrotron DESY, Hamburg, Germany

Abstract

A new diffraction limited light source PETRA IV (DESY, Germany) with ultra-low emittance is currently being designed as an upgrade of the 3rd generation light source PETRA III. For transverse beam position measurements, beam position monitors (BPMs) will be used as an essential part of the beam diagnostic system. There will be a total of about 800 BPMs distributed along the 2.3 km storage ring. The inner diameter of the standard beam pipe, and therefore of most of the BPM chambers, will be 20 mm.

The primary purpose of the systems is to provide high-resolution measurements of the transverse position of the electron beam. By specification, the impact of the mechanical tolerances on the position readings should be below 150 µm which is essential for the commissioning of the machine. To achieve this goal, the dependence of the accuracy of the beam position measurement on the tolerances of each manufactured part of the BPM was studied. This paper summarizes development and optimization of each part of the BPM by using EM simulations performed with CST Studio Suite.

INTRODUCTION

Similar to the PETRA III synchrotron ring, the standard button pickup electrodes BPMs will be used in PETRA IV. BPMs are the largest part of the PETRA IV diagnostic system. For the commissioning of the machine, an absolute beam position measurements accuracy of ≤500 µm is required [1]. The following three main factors contributes to that number:

- manufacturing tolerances;
- tolerances from electronic part;
- tolerances from the BPMs alignment.

This article considers only the contribution of manufacturing tolerances to the accuracy of BPM measurement, which should not exceed the defined 150 µm.

DESIGN ASPECTS

During BPM development, the following goals were pursued:

- to have as few parts as possible to reduce the influence of the manufacturing tolerances on the beam position reading;
- compactness;
- ease of manufacture and assembly;
- reliability and ease of troubleshooting during operation.

Various shapes of the feedthroughs and buttons were considered, calculated, and simulated. The version of the BPM presented in this paper is currently being considered as the main candidate.

Assembly Overview

The final assembly of the BPM is shown in Fig. 1. Each BPM contains the main body and four feedthroughs with buttons. Before feedthroughs are inserted and welded to the main body, their electrical characteristics will thoroughly be measured to find pairs with equal characteristics. The overall dimensions of the BPM body are 72 x 72 x 31 mm. Additional cable holder will be attached to each BPM.

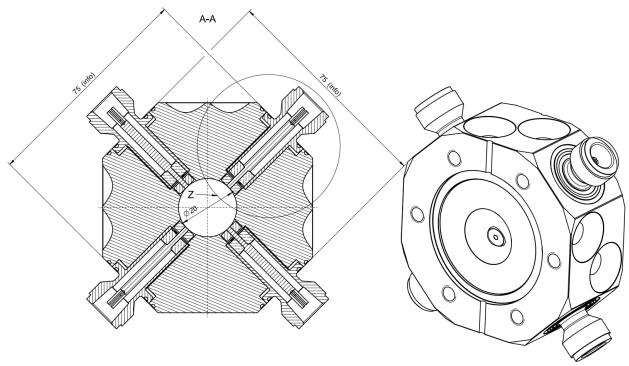


Figure 1: BPM assembly overview.

Feedthroughs with Buttons

Each feedthrough consists of the following parts:

- the body of the feedthrough with inner diameter of 7.5 mm and attached to it N-type connector;
- the flat button without any skirt around it with a diameter of 7 mm and a thickness of 3 mm made of alloy C-22. The gap between the button and the insulator is 1 mm. When feedthrough is inserted into the main body, the gap between the button and the surrounding main body is 0.25 mm;
- the central pin with diameters of 3.04 mm to match 50 Ohm impedance. From one side it is connected to the button by laser welding and on the other, it forms a N-type female connector. The material is the same as that of the button - alloy C-22;
- the 5 mm thick insulator;
- three channels on the outer surface of the assembled feedthrough to help vacuum pumping (see Fig. 2).

ELECTROMAGNETIC SIMULATION

Extensive electromagnetic simulations have been performed by the CST Studio Suite [2] to study how the manufacturing tolerances affect the signal and therefore the beam position measurements. The model from the CST Sudio Suite used for the tolerance study is shown in Fig. 3. The beam parameters of the PETRA IV timing mode specified in Table 1 were used for all the simulations.

Content from this work may be used under the terms of the CC BY 4.0 licence (© 2022). Any distribution of this work must maintain attribution to the author(s), title of the work, publisher, and DOI

ISBN: 978-3-95450-241-7 ISSN: 2673-5350 doi:10.18429/JACoW-IBIC2022-TUP13

Content from this work may be used under the terms of the CC BY 4.0 licence (© 2022). Any distribution of this work must maintain attribution to the author(s), title of the work, publisher, and DOI

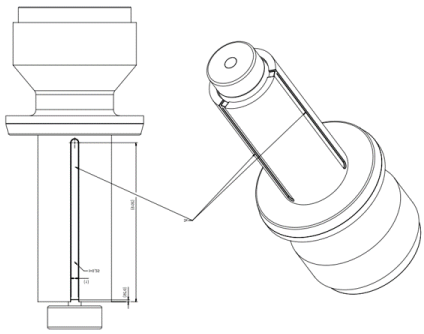


Figure 2: Three channels to help vacuum pumping.

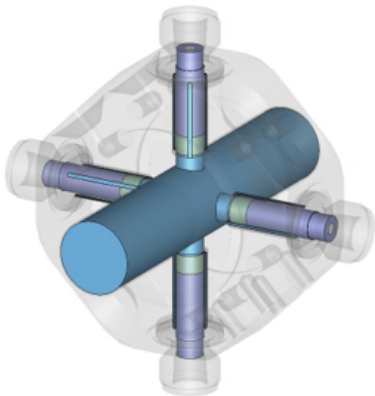


Figure 3: A BPM model from CST Studio Suite.

Table 1: PETRA IV Electron Beam Parameters [1] Used for Simulation and Analysis

Energy [GeV]	6
Bunch charge [nC]	7.68
Bunch length [mm]	13.2 (44 ps)
Bunch spacing [ns]	4

The simulations were performed for a single bunch with a Wakefield solver. Frequency range was set to the maximum of 20 GHz. At the end of each feedthrough, the voltage monitors were placed. Initial beam position was set to the center of the beam pipe.

To find out how tolerances affect the beam position reading, the dimensions and position of the one feedthrough were left variable (see Fig. 4) while the other three were fixed at nominal dimensions. Only one dimension of the variable feedthrough was changed at a time within the manufacturing tolerance of ±50 µm. The beam position was then calculated based on the difference of voltages obtained from the voltage monitors.

Output Signals; Beam Position Reading

A typical signal induced by a single bunch from a button pickup obtained from the voltage monitor in the time and frequency domains is shown in Fig. 5. Resonances at higher frequencies are not observed in simulation. This reflects good design decisions and results in a smooth and

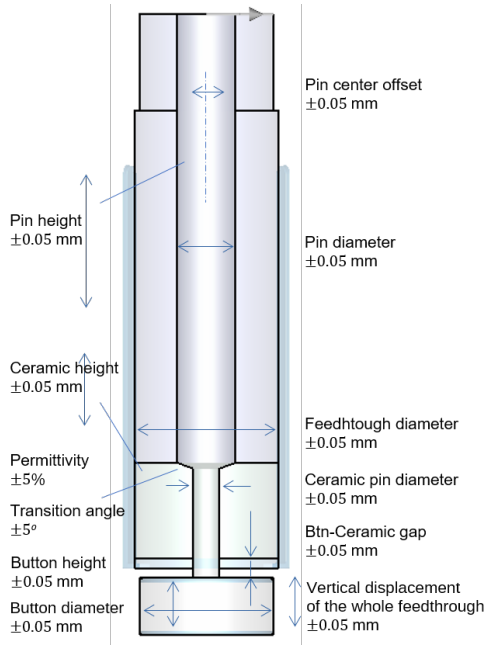


Figure 4: Feedthrough dimensions along with manufacturing tolerances that were used to set up the simulations for tolerance study.

fast (within ≈1.5 ns) decaying signal which will not interfere with the signal induced by the following bunch in 4 ns.

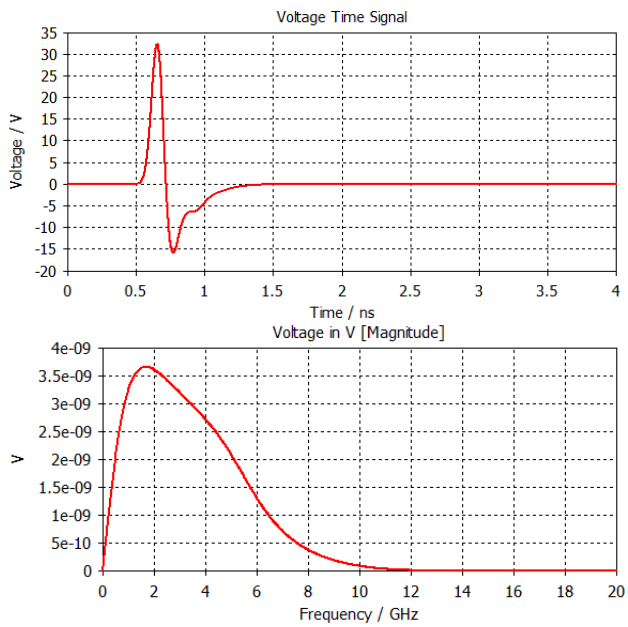


Figure 5: Signal from the feedthroughs in the time and frequency domains.

To determine beam position, the difference-over-sum ($\Delta\backslash\Sigma$) method was used

$$Horizontal = K_x \frac{(V1+V2)-(V3+V4)}{V1+V4+V2+V3}$$
$$Vertical = K_y \frac{(V1+V4)-(V2+V3)}{V1+V4+V2+V3}, \quad (1)$$

ISBN: 978-3-95450-241-7 ISSN: 2673-5350 doi:10.18429/JACoW-IBIC2022-TUP13

where K_x and K_y are monitor constants, and V_N is the voltage amplitude obtained from the voltage monitor of the corresponding N_{th} feedthrough (see Fig. 6) at the frequency of 500 MHz which is the read-out frequency of the electronics for PETRA IV.

The monitor constants can be derived from the formula in Eq. (1) with a known small (on a µm scale) beam displacement from its central position.

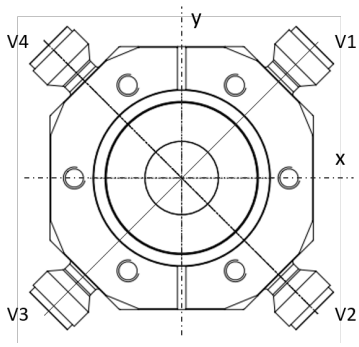


Figure 6: Alignment of BPM and voltage monitors to calculate the horizontal and vertical position of the beam by Eq. (1).

Tolerance Study Results

The beam position reading as a dependent value on the tolerances is shown in Fig. 7. The largest effects on the beam position reading are the vertical displacement of the feedthrough when the button goes inward/outward of the beam pipe and the deviation of the inner diameter of the feedthrough.

The effect of all tolerances on the beam position reading can be found as

$$S = \sqrt{\sum_{t=1}^{n} x_t^2} = 0.124\,\text{mm}, \qquad (2)$$

where x_t is a beam position reading at each tolerance value t applied to the nominal dimensions.

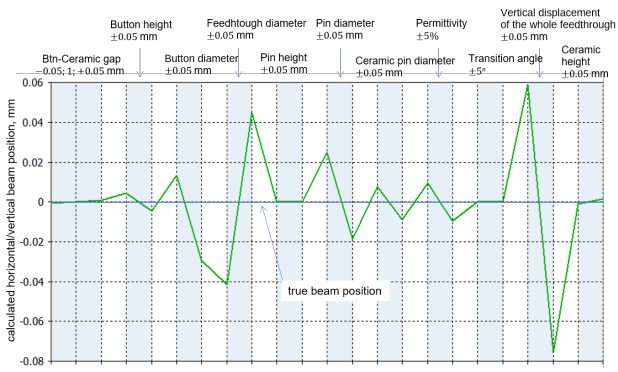


Figure 7: The dependence of the beam position reading on the manufacturing tolerances of the feedthrough with button.

SUMMARY

An extensive study on the influence of the manufacturing tolerances on beam position reading has been performed. It was found that the present manufacturing tolerances will theoretically reduce BPM resolution to 124 µm which satisfies the required 150 µm.

Further tolerance study of the read-out electronics and alignment process of the BPM for PETRA IV is an ongoing task.

ACKNOWLEDGEMENTS

The PETRA IV project team acknowledges funding of the technical design phase granted by the Behörde für Wissenschaft, Forschung, Gleichstellung und Bezirke (BWFGB) of the Freie und Hansestadt Hamburg, as well as by the Bundesministerium für Bildung und Forschung (BMBF) under the contract DES21TDR.

REFERENCES

[1] "PETRA IV. Upgrade of PETRA III to the Ultimate 3D X-ray Microscope. Conceptual Design Report", Deutsches Elektronen-Synchrotron DESY, Hamburg, Germany, 2019. https://bib-pubdb1.desy.de/record/426140/files/DESY-PETRAIV-Conceptual-Design-Report.pdf

[2] Computer Simulation Technology, http://www.cst.com

Content from this work may be used under the terms of the CC BY 4.0 licence (© 2022). Any distribution of this work must maintain attribution to the author(s), title of the work, publisher, and DOI

ISBN: 978-3-95450-241-7 ISSN: 2673-5350 doi:10.18429/JACoW-IBIC2022-TUP15

NEW GAS TARGET DESIGN FOR THE HL-LHC BEAM GAS VERTEX PROFILE MONITOR

H. Guerin*,[1], R. De Maria, R. Kersevan, B. Kolbinger, T. Lefevre, M. T. Ramos Garcia, B. Salvant, G. Schneider, J. W. Storey, CERN, Geneva, Switzerland
S. M. Gibson, Royal Holloway, University of London, Surrey, UK
[1]also at Royal Holloway, University of London, Surrey, UK

Abstract

The Beam Gas Vertex (BGV) instrument is a novel non-invasive transverse beam profile monitor under development for the High Luminosity Upgrade of the LHC (HL-LHC). Its principle is based on the reconstruction of the tracks and vertices issued from beam-gas inelastic hadronic interactions. The instrument is currently in the design phase, and will consist of a gas target, a forward tracking detector installed outside the beam vacuum chamber and computing resources dedicated to event reconstruction. The transverse beam profile image will then be inferred from the spatial distribution of the reconstructed vertices. With this method, the BGV should be able to provide bunch-by-bunch measurement of the beam size, together with a beam profile image throughout the whole LHC energy cycle, and independently of the beam intensity. This contribution describes the design of the gas target system and of the gas tank of the instrument.

INTRODUCTION

With the foreseen High-Luminosity upgrade of the Large Hadron Collider (HL-LHC), knowledge of the beam emittance during the entire energy cycle will be critical for the machine commissioning. The Beam Gas Vertex (BGV) monitor being developed for this scope, proposes to use beam-gas inelastic hadronic interactions in order to provide a transverse beam size and beam profile measurement. As illustrated in Fig. 1, a noble gas is injected in a dedicated vacuum chamber to generate the beam-gas interactions. The tracks of issued secondary particles are detected by a forward tracking detector, located downstream of the gas target and outside the vacuum. Tracks and vertices are reconstructed with dedicated computing resources, and the beam size and profile are then inferred from the spatial distribution of reconstructed vertices. The instrument is being designed with the aim to achieve a beam size measurement accuracy $< 5\%$ and provide a bunch-by-bunch beam size measurement with a relative precision of a few percent within about 1 min, throughout the full energy cycle, and independent of the beam intensity.

A demonstrator device [1, 2] was installed and operated close to the Interaction Point 4 (IP4) of the LHC during Run 2 and demonstrated the feasibility of using beam-gas inelastic interactions to measure the beam size throughout the full LHC energy cycle and independently of the beam intensity, despite not being able to reconstruct interaction vertices. This limitation made the reconstruction of the beam profile impossible.

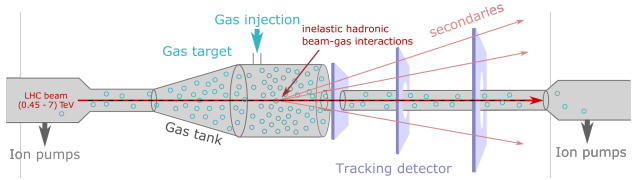


Figure 1: Sketch of the BGV instrument.

Following these results, work is ongoing to design the future instrument, which should be capable of vertexing to reach the above-mentioned specifications. A performance study based on Monte-Carlo simulation tools [3, 4] and track and vertex reconstruction analysis was carried out, in order to guide the BGV design.

The conclusions of this study lead to the choice of a compact tracker based on high resolution silicon pixel detectors. It was also decided to keep the distributed gas target system of the demonstrator, but to modify the dimensions of the vacuum chamber in order to reduce the longitudinal beam-gas interaction range and undesired radiation background, and to limit its beam impedance contribution in the LHC machine. This contribution presents the gas target and gas tank design of the future HL-LHC BGV instrument, and evaluates their impact on the machine operation.

GAS TARGET SYSTEM

Instrument Requirements

The BGV tracker was designed to detect tracks from inelastic beam-gas interactions occurring in a 1 m-long region along the beam axis and with an optimal distance of about 550 mm between the center of the gas target and the first detector plane. Most beam-gas interactions occurring outside this volume would not be used for the measurement and generate undesired background, increasing radiation levels in the LHC tunnel. Therefore, the requirements for the gas target design were to provide a uniform pressure distribution of about 1×10^{-7} mbar placed at the relevant distance from the tracker, with a quick pressure decrease outside it. Neon gas was chosen among other noble species in order not to saturate the chambers' non-evaporable getter (NEG) coating, and because remaining molecules after pumping wouldn't affect the sensibility of the leak detection systems, unlike helium and argon. Higher mass noble gases like krypton

* helene.chloe.guerin@cern.ch

Content from this work may be used under the terms of the CC BY 4.0 licence (© 2022). Any distribution of this work must maintain attribution to the author(s), title of the work, publisher, and DOI

ISBN: 978-3-95450-241-7 ISSN: 2673-5350 doi:10.18429/JACoW-IBIC2022-TUP15

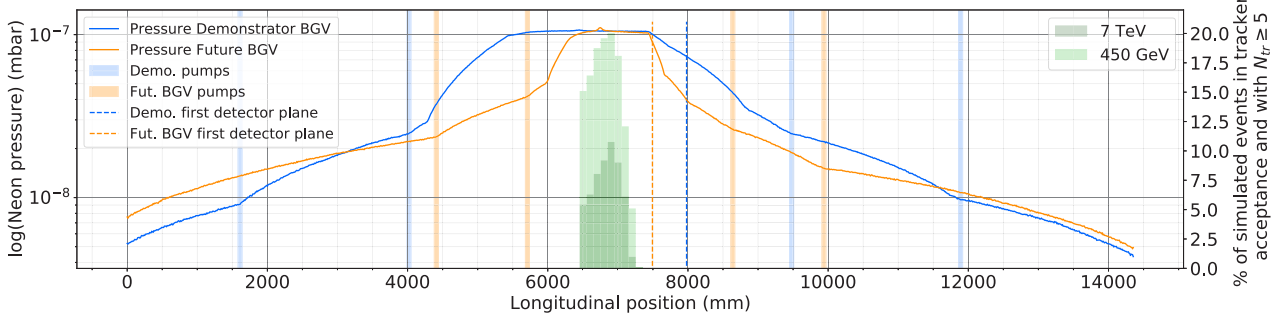


Figure 2: Longitudinal gas pressure profile of the BGV target during Ne injection, along the beam direction, as simulated with Molflow+ for both the demonstrator (blue) and future instrument (orange). The position of the ion pumps for the two designs are indicated by vertical lines of corresponding colours. Green bars show the percentage beam-gas interactions in the corresponding location, which can be reconstructed by the tracking detector (i.e. with a sufficient number of tracks N_{tr} in the tracker acceptance), at injection and flat top energies, based on Monte-Carlo simulations. The position of the first detector layer of each instrument is represented by the dashed vertical lines.

or xenon could also be considered in the future, but would require further vacuum studies.

Gas Injection System

The gas injection system proposed for the BGV has already been and is still being used in the LHC machine for other beam instruments including the demonstrator BGV [5], the Beam Gas Ionisation (BGI) monitor, and the Beam Gas Curtain (BGC) monitor [6]. As indicated in Fig. 1, the gas is injected via a capillary into the central, cylindrical part of the gas tank. The gas injected in the tank is purified with a commercial NEG filter, which reduces the concentration of contaminant from ppm to ppb level [7], and a valve allows to adjust the injected pressure. In the case of the BGV, two 500 L s^{-1} ion pumps are placed at each extremity of the central chamber, which is also surrounded by reduced aperture sections, to ensure a sharp decrease of the pressure outside the tank.

Longitudinal Gas Pressure Profile

The longitudinal gas profile of the BGV was simulated with the Molflow+ tool [8]. A parametric study of the tank dimensions was performed, starting from the demonstrator BGV setup, in order to understand how the shape of the tank and surrounding chambers impact the longitudinal gas profile. The length and diameter of each chamber and taper was considered, as well as the distance between the two pumps on each side and their proximity to the interaction chamber. The gas tank shape was thus optimised to provide a suitable pressure profile. The new longitudinal pressure profile is shown in Fig. 2, together with the one of the demonstrator. Compared to the demonstrator, the integrated pressure of the new configuration is reduced by 24%, which decreases the impact on the LHC radiation environment, while providing the required pressure in the region of interest for beam-gas interactions, at both injection and collision energies. Additional simulations, with the BGV setup included in the vacuum sectors of the foreseen locations, will be performed, as the proximity of cryogenic modules may affect the shape of the profile tails. The possible risk of Ne condensation and outgassing in cryogenic areas will also be assessed from these simulations.

GAS TANK DESIGN

The gas tank was designed taking the gas target needs into account, which were detailed in the previous section, and beam impedance and integration requirements, which are explained below. The new structure of the future instrument is shown in Fig. 3. The length and inner diameters of the different chamber parts are indicated, together with the position of the tracking detectors, first ion pumps and bellow.

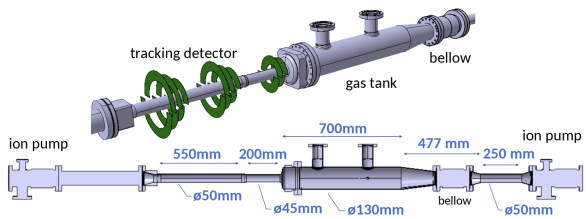


Figure 3: Most recent version of the HL-LHC BGV layout from CATIA [9] drawings.

Instrument Locations

The BGV instruments are foreseen to be installed on either side of the LHC IP4, where beam optics show little changes between injection and collision energies to facilitate beam parameters measurement, and with similar beam size in both transverse planes. The Beam 2 BGV is foreseen to be placed at the location currently occupied by the demonstrator BGV −220 m w.r.t IP4 center, where transverse β-functions cross at $\beta_x^{B2} \simeq 160$ m, and the Beam 1 instrument would be installed at +142 m w.r.t IP4 center, with a β-functions crossing of $\beta_x^{B1} \simeq 320$ m.

A critical parameter for the BGV performance is the diameter of the chamber downstream of the central gas chamber,

Content from this work may be used under the terms of the CC BY 4.0 licence (© 2022). Any distribution of this work must maintain attribution to the author(s), title of the work, publisher, and DOI

ISBN: 978-3-95450-241-7 ISSN: 2673-5350 doi:10.18429/JACoW-IBIC2022-TUP15

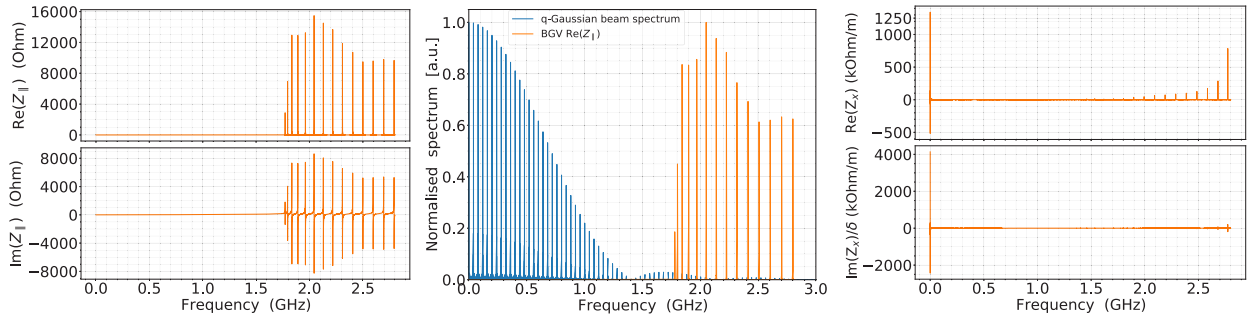


Figure 4: BGV beam coupling impedance simulated with CST Particle Studio. The real and imaginary longitudinal impedance spectrum are shown on the left figure and the transverse impedance spectrum on the right figure for the case of a transverse beam displacement of 12.5 mm. The middle plot shows the normalised beam spectrum for a q-Gaussian bunch shape, and normalised real longitudinal impedance, shifted in frequency to display the configuration with maximum dissipated power $P_{\text{loss}} = 40\,\text{W}$.

where the first detector layer is placed. Simulations have shown that most secondary particles have a small angle with respect to the beam axis, and particles with such trajectories also tend to have higher momenta, making them less prone to multiple scattering [3]. Minimising the detector beam pipe diameter is thus an important criterion in the optimisation of the tracker acceptance. At the locations foreseen for the two instruments, a beam pipe aperture of 45 mm inner diameter was agreed for the 200 mm-long chamber holding the first detector layer [10]. With such a small aperture, the chamber should be placed as close as possible to the β crossing point for the Beam 1 instrument and mechanical and alignment tolerances should be carefully considered.

Beam Coupling Impedance

Careful attention was given to the beam coupling impedance of the BGV gas tank, on the one hand because the contribution of the demonstrator was known to be non-negligible in the LHC machine [11], and on the other hand since beam instabilities due to impedance will increase with the beam intensity foreseen for HL-LHC.

A preliminary study [3] was performed with CST Particle Studio software [12], to understand how the design parameters of the gas tank impact its impedance. The main conclusions were that the diameter of the wide part of the tank is the most significant impact parameter, driving the frequency and shunt impedance of the main longitudinal resonant modes. With a longer gas tank, the number of these modes rises, but their shunt impedance also gets smaller. Finally, the taper sections can mitigate the impact of the resonant modes, but to a smaller extent compared to the two previous parameters.

Once the updated version of the tank shown in Fig. 3 was identified, its beam impedance was simulated with the wakefield solver of CST Particle Studio.

Longitudinal Impedance The real and imaginary part of the longitudinal impedance of the future gas tank design are shown in the left plots of Fig. 4. The pattern of the resonant modes is very similar to the one of the demonstrator structure [11], but with frequencies higher than 1.7 GHz (vs. >1.1 GHz for the demonstrator), and significantly smaller shunt impedance values (<16 kΩ), thanks to a smaller diameter of the wide part. The longitudinal effective impedance is obtained from the low frequency of the imaginary impedance: $Im(Z_{\parallel}/n) = 0.38\,\text{m}\Omega$. This value is almost twice smaller than the one of the demonstrator tank.

The expected power loss on the BGV was estimated based on Ohm's law, as described by Eq. (1), which considers the LHC beam of intensity I_{beam} and normalised spectrum Λ, and with the real part of the device impedance $\Re(Z_{\parallel})$. With discrete spectra, the power loss can be calculated as the sum of the contribution of each resonant mode coinciding with a beam harmonic, the fundamental being the bunching frequency $f_0 = 40\,\text{MHz}$.

$$P_{\text{loss}} = 2I_{\text{beam}}^2 \sum_{i=0}^{n} |\Lambda(\omega_i)|^2 \Re[Z_{\parallel}(\omega_i)] \,. \qquad (1)$$

The calculation was done with the most recent foreseen HL-LHC beam parameters [13], and with different bunch shapes. For each case, the impedance spectrum was shifted by a frequency varying between −20 MHz and 20 MHz, in order to consider all possible cases of overlap between the impedance resonant peaks and beam harmonics. For each bunch shape, the average power loss of all the frequency shift configurations is calculated, and the case with the maximum value is considered as worst possible configuration. Table 1 summarises the obtained results, listing for each bunch shape the average power loss value for the worst case parameters. The middle plot in Fig. 4 shows the normalised beam spectrum for a q-Gaussian bunch shape and the shifted real impedance spectrum of the BGV superimposed, in the worst case configuration. It is visible from this figure that the change of diameter of the tank shifted the impedance spectrum to higher frequencies when compared to the demonstrator, and therefore avoided the overlap with beam harmonics of relatively high intensity between 1.1 GHz and 1.5 GHz.

Content from this work may be used under the terms of the CC BY 4.0 licence (© 2022). Any distribution of this work must maintain attribution to the author(s), title of the work, publisher, and DOI

ISBN: 978-3-95450-241-7 ISSN: 2673-5350 doi:10.18429/JACoW-IBIC2022-TUP15

Table 1: Beam Induced Power Loss

Bunch shape	average P_{loss}	maximum P_{loss}
q-Gaussian	14 W	40 W
Gaussian	11 W	12 W
$\cos^2$	10 W	12 W

Transverse Impedance The transverse impedance of the HL-LHC BGV was simulated similarly. Since the BGV geometry modelled in CST is symmetrical with respect to the beam axis, the horizontal and vertical impedances are equivalent. Assuming the absence of transverse coupling between the two planes and neglecting terms of second and higher orders, the transverse impedance $Z_x(\omega)$ can be expressed as [14]: $Z_x(\omega) \simeq Z_x^0(\omega) + x_s Z_x^{\text{dip}}(\omega) + x_t Z_x^{\text{quad}}(\omega)$. A beam displacement x_s of 12.5 mm was simulated to estimate the dipolar (driving) term Z_x^{dip}, and a witness integration path displacement x_t of the same amount was simulated to derive the quadrupolar (detuning) term Z_x^{quad}. The zeroth order term $Z_x^0(\omega)$ was observed to be negligible based on simulations without offsets. The real and imaginary part of the total weighted transverse impedance are shown on the right plot of Fig. 4, weighted by the displacement $x_s = x_t = \delta$.

IMPACT ON LHC BEAM AND OPERATION

Operation Time and Radiation

When measuring beam size, the demonstrator BGV was operated with the gas profile shown in Fig. 2 and with an average plateau pressure of 1.4×10^{-7} mbar. This level was the same for both proton and ion runs, and the gas injection was usually turned on for multiple hours, and sometimes during most of the LHC energy cycle. Analyses of the total ionising dose rates and high energy hadron equivalent fluence in the vicinity of the demonstrator revealed that when turned ON, the BGV became the main source of radiation in this region [15]. An operation time of about 2 h per fill would be a minimum to measure beam size and emittance at the key phases of the energy cycle, including the ramp, and possibly calibrate the Beam Synchrotron Radiation Monitor (BSRT) at collision energy for longer measurements. Further studies are ongoing to estimate a maximum operation time, which will be limited by the radiation to the nearby active and passive instrument components.

Emittance Growth and Beam Half-Life Time

The BGV gas target is expected to have a negligible effect on the beam emittance and lifetime.

Considering first the beam particles' scattering on the gas target, and for a 1-σ beam size, the emittance growth per turn $\Delta\epsilon$ due to the presence of the BGV gas target can be calculated with Eq. (2), as detailed in Ref. [16]. In this formula, q_p is the charge number of the projectile, ie. of a proton in the beam, of momentum p and relativistic velocity β_r, and $\bar{\beta}_x$ represents the average transverse β-function along the gas target of length L. In the case of the BGV, the radiation length of the neon target is $L_{\text{rad, Ne}} \simeq L_{\text{rad, Ne, 1atm}}/(\bar{P}/1\text{ atmosphere}) = 1.2 \times 10^{13}$ m, where $\bar{P} = 2.72 \times 10^{-8}$ mbar is the average pressure along the gas target.

$$\Delta\epsilon = \frac{1}{2} q_p^2 \left(\frac{13.6\,\text{MeV}}{p\beta_r}\right)^2 \bar{\beta}_x \frac{L}{L_{\text{rad}}} \quad . \tag{2}$$

The normalised emittance growth rate $\Delta\epsilon_n$ can be expressed in $\mu\text{m}\,\text{h}^{-1}$ by scaling $\Delta\epsilon$ with the beam relativistic velocity β_r, Lorentz factor γ_L of the corresponding energy and with the LHC revolution frequency.

The resulting values are summarised in Table 2 for each beam at injection and collision energy. Emittance growth rates per fill of 0.16 % + 0.01 % = 0.17 % for Beam 1 and 0.08 % + 0.005 % = 0.085 % for Beam 2 are thus expected for the BGV operated for 1 h at injection and 1 h at collision energy. In the case where the gas injection would be turned ON several hours per fill, these values would stay way below the 10%-15% budget proposed for the beam size measurement in Ref. [17].

Table 2: Elastic Scattering Emittance Growth

Beam and Energy	$\Delta\epsilon$ (π rad m)	$\Delta\epsilon_n$ ($\mu\text{m}\,\text{h}^{-1}$)
Beam 1, 450 MeV	1.9×10^{-19}	3.2×10^{-3}
Beam 1, 7000 MeV	7.7×10^{-22}	2.0×10^{-4}
Beam 2, 450 MeV	9.3×10^{-20}	1.6×10^{-3}
Beam 2, 7000 MeV	3.8×10^{-22}	1.0×10^{-4}

In addition, calculating the beam lifetime with considering the rate of both elastic and inelastic interactions between beam protons and the BGV target molecules can gauge the amount of beam particles impacted by the gas target. Considering the new gas profile shown in Fig. 2, the half-life time of the HL-LHC proton beam would be 3 years. The impact of the BGV target on the beam lifetime can thus be considered negligible, similarly to the fraction of the beam protons interacting with the BGV target.

CONCLUSION

With the experience gained with the demonstrator BGV and with various simulation studies, a new gas target and gas tank designs are proposed for the HL-LHC BGV instrument. The impact of the BGV on the HL-LHC beam and operation was estimated based on simulation results, and will be smaller compared to the demonstrator, while ensuring the instrument's performance. The full design of the HL-LHC BGV will be detailed in a design report and presented in a review in October 2022.

ACKNOWLEDGEMENTS

The authors wish to thank Giuseppe Bregliozzi for his advises and feedback along the gas target design, together with the impedance working group for his support and comments regarding the gas tank impedance study. Thanks also to Daniel Prelipcean for his work on the radiation impact of the BGV.

Content from this work may be used under the terms of the CC BY 4.0 licence (© 2022). Any distribution of this work must maintain attribution to the author(s), title of the work, publisher, and DOI

ISBN: 978-3-95450-241-7 ISSN: 2673-5350 doi:10.18429/JACoW-IBIC2022-TUP15

Content from this work may be used under the terms of the CC BY 4.0 licence (© 2022). Any distribution of this work must maintain attribution to the author(s), title of the work, publisher, and DOI

REFERENCES

[1] A. Alexopoulos *et al.*, "Non-invasive LHC Transverse Beam Size Measurement Using Inelastic Beam-Gas Interactions," *Phys. Rev. Accel. Beams*, vol. 22, no. 4, p. 042 801, 2019. doi:10.1103/PhysRevAccelBeams.22.042801

[2] B. Wurkner, "Measurement of the LHC Beam Profile Using the Beam Gas Vertex Detector," Ph.D. thesis, Vienna, Tech. University, Germany, 2019.

[3] H. Guerin *et al.*, "The HL-LHC Beam Gas Vertex Monitor - Simulations for Design Optimisation and Performance Study," in *Proc. IPAC'21*, Campinas, Brazil, May 2021, pp. 2120–2123. doi:10.18429/JACoW-IPAC2021-TUPAB278

[4] B. Kolbinger *et al.*, "The HL-LHC Beam Gas Vertex Monitor - Performance and Design Optimisation Using Simulations," in *Proc. IBIC'21*, Pohang, Rep. of Korea, 2021, pp. 249–253. doi:10.18429/JACoW-IBIC2021-TUPP21

[5] G. Bregliozzi, V. Baglin, and P. Chiggiato, "Assessment of New Components to be Integrated in the LHC Room Temperature Vacuum System," 4 p, 2014. https://cds.cern.ch/record/1968548

[6] O. Sedlacek *et al.*, "HL-LHC Beam Gas Fluorescence Studies for Transverse Beam Profile Measurement," presented at IBIC'22, Kraków, Poland, Sep. 2022, paper TUP17, this conference.

[7] G. Bregliozzi, "Neon Venting of Activated NEG Beam Pipes in the CERN LHC Long Straight Sections without Losing Vacuum Performance," in *Proc. PAC'09*, Vancouver, Canada, May 2009, paper MO6RFP006, pp. 360–362. https://jacow.org/PAC2009/papers/MO6RFP006.pdf

[8] R. Kersevan and M. Ady, "Recent Developments of Monte-Carlo Codes Molflow+ and Synrad+," in *Proc. IPAC'19*, Melbourne, Australia, May 2019, pp. 1327–1330. doi:10.18429/JACoW-IPAC2019-TUPMP037

[9] *CATIA*. https://www.3ds.com/fr/produits-et-services/catia/

[10] R. D. Maria, private communication, 2022. https://indico.cern.ch/event/1164689/

[11] P. Hopchev *et al.*, "Beam gas vertex (bgv) demonstrator of a beam profile monitor in lhc," LHC-BGV-EC-0002, EDMS 1324635, 2014. https://edms.cern.ch/document/1324635/1.0

[12] *CST Microwave Studio*. http://www.cst.com

[13] R. Tomas Garcia *et al.*, "HL-LHC Run 4 proton operational scenario," CERN, Tech. Rep., 2022. http://cds.cern.ch/record/2803611

[14] S. Heifets, A. Wagner, and B. Zotter, "Generalized impedances and wakes in asymmetric structures," 1998. doi:10.2172/663316

[15] D. Prelipcean, "BGV beam-gas collisions at IR4 and related radiation levels and heat loads," 2022. https://indico.cern.ch/event/1129683/

[16] D. Möhl, "Sources of emittance growth," 2006. doi:10.5170/CERN-2006-012.45

[17] G. Arduini, A. Dabrowski, M. Lamont, J. Wenninger, and K. Wittenburg, "LHC Beam Size Measurement Review: Findings, comments and recommendations," 2019. https://indico.cern.ch/event/837340/

ISBN: 978-3-95450-241-7 ISSN: 2673-5350 doi:10.18429/JACoW-IBIC2022-TUP16

FOCUS: FAST MONTE CARLO APPROACH TO COHERENCE OF UNDULATOR SOURCES

M. Siano*, B. Paroli, M. A. C. Potenza, Università degli Studi di Milano, Milan, Italy
G. Geloni, European XFEL, Schenefeld, Germany
D. Butti, T. Lefevre, S. Mazzoni, G. Trad, CERN, Geneva, Switzerland
U. Iriso, A. A. Nosych, L. Torino, ALBA-CELLS, Cerdanyola del Vallés, Spain

Abstract

We present *Fast Monte-CarlO approach to Coherence of Undulator Sources* (FOCUS), a new GPU-based code to compute the transverse coherence of X-ray radiation from undulator sources. The code relies on scaled dimensionless quantities and analytic expressions of the electric field emitted by electrons in an undulator. A consistent use of Fourier optics and statistical optics naturally leads to the core structure of the code, which exploits GPUs for massively parallel computations. We validate our approach by direct comparison with *Synchrotron Radiation Workshop* (SRW), evidencing a reduction in computation times by up to five orders of magnitude on a consumer laptop. Finally, we show examples of applications to beam size diagnostics.

INTRODUCTION

Computational tools are or fundamental importance at current synchrotron radiation facilities. The high complexity of modern X-ray beamlines and the need to properly characterize the emitted X-ray wavefronts as a function of the source parameters demand for accurate numerical codes.

To this aim, several software packages have been developed, based either on ray tracing or on wave optics [1–4]. Among them, *Synchrotron Radiation Workshop* (SRW) has been extensively validated at different facilities, and has become a reference in the accelerator and X-ray optics communities.

Simulations of the transverse coherence of X-ray beams are among the most challenging tasks and must rely on a statistical description of wave optics. The standard approach involves multi-electron simulations based on Monte Carlo sampling techniques. More recently, the coherent-mode decomposition method [5] has been applied to describe the transverse coherence properties of X-ray beams from undulator sources [6]. However, both methods are quite demanding in terms of computer resources and computation times.

Here we describe a new code, natively running on GPUs, to compute the transverse coherence of undulator X-ray radiation as a function of the electron beam parameters [7]. The code is named *Fast Monte CarlO approach to Coherence of Undulator Sources* (FOCUS) and relies on analytic expressions of the electric field obtained in free space. A consistent use of Fourier optics and statistical optics naturally leads to the massively parallel code implementation. FOCUS is written in C++ language accelerated with CUDA to harness the compute capabilities of modern GPUs. Compared to multi-electron SRW simulations running with multi-threading parallelization, FOCUS achieves a remarkable reduction in computation times by up to five orders of magnitude on a consumer laptop. This enables fast and accurate characterization of the transverse coherence properties of the emitted X-ray beam as a function of the electron beam parameters.

* mirko.siano@unimi.it

THEORETICAL BACKGROUND

Let $\vec{E}(\vec{x}, z)$ be the slowly-varying envelope of the Fourier transform of the electric field (hereafter, simply the field) emitted by an ultra-relativistic electron moving through a planar undulator. Here $\vec{x} = (x, y)$ denotes transverse coordinates over an observation plane at a distance z from the undulator center. In the ultra-relativistic regime $\gamma \gg 1$, γ being the Lorentz factor, the field $\vec{E}(\vec{x}, z)$ is determined by solving paraxial Maxwell equations [8]. In addition, under the so-called resonant approximation, the vertical polarization component can be neglected and the vector field reduces to a scalar quantity [8]. For distances $z \gg L_w$, L_w being the undulator length, the following general expression for the horizontally polarized field is valid [8]:

$$\hat{E}(\hat{\vec{\theta}}, \hat{z}) = \frac{e^{i\phi_s}}{\hat{z}} \mathrm{sinc}\left(\frac{\hat{C} - \hat{\delta}_E}{2} + \frac{\zeta^2}{4}\right). \tag{1}$$

In Eq. (1) we have defined scaled quantities and dimensionless parameters as follows [8]:

$$\begin{aligned}
&\hat{E} = -\frac{2c^2\gamma}{K\omega e A_{JJ,h}} E \\
&\hat{\vec{x}} = \vec{x}\sqrt{\frac{\omega}{L_w c}} \qquad \hat{z} = \frac{z}{L_w} \qquad \hat{\vec{\theta}} = \frac{\hat{\vec{x}}}{\hat{z}} \\
&\hat{\vec{l}} = \vec{l}\sqrt{\frac{\omega}{L_w c}} \qquad \hat{\vec{\eta}} = \vec{\eta}\sqrt{\frac{\omega L_w}{c}} \\
&\hat{C} = 2\pi N_w \frac{\omega - h\omega_1}{\omega_1} \qquad \hat{\delta}_E = 4\pi N_w h \frac{\delta\gamma}{\gamma} \\
&\phi_s = \frac{\hat{z}}{2}\left|\hat{\vec{\theta}} - \frac{\hat{\vec{l}}}{\hat{z}}\right|^2 \qquad \zeta = \left|\hat{\vec{\theta}} - \frac{\hat{\vec{l}}}{\hat{z}} - \hat{\vec{\eta}}\right|.
\end{aligned} \tag{2}$$

In Eq. (2),

- ω is the angular frequency of the emitted radiation
- $\lambda = 2\pi c/\omega$ is the radiation wavelength

Content from this work may be used under the terms of the CC BY 4.0 licence (© 2022). Any distribution of this work must maintain attribution to the author(s), title of the work, publisher, and DOI

ISBN: 978-3-95450-241-7 ISSN: 2673-5350 doi:10.18429/JACoW-IBIC2022-TUP16

Content from this work may be used under the terms of the CC BY 4.0 licence (© 2022). Any distribution of this work must maintain attribution to the author(s), title of the work, publisher, and DOI

- c is the speed of light
- K is the undulator strength parameter
- $-e$ is the electron charge
- h is the harmonic number of the radiation emitted by the undulator
- $A_{JJ,h} = (-1)^{(h-1)/2}[J_{(h-1)/2}(u) - J_{(h+1)/2}(u)]$
- $u = hK^2/[2(2+K^2)]$
- J_n is the Bessel function of the first kind of order n
- N_w is the number of undulator periods
- $\omega_1 = 4\pi\gamma^2 c/[\lambda_w(1+K^2/2)]$ is the first harmonic of the undulator
- λ_w is the undulator period
- $\vec{l}$ and $\vec{\eta}$ are the electron offset and deflection, respectively
- $\Delta\gamma/\gamma$ is the relative energy deviation due to the finite energy spread of the electron beam.

Thanks to the paraxial approximation, ensured by the ultra-relativistic regime, we can apply Fourier optics methods to determine the electric field at any $\hat{z}$ [9]. In particular, the field in Eq. (1) can be described as a laser-like beam originating from a virtual source located at the undulator center and exhibiting a plane wavefront, similarly to the waist of a laser beam [8]. The field distribution of such virtual source is related to the inverse Fourier transform of the far-field pattern in Eq. (1), while the field at any $\hat{z}$ downstream the undulator center can be expressed as [8]:

$$\hat{E}(\hat{\vec{\theta}},\hat{z}) = e^{i\phi_s} e^{-i\frac{\hat{z}}{2}\zeta^2}\left[\mathrm{Ei}\left(\frac{i\hat{z}^2\zeta^2}{2\hat{z}-1}\right) - \mathrm{Ei}\left(\frac{i\hat{z}^2\zeta^2}{2\hat{z}+1}\right)\right], \quad (3)$$

where Ei is the exponential integral function. Equation (3) is valid at perfect resonance $\hat{C} = 0$ and in the absence of energy spread. It reduces to Eq. (1) in the far-field limit $\hat{z} \gg 1$.

The transverse coherence properties of the emitted X-ray radiation are described by the two-point field correlation function known in statistical optics as the Spectral Degree of Coherence (SDC) [5]:

$$\mu(\hat{\vec{\theta}}_1,\hat{\vec{\theta}}_2,\hat{z}) = \frac{\langle \hat{E}(\hat{\vec{\theta}}_1,\hat{z})\hat{E}^*(\hat{\vec{\theta}}_2,\hat{z})\rangle}{\langle|\hat{E}(\hat{\vec{\theta}}_1,\hat{z})|^2\rangle^{1/2}\langle|\hat{E}(\hat{\vec{\theta}}_2,\hat{z})|^2\rangle^{1/2}}, \quad (4)$$

where angular brackets denote ensemble averages over the phase space density of the electron beam at the undulator center. For $\lambda \ll l_{\mathrm{bunch}}$, being l_{bunch} the bunch length, each electron emits independently on the others. This naturally leads to a description of the radiation SDC in terms of single-electron contributions only, which is particularly suitable for massively parallel implementations based on Monte Carlo sampling techniques:

$$\langle f(\hat{\vec{\theta}},\hat{z})\rangle = \frac{1}{N_e}\sum_{k=1}^{N_e} f(\hat{\vec{\theta}},\hat{z},\hat{\vec{l}}_k,\hat{\vec{\eta}}_k,\hat{\delta}_k), \quad (5)$$

where $f(\hat{\vec{\theta}},\hat{z})$ denotes quantities between brackets on the right-hand side of Eq. (5) and N_e is the number of electrons in the beam.

STRUCTURE OF THE CODE

FOCUS exploits the analytical expressions of the electric field in Eqs. (1) and (3) to compute the ensemble averages in Eq. (5). Since terms in the summations refer to different electrons, they can be simultaneously evaluated through the concurrent execution of many parallel threads.

The general workflow of FOCUS is sketched in Fig. 1, where we also highlight operations running either on the CPU or on the GPU.

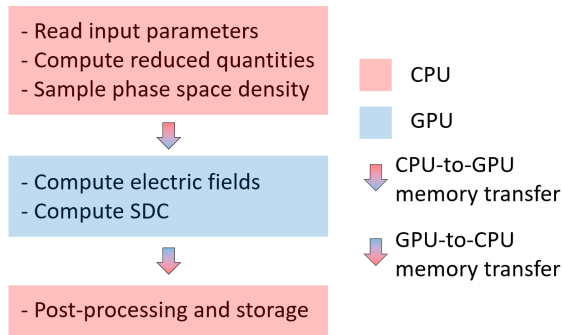


Figure 1: General FOCUS workflow.

First, the main parameters required to run the simulation are imported from external text files, which makes data input quite easy and flexible. Reduced parameters are derived based on Eq. (2). Then the phase space density of the electron beam is sampled either by an internal method relying on random number generators, or by reading values from a user-supplied file. This latter option is useful for benchmark purposes, as well as to assess the influence of non-gaussian beams on the coherence properties of the emitted X-ray beam. Computation is then moved from the CPU to the GPU. The terms in the summations in Eqs. (4) and (5) are computed in parallel through the concurrent execution of many threads on the processing cores residing on the graphic card. The final sum in Eq. (5) is also computed on the GPU by means of a parallel algorithm. Results are then transferred back onto the CPU for final post-processing and storage.

BENCHMARK WITH SRW

We validate FOCUS by direct comparison with SRW for N_e varying from 10 to 10^5. SRW simulations are run in parallel by exploiting multi-threading parallelization on the CPU. For each simulation, the same electron offsets, deflections and relative energy deviations are used in both FOCUS

ISBN: 978-3-95450-241-7 ISSN: 2673-5350 doi:10.18429/JACoW-IBIC2022-TUP16

and SRW. To showcase the results of such comparison, we consider the NCD-SWEET undulator source at the ALBA Synchrotron Light Source as a typical case study for current third-generation machines. The main parameters are summarized in Table 1.

Table 1: Main Parameters of the NCD-SWEET Undulator Source

Quantity	Parameter	Value
Electron beam energy	E	3 GeV
Undulator parameter	K	1.56
Number of periods	N_w	92
Period length	λ_w	21.6 mm
Harmonic number	h	7
Observation distance	z	33 m
Hor. beam size	$\sigma_{\mathrm{beam,x}}$	130 µm
Hor. beam divergence	$\sigma'_{\mathrm{beam,x}}$	48 µm
Ver. beam size	$\sigma_{\mathrm{beam,y}}$	6 µm
Ver. beam divergence	$\sigma'_{\mathrm{beam,y}}$	5 µm
Energy spread	Δ_E	$1.05 \cdot 10^{-3}$

We report in Fig. 2 examples of the simulated horizontal and vertical profiles of the SDC. FOCUS results match SRW simulations, even reproducing the spurious fluctuations of the SDC at large Δx and Δy due to the relatively low number of sampled electrons. Results also show that increasing the number of electrons in the beam to values in the order of 10^4 or larger is effective in suppressing such oscillations.

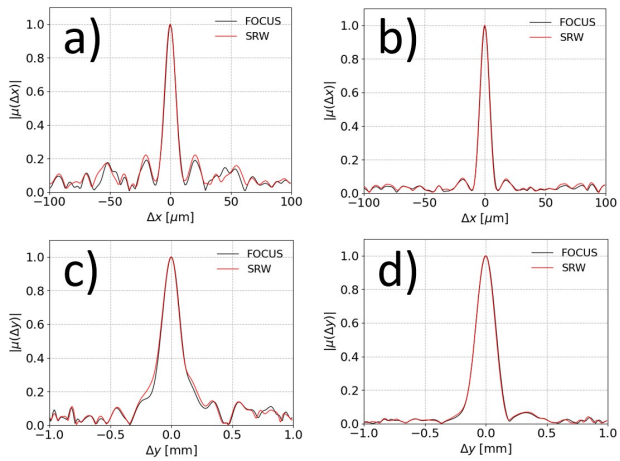


Figure 2: Benchmark of FOCUS with SRW. Results for the horizontal (a,b) and vertical (c,d) profiles of the SDC are shown, for $N_e = 10^3$ (a,c) and $N_e = 10^4$ (b,d).

We compare FOCUS and SRW computation times in Fig. 3. FOCUS achieves a remarkable reduction in computation times by up to five orders of magnitude with respect to SRW simulations. We also notice that the computation time of FOCUS does not scale linearly with N_e, opposite to the SRW case. Thanks to the concurrent execution of many parallel threads, the computation time of FOCUS is roughly constant for $N_e < 10^4$, and scales linearly with N_e only when all GPU resources are fully utilized, for N_e in the order of 10^5 or larger. For $N_e = 10^6$, FOCUS simulations require 3-4 seconds, whereas the same SRW computations would take 5 days.

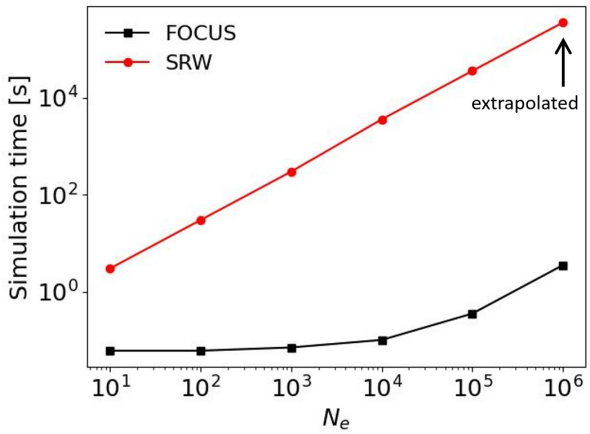


Figure 3: Comparison between FOCUS and SRW simulation times.

These results refer to a consumer laptop with a dual-core CPU and a NVIDIA GeForce 940MX graphic card with 512 CUDA cores. More modern, high-end GPUs with more CUDA cores and dedicated graphics memory can in principle achieve even better performances.

APPLICATIONS TO BEAM DIAGNOSTICS

Interferometric beam size measurements rely on the application of the well-known van Cittert and Zernike theorem to retrieve the electron beam size from the measured transverse coherence of X-ray radiation [5]. However, applicability of the van Cittert and Zernike theorem to undulator sources is highly debated, especially along the vertical direction in presence of beam emittances comparable to, or smaller than, the radiation wavelength [10–12].

Here we take advantage of the computation speed of FOCUS and thoroughly investigate the validity of the van Cittert and Zernike theorem for the NCD-SWEET undulator source. To this aim, we compute the horizontal and vertical profiles of the SDC for different beam sizes by performing accurate FOCUS simulations with $N_e = 10^6$-10^7 to limit random fluctuations in the results to a few per mils or less. Coherence profiles are then fitted to a Gaussian function to extract the transverse coherence length, here defined as the rms width of the SDC. Results are reported in Fig. 4, alongside with predictions based on the van Cittert and Zernike theorem.

Along the horizontal direction, the rigorous statistical optics approach and the van Cittert and Zernike theorem perfectly agree. The same applies along the vertical direction for beam sizes in the order of tens of micrometers. Opposite to these cases, deviations arise as the beam size is decreased to a few micrometers. Discrepancies are larger for smaller beam sizes. For example, for a vertical beam size of 3 µm the van

Content from this work may be used under the terms of the CC BY 4.0 licence (© 2022). Any distribution of this work must maintain attribution to the author(s), title of the work, publisher, and DOI

ISBN: 978-3-95450-241-7 ISSN: 2673-5350 doi:10.18429/JACoW-IBIC2022-TUP16

Content from this work may be used under the terms of the CC BY 4.0 licence (© 2022). Any distribution of this work must maintain attribution to the author(s), title of the work, publisher, and DOI

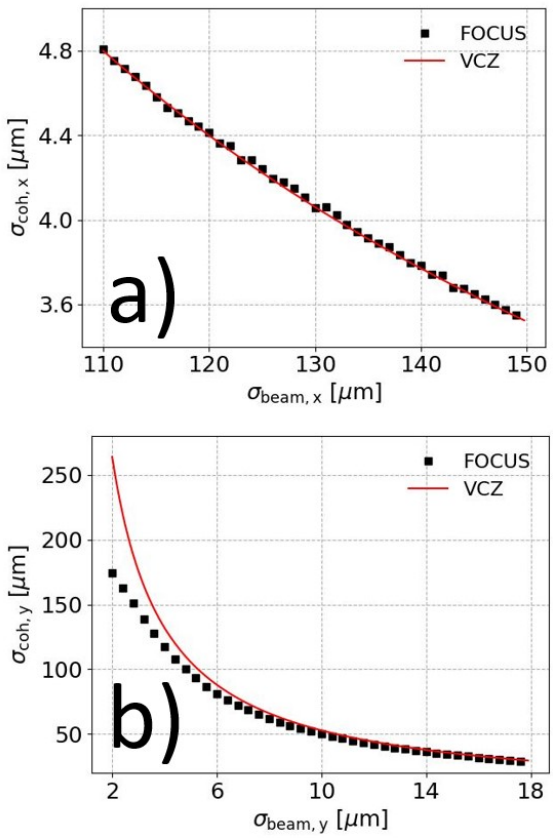


Figure 4: Simulated horizontal (a) and vertical (b) transverse coherence length as a function of the beam size for the NCD-SWEET undulator source, and comparison with predictions based on the van Cittert and Zernike theorem (VCZ).

Cittert and Zernike theorem would over-estimate the transverse coherence length by roughly 25% (175 µm, compared to 140 µm). On the other way around, this implies that interferometric beam size measurements based on the van Cittert and Zernike theorem would overestimate the beam size by roughly 25%, since a vertical beam size of 3.8 µm would be inferred from a measured transverse coherence length of 140 µm. Notice that such relative error of roughly 25% would then propagate to a relative error of roughly 50% in the emittance estimation. Therefore, although deviations between the two models are small for current third-generation facilities, they are however indicative of larger deviations which will become evident in future fourth-generation synchrotron light sources with micron-sized electron beams, especially close to the diffraction limit.

CONCLUSIONS

We have described *Fast Monte CarlO approach to Coherence of Undulator Sources* (FOCUS), a new GPU-base simulation code to compute the transverse coherence of X-ray radiation from ultra-relativistic electrons in an undulator source. We have validated FOCUS through a direct comparison with multi-electron SRW simulations. Besides accurately reproducing SRW results, FOCUS achieves a remarkable reduction in computation times by up to five orders of magnitude on a consumer laptop. Finally, we have shown an example of application to beam size measurements in presence of small beam emittances. These results might be of interest in view of next-generation light sources close to the diffraction limit.

We remark that FOCUS is complementary to existing codes like SRW. In particular, the aim of FOCUS is to fast evaluate the transverse coherence properties of the emitted X-ray beams as a function of the electron beam parameters, to support and help preparing more advanced and detailed simulations with traditional codes like SRW.

REFERENCES

[1] O. Chubar and P. Elleaume, "Accurate and efficient computation of synchrotron radiation in the near field region", in *Proc. EPAC'98*, Stockholm, Sweden, 1998, paper THP01G, pp. 1177–1179.

[2] T. Tanaka and H. Kitamura, "SPECTRA: a synchrotron radiation calculation code", *J. Synchrotron Rad.*, vol. 8, pp. 1221–1228, 2001. doi:10.1107/S090904950101425X

[3] K. Klementiev and R. Chernikov, "Powerful scriptable ray tracing package XRT", in *Proc. SPIE 9209, Advances in Computational Methods for X-ray Optics III*, San Diego, CA, USA, 2014, p. 92090A. doi:10.1117/12.2061400

[4] M. Sanchez del Rio, N. Canestrari, F. Jiang, and F. Cerrina, "SHADOW3: a new version of the synchrotron X-ray optics modeling package", *J. Synchrotron Rad.*, vol. 18, pp. 708–716, 2011. doi:10.1107/S0909049511026306

[5] L. Mandel and E. Wolf, *Optical Coherence and Quantum Optics*, Cambridge, MA, USA: Cambridge University Press, 1995.

[6] M. Glass and M. Sanchez del Rio, "Coherent modes of X-ray beams emitted by undulators in new storage rings", *Europhys. Lett.*, vol. 119, p. 34004, 2017. doi:10.1209/0295-5075/119/34004

[7] M. Siano *et al.*, "FOCUS: Fast Monte CarlO approach to Coherence of Undulator Sources", submitted for publication.

[8] G. Geloni, E. Saldin, E. Schneidmiller, and M. Yurkov, "Fourier treatment of near-field synchrotron radiation theory", *J. Opt. Commun.*, vol. 276, pp. 167–179, 2007. doi:10.1016/j.optcom.2007.03.051

[9] J. W. Goodman, *Introduction to Fourier Optics*, Greenwood Village, CO, USA: Ben Roberts & Company, Englewood, 2007.

[10] G. Geloni, E. Saldin, E. Schneidmiller, and M. Yurkov, "Transverse coherence properties of X-ray beams in third-generation synchrotron light sources", *Nucl. Instrum. Methods Phys. Res. A*, vol. 588, pp. 463–493, 2008. doi:10.1016/j.nima.2008.01.089

[11] C. Thomas, P. Dudin, and M. Hoesch, "Coherence of a near diffraction limited undulator synchrotron radiation source", *J. Opt. Commun.*, vol. 359, pp. 171–176, 2016. doi:10.1016/j.optcom.2015.09.045

[12] M. Siano *et al.*, "Two-dimensional electron beam size measurements with X-ray heterodyne near field speckles", *Phys. Rev. Accel. Beams*, vol. 25, p. 052801, 2022. doi:10.1103/PhysRevAccelBeams.25.052801

ISBN: 978-3-95450-241-7 ISSN: 2673-5350 doi:10.18429/JACoW-IBIC2022-TUP17

HL-LHC BEAM GAS FLUORESCENCE STUDIES FOR TRANSVERSE PROFILE MEASUREMENT

O. Sedlacek *[1,2], O. Stringer[2], C. Welsch[2], H. Zhang[2]
University of Liverpool, Liverpool, UK
M. Ady, A. R. Churchman, S. Mazzoni, M. Sameed, G. Schneider,
C. C. Sequeiro, K. Sidorowski, R. Veness, CERN, Geneva, Switzerland
P. Forck, S. Udrea, GSI, Darmstadt, Germany
[1]also at CERN, Geneva, Switzerland
[2]also at Cockcroft Institute, Daresbury, Warrington, UK

Abstract

In a gas jet monitor, a supersonic gas curtain is injected into the beam pipe and interacts with the charged particle beam. The monitor exploits fluorescence induced by beam-gas interactions, thus providing a minimally invasive transverse profile measurement. Such a monitor is being developed as part of the High Luminosity LHC upgrade at CERN. As a preliminary study, the fluorescence cross section of relevant gases must be measured for protons at 450 GeV and 6.8 TeV (i.e. the LHC injection and flat top energies). In these measurements, neon, or alternatively nitrogen gas, will be injected into the LHC vacuum pipe by a regulated gas valve to create an extended pressure bump. This work presents the optical detection system that was installed in 2022 in the LHC to measure luminescence cross-section and horizontal beam profile. Preliminary measurements of background light and first signals are presented in this paper.

INTRODUCTION

During the Long Shutdown 3 (LS3, from 2026 to 2028) the Large Hadron Collider (LHC) will undergo a major upgrade to deliver higher luminosity [1], which will involve many new technologies including novel beam diagnostics. A gas jet monitor - Beam Gas Curtain (BGC) monitor - exploiting fluorescence is well-suited for such an environment as it provides non-invasive or minimally invasive profile measurements in the presence of high HL-LHC beam power and strong magnetic fields. The monitor [2–7] is based on a supersonic gas curtain propagating into the path of the beams at 45° that would allow an observation of the 2D transverse distributions from above. The beam excites the gas atoms through collisions which, after deexcitation, emit photons. The distribution of photons is then directly related to the distribution of the original beam. To optimize the detector it is important to know the light yield of the fluorescence process with working gases, such as neon and nitrogen, and protons at 6.8 TeV. Currently, the cross-sections at such high energies are extrapolated through many orders of magnitude from information found in literature at much lower energies [8]. To address this lack of data, an experiment was carried out in 2018 in the LHC to measure neon fluorescence yield at the LHC beam energies, but due to a high background and a low cross-section, only the fluorescence caused by heavy lead ions at the injection energy was measured. Therefore, a new experimental setup was installed at the LHC with many improvements implemented in order to reduce synchrotron radiation background and to improve the sensitivity. The experimental setup is described in this paper, together with the first measurements performed during beam operation in 2022.

* Ondrej.Sedlacek@cern.ch

EXPERIMENTAL SETUP

A new imaging system was designed and installed at the LHC point 4 on the 'Beam 1' line (i.e. beam propagating clockwise) in a vacuum chamber equipped with a gas injection system with the aim of measuring the LHC beam-induced fluorescence yield of neon at 585 nm. Neon gas is injected at a pressure of 5×10^{-8} mbar to minimise its effect on the beam quality while providing enough gas atoms for the beam to collide with. The observed process is an emission line of neutral Ne which is due to the $2s^2 2p^5 ({}^2P^0_{1/2}) 3p^2[1/2]_0 \rightarrow 3s^2[1/2]_1$ transition at 585.4 nm [2, 9].

Figure 1 depicts the whole experimental setup including the camera module which measures the distribution of the emitted photons. An optical line is installed on top of a window flange, imaging the photons with an apochromatic triplet lens with an aperture of 40 mm and a focal length of 160 mm ideal for near-1:1 imaging conditions. The lens provides a high transmittance of approximately 80 % over the wavelengths of interest. In front of the sensor, a filter wheel is installed with one empty filter socket, one blocking filter and one 585 ± 10 nm filter. The blocking filter is a completely opaque screen stopping any photons from reaching the sensor and is used for background studies. The 585 ± 10 nm filter then allows the fluorescence signal to be measured while reducing other sources of background light. The fluorescence light is measured by a two-stage image intensifier reaching single-photon detection sensitivity [10].

The experimental chamber was installed during the 2021-22 LHC Year-End Technical Stop (YETS), in a position where low levels of synchrotron radiation are expected. To minimise the reflection of synchrotron radiation, the vacuum chamber was also blackened by amorphous carbon coating with a reflectivity of 14 %. An ultra-low reflectivity black

Content from this work may be used under the terms of the CC BY 4.0 licence (© 2022). Any distribution of this work must maintain attribution to the author(s), title of the work, publisher, and DOI

ISBN: 978-3-95450-241-7 ISSN: 2673-5350 doi:10.18429/JACoW-IBIC2022-TUP17

Content from this work may be used under the terms of the CC BY 4.0 licence (© 2022). Any distribution of this work must maintain attribution to the author(s), title of the work, publisher, and DOI

contrast plate with multi-layered coating with a reflectivity of 0.25 % was also installed at the bottom of the chamber on the opposite side of the vacuum window to minimise background light reaching the camera.

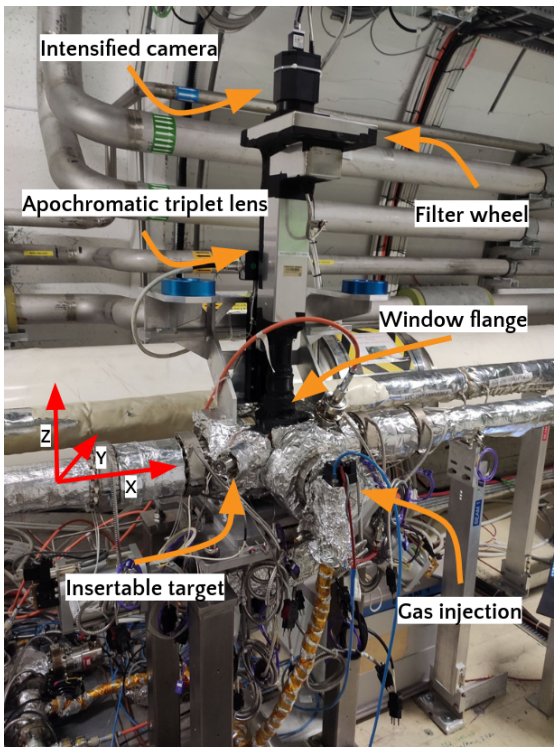


Figure 1: The experimental setup installation in the LHC, consisting of a blackened chamber, a gas injection system and a camera module.

OPTICAL SYSTEM

The extrapolated cross-section of the fluorescence is 4.7×10^{-22} cm^2 [8]. In order to cope with such a low light yield, the optical system was designed to demagnify the final image and increase the number of photons per pixel, while keeping the resolution small enough to measure the LHC beam size and maintaining the optical acceptance as large as possible. The final trade-off magnification of the system is set to 0.205 with 10.5 pixels per 300 µm corresponding to the LHC beam σ. Therefore, the solid angle of the system is 1.8×10^{-2} sr and its acceptance is 1.4×10^{-3}.

The Modulation Transfer Function (MTF) of the optical module was measured to evaluate the optical performance of the system. The resulting MTF is summarized in Table 1 which shows that for the expected beam size of 1.2 mm (4σ) the MTF is >46 % and in the order of 300 µm (σ) the MTF is still >26 %. The measurements were carried out at 585 nm using a movable optical target.

LHC BACKGROUND MEASUREMENTS

Background measurements in presence of the LHC beam at 6.8 TeV without injecting gas are shown in Figs. 2-4 and discussed below. In the figures, the beam propagates along the X-axis from left to right. The Y-axis corresponds to the horizontal direction transverse to the beam's trajectory as labeled in Fig. 1. With no gas injection in these measurements, the signal observed on the camera corresponds to the background signals caused by different sources.

Table 1: Measured Modulation Transfer Function (MTF) of the optical module installed at LHC showing MTF >46 % for 1.2 mm corresponding to 4σ of the LHC beam.

MTF [%]	line/mm
46	1.000
38	0.500
26	0.250
13	0.125

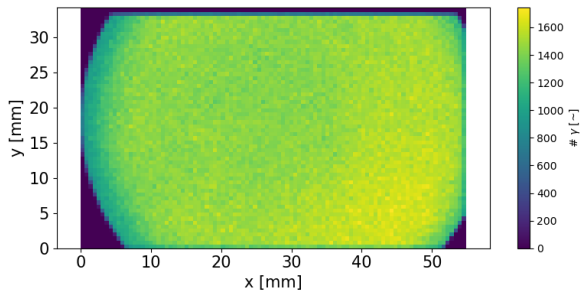


Figure 2: Background measurement in presence of the LHC beam at 6.8 TeV with a blocking filter. The measured signal yield corresponds to the beam loss induced photon-like signal as measured by the camera.

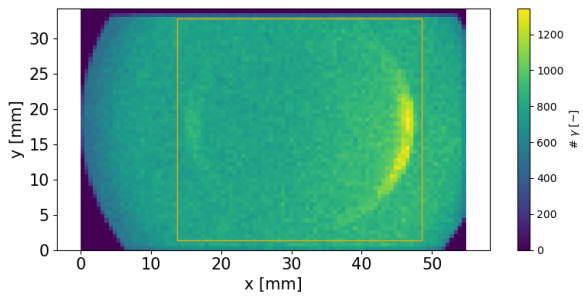


Figure 3: Measurement of the LHC beam at 6.8 TeV with a 585 ± 10 nm filter corresponding to the distribution of beam loss induced signal and synchrotron radiation observed by the camera module.

The dark counts from the camera and the optical light background measured without beam were found to be negligible. The natural beam losses at those locations typically come from the interaction of the beam with rest-gas molecules. They generate particle showers that can induce photon-like signals while crossing the MCP. The beam loss (and negligible dark counts) signal was measured using the blocking plate in the optical filter wheel such that no photon would reach the camera. Figure 2 shows that in such a case the

ISBN: 978-3-95450-241-7 ISSN: 2673-5350 doi:10.18429/JACoW-IBIC2022-TUP17

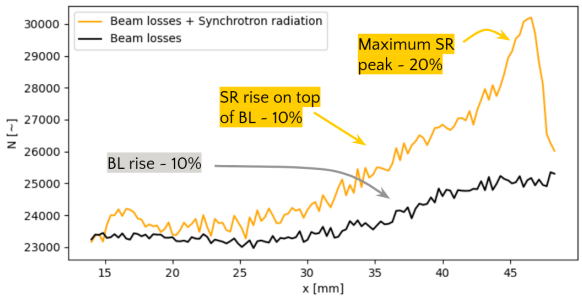


Figure 4: X projection (sum across y) of measurements with the 585 ± 10 nm (orange line) and Blocking (black line) filter.

distribution of losses is not perfectly homogeneous. A horizontal projection of the image, depicted in Fig. 4, clearly demonstrates that the photon distribution is not perfectly homogeneous which is not fully understood at this stage.

The synchrotron radiation background at the 585 nm wavelength was then measured by replacing the blocking filter with the 585 nm optical band-pass filter. The corresponding image is shown in Fig. 3. It clearly shows that, at the top energy, synchrotron radiation, generated in the surrounding dipole magnets, is the main source of optical light background for this measurement. As shown in Fig. 4, the distribution of synchrotron radiation presents an even larger inhomogeneity.

Integrating over all pixels of the image in Fig. 3, the synchrotron radiation accounts for only 3.7 % of all observed signals. Additionally, if we consider only the area around the window flange (e.g area of the image that is looking inside of the tbeam pipe), depicted as the orange rectangle in Fig. 3, then the synchrotron radiation makes up about 6 % of all signals.

Overall the synchrotron radiation levels are quite low, especially in comparison to the previous measurements carried out in 2018. The tests performed at a different location in the LHC and using a different setup demonstrated that synchrotron radiation accounted for 30 % of the signal. The measurements done in 2018 had also much higher beam loss signals, therefore it is difficult to quantify by how much the synchrotron radiation background has been reduced. Nonetheless, this is a very valuable improvement which can be attributed to the new vacuum chamber with blackened, light-absorptive internal surfaces.

SIGNAL VS BACKGROUND

With the presented experimental setup and the current settings, the expected level of fluorescence signal should be visible above the background if using a sufficient integration time. In the present configuration, the fluorescence signal should appear as a continuous horizontal band in the image. Due to the inhomogeneity of the background, the fluorescence signal should appear more clearly in the central part of the images as shown in Fig. 5 by the orange box.

The results presented in Figs. 5 and 6, show a small fluorescence signal at the expected position. This first, but

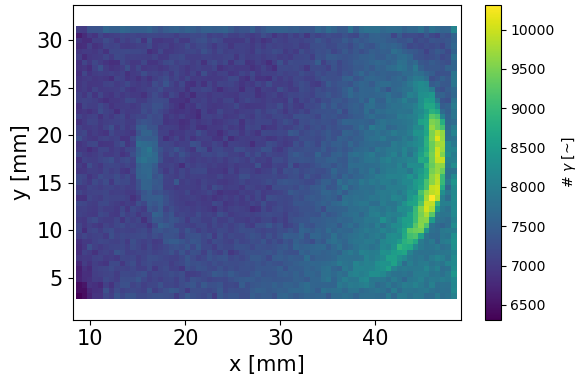


Figure 5: Image acquired using the 585 ± 10 nm filter.

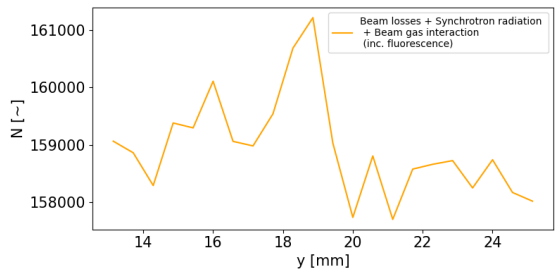


Figure 6: Vertical projection of image depicted in Fig. 5.

very encouraging, measurement was carried out with a gas pressure at the interaction point in the order of 2×10^{-8} mbar, and with ~ 2000 nominal bunches at 6.8 TeV. The measurement's integration time was 450 s.

CONCLUSIONS

New imaging and gas injection systems were installed in the LHC to measure the neon fluorescence light yield with protons at 6.8 TeV. A first set of measurements showed that beam loss and synchrotron radiation signals dominate the background with synchrotron radiation accounting for 6 % of all observed signals in the central area of the image and beam losses to the remaining 94 %. In those conditions, a small fluorescence signal was observed for the very first time with protons at 6.8 TeV using a long integration time. More measurements will be performed in the coming months as the LHC intensity ramp up continues. In the next phase of our work, we will concentrate on neon fluorescence cross section at the injection and top energies with both protons and heavy ions. In the coming year, the gas injection system will be replaced with a supersonic gas curtain that would enable the local gas density to be increased by two orders of magnitude. This will result in more precise measurements of the fluorescence cross section and non-invasive beam profile measurements.

ACKNOWLEDGMENTS

This work was supported by STFC under grant agreement ST/P006752/1 and is a part of HL-LHC project.

Content from this work may be used under the terms of the CC BY 4.0 licence (© 2022). Any distribution of this work must maintain attribution to the author(s), title of the work, publisher, and DOI

ISBN: 978-3-95450-241-7 ISSN: 2673-5350 doi:10.18429/JACoW-IBIC2022-TUP17

Content from this work may be used under the terms of the CC BY 4.0 licence (© 2022). Any distribution of this work must maintain attribution to the author(s), title of the work, publisher, and DOI

REFERENCES

[1] G. Apollinari *et al.*, "High luminosity large hadron collider HL-LHC", 2017. doi:10.48550/arXiv.1705.08830

[2] S. Udrea *et al.*, "Development of a Fluorescence Based Gas Sheet Profile Monitor for Use With Electron Lenses: Optical System Design and Preparatory Experiments", in *Proc. 6th Int. Beam Instrumentation Conf. (IBIC'17)*, Grand Rapids, MI, USA, Aug. 2017, pp. 359–363. doi:10.18429/JACoW-IBIC2017-WEPCC08

[3] A. Salehilashkajani *et al.*, "Commissioning of the Prototype for a New Gas Curtain Beam Profile Monitor Using Beam Induced Fluorescence for HL-LHC", in *Proc. 10th Int. Particle Accelerator Conf. (IPAC'19)*, Melbourne, Australia, May 2019, pp. 2709–2712. doi:10.18429/JACoW-IPAC2019-WEPGW093

[4] V. Tzoganis and C. P. Welsch. "A non-invasive beam profile monitor for charged particle beams", *Appl. Phys. Lett.*, vol. 104, no. 20, p. 204104, 2014. doi:10.1063/1.4879285

[5] H. D. Zhang *et al.*, "A Supersonic Gas-Jet Based Beam Induced Fluorescence Prototype Monitor for Transverse Profile Determination", in *Proc. 8th Int. Particle Accelerator Conf. (IPAC'17)*, Copenhagen, Denmark, May 2017, pp. 458–461. doi:10.18429/JACoW-IPAC2017-MOPAB139

[6] H. D. Zhang *et al.*, "A Supersonic Gas Jet-Based Beam Profile Monitor Using Fluorescence for HL-LHC", in *Proc. 9th Int. Particle Accelerator Conf. (IPAC'18)*, Vancouver, Canada, Apr.-May 2018, pp. 1891–1894. doi:10.18429/JACoW-IPAC2018-WEPAF034

[7] A. Salehilashkajani *et al.*, "A gas curtain beam profile monitor using beam induced fluorescence for high intensity charged particle beams", *Appl. Phys. Lett.*, vol. 120, no. 17, p. 174101, 2022. doi:10.1063/5.0085491

[8] S.Udrea and P. Forck, "Milestone 1.6 report", GSI, Darmstadt, Germany, 2018.

[9] M. Eckhardt, D. Hasselkamp, and K.H. Schartner, "Neon 3p-excitation by proton impact (100 keV-1 MeV): Cross sections and line polarization", *Z Physik A*, Dec. 1979, vol. 292, pp. 337–345. doi:10.1007/BF01546431

[10] S. Udrea *et al.*, "Development of a fluorescence based gas sheet profile monitor for use with electron lenses: Optical System design and preparatory experiments", in *Proc. 6th Int. Beam Instrumentation Conf. (IBIC'17)* Grand Rapids, MI, USA, Aug. 2017. doi:10.18429/JACoW-IBIC2017-WEPCC08

ISBN: 978-3-95450-241-7 ISSN: 2673-5350 doi:10.18429/JACoW-IBIC2022-TUP18

HIGH-RESOLUTION INTERFEROMETRIC BEAM-SIZE MONITOR FOR LOW-INTENSITY BEAMS

B. Alberdi-Esuain*,[1], J.-G. Hwang, T. Kamps[1]
Helmholtz-Zentrum Berlin für Materialien und Energie, Berlin, Germany
[1]also at Humboldt Universität zu Berlin, Berlin, Germany

Abstract

Plasma-based accelerator technology is reaching a mature state, where applications of the beam for medical sciences, imaging, or as an injector for a future large-scale accelerator-driven light source become feasible. Particularly, the requirements for beam injection into a storage-ring-based light source are very strict with regards to beam quality and reliability. A non-invasive diagnostics greatly helps to reduce the commissioning time of the machine. We present a device suitable for online, non-destructive monitoring of the transverse spot size of the injected beam. In order to measure lateral beam sizes with a few-µm resolution, the technique uses an interferometric regime of coherent synchrotron radiation that is enabled by a sub-femtosecond short bunch-length. Simulations of the photon flux and the retrieval of the beam spot-size are performed for different bandwidth filters in order to define the bandwidth acceptance. Results show the potential of the proposed system that achieves precise retrieval of the complex degree of coherence at an extremely low photon intensity similar to those expected towards the plasma-acceleration injectors.

INTRODUCTION

In the last years, the laser plasma-accelerator technology has advanced enough to produce charged-particle beams stably with ultra-low-emittances in 6D phase-space [1]. These achievements have enabled the application of plasma-accelerator technology for low-energy and high-quality injectors. Recent research evidence that the repetition rate of such a technique is not limited by plasma recovery time in the plasma cell, so it is promising to reach MHz repetition [2]. This feature opens a possibility to supersede the state-of-the-art injectors. Currently, there is an ongoing global effort aimed towards designing a compact plasma-wakefield accelerator as an injector for future large-scale accelerator-driven light sources such as Athena$_e$ [3] or cSTART [4] for injection into ring-based light-sources, high-average-power plasma wakefield research with FLASHForward [5] or projects to apply this technology for free electron lasers directly [1]. These novel injectors can generate electron beams with an extremely low-emittance on the order of $\gamma\epsilon_{x,y} = 0.05\,\text{mm}\cdot\text{mrad}$ for pC to sub-pC bunch charges. The important beam parameters of these facilities are listed in Table 1.

Diagnostics techniques are following the steps forward of laser-plasma accelerators closely, particularly the non-invasive spot-size measurement which inherently gives the beam emittance information. The characterisation of the electron distribution with the sufficient resolution is challenging due to the extremely small beam emittances and intensities in plasma-wakefield accelerators. Techniques that employ scintillation screens are widely used for similar beam conditions [6], but this deteriorates the beam quality noticeably or even it causes beam loss in the following section. On the other hand, synchrotron-radiation-based monitors is inadequate since light intensity by incoherent synchrotron radiation (ISR) is insufficient owing to the low electron intensity. However, the key feature of the laser-wakefield accelerators, temporally short bunch enables the arising of coherent synchrotron radiation (CSR) in the visible region, which enhances the photon flux significantly in a bending magnet. The photon flux by CSR provides sufficient intensity to place an interferometric beam size monitor (IBSM) which measures the lateral distribution of electrons by the spatial coherency of the interference pattern in the detector [7]. The use of the diffraction regime enhances the spatial resolution by two orders of magnitude, reaching µm-resolutions [8] and this has been applied to many storage-ring-based light sources [9–11]. By extension, we have designed and demonstrated the high-resolution IBSM for extreme beam conditions [12]. However, the detailed aspects of the bandwidth acceptance and beam spot-size retrieval are not fully discussed in the paper. Hence, numerical simulations for investigating the effect of bandwidth and for estimating the propagation of this error to the beam-size retrieval are explained. A scheme of the working principle of our design can be seen in Fig. 1.

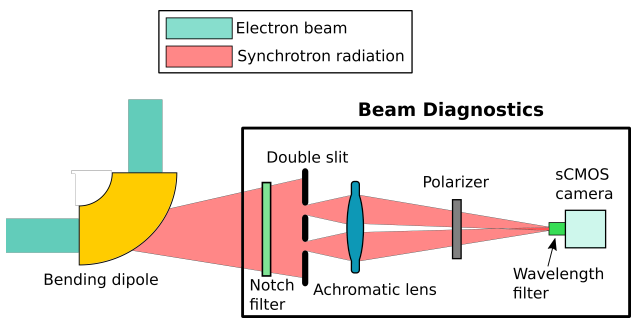


Figure 1: Schematic layout of the interferometry beam size monitor (IBSM) with a scientific complementary metal–oxide–semiconductor (sCMOS) camera for a plasma-wakefield accelerator.

* benat.alberdi_esuain@helmholtz-berlin.de

Content from this work may be used under the terms of the CC BY 4.0 licence (© 2022). Any distribution of this work must maintain attribution to the author(s), title of the work, publisher, and DOI

ISBN: 978-3-95450-241-7 ISSN: 2673-5350 doi:10.18429/JACoW-IBIC2022-TUP18

Content from this work may be used under the terms of the CC BY 4.0 licence (© 2022). Any distribution of this work must maintain attribution to the author(s), title of the work, publisher, and DOI

Table 1: Major Beam Parameters of Research Projects for a Plasma-wakefield Acceleration-based Injector Relevant for Our Case Study

	Energy (MeV)	$\gamma\epsilon$ (mm·mrad)	Bunch charge (pC)	Bunch length (fs)	Beam size at $\beta_{x,y}$=1 m (μm)
Athena$_e$ [3]	200	0.05	0.38-2.77	0.2-0.62	11
cSTART [4]	50	≤3	27.5	≤10	174
Shanghai LWFA [1]	490	≤3	50	/	15

METHODS

Double Slit Interference for 2D Gaussian Beams

The intensity distribution of interference fringes generated by a double-slit is found by using the basic theory of spatial coherence of light and the van Cittert-Zernike theorem which explains that the Fourier transform of the intensity distribution function of a distant, incoherent source is equal to its complex degree of spatial coherence (also known as interferometric visibility) under certain conditions. Assuming a Gaussian distribution of the source, the intensity distribution of the photons at the screen for a horizontal double slit can be presented for monochromatic light as

$$I(x,y) = I_0 + (I_1 + I_2)\,\mathrm{sinc}^2\left(\frac{\pi w_x x}{\lambda f}\right)\mathrm{sinc}^2\left(\frac{\pi w_y y}{\lambda f}\right)\cdot \left[1 + |\gamma_{12}|\cos\left(\frac{2\pi D_x x}{\lambda f} + \phi\right)\right], \quad (1)$$

where I_1 and I_2 are the photon intensity at two holes, respectively, w_x and w_y are the slit opening in horizontal and vertical directions, and γ_{12} is the visibility (complex degree of spatial coherence), f is the focal length of the objective lens, D_x is the slit separation, ϕ represents the phase differences between the two incident waves, and I_0 denotes the constant offset preset the value for a detector to compensate for negative values owing to random noise. For a Gaussian distributed source, the absolute value of the complex degree of coherence can furthermore be simplified as

$$\sigma_x = \frac{\lambda L}{\pi D_x}\sqrt{\frac{1}{2}\ln\frac{1}{|\gamma_{12}|}}, \quad (2)$$

where σ_x is the rms horizontal beam size and L is the distance from the source point to the slit. This relation allows quantifying the absolute beam size directly.

Operational Limit and Bandwidth Acceptance

In the previous study, it has proven that that the operating limit of the IBSM technique using the state-of-the-art single-photon camera is about 5 photons/pixel at the peak, which corresponds to a S/N ratio of about 4. This is equivalent to a total flux of 2×10^4 photons/s. The numerical simulation includes photon shot-noise which is caused by statistical quantum fluctuations and can be modeled by a Poisson process. However, the IBSM monitor requires primarily the obstacles such as a double slit for inducing diffraction generation, a polarization filter for rejecting the π-polarization component, and a wavelength filter for generating quasi-monochromatic light, which reduces the number of photons by two orders of magnitudes. It is generally not suitable for low flux beams which is the case for Athena$_e$ and cSTART projects. The photon flux can be escalated by widening the bandwidth of the filter and also can be enhanced by CSR generated by a short bunch. To estimate the photon flux by ISR and CSR for two cases of the plasma-wakefield accelerator, numerical simulations are performed using SPECTRA code [13] with beam parameters of Athena$_e$ and cSTART listed in Table 1. A magnetic field of 0.85 T in the bending magnet is used for the simulations and obstacles such as the optical wavelength filter and a double-slit with a slit opening of $3 \times 3\,\mathrm{mm}^2$ is included. The results are shown in Fig. 2.

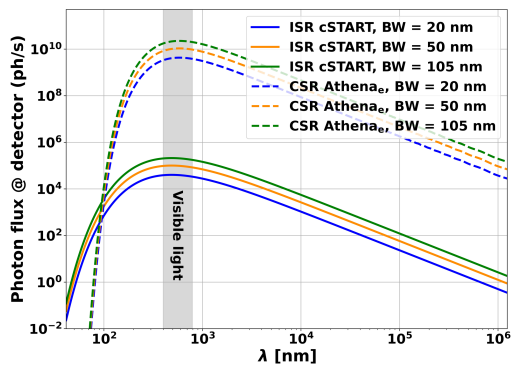


Figure 2: Photon flux at the detector for Athena$_e$ and cSTART beam parameters from Table 1 with various bandwidths. The photon flux by CSR shown here is calculated with the lower case of the bunch charge (0.38 pC) in Athena$_e$.

Taking the diminution of photon flux by the obstacles into account, the photon flux by ISR at the detector is 3.4×10^3 photons/s for the Athena$_e$ and 2.9×10^4 photons/s for cSTART at a bandwidth of 100 nm. Despite the photon flux of ISR for Athena$_e$ can not reach the operating limit, $\sim 2 \times 10^4$ photons/s, defined by the numerical simulation with the total noise and quantum efficiency of the camera, the photon flux by CSR overwhelms the limit easily which evidences that a narrow filter can be used. However, the photon flux by ISR for cSTART can overcome the operating limit by expanding the bandwidth of the filer. The wider the bandwidth of the filter, the greater the number of photons in the detector, but the dilution of the visibility caused by phase differences of non-monochromatic light becomes more severe, resulting in inaccurate beam size measurements since

ISBN: 978-3-95450-241-7 ISSN: 2673-5350 doi:10.18429/JACoW-IBIC2022-TUP18

the effect of a finite bandwidth is not accounted in Eq. (1). In order to quantify the effect of the bandwidth in the beam size determination, numerical simulations are performed based on Monte-Carlo method. Two-dimensional coordinates of photons at the detector were generated for a specified photon intensity with a random uniform distribution of the wavelength and probability density function that follows Eq. (1). Then, an artificial image was generated by counting the number of particles within a finite size of a pixel and adding Poisson noise onto each pixel. Each image is first projected into the slit axis and is analyzed based on fitting with an analytical formula. The projections simulated with various bandwidths at a visibility value of 0.5 are shown in Fig. 3. It is clear that the fringes are not significantly

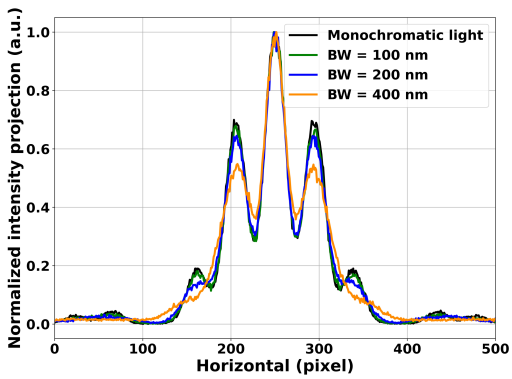


Figure 3: Simulated interference pattern at the detector for a visibility value of $|\gamma_{1,2}| = 0.5$ with various bandwidths. The simulations have been performed with a flux of 1×10^5 photon/s at the detector.

distorted for a bandwidth below 100 nm, but the distortion is non-negligible for larger bandwidths.

In order to estimate the statistical fluctuation of the visibility retrieval, the analysis is repeated for fifty different images generated for each intensity at various visibility values. The visibility can be adjusted by changing the experimental set-up such as magnitudes of L, λ and D to get a desired visibility for a given spot size. Therefore, the calculation has been performed with various visibilities. Fig. 4 shows that the retrieved visibility is underestimated for large visibilities and overestimated for the lowest ones. The error is minimized around visibility of 0.5. Therefore, to obtain the reliability of the monitor, the visibility is necessary to be tailored to the intermediate values by changing the experimental set-up. The measurement accuracy is improved with photon flux, which can be enhanced by widening the bandwidth of a wavelength filter. An increasing bandwidth decreases the visibility retrieval accuracy and, as a consequence, the beam-size resolution.

In order to estimate the measurement error in the beam size determination quantitatively, the relative error of the beam size calculation as a function of the bandwidth at various visbilities are computed. The error transfer from relative visibility retrieval error($|\Delta\gamma/\gamma|$) to spatial resolution ($\Delta\sigma$) is calculated according to the following equation: $\Delta\sigma = \lambda L / \left(2\pi D\sqrt{2\ln|1/\gamma|}\right) \times |\Delta\gamma/\gamma|$. The result is shown in Fig. 5.

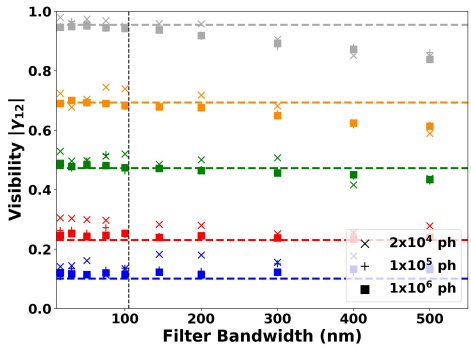


Figure 4: The retrived visibility as a function of the bandwidth at different photon fluxes and visibility (in dashed horizontal lines).

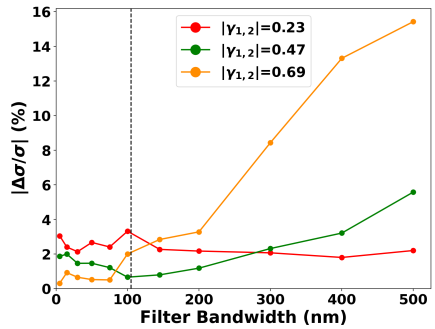


Figure 5: Relative error of the retrieved beam spot-size as a function of the bandwidth at intermediate $|\gamma_{1,2}|$ values, which depend on the beam spot-size and the experimental set-up.

For the intermediate visibility values of 0.47 and 0.69 with the chosen bandwidth of 105 nm for our device, the error of the beam size measurement remains below a few percentages. It also indicates that the smaller visibility has much less error when the bandwidth is increased because the local minima of the interference fringe raise for the lower visibility, resulting in immune to the statistical error that has been introduced by the bandwidth. The error of the visibility retrieval is smaller than 3.6% at the operating limit with a bandwidth of 105 nm. This results in a spatial resolution of fewer than 1 µm since the beam size is in the order of tens of micrometers due to the extremely low emittance. It can be also improved significantly by narrowing the bandwidth of the wavelength filter. This shows that as long as the photon flux is kept over the operating limit, a narrow bandwidth acceptance is preferred.

Content from this work may be used under the terms of the CC BY 4.0 licence (© 2022). Any distribution of this work must maintain attribution to the author(s), title of the work, publisher, and DOI

ISBN: 978-3-95450-241-7 ISSN: 2673-5350 doi:10.18429/JACoW-IBIC2022-TUP18

Content from this work may be used under the terms of the CC BY 4.0 licence (© 2022). Any distribution of this work must maintain attribution to the author(s), title of the work, publisher, and DOI

CONCLUSIONS

Plasma-wakefield accelerators produce a high quality beams with a low average beam-current which results in a lack of the photon intensity by synchrotron radiation, so this feature calls for research and development for high spatial-resolution diagnostics that can be operated at a low photon intensity. For the Athena$_e$ project, the beams have a temporal size of sub-femtosecond which is comparable to or even shorter than the wavelength of visible light, producing intense CSR. This enables the implementation of the interferometric technique that can achieve a few-μm spatial resolution. However, for the beams in cSTART that have a bunch length longer than the wavelength, it demands a broad filter to achieve the photon flux greater than the operating limit. Therefore, we have studied the effects of the bandwidth in the beam-size retrieval error. The statistical error of the IBSM by the quasi-monochromatic light is investigated for estimating the measurement accuracy of an absolute lateral size at the extreme beam condition. The error of the visibility retrieval is less than 3.6% at the operating limit with a bandwidth of 105 nm for a cSTART beam condition. This results in a spatial resolution of fewer than 1 μm.

REFERENCES

[1] W. Wang *et al.*, "Free-electron lasing at 27 nanometres based on a laser wakefield accelerator", *Nature*, vol. 595, pp. 516–520, 2021. doi:10.1038/s41586-021-03678-x

[2] R. D'Arcy *et al.*, "Recovery time of a plasma-wakefield accelerator", *Nature*, vol. 603, pp. 58–62, 2022. doi:10.1038/s41586-021-04348-8

[3] B. Marchetti *et al.*, "Technical Design Considerations About the SINBAD-ARES Linac", in *Proc. IPAC'16*, Busan, Korea, May 2016, pp. 112–114. doi:10.18429/JACoW-IPAC2016-MOPMB015

[4] B. Härer *et al.*, "Non-Linear Features of the cSTART Project", in *Proc. IPAC'19*, Melbourne, Australia, May 2019, pp. 1437–1440. doi:10.18429/JACoW-IPAC2019-TUPGW020

[5] R. D'Arcy *et al.*, "FLASHForward: plasma wakefield accelerator science for high-average-power applications", *Philos. Trans. R. Soc. London, Ser. A*, vol. 377, 2019. doi:10.1098/rsta.2018.0392

[6] M. C. Downer, R. Zgadzaj, A. Debus, U. Schramm, and M. C. Kaluza, "Diagnostics for plasma-based electron accelerators", *Rev. Mod. Phys.*, vol. 90, p. 035002, 2018. doi:10.1103/RevModPhys.90.035002

[7] T. Mitsuhashi, "Beam Profile and Size Measurement by SR Interferometers", in *Beam Measurement: Proceedings of the Joint US-CERN-Japan-Russia School on Particle Accelerators*, Editors S-i. Kurokawa, S.Y. Lee, E. Perevedentsev and S. Turner, p. 399–427, World Scientific, Singapore, 1999.

[8] T. Naito and T. Mitsuhashi, "Very small beam-size measurement by a reflective synchrotron radiation interferometer", *Phys. Rev. ST Accel. Beams*, vol. 9, p. 122802, 2006. doi:10.1103/PhysRevSTAB.9.122802

[9] C. Kim *et al.*, "Two-dimensional SR interferometer for PLS-II", *J. Korean Phys. Soc.*, vol. 58, pp. 725–729, 2011. doi:10.3938/jkps.58.725

[10] L. Torino and U. Iriso, "Transverse beam profile reconstruction using synchrotron radiation interferometry", *Phys. Rev. ST Accel. Beams*, vol. 19, p. 122801, 2016. doi:10.1103/PhysRevAccelBeams.19.122801

[11] M. Koopmans, P. Goslawski, J. G. Hwang, M. Ries, M. Ruprecht, and A. Schaelicke, "Status of a Double Slit Interferometer for Transverse Beam Size Measurements at BESSY II", in *Proc. IPAC'17*, Copenhagen, Denmark, May 2017, pp. 149–152. doi:10.18429/JACoW-IPAC2017-MOPAB032

[12] J.-G. Hwang *et al.*, "Monitoring the size of low-intensity beams at plasma-wakefield accelerators using high-resolution interferometry", *Commun. Phys.*, vol. 4, 2021. doi:10.1038/s42005-021-00717-x

[13] T. Tanaka and H. Kitamura, "SPECTRA: a synchrotron radiation calculation Code", *J. Synchrotron Radiat.*, vol. 8, pp. 1221–1228, 2001. doi:10.1107/S090904950101425X

ISBN: 978-3-95450-241-7 ISSN: 2673-5350 doi:10.18429/JACoW-IBIC2022-TUP19

VISIBLE RANGE POLARIZED IMAGING FOR HIGH RESOLUTION TRANSVERSE BEAM SIZE MEASUREMENT AT SOLEIL

M. Labat*, A. Bence, A. Berlioux, B. Capitanio, G. Cauchon,
J. Da Silva, N. Hubert, D. Pédeau, M. Thomasset
Synchrotron SOLEIL, Gif-sur-Yvette, France

Abstract

SOLEIL storage ring is presently equipped with three diagnostics beamlines: two in the X-ray range (pinhole cameras) and one in the visible range. The visible range beamline relies on a slotted copper mirror extracting the synchrotron radiation from one of the ring dipoles. The extracted radiation is then transported down to a dedicated hutch in the experimental hall. Up to now, this radiation was split into three branches for rough monitoring of the beam transverse stability, bunch length measurements and filling pattern measurements. In the framework of SOLEIL's upgrade, we now aim at developing a new branch for high resolution beam size measurement using polarized imaging. This work presents the various modifications recently achieved on the beamline to reach this target, including a replacement of the extraction mirror, and preliminary results towards transverse beam size measurement.

INTRODUCTION

SOLEIL storage ring presently delivers synchrotron radiation to 29 beamlines. The stability of the delivered photon beams, a main figure of merit for users, relies on an accurate monitoring of the electron beam orbit and electron beam size / emittance at users source points. Presently, two beamlines in the X–ray range are dedicated to beam transverse size diagnostics, relying on pinhole camera systems. The high-resolution pinhole cameras' measurements are used in a feedback loop to maintain the vertical emittance within $\pm 5\%$. Despite the high reliability of those pinhole cameras, it would be reassuring to have an additional beam size measurement based on a different technique for redundancy and further verification of the absolute emittance value. This is the main reason why, for three years, we have been working on the upgrade of our third diagnostics beamline, the MRSV beamline (Visible Synchrotron Radiation Monitor) in the visible range, to implement an additional high–resolution beam size measurement based on π polarized imaging [2]. This development also turns to be of high interest in the perspective of SOLEIL–II: it might be indeed the only way to obtain, together with a pinhole camera, two beam size measurements with two different dispersion functions for energy spread retrieval. It is finally worth mentioning that, thanks to the high available photon flux on the MRSV beamline, beam size measurements should be achievable down to very low, ≈1 mA, currents (whereas pinhole cameras can't be operated below 10 mA) and could be run above the kHz range at 500 mA (whereas pinhole cameras are limited to the 10 Hz range). This work presents the main steps of the upgrade of the MRSV beamline together with preliminary results.

GENERAL LAYOUT

The experimental layout of the MRSV beamline is presented in Fig. 1.

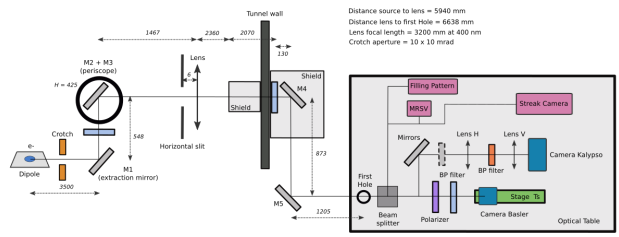


Figure 1: Layout of the MRSV beamline.

The Synchrotron Radiation (SR) of one of the ring dipoles (ANS-C01) is extracted using a slotted mirror, the slot being centered on the beam axis to let SR X–rays go through. The collected photons have a wavelength λ spanning from ≈ 190 to nearly 900 nm. The SR is then transported via a set of mirrors, including a periscope, down to a hutch in the experimental hall. On the beam path inside the tunnel are successively placed a slit and a lens. At the arrival on the optical bench in the hutch, the SR is split into several branches.

Initially, three branches were implemented (see pink boxes in Fig. 1): one with a fast diode for filling pattern measurement, one with a Streak Camera for bunch length measurement and one with a standard Ethernet camera for a coarse imaging of the beam at the source point. We added two new branches to test higher resolution / higher speed imaging systems for beam size retrieval at the source point of the MRSV beamline. We will focus in the following on the high resolution branch (see bottom branch in Fig. 1).

NEW EXTRACTION MIRROR

The initial extraction mirror was already a slotted mirror but without optimized cooling system. In standard operation at 500 mA, when the mirror was inserted in the *slot–insertion* mode, i.e. with its slot centered vertically on the SR fan, its temperature was continuously raising without reaching an equilibrium, preventing its safe use. A new design was therefore optimized in–house in order to guarantee a fast thermal equilibrium of the mirror at 500 mA and to ensure a surface

* marie.labat@synchrotron-soleil.fr

Content from this work may be used under the terms of the CC BY 4.0 licence (© 2022). Any distribution of this work must maintain attribution to the author(s), title of the work, publisher, and DOI

ISBN: 978-3-95450-241-7 ISSN: 2673-5350 doi:10.18429/JACoW-IBIC2022-TUP19

Content from this work may be used under the terms of the CC BY 4.0 licence (© 2022). Any distribution of this work must maintain attribution to the author(s), title of the work, publisher, and DOI

distortion at this equilibrium below $\lambda/2$ with λ=400 nm. The final system is shown in Fig. 2. The mirror was manufactured by Kircheim Optics company. It is a 15 mm thick bulk of Copper (CuC_2) drilled by a 5.6 mm height slot. Its incident surface is coated with an enhanced Aluminium deposit allowing high reflectivity down to 200 nm. The mirror was characterized by the Optics Group of SOLEIL upon its receipt. The measurements revealed that the flatness was below 200 nm peak–to–valley, the rugosity less than 3 nm even nearby the slot edges and the overall radius of curvature above 15 km, i.e. fully beyond the initial specifications. At the rear of the mirror, a Macor ceramic plate enables to hold a set of height thermocouples of K type. Six of them are placed all around the slot and aligned in order to go slightly beyond the mirror shadow (by 0.3 mm) and intercept the SR fan. They enable the accurate vertical centering of the mirror on the SR fan. The other two thermocouples are placed at the bottom of the ceramic plate and aligned to go slightly beyond the mirror bottom shadow. Those are used for a *surf–insertion* of the mirror (the mirror is *surfing* on the top–half of the SR fan to allow larger orbit deviations during machine studies). Two additional thermocouples are forced into the edge faces of the mirror in order to probe the mirror body temperature.

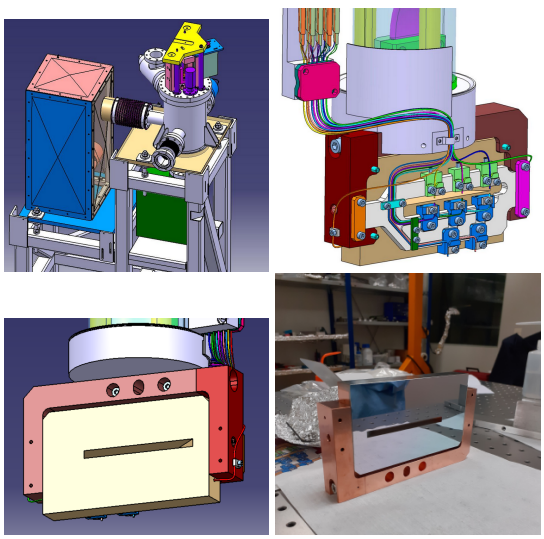


Figure 2: 3D views of the new extraction mirror and picture of the mirror before its installation.

The mirror is then gripped in a copper fork in order to minimize possible stress distortions. Thin (30 µm) Indium foils were inserted in between the mirror edge faces and the fork to optimize the heat transfer from the mirror to the fork. The fork is itself screwed on the bottom tap of an inverted bellow (air inside, vacuum outside). Inside this bellow, a rod enables to insert/extract the mirror while a large copper braid finalizes the heat transfer from the fork to the outside of the vacuum chamber housing the mirror, i.e. to the tunnel ambient air. The mirror is therefore simply but efficiently air–cooled. In standard operation, the total incident power on the mirror is expected to be 3.5 W (possibly 4.5 W at maximum orbit deviation). According to thermal simulations, in these conditions, the mirror is expected to reach an equilibrium temperature of 34°C and to suffer a maximum distortion of 300 nm peak-to-valley nearby the slot.

The mirror was installed in January 2022. After few hours of conditioning, it was inserted in the *slot–insertion* mode at 500 mA: the measured equilibrium temperature, reached within few tens of minutes, was 33°C, in excellent agreement with calculations, while no significant distortion of the radiation wavefront could be observed downstream while increasing the current, indicating negligible distortion of the mirror surface. Thanks to this main upgrade, it is now possible to operate the MRSV beamline with the extraction mirror in *slot–insertion* mode in standard operation at 500 mA.

NEW BEAMLINE COMPONENTS

Unfortunately, the upgrade of the extraction mirror was insufficient to achieve high resolution beam size measurements. Other beamline components too needed a refurbish/upgrade.

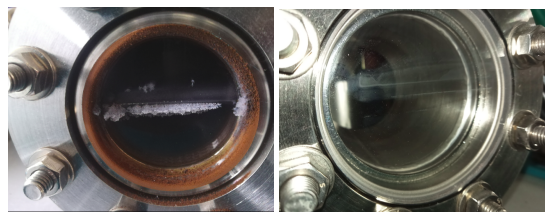


Figure 3: Pictures of the UHV Fused Silica window. Left: after 10 years of operation. Right: after 2 years of operation.

UHV Viewport

The first optical component downstream of the extraction mirror is a viewport ensuring the transition between the Ultra–High–Vacuum (UHV) of the chamber housing the extraction mirror and the ambient air of the tunnel housing the downstream components of the beamline. Since the first hours of the MRSV beamline, the viewports successively installed are made of standard Fused Silica. Recently, we realized that a couple of years of operation were enough to seriously damage the viewport as shown in Fig. 3: a white *snow* is deposited on the air–side of the viewport, nearby the mirror slot edges projection, and a whitening of the viewport is observed all over the surface where the collected SR is transmitted. Such damage is bearable during several years for one using the photon flux, but becomes unbearable within less than one year to exploit the SR wavefront. The Optics Group of SOLEIL investigated the origin of this fast damage and recently reached conclusions of high interest. The damage seems to come from two processes. (1) Inside the viewport, water molecules can get trapped during the annealing process of the Fused Silica. The SR UV photons would then dissociate those molecules and create trapped Hydrogen molecules responsible for the whitening of the viewport. (2) On the outer/air side of the viewport, the exiting SR UV photons (at λ <240 nm, probably more specifically at λ=185 nm) convert the oxygen in the air into atomic oxygen through photolysis, leading to the production of ozone. The

ISBN: 978-3-95450-241-7 ISSN: 2673-5350 doi:10.18429/JACoW-IBIC2022-TUP19

ozone would then itself be transformed through photolysis by the SR UV photons at λ <350 nm. The products of all those reactions are extremely oxidizing, especially for metals, and cause a localized de–polishing of the window surface in addition to a white deposit. This viewport degradation is of great harm for a high–resolution beam size measurement, creating a diffraction pattern in the image plane. Our observations showed that our damaged window was transmitting indeed as if there was a 1 mm thick line obstacle on the beam path (at the lens location). Building on those results, two actions are under way: the purchase of new type of windows to reduce the in–bulk effect and a main beamline update to enclose the light path under primary vacuum down to the image plane to reduce the exit surface (*snow*) effect. Regarding new windows, we systematically compared all available options from manufacturers. It came out that three types of alternative substrates could be more transmissive in the 180–250 nm range: CaF_2, MgF_2 and EUV Grade Fused Silica. CaF_2, MgF_2 windows are crystalline glass, i.e. potentially more pure (without trapped water molecules), and can transmit up to λ=1000 nm. But they are significantly more expensive than EUV Grade Fused Silica and slightly less transmissive in the 180–200 range. EUV Excimer Grade Fused Silica windows, initially optimized for excimer laser users, are now available with homogeneity grade A and inclusion class 0 with excellent surface quality. Two items were already ordered and should be installed before the end of the year.

Periscope Mirrors

A few centimeters downstream of the viewport, a periscope lowers the SR beam out of the electron beam orbit plane. The two mirrors mounted on the periscope are made of a Zerodur substrate coated with Silver. But those mirrors are also suffering a fast damaging as shown in Fig. 4. There is no *snow* deposited since the shortest wavelengths do not get through more than a few centimeters of air, but the mirrors are depolished all over the SR incident surface. This depolishing starts affecting the SR wavefront wihtin a year of operation. To try increasing the lifetime of those mirrors, we decided to test a new coating. A new pair of enhanced UV Aluminium coated mirrors was installed during summer shutdown. Even if this coating is confirmed to be more resistant to UV radiation, the enclosing of the periscope under vacuum might remain mandatory.

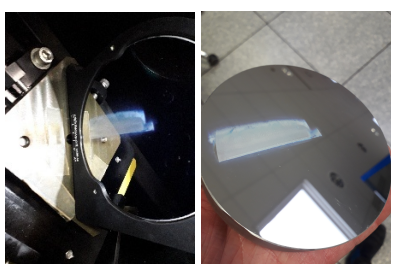


Figure 4: Pictures of the Silver coated periscope mirrors after several years of operation.

Other Optical Components

Still inside the tunnel, a motorized slit enables to control the horizontal collection angle θ_x from 0 up to 10 mrad. Immediately following this slit, a f=3200 mm cylindrical lens refocusses the SR with non–negligible chromatic effects. This lens is indeed 7 mm thick on–axis and made of Fused Silica. Up to now, no degradation of the lens could be observed. After passing through a thick shielding via a 45° incidence mirror, the SR reaches the optical table of the diagnostics hutch. Using a few beamsplitters as shown in Fig. 1, the SR is dispatched towards five branches. The last bottom branch is the one dedicated to attempt high resolution beam size measurements. According to preliminary simulations, the highest resolutions are expected to be reached using π polarized SR. A transmission type linear polarizer can therefore be mounted on a rotation stage. The SR is also monochromatized with a bandpass filter of 5 nm–fwhm centered at λ=405 nm. The SR transverse distribution in the image plane is finally recorded with a CMOS camera (acA1920-50 gm from Basler) which pixel pitch is 5.86 µm.

BEAMLINE MODELLING

To achieve a high resolution beam size retrieval from π polarized imaging, an accurate modelling of the beamline is mandatory. We used for that the SRW (*Synchrotron Radiation Workshop*) code [1]. The beamline is modelled taking into account the crotch absorber aperture, the extraction mirror slit, the aperture of the horizontal slit, the focussing of the lens and the polarizer transmission. The 2D SR wavefront (in x and y the transverse coordinates) is computed in multi–electron mode –to take into account the finite electron beam emittance at source point– for a single photon wavelength λ=405 nm (we checked that the 5 nm–fwhm bandpass filter allowed to work in this monochromatic approximation).

PRELIMINARY IMAGING RESULTS

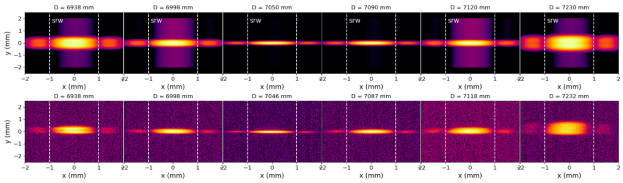
Before addressing beam size measurements strictly speaking, major efforts were made to obtain an excellent agreement between simulated and measured transverse distributions both over a large field of view and as a function of many parameters (polarizer angle, distance to image plane, horizontal collection angle, vertical position of the extraction mirror, etc..). Those long term efforts revealed to be extremely helpful to identify the faulty components of the beamline (as mentioned above). For the sake of simplicity, only two scans are presented here, scans that we however believe to be the most illustrative of the quality of our new extraction mirror and of the consequent level of agreement we could reach up to now. The first scan, presented in Fig. 5, is versus D the distance from the lens to the camera. The second scan, presented in Fig. 6, is versus θ_x the horizontal collection angle. In both scans, measurements (bottom line) are compared to simulations (upper line) using the extraction mirror in (a) *full–insertion* and (b) *slot–insertion* mode, without polarizer, and for a collection angle θ_x=0.5 mrad

Content from this work may be used under the terms of the CC BY 4.0 licence (© 2022). Any distribution of this work must maintain attribution to the author(s), title of the work, publisher, and DOI

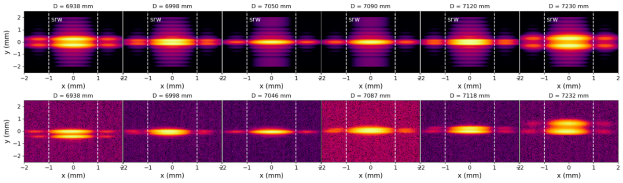
ISBN: 978-3-95450-241-7 ISSN: 2673-5350 doi:10.18429/JACoW-IBIC2022-TUP19

Content from this work may be used under the terms of the CC BY 4.0 licence (© 2022). Any distribution of this work must maintain attribution to the author(s), title of the work, publisher, and DOI

allowing to observe the diffraction pattern from the horizontal slit. For mirror safety reasons, experimental data were recorded at I=1.7 mA to avoid any mirror damage / distortion. The agreement between measurements and simulations is excellent, mainly resulting from the high quality of the optics.

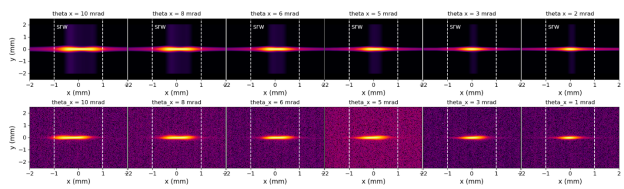


(a)

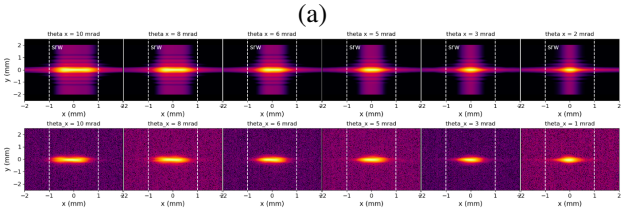


(b)

Figure 5: Intensity distributions versus D using the extraction mirror in (a) *full–insertion* mode and (b) *slot–insertion* mode. In (a) and (b): (upper line) simulations, (bottom line) measurements. Main conditions: θ_x=0.5 mrad, θ_y=10 mrad, no polarizer, λ=405 nm. Experimental parameters: I=1.7 mA. Simulation parameters: f_x=3194 mm, f_y=3227 mm.



(a)



(b)

Figure 6: Intensity distributions versus θ_x using the extraction mirror in (a) *full–insertion* mode and (b) *slot–insertion* mode. In (a) and (b): (upper line) simulations, (bottom line) measurements. Main conditions: D=7.06 m, θ_y=10 mrad, no polarizer, λ=405 nm. Experimental parameters: I=1.7 mA. Simulation parameters: f_x=3194 mm, f_y=3227 mm.

TOWARDS BEAM SIZE MEASUREMENTS

Heartened by the good agreement between measurements and simulations, we are now about to move on to strictly speaking beam size measurements. According to SRW, the highest resolution in terms of vertical beam size measurements should be reached using a vertical (π) polarization. A preliminary scan versus D in π polarization and using the mirror in *slot–insertion* mode is shown in Fig. 7. The once more excellent agreement between simulations and measurements allow us to be confident for close future absolute and high–resolution beam size measurements.

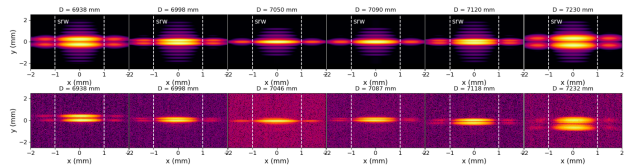


Figure 7: Intensity distributions versus D using the extraction mirror in *slot–insertion* mode. (Upper line) simulations, (bottom line) measurements. Main conditions: θ_x=0.5 mrad, θ_y=10 mrad, vertical polarizing, λ=405 nm. Experimental parameters: I=1.7 mA. Simulation parameters: f_x=3194 mm, f_y=3227 mm.

CONCLUSION

We presented here the recent developments performed on our visible range diagnostics beamline.

We recently realized how fast our optics were being damaged and we reported here the fundamental mechanisms that we believe to be leading to this fast damaging. Relying on this new knowledge, and strongly encouraged by the perspective of SOLEIL upgrade, we are now working on the improvement of our optics lifetime.

We also reported on systematic comparisons between measured and simulated radiation distribution in the beamline image plane. The excellent agreement recently reached appears very reassuring for a moving on towards absolute beam size retrieval.

We could also recently confirm that, thanks to the high SR photon flux, π polarized imaging based beam size measurements are feasible down to ≈ 1.7 mA, i.e. in a low current range where pinhole cameras are inoperable from lack of signal. This also means that at 500 mA, π polarized imaging can be run at a much higher repetition rate than pinhole cameras. The door seems opened for high–resolution and high repetition rate (> 1 kHz) beam size measurements in the visible range.

REFERENCES

[1] O. Chubar and P. Elleaume, "Accurate and Efficient Computation of Synchrotron Radiation in the Near Field Region", in *Proc. EPAC'98*, Stockholm, Sweden, Jun. 1998, paper THP01G, pp. 1177–1179.

[2] A. Andersson *et al.*, "Determination of a small vertical electron beam profile and emittance at the Swiss Light Source", *Nucl. Instrum. Methods Phys. Res., Sect. A*, vol. 591, pp. 437–446, 2008. doi:10.1016/j.nima.2008.02.095

ISBN: 978-3-95450-241-7 ISSN: 2673-5350 doi:10.18429/JACoW-IBIC2022-TUP20

CORRECTIONS FOR SYSTEMATIC ERRORS IN TRANSVERSE PHASE SPACE MEASUREMENTS AT PITZ

C. Richard*, Z. Aboulbanine, G. Adhikari, N. Aftab, P. Boonpornprasert, G. Georgiev, M. Gross, A. Hoffmann, M. Krasilnikov, X.-K. Li, A. Lueangaramwong, R. Niemczyk, H. Qian, F. Stephan, G. Vashchenko, T. Weilbach, Deutsches Elektronen-Synchrotron DESY, Zeuthen, Germany

Abstract

The Photo Injector Test Facility at DESY in Zeuthen (PITZ) characterizes and optimizes electron sources for use at FLASH and European XFEL. At PITZ, the transverse phase space is measured using a single slit scan and scintillator screen method. With the trend in photoinjectors towards lower current and emittance, these measurements become increasingly influenced by systematic errors including camera resolution and scintillator response due to smaller spot sizes. This study investigates the effects and corrections of the systematic errors for phase space measurements at PITZ.

INTRODUCTION

The Photo Injector Test Facility at DESY in Zeuthen (PITZ) commissions and characterizes electron guns for use in Free Electron Lasers (FEL) at FLASH and European XFEL [1]. For FEL operation, the transverse emittance is a key parameter for optimizing the gain length [2]. To characterize the electron guns, PITZ measures the emittance using a single slit emittance scanners. These devices measure the transverse phase space by stepping a narrow slit through the beam to only allow particles at a given position to pass. The profiles of passed beamlets are measured with a camera capturing the signal on a downstream scintillator screen to measure the angular distribution [3]. The systematic errors in this system have previously been studied for the PITZ emittance scanners [4, 5] and it was found that one of the primary systematic errors in this system is the resolution of the camera. However, these studies focused on the effect of the camera resolution on full beam measurements not beamlet measurements and do not quantify the effects on the measured emittance. The effect of the slit width on the measured emittance has also be been estimated [6, 7], but, for simplification, it was assumed the beam had no $x - x'$ coupling and the camera effects were excluded. In addition, previous studies do not propose corrections for the systematic errors and it is desired to correct for these errors so accurate emittance measurements can be made.

SYSTEMATIC ERRORS FROM SLIT SIZE

To measure the transverse position profile, the emittance scanner uses a 50 µm slit that is stepped across the beam. With this method, the measured profile is the convolution of the beam profile with the slit opening. Therefore, the measured rms beam size $\sigma_{x,m}$ can be corrected using

$$\sigma_{x,m}^2 = \sigma_{x,t}^2 + \sigma_s^2 \ , \qquad (1)$$

* christopher.richard@desy.de

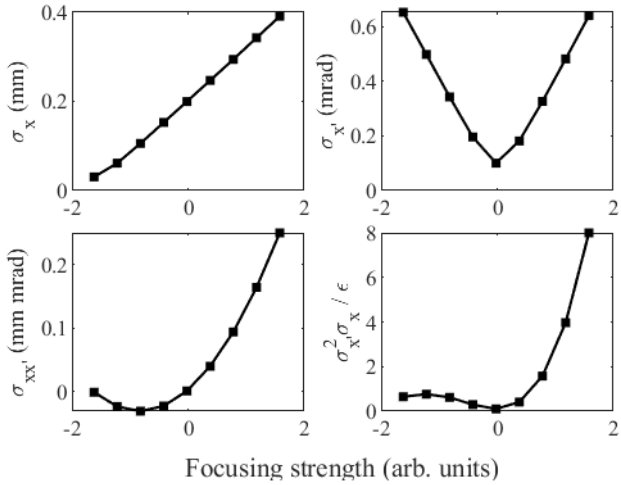


Figure 1: rms parameters of the synthetic optics scan used to test the correction methods. The geometric emittance is 0.02 mm·mrad.

where $\sigma_{x,t}$ is the true rms beam size and $\sigma_s = 50\,\mu\text{m}/\sqrt{12} \approx 14\,\mu\text{m}$ is the rms size of the slit. This results in a ~0.5% increase in $\sigma_{x,m}$ when $\sigma_{x,t} \approx 0.15$ mm which is typical at PITZ and ~5% error when $\sigma_{x,t} \approx 0.05$ mm. This also effects the measured geometric emittance measured rms emittance

$$\epsilon_m = \sqrt{\sigma_{x,m}^2 \sigma_{x',m}^2 - \sigma_{xx',m}^2} \ , \qquad (2)$$

where $\sigma_{x,m}^2 =< x^2 >$, $\sigma_{x',m}^2 =< x'^2 >$, and $\sigma_{xx',m} =< xx' >$ is a correlation term. The measured emittance can be corrected by the substitution $\sigma_{x,m}^2 \rightarrow \sigma_{x,m}^2 - \sigma_s^2$ into Eq. (2).

To study the effect on the measured emittance, a linear model of the emittance scanner was made in Matlab [8]. The model takes particles from an 4D input distribution and separates them into beamlets based on their x position replicate the slit mask. Each beamlet is then propagated through a drift length to the screen location and heat maps of the particle densities are made to replicate the screen response. To simulate beams with a range parameters similar to what is measured at PITZ, a Gaussian distribution is generated with geometric emittance $\epsilon_g = 0.02$ mm·mrad, put through a thin lens kick and a 30 cm drift length, then processed with the emittance scanner model. The resulting beam parameters at the start of the emittance scanner are shown in Fig. 1.

The measured, uncorrected rms emittance increases as the beam size decreases as expected from Eq. (1) and can be corrected (see Fig. 2). However, the emittance also significantly

Content from this work may be used under the terms of the CC BY 4.0 licence (© 2022). Any distribution of this work must maintain attribution to the author(s), title of the work, publisher, and DOI

ISBN: 978-3-95450-241-7 ISSN: 2673-5350 doi:10.18429/JACoW-IBIC2022-TUP20

Content from this work may be used under the terms of the CC BY 4.0 licence (© 2022). Any distribution of this work must maintain attribution to the author(s), title of the work, publisher, and DOI

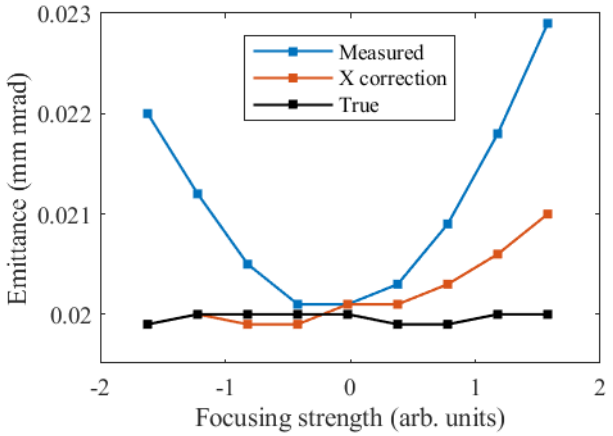


Figure 2: The rms geometric emittance increases due to the slit size as the beam size decreases. It also increases at large beam sizes due to the large $x - x'$ coupling causing the emittance to be very sensitive to the calculated rms values. Variation in the true emittance are due to statistical fluctuations.

increases when the beam size is large. This is caused by the strong $x - x'$ coupling making the calculated emittance sensitive to small changes in any of the rms parameters. The sensitivity of the emittance is found by taking the derivative with respect to σ_x

$$\mathrm{d}\epsilon = \frac{\sigma_{x'}^2 \sigma_x}{\epsilon} \mathrm{d}\sigma_x. \tag{3}$$

Due to this sensitivity, using Eq. (1) to correct the emittance improves the measured value, but does not completely correct for the effect of the slit. To avoid this sensitivity to small changes in the rms parameters, measurements should be taken when $\sigma_{x'}^2 \sigma_x / \epsilon \lesssim 1$.

CAMERA RESOLUTION SYSTEMATIC ERRORS

The non-zero pixel size of the camera causes the camera to have a point spread function (PSF), i.e. the camera will record a finite sized signal form an infinitesimally sized input signal. This causes the images recorded by the camera to be a convolution of the true image with the PSF. This can cause a significant increase in the measured size of the beamlets size when the true rms size is comparable to the rms size of the PSF.

Determining the Point Spread Function

Assume the PSF is Gaussian with standard deviation σ_p

$$p(x) = \frac{1}{\sqrt{2\pi}\sigma_p} e^{-\frac{x^2}{2\sigma_p^2}}. \tag{4}$$

The rms size of the PSF is related to camera's optical resolution with the modulation transfer function z (MTF) [5]

$$z(\omega) = \int_{-\infty}^{\infty} p(x) e^{-i\omega x} dx = e^{-\frac{1}{2}\sigma_p^2 \omega^2}. \tag{5}$$

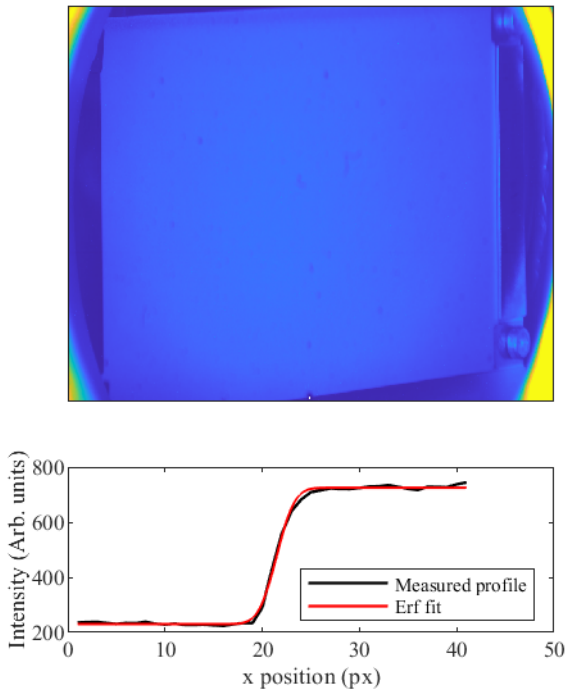


Figure 3: Image of an scintillator screen with a light shining on it (top). The intensity profile of the left edge of the screen was fitted to an error function to determine the rms PSF (bottom).

The optical resolution ω_0 in px/mm of the camera can be defined by

$$z(\omega_0) = 0.1 \tag{6}$$

which gives

$$\sigma_p = \sqrt{2\ln(10)} \approx 2.14 \text{ px}. \tag{7}$$

This can be converted to a length by dividing by ω_0. For the presented measurements, the camera's optical resolution is $\omega_0 = 28.8$ px/mm giving an rms PSF $\sigma = 74$ µm.

The rms size of the PSF can be verified by using an image taken at a screen station with a light illuminating the screen. On the edges of the image, metal brackets can be seen that hold the scintillator screen (see Fig. 3). Assuming the brackets have a hard edge and the PSF is Gaussian, then the intensity profile across the edge will be an error function corresponding to the integral of the PSF. For the image in Fig. 3, the intensity profile of 50 rows of pixels at the center of the left edge were fit to an error function. The measured rms PSF was $\sigma_p = 2.01 \pm 0.11$ px which agrees the theoretical MTF approach.

PSF Effects on Measured Distributions

The camera in the emittance scanner measures the response of the scintillator screen from beamlets that pass through the slit. The angular profile of the beam at the slit

ISBN: 978-3-95450-241-7 ISSN: 2673-5350 doi:10.18429/JACoW-IBIC2022-TUP20

location is assumed to be proportional to the spatial profile of the passed beamlet. However, the recorded images are the 2D convolution of the true screen responses with the PSF. Therefore, the measured rms beamlet sizes σ_{bl_m} can be estimated as

$$\sigma_{bl,m}^2 = \sigma_{bl,t}^2 + \sigma_p^2 \ , \tag{8}$$

where σ_{bl_t} is the true rms beamlet size. Assuming a the size of the slit is negligible, the rms size of the beamlet on the screen can be related to the rms parameters of the beam

$$\sigma_{bl,t} = \frac{\epsilon_t}{\sigma_{x,t}} L = L\sqrt{\sigma_{x',t}^2 - \frac{\sigma_{xx',t}^2}{\sigma_{x,t}^2}} \ , \tag{9}$$

where $L = 3.133$ m is the drift length between the slit and the screen. Assuming $\sigma_{xx',t} \approx 0$ and $\sigma_{x',t} \approx 0.15$ mrad then $\sigma_{bl,t} \approx 0.3$ mm. Using Eq. (8) and $\sigma_p = 74$ µm, this results in a ~3% increase in the measured beamlet size.

To study the effect of the PSF, the Matlab model of the emittance scanner was modified to convolved the heat maps of the beamlet particle densities with a Gaussian PSF with σ_p defined by Eq. (7). In addition, Gaussian noise can be added then removed from the images to replicate the image processing.

When the beamlet distributions are convolved with the PSF, the increase in the measured emittance is dominated by the effect of the slit size for small σ_x (i.e. lower focusing strength in Fig. 4 top). As the focusing strength and $\sigma_{x,t}$ increase, firstly, $\sigma_{x'}$ becomes small causing the beamlet sizes to decrease, resulting in a larger increase on their measured size due to the PSF, and therefore a larger measured emittance. As the focusing strength continues to increase, all $\sigma_{x',t}$ and $\sigma_{xx',t}$ start to increase (see Fig. 1). This increases the sensitivity of the measured emittance to the measured rms value and the error continues to increase. In these regions, there is ~5% increase in the measured emittance compared to the case without convolving with the PSF.

The effects of the slit and PSF can result in >20% increase in the measured emittance if $\sigma_{x,t}$ or $\sigma_{x',t}$ is too small or $\sigma_{xx',t}$ is too large. These effects are significant enough that even when Gaussian noise was added at 1% of the peak intensity then removed, the measured emittance can still be larger than the 100% emittance (see Fig. 4). The noise 1% noise level is a rough upper bound to measurements taken at PITZ with typical noise levels being around 0.5%.

Beamlet Image Correction

In order to correct for the effects of the camera resolution, the beamlet images must be deconvolved from the PSF. The best results for the 2D deconvolution were achieved using 5 iteration of the Richardson-Lucy algorithm with a regularization parameters of 0.1 [9]. In addition, the effect of the slit size is corrected as described above. Note, the corrected emittances should be compared to the true emittances but rather the emittances from images without the PSF convolution and with the slit correction applied $\epsilon_{\text{slit},c}$ as these are

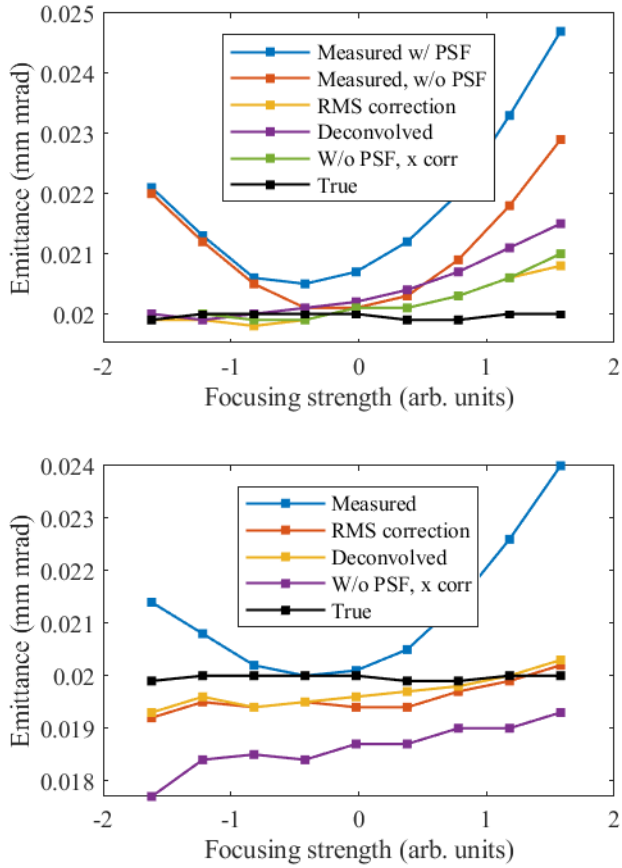


Figure 4: Measured and corrected rms geometric emittances for the cases with no noise present (top) and noise added then removed (bottom). The corrected values should be compared to the case of "W/o PSF, x corr", i.e. no PSF effects and corrected with Eq. (1), rather than the true emittance as this is the measured result without convolving with the PSF.

the best achievable results. Without added noise, deconvolving the beamlet images corrects for effects of the PSF on the emittance to <3% of $\epsilon_{\text{slit},c}$ for the simulated parameter range (see Fig. 4). The deconvolution does not reproduce the exact emittance because deconvolution algorithm was optimized assuming the presence of noise which causes the deconvolution process to be noisy and ill-posed problem. Therefore, when tuning the algorithm, the suppression of artifacts was valued more than exact replication.

While the deconvolution algorithm improves the measured emittance, it is slow, taking upward of 2.5 min depending on the number of beamlet images, and can possibly lead to nonsensical results due to noise. Instead, if detailed phase space measurements are not required, it may preferable to only correct the rms parameters. By plugging Eq. (9) into Eq. (8) and assuming the measured beamlet size also follows Eq. (9) but using the measured rms parameters, the correction to $\sigma_{x',m}$ can be approximated by

$$\sigma_{x',m}^2 = \sigma_{x',t}^2 + \sigma_p^2/L^2 \ , \tag{10}$$

where $\sigma_{x',m}$ is the measured rms angle and $\sigma_{x',t}$ is the true rms angle. This effectively assumes the x' distribution was

Content from this work may be used under the terms of the CC BY 4.0 licence (© 2022). Any distribution of this work must maintain attribution to the author(s), title of the work, publisher, and DOI

ISBN: 978-3-95450-241-7 ISSN: 2673-5350 doi:10.18429/JACoW-IBIC2022-TUP20

Content from this work may be used under the terms of the CC BY 4.0 licence (© 2022). Any distribution of this work must maintain attribution to the author(s), title of the work, publisher, and DOI

convolved with a Gaussian with rms size σ_p/L instead of the individual beamlets being convolved. Applying this correction to the measured emittance results in agreement within 1% to $\epsilon_{\mathrm{slit},c}$.

In the case when noise is added then removed (see Fig. 4 bottom), the two PSF correction methods agree with each other within 2%. However, the agreement with the non-convolved, slit corrected results is spoiled across the entire beam parameter range. This may be caused by the convolved beamlets being larger than the non-convolved ones and therefore, the noise cut had less of an effect on the measured beamlet sizes.

MEASURED RESULTS

These corrections for the PSF can be applied to measurements taken at PITZ. The results in Fig. 5 are from a typical scan of the strength of a solenoid magnet located at the electron gun to find the current setting with minimum emittance for a 19.5 MeV, 250 pC beam. When the PSF and slit corrections are applied the measured emittance is reduced by 3 - 15% and the results from the 2D deconvolution and the rms parameter correction agree within 2% (see Fig. 5). For these measurements, $\sigma_x'^2\sigma_x/\epsilon < 1$ therefore the errors due to large $\sigma^2_{xx'}$ are minimal. The measured rms sizes are $\sigma_x \approx 0.2$ mm and $\sigma_{x'} \approx 0.15$ mrad. Using Eqs. (1) and (10), the corrections for the slit size will be <0.5% and corrections for the PSF will be ~3% which roughly agrees with the measured values for lower solenoid currents. These corrections shift the minimum measured emittance setting of the solenoid by 1 A which can have an impact on the beam dynamics and tuning of the accelerator.

CONCLUSION

Phase space measurements at PITZ using a single slit scanner can be improved by correcting the beamlet images for the effects of the camera PSF and slit size. The correction can be performed by deconvolving the measured beamlet images or by applying corrections to the measured rms parameters. The measured emittance is significantly affected when the beam size is comparable to the slit size and when the beamlet size at the scintillator screen is comparable to the rms PSF. Both of these cases can be reliably corrected. However, when the beam is strongly $x - x'$ coupled, the measured emittance becomes very sensitive to the exact measured size and the measurements become unreliable.

These corrections improve the dominant linear systematic errors and help define a range of beam parameters where the emittance measurements can be trusted. However, in addition, future studies must be conducted to correct for non-linear effects such as space charge effects on the beamlets [4] and the non-linear response of the scintillator [10].

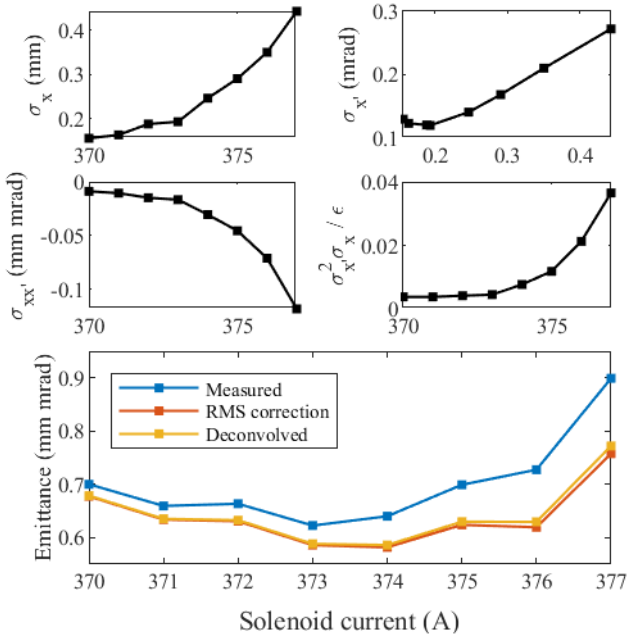


Figure 5: Measured rms parameters of the at the emittance scanner for a range of gun solenoid currents. The corrections reduce the measured emittance by 3 - 15% can change the solenoid current for the minimum emittance from 373 A to 374 A.

REFERENCES

[1] M. Krasilnikov *et al.*, "Experimentally minimized beam emittance from an *L*-band photoinjector", *Phys. Rev. ST Accel. Beams*, vol. 15, p. 100701, 2012. doi:10.1103/PhysRevSTAB.15.100701

[2] E. J. Jaeschke *et al.*, *Synchrotron Light Sources and Free Electron Lasers*, p. 155, Springer International Publishing, Switzerland, 2016. doi:10.1007/978-3-319-14394-1

[3] L. Staykov, "Design Optimization of an Emittance Measurement System at PITZ", in *Proc. DIPAC'05*, Lyon, France, Jun. 2005, paper POT032, pp. 220–222.

[4] L. Staykov, "Characterization of the transverse phase space at the photo-injector test facility in DESY, Zeuthen site", Ph.D. thesis, University Hamburg, Hamburg, Germany, 2008.

[5] R. Spesyvtsev, "Transverse Beam Size Measurement Systems at Photo Injector Test Facility in Zeuthen", master's thesis, Karazin Kharkiv National University, Kharkiv, Ukraine, 2007.

[6] R. Niemczyk, "Subpicosecond-resolved emittance measurements of high-brightness electron beams with space charge effects at PITZ", Ph.D. thesis, University Hamburg, Hamburg, Germany, 2021.

[7] G. Vashchenko, "Tranverse Phase Space Studies with the New CDS Booster Cavity at PITZ", Ph.D. thesis, University Hamburg, Hamburg, Germany, 2013.

[8] The MathWorks Inc., MATLAB, version 9.9.0.1570001 (R2020b), Natick, Massachusetts, 2020.

[9] D. Biggs and M. Andrews, "Acceleration of Iterative Image Restoration Algorithms", *Appl. Opt.*, vol. 36, no. 8, pp. 1766-1775, 1997. doi:10.1364/AO.36.001766

[10] G. Kube, S. Liu, A. I. Novokshonov, and M. Scholz, "A Simple Model to Describe Smoke Ring Shaped Beam Profile Measurements With Scintillating Screens at the European XFEL", in *Proc. IBIC'18*, Shanghai, China, Sep. 2018, pp. 366–370. doi:10.18429/JACoW-IBIC2018-WEOC03

ISBN: 978-3-95450-241-7 ISSN: 2673-5350 doi:10.18429/JACoW-IBIC2022-TUP21

SCINTILLATOR NON-PROPORTIONALITY STUDIES AT PITZ

A. Novokshonov*, G. Kube, S. Strokov
Deutsches Elektronen-Synchrotron DESY, Hamburg, Germany,
Z. Aboulbanine, G. D. Adhikari, N. Aftab, P. Boonpornprasert, G. Z. Georgiev,
J. D. Good, M. Gross, C. Koschitzki, M. Krasilnikov, X. Li, O. Lishilin,
A. Lueangaramwong, D. Melkumyan, F. Mueller, A. Oppelt, H. Qian,
F. Stephan, G. Vashchenko, T. Weilbach,
Deutsches Elektronen-Synchrotron DESY, Zeuthen, Germany

Abstract

A standard method to measure beam profiles is to use scintillating screens. Such technique is used e.g. at the European XFEL in order to overcome coherence effects in case of OTR based diagnostics. However, already during the XFEL commissioning, the standard screen material LYSO:Ce has revealed a new problem - non-proportionality effects. The reason is a high electron bunch density. Therefore it was decided to exchange LYSO:Ce by GAGG:Ce, as the material has not shown any signs of non-proportionality in a series of measurements at the XFEL. Nevertheless, further studies are ongoing. The last measurement campaign has been carried out at PITZ (DESY Zeuthen) which has two important advantages compared to the XFEL: (1) a higher bunch charge and (2) a lower electron energy. Five different scintillating materials have been investigated: LYSO:Ce, YAP:Ce, YAG:Ce, LuAG:Ce and GAGG:Ce. The present work comprises the results of the latest measurements.

INTRODUCTION

The European XFEL uses scintillating screens for standard beam profile diagnostics. $Lu_{2(1-x)}Y_{2x}SiO_5$:Ce (LYSO) has been chosen as its resolution was the best compared to other materials [1, 2]. However, during the commissioning of the XFEL the measured emittances were larger than expected [3, 4]. In addition, bunches with charges above a few hundreds of pC showed a *smoke-ring* like shape with a drop of intensity right in the center. An example of such shape is shown in Fig. 1. It was supposed that this observation is caused by the scintillator material itself [5].

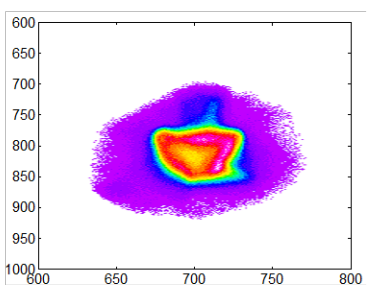


Figure 1: A typical picture received with the LYSO screen.

* artem.novokshonov@desy.de

This effect in principle is well-known in high-energy physics and is called *non-proportionality of scintillators* [6–8]. The more energy a particle looses per unit length in a scintillator volume, the less light output the scintillator will produce. In other words, the light output depends on the deposited energy density. In calorimetric measurements in high-energy physics it results in a non-proportional response [8] at different energies of an incoming particle, as the energy losses depend on its energy (see Fig. 2).

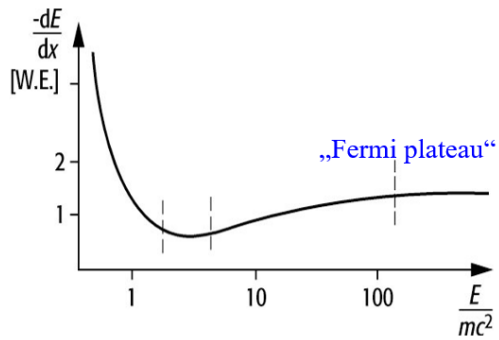


Figure 2: The dependence of particle energy losses in a media on the particle energy.

The effect is especially pronounced at low particle beam energies because the losses per unit length are largest, see Fig. 2. However, in the case of particle beam diagnostics for ultra-relativistic electron beams (as it is the case for the XFEL) the energy losses are smaller, characterized by the so called *Fermi plateau* in the energy loss curve Fig. 2. In addition, scintillators normally used for diagnostics purposes have thicknesses in the order of only a few hundreds of microns, hence the energy loss in the material is negligible compared to the total particle energy. As pointed out in Ref. [5], in this situation it is not the particle energy but the density of the impinging particles which leads to excitonic quenching effects, thus resulting in a non-linear light output. At the XFEL an electron bunch may contain up to 10^{10} particles with a typical size of $\sigma_x \times \sigma_y = 200 \times 200\ \mu m^2$, and the energy density necessary for quenching is reached directly via the initial particle density. This is nicely demonstrated in Fig. 1 where the lowest light output is located exactly in the center of the beam, i.e. the region with the largest particle density.

Content from this work may be used under the terms of the CC BY 4.0 licence (© 2022). Any distribution of this work must maintain attribution to the author(s), title of the work, publisher, and DOI

ISBN: 978-3-95450-241-7 ISSN: 2673-5350 doi:10.18429/JACoW-IBIC2022-TUP21

Content from this work may be used under the terms of the CC BY 4.0 licence (© 2022). Any distribution of this work must maintain attribution to the author(s), title of the work, publisher, and DOI

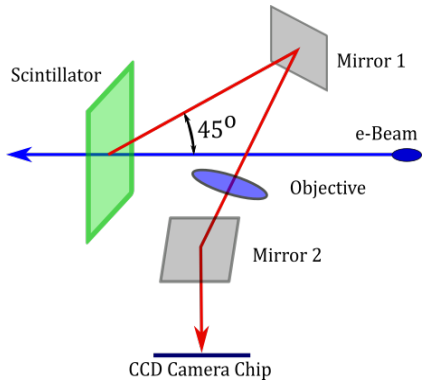


Figure 3: Scheme of the measurements.

In order to investigate this effect in more detail, a series of measurements was conducted at the XFEL which are partly described in Ref. [9]. Four additional scintillators have been selected in order to prove the assumption and to find a possible substitutes for the LYSO target:

- $Y_3Al_5O_{12}$:Ce (YAG)
- $YAlO_3$:Ce (YAP)
- $Lu_3Al_5O_{12}$:Ce (LuAG)
- $Gd_3Al_2Ga_3O_{12}$:Ce (GAGG).

Main criteria was the linearity of the light output as function of the charge density, while the scintillator with the most linear dependence is the most suitable one. It was demonstrated that GAGG screens show a very proportional light output which coincides with the theoretical assumption in Ref. [5].

Nevertheless, the subject of scintillator linearity is of utmost interest for the diagnostics community because several screen materials are in use at various accelerators with a wide range of parameters, see e.g. Ref. [10]. Especially particle densities available at modern linac based FELs may reach the critical limit, thus deteriorating beam profile measurements. In order to explore the limits of non-proportionality it was decided to continue the studies at the Photo Injector Test Facility PITZ at DESY Zeuthen. PITZ is advantageous for such kind of measurements because of the higher achievable beam charge compared to the XFEL and its lower electron energy.

EXPERIMENTAL SETUP

PITZ is used for the optimization of high-brightness electron guns for the European XFEL and FLASH. The beam main parameters are

- elctron energies up to 22 MeV
- bunch charges up to 5 . . . 6 nC
- bunch repetition rate 10 Hz.

The measurement principle was to investigate the light yield dependency as function of the bunch particle density (as it was already the case for the XFEL studies). A scheme of the experimental setup is shown in Fig. 3. Five scintillating screens (YAG, YAP, LuAG, GAGG and LYSO) are installed on a single holder and can be moved in the beam path by a stepper-motor driven mover. The screens are oriented perpendicular to the electron beam axis.

The optical part of the setup consists of 2 mirrors, an objective lens and a camera. The mirrors are used to extract the light out of the vacuum chamber and to guide it through the optical components to the camera system. A *Schneider-Kreuznach 5.6/180* objective was used in so-called Scheimpflug geometry, thus compensating depth-of-field effects caused by the 45° observation geometry. An *Allied Vision GC1350* CCD camera was used for image detection. Beam focusing in the screen plane could be performed by a set of 5 quadrupoles right before the experimental station. In order to modify the charge density the bunch charge was varied. The camera settings were chosen such that the gain was set to 0 (lowest electronical noise contribution), and the smallest possible exposure time was selected (which typically amounted to 10 µs). However, a larger exposure time would not change anything because the scintillator decay times are in the nano second region which is fast enough compared to the micro second exposure times.

RESULTS

Figure 4 show images of the same beam spot, but taken with different scintillators for a bunch charge of 2 nC and a spot size of $\sigma_x \times \sigma_y = 120 \times 50$ µm^2. The spot size was determined by means of the GAGG scintillator because it is the most reliable material. Even at high charge densities the GAGG based beam spot is well fitted by a Gaussian distribution, while the YAG and LuAG based images are already clearly saturated, resulting in a flattening in the center of the beam image. As can be seen from this figure, the only material that clearly demonstrates a smoke-ring shaped

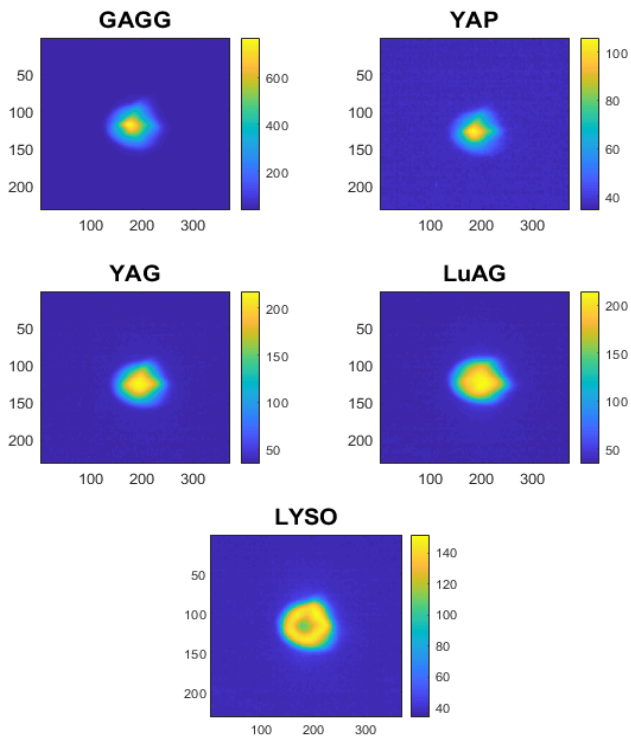


Figure 4: Comparison of the same beam spot measured with different scintillators.

ISBN: 978-3-95450-241-7 ISSN: 2673-5350 doi:10.18429/JACoW-IBIC2022-TUP21

beam profile is LYSO, an observation which reproduces the results from the XFEL measurements. Nevertheless, both YAG and LuAG seem to be close to the quenching threshold of the excitation carriers inside the crystal. However, during the course of this measurement it was not possible to reach higher charge densities and to produce a smoke-ring shaped beam profile with YAG and LuAG as a consequence.

As expected from the discussion in Ref. [5], GAGG and YAP show the best results. Reason seems to be (1) for GAGG the gadolinium content which allows that excitation carriers can rapidly transfer their energy to excited states of gadolinium, thus resulting in a rapid migration of this energy among the Gd sub–lattice, resp. (2) for YAP the high mobility of excitonic carriers which may reduce the quenching probability. The only difference between GAGG and YAP image is the much smaller light output from YAP. Besides the YAP light yield which is much smaller than the one for GAGG, the YAP radiation spectrum peaks at about 375 nm which is quite off from the maximum of the camera quantum efficiency at about 540 nm. As result the YAP image is more noisy than the GAGG based beam spot.

Figure 5 shows the results of the next measurement series. In this case the bunch charge was increased while the quadrupole settings were kept constant, and for each charge and scintillator material a series of spot size measurements was taken. For each recorded image the projected beam spot was fitted with a Gaussian distribution, and the results are combined in this figure. It should be noted that a variation of the bunch charge automatically results in a small change of the beam size due to the modification of the injector laser attenuation and the space charge as the consequence. However, even with this small additional size modification the peak charge density was increased with increasing charge which was the primary intention of this measurement.

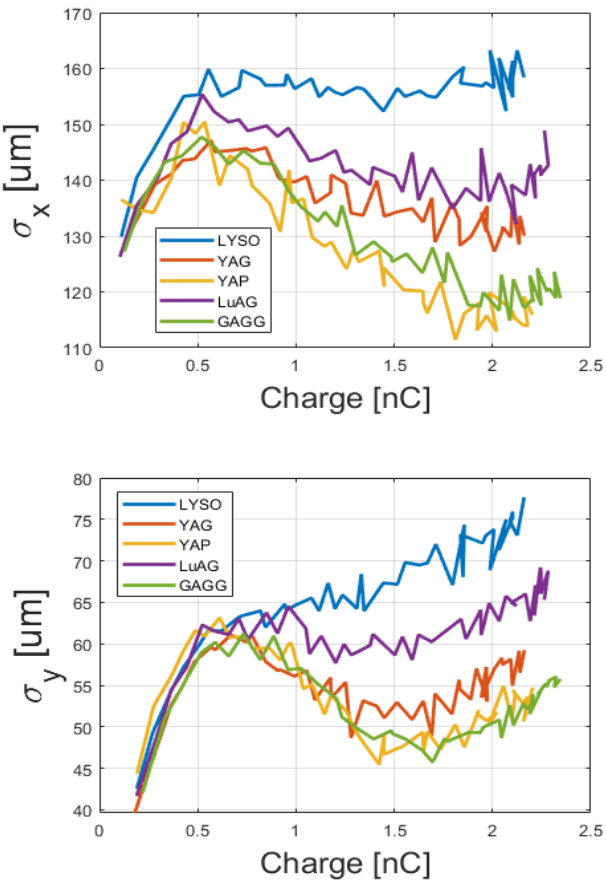


Figure 5: Comparison of projected horizontal (top) and vertical (bottom) beam sizes as function of the bunch charge.

Comparing the projected beam sizes, it is obvious to see large differences between YAG/LuAG at the one hand and GAGG/YAP at the other hand. While the spot sizes are in agreement up to charges between 0.5 nC and 1 nC, for larger bunch charges the difference is steadily increasing. It is interesting to note that the smoke-ring shapes for LYSO clearly appears only at charges above 1 nC (20 fC/μm^2), however the measured sizes are already much larger at smaller bunch charges compared to the measurements from other scintillating materials.

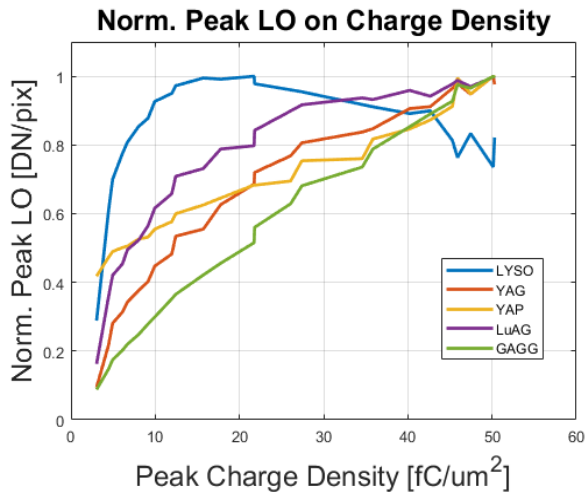


Figure 6: Normalized peak light output as function of the peak charge density.

The experience with the analysis of scintillator non-proportionalities based on beam spot measurements indicated that the extracted beam sizes are not the proper way to estimate this effect. For this purpose the light output as function of the charge density dependence is a better measure as indicated in Fig. 6. The peak charge density was defined by the beam sizes derived with the GAGG and the charge measured at each measurement. And the peak LO is an average of the 3×3 pixels area of the exact scintillator picture. As can be seen, the LYSO light output grows up to a level of ≈15 fC/μm^2 (≈0.75 nC), afterwards it even drops due to quenching of the excitonic carriers. Hence the level is a critical one for the LYSO. Also from the figure it may be concluded that both YAG and LuAG based measurements seem to approach a plateau at the end of the graph. On the other hand, YAP and GAGG based measurements show a more or less linear increase of the light output with increasing charge density. This linear behavior is exactly

Content from this work may be used under the terms of the CC BY 4.0 licence (© 2022). Any distribution of this work must maintain attribution to the author(s), title of the work, publisher, and DOI

ISBN: 978-3-95450-241-7 ISSN: 2673-5350 doi:10.18429/JACoW-IBIC2022-TUP21

Content from this work may be used under the terms of the CC BY 4.0 licence (© 2022). Any distribution of this work must maintain attribution to the author(s), title of the work, publisher, and DOI

what is needed from a scintillator for accurate beam profile diagnostics.

CONCLUSION

The measurements presented in this article extend the range of charge densities for five scintillating materials in use for electron beam profile diagnostics. As expected from previous measurements, the scintillator material which is mainly affected by non-linearity effects is LYSO. Besides, it could be shown that materials like YAG and LuAG which are widespread in use indicate significantly higher measured spot sizes at beam peak charge densities larger than 20 fC/μm^2 (corresponding to a charge of about 1 nC and a beam spot size of about $\sigma_x \times \sigma_y = 140 \times 55$ μm^2). However, at the other hand it could be demonstrated that GAGG and YAP behave very linear over the whole range of bunch charges under investigation. As consequence, the presented measurements underline the necessity to replace LYSO based screens by GAGG in order to achieve reliable beam profile measurements. This is especially true having in mind that the planned maximum beam charge at the XFEL will not be larger than 1 nC.

REFERENCES

[1] G. Kube, C. Behrens, and W. Lauth, "Resolution Studies of Inorganic Scintillation Screens for High Energy and High Brilliance Electron Beams", in *Proc. IPAC'10*, Kyoto, Japan, May 2010, paper MOPD088, pp. 906–908.

[2] G. Kube, C. Behrens, C. Gerth, B. Schmidt, W. Lauth, and M. Yan, "Inorganic Scintillators for Particle Beam Profile Diagnostics of Highly Brilliant and Highly Energetic Electron Beams", in *Proc. IPAC'12*, New Orleans, LA, USA, May 2012, paper WEOAA02, pp. 2119–2121.

[3] B. Beutner, "European XFEL injector commissioning results", in *Proc. FEL'17*, Santa Fe, NM USA, August 2017, pp. 381-385. doi:10.18429/JACoW-FEL2017-WEA01

[4] D. Nölle, "The Diagnostic System at the European XFEL; Commissioning and First User Operation", in *Proc. IBIC'18*, Shanghai, China, Sep. 2018. pp. 162–168. doi:10.18429/JACoW-IBIC2018-TUOA01

[5] G. Kube, S. Liu, A.I. Novokshonov, and M. Scholz, "A Simple Model to Describe Smoke Ring Shaped Beam Profile Measurements With Scintillating Screens at the European XFEL", in *Proc. IBIC'18*, Shanghai, China, Sep. 2018. pp. 366–370. doi:10.18429/JACoW-IBIC2018-WEOC03

[6] A. N. Vasil'ev, "Relaxation of hot electronic excitations in scintillators: account for scattering, track effects, complicated electronic structure", in *Proc. SCINT'99*, pp. 43-52, 1999.

[7] G. Bizzari, W. W. Moses, J. Singh, A. N. Vasil'ev and R. T. Williams, "An analytical model of nonproportional scintillator light yield in terms of recombination rates", *J. Appl. Phys.*, vol. 105, p. 044507, 2009. doi:10.1063/1.3081651

[8] W. W. Moses, G. A. Bizzari, R. T. Williams, S. A. Payne, A. N. Vasil'ev, J. Singh, Q. Li, J. Q. Grim and W.-S. Choong, "The origins of scintillator non-proportionality", *IEEE Trans. Nucl. Sci.*, vol. 59, pp. 2038-2043, 2012. doi:10.1109/TNS.2012.2186463

[9] G. Kube, A. Novokshonov, S. Liu and M. Scholz, "Identification and Mitigation of Smoke-Ring Effects in Scintillator-Based Electron Beam Images at the European XFEL", in *Proc. FEL'19*, Hamburg, Germany, Aug. 2019, pp. 301–306. doi:10.18429/JACoW-FEL2019-WEB01

[10] B. Walasek-Höhne, P. Forck, K. Hoehne, R. Ischebeck, and G. Kube, "Screens for High Precision Measurements", in *Proc. IBIC'19*, Malmö, Sweden, Sep. 2019, pp. 242–248. doi:10.18429/JACoW-IBIC2019-TUBO01

ISBN: 978-3-95450-241-7 ISSN: 2673-5350 doi:10.18429/JACoW-IBIC2022-TUP23

COMMISSIONING OF THE TIMING SYSTEM AT ESS

A. Gorzawski*, G. Fedel, J. J. Jamroz, J. P. S. Martins, N. Milas
ESS, European Spallation Source, Lund, Sweden

Abstract

The European Spallation Source (ESS), currently under construction and initial commissioning in Lund, Sweden, will be the brightest spallation neutron source in the world, when its driving proton linac achieves the design power of 5 MW at 2 GeV. Such a high power requires production, efficient acceleration, and almost no-loss transport of a high current beam, thus making design and beam commissioning of this machine challenging. The commissioning runs of 2021 and early 2022 were the first where the master timing system for the linac was fully available. As a consequence of that, the beam actuators and beam monitoring equipment relied fully on timing events sent across the machine, not only to be triggered to act but also to get the configuration. In this paper, we describe the timing system as available today, present how we define and create the beam pulses using the available parameters. We also present planned future upgrades and other outlook for the system.

INTRODUCTION

ESS is a collaboration of 17 European nations and its objective is to be the world's most powerful spallation neutron source [1]. The neutrons are produced by a 5 MW proton beam hitting a solid, rotating tungsten target at a distance of 600 m from the ion source. The ESS linac, the driver of the protons onto the target, requires site-wise synchronisation in order to accelerate the desired beam through its components. The production of the proton beam begins with the ion source providing the pulse of protons with an optimized current and of a given length [2]. Later, the two choppers (LEBT and MEBT) shape the pulse to the desired pulse length. The acceleration is given by the radio-frequency cavities pulsing at the correct moment. The overall repetition rate is a consequence of the definition of the arbitrary number of consecutive set of timing events (cycles), that are pre-loaded before the ion source starts producing the beam. Last but not least, the beam pulse current is primarily controlled by the IRIS settings, and does not belong to the timing system.

The combination of the three beam parameters, i.e. beam repetition rate, beam pulse length and beam current defines the envelope of the accelerator working point defined as a beam mode. At any time of the machine operation, the Fast Beam Interlock System (FBIS [3]) with Beam Current Monitors (BCMs) is supervising the compliance to the beam mode, i.e. asserting if the produced beam pulse belongs to the allowed parameter space. Pulse timing information distributed to the BCMs containing the planned beam pulse position in the cycle has therefore also a machine protection purpose.

Figure 1 shows schematic of the ESS linac. The actuators are located within the beginning of the line (e.g. source and choppers), at the very end of the line (target raster magnets), and along the full linac (RF stations). The proton beam instrumentation devices, e.g. Beam Current Monitors (BCMs), Beam Position Monitors (BPMs), Faraday Cups (FCs) and Beam Loss Monitors (BLMs) are located along the line.

The ESS distributed control system is based on Experimental Physics and Industrial Control System (EPICS [4]). The full synchronisation is provided by a distributed timing system with its own network infrastructure, and it is operated within a *Beam Production* environment. The entire timing system is configured with the pre-created timing tables, that consists a definition of supercycles, namely sequenced definitions of what the RF/actuators and instrumentation do in the given cycle. This paper summarises the efforts put in the beam commissioning of the Normal Conducting Linac, i.e. from the ion source to the DTL1 FC.

TIMING SYSTEM

The main role of the ESS timing system is to generate, acquire and distribute RF $\approx$ 704.42 MHz based timing signals:

- Synchronous clock, mostly RF/8 = 88 MHz.
- Machine synchronous and asynchronous events.
- Trigger events as a derivative of timing events.
- Data bus (a.k.a. data buffer) with beam and machine parameters.
- Absolute time reference.
- Orchestrate EPICS record processing and acquisition.

In addition, those features are utilized for troubleshooting of different distributed subsystems. The timing hardware is based based on Micro Telecommunications Computing Architecture (MTCA [5]). The detailed concept was described in [6]. Figure 2 presents the timing system topology. The Timing Master (TM) is the main timing system gateway for the operation control while event receivers (EVRs) embedded within TDMS perform synthesis of the received information into the timing signals required by a particular subsystem.

Supercycle Engine

The ESS machine ticks in $\approx$ 71.43 ms cycles ($\approx$ 14 Hz). The cycles can be added together making a meaningful supercycle, so a collection of cycles. The operation team defines each supercycle and a certain supercycle is played during different site acceptance tests, or site integration tests, or the ESS production operation. The ESS machine ticking is produced by the ESS in-house EPICS module called Supercycle

* arek.gorzawski@ess.eu

Content from this work may be used under the terms of the CC BY 4.0 licence (© 2022). Any distribution of this work must maintain attribution to the author(s), title of the work, publisher, and DOI

ISBN: 978-3-95450-241-7 ISSN: 2673-5350 doi:10.18429/JACoW-IBIC2022-TUP23

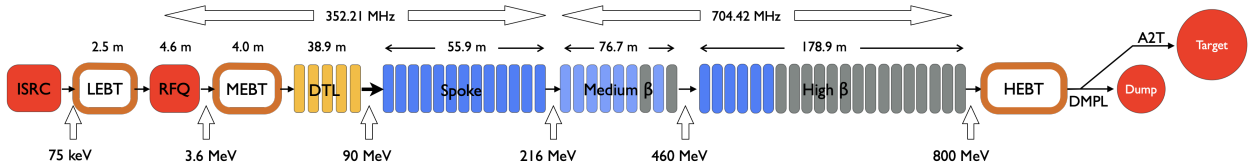


Figure 1: Block view of the ESS linac. First commissioning of the timing in 2021 and 2022 covered the Ion Source, LEBT, RFQ, MEBT and the first DTL1 tank. The two colour (blue and grey) highlight the two energies that different periods of commissioning will bring in the future. Picture courtesy Mamad Eshraqi.

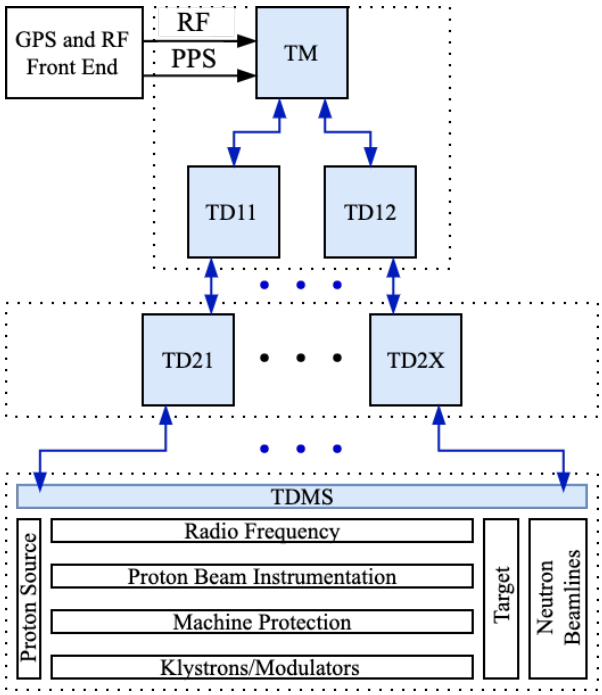


Figure 2: ESS timing network - tree topology. Timing Master (TM); Timing Distribution (TD); TDX_1X_2: X_1 - tree layer, X_2 - ID, TD2X contains X = 22 currently; Timing Distribution to Machine Subsystem (TDMS).

Engine (SCE) which is an extension of mrfioc2 [7] EPICS driver running on the Timing Master. In addition, the engine runs routines supporting asynchronous and synchronous management, safety (inhibiting required ESS actuators), the data bus and the overall system status.

Timing Events

Within the arbitrary defined timing events for the accelerator use, three main groups can be isolated:

- Longitudinal beam shaping: Ion Source Magnetron; LEBT chopper; MEBT chopper,
- Beam pulse: Beam pulse position; RF start,
- Beam monitoring: Acquisition.

These events are used as a base for the cycle definition. Along the cycle, a dedicated data buffer is sent, it contains the beam mode and beam destination, and also dedicated cycle dependent beam parameters like intended beam energy and current for the purpose of the beam loading compensation provided by the LLRF. All of the events definitions and data buffer definitions are kept as the configuration of the *Supercycle Engine* in the dedicated git repository [8].

BEAM PRODUCTION

Figure 3 illustrates the time-in-the-cycle distribution of the events and the data buffer along with the actual beam window. The fixed beam window is established for protection purposes, i.e. there shall never be a beam outside that window. The delays between the events are part of the design such that the dedicated equipment has enough time to configure itself before the beam arrives [9]. Those delays between the events consist of three contributions: the HW network (e.g. cables), the device processing time and the Time of Flight (ToF) between the different positions. The aim of the general commissioning is to identify all three groups and distribute (include) at different levels, i.e. EVRs configuration and/or a supercycle definition.

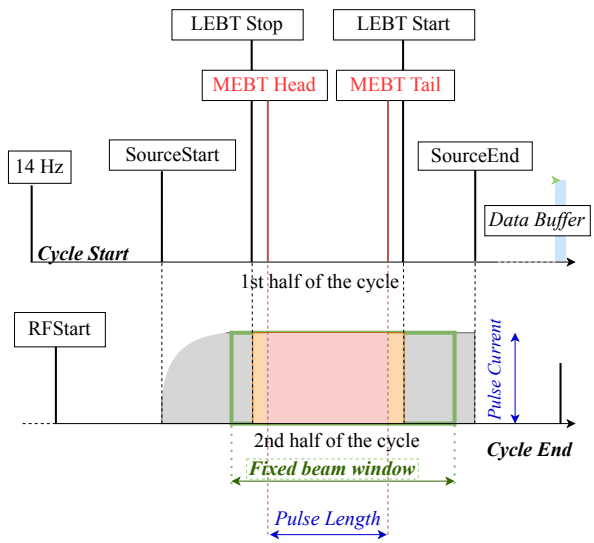


Figure 3: The schematic breakdown of the ESS beam pulse (≈ 71.43 ms) that consists: the events available for each cycle (solid squared black labels) the reserved; source pulse (grey), the fixed beam window (green region); the chopped beam (orange/red) of a given pulse length will be placed inside the fixed beam window. The pulse current is not a parameter of timing and it is shown only for the illustration.

Content from this work may be used under the terms of the CC BY 4.0 licence (© 2022). Any distribution of this work must maintain attribution to the author(s), title of the work, publisher, and DOI

ISBN: 978-3-95450-241-7 ISSN: 2673-5350 doi:10.18429/JACoW-IBIC2022-TUP23

From the control room perspective, the whole timing system is controlled via the *Beam Production* layer that interfaces more than only timing ecosystem via EPICS through the CSS Studio Phoebus suite [10]. The *Beam Production* operator interface (BP OPI) allows to control the Beam Mode and the Beam destination. Whereas both of them are part of the data buffer being sent to all EVRs they are set via BP OPI from the control room only. All receivers can read that and setup their configurations according to the selected mode and destinations (see commissioning section). The BP OPI allows to load the intended super cycle definition and (though at the time of the tests it was not available) setup the beam current settings, via a separate EPICS channel. The timing tables (in the first iteration) are persisted as CSV files and stored in the shared file repository. Figure 4 illustrates the front panel of the BP OPI, where most of the controls to set and prepare the machine and send beam pulses are available. Dedicated top-level overview that includes status from the FBIS and status of the magnetron are highlighted to simplify troubleshooting.

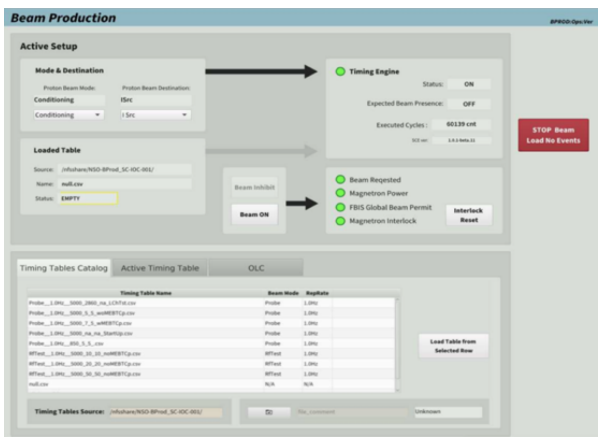


Figure 4: Front panel of the *Beam Production* OPI. It allows to control the Beam Mode and Destination (top left) the loaded timing tables (bottom) and switch ON/OFF beam.

Between the control room screens and timing system, there is another layer of *Beam Production* suite that provides all the advanced logic. As part of the internal checks, the intended (loaded) timing table can be checked if it fits the currently set beam mode in order to avoid the violation of the allowed parameters envelope. A pre-warning is visible for the operator, indicating that the intended configuration may not be supported by the FBIS. The *Beam Production* consists of ESS dedicated Input/Output Controller (IOC). Contrary to the timing engine, this controller has ESS-specific implementation of the beam mode compatibility. The main further improvements that were prototyped and tested in the later commissioning were: (a) to include the control on over the IRIS via dedicated calibration curves, (b) move the timing tables definition into the EPICS layer using the normative types, namely the NTTables. Both of these features will become operationally available in the future commissioning periods in 2023.

COMMISSIONING IN 2021/2022

Recently three designated periods of hardware and beam commissioning were assigned [11]. The timing system was available for the first of them for the first time at ESS and it is when most of the initial dry runs and setup took place. The following milestones were achieved:

1. *October 2021 - December 2021*, the MEBT FC commissioning with small current beam, first time with the timing system available,
2. *February 2022 - March 2022*, MEBT FC, commissioning with high current beam,
3. *May 2022 - July 2022*, DTL1 FC commissioning, low and high current beam.

Managing the Timing Tables

Throughout the commissioning phases the creation of the timing tables was done using the automated tool (external python notebook). The generated setup files were then sent to the shared repository and available for the system to pick up and load upon request.

The creation, the storage, the file format, and the bug fixing were heavily practiced and revision during all three periods of the commissioning. Throughout the commissioning and as an outcome we allocated resources to build a dedicated tool for editing (aka. Supercycle Editor), storing and verifying the available timing tables. While the prototypes were available during the 3rd commissioning phase, the production tool will come later in the future commissioning phase in early 2023. The validation (semantic and numeric) was implemented at the end of 1st commissioning period in the *Beam Production* IOC and it was extended during the later commissioning.

Ion Source, Choppers and RF Systems

The initial setup of the ion source timing was handled within the pre-commissioning dry runs. The magnetron timing interface setup went smooth and the timing signals were properly propagated from day one of the beam commissioning.

The LEBT Chopper works with a gate trigger type, in which the output trigger rising edge is generated by a dedicated event and the falling edge is generated by another event. This feature was configured in the EVR with the flip-flop resource. For the MEBT Chopper, a different setup is needed, as two trigger pulses must be generated for every cycle: one at the beginning (head) of the proton pulse and another one at the end (tail). On the EVR side this is implemented by using two different events to trigger the same delay generator (pulser). As the MEBT Chopper is powered by two units of high-voltage power supplies, special output modules with sub-nanoseconds delay tuning are used in the EVR. This is required in order to properly match the arrival of both high-voltage pulses on the MEBT Chopper striplines in the tunnel. The setup of the timing for both choppers was handled in the pre-commissioning dry runs and everything worked fine after the calibration of the delays in the EVRs.

Content from this work may be used under the terms of the CC BY 4.0 licence (© 2022). Any distribution of this work must maintain attribution to the author(s), title of the work, publisher, and DOI

ISBN: 978-3-95450-241-7 ISSN: 2673-5350 doi:10.18429/JACoW-IBIC2022-TUP23

Content from this work may be used under the terms of the CC BY 4.0 licence (© 2022). Any distribution of this work must maintain attribution to the author(s), title of the work, publisher, and DOI

The setup of the LLRF (and the RF in general) required a bit more follow up. Main issue that was isolated was related to the fact how ESS cavities are powered. The NCL's cavities share the modulator (i.e. one modulator per two cavities), that receives the pulsing signal from the individual cavity's LLRF. We proposed disentangling and implemented this by allowing the modulator to pulse at 14 Hz independently of the selected supercycle, and produce RF power as requested by the super cycle. To achieve that, a concept of *Global*, *Mixed* and *Island* modes of EVRs was introduced. In *Global* timing the local EVR was entirely following the supercycle, in the *Island* mode the local EVR was running completely isolated and unaware of global timing. Extremely handful came the *Mixed* timing mode where EVR can follow specific frequency events: 1 , 2 , 3.5 , 7 and 14 Hz. This solution allowed for a simultaneous beam run and RF conditioning activities where both could progress at different effective frequency, i.e. provide beam tests at 1 Hz and push the RF conditioning at 14 Hz.

Beam Monitoring Devices

We isolated the BCMs that required an immediate, i.e. pre-commissioning runs, in order to get ready for the beam commissioning. During the dry runs we tested the response of the all chain for controlling the beam mode and destination, loading the test timing tables that contained the simple cycles on which we tested simple EVR responses.

In order to fulfill one of the requirements, i.e. all events should come early in the cycle to allow devices to load proper configuration [9], delays were implemented in the cycle definition as well as in the EVRs. Delays configurations are stored in the SaveAndRestore [12] application and are part of the pre-restart checks.

Further simplification in this configuration is foreseen, i.e. stepping away from the common delay in the EVRs and Supercycle Tables, and it is planned to be tested during the dry runs before the commissioning phases on 2023. ESS machine protection (FBIS) heavily relays on the BCM functionality where the beam mode and beam destination data allows to load the dedicated Look up Tables (LUT). As part of the dry run, this was verified for each available BCMs and FCs. The latter, as the commissioning was progressing, were successively added tested with similar dry runs before each commissioning run. Figure 5 shows one of the first beam pulses sent to the MEBT FC that was chopped using both choppers. More on the performance of the beam instrumentation can be found in [13].

Data Storage Concerns

During all three periods of the commissioning almost every day we experienced data acquisition and/or storage issues. Commissioning the timing events and triggering the data acquisition is subject to a constant analysis of the high resolution wave forms. This post analysis heavily relays on the availability of the proper time-stamping of the data. To solve the recurring issues the concept of the Synchronous data system was supported and re-introduced [14].

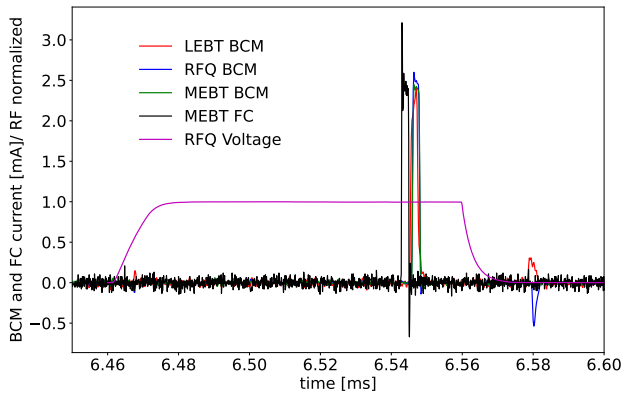


Figure 5: The aligned wave-forms triggered at the same acquisition event. All captured during one of the commissioning days in 2021.

SUMMARY

The beam runs and test with a configured timing system were performed for the first time at the ESS. The accelerator devices were configured, commissioned and handed over to operations. During tests we found few showstoppers that required in house adjustments. The outcome of these findings (i.e. event distribution, event delays or supercycle definitions) are identified and put in the list to improve before the next rounds of commissioning. There is an active effort put in consolidation of the scattered tools to manage and handle timing configurations. The beam commissioning activities will restart in the spring 2023 and many of the new top level features will be available for the commissioning and operation team.

ACKNOWLEDGMENTS

The authors would like to thank all people involved in the ESS Linac operation, hardware and beam commissioning team for their continuous support and input.

REFERENCES

[1] R. Garoby *et al.*, "The European Spallation Source Design", *Phys. Scr.*, vol. 93 p. 014001, 2017. doi:10.1088/1402-4896/aa9bff

[2] R. Miyamoto *et al.*, "Highlights from the first beam commissioning stage at ESS for its ion source and low energy beam transport", *J. Instrum.*, vol. 15, 2020. doi:10.1088/1748-0221/15/07/p07027

[3] S. Gabourin, M. Carroll, S. Kövecses de Carvalho, A. Nordt, S. Pavinato, and K. Rosquist, "The ESS Fast Beam Interlock System: First Experience of Operating With Proton Beam", presented at the LINAC'22, Liverpool, UK, Aug.-Sep. 2022, paper MOPORI17, to be published.

[4] Experimental Physics and Industrial Control System (EPICS), https://epics-controls.org, https://docs.epics-controls.org/en/latest

[5] PICMG MicroTCA Overview, https://www.picmg.org/openstandards/microtca

ISBN: 978-3-95450-241-7 ISSN: 2673-5350 doi:10.18429/JACoW-IBIC2022-TUP23

[6] J. J. Jamroz, J. Cereijo García, T. Korhonen, and J. H. Lee, "Timing System Integration with MTCA at ESS", in *Proc. ICALEPCS'19*, New York, NY, USA, Oct. 2019. doi:10.18429/JACoW-ICALEPCS2019-WEPHA071

[7] EPICS driver for Micro Research Finland event timing system devices, version 2 (mrfioc2), https://github.com/epics-modules/mrfioc2

[8] ESS Reference Tables "reftabs", https://gitlab.esss.lu.se/icshwi/reftabs

[9] N. Milas *et al.*, "Time Structure of the Proton Beam Pulses in the LINAC", ESS-1837307.

[10] Control System Studio, https://controlsystemstudio.org

[11] D. C. Plostinar *et al.*, "Status of the Normal Conducting Linac at the European Spallation Source", in *Proc. IPAC'22*, Bangkok, Thailand, Jun. 2022, pp. 2019–2022. doi:10.18429/JACoW-IPAC2022-WEPOTK001

[12] EPICS Save and Restore tool, https://gitlab.esss.lu.se/ics-software/jmasar-service

[13] T. Shea *et al.*, "Beam Instrumentation Performance During Commissioning of the ESS RFQ, MEBT and DTL", presented at the IBIC'22, krakow, Poland, Sep. 2022, paper MOP07, this conference.

[14] R. Titmarsh *et al.*, "Synchronous Data System at the European Spallation Source", presented at the IBIC'22, krakow, Poland, Sep. 2022, paper MOP040, this conference.

Content from this work may be used under the terms of the CC BY 4.0 licence (© 2022). Any distribution of this work must maintain attribution to the author(s), title of the work, publisher, and DOI

ISBN: 978-3-95450-241-7 ISSN: 2673-5350 doi:10.18429/JACoW-IBIC2022-TUP25

SIMULATION AND MEASUREMENTS OF THE FAST FARADAY CUPS AT GSI UNILAC

R. Singh*[1], S. Klaproth[2], P. Forck[1], T. Reichert[1], A. Reiter [1], G. Rodrigues[3]
[1]GSI Helmholtz Center for Heavy Ion Research, Darmstadt, Germany
[2]Technische Hochschule Mittelhessen, Friedberg, Germany
[3]Inter University Accelerator Center, New Delhi, India

Abstract

The longitudinal charge profiles of the high intensity heavy ion beam accelerated at the GSI UNILAC up to 11.4 MeV/u can differ significantly in consecutive macro-pulses. Variations in bunch shape and mean energy were also observed within a single macro-pulse. In order to have an accurate and fast determination of bunch shape and its evolution within a macro-pulse, a study of fast Faraday Cup designs is underway at GSI. In this contribution, we present CST particle in cell (PIC) simulations of radially coupled co-axial Fast Faraday Cup (RCFFC) and conventional axially coupled FFC (ACFFC) design. The simulation results are compared to the measurements performed under comparable beam conditions primarily with RCFFCs. A rather large impact of secondary electron emission is observed in simulations and experiments. The biasing of the FFC central electrode as a mitigation mechanism on the measured profiles is discussed.

INTRODUCTION

Measurement of longitudinal beam parameters such as kinetic energy, the energy spread, and spread in particle time of arrival with respect to the RF is essential in linear accelerators (LINACs). Kinetic energy measurements are performed using the Time of Flight (ToF) between two or more phase probes (also referred as pick-ups/BPMs) and are routinely done at several locations along the UNILAC. The correlated distributions of beam energy spread and time of arrival with respect to RF phase or "phase spread" with respect to synchronous particle form an ellipse in longitudinal phase space. Typical strategy of determining full longitudinal phase space ellipse is by measuring one of the projection of longitudinal phase space under controlled longitudinal optics settings [1]. The problem of longitudinal emittance determination is thus reduced to precise measurement of the longitudinal charge distribution. The measurement of phase/time of arrival spread also referred to as "longitudinal charge distribution" or often just "bunch length" or "bunch shape" and is typically more accessible for direct measurements. Fast Faraday cups (FFCs) are variants of the regular Faraday cups optimized for measuring fast time varying charge distributions. In order to measure short bunch signals in ns regime, the FFC structures are carefully designed to match the signal termination impedance along with measures for suppression of field dilution and secondary electrons.

In this upcoming section, we will show the simulations of two FFC designs, a) in the first design, the beam is radially coupled into a coaxial cable via a blind hole [2] which is compared with a second design b) the traditional and commercially available axially coupled tapered co-axial cable design [3]. The simulation details and signals induced by beam in the FFC structure in presence of secondary electron emission are discussed. In the following section, measurements with ion beam performed with these FFCs are discussed.

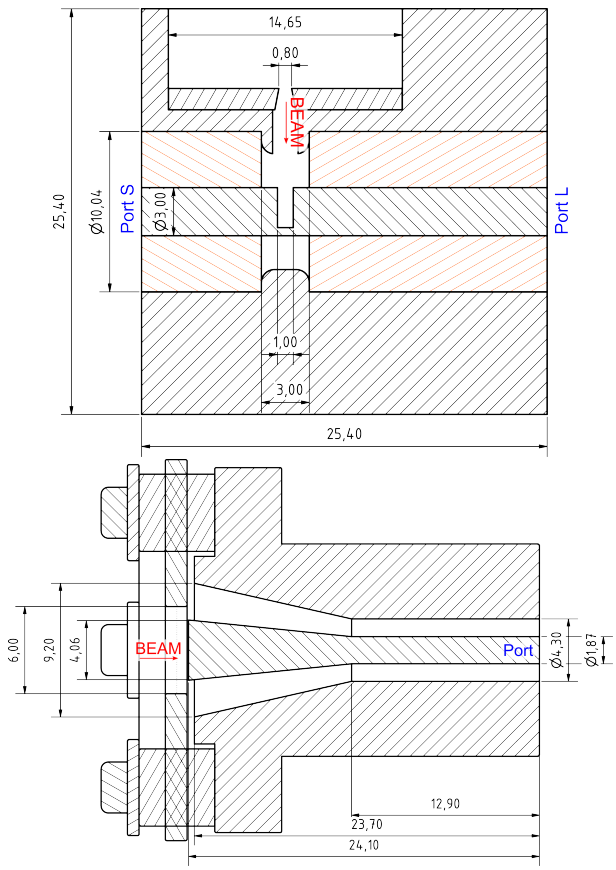


Figure 1: Schematic of the two co-axial FFCs investigated in this manuscript. (Top) Radially coupled FFC and (bottom) Axially coupled FFC. The beam incidence and port for signal coupling are indicated.

SIMULATIONS

Both FFC designs are shown in Fig. 1 which are simulated with the PIC solver of CST EM Studio and ion beam as input.

* r.singh@gsi.de

Content from this work may be used under the terms of the CC BY 4.0 licence (© 2022). Any distribution of this work must maintain attribution to the author(s), title of the work, publisher, and DOI

ISBN: 978-3-95450-241-7 ISSN: 2673-5350 doi:10.18429/JACoW-IBIC2022-TUP25

In addition to ensuring matched signal transmission, these simulations study the deformations in the measured time structure of the beam due to secondary electron yield and field elongation for non-relativistic ion beams.

The first design (RCFFC) where beam enters radially into the co-axial structure is shown in Fig. 1 (top). The basic idea behind the design is coupling of beam through a blind hole from the side of a co-axial through the dielectric medium into the central conductor. The choice of hole width (1 mm) and depth (2.8 mm) is to minimize the escape of emitted secondary electrons. The blind hole in the central conductor of the co-axial is covered with a Titanium Zirconium Molybdenum Alloy (TZM) disk with a small 0.8 mm hole with the dual purpose of reducing field dilution effects [4] and tolerating the heat deposited by the beam. A detailed discussion of the design can be found here [2]. A modification of this design geared towards lower intensity beams is discussed in another contribution of this conference [5]. The second

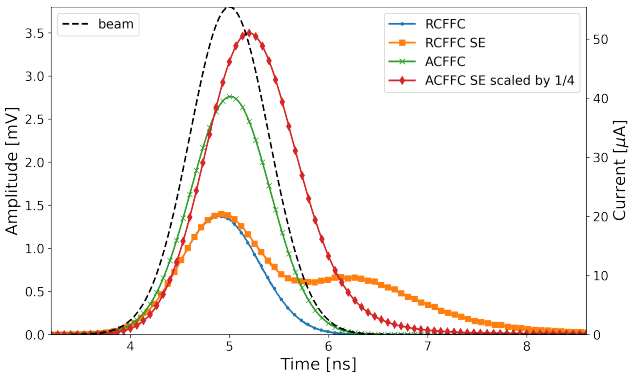


Figure 2: Induced signal with and without secondaries for both FFC designs ($\beta = 0.15$, $\sigma = 400$ ps).

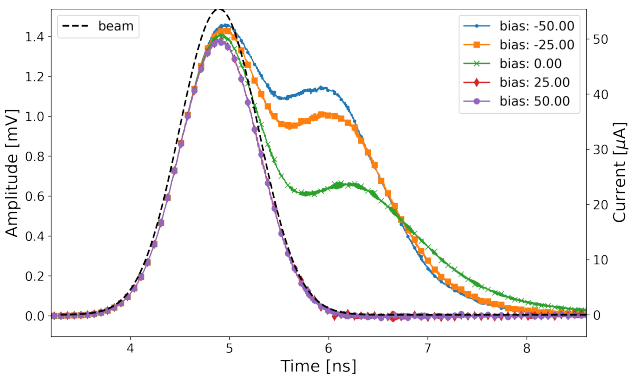


Figure 3: The effect of biasing on the induced signal for radially coupled FFC ($\beta = 0.15$, $\sigma = 400$ ps).

FFC design is the traditional open ended tapered axially coupled co-axial structure [3] shown in Fig. 1 (bottom). The core idea is to enlarge the co-axial cable via a taper while maintaining 50 Ω impedance. There is a grid in front to avoid passage of the beam pre-field which leads to dilution of the measured profile. A comparable design is available on loan from Bhabha atomic research center (BARC) and was used for some of the verification measurements.

The ion induced secondary electron yield and energy spectra have been widely studied in literature [6–9] and some recent studies in context of secondary electron grids for transverse profile measurement of ion beams are discussed here [10]. The backward secondary electron yield per incident ion can be estimated using the Bethe-Bloch formula for the stopping power of charged particle beam on a target. The number of secondary electrons N_e is thus proportional to the square of charge state Z of the incident ion and target electron density n of the FFC material.

$$N_e \propto nZ^2 \cdot N_{ion} \quad (1)$$

Empirical estimates from literature suggest emission of about 10-15 e^- for 8.0 MeV/u O^{5+} ion normally incident with energy of on a copper target [8, 11, 12]. For 8.6 MeV/u Ar^{10+}, this gives about 50 e^- per incident ion and this estimate has been used in our simulations. The secondary electron yield also has a strong dependence on the angle of incidence with respect to surface normal θ. For smooth surfaces the yield is proportional to sec θ [13]. Even for normally incident beam $\theta = 0$, the roughness of the surface could lead to an increased secondary yield due to random distribution of incidence angles, however this effect is not considered in this paper. The secondary electron emission from the surface follows a cosine distribution with respect to target normal [14]. For the radially coupled FFC discussed above with 1 mm diameter and 2.5 mm depth, about 15 % of electrons should exit the blind hole potentially causing the deformation in the induced signal. The energy spectra of the majority of secondary electrons is known to below 50 eV [15, 16]. The secondary electron energy spectra simulated in CST uses the Vaughan model parameterisation [17]. The simulation results showing the induced signal for a longitudinal charge distribution with $\sigma = 400$ ps for $\beta = 0.15$ with and without secondaries for both FFC designs are shown in Fig. 2. There is a clear deformation of induced signal on the FFC for both designs with the secondaries. That is related to the secondary electron emission and the time these low energy electrons require to leave the area near the central conductor of the FFC. Figure 3 shows the effect of biasing the central conductor for radially coupled FFC under different bias voltages. It is clear that +ve bias on the central conductor suppresses the electrons leaving the blind hole and deformation of the induced signal. The field dilution effect is not visible for 400 ps bunches, and becomes more relevant for shorter bunches, e.g. < 100 ps especially for ACFFC.

EXPERIMENTS

Most of the measurements were performed with the radially coupled FFC at the exit of the X2 beam line with ion beam energy of 8.6 MeV/u. Previous measurements with a beam of lower energy and charge state and a comparison of the FFC with a Feschenko monitor are reported here [18]. These measurements were performed with a DC biasing scheme of the FFC central conductor as shown in Fig. 4. Biasing is performed to influence the motion of secondary

Content from this work may be used under the terms of the CC BY 4.0 licence (© 2022). Any distribution of this work must maintain attribution to the author(s), title of the work, publisher, and DOI

ISBN: 978-3-95450-241-7 ISSN: 2673-5350 doi:10.18429/JACoW-IBIC2022-TUP25

Content from this work may be used under the terms of the CC BY 4.0 licence (© 2022). Any distribution of this work must maintain attribution to the author(s), title of the work, publisher, and DOI

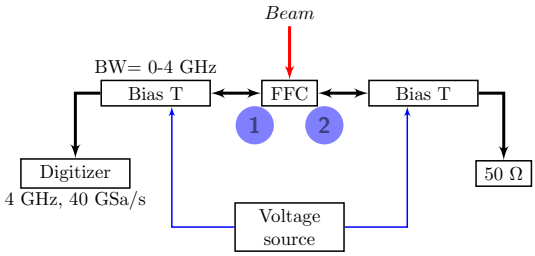


Figure 4: The symmetric biasing scheme ensures that there is no current flow through the FFC due to the biasing.

electrons emitted due to the beam irradiation. The biasing scheme ensures that no DC current flows through the FFC due to the bias voltage. This first measurement was performed with a 0.4 mA O^{6+} beam in 2021 campaign and the bunch length evolution along the full macro-pulse is shown in Fig. 5 for three bias settings. For case with zero biasing voltage, we observe a significant bunch "tail" of around 3 ns in the measured profile. The tail was suppressed on application of +ve bias and is further increased on application of −ve bias inline with the simulations. Although the electrons are created almost instantaneously after the beam hits the central conductor, the additional signal due to electron emission is only induced after electrons leave the blind hole as discussed earlier. 1 - 10 eV electrons possess a velocity of 0.6 to 2 mm/ns and need between 1 - 3 ns to exit the blind hole in the central conductor forming the long tail. There is a reflection at around 40 degrees which vanishes when the biasing scheme was removed. Fig. 6 shows the averaged bunch calculated for the whole macro-pulse. The second smaller peak is clearly visible along with the reflection as annotated in the plot.

Similar measurement was performed with Ar^{10+} beam also at 8.6 MeV/u in the 2022 campaign where the machine settings were different. The averaged bunch shape measurement in a 50 µs pulse as a function of DC bias applied on FFC central conductor is shown in Fig. 7 (top). The Phase Probe (PP) signal installed 0.5 m upstream of the FFC is shown in Fig. 7 (bottom) and shows that the beam conditions were stable during the measurement. Typically convolution of FFC signal with the field elongation expression can be used to estimate the true charge state distribution [4].

The charge profile measured by FFC were compared with the phase probe signal. Figure 8 shows the estimated bunch width (4σ) as a function of bias voltage after erasing the signal below 10 % of maximum amplitude. The bunch width seems to saturate around 30 V. Other measurements reported in literature [3, 10] suggest that more than 90 % electrons have energies below 30 eV and 30 - 50 V DC bias should be sufficient to suppress the signal distortion due to secondary emission. Figure 9 shows the comparison of ACFFC and RCFCC under comparable machine settings. We should however note that due to unavailability of sufficient feedthroughs, the measurements with the two FFCs were done on different days. The ACFFC consistently shows

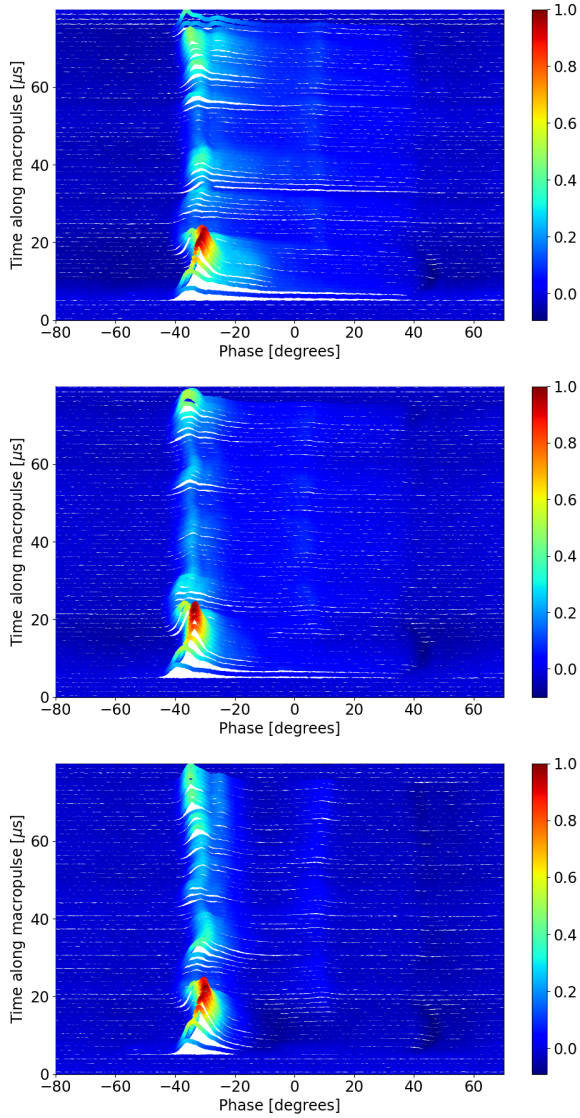


Figure 5: The waterfall plot showing the full macro-pulse for various DC bias voltages applied on central conductor of the radially coupled FFC −25 V (top) 0 V (middle) and 25 V (bottom).

a dip at the tail of bunch and seems to be less affected by secondary emission. Currently, it is speculated that the dip at the end is caused by particles which interact with central conductor of ACFFC due to its pre-field but are not deposited on it causing a phase probe like behavior.

CONCLUSION

We have studied two FFC designs by means of CST simulations taking the secondary emission and external biasing voltage into account. Measurements under similar beam conditions are reported where a strong distortion in the longitudinal charge profile measurement due to secondary electrons is observed. External DC biasing of central conductors is shown to mitigate the distortion to a large extent.

ISBN: 978-3-95450-241-7 ISSN: 2673-5350 doi:10.18429/JACoW-IBIC2022-TUP25

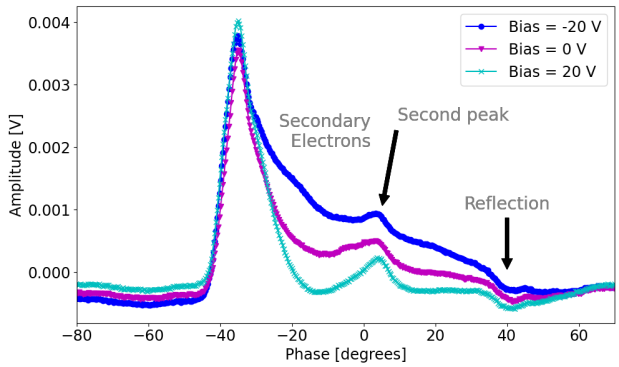


Figure 6: The longitudinal charge profile measurement averaged for a macro-pulse with application of various DC bias voltages on the radially coupled FFC central conductor.

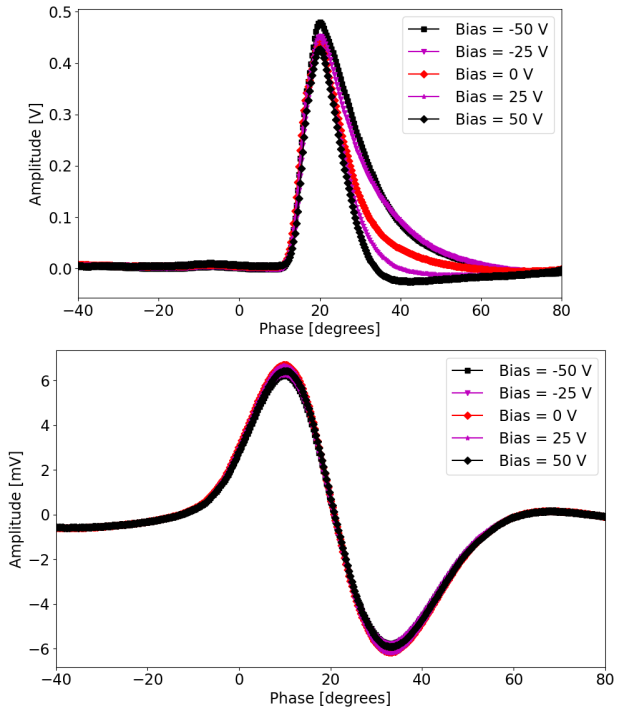


Figure 7: The FFC and preceding phase probe signal for various bias voltages.

ACKNOWLEDGEMENTS

This work is supported by the German Federal Ministry of Education and Research (BMBF) under contract no. 05P21RORB2. Joint Project 05P2021 - R&D Accelerator (DIAGNOSE). R. Singh and G. Rodrigues acknowledge the support received under VAJRA project (VJR/2018/000115) from Department of Science and Technology, India. D. Sun, A. Shemyakin and V. Scarpine are gratefully acknowledged for providing the RCFFC on loan. We thank J. Matthew for providing the ACFFC on loan.

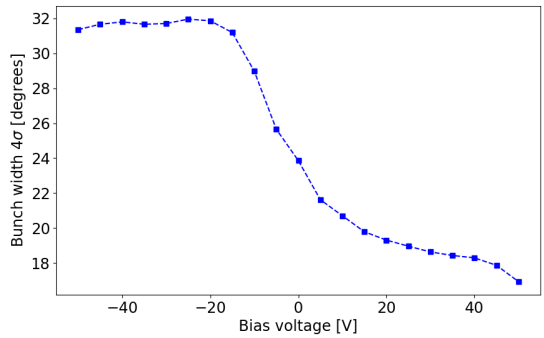


Figure 8: The longitudinal charge profile measurement averaged for a macro-pulse with application of various DC bias voltages on the FFC central conductor.

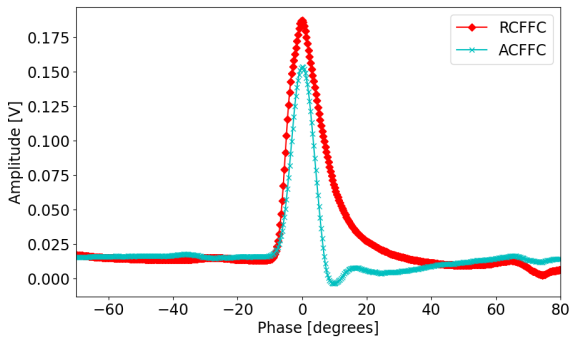


Figure 9: Bunch shape measurements comparison between the axially coupled coaxial structure and the radially coupled coax FFC under comparable machine settings without any biasing.

REFERENCES

[1] S. Lauber *et al.*, "Longitudinal phase space reconstruction for a heavy ion accelerator", *Phys. Rev. Accel. Beams*, vol. 23, p. 114201. doi:10.1103/PhysRevAccelBeams.23.114201

[2] J.-P. Carniero *et al.*, "Longitudinal beam dynamics studies at the PIP-II injector test facility", *Int. J. Mod. Phys. A*, vol. 34, no. 36, 2019. doi:10.1142/S0217751X19420132

[3] W. R. Rawnsley *et al.*, "Bunch shape measurements using fast Faraday cups and an oscilloscope operated by LabVIEW over Ethernet", *AIP Conf. Proc.*, vol. 546, p. 547, 2000. doi:10.1063/1.1342629

[4] R. Singh, "Longitudinal diagnostics R&D at GSI UNILAC", in *Proc. HIAT'22*, Darmstadt, 2022, to be published.

[5] G. Rodrigues *et al.*,"Studies on Radially Coupled Fast Faraday Cups to Minimize Field Dilution and Secondary Electron Emission at Low Intensities of Heavy Ions", presented at the IBIC'22, Kraków, Poland, Sep. 2022, paper WEP28, this conference.

[6] E. J. Sternglass, "Theory of Secondary Electron Emission by High-Speed Ions", *Phys. Rev.*, vol. 108, no. 1, 1957. doi:10.1103/PhysRev.108.1

[7] H. Rothard *et al.*, "Secondary-electron yields from thin foils: A possible probe for the electronic stopping power of heavy

Content from this work may be used under the terms of the CC BY 4.0 licence (© 2022). Any distribution of this work must maintain attribution to the author(s), title of the work, publisher, and DOI

ISBN: 978-3-95450-241-7 ISSN: 2673-5350 doi:10.18429/JACoW-IBIC2022-TUP25

ions", *Phys. Rev. A*, vol. 41, no. 5, p. 2521, 1990. doi:10.1103/PhysRevA.41.2521

[8] A. Koyama, T. Shikata and H. Sakairi, "Secondary electron emission from Al, Cu, Ag and Au metal targets under proton bombardment", *Jpn. J. Appl. Phys.*, vol. 20, no. 1, pp. 65-70, 1981. doi:10.1143/JJAP.20.65

[9] D. Hasselkamp, K. G. Lang, A. Scharmann and N. Stiller, "Ion induced electron emission from metal surfaces", *Nucl. Instrum. Methods*, vol. 180, no. 2–3, pp. 349-356, 1981. doi:10.1016/0029-554X(81)90076-8

[10] A. Reiter *et al.*, "Investigation of Cross Talk in Secondary Electron Emission Grids", Technical Note LOBI-TN-SEM-2012-001, GSI, Darmstadt, 2012.

[11] O. Benka, A. Schinner, T. Fink and M. Pfaffenlehner, "Electron-emission yield of Al, Cu, and Au for the impact of swift bare light ions", *Phys. Rev. A*, vol. 52, no. 5, pp. 3959-3965, 1995. doi:10.1103/PhysRevA.52.3959

[12] A. F. Haque *et al.*, "Proton-induced secondary electron emission from elemental solids over the energy domain 1 keV–1000 MeV", *Results Phys.*, vol. 15, p. 102519, 2019. doi:10.1016/j.rinp.2019.102519

[13] D. Hasselkamp, H. Rothard, K. O. Groeneveld, J. Kemmler, P. Varga and H. Winter, "Particle Induced Electron Emission 2", vol. 4, p. 25, Springer-Verlag, Berlin/Heidelberg, 1992.

[14] H. Rothard *et al.*, "Differential multi-electron emission induced by swift highly charged gold ions penetrating carbon foils", *Nucl. Instrum. Methods Phys. Res., Sect. B*, vol. 258, pp. 91–95, 2007. doi:10.1016/j.nimb.2006.12.132

[15] D. Hasselkamp, S. Hippler and A. Scharmann, "Ion induced secondary electron spectra from clean metal surfaces", *Nucl. Instrum. Methods Phys. Res., Sect. B*, vol. 18, pp. 561-565, 1987. doi:10.1016/S0168-583X(86)80088-X

[16] N. V. Sydorenko, S. I. Kononenko and V. P. Zhurenko, "Mean energy of electrons emitted from solid unders swift light ion bombardment", *Journal of Kharkiv University*, no. 657, pp. 81-84, 2005.

[17] J. R. Vaughan, "Secondary Emission Formulas", *IEEE Trans. Electron Devices*, vol. 40, no. 4, 1993. doi:10.1109/16.202798

[18] R. Singh *et al.*, "Comparison of Feschenko BSM and Fast Faraday Cup with Low Energy Ion Beams", in *Proc. IBIC'21*, Pohang, Korea, Sep. 2021, pp. 407–411. doi:10.18429/JACoW-IBIC2021-WEPP16

Content from this work may be used under the terms of the CC BY 4.0 licence (© 2022). Any distribution of this work must maintain attribution to the author(s), title of the work, publisher, and DOI

ISBN: 978-3-95450-241-7 ISSN: 2673-5350 doi:10.18429/JACoW-IBIC2022-TUP28

COHERENT DIFFRACTION RADIATION FOR LONGITUDINAL ELECTRON BEAM CHARACTERISTICS

R. Panaś*, NSRC SOLARIS, Kraków, Poland
A. Curcio, CLPU, Villamayor, Spain
K. Łasocha, Jagiellonian University, Kraków, Poland

Abstract

For the need of diagnostics of the longitudinal electron beam characteristics at the first Polish free electron laser (PolFEL) project, a Coherent Diffraction Radiation (CDR) system is being developed and tested. It will allow for non-destructive bunch length measurement based on the power balance of CDR radiation collected by Schottky diodes in different ranges of (sub-)THz radiation. The first tests and measurements will be performed at the end of the SOLARIS synchrotron injector linac, where the beam has been already characterized and aligned. In this paper the theoretical background of the measurement, calculations and first experimental achievements will be presented.

COHERENT DIFFRACTION RADIATION

Electromagnetic radiation is emitted when a beam of charged particles accelerates or changes medium of propagation (abruptly or continously in terms of the local electromagnetic susceptibility) [1, 2]. If the emitted wavelength is comparable or greater than the bunch length, the radiation is said "coherent" because the contributions from the single particles within the beam interfere constructively and the bunch emits as a whole. In that case the emitted radiation power is proportional to the square of the bunch form-factor and increases with decreasing bunch length. For bunch lengths on the picosecond scale variations in the peak current can be easily monitored by GHz-THz detectors like Schottky diodes [3, 4]. For shorter bunches far-infrared diagnostics are needed, for example spectrometers [5]. If the goal is to infer a relative information of the bunch compression, then a source of coherent radiation coupled to a power-detector can provide this information, since for a detected frequency which is high-enough the amount of detected power scales with the shortness of the emitting bunch. Coherent radiation can be coupled out of the beamlines through suitable transparent windows, eventually transported in air into power-detectors. For the diagnostic purposes of the PolFEL project [6], Coherent Diffraction Radiation (CDR) will be exploited, which allows for non-destructive bunch length measurements. Diffraction radiation is the radiation that a bunch of particles emits when crossing two regions of limited size with different index of refraction [7]. This can be accomplished if the beam passes through a hollow disk of dense material. If the disk surface is metallic the radiation is emitted from localized layers of that surface, in such a way that the beam properties are imprinted into the emitted radiation at the transition plane and can be exploited for diagnostics. The fact that the disk is hollow allows for the beam not to be scattered and the emittance be preserved (the field lines polarize the radiator even if the particles do not propagate inside it). The spectral angular distribution of energy emitted backward in the form of diffraction radiation from a perfectly conducting round disk, with an internal and external radius equal to respectively a and b, can be described with the following formula [8, 9]:

$$\frac{d^2I}{d\omega d\Omega} = |F(\omega)|^2 \times \frac{Q^2}{(4\pi^3\epsilon_0 c^5\beta^4\gamma^2)} \times \times \left| \int_a^b d\rho\rho K_1\left(\frac{\omega\rho}{\beta\gamma c}\right) J_1\left(\frac{\omega\rho}{c\sin\theta}\right) e^{\frac{j\omega^2\rho^2}{2c^2}} \right|^2, \quad (1)$$

where Q denotes the bunch charge, ϵ_0 is vacuum permittivity, c is the velocity of light, β is the ratio of particle velocity and the velocity of light and γ is the Lorentz factor. The quantity $F(\omega)$ is called *bunch form factor* and strictly depends on the shape of the electron bunch. An example of spectral-angular distribution of emitted CDR energy is shown in Fig. 1.

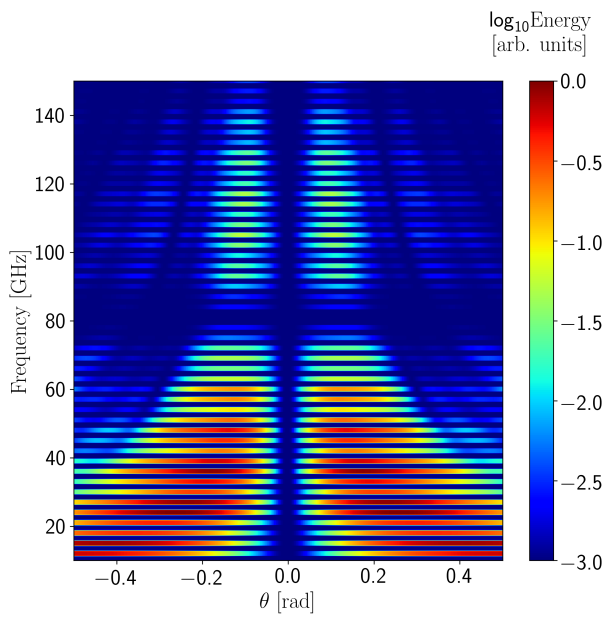


Figure 1: CDR spectral-angular distribution for the SOLARIS injector bunch repetition pattern and beam energy of 550 MeV. The radiator diameter has been set to 5 cm with 1 cm diameter hole for non-destructive diagnostics.

* roman.panas@uj.edu.pl

Content from this work may be used under the terms of the CC BY 4.0 licence (© 2022). Any distribution of this work must maintain attribution to the author(s), title of the work, publisher, and DOI

ISBN: 978-3-95450-241-7 ISSN: 2673-5350 doi:10.18429/JACoW-IBIC2022-TUP28

Content from this work may be used under the terms of the CC BY 4.0 licence (© 2022). Any distribution of this work must maintain attribution to the author(s), title of the work, publisher, and DOI

BUNCH LENGTH MEASUREMENT

The diagnostic technique considered for PolFEL is based on the power balance of CDR radiation collected by Schottky diodes in different ranges of sub- THz radiation. As seen from Eq. (1), the emitted energy depends on the bunch length through the form factor $F(\omega)$. If the transverse size of the bunch is negligible, one has

$$F(\omega) = \int_{-\infty}^{\infty} I(t) e^{j\omega t}\, dt, \qquad (2)$$

where $I(t)$ is the normalized dimensionless beam current passing through the disk. Simply speaking, the form factor is the Fourier transform of the beam current. In certain cases, for example when the beam consists of a single Gaussian bunch, an exact analytical formula for the form factor can be given, parametrized by the RMS bunch length. This parameter can be then experimentally retrieved by calculating the ratio of CDR power at two distinct frequencies and comparing it to the theoretical predictions given by Eq. (1). The described technique is not limited to only one type of radiation, and has been previously demonstrated with measurements based on CDR [3] and Coherent Cherenkov Diffraction Radiation [4]. First tests for PolFEL [10] will be conducted at SOLARIS [11], on a diagnostic station at the end of the injector linac, just before the beam dump, placed for this and other experimental purposes . In the SOLARIS linac the beam is bunched, with the 3 GHz bunch repetition rate. The shape of a single bunch differs from the Gaussian and the bunch intensity is modulated proportionally to the 100 MHz sinewave [12, 13]. As result the corresponding form factor also differs from the smooth form factor of a single Gaussian bunch as presented in Fig. 2.

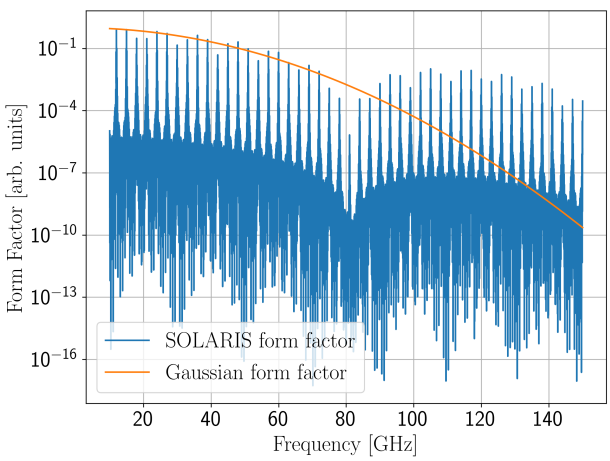


Figure 2: Form factors calculated for SOLARIS injector bunch train and a single Gaussian bunch. In both cases the RMS bunch length is equal to 5 ps.

Although deriving the information on the bunch length from a narrow frequency band is not possible, due to the oscillatory character of the form factor, the bunch length might be derived from the cumulative power within the broader frequency bands. In Fig. 3 the ratios of the CDR power expected in SOLARIS within three frequency bands is plotted as a function of the RMS bunch length. The bands correspond to the bands of commercially available Shcottky diodes offered by Eravant [14]. As can be seen, combination of 50-75 GHz diode with any of two other diodes can provide a sensitive measure of the bunch length, but only for bunches shorter than approximately 6.5 ps. The longer bunches can be however measured using the less sensitive 26.5-40 GHz / 33-50 GHz ratio.

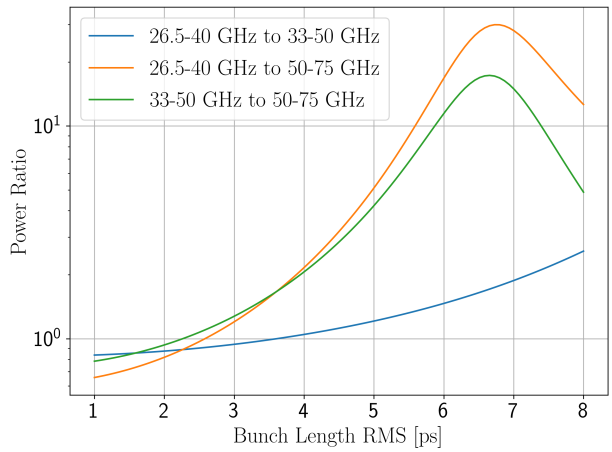


Figure 3: Ratios of CDR power emitted in distinct frequency band, as a function of RMS bunch length.

EXPERIMENTAL SETUP

The first step taken when preparing the setup for measuring the longitudinal electron beam profile using CDR radiation was to place the YAG screen about 20 cm behind 0.15 mm thick flange at the end of the linac in beam dump section. A series of tests was carried out on how the electron profile can be modifed by linac magnets settings, but ultimately it was left with the original machine setup, because the linac had to remain operational so as not to interfere with the operation of the synchrotron. Afterwards the YAG screen was replaced with a CDR radiator in the form of metal coated mirror at an angle of 45° to the incident electron beam. The reason for using a metallic mirror as a radiator instead of a hollow disc was to induce transition radiation, which facilitated the alignment process. In order to focus radiation on the detector, a golden coated parabolic mirror was placed in the setup. The fact that the emitted transition radiation contains part of the visible spectrum, and reflects off the Ø3" 90° Off-axis parabolic mirror in the same way like CDR radiation, makes it possible to use optical CCD camera as radiation focus detector. In this way the location for the Schottky diodes was determined. Placing the latters there and measuring the CDR signal will be the next action to take. In parallel and for more general purposes, a remote controlled lens was mounted on the diagnostic camera for prototyping and testing. The system has been built with a

ISBN: 978-3-95450-241-7 ISSN: 2673-5350 doi:10.18429/JACoW-IBIC2022-TUP28

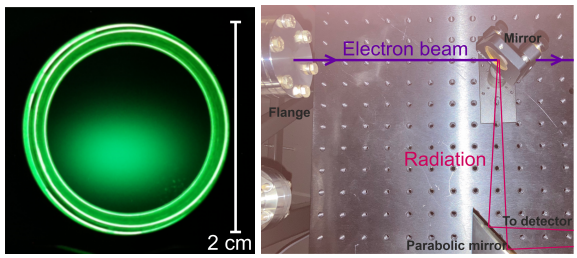


Figure 4: Transverse electron beam profile measured with YAG screen at radiator position and top view of longitudinal profile measurement set-up at SOLARIS.

widely available and low cost Canon EF lens that is also compatible with a general purpose Canon still cameras. The electronic control system was made using a STM32 microprocessor and an Ethernet controller chip. These controllers may be mounted on the other diagnostics cameras in the linac or even at the Pinhole diagnostic beamline in the SOLARIS ring. At the diagnostic station before the beam dump we have for now mounted a Raspberry Pi camera with a in-house modified hardware that has the ability to be triggered from the timing system. Thanks to this it is possible to take a synchronized beam image just when the radiator is hit and light is emitted, as in Fig. 4.

CONCLUSION

In this contribution the first steps made at SOLARIS towards an experimental test of the CDR-based electron bunch length measurement for PolFEL have been presented. As a parallel development, an imaging system with automatic focusing and trigger has been successfully commissioned during the setup construction. Additionally, tools for processing the measured data and calculating the bunch length have been developed. The Schottky diodes purchase process is currently underway. After placing them in the setup, first results will be obtained, analyzed and compared to the expected values in order to verify the correctness of measurements and calculations. If all tests pass, analogous setups will be implemented for the PolFEL project.

REFERENCES

[1] J. D. Jackson, *Classical electrodynamics*. American Association of Physics Teachers, 1999.

[2] V. L. Ginzburg, "Radiation by uniformly moving sources (Vavilov-Cherenkov effect, transition radiation, and other phenomena)," *Phys. Usp.*, vol. 39, no. 10, pp. 973–982, 1996. doi:10.1070/PU1996v039n10ABEH000171

[3] A. Curcio *et al.*, "Beam-based sub-thz source at the cern linac electron accelerator for research facility," *Phys. Rev. Accel. Beams*, vol. 22, no. 2, p. 020 402, 2019. doi:10.1103/PhysRevAccelBeams.22.020402

[4] A. Curcio *et al.*, "Noninvasive bunch length measurements exploiting Cherenkov diffraction radiation," *Phys. Rev. Accel. Beams*, vol. 23, no. 2, p. 022 802, 2020. doi:10.1103/PhysRevAccelBeams.23.022802

[5] T. J. Maxwell *et al.*, "Coherent-radiation spectroscopy of few-femtosecond electron bunches using a middle-infrared prism spectrometer," *Phys. Rev. Lett.*, vol. 111, no. 18, p. 184 801, 2013. doi:10.1103/PhysRevLett.111.184801

[6] A. I. Wawrzyniak *et al.*, "Concept of Electron Beam Diagnostics for PolFEL," in *Proc. IPAC'22*, Bangkok, Thailand, 2022, pp. 1055–1058. doi:10.18429/JACoW-IPAC2022-TUPOPT025

[7] A. Potylitsyn, "Transition radiation and diffraction radiation. similarities and differences," *Nucl. Instrum. Methods Phys. Res., Sect. B*, vol. 145, no. 1, pp. 169–179, 1998. doi:10.1016/S0168-583X(98)00384-X

[8] S. Casalbuoni, B. Schmidt, P. Schmüser, V. Arsov, and S. Wesch, "Ultrabroadband terahertz source and beamline based on coherent transition radiation," *Phys. Rev. ST Accel. Beams*, vol. 12, no. 3, p. 030 705, 2009. doi:10.1103/PhysRevSTAB.12.030705

[9] A. Curcio *et al.*, "Diffractive shadowing of coherent polarization radiation," *Phys. Lett. A*, vol. 391, p. 127 135, 2021. doi:10.1016/j.physleta.2020.127135

[10] R. Nietubyć *et al.*, "Status of PolFEL project," in *Proc. SRF'21*, East Lansing, MI, USA, Jun.-Jul. 2021, pp. 566–570. doi:10.18429/JACoW-SRF2021-THPFAV003

[11] A. I. Wawrzyniak, R. Panaś, A. Curcio, M. Knafel, G. Kowalski, and A. Marendziak, "Solaris synchrotron performance and operational status," *Nucl. Instrum. Methods Phys. Res., Sect. B*, vol. 493, pp. 19–27, 2021. doi:10.1016/j.nimb.2021.01.020

[12] A. Curcio, R. Panaś, M. Knafel, and A. Wawrzyniak, "Liouville theory for fully analytic studies of longitudinal beam dynamics and bunch profile reconstruction in dispersive lines," *Nucl. Instrum. Methods Phys. Res., Sect. A*, vol. 986, p. 164 755, 2021. doi:10.1016/j.nima.2020.164755

[13] A. Curcio, M. A. Knafel, G. W. Kowalski, R. Panaś, M. Waniczek, and A. I. Wawrzyniak, "Bunch Length Characterizations for the Solaris Injector LINAC," in *Proc. IPAC'21*, Campinas, Brazil, May 2021, pp. 2117–2119. doi:10.18429/JACoW-IPAC2021-TUPAB277

[14] Eravant. https://www.eravant.com/.

Content from this work may be used under the terms of the CC BY 4.0 licence (© 2022). Any distribution of this work must maintain attribution to the author(s), title of the work, publisher, and DOI

ISBN: 978-3-95450-241-7 ISSN: 2673-5350 doi:10.18429/JACoW-IBIC2022-TUP29

ZnO(In) SCINTILLATION LIGHT SPECTRA INVESTIGATION FOR HEAVY ION DETECTOR APPLICATION*†

M. Saifulin[1,‡], P. Boutachkov, C. Trautmann[1], B. Walasek-Höhne
GSI Helmholtz Center for Heavy Ion Research, Darmstadt, Germany
P. Rodnyi, I. Venevtsev, Peter the Great Polytechnic University, St. Petersburg, Russia
E. Gorokhova, JSC S.I. Vavilov State Optical Institute, St. Petersburg, Russia
[1]also at Technical University Darmstadt, Darmstadt, Germany

Abstract

ZnO-based ceramics are known as promising scintillators exhibiting light emission in the ultraviolet (UV) spectral region (~390 nm) and ultrafast decay times (<1 ns). They are of great interest for applications in scintillation counters and screens at high-energy heavy ion accelerators. In this contribution, the deterioration of scintillating properties of ZnO-based ceramics subjected to heavy ion exposure at high doses is investigated. The scintillation light spectra of ZnO(In) as a function of fluence for 4.8 MeV/u ^{48}Ca and ^{197}Au ions were studied. We observed that the deterioration of the scintillation intensity with increasing fluence follows the Birks-Black model.

INTRODUCTION

Zinc oxide is a multi-functional material with many applications due to its interesting properties [1, 2]. In particular, since the 1960s it has been known as a promising scintillation material that exhibits sub-nanosecond fast light emission at room temperature [3–5]. Previously, pure and doped ZnO has been produced in various forms (powder, thin films, single- and poly-crystals, and ceramics) with the purpose of detecting different types of ionizing radiation [6–9].

Recent studies and technological advances have made it possible to produce bulk pieces of indium- and gallium-doped zinc oxide ceramics (ZnO(In) and ZnO(Ga)) by uniaxial hot pressing in vacuum [10, 11]. These scintillating ceramics become highly interesting for heavy-ion radiation detection at accelerator facilities like GSI and the future FAIR facility in Darmstadt, Germany [12]. ZnO(In) and ZnO(Ga) scintillators are considered as promising candidates to substitute plastic scintillator BC400 commonly used for beam intensity monitoring and spill micro-structure characterization at SIS-18 synchrotron, where ion beams from proton to uranium with energies from 150 MeV/u to 4.5 GeV/u can be obtained.

As a part of a research and development project for a radiation-resistant fast scintillation detector, we report on the performance and in-situ characterization of ZnO(In) ceramics scintillation light spectra change as a function of ion fluence.

ZnO(In) SCINTILLATION SPECTRA

The investigated ZnO(In) ceramic sampels were produced in the form of 8 mm × 8 mm × 0.4 mm size plates at the Joint Stock Company "Research and Production Corporation S.I. Vavilova" (St. Petersburg, Russia). The samples were produced with 0.046 at % In^{3+} dopping concentration. Samples density estimated from mass and volume measurements was 4.66 g/cm^2.

In-situ characterization of scintillation light spectra was performed using 4.8 MeV/u energy ^{48}Ca and ^{197}Au ions from UNIversal Linear ACcelerator (UNILAC) of the GSI Helmholtz Center for Heavy Ion Research GmbH (Darmstadt, Germany) [13]. The irradiations were carried out at room temperature in vacuum at a beam incidence angle of 45° with respect to the sample surface.

Scintillation light was collected with a lens placed in front of the ion-incident surface of the sample. The collected light was transfered via a light guide to an Ocean Optics QE-Pro spectrometer. The acquired spectra were corrected for dark counts and normalized by the number of ions that hit the sample during the spectrum acquisition.

Figure 1 shows how the scintillation light spectrum of ZnO(In) ceramic sample changes as a result of 4.8 MeV/u ^{48}Ca ion irradiation. The spectra have only one emission

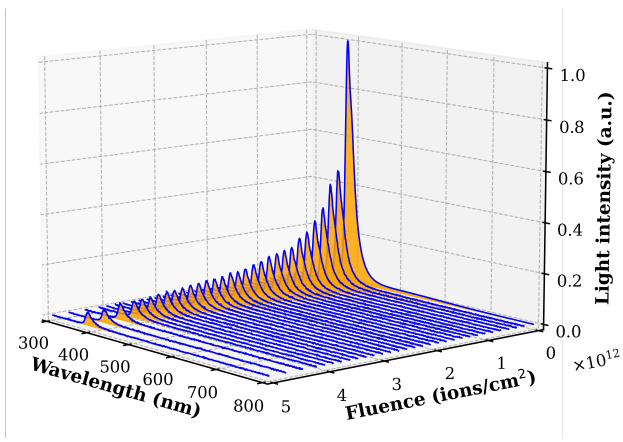


Figure 1: Spectra of ZnO(In) ceramic as a function of 4.8 MeV/u ^{48}Ca ion fluence.

band in the ultraviolet (UV) light region with a maximum at around 387 nm. The observed peak corresponds to the near-band-edge emission (NBE) known for scintillation decay times less than nanosecond. With increasing fluence, the

* The results presented in this contribution are based on the work performed before the 24th of February, 2022.
† DLR funded this work within the ERA.Net RUS Plus Project RUS_ST2017-051.
‡ m.saifulin@gsi.de (corresponding author)

Content from this work may be used under the terms of the CC BY 4.0 licence (© 2022). Any distribution of this work must maintain attribution to the author(s), title of the work, publisher, and DOI

ISBN: 978-3-95450-241-7 ISSN: 2673-5350 doi:10.18429/JACoW-IBIC2022-TUP29

intensity of this NBE band drops considerably. No new light emission bands are formed as a result of the ion irradiation, not even at the highest fluences reached, 5×10^{12} Ca-ions/cm^2 and 2×10^{11} Au-ions/cm^2.

BIRKS-BLACK MODEL FIT

The Birks-Black model [14] was used to fit the observed NBE peak intensity reduction as a function of Ca and Au ion fluence. According to this model, the reduction of the scintillation light intensity can be presented as:

$$\frac{I(\Phi)}{I_0} = \frac{1}{1+\frac{\Phi}{\Phi_{1/2}}}, \quad (1)$$

where I_0 is the initial scintillation light intensity, and $\Phi_{1/2}$ is the critical fluence at which the scintillation light intensity is reduced by 50% of the initial value.

Figure 2 shows the NBE peak intensity as a function of the Ca and Au ion fluence. The intensity evolution follows the Birks-Black model for both ion species. The critical fluence values extracted from a fit of Eq. (1) to the data are 3.3×10^{11} Ca-ions/cm^2 and 3.5×10^{9} Au-ions/cm^2, respectively.

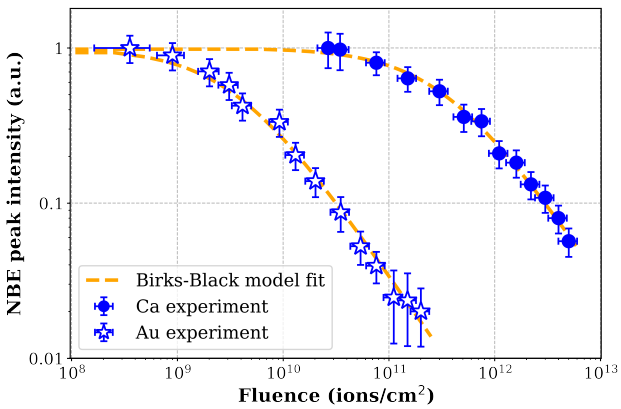


Figure 2: Intensity of the NBE peak (387 nm) of the scintillation spectrum as a function of irradiation fluence using ^{48}Ca ions (full circles) and ^{197}Au ions (open stars). The dashed line represent fits with Eq. (1) from the Birks-Black model.

CONCLUSIONS

ZnO-based scintillating ceramics are promising materials to be used for heavy-ion particle detection applications. In this work, ZnO(In) scintillating ceramics were exposed to 4.8 MeV/u ^{48}Ca and ^{197}Au ion beams in order to investigate the changes in scintillation light spectrum as a function of swift heavy ion fluence. The scintillation light intensity follows the trend predicted by the Birks-Black model. As a result of high fluence irradiation, no new peak formation was observed up to 5×10^{12} Ca-ions/cm^2 and 2×10^{11} Au-ions/cm^2 irradiation at 4.8 MeV/u energy.

REFERENCES

[1] Ü. Özgür *et al.*, "A comprehensive review of ZnO materials and devices," *J. Appl. Phys.*, vol. 98, no. 4, pp. 1–103, 2005. doi:10.1063/1.1992666

[2] C. Klingshirn *et al.*, "65 years of ZnO research–old and very recent results," *Phys. Status Solidi B*, vol. 247, no. 6, pp. 1424–1447, 2010. doi:10.1002/pssb.200983195

[3] W. Lehmann, "Edge emission of *n*-type conducting ZnO and CdS," *Solid-State Electron.*, vol. 9, no. 11-12, pp. 1107–1110, 1966.

[4] D. Luckey, "A fast inorganic scintillator," *Nucl. Instrum. Methods Phys. Res. A*, vol. 62, no. 1, pp. 119–120, 1968. doi:10.1016/0029-554X(68)90628-9

[5] T. Batsch, B. Bengtson, and M. Moszyński, "Timing properties of a ZnO(Ga) scintillator (NE843)," *Nucl. Instrum. Methods Phys. Res. A*, vol. 125, no. 3, pp. 443–446, 1975. doi:10.1016/0029-554X(75)90262-1

[6] J. S. Neal, L. A. Boatner, N. Giles, L. Halliburton, S. Derenzo, and E. Bourret-Courchesne, "Comparative investigation of the performance of ZnO-based scintillators for use as α-particle detectors," *Nucl. Instrum. Methods Phys. Res. A*, vol. 568, no. 2, pp. 803–809, 2006. doi:10.1016/j.nima.2006.09.041

[7] J. S. Neal *et al.*, "Investigation of ZnO-based polycrystalline ceramic scintillators for use as α-particle detectors," *IEEE Trans. Nucl. Sci.*, vol. 56, no. 3, pp. 892–898, 2009. doi:10.1109/TNS.2008.2004702

[8] C. Liang *et al.*, "Experimental study on scintillation efficiency of ZnO:In to proton response," *Chin. Phys. C*, vol. 35, no. 11, p. 1037, 2011. doi:10.1088/1674-1137/35/11/011

[9] R. Sahani, C. Kumari, A. Pandya, and A. Dixit, "Efficient alpha radiation detector using low temperature hydrothermally grown ZnO:Ga nanorod scintillator," *Sci. Rep.*, vol. 9, no. 1, pp. 1–9, 2019. doi:10.1038/s41598-019-47732-1

[10] E. Gorokhova *et al.*, "Development and study of ZnO:In optical scintillation ceramic," *J. Opt. Technol.*, vol. 82, no. 12, pp. 837–842, 2015. doi:10.1364/JOT.82.000837

[11] E. I. Gorokhova *et al.*, "Structural, optical, and luminescence properties of ZnO:Ga optical scintillation ceramic," *J. Opt. Technol.*, vol. 85, no. 11, pp. 729–737, 2018. doi:10.1364/JOT.85.000729

[12] G. Rosner, "Future facility: FAIR at GSI," *Nucl. Phys. B*, vol. 167, pp. 77–81, 2007. doi:10.1016/j.nuclphysbps.2006.12.089

[13] W. Barth, L. Dahl, J. Glatz, L. Groening, S. G. Richter, and S. Yaramishev, "Achievements of the High Current Beam Performance of the GSI Unilac," in *Proc. EPAC'04*, Lucerne, Switzerland, Jul. 2004.

[14] J. Birks and F. Black, "Deterioration of anthracene under α-particle irradiation," *Proc. Phys. Soc. London, Sect. A*, vol. 64, no. 5, p. 511, 1951. doi:10.1088/0370-1298/64/5/112

Content from this work may be used under the terms of the CC BY 4.0 licence (© 2022). Any distribution of this work must maintain attribution to the author(s), title of the work, publisher, and DOI

ISBN: 978-3-95450-241-7 ISSN: 2673-5350 doi:10.18429/JACoW-IBIC2022-TUP30

BEAM INTENSITY MEASUREMENT IN ELENA USING RING PICK-UPs

O. Marqversen†, D. Alves, CERN, Geneva, Switzerland

Abstract

A bunched beam intensity measurement system for the CERN Extra Low ENergy Antiproton (ELENA) ring, using a cylindrical shoe-box electrostatic pick-up from the existing orbit system, is presented. The system has been developed to measure very challenging beam currents, as low as 200 nA corresponding to intensities of the order of 10^7 antiprotons circulating with a relativistic beta of the order of 10^{-2}.

In this work we derive and show that the turn-by-turn beam intensity is proportional to the baseline of the sum signal and that, despite the AC-coupling of the system, the installed front-end electronics, based on a charge amplifier, not only guarantees the preservation of the bunch shape (up to a few tens of MHz), but also allows for an absolute calibration of the system. In addition, the linearity of the intensity measurements and their independence with respect to average beam position is evaluated using a standard electromagnetic simulation tool. Finally, experimental measurements throughout typical antiproton deceleration cycles are presented and their accuracy and precision are discussed.

THE MEASUREMENT SYSTEM

This newly developed intensity measurement system is an add-on to the Extra Low ENergy Antiproton (ELENA) ring orbit system [1], using the already available sum signal from one ring Pick-Up (PU). In terms of hardware, the add-on consists of an Analog to Digital Converter (ADC) mounted on a PCIExpress bus [2] integrated in a front-end computer installed in the CERN control system, in order to digitise the PU sum signal.

ELECTROSTATIC PICK-UP AS A CHARGE MONITOR

As an alternative, or a complement, to the standard beam current transformers, an electrostatic orbit PU can be used to measure the intensity of bunched beams, either in a beam line or in a ring.

The Charge Found from the Output Voltage

The beam intensity can be found from the integrated output voltage from an electrostatic PU:

The charge Q, induced in the inner surface of a cylindrical PU is given by

$$Q = Q_b = \rho V \tag{1}$$

where ρ is the beam charge density [charge/m^3], V is the volume enclosed by the PU and Q_b is the portion of the beam charge contained in this volume.

The current density, J is given by

$$J = \frac{i}{A} = \rho\beta c \tag{2}$$

where i is the beam current, A its transverse area and βc its speed. Combining Eq. (1) and Eq. (2) we get

$$Q = \frac{i}{\beta c A} V = \frac{L}{\beta c} i \tag{3}$$

where L is the length of the PU.

The current i_z, drawn from the PU (as shown in Fig. 1), can be written as

$$i_z = \frac{dQ_b}{dt} = \frac{1}{\beta c} \cdot L \cdot \frac{di_b}{dt} \tag{4}$$

This current is split in two in the load impedance, Z, which is assumed to consist of a resistor, R, in parallel with a capacitor, C_L. C_L is in parallel with the pick-up capacitance, C_{pu}, and can be combined into a single capacitance, C, thus including both the PU and the load.

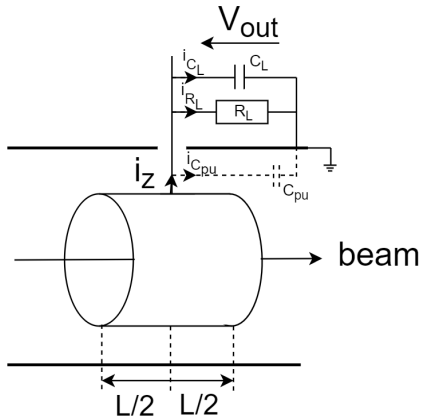


Figure 1: A circular electrostatic pick-up.

Ohm's law is used to get the voltage on the output, V_{out}:

$$i_z = i_R + i_C \tag{5}$$

where:

$$i_R = \frac{V_{out}}{R} \quad \text{and} \quad i_C = \frac{dQ_c}{dt} = C\frac{dV_{out}}{dt} = RC\frac{di_R}{dt}$$

The transfer function can be calculated by combining Eqs. (4) and (5) and differentiating assuming sinusoidal inputs to obtain:

$$\frac{i_R}{i_b} = \frac{L}{\beta c} \cdot \frac{j\omega}{1+j\omega RC} \tag{6}$$

The V_{out} on the load is found by multiplying the current, i_R, with the resistance, R (Ohm's law):

$$V_{out} = R \cdot i_R = \frac{L}{\beta c C} \cdot \frac{j\omega RC}{1+j\omega RC} \cdot i_b \tag{7}$$

Equation (7) is a standard first order high pass transfer function.

A bunched beam in a circular accelerator will have a periodic spectrum consisting of all harmonics (H) of the revolution frequency, where the amplitude ratio between harmonics will be dependent upon bunch shape as indicated in Fig. 2.

† ole.marqversen@cern.ch

Content from this work may be used under the terms of the CC BY 4.0 licence (© 2022). Any distribution of this work must maintain attribution to the author(s), title of the work, publisher, and DOI

ISBN: 978-3-95450-241-7 ISSN: 2673-5350 doi:10.18429/JACoW-IBIC2022-TUP30

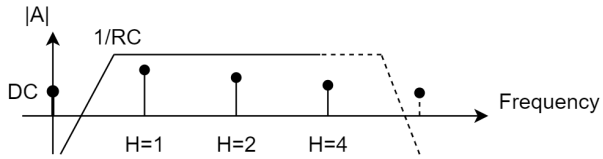


Figure 2: The high pass transfer function of the system.

Ensuring in the design, by appropriately choosing R and C, that all beam harmonics are inside the passband, will preserve the shape of the bunches [3]. Care should also be taken as to ensure that the upper cut off frequency is high enough to include all harmonics with relevant power. The revolution frequency in ELENA changes during deceleration from 1.056 MHz to 144 kHz. The low cut off frequency, $\omega_0 = 1/RC$, will determine the so-called droop time for the cancellation of the DC component. By controlling the low cut off frequency one can also ensure that $1 \ll j\omega RC$, in which case the system will work in a regime where Eq. (7) reduces to

$$V_{out} = R \cdot i_R = \frac{L}{\beta c} \cdot \frac{1}{C} \cdot i_b \qquad (8)$$

The total beam charge, Q_{beam}, can be calculated by integrating the beam current, i_b, over one revolution period, T_0, to give

$$Q_{beam} = \int_o^{T_0} (i_b - i_{baseline}) dt = \\ = C \cdot \frac{\beta c}{L} \int_0^{T_0} (V_{out} - V_{baseline})\, dt \qquad (9)$$

The baseline subtraction is needed otherwise the integral will be zero as the PU is not sensitive to the DC component of the beam spectrum. One can see from Eq. (9) that the knowledge of the beam speed, PU length and total capacitance is needed to get an absolute measurement.

Charge Amplifier

By using a charge (transimpedance) amplifier, see Fig. 3, the sensitivity of measurement can be increased as the total capacitance, C (normally the sum of the PU capacity and the load impedance capacity), becomes essentially $C_{feedback}$:

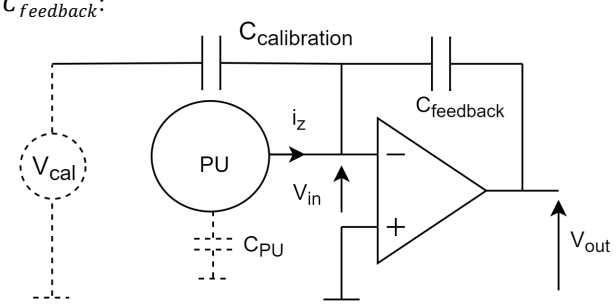


Figure 3: Ideal charge (transimpedance) amplifier, connected to PU and calibration signal input.

Ideally (i.e. for infinite open-loop gain), the feedback around the amplifier will ensure zero voltage at the input terminal, i.e. V_{in} vanishes on the PU. The PU capacitance, C_{PU} is therefore not charged and will not influence the sensitivity. In the ELENA system, a $C_{feedback}$ of 1 pF is used and the ideal operational amplifier shown in Fig. 3 is made up using a discrete input stage of JFETs and a feedback resistor to control the low pass frequency cut-off (~200 Hz) [4]. The open loop gain of this amplifier, in the pass band, is 70 dB, thus ensuring essentially a zero voltage on the input (V_{in} = 0 V).

The charge amplifier will charge the input current onto the capacitor, $C_{feedback}$, and output the integral of i_z as V_{out}. Substituting i_b from Eq. (4) into Eq. (8), we get

$$V_{out} = -\frac{1}{C_{feedback}} \int i_z\, dt = -\frac{1}{C_{feedback}} \cdot \frac{L}{\beta c} \cdot i_b \qquad (10)$$

i.e. using a charge amplifier the total capacitance, C in Eq. (9), reduces to $C_{feedback}$ = 1 pF. The capacitance, C_{PU}, for an ELENA orbit PU is ~25 pF. If one assumes 5 pF on the amplifier input, then C would be ~30 pF. The use of charge amplifiers can therefore increase the sensitivity by ~30 dB. For 10^7 charges V_{out} is ~6 mV with the charge amplifier, as opposed to ~210 μV if a voltage amplifier was used.

Integrating the Signal from a PU

As previously stated, for a system where all relevant beam harmonics are within the passband and only the DC part is filtered out, the bunch shape is conserved. With the bunch shape conserved, the intensity can be obtained for a single passage of the beam, using Eq. (9). The area to be found by integration is marked as A1 in Fig. 4. The baseline is the voltage drop marked as $V_{baseline}$ in Fig. 4. If the measurement system has a DC offset, this can be accounted for by measuring the baseline with no beam.

For a circulating beam, after the droop time has passed, no DC is left and the base line is flat (assuming only small and/or slow beam losses when compared to the revolution period). With reference to Fig. 4, this means that the area A2 + A3 = A4. What is needed is A1, which is equal to A4 + A5 so, substituting A4 by A2 + A3, we can see that A1 = A2 + A3 + A5 = A6:

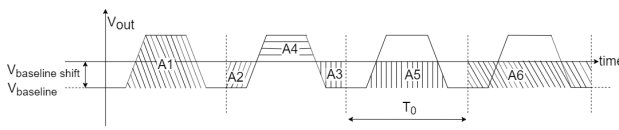


Figure 4: Circulating bunched beam example.

The integral of the output voltage can thus be found as the baseline shift multiplied by the revolution period to give

$$\int V_{out} dt = V_{baseline} \cdot \frac{L_{ELENA}}{\beta c} \qquad (11)$$

where L_{ELENA} is the circumference of the machine. By using this baseline shift to calculate the integral of V_{out} in Eq. (9) the beam intensity, Q_{beam} can be found:

$$Q_{beam} = C \cdot \frac{\beta c}{L} \int V_{out} dt = \\ = C_{feedback} \cdot V_{baseline} \cdot \frac{L_{ELENA}}{L} \qquad (12)$$

Equation (12) shows that the intensity measurement conveniently becomes independent of the beam energy and only depends on known constants.

Content from this work may be used under the terms of the CC BY 4.0 licence (© 2022). Any distribution of this work must maintain attribution to the author(s), title of the work, publisher, and DOI

ISBN: 978-3-95450-241-7 ISSN: 2673-5350 doi:10.18429/JACoW-IBIC2022-TUP30

Content from this work may be used under the terms of the CC BY 4.0 licence (© 2022). Any distribution of this work must maintain attribution to the author(s), title of the work, publisher, and DOI

Finding the Base Line

In the ELENA system, the baseline shift is found in software after signal digitalisation. Both the baseline without beam and the baseline with beam, i.e. the baseline shift, can be derived by taking the average of all time samples within a percentile interval. This percentile interval should ideally be set so that only the digitised samples with a signal level corresponding to the baseline (i.e. approximately around -1000 as can be seen in the left plot of Fig. 5) is included in the averaging. The settings for the percentile interval are empirically tuned and may depend on the bunch shape. A measurement of the PU sum signal and its cumulative distribution is shown in Fig. 5. Typically, only the data samples over the 1% percentile and below the 25 to 50% percentiles are taken and averaged to find the baseline.

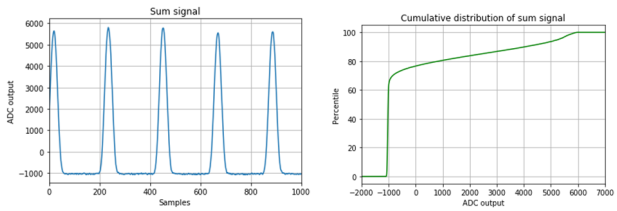


Figure 5: Left the time sampled sum signal. Right the corresponding cumulative distribution.

The typically used sampling rate of the system is set to 125MSPS. The sum signal, shown in Fig. 5, was obtained with a beam of approximately $3 \cdot 10^7$ anti-protons decelerated to 100 keV (kinetic energy). The revolution frequency at this final stage of the ELENA cycle is of 144 kHz and the beam was bunched at RF harmonic 4 in this 30.4 m long ring.

Absolute Calibration

The accuracy of the beam intensity calculated using Eq. (12) will depend on how accurately $C_{feedback}$ and $V_{baseline}$ are known, assuming we know L and L_{ELENA} with infinite precision. As the baseline shift is measured using an ADC, it is required to know the voltage gain in between the charge amplifier output and the ADC input, as well as the voltage to bit conversion factor of the ADC. The amplifier gain and ADC parameters are straightforward to know and can be measured to sufficient precision using a standard network analyser. In the case of ELENA, the feedback capacitor, $C_{feedback}$ in Eq. (12), is a high precision capacitor, mounted inside the charge amplifier. The value of this capacitor was estimated by applying a calibration signal (V_{cal} in Fig. 3) via another high precision capacitor, $C_{calibration}$ = 1 pF. In this configuration, the circuit can be seen as a standard inverting operational amplifier with a gain, A_v given by

$$A_v = -\frac{Z_{feedback}}{Z_{source}} = -\frac{\frac{1}{j\omega C_{feedback}}}{\frac{1}{j\omega C_{calibration}}} = -\frac{C_{calibration}}{C_{feedback}} \quad (13)$$

Since both the source impedance, $C_{calibration}$ and $C_{feedback}$, suffer from stray capacity, this limits the precision of this measurement. The measurement precision of $C_{feedback}$ is currently deemed to be the dominant error source in the system. At present, there are no alternative instruments capable of measuring the absolute beam intensity in the ELENA ring, thus making it impossible to perform a cross-calibration.

BEAM POSITION SENSITIVITY

To evaluate the intensity measurements sensitivity to beam position, simulations have been performed in CST Studio Suite [5]. Two models have been evaluated: Model 1: One metal cylinder 1 mm thick, 120 mm long, 66 mm diameter inside an 80 mm diameter metal beam pipe. Model 2: (see Fig. 6) as model 1, but with a 2 mm linear cut in the ring to make it position sensitive. The model 2 is similar to the actual orbit PUs in ELENA [6, page 4].

Simulations have been performed at beam speeds corresponding to β = 1 and β = 0.6, and with 10^7 charges in an approximately 5 m long (measured at 50% of the maximum amplitude) Gaussian bunch. The output is monitored using the voltage probes (the small grey arrows) shown at the top and bottom of Fig. 6.

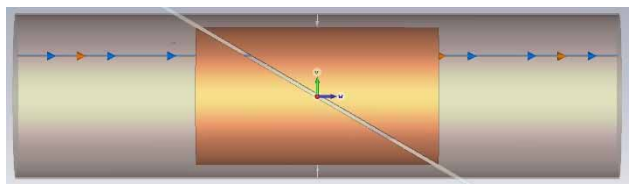


Figure 6: The 3D model of ELENA PU.

Circular PU

For model 1 the beam position is simulated at the PU centre, and moved transversally in 5 mm steps, to 25 mm off centre. The integral over time of the output voltage for each beam offset position and β value is also calculated in the simulation. A negligible (< 0.1%) change in the integrated output voltage is observed with respect to changes in the beam position. The ratio between the time integrated output voltage for the different β values is the ratio of β values themselves, as expected from Eq. (9).

Sweeping the number of charges or sweeping the bunch length reveals no non-linearities. These simulations do not include the front-end electronics.

Linear Cut Circular PU

For model 2 the beam position is simulated at the PU centre, in one case with a 20 mm offset in the horizontal plane, with the same offset in the vertical plane and finally with the same offset simultaneously in both planes. In Fig. 7 the blue curves correspond to centred beams and to vertical offset beams for both β = 1 (leftmost set of curves) and β = 0.6 (rightmost set of curves). The red curves correspond to the output signal from the PU plate towards which the beam is offset and the green curves correspond to the opposite PU plate for both β = 1 and β = 0.6. For a centred beam, and as expected, the integrated output voltage is unchanged when the beam is moved in the vertical plane. A difference in the two signals is seen when the beam is moved in the horizontal plane, as expected for a horizontal PU. When moved in the horizontal plane, the sum of the

ISBN: 978-3-95450-241-7 ISSN: 2673-5350 doi:10.18429/JACoW-IBIC2022-TUP30

integrals of the output voltages of each plate is the same as the sum of integrals of the same plates when the beam is centred, as one would expect. The ratios for the sum of the integrated output signals for the two different energies is, as expected from Eq. (9), β. This means that the increased bending of the field lines in the case of low beta does not affect the measured output or its integral.

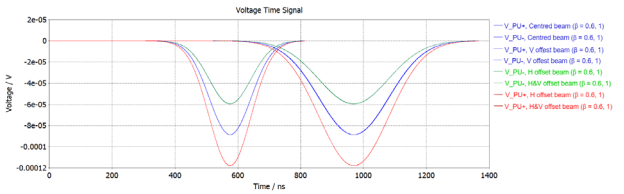


Figure 7: Beam position and β sweep for linear cut PU.

MEASUREMENTS

This system, installed in ELENA, uses Eq. (12) to provide an intensity measurement, every 1 ms, during the ELENA deceleration cycle. A typical output is shown in Fig. 8 where injection occurs at approximately 2.8 s, when the beam coming from the CERN Antiproton Decelerator (AD) is injected. Due to the high pass characteristic of the system, this approach is only valid while the beam is bunched. Therefore, the "zero-intensity" intervals which appear between 4.5 s to 6.8 s and 8.8 s to 11 s occur exactly when the beam is de-bunched and cooled.

Also due to the high pass characteristic of the PU together with the charge amplifier, the droop time is, in the current setup, of the order of a few hundreds of µs, i.e. less than one measurement period.

An overshoot consisting of the first two points of the measurement at injection is observed. This overshoot, which normally would indicate beam loss at injection is *not* believed to be real by the ELENA operators. Further studies are required to understand whether it is indeed so.

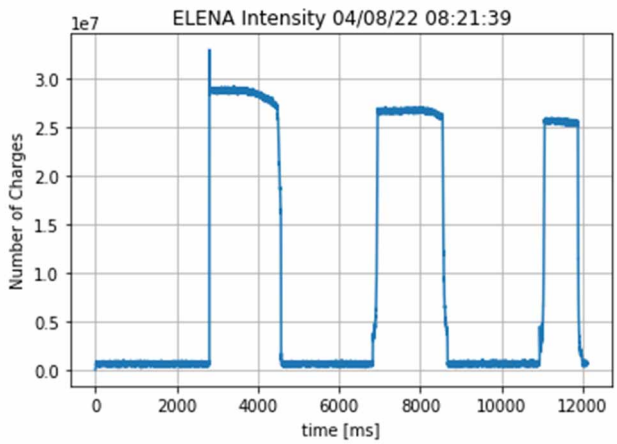


Figure 8: The Intensity as measured in the bunched periods of the ELENA deceleration cycle.

The number of charges was compared to that of the Cryogenic Current Comparator (CCC) [3], installed in the AD ring. Not considering the overshoot at injection, the proposed method measures approximately 85% of the intensity measured by the CCC.

CONCLUSIONS

A system capable of measuring low intensity (few 10^7 charges) antiproton beams, when bunched during the CERN ELENA deceleration cycle, was presented. The system is based on the sum signal from a circular linearly cut electrostatic PU also used by the ELENA orbit system. It has been shown that the baseline shift, caused by the high pass transfer function of the PU can be used to measure the absolute intensity, provided that the system bandwidth covers all relevant harmonics of the bunched beam spectrum. The baseline shift method does not seem to be affected by relativistic effects, as indicated by the CST simulations (only $\beta = 1$ and $\beta = 0.6$ evaluated). When compared to voltage amplifiers, the use of charge amplifiers as the first amplifier in the chain gives an advantage in terms of sensitivity, though stray capacitance sets a limit to the absolute accuracy of the intensity measurement if the feedback capacitor is taken to very low values. In this system the feedback capacitor is approximately 1 pF and the estimated sensitivity gain 30 dB.

It has been shown, via simulations, that the position sensitivity of the sum signal is negligible, making an electrostatic PU an interesting intensity sensor.

Measurements from the ELENA system were presented. Since no alternative reliable intensity measurement exists in ELENA, it is challenging to validate the accuracy of this measurement. By design, the absolute accuracy of the system is currently limited by the accuracy of the knowledge of the feedback capacitor capacitance, including its stray capacitance once mounted and used in the charge amplifier configuration. At present, this system provides successfully relative intensity measurements during the ELENA cycle. Further studies will be continued with the goal of providing more accurate absolute intensity measurements.

REFERENCES

[1] O. Marqversen *et al.*, "The orbit measuring system for the CERN extra low energy anti-proton ring", in *Proc. IBIC'17*, Grand Rapids, MI, USA, Aug. 2017, pp. 206-208. doi:10.18429/JACoW-IBIC2017-TUPCF05

[2] Spectrum Instrumentation, https://spectrum-instrumentation.com/products/families/44xx_index.php

[3] G. Gelato, "Beam current and charge measurements", in *Beam instrumentation*, ed. J. Bosser, CERN, Geneve, Switzerland, Rep. CERN–PE–ED 001–92, p. 185, Nov. 1994.

[4] R. Marco-Hernández *et al.*, "A Low-Noise Charge Amplifier for the ELENA Trajectory, Orbit, and Intensity Measurement System", *IEEE Trans. Nucl. Sci.*, vol. 64, pp. 2465-2473, Sep. 2017. doi:10.1109/TNS.2017.2740238

[5] CST Studio Suite, https://www.3ds.com/products-services/simulia/products/cst-studio-suite/

[6] R. Marco-Hernández *et al.*, "AD and ELENA orbit, trajectory and intensity measurement system", *J. Instrum.*, vol. 12, p. P07024, 2017. doi:10.1088/1748-0221/12/07/p07024

Content from this work may be used under the terms of the CC BY 4.0 licence (© 2022). Any distribution of this work must maintain attribution to the author(s), title of the work, publisher, and DOI

ISBN: 978-3-95450-241-7 ISSN: 2673-5350 doi:10.18429/JACoW-IBIC2022-TUP31

THE CRYOGENIC CURRENT COMPARATOR AT CRYRING@ESR*

L. Crescimbeni†, D. M. Haider†, A. Reiter, M. Schwickert, T. Sieber
GSI Helmholtz Centre for Heavy Ion Research, Darmstadt, Germany
H. De Gersem, N. Marsic, W. F. O. Mueller, TU Darmstadt, Darmstadt, Germany
M. Schmelz, R. Stolz, V. Zakosarenko[3], Leibniz IPHT, Jena, Germany
F. Schmidl, Friedrich-Schiller-University Jena, Jena, Germany
T. Stoehlker[1,2], V. Tympel, Helmholtz Institute Jena, Jena, Germany
[1]also at GSI Helmholtz Centre for Heavy Ion Research, Darmstadt, Germany
[2]also at Institute for Optics and Quantum Electronics, Jena, Germany
[3]also at Supracon AG, Jena, Germany

Abstract

The Cryogenic Current Comparator (CCC) at the heavy-ion storage ring CRYRING@ESR at GSI provides a calibrated non-destructive measurement of beam current with a resolution of 10 nA or better. With traditional diagnostics in storage rings or transfer lines a non-interceptive absolute intensity measurement of weak ion beams (< 1 µA) is already challenging for bunched beams and virtually impossible for coasting beams. Therefore, at these currents the CCC is the only diagnostics instrumentation that gives reliable values for the beam intensity independently of the measured ion species and without the need for tedious calibration procedures. Herein, after a brief review of the diagnostic setup, an overview of the CCC operation with different stored ion beams at CRYRING is presented. The current reading of the CCC is compared to the intensity signal of various standard instrumentations including a Parametric Current Transformer (PCT), an Ionization Profile Monitor (IPM) and the Beam Position Monitors (BPMs). It could be shown that the CCC is a reliable instrument to monitor changes of the beam current in the range of nA.

INTRODUCTION

The non-destructive and absolute monitoring of ion beams with an intensity in the order of nA plays an essential role in accelerator facilities that produce slowly extracted ions for nuclear physics research or rare isotopes and antiprotons in storage rings. In general, for coasting beams standard diagnostic systems are not able to provide measurements in the range of nA without major efforts. Even then, the instruments that can provide some information in this range have problems to deliver the high precision and reliability that is required (e.g. Schottky [1]), or are destructive, at least partially, reducing severely the possibility of using them as monitoring devices in storage rings (e.g. Faraday Cups and Secondary Electron Monitors) or are limited to bunched beams (BPM, Integrating Current Transformer).

The Cryogenic Current Comparator (Fig.1) is a superconductive device that can measure currents in the order of nA detecting the magnetic field of the beam itself. The CCC uses a DC Superconducting Quantum Interference Device (SQUID) as a highly sensitive magnetometer, shielded from external magnetic fields thanks to an elaborate superconductive magnetic shielding, to provide absolute high-precision measurement of low-intensity currents while being non-destructive and easy to calibrate.

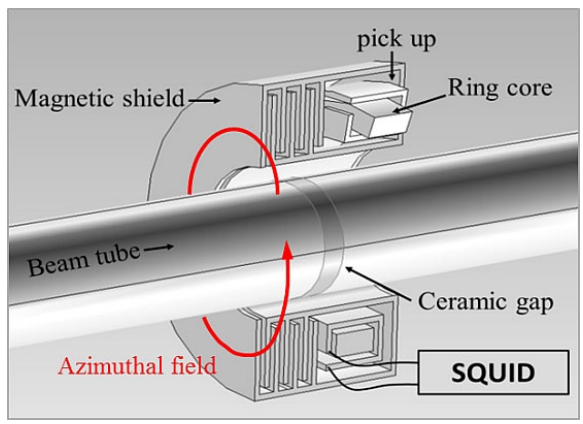


Figure 1: Schematic view of the CCC.

Five CCCs are planned to be installed in the FAIR facility and, in preparation, a prototype was installed in the heavy-ion storage ring CRYRING@ESR at GSI to be tested with beam. The prototype is based on the FAIR-Nb-CCC-XD [2] that is part of the family of CCC-XD that has been developed for the use with large beam-lines diameters (e.g. at Antiproton Decelerator at CERN [3]) and that was adapted to the beamline dimensions at FAIR (Ø 150 mm). At CRYRING, the CCC was operated with several different ion species (D^+, O^{6+}, Nb^{2+}, Pb^{78+}, U^{91+}) and various beam conditions (e.g. coasting/bunched) with beam intensities between 5 nA and 20 µA to demonstrate the detector performance that can be expected for FAIR.

COMMISSIONING IN CRYRING

The CCC detector is allocated in a newly manufactured beamline cryostat developed in collaboration with ILK Dresden§ to fulfil the needs of the installation at FAIR [4]. The SQUID sensor of the CCC is a highly sensitive magnetometer and is susceptible to external perturbations.

*Work supported by AVA – Accelerators Validating Antimatter the EU H2020 Marie-Curie Action No. 721559 and by the BMBF under contract No 05P21SJRB1.
†l.crescimbeni@gsi.de, d.haider@gsi.de
§ILK Dresden gGmbH, Dresden, Germany
¶Model PT415 from Cryomech Inc, Syracuse, NY, USA

Content from this work may be used under the terms of the CC BY 4.0 licence (© 2022). Any distribution of this work must maintain attribution to the author(s), title of the work, publisher, and DOI

ISBN: 978-3-95450-241-7 ISSN: 2673-5350 doi:10.18429/JACoW-IBIC2022-TUP31

Therefore, the cryostat provides a very stable operating pressure and temperature, necessary to ensure the stable operation of the detector. The system is equipped with a local helium liquefier[¶] which at CRYRING allowed a continuous operating time of 7 days which will be expanded in the future to complete stand alone operation [5].

Moreover, it is necessary to have a mechanical isolation from the accelerator environment to suppress mechanical perturbations, which is achieved using a support system composed of stainless steel filled with sand and equipped with a dedicated dampening mat. The beamline and the liquefier are connected with mechanical bellows, and the vacuum pumps are equipped with damping elements.

After the installation at the beamline, the detector was calibrated with a reference current that simulates the beam. The calibration line is composed of a wire parallel to the beamline that passes through the CCC and is connected to a function generator. This setup allows the in-situ calibration of the CCC with waveforms of chosen shape, intensity and frequency. The calibration showed that the CCC is able to measure currents below 10 nA limited by the fluctuation of the baseline on the scale of several nA. Larger baseline fluctuations were mainly due to two noise sources, the stray field of the ramp of nearby dipole magnets and the vibration of the CCCs own helium liquefier. Using data collected in several "dry runs" it was possible to identify the noise and to develop a correction for these baseline drifts. This is possible because the dipole ramp is strongly deterministic, and the liquefier noise is periodic with a period of 1.4 Hz. This leads to a noise-limited current resolution in the accelerator environment that is not far from the value that was achieved in the laboratory [2].

CRYRING MEASUREMENT

Following the commissioning reported in detail last year [5], the accuracy of the CCC was tested with beam at CRYRING. Figure 2 shows the beam intensity of a bunched deuterium beam throughout the accelerator cycle. Shown in light green is the data collected by the CCC, after applying the liquefier and the dipole ramp correction. Even if the phases of the machine cycle (injection, acceleration, flattop) are clearly visible, the signal is affected by noise. A large part of the noise originates in the bunch structure of the beam, which at the low injection energy of 300 keV/u can partly be resolved by the CCC. The remaining noise contribution is due to the intrinsic noise of the magnetic core and due to external perturbations. For DC beam current measurements both can be strongly attenuated with an analogue low-pass filter (e.g., at 20 Hz) or by performing a digital averaging of the data (Fig. 2, dark green). A noise-limited current resolution of better than 10 nA_{rms} at the full detector bandwidth of roughly 200 kHz could be shown.

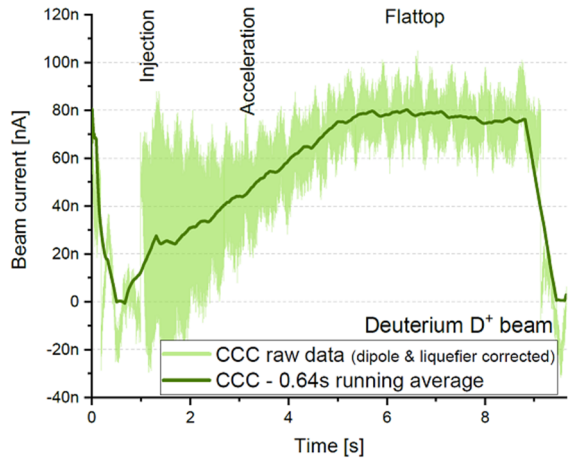


Figure 2: CCC measurement of a low-current bunched beam of deuterium D^+ (5 MeV/u at flattop). Dipole ramp and liquefier noise corrected (light green) with a bandwidth of about 200 kHz [2] and smoothed with a running average (dark green).

Coasting Beam

After this first demonstration of the performance, we proceeded with the comparison of the CCC with existing instrumentations in the CRYRING. The first one shown here is the confrontation with a Parametric Current Transformer (PCT) and with an Ionization Profile Monitor (IPM) for the measurement of unbunched beam. Figure 3 shows the exponential loss of beam current for a coasting $^{238}U^{91+}$ beam with a peak beam intensity of around 18 µA (identical results obtained for $^{208}Pb^{78+}$ beam). Due to the large noise associated with the signal of the PCT and of the IPM, both were smoothed with a running average to allow a sensible comparison. The count rate of the IPM (order of 60kHz) was converted to an absolute current with a linear calibration factor that was determined using the calibrated CCC signal. The 3dB-bandwidth of the CCC was restricted to 11.3 kHz (required due to "high intensity" operation") but no signal correction (dipole or liquefier) was applied.

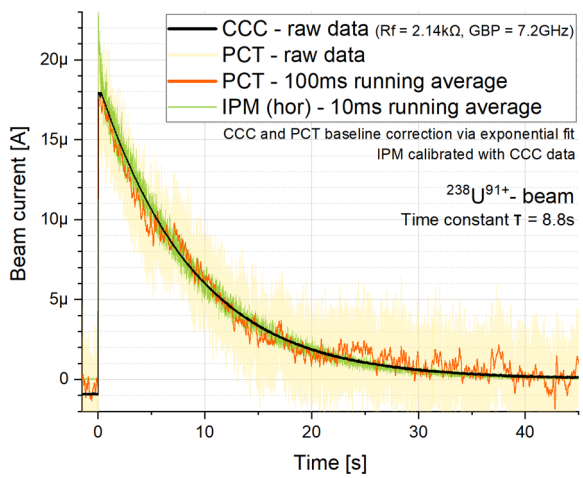


Figure 3: Coasting beam current measurement of a $^{238}U^{91+}$ beam performed with CCC (black), with PCT (orange) and IPM (green). The CCC provides a superior current resolution.

Content from this work may be used under the terms of the CC BY 4.0 licence (© 2022). Any distribution of this work must maintain attribution to the author(s), title of the work, publisher, and DOI

ISBN: 978-3-95450-241-7 ISSN: 2673-5350 doi:10.18429/JACoW-IBIC2022-TUP31

Content from this work may be used under the terms of the CC BY 4.0 licence (© 2022). Any distribution of this work must maintain attribution to the author(s), title of the work, publisher, and DOI

Figure 3 shows that the current measurement performed by the CCC was affected by substantially less noise and subsequently could provide a significantly better current resolution, even at beam intensities that are rather large for the CCC. For the PCT a current noise of 1.9 μA_{rms} with a bandwidth of 100 Hz was determined while the IPM showed a noise of around one μA_{rms}. For the direct comparison, Table 1 gives a list of the noise-limited current resolution of the intensity diagnostics at CRYRING.

In addition, we must consider the limitations of the PCT and of the IPM. First of all, the PCT – even with averaging multiple accelerator cycles – it not suited for intensities smaller than about 5 µA which means there is no possibility to obtain a calibrated measurement with weaker intensities. The IPM can detect much lower currents, however, it has two main problems. First, the measure is not calibrated and strongly depends on the measurement parameter. The calibration of the IPM can be performed only by referring to another device able to measure the beam current, in the data acquisition at CRYRING the CCC has been used as calibration device. Second, at low beam energies it can significantly affect the beam. For low-energy beam the electromagnetic field used to collect the secondary ions act as a disturbance on the beam, making the IPM a destructive device, even if not completely.

Bunched Beam

Excellent specialized diagnostics already exists for low intensity bunched beams. The second comparison was performed with the intensity signal obtained from the sum signal of a Beam Position Monitor (BPM) and with the calibrated signal of an Integrating Current Transformer (ICT), using bunched $^{2}D^{+}$ and $^{16}O^{6+}$ beam. At CRYRING the optimal current noise of the ICT is 1 nA_{rms} or larger at a bandwidth of 20 Hz [6] which is comparable to the CCC. The noise level of the BPM can be as low as 100 pA_{rms} (@ 20 Hz) which exceeds today's measurement capacity of the CCC (see Tab. 1). However, the BPM signal needs to be calibrated to obtain a current measurement and both the ICT and BPM are restricted to bunched beams which makes the CCC a much more versatile device.

Table 1: Comparison of Intensity Diagnostics at CRYRING

Instrument	Current noise (bandwidth)	Comments
CCC	< 10 nA_{rms} (200 kHz)	Calibrated
PCT	~ 1.9 μA_{rms} (100 Hz)	Calibrated
IPM	~ 1 μA_{rms} (parameter dep.)	Uncalibrated
ICT	≥ 1 nA_{rms} (20 Hz) [6s]	Calibrated, bunched beam
BPM	~ 100 pA_{rms} (20 Hz) [6]	Uncalibrated, bunched beam

LIMITATIONS

The CCC primarily is a diagnostic to monitor small, gradual changes of the beam intensity of (coasting) beams with high precision. When intensities are larger, the associated slew rates during the injection of the bunched beam can easily exceed the slew rate limit of the detector of approximately 0.16 µA/µs (with f ≤ 200 kHz) [2]. Excessive slew rates lead to local artefacts or to a measurement offset. The slew rate limit at higher frequencies depends on the corresponding pick-up sensitivity of the CCC, which significantly drops beyond 200 kHz.

Figure 4 shows the beam current of a deuterium D^{+} beam measured by the CCC and by the PCT, which was used as a reference signal. The signal of the CCC is distorted during most of the accelerator ramp due to a slew rate of the bunched beam that exceeds the limitation of the detector. Once the revolution frequency is larger than the sensitive bandwidth of the CCC of 200 kHz, the signal can be tracked accurately and can be used to obtain the absolute beam current. Any offset of the CCC measurement as a result of the exceeding slew rate can be corrected using the zero-current baseline of the empty accelerator after the beam dump. Effectively, only the information about the beam intensity during the time in which the slew rate was exceeded is lost.

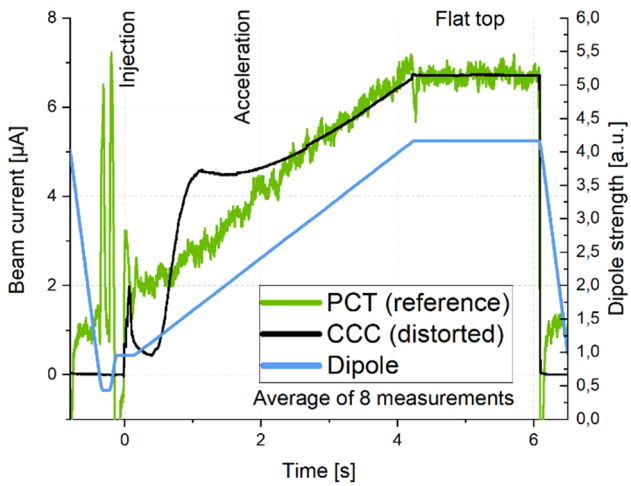


Figure 4: Averaged current measurement of a bunched beam of deuterium D^{+} (5 MeV/u with revolution frequency of 572 kHz at flattop) with the PCT (green) and with the CCC (bandwidth of 200 kHz). The dipole ramp is shown in blue.

In order to increase the slew rate limit of the CCC the sensitive bandwidth of the pick-up can be reduced. Following the first measurements with beam, a low-pass filter with a 3dB-bandwidth of 11.3 kHz was installed to the pick-up of the CCC to reduce the sensitivity at the typical operating frequencies at CRYRING (≥ 130 kHz). In principle, arbitrary signal filters can be installed to adapt the CCC to the required slew rates. However, each resistance adds a thermal noise to the system that can significantly deteriorate the current resolution of the CCC. Therefore, a balance between the required low-current resolution and

ISBN: 978-3-95450-241-7 ISSN: 2673-5350 doi:10.18429/JACoW-IBIC2022-TUP31

the maximum slew rate must be found depending on the operating scenario. An improvement of the maximum slew rate of the CCC detector itself based on two parallel, specialized SQUIDs is currently under investigation.

CONCLUSIONS

The results of the test of the FAIR CCC prototype at CRYRING is highly satisfactory. The cryostat works as expected, providing a reliable shield for external disturbances (magnetic and mechanical ones) and a stable temperature and pressure environment for the CCC. This allowed us to perform the measurement in the noisy accelerator environment maintaining a resolution almost comparable with the one achieved in the laboratory (better than 10 nA).

The comparison of the measurement collected by the CCC with the ones obtained with standard instrumentation is highly promising. Even if our CCC is still a prototype it showed a better resolution than all the standard detectors used for monitoring coasting beams in CRYRING allowing access to high-precision measurement of beam current also for coasting beams that are often requested by experiments. At the same time, the CCC provides a fast, non-destructive measurement of low-intensity beam currents.

As expected, the measurement performed with the CCC is independent from the ion species. The test performed with a full spectrum of ion species and beam conditions has shown accurate measurement results and better resolution than the one achieved with the standard instrumentation.

FUTURE PLANS

The prototype of the CCC has still an improvement margin. The future plans regarding the development of the new CCC have two main directions that we will discuss briefly: the first is the optimization of the cryogenic support system and the second is the development of a new CCC for better performance of the detector itself.

For the optimization of the cryogenic support system the focus is on the resolution of the problems regarding the limited operation time, which is in contradiction with to the requirement of a stand alone system. With the development of a new thermal shield with improved enthalpy cooling on the helium exhaust line it's possible to maximize the liquefier efficiency. Moreover, an active pressure control system is under development, this system will allow us to keep the pressure at the required value for maximum liquefier performance. Moreover, we are working on reducing the heat load inside the cryostat, thanks to additional placement of Multi-Layer Insulation (MLI) and minimization of the possible heat input sources.

Furthermore, we are working on the development of a new CCC made from lead, coreless and with an axial shield geometry. This new model is expected to be less sensitive to external perturbations, in particular low-frequency ones, caused by magnetic field caught inside the core material [7] (for CCC version with core) and by mechanical disturbances, allowing an increase of the resolution of the detector itself. Moreover, it will also allow us to increase the slew rate limit, thanks to the implementation of two parallel SQUID systems. This allows us to track faster slew rates and therefore to increase the dynamic range of the CCC. Our desired value should be 10 times higher, to cover the full intensity range at all locations of GSI and FAIR. The slew rate limitations that have been found during our measurement in CRYRING will be checked in a new measurement campaign with the coreless lead axial CCC.

REFERENCES

[1] M.E. Angoletta *et al.*, "Schottky Based Intensity Measurements and Errors Due to Statistical Fluctuations", in *Proc. 8th Int. Particle Accelerator Conf. (IPAC'17)*, Copenhagen, Denmark, p. 385-388, Sep. 2017. doi:10.18429/JACOW-IPAC2017-MOPAB112

[2] P. Seidel *et al.*, "Cryogenic current comparators for larger beamlines", *IEEE Trans. Appl. Supercond.*, vol. 28, no. 4, pp. 1601205, Jun. 2018. doi:10.1109/TASC.2018.2815647

[3] M. Fernandes *et al.*, "Non-perturbative measurement of low-intensity charged particle beams", *Supercond. Sci. Technol.*, vol. 30, pp. 015001, Nov 2016. doi:10.1088/0953-2048/30/1/015001

[4] D.M. Haider *et al.*, "Versatile beamline cryostat for the Cryogenic Current Comparator (CCC) for FAIR", *in Proc. 8th Int. Beam Instrum. Conf. (IBIC'19)*, Malmö, Sweden, p. 78-81, Sep. 2019. doi:10.18429/JACoW-IBIC2019-MOPP007

[5] D.M. Haider *et al.*, "Commissioning of the Cryogenic Current Comparator (CCC) at CRYRING", *in Proc. 10th Int. Beam Instrum. Conf. (IBIC'21)*, Pohang, Rep. of Korea, p. 349-352, Sep. 2021. doi:10.18429/JACoW-IBIC2021-WEOB02

[6] A. Paal *et al.*, "Bunched Beam Current Measurements with 100 pA RMS resolution at CRYRING", *in Proc.10th European Part. Acc. Conf. (EPAC'06)*, Edinburgh, UK, Jun. 2006, paper TUPCH080, p. 1196.

[7] V. Zakosarenko *et al.*, "Coreless SQUID-based cryogenic current comparator for non-destructive intensity diagnostics of charged particle beams", *Supercond. Sci. Technol.*, vol. 32, Dec. 2018, pp. 014002. doi:10.1088/1361-6668/aaf206

Content from this work may be used under the terms of the CC BY 4.0 licence (© 2022). Any distribution of this work must maintain attribution to the author(s), title of the work, publisher, and DOI

ISBN: 978-3-95450-241-7 ISSN: 2673-5350 doi:10.18429/JACoW-IBIC2022-TUP32

DIFFERENTIAL CURRENT TRANSFORMER FOR BEAM CHARGE MONITORING IN NOISY ENVIRONMENTS

H. Maesaka†, [1], T. Inagaki[1], RIKEN SPring-8 Center, Sayo, Hyogo, Japan
K. Yanagida, H. Dewa, JASRI, Sayo, Hyogo, Japan
K. Ueshima, QST, Sendai, Miyagi, Japan
[1]also at JASRI, Sayo, Hyogo, Japan

Abstract

We designed and produced a new differential current transformer (CT) for electron beam current and charge measurement in noisy environments, such as near a high-power pulse generator. This differential CT has four pickup wires coiled at equal intervals (90 degrees) on a toroidal core. Each coil has two turns and the midpoint of the coil is connected to the body ground so that a balanced differential signal is generated. A beam pipe with a ceramics insulation gap is inserted into the toroidal core to obtain a signal from a charged-particle beam. The four balanced differential signals are transmitted through a Category-6 twisted pair cable and fed into an amplifier unit. The four signals are then summed by the amplifier and digitized by an MTCA.4 high-speed AD converter. We produced differential CTs and installed them into the new injector linac of NewSUBARU. Before the installation, we confirmed basic performances such as the beam current sensitivity of 1.24 V/A, wide frequency response of up to 100 MHz, etc. The beam test was performed at the new linac of NewSUBARU and beam charge measurement performance, common-mode noise cancellation, etc. were evaluated. The differential CTs have been utilized for stable beam charge monitoring in the NewSUBARU linac.

INTRODUCTION

Reliable monitoring of the charge and current of a particle beam is important for most particle accelerators. A current transformer (CT) is often used as a non-invasive beam charge and current monitor. The signal output of a CT is usually designed as a single-ended coaxial line. If a single-ended CT is located near a pulsed high-power component, a common-mode noise can be overlapped with a beam signal and the noise can deteriorate the measurement accuracy.

To mitigate the noise from the high-power component, a differential CT was proposed and utilized in the X-ray free-electron laser, SACLA [1, 2]. This differential CT has four single-turn coils around a toroidal magnetic core, where two coils generate positive signals and the other two generate negative signals. A common-mode noise can be canceled out by subtracting the positive and negative signals. Since each signal output is a single-ended coaxial line, however, a preamplifier or a balun near the differential CT is required to transform two differential single-ended signals into a balanced differential line for long signal transmission.

A new 3 GeV light source project, NanoTerasu [3, 4], was proposed and it is now being constructed in Sendai, Japan. Before the construction of NanoTerasu, a new injector linac for the NewSUBARU storage ring [5] was constructed as a prototype of the NanoTerasu linac [6]. One of the most important design concepts of these accelerators was low-cost and easy maintainability. A differential CT should also be low-cost and the number of components in the system should be as small as possible. Therefore, we designed a new differential CT that did not need a preamplifier near the CT.

DESIGN

A new differential CT aims to extract a balanced differential signal directly from a coil. Therefore, we designed a CT having two-turn pickup coils wound on a toroidal magnetic core and the midpoint of each coil is grounded. A schematic view of the new differential CT is shown in Fig. 1. Four pickup coils are attached to a toroidal core at equal intervals (90 degrees) and a beam pipe with a ceramics gap is inserted into the core. The toroidal core is Finemet FT-3KM F7555G supplied from Hitachi Metals, which has enough permeability as high frequency as 1 GHz. An 11 Ω resistor is attached to each coil in parallel to attenuate a beam signal. The signals from pickup coils are extracted from four LEMO 0S302 series 2-pin connectors. A photograph of the differential CT is shown in Fig. 2. The four balanced differential signals are transmitted to a readout electronics by a Category-6 (CAT6) S/FTP cable for Ethernet, which has good high-speed signal transmission characteristics and a reasonable price.

The beam current sensitivity of each turn of the pickup coil is 0.125 A/A since the number of total turns is 8. The voltage sensitivity of the output to the beam would be 12.5 V/A without any parallel resistors since the characteristic impedance of the balanced differential line is 100 Ω. Since the sensitivity of around 1 V/A is easy to deal with for us, an 11 Ω metal-film resistor (±0.1 % accuracy) is inserted in parallel with the pickup coil to attenuate the signal amplitude. The sensitivity is reduced by a factor of 0.099 and the current and voltage sensitivity are finally decreased to 0.0124 A/A and 1.24 V/A, respectively, which corresponds to –35 dB relative to the beam current.

The readout electronics consists of an amplifier unit and a high-speed digitizer. The block diagram of the amplifier unit is shown in Fig. 3. The S/FTP cable from a differential CT is received by an M12 X-coded connector, which is more reliable than an RJ-45 modular connector. Common-

† maesaka@spring8.or.jp

Content from this work may be used under the terms of the CC BY 4.0 licence (© 2022). Any distribution of this work must maintain attribution to the author(s), title of the work, publisher, and DOI

ISBN: 978-3-95450-241-7 ISSN: 2673-5350 doi:10.18429/JACoW-IBIC2022-TUP32

mode noise in each balanced differential signal is suppressed by a common-mode choke filter and a high-frequency component is blocked by a low-pass filter having a cutoff frequency of 10 MHz. The filtered differential signal is converted to single-ended by a differential amplifier. The four signals are then summed and outputted from SMA connectors. The signal from the amplifier unit is recorded by a high-speed digitizer, such as SIS8325 [7] (250 MSPS, 16 bits).

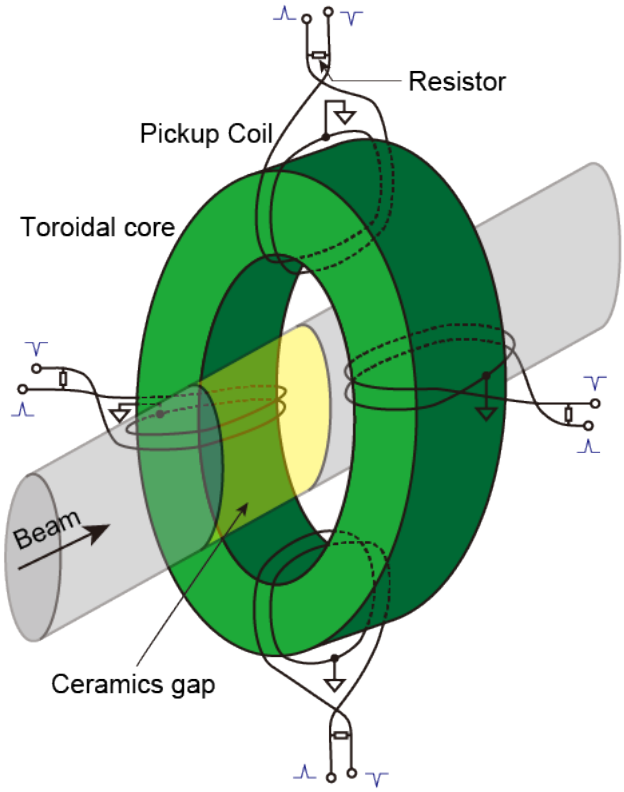


Figure 1: Schematic view of the differential CT.

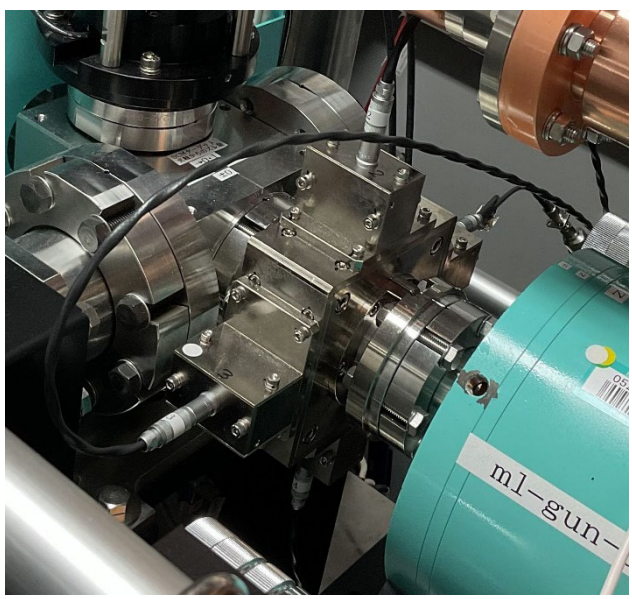


Figure 2: Photograph of a differential CT installed in the new injector linac of NewSUBARU.

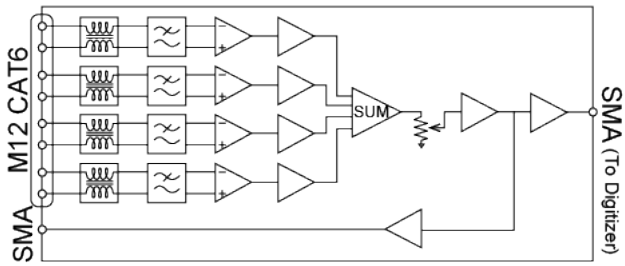


Figure 3: Block diagram of the amplifier unit.

LABORATORY TEST RESULTS

We produced differential CTs for the new linac for NewSUBARU and evaluated electrical response before installation. A schematic view of the response measurement setup is shown in Fig. 4. An electron beam was simulated by a rod in the beam pipe and two taper lines were connected to both ends of the pipe to adapt the 50 Ω coaxial transmission line smoothly.

The frequency response was measured by a 4-port vector network analyzer (VNA). Two ports are connected to both ends of the taper lines and the other two were connected to one of the four differential outputs (one port for the positive pin and the other for the negative). The unused three outputs were terminated by 100 Ω resistors. The frequency response from the beam port to the normal mode of each output is plotted in Fig. 5. The responses of the four outputs were almost flat and identical up to 100 MHz. The insertion loss was –36 dB in the low-frequency region, which was consistent with the design value. The frequency response to the common mode is plotted in Fig. 6. The signal from the beam to the common mode is suppressed by approximately 30 dB compared to the normal mode up to 10 MHz.

The pulse response was also tested by using a fast pulse generator. A rectangular pulse of 5 V height and 1 ns width was applied to the beam port, corresponding to a 100 mA beam current and a 100 pC beam charge. The output waveforms are shown in Fig. 7. The peak voltage is 0.08 V, which is –36 dB of 5 V. The pulse width is 1.4 ns FWHM, which is fast enough for our application.

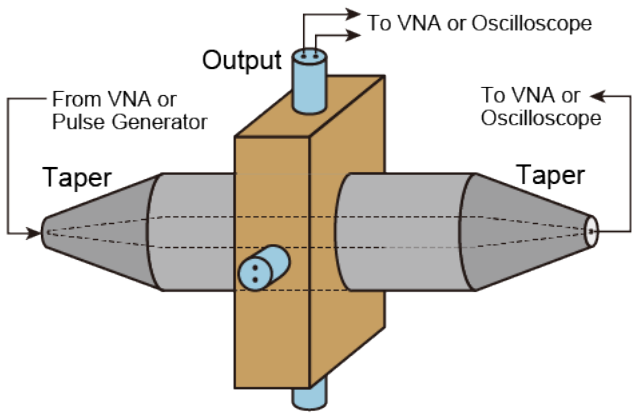


Figure 4: Schematic view of the response measurement setup.

Content from this work may be used under the terms of the CC BY 4.0 licence (© 2022). Any distribution of this work must maintain attribution to the author(s), title of the work, publisher, and DOI

ISBN: 978-3-95450-241-7 ISSN: 2673-5350 doi:10.18429/JACoW-IBIC2022-TUP32

Content from this work may be used under the terms of the CC BY 4.0 licence (© 2022). Any distribution of this work must maintain attribution to the author(s), title of the work, publisher, and DOI

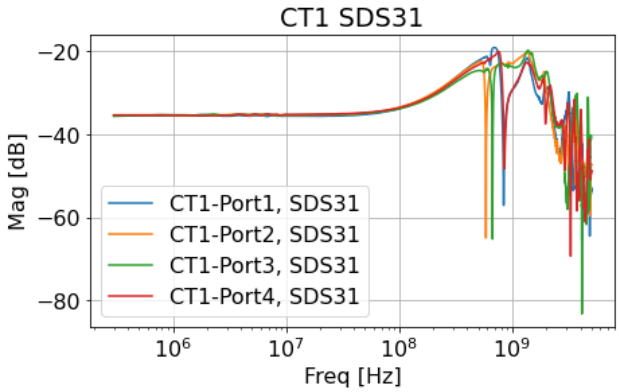


Figure 5: Frequency response of the transmission coefficient from the beam port to the normal mode of each output channel.

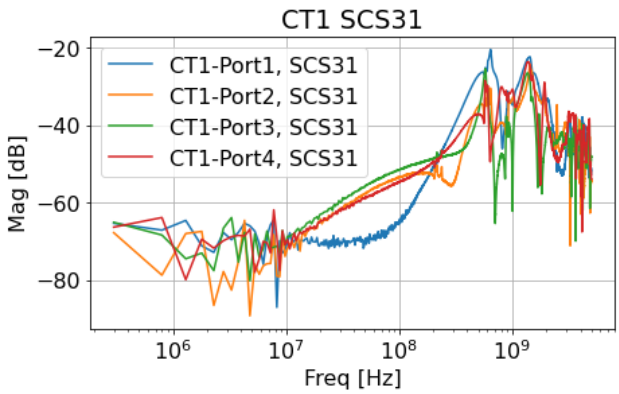


Figure 6: Frequency response from the beam port to the common mode of each output channel.

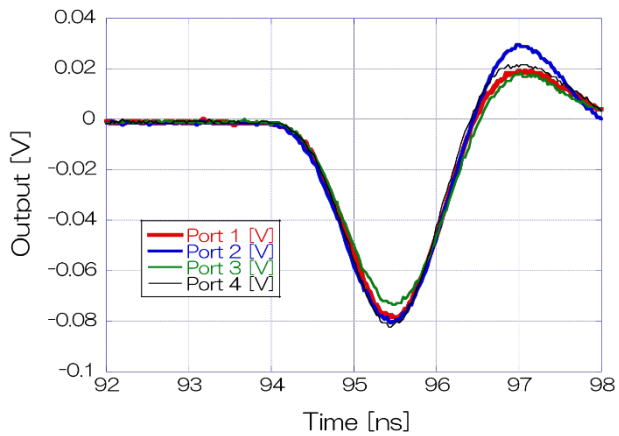


Figure 7: Output waveforms from a rectangular pulse of 5 V height and 1 ns width.

BEAM TEST RESULTS

After the construction of the new linac for NewSUBARU, we tested the differential CT with an actual electron beam. A signal waveform from a differential CT is shown in Fig. 8. The beam charge was approximately 1 nC in this case and the signal was taken by an oscilloscope with a coaxial cable of approximately 20 m-long. A short pulse width of less than 1 ns FWHM was observed, which was fast enough for our application. The pedestal level was not affected by common-mode noise from high-power components near the CT. When a single pin of the CT was observed, the fluctuation of the ground level was significantly larger than the balanced differential signal. Thus, the noise tolerance of the differential CT was confirmed to be sufficient.

Figure 9 shows a waveform taken by a SIS8325 MTCA.4 digitizer after an amplifier unit. The beam charge of this waveform was approximately 0.5 nC. The pulse width was stretched to about 20 ns FWHM by a low-pass filter in the amplifier unit. The peak value is used for calculating the beam charge. The beam charge data have been stably recorded to the database system of NewSUBARU and utilized for the stable operation of the injector linac.

Figure 10 shows a waveform when one wire in the CAT6 differential cable was accidentally disconnected. The ground level is heavily disturbed by common-mode noise from a high-power pulse component. The noise level is comparable to the beam signal and it is difficult to monitor the beam charge precisely. Since the disconnected floating wire can be an antenna to receive the noise, the observed noise is somewhat enhanced. However, a conventional single-ended CT is thought to be affected by this noise to some extent. Thus, the noise suppression capability of the differential CT is important for precise beam charge monitoring in a noisy environment.

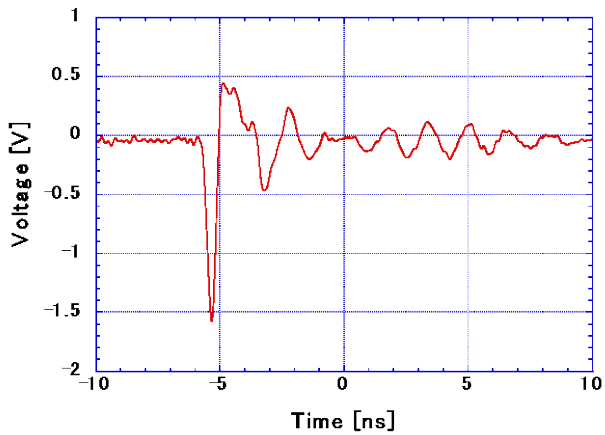


Figure 8: Beam signal waveform of a differential CT.

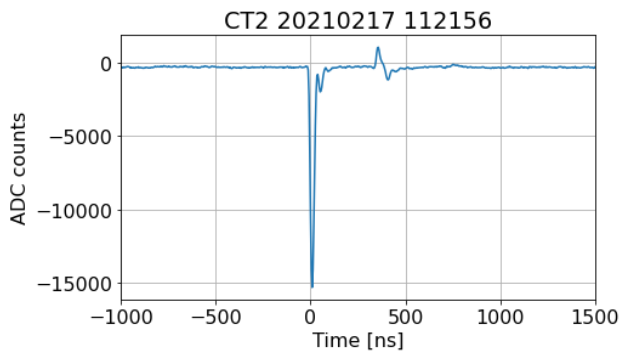


Figure 9: Beam signal waveform taken by an MTCA.4 digitizer. The sampling rate is 238 MHz and the ADC full scale is ±32767.

ISBN: 978-3-95450-241-7 ISSN: 2673-5350 doi:10.18429/JACoW-IBIC2022-TUP32

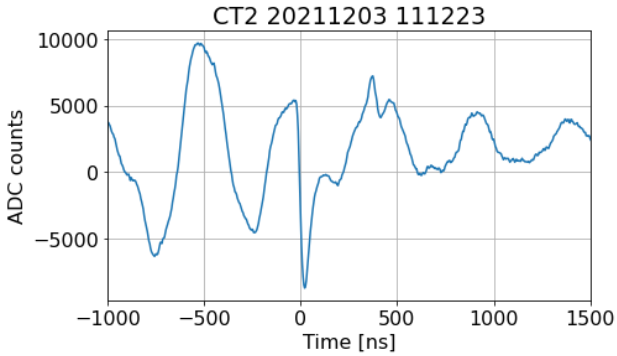


Figure 10: Abnormal waveform when one wire of the CAT6 cable was disconnected.

SUMMARY

We designed a new low-cost differential CT to monitor the current and charge of an electron beam without common-mode noise from high-power components. This differential CT was installed into the new injector linac of NewSUBARU and will be used in the linac of NanoTerasu. This differential CT has a toroidal magnetic core with four two-turn pickup coils and the midpoint of each coil is grounded to generate a balanced differential signal. A readout electronics consisting of an amplifier unit and an MTCA.4 high-speed digitizer was also developed. Electrical characteristics of the differential CT, such as frequency response and pulse response, were evaluated in a laboratory and the results were consistent with the design. The beam current sensitivity was 1.24 V/A and the frequency response was sufficiently flat up to 100 MHz. The differential CT was tested with an actual electron beam during the beam commissioning of the new linac for NewSUBARU. Appropriate waveforms of electron beams were observed as expected and the CT data have been utilized for stable operation of NewSUBARU.

REFERENCES

[1] A. Higashiya, H. Maesaka, and Y. Otake, "Development of a Beam Current Transformer for the X-FEL Project in SPring-8", in *Proc. 29th Int. Free Electron Laser Conf. (FEL'07)*, Novosibirsk, Russia, Aug. 2007, paper WEPPH051, pp. 464-467.

[2] Y. Otake *et al.*, "Beam monitor system for an x-ray free electron laser and compact laser", *Phys. Rev. ST Accel. Beams* vol. 16, p. 042802, Apr. 2013. doi: 10.1103/PhysRevSTAB.16.042802

[3] "Accelerator design report for 3-GeV Next-Generation Synchrotron Radiation Facility", National Institutes for Quantum and Radiological Science and Technology (QST) and Institute for Advanced Synchrotron Light Source, Japan, Sep. 2020. https://www.qst.go.jp/uploaded/attachment/18596.pdf

[4] N. Nishimori, "A New Compact 3 GeV Light Source in Japan", in *Proc. 13th Int. Particle Accelerator Conf. (IPAC'22)*, Bangkok, Thailand, Jun. 2022, pp. 2402-2406. doi:10.18429/JACoW-IPAC2022-THIXSP1

[5] A. Ando *et al.*, "Isochronous storage ring of the New SUBARU project", *J. Synchrotron Rad.*, vol. 5, pp. 342-344, May 1998. doi:10.1107/S0909049597013150

[6] T. Inagaki *et al.*, "Construction of a Compact Electron Injector Using a Gridded RF Thermionic Gun and a C-Band Accelerator", in *Proc. 12th Int. Particle Accelerator Conf. (IPAC'21)*, Campinas, Brazil, May 2021, pp. 2687-2689. doi:10.18429/JACoW-IPAC2021-WEPAB039

[7] SIS8325 MTCA.4 Digitizer, Struck Innovative Systeme, https://www.struck.de/sis8325.html

Content from this work may be used under the terms of the CC BY 4.0 licence (© 2022). Any distribution of this work must maintain attribution to the author(s), title of the work, publisher, and DOI

ISBN: 978-3-95450-241-7 ISSN: 2673-5350 doi:10.18429/JACoW-IBIC2022-TUP34

LHC SCHOTTKY SPECTRUM FROM MACRO-PARTICLE SIMULATIONS

C. Lannoy[1,*], D. Alves, N. Mounet, CERN, Geneva, Switzerland
K. Lasocha, Institute of Physics, Jagiellonian University, Kraków, Poland
T. Pieloni, EPFL, Lausanne, Switzerland
[1]also at EPFL, Lausanne, Switzerland

Abstract

We introduce a method for building Schottky spectra from macro-particle simulations performed with the PyHEADTAIL code, applied to LHC beam conditions. In this case, the use of a standard Fast Fourier Transform (FFT) algorithm to recover the spectral content of the beam becomes computationally intractable memory-wise, because of the relatively short bunch length compared to the large revolution period. This would imply having to handle an extremely large amount of data for performing the FFT. To circumvent this difficulty, a semi-analytical method was developed to compute efficiently the Fourier transform. The spectral content of the beam is calculated on the fly along with the macro-particle simulation and stored in a compact manner, independently from the number of particles, thus allowing the processing of one million macro-particles in the LHC, over 10 000 revolutions, in a few hours, on a regular computer. The simulated Schottky spectrum is then compared against theoretical formulas and measurements of Schottky signals previously obtained with lead ion beams in the LHC.

INTRODUCTION

Schottky signals contain information on various beam and machine parameters, such as momentum spread, betatron tune, synchrotron frequency and chromaticity, among others. The basic theory of Schottky signals predicts how all of these parameters express themselves in the recorded signal, after it is transformed to the frequency domain. This topic is treated in detail in a classical work by Boussard [1]. The developed theory is however limited only to the simplified beam dynamics and does not include, e.g., collective effects and beam interaction with the vacuum chamber through impedance. Due to the complex theoretical description of such effects, it is most suitable to study their impact on Schottky spectra using multi-particle simulations, as done in [2], where the effect of space charge was investigated.

Obtaining a Schottky spectrum from multi-particle simulations in the case of the CERN Large Hadron Collider (LHC), is particularly challenging computationally due to the highly sparse characteristic of the current signal produced by a single bunch. While discretising the current signal in time, and applying the FFT algorithm to retrieve the spectral content of the beam is manageable for smaller accelerators, typically having smaller revolution periods and longer bunches, like the CERN Proton Synchrotron (PS), this is unfortunately intractable memory-wise for the LHC. As a conservative estimate, for the LHC revolution frequency $f_0 \approx 11245.5$ Hz, if we sample a 1 ns long bunch with 100 points (which corresponds to a sampling frequency of 100 GHz) over 10 000 turns, we would have to store an array of $10^{11+4}/f_0 \sim 10^{11}$ signal samples[1] or around 1 TB of data, hence the need of an alternative approach.

The study presented herein is based on simulations performed with PyHEADTAIL [3, 4], a macro-particle code that can be used to track turn-by-turn the six-dimensional phase space evolution of a bunch, possibly including the effects of direct space charge and beam-coupling impedances (although this capability is not yet used for this study). The following section will present the method used to post-process the data from PyHEADTAIL and reconstruct the Schottky spectra, while the third section will compare the simulation results against theoretical formalisms and measurements from LHC ion beams.

METHOD

To simulate Schottky spectra one generates a set of macro-particles following an initial phase-space distribution, and then tracks turn-by-turn the macro-particles using the machine optics. The Schottky spectra are computed using an analytical Fourier transform, performed turn-by-turn at the same time as the tracking.

Longitudinal and Transverse Phase Space

An accurate description of the longitudinal phase space is necessary since the average Schottky spectrum explicitly depends on the distribution of synchrotron oscillation amplitudes [1]. For LHC lead ion bunches, the synchrotron oscillation amplitudes $\widehat{\tau}$ approximately follow a Rice distribution [5]. The amplitude of the momentum deviation $\widehat{\Delta p}$ can be deduced from $\widehat{\tau}$ by substituting Eq. (4) in Eq. (11) from [6], which yields

$$\widehat{\Delta p} = \frac{p_0}{|\eta|}\widehat{\tau}\left(1 - \frac{(h_{rf}\omega_0\,\widehat{\tau})^2}{16}\right)\Omega_0 \,,$$

with p_0 the reference momentum, η the slippage factor, Ω_0 the nominal angular synchrotron frequency[2], h_{rf} the radio frequency harmonic and ω_0 the angular revolution frequency of the LHC. The initial position with respect to the synchronous particle z and momentum deviation Δp of each

[1] Most of these will be zeros and while Sparse Fourier Transform algorithms exist, these are only applicable to sparse output signals.

[2] By nominal synchrotron frequency we mean the synchrotron frequency of the synchronous particle, for which the synchrotron amplitude vanishes.

* christophe.lannoy@cern.ch

Content from this work may be used under the terms of the CC BY 4.0 licence (© 2022). Any distribution of this work must maintain attribution to the author(s), title of the work, publisher, and DOI

ISBN: 978-3-95450-241-7 ISSN: 2673-5350 doi:10.18429/JACoW-IBIC2022-TUP34

particle can then be computed from their synchrotron amplitude and phase[3] using Eqs. (10) and (12) of [6]:

$$z_i = \beta\, c\, \widehat{\tau_i}\, \cos(\phi_i), \qquad \Delta p_i = \widehat{\Delta p_i}\, \sin(\phi_i).$$

The initial transverse positions and momenta are instead obtained assuming a 2D Gaussian distribution in phase space.

Analytical Fourier Transform

Longitudinal Spectrum The current of a single particle i as seen from a pickup, can be expressed as

$$i_i(t) = q \sum_{n=0}^{N_t} \delta(t - nT_0 - \tau_{n,i}),$$

where δ is the Dirac delta function, N_t the number of turns, q the charge of the particle, $f_0 = 1/T_0$ the LHC revolution frequency, and $\tau_{n,i}$ the time difference between the particle i and the synchronous particle at turn n. The current produced by one bunch is simply obtained by summing the contributions of the N_p particles constituting the bunch:

$$i(t) = q \sum_{i=1}^{N_p} \sum_{n=0}^{N_t} \delta(t - nT_0 - \tau_{n,i}).$$

We proceed by computing analytically the Fourier transform

$$\widetilde{i(\omega)} = \int_{-\infty}^{\infty} i(t) e^{j\omega t} dt = q \sum_{n=0}^{N_t} e^{j\omega n T_0} \sum_{i=1}^{N_p} e^{j\omega \tau_{n,i}}. \quad (1)$$

To evaluate numerically this last expression we would have to store in memory the $N_t \times N_p$ numbers $\tau_{n,i}$ and to compute $O(N_t N_p N_f)$ exponentials, where N_f is the number of frequencies we want to plot. Both these requirements are highly limiting the number of particles we can simulate. We expect that the number of macro-particles required to make the PyHEADTAIL simulation realistic would be at least $N_p \sim 10^6$. Typical values for the number of turns and frequencies are $N_t \sim N_f \sim 10^4$ and come respectively from the acquisition time and spectral resolution of the LHC Schottky Monitor.

The spectrum in Eq. (1) can be computed more efficiently by replacing the right-hand exponential by its Taylor expansion. Since we are interested in the frequency domain of the LHC Schottky monitor working at the $h = 427725$ harmonic of the revolution frequency, the maximal value of the right-hand exponential argument will be $(\omega\tau)_{max} \approx 30$ (with $f_0 \approx 11.2455$ kHz and $\tau_{max} \sim 1$ ns) and will typically span over a maximum range of $|\Delta\omega|\ \tau_{max} \sim 10^{-5}$ for the sidebands satellites (e.g. for ~ 20 of them spaced by the nominal synchrotron frequency $f_s \sim 65$ Hz and for a fractional part of the tune $q_x \sim q_y \sim 0.3$). Expanding each exponential around $\omega_c \tau_{n,i}$ with $\omega_c = 2\pi h f_0$, instead of using the MacLaurin expansion, will allow the series to converge faster and to save some memory. The required number of terms, N_l, can be estimated by computing an upper bound for the rest of the Taylor expansion, which showed that $N_l = 4$ is typically sufficient for the simulation parameters stated above. Equation (1) is then replaced by

$$\begin{aligned}\widetilde{i(\omega)} &= q \sum_{n=0}^{N_t} e^{j\omega n T_0} \sum_{i=1}^{N_p} \sum_{l=0}^{N_l} \frac{e^{j\omega_c \tau_{n,i}}}{l!} (j\omega\tau_{n,i} - j\omega_c \tau_{n,i})^l \\ &= q \sum_{n=0}^{N_t} e^{j\omega n T_0} \sum_{l=0}^{N_l} \frac{j^l(\omega - \omega_c)^l}{l!} \sum_{i=1}^{N_p} e^{j\omega_c \tau_{n,i}} (\tau_{n,i})^l.\end{aligned}$$

By introducing the variables $\mathcal{L}_{n,l}$ and $\alpha_l(\omega)$ defined as

$$\mathcal{L}_{n,l} = \sum_{i=1}^{N_p} e^{j\omega_c \tau_{n,i}} (\tau_{n,i})^l, \qquad \alpha_l(\omega) = \frac{j^l(\omega - \omega_c)^l}{l!},$$

the previous expression can be written in the compact form

$$\widetilde{i(\omega)} = q \sum_{n=0}^{N_t} e^{j\omega n T_0} \sum_{l=0}^{N_l} \alpha_l(\omega)\ \mathcal{L}_{n,l}. \quad (2)$$

Computing all the $\mathcal{L}$ coefficients requires $O(N_t N_p)$ operations; the summation over N_l can be considered as $O(1)$, hence computing the spectrum thereafter takes $O(N_t N_f)$ operations. The total cost of evaluating Eq. (2) is then $O(N_t N_p)$ since $N_f << N_p$.

Transverse Spectrum A similar derivation can be performed for the transverse Schottky spectrum. With the dipole moment of a macro-particle i defined as $d_i(t) = x_i(t)\ i_i(t)$, we get a similar expression as Eq. (2):

$$\widetilde{d(\omega)} = q \sum_{n=0}^{N_t} e^{j\omega n T} \sum_{l=0}^{N_l} \alpha_l(\omega)\ \mathcal{T}_{n,l} \quad (3)$$

using the definition

$$\mathcal{T}_{n,l} = \sum_{i=0}^{N_p} x_{n,i}\ e^{j\omega_c \tau_{n,i}} (\tau_{n,i})^l,$$

where $x_{n,i} = x_i(t = nT_0 + \tau_{n,i}) \approx x_i(t = nT_0)$ is the horizontal transverse position of the particle i when passing in front of the detector at turn n.

Beside the considerable gain in computation time, another advantage of the formalism of Eqs. (2) and (3) is that the $\mathcal{L}$ and $\mathcal{T}$ coefficients can be calculated simultaneously with the tracking done in the PyHEADTAIL simulation. Hence there is no need to keep in memory the extremely large arrays of $\tau_{n,i}$, $x_{n,i}$ and $y_{n,i}$ for each turn and each particle - all the necessary information is contained in the $N_t \times N_l$ coefficients $\mathcal{L}$ and $\mathcal{T}$. Since the number of these coefficients does not depend on the number of macro-particles, we can increase the latter without any memory issue.

[3] Synchrotron phases are assumed to be uniformly distributed.

Content from this work may be used under the terms of the CC BY 4.0 licence (© 2022). Any distribution of this work must maintain attribution to the author(s), title of the work, publisher, and DOI

ISBN: 978-3-95450-241-7 ISSN: 2673-5350 doi:10.18429/JACoW-IBIC2022-TUP34

Content from this work may be used under the terms of the CC BY 4.0 licence (© 2022). Any distribution of this work must maintain attribution to the author(s), title of the work, publisher, and DOI

Simulation Procedure

Figure 1 sketches the full simulation procedure. Note that we use the smooth approximation for the machine optics, and (unless stated otherwise) a non-linear RF system (hence leading to synchrotron frequency spread).

The spatial coordinates $x_{n,i}$, $y_{n,i}$ and $z_{n,i}$ of each marco-particle at each turn, obtained from PyHEADTAIL, are plugged into Eqs. (2) and (3) to reconstruct the longitudinal and transverse Schottky spectra. Finally, averaging these spectra over several random draws for the initial bunch, makes the characteristic Bessel satellites of the spectra appear. This final step is needed since the variance of the power spectral density of the non-central synchrotron satellites is proportional to the square of the number of simulated particles, due to the random phases of synchrotron motion. Therefore, adding more particles to the simulation procedure will not make the spectrum converge to its true average.

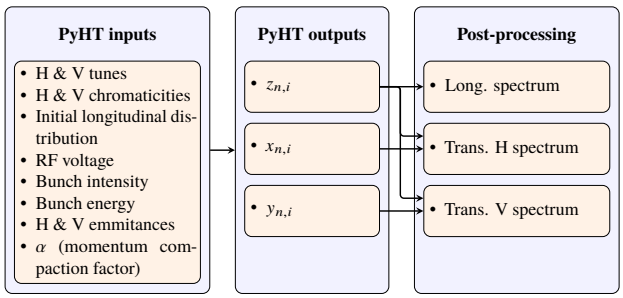


Figure 1: Schottky spectrum simulation procedure.

RESULTS

The method presented in the previous section is benchmarked against experimental Schottky spectra obtained with lead ion beams during LHC Run 2. The Schottky data consists of horizontal measurements of beam 2 taken at injection energy for the fill 7443.

Among the PyHEADTAIL input parameters described in Fig. 1, some are based on the fitting of the experimental spectrum as done in [5] and allows to determine precise machine parameters for the specific fill we want to reproduce. The parameters based on this fitting procedure are horizontal and vertical tunes, horizontal and vertical chromaticities, synchrotron amplitude distribution and nominal synchrotron frequency. The other parameters needed by PyHEADTAIL such as emmitances or bunch intensity and energy, come from direct measurements or machine design. Table 1 summarises the values of these parameters.

Table 1: PyHEADTAIL Simulation Parameters for Fill 7443

Intensity	1.76×10^8 ions per bunch
Energy per ion	36.9 TeV
Ion charge	82 e
Ion mass	193.687 GeV/c^2
ϵ_x, ϵ_y	1.5 µm
Tunes	$Q_x = 64.2827$, $Q_y = 59.2985$
Chromaticities	$Q'_x = 18.56$, $Q'_y = 11.64$
α	3.479×10^{-4}
h_{rf}	35640
RF voltage[4]	8.22 MV
LHC circumference	26.659 km
Rice parameters of $\hat{\tau}$ distribution	$\sigma = 1.306$ ns, $b = 0.216$

Figure 2 presents an overall view of the simulated longitudinal and transverse horizontal Schottky spectra obtained using Eqs. (2) and (3) respectively and plotted on the same frequency axis (frequencies in the plot have been shifted to the first harmonic). Figure 3 is a detailed view of these spectra compared against the experimental measurements of fill 7443. As visible from the plots, the agreement between simulations and measurements is very good. One can also observe that the effect of chromaticity, which makes the upper betatron sideband higher and thinner than the lower sideband, is well reproduced by the simulation.

[4] The RF voltage is computed from the fitted nominal synchrotron frequency $f_s = 64.67$ Hz with Eq. (110) of [7] and does not correspond to the measured RF voltage of 7.5 MV. This discrepancy is currently being investigated.

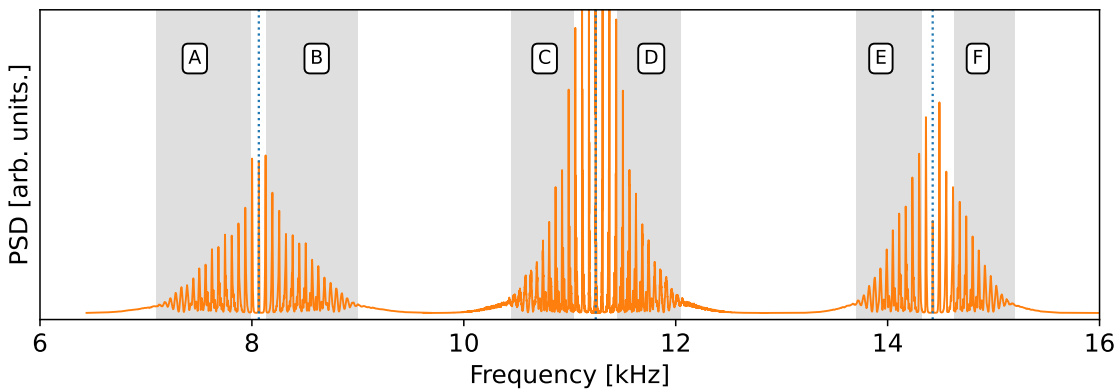


Figure 2: Simulated longitudinal (C, D) and transverse horizontal (A, B, E, F) Schottky spectra for the machine and beam configuration of LHC fill 7443. The dotted lines indicate respectively (from left to right): $(1 - Q_x) f_0$, f_0 and $(1 + Q_x) f_0$.

ISBN: 978-3-95450-241-7 ISSN: 2673-5350 doi:10.18429/JACoW-IBIC2022-TUP34

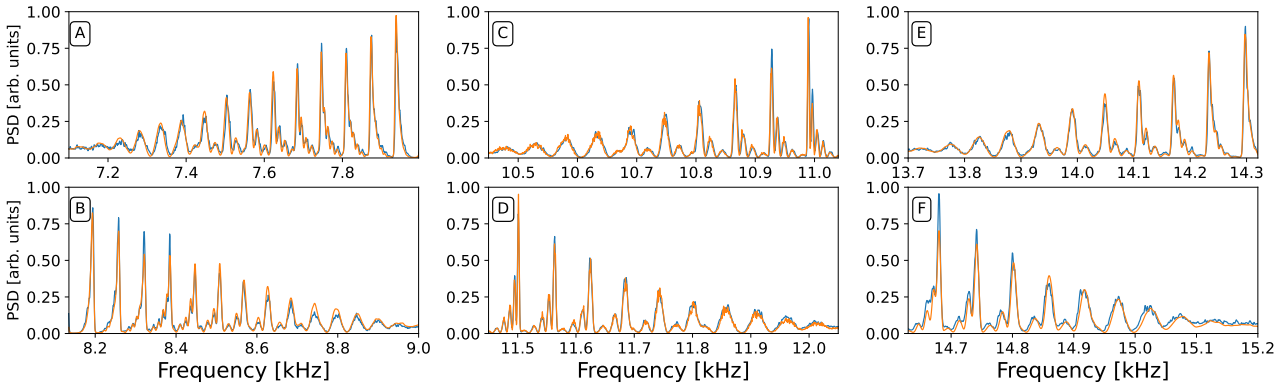


Figure 3: Measured (blue lines) longitudinal and transverse horizontal Schottky spectra compared with the simulated spectra (orange lines) for LHC fill 7443. The A–F region labels correspond to the frequency ranges of the shaded regions on Fig. 2.

Theoretical Comparison

Finally, we will compare the simulations against two theory-based methods suitable to reconstruct the Schottky spectrum. The first method is based on the Monte Carlo approach presented in [8]. It consists in drawing randomly, for each particle, a synchrotron oscillation time-amplitude $\widehat{\tau_i}$ and an initial synchrotron phase φ_{s_i} from a Rice and a uniform distribution respectively. Using the theoretical formula for the longitudinal spectrum of each particle i [1]

$$i_i(t) = q f_0 \sum_{n,p=-\infty}^{\infty} J_p(n\omega_0 \widehat{\tau_i})\, e^{j(n\omega_0 t + p\Omega_{s_i} t + p\varphi_{s_i})},$$

the Fourier transform of each individual particle can be directly deduced using the expresssion giving $\Omega_{s_i}(\widehat{\tau_i})$ from [6]. The Fourier transform being a linear operation, we can sum over the single-particle spectra in the complex plane using the sliding window method of [8] and taking the squared magnitude of this sum gives the Power Spectral Density (PSD) of the whole bunch (i.e. the Schottky spectrum). Finally, as done for PyHEADTAIL simulations, we need to average the PSD over several random draws for the initial bunch.

The transverse spectrum is obtained in a similar fashion by drawing an additional initial betatron phase φ_{β_i} from a uniform distribution and using the general expression for the dipole moment [9]

$$d_i(t) = q f_0 \frac{\widehat{x}}{2} \sum_{n,p=-\infty}^{\infty} J_p(\chi_{i,n}^{\pm}) e^{j(t[(n\pm Q)\omega_0 + p\Omega_{s_i}] \pm \varphi_{\beta_i} + p\varphi_{s_i})},$$

where

$$\chi_{i,n}^{\pm} = \left(n\widehat{\tau_i} \pm \frac{\widehat{Q_i}}{\Omega_{s_i}} \right) \omega_0.$$

Figure 4 shows a comparison between the results of our proposed simulation-based method, the Monte Carlo method, the matrix formalism developed in Refs. [5] and [9], and real measurements for two different regions of the Schottky spectrum. All the spectra have been normalised and are in very good agreement with each other.

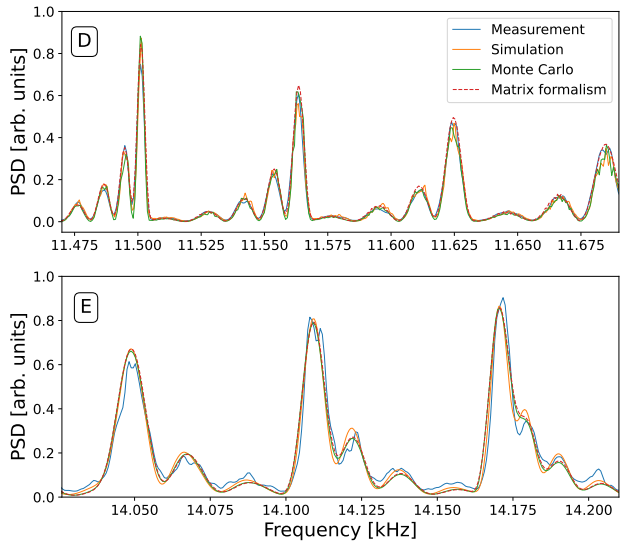


Figure 4: Comparison between measured, simulated and theory based longitudinal (D) and transverse horizontal (E) Schottky spectra for LHC fill 7443.

CONCLUSION

The aim of this work was to validate the development of a new method for calculating Schottky spectra from macro-particle simulations. This method will enable future studies on how effects such as beam-coupling impedances impact the measured spectra. After discussing the high computational resource requirements of traditional FFT algorithms when performing simulations for LHC beam and machine conditions, we showed how one can achieve a substantial reduction of its computational complexity. This method allows to closely reproduce the Schottky spectrum of a given LHC fill. The obtained results were shown to be in good agreement with reference measurements as well as with other theory-based methods, and reproduce the overall shape of the spectrum together with the detailed internal structure of the synchrotron satellites, as shown in Figs. 3 and 4.

Content from this work may be used under the terms of the CC BY 4.0 licence (© 2022). Any distribution of this work must maintain attribution to the author(s), title of the work, publisher, and DOI

ISBN: 978-3-95450-241-7 ISSN: 2673-5350 doi:10.18429/JACoW-IBIC2022-TUP34

Content from this work may be used under the terms of the CC BY 4.0 licence (© 2022). Any distribution of this work must maintain attribution to the author(s), title of the work, publisher, and DOI

REFERENCES

[1] D. Boussard, "Schottky noise and beam transfer function diagnostics," CERN. Geneva, Switzerland, Rep. CERN-SPS-86-11–ARF, 1986. doi:10.5170/CERN-1987-003-V-2.416

[2] O. Boine-Frankenheim and V. Kornilov, "Transverse schottky noise spectrum for bunches with space charge," *Phys. Rev. ST Accel. Beams*, vol. 12, p. 114 201, 2009. doi:10.1103/PhysRevSTAB.12.114201

[3] K. S. B. Li *et al.*, "Code development for collective effects," in *Proc. HB'16, Malmö, Sweden*, 2016, pp. 362–367. doi:10.18429/JACoW-HB2016-WEAM3X01

[4] *PyHEADTAIL code repository*. https://github.com/PyCOMPLETE

[5] K. Lasocha and D. Alves, "Estimation of longitudinal bunch characteristics in the LHC using Schottky-based diagnostics," *Phys. Rev. Accel. Beams*, vol. 23, p. 062 803, 2020. doi:10.1103/PhysRevAccelBeams.23.062803

[6] D. Alves and K. Lasocha, "Kalman filter-based longitudinal phase-space reconstruction method for hadron machines," *Phys. Rev. Accel. Beams*, vol. 24, p. 072 801, 2021. doi:10.1103/PhysRevAccelBeams.24.072801

[7] L. Rinolfi, "Longitudinal Beam Dynamics Application to synchrotron," CERN. Geneva, Switzerland, Rep. CERN-PS-2000-008–LP, 2000. https://cds.cern.ch/record/446961

[8] M. Betz, O. R. Jones, T. Lefevre, and M. Wendt, "Bunched-beam Schottky monitoring in the LHC," *Nucl. Instrum. Methods Phys. Res. A*, vol. 874, pp. 113–126, 2017. doi:10.1016/j.nima.2017.08.045

[9] K. Lasocha and D. Alves, "Estimation of transverse bunch characteristics in the LHC using Schottky-based diagnostics," *Phys. Rev. Accel. Beams*, vol. 25, p. 062 801, 2022. doi:10.1103/PhysRevAccelBeams.25.062801

ISBN: 978-3-95450-241-7 ISSN: 2673-5350 doi:10.18429/JACoW-IBIC2022-TUP35

FIRST RF PHASE SCANS AT THE EUROPEAN SPALLATION SOURCE

Y. Levinsen*, M. Akhyani, R. Baron, E. Donegani, M. Eshraqi, A. Garcia Sosa,
H. Hassanzadegan, B. Jones, N. Milas, R. Miyamoto, D. Noll, I. Vojskovic, R. Zeng
European Spallation Source, Lund, Sweden
F. Grespan, INFN, Italy
I. Bustinduy, ESS-Bilbao, Bilbao, Spain

Abstract

The installation and commissioning of the European Spallation Source is currently underway at full speed, with the goal to be ready for first neutron production by end of 2024. This year we accelerated protons through the first DTL tank. This included the RFQ, 3 buncher cavities in the medium energy beam transport as well as the DTL tank itself as RF elements. At the end of the DTL tank we had a Faraday cup acting as the effective beam stop. This marks the first commissioning when RF matching is required for beam transport. In this paper we discuss the phase scan measurements and analysis of the buncher cavities and the first DTL tank.

INTRODUCTION

The European Spallation Source (ESS) is designed as the world brightest neutron source, driven by a 5 MW proton beam that is accelerated to 2 GeV. The proton linac driver consists of a normal conducting (NC) front end that brings the beam energy to around 90 MeV, followed by a super conducting (SC) section and finally a beam transport to the rotating tungsten target wheel. The linac features a very long beam pulse length of 2.86 ms, with a 14 Hz repetition rate. The NC radiofrequency (RF) and hence beam bunch frequency is at 352.21 MHz. The two last SC families operate at twice that frequency, 704.42 MHz.

The first beam commissioning of the ESS linac commenced in 2018-19, including the ion source (IS) and the low energy beam transport (LEBT) [1, 2]. The second stage of commissioning started in the fall of 2021, included the radio-frequency quadrupole (RFQ) and the medium energy beam transport (MEBT). This run continued with some minor interruptions until the next step which sent beam through the first drift tube linac (DTL) tank, starting at the end of May 2022 and continuing until mid July. For this stage the buncher cavities in the MEBT were also made available, which marked the first time beam-based RF matching was possible and necessary.

In this paper we will discuss the initial experience in matching the RF phase and amplitude using the phase scan technique primarily for the buncher cavities and also for the first DTL tank. A more general overview of the MEBT characterisation is presented in [3]. Prerequisites for this work is also to have good diagnostics [4], and a well functioning timing system [5]. For the bunchers, the primary signal to look at is the beam position monitor (BPM) phase response. For the DTL we have transmission scans as well as the response signals of the internal BPMs in the tank.

* yngve.levinsen@ess.eu

SIMULATIONS

Our primary simulation software is TraceWin [6], as well as OpenXAL [7] meant primarily for online modelling though usable for any simulation where an envelope model is sufficient. That essentially translates to effects where a linear space charge model is sufficient. In both cases, each gap in the bunchers and DTL is modeled as a drift-kick-drift.

RF phase scans are performed by modulating the amplitude and phase of an RF element, and monitoring the Time of Flight (ToF) of the beam downstream of the element. In general the absolute value of the ToF is not known, so most commonly one then instead looks at the change in BPM phase signal(-s) and compares with model expectation.

For modelling RF cavities one often refers to the transit time factor (TTF), which follows

$$T = \frac{1}{\int E_z dz}\left[\int E_z \cos\omega t dz - \tan\phi \int E_z \sin\omega t dz\right]. \quad (1)$$

Here E_z is the longitudinal on-axis field amplitude that generally depend on z, and ω is the RF frequency. V_0 is the integrated field amplitude E_z. ϕ is the relative phase arrival of the particle. The time t is a function of z through the speed of the particle. Through the TTF we can then get the simple formula for the the net energy gain traversing the cavity, which becomes

$$\Delta W = qV_0 T\cos\phi, \quad (2)$$

where q is the charge of the particle, and V_0 is the integrated field (denominator of (1)). For $\phi = 0$ we then have what we call "on crest" acceleration, which gives the maximum energy gain, but then with no longitudinal focusing. In fact there is even defocusing on half of the bunch, since particles arriving early (or late) and would need a higher energy kick to "catch up" instead get a lower energy kick falling further behind the synchronous particle.

Buncher cavities run at $\phi = -90°$, which provides no acceleration but maximum longitudinal focusing. These are rather simple cavities generally speaking, providing sine-like signatures in phase space downstream that are relatively easy to analyse (differing for example from DTL signatures). As we can understand from Eq. (1), even if the net energy gain is zero, the transit time still depends on the amplitude of the cavity. This can be understood from the fact that the cavity has a finite size and the particle is travelling slower than the speed of light. If $\phi = -90°$, the particle arrives at the entrance of the cavity early and experience a slight deceleration. In the middle of the cavity there is no acceleration, while in the second half there is a comparatively positive acceleration

Content from this work may be used under the terms of the CC BY 4.0 licence (© 2022). Any distribution of this work must maintain attribution to the author(s), title of the work, publisher, and DOI

ISBN: 978-3-95450-241-7 ISSN: 2673-5350 doi:10.18429/JACoW-IBIC2022-TUP35

Content from this work may be used under the terms of the CC BY 4.0 licence (© 2022). Any distribution of this work must maintain attribution to the author(s), title of the work, publisher, and DOI

which nets out as 0 acceleration. However the particle will have travelled on average with a slightly lower energy through the cavity than if it was turned off. This is why one commonly looks at the phase variation between 2 downstream BPMs rather than just a single BPM. The RF relative phase is found when there is no amplitude dependency on the phase between the two downstream BPMs.

In the commissioning run presented here, we have no downstream BPMs of the DTL to look at, so we are left with analysing the transmission and the signature curves of internal BPMs.

Buncher Cavities

There are 3 buncher cavities in the MEBT to focus the beam longitudinally and match to the DTL following. The first buncher stops the rather strong debunching arizing from space-charge forces out of the RFQ to maintain a reasonable beam size through the transport section, and would ideally be placed more or less as close to the RFQ exit as possible. The second maintains stable longitudinal envelope and operates at about half the strength of the two other bunchers. The last is primarily responsible for matching to the DTL and would again ideally be placed as close to the DTL entrance as possible. This last buncher operates quite close to the maximum field possible with these bunchers.

All bunchers operate at −90° from the accelerating phase, which means that the centroid is unaffected. The head of the bunch (arriving early) will experience a deceleration kick, and the late tail of the bunch will experience an accelerating kick.

The −90° is conceptually quite easy to find for such a cavity. It is essentially the phase where the downstream ToF does not depend on the cavity amplitude. However, the transit through a finite length cavity at this phase, the beam initially experience some decelaration, in the middle of the cavity zero acceleration, and then some acceleration again at the end of the cavity again to reach the net acceleration of zero. This means the transit time through the cavity does depend on the amplitude at the correct phase. This is the motivation for measuring the ToF between two downstream BPMs rather than just one. A BPM far downstream would be showing an intersection point very close to −90°, as the variation in transit time becomes small in comparison to the variation in ToF.

In Fig. 1 we demonstrate how the single BPM fit would look for our first MEBT buncher. The intersection of the curves from a given BPM is not exactly at −90°, and the discrepancy is strongest for the closest BPM2, while for the other 2 BPMs we are close to the expected measurement errors in this example. It is still preferred to use 2 BPM for ToF since it is fully model independent, but single BPM fit can be useful to improve statistical understanding of the fit.

A secondary effect here is that if we do a sine fit of each phase curve to find the −90°, the relative effect of the transit time increases somewhat. It was found in simulations that this effect is well below the measurement uncertainties we are working with in the data for this commissioning round.

When we later in the paper quote a single BPM fit, we then subtract the offset expected from a simulated fit using our field map model.

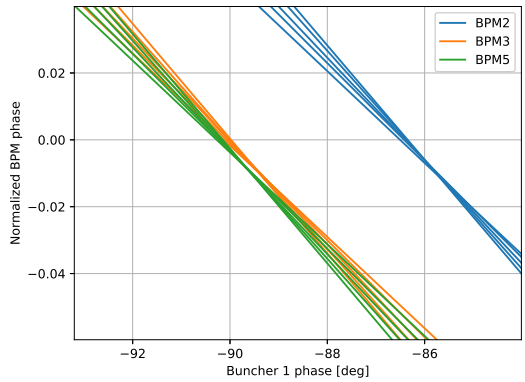


Figure 1: Simulated phase curves of BPMs as a function of buncher RF phase for varying buncher field amplitude. The colours represent different BPMs and the different curves of same colour are for different amplitudes. The point where curves intersect represent the cavity phase where this signal is amplitude independent.

DTL

Figure 2 show the simulated phase signatures of the internal BPMs to the DTL tank. Interesting to note is that the first BPM should follow a rather simple sine-like signature, with a minima close to $\phi = 0$. The first BPM will also have a good transmission for a larger range of RF phases. On top of that it should be added that unwrapping the signals of the later BPMs requires a very fine grained phase scan, as well as accurate BPM signals. For example BPM4 in simulation shows a phase variation of over 5000° in phase during the full 360° scan. BPM1 shows 80° variation.

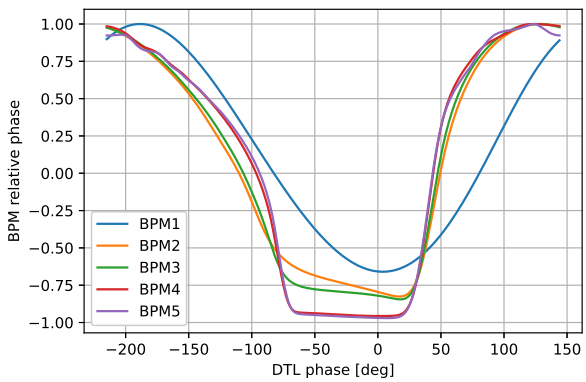
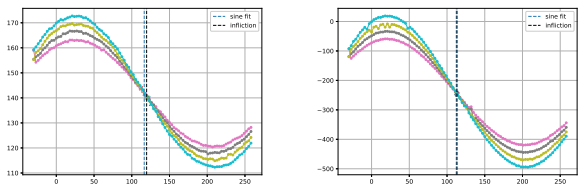


Figure 2: The simulated phase signatures of the 5 first internal BPMs in the DTL tank. The 6th BPM signal seems unstable for several phases, so it is excluded from this plot. Each signal is divided by the maximum so all signatures can be compared in the same plot.

ISBN: 978-3-95450-241-7 ISSN: 2673-5350 doi:10.18429/JACoW-IBIC2022-TUP35

Table 1: Phase set points for buncher 1, from analysing different BPM and/or BPM pair signals from a specific RF phase scan. For the intersect method the median of all curve intersects is used, for sine fit the mean of the phase from each amplitude curve is used.

BPM	Intersection		Sine-fit	
	median	error	mean	error
BPM2	110.92	3.93	111.48	0.39
BPM3	112.56	0.26	112.82	2.22
BPM5	109.04	0.43	111.21	3.00
BPM2 - BPM3	112.66	0.33	110.52	0.11
BPM2 - BPM5	108.53	0.64	107.39	0.62



(a) BPM2 (b) BPM3 - BPM2

Figure 3: Phase scan curves for buncher 1, for two of the BPM responses evaluated.

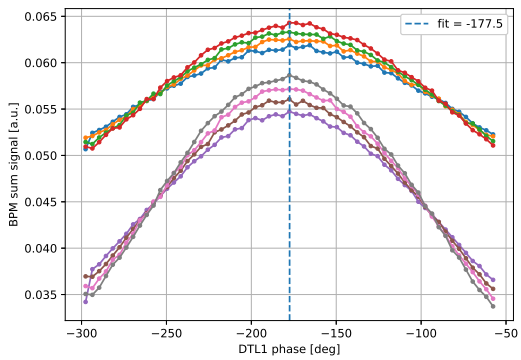


Figure 4: The sum signals from 2 BPMs during a phase scan of the second buncher. The maximum of the curve fit should indicate the −90° phase.

RESULTS

Bunchers

Figure 3 show scan curves for buncher 1, both single BPM and difference signal between two downstream BPMs. We see that ta large both signals seem similar and clean enough to analyse. The vertical lines show the estimated -90° operating phase by using sine fit as well as averaging the intersections of the lines. We see that the two methods overlap quite well. Table 1 lists a complete overview of fit results for the signals considered for matching buncher 1.

In Fig. 4 we show data of the BPM sum signal from the 5th and 6th BPM during a phase scan of the second buncher. A maximum from a fitted line of these curves are found to be −177.46°±1.54°. This can be compared to −180.4° from the sine fit of the phase signals mentioned earlier.

Table 2: Summary of the matched amplitude and phase set points for the 3 bunchers in the ESS MEBT. For evaluating phase the sine fit was chosen.

Cavity	Amplitude [kV]	Phase [°]
Buncher 1	131.81±0.78	112.61±0.30
Buncher 2	62.85±0.20	−180.45±1.39
Buncher 3	163.98±0.66	31.72±0.39

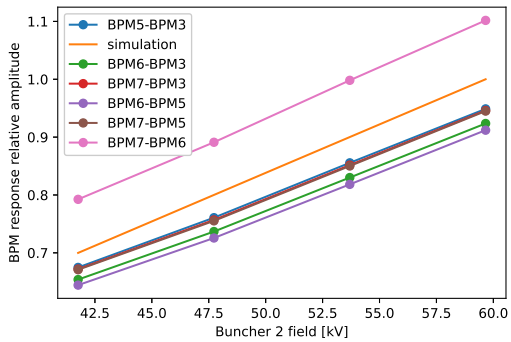


Figure 5: Buncher 2 amplitude fit to model. The curves show the relative amplitude, so 1.0 for the nominal 59.66 kV would imply no correction.

The amplitude we evaluate by comparing the amplitude of a sine fit to the simulation. In Fig. 5 we show an example of such a fit for buncher 2. In this example we see that 3 BPMs agree very precisely to a correction of about 5.3%, while any pair involving BPM6 do not fit to this correction.

In Tab. 2 we have summarised the obtained matched parameters for phase and amplitude of the three bunchers. Here we can add that the stability of phase is worse than the error of the measurement indicates, typically we would get consistent results from multiple scans within 1-2 degrees but not less. The error reported is the sum of squared errors of the individual curve fits and the variation of the values obtained from each individual curve.

For the third buncher we find a fit which gives a higher amplitude set point than the design maximum of 160 kV. Various measurement and fitting methods so far has found results in the range of 10-13% increase necessary. We conclude for now that the 3rd buncher most likely will need to run very close to the maximum possible field. Before we have beam transport through a larger part of the linac it is challenging to conclude on how accurate these fits are.

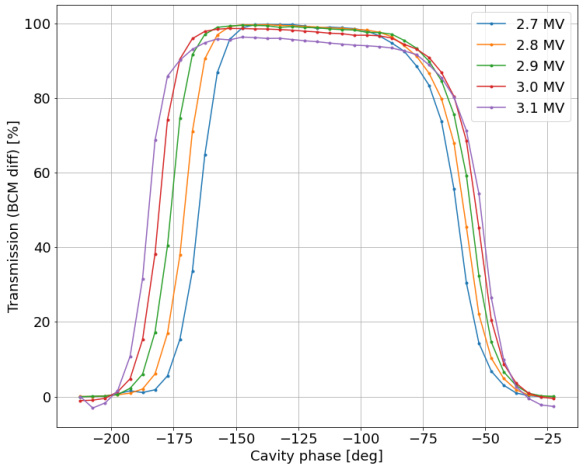
DTL

The main goal for the DTL commissioning with beam in this run was to get the beam through the cavity and secondly to get the full current through. Both of these were achieved shortly after we had the green light for the respective beam modes [8]. Additionally a full RF conditioning, getting to the nominal RF pulse was a main goal for the DTL [9].

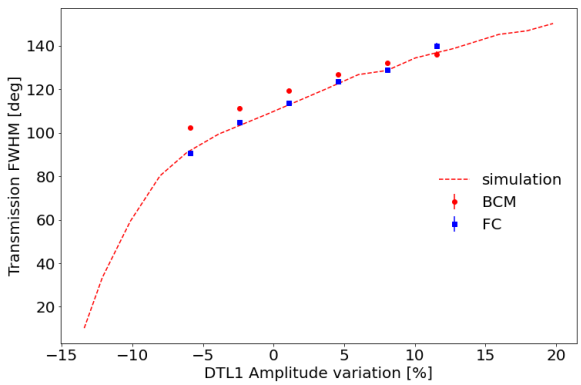
Content from this work may be used under the terms of the CC BY 4.0 licence (© 2022). Any distribution of this work must maintain attribution to the author(s), title of the work, publisher, and DOI

ISBN: 978-3-95450-241-7 ISSN: 2673-5350 doi:10.18429/JACoW-IBIC2022-TUP35

Content from this work may be used under the terms of the CC BY 4.0 licence (© 2022). Any distribution of this work must maintain attribution to the author(s), title of the work, publisher, and DOI



(a) Transmission



(b) FWHM fit

Figure 6: Transmission curves (a) during an RF phase scan of the DTL at different amplitudes, and a fit of the FWHM of the transmission (b) to the simulations as a way to find the amplitude correction.

DTL Transmission and Amplitude Set Point

We succeeded to obtain a few phase scan sets of the DTL, however we encountered some technical obstacles with signal processing, and (apparent) noise from strong harmonics of the RF source at the operating frequency of the diagnostics, which is twice the RF frequency in these sections of the linac.

The transmission was measured with a beam current monitor (BCM) at the end of the tank, as well as a Faraday cup (FC) that was placed shortly after the tank as an effective beam stop for this commissioning run. In Fig. 6a we show the transmission measured with the BCM. At a glance this corresponds reasonably well to what is expected from simulations.

In Fig. 6b we look at the FWHM of each transmission curve, and compare that to the model predictions. In simulations [10] we have found that this method should be less dependent on e.g. input beam parameters. The FWHM fit provides an estimate for the amplitude correction, and in this scan we found that 2.9 MV/m should be the closest match for the design 3.0 MV/m transmission signature. This is within the estimated RF calibration error.

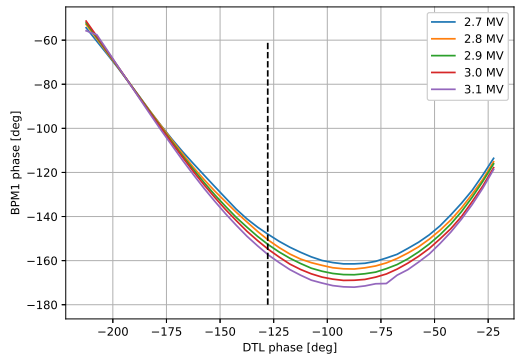


Figure 7: Measured phase signal of the first BPM in the tank as a function of the DTL phase signal, for different amplitudes. The working point from the fit is marked with dashed black line.

DTL BPM Signals and Phase Set Point

As discussed earlier, the first BPM in the tank should be an interesting candidate for finding the correct phase for the DTL. In Fig. 7 we see that during these scans there is indeed a similar curve, and the minima of each curve should be close to the 0° phase of the cavity. If we look closer at the simulation data, we find that the minima should be around 3.5-4° for the nominal field, and slowly increasing as the field increases. In our measurements we find instead a slowly reducing minima phase, from $-88.7°$ at 2.7 MV m^{-1} to $-89.5°$ at 3.1 MV m^{-1}. If we assume that the average of these curves should follow the simulated offset of 3.61°, and subtract the 35° operating point (from design), we land at an operating phase of $-127.8°$.

SUMMARY AND OUTLOOK

During the 2022 commissioning run of the ESS front-end, we successfully sent beam through the RFQ, MEBT and the first DTL tank. This was the first time we performed beam-based RF matching. We found a reasonably good set of reference amplitude and phase points for the bunchers and DTL1, and decent consistency between measurements and methods. A complete evaluation of the quality of the longitudinal beam transport will probably not be possible before a larger part of the linac is installed. Going more in details, there are still inconsistencies between the discussed fitting methods as well as diagnostic signal processing that needs to be ironed out or accounted for before the goal of an automated setup procedure could be materialised.

ACKNOWLEDGEMENTS

We would like to acknowledge the operations team for their tireless efforts making this a successful commissioning run, and the numerous other colleagues who contribute in various ways to the commissioning.

REFERENCES

[1] M. Eshraqi *et al.*, "First Protons in the ESS LINAC," *J. Surf. Invest.*, vol. 14, S42–S49, 2020. doi:10.1134/S1027451020070137

ISBN: 978-3-95450-241-7 ISSN: 2673-5350 doi:10.18429/JACoW-IBIC2022-TUP35

[2] R. Miyamoto *et al.*, "Highlights from the first beam commissioning stage at ESS for its ion source and low energy beam transport," *J. Instrum.*, vol. 15, P07027, 2020. doi:10.1088/1748-0221/15/07/P07027

[3] N. Milas *et al.*, "Beam tuning studies in the ess mebt," presented at IBIC'22, Krakow, Poland, Sep. 2022, paper MO2C2, this conference.

[4] T. Shea *et al.*, "Beam instrumentation performance during commissioning of the ESS RFQ, MEBT and DTL," presented at IBIC'22, Krakow, Poland, Sep. 2022, paper MOP07, this conference.

[5] N. Milas *et al.*, "Commissioning of the timing system at ESS," presented at IBIC'22, Krakow, Poland, Sep. 2022, paper TUP23, this conference.

[6] D. Uriot and N. Pichoff, *TraceWin,* https://www.dacm-logiciels.fr/tracewin

[7] A. P. Zhukov *et al.*, "Open XAL Status Report 2022," in *Proc. IPAC'22*, Bangkok, Thailand, 2022, pp. 1271–1274. doi:10.18429/JACoW-IPAC2022-TUPOTK029

[8] R. Miyamoto *et al.*, "Beam commissioning of the normal conducting part and status of the ESS project," presented at LINAC'22, Liverpool, UK, Aug.-Sep. 2022, paper MO1PA02, to be published.

[9] F. Grespan *et al.*, "High Power RF Conditioning of the ESS DTL1," presented at LINAC'22, Liverpool, UK, Aug.-Sep. 2022, paper TUPOJO09, to be published.

[10] E. Nilsson, Private comm.

Content from this work may be used under the terms of the CC BY 4.0 licence (© 2022). Any distribution of this work must maintain attribution to the author(s), title of the work, publisher, and DOI

ISBN: 978-3-95450-241-7 ISSN: 2673-5350 doi:10.18429/JACoW-IBIC2022-TUP36

BEAM CHARACTERIZATION OF SLOW EXTRACTION MEASUREMENT AT GSI-SIS18 FOR TRANSVERSE EMITTANCE EXCHANGE EXPERIMENTS

J. Yang[1,*], P. Boutachkov, P. Forck, T. Milosic, R. Singh, S. Sorge
GSI Helmholtzzentrum für Schwerionenforschung GmbH, Darmstadt, Germany
[1]also at Goethe Universität, Frankfurt am Main, Germany

Abstract

The quality of slowly, typically several seconds, extracted beams from the GSI synchrotron SIS18 is characterized with respect to the temporal spill stability, the so-called spill micro structure on the 100 µs scale. A pilot experiment was performed utilizing transverse emittance exchange to reduce the beam size in the extraction plane, and the improvement of spill micro structure was found. Important beam instrumentation comprises an Ionization Profile Monitor for beam profile measurement inside the synchrotron and a plastic scintillator at the external transfer line for ion counting with up to several 10^6 particles per second and 20 µs time slices. The performant data acquisition systems, including a scaler and a fast Time-to-Digital Converter (TDC), allow for determining the spill quality. The application of the TDC in the measurements and related MAD-X simulations are discussed.

INTRODUCTION

Temporary beam stability within 100 µs of the slowly extracted beam from the GSI SIS18 synchrotron is crucial for fixed-target experiments. Beam instrumentation plays an essential role in the slow extraction investigation into searching for better methods that could mitigate the spill micro structure.

SIS18 has a circumference of 216.72 m and a beam rigidity of up to 18 Tm. Tune-swept slow extraction is regularly performed. The third-order resonance excited by the sextupolar field is fed by increasing the strength of two fast quadrupoles. The extracted beam, referred to as a spill, has a temporal variation on time scales of micro-to-milliseconds, which is also called spill micro structure [1]. The reason is related to the power supply ripples which act on the quadrupole magnet, leading to the unintended variation of the machine tune [2]. The spill micro structures are mitigated if the machine tune during the extraction is set closer to the resonance tune, which results in a larger spread of the transit times [3]. That can be achieved not only by proper lattice settings, e.g. lower sextupole strengths but also by reducing the beam size (emittance) in the extraction plane. The latter is applied for this study. Since the beam is injected into the synchrotron by horizontal multi-turn injection, the horizontal emittance is significantly larger than the vertical emittance. One of the possible techniques to get a smaller beam is to benefit from the transverse emittance exchange effect to reduce the beam size at the extraction plane under a suitable emittance exchange condition [4]. The emittance exchange effect has already been successfully observed at SIS18 due to residual skew quadrupole components, described in [5]. It was executed by utilizing linear horizontal-vertical betatron coupling while the horizontal tune Q_x crosses the coupling resonance in a short time. The resonance in SIS18 is defined by $Q_x = Q_y + 1$. Tune-swept slow extraction measurement with transverse emittance exchange was performed using a $E = 300$ MeV/u Ar^{18+} coasting beam [6]. By performing emittance exchange, beam size at the extraction plane was reduced, and the improvement of the spill micro structure was found.

Essential beam instrumentation was used for different purposes in the slow extraction experiment utilizing emittance exchange: firstly, an Ionization Profile Monitor (IPM) [7] was used for the observation and measurement of the beam profiles during the transverse emittance exchange; secondly, a plastic scintillator [8] was used for particle counting while performing slow extraction; moreover, data acquisition systems were used to characterize the spill signals, including a scaler [9] and a fast Time-to-Digital Converter (TDC) [10].

This contribution will present the application example of the above-mentioned beam instrumentation used in the recent slow extraction investigation utilizing transverse emittance exchange. The experiment results concerning spill characterization and related simulations are discussed in detail.

MEASUREMENTS

Beam Profile

The online observation of the transverse emittance exchange effect is essential in the investigation and ensures the beam size condition for the following slow extraction.

During the emittance exchange process, tune crossing was executed by moving the horizontal tune from 4.17 to 4.2995 within 40 ms; meanwhile, the vertical tune was kept constant at 3.24. The resultant horizontal emittance reduction and vertical emittance increase were observed by the IPM [7], which is installed inside the SIS18 synchrotron ring for beam profile measurement. The profile readout period of the IPM is 10 ms. The signals from the detector within 50 µs were integrated and formed one profile data. By calculating the widths of beam profiles, beam size evolution along with the time in one acceleration cycle was obtained. The emittance exchange effect was evidently demonstrated in Fig. 1. It

* Jia.Yang@gsi.de

Content from this work may be used under the terms of the CC BY 4.0 licence (© 2022). Any distribution of this work must maintain attribution to the author(s), title of the work, publisher, and DOI

ISBN: 978-3-95450-241-7 ISSN: 2673-5350 doi:10.18429/JACoW-IBIC2022-TUP36

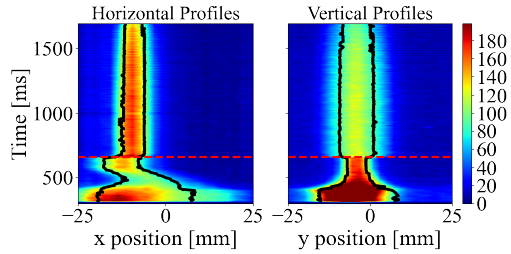


Figure 1: Beam size evolution at horizontal and vertical plane in one acceleration cycle when emittance exchange was executed. The black lines represent the standard deviation of the beam profiles with respect to the beam centers.

could be estimated that by utilizing transverse emittance exchange, the horizontal beam size (1σ) shrunk approximately from 4.9 mm to 3.1 mm, while the vertical beam size (1σ) increased approximately from 2.8 to 5.2 mm. The estimated horizontal RMS emittance reduced from 1.9 mm·mrad to 0.75 mm·mrad, while the vertical emittance increased from 1.04 mm·mrad to 3.37 mm·mrad. In addition, the time of the emittance exchange was around 660 ms (marked as a red dashed line) after the start of the acceleration cycle.

Spill Measurement

Detector and DAQs The choice of detectors to be used in the spill measurement depends on particle extraction rate and beam energy [1]. In this measurement, the extracted particles were counted by a plastic scintillator inside the transfer line with an extraction rate of up to several 10^6 particles per second [8]. The scintillator is made of BC400, with a square area of 75×75 mm^2 and a thickness of 1 mm. The advantages of the plastic scintillator are that single particle counting can be achieved, and there is no noise in the detected signals; therefore, the signal could be directly compared with simulations [11]. Particle signals were discriminated by the 300 MHz discriminator that connected to the scintillator [11].

There are two alternative data acquisition electronics systems to characterize the data. The counts from the discriminator were read out by either a scaler counting system with a minimum readout time of 10 µs [9] or TDC with the RMS time resolution of 35 ps per input channel [10]. Besides the information that the scaler counting system can provide, the TDC provides high-resolution time structure information, including the particles' arrival time with respect to the ring RF cavity frequency and particle interval distribution with respect to the subsequent particle. This information can be observed in an online display tool for operation and measurement, and can also be reconstructed from the recorded binary data using a TDC exporter with user-defined settings in offline data analysis [10].

Spill Time Structure from TDC In order to demonstrate the data information which could only be provided by the TDC, an example of a bunched beam slow extraction is given below. Figure 2 shows the particle interval distribution (a) and particle arrival distribution with respect to the ring RF cavity frequency (b) of the same spill. In this case, the displayed time structure was limited within the user-defined particle intervals range of 2 µs. Both subfigures' horizontal and vertical bin sizes are 1 ns and 0.05 s. In both subfigures, projections of 2-dimensional data were depicted in the left and upper side plots. In subfigure (a), the horizontal axis is the particle intervals, while in subfigure (b), it is the particle arrival time with respect to the ring RF cavity frequency; the vertical axes in both subfigures are the extraction time. The left projections in both subfigures show the total particle counts in a user-defined bin length along with the extraction time. Moreover, the top projections show the total distributions of particle arrival time with respect to the subsequent particle (a) or ring RF cavity frequency over the full extraction time (b).

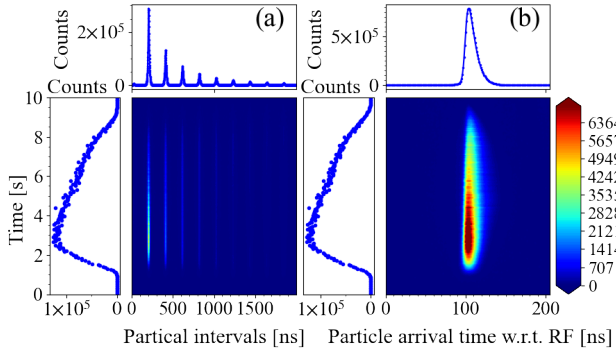


Figure 2: Particle interval distribution and particle arrival distribution of spills extracted in bunched beam slow extraction (RF voltage = 505 V).

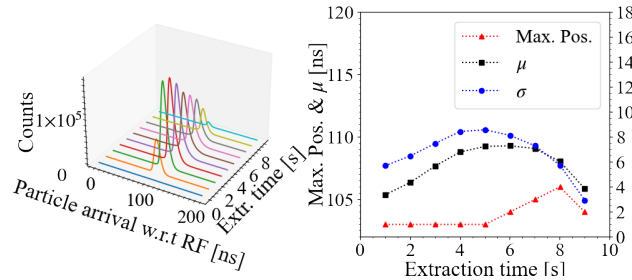


Figure 3: Time structures of spill slices in a bunched beam slow extraction (RF voltage = 505 V), obtained from TDC.

The time structures of the spills in different time slices during the extraction were also evaluated. The 3-dimensional plot of the particle arrival distributions of the same spill in 10 different time slices is shown in left subfigure of Fig. 3, while the right subfigure depicts the position of maximum counts, mean value and standard deviation of the corresponding distributions; for different spill slices, the position of the maximum, the center and the width of the particle arrival time with respect to the ring RF cavity frequency vary along the extraction time. The same evaluations were executed for the spills extracted with different RF voltages. Figure 4

Content from this work may be used under the terms of the CC BY 4.0 licence (© 2022). Any distribution of this work must maintain attribution to the author(s), title of the work, publisher, and DOI

ISBN: 978-3-95450-241-7 ISSN: 2673-5350 doi:10.18429/JACoW-IBIC2022-TUP36

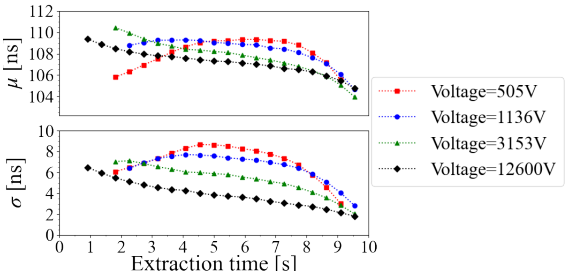


Figure 4: Comparison of the statistical moments of spill slices in bunched beam slow extractions with different RF voltages.

demonstrates the mean values and standard deviations of the particle arrival distributions of the spill slices from bunched beam slow extractions using different RF voltages: 505, 1136, 3153 and 12600 V. The time structures of the spills extracted with different RF voltages have different variation behaviors during extraction.

SPILL CHARACTERIZATION

The performant data acquisition system and data analysis tools offer evaluation for both the time and frequency domain. Details of spill characterization can be found in [1], definitions of time-dependent quantities such as standard deviation, duty factor, and maximum-average ratio were described. A higher duty factor and lower max-average ratio indicate better micro spill structure. The quality of the entire spill is characterized by weighted duty factors and weighted maximum-average ratios [12]. In this measurement, spill data was recorded using both data acquisition systems discussed in the previous section. Data obtained by the scaler system with the readout time of 21 μs was evaluated, and depicted in [6]. The statistical moments of every 500 data points were evaluated and formed one evaluation interval, equivalent to 10.5 ms in time. The improvement of the spill quality was found by using transverse emittance exchange.

TDC data The TDC system provides more information. As shown in Fig. 5 for the coasting beam slow extraction, particle interval distribution evolution of the spills extracted with (a) and without (b) utilizing emittance exchange were measured by using the TDC application. The horizontal and vertical bin sizes for both cases are 5 ns and 21 μs. Particle interval distributions in different time slices were evaluated as well, as shown in Fig. 6. The corresponding times were marked out in Fig. 5 with white dashed lines.

Spill quality characterization in terms of duty factor and spill particle interval distribution was executed. The TDC data was converted with a readout time of 21 μs for duty factor evaluation, the same as the scaler system settings of this measurement. The evaluation interval is 31.5 ms. Figure 7 depicts the time-dependent duty factor evaluations, which shows better spill micro structures in the second half of the spill extracted with emittance exchange. Weighted duty factors were evaluated to characterize the quality of the

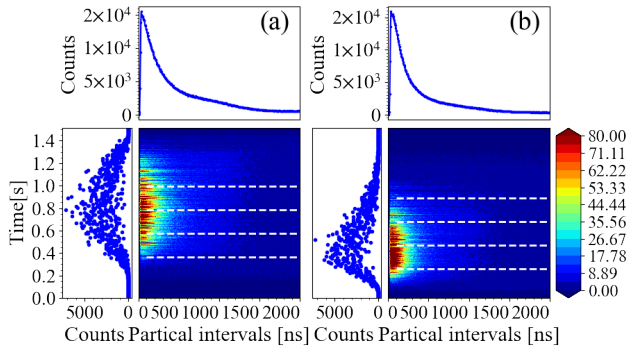


Figure 5: Particle interval distributions of spills extracted with (a) and without (b) transverse emittance exchange.

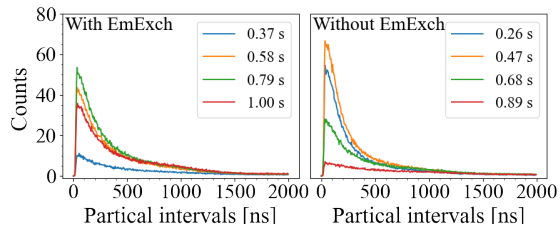


Figure 6: Particle interval distributions in different time slices of spills extracted with and without transverse emittance exchange.

entire spills for both cases. It increased from 0.49 to 0.64 after introducing the transverse emittance exchange.

The particle interval distributions in a selected extraction time window of 0.315 s duration in a high count rate region were evaluated and compared to their corresponding hypothetical Poisson distributions (dashed lines) calculated from the average count rate in the same time window length, shown in Fig. 8. The vertical axis is the counts normalized by the total spill counts in the selected duration; the mean particle intervals of the Poisson distributions for both cases were marked with corresponding colors. As depicted in the figure, a smaller distance between the particle interval distribution and its corresponding Poisson distribution suggests a smoother spill. The differences between measured particle interval distributions and corresponding Poisson distributions are consistent with the distances between the time-dependent duty factor evaluation results and corresponding Poisson distribution limits (shown in Fig. 7).

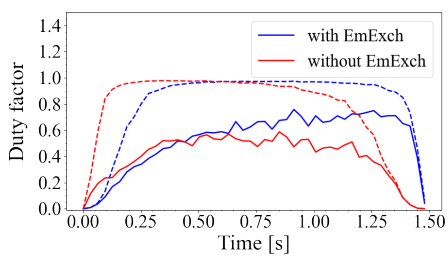


Figure 7: Comparison of measured time-dependent duty factors with corresponding Poisson limits (dashed lines) of spills obtained with and without emittance exchange.

Content from this work may be used under the terms of the CC BY 4.0 licence (© 2022). Any distribution of this work must maintain attribution to the author(s), title of the work, publisher, and DOI

ISBN: 978-3-95450-241-7 ISSN: 2673-5350 doi:10.18429/JACoW-IBIC2022-TUP36

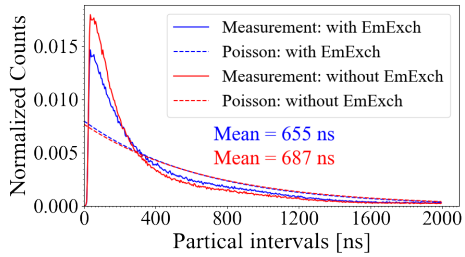


Figure 8: Comparison of measured particle interval distributions of spills in a selected extraction duration with corresponding hypothetical Poisson distributions obtained with and without emittance exchange.

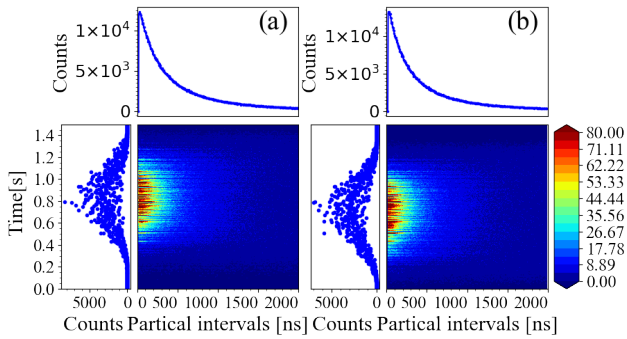


Figure 9: Simulated particle interval distributions of spills extracted with (a, beam size = 3.1 mm) and without (b, beam size = 4.9 mm) emittance exchange.

SIMULATION

The validity of the method for spill quality improvement by reducing the beam size on the extraction plane was verified by particle tracking simulations using the thin-lens tracking module in MAD-X [13] within the Python environment [14]. 1.2×10^6 particles with the kinetic energy of 300 MeV/u were tracked over 1354071 revolution turns for a 1.5 s extraction time. The momentum spread of the beam was set as 5×10^{-4} as the maximum length for Gaussian distribution truncated at $\pm 2\sigma$ [3]. Power supply ripples were introduced to quadrupoles as sine waves consisting of a few frequency components (50, 100,150, 300 and 600 Hz) with different ratios: 0.25, 0.3, 0.2, 0.3, 0.7; the amplitude of the ripples was normalized to 0.35 $\times 10^{-5}$. A bandwidth (0-20 kHz) limited white noise signal was applied. The parameters of the power supply ripples were adjusted to adapt to the measurement. Simulations for different horizontal beam sizes were executed with the same power supply ripples input, but the tune ramps were modified.

The particle interval distributions were constructed with the simulated particle tracking data, shown in Fig. 9. Particle intervals below 20 ns are ignored, corresponding to the dead time of the scintillator electronics. The comparison of the particle interval distributions in a selected extraction duration within a high count rate region with corresponding hypothetical Poisson distribution was shown in Fig. 10, the tendency of which is consistent with the measurement

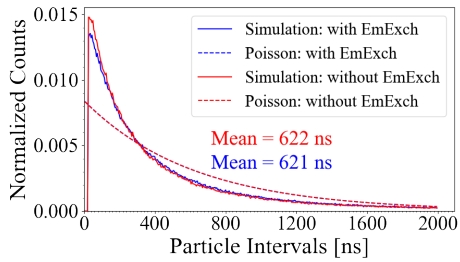


Figure 10: Comparison of simulated particle interval distributions of spills in a selected extraction duration with corresponding hypothetical Poisson distributions obtained with and without emittance exchange.

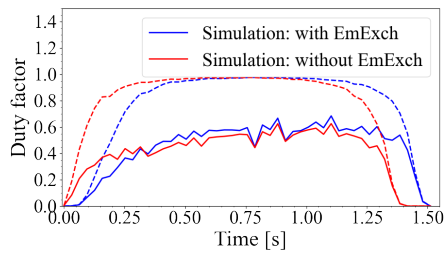


Figure 11: Comparison of simulated time-dependent duty factors with corresponding Poisson limits (dashed lines) of spills extracted with and without emittance exchange.

results shown in Fig. 8. Figure 11 shows the simulated time-dependent duty factor with an evaluation interval of 31.5 ms. The weighted duty factor of the spill extracted from the larger beam (0.51) is lower than it (0.56) from the smaller beam. Characterization of the simulated spills agrees with the measurement that a spill extracted from a horizontally narrower beam has a better micro spill structure.

CONCLUSION

This contribution presented the application of the beam instrumentation in the slow extraction measurement via transverse emittance exchange performed at SIS18. The beam instrumentation consists of Ionization Profile Monitor, Scintillator, and two data acquisition systems (scaler, fast Time-Digital-Converter) were used in the measurement. Analysis of the data acquired from TDC was discussed. Particle tracking simulations were performed to reproduce the measurement results obtained from TDC, and the TDC-like data were achieved in the simulation. Both experimental results and simulations agree with the fact that a horizontally narrow beam leads to a better spill micro structure.

ACKNOWLEDGEMENTS

The authors wish to thank SIS colleagues and the beam operation team at SIS18 for their great support in carrying out the measurement. Sajjad Hussain Mirza (DESY) and Rebecca Taylor (CERN) are acknowledged for discussions regarding MAD-X simulation. This project has received funding from the European Union's Horizon 2020 Research and Innovation programme under GA No 101004730.

Content from this work may be used under the terms of the CC BY 4.0 licence (© 2022). Any distribution of this work must maintain attribution to the author(s), title of the work, publisher, and DOI

ISBN: 978-3-95450-241-7 ISSN: 2673-5350 doi:10.18429/JACoW-IBIC2022-TUP36

Content from this work may be used under the terms of the CC BY 4.0 licence (© 2022). Any distribution of this work must maintain attribution to the author(s), title of the work, publisher, and DOI

REFERENCES

[1] R. Singh, P. Boutachkov, P. Forck, S. Sorge, and H. Welker, "Slow Extraction Spill Characterization From Micro to Milli-Second Scale", in *Proc. IPAC'18*, Vancouver, Canada, Apr.-May 2018, pp. 2095–2098. doi:10.18429/JACoW-IPAC2018-WEPAK007

[2] L. Badano *et al.*, "Proton-Ion Medical Machine Study (PIMMS), 1", CERN, Geneva, Switzerland, Rep. CERN/PS 99-010, 1999.

[3] S. Sorge, P. Forck, and R. Singh, "Measurements and Simulations of the Spill Quality of Slowly Extracted Beams from the SIS-18 Synchrotron", in *Proc. IPAC'18*, Vancouver, Canada, Apr.-May 2018, pp. 924–926. doi:10.18429/JACoW-IPAC2018-TUPAF081

[4] A. Franchi, E. Métral, and R. Tomás, "Emittance sharing and exchange driven by linear betatron coupling in circular accelerators", *Phys. Rev. ST Accel. Beams*, vol. 10, p. 064003, 2007. doi:10.1103/PhysRevSTAB.10.064003

[5] R. Singh, P. Forck, G. Franchetti, T. Giacomini, and P. Kowina, "Observation of dynamic transverse emittance exchange in SIS-18", GSI Helmholtzzentrum für Schwerionenforschung, Darmstadt, Germany, Rep. GSI Report 2015-1, p. 488. 2014. doi:10.15120/GR-2015-1-FG-SIS18-02

[6] J. Yang, P. Forck, T. Giacomini, P. J. Niedermayer, R. Singh, and S. Sorge, "Improvement of Spill Quality for Slowly Extracted Ions at GSI-SIS18 via Transverse Emittance Exchange", in *Proc. IPAC'22*, Bangkok, Thailand, Jun. 2022, pp. 2093–2095. doi:10.18429/JACoW-IPAC2022-WEPOTK021

[7] T. Giacomini, P. Forck, J. G. De Villiers, J. Dietrich, and D. A. Liakin, "Ionization Profile Monitors - IPM @ GSI", in *Proc. DIPAC'11*, Hamburg, Germany, May 2011, paper TUPD51, pp. 419–421.

[8] P. Forck, "Lecture Notes on Beam Instrumentation and Diagnostics", in *Joint University Accelerator School*, 2021, pp. 31–35.

[9] T. Hoffmann, P. Forck, D. A. Liakin, "New Spill Structure Analysis Tools for the VME Based Data Acquisition System ABLASS at GSI", *AIP Conf. Proc.*, vol. 868, p. 343, 2006. doi:10.1063/1.2401422

[10] T. Milosic, P. Forck, and R. Singh, "Sub-ns Single-Particle Spill Characterization for Slow Extraction", in *Proc. IBIC'21*, Pohang, Rep. of Korea, May 2021, pp. 438–442. doi:10.18429/JACoW-IBIC2021-WEPP28

[11] P. Forck *et al.*, "Measuement of the spill structure on a wide time range at GSI", in *Proc. ARIES Slow Extraction Workshop 2017*, CERN, Geneva, Switzerland, Nov. 2017.

[12] R. Singh, P. Forck and S. Sorge, "Reducing fluctuations in slow-extraction beam spill using transit-time-dependent tune modulation", *Phys. Rev. Appl.*, vol. 13, pp. 044076, 2020. doi:10.1103/PhysRevApplied.13.044076.

[13] W. Herr and F. Schmidt, "A MAD-X Primer", CERN, Geneva, Switzerland, Rep. CERN-AB-2004-027-ABP, 2004.

[14] K. Fuchsberger and Y. I. Levinsen, "PYMAD – Integration of MADX in PYTHON", in *Proc. IPAC'11*, San Sebastian, Spain, Sep. 2011, paper WEPC119, pp. 2289–2291.

ISBN: 978-3-95450-241-7 ISSN: 2673-5350 doi:10.18429/JACoW-IBIC2022-TUP38

DEEP NEURAL NETWORK FOR BEAM PROFILE CLASSIFICATION IN SYNCHROTRON

Michał Piekarski*,[1], NSRC SOLARIS, Jagiellonian University,
[1]also at AGH University of Science and Technology, Kraków, Poland

Abstract

The main goal of National Synchrotron Radiation Centre (NSRC) Solaris is to provide scientific community with high quality synchrotron light. To achieve this, it is necessary to constantly monitor many subsystems responsible for beam stability and to analyze data about the beam itself from various diagnostic beamlines. In this work a deep neural network for transverse beam profile classification is proposed. Main task of the system is to automatically assess and classify transverse beam profiles based solely on the evaluation of the beam image from the Pinhole diagnostic beamline at Solaris. At the present stage, a binary assignment of each profile is performed: stable beam operation or unstable beam operation / no beam. Base model architecture consists of a pre-trained convolutional neural network (CNN) followed by a densely-connected classifier and the system reaches accuracy at the level of 94.10%. The model and the results obtained so far are discussed, along with plans for future development.

INTRODUCTION

Solaris is a third generation light source (shown in Fig. 1) operating at the Jagiellonian University in Kraków, Poland [1]. This advanced and complex scientific infrastructure offers new highly innovative research opportunities for areas including physics, medicine and nanotechnology. Currently at Solaris five experimental beamlines offering various techniques, e.g.: photoemission electron microscopy, X-ray absorption spectroscopy, ultra angle-resolved photoemission spectroscopy or multi-scale X-ray and multimodal imaging, are available to the scientific community whereas another three are already at advanced level of construction and commissioning. Moreover, Solaris is also a National Cryo-EM Centre, with two latest generation cryo-electron microscopes enabling life science researchers to unravel life at the molecular level [2].

Synchrotron control system is large, distributed and controls hundreds of devices and reads measurement and diagnostic data out of thousands. Moreover, due to a complexity of physical phenomena that occurs during the operation i.e. electron injection, beam tuning and beam decay, it is often difficult to quickly determine the reason of beam instabilities or its lost. Manual inspection performed even by an experienced operator is not able to extract full information from hundreds of diagnostic signals, which carry a lot of important information about the state of the machine. The purpose of this work is to present a system that could help operators in detecting potential threats and, in the future, to serve as a tool for predicting anomalies, beam loss or equipment failure.



Figure 1: NSRC Solaris [3].

The use of artificial intelligence (AI) techniques, including machine learning and neural networks, for signal analysis, prediction or anomaly detection has a long history. As the accelerators serve as an interesting research area also here we observe a huge interest in the anomaly detection area where new methods are developed, validated and deployed to solve existing problems regarding the operation of synchrotron radiation systems. Classic neural networks or machine learning frameworks take advantage of archived data of beam position in the storage ring in order to determine the appropriate orbit correction to minimize the proposed cost function [4, 5]. The problem of anomaly detection and failure prediction in the accelerator control systems has also been discussed during the ICALEPCS or IBIC conferences and different approaches has been proposed [6, 7]. Finally, various applications of artificial intelligence based systems has been identified in the fields like beam stabilization, autonomous operation, optimisation and performance improvements [8–10]. Since there is such a high demand on a precise and reliable AI-based systems I propose a deep neural network (DNN) for transverse beam profile classification as a support tool for operators.

BEAM PROFILE CLASSIFICATION SYSTEM

In this section a transverse beam profile classification model based on deep, convolutional neural network is presented. Main idea behind it is to use Pinhole diagnostic beamline beam profiles and employ transfer learning methods to build suited classifier on top of the pre-trained architecture.

* michal.piekarski@uj.edu.pl, piekarski@agh.edu.pl

Content from this work may be used under the terms of the CC BY 4.0 licence (© 2022). Any distribution of this work must maintain attribution to the author(s), title of the work, publisher, and DOI

ISBN: 978-3-95450-241-7 ISSN: 2673-5350 doi:10.18429/JACoW-IBIC2022-TUP38

Content from this work may be used under the terms of the CC BY 4.0 licence (© 2022). Any distribution of this work must maintain attribution to the author(s), title of the work, publisher, and DOI

Deep Neural Networks

Deep neural networks have become very popular, resulting in their appearance in many applications and models. It is an attempt to map to some extent the activity of the human brain. Neural networks quickly proved to be effective in solving problems that typical programs or algorithms do not cope with or become too complicated to use. An important feature of the networks is that the they are effective even if the creator of the network himself does not quite know the algorithm that could solve the problem. Only knowledge of the problem and the appropriate selection of parameters and architecture are required. This greatly expands the possibilities of using such models for practical cases. The neural networks after proper training are able to learn a certain process and detect a moment of anomaly or deviation from the norm. The key to success in this case is having sufficiently large retrospective data that can be used to show examples of relationships and correlations.

Convolutional neural networks, which are subset of deep neural networks, proved to be successful in classification and recognition tasks. The convolution operation in terms of image processing is a filtering process. A filter (convolution mask) is moved through the image and the sum of products of the corresponding values is calculated. Parameters are usually the window (mask) size and the number of pixels by which the mask moves in each step. The goal of the first convolution layers is to reveal general image features such as edges and simplest shapes. Those deeper ones can already indicate whole shapes and high-level features.

Transfer Learning

Deep neural network models require not only computational resources but also huge amount of training, validation and testing data in order to tune all parameters well which is the main limitation in building deep networks from scratch Moreover, sometimes an experiment cannot be repeated or data gathering can be dangerous or very expensive so often scientists end up with a limited amount of data. While observing the ability of DNN to generalize on big datasets one of the possibilities is to use transfer learning. Its main idea is to share base model of a neural network, build only classifier on top of it and by this architecture solve similar issue [11].

The decision of choosing the transfer-learning strategy has been done based on the amount of data in the dataset. I have also decided to use the soft fine-tuning strategy. Main idea is to unlock some of the layers of base model and train both new classifier on top and those few layers (original weights are used as a starting point). This method can improve models' performance by tuning architecture to its new task. Taking into account that the pre-trained model has been well trained on a huge database I kept a small learning rate (only for the classifier) to ensure that I don't distort the CNN weights too much.

Proposed Beam Profile Classification Solution

The main purpose of the proposed solution is automatically assess and classify transverse beam profiles based only on the evaluation of the beam image from the Pinhole diagnostic beamline. Due to the complexity of the operation, Solaris has a distributed control system that gathers diagnostic signals from thousands of devices, processes them and finally controls many setpoints and moving elements. Measurement data from most devices are read and archived using dedicated archiving system. Different kind of signals (scalars, 1D or 2D) are stored in the database and are easily accessible for further analysis and comparison.

For the emittance and beam size monitoring and measurements Pinhole diagnostic beamline has been setup. It is based on X-ray radiation extracted from the dipole through a diamond window, a pinhole cross down to the scintillator crystal where is converted to the visible light. The optical light from scintillator is imaged by a CCD camera [12]. Overview of the Pinhole beamline has been shown in Fig. 2. The Pinhole beamline allows for online monitoring of the transverse beam profile and the emittance thus beam stability during electron beam decay. Example of data extracted from this diagnostic beamlie at Solaris has been shown in Fig. 3.

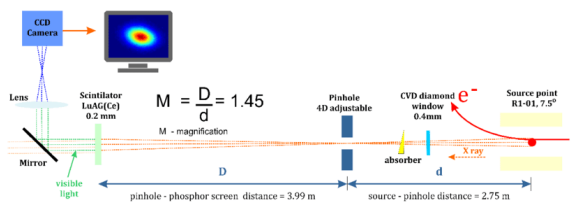
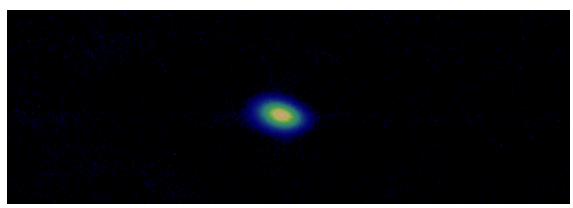
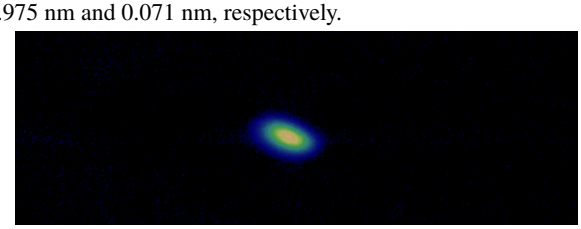


Figure 2: The Pinhole diagnostic beamline [12].



(a) High beam quality, horizontal and vertical emmitances are 9.975 nm and 0.071 nm, respectively.



(b) Low beam quality, horizontal and vertical emmitances are 15.047 nm and 0.093 nm, respectively.

Figure 3: Example images taken by the Pinhole diagnostic beamline in Solaris Radiation Centre.

Database for this research has been created from scratch, gathering raw transverse beam profiles from the CCD camera

ISBN: 978-3-95450-241-7 ISSN: 2673-5350 doi:10.18429/JACoW-IBIC2022-TUP38

as well as both vertical and horizontal emmitances. Following with the Solaris archiving standards and requirements, data were collected with a period of 3 s. Presented architecture has been trained using nearly 137000 Pinhole images and the corresponding emittance values. As the emittance is an important property of the beam, directly determining its quality and stability it was used to label the dataset by thresholding both horizontal and vertical emittances. Good quality beam threshold values were determined empirically and are: [5 nm, 11 nm] and [0.05 nm, 0.08 nm] for horizontal and vertical emittances, respectively. Finally, image is considered as anomaly if the emittance values go beyond the specified range in both planes simultaneously.

Architecture for Pinhole diagnostic images evaluation has been created in soft fine-tuning strategy using InceptionV3 as a base model. To achieve better performance, apart from the classifier, last three layers of the base network have been unfrozen and subjected to training. The system operation diagram has been presented in Fig. 4.

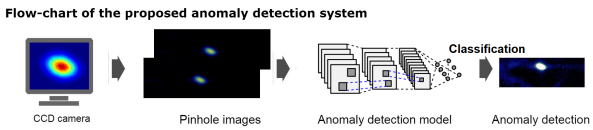


Figure 4: The streamline of proposed neural network based framework.

In the proposed system, the classifier has been created specifically for the problem of recognizing two classes: correct and not correct beam shape. It consists of three layers. The first is the Fully-Connected layer with ReLU activation function, the next is the Dropout layer and the classifier finishes the Fully-Connected output layer with two outputs and the Softmax activation function. At each of these outputs, the network calculates the probability that the input image is an anomaly or is correct. Hyperparametes setting for the proposed system has been shown in Table 1.

Table 1: Overview of the Hyperparameters Settings for the Proposed CNN Model

Parameters	InceptionV3
Topological depth	189
Input shape	134, 390, 3
Dropout rate	0.2
Epochs	50
Loss function	Categorical cross-entropy
Metrics	Accuracy
Fine-tuning	Last three conv-layers
Optimizer	Adam

Tests and Results

At the stage of preparation and initial data processing, two datasets have been obtained: training and validation. They come from completely different periods of time, which ensures the reliability of the results obtained in tests. Accuracy of the proposed system is 95.20% and 94.10% for those datasets respectively, which shows that the network classifies images very well. Moreover, it can also be concluded that the system was not overfitted. For further evaluation of the model, confusion matrix was created (see Table 2). The system should have as many classifications as possible on the diagonal of the confusion matrix (correct classification), and when there is a mistake it should be FP (false positive) type. It means that it is a false alarm which can be easily verified by duty operator.

Table 2: Confusion Matrix

Actual class	Predicted class	
	positive	negative
positive	62037	3559
negative	6574	100592

CONCLUSION AND FUTURE WORK

The paper presents the design of deep neural network based system for transverse beam profile classification. It was inspired by earlier research conducted using various machine learning and deep learning techniques in accelerators. It has been proved that using deep neural network based systems can achieve high accuracy in electron beam quality assessment. What is worth emphasizing is a fact that it can be done based directly from raw Pinhole image without having to calculate any physical beam parameters. Such a system could certainly serve as a support for the Operators giving valuable information on the current machine performance.

The system has great development potential. The next stage will be real time Pinhole image capturing and their classification. Further modifications may include extending the number of classes to find more meaningful and potentially useful beam states for the Operators and to include the Solaris' state machine.

ACKNOWLEDGEMENTS

The presented work has been achieved in collaboration with AGH University of Science and Technology in Kraków as a part of a PhD thesis.

REFERENCES

[1] A. I. Wawrzyniak *et al.*, "Solaris a new class of low energy and high brightness light source", *Nucl. Instrum. Methods Phys. Res., Sect. B*, vol. 411, pp. 4–11, 2017. doi:10.1016/j.nimb.2016.12.046

[2] A. I. Wawrzyniak, R. Panaś, A. Curcio, M. Knafel, G. Kowalski, and A. Marendziak, "Solaris synchrotron performance and operational status", *Nucl. Instrum. Methods Phys. Res., Sect. B*, vol. 493, pp. 19-27, 2021. doi:10.1016/j.nimb.2021.01.020

[3] SOLARIS website, https://synchrotron.uj.edu.pl

Content from this work may be used under the terms of the CC BY 4.0 licence (© 2022). Any distribution of this work must maintain attribution to the author(s), title of the work, publisher, and DOI

ISBN: 978-3-95450-241-7 ISSN: 2673-5350 doi:10.18429/JACoW-IBIC2022-TUP38

Content from this work may be used under the terms of the CC BY 4.0 licence (© 2022). Any distribution of this work must maintain attribution to the author(s), title of the work, publisher, and DOI

[4] E. Meier, G. LeBlanc, and Y. E. Tan, "Orbit Correction Studies using Neural Networks", in *Proc. IPAC'12*, New Orleans, LA, USA, May 2012, paper WEPPP057, pp. 2837–2839.

[5] J. P. Edelen, K. Bruhwiler, E. G. Carlin, C. C. Hall, K. A. Brown, and V. Schoefer, "Machine Learning Based Tuning and Diagnostics for the ATR Line at BNL", in *Proc. ICALEPCS'21*, Shanghai, China, Oct. 2021, pp. 803–808. doi:10.18429/JACoW-ICALEPCS2021-THAL04

[6] F. M. Tilaro, B. Bradu, M. Gonzalez-Berges, F. Varela, and M. Roshchin, "Model Learning Algorithms for Anomaly Detection in CERN Control Systems", in *Proc. ICALEPCS'17*, Barcelona, Spain, Oct. 2017, pp. 265–271. doi:10.18429/JACoW-ICALEPCS2017-TUCPA04

[7] M. Reščič, W. Blokland, and R. Seviour, "Using Machine Learning Tools to Predict Accelerator Failure", presented at IBIC'20, Santos, Brazil, Sep. 2020, paper THAO02, unpublished.

[8] L. Vera Ramiréz *et al.*, "Machine Learning Tools Improve BESSY II Operation", in *Proc. ICALEPCS'21*, Shanghai, China, Oct. 2021, pp. 784–790. doi:10.18429/JACoW-ICALEPCS2021-THAL01

[9] S. Pioli *et al.*, "Machine Learning Based Middle-Layer for Autonomous Accelerator Operation and Control", in *Proc. ICALEPCS'21*, Shanghai, China, Oct. 2021, pp. 797–802. doi:10.18429/JACoW-ICALEPCS2021-THAL03

[10] S. C. Leemann, "Machine Learning-based Beam Size Stabilization", presented at the 9th Int. Beam Instrum. Conf. (IBIC'20), Santos, Brazil, Sep. 2020, paper THAO01, unpublished.

[11] P.-H. E. Su and Li Yingzhen, "Transfer learning", https://citeseerx.ist.psu.edu/viewdoc/download?doi=10.1.1.715.3906\&rep=rep1\&type=pdf

[12] A. Kisiel, A. M. Marendziak, M. Ptaszkiewicz, and A. I. Wawrzyniak, "X-ray Pinhole Camera for Emittance Measurements in Solaris Storage Ring", in *Proc. IPAC'19*, Melbourne, Australia, May 2019, pp. 3084–3087. doi:10.18429/JACoW-IPAC2019-WEPRB116

ISBN: 978-3-95450-241-7 ISSN: 2673-5350 doi:10.18429/JACoW-IBIC2022-TUP39

NEURAL NETWORK INVERSE MODELS FOR IMPLICIT OPTICS TUNING IN THE AGS TO RHIC TRANSFER LINE

J. P. Edelen, N. M. Cook, J. Einstein-Curtis, RadiaSoft LLC, Boulder, CO, USA
K. A. Brown, V. Schoefer, BNL, Upton, NY, USA

Abstract

One of the fundamental challenges of using machine-learning-based inverse models for optics tuning in accelerators, particularly transfer lines, is the degenerate nature of the magnet settings and beam envelope functions. Moreover, it is challenging, if not impossible, to train a neural network to compute correct quadrupole settings from a given set of measurements due to the limited number of diagnostics available in operational beamlines. However, models that relate BPM readings to corrector settings are more forgiving, and have seen significant success as a benchmark for machine learning inverse models. We recently demonstrated that when comparing predicted corrector settings to actual corrector settings from a BPM inverse model, the model error can be related to errors in quadrupole settings. In this paper, we expand on that effort by incorporating inverse model errors as an optimization tool to correct for optics errors in a beamline. We present a toy model using a FODO lattice and then demonstrate the use of this technique for optics corrections in the AGS to RHIC transfer line at BNL.

INTRODUCTION

Machine learning (ML) has seen a significant growth in its adoption for widespread applications. In particle accelerators, ML has been identified as having the potential for significant impact on modeling, operation, and controls [1, 2]. These techniques are attractive due to their ability to model nonlinear behavior, interpolate on complicated surfaces, and adapt to system changes over time. This has led to a number of dedicated efforts to apply ML, and early efforts have shown promise.

For example, neural networks (NNs) have been used as surrogates for traditional accelerator diagnostics to generate non-interceptive predictions of beam parameters [3, 4] or for a range of machine tuning problems utilizing inverse models [5]. When used in conjunction with optimization algorithms, neural networks have demonstrated improved switching times between operational configurations [6]. Neural network surrogate models have also been demonstrated to significantly speed up multi-objective optimization of accelerators [7]. Additionally, ML has been of interest for anomaly detection for root cause analysis [8] and for outlier detection, using large data-sets of known good operational states [9], using autoencoders.

In this work we seek to apply ML methods — for both tuning and anomaly detection — on the AGS to RHIC transfer line at Brookhaven National Laboratory. Specifically, we employ the use of inverse models for these applications. The application of inverse models for anomaly detection is a burgeoning area of research in many other fields that has not seen much attention in particle accelerators. Here we present our work towards implementing inverse models to detect errors in quadrupoles using only beam position monitors and corrector data. We will demonstrate the utility of this approach using a toy model, and then show how it scales to a larger system such as the AGS to RHIC transfer line. We will then show results of training inverse models using data from the machine and discuss future work for this effort.

FODO BENCHMARK

Before applying our technique to the ATR line, we first demonstrate the efficacy of our technique using a toy problem. Here we consider a linear system comprised of two quadrupoles, four beam position monitors and two correctors that operate in both the horizontal and vertical plane. The training data consisted of 5000 examples simulated by randomly changing corrector strength and the initial beam position. The model was trained to predict the corrector setting for a given set of BPM readings. The network architecture was optimized as a function of the number of layers as well as the nodes per layer to improve training loss without over-fitting. Figure 1 shows the model prediction compared to the ground truth for each of the correctors (kickers). The relationship is almost perfectly linear in all cases, indicating the model is well trained.

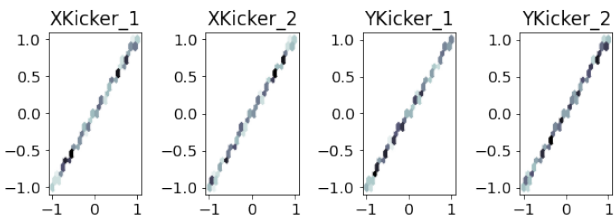


Figure 1: Real corrector setting on the x-axis with inverse model output result on the y-axis. The plots show a well-trained inverse model.

To evaluate the neural network against standard linear model benchmarks, we trained a linear model using the same data as the neural network. We also introduced different sextupole strengths to the lattice in order to understand the impact of a simple nonlinearity on the system. The linear model was compared to the neural network model for each case. Figure 2 shows the RMS prediction error on the test data for each of the correctors and the aggregate error which is computed as the sum of the squares of the individual corrector errors.

Content from this work may be used under the terms of the CC BY 4.0 licence (© 2022). Any distribution of this work must maintain attribution to the author(s), title of the work, publisher, and DOI

ISBN: 978-3-95450-241-7 ISSN: 2673-5350 doi:10.18429/JACoW-IBIC2022-TUP39

Content from this work may be used under the terms of the CC BY 4.0 licence (© 2022). Any distribution of this work must maintain attribution to the author(s), title of the work, publisher, and DOI

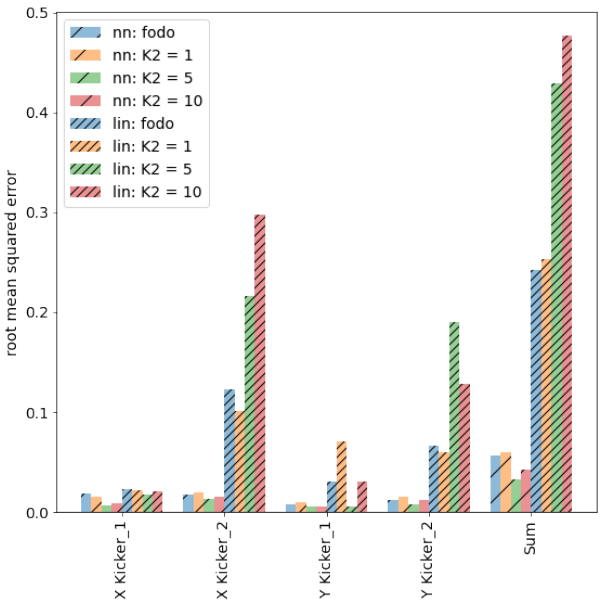


Figure 2: RMS prediction error for kickers in the FODO and nonlinear system based on model type and nonlinearity strength.

We see that the neural network does a better job at predicting the corrector settings even for the linear model case. There is also a weak improvement in the model prediction for the lattice with a sextupole component. This gives a good indication that the neural network will be a better solution in general even for the linear case.

Next we tested the model using data with systematically introduced errors in individual quadrupoles. We ran the MAD-X simulations with random corrector strengths and initial beam positions for a fixed quadrupole strength error. We then compared the predicted corrector settings to the actual corrector settings as we varied the quadrupole error. Figure 3 shows the model error as a function of both the quadrupole strengths being varied. Here we see a well-defined minima around the nominal lattice configuration, which is a quadrupole error of unity.

ATR STUDIES

Next we applied this concept to the UW line in the ATR. The problem is a bit more complex as there are now not just quadrupoles, correctors, and BPMs, but also combined function bends and vertical bends. Moreover there are comparatively few BPMs and correctors — only 26 and 14 respectively — making the model more subject to degeneracies. This combined with the 19 quadrupoles significantly increases the complexity of the problem space.

We trained the inverse model using 5000 samples, randomly varying the corrector strengths and beam initial positions. During our initial training of the inverse model four correctors (utv4, uth6, utv7, and wth1) were not well fit. In future work we will address this issue, however, for studies presented here we simply removed those four correctors

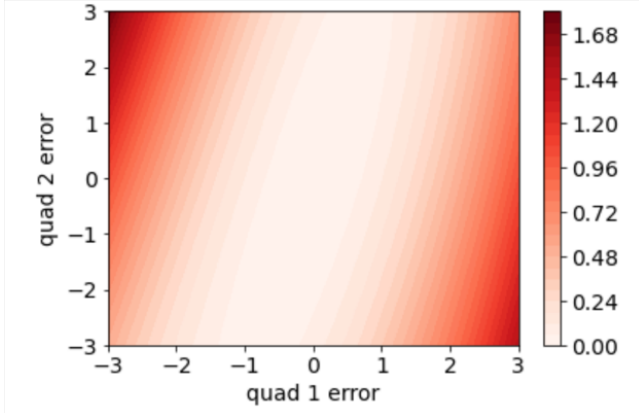


Figure 3: Model error as a function of quadrupole strength error as we vary both quads in the FODO cell.

from the prediction. For the correctors we did include we see very good agreement between the model prediction and the ground truth. We then included single quadrupole errors to evaluate the feasibility of detecting such an error with the inverse model. Figure 4 shows the predicted corrector settings vs the ground truth for three cases. Black is the beamline without any quadrupole errors. Blue is the beamline with a single quadrupole excitation error of negative 20%. Red is the same quadrupole error as blue but with a positive 20% excitation. Here we can clearly see the model can detect the error and even can pinpoint the location of the quadrupole error.

For tuning it is important to understand how the model error varies as each quadurpole magnet is changed. Figure 5 shows the model error as a function of quadrupole strength for six of the magnets in the beamline. Here we can clearly see that the model has very different sensitivities to different magnets. Moreover the model error is not always centered around the nominal excitation. To address this we consider the use of ensemble methods.

ENSEMBLE METHODS

Ensemble methods allow one to generate an aggregate prediction when individual models don't perform as well. This is especially helpful when the model is less sensitive to the particular quadrupole error. Figure 6 shows the model error as a function of quadrupole strength for an ensemble of 25 models. Each model is trained on the same data, however, random initializations are used for the weights.

When we aggregate the output of these models we see a clear improvement in the model error as a function of quadrupole strength. Figure 6 shows the median and the mean error of the ensemble predictions as a function of quadrupole strength. Note that the a quadrupole strength of zero is no error in the quadrupole setting. Compared with Fig. 5, the curves that were not centered around the correct quadrupole excitation are now behaving correctly. While the relationship between model error and quadrupole excitation is not the same strength along the beamline, this approach

ISBN: 978-3-95450-241-7 ISSN: 2673-5350 doi:10.18429/JACoW-IBIC2022-TUP39

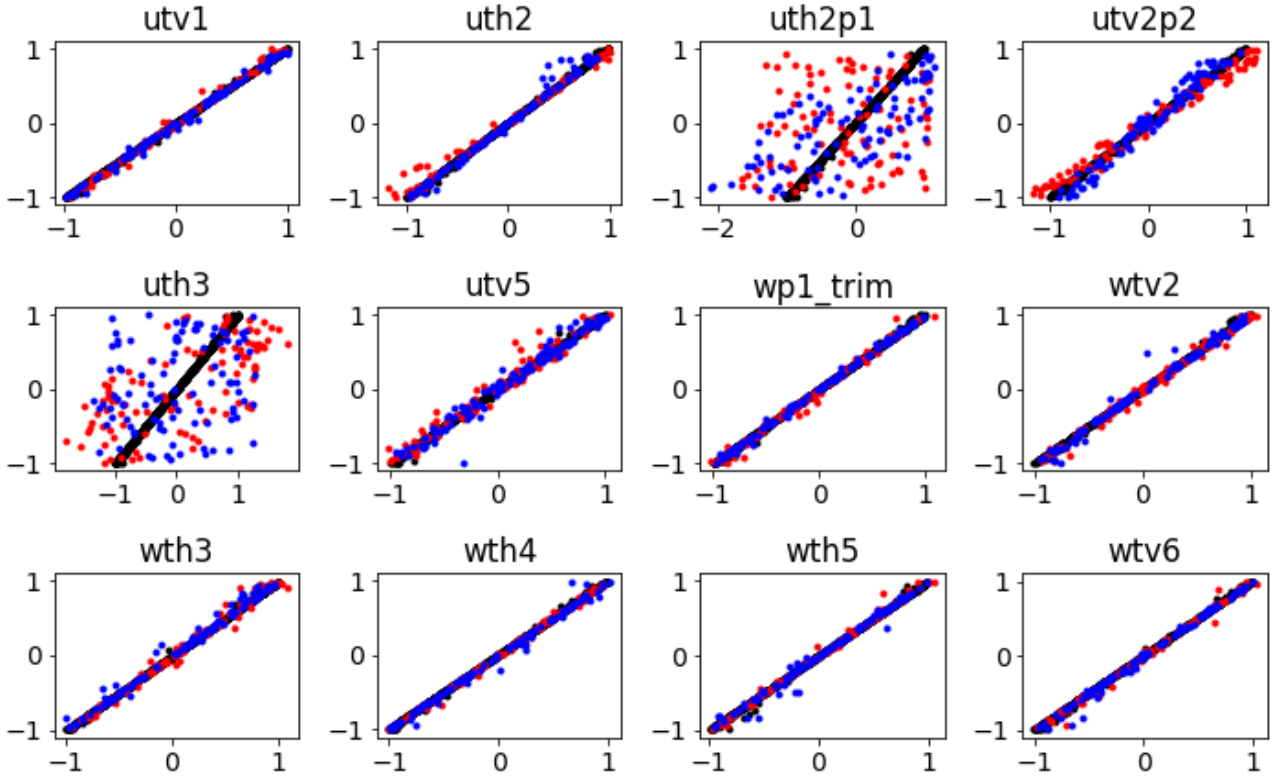


Figure 4: Black: model prediction vs ground truth with no quadrupole errors. Blue: model prediction vs ground truth for a negative 20% quadrupole error. Red: model prediction vs ground truth for a positive 20% quadrupole error.

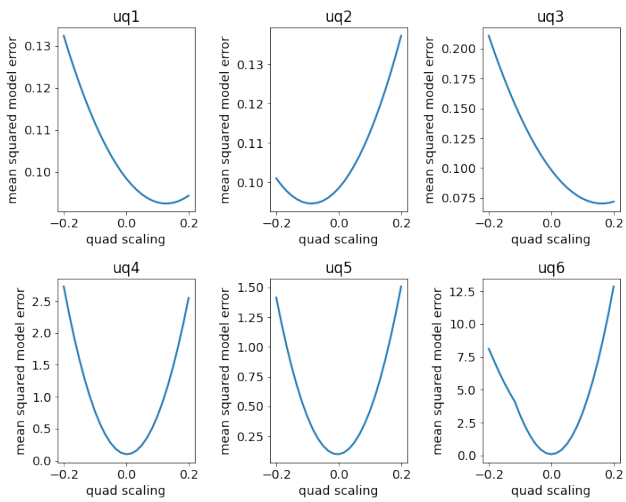


Figure 5: Model error as a function of quadrupole strength for six of the magnets.

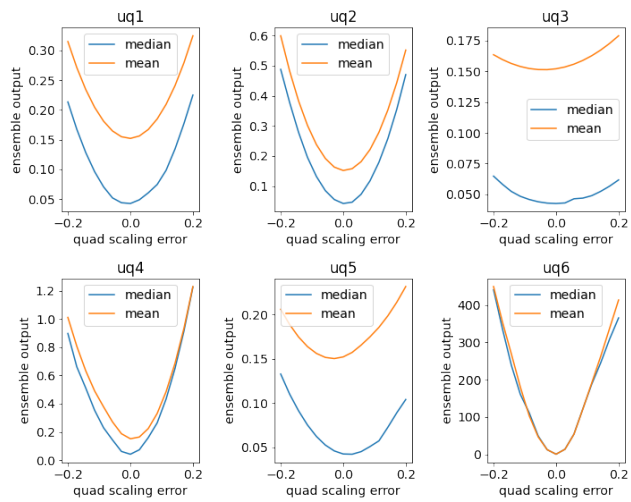


Figure 6: Model error as a function of the quadrupole excitation strength for six of the quadrupoles. Here we show the median and mean output of the ensemble.

demonstrates that an ensemble can improve the performance of the inverse model method.

Another advantage of the ensemble method is gaining uncertainty information. This is important when using the method as a diagnostic as the uncertainty in the diagnostic is an important consideration for operations. Figure 7 shows the ensemble output with the uncertainty (standard deviation in the ensemble) as the shaded region.

There is a clear correlation between the quadrupoles with high uncertainty and the quadrupoles that didn't have a good correlation between the model error and the quadrupole errors in Fig. 5.

Content from this work may be used under the terms of the CC BY 4.0 licence (© 2022). Any distribution of this work must maintain attribution to the author(s), title of the work, publisher, and DOI

ISBN: 978-3-95450-241-7 ISSN: 2673-5350 doi:10.18429/JACoW-IBIC2022-TUP39

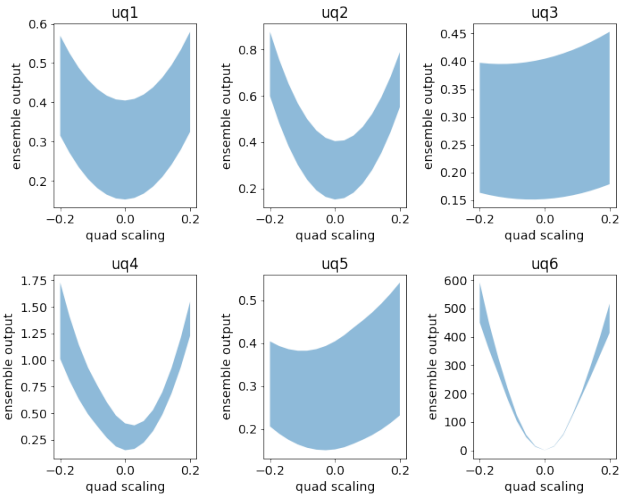


Figure 7: Model error as a function of the quadrupole strength for six of the quadrupoles. Here we show the ensemble mean and the variance.

CONCLUSIONS

In this paper we have refined the use of a neural network inverse model to detect quadrupole strength errors when trained on bpm and corrector data for a nominal setup. This method can be used as a diagnostic or for model-based tuning. We also show the use of ensemble methods to improve the quality of the model prediction; additionally, ensemble methods can provide a rudimentary uncertainty metric. We are continuing to refine our techniques in addition applying our technique to measured data collected during this period of performance.

ACKNOWLEDGEMENTS

This material is based upon work supported by the U.S. Department of Energy, Office of Science, Office of Nuclear Physics under Award Number DE-SC0019682

REFERENCES

[1] A. L. Edelen, S. Biedron, B. Chase, D. Edstrom, S. Milton, and P. Stabile, "Neural networks for modeling and control of particle accelerators," *IEEE Trans. Nucl. Sci.*, vol. 63, no. 2, pp. 878–897, 2016. doi:10.1109/TNS.2016.2543203

[2] A. Edelen *et al.*, "Opportunities in machine learning for particle accelerators," 2018. doi:10.48550/arXiv.1811.03172

[3] C. Emma, A. Edelen, M. Hogan, B. O'Shea, G. White, and V. Yakimenko, "Machine learning-based longitudinal phase space prediction of particle accelerators," *Phys. Rev. Accel. Beams*, vol. 21, no. 11, p. 112 802, 2018. doi:10.1103/PhysRevAccelBeams.21.112802

[4] A. Edelen, S. Biedron, S. Milton, and J. Edelen, "First steps toward incorporating image based diagnostics into particle accelerator control systems using convolutional neural networks," 2016. doi:10.48550/arXiv.1612.05662

[5] A. L. Edelen, S. Biedron, S. V. Milton, and P. J. M. van der Slot, "Using A Neural Network Control Policy For Rapid Switching Between Beam Parameters in an FEL," in *Proc. FEL'17*, Santa Fe, NM, USA, Aug. 2017, pp. 488–491. doi:10.18429/JACoW-FEL2017-WEP031

[6] A. Scheinker, A. Edelen, D. Bohler, C. Emma, and A. Lutman, "Demonstration of model-independent control of the longitudinal phase space of electron beams in the linac-coherent light source with femtosecond resolution," *Phys. Rev. Lett.*, vol. 121, no. 4, p. 044 801, 2018. doi:10.1103/PhysRevLett.121.044801

[7] A. Edelen, N. Neveu, M. Frey, Y. Huber, C. Mayes, and A. Adelmann, "Machine learning for orders of magnitude speedup in multiobjective optimization of particle accelerator systems," *Phys. Rev. Accel. Beams*, vol. 23, no. 4, p. 044 601, 2020. doi:10.1103/PhysRevAccelBeams.23.044601

[8] J. P. Edelen and C. C. Hall, "Autoencoder based analysis of rf parameters in the fermilab low energy linac," *Information*, vol. 12, no. 6, p. 238, 2021. doi:10.3390/info12060238

[9] J. P. Edelen and N. M. Cook, "Anomaly detection in particle accelerators using autoencoders," 2021. doi:10.48550/arXiv.2112.07793

Content from this work may be used under the terms of the CC BY 4.0 licence (© 2022). Any distribution of this work must maintain attribution to the author(s), title of the work, publisher, and DOI

ISBN: 978-3-95450-241-7 ISSN: 2673-5350 doi:10.18429/JACoW-IBIC2022-TUP40

PHOTON POLARIZATION SWITCH AT ALBA

L. Torino*, G. Benedetti, F. Fernández, U. Iriso, Z. Martí, J. Moldes, D. Yepez
ALBA-CELLS, Cerdanyola del Vallès, Spain

Abstract

The polarization of the synchrotron radiation produced by a bending magnet can be selected by properly choosing the vertical emission angle. At beamlines this can be done by moving a slit to block unwanted polarization: this method is time consuming and not very reproducible. Another option is to fix the slit position, generate a local bump with the electron beam, and vary the emission angle at the source point such that the sample is illuminated with the desired polarization. At ALBA, we have implemented this option within the Fast Orbit Feedback, which allows to perform the angle switch in less than one minute without affecting other beamlines. This report describes the implementation of this technique for the dipole beamline MISTRAL at the ALBA Synchrotron.

INTRODUCTION

Some experimental techniques, such as imaging in the magnetic domain, take great advantage from using different polarizations of synchrotron radiation. At ALBA, the MISTRAL beamline is devoted to these technique and a fast and reliable polarization selection mechanism is demanded.

The polarization of the synchrotron radiation produced by a bending magnet is distributed as a function of the emission angle, as depicted in Fig. 1. Until last year, polarization was

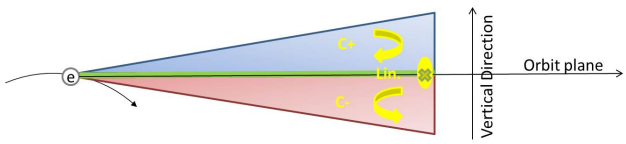


Figure 1: Synchrotron radiation produced by an electron beam passing through a bending magnet: the polarization is different according to the emission angle (C+: Circular Positive, C-: Circular Negative, Lin.: Linear).

selected by means of movable slits. This process works fine but creates problem of optics stability related with heat-load of components: when changing the mask position, a different part of the optics is enlightened and time for thermalisation is needed for thermal stabilization. Moreover, since the radiation follows a different optical path, the sample location also had to be adjusted, making the process unpractical and time consuming.

Another approach, already experimented at PSI [1], is to generate bumps with the electron beam. Doing this the radiation follows always the same optical path, and the desired polarization can be selected without varying the position of the slit.

* ltorino@cells.es

At ALBA, we decided to implement the Polarization Switch for the MISTRAL beamline within the Fast Orbit FeedBack (FOFB) architecture.

SWITCHING MECHANISM

In order to switch the polarization of synchrotron radiation, the idea is to create bumps at the MISTRAL source point so to locally change the direction of the orbit plane. In this way, when switching polarization, the position of the electron beam is kept while the angle changes, allowing to select a different polarization. Figure 2 shows the bump necessary to obtain positive and negative circular polarization.

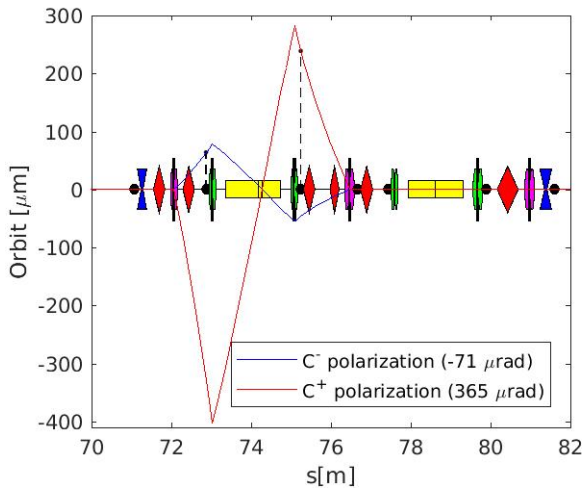


Figure 2: Bump to select different polarization at MISTRAL source point: negative polarization in blue, positive polarization in red. The dashed line represents the position of BPMs involved in the bump. The asymmetry is due to the initial alignment of the beamline.

At ALBA, before the switching mechanism was implemented, it was not possible to generate such a bump during normal operation since a FOFB system is running to keep the distortion with respect to to the golden orbit lower than 1 µm RMS.

At the beginning, the choice of not changing the FOFB code was taken, and thus an online modification to the golden orbit was discarded. The other option was then to displace offsets of BPMs involved in the bump to "trick" the FOFB system to actually produce it.

The formula to obtain the beam position x from a BPM button is:

$$x = k_x \frac{\Delta}{\Sigma} - \delta x$$

Content from this work may be used under the terms of the CC BY 4.0 licence (© 2022). Any distribution of this work must maintain attribution to the author(s), title of the work, publisher, and DOI

ISBN: 978-3-95450-241-7 ISSN: 2673-5350 doi:10.18429/JACoW-IBIC2022-TUP40

Content from this work may be used under the terms of the CC BY 4.0 licence (© 2022). Any distribution of this work must maintain attribution to the author(s), title of the work, publisher, and DOI

where k_x is the BPM sensitivity and $\frac{\Delta}{\Sigma}$ depends on the real position of the beam within the buttons. δx is the BPM offset that takes into account mechanical imperfection of BPM blocks and defects related with the electronics. The offset is obtained by Beam Based Alignment [2] and it is usually fixed unless any change in the electronics occurs.

The FOFB ensures that x is always as close as possible to the ideal beam position provided by the golden orbit within 1 µm RMS. An offset variation (δx) with the FOFB running would then produce a real displacement of the beam. Producing a synchronous offset variation in two BPMs, one before and one after the source point, generates the bump.

ALBA FOFB

ALBA FOFB system is a distributed system based on Diamond Communication Controller (for BPMs) and PSI protocol (for power supplies) working at 5 kHz and dumping frequencies up to 100 Hz [3–5].

At a glance, it is composed of 88 BPMs and correctors in the horizontal plane and 87 BPMs + 1 XBPM and 88 correctors in the vertical plane. For each of the 16 ALBA sectors, data from 7 or 8 BPMs are collected and treated by a FOFB processing node which also controls correctors power supplies.

Libera Brilliance electronics are used for BPM data treatment and a Libera Photon is used for the X-BPM [6]. Horizontal and vertical position is then collected to the processing node via an FPGA used as sniffer. Data are then passed to a CPU in which the correction is calculated and sent to correctors.

At ALBA the XBPM located in the MISTRAL frontend is integrated in the FOFB since the early time of operation. Strong thermalisation drifts were observed when the machine was still operating in decay mode [7]. The heat load of the accelerator beam pipe was provoking a drift with respect to the frontend, visible in the XBPM (Fig. 3), which has been finally compensated by adding this device in the FOFB loop.

IMPLEMENTATION OF POLARIZATION SWITCH

As explained in previous sections, the polarization switch is performed by modifying offsets of two BPMs to perform a local bump around the MISTRAL source point. The goal is to achieve

$$\frac{\text{Orbit Distortion}}{\text{Vertical Beam Size}} < 5\%$$

when moving from one polarization to the other, so that the process is transparent for other beamlines.

To achieve this requirement, a BPM-corrector pair for the vertical plane had to be added. Also, since the beam is passing off-center in the nearby quadrupoles when one of the polarizations is selected, an extra skew was added to correct the coupling.

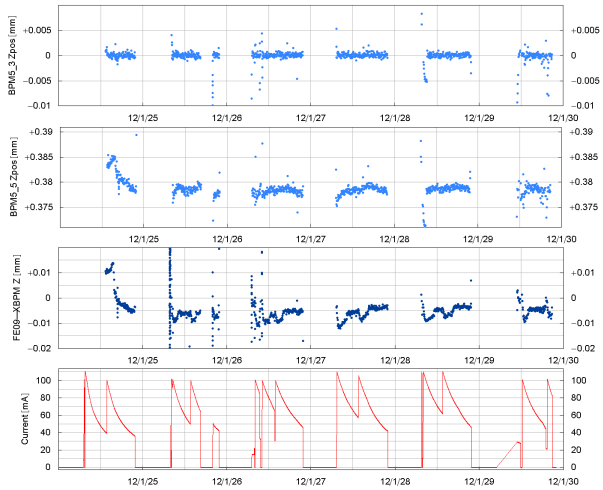


Figure 3: Drift of the x-ray beam when using only electron BPMs in the FOFB. First two plots in light blue represent the position measured at BPMs (in the loop), while the third plot is the position measured at the XBPM (mind the vertical scale). Finally, in the last plot, the current during decay mode.

During operation, two BPMs and the XBPM are involved in the swap. Two of them are used to perform the bump and another to monitor the performance.

BPMs Offset Change

The final offset to produce the bump is in the orders of hundreds of µm, thus little steps in the order of 1 µm at a 20 Hz rate are used to go from one position to the other to minimize perturbation.

It has been observed that the BPMs device server was not fast enough to send the "change of offset" command. Figure 4 shows the response of the FOFB when data were sent at 10 Hz: glitches due to the sudden change of offset only appear at a rate of roughly 1 Hz.

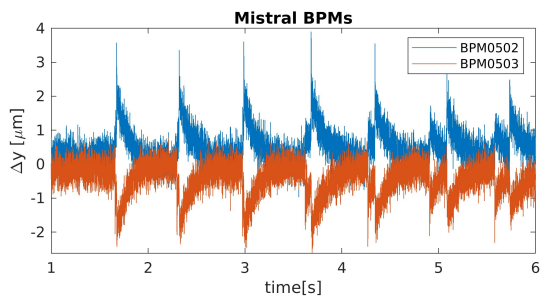


Figure 4: Response of the FOFB to a change of offset of 4 µm at a rate of 10 Hz, the actual offset change appears at a frequency of 1 Hz

For this reason, a script to modify the offset directly running in the Libera has been developed. On the other hand, in order to run the software the device server of the specific BPM has to be off. This is not a problem with FOFB or

ISBN: 978-3-95450-241-7 ISSN: 2673-5350 doi:10.18429/JACoW-IBIC2022-TUP40

interlock, since everything runs by hardware. Some disadvantages appear with the archiving system, taking data from the device server. This has been solved by acquiring and decimating data directly from the Fast Archiver [8].

Gain and Regularization

Also, a trade between speed and noise when moving from a position to another of the bump had to be found. The chosen solution was to decrease the regularization of the inverse response matrix (α) and integral gain of the PID (K_i) only in the sector of MISTRAL source point. Several tests were performed showing this was the good compromise, as presented in Fig. 5. At ALBA, the typical values are $\alpha = 1$ and $K_i = 1000$, while, after the implementation of the polarization switch, the regularization and gain for the MISTRAL sector are set to $\alpha_{loc} = 0.01$ $K_{i,loc} = 100$.

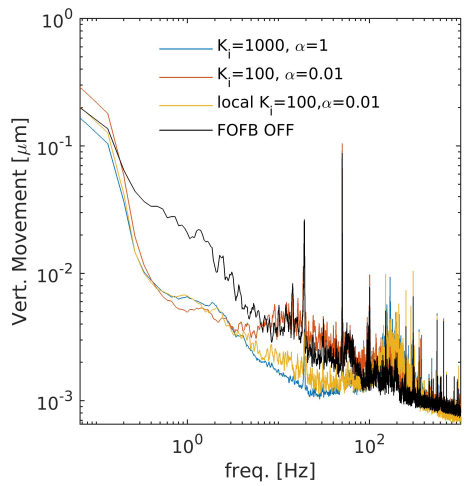


Figure 5: ALBA beam spectrum without FOFB (black) and with FOFB using different regularization (α) and feedback gains (K_i). In yellow the chosen combination: local $\alpha = 0.01$ and $K_i = 100$.

XBPM Range

The bump for polarization switch can be performed using either two standard BPMs or using one BPM (the one before the MISTRAL source) and the XBPM.

After discussions with the beamline, the second option was chosen in order to guarantee photon beam stability at the frontend. The main disadvantage related with this choice is the lack of linearity of this detector over the whole span of the bump. Moreover, position measurement accuracy strongly depends on the range in which the Libera Photon is operating.

Another issue comes from the fact that the XBPM electronics is close to the cross between two different operation ranges. Figure 6 shows a a bump performed using the two electrons BPMs and monitored using the XBPM for several acquisitions: while the bump is changing, the range of the XBPM changes generating some glitches, which the FOFB attempts to correct, generating perturbations.

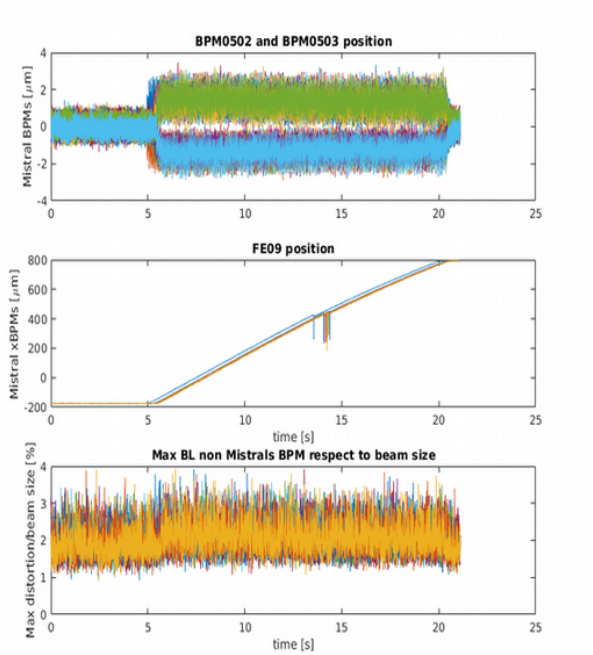


Figure 6: Top: position at the BPMs where the bump is generated. Center: position at the XBPM used to monitor the bump (note the glitches in the center). Bottom: perturbation generated in BPMs of other beamlines.

To avoid these glitches, the auto-range functionality of the Libera Photon has to be disabled. This creates some problems when injecting from zero current and trying to start to correct the orbit at 2 mA while using a range suitable for 2 mA. This leads to saturation of the FOFB and, as a consequence, to beam loss. To avoid this, the polarization switch operation mode can be activated only at full current.

Beam Size

Finally, a feed-forward on the vertical beam size has to be used to maintain it constant when bumps are active. To do so, a new skew magnet was added. Figure 7 shows the beam size with and without the feed-forward for different polarization which can be identified with different positions in the monitoring BPM.

OPERATION

After several tests performed during machine dedicated time in collaboration with MISTRAL beamline, the polarization switch operation mode is available for user since December 2021. A Graphical User Interface (GUI, Fig. 8) allows to arm and to select the desired polarization. Little adjustment to the bump in steps of 5 µm can be performed if requested from the beamline.

The operation mode can be enabled or disabled directly from the general Insertion-Device GUI. If the operation mode is enabled, polarization switch can be performed directly from the beamline via a Tango gateway.

Content from this work may be used under the terms of the CC BY 4.0 licence (© 2022). Any distribution of this work must maintain attribution to the author(s), title of the work, publisher, and DOI

ISBN: 978-3-95450-241-7 ISSN: 2673-5350 doi:10.18429/JACoW-IBIC2022-TUP40

Content from this work may be used under the terms of the CC BY 4.0 licence (© 2022). Any distribution of this work must maintain attribution to the author(s), title of the work, publisher, and DOI

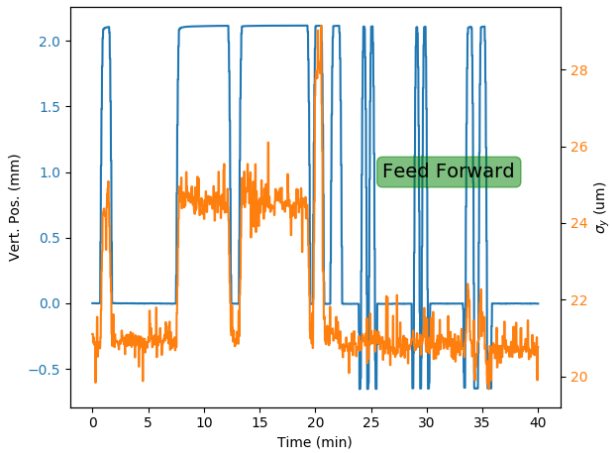


Figure 7: Vertical beam size when performing polarization switch with and without the feed-forward. Blue: position of the beam at the monitoring BPM. Orange: beam size.

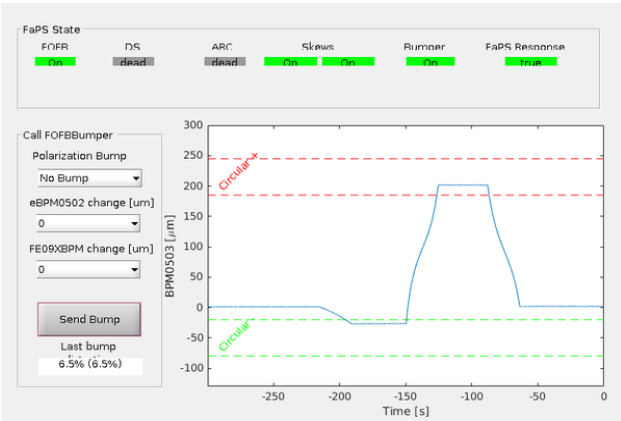


Figure 8: GUI used in the control room to arm and control polarization switch.

For all the possible polarization changes, the average perturbation seen from BPMs which are not involved in the bump is always lower than 5%, as shown in Table 1.

Table 1: Perturbation of the Orbit with respect to the Beam Size when Switching Polarization

	C+	C-	0	Lin.
C+	–	5%	4.6%	4.3%
C-	5%	–	3.8%	3.8%
0	4.6%	3.8%	–	3.9%
Lin.	4.3%	4.6%	4.3%	–

SUMMARY

A polarization switch operation mode has been developed at ALBA for the MISTRAL beamline. The polarization of the synchrotron radiation is selected performing a bump at the MISTRAL source point to modify the emission angle and select only the desired polarization.

Since December 2021, this operation mode is available for the beamline which can perform the switch without interaction with the control room.

Techniques such as magnetic imaging have already taken advantages of this type of operation showing interesting details that could not be achieved before at ALBA.

ACKNOWLEDGEMENTS

Authors would like to thank M. Böge from PSI for useful discussions. Many thanks MISTRAL, and ALBA operation group for the participation in the development and the definition of the new operation mode.

REFERENCES

[1] M. Böge, U. Flechsig, J. Raabe, and T. Schilcher, "Fast polarization switching at the SLS microspectroscopy beamline POLLUX", in *Proc. EPAC'06*, Edinburgh, UK, Jun. 2006, paper THPLS138, pp. 3610–3612.

[2] Z. Martí, G. Benedetti, U. Iriso, E. Morales, and A. Franchi, "Fast beam-based alignment using AC excitations", in *Proc. IBIC'21*, Pohang, Korea, Sep. 2021, paper MOOC01.

[3] A. Olmos *et al.*, "First steps towards a fast orbit feedback at ALBA", in *Proc. IBIC'13*, Oxford, UK, Sep. 2013, paper WEPC22, pp. 727–730.

[4] I. S. Uzun, R. Bartolini, G. Rehm, J. A. Dobbing, M. T. Heron, and J. Rowland, "Initial design of the fast orbit feedback system for DIAMOND Light Source", in *Proc. ICALEPCS'05*, Geneva, Switzerland, Oct. 2005, paper P3_030.

[5] F. Jenni and L. Tanner, "Digital control for highest precision accelerator power supplies", in *Proc. PAC'01*, Chicago, IL, USA, Jun. 2001, paper FPAH010, pp. 3681–3683.

[6] http://www.i-tech.si

[7] J. Marcos and M. Munoz, "Slow orbit feedback and beam stability at ALBA", in *Proc. IPAC'13*, Shanghai, China, May 2013, paper WEPME038, pp. 3010–3012.

[8] I. S. Uzun and M. G. Abbott, "CERN open hardware experience: upgrading the Diamond fast archiver", in *Proc. ICALEPCS'15*, Melbourne, Australia, Oct. 2015, pp. 901–904. doi:10.18429/JACoW-ICALEPCS2015-WEPGF089

ISBN: 978-3-95450-241-7 ISSN: 2673-5350 doi:10.18429/JACoW-IBIC2022-TUP41

MULTI-DIMENSIONAL FEEDFORWARD CONTROLLER AT MAX IV

C. Takahashi*, A. Freitas†, V. Hardion, M. Holz, M. Lindberg, M. Sjöström, H. Tarawneh
MAX IV Laboratory, Lund, Sweden

Abstract

Feedforward control loops are used in numerous applications to correct process variables. While feedforward control loops correct process variables according to the expected behavior of a system at any given setpoint, feedback loops require measurements of the output to correct deviations from the setpoint. At MAX IV, a generic multi-dimensional input and output feedforward controller was implemented using TANGO Control System. This paper describes the development and use cases of this controller for beam orbit and optics corrections at MAX IV.

INTRODUCTION

MAX IV Laboratory is a fourth-generation light-source facility comprised of a 3 GeV storage ring, a 1.5 GeV storage ring, and a linear accelerator that serves as a full-energy injector to the rings and as a driver for the Short Pulse Facility. Yearly, the laboratory receives around 1000 users from academia, research institutes, industry, and government agencies through user access programs. With this, MAX IV has consistently delivered to users at 300 mA and 400 mA, on the 3 GeV and 1.5 GeV storage rings respectively.

The MAX IV distributed control system is composed of a three-layer architecture, in which TANGO [1] is the distributed control framework used on the middle layer to interface the equipment available in the facility and supervise their operation. The critical tasks are handled by dedicated hardware, and, from the client layer, Python and Matlab scripts can be used to interact with TANGO.

TANGO allows the implementations of devices to interface with real-world equipment and also to act on them according to a desired logic. In this context, TANGO devices can be used to implement controllers that read signals and actuate on other devices. Controllers act on system output in order to guarantee its stability and robustness by compensating for disturbances in the system. In this context, the controller can either react to errors on the output signal/setpoint or react to the input disturbance against an expected value. The first category is named feedback control, and the last one is feedforward control. While feedback control is more common in the literature and has obvious importance in stabilizing the system and satisfying its robustness requirements, feedforward control is required when large disturbances occur on a well-tracked system [2]. At MAX IV, the beam orbit and optics fall under the second category. These systems are controlled and have excellent tracking performance; however, they are subject to disturbances determined by insertion devices (ID) undulators positions. Thus, it became necessary to implement a Multi-Dimensional Feedforward device to compensate that.

The first section of this paper will describe the general multi-dimensional feedforward device implemented at MAX IV, and the second section will detail some of its applications on the accelerator.

FEEDFORWARD CONTROL

Generally, feedforward control measures the disturbances on the input beforehand and adjusts the manipulated variable in order to minimize the deviation on the controlled variable [3]. Furthermore, when the effects of the disturbances can not be eliminated by the feedback loop alone, the feedforward controller can improve the overall performance of the system [2]. In this context, an ideal feedforward compensator could be derived by multiplying the transfer function of the disturbance by the inverse of the process variable; however, this realization is frequently unfeasible, unstable, or non-causal [4]. Therefore, different feedforward devices implementations have been proposed in the literature. The TANGO feedforward device implemented at MAX IV has a minimalist approach to a multi-dimensional controller.

Overall, it is necessary that the systems are already stable and tracked before using a feedforward strategy. In this context, feedforward controllers are often used jointly with a closed loop feedback control [2, 4]. Figure 1 presents a generic diagram of a feedforward-feedback control loop in which the feedforward controller compensates the disturbances. Hence, disturbances do not travel through the whole control path, minimizing the risks of oscillations and over-corrections.

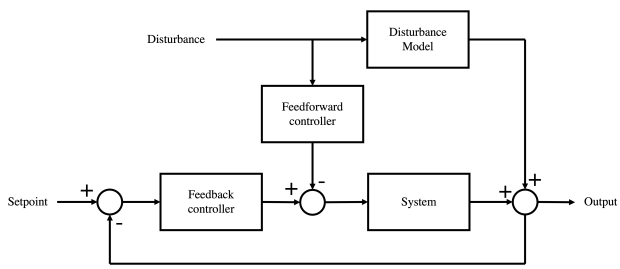


Figure 1: Block diagram of feedforward-feedback control system.

The ideal feedforward controller should compensate the disturbance according to its transfer function. Given that, $D(s)$ and $Y(s)$ are, respectively, the disturbance and the system output, $G_c(s)$ and $G_f(s)$ are the feedback and feedforward controllers and $G_p(s)$ represents the transfer function of the disturbance, then the control loop transfer function is given by Eq. (1). This equation should be zero to reject the

* carla.takahashi@maxiv.lu.se
† aureo.freitas@maxiv.lu.se

Content from this work may be used under the terms of the CC BY 4.0 licence (© 2022). Any distribution of this work must maintain attribution to the author(s), title of the work, publisher, and DOI

ISBN: 978-3-95450-241-7 ISSN: 2673-5350 doi:10.18429/JACoW-IBIC2022-TUP41

Content from this work may be used under the terms of the CC BY 4.0 licence (© 2022). Any distribution of this work must maintain attribution to the author(s), title of the work, publisher, and DOI

disturbance [2].

$$\frac{Y(s)}{D(s)} = \frac{G_d(s) - G_f(s)G_p(s)}{1 + G_c(s)G_p(s)} \tag{1}$$

Hence, the feedforward controller transfer function is given by Eq. (2). With this, it is possible to notice that a strict modeling of the disturbance is necessary. However, modeling the disturbances thoroughly enough to reject disturbances altogether is unpractical at best and impossible for most applications. Thus, pragmatically, feedforward control is commonly added only for vital disturbances, and the feedback loop is responsible for compensating minor disturbances.

$$G_f(s) = \frac{G_d(s)}{G_p(s)} \tag{2}$$

Alternatively, feedforward devices can compute preemptive control actions according to mathematical approximations instead of deriving them from an analytical model. In this case, the controller action should compensate for disturbances according to any arbitrary approximation that fits the system. Hence, the feedforward controller response in time can be given by:

$$g_f(t) = f(d(t)) \tag{3}$$

in which $g_f(t)$ is the feedforward controller output, $d(t)$ is the disturbance in time and $f(\cdot)$ is an arbitrary function.

TANGO Device

The feedforward TANGO device at MAX IV has a general implementation in Python, with multiple-input and multiple-output (MIMO) support. It implements an arbitrary compensation based on mathematical interpolation, as modeling the disturbances was unfeasible. The device properties, described in Table 1, define the controller static characteristics, such as the sensors and actuators lists, and also contain the measurements of disturbances and actuator responses necessary to compensate them. Table 2 contains the attribute list and the commands available to interact with the device. The state-machine of the device contains the states described on Table 3 and behaves according to Fig. 2.

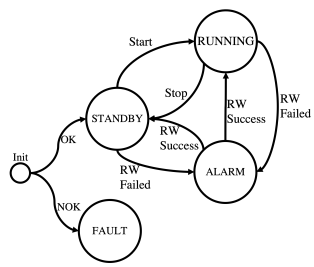


Figure 2: State-machine of the feedforward TANGO device.

The feedforward device was implemented as a Timed-Facade TANGO device [5]; therefore, by default, its main task is triggered periodically according to the polling period of the UpdateTime command, with a maximum frequency

Table 1: TANGO Feedforward Device Configurable Properties

Property	Description
ActuatorsList	List of TANGO attributes used as actuators.
SensorsList	List of TANGO attributes used as sensors.
SensorsMatrix	Matrix with disturbance values for the controller response interpolation.
ResponseMatrix	Matrix with measured feedforward responses for the controller response interpolation.

Table 2: TANGO Feedforward Device User Available Attributes and Commands

Attributes	Description
sensors_last	Current values of sensors signals.
actuators_last	Current values of actuators signals.
actuators_next	Next values of the actuators signals, regardless of the state.
Time	Timestamp of last control loop action.
Commands	**Description**
Start	Start control loop.
Stop	Stop control loop.
UpdateTime	Trigger control action. It is a polled command.

Table 3: TANGO Feedforward Device States

State	Event
STANDBY	Control loop is not running.
RUNNING	Control loop is running.
FAULT	Critical error in the loop.
ALARM	Error to read or write to sensors or actuators.

of 100 Hz. With this, as presented in the state-machine in Fig. 2, the controller should, ideally, be either RUNNING, so that the control action is performed whenever the UpdateTime is polled, or on STANDBY, when the correction is not applied. In this context, the UpdateTime polling period must be defined according to the system requirements. There are also two exception states: FAULT and ALARM. The first one occurs when the controller faces a critical issue, such as missing interpolation data or the sensors or actuators can not be found, and, thus, it can not be recovered without intervention from the operator. Otherwise, the ALARM state happens mainly when the sensors and actuators can not be read or written to for some reason, this error can be transient, and the controller might recover on its own.

The control action of this device is calculated according to Eq. (3) in which the $f(\cdot)$ function is a piece-wise linear

ISBN: 978-3-95450-241-7 ISSN: 2673-5350 doi:10.18429/JACoW-IBIC2022-TUP41

interpolation of actuator values according to the sensor input. If sensor values are outside the range, nearest point interpolation is used instead to calculate the actuator value. In this case, the values stored on the SensorMatrix and ResponseMatrix properties are used to create the linear and nearest interpolators using SciPy [6], and, every polling cycle, a new actuator value is calculated by the interpolators given the sensor readings. In this implementation, it is important to notice that the output is the actual actuator value and not a correction added to the actuator's current value.

APPLICATIONS AT MAX IV

Orbit Correction

At MAX IV, the transverse stability of the beam is essential for the requirements of the light source provided by the facility. With this motivation, the orbit is rigorously controlled on feedback loops employing Libera Brillance+ for beam positioning monitors and hardware-based Fast Orbit Feedback (FOFB) control at 10 kHz. Also, an additional MIMO controller implemented in TANGO is used for Slow Orbit Feedback (SOFB) control at 10 Hz [7]. Still, the beam orbit is subject to distortions caused by the insertion devices undulators. In this sense, the IDs cause a disturbance on the beam orbit, which vary according to the configuration of the undulator, such as the gap distance between the magnet blocks and the phase translation [8]. In this context, the feedforward controller is used to minimize the beam orbit displacement caused by the insertion devices for any given configuration of the undulator.

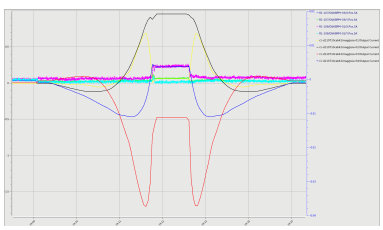


Figure 3: Actuator signals and beam position measurements for Species beamline ID.

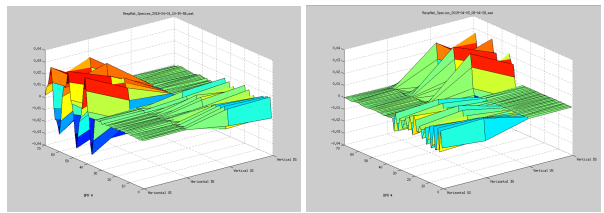
For the orbit correction, the feedforward control uses the undulator gap distance as the disturbance and the correction magnets, coils, or strips as actuators. In this case, the TANGO device SensorList receives the position TANGO attribute of the insertion device, and the ActuatorList contains the current attributes of the TANGO device of the PowerSupplies that drive the correction devices. Thus the output current of the corrector magnets power supplies change, reacting the beam position variations, as seen in Fig 3.

The definition of the response matrix is an exhaustive process, presented in Fig. 4 in which the orbit is corrected to match the Golden Orbit, and the response matrix is calculated for each gap and phase combination.

During the estimation of the response matrix, the distortion on the beam orbit can be measure on the corrector

```
Move ID to maximum Gap and initial Phase.
Correct the orbit.
Golden Orbit ← orbit.
for each phase in possible phases do
    while gap ≥ minimum gap do
        Correct orbit to match Golden Orbit
        ResponseMatrix ← Actuator values
        Move to next gap
    end while
end for
```

Figure 4: Process to define the feedforward response matrix.



(a) Distortion (b) Respones Matrix

Figure 5: Vertical distortion showed up in the horizontal plane and vice versa due to the Species beamline ID and the estimated response matrix. The horizontal up-stream(US), horizontal down-stream(DS), vertical US and vertical DS are the corrector magnets power supplies.

magnets as shown in Fig. 5(a) from which the response matrix on Fig. 5(b) was derived.

This step is essential and requires meticulous work since the quality of the control action depends on the final matrices. In this context, the number of gap positions used will also greatly affect the quality of the response since the interpolation between any two consecutive points is considered to be linear. If two adjacent gap positions are too distant, any non-linearity between them will be disregarded, which can significantly impact the overall control performance.

Since the displacement on the orbit also depends on the phase configuration of the undulator, the MAX IV Elliptically Polarizing Undulators (EPU's), which allow different phase modes, required modifications on the base feedforward device. The updated device can store and switch between multiple matrices in order to compensate distortions in different phases for any gap position.

Trajectory Correction A special case of the beam displacement appear on the linear accelerator beam trajectory because of the Short Pulse Facility (SPF). This issue arises from reasons similar to the ring orbit displacement, however, the system affected, in this case, is the linear accelerator instead of the rings. Hence, it is said that the injection to SPF causes a disturbance on the beam trajectory and the feedforward controller is used to correct that. As with the orbit correction feedforward devices, the sensor for this controller is the gap distance of the SPF ID and the actuators are the power supplies driving the correction magnets. The tuning process of the SPF feedforward is also the same.

Content from this work may be used under the terms of the CC BY 4.0 licence (© 2022). Any distribution of this work must maintain attribution to the author(s), title of the work, publisher, and DOI

ISBN: 978-3-95450-241-7 ISSN: 2673-5350 doi:10.18429/JACoW-IBIC2022-TUP41

Content from this work may be used under the terms of the CC BY 4.0 licence (© 2022). Any distribution of this work must maintain attribution to the author(s), title of the work, publisher, and DOI

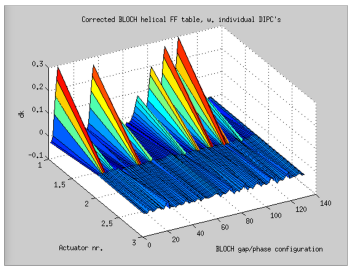
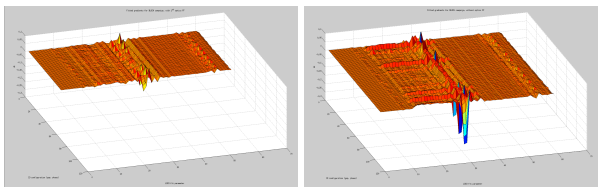


Figure 6: BLOCH ID feedforward response matrix for the helical phase mode.



(a) First FF tuning (b) No FF

Figure 7: Fitted gradients of the SQFO for various BLOCH ID gaps and phase combinations with optics feed-forward control and without optics feed-forward control.

Linear Optics Correction

Another issue with the insertion devices is the ID's intrinsic focusing, which affects the symmetry and periodicity of the ring lattice. Due to the physical characteristics of undulators, they cause a similar effect as the dipole edge focusing; thus, some distortion occurs when the beam traverses the periodic magnetic field in the ID. Furthermore, a small quadrupole focusing is also expected, as imperfections on the ID would cause its residual magnetic field integral to be different from zero [8]. Differently from the ID disturbance on the orbit, which results in a displacement of the orbit, the ID's residual quadrupole field causes a beam shape distortion.

In this case, similarly to the orbit correction, the sensors for the feedforward TANGO device are the undulator gap distances, represented by the ID device TANGO position attributes, and the actuators are the current attributes of the power supplies of the corrector magnets. However, the definition of the response matrix for the optics correction is done by using the Local Optics from Closed Orbit (LOCO) algorithm. The LOCO algorithm generates a linear optics ideal model with the open gaps and a working model with the closed gap. The magnet corrections are chosen so that the closed gap model matches the ideal one; thus, the opposite of the difference between the two models should be applied to the machine in order to compensate for the ID's disturbances. With adjusted feedforward response matrices, represented in Fig. 6, the feed-forward control on the optics subsystem can significantly reduced amplitude of the SQFO strengths as seen in Fig. 7.

FUTURE WORKS

According to continuous software development and support, the feedforward TANGO device is constantly under improvement. New features are delivered based on use cases requirements and stakeholders requests. Thus, some future development is already planned for in order to fulfill issues observed during operation and commissioning. In this context, a slew-rate capability is intended to be added to improve controlability of the corrector magnets. In mid and long term perspectives, the device can be modified to accept external triggers based on TANGO event system instead of periodic polling, which will allow it to be synchronized with the machine timing system; and it is possible to adopt an adaptive approach to build the sensor and response matrices using machine-learning or adaptive and predictive control.

CONCLUSION

The generic Multi-Dimensional Feedforward TANGO Device was implemented at MAX IX in order to improve the performance of the beam orbit and optics control. This device is suitable for both MIMO and single-input single-output (SISO) applications and can be used in any system which has a constrained operational region. The only requirements are that the sensors and actuators are available as TANGO Attributes and that the sensors and actuators' measurements are available to create the response matrices. In this context, the quality of the feedforward control is heavily dependent on the number of points available in the sensor and response matrices, as it directly impacts the quality of the interpolation. Likewise, the quality of the values on the sensor and response matrices also heavily impacts the quality of the control action. In this sense, they should be a careful calibration process to extract the correct matrices.

REFERENCES

[1] TANGO Controls, http://www.tango-controls.org

[2] L. Liu *et al.*, "Industrial feedforward control technology: a review", *J. Intell. Manuf.*, vol. 30, pp. 2819–2833, 2019. doi:10.1007/s10845-018-1399-6

[3] W. A. Poe and S. Mokhatab, *Modeling, Control, and Optimization of Natural Gas Processing Plants*, Gulf Professional Publishing, 2017. doi:10.1016/C2014-0-03765-3

[4] J. L. Guzmán *et al.*, "Performance indices for feedforward control", *J. Process Control*, vol. 26, pp. 26–34, 2015. doi:10.1016/j.jprocont.2014.12.004

[5] TANGO Facade Device, https://tango-facadedevice.readthedocs.io/en/latest/index.html

[6] SciPy Interpolation, https://docs.scipy.org/doc/scipy/reference/interpolate.html

[7] P. J. Bell, V. H. Hardion, M. Lindberg, V. Martos, and M. Sjöström, "A General Multiple-Input Multiple-Output Feedback Device in Tango for the MAX IV Accelerators", in *Proc. ICALEPCS'19*, New York, NY, USA, Oct. 2019. doi:10.18429/JACoW-ICALEPCS2019-WEPHA012

[8] H. Månefjord, D. Hill, "Commissioning of the First Insertion Devices on the 1.5 GeV Storage Ring in MAX IV", M.S. thesis, EIT, LTH, Lund University, Lund, Sweden, 2018. https://www.eit.lth.se/sprapport.php?uid=1077

ISBN: 978-3-95450-241-7 ISSN: 2673-5350 doi:10.18429/JACoW-IBIC2022-TUP42

FAST ORBIT FEEDBACK UPGRADE AT SOLEIL

R. Broucquart†, N. Hubert, Synchrotron SOLEIL, Gif-Sur-Yvette, France

Abstract

In the framework of the SOLEIL II project, the diagnostics group must anticipate ahead of the dark period the upgrade of important system like the BPM electronics, the timing system end the Fast Orbit Feedback (FOFB). The FOFB is a complex system that is currently embedded in the BPM electronics modules (eBPM). A new flexible stand-alone platform is under conception to follow the future upgrades of surrounding equipment, and to allow the integration of future correction schemes. In this paper we will present the current status of technical decisions, tests and developments.

CONTEXT

SOLEIL II aims at outstanding performances on the beam physics, qualified with renewed instrumentations. Most of the equipment linked to the FOFB will have to be updated to either accommodate these new performances (corrector magnets and their power supplies) or because they have reached obsolescence (BPM electronics, timing system).

The eBPMs (Libera Electron) currently host a major part of the FOFB system: 1) they are linked with a fast dedicated network to exchange the measured positions in all bpm location, 2) they compute the correction to apply from the given response matrix and 3) they communicate with the corrector magnet Power Supplies Controller (PSC) to apply the correction on beam.

These features have been embedded in the FPGA located inside those electronics. Most are custom developments or integration of the Diamond Light Source Communication Controller (DLS CC) [1]. This entanglement makes it difficult to upgrade the eBPMs, having to deal with two major applications: position monitoring and FOFB.

As FOFB system are very dependent on the machine layout, boundary systems and stabilization strategy, it has been decided to keep this system as an in-house development. To ease the integration, our strategy is to first segregate the FOFB system on a new dedicated platform. This platform will be interfaced with current eBPMs, PSC and timing system. It will evolve with the upgrade of each of these boundary systems.

On a feature perspective, the initial goal is to reproduce the actual features, operation control interface and performances. Future features will then be added: augmented monitoring, special mode of operation for fast lattice parameters measurements, new correction scheme… With the evolution of boundary systems and features in mind, a new modular FOFB system has been proposed.

† romain.broucquart@synchrotron-soleil.fr

SPECIFICATIONS AND GOALS

- Functionalities reproduced: With the new FOFB system platform, obtain the same service as provided currently.
- Increased performances: Communication latency and data rate will be improved, and with the leverage of a reduced latency of the future eBPMs, it will unlock a larger correction bandwidth. Performances evolution are given in Table 1.
- Follow machine evolution: SOLEIL II will bring down beam dimensions and thus stability requirements. With new correctors magnets and power supplies, the FOFB system shall attain lower stability dimensions.
- Offer new features: The new platform will allow new monitoring and fast lattice parameters measurement, such as fast response matrix identification or fast beam based alignment.

Table 1: FOFB Performances Evolution

	Actual FOFB	Future FOFB
# BPM	122	~180
# Corrector	50 H & V	*To be defined*
Data rate	10 kHz	100 kHz
Correction BW	150 Hz	1 kHz
Latency (communication and computation)	100 µs	10 µs
Stability	10 % of beam size 20 µm H ; 0.8 µm V	5% of beam size 50 nm H & V

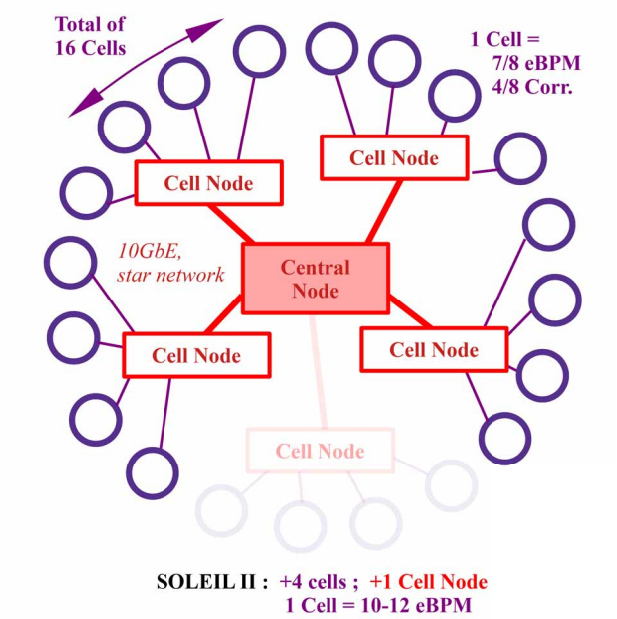


Figure 1: Network Topology.

Content from this work may be used under the terms of the CC BY 4.0 licence (© 2022). Any distribution of this work must maintain attribution to the author(s), title of the work, publisher, and DOI

ISBN: 978-3-95450-241-7 ISSN: 2673-5350 doi:10.18429/JACoW-IBIC2022-TUP42

Content from this work may be used under the terms of the CC BY 4.0 licence (© 2022). Any distribution of this work must maintain attribution to the author(s), title of the work, publisher, and DOI

ROPOSED SYSTEM

The proposed system is supported by several hardware platforms linked in a dedicated network. In the following section we will present technical choices for every aspect of the system.

Dedicated Network

The FOFB system is at the interconnection of multiple eBPMs and PSCs, all scattered in the synchrotron building. On the current system [2], all Libera Electron are linked to 2-3 neighbours, making a redundant ring network. This topology naturally provides redundancy, but the communication latency grows with the number of endpoints. The ring topology is efficient for the current implementation of the correction computation, with a distributed matrix multiplication which may not be possible for future correction schemes. For the new system, we envision that a centralized computation will ease the implementation of features such as the interface with Slow Orbit Feedback, complex controller or correction scheme adaptability to injection event.

A star topology naturally provides a central node that connects to every end points. We will use this topology for our core network made of a Central Node and 4 Cell Nodes as shown in Fig. Error: Reference source not found. The direct fast connexion between the Central Node and Cell Nodes will be the backbone of the network, with a protocol independent of the boundary systems. For this protocol, we selected to forge custom packets encapsulated in Ethernet MAC frames, running on a 10GbE fiber link. As SOLEIL II increases the number of endpoints (eBPMs and PSCs), we can extend the network by adding one Cell Node.

The selection of an Ethernet based protocol enable us to use on the shelf solution if required, such as network switches. While Ethernet is not originally aimed at low latency, it provides proved robustness and basics features that we require. We do not use a full TCP/UDP and IP stack, as we do not require generic routing and addressing. Frames structures are defined in Fig. 2. As single Ethernet frame can contain up to 149 position data or 248 correction data and will be carried in around 1.2 µs over a 10GbE link.

Cell Nodes will be connected to the boundary systems using the interface required by them. Cell Nodes act as gateway in our network, aggregating data packets from the eBPMs and dispatching correction packets to PSCs. The topology of this outer network depends on the solution used for eBPMs and PSCs. For the first phase, Cell Nodes will simply tap in the eBPM ring network and will be connected directly to the PSCs, keeping the same communication latency. With new eBPMs, we can assume a 1 Gbps link between a Cell Node and eBPMs. This leads to a transmission time of a little above 1 µs for 12 eBPMs aggregated over the same interface (10 bytes per eBPM, no overhead considered).

Redundancy is not naturally covered by this new topology. On the current FOFB system, rare optical fiber connexion incident can occur, solved by restarting the SFP modules. The new topology will be more vulnerable to this kind of problem. It can be tempered for example by opting for high grade SFP modules, or running two parallel connexion (cold or hot swap). To minimize the down time, automatic routine can be developed to restart the module and restart the system faster.

Hardware Platform

For development and maintenance simplicity, we aimed at an identical platform for the Cell Nodes and Central Node. The Micro TCA standard (MTCA) is common in accelerator facilities. This standard allows a very good flexibility: chassis size and complexity, vast selection of AMC board, adding custom RTM board.

For our application, we selected the DAMC-FMC2ZUP board [3]. It mainly features 2 FMC slots with 16 and 8 transceivers – giving us flexibility on interfaces – and a Zynq Ultrascale+ SOC – providing FPGA and CPU supports. As this AMC board provide enough resources alone, we selected a small, cost-efficient MTCA chassis [4] to host it.

For communication with current eBPMs and central node, we selected a 4SFP+ FMC [5] as we only need a few. This solution can be upgraded by doubling it and/or increasing the number of interfaces with double QSFP+ or MPO interfaces.

For communication with the current PSCs, we need up to 32 serial interfaces per Cell Node. Given the very high density, the simplicity of the interfaces and the short life span of this solution, we chose to design a custom RTM board, named CACTUS. This board simply contains RS422 drivers connected to the AMC board and RJ45 connectors. Simple CAT5 cables will carry signals on 4 differential pairs, routed to cell racks and split there. In the future, the communication to the SOLEIL II PSCs will

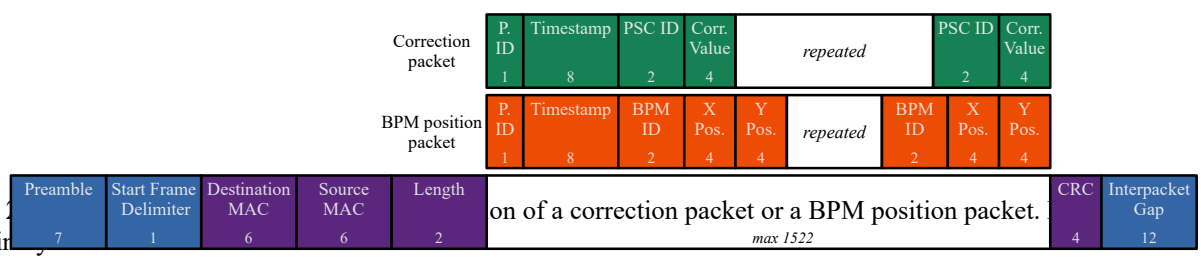


Figure 2
given in

ISBN: 978-3-95450-241-7 ISSN: 2673-5350 doi:10.18429/JACoW-IBIC2022-TUP42

be move to a high speed – low latency – protocol and interface. The CACTUS board will be then removed.

The DAMC-FMC2ZUP also provides a high density interface for timing. It can accept clock & trigger LVDS signals – compatible with the current local cell timing distribution at SOLEIL – or it also provides compliance with White Rabbit timing distribution – a possible candidate for SOLEIL II.

The platform obtained can be upgraded for still unspecified usages: integration of XBPM is foreseen, the interface to future PSC is still unknown. These usage will be supported by either increasing the number of SFP+ interfaces, or using a new FMC, AMC or RTM board.

In case of a platform failure, the orbit stability is degraded until the platform is replaced by a spare. As the platform is composed of several modules, the reparation can be eased by replacing only the defective part. The total cost of the hardware platform amount to about 12k€.

FPGA Firmware

A lot of functionalities will be embedded in the FPGA matrix of the SOC: high speed communication, correction computation, data capture… These functionalities will evolve with the FOFB system and the boundary systems.

To stir the development to a maintainable and evolutive format, we decided to use the FWK project framework developed by DESY MSK [6]. This cut down big project into modules, adding automation to organize, test, build and reproduce. Choosing FWK also provides good compatibility with ChimeraTK (presented in next section), and allows block exchange with other facilities using this framework.

The main modules used in our project are represented in Fig. 3 and listed below (not exhaustive, development under progress).

- COMBPM: receive and decode the eBPM data stream. It translates the BPM frames to AXI4-Stream packets. It provides packet filtering. For now, it only aims at decoding Libera Electron DLS CC stream, but it will be completed with the required capacity for the future eBPMs.
- COMCELLNODE: data exchange based on 10GbE MAC and PHY. Additional modules prepare BPM and correction packets to encapsulate in MAC frames, or decapsulate them for local processing.
- COMCORR: Route and encode correction data to the destination PSC. As for the COMBPM module, this module will evolve with future PSCs.
- CORRECTION: Apply the correction algorithm on the BPM data to obtain the correction data.
- TIMING: Receive clock and trigger and maintain a local time synchronized with the machine clock (turn by turn clock).

Using the widely known AXI4-Stream for data stream and AXI4 Memory Mapped for register access enable us to leverage generic IP such as AXIS interconnects.

The main challenge encountered so far was the configuration of the transceivers, because one quad is affected with two very different protocols, which require a custom configuration of the QPLL (Quad PLL).

Software Stack

SOLEIL II will keep Tango as the Control System. Current operation of the FOFB is piloted from Matlab GUI, which interact on a main Tango device dispatching configuration and retrieving status of all eBPMs and PSC Tango devices.

To keep up with the FOFB system evolution, we are in the process of deploying a very flexible software stack. The CPU part of the SOC runs an embedded Linux, which we will leverage to host services for control. We aim at using ChimeraTK [7] to build an OPCUA server, offering remote access to control and status registers of the FPGA modules.

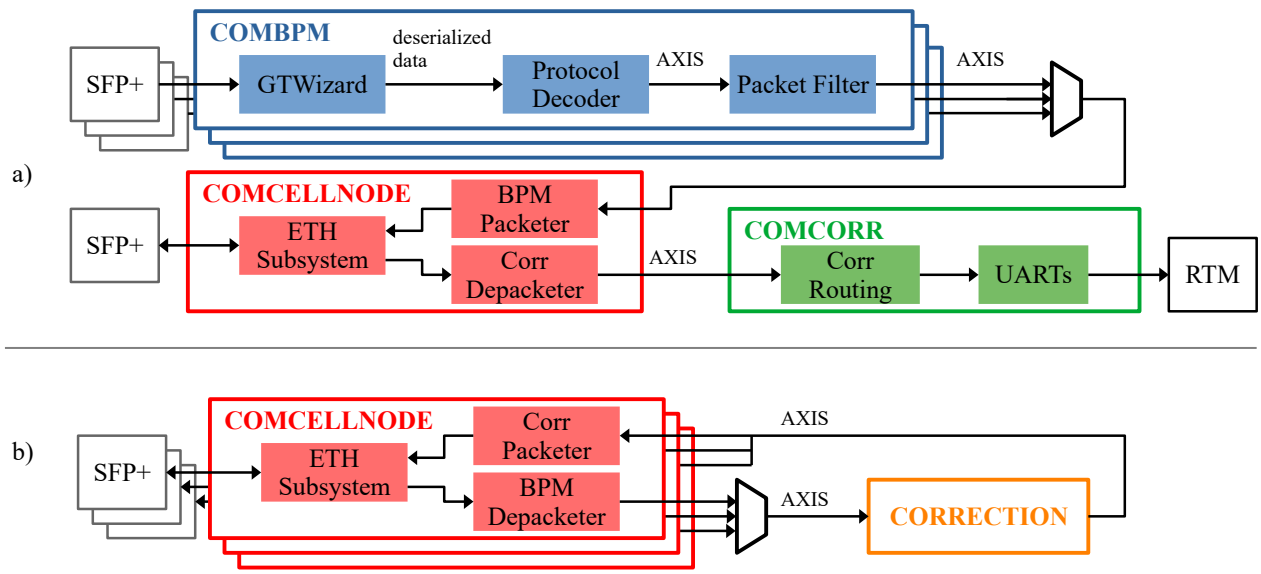


Figure 3: Overview of FPGA firmware modules for a) Cell Nodes and b) Central Node

Content from this work may be used under the terms of the CC BY 4.0 licence (© 2022). Any distribution of this work must maintain attribution to the author(s), title of the work, publisher, and DOI

ISBN: 978-3-95450-241-7 ISSN: 2673-5350 doi:10.18429/JACoW-IBIC2022-TUP42

Content from this work may be used under the terms of the CC BY 4.0 licence (© 2022). Any distribution of this work must maintain attribution to the author(s), title of the work, publisher, and DOI

This on-board OPCUA server will be contacted from a generic Tango device server, acting as a OPCUA client. This will allow very simple access from SOLEIL control system to the FPGA modules. When changing the FPGA registers, this whole software stack can be quickly updated with map files, without requiring compilation.

For important data captures – i.e. hundreds of points, for identification measures or debug – we aim at using Direct Memory Access (DMA) to move the data in the AMC DDR. Another service – still to be defined – will then operate an upload to remote storage or allow a download from a client.

PROJECT STATUS

Despite the strain on electronic productions chains, we now gathered all the platforms for operation. Prototyping and tests were already run on a first platform.

- Communication with eBPM was validated in lab, then by taping in the real network. As we only read the data stream, we are able to capture data during normal operation.
- 10GbE was validated in lab, with loopbacks at transceivers and cable. Additional tests were made with an Ethernet switch [8], mainly to measure the minimal latency obtain with such device, but it also cross-check our Ethernet interface (signals and frame) with a commercial solution.
- Communication with current PSC was validated in lab, using a RS422 FMC board.
- Timing signals – clock and trigger – from our current Cell local board were correctly used in lab.
- We also integrated a double QSFP+ board to validate the possibility to increase interface density.

The custom RTM board will be under test from September 2022. A small network of 1 Cell Node and 1 Central Node will be deployed on the running eBPM network by the end of 2022. It will run in open loop (not driving actual PSCs). During 2023, this network will be then increased to its full size and real scale test with closed loop will take place during machine test runs. We aim at an operational status by summer 2023. Next major step dates depend on boundary systems evolutions.

CONCLUSION

The new FOFB is under development at SOLEIL, getting from prototype to a first version. As the system is found at the intersection of several applications and systems, all expected to change, we opted for a very flexible platform. To manage integration with specific equipments and SOLEIL control system, his project requires hardware, FPGA and software developments.

ACKNOWLEDGEMENTS

We would like to thank J. Bisou, A. Bence, G. Pichon, S. Zhang, Y.M. Abiven and F. Bouvet from SOLEIL for their work or views on the project.

We equally thank C. Guemues, L. Butkowski and M. Killenberg from DESY for their help with FWK and ChimeraTK.

REFERENCES

[1] I. S. Uzun, R. Bartolini, G. Rehm, J. A. Dobbing, M. T. Heron, and J. Rowland, "Initial Design of the Fast Orbit Feedback System for DIAMOND Light Source", in *Proc. ICALEPCS'05*, Geneva, Switzerland, Oct. 2005, paper P3_030.

[2] N. Hubert *et al.*, "Commissioning of SOLEIL Fast Orbit Feedback system", in *Proc. BIW'08*, Lake Tahoe, CA, USA, May 2008, paper WECOTC02, pp. 337-341.

[3] DAMC-FMC2ZUP, CAENels, https://www.caenels.com/products/damc-fmc2zup

[4] 11850-29, Schroff-nVent, https://schroff.nvent.com/en-us/products/enc11850-029

[5] FMC-4SFP, CAENels https://www.caenels.com/products/fmc-4sfp

[6] FWK, DESY, https://gitlab.desy.de/fpgafw/fwk

[7] ChimeraTK, DESY https://github.com/ChimeraTK

[8] R. Broucquart, "Future Fast Orbit Feedback for SOLEIL", presented at the 10th MTCA Workshop, Virtual, DESY, Hamburg, Germany, Dec. 2021, unpublished.

ISBN: 978-3-95450-241-7 ISSN: 2673-5350 doi:10.18429/JACoW-IBIC2022-TUP43

REQUIREMENTS AND STATUS OF PETRA IV FAST ORBIT FEEDBACK SYSTEM

S.H. Mirza*, A. Aloev, H.T. Duhme, B. Dursun, A. Eichler, S. Jablonski,
J. Klute, F. Ludwig, S. Pfeiffer, H. Schlarb, B. Szczepanski
Deutsches Elektronen-Synchrotron DESY, Hamburg, Germany
G. Rehm, Helmholtz-Zentrum Berlin für Materialien und Energie/BESSYII, Berlin, Germany

Abstract

PETRA IV is the upcoming low-emittance, 6 GeV, fourth-generation light source at DESY Hamburg. It is based upon a six-bend achromat lattice with additional beamlines as compared to PETRA III. Stringent stability of the electron beam orbit in the ring will be required to achieve a diffraction-limited photon beam quality. In this regard, the requirements and the proposed topology of the global orbit feedback system are discussed for expected perturbations. An initial analysis based upon system requirements, design and modelling of the subsystems of the orbit feedback system is also presented.

INTRODUCTION

Multi-bend achromat (MBA) lattice design in fourth-generation light sources provides the possibility of achieving a high degree of transverse coherence and brightness of photon beams by generating extremely low emittance electron beams. But the effort must be complemented by the transverse orbit stability against dipolar perturbations arising within the ring and from ground motion. Moreover, the transverse orbit stability requirement has drastically increased in the fourth-generation light sources also due to the smaller size of the electron beam in both transverse planes.

The upcoming PETRA IV of DESY Hamburg, which is an upgrade of the existing ring of PETRA III will have a six-bend achromat lattice [1] with additional beamlines having transverse beam position and pointing angle stability requirement of 5% to 10% of the electron beam size and divergence, respectively. A fast orbit feedback (FOFB) system is being developed to achieve disturbance rejection up to 1 kHz on the closed orbit. The main strategy for designing the FOFB system is to identify the requirements and design the subsystems around these requirements using lattice-based simulations.

The required performance criteria for the fast orbit correction is defined by the beam size and divergence at insertion devices (given in Table 1).

Even a generally accepted target of keeping RMS variation of electron beam position and pointing angle to 10% of RMS beam size and divergence [2] requires stabilization of 297 nm and 100 nrad (RMS) in the vertical plane of PETRA IV. The beam size and divergence are given with $\sigma = \sqrt{\beta\epsilon + \sigma_E^2\eta^2}$ and $\sigma' = \sqrt{\frac{\epsilon}{\beta}}$, where ϵ and β are the emittance and beam size, respectively. The energy spread

* sajjad.hussain.mirza@desy.de

Table 1: Electron Beam Parameters at IDs

Parameter	Value
$\beta_{x,y}$ (m), standard cell	2.2
$\beta_{x,y}$ (m), flagship IDs	4
Nat. emittance $\epsilon_{x,y}$ (pm rad)	20, 4
Beam size $\sigma_{x,y}$ (µm), standard cell	6.6, 2.97
Beam div. $\sigma'_{x,y}$ (µrad), standard cell	3.02, 1.34
Beam size $\sigma_{x,y}$ (µm), flagship IDs	8.9, 3.98
Beam div. $\sigma'_{x,y}$ (µrad), flagship IDs	2.23, 1.0

σ_E and the dispersion η is assumed to be zero at the location of IDs. The reuse of the old tunnel of PETRA III will come with relatively larger static and dynamic errors [3]; a stability task force was formed to model the error spectrum. The ground motion is expected to be below 100 Hz, but a disturbance rejection bandwidth of 1 kHz is targeted to achieve reasonable attenuation on the lower side of the frequency spectrum where most of the disturbances are expected. This is necessary to achieve the above-mentioned stability criteria, which further requires a latency-optimized system. The update rate of the closed loop is planned to be 130 kHz (equal to the revolution frequency) to reduce the latency in the closed loop. In this case, the betatron frequencies ($\nu_x = 23.43$ kHz and $\nu_y = 35.156$ kHz) cannot be disregarded in the FOFB modelling, because they are within the Nyquist sampling frequency and they may be in the region where the sensitivity function (transfer function from disturbance to output) could have a magnitude larger than 1.

This contribution discusses the proposed topology for the global FOFB system. In addition, analytical modeling of the subsystems is presented, which plays an important role in their design and in identifying the technical challenges to achieve 1 kHz disturbance rejection for SISO simulation.

PROPOSED TOPOLOGY FOR THE FOFB SYSTEM

FOFB system for PETRA IV is planned to perform orbit correction for the full range of disturbance spectrum, i.e. from quasi-DC to high frequency (1 kHz). The slow correctors distributed along the ring will correct large and slow orbit offset drifts. The FOFB system will correct fast perturbations referenced to the orbit maintained by slow correctors during machine commissioning. A total of 789 beam position monitors (BPMs) and 322 fast correctors in the vertical plane, and 200 fast correctors in the horizontal plane will

Content from this work may be used under the terms of the CC BY 4.0 licence (© 2022). Any distribution of this work must maintain attribution to the author(s), title of the work, publisher, and DOI

ISBN: 978-3-95450-241-7 ISSN: 2673-5350 doi:10.18429/JACoW-IBIC2022-TUP43

Content from this work may be used under the terms of the CC BY 4.0 licence (© 2022). Any distribution of this work must maintain attribution to the author(s), title of the work, publisher, and DOI

be available for the FOFB. The FOFB system for PETRA IV is planned to have an extended star topology which will have 1 global central node marked as "GLO" between supply building 12 and 13 and 15 local nodes (LOC), see Fig. 1.

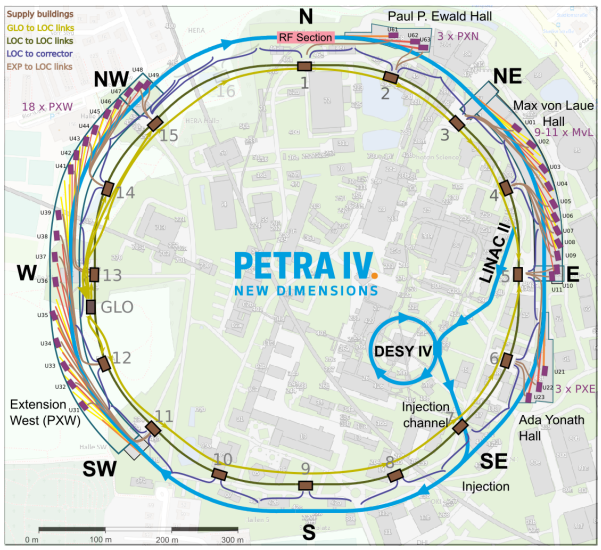


Figure 1: Supply buildings across the ring to serve as local stations for BPM and corrector data collection and distribution.

BPM crates and power supply (PS) racks will be peripheral nodes for each local star. BPM crates are planned in the MicroTCA.4 form factor, housing multiple BPM processors coupled with a data aggregation AMC for transferring the corresponding BPM data to LOC. PS units are planned to be distributed into racks with a single optical link per rack. Various options such as optical splitters are being considered to distribute the data locally to the individual PSs. The GLO and LOC are planned as similar hardware, which will also have the MicroTCA.4 form factor. GLO will have bidirectional optical links up to 1.2 km long with all 15 LOCs. Each LOC will be connected to the local BPM crates and local PS racks with optical links. Optical links to both neighbouring LOCs (upstream and downstream) and experimental stations are also considered. Figure 2 shows the simplified block diagram for central data processing.

The main idea behind such a topology is establishing a latency-optimized global system. Data propagation within the MicroTCA.4 backplanes is latency-optimized in order of 270 ns, while the optical cable paths are bandwidth-optimized. Data transfer times are up to 6 µs for the longest communication path between LOC and GLO, and we expect a latency of less than one microsecond for each local communication, i.e. LOC to PS and BPM.

ANALYTICAL MODELLING OF SUBSYSTEMS

This section describes the main transfer characteristics of individual subsystems in the signal chain for the FOFB system. The starting point will be the signal detection by

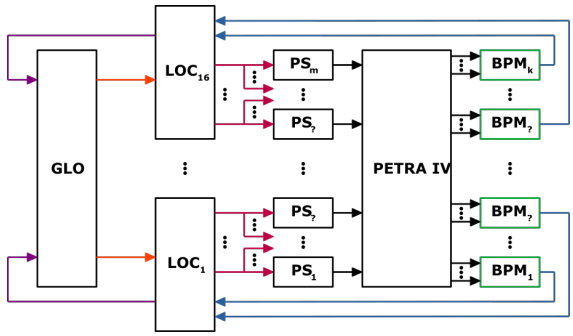


Figure 2: Simplified block diagram for central data processing around the PETRAIV ring. Optical communication links, displayed as colored lines, from up to k=789 BPMs via up to 16 LOCs and 1 GLO to about 522 PS, locally distributed over the corresponding LOC.

the BPM, followed by the corrector power supply up to the considered beam dynamics.

Beam Position Monitor

Button BPMs with four distributed pickups will be located around the ring. The BPM electronics is based on Libera Brilliance+ system [4] providing turn-by-turn data with a resolution of at least 100 nm and an update rate of 130 kHz [5]. This data should be free of switching artifacts and with a maximum latency of 3 turns, i.e. latency of about 23 µs. The latency, orbit resolution, and noise modelling of the BPM electronics are the most important elements for the simulation.

Corrector Power Supply

The power supply design is not finalized yet, but the considered option includes two paths: slow regulation (feedback based) up to a maximum of a few hundred Hertz for mainly slow drift compensation and fast uncontrolled (feed-forward) regulation for fast correction to overcome mismatch in the current readback using DCCT at the PS output. This solution provides low latency, the update rate of 130 kHz, no feedback, but a lead-lag component is required for the fast corrector coil to reach at least 1.3 kHz open-loop bandwidth.

Cable and Corrector Magnets

Cables with lengths up to 200 m are required between the corrector power supplies and the magnets to keep the power electronics outside the tunnel. This puts special demands on the cable itself, like low losses, radiation hardness and other aspects discussed in the following.

All 3 horizontal and 2 out of 4 vertical fast correctors per cell (in the current lattice of PETRA IV) overlap the locations of slow correctors. So the combined AC/DC corrector magnet design is proposed capable of 800 µrad DC deflection (twice the value predicted by static error analysis [3]) and 30 µrad integrated deflection up to 1 kHz. The aperture diameter of 25 mm and length no longer than 150 mm are the design parameters from the lattice point-of-view. The proposed design is based on the layout of the 8-pole correc-

ISBN: 978-3-95450-241-7 ISSN: 2673-5350 doi:10.18429/JACoW-IBIC2022-TUP43

tor magnet for APS-U [6]. This layout allows improved field quality for both deflection planes created by the main and auxiliary coils. The schematic is shown in Fig. 3.

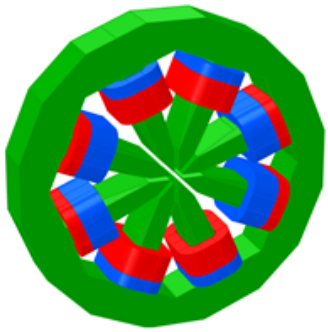


Figure 3: Combined corrector layout for PETRA IV. The main and auxiliary coils are represented by inner and outer coils, respectively, with blue representing horizontal correctors and red representing vertical correctors.

At a certain ratio of ampere-turns in these coils, it is possible to minimize the 3rd and 5th harmonics (b_3 and b_5). In practice, main and auxiliary coils are connected in series. The number of turns is chosen as a compromise between the field quality, inductance and maximum current. For example, Table 2 shows relative (to dipole) integrated harmonics, maximum current and inductance for 65/27 and 70/29 turns in the main and auxiliary coils.

Table 2: Number of turns in main and auxiliary coils, maximum DC current I (A) and inductance L of fast corrector magnets. The integrated harmonics are given relative to the main dipole harmonic b_1 (values in 10^{-4}).

Turns	L [mH]	I [A]	$\mathbf{b_3}$	$\mathbf{b_5}$	$\mathbf{b_7}$	$\mathbf{b_0}$
65/27	23.0	22.3	2.5	0.90	278	−26.6
70/29	26.4	20.7	−3.2	−1.0	278	−26.6

The bandwidth of magnet core (eddy current effect) is modelled to be 10 kHz based upon measurements of similar correctors at APS-U (private communication). First simulations of PS, cable and magnet depict an additional challenge in terms of cable-magnet resonance, dominated by large magnet inductance and capacitance of such a long cable. In first order, this is given as a series LC circuit as

$$f_{\text{res}} = \frac{1}{2\pi\sqrt{L_{\text{mag}} C_{\text{cable}} l_{\text{cable}}}}\,, \tag{1}$$

where L_{mag} is the magnet coil inductance, C_{cable} is the cable capacitance per meter and l_{cable} is the length of the cable. Figure 4 shows the corresponding notch in the source current at 8.3 kHz. This notch creates uncertainty between source current and magnet current at frequencies around the notch. Hence a closed-loop current controller shall be limited to a few hundred Hz. Therefore, the proposed solution is to use a feed-forward circuit for kHz regime based upon a closed-loop of global FOFB beam-based system while a closed-loop

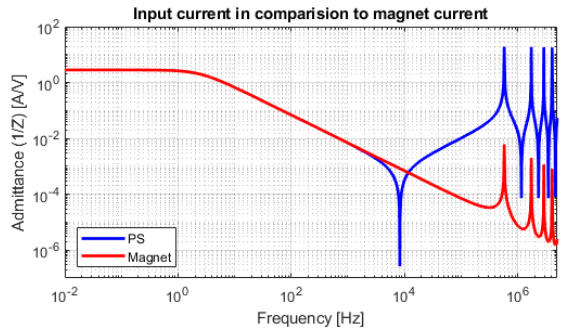


Figure 4: The notch in current in the coaxial cable connected with magnet coil, at 8.3 kHz seen by the source point of view.

current controller up to 100 Hz only for drift compensation of the set point. In this case, the overall open-loop bandwidth shall significantly reduce and currently, estimation (based upon current design considerations) is 1.3 kHz. The corrector coil transfer function (voltage to current) shall be overtaken by the action of this PS with a lead-lag component. Furthermore, the cable resonances are found to be $f_{\text{peak}} = \frac{cN_{1,3,5,\ldots}}{4\sqrt{\epsilon_r \mu_r} l}$, where c is the speed of light, ϵ_r is the relative permittivity, and μ_r is the relative permeability. The peaks are shifted towards lower frequency by the increase of cable length and should not overlap with the multiples of betatron tunes.

Vacuum Chamber

The eddy currents in the vacuum chamber placed inside an electromagnet act like a low-pass filter attenuating the magnetic field inside the chamber. If the skin depth of material is larger than the thickness of the chamber, its response can be modelled as a first order filter given as,

$$G_{vac} = \frac{\omega_0}{s+\omega_0},\ \omega_0 = \frac{1}{\tau},\ \tau = \frac{1}{2}\mu_0 \sigma a d \tag{2}$$

where, $\mu_0 = 4\pi\times10^{-7}$ H/m, σ is conductivity, a is the internal radius and d is the thickness of chamber [7]. In order to make the eddy current effects non-dominant, 1 mm thick stainless steel chamber of radius 10.5 mm is requested for the fast correctors (BW=17.8 kHz), contrary to the alternate option of copper (BW=770 Hz, for 0.5 mm thickness). Remark: inner coating might be necessary that can reduce the bandwidth down to 7 kHz. This aspect is currently under discussion for impedance matching and ignored for simulations presented here.

Beam Dynamics

Orbit Response Matrix The pseudo-inverse of the orbit response matrix (ORM) serves as the machine model for the calculation of the corrector settings for a given perturbed orbit. The elements of the ORM are given as,

$$R_{mn} = \frac{\sqrt{\beta_m \beta_n}}{2\sin(\pi Q)} \cos\left(Q\pi - |\mu_m - \mu_n|\right) \tag{3}$$

where β and μ denote the beta function and phase advance at BPM and corrector locations marked as m and n respectively,

Content from this work may be used under the terms of the CC BY 4.0 licence (© 2022). Any distribution of this work must maintain attribution to the author(s), title of the work, publisher, and DOI

ISBN: 978-3-95450-241-7 ISSN: 2673-5350 doi:10.18429/JACoW-IBIC2022-TUP43

Content from this work may be used under the terms of the CC BY 4.0 licence (© 2022). Any distribution of this work must maintain attribution to the author(s), title of the work, publisher, and DOI

in the given plane. Q is the coherent betatron tune of the storage ring. The condition numbers of PETRA IV ORMs (ratio of highest to lowest singular values) are 322.8 and 765 for horizontal and vertical planes, respectively.

Betatron Oscillations

The betatron excitation needs to be taken into account as mentioned in the introduction section. The transfer function model between a corrector and a BPM for betatron excitation is given as,

$$H_{mn} = \sqrt{\beta_m \beta_n}\ \mathrm{Im}\left(\frac{e^{j(\mu_m - \mu_n)}}{s + \frac{1}{\tau} - j\nu}\right) \tag{4}$$

where τ is the damping time constant and $\nu_{x,y} = 2\pi Q_{x,y} f_{\mathrm{rev}}$, [8]. For SISO simulation, it is modelled as a damped second-order low-pass filter with $H = \frac{p_1 p_2}{(s-p_1)(s-p_2)}$, where $p_i = -(\frac{1}{\tau} \pm j\omega_t)$.

Synchrotron Oscillations

The beam's momentum deviation ΔP with respect to nominal momentum P_0 produces a closed orbit distortion through the dispersion function D as $x_D = \frac{\Delta P}{P_0} D$. The momentum deviation is not a constant but rather oscillates with the synchrotron oscillation frequency resulting into "fast" orbit oscillations [9] making the synchrotron frequency relevant for PETRA IV FOFB system where the $\Omega_t = 600$ Hz (within the disturbance rejection bandwidth).

Single-Input-Single-Output Simulations

A first-hand estimation of the full open-loop transfer function and delay budget for the FOFB system is made based upon analytical modelling of the subsystems discussed above and depicted in Fig. 5. The estimation is done for the worst-case scenario (for maximum delay paths from LOC to GLO stations). Figure 6 shows the simulated Bode plots for the vacuum chamber, corrector magnet eddy current effect, power supply and their combined transfer function with a net open-loop bandwidth of 1.26 kHz. Similarly, a total delay of 83 µs is estimated ($\tau_{\mathrm{d,BPMs}}$=23 µs, $\tau_{\mathrm{d,controller}}$=30 µs, $\tau_{\mathrm{d,LOC\text{-}GLO}}$=15 µs, $\tau_{\mathrm{d,PS\text{-}cable}}$=15 µs). Figure 6 also shows the total response adding the betatron resonance ($\nu_x = 23.43$ kHz and $\nu_y = 35.156$ kHz) with decay constants ($\tau_x = 17$ ms and $\tau_y = 22$ ms) for both planes, in

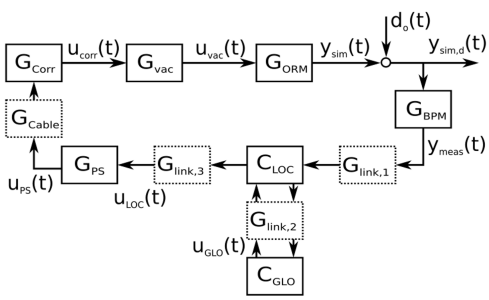


Figure 5: Closed-loop schematic of the FOFB system identifying the individual subsystems.

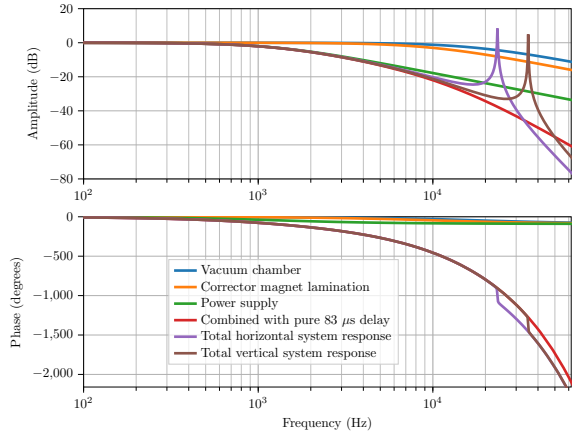


Figure 6: Open-loop transfer function of subsystems.

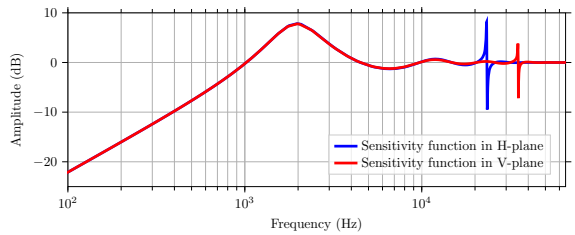


Figure 7: Disturbance-to-output sensitivity function

the absence of multi bunch feedback. The synchrotron oscillations are ignored in these simulations. The closed-loop simulation in the SISO domain is performed using a PI controller, with closed-loop bandwidth three times of open-loop bandwidth. Disturbance rejection of 1 kHz seems feasible as depicted by the disturbance-to-output sensitivity function in Fig. 7, for the subsystems described above.

SUMMARY

This paper presents a preliminary analysis of requirements and proposed topology for the global FOFB system for PETRA IV. Analytical subsystem modelling is also presented in order to evaluate the feasibility 1 kHz disturbance rejection bandwidth.

REFERENCES

[1] I. V. Agapov *et al.*, "PETRA IV Storage Ring Design", in *Proc. IPAC'22*, Bangkok, Thailand, Jun. 2022, pp. 1431–1434. doi:10.18429/JACoW-IPAC2022-TUPOMS014

[2] G. Rehm, "Achieving and measuring sub-micrometer beam stability at 3rd generation light sources", *J. Phys. Conf. Ser.*,vol. 425, p. 042001, 2013. doi:10.1088/1742-6596/425/4/042001

[3] T. Hellert *et al.*, "Error Analysis and Commissioning Simulation for the PETRA-IV Storage Ring", in *Proc. IPAC'22*, Bangkok, Thailand, Jun. 2022, pp. 1442–1444. doi:10.18429/JACoW-IPAC2022-TUPOMS018

[4] P. Paglovec *et al.*, "The RF BPM Electronics Concept and Developments for the PETRA IV project at DESY", MicroTCA Workshop (DESY), 2021. {https://bib-pubdb1.desy.de/record/473042}

ISBN: 978-3-95450-241-7 ISSN: 2673-5350 doi:10.18429/JACoW-IBIC2022-TUP43

[5] G. Kube *et al.*, "Upgrade of the BPM long term drift stabilization scheme based on external crossbar switching at PETRA III", presented at IBIC'22, Kraków, Poland, Sep. 2022, paper WEP08, this conference.

[6] M. Jaski, "APS Upgrade: Magnets", ASD Seminar, Apr. 2017. https://www.aps.anl.gov/files/APS-Uploads/ASDSeminars/2017/2017-04-12-Jaski.pdf

[7] B. Podobedov *et al.*, "Eddy Current Shielding by Electrically Thick Vacuum Chambers", in *Proc. PAC'09*, Vancouver, Canada, May 2009, paper TH5PFP083, pp. 3398–3400. https://jacow.org/PAC2009/papers/TH5PFP083.pdf

[8] Y. Cheng, "Dynamic Closed Orbit Correction", in *Proc. PAC'93*, Washington D.C., USA, Mar. 1993, pp. 2269–2271. https://jacow.org/p93/PDF/PAC1993_2269.PDF

[9] P. Kallakuri *et al.*, "Coupled bunch mode zero correction using orbit measurements and rf system phase feedback", *Phys. Rev. Accel. Beams*, vol. 25, p. 082801, 2022. doi:10.1103/PhysRevAccelBeams.25.082801

Content from this work may be used under the terms of the CC BY 4.0 licence (© 2022). Any distribution of this work must maintain attribution to the author(s), title of the work, publisher, and DOI

ISBN: 978-3-95450-241-7 ISSN: 2673-5350 doi:10.18429/JACoW-IBIC2022-TU3I1

INVESTIGATING THE TRANSVERSE DYNAMICS OF ELECTRON BUNCHES IN LASER-PLASMA ACCELERATORS

A. Koehler*,[1], German Aerospace Center (DLR e.V.), Fassberg, Germany
[1]previously at Helmholtz-Zentrum Dresden – Rossendorf, Dresden, Germany

Abstract

The demonstrations of GeV electron beams and FEL radiation driven by a centimeter-scale device illustrate the tremendous progress of laser-plasma accelerators. In such applications, beam divergence and size, along with beam energy and charge, are critical parameters of electron beams. An insight on the transverse parameters and their dynamics such as beam decoherence can be obtained by diagnostics complemented by betatron radiation detectors. This talk will also provide a brief overview of recent techniques for accessing the transverse phase space.

INTRODUCTION

Relativistic electron sources represent an important tool in basic and applied sciences. The best examples are synchrotron light facilities and free-electron lasers (FELs), in which electrons produce extremely short and bright flashes of light as they pass through periodic structures. This radiation allows us to study ultrashort processes and nonequilibrium states in biology, chemistry, and materials science. However, the radiofrequency technology generally used limits the maximum electron current and thus the available radiation intensity due to its accelerating structures. Ultimately, this leads to huge, expensive accelerators that can only be made available to a small group of users. In contrast to conventional accelerators, plasma accelerators produce highly relativistic electrons of up to several GeV at much shorter acceleration lengths of only a few millimeters. Because of the high beam currents enabled by the plasma medium, they are ideally suited for driving FELs, as demonstrated recently [1, 2].

Plasma accelerators can be driven by intense laser radiation, e.g. in laser wakefield acceleration (LWFA) schematically shown in Fig. 1. In LWFA, a high-intensity laser pulse propagates through an underdense plasma of density n_e, exciting plasma waves of frequency $\omega_p = \sqrt{n_e e^2/(m_e \epsilon_0)}$. Here, e, m_e and ϵ_0 are the elementary charge, the electron mass, and the vacuum permittivity, respectively. The waves are excited by the ponderomotive force of the laser pulse, which displaces electrons from high intensity regions. At relativistic laser intensities, the electrons are completely pushed from the high intensity regions by the laser pulse. Due to their large mass, the ions remain behind and form a plasma cavity or a so-called bubble [3]. Electrons in a plasma cavity experience a longitudinal accelerating electric field and gain the energy γ. In the transverse plane, the plasma's electric and magnetic fields continuously focus

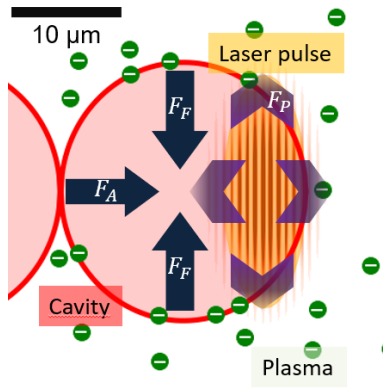


Figure 1: Schematic of LWFA. The laser pulse moves from left to right. F_P, F_F and F_A are the ponderomotive force of the laser pulse and the focusing and accelerating forces of the cavity on injected electrons, respectively.

the electrons and cause them to oscillate at the betatron frequency $\omega_\beta = \omega_p/\sqrt{2\gamma}$ and wavelength λ_β. The resulting betatron radiation enables the study of beam dynamics inside the plasma as well as it provides a broadband, ultrashort x-ray source [4].

The characteristics of betatron radiation can be compared with radiation from undulators and wigglers [5]. The dimensionless wiggler parameter for LWFA depends on the betatron radius r_β as

$$K = 2\pi\gamma\frac{r_\beta}{\lambda_\beta}. \quad (1)$$

The betatron radius is the amplitude of the electron orbit during acceleration. The betatron radiation spectrum is synchrotron-like and is described by the critical energy $E_c = 3\gamma^2 K h\omega_\beta$, where h is the Planck constant.

Typical LWFA operating at plasma densities of $1 \times 10^{19}\,\mathrm{cm}^{-3}$ possesses plasma wavelengths of 10 µm. When the accelerated electrons reach energies of about 250 MeV at typical r_β of 1 µm, then $K \approx 10$ indicates the wiggler regime and the emitted spectrum has a critical energy of about 10 keV.

The paper is structured as follows: First, a basic setup for LWFA is shown, including commonly utilized betatron diagnostics. Then, very briefly, betatron decoherence is introduced. Finally to a short summary, laser-acceleration methods of other particles are mentioned.

* Alexander.koehler@dlr.de

Content from this work may be used under the terms of the CC BY 4.0 licence (© 2022). Any distribution of this work must maintain attribution to the author(s), title of the work, publisher, and DOI

ISBN: 978-3-95450-241-7 ISSN: 2673-5350 doi:10.18429/JACoW-IBIC2022-TU3I1

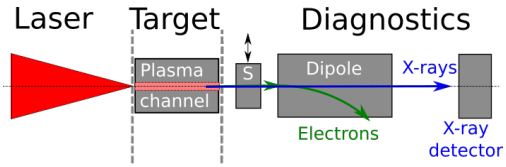


Figure 2: Schematic example of an LWFA setup. The retractable detector S can be, for example, a scintillation screen or a current transformer for the electron beam.

SETUP AND BUNCH DIAGNOSTICS

Basic Components of an LWFA Setup

As shown in Fig. 2, a typical LWFA setup consists of three components: a high-power laser system, a target, and diagnostics. The laser system, for example, delivers a pulse energy of several joules at pulse durations in the range of 100 to 30 fs [6]. To achieve high intensities, the laser pulse is focused down to spot sizes of 10s of µm on the target, that are comparable with the plasma wavelength. Jets from gas nozzles and gas-filled capillaries operated with easily ionizable gases such as helium or hydrogen can be used as targets. Both differ in adjustable plasma densities and lengths and depend on the deployed injection scheme. The highly versatile diagnostics analyze the properties of electrons that are accelerated by and copropagate with the laser pulse [7]. Charge can be detected either by fast current transformers or by charge-calibrated scintillation screens [8]. Typically, at least an electron spectrometer is utilized for obtaining an energy-resolved spectrum. The spectrometer's dipole magnet deflects the accelerated electrons on a calibrated screen.

Betatron Diagnostics

The betatron spectrum can be reconstructed by detecting single photons with a CCD X-ray camera [9]. Another method is to use dispersive elements such as crystals or powders [10]. Both detection methods have advantages and disadvantages. Single photon detection requires a sufficiently low intensity on the chip, since typically only about 1% to 5% of the detector's pixels may be hit by a photon to be able to isolate single photon events. On the other hand, only the low-energy part of the betatron spectrum can be efficiently scattered by a Bragg crystal, since the resolution at high X-ray energies is too low. Therefore, single photon detectors are placed several meters away from the source, while crystal-based detectors are typically only one meter away to collect a sufficient amount of photons. Alternatively, when space is restricted, a set of multiple foils can be assembled to pass only parts of the spectrum.

Betatron spectroscopy is a non-invasive and indirect diagnostic method. Figure 3 shows an example of a measured betatron spectrum. Single photon detectors may suffer from the high photon flux. In this case, the number of detected photons can be reduced by filter foils, which are the main source of attenuation of the red shaded area. The betatron radius can be acquired by the spectral shape. The spectrum

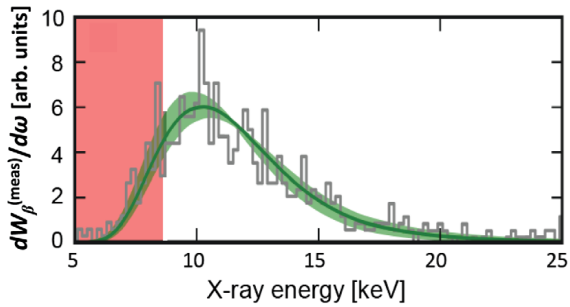


Figure 3: Example of a measured betatron spectrum with single photon detectors. The solid black histogram shows the photons counted per energy bin. The solid green line is the best fit for a betatron radius of 0.8 µm. The red shaded area is the lower detection limit due to beam line transmission and detector efficiency. From [7].

is dominated by the radiation emitted at the end of the acceleration, i.e. still in the plasma.

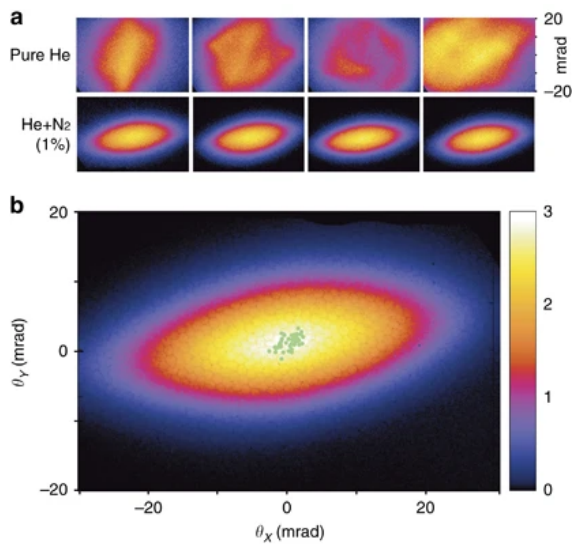


Figure 4: The typical spatial profile of betatron radiation depends on the way electrons are injected into the accelerator. (a) shows two different gas mixtures that can be used to tune the profile and thus the electron orbits. (b) is the average signal over 50 consecutive shots using He+N_2 as the gas mixture. From [11].

Beside the spectrum, the spatial profile of the radiation can provide information about the orientation of the electron orbits during acceleration [11]. Depending on the type of injection, the accelerated electrons will perform betatron oscillations in one prefered plane or in both transverse planes, resulting in elliptic or circular beam profiles, as presented in Fig. 4. The spatial profile can be detected by carefully light shielded scintillators, such as CsI or Lanex [8] that has to be protected from residual laser light and energetic electrons.

Content from this work may be used under the terms of the CC BY 4.0 licence (© 2022). Any distribution of this work must maintain attribution to the author(s), title of the work, publisher, and DOI

ISBN: 978-3-95450-241-7 ISSN: 2673-5350 doi:10.18429/JACoW-IBIC2022-TU3I1

Content from this work may be used under the terms of the CC BY 4.0 licence (© 2022). Any distribution of this work must maintain attribution to the author(s), title of the work, publisher, and DOI

Complementing Diagnostics

The high beam divergence of electrons from LWFA compared to RF-based accelerators allows short drift distances to determine the beam divergence σ_θ despite high energies. A very elegant method is to use the non-dispersive plane of a dipole magnet while the electron energy γ is detected simultaneously in the dispersive plane. Then, the beam size σ_r can be deduced from the critical energy, allowing to estimate the normalized emittance by an elaborated model [12]. For LWFA, emittances as low as 0.1 mm · mrad up to several mm mrad has been reported [7, 13].

BUNCH DECOHERENCE

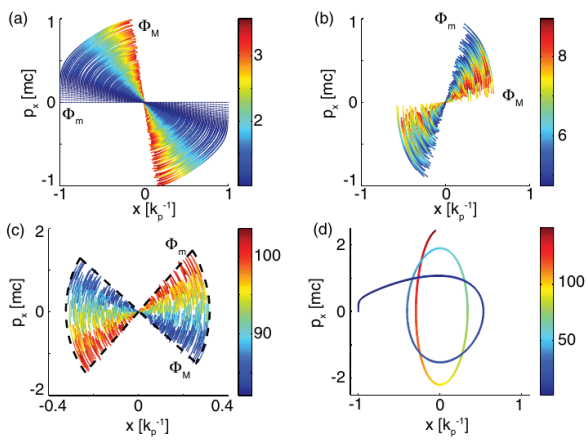


Figure 5: Transverse phase space (x, p_x) during the decoherence process. The color indicates the electron energy γ. (a)-(c) are taken at different times during acceleration. (a) is at the beginning of the acceleration ($\gamma \approx 2$), (b) is after a small energy gain ($\gamma \approx 7$), and (c) after a larger energy gain ($\gamma \approx 95$). (d) is the phase space trajectory for a single randomly selected particle. From [14].

One phenomenon that can be studied with LWFA due to the constant focusing in the plasma channel is the decoherence of the bunch [14, 15]. In the transverse phase space of location and momentum, the electron orbits describe circular paths that are traversed more slowly with progressive adiabatic acceleration. Due to the energy dependence of the betatron frequency, it happens that electron groups with different energies can twist relative to each other and also overtake each other, as shown in Fig. 5. The result is a dynamically evolving normalized emittance that can be minimized under optimal conditions.

CONCLUSION

LWFA has become a reliable source and acceleration method for relativistic electrons [16, 17]. At the same time, diagnostics that detect the beam parameters [18] or resolve the very compact plasma structures [19, 20] have also become more sophisticated. In this paper, only a small part of this could be described.

Plasma-based accelerators allow colliders and FELs to be designed much more compactly, making them accessible to a wider range of users. With the availability of inherently synchronized laser pulses, laboratories with LWFA sources also offer unique opportunities for pump-probe setups for investigation with multiple beam types (electrons, X-rays, infrared and visible laser radiation) [21].

ACKNOWLEDGEMENTS

The author would like to thank the conference organizers and the DLR for their support and for the opportunity to present an invited talk.

REFERENCES

[1] W. Wang *et al.*, "Free-electron lasing at 27 nanometres based on a laser wakefield accelerator", *Nature*, vol. 595, pp. 516–520, 2021. doi:10.1038/s41586-021-03678-x

[2] R. Pompili *et al.*, "Free-electron lasing with compact beam-driven plasma wakefield accelerator", *Nature*, vol. 605, pp. 659–662, 2022. doi:10.1038/s41586-022-04589-1

[3] A. Pukhov and J. Meyer-ter-Vehn, "Laser wake field acceleration: the highly non-linear broken-wave regime", *Appl. Phys. B: Lasers Opt.*, vol. 74, pp. 355–361, 2002. doi:10.1007/s003400200795

[4] F. Albert and A. G. R. Thomas, "Applications of laser wakefield accelerator-based light sources", *Plasma Phys. Controlled Fusion*, vol. 58, p. 103001, 2016. doi:10.1088/0741-3335/58/10/103001

[5] S. Corde *et al.*, "Femtosecond x rays from laser-plasma accelerators", *Rev. Mod. Phys.*, vol. 85, pp. 1–48, 2013. doi:10.1103/RevModPhys.85.1

[6] U. Schramm *et al.*, "First Results with the Novel Peta-Watt Laser Acceleration Facility in Dresden", in *Proc. IPAC'17*, Copenhagen, Denmark, May 2017, pp. 48–52. doi:10.18429/JACoW-IPAC2017-MOZB1

[7] M. C. Downer *et al.*, "Diagnostics for plasma-based electron accelerators", *Rev. Mod. Phys.*, vol. 90, p. 035002, 2018. doi:10.1103/RevModPhys.90.035002

[8] T. Kurz *et al.*, "Calibration and cross-laboratory implementation of scintillating screens for electron bunch charge determination", *Rev. Sci. Instrum.*, vol. 89, p. 93303, 2018. doi:10.1063/1.5041755

[9] A. Köhler *et al.*, "Single-shot betatron source size measurement from a laser-wakefield accelerator", *Nucl. Instrum. Methods Phys. Res., Sect. A*, vol. 829, p. 265, 2016. doi:10.1016/j.nima.2016.02.031

[10] M. Šmíd *et al.*, "Highly efficient angularly resolving x-ray spectrometer optimized for absorption measurements with collimated sources", *Rev. Sci. Instrum.*, vol. 88, p. 063102, 2017. doi:10.1063/1.4986464

[11] A. Doepp *et al.*, "Stable femtosecond X-rays with tunable polarization from a laser-driven accelerator", *Light Sci. Appl.*, vol. 6, p. e17086, 2017. doi:10.1038/lsa.2017.86

[12] A. Curcio *et al.*, "Trace-space reconstruction of low-emittance electron beams through betatron radiation in laser-plasma accelerators", *Phys. Rev. Accel. Beams*, vol. 20, p. 012801, 2017. doi:10.1103/PhysRevAccelBeams.20.012801

ISBN: 978-3-95450-241-7 ISSN: 2673-5350 doi:10.18429/JACoW-IBIC2022-TU3I1

[13] G. Plateau *et al.*, "Low-Emittance Electron Bunches from a Laser-Plasma Accelerator Measured using Single-Shot X-Ray Spectroscopy", *Phys. Rev. Lett.*, vol. 109, p. 64802, 2012. doi:10.1103/PhysRevLett.109.064802

[14] X. Xu *et al.*, "Phase-Space Dynamics of Ionization Injection in Plasma-Based Accelerators", *Phys. Rev. Lett.*, vol. 112, p. 035003, 2014. doi:10.1103/PhysRevLett.112.035003

[15] A. Koehler *et al.*, "Restoring betatron phase coherence in a beam-loaded laser-wakefield accelerator", *Phys. Rev. Accel. Beams*, vol. 24, p. 091302, 2021. doi:10.1103/PhysRevAccelBeams.24.091302

[16] J. Götzfried *et al.*, "Physics of High-Charge Electron Beams in Laser-Plasma Wakefields", *Phys. Rev. X*, vol. 10, p. 041015, 2020. doi:10.1103/PhysRevX.10.041015

[17] A. R. Maier *et al.*, "Decoding Sources of Energy Variability in a Laser-Plasma Accelerator", *Phys. Rev. X*, vol. 10, p. 031039, 2020. doi:10.1103/PhysRevX.10.031039

[18] A. Seidel *et al.*, "Characterizing ultralow emittance electron beams using structured light fields", *Phys. Rev. Accel. Beams*, vol. 24, p. 012803, 2021. doi:10.1103/PhysRevAccelBeams.24.012803

[19] S. Schöbel *et al.*, "Effect of driver charge on wakefield characteristics in a plasma accelerator probed by femtosecond shadowgraphy", *New J. Phys.*, vol. 24, p. 083034, 2022. doi:10.1088/1367-2630/ac87c9

[20] M. B. Schwab *et al.*, "Visualization of relativistic laser pulses in underdense plasma", *Phys. Rev. Accel. Beams*, vol. 23, p. 032801, 2020. doi:10.1103/PhysRevAccelBeams.23.032801

[21] B. Kettle *et al.*, "Single-Shot Multi-keV X-Ray Absorption Spectroscopy Using an Ultrashort Laser-Wakefield Accelerator Source", *Phys. Rev. Lett.*, vol. 123, p. 254801, 2019. doi:10.1103/PhysRevLett.123.254801

Content from this work may be used under the terms of the CC BY 4.0 licence (© 2022). Any distribution of this work must maintain attribution to the author(s), title of the work, publisher, and DOI

ISBN: 978-3-95450-241-7 ISSN: 2673-5350 doi:10.18429/JACoW-IBIC2022-TU3C2

ANGULAR-RESOLVED THOMSON PARABOLA SPECTROMETER FOR LASER-DRIVEN ION ACCELERATORS

C. Salgado-López*, J. I. Apiñaniz, A. Curcio, D. de Luis, J. L. Henares,
J. A. Pérez-Hernández, L. Volpe, G. Gatti
Centro de Láseres Pulsados (CLPU), Villamayor (Salamanca), Spain

Abstract

Laser-plasma driven accelerators have become reliable sources of low-emittance, broadband and multi-species ion beams, presenting cut-off energies above the MeV-level. We report on the development, construction, and experimental test of an angle-resolved Thomson Parabola (TP) spectrometer for laser-accelerated multi-MeV ion beams which is able to distinguish between ionic species with different q/m ratio. The angular resolving power is achieved due to an array of entrance pinholes and it can be simply adjusted by modifying the geometry of the experiment and/or the pinhole array itself. The analysis procedure allows for different ion traces to cross on the detector plane, which greatly enhances the flexibility and capabilities of the detector. A full characterization of the TP magnetic field has been implemented into a relativistic code developed for the trajectory calculation of each beamlet. High repetition rate compatibility is guaranteed by the use of a MCP or plastic scintillator as active particle detector. We describe the first test of the spectrometer at the 1 PW VEGA 3 laser facility at CLPU, Salamanca (Spain), where up to 15 MeV protons and carbon ions from a 3-micron laser-irradiated metallic foil are detected. A second set of experimental measurements is shown, where highly magnified traces are obtained which leads to a possible transversal beam emittance estimation.

INTRODUCTION

Since the invention of the Chirped Pulse Amplification [1], the range of accesible light intensities on focus for ultrabright lasers has only increased. Such enhancement paved the way for laser-plasma particle accelerators (LPA), mainly focused on ions [2] and electrons [3]. The applications of such accelerated beams profit from the low-emmitance and ultrashort duration of the beams, wel-fitted characteristics for practical employments. Specifically, since the demonstration of collimation and monochromatisation of LPA multi-MeV ion beams [4, 5], their potential employments have attained plenty of attention, including ultrafast proton probing [6], isochoric heating of dense plasmas [7], fast ignition of inertial confinement fusion reactions [8] and medical purposes [9] among others.

Due to the specific LPA beam characteristics, one of the most widely used diagnostics for laser-driven ion accelerators are Thomson Parabola (TP) spectrometers [10]. First developed by Thomson in 1907, they are in-line diagnostics which sort the particles depending on their energy, momentum and charge-to-mass ratio. The latter is specially useful in LPA scenario where the acceleration of multi-species beam is frequent. The main drawback of TPs is the incapability of deconvolving the spatial distribution of the measured beam as only a particular angle of the beam with an insignificant spread is evaluated because of the use of an entrance pinhole mask. Previous studies with different detectors, focused on analysing the spatial structure of the beams, showed that the most common laser based ion acceleration mechanism, the Target Normal Sheath Acceleration or TNSA [2], emits extraordinarily low-emittance beams from a source with a diameter as big as a few hundreds of micrometers and a total beam divergence of 20°. In order to retrieve spatial information about the beam other methods could be use, as stacks of radiochromic films or scintillators [11] which nevertheless fail when attempting to have fine spectral resolution. We present a multi-pinhole Thomson Parabola spectrometer, which combines sharp spectral and angular accuracy, besides the ionic species sorting capability.

DESIGN

Thomson Parabola spectrometers work according to magnetic an electric sector spectrometer principles. The entrance pinhole selects a beamlet composed by ions with specific q/m. Parallel (or anti-parallel) magnetic (B) and electric (E) dipoles deflect the ions in orthogonal directions. Such particles are detected in a two-dimensional spatially resolved particle-sensitive detector. In paraxial approximation with perfect fields, the particles will draw a parabolic trace onto the detector (given simply by Lorentz force) as

$$y^2 = \frac{q}{m}\frac{B^2 l_2 l_3}{E}x, \tag{1}$$

where l_2 dipole length, l_3 the particle free-flight distance after the deviation, being the fields parallel to the x-axis. As seen, different charge-to-mass ratio particles will describe different traces and the position of the particle onto the trace will describe its kinetic energy.

We propose a modification of the basic TP design which consist on the substitution of the entrance pinhole by a mask in which several pinholes are drilled. The array of holes chops the incoming beam into several beamlets which are simultaneously detected, resulting in a tomography-like spectral measurement with tunable spatial-resolved information [12]. Figure 1 shows the basic device design.

Previous works [13–15] showed similar measurement strategies but most of the cases dismissing the electric field (and therefore the q/m differentiation) or limited their detec-

* csalgado@clpu.es

Content from this work may be used under the terms of the CC BY 4.0 licence (© 2022). Any distribution of this work must maintain attribution to the author(s), title of the work, publisher, and DOI

ISBN: 978-3-95450-241-7 ISSN: 2673-5350 doi:10.18429/JACoW-IBIC2022-TU3C2

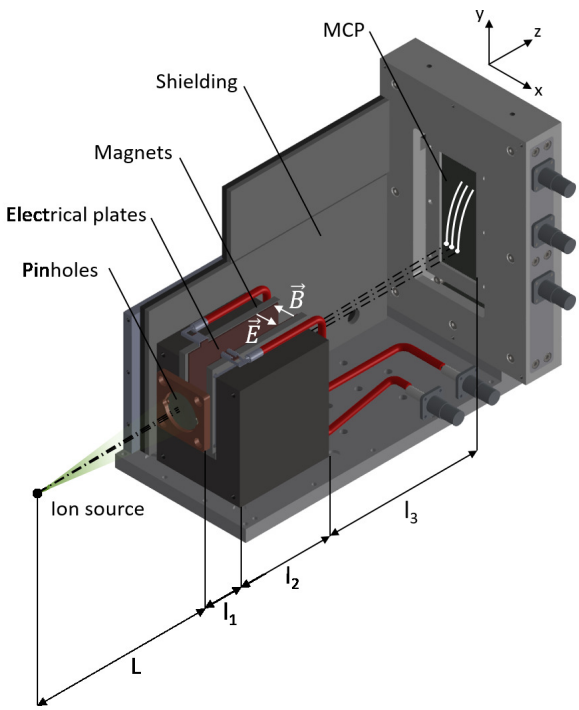


Figure 1: Multi-pinhole TP spectrometer design.

tion geometries in order to avoid crossing traces on the detector [16]. We propose a more general approach of such device which can apply the electric and magnetic field for identifying different q/m ions and measuring their spectrum at different beamlets backed by a generic post-processing methods which accounts for trace crossing. A three-dimensional numerical solver was developed for trajectory simulation and provides the expected traces and the energy-position relation for the required species, which includes a Hall probe characterization of the magnetic field. In the presented configuration proton energies between 300 keV and 25 MeV are accessible; uncertainty at 20 MeV has been estimated to be around 1 MeV.

Trace crossings at the detector produce peak artifacts in the spectrum. Interpretation of such events starts with the identification of the species involved in each cross. Only artifacts producing significant distortion are treated; the peaks that are still observable after applying a Gaussian smoothing over the data are removed, by removing the relevant peak width and performing a linear interpolation between the gap edges. Such interpolation is considered to follow the data trend within its root main squared deviation.

EXPERIMENTAL TESTS

In this section we show two experimental tests of the detector performed under different experimental conditions. Both were performed at the VEGA 3 petawatt laser facility at Centro de Láseres Pulsados (CLPU, Spain). VEGA 3 is a Titanium:Sapphire system ($\lambda = 0.8\,\mu$m) which delivers p-polarized pulses, up to 30 J and as short as 30 fs. The pulses are focalized by a F/11 off-axis parabolic mirror into a 10 µm full width at half maximum, which implies an averaged laser intensity over 10^{19} W/cm^2. The target was a micrometric-thick Al planar foil irradiated at 10° from the target normal in the horizontal plane.

Low Spatial Resolution Test

In this first commissioning test ion acceleration was detected by the multi-pinhole set at a distance from the source $L = 508$ mm. A microchannel-plate (MCP) attached to a phosphor screen was used as active detector, which has the advantage of being well-fitted for high repetition rate (HHR) operation. As shown in Fig. 2, traces were imaged onto a scientific CMOS with a calibrated imaging system. The mask in this case was made of a W substrate with $n = 3$ drilled pinholes of $d = 200\,\mu$m evenly separated by $a = 3$ mm.

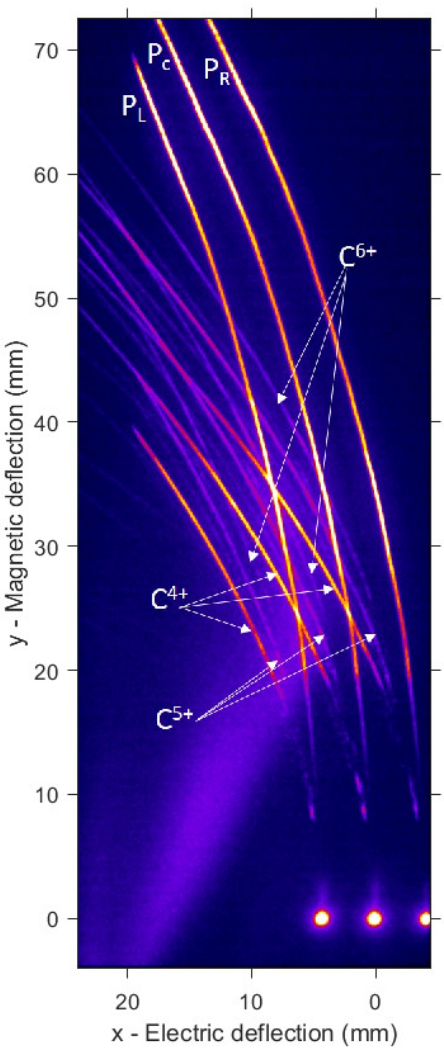


Figure 2: Multi-pinhole TP traces from a single laser shot at VEGA 3.

A single beamlet proton spectrum is plotted in Fig. 3, together with the traces intersection signal which are removed.

In such geometrical configuration, the separation between the angles probed ($\alpha \approx a/(L) = 0.3°$) is small when com-

Content from this work may be used under the terms of the CC BY 4.0 licence (© 2022). Any distribution of this work must maintain attribution to the author(s), title of the work, publisher, and DOI

ISBN: 978-3-95450-241-7 ISSN: 2673-5350 doi:10.18429/JACoW-IBIC2022-TU3C2

Content from this work may be used under the terms of the CC BY 4.0 licence (© 2022). Any distribution of this work must maintain attribution to the author(s), title of the work, publisher, and DOI

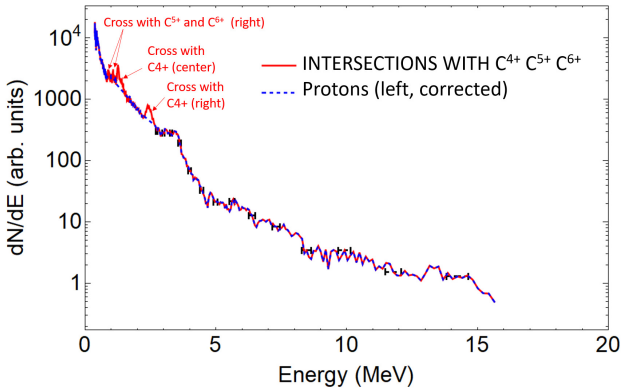


Figure 3: Left beamlet proton (P_L) spectrum from Fig. 2. Dashed blue: corrected spectrum. Red: raw spectrum.

pared to the total divergence of the beam. Therefore modest differences between different beamlet spectra are expected. Such conjecture is confirmed after the data analysis, as seen in the spectra shown in Figs. 4 and 5. For sake of comparison Fig. 6 shows the spectra of different ion species of the same beamlet.

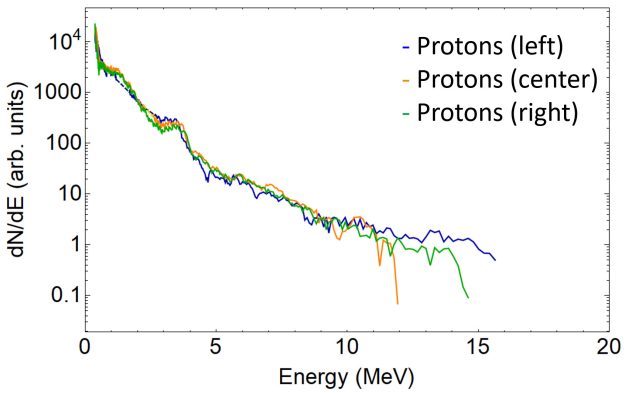


Figure 4: Left, center and right proton beamlets (P_L, P_C and P_R) spectra from traces of Fig. 2.

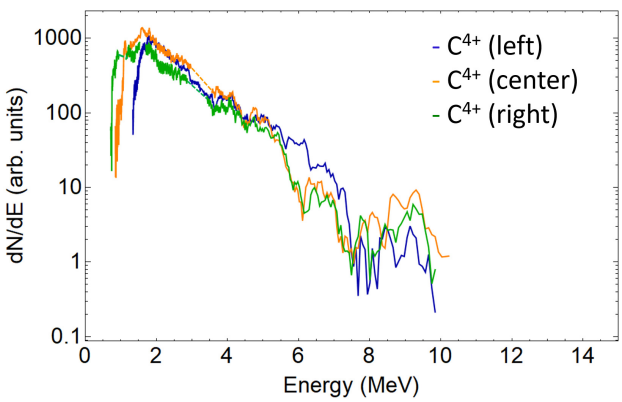


Figure 5: Left, center and right C^{4+} beamlets spectra from traces of Fig. 2.

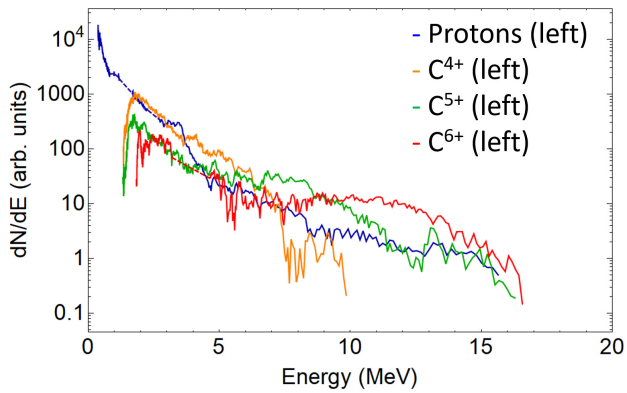


Figure 6: Left beamlet spectra for protons P_L and C^{4+}, C^{5+} and C^{6+} from traces of Fig. 2.

High Spatial Resolution Test

The results of a second test are shown, whose goal was attempting to improve as much as possible the spatial resolution of the detector. For such purpose, the experimental geometry was accordingly modified mainly by bringing the detector closer to the interaction point ($L = 15$ mm, $n = 13$, $a = 500\,\mu$m, $d = 100\,\mu$m). Such change results in larger beam area measured and greater angular separation between beamlets ($\alpha = 2°$) and higher acceptance of each pinhole, therefore producing thicker traces. For this case a HHR-compatible scintillating screen BC-400 was directly used as active detector. A 12 µm thick pokalon (plastic) foil was used to protect the scintillator from optical radiation and simultaneously shield it against heavier ions. As only protons where detected after the shielding, q/m was unique for all particles and electric field was switched off. A Lanex scintillating screen was used for measuring the x-ray non-deflected reference point of each pinhole.

Figure 7 shows the typical proton traces of this experimental test. Observable cut-off energy is approximately 15 MeV, similarly as in the previous test. Clear features (as trace thickness and direction) are identified to change at different energies. Following the working principle of the pepper-pot method [17], from such data it is in principle possible to infer, in a restricted area of the full beam profile, the spectrally-resolved horizontal phase-space of the beam and therefore estimate the local rms horizontal emittance ϵ considering that

$$\epsilon_x = \sqrt{< x^2 >< x'^2 > - < xx' >^2}, \qquad (2)$$

where x is the particle transverse position and x' its transverse momentum.

CONCLUSION

A newly developed diagnostic tool is presented. Its operation is based on the Thomson Parabola working principle and therefore able to differentiate between ionic species and presents a fine and wide spectral range of detection, which makes it well-fitted to measure characteristics of typical laser-driven ion beams. Furthermore, tomography-like

ISBN: 978-3-95450-241-7 ISSN: 2673-5350 doi:10.18429/JACoW-IBIC2022-TU3C2

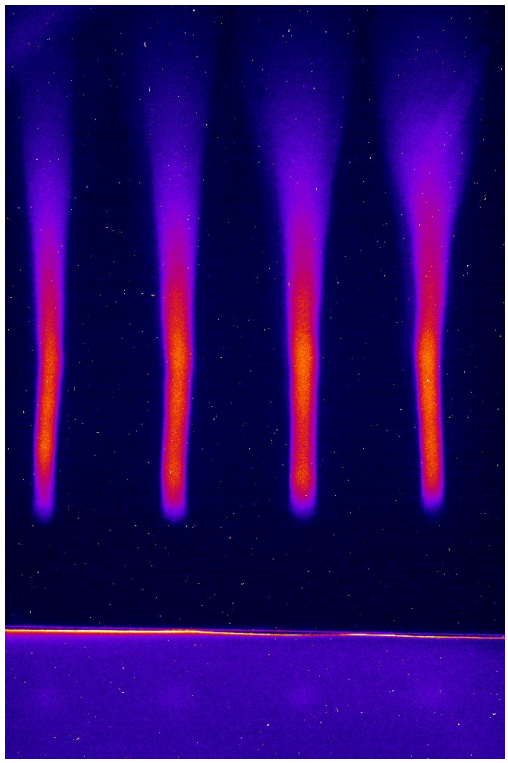


Figure 7: Proton traces at highly magnified experimental test.

measurements of the beam with varying angular resolution—depending on the detecting geometry—can be performed thanks to a mask of entrance pinholes. A post-processing method is introduced, making it possible to account for trace crosses at the detector plane. Moreover, a feasible method for specie/spectrum-resolved (restricted) phase-space estimation with the device is presented. Such simultaneous study of beam parameters makes this tool practical for characterization of LPA beams, which present a high degree of laminarity [18] and therefore are well adapted for possible application after beamline transport [19].

ACKNOWLEDGEMENTS

We thank the staff of CLPU involved in the experimental campaigns where the spectrometer was commissioned, including scientific and technical areas, radio-protection department, engineering and administration sections. Special mention to D. Arana for his job on the workshop. Funding from LASERLAB-EUROPE V (Grant Agreement No. 871124, EU Horizon 2020 research and innovation program), IMPULSE (Grant Agreement No. 871161, EU Horizon 2020 researhc and innovation program) and Grant No. CLP263P20 (Junta de Castilla y León) are acknowledged.

REFERENCES

[1] D. Strickland and G. Mourou, "Compression of amplified chirped optical pulses", *Opt. Commun.*, vol. 55, pp. 447-449, Oct. 1985. doi:10.1016/0030-4018(85)90120-8

[2] A. Macchi, M. Borghesi, and M. Passoni, "Ion acceleration by superintense laser-plasma interaction", *Rev. Mod. Phys.*, vol. 85, pp. 751-793, May 2013. doi:10.1103/RevModPhys.85.751

[3] E. Esarey, C. B. Schroeder and W. P. Leemans, "Physics of laser-driven plasma-based electron accelerators", *Rev. Mod. Phys.*, vol. 81, pp. 1229-1285, Jul. 2009. doi:10.1103/RevModPhys.81.1229

[4] S. Ter-Avetisyan *et. al.*, "First demonstration of collimation and monochromatisation of a laser accelerated proton burst", *Laser Part. Beams*, vol. 26, pp. 637-642, Nov. 2008. doi:10.1017/S0263034608000712

[5] T. Toncian *et. al.*, "Ultrafast Laser-Driven Microlens to Focus and Energy-Select Mega-Electron Volt Protons", *Science*, vol. 312, pp. 410-413, Apr. 2006. doi:10.1126/science.1124412

[6] S. Malko *et. al.*, "Proton stopping measurements at low velocity in warm dense carbon", *Nat. Commun.*, vol. 13, no. 2893, May 2022. doi:10.1038/s41467-022-30472-8

[7] P. Patel *et. al.*, "Isochoric heating of solid-density matter with an ultrafast proton beam", *Phys. Rev. Lett.*, vol. 91, p. 1225004, Sep. 2003. doi:10.1103/PhysRevLett.91.125004

[8] M. Roth *et. al.*, "Fast Ignition by Intense Laser-Accelerated Proton Beams", *Phys. Rev. Lett.*, vol. 86, pp. 433-439, Jan. 2001. doi:10.1103/PhysRevLett.86.436

[9] I .Spencer *et. al.*, "Laser generation of proton beams for the production of short-lived positron emitting radioisotopes", *Nucl. Instrum. Methods Phys. Res. Sect. B.*, vol. 183, pp. 449-458, Oct. 2001. doi:10.1016/S0168-583X(01)00771-6

[10] J. Thomson, "On rays of positive electricity", *Lond. Edinb. Dubl. Phil. Mag. Sci.*, vol. 13, pp. 561–575, 1907. doi:10.1080/14786440709463633

[11] M. Huault *et. al.*, "A 2D scintillator-based proton detector for high repetition rate experiments", *High Power Laser Sci. Eng.*, vol. 7, p. e60, Dec. 2019. doi:10.1017/hpl.2019.43

[12] C. Salgado-López *et. al.*, "Angular-resolved Thomson parabola spectrometer for laser-driven ion accelerators", *Sensors*, vol. 22, p. 3239, Apr. 2022. doi:10.3390/s22093239

[13] H. Chen *et. al.*, "An imaging proton spectrometer for short-pulse laser plasma experiments", *Rev. Sci. Instrum.*, vol. 81, p. 10D314, Sep. 2010. doi:10.1063/1.3483212

[14] S. Ter-Avetisyan *et. al.*, "Tomography of an ultrafast laser driven proton source", *Phys. Plasma*, vol. 17, p. 063101, Jun. 2010. doi:10.1063/1.3428740

[15] S. Yang *et. al.*, "A two-dimensional angular-resolved proton spectrometer", *Rev. Sci. Instrum.*, vol. 87, p. 103301, Oct. 2016. doi:10.1063/1.4963706

[16] Y. Zhang *et. al.*, "An angular-resolved multi-channel Thomson parabola spectrometer for laser-driven ion measurement", *Rev. Sci. Instrum.*, vol. 89, p. 093302, Sep. 2018. doi:10.1063/1.5042424

[17] S. Humphries, *Charged Particle Beams*, New York, NY, USA: Wiley and Sons, 1990.

Content from this work may be used under the terms of the CC BY 4.0 licence (© 2022). Any distribution of this work must maintain attribution to the author(s), title of the work, publisher, and DOI

ISBN: 978-3-95450-241-7 ISSN: 2673-5350 doi:10.18429/JACoW-IBIC2022-TU3C2

[18] M. Borghesi *et. al.*, "Multi-MeV proton source investigations in ultraintense laser-foil interactions", *Phys. Rev. Lett.*, vol. 92, p. 055003, Feb. 2004. doi:10.1103/PhysRevLett.92.055003

[19] M. Schollmeier *et. al.*, "Controlled transport and focusing of laser-accelerated protons with miniature magnetic devices", *Phys. Rev. Lett.*, vol. 101, p. 055004, Aug. 2008. doi:10.1103/PhysRevLett.101.055004

Content from this work may be used under the terms of the CC BY 4.0 licence (© 2022). Any distribution of this work must maintain attribution to the author(s), title of the work, publisher, and DOI

ISBN: 978-3-95450-241-7 ISSN: 2673-5350 doi:10.18429/JACoW-IBIC2022-TU3C3

LINAC4 LASER PROFILE AND EMITTANCE METER COMMISSIONING

A. Goldblatt*, F. Roncarolo, J. Tagg, O. Andreassen, CERN, Geneva, Switzerland
T. Hofmann, Bobst Mex SA, Lausanne, Switzerland
G. E. Boorman, A. Bosco, S. M. Gibson, John Adams Institute, Royal Holloway, United Kingdom

Abstract

The CERN LINAC4 is now equipped with two laser profile and emittance meters, a basically non destructive measurement of the transverse beam profile, not limited by the beam power density. The light of a pulsed laser is transported through optical fibers and focused into the 160 MeV/c H^- beam. The interaction of this laser "wire" with the H^- ions detaches electrons that are collected by an electron-multiplier, while the resulting H^0 particles, after being separated from the main H^- beam by a dipole magnet, are recorded by a diamond strip detector, located a few meters away from the interaction point. The transverse beam emittance and profile are reconstructed from the laser by a stepped scan through the H^- beam. After several years of feasibility tests and prototyping, this paper presents the details about the final hardware implementation, operational aspects, and the 2022 experimental results.

INTRODUCTION

Since 2019, when being connected as injector to the Proton Synchrotron Booster (PSB), LINAC4 serves as source of all CERN proton beam formats. While its predecessor LINAC2 was producing 50 MeV/c protons, LINAC4 accelerates H^- ions up to 160 MeV/c which are converted into protons – via a thin stripping foil – during injection into the four rings of the PSB. During the construction and commissioning of the LINAC4, a novel laser-based system was developed to measure the transverse beam profile and emittance in a non destructive way. After several years of design and testing, two systems were installed in strategic locations, both receiving 160 MeV/c H^- beams. The instrument operates on the *photo-detachment* principle, i.e. a laser-based stripping of the weakly coupled, second electron of the H^- ion, described in detail in [1–4]. The light of a pulsed laser is transported through optical fibers and focused to a cross section of about 140 µm diameter into the H^- beam. For each LINAC pulse, approximately 7% of the ions interacting with the laser are fully stripped. As depicted in Fig. 1:

- at the interaction point (IP) the detached free electrons are bent by a short dipole (weakly affecting the main beam) into an electron-multiplier tube (EMT).
- the neutral H^0 particles are measured on a diamond strip detector a few meters downstream, after being separated from the H^- beam by a main linac dipole.

The laser is scanned in well defined increments horizontally (H) or vertically (V) through the H^- beam. Correlating the laser positions at the IP with the EMT and diamond detector signals allows the reconstruction of the beam profile and emittance, respectively, similar to a classical slit-grid emittance-meter.

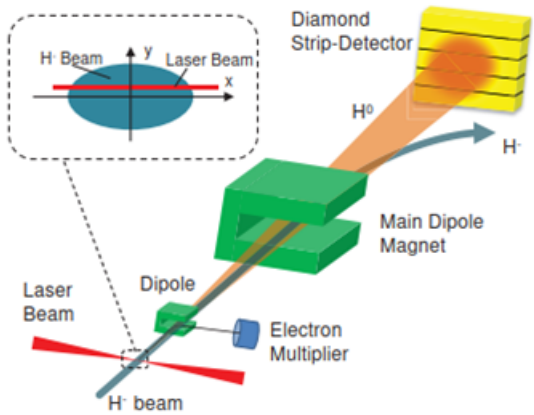


Figure 1: Concept of the laser emittance meter.

HARDWARE IMPLEMENTATION

It was decided to implement two systems to guarantee redundancy, and also to be complementary. The first system was installed at the end of the linac, before the first horizontal bend to the PSB transfer line. Here the beam emittance is dominated by the the beam size wrt. the dispersion. The second system is located between two main dipole magnets in the transfer line, where the H^0 background due to beam gas stripping is low. The distance between the H^0 detectors and the laser IP, 4.5 and 7 m, was chosen to have a convenient phase advance for sampling the angles of the emittance ellipse, like performed in slit-grid emittance-meters. The laser source, located in a dedicated hutch in the LINAC4 klystron hall, consists of an infrared laser with adjustable power, frequency and pulse length, with charateristics detailed in Table 1. The beam quality factor ensures a small beam diameter and long *Rayleigh* range at the interaction point, which is crucial to achieve a good resolution. The laser beam is transported from the surface to the interaction points in the LINAC4 tunnel through large mode area optical fibers with a special end-facet, designed to withstand the laser power density. Each of the two instruments receives two fibers of 30 and 70 m length to reach the two IP locations, for horizontal and vertical laser scans.

The diamond strip detector is composed of two motorized sensors, each having 28 channels with a pitch of 0.34 mm. They were produced by a polycristalline chemical vapor deposition (pCVD) method and are radiation tolerant. Two

* aurelie.goldblatt@cern.ch

Content from this work may be used under the terms of the CC BY 4.0 licence (© 2022). Any distribution of this work must maintain attribution to the author(s), title of the work, publisher, and DOI

ISBN: 978-3-95450-241-7 ISSN: 2673-5350 doi:10.18429/JACoW-IBIC2022-TU3C3

Content from this work may be used under the terms of the CC BY 4.0 licence (© 2022). Any distribution of this work must maintain attribution to the author(s), title of the work, publisher, and DOI

sizes are used, 20 20 or 32 10 mm. The diamond detector signals are amplified in the LINAC4 tunnel and transported to the surface where the digital data acquisition system is located. The electron-multiplier tube (Hamamatsu model R2362) has an aperture diameter of 20 mm and a gain of approximately 10^6. The laser hutch and the optical breadboards in the tunnel are equipped with photodiodes, energy meters and digital cameras to setup, tune and periodically control the laser-fiber coupling, transmission and focusing. A PXI system from National Instruments [5] handles the control and acquisition. It contains a PXIe controller (running LabVIEW RT 2017), a timing/synchronisation card, a general purpose DAQ card, and the ADCs for the signals digitization. The sampling frequency of the diamond detector ADC is 50 MHz, while the ADCs for the electron multiplier and photodiodes clock at 120 MHz. The controller include FPGAs for the entire low level control and real time signal processing, and was recently integrated to the CERN control and read-out infrastructure (FESA [6]).

Table 1: Laser Specifications

Model	Spectra Physics VPFL-ISP-POD-50
Wavelength	1064 nm
Power	Average 50 W, max peak 30 kW
Frequency	Single shot to 2 MHz, used 500 kHz
Pulse width	2 to 250 ns, used 100 ns
M^2	1.3

OPERATIONAL ASPECTS

The final beam commissioning of the laser emittance meter started in 2018 with a temporary version of timing architecture, which later in 2020 was upgraded to include the synchronization between LINAC4 and the PSB. The LINAC4 beam consists of RF macro-pulses of up to 650 µs duration every 1.2 s, filled with micro-bunches created by the RF accelarating structures operating at 352 MHz. A fast RF chopper, located in the 3 MeV medium energy beam transport (MEBT) is used to tune the macro-pulse filling factor following the PSB user request, and creates empty buckets required for the LINAC4 beam injection into the four PSB rings[1], and the ones necessary for the multi-turn injection into each ring. Each 1 µs duration PSB turn must have a 300 ns empty gap for beam injection and extraction. The laser is pulsed synchronous with the chopper at a fixed frequency, typically at 500 kHz. Therefore, several timing signals are directly linked between the RF chopper system and the DAQ system of the laser emittance meter: the laser is synchronized to the 1 MHz PSB revolution frequency, while start and end of the data acquisition are triggered by the timing signals of the four PSB rings that define start and end of the beam injection. In that way each laser wire data chunk in a LINAC4 macro-pulse can be automatically associated to the beam for a particular PSB ring. The time delays of both, laser pulse and data acquisition are adjustable in steps of 10 ns, which can be used to sample different parts of the macro-pulse. During a measurement scan, the laser and diamond positions change every 1.2 s. A full scan takes about ten minutes in order to achieve a good resolution of the phase space ellipse. For the reconstruction of the beam profile and emittance from the raw data, the pulse signals of the diamond strip-detector have to be integrated and their channel position have to be correlated to the actual position of the laser beam at the IP. As illustrated in Fig. 2, this is performed in the FPGA "on the fly" during the scan. The EMT pulse data is processed ans included via software at the end of each scan, as discussed in the next section.

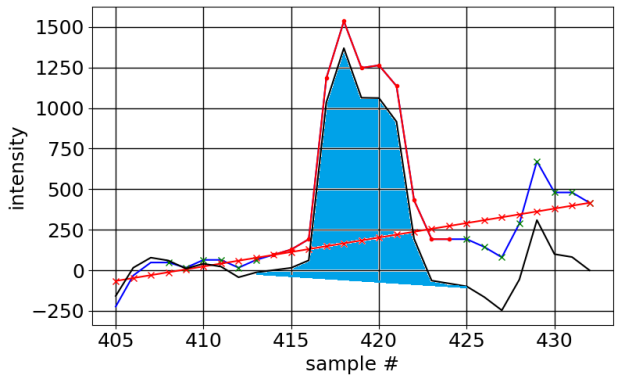


Figure 2: The FPGA process the diamond data by subtracting the background, summing the pulse area (in blue) and saves the resulting value.

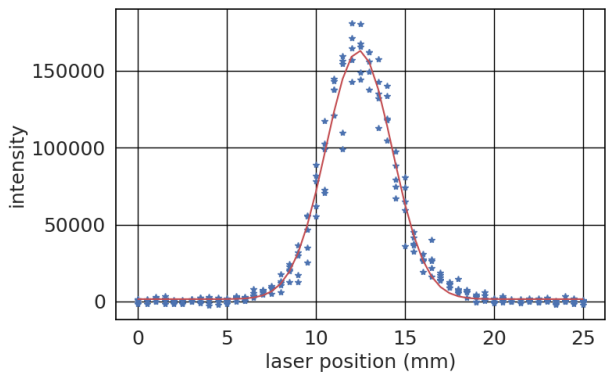


Figure 3: Reconstructed profile from the electron multiplier data.

DATA PROCESSING

Presently, the profile and emittance reconstruction algorithms are performed via Python routines launched at the end of a scan. For each laser sampling point along the beam pulse, e.g. each 2 µs if the laser pulse rate is set to 500 kHz:

[1] The very last part of the LINAC4-PSB transfer line is equipped with a *fast distributor*, based on a combination of pulsed magnets and septas, splitting the macro-pulse into the four PSB rings.

ISBN: 978-3-95450-241-7 ISSN: 2673-5350 doi:10.18429/JACoW-IBIC2022-TU3C3

- the EMT pulse integral as function of laser position provides a data point according to the beam transverse beam profile and correspondent size (via a Gaussian fit). An example of a complete scan is shown in Fig. 3.

- the correlation of the laser positions and the H^0 beamlet profiles measured by the diamond strip detectors, together with the known distance between laser-H^- beam IP and diamond detector allows inferring the beamlet position and divergence, and thus reconstruct the H^- beam transverse phase space.

The transverse emittance is estimated by calculating the phase space ellipse area after subtraction of the background by applying a data intensity threshold. Determining the optimal threshold to suppress background while not excluding beam tails in the position and angle coordinates is not always trivial and deterministic. It turned out to be reasonable to estimate the correct threshold near the inflection point of the curve. An example of the emittance values obtained as function of the threshold (expressed as percentage of the phase space maximum) is shown in Fig. 4.

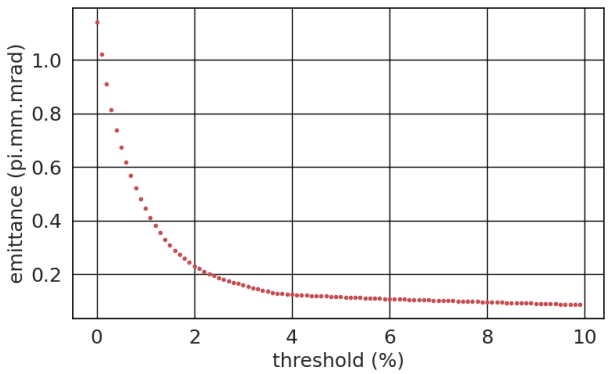


Figure 4: Example of vertical normalized emittance values as calculated for different applied thresholds.

Comparison of EMT and Diamond Profiles

The projection of the emittance phase-space H or V ellipse, measured by the diamond detector, along the position axis gives the corresponding H or V beam profile, and can be compared to the direct profile measurement utilizing the EMT. Both methods use the same laser scan and the resulting photo-detachment, but are based on different, independent detection techniques, counting detached electrons vs. profiling H^0 beamlets. So far, our beam studies show a good the agreement between the two techniques, with the results to be well within a 0.5% difference in the H plane when comparing the measured beam size along the macro-pulse, as Fig. 5 shows.

However, the vertical beam sizes measured by the the EMT appeared to be smaller compared to the measurement from the projection of the phase-space ellipse. The EMT profiles also show evidence of sharply decreasing tails, which may be a hint to the effect of a beam *scraping*. Therefore, we are now investigating the combined effects of

(i) a limited EMT detector acceptance.

(ii) the vertical beam size at this location appears to be larger than the horizontal beam size.

(iii) the field strength of the short magnet used to bend the stripped electrons is set to a single value for the entire laser scan, optimized to get the highest signal with the laser hitting the H^- beam center.

(iv) a possible tilt of the bending magnet introducing H-V coupling, and thus a vertical kick of the detached electron beam.

As the EMT is not movable, the study of these hypothesis will require dedicated machine development time to perform multiple laser scans with different magnet settings[2].

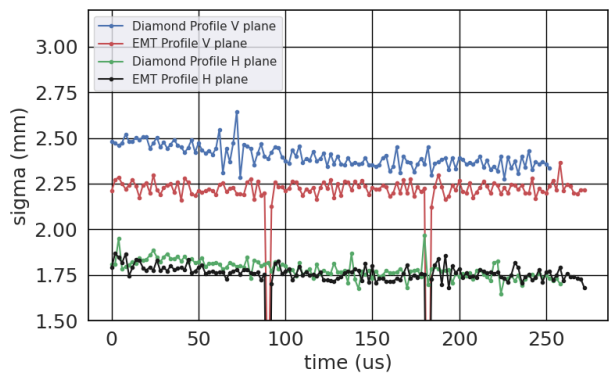


Figure 5: Diamond and EMT profiles along the macropulse.

Diamond Detector Signal Perturbation

The first measurements in 2022 of the beam emittance along the LINAC4 pulse revealed the presence of a perturbation, common to all diamond detector channels. As shown in Fig. 6, without any filtering a strong signal, larger than emittance variation along the macro-pulse, perturbs the emittance measurement.

A *Fourier* analysis of the integrated diamond detector signals, with the detectors in the parking position, confirms an unwanted strong, signal harmonic at ≈ 50 kHz, see Fig. 7. A Fast *Fourier* Transformation (FFT) of the integrated signals of all diamond detector channels exposed to the H^0 beam reveals the beam itself seems to contain frequency components which perturb the diamond signal, see Fig. 8.

During a stop in the 2022 run, it was possible to identify a 2 MHz perturbation signal, taking its source in the individual cables transporting the diamond raw signals before integration from the detectors to the pre-amplifiers few meters away. After integration of the diamond pulse signals, this could explain the observed 50 kHz artifact. During the upcoming

[2] Even if the effect on the main beam is weak, the H^- beam trajectory always has to be re-adjusted for each change of the magnet field.

Content from this work may be used under the terms of the CC BY 4.0 licence (© 2022). Any distribution of this work must maintain attribution to the author(s), title of the work, publisher, and DOI

ISBN: 978-3-95450-241-7 ISSN: 2673-5350 doi:10.18429/JACoW-IBIC2022-TU3C3

Content from this work may be used under the terms of the CC BY 4.0 licence (© 2022). Any distribution of this work must maintain attribution to the author(s), title of the work, publisher, and DOI

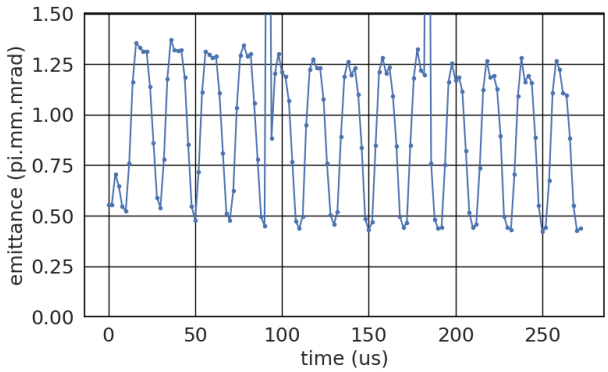


Figure 6: Emittance reconstruction from the integrated the diamond detector raw data along the macro-pulse.

winter stop at the end of 2022 it is foreseen to review the shielding, routing and grounding of all cables. Meanwhile, applying a digital notch filter during the data processing resulted to be very effective in filtering the 50 kHz perturbation. It should be noted, this 50 kHz perturbation signal on the diamond detectors, while perturbing the emittance calculation, does not affect the beam size measurements inferred from the phase space projection, it only adds an offset on the measured beam profiles.

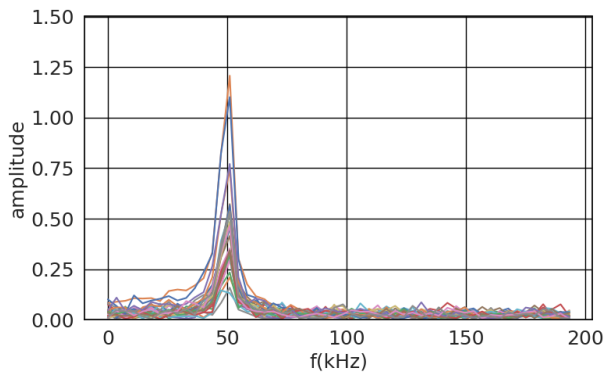


Figure 7: FFT of the integrated data, with diamond detector out of beam. Each line corresponds to a diamond detector channel.

Emittance Measurements

Fig. 9 shows a typical emittance measurement from the laser emittance meter located in the transfer line, as reconstructed phase space ellipse from the diamond data for one pulse along of the LINAC4 macropulse. As shown in Fig. 10, the vertical emittance along the LINAC4 macropulse decresases during the first 150 µs section, until it reaches a similar emittance value (in the 2nd and 3rd 150 µs sections) as the emittance measured in the horizontal plane, which almost matches the emittance measured by the wire scanners, generally used as reference. The notch filter used to suppress the 50 kHz perturbation of the integrated diamond data is suspected adding some unwanted "edge" effects to the calculation of the emittance along the macropulse. More investigations will be made, as well as measurements with the laser emittance meter system located towards the LINAC4 dump line.

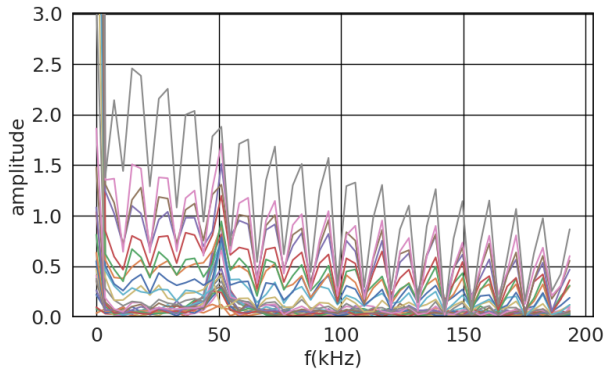


Figure 8: FFT of the raw diamond detector data. Each line corresponds to a diamond channel. The channels exposed to the H^0 beam show multiple harmonics.

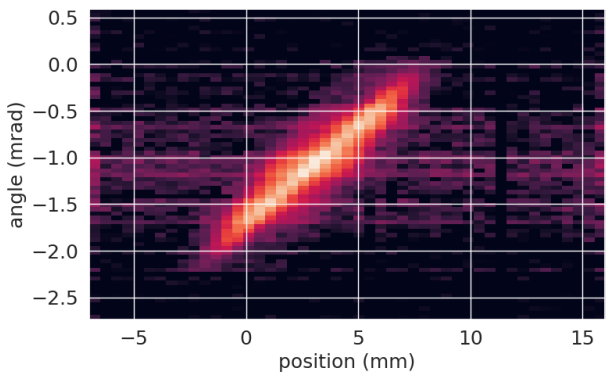


Figure 9: Example of vertical phase space ellipse measured by the laser emittance meter from one laser pulse of the macropulse.

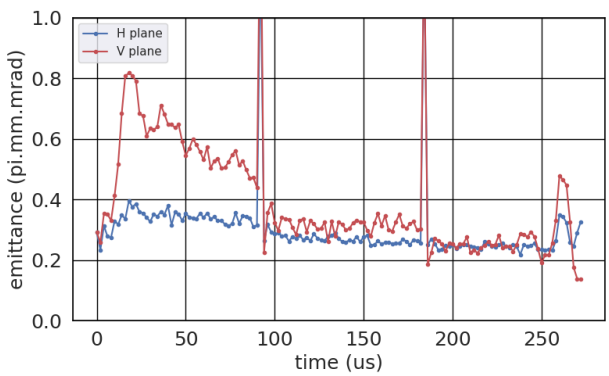


Figure 10: Normalized emittance along the macropulse measured by the laser emittance meter.

ISBN: 978-3-95450-241-7 ISSN: 2673-5350 doi:10.18429/JACoW-IBIC2022-TU3C3

CONCLUSION AND OUTLOOK

The completion of the commissioning of the laser emittance meter at the beginning of year 2022 allowed first systematic measurements in view of assessing the performance of the instrument. It appeared the quality of the emittance measurement from the diamond sensors is degraded by the presence of periodic perturbation signal that has an electrical origin, but seems as well transported by the LINAC4 beam. A digital notch filter is used to effectively supress the electrical perturbation signal, but it is planned to improve the shielding of the signal cables during the next winter technical stop.

The emittance measured along the LINAC4 macropulse by the laser emittance meter located in the transfer line shows some unexpected behavior in vertical plane that might have its origin from the filtering. More analysis will be performed to understand this phenomena and other measurements with the laser emittance meter located towards the beam dump line will bring other interesting material to study.

In the near future, different hardware and software strategies will be explored to improve the performance of the laser emittance meter. The comparison with other emittance and profile instruments will be performed as well.

ACKNOWLEDGEMENTS

We would like to thank our colleagues from CERN and Royal Holloway Institute for their strong past and present involvement, work and support on this project.

REFERENCES

[1] T. Hofmann, "Development of a Laser-based Emittance Monitor for Negative Hydrogen Beams", Ph.D. thesis, University of Erlangen-Nuremberg, Germany, 2017.

[2] T. Hofmann, U. Raich, F. Roncarolo, G. E. Boorman, A. Bosco and S. M. Gibson, "Results From the Laserwire Emittance Scanner and Profile Monitor at CERN's Linac4", in *Proc. LINAC'16*, East Lansing, MI, USA, Sep. 2016, pp. 715–719. doi:10.18429/JACoW-LINAC2016-TH2A02

[3] T. Hofmann, G. E. Boorman, A. Bosco, S. M. Gibson and F. Roncarolo, "Commissioning of the Operational Laser Emittance Monitors for LINAC4 at CERN", in *Proc. IPAC'18*, Vancouver, Canada, Apr.-May 2018, pp. 2357–2360. doi:10.18429/JACoW-IPAC2018-WEPAL074

[4] R. E. Shafer, "Laser diagnostic for high current H– beams", *AIP Conference Proceedings*, vol. 451, no. 1, pp. 191–198, 1998. doi:10.1063/1.56999

[5] National Instruments, https://www.ni.com/.

[6] A. Guerrero, J. J. Gras, J-L. Nougaret, M. Ludwig, M. Arruat and S. Jackson, "CERN Front-End Software Architecture for Accelerator Controls", in *Proc. ICALEPCS'03*, Gyeongju, Korea, Oct. 2003, paper WE612, pp. 342–344.

Content from this work may be used under the terms of the CC BY 4.0 licence (© 2022). Any distribution of this work must maintain attribution to the author(s), title of the work, publisher, and DOI

ISBN: 978-3-95450-241-7 ISSN: 2673-5350 doi:10.18429/JACoW-IBIC2022-TU3C4

A HIGH PERFORMANCE SCINTILLATOR ION BEAM MONITOR*

D. S. Levin†, University of Michigan, Ann Arbor, MI, USA
P. S. Friedman, Integrated Sensors LLC, Palm Beach Gardens, FL, USA
T. Ginter, Michigan State University, East Lansing, MI, USA
C. Ferretti, A. Kaipainen, N. Ristow, University of Michigan, Ann Arbor, MI, USA

Abstract

A high-performance Scintillator Ion Beam Monitor (SBM) provides diagnostics across an extremely wide range of isotopes, energies, and intensities employing a machine-vision camera with two novel scintillator materials moveable into/out of the beam without breaking vacuum. Scintillators are: 1) a semicrystalline polymer material (PM), film, 1 – 200 µm thick; and 2) a 100 – 400 µm thick opaque sheet consisting of a hybrid of an *inorganic-polymer* (HM) hybrid matrix. The SBM was demonstrated at the Facility for Rare Isotope Beams (FRIB, East Lansing, MI) providing real-time beam profile and rate analysis spanning more than five orders of magnitude *including visualization of single ion signals*. It may replace FRIB reference detectors: a phosphorescent beam viewer, a Faraday cup, a microchannel plate, and a silicon detector.

INTRODUCTION

Ion beam laboratories such as the Facility for Rare Isotope Beams (FRIB) feature many experimental beam lines requiring extensive, and potentially very expensive beam tuning. For example, the 2023 FRIB operating budget is nearly $100M [1], distributed over some 3100 active beam hours suggests an hourly beam operating cost on the order of $30k. Other facilities such as ANL, JLab, BNL/NASA require high performance scintillator detectors for charged particle counting over a wide dynamic range. High usage costs put a premium on technologies that enable the beam to be imaged, focused and otherwise tuned for research use with minimal time overhead and maximum versatility and spatial precision. The Scintillator Ion Beam Monitor system‡ (SBM) hardware/software beam detector and analysis suite is designed to meet these requirements. This article describes the SBM and recent experiment results.

The SBM hardware employs a machine-vision camera combined with a fast, large aperture lens and two proprietary thin scintillator materials. The scintillators mount on a multi-target cassette controlled by a robotic arm that allows them to be swapped or translated in/out of the beam without breaking vacuum. This detector is fabricated in a six-way stainless steel cross (6WC) composed of the three orthogonal transepts and can be configured directly into a high vacuum beamline. Figure 1 shows the 6WC mounted on a support stage for positioning in a beam, and a cross-sectional view showing the ladder or cassette of scintillator targets. A high resolution (megapixels), low-noise (2.4 photoelectrons RMS/ADC bin) CMOS sensor collects the scintillation light along the vertical branch line through a clear port window with a fast (*f*/0.9) lens. The field of view and depth of field are sufficient to image the entire target region.

Scintillators

Two types of proprietary scintillators are employed in the SBM: (1) Polymer Material (PM) – a semicrystalline polymer developed as a resilient thin film primarily for packaging applications. It was discovered to be an intrinsic scintillator with superior physical properties and higher light-yield than most plastic scintillators based on polyvinyltoluene and/or polystyrene. Because PM is semicrystalline, it has a "hazy" appearance. The PM-scintillator is highly radiation damage resistant. It produces a much stronger photodetector signal in our 6WC than other plastic scintillators tested such as BC-400 [2]. Various scintillator thicknesses from 200 µm to 1 µm have been tested. These thin films are particularly attractive for transmissive applications such as external beam radiation therapy (EBRT) where it is necessary for the imaging target to remain in the beam during treatment; (2) Hybrid Material (HM) is an *inorganic-polymer* material, is non-hygroscopic, is radiation damage resistant, is available in both thin and large area sizes, and can generate up to order of magnitude stronger signals per unit thickness than CsI(Tl). These large signals are attributed primarily to the photon transport; photons do not internally reflect and are emitted readily from the surface. The HM photon yield itself per energy deposited might be similar to CsI(Tl), in the range of 48000 – 65000 photons/MeV [3, 4]. Being polycrystalline in nature, it is visually opaque and incapable of total internal reflection, thus resulting in (1) a higher percentage of photons escaping from the film surface, (2) reduced back surface reflection and more accurate beam imaging and dosimetry. Two types of HM (HM_1 and HM_2) are included for SBM use, differentiated by their dopants, light yields, and decay times in the µs versus ms range respectively.

EXPERIMENTAL RESULTS

The SBM has been evaluated experimentally in various laboratories and with different radiation sources. Initial tests focused on scintillator performance using low-rate alpha and beta sources (^{241}Am, ^{90}Sr). Beam tests at FRIB using a 3 MeV/n ^{86}Kr beam in Sept. 2021, were followed at the Michigan Ion Beam Lab (MIBL) with high intensity 1 – 5 MeV protons, and at the Notre Dame Radiation

* Work supported by SBIR Phase-II award from the DOE Office of Science to Integrated Sensors, LLC (Award No. DE-SC0019597).
† dslevin@umich.edu
‡ An Integrated Sensors patented product

Content from this work may be used under the terms of the CC BY 4.0 licence (© 2022). Any distribution of this work must maintain attribution to the author(s), title of the work, publisher, and DOI

ISBN: 978-3-95450-241-7 ISSN: 2673-5350 doi:10.18429/JACoW-IBIC2022-TU3C4

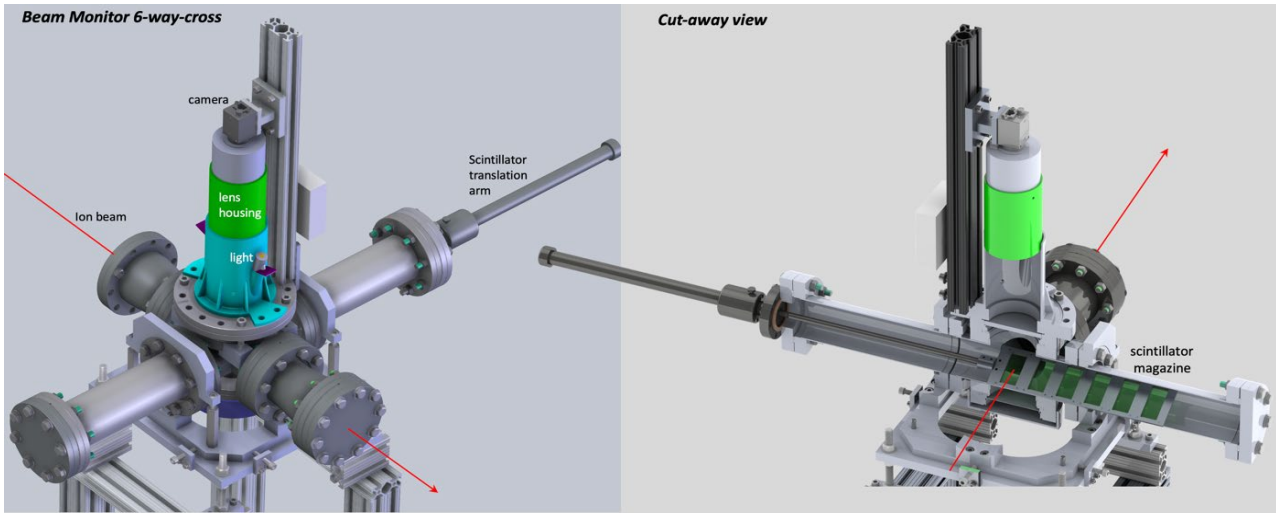


Figure 1: The six-way cross (6WC) mounted on a support stage (left); cut-away view showing the internal scintillator cassette (right).

Laboratory using fast, intense bunches of 8 MeV electrons. Selected results are presented here.

Benchtop Scintillator Tests

Initial test-bench experiments were conceived to evaluate HM and PM scintillator performance with respect to reference standards. The setup was arranged in a dark box using the 6WC components and a similar optical layout. The camera imaged 2 x 4 cm^2, 105 – 435 µm thick HM and 1.25 mm thick unpolished CsI(Tl), scintillator targets over a range of viewing angles. The radiation source was a 2.4 mCi ^{90}Sr button that produced a 3 mm diameter beam of ~1 MeV b$^-$ particles. Images of this beam are shown in Figure 2 for a 0° viewing angle. The top panel shows the beam imaged on CsI(Tl), which may be compared to the same beam on a HM_2 target in the lower panel. The intense inner beam core corresponds to the 3 mm source bore. The significant feature of these tests is

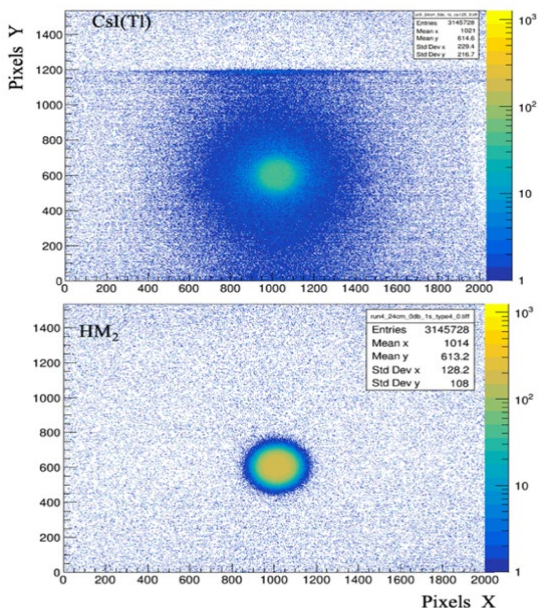


Figure 2: Image of a b$^-$ from ^{90}Sr on 1.25 mm thick CsI(Tl) (top) and 0.435 mm HM_2 (bottom).

1) the HM image is clean with well-defined beam since there are no internal reflections that distort or otherwise cause the beam image to bloom; 2) the relative signal strength of HM to CsI(Tl) scintillator, normalized to the material thickness: (units of ADC counts/mm) ranges from 5.4 to 12.2 (±10%) for HM_1 & HM_2 respectively. Furthermore, we note that the tested *unpolished* CsI would yield more front surface photon emission than a polished crystal. Using the same experimental setup the signal from commercial BC-400 scintillator relative to PM type of similar thickness was compared. The results are shown in Figures 3 top and bottom respectively. The ADC

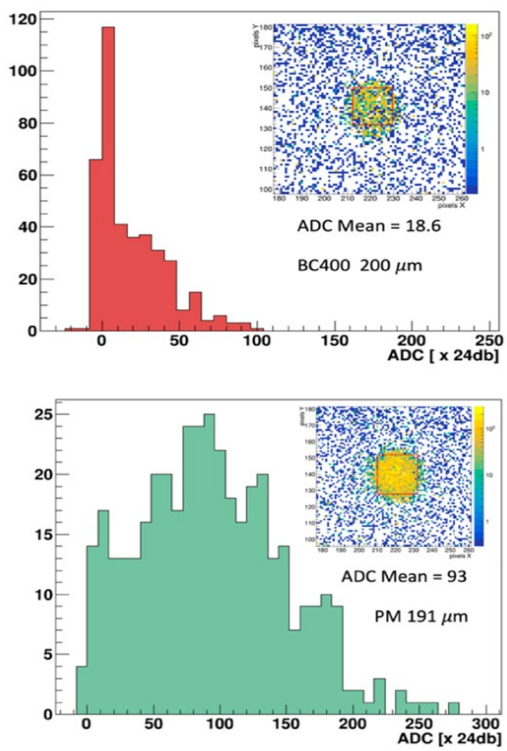


Figure 3: Inset is image of ^{90}Sr b$^-$ source on BC-400 (top) and PM (bottom). ADC spectra are from the red frame signal regions.

Content from this work may be used under the terms of the CC BY 4.0 licence (© 2022). Any distribution of this work must maintain attribution to the author(s), title of the work, publisher, and DOI

ISBN: 978-3-95450-241-7 ISSN: 2673-5350 doi:10.18429/JACoW-IBIC2022-TU3C4

Content from this work may be used under the terms of the CC BY 4.0 licence (© 2022). Any distribution of this work must maintain attribution to the author(s), title of the work, publisher, and DOI

distributions pertain to the hits within a fiducial signal region indicated by the red square frame. The PM image is much more filled in and the average ADC value is nearly 5 times larger. We note that this is not attributed to higher light yields as both materials likely have similar efficiency. Because PM is semi-crystalline and hazy, photons easily escape the planar surfaces towards the lens. The BC-400 is clear with smooth, specular surfaces; light internally reflects and escapes mostly out the edges where it is not collected by the lens.

FRIB Beam Test Results

At FRIB PM and HM_2 scintillators were tested. (Here HM=type 2). In-house diagnostic systems were used as a beam current reference, including a Faraday cup above 25,000 particles/s (pps), a silicon detector for counting rates below 100 pps, and a microchannel plate (MCP) that was used for the $10^{2\text{-}3}$ pps range. Intermediate hit rates ($> 10^3$ pps) were determined by calibrated beam attenuators. The SBM was evaluated at rates that extend from 520,000 pps down to effectively single, isolated particles at a total rate of ~5-10 pps distributed over an area of several mm^2. Figure 4 specifically shows these single particle hits on HM scintillator for a 1 s frame exposure (1 Hz frame rate). Figure 5 shows the hit profile for a ~50 pps beam for HM (left) and a reference CsI(Tl) 1.25 mm thick, unpolished scintillator (right) for comparison. In CsI(Tl) the beam is barely visible while in HM a clear beam image emerges. The integrated photon signal over the beam area is much larger for HM vs CsI(Tl).

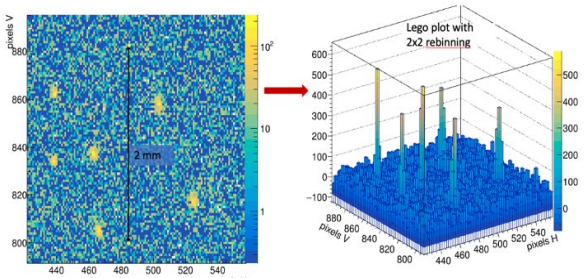


Figure 4: Individual ^{86}Kr hits on HM type scintillator. Camera frame exposure time = 1 s, beam rate ~5-10 pps.

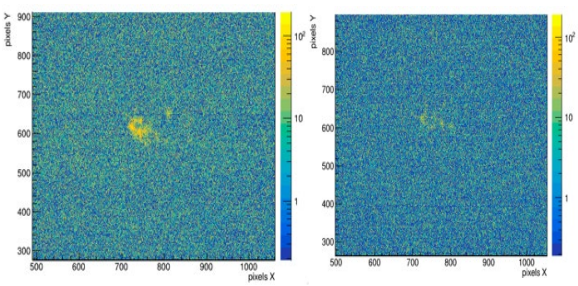


Figure 5: Image of a 50 pps beam on HM scintillator (left) and CsI(Tl) (right).

An updating low rate beam position tracking validation was conducted in real-time by the control room engineers incrementally translating the above 50 pps beam over a ~1 cm square region. The SBM tracking algorithm finds the beam centroid in the background subtracted images, performs perspective transforms and the necessary rotations to then present the centroids and widths in the beam coordinate system to the control room *in real-time.* Figure 6 (top left, top right) shows the history of the motion along the beam X and Y coordinates; the bottom left shows the RMS beam width and the bottom right shows the full 2D reconstructed beam position movement over a period of a few minutes.

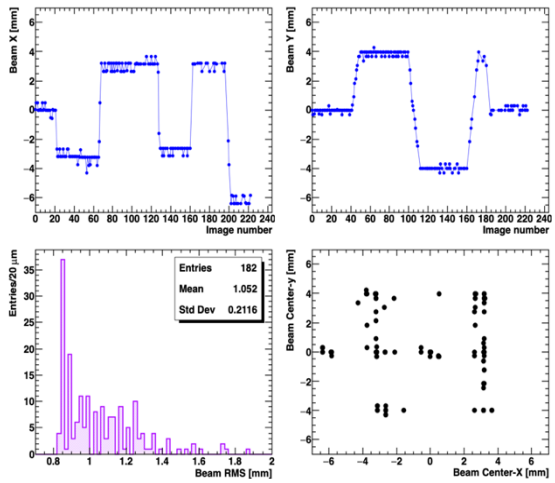


Figure 6: Tracking history of a low-rate (50 pps) beam motion. Top left, right: X and Y coordinate history where image frames are 1 s apart. Bottom left is the RMS beam radius and bottom right shows the 2D map of beam centroid positions.

Linearity and dynamic range: The signal response vs beam rate of HM scintillator at FRIB was measured by integrating the background-subtracted ADC signal over the entire area of the beam profile. This integral was then normalized to the average single particle signal. To obtain the single particle normalization constant, each of several hundred isolated ^{86}Kr hits in all low-rate data sets, as exemplified in Figure 4, were integrated out to the maximum hit radius. The results of this measurement are shown in Figure 7. The X coordinate axis reports the corresponding beam currents provided by FRIB beam control. These are based on the outputs of three rate-specific FRIB detectors (silicon strip detector, MCP,

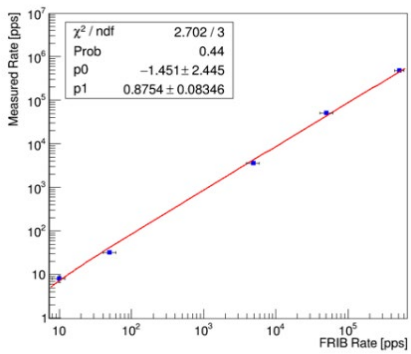


Figure 7: The SBM measured beam rate in HM scintillator plotted against the rates provided from three different FRIB reference detectors.

ISBN: 978-3-95450-241-7 ISSN: 2673-5350 doi:10.18429/JACoW-IBIC2022-TU3C4

Faraday cup), and on the use of calibrated beam attenuators that provide current estimates. The estimated total rate uncertainty of these rates is ~20%. The salient feature of Figure 7 is that the SBM result is linear within the fit error, and it tracks the beam current from single hits to five orders of magnitude.

MIBL Results

The SBM was staged in a higher current (1 – 10 nA), low energy (1 – 5.4 MeV) proton beam with the objective of measuring radiation degradation in PM type scintillators at high ionizing dose rates. In these experiments the beam was rastered over a 1 cm^2 aperture to produce a current density at the scintillator target of 4 nA/cm^2. Thin (1 – 200 µm) PM scintillators were evaluated for signal output, image quality and radiation degradation. For these high exposure rates in vaccuum of over 300 Gy/s, the average signal was observed to diminish by 0.5 ± 0.1 %/kGy as shown in Figure 8, for PM samples of varying thickness. Notably, when the samples are left in air, they tend to recover over a time of a few hours. Figure 9 shows the UV excited scintillation light yields measured post-irradiation for several PM samples of varying thickness, and for 20 kGy integrated dose. For reference, a commercial scintillator type EJ260 is also shown. The commercial product suffers greater signal loss, but recovers partially in 2 hours (later data were not acquired). Other measurements of EJ260 show, after 2 months, a 10% drop in transmittance at 550 nm for 5 x 10^{11} protons/cm^2 at 150 MeV (approximately 43 kGy) [5].

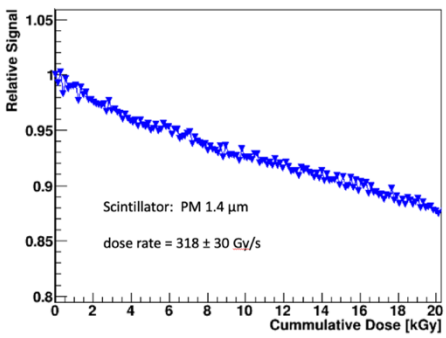


Figure 8: Relative signal in 1.4 µm thick PM scintillator during exposure at MIBL from 5.4 MeV protons at a dose rate of 318 Gy/s.

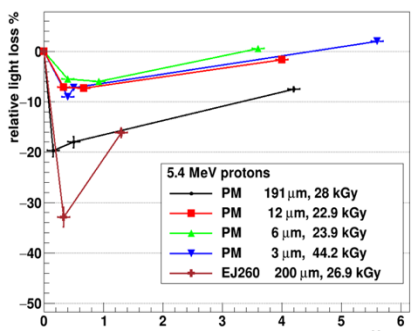


Figure 9: The UV induced scintillation signal strength vs recovery time in air for PM scintillators after exposure to 5.4 MeV protons.

CONCLUSIONS

The SBM is a verstaile instrument with a demonstrated ability to profile ion beams from low rates (single particles) to 10 nA currents using two novel scintillators mounted on a mult-target casette. High sensitivity HM scintillators readily detect single particles and low rate beams. PM type scintillators are shown to produce stronger signals than common commercial varieties. The PM can also be ultra-thin, with micron thickness and be partially or fully transmissive to ion beams. Scintillators are inserted into/out of the beam without breaking vacuum. A data acquistion and analysis software package is able to detect, measure and display beam profiles in real-time, enabling the SBM to be an effective beam tuning instrument.

REFERENCES

[1] Office of Chief Financial Officer, "Department of Energy: FY 2023 Congressional Budget Request, Volume 5", Office of Chief Financial Officer, Mar. 2022, https://www.energy.gov/cfo/articles/fy-2023-budget-justification

[2] Saint Gobain, "Saint-Gobain Crystals: BC400, BC-404, BC-408, BC-42, BC-416 Data Sheet", 2022. https://www.crystals.saint-gobain.com/radiation-detection-scintillators/plastic-scintillators/bc-400-bc-404-bc-408-bc-412-bc-416

[3] J. de Haas, P. Dorenbos, and C. van Eijk, "Measuring the absolute light yield of scintillators", *Nucl. Instrum. Methods Phys. Res., Sect. A,* vol. 537, pp. 97-100, 2005. doi:10.1016/j.nima.2004.07.243

[4] E. Shibamura, S. Saski, and N. Tran, "Systematic Study of Inorganic and Organic Scintillator Light Yields", in *Proc. Int. Symp. on Radiation Detectors and Their Uses (ISRD2016)*, Tokyo, Japan, 2016, vol. 11. doi:10.7566/JPSCP.11.020004

[5] V. Dormenev, K. Brinkman, R. Korjik, and R. Novotny, "Study of properties of the plastic scintillator EJ-260 under irradiation with 150 MeV protons and 1.2MeV gamma-rays", in *J. Phys. Conf. Ser.*, May 2016, Daegu, South Korea, 2017, vol. 928, p. 012035. doi:10.1088/1742-6596/928/1/012035

Content from this work may be used under the terms of the CC BY 4.0 licence (© 2022). Any distribution of this work must maintain attribution to the author(s), title of the work, publisher, and DOI

ISBN: 978-3-95450-241-7 ISSN: 2673-5350 doi:10.18429/JACoW-IBIC2022-WE1C2

AN X-RAY BEAM PROPERTY ANALYZER BASED ON DISPERSIVE CRYSTAL DIFFRACTION

N. Samadi†, C. Ozkan Loch, G. Lovric, Paul Scherrer Institut (PSI), Villigen PSI, Switzerland
X. Shi, Advanced Photon Source, Argonne National Laboratory, Lemont, USA

Abstract

The advance in low-emittance X-ray sources urges the development of novel diagnostic techniques. Existing systems either have limited resolution or rely heavily on the quality of the optical system. An X-ray beam property analyzer based on a multi-crystal diffraction geometry was recently introduced. By measuring the transmitted beam profile of a dispersive Laue crystal downstream of a double-crystal monochromator, the system can provide a high-sensitivity characterization of spatial source properties, namely, size, divergence, position, and angle in the diffraction plane of the system at a single location in a beamline. In this work, we present the experimental validation at a super-bending magnet beamline at the Swiss Light Source and refine the method to allow for time-resolved characterization of the beam. Simulations are then carried out to show that the system is feasible to characterize source properties at undulator beamlines for fourth-generation light sources.

INTRODUCTION

Fourth-generation synchrotron facilities [1-3] have brought the needs and challenges in developing advanced source property diagnostics. A complete characterization of the source position, angle, size, and divergence is critical for not only the electron source study but also the beamline experiment optimization. Many efforts have been dedicated to searching for the best diagnostic tools with different approaches, such as direct imaging [4-6], interferometry-based [7-9], and dispersion-based methods [10, 11]. Since each technique has advantages and limitations, we have concluded in a recent review [12] that the combination of multiple techniques may be advantageous.

Most recently, an X-ray beam property analyzer (XBPA) based on a multi-crystal diffraction geometry has been proposed and demonstrated to measure source properties with high resolution and sensitivity [13], showing great potential for X-ray beam quality characterization at next-generation light sources. Here, we first review the theoretical model of the XBPA system, followed by an experimental demonstration at a super-bending magnet beamline at the Swiss Light Source (SLS), performed with an ultra-fast detector. Finally, we summarize the simulation results of the XBPA for analyzing the source properties of an undulator beamline, as proposed in the course of the SLS upgrade.

XBPA SYSTEM DESCRIPTION

The XBPA system together with the physical model and fundamental equations is described in detail in [13]. A schematic is shown in Fig. 1. The XBPA system uses a crystal monochromator (e.g., a double-crystal monochromator (DCM) is the most commonly used) to generate a narrow-bandwidth (in the order of $\Delta E/E \approx 10^{-4}$) beam with the energy spread in the diffraction direction (e.g., vertical direction for a vertical deflecting monochromator), as shown in Fig. 1(a). The flat beam downstream of the monochromator is a near-Gaussian profile, as shown in Fig. 1(b), that contains the source angle and divergence information. By placing a Laue crystal in the dispersion geometry tuned to the central energy of the monochromator, a small spatial portion of the beam will be diffracted away, leaving a valley in the transmitted beam profile, as shown in Fig. 1(c). The width and location of the valley contain the source position and size information. By analyzing both the flat and transmitted beam profiles, the spatial properties of the photon source in the diffraction direction can be fully extracted.

When the source has a fixed position, but the beam is tilted by an angle, the flat beam will move vertically according to the angle and the source-to-detector distance. However, the Laue-transmitted beam valley location will not move, as the monochromator will select out the same energy from the angular distribution of the source, or the central energy line (dashed line in Fig. 1) will not move. On the other hand, if the source is fixed in angle but moves vertically in position, not only the flat beam will move vertically, but the valley position will also move vertically the same amount as the source motion (i.e., a parallel vertical shift of the dashed central energy line in Fig. 1). Thus, there is a simple relationship between the vertical source angle (y_s') and position (y_s) and the measured flat beam location

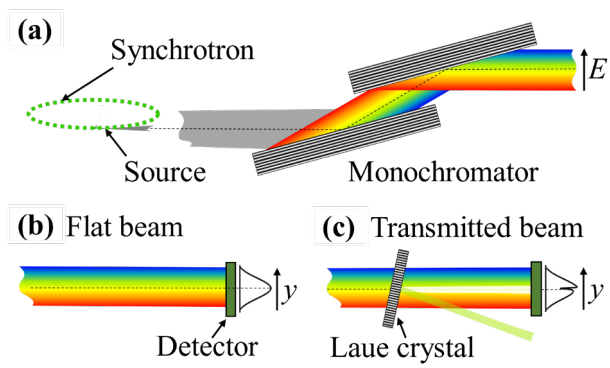


Figure 1: Schematic of the XBPA system containing the crystal monochromator, the Laue crystal in dispersion geometry downstream of the monochromator, and the detector. (a) shows a double-crystal monochromator geometry, (b) and (c) show the flat beam without the Laue crystal and the transmitted beam with the Laue crystal tuned to the central energy of the monochromator, respectively.

† nazanin.samadi@psi.ch

Content from this work may be used under the terms of the CC BY 4.0 licence (© 2022). Any distribution of this work must maintain attribution to the author(s), title of the work, publisher, and DOI

ISBN: 978-3-95450-241-7 ISSN: 2673-5350 doi:10.18429/JACoW-IBIC2022-WE1C2

(y_{flat}) and Laue-transmitted beam vally location (y_{valley}). This can then be used to determine the vertical source position and angle [13] by,

$$y_s = y_{\mathrm{valley}} \tag{1}$$

and

$$y_s' = \frac{y_{\mathrm{flat}} - y_s}{d}, \tag{2}$$

where d is the source-to-detector distance.

Similarly, the source size and divergence information can be extracted from the measured flat beam profile and the Laue-transmitted beam (valley) profile. Since the valley profile is not Gaussian, a simple Gaussian fitting will not work. Instead, we extract the source profile $I_s(y)$ through curve fitting the measured valley profile $I_{\mathrm{valley}}(y)$ given by,

$$I_{\mathrm{valley}}(y) = \frac{I_{\mathrm{trans}}(y)}{I_{\mathrm{flat}}(y)}, \tag{3}$$

where $I_{\mathrm{trans}}(y)$ and $I_{\mathrm{flat}}(y)$ are the measured Laue-transmitted and flat beam profiles, respectively. The curve fitting is performed by minimizing the error function in a discrete form defined as [13],

$$err = \left\{\frac{1}{n}\sum_{i=1}^{n}\left[I_{\mathrm{point}}(y_i) * I_s(y_i) - I_{\mathrm{valley}}(y_i)\right]^2\right\}^{1/2}, \tag{4}$$

where i is the pixel index on the detector along the vertical direction, n is the total number of pixels and $*$ is the convolution operator. The $I_{\mathrm{point}}(y)$ is the theoretical valley profile that can be accurately calculated using dynamical theory [14]. Assuming a Gaussian source profile,

$$I_s(y) = \exp\left[-\frac{(y - y_s)^2}{2\sigma_y^2}\right]. \tag{5}$$

The sigma source size σ_y can thus be extracted from the curve fitting process. Finally, the source divergence $\sigma_{y'}$ can be derived from the flat beam size, σ_{flat}, assuming a Gaussian flat beam distribution, given by,

$$\sigma_{y'} = \frac{1}{d}\left(\sigma_{\mathrm{flat}}^2 - \sigma_y^2\right)^{1/2}.$$

EXPERIMENTAL DEMONSTRATION

The first experimental demonstration of the XBPA system was carried out at the SLS optics beamline (X05DA dipole magnet) [15], and the results were reported in [13]. Here we show data from a new experiment performed at the X02DA TOMCAT beamline (2.9 Tesla super-bending magnet) at the SLS. A Si (1,1,1) fixed-exit double-crystal monochromator (DCM) at approximately 7 m from the source was used to tune the X-ray energy to around 20 keV. A 1× objective lens coupled to a 300-micron LuAG scintillator and an ultra-fast CMOS detector [16] was used to capture images with an effective pixel size of 11×11 μm^2.

A 350 μm thick Si (1,1,1) Laue crystal was placed in a dispersive geometry against the DCM at 25.1 m from the source. The Laue crystal was tuned to the central energy of the DCM to diffract at 20 keV. The detector was placed at 25.2 m from the source and collected the flat beam (without the Laue crystal) and the transmitted beam images through the Laue crystal. The measurements were performed with different acquisition times (down to milliseconds level), thanks to the high flux provided by the super-bending magnet source. The results presented here use an acquisition time of 40 ms for a single image.

Figure 2(a) shows the dark-corrected flat beam image and its integrated 1D profile, $I_{\mathrm{flat}}(y)$, (black dashed curve), and Figure 2(b) shows the dark-corrected transmitted beam image through the Laue crystal with its integrated 1D profile, $I_{\mathrm{trans}}(y)$, (black solid curve). Note that the 1D profiles were obtained by integrating over the central 500 horizontal pixels of each 2D beam image. Figure 2(c) shows the valley profile, $I_{\mathrm{valley}}(y)$, (solid curve) and the numerically fitted profile (dashed curve). The vertical source size was measured to be σ_y = 17±2 μm (rms), as compared to a recent result (17-18 μm rms) using zone plate imaging [17] and the previously measured values (15 μm rms, or 35 μm FWHM) based on the fractional Talbot effect [18]. The error bar was determined as the standard deviation of 20 measurements (each measurement was an average of 10 images). Note that the beam profile in Fig. 2(a) is not a perfect Gaussian shape with a brighter central part, which is caused by the superposition of the third-harmonic beam (Si(3,3,3) diffraction of the 60 keV beam). Thus, the fitting has been performed using Eq. (4) with $I_{\mathrm{point}}(y)$ constructed as a sum of the first and the third harmonic contributions assuming a specific ratio (4:1, estimated from the bending magnet spectrum and scintillator photon yield).

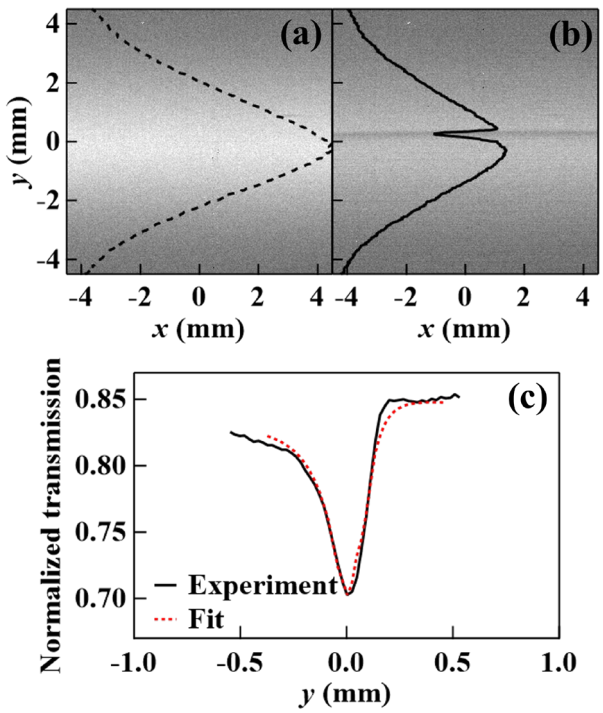


Figure 2: Images of (a) the flat beam and its 1D integrated profile, $I_{\mathrm{flat}}(y)$, (dashed curve) and (b) the Laue-transmitted beam and its 1D integrated profile, $I_{\mathrm{trans}}(y)$, (solid curve). (c) Normalized transmission (valley) profiles from the experiment, $I_{\mathrm{valley}}(y)$, (solid curve) the numerical fit (dashed curve).

Content from this work may be used under the terms of the CC BY 4.0 licence (© 2022). Any distribution of this work must maintain attribution to the author(s), title of the work, publisher, and DOI

ISBN: 978-3-95450-241-7 ISSN: 2673-5350 doi:10.18429/JACoW-IBIC2022-WE1C2

Content from this work may be used under the terms of the CC BY 4.0 licence (© 2022). Any distribution of this work must maintain attribution to the author(s), title of the work, publisher, and DOI

Since the bending magnet source size is dominated by the electron beam, $I_s(y)$ in Eq (4) stays the same.

UNDULATOR SOURCE PROPERTY CHARACTERIZATION

The resolution of the XBPA system is determined by the diffraction bandwidth of the monochromator and Laue crystal. In order to measure an undulator source, especially at low-emittance light sources, the crystal bandwidth has to be significantly smaller than the angular divergence of the source. Otherwise, the valley in the transmitted beam may be too wide compared to the beam width, which makes it challenging to extract the valley profile using Eq. (3). One solution is to use a high-index reflection of the crystals.

We next simulate the feasibility of the XBPA system in measuring undulator source properties using the *Shadow-Oui* ray-tracing program [19] in the *OASYS* environment [20]. The photon source parameters (including both contributions from the electron and undulator radiation) used are σ_y= 5.9 µm and $\sigma_{y'}$ = 3.6 µrad. The monochromator is a Si(333) Bragg DCM, and the Laue crystal is a symmetric Si(333) Laue crystal with a thickness of 0.25 mm. The diffraction/transmission profiles of the Laue crystal are generated by the *XCRYSTAL* module [21] before being used in the ray tracing. The detector is at d = 15 m from the source. For each simulation, 5×10^6 rays are used to achieve sufficient statistics.

Five sets of simulations (virtual experiments) were carried out: (1) the nominal case with no source parameter changes, (2) the source position y_s shifted by 1.77 µm, (3) the source angle y_s' tilted by 0.57 µrad, (4) the source size reduced to σ_y= 4.72 µm, and (5) the source divergence reduced to $\sigma_{y'}$= 3.43 µrad. The simulated flat beam profiles and transmission profiles are shown in Fig. 3. The extracted source parameters are summarized in Table 1. The XBPA system can correctly isolate and measure source position, angle, size, and divergence changes, making it a promising source diagnostic tool for undulator sources.

Table 1: Results of Source Property Simulation

#	Input change	Output (extracted from simulation)
(1)	σ_y = 5.9 µm $\sigma_{y'}$ = 3.6 µrad	y_s = 0, y_s' = 0 σ_y = 5.72 µm, $\sigma_{y'}$ = 3.64 µrad
(2)	y_s = 1.77 µm	y_s = 1.76 µm, $\Delta y_s'$ = −0.003 µrad
(3)	y_s' = 0.57 µrad	Δy_s = 0.00 µm, y_s' = 0.565 µrad
(4)	σ_y = 4.72 µm	σ_y = 4.66 µm, $\Delta\sigma_{y'}$ = 0.004 µrad
(5)	$\sigma_{y'}$ = 3.43 µrad	$\Delta\sigma_y$ = 0.11 µm, $\sigma_{y'}$ = 3.47 µrad

CONCLUSION

Here we have described how the XBPA system can be used to characterize the source properties at synchrotron light sources. Measurements of the TOMCAT super bending magnet beamline source size have been demonstrated and give a good agreement with previous results. Simulations were conducted to show the feasibility of using the XBPA system to characterize the undulator source position, angle, size, and divergence at low-emittance light sources. The XBPA system is a promising source diagnostic tool for different beamlines and photon energies.

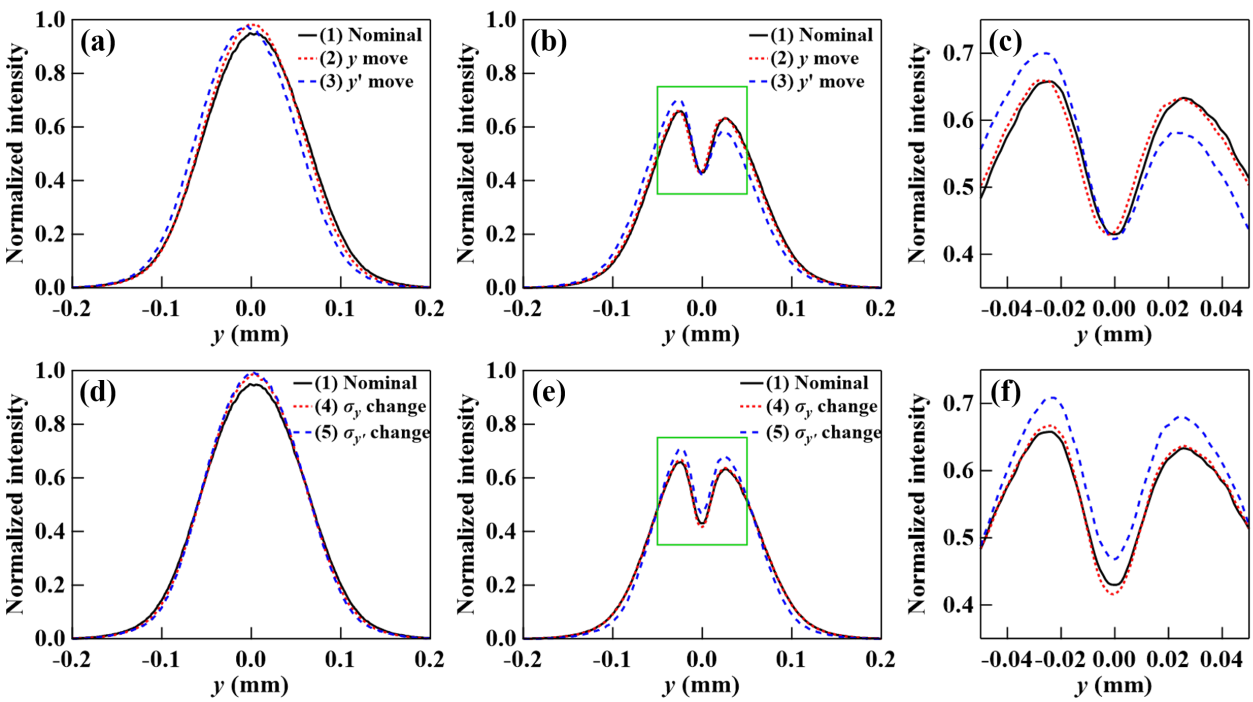


Figure 3: Simulated flat beam profiles (a and d) and Laue-transmitted beam profiles (b and e) of an undulator with different source parameters (see text and Table 1 for details of the five sets of simulations). Figures (c) and (f) are the enlarged regions (green boxes) of (b) and (e), respectively.

ISBN: 978-3-95450-241-7 ISSN: 2673-5350 doi:10.18429/JACoW-IBIC2022-WE1C2

REFERENCES

[1] M. Eriksson, J. F. Van Der Veen, and C. Quitmann, *"Diffraction-Limited Storage Rings-A Window to the Science of Tomorrow"*, *J. Synchrotron Radiat.,* vol. 21, p. 837, 2014. doi:10.1107/S1600577514019286

[2] P. F. Tavares, S. C. Leemann, M. Sjöström, and Å. Andersson, *"*The MAX IV Storage Ring Project*"*, *J. Synchrotron Radiat.,* vol. 21, p. 862, 2014. doi:10.1107/S1600577514011503

[3] M. Borland *et al.*, "The Upgrade of the Advanced Photon Source", in *Proc. IPAC'18*, Vancouver, Canada, Apr.-May, 2018, pp. 2872-2877. doi:10.18429/JACoW-IPAC2018-THXGBD1

[4] C. Thomas, G. Rehm, I. Martin, and R. Bartolini, *"*X-Ray Pinhole Camera Resolution and Emittance Measurement*"*, *Phys. Rev. ST Accel. Beams*, vol. 13, p. 022805, 2010. doi:10.1103/PhysRevSTAB.13.022805

[5] H. Sakai e*t al.*, *"*Improvement of Fresnel Zone Plate Beam-Profile Monitor and Application to Ultralow Emittance Beam Profile Measurements*"*, *Phys. Rev. ST Accel. Beams,* vol. 10, p. 042801, 2007. doi:10.1103/PhysRevSTAB.10.042801

[6] D.-C. Zhu, J.-H. Yue, Y.-F. Sui, D.-H. Ji, J.-S. Cao, K.-R. Ye, S.-Q. Tian, J. Chen, and Y.-B. Leng, *"*Performance of Beam Size Monitor Based on Kirkpatrick–Baez Mirror at SSRF*"*, *Nucl. Sci. Tech.*, vol. 29, p. 148, 2018. doi:10.1007/s41365-018-0477-y

[7] T. Naito and T. Mitsuhashi, *"*Very Small Beam-Size Measurement by a Reflective Synchrotron Radiation Interferometer*"*, *Phys. Rev. ST Accel. Beams*, vol. 9, p. 122802, 2006. doi:10.1103/PhysRevSTAB.9.122802

[8] J. Corbett, X. Huang, J. Wu, C. L. Li, T. Mitsuhashi, Y. H. Xu, and W. J. Zhang, "Transverse Beam Profiling and Vertical Emittance Control with a Double-Slit Stellar Interferometer", in *Proc. IBIC'16*, Barcelona, Spain, Sep. 2016, pp. 236-239. doi:10.18429/JACoW-IBIC2016-MOPG70

[9] X. Shi, S. Marathe, M. J. Wojcik, N. G. Kujala, A. T. Macrander, and L. Assoufid, *"*Circular Grating Interferometer for Mapping Transverse Coherence Area of X-Ray Beams*"*, *Appl. Phys. Lett.*, vol. 105, p. 041116, 2014. doi:10.1063/1.4892002

[10] N. Samadi, B. Bassey, M. Martinson, G. Belev, L. Dallin, M. De Jong, and D. Chapman, *"*A Phase-Space Beam Position Monitor for Synchrotron Radiation*"*, *J. Synchrotron Rad.*, vol. 22, p. 946, 2015. doi:10.1107/S1600577515007390

[11] N. Samadi, X. Shi, L. Dallin, and D. Chapman, *"*A Real-Time Phase-Space Beam Emittance Monitoring System*"*, *J. Synchrotron Radiat.,* vol. 26,. p. 1213, 2019. doi:10.1107/S1600577519005423

[12] N. Samadi, X. Shi, L. Dallin, and D. Chapman, *"*Source Size Measurement Options for Low-Emittance Light Sources*"*, *Phys. Rev. Accel. Beams*, vol. 23, p. 024801, 2020. doi:10.1103/PhysRevAccelBeams.23.024801

[13] N. Samadi, X. Shi, C. Ozkan Loch, J. Krempasky, M. Boege, D. Chapman, and M. Stampanoni, *"*A Spatial Beam Property Analyzer Based on Dispersive Crystal Diffraction for Low-Emittance X-Ray Light Sources*"*, *Sci. Rep.*, under review, 2022.

[14] W. H. W. Zachariasen, *Theory of X-Ray Diffraction in Crystals*, New York: John Wiley, 1945.

[15] U. Flechsig, A. Jaggi, S. Spielmann, H. A. Padmore, and A. A. MacDowell, *"*The Optics Beamline at the Swiss Light Source*"*, *Nucl. Instrum. Methods Phys. Res. Sect. A*, vol. 609, p. 281, 2009. doi:10.1016/j.nima.2009.07.092

[16] R. Mokso *et al., "GigaFRoST:* The Gigabit Fast Readout System for Tomography*"*, *J. Synchrotron Radiat.*, vol. 24, p. 1250, 2017. doi:10.1107/S1600577517013522

[17] C. Ozkan Loch, A. Bonnin, J. Vila-Comamala, N. Samadi, A. M. M. Stampfli, and R. Ischebeck, *"*SLS 2.0 – Status of the Diagnostics*"*, presented at IBIC'2022, Krakow, Poland, Sep. 2022, paper MOP01, this conference.

[18] G. Lovric, P. Oberta, I. Mohacsi, M. Stampanoni, and R. Mokso, *"*A Robust Tool for Photon Source Geometry Measurements Using the Fractional Talbot Effect*"*, *Opt. Express*, vol. 22, p. 2745, 2014. doi:10.1364/OE.22.002745

[19] L. Rebuffi and M. Sánchez del Río, *"*ShadowOui: A New Visual Environment for X-Ray Optics and Synchrotron Beamline Simulations*"*, *J. Synchrotron Rad.,* vol. 2, p. 1357, 2016. doi:10.1107/S1600577516013837

[20] L. Rebuffi and M. Sanchez del Rio, *"*OASYS (OrAnge SYnchrotron Suite): An Open-Source Graphical Environment for X-Ray Virtual Experiments*"*, in *Proc. SPIE*, vol. 10388, p. 103880S, 2017. doi:10.1117/12.2274263

[21] M. Sanchez, N. Perez-bocanegra, X. Shi, and V. Honkimäki, *"*Simulation of X-Ray Diffraction Profiles for Bent Anisotropic Crystals*"*, *J. Appl. Crystallogr.*, vol. 48, p. 477, 2015. doi:10.1107/S1600576715002782

Content from this work may be used under the terms of the CC BY 4.0 licence (© 2022). Any distribution of this work must maintain attribution to the author(s), title of the work, publisher, and DOI

ISBN: 978-3-95450-241-7 ISSN: 2673-5350 doi:10.18429/JACoW-IBIC2022-WE2C2

BEAM STABILITY IN THE MAX IV 3 GeV STORAGE RING

J. Breunlin*, G. Felcsuti, MAX IV Laboratory, Lund University, Sweden

Abstract

The MAX IV Laboratory, inaugurated in 2016, hosts a 3 GeV ultra-low emittance storage ring, a 1.5 GeV storage ring and a linear accelerator driven Short Pulse Facility to deliver synchrotron radiation to scientific users. A Stability Task Force has been assigned to ensure the delivery of stable beams since early on in the design phase of the laboratory and is continuing its work in an ongoing and multi-disciplinary effort. Measurements of the electron beam stability resulting from the passive stabilization approach taken for the two storage rings will be presented, as well as figures of beam stability with the Fast Orbit Feedback system in operation. Each ID beamline in the 3 GeV storage ring is equipped with a pair photon beam position monitors that are currently used to complement the electron beam position monitors. In the light of the city development around the MAX IV campus, maintaining the good mechanical stability of the laboratory has to be seen as an ongoing effort. A number of studies are being performed to identify possible risks and to decide where measures need to be taken.

INTRODUCTION

The MAX IV 3 GeV storage ring, is optimized for the production of high-brightness X-rays and features a 20-fold seven-bend achromat lattice reaching a bare lattice emittance of 328 pm rad [1, 2]. The emittance coupling is adjusted for a routine delivery beam with a vertical emittance of 8 pm rad. All user beamlines use insertion devices (IDs). The RMS electron beam sizes in the source points are 52.0 µm horizontally and 4.0 µm vertically when considering the horizontal emittance reduction by ID radiation damping.

In order to achieve our overall stability goal, a beam stability better than 10 percent of the RMS beam size, the tolerances on magnet stability of 20 nm to 30 nm RMS displacement had been defined during the project phase [3]. This is achievable also because the very good initial 'green field' ground vibration levels have not increased significantly by the presence of the laboratory.

This paper shows examples of the work of the MAX IV Stability Task Force covering mechanical stability topics and floor vibration, the orbit stability of the stored electron beam, the role of orbit feedback systems, as well as position and angle stability studies with the synchrotron radiation (SR) beam from IDs.

MECHANICAL STABILITY

Mechanical stability at MAX IV is in general achieved by passive systems [3]. While internal vibration sources are easily controlled by passive isolators, disturbances originating outside the borders of the facility must be dealt with differently: by careful design of the support structures, and by early involvement in planned projects near the laboratory. A few examples are mentioned below.

During the design phase of the facility, the main mechanical stability concern was heavy traffic on the nearby motorway (distance approx. 120 m). Here the special floor structure designed to mitigate traffic-related disturbances together with the implementation of a policy ensuring stiff foundations (by prescribing a goal for the lowest resonance frequencies for structures supporting accelerator and beamline components) turned out to be very successful. Even though vibration peaks due to heavy traffic are clearly observable in the floor of the laboratory (see the correlation between vibration peak count and heavy vehicle count in Fig. 1), as of today, only minor disturbances to beamline operations have been related to traffic. The vibration levels caused by motorway traffic are typically used as a reference to evaluate the impact of future projects in the vicinity of the laboratory.

MAX IV was one of the first buildings in Brunnshög, a quickly developing district of Lund where office buildings, research facilities and residential homes for 40 000 inhabitants will be built the coming decades. As the city is growing around the MAX IV Laboratory, the nature of addressing mechanical stability changes. The main focus has been shifted from ensuring proper design towards influencing potentially vibration-generating projects planned in close proximity to our operations. In practice, our concerns regarding mechanical stability are raised in early planning phase through discussions with policymakers and urban developers about the location and design of their projects. For instance, track vibration isolation of a new tramway line close to the laboratory was implemented thanks to the cooperation with the municipality, and as a result, no detectable influence has been observed on the accelerator since the tram has been in operation since the end of 2020.

Currently, we are involved in the decision on where to introduce speed bumps on nearby roads. To minimize the risk of disturbing ambient vibrations at the laboratory, tests were conducted in collaboration with the municipality to determine safe distances for different bump profiles, vehicle weights, and speeds, see Fig. 2.

ELECTRON BEAM STABILITY

The Slow Orbit Feedback (SOFB) system is designed to correct the electron orbit at repetition rates up to 10 Hz in order to handle slow drifts [4]. A total of 200 beam position monitors (rf-BPMs) are available in each plane as well as 200 horizontal and 180 vertical corrector magnets. The targeted orbit stability is achievable with the SOFB only during operation (see Fig. 3); a result of the excellent passive stability of the storage ring. Integrated up to 1 kHz

* jonas.breunlin@maxiv.lu.se

Content from this work may be used under the terms of the CC BY 4.0 licence (© 2022). Any distribution of this work must maintain attribution to the author(s), title of the work, publisher, and DOI

ISBN: 978-3-95450-241-7 ISSN: 2673-5350 doi:10.18429/JACoW-IBIC2022-WE2C2

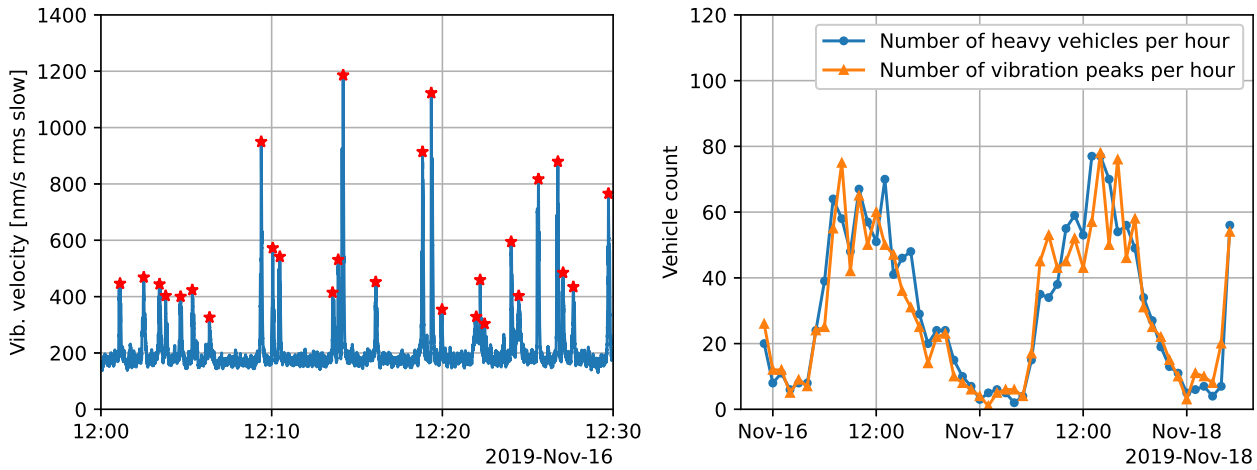


Figure 1: Left diagram: floor vibration time history (blue) and vibration peaks (red asterisks). Right diagram: comparison of the number of floor vibration peaks per time interval (blue) to the number of heavy vehicles on the nearby motorway (orange), measured by the Swedish road traffic authorities.

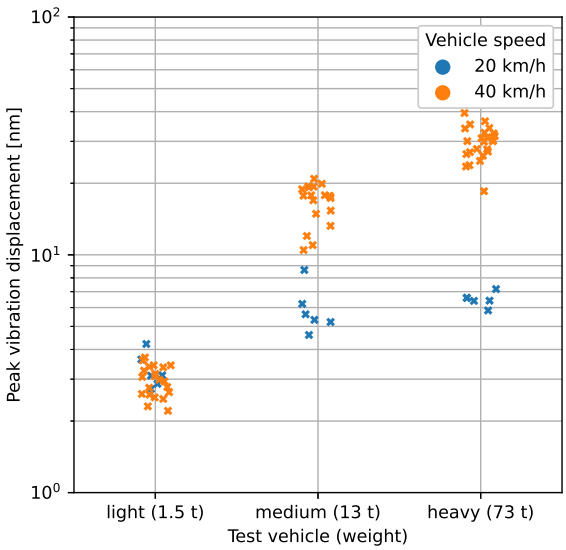


Figure 2: Results of an experimental study with vehicles driven over a speed bump. Floor vibration peak amplitudes for different test vehicle weights and speeds.

the horizontal RMS orbit displacement at beam position monitors closest to ID source points is 738 nm horizontally and 192 nm vertically.

Since the design of the slow correctors, iron core magnets and copper vacuum chambers, pose a physical restriction to the bandwidth of the SOFB system, an independent Fast Orbit Feedback (FOFB) [5] is installed using fast window-frame magnets at locations with stainless steel vacuum chambers. These fast correctors are of limited range and a periodical off-loading to the SOFB is required to avoid saturation, a principle that is also implemented at the Synchrotron Soleil [6].

The important role of the FOFB in the 3 GeV ring is the supression of orbit perturbations caused by transients induced by ID gap (or phase) movements, for which neither the SOFB nor the deployed ID orbit feed-forward system are fast enough. With the FOFB operating during user beam delivery ID gap and phase changes are transparent to the other user beamlines.

X-RAY BEAM POSITION MONITORING

Situated upstream of all beamline optics the frontend X-ray Beam Position Monitors (XBPMs) provide a valuable diagnostics tool for the SR delivered to each beamline and offer, due to the difference in their working principle, a complementary measurement to the rf-BPMs on the electron beam.

All of the ten insertion device beamlines at the MAX IV 3 GeV storage ring that are receiving SR today are equipped with a pair of XBPMs in their frontends [7]. Each XBPM head is equipped with four tungsten blades in a x-shape geometry. The blades interact with the outer region of the SR from the ID via the photoelectric effect and the resulting photocurrents are measured with electrometers [8]. Calibration of position is done on the control system level. The XBPM system is currently optimized for long term monitoring and archiving of position data.

XBPM measurements have confirmed the effectiveness of the SOFB and especially the FOFB in terms of stability of the delivered photon beams. The targeted observation of potential photon beam position drifts over time periods of hours to days, however, proved to be difficult because of the XBPM's intrinsic dependency on ID gap and phase as well as a dependency on stored beam current. Nevertheless, the combination of rf-BPM data, orbit corrector magnet currents

Content from this work may be used under the terms of the CC BY 4.0 licence (© 2022). Any distribution of this work must maintain attribution to the author(s), title of the work, publisher, and DOI

ISBN: 978-3-95450-241-7 ISSN: 2673-5350 doi:10.18429/JACoW-IBIC2022-WE2C2

Content from this work may be used under the terms of the CC BY 4.0 licence (© 2022). Any distribution of this work must maintain attribution to the author(s), title of the work, publisher, and DOI

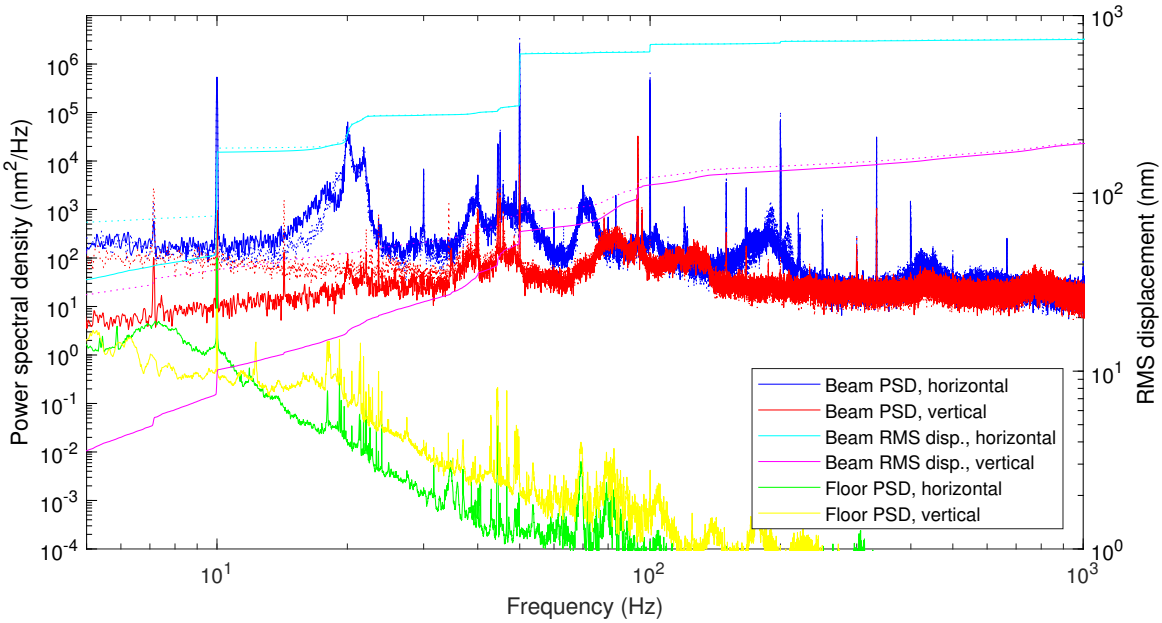


Figure 3: Electron beam motion (red and blue) and floor vibration (green and yellow) power spectral densities (on the left axis) as well as integrated RMS displacement of the electron beam in the horizontal and vertical plane (cyan and magenta, respectively, on the right axis) as a function of frequency. The electron beam data was measured with rf-BPMs flanking ID source points. The dotted lines show beam motion with only SOFB active while the solid lines show beam motion with active FOFB.

and XBPM data allow studies of the behaviour of both types of beam position diagnostics as well as an improvement of source stability.

CONCLUSIONS AND OUTLOOK

The MAX IV approach to beam stability is to a large extend based on the mechanical stability of the facility and its surroundings. The coming years in which a new city district will be developed in our neighborhood will require careful observation and possibly intervention in order to maintain our stability goals.

Slow and Fast Orbit Feedback systems are in daily user operation, stabilizing the orbit in the presence of slow drifts as well as fast perturbations for example from ID motion. Further improvement of the FOFB, for example the increase of its correction bandwidth require beam time and are planned for the near future. The installation and commissioning of a corresponding system in the MAX IV 1.5 GeV ring is ongoing.

XBPMs are currently in use for continuous monitoring. During the past months the option to change readout electronics to Libera Photon [9] has been investigated, a system that would allow for a much more efficient integration of the XBPMs into the existing rf-BPM system. In-house research is ongoing regarding alternative XBPM heads for the frontends of the 3 GeV ring [10].

REFERENCES

[1] P. F. Tavares *et al.*, "The MAX IV Storage Ring Project", *J. Synchrotron Radiat.*, vol. 21, pp. 862–877, 2014. doi:10.1107/S1600577514011503

[2] P. F. Tavares *et al.*, "Commissioning and first-year operational results of the MAX IV 3 GeV ring", *J. Synchrotron Radiat.*, vol. 25, pp. 1291–1316, 2018. doi:10.1107/S1600577518008111

[3] MAX IV Laboratory, "MAX IV Detailed Design Report", 2010.

[4] M. Sjöström, J. Ahlback, M. A. G. Johansson, S. C. Leemann, and R. Nilsson, "Orbit Feedback System for the MAX IV 3 GeV Storage Ring", in *Proc. IPAC'11*, San Sebastian, Spain, Sep. 2011, paper MOPO010, pp. 499–501.

[5] P. Leban, E. Janezic, and M. Sjöström, "Fast Orbit Feedback Application at MAX IV and SOLARIS Storage Rings", in *Proc. IPAC'14*, Dresden, Germany, Jun. 2014, pp. 1748–1750. doi:10.18429/JACoW-IPAC2014-TUPRI078

[6] N. Hubert, L. Cassinari, J. Denard, A. Nadji, and L. S. Nadolski, "Global Fast Orbit Feedback System Down to DC using Fast and Slow Correctors", in *Proc. DIPAC'09*, Basel, Switzerland, May 2009, paper MOOC01, pp. 27–31.

[7] A. Bartalesi, "The XBPM Project at MAX IV Frontends, Overview and First Results", in *Proc. MEDSI'18*, Paris, France, Jun. 2018, pp. 340–342. doi:10.18429/JACoW-MEDSI2018-THPH03

[8] J. A. Avila-Abellan *et al.*, "Em# Electrometer Comes to Light", in *Proc. ICALEPCS'17*, Barcelona, Spain, Oct. 2017, pp. 137–142. doi:10.18429/JACoW-ICALEPCS2017-TUAPL04

ISBN: 978-3-95450-241-7 ISSN: 2673-5350 doi:10.18429/JACoW-IBIC2022-WE2C2

[9] A. Kosicek and P. Leban, "Libera Brilliance and Libera Photon Working Together in Fast Orbit Feedback", in *Proc. ICALEPCS'09*, Kobe, Japan, Oct. 2009, paper THP070, pp. 797–799.

[10] P. Ilinski, "Novel Photoemission Type of X-ray Beam Position Monitor for the 'White' Undulator Radiation", presented at the IBIC'22, Krakow, Poland, paper MOP44, this conference.

Content from this work may be used under the terms of the CC BY 4.0 licence (© 2022). Any distribution of this work must maintain attribution to the author(s), title of the work, publisher, and DOI

ISBN: 978-3-95450-241-7 ISSN: 2673-5350 doi:10.18429/JACoW-IBIC2022-WE2I3

ADAPTIVE FEEDFORWARD CONTROL OF CLOSED ORBIT DISTORTION CAUSED BY FAST HELICITY-SWITCHING UNDULATORS

M. Masaki†, S. Takano[1], T. Watanabe[1], T. Fujita, H. Dewa, T. Sugimoto[1], M. Takeuchi
JASRI, Hyogo, Japan
H. Maesaka[2], K. Soutome, T. Fukui, H. Tanaka, RIKEN SPring-8 Center, Hyogo, Japan
K. Kubota, SPring-8 Service Co. Ltd., Hyogo, Japan
[1]also at RIKEN SPring-8 Center, Hyogo, Japan
[2]also at JASRI, Hyogo, Japan

Abstract

We developed a new correction algorithm for closed orbit distortion (COD) based on adaptive feedforward control (AFC). The AFC system integrated into the SPring-8 storage ring has proved to be effective in suppressing the fast COD with repetitive patterns caused by helicity-switching undulators. The scheme aims to counteract error sources by feedforward correctors at the position or in the vicinity of error sources to avoid a potential risk of unwanted local orbit bumps, which is known to exist for the global orbit feedback. The new option, AFC, is especially advantageous when an error source causes an angular fluctuation of photon beams such as a fast orbit distortion near undulators. The AFC provides a complementary capability to a so-called fast global orbit feedback (FOFB) for coming next-generation light sources where ultimate light source stability is essentially demanded.

INTRODUCTION

Storage-ring-based light sources have been become essential facilities for photon sciences and related applications including industrial purposes. One of the key advantages for light source users is the brightness of light, which is also related to the degree of transverse coherence. However, high photon beam stability is also essential for successful developments, along with high brightness. In modern or future light sources, the pointing stability of photon beam should be sufficiently smaller than the electron beam size to achieve the inherent light source performance. Beam orbit disturbances in a storage ring can be caused by a variety of error sources. For examples, (i) mechanical motions of magnets or vacuum chambers due to ground motion, cooling water, (ii) electro-magnetic noise of magnet power supplies or RF sources, (iii) magnet pole gap or phase motions, polarization switching kickers of insertion devices (IDs). These disturbances can be suppressed by orbit feedback and feedforward controls, or elimination of the error source itself. In the case that the error sources are unknown, slow or fast global orbit feedback can be an effective countermeasure. On the other hand, when the error sources are known, an ideal solution is to remove the error source itself, but not feasible for all sources. For an example, in the case of ID-derived orbit disturbance due to gap motion or fast switching kicker, feedforward corrections are often used without removing the error sources. The feedforward counter kicks in the vicinity of the error kicks are very effective.

In the SPring-8 storage ring, two twin-helical undulators (THUs) with fast kicker systems: ID23 and ID25 [1, 2] were installed for periodic photon helicity switching in X-ray magnetic circular dichroism experiments at beamlines. Orbit variations due to periodic excitation of the kicker magnets on demand from user experiments have been observed for years, even though ID23 and ID25 are equipped with fast corrector magnets for feedforward corrections to suppress them. The periodic orbit fluctuations, which are synchronized with the kicker excitation, gradually grew up to 10 μm (RMS) or more because of the deterioration with time of feedforward correction accuracy.

To address this issue, based on a fundamental orbit correction strategy to directly counteract an error source to be corrected, we have taken the following points into consideration: (i) the error sources are identified at the two THUs, (ii) the feedforward correction is already equipped, and (iii) the degradation rate of the correction accuracy is slow. We have introduced, instead of a conventional fast global orbit feedback, a new COD correction algorithm based on adaptive feedforward control (AFC) [3], in which the feedforward tables are dynamically updated. The COD variations originating in the two error sources (ID23 and ID25) are independently suppressed by the new AFC system. Our goal for the orbit stabilization is to suppress the COD fluctuations of less than 1 μm RMS during the kicker excitation in a transparent manner where experimental users cannot observe any periodic disturbance.

HELICITY-SWITCHING UNDULATORS OF SPRING-8

Schematics of the THU installed in the SPring-8 storage ring are illustrated in Fig. 1. The twin helical switching system consists of the two helical undulators for right- and left-handed circular polarizations, placed on the upstream and downstream sides, respectively. Five kicker magnets make the dynamical horizontal orbit bumps (orbit A and B as shown in Fig. 1) alternately, for periodic optical helicity switching. The switching-frequency for ID23 is 1 Hz; ID25 can be switched at either 1 or 0.1 Hz. When the electron beam orbit is switched to the orbit A, the radiation from the upstream undulator propagates horizontally off-axis and is

† masaki@spring8.or.jp

Content from this work may be used under the terms of the CC BY 4.0 licence (© 2022). Any distribution of this work must maintain attribution to the author(s), title of the work, publisher, and DOI

ISBN: 978-3-95450-241-7 ISSN: 2673-5350 doi:10.18429/JACoW-IBIC2022-WE2I3

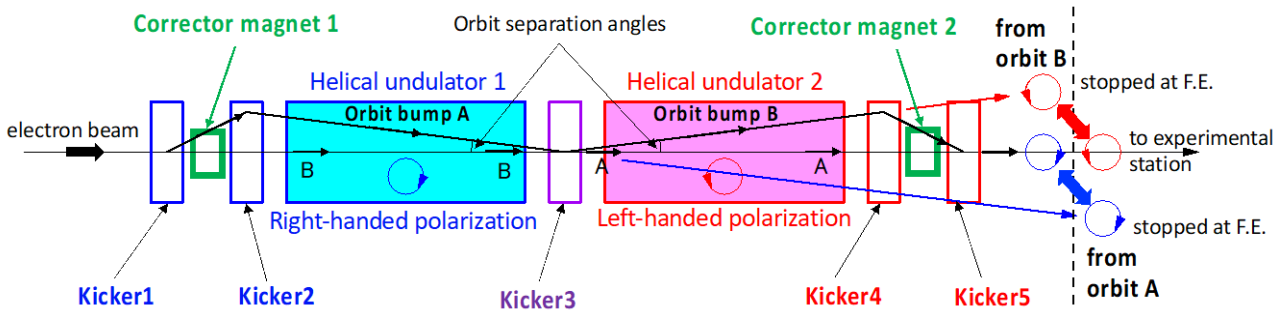


Figure 1: Schematic top view of the twin-helical undulator of SPring-8 with the horizontal kicker system for helicity switching. The orbit separation angles are 300 μrad and 100 μrad for ID23 and ID25, respectively.

stopped at the front-end absorber in the beamline, whereas the radiation from the downstream undulator propagates along the beamline axis and reaches the experimental station. On the other hand, switching to the orbit B makes revered situation. Thus, by switching these two orbits (A and B) repeatedly, the circularly polarized light with alternate helicities is provided for the user's experiments. The photon beam separation angle by the orbits A and B is 300 μrad for ID23 and 100 μrad for ID25. The five kicker magnets are excited with periodic trapezoidal patterns. As a typical example, the excitation pattern of ID23 kickers with a repetition frequency of 1 Hz is shown in Fig. 2. The kickers 1,2,3 to make the orbit bump A are excited in the time range from 0 s to 0.5 s, whereas the kickers 3,4,5 to make the orbit bump B are excited from 0.5 s to 1s.

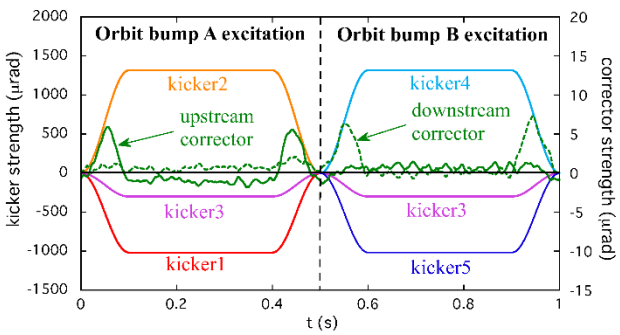


Figure 2: Kicker excitation patterns and examples of excitation patterns for corrector magnets of ID23 for switching at 1 Hz.

The imperfect closure of orbit bumps due to the kicker errors in the THU is supposed to be cancelled out by the feedforward control of two fast air-core corrector magnets placed on both ends of the THU. The waveform-pattern signals to drive the power supplies for the kicker magnets and the fast corrector magnets are generated by a pattern board on a VME system which is prepared for each of ID23 and ID25, separately. The pattern board is equipped with 16 bits D/A converters and outputs the waveform-pattern data sampled synchronously with an internal clock. The clock rate is set to 5 kHz or 1 kHz for the kicker switching frequency of 1 Hz or 0.1 Hz, respectively. While driving the kickers and the fast corrector magnets at 1 Hz or 0.1 Hz, the pattern board also provides the trigger signal outputs synchronized with the kicker pattern excitation.

The feedforward correction tables of fast corrector magnets used to be updated a few times a year. However, as the correction accuracy gradually degraded with time, we sometimes observed periodic orbit fluctuations in the horizontal plane, typically of several microns during the helicity switching, which was detrimental to user experiments. The causes of this deterioration remain unclear, despite having been painstakingly investigated by the Insertion Device Group. This led to the need for an adaptive feedforward system that can dynamically and automatically update the correction tables without stopping the demanded helicity switching in user experiments.

ADAPTIVE FEEDFORWARD CONTROL

We overview the AFC system for helicity-switching undulators developed at SPring-8 [3] by focusing on its specific features and summarizing results from the beam test and operation experiences in the user time.

Key Points of the AFC

In order to mitigate the problem of the periodic orbit perturbation during the optical helicity switching, we have developed the AFC system, which is equipped with dedicated fast BPMs with sufficient time response to detect the orbit variations precisely. The following points are important for the AFC to work effectively: (1) Automatic updating of the correction tables without stopping the helicity switching for user experiments, (2) High-precision and efficient extraction of only error kicks due to the THUs, (3) Even if simultaneous helicity-switching of the two THUs, well-resolving each counter kick, (4) Resistant to orbit perturbations due to error sources other than the THUs.

Correction Scheme

Periodic COD fluctuation occurred in the horizontal plane synchronized to the kickers' driving frequency of 1 or 0.1 Hz during the switching at the two THUs. The observed periodic fluctuation contains frequency components up to several tens of Hz, but these are sufficiently slow compared to the radiation damping time of millisecond order. Therefore, we considered that the orbit distortion at each moment in the switching period can be analyzed as a superposition of instantaneous CODs caused by time-dependent multiple error kicks at the kickers.

Content from this work may be used under the terms of the CC BY 4.0 licence (© 2022). Any distribution of this work must maintain attribution to the author(s), title of the work, publisher, and DOI

ISBN: 978-3-95450-241-7 ISSN: 2673-5350 doi:10.18429/JACoW-IBIC2022-WE2I3

Content from this work may be used under the terms of the CC BY 4.0 licence (© 2022). Any distribution of this work must maintain attribution to the author(s), title of the work, publisher, and DOI

As shown in Fig. 1, each of the orbit bumps A and B is produced by exciting three kickers in a THU. Since the imperfect closure of the three-kicker orbit bump has two error kicks, the leakage of COD variation outside the THU can be suppressed by adding two counter-kicks by exciting the two corrector magnets placed beside the kicker magnets in each THU. The betatron phase difference between the two THUs, ID23 and ID25, is approximately 660° in the horizontal direction, around the ideal value (i.e., an odd multiple of 90°) for resolving the error sources relevant to each THU by observing the distribution of orbit distortion along the storage ring. Therefore, we decided to determine the values for the counter-kicks of the corrector magnets in the two THUs by measuring the orbit variation with multiple BPMs placed along the storage ring. The four counter-kicks for the two THUs can be approximately determined with the data of orbit distortion obtained at four BPMs placed on the ring by solving,

$$-x_{BPM,i}(t) = \sum_{j=1}^{n} R_{ij}\theta_{corr,j}(t)\,, \qquad (1)$$

where $\theta_{corr,j}(t)$ and $x_i(t)$ are the time-dependent counter kick angle at the j-th corrector magnet and the observed beam position displacement at the i-th BPM, respectively. The response-matrix element between the kicker and BPM is

$$R_{ij} \equiv \frac{\sqrt{\beta_i\beta_j}}{2\sin(\pi\nu)}\cos\left(\pi\nu - |\mu_i - \mu_j|\right), \qquad (2)$$

where the parameters β_i, β_j are beta functions at the i-th BPMs and the j-th kickers; ν is the betatron tune; and μ_i-μ_j is the betatron phase advance between the kicker and the BPM, respectively.

System Overview

Figure 3 shows an overview of the AFC system at SPring-8. To resolve the four counter kicks of the corrector magnets even while the two THUs are switching the helicity at the same frequency, we carefully selected four out of the total 286 BPM heads on the storage ring. Each of the selected BPM heads is connected to a newly developed fast MTCA.4-based readout circuit [4] to detect the periodic COD variations with sufficient precisions. We selected two BPMs (namely, 23-2 and 46-2) sensitive to horizontal kicks in ID23, and two others (24-5 and 35-2) for ID25, considering the betatron phases between the IDs and the BPM heads. The measured values of the response matrix elements between the selected BPMs and the fast corrector magnets for ID23/25 are listed in Table 1. The periodic COD variations during the kicker operations are measured by using the fast acquisition (FA) mode of the BPM circuit with a sampling rate of 10 kHz. The two trigger signals synchronized with the kicker drivers of THUs, ID23 and ID25, are fed to a digitizer board on the common MTCA.4 system for the BPM23-2 and 24-5. The other two BPM data are synchronized with the kickers by marking with the common timestamps of the fed trigger signals which are shared on the control network of the accelerator. The correction patterns are updated by adding the counter-kick patterns calculated from the 4-BPM data to the previous patterns.

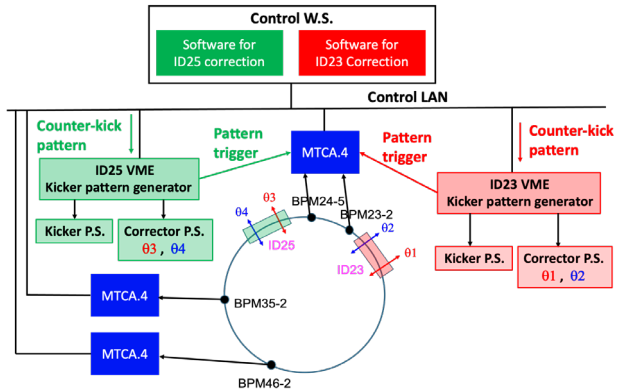


Figure 3: Overall picture of the adaptive feedforward control system at SPring-8.

Table 1: Measured 4-by-4 Horizontal Response Matrix

R_{ij} (m/rad)	ID23-U (θ_1)	ID23-D (θ_2)	ID25-U (θ_3)	ID25-D (θ_4)
BPM23-2 (x_1)	+26.4	+25.6	-3.07	+1.05
BPM24-5 (x_2)	+0.623	-3.29	+25.6	+25.8
BPM35-2 (x_3)	-2.08	+1.66	-22.8	-20.2
BPM46-2 (x_4)	-18.2	-20.9	+6.69	+2.71

Folding and Filtering Processes of BPM Data

To achieve orbit correction accuracy of less than 1 μm (rms), the counter-kick errors of the fast correctors need to be within 0.05 μrad (rms). The keys of BPM data processing are random noise reduction to secure sub-micron resolution and filtering to eliminate contamination due to error kicks other than the THUs. For low-noise extraction of the periodic COD variation, the BPM data of several tens of periods in length is folded at the period of the helicity switching. In the case of helicity switching at 1 Hz, for example, the BPM data sampled at 10 kHz of 60 periods in length is firstly fast-Fourier-transformed (FFT) in the frequency range from –5 kHz to +5 kHz. We then pick up every peak accurately at the repetition frequency of the switching kicker and its harmonic frequencies by spline interpolation of the FFT spectrum. Inverse Fourier transform of the data picked-up at the fundamental and harmonic frequencies yields the time profile of periodic orbit variation folded at the period of the helicity switching. In the case of helicity switching at 0.1 Hz, the BPM data of 10 periods in length is folded by a similar procedure. For high frequency noise reduction, the 5-th orders Butterworth numerical low-pass filter is applied to the data in the frequency domain before the inverse Fourier transform. The filter cut-off frequency is 100 Hz and 30 Hz for switching at 1 Hz and 0.1 Hz, respectively. To accurately counteract error sources, it is important to compensate time response (phase delay) of the AFC correction loop itself. The phase delay in the frequency domain was derived from a step response of the BPMs measured by exciting the correctors with a step function. The phase delay compensation was incorporated into a phase function of the complex low-pass filter.

ISBN: 978-3-95450-241-7 ISSN: 2673-5350 doi:10.18429/JACoW-IBIC2022-WE2I3

By this folding and filtering processes of raw BPM data, we can obtain an averaged and smoothed one-cycle time profile of the periodic orbit variation at the switching frequency. After the folding and the filtering, the random noise level of the BPM data is 0.2 μm (rms).

Counter Kick Calculation

In our AFC system, counter-kick patterns for the four corrector magnets in the two THUs are calculated using the processed four BPMs data by solving Eq.(1) with the singular value decomposition (SVD) method. The 4-by-4 response matrix elements R_{ij} between the BPMs and the correctors are measured as shown in Table 1. In the case of the simultaneous helicity switching of ID23 and ID25, the corresponding singular values of the 4-by-4 response matrix are shown in Table 2, in descending order from four modes #1 to #4. Solving Eq.(1) with the SVD using all the four modes is equivalent to simply multiplying the inverse of the response matrix. Calculated CODs (RMS of values at the four BPMs) corresponding to each mode excited by a random kick of 0.1 μrad (1σ) at each corrector magnet are shown in Table 2. The CODs of modes #1 and #2 are the main components of the orbit variation and are larger than that of the modes #3 and #4. The CODs of modes #1 and #2 apparently need to be corrected. Modes #3 and #4 have significantly smaller contributions to the orbit variation. However, solving by using only two modes of #1 and #2 resulted in calculated counter-kicks with an inappropriate kick angle and sign. Comparing the BPM noise-derived errors of the counter-kicks between "3-mode case" correcting modes #1 through #3 except mode #4, and "4-mode case" correcting all four modes, the former is 0.05 μrad (1σ) and the latter is 0.1 μrad (1σ), indicating that the "4-mode case" does not satisfy the target correction-kick accuracy of 0.05 μrad (1σ). Therefore, we decided to calculate the counter-kicks in the "3-mode case" (discarding mode #4).

Table2: Singular Values of the 4-by-4 Response Matrix. RMS values of calculated CODs in micron unit at the 4-BPMs corresponding to each mode when the random kick of 0.1 μrad (1σ) is given at each correction kicker.

Mode #	Singular Values	ID23-U kick	ID23-D kick	ID25-U kick	ID25-D kick
1	50.4	0.94	1.2	3.9	1.3
2	43.7	1.3	1.2	0.84	1.0
3	1.89	0.05	0.04	0.05	0.06
4	1.22	0.03	0.04	0.03	0.02

In the case of the solo helicity switching of ID23 or ID25, counter-kick patterns at the two corrector magnets for each of ID23 and ID25 are calculated from the four-BPM data by solving Eq. (1) with SVD using all modes with two singular values of the 4-by-2 response matrix, in other words, multiplying by the pseudo-inverse response matrix. The errors in the solved counter kicks derived from the BPM error of 0.2 μm (1σ) are about 0.03 μrad (1σ) for both ID23 and ID25, which satisfy the target correction kick accuracy.

Experimental Verifications

The new correction scheme based on the AFC was experimentally verified and successful for both solo and simultaneous switching at ID23 and ID25. Here, as an example, a demonstration for simultaneous 1 Hz switching is described. Orbit fluctuations were detected at all the four BPMs with the initial correction patterns in the feedforward correction tables for the two THUs. Following the aforementioned procedure, we obtained the counter-kick data for updating the feedforward correction tables for both IDs. The calculation of counter-kick data for each ID was separately processed by using all the four BPM data synchronized with the respective kicker triggers. The observed periodic orbit variations before and after modifying the correction patterns, along with the frequency-domain orbit fluctuation, are shown in Fig. 4, in which the periodic COD variations folded at the period of the kicker trigger for ID23 are shown. The pole gaps were 20 mm and 60 mm for ID23 and ID25, respectively. After the modification of the feedforward correction pattern, the horizontal COD fluctuations were drastically damped to the background level without helicity switching. We also checked for adverse effects of the horizontal corrections on the vertical COD as that could be induced by, e.g., tilted magnetic field in the fast corrector magnets due to fabrication and installation errors. The horizontal corrections worked well without compromising on the vertical beam stability.

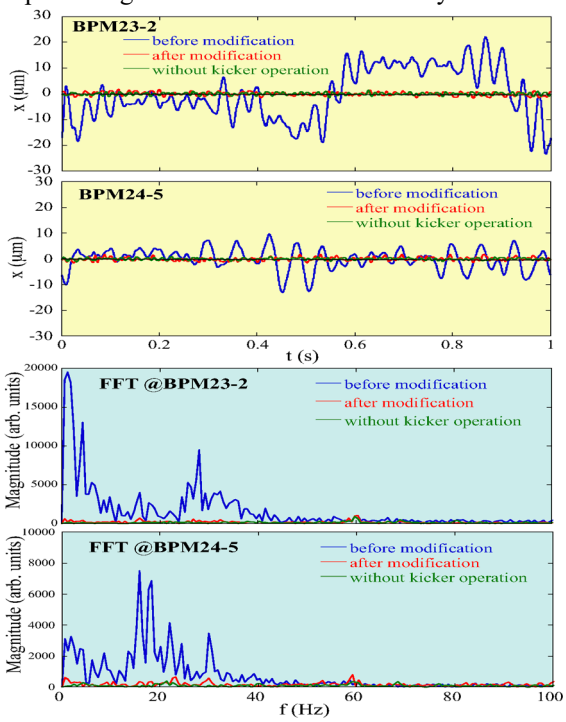


Figure 4: Example of the simultaneous 1 Hz switching of ID23 and ID25. Horizontal orbit fluctuations and their FFT spectra before and after modification of the correction patterns are shown.

Long-term Performance

We applied the developed AFC to the helicity switching of ID23 during the user time operation to confirm its long-

Content from this work may be used under the terms of the CC BY 4.0 licence (© 2022). Any distribution of this work must maintain attribution to the author(s), title of the work, publisher, and DOI

ISBN: 978-3-95450-241-7 ISSN: 2673-5350 doi:10.18429/JACoW-IBIC2022-WE2I3

Content from this work may be used under the terms of the CC BY 4.0 licence (© 2022). Any distribution of this work must maintain attribution to the author(s), title of the work, publisher, and DOI

term performance in suppressing the periodic COD variations. The feedforward correction patterns were automatically updated at 10 minutes intervals at that time. Figure 5 shows the RMS-fluctuation trend of the periodic COD patterns (chosen as an indicator of the magnitude of the periodic orbit fluctuation at 1 Hz) observed by BPM23-2, together with the pole gap of ID23. With the AFC, the orbit variation was successfully suppressed below the target value of 1 μm (rms) over the long period of term. The orbit fluctuation jumped up just after the ID23 pole gap changed, but it was promptly reduced by a subsequent correction by the AFC system.

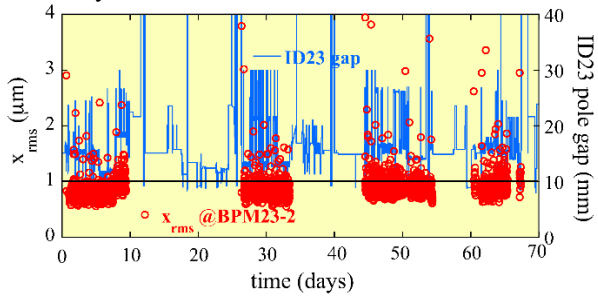


Figure 5: Example of RMS horizontal orbit fluctuation (red dots) with the continuous AFC operation during the ID23 helicity switching. Blue line shows the pole gap of ID23.

WHY NOT USE FAST ORBIT FEEDBACK

Potential Risk of FOFB

Fast orbit feedback (FOFB) is based on a global orbit correction scheme for fast orbit variations. The global correction has the advantage that it can be available in situations where error sources in a ring cannot be identified. However, the correction accuracy is limited by the number and placement of BPMs and correctors. There is a potential risk of unwanted orbit distortions or local bumps, because the correctors are not always placed at the positions or in the vicinity of the error sources.

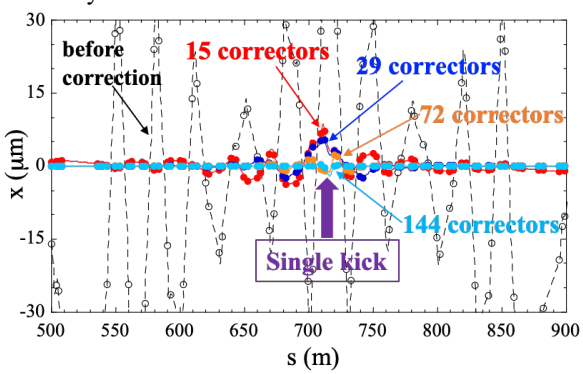


Figure 6: COD correction accuracy depending on the number of correctors with equal spacing, assuming an error source of horizontal single kick of 1 μrad at s=716.05 m. Dots show the horizontal orbits at the BPMs.

We simulated assuming the optics of the SPring-8 storage ring. Simulation conditions are assumed to be as follows: 1) an error source is a horizontal single kick of 1 μrad at s=716.05 m in the ID25 section, 2) numbers of correctors are assumed to be 15, 29, 72, and 144 with equal spacing, and 3) number of BPMs to detect the COD is fixed to be 286 which is all BPMs of the ring. The simulation results in Fig. 6 show that the COD correction accuracy depends on the number of correctors. A small number of the correctors results in unwanted orbit bumps around the error kick. Only the case of 144 correctors shows that such the local orbit bump dose not almost appear, in which the correctors exist within a few meters from the error kick.

Advantage of the AFC

In case that error sources are known, the AFC is much more advantageous than FOFB of the global correction scheme. On the AFC based on a source suppression scheme, the dedicated fewer correctors placed near error sources counteract them efficiently and precisely. A feedforward control such as the AFC is particularly suitable for correcting ID-induced orbit variations. Because we can grasp in advance the characteristics of the error kicks. In an ID section, which is a drift space, at least two correctors up- and down-stream near the error source would be sufficient, not to leak the orbit distortion outside the section. In this case, two counter kicks are approximately allocated in the ratio of the distances from the error kick to each corrector.

CONCLUSION

The development and verification of a new COD correction technique with the adaptive feedforward control (AFC) have been successfully done at SPring-8. The AFC works well for suppressing fast periodic orbit fluctuations during user time operation using the helicity-switching undulators with kickers. It keeps the COD fluctuation suppressed with sub-micron order for a long time.

Toward ultimate photon beam stability for next-generation light sources, relying solely on the global correction scheme, including FOFB, is not sufficient. When the error source is known, for example such as an insertion device origin, a source suppression scheme such as the AFC can be very effective. We believe that the global correction and the source suppression, both of the schemes in a complementary relationship, are indispensable in achieving the ultimate photon beam stability in future light sources.

REFERENCES

[1] T. Hara *et al.*, "Spring-8 twin helical undulator", *J. Synchrotron Radiat.*, vol. 5, pp. 426-427, 1998. doi:10.1107/S0909049597015719

[2] T. Hara *et al.*, "Helicity switching of circularly polarized undulator radiation by ocal orbit bumps", *Nucl. Instrum. Methods Phys. Res., Sect. A*, vol. 498, pp. 496-502, 2003. doi:10.1016/S0168-9002(02)02145-9

[3] M. Masaki *et al.*, "Adaptive feedforward control of closed orbit distortion caused by fast helicity-switching undulators", *J. Synchrotron Radiat.*, vol. 28, pp. 1758-1768, 2021. doi:10.1107/S160057752101047X

[4] H. Maesaka *et al.*, "Development of MTCA.4-Based BPM Electronics for SPring-8 Upgrade", in *Proc. IBIC'19*, Malmö, Sweden, Sep. 2019, pp. 471-474. doi:10.18429/JCoW-IBIC2019-WEBO03

ISBN: 978-3-95450-241-7 ISSN: 2673-5350 doi:10.18429/JACoW-IBIC2022-WE2C4

RF SYSTEM-ON-CHIP FOR MULTI-BUNCH AND FILLING-PATTERN FEEDBACKS*

P. Baeta†, B. Keil, G. Marinkovic, Paul-Scherrer-Institut (PSI), Villigen, Switzerland

Abstract

We have evaluated an RF System-on-Chip (RFSoC) as a platform to implement the multi-bunch (bunch-by-bunch) feedback and the filling pattern (single bunch charge) measurement system for the Swiss Light Source (SLS) upgrade project, the SLS 2.0. This paper presents the status and first results of a preliminary design of the feedback systems using an RFSoC evaluation board, including test measurements at the SLS.

INTRODUCTION

The Swiss Light Source (SLS) is a synchrotron light source at Paul Scherrer Institute (PSI), and it has been in user operation since June 2001. The SLS beamlines cover research areas such as, but not exclusively, atomic and molecular science, material science, environmental and earth science, and life and medical science. To preserve the high scientific output of SLS, PSI plans an upgrade of SLS, the SLS 2.0. The SLS storage ring will be replaced, and an innovative magnet lattice with reverse bends will provide up to 60-fold higher brightness for hard X-rays [1]. Moreover, aging systems of the SLS will be exchanged, including the storage ring multi-bunch feedback (MBFB) and filling pattern feedback (FPFB). In this context, an RF System-on-Chip (RFSoC) from Xilinx/AMD [2] has been evaluated as a possible solution to substitute the existing technology of the MBFB and FPFB systems in operation at the SLS [3, 4]. The RFSoC integrates multi-core CPUs, FPGA fabric, high-speed analog-to-digital (ADC), and digital-to-analog data converters (DAC) with several Giga-samples per second (Gs/s) on a single chip. We have used the ZCU111 kit from Xilinx/AMD to evaluate the RFSoC [2]. The ZCU111 evaluation board features an RFSoC with eight 12-bit 4 Gs/s ADCs, eight 14-bit 6.5 Gs/s DACs, a 4-core 64-bit, and a 2-core 32-bit ARM CPU. In addition, the RFSoC provides various data storage and communication interfaces, including multi-gigabit links and Ethernet.

The following sections of the paper describe the implementation of a three-dimensional multi-bunch feedback (MBFB) and the measurement of the relative charge in each bunch (filling pattern) at the SLS storage ring with the RFSoC, using RF beam position monitor (BPM) signals.

HARDWARE

Figure 1 shows the hardware setup installed in the SLS storage ring for developing and testing the MBFB and filling pattern measurement using the RFSoC. A BPM with four capacitive button electrodes is connected to RF hybrids, generating: The sum signal, S, proportional to the bunch charge; the horizontal, X, and vertical, Y, signals proportional to the product of transverse bunch position offset and charge. The ZCU111 is the core component of the system. The device acquires and samples the X, Y, and S signals with its ADCs, and generates the correction signals with its DACs. The correction signals are amplified and drive the MBFB kickers. In addition, acquired signal S is used to measure the filling pattern.

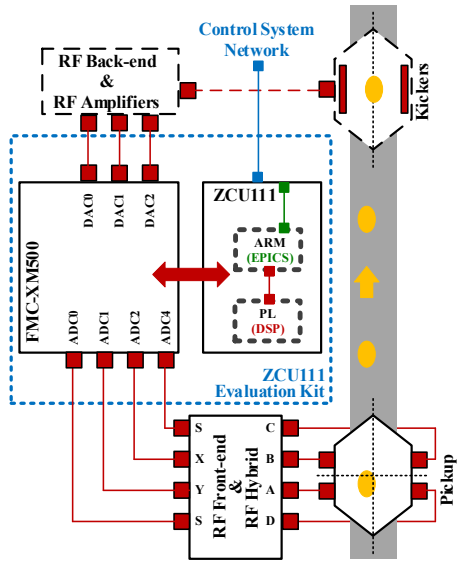


Figure 1: Hardware block diagram of the RFSoC-based multi-bunch feedback and filling pattern measurement.

The current MBFB system at SLS, presented in [3], has been in operation since 2006. The system has a commercial RF front-end (RFFE), which mixes the BPM signals from 1.25-1.5 GHz range down to baseband. The RFFE provides to ADCs: The transverse position signals, X and Y, and the phase signal for the longitudinal position, S. The signals X, Y, and S are sampled each by an 8-bit 500 Mega-samples per second (Ms/s) ADC. The signals are processed on a Virtex-2 FPGA with firmware implemented in VHDL at PSI. The driving signals for the transverse and longitudinal MBFB kickers are generated each by an 8-bit 500 Ms/s DAC. Each DAC directly drives the RF power amplifiers of transverse strip line kickers for X and Y channels. The longitudinal plane has an analog upconverter to transform the baseband (0-250 MHz) DAC signal to 1.25-1.5 GHz for the power amplifier of the longitudinal kicker.

The primary goal of the first MBFB implementation on the RFSoC was to facilitate the comparison with the current SLS system. Therefore, the new RFSoC firmware is functionally compatible with the analog signal conditioning of the current system. Consequently, the new and existing MBFB system electronics can be exchanged or even operated in parallel, enabling live switching between the two systems using combiners/splitters.

At SLS, the current FPFB measures the bunch charge with an avalanche photodiode (APD), using synchrotron

† pedro.baeta@psi.ch

Content from this work may be used under the terms of the CC BY 4.0 licence (© 2022). Any distribution of this work must maintain attribution to the author(s), title of the work, publisher, and DOI

ISBN: 978-3-95450-241-7 ISSN: 2673-5350 doi:10.18429/JACoW-IBIC2022-WE2C4

Content from this work may be used under the terms of the CC BY 4.0 licence (© 2022). Any distribution of this work must maintain attribution to the author(s), title of the work, publisher, and DOI

radiation photons in the visible range [4]. The APD signal is digitized in oversampling mode with a VMEbus ADC board at 500 Ms/s. Embedded real-time software calculates the filling pattern using the acquired signals during the interval between the injections of consecutive top-up injection cycles. The filling pattern information is used to sort the electron bunches by charge. Finally, the sorted bunch indices are used to control the injections of the next top-up cycle. There are typically 15 single-bunch injections of 0.15 nC each at 3 Hz every few minutes. The FPFB fills at first bunches with the largest charge deficit from the user-defined filling pattern, and keeps the SLS ring beam current of usually 400 mA within a window of typically 2 mA.

In contrast to the RFSoC-based MBFB, the new filling pattern measurement with the RFSoC uses direct sampling of the BPM sum signal, S, without any analog signal preconditioning. Moreover, a unique firmware realizes both systems on the ZCU111 board.

FIRMWARE AND SOFTWARE

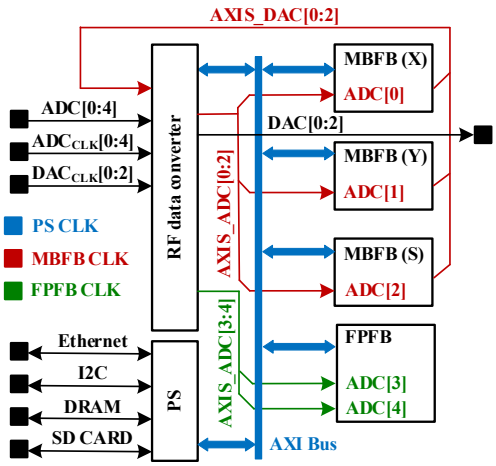


Figure 2: Firmware block diagram of the RFSoC-based multi-bunch feedback and filling pattern measurement.

Figure 2 shows the firmware block diagram of the systems on the RFSoC. The MBFB and the FPFB cores implement the multi-bunch feedback and the data acquisition for the FPFB, respectively. The central IP core of the design is the Xilinx RF Data Converter, which configures the ADCs and DACs and instantiates their interfaces to the programmable logic (PL) [2]. The ADC and DAC data are streamed from/to the AD/DA RF Data Converter core via AXI stream interfaces. The processing system (PS) core instantiates the ARM CPUs. The Ethernet interface of the PS communicates with the control system via an EPICS IOC running on the ARM CPU of the RFSoC. The AXI bus connects the PS to other IP Cores of the design. The I2C bus is used to control the peripherals of the ZCU111, including on-board PLLs that define the clock frequencies of the PL and sampling frequencies of the data converters. The ZCU111 uses the SLS machine reference clock of the ring central RF systems (f_{RF} = ~500 MHz). The clocks of the data converters and PL are synchronized to this reference clock and thus to the electron beam revolution frequency.

The ADCs and DACs 0 to 2 of the RFSoC, used for the MBFB, run at 8 × f_{RF} (~4 Gs/s), the red clock network in Fig. 2. The harmonic number of the SLS ring is 480. Thus, the ADC and DAC acquire eight samples per bunch and $N = 8 \times 480$ samples per storage ring revolution. Moreover, the ADC and DAC tiles of the RFSoC are configured in multi-tile synchronization (MTS) mode to guarantee temporal sample alignment among ADCs and DACs, as well as a reproducible latency from ADC to DAC after a power cycle of the system [2]. The ADCs 3 and 4, used for the FPFB, operate at a different clock (close to 4 Gs/s), the green network in Fig. 2. So that an interleaving scheme increases the effective sampling rate of these ADCs. The sampling frequency f_S is set to acquire a fractional number of samples per beam turn

$$f_s = \frac{f_{RF} \times 8 \times (M \times N - 1)}{(N \times M)}, \quad (1)$$

where N is the number of samples per beam turn, and M is the interleaving factor. The data, acquired over M turns, is interleaved, resulting in a waveform with M-fold higher effective sampling rate. In the prototype system, M is set to 16, providing an effective sampling rate of ~ 64 Gs/s.

Multi-bunch Feedback (MBFB) Systems

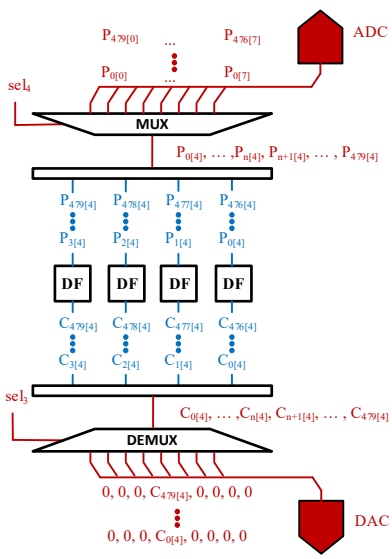


Figure 3: Data processing path of the MBFB System.

Figure 3 shows the signal processing path for the three MBFB planes. The interface between ADCs and PL operates at f_{RF} (~500 MHz), providing eight samples in parallel. Next, the 8 × f_{RF} (~4 Gs/s) data stream is decimated to 500 Ms/s by selecting one out of 8 samples, P_i, of the position signal. The resulting 500 Ms/s data stream is demultiplexed four times, generating four streams with 125 Ms/s for easier timing closure of the FPGA firmware. The bunch position P_i of each bunch is processed by digital filters (DF), resulting in the bunch correction signal C_i. In the output stage, the user can choose, with 250 ps resolution, when to apply the bunch correction signal C_i to kick the bunch with index i, b_i. Figure 4 shows the digital signal processing paths for the longitudinal (4a) and the two transverse (4b) planes of the MBFB. The IIR filters, gain stages,

ISBN: 978-3-95450-241-7 ISSN: 2673-5350 doi:10.18429/JACoW-IBIC2022-WE2C4

and generic FIR filters can be reconfigured to damp coherent bunch oscillations. For the prototype, the DF used in the longitudinal and transverse planes of the MBFB system is functionally equivalent to the filters presented in [3].

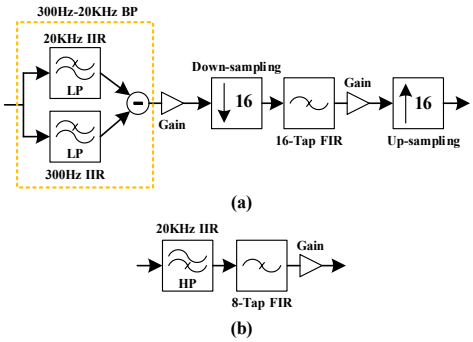


Figure 4: Block diagram of the digital filters for the longitudinal (a) and transverse (b) planes of the MBFB.

Filling Pattern Feedback (FPFB) System

The firmware of the test implementation of the FPFB using the RFSoC system consists of data acquisition blocks, which record the input data stream of ADCs 3 and 4, shown in Fig. 2. ADC 3 samples the revolution clock (reference for bunch indexing) and ADC 4 the sum signal, S (providing bunch charge and bunch arrival-time information). The acquisition core supports automatic trigger detection by level or external triggering, storing up to 512k samples for all ADC channels. Moreover, data can be acquired continuously or in multiple segments with user-defined length and inter-segment gaps. The communication and configuration of the acquisition core are done via AXI bus. The recorded data and configuration parameters can be accessed via EPICS channels.

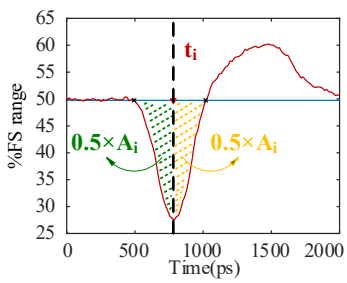


Figure 5: Sum signal, S, for one bunch windows of 2 ns, illustrating a single bunch pulse of the bunch train. The area A_i between the negative pulse (red curve) and the baseline (blue curve) is used to estimate the charge of the bunch b_i. Time t_i, which splits A_i in two equal parts, is an estimate for the arrival time of b_i.

The bunch charge and arrival time have been calculated offline on a PC in Python, with the acquired BPM data from the EPICS IOC running on the RFSoC. This first approach provided the flexibility to test different algorithms for the final version, which will be deployed in firmware/real-time embedded software.

Figure 5 shows a single bunch pulse from the sum signal, S. Each bunch window is 2 ns long, where A_i is the area between the negative pulse, red curve, and the baseline, blue curve. The baseline is the mean value of S in the bunch window. The charge of each bunch b_i is equal to a common factor k times the calculated area A_i. The bunch index i is assigned such that bunch zero is the first bunch after the revolution clock, and bunch 479 is the last before a new turn. The bunch arrival time of b_i is the time t_i, which splits the area A_i equally by two.

STATUS AND OUTLOOK

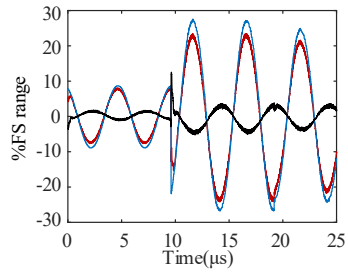


Figure 6: Hardware (red curve) and expected response (blue curve) of the transverse MBFB system (X-plane) for an arbitrary input. The black curve corresponds to the absolute error of the hardware response.

Multi-bunch Feedback (MBFB) Systems

The present prototype of the MBFB system has been designed to be functionally equivalent to the existing MBFB, aiming to evaluate if the RFSoC technology suits the application. In the first step, we verified that the latency from ADC to DAC of the RFSoC is reproducible after a power cycle of the ZCU111. While the old system has an external clock shifter, the RFSoC system latency can be adjusted on-chip in steps of 250ps via EPICS. Next, the data processing functionality of the MBFB was verified by firmware simulation and by feeding generated test signals into the new hardware and comparing the response to a software reference model. Figure 6 illustrates the functional verification of the MBFB system, showing the hardware and the expected response for the horizontal plane. Attenuation along the analog signal path leads to the difference between the two responses. Beam tests of the MBFB are planned for the following months. First, a one-to-one replacement of the present MBFB hardware with the new hardware is intended, keeping the analog down/up converters of the old system. Next, the external analog up converter for the longitudinal kicker will be removed, and the RFSoC will directly synthesize the kicker drive waveform (up to 1.5 GHz for SLS and 1.75 GHz for SLS 2.0). In addition, replacing the present analog downconverter RF front-end (RFFE) for the BPM signals is planned. For the new RFFE, we consider directly sampling the BPM signals with suitable signal bandwidth, gain and delay adjustment, aiming to process all ADC signals at the full sample rate of 4 Gs/s. Moreover, we are evaluating the option to digitally calculate X, Y, and S from the four button signals.

Content from this work may be used under the terms of the CC BY 4.0 licence (© 2022). Any distribution of this work must maintain attribution to the author(s), title of the work, publisher, and DOI

ISBN: 978-3-95450-241-7 ISSN: 2673-5350 doi:10.18429/JACoW-IBIC2022-WE2C4

Content from this work may be used under the terms of the CC BY 4.0 licence (© 2022). Any distribution of this work must maintain attribution to the author(s), title of the work, publisher, and DOI

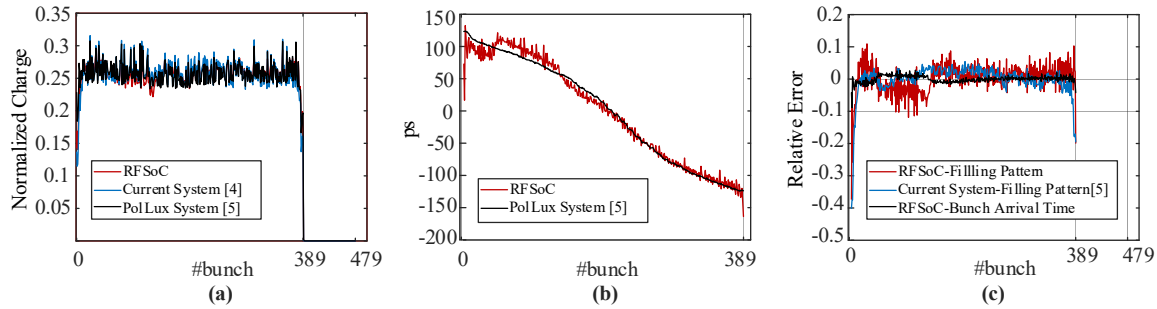


Figure 7: Measurements of the bunch (a) charge and (b) arrival time in the SLS. (c) Relative error of the bunch charge and arrival time measurements using a soft X-ray photon counting system of the SLS PolLux beamline as reference [5].

For SLS 2.0, we consider implementing more advanced diagnostics and feedback algorithms, such as excitation-damping measurements, betatron and synchrotron tune measurement, and automated tuning. The lack of logic resources in the current SLS Virtex-2 hardware limits the scalability and modernization of its algorithms.

Filling Pattern Feedback (FPFB) Systems

Figure 7 shows the measurement results of the bunch charge and arrival time obtained at the SLS storage ring. Figure 7a compares the bunch charge measurement of the RFSoC implementation against the existing system presented in [4] and with a soft X-ray photon counting system of the SLS PolLux beamline described in [5]. Figure 7b compares the bunch arrival-time measurements for different methods, and Fig. 7c compares the system performance using the PolLux system as a reference [5].

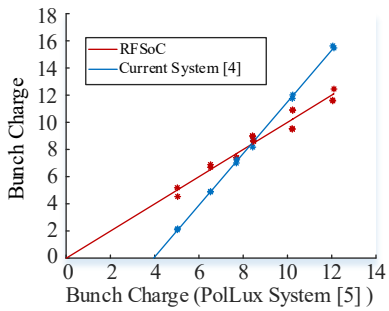


Figure 8: Linearity of the bunch charge measurement for current and RFSoC system, measured at the SLS ring.

The linearity of the bunch charge measurement was evaluated by measuring the charge of a single bunch for different bunch charges with three different systems: The current system [4], the RFSoC, and the PolLux system. The latter is used as a reference for the other systems due to its superior linearity and negligible offset. Figure 8 shows that the RFSoC has a smaller offset than the current system [4] and good linearity. The noise of the RFSoC system can be further improved by averaging longer than the present 128 µs.

For the filling pattern measurement using the RFSoC, the algorithms to calculate bunch charge and bunch arrival-time have been implemented in Python, running offline on a PC. As a next step, we will implement the data processing algorithms in firmware and real-time software on the RFSoC and close the feedback loop. Moreover, we plan to reduce systematic errors in the RFSoC-based filling-pattern measurement. This includes minimizing the impact of reflections on the long cables (from BPM to electronics) on the measurement result.

CONCLUSION

We have evaluated the suitability of RFSoC technology for implementing the MBFB and FPFB of SLS 2.0. While porting the functionality of the existing MBFB implantation to the newer technology, our tests show that the RFSoC meets the requirements for an MBFB system, providing additional resources for future advanced features not feasible with our current SLS hardware. Regarding the FPFB, we have implemented and successfully tested bunch charge and bunch arrival-time measurement using the RFSoC using raw button BPM sum signals. Performance comparisons with the existing systems show that the RFSoC is adequate to measure the filling pattern and has the resources to close the feedback loop by controlling injection and gun charge in real-time. Finally, for both systems, direct sampling of BPM signals and kicker driving is envisaged, using the fast ADCs and DACs of the RFSoC with new simplified analog pre- and postconditioning.

ACKNOWLEDGMENTS

The authors would like to thank Joerg Raabe and Simone Finizio for their support during the experiments in the PolLux (X07DA) beamline of the SLS.

REFERENCES

[1] A. Streun, “SLS 2.0, the Upgrade of the Swiss Light Source”, in *Proc. IPAC'22*, Bangkok, Thailand, Jun. 2022, pp. 925-928. doi:10.18429/JACoW-IPAC2022-TUPOST032

[2] Xilinx, https://www.xilinx.com/products/boards-and-kits/zcu111.html

[3] M. Dehler, G. Marinkovic, P. Pollet, and T. Schilcher, “State of the SLS Multi-bunch Feedback”, in *Proc. APAC'07*, Indore, India, Jan.-Feb. 2007, paper TUPMA014, pp. 118-120.

[4] B. Kalantari, T. Korhonen, and V. Schlott, “Bunch Pattern Control in Top-up Mode at the SLS”, in *Proc. EPAC'04*, Lucerne, Switzerland, Jul. 2004, paper THPLT186, p. 2885.

[5] S. Finizio, S. Mayr, and J. Raabe, “Time-of-arrival detection fir tuine-resolved scanning transmission X-ray microscopy imaging”, *J. Synchrotron Radiat.*, vol. 27, pp. 1320-1325, 2020. doi:10.1107/S1600577520007262

ISBN: 978-3-95450-241-7 ISSN: 2673-5350 doi:10.18429/JACoW-IBIC2022-WEP04

DUAL CHANNEL FMC HIGH-VOLTAGE SUPPLY

W. Viganò *, J. Emery, M. Saccani, CERN, Geneva, Switzerland

Abstract

The Beam Loss Monitoring (BLM) detectors and electronics are installed in the CERN accelerators to provide measurements of the beam loss and to protect from excessive losses. The majority of the BLM detector types require voltage biasing up to 2000 V_{DC} with a possibility to generate patterns to verify the connection chain from the detectors to the front-ends.

Currently, the power supply solution consists of Components Off-The-Shelf (COTS) large format power supplies with additional custom electronics and various interconnections to provide monitoring and remote control. For this reason, a market search has been done to identify a high reliability module suitable for dedicated BLM installations composed of a few detectors. The outcome of this market survey has justified the need to design a low-cost custom board, compatible with the CERN infrastructure and different detector types, as well as easily customizable to cover various installation architectures and needed voltage ranges.

The main characteristics of the developed board are: autonomy and full remote control; common hardware for different applications with a change of the DC\DC converter and a few components; smaller size than what is currently used as High-Voltage (HV) power supplies; multiple different high voltage or low voltage outputs for specific applications with the default design consisting of two positive high voltage outputs and one low voltage output; μV voltage sensing and mA current sensing capabilities; protection against overvoltage.

INTRODUCTION

The present article describes the design and test methodologies adopted to build and validate a dual channel high voltage supply in a FMC form factor. It will be used to bias BLM diamond detectors and mobile installations of ionization chambers and other beam instrumentation detectors in the CERN accelerators.

Next chapters highlight the effort put on the safety and operability aspects of the design related to the small form factor as well as the versatility and adaptability of the card for multiple use cases and applications.

DEVELOPMENT STRATEGY

Specifications

The first phase of the design focused on collecting specifications from all BLM systems at CERN, which are based mainly on ionization chambers with various dimensions and shapes, diamond detectors and silicon photomultipliers.

The outcome of the investigation is summarised in Table 1. A development baseline was defined to be a common platform for most of the BLM detectors with a board able to generate two high-voltage outputs and one low voltage output settable in a pre-defined range.

To minimize the development time, and to make the board compatible with several other platforms, the FPGA Mezzanine Card (FMC) form factor has been selected.

The CERN Beam Instrumentation Group has developed and already produced a large quantity of Intel Arria V based VME64x carrier for one High Pin Count (HPC) FPGA Mezzanine Card (FMC, VITA 57) called VFC-HD [1].

The additional requirements for FMC High-Voltage Supply were to keep the standard front panel width of 4HP, use SHV connector for high-voltage outputs and LEMO connectors for low voltage outputs. As an additional feature, it should be possible to plug adjacent boards into a VME crate without any risk of electrical discharges.

Table 1: Default Version Specifications

Version	Min Voltage [V]	Max Voltage [V]
V1	+175	+1734
V2	-175	-1734
V3	+5	+10

IMPLEMENTATION

Electronic Design

An XP Power AG Series DC/DC converter is the core component in the developed design. The AG Series is a broad line of ultra-miniature DC to HV DC converters that sets an industry standard in high-voltage miniaturization. Module are available in three categories of input voltages: 5 V, 12 V and 24 V. We have decided to use the 12 V series as default because it is the best compromise between the voltage and current level for the VME standard. Nevertheless, the FMC board is designed to be compatible with the 5 V series as well. The AG Series offers modules with positive or negative output voltages ranging from 100 V to 6000 V. The FMC High-Voltage Supply board is designed to work safely up to 2000 V. A possible extension up to 3000 V is still under evaluation.

Figure 1 shows a block diagram of the high-voltage interface. From the FMC connector, the mezzanine receives the +12 VDC power rail for the HV DC/DC converters and the +3.3 VDC power rails to the digital circuitry. A power enable digital signal is used to control, using Pulse Width Modulation (PWM), the +12 V_{DC} rail making it possible to adjust the main HV DC/DC accordingly, with the XP Power AG series that works at 12 V_{DC} or at 5 V_{DC}, while the voltage regulator is fine-

* william.vigano@cern.ch

Content from this work may be used under the terms of the CC BY 4.0 licence (© 2022). Any distribution of this work must maintain attribution to the author(s), title of the work, publisher, and DOI

ISBN: 978-3-95450-241-7 ISSN: 2673-5350 doi:10.18429/JACoW-IBIC2022-WEP04

Content from this work may be used under the terms of the CC BY 4.0 licence (© 2022). Any distribution of this work must maintain attribution to the author(s), title of the work, publisher, and DOI

tuned by a DAC and additional dedicated circuitry. The high-voltage output is monitored by a high-resolution ADC through a 1:1000 high-voltage divider. An auxiliary ADC measures the primary side of the HV DC/DC converter to indirectly monitor the power consumption at the output, and at the same time to allow a supervision algorithm to control power dissipation.

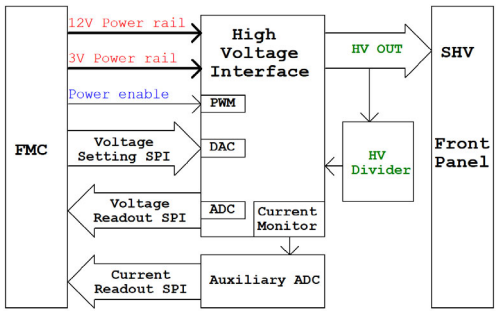


Figure 1: HV Supply basic block diagram.

Both high-voltage outputs available on the developed board have the same independent structure except for the auxiliary ADC which is shared by all output interfaces for the current consumption measurement. The low-voltage output has the same structure except for the HV divider (which is just a low voltage divider) and the ADC, since the auxiliary ADC, shared with the other output interfaces, is used for both output voltage read out and current measurement.

Figure 2 gives a global overview of the board structure: all connections through the FMC connector are on the left, while on the right side of the figure there is the front panel which carries two SHV connectors for the high-voltage outputs and also two LEMO connectors for the low voltage output. For the low-voltage outputs, we decided to bring out both the direct +12 V_{DC} (coming from the VME and controlled by a switch) and the adjustable output voltage.

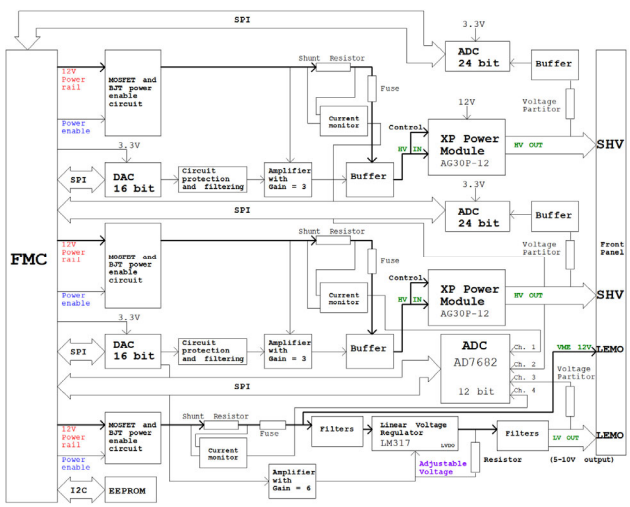


Figure 2: HV Supply detailed block diagram.

All interfaces share the same architecture, but they are independent from each other. Consequently, five independent SPI buses are routed to the FMC connector. An EEPROM is also present on the board and connected by I^2C as requested by the FMC standard specifications.

Figure 3 shows the circuitry used to control the HV DC/DC modules. The power enable circuit, controlled by the HV_ENABLE input, uses a BJT connected to a PMOS gate to safely control the 12 V power supply for the rest of the driver circuit. The PMOS source is connected to the 12 V power rail of the VME. This 12 V rail supplies the amplifiers and the BJT in the DAC amplifier circuit. Therefore, when the PMOS is off, the 12 V rail does not supply the amplifiers and BJT, and no HV signal is created. The circuit is simple but robust enough for our needs. When there is no power enable signal, the BJT does not conduct and the PMOS is off. When the power enable signal is on, the 3.3 V signal activates the BJT. This biases the PMOS gate allowing the PMOS to fully conduct and transmit the 12 V to the rest of the circuit. After the PMOS, there is a shunt resistor used to monitor the current consumption of the entire HV circuit (HV Driver, HV DC/DC Converter and HV Control Circuit). The current consumption is then measured as a voltage signal through a shunt connected to a current amplifier. This signal is digitized by an ADC and sent through SPI to the carrier board FPGA.

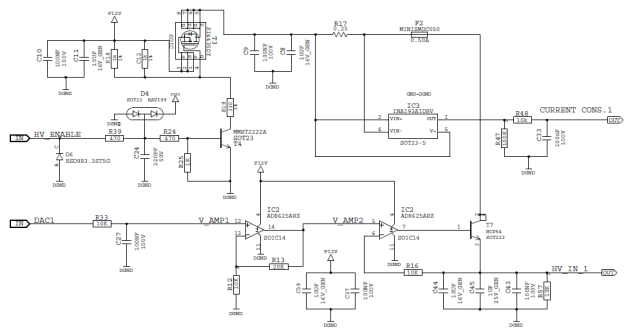


Figure 3: HV interface electrical drawing.

The HV_ ENABLE signal is a PWM with a duty cycle settable from 0 to 100%. For HV DC/DC converters that work with an input voltage of 5 V instead of 12 V, the power dissipation on the BJTs can be optimized by driving the power enable circuit with a 100 kHz PWM control signal @ 50% duty cycle.

In such a case, the output voltage of the enabling circuit becomes 6 V and the HV DC/DC output can be controlled by the DAC avoiding excessive power dissipation on the BJTs.

PCB Design

Functions on the PCB have been distributed as shown in Figure 4 and Figure 5. Most of the active and passive components are located on the top side of the board, while the bottom side is mostly dedicated to the high-voltage circuitry and power dissipation areas for active components. To increase the power dissipation performance, the PCB solder mask has been removed from the dissipation areas, in addition capped and filled vias

ISBN: 978-3-95450-241-7 ISSN: 2673-5350 doi:10.18429/JACoW-IBIC2022-WEP04

have been selected. In such way we have maximized the dissipation area and its thermal exchange.

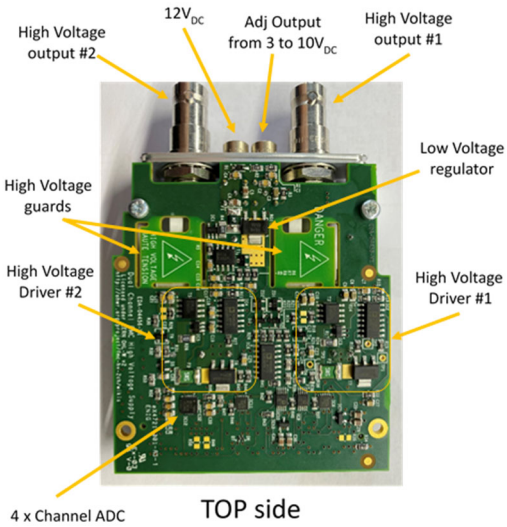


Figure 4: Board picture - top side.

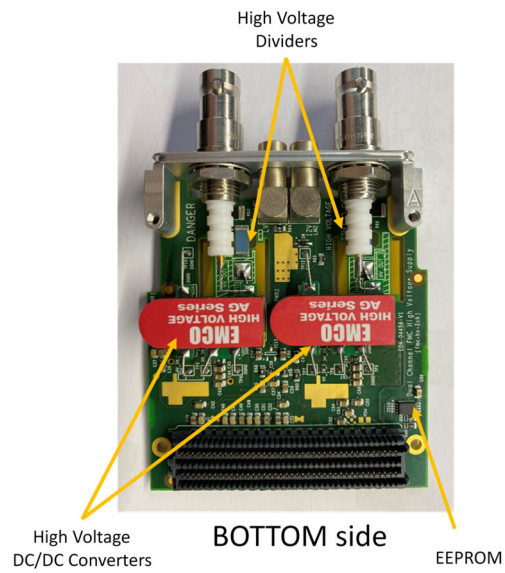


Figure 5: Board picture - bottom side.

The PCB design required particular attention due to the presence of high-voltage, which is a potential source of safety issues, electrical discharges, and current leakage. For these reasons, dedicated high-voltage guards have been created on the PCB by applying the following rules:

- A single wire connects the SHV connector to the HV DC/DC converter and the PCB pad for the HV divider.
- Except for the soldering pad of the HV wire (bottom side), all copper is removed in all PCB layers up to the top side in the HV high area.
- The minimum distance between HV copper and all other lines is greater than 5 mm in all directions.
- The PCB substrate has a Comparative Tracking Index (CTI) 0 for voltages greater than 600V.

Figure 6 highlights the layout implemented to build the high-voltage guards.

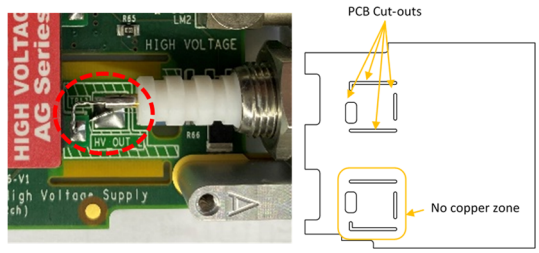


Figure 6: High-Voltage guards.

Detailed Documentation

The design is managed in Open Hardware Repository OHWR [2]. Detailed documents for the electronic design including the layout and the hardware design manual are available and public on the CERN EDMS archive [3].

Testing

Board testing was possible after its integration on the VFC-HD carrier, and thanks to the creation of a generic firmware (FW) interface module. The FW is based on a wishbone bus and available on the OHWR website.

In parallel to the FW creation, a script interface was written to allow both sending of commands through the VME bus and monitoring the HV power supply parameters. Such an interface allowed us to perform a full basic verification of the board and to successfully test it with the CERN ionization chamber and diamond BLM detectors. With a custom version of the board, it was possible to use it to directly drive a commercial Heinzinger NCE 3000 series high-voltage and high-power supply.

After the basic verifications, a successful safety check was performed by testing integration in a 19' chassis with adjacent boards. All power dissipation areas on the PCB were monitored with a FLIR E8 infrared camera. The HV power supply was installed without ventilation to create a non-nominal worst-case condition to check the limit of the design. In the worst case, the board hot spots were about 20 degrees Celsius above ambient temperature which accordingly to the calculation a reliable working condition.

Firmware

A low-level generic firmware was designed to validate the HV FMC prototype. As shown in Figure 7, the firmware implements control and status signals, 3 PWM modules, 5 SPI masters associated with a custom Finite State Machine (FSM) managing the ADC and DAC protocols and an I2C master with a standard Wishbone slave input interface.

This basic firmware was tested on a complete GHDL/GTKWave testbench instantiating a model of every component of the FMC. All the files are available on the OHWR.

Content from this work may be used under the terms of the CC BY 4.0 licence (© 2022). Any distribution of this work must maintain attribution to the author(s), title of the work, publisher, and DOI

ISBN: 978-3-95450-241-7 ISSN: 2673-5350 doi:10.18429/JACoW-IBIC2022-WEP04

Content from this work may be used under the terms of the CC BY 4.0 licence (© 2022). Any distribution of this work must maintain attribution to the author(s), title of the work, publisher, and DOI

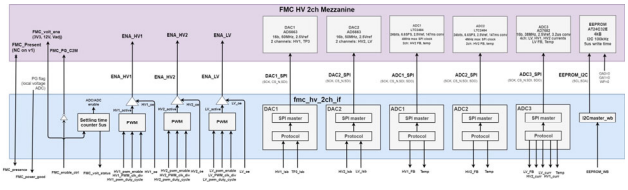


Figure 7: Low-level interface firmware architecture.

Control Algorithm

A control algorithm with two main functions is required inside the FPGA to operate the board efficiently. Firstly, it oversees the output voltage and steers it as close as possible to the set point. Secondly, it makes sure that the core module of the board that provides the high voltage is operated safely. These functionalities are necessary to operate the core module as its output voltage is set by not only the input voltage but also by the load attached to its secondary side. This load can have a resistive, capacitive, or inductive behaviour, thus making it difficult to operate without voltage feedback. In addition, the module needs to be protected against overvoltage and overcurrent.

Figure 8 shows the typical input-output characteristics of the DC-HVDC module for different loads as per the manufacturer's datasheet. The dashed line shows how much the output voltage can differ with a constant input voltage but under different loads. Without a load, the output voltage can damage the module as it crosses the safe operating limit (red line).

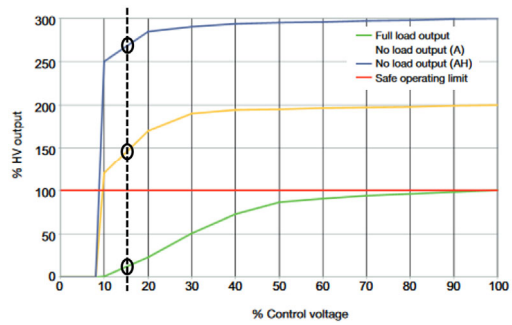


Figure 8: Module output voltage versus input voltage.

The load was modelled using Simulink to test different strategies for the feedback controller and select the optimal one. Figure 9 shows, as blue blocks, the feedback-based voltage and current controller selected for implementation. It is built around one integrator with a gain and a saturation to select the maximum voltage rate.

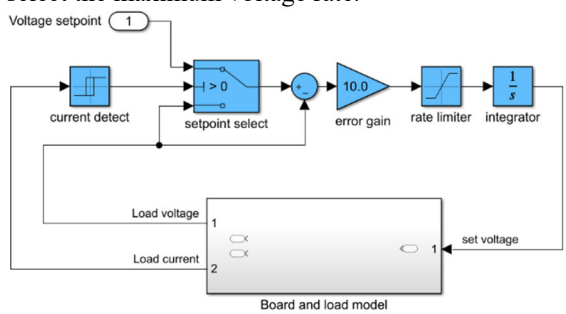


Figure 9: Voltage/current feedback controller principle.

The current limit detection controls a switch that lowers the set voltage until the current goes below the limit, making the module compatible with capacitive loads which will be charged with the highest possible current until they reach the desired voltage.

Figure 10 illustrates a simulation scenario where the set voltage (black line) is too high for the module with the load sinking too much current, therefore forcing the algorithm to limit the output voltage (red line).

The oscillation level is the set by the hysteresis selected in the current detection module.

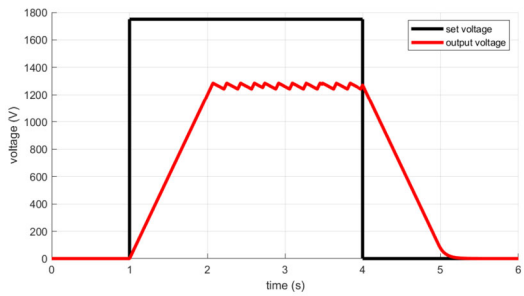


Figure 10: Simulated behaviour with a load drawing excessive current.

The selected algorithm is written in VHDL and simulated with traditional HDL tools. While Simulink models are generally 64 bits floating points number representation, the FPGA implementation uses lower precision to limit resources usage. The simulation with 32 bits fixed point numbers shows satisfactory precision and will be used for the final implementation.

The algorithm is still in development and an additional test campaign will be carried out as soon it is ready.

CONCLUSIONS

The first version of the dual channel FMC high voltage supply has been successfully validated, and all design details including the design manual, the low-level firmware and the control algorithm are public and available on the OHWR.

By following the design methodology described in this article, we have optimized the development time and maintained the flexibility by using a standard platform and selecting a core component which offers a large selection of output levels.

REFERENCES

[1] A. Boccardi, M. Barros Marin, T. Levens, B. Szuk, W. Viganò, and C. Zamantzas, "A Modular Approach to Acquisition Systems for Future CERN Beam Instrumentation Developments," in *15th International Conference on Accelerator and Large Experimental Physics Control Systems*, 2015, THHB2O02. doi:10.18429/JACoW-ICALEPCS2015-THHB2O02

[2] CERN, CERN Open Hardware License (CERN OHL), http://www.ohwr.org/projects/cernohl/wiki

[3] Dual Channel FMC High Voltage Supply CERN EDMS archive: https://edms.cern.ch/item/EDA-04456-V1-1/0

ISBN: 978-3-95450-241-7 ISSN: 2673-5350 doi:10.18429/JACoW-IBIC2022-WEP06

AN LHC PROTECTION SYSTEM BASED ON FAST BEAM INTENSITY DROPS

M. Gasior, T. Levens, CERN, Geneva, Switzerland

Abstract

The Large Hadron Collider (LHC) is protected against potentially dangerous beam losses by a distributed system based on some four thousand beam loss monitors. To provide an additional level of safety, the LHC has been equipped with a system to detect fast beam intensity drops and trigger a beam dump for potentially dangerous rates. This paper describes the architecture of the system and its signal processing, optimized to cope with dump thresholds in the order of 0.01% of the circulating beam intensity. The performance of the installed system is presented based upon beam measurements.

INTRODUCTION

The LHC Beam Charge Change Monitor (BCCM), also called the dI/dt system, is specified to trigger beam dumps for beam losses exceeding thresholds in six integration windows in two beam energy ranges, as summarised in Table 1. The integration window lengths, expressed in units of the LHC revolution period T_r (≈ 89 μs), have been chosen to correspond to integration periods of the Beam Loss Monitoring (BLM) system. The BCCM is required to operate for beam intensities from 5×10^9 elementary charges (q_0) for a single pilot bunch, up to 6×10^{14} q_0 for ≈ 2800 physics beam bunches of 2.1×10^{11} q_0, resulting in the intensity dynamic range of ≈ 10^5 and the beam signal dynamic range of ≈ 40. Thus, the smallest beam dump threshold of 0.5×10^{11} q_0 for the longest integration window in the high energy range corresponds to an intensity change of ≈ 0.008%. Such challenging beam dump threshold levels and the required operational reliability have proved to be very difficult to satisfy at the same time. The BCCM system design described in this paper was preceded by a few prototypes and the experience gained at each stage contributed to the improving performance.

The initial prototype of the system was based on signals from Fast Beam Current Transformers (FBCTs), with 16-bit ADCs sampling at 160 MHz and IQ narrowband processing of the 40 MHz beam component implemented in an FPGA [1]. A mayor limitation of the first prototype was the beam sensor itself, as its readings were beam position dependent [1]. This triggered a development of a new technology, resulting in Wall Current Transformers (WCTs) [2], which removed the beam position dependence problem [3] and finally replaced the FBCTs. Then the WCT signals were used in the next version of the BCCM and the signal processing was updated. However, this version had not achieved the required reliability to work as an LHC protection system without triggering false dumps. Finally, the architecture of the BCCM was revised and the system was completely rebuilt according to the design described in this paper.

Table 1: BCCM Beam Dump Threshold Levels in 10^{11} q_0

Beam energy	Integration window lengths in T_r units					
	1	4	16	64	225	1125
< 0.5 TeV	6	6	6	6	6	6
≥ 0.5 TeV	3	3	3	3	2	0.5

The most fundamental change in the new BCCM is the source of the beam signal, where the WCT has been replaced by the sum signal of a beam position monitor (BPM). This way the development of the BCCM became independent of the beam intensity measurement system, which is critical for the LHC operation and therefore any changes to its parameters were very difficult. This was previously posing serious limitations during the development of the BCCM. The BPM also provides larger signals than the WCM, which contributes to the improved noise performance of the present system.

The signal processing now used in the BCCM provides a few improvements and simplifications:

- the fast beam signals are rectified, allowing the system bandwidth to be strongly limited by low-pass filters already before the ADC;
- in consequence, the beam synchronous ADC sampling could be lowered to 40 MHz, allowing to use high signal-to-noise ratio ADCs and facilitating the digital signal processing;
- the idea of one revolution digital delay line was introduced: the beam signal changes are calculated as plain differences of one revolution period integrals, allowing simple, reliable and efficient signal processing;
- the ADC sampling phase does not need to be adjusted to the beam signal, increasing the simplicity and robustness of the system operation.

The new LHC BCCM system based on the mentioned features is described in the following sections and its performance illustrated with beam measurements.

SYSTEM ARCHITECTURE

The block diagram of the BCCM is shown in Fig. 1, along with signals sketched in key nodes of the system. The signals from four electrodes of a BPM are first processed by 80 MHz non-reflecting low-pass filters (NRLP), amplified by RF amplifiers (RFA) and then combined to remove their beam position dependence. The resultant signal is rectified by an envelope detector (ED), which allows subsequent strong low-pass filtering, essential to limit the system bandwidth and in consequence noise. The filtered signal is digitised by a 16-bit ADC (LTC2204) sampling at 40 MHz derived from the 400 MHz LHC RF frequency. The ADC samples are processed by an FPGA

Content from this work may be used under the terms of the CC BY 4.0 licence (© 2022). Any distribution of this work must maintain attribution to the author(s), title of the work, publisher, and DOI

ISBN: 978-3-95450-241-7 ISSN: 2673-5350 doi:10.18429/JACoW-IBIC2022-WEP06

Content from this work may be used under the terms of the CC BY 4.0 licence (© 2022). Any distribution of this work must maintain attribution to the author(s), title of the work, publisher, and DOI

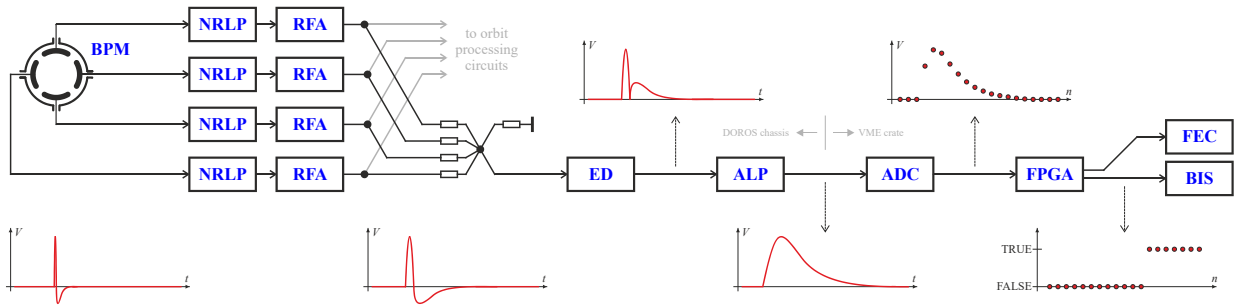


Figure 1: Block diagram of the BCCM system. BPM – Beam Position Monitor, NRLP – Non-Reflecting RF Low Pass filter, RFA – RF Amplifier, ED – Envelope Detector, ALP – Active Low Pass filter, FEC – Front-End Computer.

(ARRIA V), which generates the beam dump triggers to the LHC Beam Interlock System (BIS).

The BCCM triggers a beam dump when a beam intensity change rate in one of the six integration windows is above the corresponding dump threshold level. A beam dump is also requested upon certain system error conditions, such as the lack of the 400 MHz RF signal or a sample reaching the ADC full scale limit.

To implement energy dependent thresholds, the BCCM also receives the beam energy information from the LHC timing system. In case this information is missing, the beams will not be dumped but instead the system operates with the worst-case settings, in the high energy range with the safer dump thresholds.

A VME front-end computer (FEC) receives data from the FPGA every second and provides all functionalities, which are not time- nor machine-safety critical, like system setup, operation monitoring and data logging. All FPGA signal processing is implemented as fixed-point integer arithmetic, so the FEC also provides all translation between intensities measured in charges and the integer equivalents.

Each of the LHC beams is equipped with two redundant BCCM systems which must be operational at all times. If any system detects an abnormal beam intensity change, dump triggers are issued within microseconds for both beams. The four BCCM systems consists of two 1U 19" chassis accommodating the analog processing, two 3U VME crates hosting the FPGA boards, the ADC mezzanines and interface to the BIS. A part of the analog processing, marked on the system block diagram in Fig. 1, is shared with the DOROS system [4]. The system provides amplitudes of beam signals on each electrode of the system BPMs, along with their beam position readings used for BCCM operation monitoring.

SIGNAL PROCESSING

The key part of the BCCM analog signal processing is the beam signal rectification, realised with an RF envelope detector ADL5511. This allows the bandwidth of the rectified signals to be well limited by the following active low pass filters. The strong filtering causes the beam pulses to overlap as it will be shown in the next section, however, low-pass filtering conserves the signal integrals, so even the acquired signals have quite different forms than the beam signals, their integrals are maintained.

The beam synchronous sampling of the ADC allows the FPGA to synchronise to the LHC revolution period by working on sets of 3564 ADC samples. Then the one revolution period ($1T_r$) integrals are calculated as simple sums of samples with the amplitudes above a threshold, which prevents integrating the noise from the samples with no beam signal. The Simpson integration method was also tried with the hope for smaller integration noise, but no advantage was observed over the simplest rectangle method.

The $1T_r$ intensity change is just a difference of $1T_r$ integrals from two consecutive turns and the intensity changes for the other five integration windows are similarly calculated. The intensity changes in the six windows are compared every revolution period to the corresponding beam dump thresholds.

The dump thresholds are expressed in absolute beam intensity losses, so the system needs to know the actual intensity of the circulating beam. To avoid dependences upon other systems, the intensity is obtained locally by scaling the beam signal integrals evaluated by the BCCM to correspond to the intensity readings of the LHC BCTs.

BEAM MEASUREMENT EXAMPLES

The effect of the heavy low-pass filtering of the beam signal is shown in Fig. 2, presenting an example of the normalised raw ADC samples for one revolution period with the LHC fully filled. The fact that the beam pulses spaced by 25 ns overlap is documented in Fig. 3, showing with finer time resolution a 2 µs segment of Fig. 2. The system can efficiently operate with such slow signals, since the overlap is identical in consecutive revolution periods, so are the revolution integrals, resulting in zero difference when the beam intensity is constant. It can be seen that the risetime of the signal is about six 25 ns sampling periods, which corresponds to the system bandwidth of about 2 MHz. The long signal tail seen between the bunch trains is a feature of the envelope detector chip used, but again, due to the chosen digital signal processing, this defect has no importance for the proper operation of the system.

Typical BCCM operation during a short full LHC beam cycle is illustrated in Fig. 4, showing the beam intensity and its maximal drops in the three shortest integration windows for which the system operates well. The BCCM properly detects injection losses, which go up to some 30%

ISBN: 978-3-95450-241-7 ISSN: 2673-5350 doi:10.18429/JACoW-IBIC2022-WEP06

of the dump threshold for the $4T_r$ integration window and about 40% of the system maximal beam intensity. With higher intensities the injection losses could increase, so the specification of the system must be revised to assure at the same time a safe operation of the LHC and prevent the BCCM system from triggering unnecessary dumps.

The relative accuracy of the intensity readings provided by both redundant BCCMs of LHC beam 1 (B1) as compared to a Fast BCT and a DC BCT is presented in Fig. 5, showing the corresponding normalised intensities at the beginning and at the end of a 13.5 h beam cycle. It is seen that the BCCMs follow the BCTs through the energy ramp within ≈0.5%. Small ripples seen in the BCCM readings are caused by bunch length fluctuations related to a longitudinal emittance blow-up (LEBU) [5] used to prevent the bunch length shortening over the beam acceleration. During the next 13 h of the beam cycle at 6.8 TeV the bunch length shrinks from ≈1.2 ns to ≈0.8 ns, causing the BCCM readings, originating from BPMs which are high-pass systems, to be larger than the BCT readings by around 3%. Such errors are completely acceptable, especially since the BCCM readings are overestimated and so the dump triggers will be then issued for smaller loss rates than specified.

Intensity drop examples for the two longest integration windows are presented in Fig. 6. For this particular cycle, the LEBU was accidentally only operational for beam 2 (B2), causing fast bunch length changes only for this beam. The changes were converted by the BPM to beam signal amplitude fluctuations, which were misinterpreted by the BCCM as intensity changes. The lack of the longitudinal blow-up for B1 caused a beam dump seen in Fig. 7, presenting revolution-by-revolution normalised intensities for both beams. Oscillations with amplitudes in the order of a few 10^{-4}, related to the bunch synchrotron motion, are present only for B2 on both shown records, at the dump and 52 s earlier. The normalised intensities of B1 for which the LEBU was missing show only noise.

The unexpectedly large and fast bunch length changes caused by the LEBU limit the present performance of the BCCM system for the three longest integration windows, whose lengths are comparable to the beam synchrotron period. First tests have shown that the LEBU influence can be reduced by making the integration window lengths a multiple of the synchrotron period. However, as this period changes during the acceleration by a factor of two, such window lengths are a compromise and therefore can reduce the LEBU influence by only a few times. Other options of how to cope with the LEBU are under discussion. In short term the system could operate with a third energy range covering the period of LEBU activity, for which the dump thresholds could be raised. An ultimate solution would be to use a beam signal sensor with no bunch length dependence. The first obvious candidate is the BCT system based on WCTs, whose upgrades have been now finalised and therefore its signals should be easier to use than in the past. However, the WCT signals are lower than the BPM ones currently used and it must be carefully checked whether they are sufficient for a reliable BCCM operation.

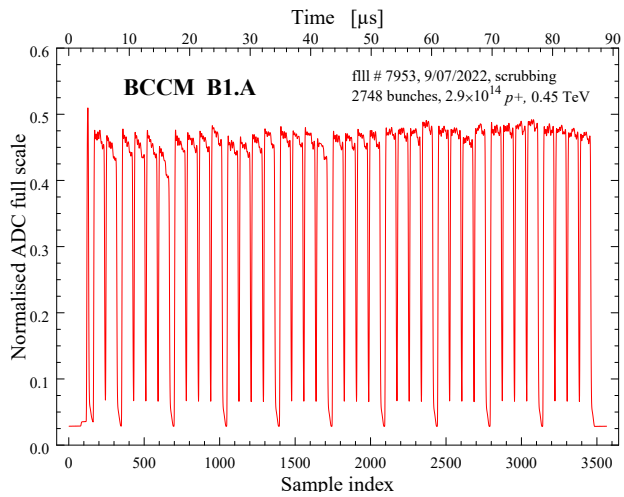


Figure 2: Normalised raw ADC samples over one revolution period with the LHC fully filled with protons (p+) during the 2022 scrubbing run.

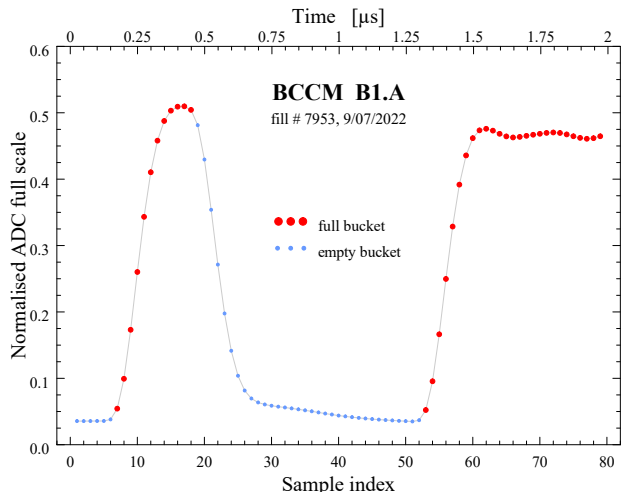


Figure 3: Zoom on a 2 μs segment of the ADC samples shown in the above Fig. 2.

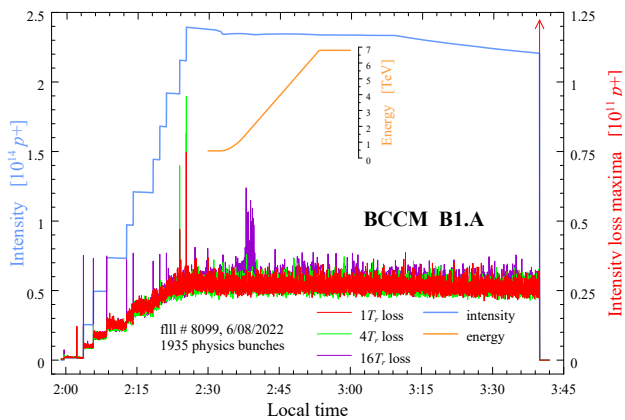


Figure 4: An example of BCCM signals during a full LHC beam cycle. Please note the 2000-fold difference in the scales for the left and right axes.

Content from this work may be used under the terms of the CC BY 4.0 licence (© 2022). Any distribution of this work must maintain attribution to the author(s), title of the work, publisher, and DOI

ISBN: 978-3-95450-241-7 ISSN: 2673-5350 doi:10.18429/JACoW-IBIC2022-WEP06

Content from this work may be used under the terms of the CC BY 4.0 licence (© 2022). Any distribution of this work must maintain attribution to the author(s), title of the work, publisher, and DOI

There was no observation of any dependence of BCCM readings on beam position changes in the used BPMs. The BPMs are not far from the RF cavities, so larger position changes should not be expected. This has been confirmed with measurements provided by the DOROS system using signals from the same BPMs.

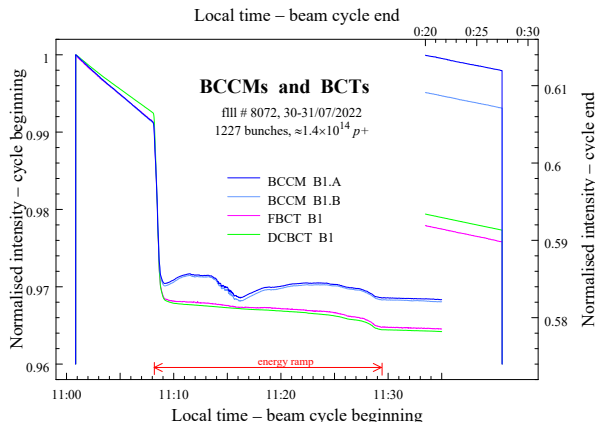


Figure 5: Comparison of BCCM and BCT normalised intensities at the beginning and the end of a beam cycle.

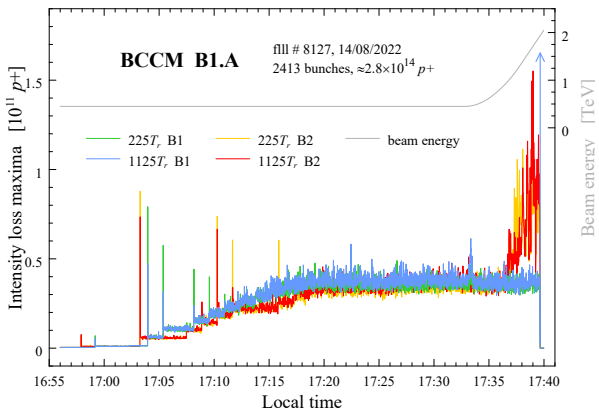


Figure 6: BCCM intensity losses in the two longest integration windows for B1 and B2 with the longitudinal emittance blow-up disabled and enabled, respectively.

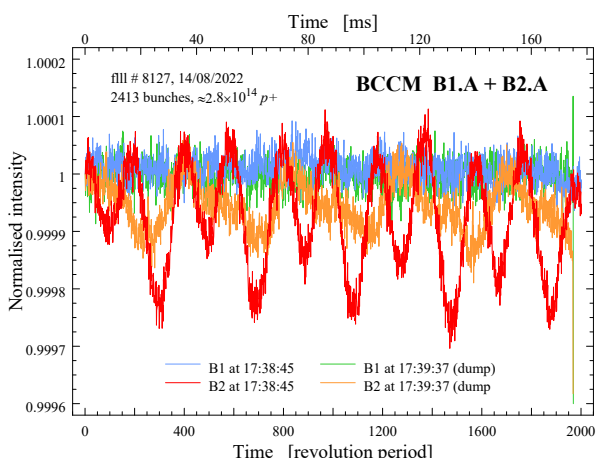


Figure 7: Normalised B1 and B2 intensities corresponding to the intensity losses shown in the above Fig. Note that the longitudinal emittance blow-up is present only for B2.

SUMMARY AND OUTLOOK

The LHC BCCM system is based on beam signals from four sensors for both beams and is able to detect all beam losses, since it acts on the total beam intensity. Therefore, it very well complements the distributed LHC BLM system that make use of four thousand detectors and measures localised beam losses. The presented system, after many years of development, has finally achieved the required sensitivity and the reliability expected from a system from which a single 25 ns ADC sample can trigger a beam dump.

The 2022 LHC run is being used to optimise the BCCM before unmasking its dump triggers, planned for the LHC restart in 2023. To become a part of the LHC machine protection system, the BCCM must undergo an elaborate commissioning procedure with beam [6], so it is very important to minimise the probability that any system setting would need be changed, as then the commissioning must have to be repeated.

The BCCM 2022 operation revealed some sensitivity to the longitudinal emittance blow-up for the three longest integration windows. This discovery is currently under discussion and corrections to the integration window lengths as well as to the dump threshold values are being evaluated.

ACKNOWLEDGEMENTS

The authors are indebted to all members of the CERN Beam Instrumentation Group and the LHC Machine Protection Panel, who contributed to the long development of the BCCM, especially to Diogo Alves, David Belohrad, Michal Krupa, Jan Uythoven and Daniel Wollmann.

REFERENCES

[1] Belohrad, J. M. Belleman, L. K. Jensen, M. Krupa, and A. Topaloudis, "The LHC Fast Beam Current Change Monitor", in *Proc. IBIC'13*, Oxford, UK, Sep. 2013, paper WEPF29, pp. 887-890.

[2] M. Krupa and M. Gasior, "The Wall Current Transformer - a New Sensor for Precise Bunch-by-Bunch Intensity Measurements in the LHC", in *Proc. IBIC'16*, Barcelona, Spain, Sep. 2016, pp. 568-571. doi:10.18429/JACoW-IBIC2016-WEAL02

[3] M. Krupa *et al.*, "Summary of LHC MD 398: Verification of the dependence of the BCTF measurements on beam position and bunch length", CERN-ACC-Note-2015-0031.

[4] M. Gasior, G. Baud, J. Olexa, and G. Valentino, "First Operational Experience with the LHC Diode ORbit and OScillation (DOROS) System", in *Proc. IBIC'16*, Barcelona, Spain, Sep. 2016, pp. 43-46. doi:10.18429/JACoW-IBIC2016-MOPG07

[5] P. Baudrenghien *et al.*, "Longitudinal Emittance Blow-up in the LHC", in *Proc. IPAC'11*, San Sebastian, Spain, Sep. 2011, paper TUPZ010, pp. 1819-1821.

[6] M. Gasior, T. Levens, "MPS Commissioning Aspects of the Beam Charge Change Monitoring (BCCM) System", LHC OP MPS 0021, EDMS 2683896.

ISBN: 978-3-95450-241-7 ISSN: 2673-5350 doi:10.18429/JACoW-IBIC2022-WEP07

INFLUENCE OF THE BEAM INDUCED IRRADIATION ON THE CRITICAL CURRENT PHENOMENA IN SUPERCONDUCTING ELEMENTS

J. Sosnowski, NCBJ, Świerk, Poland

Abstract

In the constructions of the modern accelerators, of free electrons as is in the case of FEL-s or ionized particles as in LHC working in CERN, the ionized beam is guided by the magnetic field generated in electromagnets, more and more frequently wound up using superconducting wires. The beam's induced irradiation arises in these accelerators, which influences the properties of the superconducting elements, as wires, current leads or shields, which issue is discussed in the present paper. It is shown in which way the irradiation damages the subtle structure of superconducting materials, leading to columnar defects formation in 2D HTc superconductors. It is analysed theoretically how these nano-structural defects influence the critical current properties of the superconducting materials. In the paper is developed energetic approach, of the Ginzburg-Landau type in lowest order approximation, to the process of capturing of the magnetic pancake vortices in HTc superconductors. Various initial positions of the captured vortices are analysed, movement of them through the potential barrier leads to electric field generation. The dependence of the potential barrier on transport current is analysed. Influence of the irradiation effects on the current-voltage characteristics of superconductors are investigated then and critical current values detected, as the function of irradiation intensity, size of created then nano-defects and physical parameters such as critical temperature and elasticity forces. This analysis has therefore physical meaning and should be useful also for prediction the proper work conditions of accelerators with superconducting elements.

INTRODUCTION

Nowadays it is intensively developed nuclear accelerators technology, to which belong also linear constructions of the FEL-s type. In these facilities more and more frequently there are applied superconducting materials [1], including the HTc superconductors too. They are used in solenoids generating magnetic field, forming the electron beam at FEL-s facilities but also as current leads, resonant cavities, shields and various correctional coils, guiding the beam along the appropriate track. Before applying these new materials in accelerating machines, we should therefore to establish the sensitivity of their properties to irradiation, which appears especially in nuclear accelerators. This issue is just the subject of paper.

In the paper is discussed how irradiation arising in modern accelerating devices, caused by primary beam of ionized particles circulating in synchrotrons or electrons beam in linear FEL-s machines, will influence the current carrying properties of superconducting elements. For the case of FEL-s linear accelerators beside primary beam, in which irradiation is created by moving electrons, occur too the secondary beams, composed beside all from neutrons, γ-rays, positrons and photonic bunches. They are created during collisions of electrons with walls of accelerators.

These investigations are especially relevant for HTc superconductors, which are characterised by the subtle planar structure of 2D type, very sensitive therefore to the defects concentration. These defects are created just by the irradiation caused by the ionic or electrons beam guided in accelerators lines. For that 2D structure the ionic bombardment can lead to the columnar defect creation. At an aim of describing mathematically the influence of the irradiation, creating the nano-sized defects on superconducting elements, it has been developed the model oriented on the energy variation analysis during the dynamic interaction of nano-defects with the magnetic vortices. They are generated by external magnetic field or current flow. This general model has been applied to the defects induced by irradiation as well as mechanically formed defects, such as dislocations arising especially during the winding procedure of the superconducting coils.

BEAM IRRADIATON EFFECTS IN SUPERCONDUCTORS

Irradiation in superconducting accelerators although caused by rather small volume of ionized beam has significant influence on superconducting elements just because the superconductivity is very subtle effect. It is second order effect in perturbation range, which for many years was not explained theoretically therefore by scientists. So it can be expected that irradiation of the superconducting materials will have large influence on their properties, which concerns especially the low dimensional superconductors as two-dimensional HTc superconductors based on CuO_2 planes but also will apply to the quasi one–dimensional A15 type superconductors. This class of materials is characterized by three linear, perpendicular chains of the atoms of the transition metals. Beam irradiation of these materials, for instance Nb_3Sn wires, will lead to damage of the chains responsible for their superconducting properties. Critical temperature is then really decreasing. Also HTc superconductors, reaching already room temperature are more and more attractive from the point of view of application them in nuclear physics devices. World record of the critical temperature belongs now to the hydrogen sulphide and exceeds already room temperature. T_c = 14 ºC at H_2S + CH_4, unfortunately under very high pressure at 267 GPa. But this world record for highest T_c should be still confirmed. Second on this list is lanthanum - hydrogen compound of the composition LaH_{10} at pressure of the 170 GPa, with critical temperature of -23 ˚C [2]. To the

Content from this work may be used under the terms of the CC BY 4.0 licence (© 2022). Any distribution of this work must maintain attribution to the author(s), title of the work, publisher, and DOI

ISBN: 978-3-95450-241-7 ISSN: 2673-5350 doi:10.18429/JACoW-IBIC2022-WEP07

Content from this work may be used under the terms of the CC BY 4.0 licence (© 2022). Any distribution of this work must maintain attribution to the author(s), title of the work, publisher, and DOI

power applications of the superconductors in nuclear physics, belong nuclear accelerators, as FEL-s linear free electron laser, including built now in Poland PolFEL, in which construction appears the direct exposition of the superconducting elements to the ionizing beam irradiation. It is primary ionic beam or as in the case of FEL-s facilities beside initial electrons beam arise too the secondary beams composed from neutrons, ions, positrons, γ-rays, interacting with the superconducting elements creating nano-defects. Defects of the dislocation type are created too during winding up of the superconducting coils, leading to bending strain, this is shown in the chapter about I-V characteristics. The nano-defects act as the pinning centers capturing the pancake type vortices as is shown in Fig. 1 for layered superconductors or linear flux lines for usual low temperature superconductors. This interaction vortices with nano-sized defects is described by the system energy F, described by the following formula:

$$F(r_1,\dots,r_N) = \sum_{i=1}^{N} U(r_i) + \frac{1}{2}\sum_{i\neq j}^{N} F_{inter}(r_i - r_j) - J\emptyset_0 \sum_{i=1}^{N}(l_i - r_i) - \sum_{i=1}^{N}\frac{C(r_i-\xi)^2}{2}V_i \quad (1)$$

Equation (1) describes the energy of N magnetic pancake type vortices, specific for layered superconductors, captured on the pinning centers at positions $r_1,..r_N$. U is pinning potential of the captured pancake vortices, shown in Fig. 1, while summation runs over N captured magnetic vortices, each of them is transporting quantized magnetic flux $\Phi_0 = 2{,}07\cdot10^{-15}$ Wb. Second term in Eq. (1) describes the contribution to system energy of the inter-vortices interaction, while third expression is connected with Lorentz force, where J is electric current density. Last part in Eq. (1) determines the increase of the elasticity energy of the vortices lattice, during the shift of the vortex from equilibrium position at the process of the magnetic flux capturing. V_i describes connected with this deformation volume, while C is spring constant of the vortices lattice.

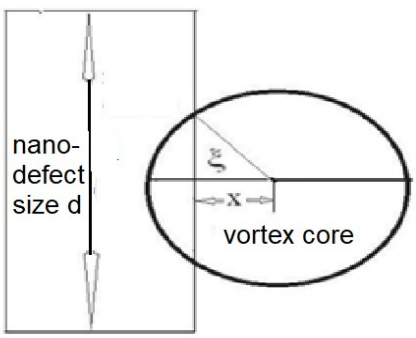


Figure 1: Schematic view of the capturing of magnetic pancake vortex on nano-sized defect of the width d>2ξ.

In Fig. 1 is shown the capturing of magnetic pancake vortex by nano-sized defect of the width d > 2ξ, where ξ is the coherence length. The movement of the vortex against capturing forces, caused by the Lorentz force leads to the potential energy U(x) of the system increase according to the relation (2), while parameter x here denotes the shift of the vortex against its initial position:

$$U(x) = \frac{\mu_0 H_c^2}{2} l\xi^2 \langle arcsin\frac{x}{\xi} - \frac{\pi}{2} + \frac{x}{\xi}\cdot\sqrt{1-\left(\frac{x}{\xi}\right)^2}\rangle - jB\pi\xi^2 lx \quad (2)$$

In Eq. (2) H_c is thermodynamic critical magnetic field, μ_0 magnetic permeability of vacuum, while l the thickness of the superconducting layer. Existence of the potential energy U(x) varying with the vortex deflection from the initial position against the capturing center, according to the Lorentz force leads to the potential barrier ΔU uprise, which should pass vortex in the flux creep process. The potential barrier arising then reaches the maximum for the vortex deflection $x = x_m$, where x_m is given by the relation joining the cartesian units with current representation:

$$x_m = \xi\sqrt{1-\left(\frac{I}{I_c}\right)^2} \quad (3)$$

The transformation to the current representation brings new expressions for single vortex potential barrier ΔU:

$$\Delta U(i) = \frac{\mu_0 H_c^2}{2} l\xi^2 \langle arcsin\frac{d}{2\xi} - arcsini + \frac{d}{2\xi}\cdot \sqrt{1-\left(\frac{d}{2\xi}\right)^2} - i\left[\sqrt{1-i^2} + arcsin\frac{d}{2\xi} - \frac{\pi}{2} + \frac{d}{2\xi}\cdot \sqrt{1-\left(\frac{d}{2\xi}\right)^2}\right]\rangle + \propto \xi^2\left(\sqrt{1-i^2}-2\right)\cdot\sqrt{1-i^2} \quad (4)$$

$$\Delta U(i) = \frac{\mu_0 H_c^2}{2} l\xi^2 \langle arcsin\frac{d}{2\xi} - arcsin\, i + \frac{d}{2\xi}\cdot\left(1 + \sqrt{1-\left(\frac{d}{2\xi}\right)^2}\right) + i\left[-\sqrt{1-i^2} - arcsin\frac{d}{2\xi} + \frac{\pi}{2} - d/2\xi\cdot(1 + \sqrt{1-\left(\frac{d}{2\xi}\right)^2})\right]\rangle \quad (5)$$

$$\Delta U(i) = \frac{\mu_0 H_c^2}{2} l\xi^2 \langle 2arcsin\frac{d}{2\xi} - arcsin\, i + \frac{d}{2\xi}\cdot\sqrt{1-\left(\frac{d}{2\xi}\right)^2} + i\left[-\sqrt{1-i^2} - 2arcsin\frac{d}{2\xi} + \frac{\pi}{2} - d/\xi\cdot\sqrt{1-\left(\frac{d}{2\xi}\right)^2}\right]\rangle \quad (6)$$

In Eq. (4) $i = I/I_c$ is reduced transport current and has been considered here case of half-captured initially vortex on beam's irradiation created nano-defect. As well as it has been included too term describing the elasticity forces described by parameter α proportional to spring constant C from Eq. (1). In Eq. (5) is given case of temporary initially captured vortices, while in Eq. (6) of totally captured, respectively. In half captured vortex is still kept the structure of the circulating currents in the vortex, while fully captured vortex configuration is most favourable energetically [3]. Figure 2 presents the variation with current height of the potential barrier, which should pass vortex in the flux creep process movement for these cases, it is for totally captured initially vortex, temporary and half pinned respectively, on beam's irradiation created nano-defects.

ISBN: 978-3-95450-241-7 ISSN: 2673-5350 doi:10.18429/JACoW-IBIC2022-WEP07

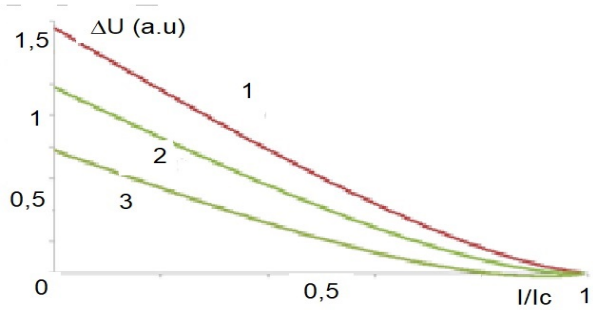


Figure 2: Dependence of the potential barrier ΔU on reduced to critical, transport current, for various initial captured vortex positions: (1) $x_0 = -\xi$ (fully captured), (2) $x_0 = -\xi/2$ (partly captured), (3) $x_0 = 0$ (half captured).

ANALYSIS OF SUPERCONDUCTING I-V CHARACTERISTICS

Discussed in the previous point potential barrier height ΔU has crucial meaning for determining the I-V characteristics and then critical current I_c of the superconducting materials. Useful at that aim is the general relation (7), describing the generated electric field E for the forward and backward flux creep processes, as the function of $i = I/Ic$, the reduced to critical transport current:

$$E = B\omega\, a\left(e^{\frac{-\Delta U(0)(1+i)}{k_B T}} - e^{\frac{-\Delta U(i)}{k_B T}}\right) \quad (7)$$

B is here applied magnetic induction, a distance between nearest capturing pinning centers, ω flux creep process frequency, k_B Boltzmann's constant, T temperature.

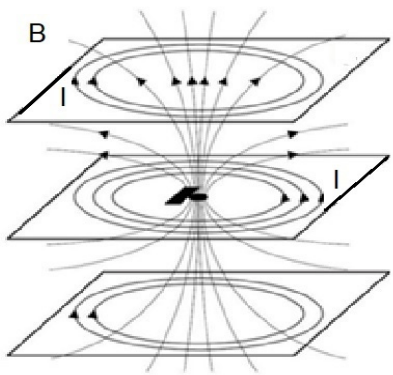


Figure 3: View of the vortex - pinning center interaction in the multi-layered superconductors.

It should be noticed that for some especial structures, as for instance 2D high temperature superconductors it can be taken into account too the interlayered vortex – pinning center interaction, as it shows Fig. 3, giving additional contribution to system energy, described by Eq. (1). From Fig. 3 follows that circulating currents in neighbouring layers have opposite direction, which means that interlayered vortices attract. In the same layer the vortices generate parallel magnetic field which results in the repulsion effect and forming the hexagonal vortex lattice.

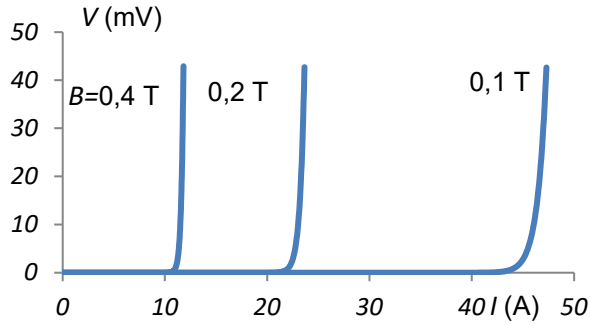


Figure 4: Calculated the current-voltage characteristics of subjected to bending strain HTc superconductor, as the function of the static, external magnetic induction.

The results of the calculations influence on the current-voltage characteristics of bent HTc superconductors, of the static magnetic field are shown in Fig. 4 and predict rapid decrease critical current, as is really observed. It should be noticed also that above model allows too predict current-voltage characteristics in dynamic case, as it shows Fig. 5.

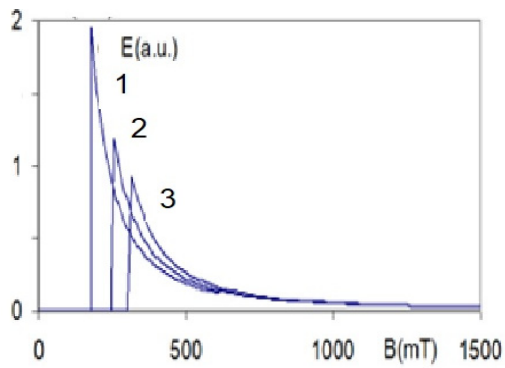


Figure 5: Theoretically calculated influence of the magnetic field sweep rate on the dynamic current-voltage characteristics anomalies in varying magnetic field: (1) 20 mT/s, (2) 30 mT/s, (3) 45 mT/s.

In Fig. 5 are presented calculated dynamical anomalies of the current-voltage characteristics in HTc superconducting slab in the slowly varying magnetic field. These anomalies observed us previously on various HTc superconductors as YBaCuO, HoBaCuO, BiSrCaCuO ceramics are sensitive to the magnetic field sweep rate, current amplitude, temperature. Generally they depend on sample quality and velocity of the magnetic flux diffusion into superconductors, so can be used in principle as superconducting sensor for measuring the electromagnetic properties of superconducting materials.

Presented in previous part static model allows also to determine the materials parameters of the investigated superconductors. At that purpose [3] fitting procedure of experimental and calculated I-V characteristics has been performed and the surface concentration of the inherent defects established as equal to $3 \cdot 10^{10}$ cm^{-2}, for sintered PbBiSrCaCuO superconductor. Such comparison can be used as new method of superconductors characterisation, allowing just to determine this way their state of purity.

Content from this work may be used under the terms of the CC BY 4.0 licence (© 2022). Any distribution of this work must maintain attribution to the author(s), title of the work, publisher, and DOI

ISBN: 978-3-95450-241-7 ISSN: 2673-5350 doi:10.18429/JACoW-IBIC2022-WEP07

Content from this work may be used under the terms of the CC BY 4.0 licence (© 2022). Any distribution of this work must maintain attribution to the author(s), title of the work, publisher, and DOI

INFLUENCE OF BEAM RADIATION ON Ic

Discussed potential barrier ΔU has crucial meaning for determining the current-voltage (I-V) characteristics and then critical current I_c of the superconducting materials, because height of ΔU determines the probability of the flux creep process. In this process captured vortex under influence of the Lorentz force and current flow should pass just this potential barrier, generating electric field. For better understanding of this effect the critical current has been determined as function of various physical parameters. In Fig. 6 is presented the influence on critical current of the nano-defect size d as the function of the nano-defects concentration. It is observed here that for low irradiation generating nano-defects the critical current initially increases, reaches the maximum, while then starts to decrease. This dependence is in agreement with physical interpretation, in which initially created defects act as new pinning centers, while for higher irradiation intensity nano-defects begin above all to damage the structure of superconductors. Similar course appears at the dependence of the critical current as the function of the irradiation intensity versus the critical temperature of superconductors shown in Fig. 7. In Fig. 8 is presented the dependence of the critical current on the nano-defects concentration, proportional to beam's irradiation intensity. It is shown here the influence of the elasticity constant of vortex lattice on the critical current.

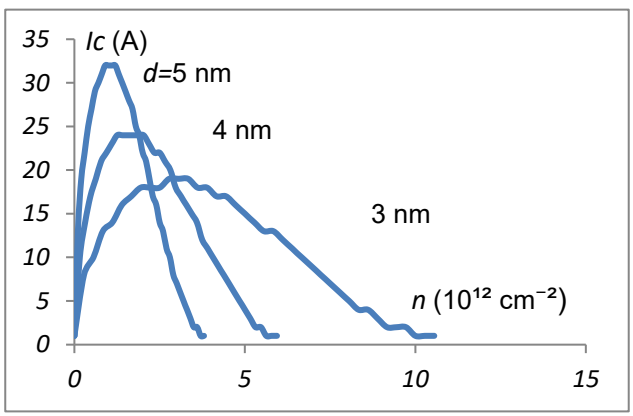


Figure 6: The influence of the nano-defect size on the dependence of the critical current versus beam's created irradiation defects surface concentration.

As it follows from runs shown in Fig. 8 the elasticity constant determining the stiffness of vortices lattice α has negative influence on the critical current. It is in agreement with physical interpretation of this phenomenon, indicating that for rigid lattice the vortices are strongly kept in regular hexagonal vortices array, so their capturing will be weak and therefore critical current appropriately smaller.

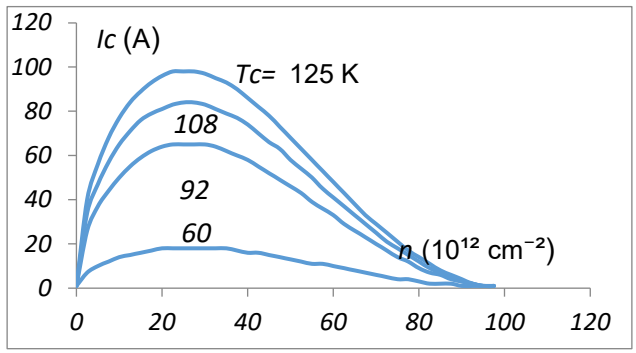


Figure 7: The influence of the critical temperature on the dependence of the critical current as the function of the beam's irradiation created defects surface concentration.

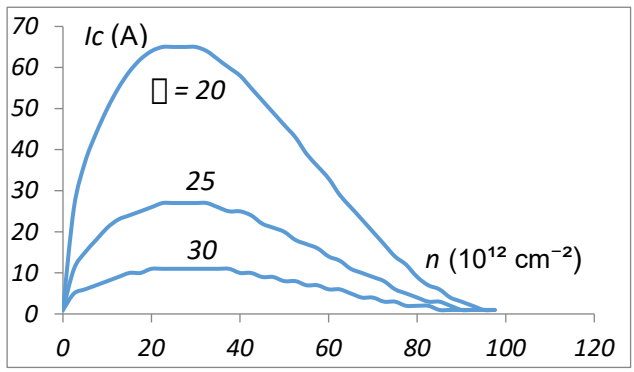


Figure 8: The influence of the vortex lattice elasticity constant α (10^{-5} eV/m^2), proportional to spring constant C, on dependence of the critical current, versus beam's created irradiation defects surface concentration.

CONCLUSIONS

In the paper is discussed important from scientific and applied point of view effect of influence beam's irradiation on the current carrying properties of the superconducting elements, more and more frequently used in modern accelerators. The creation of the nano-sized defects has been then considered and their influence on the critical current of superconductors. The energetic approach has been performed, which allowed to determine the height of potential barrier and critical current of irradiated samples.

REFERENCES

[1] J. Sosnowski, *Superconducting cryocables*, Book Publisher of Electrotechnical Institute, in Polish, pp. 1-100, 2012.

[2] M.I. Eremets *et al.,* "High-Temperature Superconductivity in Hydrides: Experimental Evidence and Details", *J. Supercond. Novel Magn.,* vol. 35, pp. 965–977, 2022. doi:10.1007/s10948-022-06148-1

[3] J. Sosnowski, "Analysis of electric current flow through the HTc multilayered superconductors", *IOP Conf. Ser.: Mater. Sci. Eng.,* vol. 113, p. 012019, 2016. doi:10.1088/1757-899X/113/1/012019

ISBN: 978-3-95450-241-7 ISSN: 2673-5350 doi:10.18429/JACoW-IBIC2022-WEP08

UPGRADE OF THE BPM LONG TERM DRIFT STABILIZATION SCHEME BASED ON EXTERNAL CROSSBAR SWITCHING AT PETRA III

G. Kube, F. Schmidt-Föhre, K. Wittenburg
Deutsches Elektronen-Synchrotron DESY, Germany
A. Bardorfer, L. Bogataj, M. Cargnelutti, P. Leban, M. Oblak, P. Paglovec, B. Repič
I-Tech, Solkan, Slovenia

Abstract

PETRA IV at DESY will be an upgrade of the present synchrotron radiation source PETRA III into an ultra low–emittance source with beam emittance of about 20 pm rad which imposes stringent requirements on the machine stability. In order to measure beam positions and control orbit stability to the required level of accuracy, a high resolution BPM system will be installed which consists of about 800 monitors with the readout electronics based on MTCA.4. In order to fulfill the requested long–term drift requirement (< 1 µm over 7 days), also the BPM cable paths have to be stabilized because of the PETRA–specific machine geometry. To achieve this, the crossbar switching concept was extended such that the analogue switching part is separated from the read–out electronics and brought as close as possible to the BPM pickup. While first measurements were presented before, meanwhile the system has undergone a major revision, especially the external switching matrix changed from a prototype setup to a system close to the final design. This contribution summarizes the latest measurements from PETRA III, demonstrating the high performance of the external stabilization concept.

INTRODUCTION

The PETRA IV project at DESY (Hamburg, Germany) aims at the construction of a diffraction limited ultra–low emittance light source operating at 6 GeV. The storage ring will be installed in the existing 2.3 km PETRA tunnel, thus it will follow the geometry of the old PETRA collider with 8 octants made of arcs, each hosting nine hybrid six bend achromatic (H6BA) cells which are connected by long straight section as shown in Fig. 1. Given the constraints on the DESY campus, only three octants will host beamlines (named OCTU in Fig. 1). Therefore, the facility will reuse the existing PETRA III experimental halls and will build a new one covering two octants of the ring in the West. The remaining octants (named OCTA) will host damping wigglers (DWs) in order to reduce the H6BA lattice emittance from approx. 43 pm rad down to the target value of 20 pm rad. The PETRA IV design operational parameters are summarized in Table 1, more information about the project and its actual status can be found e.g. in Refs. [1, 2].

The small PETRA beam emittance translates directly into much smaller beam sizes of 7 µm in both planes at the insertion device source points, thus imposing stringent requirements on the machine stability. In order to measure beam positions and control orbit stability to the requisite level of accuracy, a high resolution BPM system will be installed which consists of 787 individual monitors with the readout electronics based on MTCA.4 as technical platform. In Table 2 the BPM readout specifications are summarized.

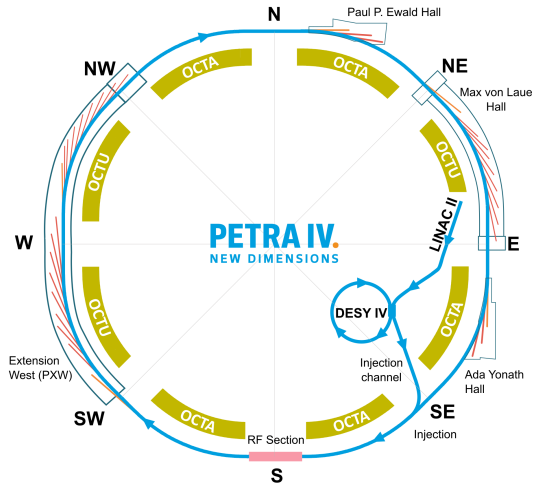


Figure 1: Layout of the PETRA IV facility. Existing experimental halls (Max von Laue, Peter P. Ewald, and Ada Yonath) will be reused, an additional experimental hall in West will be constructed.

Table 1: PETRA IV Main Parameters

Parameter	Value
energy	6 GeV
circumference	2304 m
emittance (with DWs)	20 pm rad
rel. energy spread (with DWs)	0.91×10^{-3}
momentum compaction	3.3×10^{-5}
$\beta_{x,y}$ at IDs	2.2 m, 2.2 m

As pointed out in Ref. [3], the specific PETRA IV machine geometry has to be taken into account in order to fulfil the requested long–term drift specification. This requires an additional stabilization of the BPM cable paths. Different drift compensation schemes are available and reviewed in Ref. [4]. As outcome of tests performed at PETRA III [3, 5] and of the discussion in Ref. [6] it was decided to use the principle of external crossbar switching where the analogue switching part is separated from the read–out electronics and brought as close as possible to the BPM pickup. Based on this idea DESY and the company I-Tech started a cooperation within the PETRA IV Technical Design Report (TDR) phase. Objectives are development and tests of a MTCA.4

Content from this work may be used under the terms of the CC BY 4.0 licence (© 2022). Any distribution of this work must maintain attribution to the author(s), title of the work, publisher, and DOI

ISBN: 978-3-95450-241-7 ISSN: 2673-5350 doi:10.18429/JACoW-IBIC2022-WEP08

Content from this work may be used under the terms of the CC BY 4.0 licence (© 2022). Any distribution of this work must maintain attribution to the author(s), title of the work, publisher, and DOI

Table 2: Readout electronics specifications. The single bunch / turn resolution holds for 0.5 mA bunch current, the closed orbit one for 1 kHz bandwidth, the beam current dependency for a 60 dB range with centered beam, and the long term stability should be measured over 6 days and a temperature span of ±1°C within a stabilized rack.

Requirement	Value
single bunch / single turn	< 10 µm
closed orbit resolution	< 100 nm (rms)
beam current dependence	±2 µm
long term stability	< 1 µm

based BPM system. Status of the project and preliminary evaluation of electronic prototypes under laboratory tests are reported in Ref. [7].

This contribution summarizes the latest long–term drift stability measurements performed in summer 2022 at PETRA III. While the MTCA.4 based prototypes are not yet ready to be tested in the accelerator environment, the external switching matrix (Libera XBS FE) is in the final design stage and was tested in combination with a modified Libera Brilliance+ (LB+) [8]. First measurements using different PETRA III operating modes indicate that the test setup performance fulfils the specifications for PETRA IV.

TEST SETUP AT PETRA III

A sketch of the setup in use for the PETRA III studies is shown in Fig. 2. In order to get rid of the beam jitter, a zero–offset emulator is used which consists of a combination of combiner and splitter (MACOM DS-409-4). The output signal is fed to the Libera XBS FE matrix. Outside the accelerator tunnel, the LB+ readout module is mounted in a rack located in an electronic hutch, the length of the interconnecting cables (3/8" Cellflex, LCF38-50JFN) is about 100 m. In order to synchronize the Libera XBS FE with the digital switch matrix inside the LB+, both devices are interconnected via a UTP Cat 7A cable. While the temperature

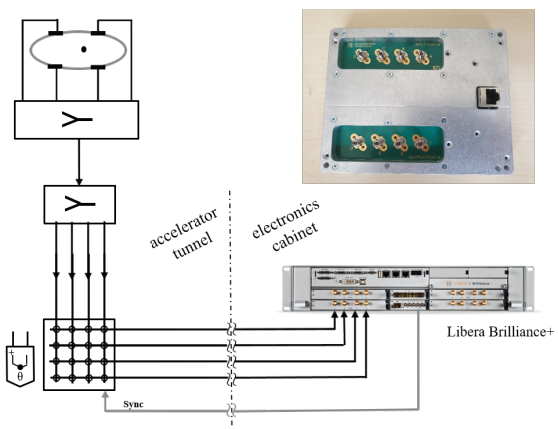


Figure 2: Principle scheme of the test setup. The photo shows the Libera XBS FE switch matrix (physical dimensions: 162.4 mm×128.4 mm×18 mm).

in the electronic hutch is stabilized to a level of ±1°C, the accelerator tunnel at the BPM location is not stabilized and temperature drifts of more than 2°C are possible throughout a week of operation. In order to measure the temperature, the XBS FE is equipped with a temperature sensor.

Compared to the setup described in Ref. [3], the main difference in the present one is the absence of the 500 MHz bandpass filter in the signal chain. Its purpose was to protect the switch matrix input from too high power, but embedding it in the zero offset emulator does not mimic a realistic situation. Instead of using bandpass filters, the Libera XBS FE uses low pass filters in the input of each signal path. Compared to a bandpass, the low pass filter characteristics has a much flatter slope and is less prone to input fluctuations.

LONG TERM STABILITY STUDIES

With the first Libera XBS FE prototype available in summer 2022, a series of measurements was performed. Each measurement lasted at least a few days. Figure 3 shows the temporal evolution of the beam current during about 5 days of user operation. In this time the machine was operated in the so called *continuous mode*, i.e. with a homogeneous filling of 480 bunches in 120 mA. Between 30,000 and 60,000

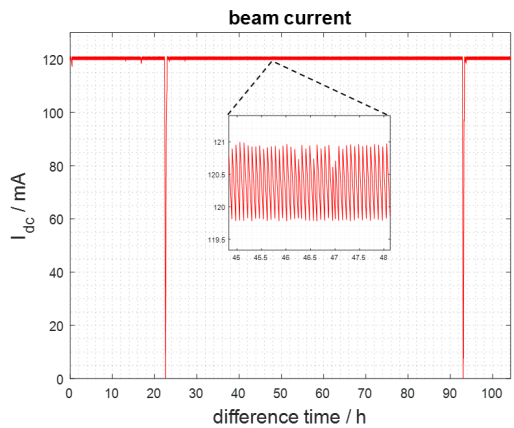


Figure 3: Beam current during user operation in July 2022. In this period PETRA III was operated with I_{dc} = 120 mA in 480 bunches. In this week two total beam losses happened. The insert indicates variations during top-up operation which keeps the current constant to a level of 1%.

data samples were recorded in Slow Acquisition (SA) mode of the readout electronics with 10 s wait time between consecutive samples. During the measurements, Digital Signal Conditioning (DSC), crossbar switching, and Automatic Gain Control (AGC) were active in the LB+.

In the following, example measurements are presented for both operational modes of PETRA III, the *continuous mode* with a homogeneous filling as described above (16 ns bunch separation), and the *timing mode* with 40 bunches in 100 mA (192 ns bunch separation). Similar modes are also planned for PETRA IV. While the development of modern ADCs is mainly driven by the telecommunication market and the

ISBN: 978-3-95450-241-7 ISSN: 2673-5350 doi:10.18429/JACoW-IBIC2022-WEP08

ADC performance therefore well suited for sinusoidal input signals (homogeneous filling), the pattern of the timing mode is challenging for a stabilization scheme. The experience from PETRA III tests using a pilot tone compensation scheme indicated at least difficulties in the performance for large bunch separations.

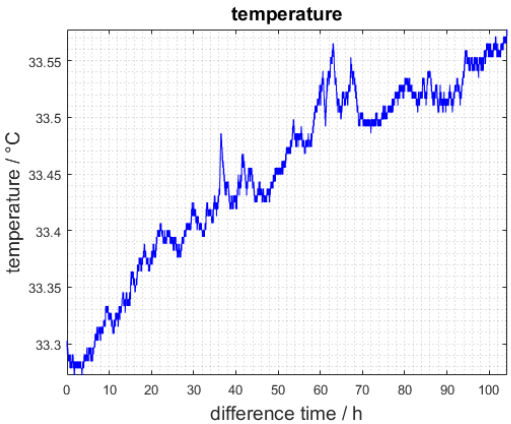


Figure 4: Temperature profile measured at the Libera XBS FE switch matrix.

Continuous Mode: Figure 4 represents the temperature profile as measured with the sensor mounted at the Libera XBS FE switching box. All data shown in this paragraph were taken simultaneously to the current dependency in Fig. 3.

Figure 5 illustrates the temporal evolution of the DSC coefficients gain and phase which both characterize the complex channel gain. As can be seen, a change in the beam current due to a beam loss is immediately visible in the gain, c.f. Fig. 3.

In Fig. 6 the position readout data from the SA data path are plotted. The monitor constant for data representation and beam position analysis amounts to $K_{x,y}$ = 10 mm throughout

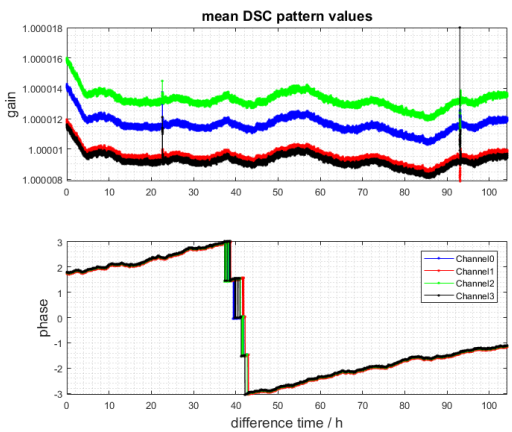


Figure 5: Temporal evolution of the mean DSC coefficients gain (top) and phase (bottom). Both parameters characterize the weighted average of the four data paths and represent a complex channel gain.

this report. In case of beam losses when there is no signal power at the input of the LB+, position readings are useless and a measure of the system noise. In order to exclude this distorting resolution influence, only data for $I_{dc} \geq 115$ mA are considered for the data analysis.

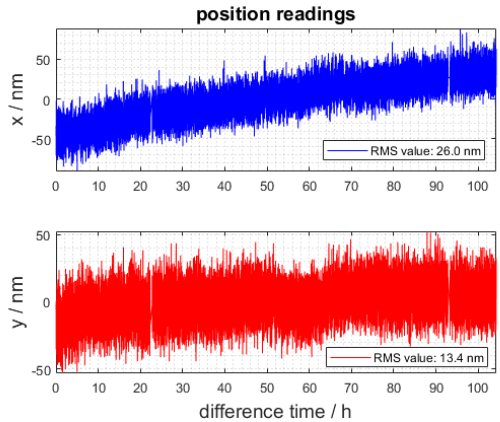


Figure 6: Position readings acquired from the SA data path. The monitor constant is $K_{x,y}$ = 10 mm.

As can be seen from this figure, the long term stability of the position data is very good. The rms values amount to 26.0 nm horizontally and 13.4 nm vertically, the peak–to–peak readings are in the order and below 100 nm which is well below the requested specification of < 1 µm. Comparing Figs. 4 and 6 there might be a small correlation between position readings and temperature profile. However, the effect is very small and the compensation scheme by external crossbar switching works well and compensates temperature together with possible humidity changes on both readout electronics and interconnecting cables.

Timing Mode: In the following a measurement is presented for timing mode operation which lasted about 8 days (192 h). In this time period there were four total beam losses and a few top-up interruptions (minimum beam current amounted to 72 mA, corresponding to a gain variation from −11 dB to −13 dB at the Libera input). The temperature profile as measured at the switching box showed a similar increasing trend than the one in Fig. 4, but with a variation of more than 1.2°C which is much larger compared to the measurements during continuous mode operation. This was most likely caused by the increased outdoor temperatures of about 30°C during the course of this measurement.

Figure 7 illustrates the temporal evolution of the DSC coefficients gain and phase as before. As can be seen from the gain coefficients, day–night variations with a period of about 24 h are clearly visible, especially at the beginning of the measurement. While fluctuations in the gain are larger compared to Fig. 5, the general trend in the phase indicates again a smooth increase (apart from the 90° phase jumps which are caused by numerical effects, but do not hamper the performance).

Content from this work may be used under the terms of the CC BY 4.0 licence (© 2022). Any distribution of this work must maintain attribution to the author(s), title of the work, publisher, and DOI

ISBN: 978-3-95450-241-7 ISSN: 2673-5350 doi:10.18429/JACoW-IBIC2022-WEP08

Content from this work may be used under the terms of the CC BY 4.0 licence (© 2022). Any distribution of this work must maintain attribution to the author(s), title of the work, publisher, and DOI

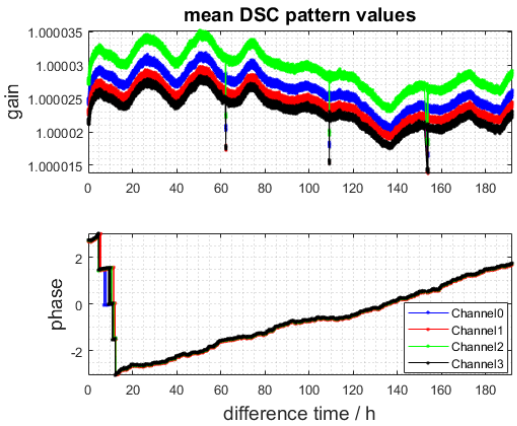


Figure 7: Temporal evolution of the mean DSC coefficients gain (top) and phase (bottom).

Figure 8 shows the corresponding position readout data from the SA data path. Again, in order to exclude distorting resolution influence due to beam losses only data for $I_{dc} \geq 95$ mA are considered for the data analysis. As can be

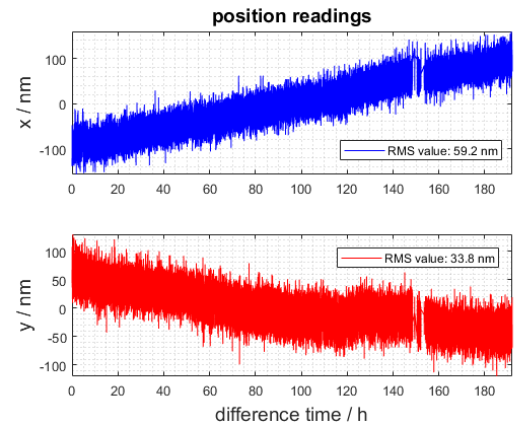


Figure 8: Position readings acquired from the SA data path.

seen, the long term stability of the position data results in rms values of 59.2 nm horizontally and 33.8 nm vertically. These values are about a factor of 2.5 worse compared to the continuous mode with its homogeneous fill pattern, nevertheless they are still well below the requested specification of < 1 µm. However, as pointed out in Ref. [3] the most temperature–drift critical element in the analogue signal chain is the external switch matrix itself, and besides also splitter and cables in front of the Libera XBS FE can contribute. As consequence it is quite likely to assume that not only the fill pattern, but also the environmental conditions during the second measurement with a measured temperature variation of more than 1.2°C at the switch matrix contribute additionally to the increased rms values. Since the tunnel temperature in PETRA IV will be stabilized to about ±1°C, larger drifts are not to be expected.

SUMMARY AND OUTLOOK

This paper summarizes BPM long–term stability studies which were performed at PETRA III using a modified LB+ with external switch matrix Libera XBS FE. These measurements indicate that the concept of external switching compensation works well, i.e. drifts in the RF front–end and from the interconnecting cables due to environmental changes are compensated to a high level. All long–term measurements performed so far indicate that the achieved readout stability is well below the specified 1 µm over one week of operation.

As next step, the MTCA based BPM system described in Ref. [7] which is an evolution of the present system will be installed and tested at PETRA III. Provided that future system tests with beam will demonstrate a comparable performance, the task to develop a prototype BPM system for the PETRA IV TDR phase is completed. Afterwards, the final step will be to transform the prototype into a system for serial production.

ACKNOWLEDGEMENTS

The PETRA IV project team acknowledges funding of the technical design phase granted by the Behörde für Wissenschaft, Forschung, Gleichstellung und Bezirke (BWFGB) of the Freie und Hansestadt Hamburg, as well as by the Bundesministerium für Bildung und Forschung (BMBF) under the contract DES21TDR.

REFERENCES

[1] I. V. Agapov *et al.*, "PETRA IV Storage Ring Design", in *Proc. IPAC'22*, Bangkok, Thailand, 2022, pp. 1431–1434. doi:10.18429/JACoW-IPAC2022-TUPOMS014

[2] R. Bartolini *et al.*, "Status of the PETRA IV Machine Project", in *Proc. IPAC'22*, Bangkok, Thailand, 2022, pp. 1475–1478. doi:10.18429/JACoW-IPAC2022-TUPOMS029

[3] G. Kube *et al.*, "Tests of the New BPM Long Term Drift Stabilization Scheme Based on External Crossbar Switching at PETRA III", in *Proc. IBIC'21*, Pohang, Korea, Sep. 2021, paper MOPP30, pp. 123. doi:10.18429/JACoW-IBIC2021-MOPP30

[4] G. Rehm, "Review of BPM Drift Effects and Compensation Schemes", presented at the IBIC'22, Krakow, Poland, Sep.2022, paper MO3I1, this conference.

[5] G. Kube, "BPM Studies in view of PETRA IV", 15th Libera Online Workshop, June 17, 2020, https://www.i-tech.si/wp-content/uploads/2021/06/6.-Gero-Kube_DESY_compressed1.pdf

[6] F. Schmidt-Foehre, G. Kube, and K. Wittenburg, "Comparison of Two Long Term Drift Stabilization Schemes for BPM Systems", in *Proc. IBIC'21*, Pohang, Korea, Sep. 2021, paper MOPP36. doi:10.18429/JACoW-IBIC2021-MOPP36

[7] P. Leban *et al.*, "Preliminary Evaluation of the MTCA.4 BPM Electronics Prototype for the PETRA IV Project", presented at the IBIC'22, Krakow, Poland, Sep.2022, paper WEP09, this conference.

[8] Libera Brilliance+, https://www.i-tech.si/products/libera-brilliance-3/.

ISBN: 978-3-95450-241-7 ISSN: 2673-5350 doi:10.18429/JACoW-IBIC2022-WEP09

PRELIMINARY EVALUATION OF THE MTCA.4 BPM ELECTRONICS PROTOTYPE FOR THE PETRA IV PROJECT

P. Leban, M. Cargnelutti, A. Bardorfer, M. Oblak, B. Repic, L. Bogataj, P. Paglovec
Instrumentation Technologies (I-Tech), Slovenia
G.Kube, F.Schmidt-Föhre, K.Wittenburg, Deutsches Elektronen-Synchrotron DESY, Germany

Abstract

Within the PETRA IV project at DESY, the synchrotron radiation source PETRA III will be upgraded into a low-emittance source. The small beam emittance and reduced beam size imply stringent requirements on the machine stability. To meet the requirements on position measurement and orbit stability, a high-resolution BPM system will be installed in the new machine, with about 800 BPMs and MTCA.4-based readout electronics.

In the TDR phase of the project, I-Tech and DESY are cooperating on the realization of a BPM prototype that will demonstrate the feasibility of reaching the PETRA IV requirements. Several analog, digital and SW parts are taken from the Libera Brilliance+ instrument and are reused in the MTCA.4 BPM prototype, with some innovations. One of them is the separation of the RF switch matrix used for long-term stabilization: placing it near the BPM enables also the long RF cables to be stabilized. An 8 channel RTM board, able to acquire signals from two BPMs was developed and is also tested.

This paper presents an overview of the BPM electronics prototype and the promising test results achieved in the Instrumentation Technologies' laboratory with the first boards produced.

PERFORMANCE REQUIREMENTS

The PETRA IV performance requirements for the BPM electronics are presented in Table 1.

Table 1: Performance Requirements for the PETRA IV BPM Electronics

Parameter	Requirement
Resolution on single bunch/turn	< 20 µm RMS (0.5 mA)
Resolution on closed orbit	< 200 nm RMS (at 200 mA in 1600 bunches, 300 Hz bandwidth)
Beam current dependence	±2 µm (0 to -60 dBm range)
Long-term stability at room temperature (25°C)	< 1 µm (6 days, ±1 K)
FOFB latency	≤ 3 turns

PROTOTYPE DESCRIPTION

The PETRA IV project requirements [1] for the BPM electronics performance could not be met with the commercially available Libera instrumentation entirely. A characteristic of the machine are the long RF cable paths between the BPM and the BPM electronics which can extend over 150 metres, up to 200 metres. The compensation mechanism in the Libera Brilliance+ instrument is not capable to compensate the disturbances along the cables which makes position readout sensitive to environmental and mechanical factors. To fulfill the 1 µm long-term stability over 6 days (ΔT = ±1 K), the RF cables must be compensated well.

Another project-specific requirement is that the BPM electronics hardware should be based on the MTCA.4 standard, with a combination of modules provided either by DESY, by commercial suppliers or developed specifically. In the time frame of the TDR phase of the project, I-Tech developed the RTM module which contains the RF front-end, analog signal conditioning components and the A/D converters. The module connects to the DESY's AMC module [2]. In each of the machine cells, all the BPM electronics, including the Fast-Orbit-Feedback (FOFB) and timing cards, are foreseen to be installed in a single 12-slot chassis. Due to space constraints, a high density of RF channels per BPM module was preferred. Taking into account other constraints, such as power consumption and cooling capabilities, the final RTM design includes 8 RF channels with standard SMA-F connectors and 2 additional RJ-45 connectors. The A/D converters are dual-channel 125 MHz/16 bit and are driven by the clock provided through the HW or SW PLL on-board the RTM module. The reference clock is locked to the turn-by-turn clock of PETRA IV provided by the timing system.

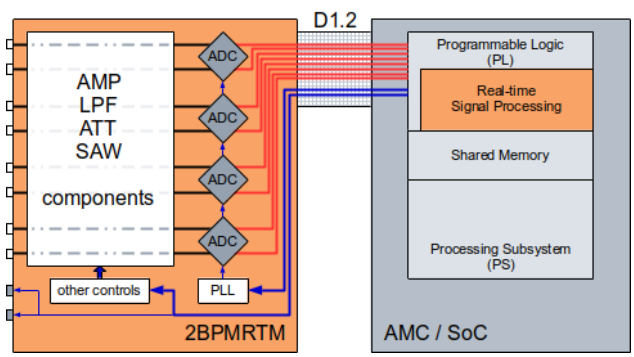


Figure 1: RTM and AMC modules used for the prototype system.

A general-purpose AMC module was used for the development phase and it utilizes a high-performance Zynq Ultrascale+ (ZUP) System-on-Chip (SoC) with 1 GB shared memory for the programmable logic (PL). According to the architecture, only the PL of the SoC is

Content from this work may be used under the terms of the CC BY 4.0 licence (© 2022). Any distribution of this work must maintain attribution to the author(s), title of the work, publisher, and DOI

ISBN: 978-3-95450-241-7 ISSN: 2673-5350 doi:10.18429/JACoW-IBIC2022-WEP09

Content from this work may be used under the terms of the CC BY 4.0 licence (© 2022). Any distribution of this work must maintain attribution to the author(s), title of the work, publisher, and DOI

used for the real-time signal processing while the processing subsystem part is only used to manage the module's housekeeping. The RTM and AMC modules are presented in Fig. 1.

STABILIZATION TECHNIQUE

The cross-bar switch was implemented in the first Libera instrument generations (Electron, Brilliance) back in 2005 and has been in use in various synchrotron machines since then. By switching, in combination with properly supported software calculations, the amplitude readings were compensated to ensure few tens of nanometers position drift over several hours or days. Since the cross-bar switches were located in the BPM module, only the RF signal path through the BPM module was compensated while the RF cables connecting the BPM with the electronics were not compensated. While majority of the synchrotron machines do not suffer from disturbances along their few ten meters of RF cable lengths, the PETRA IV project is going to be more challenging. The RF cables may have to be as long as 200 metres going through various locations with their micro-climate conditions.

After a brief brainstorming with the PETRA III Beam Diagnostics group, an idea came to implement a stand-alone module which contains the cross-bar switches with a minimum set of other components. The module should be installed in the tunnel as close to the BPM as reasonably possible and minimize the non-compensated RF cable path (Fig. 2). With such approach, the long RF cables become part of the RF signal path which is compensated by the signal conditioning algorithms in the BPM electronics. The module is powered and controlled from the RTM module through a Cat.7 Ethernet cable [3].

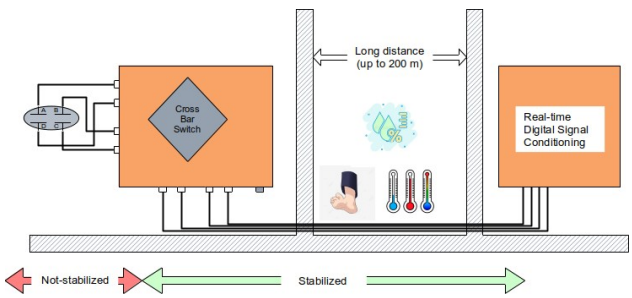


Figure 2: The module with a cross-bar switch is installed inside the tunnel. The signal conditioning algorithms in the BPM electronics compensate the disturbances along the long RF cables.

SIGNAL PROCESSING AND DATA READOUT

The analog signals are sampled by the A/D converters on the RTM module and are transferred to the AMC module over the Zone 3 connector class D1.2 interface. The raw ADC samples with approximately 8 ns time resolution are processed by several FPGA blocks that apply the bitmasks, fine-tune the time delay and specify the processing type for the turn-by-turn and multi-bunch turn-by-turn data. The buffered data is stored in the SoC's shared memory and provided to the main CPU module over the PCIe bus. The streaming data intended for fast and slow monitorings is transferred through the PCIe as well. The CPU module runs the Libera BASE software framework which supports various hardware module types and hosts the specific applications (e.g., BPM application). The application communicates with multiple AMC modules within the MTCA.4 chassis and provides a generic user interface for data readout and parameter control. The prototype version already supports various clients but generic command-line interface ("libera-ireg") will be used for testing at PETRA III. DOOCS is planned for the PETRA IV machine [4]. Fig. 3 shows the processing blocks in the AMC and CPU modules.

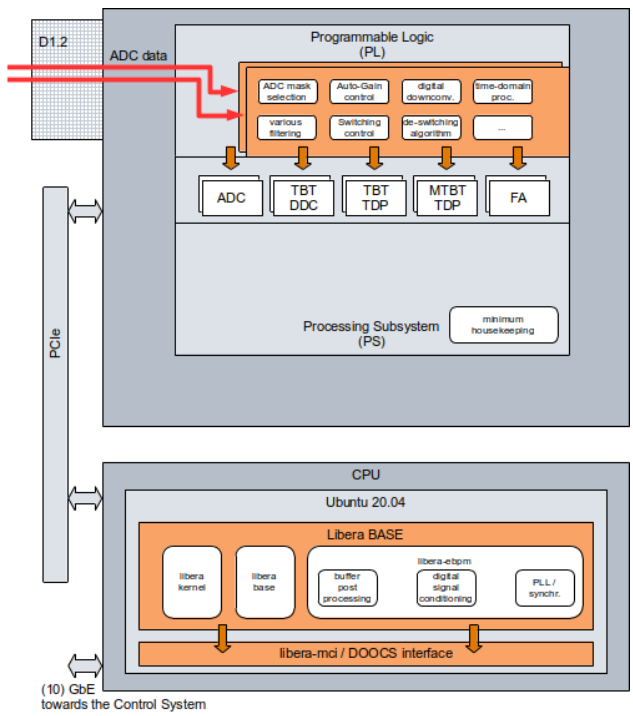


Figure 3: Signal processing, data buffers and software framework in the AMC and the CPU modules.

PROTOTYPE EVALUATION

The core parts of the Libera Brilliance+ FPGA processing were reused and transferred to the MTCA.4 prototype. This enabled quick and effective performance evaluations that were required to confirm the hardware conforms with the project requirements. Before the first production run of the RTM modules, the commercial name was set to "2BPMRTM".

2BPMRTM Module Evaluation

A subset of tests presented in this paper includes verifications of the input signal range, input noise density and crosstalk between channels.

The maximum input signal power is +4 dBm CW at nominal frequency. The RF chains are equipped with a 31 dB programmable attenuator. The input noise density

ISBN: 978-3-95450-241-7 ISSN: 2673-5350 doi:10.18429/JACoW-IBIC2022-WEP09

was measured and calculated for maximum and minimum attenuation values (31 dB and 0 dB). Results are presented in Table 2.

Table 2: Input Noise Density

Channel	Input noise density
Maximum attenuation (31 dB)	-144 dBm/Hz
Minimum attenuation (0 dB)	-169 dBm/Hz

The crosstalk between the channels is presented in Table 3. The worst crosstalk measured was -76 dB between channels B and C. The 2BPMRTM module supports 2 BPMs (8 channels). The maximum crosstalk between the 2 BPMs was measured -95 dB (BPM1 channel D, BPM2 channel A).

Table 3: Crosstalk Between the Channels on a Single BPM

	A	B	C	D
A	/	-82 dB	-88 dB	-97 dB
B	-80 dB	/	-86 dB	-95 dB
C	-90 dB	-76 dB	/	-78 dB
D	-95 dB	-94 dB	-81 dB	/

The 2BPMRTM module is shown in Fig. 4. The front-panel contains 8 SMA-F and 2 RJ-45 interfaces.

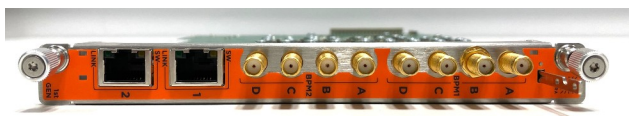


Figure 4: 2BPMRTM prototype.

Results in Laboratory Setup

The measurement performance was evaluated also using the external switching module (official name: Libera XBS FE) according to the standard testing procedure used for the Libera Brilliance+. Various cable lengths between the 2BPMRTM module and Libera XBS FE were tested ranging from few meters up to 200 meters. The monitor constant used in all measurements was Kx = Ky = 10 mm.

The short-term measurement performance was evaluated in the laboratory environment with quasi-stable temperature conditions. The test setup is used for production tests of the Libera instrumentation and uses calibrated generators. RMS values of the turn-by-turn and 10 kHz data were evaluated at input signal power from 0 dBm down to -60 dBm, CW. Figure 5 shows the results for a single plane and for signal range down to -50 dBm. The bandwidth of the turn-by-turn data is DC to ~45 kHz, the 10 kHz data has a bandwidth DC to 2 kHz.

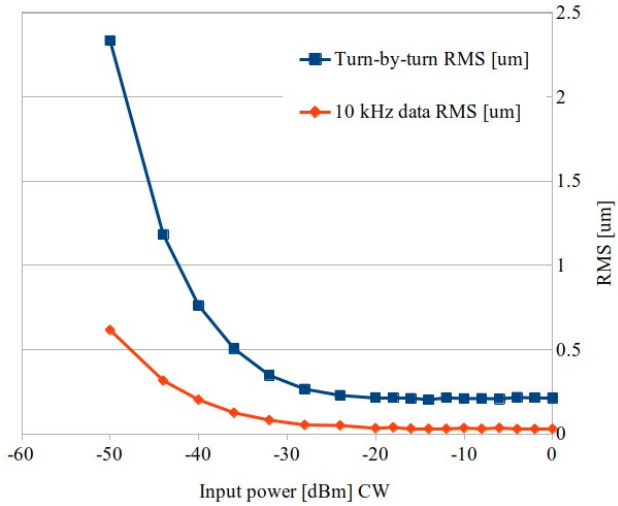


Figure 5: The turn-by-turn RMS and 10 kHz data RMS values are < 1 µm down to -40 dBm CW input signal.

The linearity (beam-current dependence) was measured under same setup as the short-term performance. Figure 6 shows the beam current dependence characteristics for centered and off-centered (~800 µm) beam conditions. While the centered conditions did not show any obvious position offset, there was a slight offset observed for off-centered conditions for the input power levels where the programmable attenuators were already open completely.

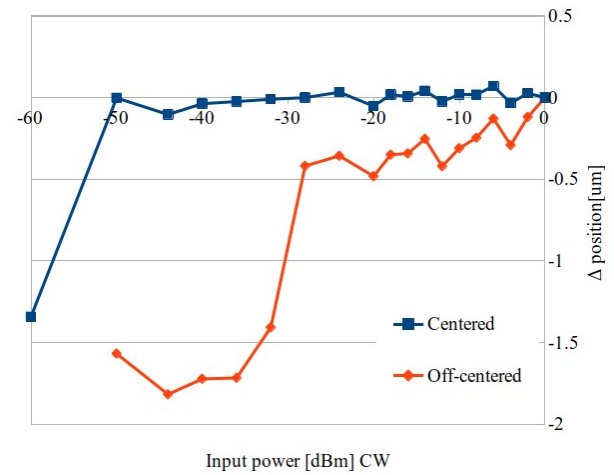


Figure 6: Beam current dependence characteristics.

Crosstalk was measured with the combination of the 2BPMRTM module and Libera XBS FE with a simulated single bunch. Results are presented in Table 4.

Table 4: Crosstalk Between the Channels of the 2BPMRTM Module and Libera XBS FE, Single Pulse

	A	B	C	D
A	/	-55 dB	-56 dB	-57 dB
B	-57 dB	/	-57 dB	-57 dB
C	-56 dB	-57 dB	/	-57 dB
D	-56 dB	-56 dB	-56 dB	/

Content from this work may be used under the terms of the CC BY 4.0 licence (© 2022). Any distribution of this work must maintain attribution to the author(s), title of the work, publisher, and DOI

ISBN: 978-3-95450-241-7 ISSN: 2673-5350 doi:10.18429/JACoW-IBIC2022-WEP09

Content from this work may be used under the terms of the CC BY 4.0 licence (© 2022). Any distribution of this work must maintain attribution to the author(s), title of the work, publisher, and DOI

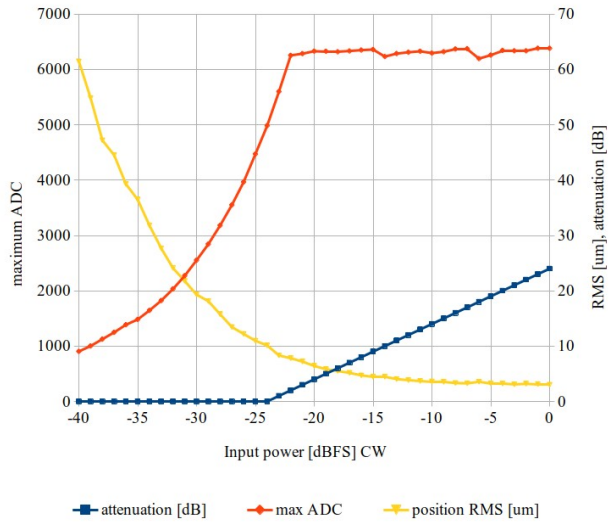


Figure 7: Measurement performance with simulated single bunch.

The single bunch was simulated by an external generator. The pulse width was approximately 1 ns. The required RMS (20 µm) is guaranteed for the input power 0 to -30 dBFS (Fig. 7). The corresponding ADC count level at -30 dBFS is approximately 2500 out of 32768 (full scale).

For the temperature drift evaluation, the whole system was placed in a temperature chamber: RF generator, MTCA.4 chassis, Libera XBS FE and 4x 22m LMR-195 RF cables. Temperature profile:

- 2 days at 25°C
- 10 hours at 20°C
- 5 hours at 25°C then 10 hours at 30°C
- 5 hours at 25°C then 20°C until end of test

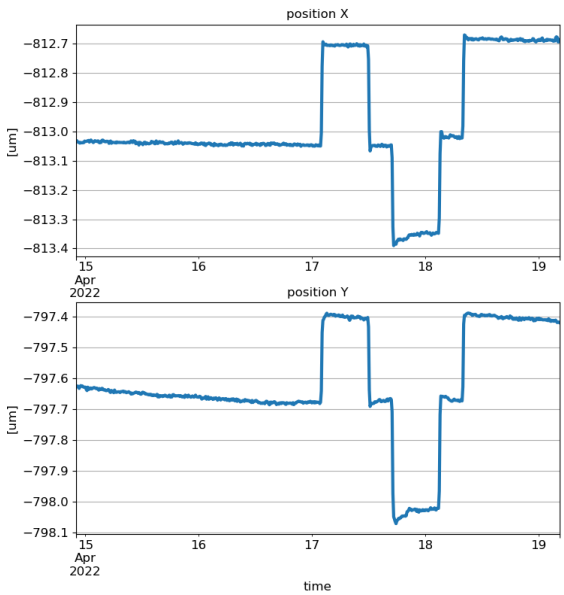


Figure 8: A four-day test in the temperature chamber.

Figure 8 shows the horizontal and vertical position readings from the test. Results are presented in Table 5.

Table 5: Longterm Stability and Temperature Dependence Tests

Property	Value
Position drift at constant temperature	<100 nm peak-to-peak
Position drift under varying temperature	100 nm/K

Results from the laboratory tests confirm the BPM performance meet majority of the requirements from Table 1. Some tests still need to be done [5].

CONCLUSIONS

The prototype BPM system for the PETRA IV project has been under development since December 2020. The first RTM module was developed, produced and tested already in March 2022 showing promising results. In the same time frame, the external switching module prototype was produced and tested with both, the Libera Brilliance+ and the RTM module. Its design and performance were confirmed with beam tests at PETRA III machine and the module had been finalized and produced as a final product in May 2022.

The results achieved with laboratory tests confirm the MTCA-based BPM system conforms with the PETRA IV requirements in all related aspects. Further tests with beam were done at PETRA III as discussed in [5]. Verification of the external switching module's radiation resistance is planned along further beam performance tests.

Main emphasis of the project is now put on the software and FPGA development, supporting also automatic gain control and few other PETRA IV specific features. Later this year, tests at PETRA III with a fully supported MTCA.4 chassis is planned.

REFERENCES

[1] PETRA IV Conceptual Design Report, https://bib-pubdb1.desy.de/record/426140/files/DESY-PETRAIV-Conceptual-Design-Report.pdf

[2] MicroTCA Technology Lab, https://techlab.desy.de/products/amc/damc_fmc2zup/index_eng.html

[3] G. Kube *et al.*, "Tests of the New BPM Long Term Drift Stabilization Scheme Based on External Crossbar Switching at PETRA III", in *Proc. IBIC'21*, Pohang, Korea, Sep. 2021, paper MOPP30, pp. 123.

[4] The Distributed Object-Oriented Control System Framework, https://doocs-web.desy.de

[5] G. Kube *et al.*, "Upgrade of the BPM Long Term Drift Stabilization Scheme Based on External Crossbar Switching at PETRA III", presented at IBIC'22, Krakow, Poland, Sep. 2022, paper WEP08, this conference.

ISBN: 978-3-95450-241-7 ISSN: 2673-5350 doi:10.18429/JACoW-IBIC2022-WEP10

DETECTION OF A DC ELECTRIC FIELD USING ELECTRO-OPTICAL CRYSTALS

A. Cristiano*[1], M. Krupa, CERN, Geneva, Switzerland
R. Hill, University of Huddersfield, UK
[1]also at University of Huddersfield, UK

Abstract

Standard Beam Position Monitors (BPM) are intrinsically insensitive to beams with no temporal structure, so-called DC beams, which many CERN experiments rely on. We therefore propose a novel detection technique in which the usual BPM electrodes are replaced with electro-optic (EO) crystals. When exposed to an electric field, such crystals change their optical properties. This can be exploited to encode the electric field magnitude onto the polarisation state of a laser beam crossing the crystal. An additional EO crystal, placed outside the vacuum chamber, can be used to control the system's working point and to introduce a sinusoidal modulation, allowing DC measurements to be performed in the frequency domain. This contribution presents the working principle of this measurement technique, its known limitations, and possible solutions to further increase the system's performance. Analytical results and simulations for a double-crystal optical chain are benchmarked against the experimental data taken on a laboratory test bench.

INTRODUCTION

Most high-energy particle accelerators rely on radiofrequency cavities to boost bunches of particles to the desired energy. The power spectral density of such beams extends to high frequencies. However, some physics experiments require particle beams without any temporal structure [1], e.g. the future Search for Hidden Particle (SHiP) experiment at CERN [2]. Since DC particle beams do not induce signals in commonly used Beam Position Monitors, other methods are used to observe their transverse position. Indirect measurements can be performed with Schottky monitors [3], but they require some integration time. On the other hand, screen-based BPMs [4] interact with the particle beam and unavoidably affect its parameters which can deteriorate the beam. To address these issues, a novel BPM based on electro-optical crystals and suitable for measurement of DC beams (EO-DC-BPM) is under development at CERN.

Under an electric field exposure, EO crystals' properties change linearly due to the Pockels effect [5]. This variation can be encoded into the polarisation state of a laser beam crossing the crystal and later decoded through interferometric or amplitude demodulation techniques. The fast response of the Pockels effect makes EO crystals suitable for high frequency diagnostic tools. A high-frequency EO BPM capable of detecting variations of the transverse position within a bunch of a particle beam is currently under development for the HL-LHC project [6]. However, EO crystals are dielectric and in a presence of a DC or quasi-DC electromagnetic field, free charge carriers move to their boundaries and create an internal electric field obstructing the external field. This reduction of the modulation depth leads to a measurement error and has limited the use of EO materials to measurements above 20 Hz [7], unless the space charge is avoided through mechanical rotary stages [8].

Until now, the EO-DC-BPM development has focused on studying the feasibility of using an optical chain based on EO-crystals for measurements of the intensity of an electrostatic field in frequency domain. A proof-of-concept test bench has been designed to scrutinize the experimentally obtained results against those expected from simulations.

ELECTRO-OPTIC DC FIELD SENSOR

The EO-DC-BPM consists of four identical optical branches arranged symmetrically around the vacuum chamber. Each branch accommodates a chain of two electro-optical crystals. One crystal is placed inside the vacuum chamber and couples to the electrostatic field of the particle beam. The other crystal remains outside and is externally modulated with a sinusoidal field to move the measurement to the frequency domain. On top of the modulation signal, a DC bias is used to tune the system and to compensate crystal drifts which can lead to measurement error.

A conceptual overview of a single optical branch of the EO-DC-BPM is shown in Fig. 1. The sensor is composed of two EO crystals made of Lithium Niobate ($LiNbO_3$) which was chosen due to its large EO coefficients, low conductivity [9] and high radiation hardness [10] compared to other EO materials. The optical axes of the crystals are aligned with the z-axis. A linearly polarised laser beam traverses the crystals along the y-axis and oscillates in x-z plane.

The input polariser fixes the laser beam's polarisation at 45° with respect to the x-axis. The laser beam then enters

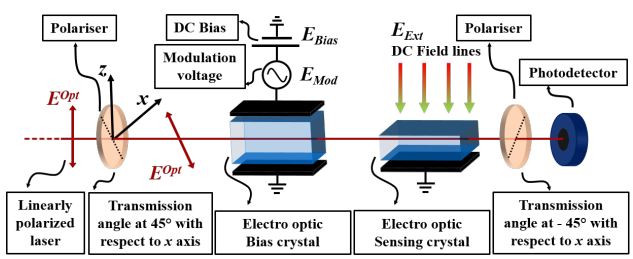


Figure 1: Schematic view of one optical branch of the EO-DC-BPM.

* antonio.cristiano@cern.ch

Content from this work may be used under the terms of the CC BY 4.0 licence (© 2022). Any distribution of this work must maintain attribution to the author(s), title of the work, publisher, and DOI

ISBN: 978-3-95450-241-7 ISSN: 2673-5350 doi:10.18429/JACoW-IBIC2022-WEP10

Content from this work may be used under the terms of the CC BY 4.0 licence (© 2022). Any distribution of this work must maintain attribution to the author(s), title of the work, publisher, and DOI

the first crystal, labelled as *EO Bias crystal* in Fig. 1. The phases of the two light components along the x-axis and z-axis are unevenly retarded because of the crystal's natural birefringency and the Pockels effect due to the external modulation field. The laser beam's polarisation is rotated again in the second crystal, *EO Sensing crystal*, in which the Pockels effect is driven by the external DC field to sense. Finally, the output polariser, rotated by 90° with respect to the first one, translates the polarisation modulation into optical power variation which can be measured by a photo-detector.

The optical chain has been modeled analytically [11] using Jones calculus [12]. The normalized output laser beam intensity is given by:

$$I = \sin^2[\alpha \cdot E_{Mod}(t) + \Gamma_0 + \Phi_0(E_{Bias}) + \Phi_1(E_{Ext})] \quad (1)$$

where $E_{Mod}(t)$ is the external sinusoidal modulation field, α is a constant term given by the physical and electro-optic properties of the bias crystal, Γ_0 is the collective phase retardation due to the natural birefringency of the two crystals, $\Phi_0(E_{Bias})$ and $\Phi_1(E_{Ext})$ describe the electro-optic properties of, respectively, the bias and sensing crystals which vary linearly with the applied electric field.

Eq. (1) constitutes the basis of the developed analytical model which supported selection of optical components for the proof-of-concept test bench. The model, developed in MATLAB, mimics the behaviour of the optical chain and accurately factors in effects related to temperature, optical wavelength and the level of doping of the crystals. It provides all the simulations results shown in the paper.

With no external field acting on the sensing crystal and with $E_{Mod} = 0$ on the bias crystal, the sensor's output light intensity depends only on E_{Bias} and is characterized by a quadratic transfer function shown in Fig. 2. The electric field equivalent to a half-period shift of the transfer function is called E_π and its value is given by:

$$E_\pi = \frac{\lambda}{L_y(n_e^3 r_{33} - n_o^3 r_{13})} \quad (2)$$

E_π corresponds to the electric field necessary to rotate the laser beam's polarisation by 180°. Each of the two crystals features its own E_π which are distinguished as $E_{\pi B}$ for the bias crystal and $E_{\pi S}$ for the sensing crystal. $E_{\pi B}$ limits the maximum useful modulation amplitude [11], whiles $E_{\pi S}$ defines, together with the acquisition chain, the resolution and the dynamic range of the optical chain.

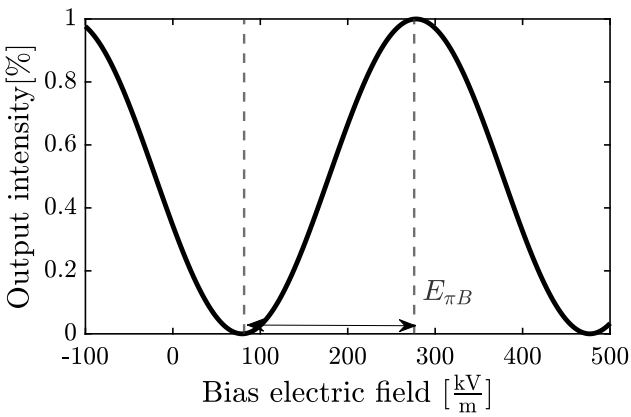


Figure 2: Transfer function of the modelled optical chain.

DC Field Measurements in Frequency Domain

The quadratic symmetry of the sensor's transfer function can be exploited to conduct DC measurements in the frequency domain. Firstly, in the absence of E_{Ext}, the DC bias is set to drive the system to one of the symmetry points (any peak or trough of the transfer function). A pure sinusoidal modulation applied around a symmetry point results in an output signal containing only even harmonics of the modulation frequency. Figure 3 shows the working point set with E_{Bias} (red dot) and the sinusoidal modulation E_{Mod} added on top (red line). The sinusoidal signal moves the working point along the transfer function, resulting in a modulated output signal containing exclusively even harmonics of the modulation frequency as shown in Fig. 4.

A DC particle beam, and its corresponding electrostatic field, acting on the sensing crystal, disrupts this symmetry by effectively shifting the working point by an amount proportional to the intensity of the measured field, as shown in Fig. 5. The resulting output signal, shown in the frequency domain in Fig. 6, contains both odd and even harmonics of the modulation frequency. Amplitudes of the odd harmonic are proportional to E_{Mod} and can therefore be used

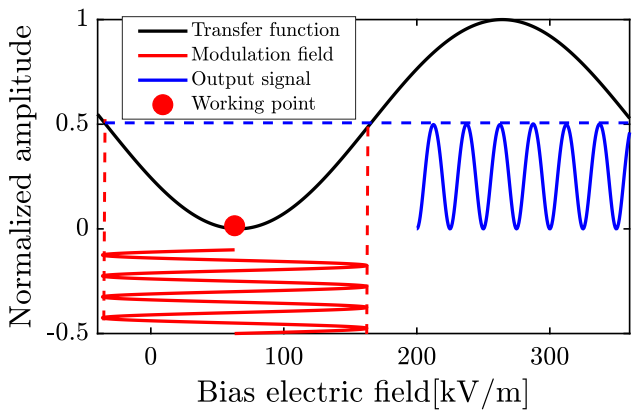


Figure 3: Output light intensity with a sinusoidal modulation applied to the bias crystal in standard condition, without electric field acting on the sensing crystal.

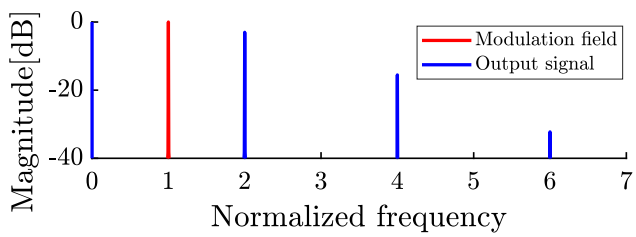


Figure 4: Spectrum of the modulation field and the modulated output intensity with no electric field acting on the sensing crystal.

ISBN: 978-3-95450-241-7 ISSN: 2673-5350 doi:10.18429/JACoW-IBIC2022-WEP10

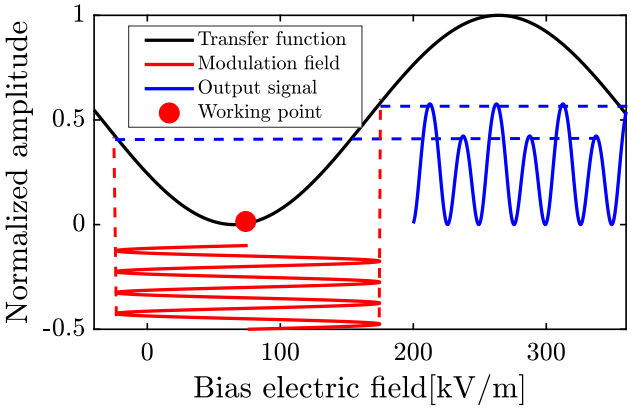


Figure 5: Output light intensity with a sinusoidal modulation applied to the bias crystal when an electric field is acting on the sensing crystal.

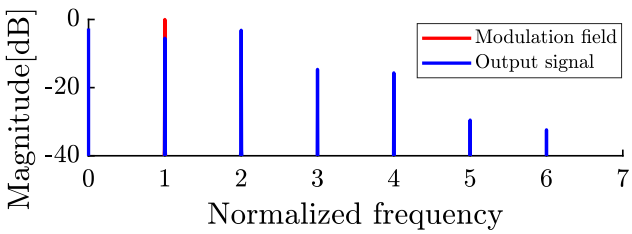


Figure 6: Spectrum of the modulation field and the modulated output intensity with an electric field acting on the sensing crystal.

to determine the relative intensity of the field under measurement [11]. Since for beam position monitoring the EO-DC-BPM does not require measurements of the absolute DC field intensity, there is no need to precisely calibrate the absolute electric field sensitivity of the sensor. Moreover, as the amplitude of the first harmonic is the strongest, the EO-DC-BPM fully relies on monitoring that component only.

EXPERIMENTAL RESULTS

The analytical model was validated experimentally with a proof-of-concept laboratory test bench shown in Fig. 7.

The test bench consists of a 60 cm long pipe with a square 45×45 mm aperture. Both vertical walls of the pipe carry removable crystal holders, annotated with a red circle in Fig. 7. The holder houses the sensing crystal and two prisms to steer the laser beam in and out of the pipe and through the crystal. The bias crystal is placed outside the pipe, between two PCBs connected to a high-voltage piezo-amplifier. The most relevant properties of the crystals are listed in Table 1.

The entire optical chain, except for the two crystals, was assembled using off-the-shelf THORLABS components. The SFL-1550P laser diode provides a 1550 nm linearly-polarised laser beam with a maximum power of 40 mW. The choice of the wavelength might seem counter-intuitive considering the figure of merit E_π defined earlier in Eq. (2). However, the selected wavelength minimizes the creation of optically induced hole-electron pairs which would otherwise be a source of unwanted space charge. The output laser beam is captured by the S122C photo-detector connected to the PM100D power meter, whose output is measured by a 10-bit oscilloscope and a signal analyzer.

A metal rod carrying a voltage up to 1 kV traverses the pipe longitudinally. The rod substitutes a DC particle beam passing through the EO-DC-BPM and acts as source of a uniform electric field for the sensing crystal. The pipe and the optical chain are fixed on a breadboard which, in turn, is mounted on a linear translation stage connected to a large optical table. The metallic rod is rigidly attached to the same optical table. Such a configuration allows the pipe and all the optics to be displaced around a stationary rod.

Table 1: Properties of the $LiNbO_3$ (5% MgO doped) Crystals Used in the EO Sensor

	Bias crystal	Sensing Crystal
$\mathbf{L_x}$ [mm]	3	5
$\mathbf{L_y}$ [mm]	40	50
$\mathbf{L_z}$ [mm]	3	2
$\mathbf{E}_\pi$ [$\frac{\mathrm{kV}}{\mathrm{m}}$]	$E_{\pi B}$ = 203.9	$E_{\pi S}$ =159

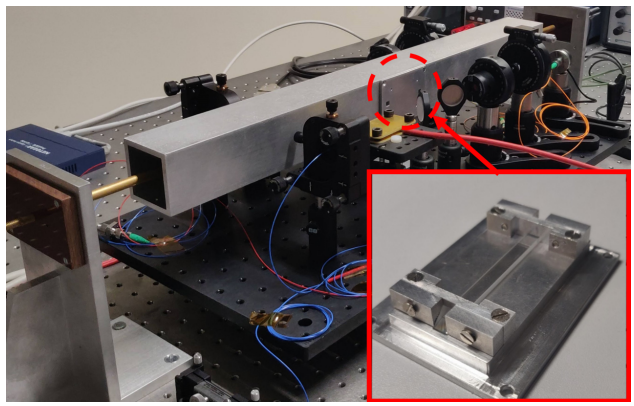


Figure 7: Proof-of-concept test bench and metallic holder highlighted.

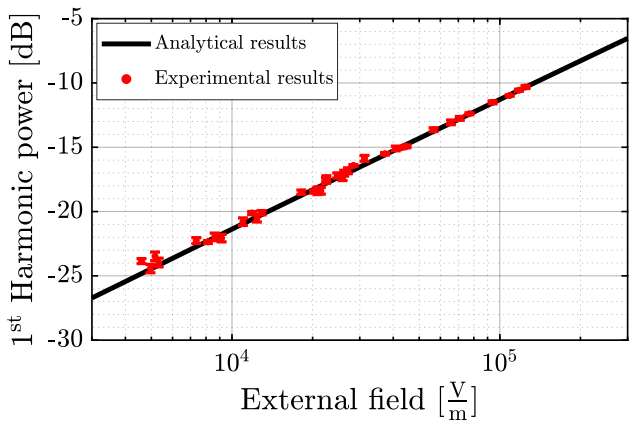


Figure 8: Experimental results of a single optical chain benchmarked with analytical ones.

Content from this work may be used under the terms of the CC BY 4.0 licence (© 2022). Any distribution of this work must maintain attribution to the author(s), title of the work, publisher, and DOI

ISBN: 978-3-95450-241-7 ISSN: 2673-5350 doi:10.18429/JACoW-IBIC2022-WEP10

Content from this work may be used under the terms of the CC BY 4.0 licence (© 2022). Any distribution of this work must maintain attribution to the author(s), title of the work, publisher, and DOI

Figure 8 shows the comparison of experimental results and analytical predictions. Data were sampled at f_s = 100 kSps while the biasing crystal was modulated at f_{Mod} = 600 Hz. The sensor measured an electric field ranging from 3 to 150 kV/m, and was limited on the lower end by the dynamic range of the used acquisition system. The maximum field was limited by the highest voltage which could be applied to the rod. Experimental observations show small discrepancies for low values of the electric field, which can be explained by several imperfections of this first proof-of-concept test bench such as space charge build-up, presence of higher harmonics in the modulation signal or uncompensated temperature drift. To better understand the reasons behind the discrepancies, a custom acquisition chain is under development to extend the dynamic range of the system. Additionally, the new acquisition chain will make it possible to simultaneously use a second optical branch installed on the opposite side of the pipe. Combining the information from the two optical chains, it will be possible to directly measure the position of the metallic rod inside the pipe.

Analytical Transverse Position Evaluation

The successful validation of the analytical model with experimental results makes estimating the transverse position resolution for an EO-DC-BPM using two symmetric optical branches possible. Table 2 summarizes the obtained results.

Table 2: Estimated transverse position measurement resolution. R* is the vacuum chamber aperture.

DAQ	I_b [A]	BW [Hz]	R* [mm]	DR [dB]	Position resolution [µm]
scope	2.8	59	45	30	3e3
custom	2.8	100	45	75	0.1
custom	0.28	100	45	75	1
custom	0.28	100	80	75	2.5

The first row gives the resolution estimate for the laboratory test bench with the same basic acquisition chain as used to obtain the experimental results presented in the previous section. The assumed beam current of 2.8 A is exactly one order of magnitude higher than the current of an unbunched beam in the SPS. The very modest 30 dB of dynamic range limits the minimum detectable displacement to 3 mm in a measurement bandwidth of 59 Hz.

The system performance can be significantly improved with a dedicated acquisition system, the development of which is currently ongoing. The new electronics will be based on the VFC acquisition card [13] together with a 24-bit ADC/DAC module, both developed at CERN. Moreover, the signal will be preconditioned with an analog circuit to isolate and amplify the first harmonic. The new system will replace the optical power meter and the 10-bit oscilloscope used to gather the first experimental data, which will lead to an effective improvement of the dynamic range by approximately 60 dB for a measurement bandwidth BW of 100 Hz. With a conservative margin of 15 dB for unknown sources of noise and nonlinearities, a dynamic range of 75 dB is deemed achievable with the new electronics. The second and third rows of Table 2 show the estimates for the developed test bench equipped with the improved acquisition system and measurement bandwidth increased to 100 Hz. The transverse position resolution decreases to less than 1 µm for the conditions of the previously discussed experiments.

The final row gives an estimate for a debunched SPS beam in a vacuum chamber with a realistic diameter of 80mm. The electric field in the crystal was computed for an improved design of the sensing crystal's holder (see Fig. 7), with no metal stripes partially covering the crystal. This leads to a 30% increase in the intensity of the electric field acting on the sensing crystal. Under these conditions, the computed resolution is 2.5 µm.

CONCLUSION

We have presented a conceptual design of a novel BPM composed of four identical EO electrostatic field sensors and capable of performing measurements of DC particle beams in the frequency domain.

The good match between the theoretical predictions of the analytical model and experimental results obtained on a purpose-built test bench confirms the feasibility of constructing such a sensor. The measurements can be applied over a wide range of electrostatic fields by varying the optical properties of the system.

Further improvements are being investigated. In particular, a custom acquisition system is under development not only to increase the resolution of the final system but also to open the possibility of studying the impact of parasitic effects of the EO crystals on the measurement's accuracy.

ACKNOWLEDGEMENTS

The authors express their gratitude to Juan Carlos Allica Santamaria, Franck Guy Guillot-Vignot, Patrick Bouvier, Morad Hamani, Thibaut Lefevre, Stefano Mazzoni, and Romain Ruffieux from the Beam Instrumentation Group at CERN, and Alberto Arteche from Royal Holloway University of London, for their help with the design and construction of the EO test bench and for the commissioning of the laser-lab. This project has received funding from the ATTRACT project funded by the EC under Grant Agreement 777222.

REFERENCES

[1] V. Kain, "Fixed Target Beams", CERN Proceedings 2, 2017.

[2] M. Anelli *et al.*, "A facility to search for hidden particles (SHiP) at the CERN SPS", arXiv preprint, 2015. doi:10.48550/arXiv.1504.04956

[3] S. Paret *et al.*, "Transverse Schottky and beam transfer function measurements in space charge affected coasting ion beams", *Phys. Rev. Spec. Top. Accel Beams*, vol. 13, no. 2,

ISBN: 978-3-95450-241-7 ISSN: 2673-5350 doi:10.18429/JACoW-IBIC2022-WEP10

p. 022802, 2010. doi:10.1103/PhysRevSTAB.13.022802

[4] R. Jung *et al.*, "Single pass optical profile monitoring", in *Proc. DIPAC 2003*, Mainz, Germany, May 2003, pp. 10-14.

[5] C. D. West and R. Clark Jones, "On the properties of polarisation elements as used in optical instruments. I. Fundamental considerations", *J. Opt. Soc. Am.*, vol. 41, no. 12, Dec. 1951, pp. 976-982. doi:10.1364/JOSA.41.000976

[6] A. Arteche, "Studies of a prototype of an electro-optic beam position monitor at the CERN super proton synchrotron", Ph.D. thesis, Royal Holloway, University of London, 2018.

[7] N. Kuwabara *et al.*, "Development and analysis of electric field sensor using LiNbO3 optical modulator", *IEEE Trans. Electromagn. Compat.*, vol 34, no. 4, Nov. 1992, pp. 391-396. doi:10.1109/15.179271

[8] J. Liu, H. Wang and Y. Li, "Research and design of rotary optical electric field sensor", in *IOP Conference Series: Materials Science and Engineering*, vol. 677, no. 5, Dec. 2019, p. 052112. doi:10.1088/1757-899x/677/5/052112

[9] R. S. Weis and T. K. Gaylord, "Lithium niobate: Summary of physical properties and crystal structure", *Appl. Phys.*, vol. 37, no. 4, Aug. 1985, pp. 191-203. doi:10.1007/BF00614817

[10] M. N. Palatnikov *et al.*, "Radiation hardness of lithium niobate nonlinear optical crystals doped with Y, Gd, and Mg", *Inorg. Mater.*, vol. 49, no. 8, Aug. 2013, pp. 821-825. doi:10.1134/S0020168513080116

[11] A. Cristiano, M. Krupa and R. Hill, "Electro-optic sensor for measuring electrostatic fields in the frequency domain", *Appl. Sci.-Basel*, vol. 12, no. 17, Sep. 2022, p. 8544. doi:10.3390/app12178544

[12] R. Clark Jones, "A new calculus for the treatment of optical systemsi. description and discussion of the calculus", *J. Opt. Soc. Am.*, vol. 31, no. 7, Jul. 1941, pp. 488-493. doi:10.1364/JOSA.31.000488

[13] A Boccardi *et al.*, "A modular approach to acquisition systems for future CERN beam instrumentation developments", in *Proc. ICALEPS'15*, Melbourne, Australia, Oct. 2015. pp. 1103–1106. doi:10.18429/JACoW-ICALEPCS2015-THHB2O02

Content from this work may be used under the terms of the CC BY 4.0 licence (© 2022). Any distribution of this work must maintain attribution to the author(s), title of the work, publisher, and DOI

ISBN: 978-3-95450-241-7 ISSN: 2673-5350 doi:10.18429/JACoW-IBIC2022-WEP12

HL-LHC BPM SYSTEM DEVELOPMENT STATUS

M. Krupa*, I. Degl'Innocenti, D. Gudkov, G. Schneider, CERN, Geneva, Switzerland
D. R. Bett, University of Oxford, UK

Abstract

The demanding instrumentation requirements of the future High Luminosity LHC (HL-LHC) require 44 newly designed Beam Position Monitors (BPM) to be installed around the ATLAS and CMS experiments in 2026–2028. Three BPM types are now in pre-series production, with two more variants under design. Close to the collision point, a set of cryogenic directive coupler BPMs equipped with a brand new acquisition system based on nearly-direct digitization will resolve the position of the two counter-rotating LHC beams occupying a common vacuum chamber. Other new button and stripline BPMs will provide not only the transverse beam position, but also timing signals for the experiments, and diagnostics for the new HL-LHC crab cavities. This contribution summarizes the HL-LHC BPM specifications, gives an overview of the new BPM designs, reports on the pre-series BPM production status and plans for series manufacturing, outlines the foreseen acquisition system architecture, and highlights the first beam measurements carried out with the proof-of-concept electronics for the directive stripline BPMs.

INTRODUCTION

The High Luminosity LHC (HL-LHC) project aims to significantly boost the LHC performance with a series of major upgrades scheduled to take place in 2026-2028 [1]. Most notably, the two regions housing the large ATLAS and CMS experiments will be overhauled including a complete replacement of the low-beta Inner Triplets (IT) with higher gradient focusing magnets to produce an even smaller beam size at the Interaction Points (IP) where the LHC beams collide. Further increase of the instantaneous luminosity will be possible thanks to crab cavities (CC) installed on each side of ATLAS and CMS. The CC installed upstream from the IP will tilt each circulating bunch transversely such that at the IP it collides head-on with the counter-rotating bunch. The CC on the other side of the IP will reverse this tilt to cancel out any transverse oscillation outside of the crabbing region between two CCs.

SYSTEM OVERVIEW

The HL-LHC ITs will require a set of new Beam Position Monitors (BPM) to reliably control the orbit of extraordinarily small beams. Moreover, additional specialized BPMs are needed near the CCs to tune and monitor the crabbing process as well as to watch for any beam instabilities [2]. In total, 44 new BPMs of 5 types will be installed as part of the HL-LHC project. Figure 1 shows the arrangement of the new BPMs on each side of the IP in the HL-LHC era.

* michal.krupa@cern.ch

The six BPMs closest to the IP (BPMQSTZA and BPMQSTZB types) are installed inside the continuous cryostat of the new HL-LHC IT where both counter-rotating beams will circulate in a common vacuum chamber. Therefore, these BPMs must be able to distinguish the position of each beam independently. Such a feature, referred to as directivity, is typical of directional coupler BPMs in which the passing beam induces signals on four long antennas (commonly called striplines) parallel to the beam motion axis [3]. The striplines are connectorised on each end and are designed such that the majority of the beam signal couples only on the upstream port with a much smaller (around 5%) parasitic signal leaking to the downstream output. To further reduce the cross-talk between the two beams, the HL-LHC directional couplers will be installed in locations where bunches of both beams arrive at different times with the temporal separation ranging from 3.9 ns (approximately 3 times larger than the bunch length) up to 10.5 ns depending on the BPM location. The measurement error due to the presence of the other beam will also be reduced through digital signal processing with a new dedicated fast-sampling data acquisition system [4]. All HL-LHC directional coupler BPMs will operate at a cryogenic temperature within the 60–80 K range. Moreover, the BPMQSTZB type BPMs will be equipped with shielding blocks made out of tungsten to decrease the ionizing dose received by the nearby superconducting magnets [5].

Further away from the IP, after the separation-recombination dipoles, both beams circulate in separate vacuum chambers. A standalone double-aperture cryogenic dipole will be equipped with two capacitive button BPMs (one per beam, BPMQBCZA/B type) installed within the magnet's cryostat and operating at 4.5–20 K. The signals of these BPMs will be measured by the currently used LHC BPM data acquisition system [6].

The remaining three room-temperature BPMs installed after the CCs will not become part of the main LHC BPM system but will instead serve very special users. The two BPTQR type BPMs will replace the initially foreseen APWL pick-ups as the main diagnostic monitors for the crab cavities. These BPMs will be connected to dedicated electronics and will combine three different BPMs in a single unit:

- a set of capacitive buttons for phasing the CCs with the beam and for filtering the CC antenna signal,
- a pair of 94 mm-long stripline antennas for the CC amplitude and noise feedback at the 800 MHz component,
- a pair of Electro-Optical (EO) buttons [7] or a pair of 400 mm-long stripline antennas for wideband measurements of beam instabilities introduced by the CCs.

The detailed BPTQR design is not yet frozen, and some technical decisions (e.g. the choice between EO buttons and stripline antennas) will be taken in the following years.

Content from this work may be used under the terms of the CC BY 4.0 licence (© 2022). Any distribution of this work must maintain attribution to the author(s), title of the work, publisher, and DOI

ISBN: 978-3-95450-241-7 ISSN: 2673-5350 doi:10.18429/JACoW-IBIC2022-WEP12

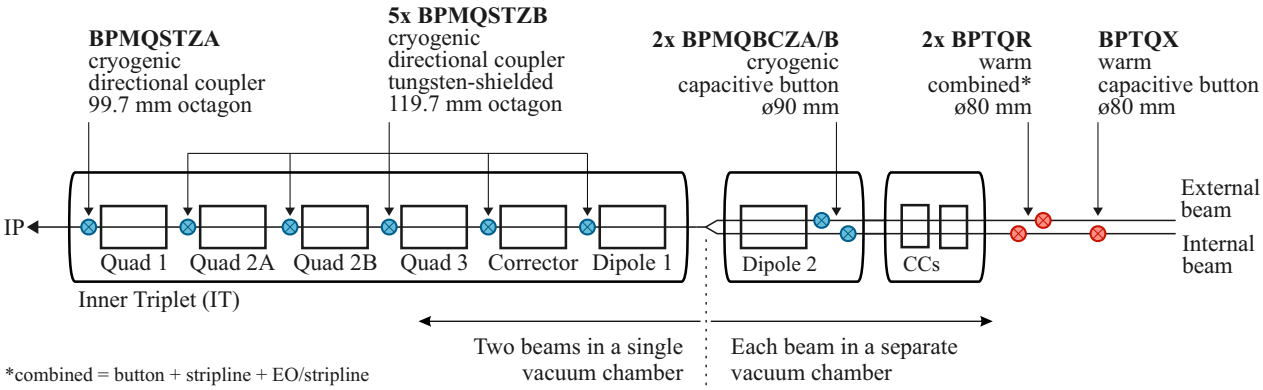


Figure 1: New BPMs foreseen to be installed in the HL-LHC era on each side of the ATLAS and CMS experiments.

The final BPTQX type BPM will replace the currently used BPTX pick-up which is part of the ATLAS and CMS experiments' trigger and timing system [8]. These capacitive button BPMs are installed only on the vacuum chamber carrying the beam travelling towards the IP and are connected to dedicated electronics managed by the experiments.

With the increased bunch intensity in the HL-LHC era, the beam-induced heat loads on accelerator components have to be managed even more carefully than in the LHC. The inner surfaces of all HL-LHC BPMs will be coated with 100 µm-thick layer of copper to improve heat transfer along the body and a thin layer of amorphous carbon to reduce the power generated due to electron cloud effects [9]. Moreover, all cryogenic BPMs will be actively cooled with liquid helium to efficiently maintain them at the temperature of the adjacent vacuum components.

PERFORMANCE SPECIFICATIONS

The LHC BPM system has three main users whose requirements drive the performance specification:

- the accelerator operators who continuously monitor and control the average beam orbit, predominantly through an automated feedback system,
- the accelerator physicists who rely on bunch-by-bunch turn-by-turn position data to measure and correct the accelerator optics as well as to tune its performance,
- the LHC experiments who calibrate the luminosity through van der Meer scans using the average beam orbit measured by the BPMs closest to the IP.

The users' requests for the HL-LHC era BPM system performance have been collected in a detailed document which currently serves as a baseline conceptual specification [10]. Table 1 provides an excerpt of some of the most demanding performance requirements for the IT BPMs. With a reduced BPM sensitivity due to the increased vacuum chamber aperture, some of the requests (e.g. one-turn one-bunch precision) call for an effective improvement by over an order of magnitude when compared to the currently used LHC BPM data acquisition system. Detailed studies spanning theoretical analysis and practical measurements are ongoing to evaluate if the requested performance can be achieved.

Table 1: Users' Requests for the HL-LHC IT BPM

Parameter	Value
Bunch charge	0.8–36 nC
Minimum bunch spacing	25 ns
Turn period	89 µs
Measurement range	±29 mm
Scale error	0.8%
Non-linearity	0.1%
Gain stability (24 h)	0.1%
Measurement offset	50 µm
One-turn one-bunch precision	15 µm
Two-beam cross-talk	0.05%

PRODUCTION OF BEAM PICK-UPS

All cryogenic HL-LHC BPMs will be integrated within the respective magnet's cryostat. The BPM installation is, therefore, one of the many steps in a long magnet assembly sequence. As the series production of HL-LHC IT magnets is already ongoing or starting soon [11, 12], the BPM manufacturing must also be carefully scheduled to ensure that the pick-ups are available when needed. Overall, 38 cryogenic BPMs (32 to be installed in the accelerator and 6 spares) will be manufactured by the CERN Main Workshop in the coming years. Figure 2 shows the most complex BPM type to be built, BPMQSTZB, which features an octagonal aperture, tungsten shielding blocks, brazed thermal links, welded cooling capillaries, and conflat knife-edges machined on a solid 316LN stainless steel body. All cryogenic HL-LHC BPMs will interface the adjacent vacuum components via custom aperture-adapting transitions made out of OFE copper.

Due to the high complexity of the cryogenic HL-LHC BPMs, their manufacturing has been split into three phases: prototyping (simplified units to test specific manufacturing methods), pre-series production (2 units per type), and series production (32 units of 3 types in total). The prototyping phase was completed by the end of 2021 and currently 6 fully-featured pre-series units are being manufactured at CERN. One of the BPM bodies after gold plating and copper coating can be seen in Fig. 3.

Content from this work may be used under the terms of the CC BY 4.0 licence (© 2022). Any distribution of this work must maintain attribution to the author(s), title of the work, publisher, and DOI

ISBN: 978-3-95450-241-7 ISSN: 2673-5350 doi:10.18429/JACoW-IBIC2022-WEP12

Content from this work may be used under the terms of the CC BY 4.0 licence (© 2022). Any distribution of this work must maintain attribution to the author(s), title of the work, publisher, and DOI

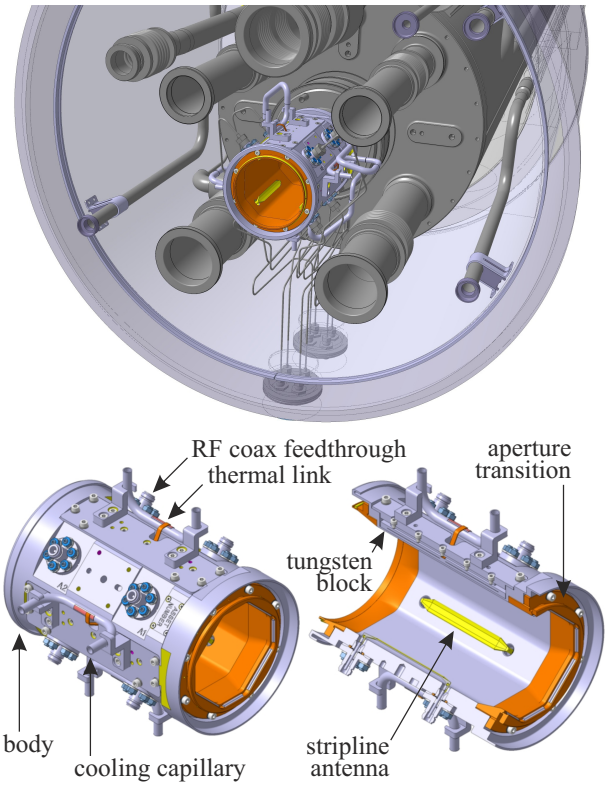


Figure 2: BPMQSTZB-type cryogenic directional coupler BPM in a magnet's cryostat (top) with its most important features marked (bottom).

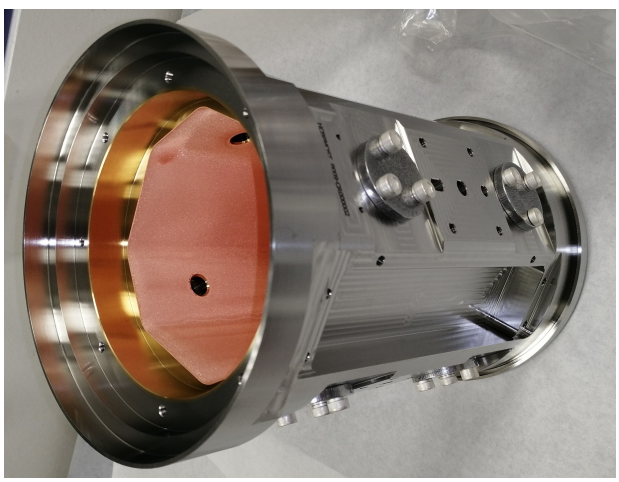


Figure 3: Gold- and copper-coated pre-series body of the BPMQSZTB-type BPM

The series production of the remaining cryogenic HL-LHC BPMs is foreseen to start once the pre-series units have been fully validated through vacuum, cryogenic, electrical, and mechanical integration tests. Installation of the first BPMs in cryogenic magnets is foreseen to take place in June 2023 and launch a campaign lasting until early 2026.

The production schedule of the room-temperature BPMs of types BPTQR and BPTQX is more relaxed as their installation is scheduled to take place only in 2028. Nevertheless, their mechanical designs are expected to be completed in 2022 (BPTQX) and 2023 (BPTQR) with production to start in 2024. Due to their simpler design and a reduced number of value-adding features, the warm BPMs are expected to be easier to manufacture than the cryogenic BPMs.

In parallel, the Mechanics and Logistics section of the CERN Beam Instrumentation Groups is designing and manufacturing a vast amount of custom tooling for BPM assembly, 3 coating procedures, quality control (mechanical, electrical, vacuum), handling, and storage.

DATA ACQUISITION SYSTEM FOR DIRECTIONAL COUPLERS

Independently of the BPM pick-up design and production, a new data acquisition platform for the cryogenic directional couplers is under development in collaboration between CERN and the University of Oxford. In contrast to the acquisition electronics used by the current LHC BPM system which relies on precise analogue signal conditioning (through amplitude-ratio to time-difference conversion), the new electronics will exploit nearly-direct digitisation of the BPM-generated signals with minimum analogue preprocessing. Due to the high radiation levels in the HL-LHC IT area, it is not possible to house the acquisition electronics directly next to the BPMs. However, favourable locations with radiation levels considered safe for commercial-grade electronics have been identified in the nearby technical galleries with the maximum cable length between a BPM pick-up and its acquisition electronics not exceeding 100 m.

Numerical studies have demonstrated that precise beam position measurements based on direct digitisation in the LHC require a sampling rate in the order of a few gigasamples per second (GSps) and a vertical resolution with an Effective Number of Bits (ENOB) reaching 10 [13]. The Xilinx Zynq UltraScale+ RFSoC [14] has recently been identified as a compelling solution for modern beam instrumentation systems [15–18]. These devices integrate multiple high-performance analogue-to-digial converters (ADC) and digital-to-analogue converters (DAC) together with a feature-rich platform which includes Digital Signal Processing (DSP) blocks, a general-purpose processor, and programmable logic on a single chip. Given its excellent datasheet performance, tests are ongoing to verify if the new data acquisition system for the HL-LHC directional coupler BPMs can be based on the RFSoC technology.

In October 2021, beams briefly circulated in the LHC for the first time after a three-year-long shutdown in order to test various systems before the accelerator fully restarted in April 2022. This period was also used to parasitically acquire preliminary beam data with an off-the-shelf ZCU111 evaluation board connected to one of two existing directional coupler BPMs installed 30–60 m away from the CMS experiment. The ZCU111 board is equipped with a Generation-1 RFSoC featuring 8 ADCs (sampling at up to 4.096 GSps with ENOB ≈ 9.5) which is sufficient to acquire all the signals generated by one directional coupler BPM. However,

ISBN: 978-3-95450-241-7 ISSN: 2673-5350 doi:10.18429/JACoW-IBIC2022-WEP12

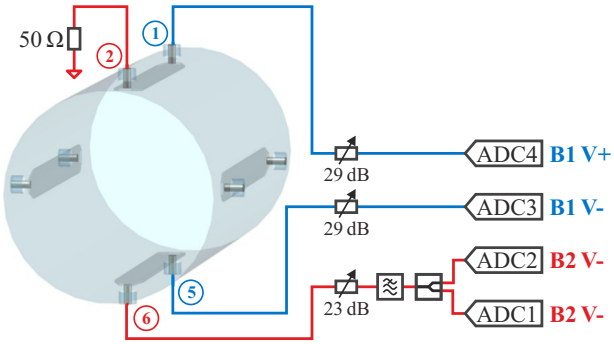


Figure 4: One of the configurations used in 2021 to acquire beam-induced BPM signals with a ZCU111 board.

due to some prototype firmware limitations, only four of the available ADCs could be used during the tests.

Even though direct digitisation calls for the signal source to be connected directly to the ADC, such an approach is not possible for the LHC BPMs. The broadband nature of beam-induced BPM signals as well as their amplitudes reaching several hundreds of volts exceed the input capabilities of even the most modern digitisers. Some limited analogue signal conditioning is therefore unavoidable and even desirable to match the BPM signals well to the ADC input capabilities. During the aforementioned 2021 beam tests, the analogue front-end consisted of a fixed 23–29 dB attenuator and a custom-made non-reflective low-pass filter with a 3 dB cut-off at 170 MHz and a sufficient anti-aliasing insertion loss (exceeding 60 dB for frequencies above 900 MHz).

The data were acquired using five different configurations, with one of them set out in Fig. 4. In this case, the vertical plane of Beam 1 BPM (ports 1 and 5) was connected without additional filtering to the ADC channels 3 and 4, while the remaining ADC channels 1 and 2 measured the split filtered signal of Beam 2 BPM bottom output (port 6) with the top port terminated with 50 Ω. The split signal measurements are particularly interesting as they allow the acquisition electronics' resolution to be evaluated independent of the real beam movement. The other tested configurations employed unsplit signals from one of two different pick-ups with or without filters and with different levels of attenuation.

As will be the case in the final system, the ADC clocks were free-running and asynchronous to the beam but phase-locked among the four used ADCs. A standard LHC timing signal was used to define the acquisition window with respect to the revolution period. All measurements were carried out with only a few well-separated bunches in each beam organized such that none of the bunches of the counter-rotating beams arrived at the BPM location near each other.

In total, nearly 700 thousand traces have been recorded in a two-day measurement period. In order to reliably compare various considered data processing and correction algorithms, no DSP was applied online and all ADC samples were saved as raw data for fully offline processing. The signals typically covered 30% to 50% of the ADC dynamic range.

The comprehensive analysis of the acquired data will be the subject of another, future manuscript. However, some preliminary results indicate that an RFSoC-based acquisition system might be the right choice for the HL-LHC directional couplers. The data acquired with a split signal hints that a one-turn one-bunch precision of under 30 µm could be achievable with the input signal covering noticeably less than half of the ADC dynamic range. An extensive analysis of waveforms synthesized such that the two beams arrive at the BPM location with the expected temporal separation proves that the developed two-beam cross-talk correction algorithm (so-called *power compensation* [4]) can efficiently minimize the impact of the pick-up's limited directivity. The analysis also substantiated that signal reflections due to imperfections in cables and connectors lead to a quantifiable reduction of the measurement precision and might require a dedicated correction procedure.

As the 2021 tests proved invaluable for the development of the new data acquisition systems for the HL-LHC directional couplers, a further data-taking campaign is foreseen in 2022. With dedicated beam time, it will be possible to configure the two beams to even better mimic the conditions expected in the HL-LHC era. Most importantly, the temporal difference between the arrival of bunches from both beams at the BPM location will be controlled through a process commonly called RF cogging.

SUMMARY AND OUTLOOK

As part of the HL-LHC project, 44 new BPM pick-ups of 5 brand new types will be installed to fulfil the ever increasing beam instrumentation and diagnostics needs of the BPM system users. Pre-series production of the most urgently needed pick-ups is already ongoing, with the remaining units to be manufactured in the coming years.

The cryogenic directional couplers are closest to the IP and see both beams circulating in a common vacuum chamber. In addition to the reduction of the two-beam cross-talk at source, a new data acquisition system based on nearly-direct digitisation and advanced DSP to reduce the measurement error is under development for those BPMs. Currently, the focus is on testing commercially available evaluation boards to qualify the RFSoC technology as viable for the HL-LHC direction couplers. Manufacturing of the first custom-made prototype boards is planned for 2024-25, with the series production expected to take place in 2026-27.

ACKNOWLEDGEMENTS

The authors would like to thank colleagues from the CERN MME, VSC, and ABP groups as well as from the HL-LHC Project Office for their overall contribution to the development of the HL-LHC BPMs. The authors are particularly grateful to A. Boccardi, K. Sidorowski, and M. Wendt from the CERN BI group for their valuable and continuous support of the work presented in this paper.

Content from this work may be used under the terms of the CC BY 4.0 licence (© 2022). Any distribution of this work must maintain attribution to the author(s), title of the work, publisher, and DOI

ISBN: 978-3-95450-241-7 ISSN: 2673-5350 doi:10.18429/JACoW-IBIC2022-WEP12

Content from this work may be used under the terms of the CC BY 4.0 licence (© 2022). Any distribution of this work must maintain attribution to the author(s), title of the work, publisher, and DOI

REFERENCES

[1] M. Zerlauth *et al.*, "The HL-LHC Project Gets Ready for Its Deployment", in *Proc. IPAC'22*, Bangkok, Thailand, Jun. 2022, pp. 50–53. doi:10.18429/JACoW-IPAC2022-MOPOST005

[2] M. Krupa, "Beam Instrumentation and Diagnostics for High Luminosity LHC", in *Proc. IBIC'19*, Malmö, Sweden, Sep. 2019, pp. 1–8. doi:10.18429/JACoW-IBIC2019-MOA002

[3] R. E. Shafer, "Characteristics of directional coupler beam position monitors", *IEEE Trans. Nucl. Sci.*, vol. 32, pp. 1933–1937, 1985. doi:10.1109/TNS.1985.4333772

[4] D. R. Bett, A. Boccardi, I. Degl'Innocenti, and M. Krupa, "Signal Processing Architecture for the HL-LHC Interaction Region BPMs", in *Proc. IBIC'21*, Pohang, Korea, Sep. 2021, pp. 100–103. doi:10.18429/JACoW-IBIC2021-MOPP24

[5] L. S. Esposito, F. Cerutti, and E. Todesco, "FLUKA Energy Deposition Studies for the HL-LHC", in *Proc. IPAC'13*, Shanghai, China, May 2013, paper TUPFI021, pp. 1379–1381.

[6] E. Calvo-Giraldo *et al.*, "The LHC Orbit and Trajectory System", in *Proc. DIPAC'03*, Mainz, Germany, May 2003, paper PT08, pp. 187–189.

[7] A. Arteche *et al.*, "Electro-Optical BPM Development for High Luminosity LHC", presented at IBIC'22, Krakow, Poland, Sep. 2022, paper TU1I1, this conference.

[8] C. Ohm and T. Pauly, "The ATLAS beam pick-up based timing system", *Nucl. Instrum. Methods Phys. Res., Sect. A*, vol. 623, pp. 558–560, 2009. doi:10.1016/j.nima.2010.03.069

[9] G. Skripka and G. Iadarola, "Beam-induced heat loads on the beam screens of the inner triplets for the HL-LHC", CERN, Geneva, Switzerland, Rep. CERN-ACC-NOTE-2018-0009, Feb. 2018. doi:10.17181/CERN.I7WJ.TNS9

[10] D. Gamba *et al.*, "Conceptual Specifications for the HL-LHC BPMs", Geneva, Switzerland, Rep. LHC-BPM-ES-0013, Apr. 2022. https://edms.cern.ch/document/2387369

[11] G. Ambrosio *et al.*, "Lessons Learned From the Prototypes of the MQXFA Low-Beta Quadrupoles for HL-LHC and Status of Production in the US", *IEEE Trans. Appl. Supercond.*, vol. 31, no. 5, 2021. doi:10.1109/TASC.2021.3058597

[12] S. I. Bermudez *et al.*, "Progress in the Development of the Nb3Sn MQXFB Quadrupole for the HiLumi Upgrade of the LHC", *IEEE Trans. Appl. Supercond.*, vol. 31, no. 5, 2021. doi:10.1109/TASC.2021.3061352

[13] A. Boccardi, I. Degl'Innocenti, L. Fanucci, and M. Wendt, "Direct Digitization and ADC Parameter Trade-off for Bunch-by-Bunch Signal Processing", in *Proc. IBIC'20*, Santos, Brazil, Sep. 2020, pp. 288–294. doi:10.18429/JACoW-IBIC2020-FRA002

[14] Xilinx, Inc., "An Adaptable Direct RF-Sampling Solution", White paper, WP489 (v1.1), 2019, https://docs.xilinx.com/v/u/en-US/wp489-rfsampling-solutions

[15] W. E. Norum, "RFSoCs in Beam Instrumentation Systems", in *Proc. IBIC'21*, Pohang, Korea, Sep. 2021, paper FROB01.

[16] J. M. Weber, J. C. Bell, M. J. Chin, W. E. Norum, and G. J. Portmann, "Advanced Light Source High Speed Digitizer", in *Proc. IBIC'20*, Santos, Brazil, Sep. 2020, pp. 132–135. doi:10.18429/JACoW-IBIC2020-WEPP16

[17] B. Keil, "Generic Hardware, Firmware and Embedded Software Platforms for Particle Accelerators", presented at IBIC'19, Malmö, Sweden, Sep. 2019, paper WEBO01, unpublished.

[18] J. E. Dusatko, "Evaluation of the Xilinx RFSoC for Accelerator Applications", in *Proc. NAPAC'19*, Lansing, MI, USA, Sep. 2019, pp. 483–486. doi:10.18429/JACoW-NAPAC2019-TUPLS13

ISBN: 978-3-95450-241-7 ISSN: 2673-5350 doi:10.18429/JACoW-IBIC2022-WEP14

CAVITY BPM ELECTRONICS FOR SINBAD AT DESY

B. Lorbeer*, M. Werner, T. Lensch, I. Kroupchenkov, H. T. Duhme, S. Vilcins, D. Lipka
Deutsches Elektronen-Synchrotron DESY, Hamburg, Germany

Abstract

The SINBAD (Short and INnovative Bunches and Accelerators at DESY) R&D accelerator is planned for studying new concepts for high gradient electron beam acceleration and the generation of ultra-short electron bunches. The accelerator called ARES (Accelerator Research Experiment At DESY) is composed of S-band accelerating structures. In order to achieve the goal of very short electron bunches the electron beam charges generated in the RF (radio frequency) Gun can vary in a range from 200 pC down to 500 fC. A new type of high resolution cavity BPM (beam position monitor) has been developed to measure the beam position with good resolution at small charge down to 500 fC. One key component in the BPM system are the custom RF front-end receiver electronics to meet the resolution requirements in the required charge range. The entire BPM system with a focus on the system design requirements and the MicroTCA based RF electronics are presented in this paper.

INTRODUCTION

The S-band electron linear accelerator ARES at DESY in Hamburg, Germany is build for studying novel acceleration techniques including a beam manipulation testbed, accelerator components and concepts for autonomous accelerator operation. Its target parameters are an energy of 50 MeV-155 MeV, a charge of 0.5 pC-200 pC. A single electron bunch at the rate of 50 Hz is generated by an RF-Gun in which the electrons are released from a cathode by making use of a photocathode laser. The machine has already been successfully commissioned and first experiments have been carried out [1–4]. The diagnostics include eight high resolution in-house developed cavity BPM (beam position monitors) which are distributed at significant locations along the 50 m long machine [5] . An overview of the machine with two BPMs currently under test is shown in Fig. 1.

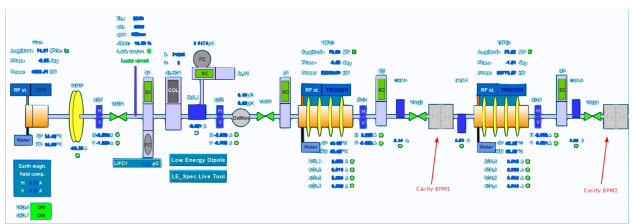


Figure 1: Extraction from ARES Linac operation panel with two cavity Beam Position Monitors.

The key specification of the cavity BPM system are position measurements at bunch charges from 500 fC up to 1 nC. The challenging requirement in precision and accuracy at the smallest charge is 5 µm in a measurement range of 100 µm while averaging over 25 bunches. The single bunch resolution requirement over a range of 700 µm is 35 µm [6].

CAVITY BEAM POSITION MONITOR

In order to determine the bunch charge and position of the electron bunch in the beam-pipe a monopole and two dipole excited modes in the cavity are necessary [7, 8]. The excited monopole mode shows a proportionality to the electron bunch charge and two excited dipole modes deliver proportionalities to the horizontal and vertical position of the electron bunch. The measured voltages are $V_{mon} \propto q$ and $V_{dipole} \propto x_{pos}, y_{pos}$ respectively. The realization of the cavities for measuring the amplitudes of monopole and dipole modes are based on a tedious design procedure of the vacuum chamber which includes electromagnetic field simulation and tolerance studies before it could be produced. More details can be found in [9]. A simplified electromagnetic simulation model of the cavity is shown in Fig. 2.

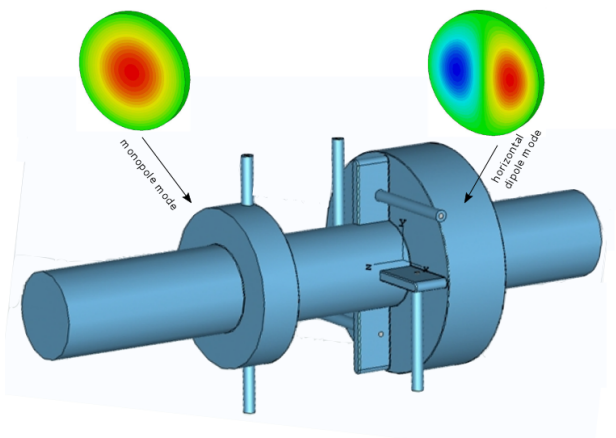


Figure 2: Simulation model of Cavity Beam Position Monitor. Monopole and dipole modes have symmetric ports to maintain symmetric fields around the beam axis. The measurement system only uses one of the ports and the other is terminated with 50 Ohm.

The mono and dipole cavity geometries have been chosen to be compatible with existing BPM monitors already installed at the E-XFEL and FLASH at DESY, Hamburg, Germany. Both machines operate with high repetition rates of the electron bunch of up to 4.5 MHz. Therefor a loaded quality factor of around 70 has been a feasible choice to avoid an overlap of subsequent bunches. The design procedure also aimed for high sensitivities of monopole and dipole cavities to deliver sufficient signal power at very low charges.

* bastian.lorbeer@desy.de

Content from this work may be used under the terms of the CC BY 4.0 licence (© 2022). Any distribution of this work must maintain attribution to the author(s), title of the work, publisher, and DOI

ISBN: 978-3-95450-241-7 ISSN: 2673-5350 doi:10.18429/JACoW-IBIC2022-WEP14

Content from this work may be used under the terms of the CC BY 4.0 licence (© 2022). Any distribution of this work must maintain attribution to the author(s), title of the work, publisher, and DOI

Significant characteristics of the cavity BPM resonators are summarized in Table 1.

Table 1: Design characteristics of monopole and dipole cavity.

Quality	Quantity
Resonance frequency f_0	3.3 GHz
Loaded Quality Factor Q_L	70
dipole Sensitivity S_{dip}	4.25 Vpk/nC/mm
monopole Sensitivity S_{mon}	43 Vpk/nC

ACQUISITION SYSTEM

The acquisition system is composed of a custom-made heterodyne RF front-end receiver, a COTS (custom of the shelf) digitizer board [10] including analog-digital converters (ADCs) and an FPGA (Field Programmable Gate Array) for pre-processing the data. A machine synchronous interrupt driven server application receives the data from the FPGA via backplane in the MicroTCA [11] crate. The signal flow of the analog signals is shown in Fig. 3.

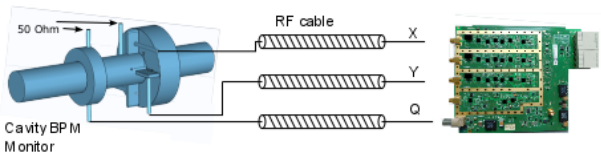


Figure 3: Analog signal flow.

A MicroTCA platform including digitizers, FPGA, CPU and timing system for the eight cavity BPMs installed in ARES is shown in Fig. 4.

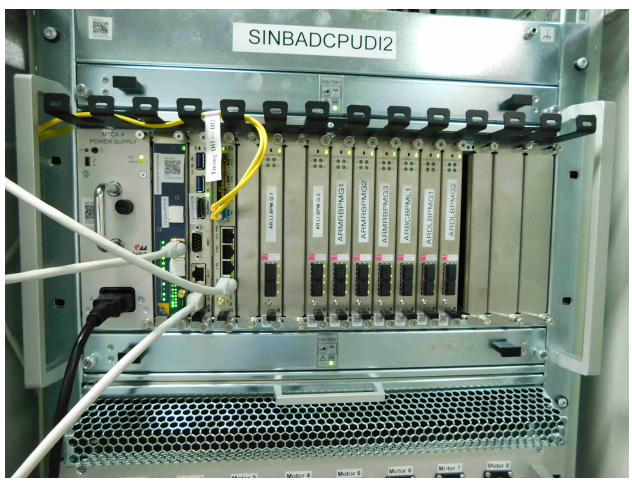


Figure 4: MicroTCA crate with digitizers, CPU, MCH, and timing system.

RF Front-End Receiver

The RF front-end receiver is composed of three equal channels and a LO (local oscillator) block. The RF signals from the cavity are band-pass filtered and can be amplified by a factor of 52 dB at the center frequency of 3.3 GHz. Step attenuators with a range from 0 - 31.75 dB make it possible to adjust the gain for different charges and make sure that the following down-conversion stages are not over-driven. During machine commissioning for different experiments the switching process of attenuators is negligible for the accuracy of the position calculation. After the amplification stages the cavity signals are demodulated to a base-band signal with the help of a synchronous LO signal at 3.301 GHz. This LO signal is generated with a software configurable integer-N phase locked loop. The base-band signal contains two independent paths for I and Q components which are delivered by the demodulator. These signals are buffered with a differential driver amplifier and are then send to the digitizer board. The minimum expected signal power for the dipole cavity resonator at a charge of 500 fC is -89 dBm with an offset position of 10 µm from center. The minimum signal power of the monopole mode cavity is -30 dBm. These expected powers levels include the RF cable losses. An RF channel isolation of better than 100 dB has been achieved. This is necessary in case of large monopole signals and very small dipole signals. A simplified block diagram of the RF front-end is shown in Fig. 5.

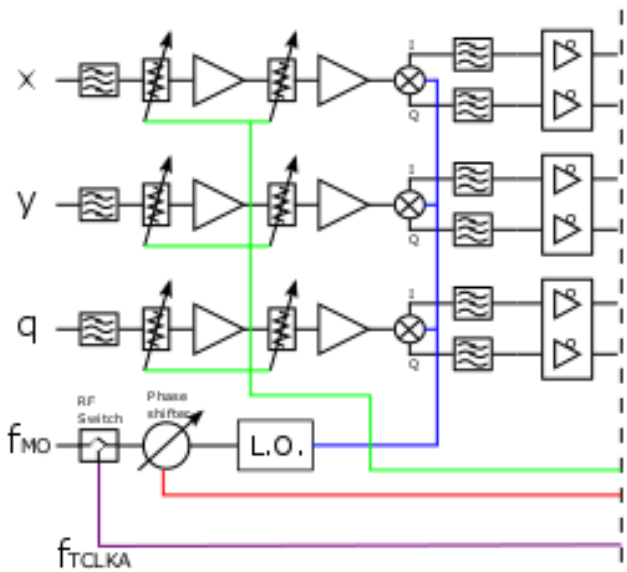


Figure 5: Block diagram of the RF front-end receiver. Green: SPI bus to adjust step-attenuator settings. Blue: LO distribution. Red: LO phase adjustement.

Firmware and Server Application

The signals from the RF front-end are digitized at a rate of 125 MHz and 16 Bits. A custom firmware to arrange the raw ADC data for further processing is implemented in an FPGA. It also includes several interfaces to the programmable RF front-end components such as an SPI interfaces for the step attenuators and PLL, an I2C interface for a DAC to adjust the LO phase with a phase shifter and several switchable gains in the x,y, and q measurement channels. Currently the

ISBN: 978-3-95450-241-7 ISSN: 2673-5350 doi:10.18429/JACoW-IBIC2022-WEP14

adjustment of the waveforms with respect to the ADC clock is done manually. A raw data waveform and interface server are displayed in Fig. 6.

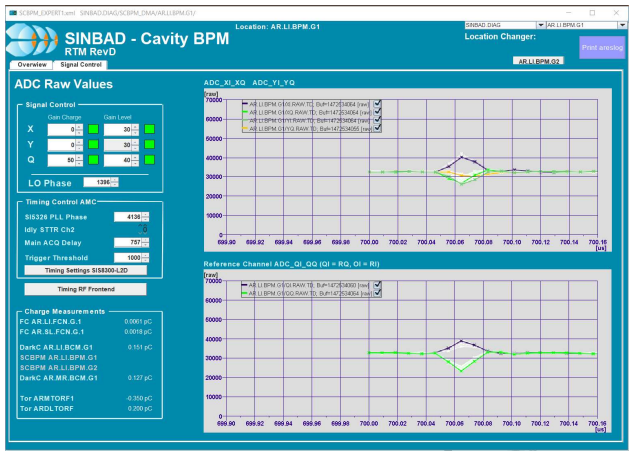


Figure 6: Signal control interface with step attenuator and gain settings, ADC timing, acquisition delay adjustment.

The calculations applied on this waveforms are implemented in a text-file based python script. The charge calibration has been cross-referenced with charge readings while the horizontal and vertical calibration have been made with magnetic steerers and a screen. Both are hard-coded in the python script. One pre-requisite of the proper usage of the system is a phase control loop which keeps the phase of the monopole q channel at an angle of 45°. Another pre-requisite is the alignment of the x and y vectors with respect to the reference channel. With this correction beam position and beam angle can be separated and the orientation of the coordinate system is adjusted.

MEASUREMENTS

First measurements with electron beam at ARES have been made and indicate promising results. The first two BPMs have been calibrated with the help of a screen and a steerer. The linear measurement range exceeds > +/- 5 mm. The standard deviation of position fluctuations including beam jitter is better than 10 µm at a charge of 1.25 pC.

CONCLUSION

Compact cavity BPM electronics can be realized with the MicroTCA form factor. Measurements at charges smaller than 1 pC is possible. The standard deviation of position measurements at these small charges fulfill the specifications. A proper implementation of the algorithm in a server platform for the control system is under way and will improve the stability and usability of the measurement system.

ACKNOWLEDGEMENTS

The authors are very grateful for tremendous support and exchange of conceptual and technical ideas with collaborative colleagues from Paul Scherer Institut (PSI) in Switzerland. Particularly these are G. Marinkovic and M. Stadler.

REFERENCES

[1] E. Panofski *et al.*, "Commissioning Results and Electron Beam Characterization with the S-Band Photoinjector at SINBAD-ARES", *Instruments*, vol. 5, no. 3, p. 28, 2021. doi:10.3390/instruments5030028

[2] F. Burkart *et al.*, "ARES Linac at DESY in Operation", presented at LINAC'22, Liverpool, United Kingdom, Aug. 2022, paper THPOJO01, unpublished.

[3] W. Kuropka *et al.*, "Commissioning of a movable bunch compressor for sub-fs electron bunches", presented at LINAC'22, Liverpool, United Kingdom, Aug. 2022, paper THPOJO02, unpublished.

[4] J. Kaiser, O. Stein and A. Eichler, "Learning-based Optimisation of Particle Accelerators Under Partial Observability Without Real-World Training", in *Proc. ICML'22*, vol. 162, pp. 10575–10585, Jul. 2022.

[5] D. Lipka, "Production of Cavity Beam Position Monitors for the Ares Accelerator at DESY", presented at IBIC'22, Kraków, Poland, Sep. 2022, paper MOP12, this conference.

[6] B. Marchetti and M. Werner, "2018-05-16 ARES Diaagnostics Electronics Specification", internal specification document, DESY, Hamburg, Germany, 2018.

[7] S. Walston *et al.*, "Performance of a high resolution cavity beam position monitor system", *Nucl. Instrum. Methods Phys. Res., Sect. A*, vol. 578, no. 1, pp. 1–22, 2007. doi:10.1016/j.nima.2007.04.162

[8] D. Lipka, "Cavity BPM Designs, Related Electronics and Measured Performances", in *Proc. DIPAC'09*, Basel, Switzerland, May 2009, paper TUOC02, pp. 280–284.

[9] D. Lipka *et al.*, "Design of a Cavity Beam Position Monitor for the ARES Accelerator at DESY", in *Proc. IBIC'18*, Shanghai, China, Sep. 2018, pp. 269–272. doi:10.18429/JACoW-IBIC2018-TUPB05

[10] *SIS8300-L2 MicroTCA.4 Digitizer*, Struck Innovative Systems, https://www.struck.de/sis8300-l2.html

[11] MicroTCA.4 specifcations source, http://www.picmg.org

Content from this work may be used under the terms of the CC BY 4.0 licence (© 2022). Any distribution of this work must maintain attribution to the author(s), title of the work, publisher, and DOI

ISBN: 978-3-95450-241-7 ISSN: 2673-5350 doi:10.18429/JACoW-IBIC2022-WEP15

XFEL PHOTON PULSE MEASUREMENT USING AN ALL-CARBON DIAMOND DETECTOR

C. Bloomer*,[1], L. Bobb, Diamond Light Source Ltd, Didcot, UK
M. E. Newton, University of Warwick, Coventry, UK
W. Freund, J. Grünert, J. Liu, European XFEL, Schenefeld, Germany
[1]also at University of Warwick, Coventry, UK

Abstract

The European XFEL can generate extremely intense, ultrashort X-ray pulses at MHz repetition rates. Single-crystal CVD diamond detectors have been used to transparently measure the photon beam position and pulse intensity. The diamond itself can withstand the power of the beam, but the surface electrodes can be damaged since a single pulse can already exceed the damage threshold of the electrode material. Presented in this work are pulse intensity and position measurements obtained at the European XFEL using a new type of all-carbon single-crystal diamond detector developed at Diamond Light Source. Instead of traditional surface metallisation, the detector uses laser-written graphitic electrodes buried within the bulk diamond. There is no metallisation in the XFEL X-ray beam path that could be damaged by the beam. The results obtained from a prototype detector are presented, capable of measuring the intensity and 1-dimensional X-ray beam position of individual XFEL pulses. These successful measurements demonstrate the feasibility of all-carbon diagnostic detectors for XFEL use.

INTRODUCTION

The European XFEL is a radiation source characterised by ultrashort pulse duration, high pulse intensities, high repetition rates, and almost complete transverse coherence. Individual pulses can contain up to 4 mJ of energy, delivered in a pulse that is less than 100 fs long [1,2]. It is important to monitor the XFEL pulse parameters such as intensity, beam size, and beam centroid position. Pulse-by-pulse capabilities are extremely useful as individual pulses vary considerably due to the stochastic nature of the light generation process in an XFEL. Making such measurements "transmissively", enabling the majority of the pulse energy to pass through the beamline into the instrument for the user experiment, is an increasingly important part of normalising data for fluctuations of the photon pulse parameters. Obtaining pulse-by-pulse X-ray beam size and position measurements in particular is extremely difficult, and there are very few techniques available that can achieve this. A general overview of XFEL beamline diagnostics can be found in Ref. [1].

On-line diagnostics that can be safely placed in the X-ray beam path and withstand the beam powers can be challenging to develop. Any beam instrumentation needs to be designed to survive the single-shot and multi-bunch beam intensities, while also making measurements of the X-ray beam without interfering with the beam delivery and user experiments. The peak power is sufficient to damage many materials placed in the beam path. Because of the extremely short pulse lengths, thermal transport does not remove any heat from intercepting diagnostics during the pulse duration itself, even for extremely good heat conductors such as copper or diamond [3], a factor exacerbated by the high repetition rate of the XFEL pulses in the MHz range. Under a sufficiently focused X-ray beam, most materials placed directly in the beam path will suffer ablation, and the upper layers of the material will vaporise due to absorption of energy from a single XFEL pulse. For this reason, instruments made of low atomic number materials such as diamond are useful, as photon absorption is lower resulting in lower absorbed power densities.

Single-crystal CVD diamond detectors show great promise for XFEL beam diagnostics. Compared to other detector materials, diamond has superior radiation tolerance, excellent thermal conductivity, and fast response times (i.e. fast charge carrier drift velocities). CVD diamond has found many uses at XFEL beamlines: as a scintillator screen material for beam profile imaging (when appropriately doped) [4], as a foil to generate backscattered photons for simple position or intensity monitoring [5], and most recently as solid-state ion-chamber flux intensity monitors [6,7]. The diamond itself can withstand the power of the beam, but the pulses can deposit sufficient energy into the detector that surface electrodes and other metallisation in the beam path may be damaged by the radiation.

Presented in this work are proof-of-principle pulse intensity and position measurements obtained at the European XFEL using a new type of all-carbon single-crystal diamond detector developed in collaboration between University of Warwick and Diamond Light Source.

DETECTOR DESIGN

The detector used for this work utilises laser-written graphitic electrodes, instead of traditional surface metallisation. These are fabricated using an ultrashort pulse laser technique. At the laser focal point there is sufficient energy deposited into the diamond that a local phase transition can take place: electrically non-conductive diamond is converted into conductive graphite. Diamond detectors using such electrodes were first demonstrated in the early 2010s [8].

These buried graphitic electrodes offer several advantages that make them more resistant to damage than surface metallised electrodes. Firstly, they very closely match the sur-

* chris.bloomer@diamond.ac.uk

Content from this work may be used under the terms of the CC BY 4.0 licence (© 2022). Any distribution of this work must maintain attribution to the author(s), title of the work, publisher, and DOI

ISBN: 978-3-95450-241-7 ISSN: 2673-5350 doi:10.18429/JACoW-IBIC2022-WEP15

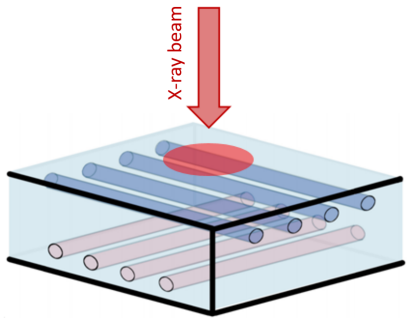


Figure 1: A sketch (not to scale) showing the electrode layout of the detector. The 'measurement' electrodes are shown in blue; the 'bias' electrodes are shown in red.

rounding diamond in terms of X-ray transmission, so the absorbed power density is much lower than that of typical titanium or aluminium electrodes, helping to prevent damage. Secondly, they are surrounded on all sides by thermally conductive diamond which can transfer away heat, unlike surface electrodes which are only connected to the diamond on one side. Finally, their thermal expansion better matches the diamond plate than surface metallisation, where a mismatch in the thermal expansion and contraction of the metallisation and the diamond can weaken the adhesion between the two and degrade the electrode.

The prototype detector used in this work has a series of buried 'strip electrodes' that can be individually read out to provide X-ray beam profile measurements. In brief, the diamond is a 'single crystal optical plus' grade CVD plate, 5.1 mm x 3.6 mm in size and 600 µm thick. The measurement strip-electrodes are located at a depth of 100 µm within the material, and the bias strip-electrodes are located at a depth of 200 µm. There is a spacing of 50 µm between each

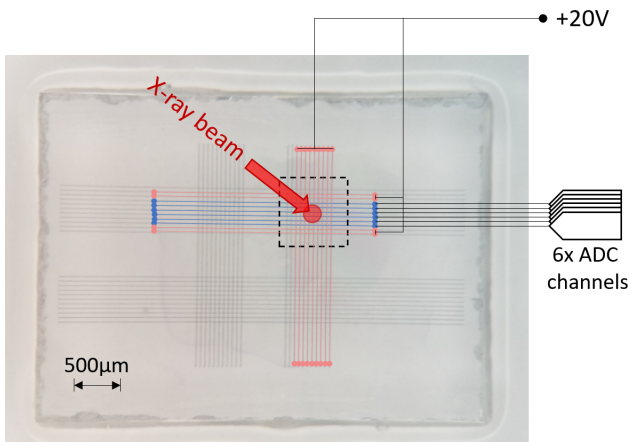


Figure 2: A photograph of the detector plate with the graphitic electrodes visible. The wiring arrangement is highlighted, showing how the 'bias' and 'measurement' electrodes are connected to the acquisition hardware. Biased 'guard rails' running parallel to the 'measurement' electrodes are used to ensure a uniform electric field within the interaction region.

individual strip-electrode. Figure 1 shows a sketch of this layout.

The graphitic electrodes are connected to the surface by vertical graphitic columns referred to as 'vias'. These are located at the edge of the diamond plate for the purpose of connecting the buried electrodes to a surface metallisation pad, well away from the centre of the detector where the beam would pass through. Further information on the design and operation of the detector, and beam profile measurements obtained from synchrotron radiation beamlines at Diamond Light Source, is presented elsewhere [9, 10]. Figure 2 shows a photograph of the diamond plate, illustrating how the strip electrodes were wired up to acquisition hardware used in these tests.

EXPERIMENTAL SET-UP

The Materials Imaging and Dynamics (MID) instrument [11] at European XFEL was used for these tests. The photon energy was 12.9 keV, and the average pulse energy before attenuation was 1.2 mJ. A CVD diamond filter was inserted upstream of the graphitic wire detector to attenuate the pulse energy for the duration of these proof-of-principle tests, and avoid damaging the detector, reducing the pulse energy at the graphitic wire detector to 0.17 mJ. The delivered beam contained 5 pulses per train at 10 Hz train repetition and 0.565 MHz intra-train pulse repetition rate (1770 ns gap between pulses in a train).

Compound refractive lenses were used to reduce the X-ray beam size at the detector to 250 µm. The diamond detector was installed at the instrument's sample point, at a distance of 970 m from the X-ray source point.

The MID instrument had six available fast ADC channels at the time of the tests, so these were connected to six of the parallel 'measurement' electrodes using lengths of coaxial cable. The ADCs were 16-bit commercial products with 108 MHz sampling rate, triggered to capture data synchronously with each pulse train.

The 'bias' electrodes were connected to a variable bias supply. For the duration of these experiments this was set to +20 V. The graphitic wires on either side of the parallel 'measurement' electrodes were also connected to the bias supply, to act as 'guard rails'. These guard rails provide two functions: to better constrain the electric field between 'measurement' and 'bias' electrodes, providing a more uniform field; and to restrict the fringe field found outside of the electrode array, and prevent extraneous charge carriers generated outside of the electrode array from being carried to the measurement electrodes.

Downstream of the location of the detector is the instrument's diagnostic end-station (DES). The DES includes tools for characterisation of the transmitted XFEL pulses, including a fast solid state intensity monitor capable of shot-by-shot measurements. This fast intensity monitor is also a diamond detector, without any position-sensing capabilities. The capabilities and operation of this intensity monitor is outlined in Ref. [6]. The intensity measurements from the graphitic

Content from this work may be used under the terms of the CC BY 4.0 licence (© 2022). Any distribution of this work must maintain attribution to the author(s), title of the work, publisher, and DOI

ISBN: 978-3-95450-241-7 ISSN: 2673-5350 doi:10.18429/JACoW-IBIC2022-WEP15

Content from this work may be used under the terms of the CC BY 4.0 licence (© 2022). Any distribution of this work must maintain attribution to the author(s), title of the work, publisher, and DOI

electrode detector can be compared to that from this existing DES intensity monitor.

BEAM INTENSITY MEASUREMENTS

The detector was installed on a motion stage to enable it to be scanned through the beam path. It was initially coarsely aligned using the stepper motor so that the X-ray beam was transmitted through the region indicated in Fig. 2. This enabled a measurement of the intensity of each of the pulses in the 5-pulse XFEL train. The ADC signal from one example train is presented in Fig. 3, along with the corresponding measurement from the DES intenstity monitor. It can be seen that there is agreement in the measured pulse heights.

Resolving the true pulse lengths (< 100 fs) is not possible for either instrument, but the pulse intensities can be compared. It is noted that a significant decay time is observed from the graphitic wire detector signals, compared to the MID intensity monitor. It is currently unclear if this is due to poor wiring or connection to the ADC, or due to some unwanted capacitances arising from within the detector. Future work should be carried out to address this question. Nonetheless, the individual pulses are clearly resolvable.

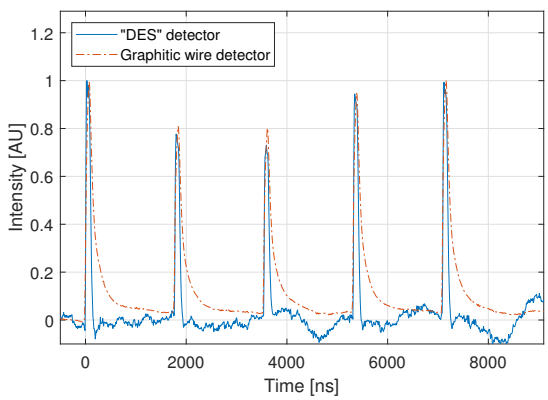


Figure 3: A measurement of the intensities of each pulse in the train. The measurement from the DES intensity monitor is compared with that from the graphitic wire detector. Intensities have been normalised to the peak intensity measured.

Figure 4 presents a comparison of measured pulse intensities from the graphitic wire detector and from the DES intensity monitor, observing the natural variation in pulse-by-pulse intensities during the experimental period. There is broad qualitative agreement between the two instruments, however the measured r.m.s. difference is 10.5 % of the graphitic wire intensity. This discrepancy is hypothesised to be due to the sensitive region of the graphitic wire detector being relatively small compared to the average incident beam size, so the full beam intensity is not measured if individual pulses vary significantly in size or position.

BEAM PROFILE MEASUREMENTS

By monitoring the signals recorded on all six acquisition channels individually, beam spatial profile information can

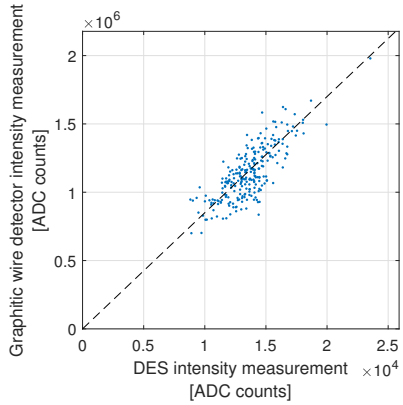


Figure 4: Pulse intensity measurements from the graphitic wire detector as a function of DES intensity measurement. A line of best fit is drawn.

be obtained. Shown in Fig. 5 is a the integrated measurement from the six channels over 20 pulse trains (100 pulses in total). Figure 6 shows the pulse profiles measured for a number of *individual* XFEL pulses from three trains.

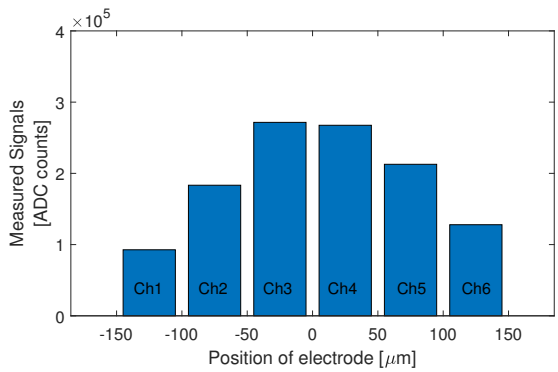


Figure 5: Vertical pulse profile measurements from the graphitic wire detector, showing the average profile obtained from 20 consecutive pulse trains.

BEAM POSITION MEASUREMENTS

A standard difference-over-sum (Δ/Σ) approach can be taken to obtain a measurement of the 1-dimensional X-ray beam position using this array of strip-electrodes.

$$Y_{\Delta/\Sigma} = \frac{(Ch1 + Ch2 + Ch3) - (Ch4 + Ch5 + Ch6)}{Ch1 + Ch2 + Ch3 + Ch4 + Ch5 + Ch6}$$

The motion stage that the detector was mounted upon was used to carry out a slow vertical stepper motor scan of the detector through the path of the XFEL beam whilst acquiring data from the six measurement electrodes. For each pulse during the scan the beam position was calculated, and is presented in Fig. 7. The dimensionless Δ/Σ is multiplied by an experimentally determined scale factor to convert it into a beam position with real-world units of millimetres. The calculated position of each individual XFEL pulse is

ISBN: 978-3-95450-241-7 ISSN: 2673-5350 doi:10.18429/JACoW-IBIC2022-WEP15

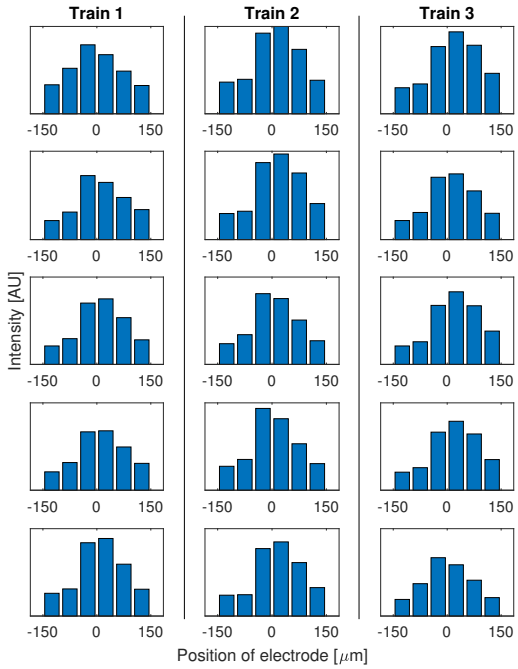


Figure 6: Vertical pulse profile measurements from individual pulses within three different 5-pulse trains.

shown in the figure (red dots), with the mean and standard deviation of the measured beam position at each step of the motor scan also displayed (blue error-bars).

The position measurement is found to be linear over about ± 0.3 mm, which is to be expected given the size of the incident beam and the electrode spacing. Stochastic shot-to-shot variation in beam position is clearly visible in this data. The measured standard deviation in individual pulse position was 0.043 mm.

FUTURE WORK

These experiments have demonstrated the feasibility of all-carbon profile monitors for XFEL pulse measurements, and indicated useful avenues for future research. This should be repeated with the full available pulse energy and maximum possible intra-train repetition rates, to demonstrate no adverse affect on the graphitic electrodes from the absorbed power. Repeating the measurements over a wider range of attenuations would also be useful to verify the intensity linearity of the detector.

The detector used in this test was optimised for 'continuous' synchrotron radiation, and not for 'RF' pulse-by-pulse measurements. Careful modelling could help produce a detector design that is better optimised for MHz XFEL measurements, and better capable of resolving individual pulses even at the highest repetition rates.

Finally, it would be beneficial to repeat these tests using new acquisition hardware with a greater number of ADC channels. This would allow for higher spatial resolution

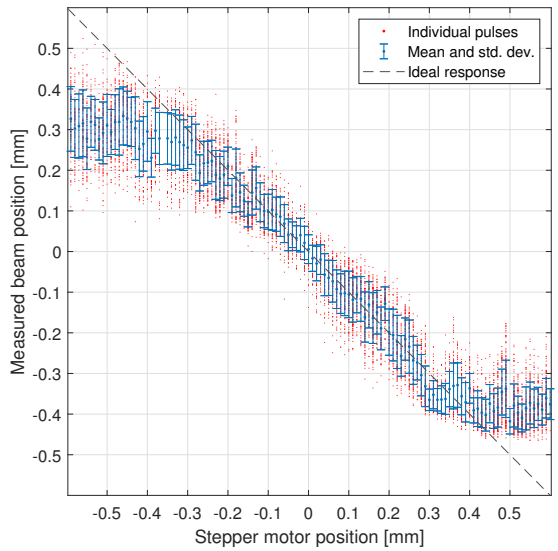


Figure 7: A scan of the detector motion stage, with a 1-dimensional beam position measurement acquired for each XFEL pulse during the scan.

than could be achieved using just the six channels that were available for these tests.

CONCLUSIONS

A proof-of-principle measurement of individual XFEL pulses arriving at MHz rates using an all-carbon graphitic electrode has been carried out. XFEL X-ray pulse intensity, 1-dimensional spatial profile, and position measurements have been obtained using the detector. The graphitic tracks survived exposure to the beam for the duration of the experiment and suffered no measurable damage.

ACKNOWLEDGEMENTS

The authors wish to acknowledge the support of many individuals and groups that aided in this research. The CVD diamond plate used to create this detector was provided by Element Six. We wish to acknowledge the contributions of P. Salter for the graphitic electrode fabrication, at the University of Oxford. The detector surface metallisation was carried out by B. Green, and the wire bonding by F. Courtney, both at the University of Warwick. Finally, the authors acknowledge the support and help of the MID instrument staff at European XFEL, in particular U. Boesenberg and A. Zozulya.

REFERENCES

[1] J. Grünert *et al.*, "X-ray photon diagnostics at the European XFEL", *J. Synchrotron Radiat.*, vol. 26, pp. 1422–1431, 2019. doi:10.1107/S1600577519006611

[2] W. Decking *et al.*, "A MHz-repetition-rate hard X-ray free-electron laser driven by a superconducting linear ac-

Content from this work may be used under the terms of the CC BY 4.0 licence (© 2022). Any distribution of this work must maintain attribution to the author(s), title of the work, publisher, and DOI

ISBN: 978-3-95450-241-7 ISSN: 2673-5350 doi:10.18429/JACoW-IBIC2022-WEP15

celerator", *Nat. Photonics*, vol. 14, pp. 391–397, 2020. doi:10.1038/s41566-020-0607-z

[3] T. Tschentscher *et al.*, "Photon Beam Transport and Scientific Instruments at the European XFEL", *Appl. Sci.*, vol. 7, p. 592, 2017. doi:10.3390/app7060592

[4] A. Koch *et al.*, "Design and initial characterisation of X-ray beam diagnostic imagers for the European XFEL", *Proc. SPIE Int. Soc. Opt. Eng.*, vol. 9512, p. 95121, 2015. doi:10.1117/12.2182463

[5] K. Tono *et al.*, "Single-shot beam-position monitor for x-ray free electron laser", *Rev. Sci. Instrum.*, vol. 82, p. 23108, 2011. doi:10.1063/1.3549133

[6] T. Roth *et al.*, "Pulse-resolved intensity measurements at a hard X-ray FEL using semi-transparent diamond detectors", *J. Synchrotron Radiat.*, vol. 25, p.p 177-188, 2017. doi:10.1107/S1600577517015016

[7] J. Bohon *et al.*, "Use of diamond sensors for a high-flux, high-rate X-ray pass-through diagnostic", *J. Synchrotron Radiat.*, vol. 29, pp. 595-601, 2022. doi:10.1107/S1600577522003022

[8] A. Oh *et al.*, "A novel detector with graphitic electrodes in CVD diamond", *Diamond Relat. Mater.*, vol. 38, pp. 9–13, 2013. doi:10.1016/j.diamond.2013.06.003

[9] C. Bloomer *et al.*, "A single-crystal diamond X-ray pixel detector with embedded graphitic electrodes", *J. Synchrotron Radiat.*, vol. 27, pp. 599–607, 2020. doi:10.1107/s160057752000140x

[10] C. Bloomer *et al.*, "Single-crystal diamond pixelated radiation detector with buried graphitic electrodes", in *Proc. IBIC'21*, Pohang, Korea, Sep. 2021, pp. 158-166. doi:10.18429/JACoW-IBIC2021-TUOA01

[11] A. Madsen *et al.*, "Materials Imaging and Dynamics (MID) instrument at the European X-ray Free-Electron Laser Facility", *J. Synchrotron Radiat.*, vol. 28, pp. 637–649, 2021. doi:10.1107/S1600577521001302

Content from this work may be used under the terms of the CC BY 4.0 licence (© 2022). Any distribution of this work must maintain attribution to the author(s), title of the work, publisher, and DOI

ISBN: 978-3-95450-241-7 ISSN: 2673-5350 doi:10.18429/JACoW-IBIC2022-WEP16

PSF CHARACTERIZATION OF THE ALBA X-RAY PINHOLES

U. Iriso, Z. Martí, A. A. Nosych, ALBA Synchrotron, Cerdanyola del Vallès, Spain
A. Cazorla, ICMAB, Campus UAB, Bellaterra, Spain
I. Mases, CERN, Geneva, Switzerland

Abstract

ALBA is currently equipped with two X-ray pinhole cameras for continuous beam size monitoring using the synchrotron radiation from two different bending magnets. The first pinhole was installed on day-1 and it is working properly since 2011 as the work-horse for the ALBA emittance measurements. The second one has been commissioned in early 2021 for redundancy purposes. This paper summarizes the exercises to characterize the Point Spread Function (PSF) of both pinhole cameras using analytical calculations, SRW simulations, and experimental measurements.

INTRODUCTION

Measuring the transverse beam size and emittance of the electron beam is an essential tool to control the machine performance. Since the ALBA commissioning in 2011, this was carried out using an X-ray pinhole camera located in FE34 [1]. During the last years, at ALBA we have performed other means to infer the beam emittance based on the Synchrotron Radiation Interferometry (SRI) [2] or Heterodyne Near Field Speckles (HNFS) [3]. Nevertheless, we found the X-ray pinhole camera as a more robust set-up, and so we have finally decided to install a second unit for redundancy purposes, this time located in FE21 - almost on the opposite side of the storage ring.

In a pinhole (see Fig. 1), the source image (the electron beam) is amplified at the image plane by a factor $X = L_2/L_1$, where L_1 is the distance between the source point and the pinhole, and L_2 corresponds to the distance between the pinhole and the image plane (YAG screen).

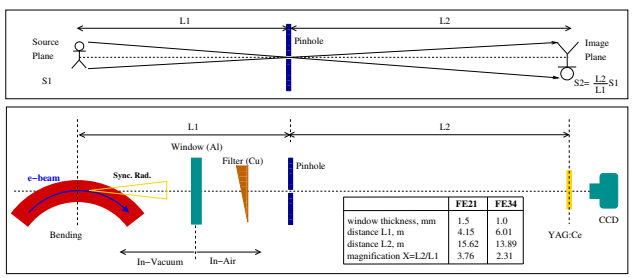


Figure 1: Top: general working principle of a pinhole imaging system. Bottom: sketch of the X-ray pinhole cameras at ALBA, with the geometrical parameters of FE21 and FE34.

But imaging with a pinhole requires a thorough characterization of the pinhole Point Spread Function (PSF, or σ_{PSF} in the following), which is the beam size measured at the image plane corresponding to a point-like source. If σ_e is the electron beam size, the size measured at the YAG screen in Fig. 1 is affected by the σ_{PSF} by:

$$\sigma^2_{\mathrm{YAG}} = (X\sigma_e)^2 + \sigma^2_{\mathrm{PSF}} \,. \tag{1}$$

This paper summarizes the exercises to characterize the PSF of both ALBA pinhole cameras using analytical calculations, SRW simulations [4], and experimental measurements using the beam lifetime. For reference, Table 1 lists the main beam parameters for both pinholes.

Table 1: Twiss Parameters at FE21 and FE34, and Main Operation Parameters of ALBA

	FE21	FE34
hor beam size, µm	55	60
ver beam size, µm	24	27
hor beta function, m	0.52	0.435
ver beta function, m	22.83	25.82
hor dispersion, mm	20.1	37.1
ver dispersion, mm	7.0	11.5
energy spread, %	$1.05{\cdot}10^{-3}$	
emittance, nm·rad	4.6	
coupling, %	0.5	
energy, GeV	2.98	

BEAMLINE SETUP

Both ALBA set-ups (see Fig. 1, bottom) follow the classical design in other light sources [5]: the source point (a bending dipole in both cases) emits synchrotron radiation, and the visible and soft X-rays part are filtered out by an Aluminium window. Furthermore, the Al-window separates vacuum from in-air components. Next a Copper filter whose length can be varied between 0 mm and 5 mm is used to attenuate or harden the X-rays before they hit the pinhole. This is a µm size hole, which is properly aligned using a motorized stage (see next sub-section). Finally, an imaging system consisting in a YAG screen with an optical set-up transforms the X-rays into visible light to form the image and obtain the beam size.

The paper focuses on the cases with and without the use of Cu filter. By optimizing the contrast in Control Room during normal operation conditions, we work with a Cu thickness of 0.3 mm. In order to compare the Cu filter effect, the paper focus the study on four cases:

(a) FE21, 1.5 mm of Al

(b) FE21, 1.5 mm of Al, and 0.3 mm of Cu

(c) FE34, 1.0 mm of Al

(d) FE34, 1.0 mm of Al, and 0.3 mm of Cu

Content from this work may be used under the terms of the CC BY 4.0 licence (© 2022). Any distribution of this work must maintain attribution to the author(s), title of the work, publisher, and DOI

ISBN: 978-3-95450-241-7 ISSN: 2673-5350 doi:10.18429/JACoW-IBIC2022-WEP16

Content from this work may be used under the terms of the CC BY 4.0 licence (© 2022). Any distribution of this work must maintain attribution to the author(s), title of the work, publisher, and DOI

As an illustrative example, Fig. 2 shows the spectrum of the FE34 coming from an ALBA dipole, and after traversing the 1 mm of Al (case "c"), and [1 mm of Al plus 0.3 mm of Cu] (case "d"). Note that with only 0.3 mm of Cu, the peak energy moves to higer energies wrt the case with only Al (from 27 keV to 39 keV).

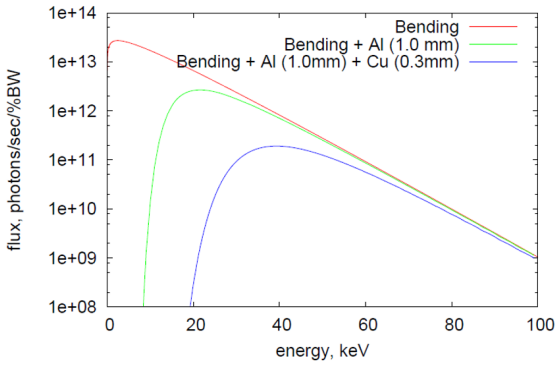


Figure 2: Spectrum of the ALBA dipole at FE34, after traversing 1 mm of Al and 0.3 mm of Cu.

Pinhole Width Measurement

One of the key systems is the pinhole itself. We use a similar design as in [5], using tungsten (W) blocks of [10x3x1] mm assembled one on top of the other, with small shims of 50, 10, and 5 µm in between (see Fig. 3). Placed vertical and horizontally, the blocks form a grid of 9 different hole sizes. Using a motorized stage, we can use one or another (pin)hole. We typically use the center hole (the one made with the shims of 10x10 µm).

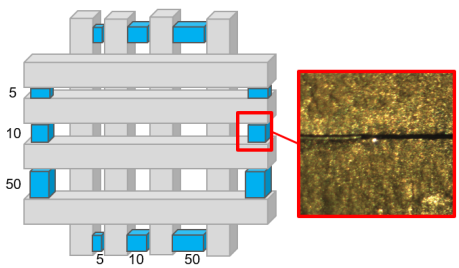


Figure 3: Left: Sketch of the pinhole block installed in FE21. Right: microscope image showing the 10 µm shim between the two W-blocks.

Prior to its installation, the different slit widths are measured with a microscope. Once installed, we repeat these measurements using the X-ray beam itself: tilting the setup from the minimum to maximum illumination, and back to minimum. The measurements results for the slits using the 10 µm spacer are summarized in Fig. 4: note that although we use 10 µm spacers, the "effective" width is actually larger (about 20 µm). This could be related to the deformation of the spacers when they are cut (see Fig. 3, right), which cannot be fully compressed using the mechanical set-up.

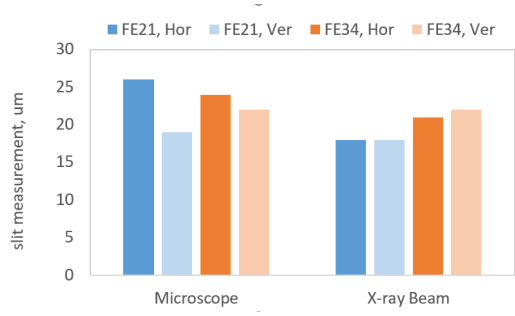


Figure 4: Measurements of the slit widths forming the pinhole in FE21 and FE34.

ANALYTICAL PSF EVALUATION

Imaging using synchrotron radiation is affected by the diffraction and blurring effects. For a given photon energy E and pinhole width w, these contributions are analytically evaluated by [5]:

$$\sigma_{\text{diff}} = \frac{\sqrt{12hc}}{4\pi}\frac{L_2}{E \cdot w}, \qquad \sigma_{\text{blur}} = \frac{w(L_1 + L_2)}{\sqrt{12}L_1}, \tag{2}$$

where c is the speed of light, h is the Planck constant and L_1, L_2 are described in Fig. 1.

But the synchrotron radiation (SR) that forms the pinhole image is not monochromatic, and so Eq. (2) must take into account the spectrum given by the ALBA bending, attenuated by the Al window and Cu filter (if in use). The numerical integration of Eq. (2) is done using

$$\sigma_{\text{DIFF}} = \int \sigma_{\text{diff}}(E)P(E)dE, \qquad P(E) = \frac{N_{\text{ph}}(E)}{\int_0^\infty N_{\text{ph}}(E)\,dE}. \tag{3}$$

Here $N_{\text{ph}}(E)$ is the photon flux for a specific energy (see Fig. 2). Then, the PSF is obtained by adding these contributions in quadrature:

$$\sigma_{\text{PSF}} = \sqrt{\sigma_{\text{blur}}^2 + \sigma_{\text{DIFF}}^2 + \sigma_{\text{screen}}^2}, \tag{4}$$

where σ_{screen} is the CCD pixel size. Solving Eqs. (3) and (4), in FE21 we find σ_{PSF}=24 µm with only Al, while it goes down to 18 µm if we use 0.3 mm of Cu. For FE34 and only Al, σ_{PSF}=22 µm and it goes down to 15 µm if we use 0.3 mm of Cu. The values of FE21 are larger due to the larger magnification.

PSF CALCULATION USING SRW

For these simulations we consider the wavefront of light emitted by a point-like ("zero emittance") beam. We perform the simulations using a 10 µm horizontal and 1 µm vertical, which is a factor ~25 smaller than the real vertical size and it is a good compromise between an optimum simulation result

ISBN: 978-3-95450-241-7 ISSN: 2673-5350 doi:10.18429/JACoW-IBIC2022-WEP16

and the CPU time. The σ_{PSF} is computed in the vertical plane because this is where the smallest beam size is achieved.

Although we have seen that recently SRW allows to perform polychromatic simulations through OASYS [6], this was not the case when we first start this study. Therefore, we have done monochromatic simulations [7] at different energies (in our case, 5 different energies). These energies are chosen considering the spectrum flux in FE21 and FE34, with and w.o. Cu filter (0.3 mm). As an example, Fig. 5 shows the normalized spectrum for the FE34 case with 0.3 mm of Cu, and with the "representative" energies (red boxes).

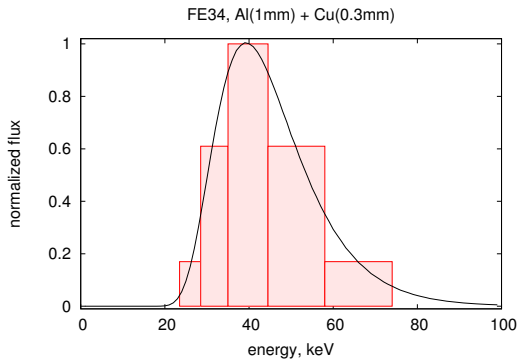


Figure 5: Normalized transmission spectra for FE34, assuming Al (1 mm) and 0.3 mm of Cu. The red squares denote the energies considered for the PSF calculation in Fig. 6.

For each these energies, SRW provides an intensity profile (Fig. 6, top), which is weighted with the values of the normalized spectrum. Next, we add these contributions in one single profile (red dots in Fig. 6, bottom). The σ_{PSF} is obtained after fitting this profile to a Gaussian function (blue line in Fig. 6 - bottom). We are currently performing polychromatic simulations using the up-to-date version of SRW to crosscheck these results.

Consistently with the analytical calculations, we obtain values of 23 and 19 µm for FE21 with and w.o. Cu, while in FE34 these are 18 and 15 µm with and w.o. Cu. Moreover, we perform this analysis for several Cu filter cases to fully characterize the PSF. Then, we fit the PSF as a function of the Cu filter thickness as shown in Fig. 7 for the case of FE21 and 5 µm slit. Then, this fit is included in the GUI that provides the beamsize in real-time in the Control Room during normal operation, so that in case operators move the Cu thickness, or change the pinhole width, the PSF is automatically updated. More details can be found in Ref. [9].

EXPERIMENTAL PSF CALCULATION

The pinhole PSF can be experimentally calculated using the Touschek lifetime, τ_T as already performed in [8]. For the ultra-relativistic case, and in ALBA conditions, we have

$$\frac{1}{\tau_T} \approx \left\langle \frac{c r_p^2 N_p}{2\sqrt{\pi}\gamma^2 \sigma_z \sigma_x \sigma_y (\Delta_E/E_0)^2} \right\rangle, \qquad (5)$$

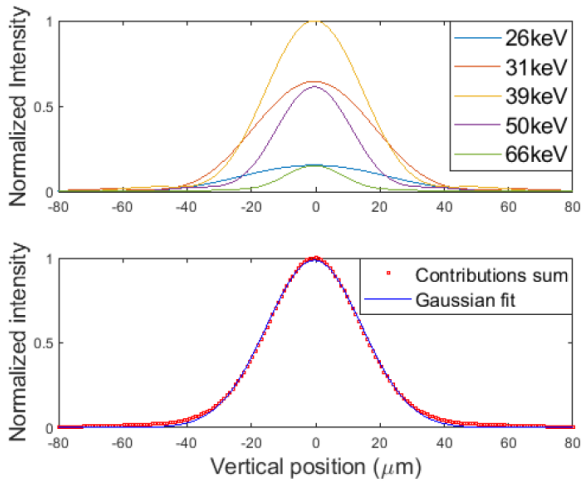


Figure 6: Top: FE34 PSF obtained at the screen for five different energies with 0.3 mm of Cu. Bottom: Sum of all PSF contributions (red dots) and Gaussian fit (blue).

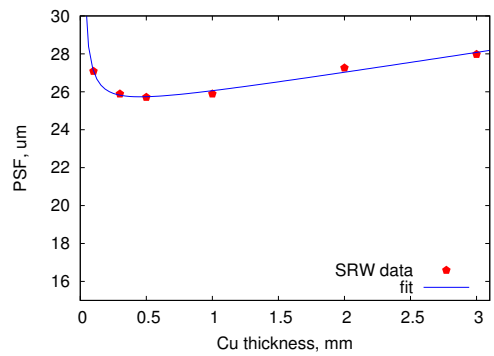


Figure 7: PSF calculation at FE21 for different Cu thickness using SRW simulations (red points) and fit (blue).

where c is the speed of light, r_p is the classical particle radius, N_{p} is the number of electrons in the bunch, σ_{z} is the bunch length, (Δ_E/E_0) is the relative energy spread. The brackets mean the average over the whole storage ring circumference. Note that Touschek lifetime is directly proportional to the average horizontal $\langle \sigma_{\mathrm{x}} \rangle$ and vertical beam sizes, $\langle \sigma_{\mathrm{y}} \rangle$.

When ALBA operates in a Touscheck dominated regime, then we can assume the measured lifetime τ is mainly the Touscheck lifetime τ_T, and so

$$\langle \sigma_{\mathrm{y}} \rangle = k \cdot \tau, \qquad (6)$$

where k is a scaling factor. If we further assume that the average vertical beam size $\langle \sigma_y \rangle$ is proportional to the beam size measured at the ALBA pinholes σ_{YAG}, then

$$\left(\frac{\sigma_{\mathrm{YAG}}}{X}\right)^2 = (k\tau)^2 + \left(\frac{\sigma_{\mathrm{PSF}}}{X}\right)^2. \qquad (7)$$

Figure 8 shows an example of such a measurement, in which the coupling is changed using different set of the skew quarupoles. At each skews settings, we measure the lifetime and the vertical beam size in both pinholes, with and w.o.

Content from this work may be used under the terms of the CC BY 4.0 licence (© 2022). Any distribution of this work must maintain attribution to the author(s), title of the work, publisher, and DOI

ISBN: 978-3-95450-241-7 ISSN: 2673-5350 doi:10.18429/JACoW-IBIC2022-WEP16

Content from this work may be used under the terms of the CC BY 4.0 licence (© 2022). Any distribution of this work must maintain attribution to the author(s), title of the work, publisher, and DOI

0.3 mm of Cu. The PSF for each case is found from the independent term in the linear fit (solid lines in Fig. 8). The final result shown in Fig. 8 is the average of 5 experiments, where the error bar includes both the fitting error as well as the spread of the measurements.

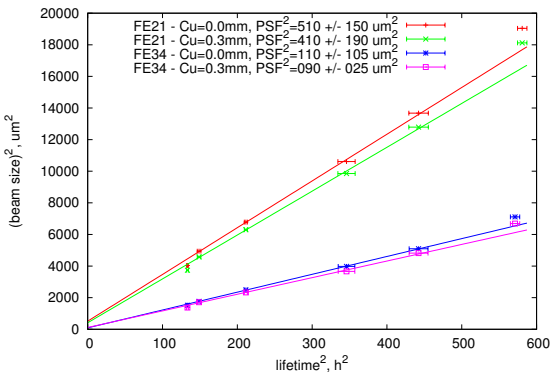


Figure 8: Lifetime evolution and beam size calculation using both pinholes for the "only Al case", and the case with "Al and Cu".

Note the large error bars in the linear fits. These stem from several reasons. First, the lifetime measurement at ALBA oscillates significantly due to the DCCT noise (see error bars in Fig. 8). Furthermore, although the measurements are performed in a regime in which the Touscheck lifetime dominates, the gas lifetime still has a non-negligible influence and so Eq. (5) is not valid in all the parameter space (this is especially relevant at high beam sizes). Finally, we note that the coupling correction is only performed with 32 skews, and this means the coupling correction is discrete and might not be uniform through the ring. This is especially relevant for low beam sizes. We note that in Fig. 8 the last and first points are not considered for the fits.

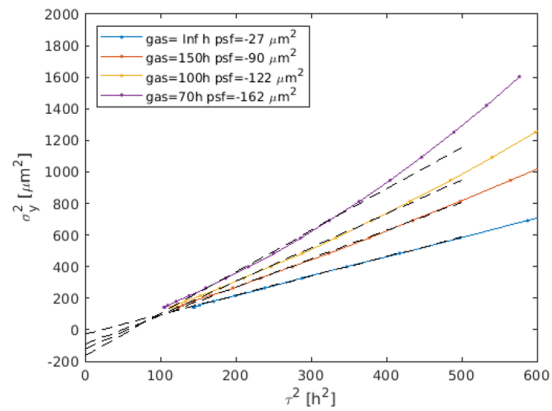


Figure 9: Lifetime evolution and expected beam size at FE34 according to the MML simulation.

Figure 9 shows a MML simulation for the FE34 case, correcting the coupling with the skew magnets and assuming different gas lifetimes. We note that even in all cases (even if we consider the gas lifetime as infinite), the expected PSF has a negative value.

RESULTS AND CONCLUSIONS

Table 2 lists the results of the PSF calculation with the three different methods for both pinholes, in case of only Al or with Al and 0.3 mm of Cu.

Table 2: Summary of the PSF Calculation at Both Pinholes Using the Three Different Methods in This Report

	FE21 Al	FE21 Al + Cu	FE34 Al	FE34 Al + Cu
Analytic	24.4	18.9	21.7	15.2
SRW	23.1	18.8	17.8	14.8
Exper.	20 ±16	20 ±15	13 ±15	13 ± 17

The values of σ_{PSF} obtained for the pinhole in FE21 are larger than the ones of pinhole in FE34 because the magnification of pinhole FE21 is larger. Despite this fact, the resolution (in terms of minimum measurable beam size) of FE21 pinhole is better than FE34. Considering that σ_{PSF}/X is the minimum beam size measurable by the pinhole camera, we obtain a minimum beamsizes of 6.5 µm for FE34, and 5.0 µm for FE21 (in the case with Cu filter of 0.3 mm).

The results using the different methods agree among them, especially between the analytical and the SRW simulations. The experimental measurements show a big error bar due to the inherent uncertainties in the experiment. We are currently performing more SRW simulations including polychromatic effects to crosscheck the results shown here.

The effect of the PSF is included in the Control Room GUI that provides in real-time the beam sizes of FE21 and FE34. The PSF is automatically updated for different hole sizes and values of the Cu thickness, as shown in [9]. Nevertheless, note that the effect of adding in quadrature σ_{PSF} to the vertical beam size is in the order of few %. Using 0.3 mm of Cu, excluding the PSF would correspond to 2.5% error in FE21, and 5% in FE34 for the typical operation values of $\sigma_y = 25$ µm. The effect of σ_{PSF} on the horizontal beam size of the image, is even smaller because $\sigma_x \sim 60$ µm.

ACKNOWLEDGEMENTS

The authors would like to acknowledge D. Heinis for the support using SRW.

REFERENCES

[1] U. Iriso, M. Alvarez, F. F. B. Fernandez, A. Olmos, and F. Perez, "Diagnostics during the ALBA Storage Ring Commissioning", in *Proc. DIPACâ€™11*, Hamburg, Germany, May 2011, pp. 280–282. https://jacow.org/DIPAC2011/papers/TUOA02.pdf

[2] L. Torino and U. Iriso, "Transverse beam profile reconstruction using synchrotron radiation interferometry", *Phys. Rev. Accel. Beams*, vol. 19, p. 122801, 2016. doi:10.1103/PhysRevAccelBeams.19.122801

ISBN: 978-3-95450-241-7 ISSN: 2673-5350 doi:10.18429/JACoW-IBIC2022-WEP16

[3] M. Siano, *et al.*, "Two-dimensional electron beam size measurements with X-ray heterodyne near field speckles", *Phys. Rev. Accel. Beams*, vol. 25, p. 052801, 2022. doi:10.1103/PhysRevAccelBeams.25.052801

[4] SRW, https://www.esrf.fr/Accelerators/Groups/InsertionDevices/Software/SRW

[5] P. Elleaume, C. Fortgang, C. Penel, and E. Tarazona, "Measuring Beam Sizes and Ultra-Small Electron Emittances Using an X-ray Pinhole Camera", *J. Synchrotron Radiat.*, vol. 2, pp. 209–214, 1995. doi:10.1107/S0909049595008685

[6] OASYS, https://www.aps.anl.gov/Science/Scientific-Software/OASYS

[7] I. Mases, A. Garcia-Santiago, and U. Iriso, "Characterization of the Point Spread Function for the X-ray pinhole cameras at ALBA Synchrotron", Treball Final de Grau, Univ. Autònoma Bellaterra, 2020. http://hdl.handle.net/2445/176714

[8] L. M. Bobb, A. F. D. Morgan, and G. Rehm, "Performance Evaluation of Molybdenum Blades in an X-ray Pinhole Camera", in *Proc. IBICâ€™16*, Barcelona, Spain, Sep. 2016, pp. 795–798. doi:10.18429/JACoW-IBIC2016-WEPG63

[9] A. A. Nosych and U. Iriso, "Real-Time Beam Detection and Tracking From Pinhole Imaging System Based on Machine Learning", in *Proc. IBICâ€™21*, Pohang, Korea, Sep. 2021, pp. 272–275. doi:10.18429/JACoW-IBIC2021-TUPP28

Content from this work may be used under the terms of the CC BY 4.0 licence (© 2022). Any distribution of this work must maintain attribution to the author(s), title of the work, publisher, and DOI

ISBN: 978-3-95450-241-7 ISSN: 2673-5350 doi:10.18429/JACoW-IBIC2022-WEP17

SECONDARY ELECTRON EMISSION (SEM) GRID FOR THE FAIR PROTON LINAC

J. Herranz, Proactive R&D, Sabadell, Spain
T. Sieber, P. Forck, GSI, Darmstadt, Germany
I. Bustinduy, A. Rodriguez Paramo, ESS Bilbao, Zamudio, Spain
A. Navarro Fernandez, CERN, Geneva, Switzerland

Abstract

New SEM-Grid has been developed for FAIR Proton Linac, the instrument consists of 2 harps fixed together in an orthogonal way. This SEM-Grid will provide higher resolution and accuracy measurements as each HARP consists of 64 tungsten wires 100 µm in diameter and 0.5 mm pitch. Each wire is fixed to a ceramic PCB with an innovative dynamic stretching system, this system assures wire straightness under typical thermal expansion due to beam heat deposition. Simulation calculations of electric field distribution have been performed, three main parameters have been optimized, wires distribution, quantity of polarization electrodes and distance between electrodes and wires. The design and production of the SEM-Grid has been performed by the company Proactive R&D that has counted on the expertise of ESS-Bilbao to define safe operation limits and signal estimation by means of a code developed specifically for this type of calculations. Preliminary validations of the first prototypes have shown excellent mechanical and electrical behaviour. After the successful beam test validations performed in June 2022, final series of the SEM-Grid will be produced to be installed on FAIR proton LINAC.

FAIR PROJECT INTRODUCTION

The FAIR [1] facility at GSI will provide antiproton and ion beams of worldwide unique intensity and quality for fundamental physics research.

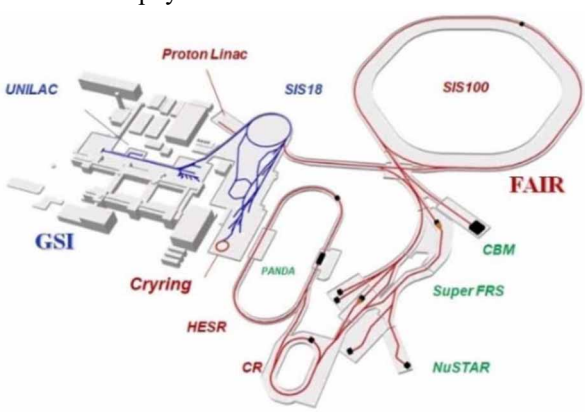


Figure 1: Layout of the FAIR facility.

The accelerator facility of FAIR, shown in Fig. 1, will include three linear accelerators, the existing UNILAC (for which a refurbishing program is currently on the way), a superconducting cw-Linac, designed mainly for intermediate energy experiments [2], and the new proton Linac (pLinac) [3]. The UNILAC and pLinac will be the main injectors of SIS18, which will in turn be an injector for SIS100, the central accelerator component of FAIR.

The pLinac consists of a novel so called 'Ladder' RFQ [4] followed by two ~10 m sections of Cross Bar H-drifttube accelerator (CH) structures [5]. The first section includes six CH modules, which are pairwise rf-coupled (Coupled CH or CCH). The second section consists of three separate modules, each connected to its own klystron. The pLinac will deliver a current up to 70 mA with a macropulse length of 35 µs (at max. 4 Hz) and a typical bunch length of 100 ps. The design energy is 68 MeV. Figure 2 shows a schematic of the pLinac and its beam instrumentation.

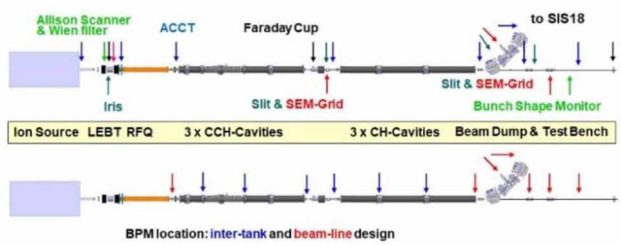


Figure 2: Schematic of the FAIR pLinac, side view, showing the location of diagnostics (upper) and BPMs, divided in cavity (inter-tank) and beamline BPMs (lower).

The overall diagnostics concept and layout of pLinac has been described in various reports, e.g. [6]. Because of the compact structure of the two CH sections, diagnostics (except BPMs) will be concentrated in the LEBT, in the MEBT behind the RFQ and in a diagnostics/rebuncher (so called SD) section between the CCH and CH parts of the pLinac. Additional beam diagnostics elements are placed in the transfer line to SIS18 as well as in a straight line to the beam dump.

Special care has been taken for the design of the SEM Grids. We expect a 1 σ beam radius of 1.5 mm in the "worst case", therefore the wire pitch cannot be larger than 0.5 mm to obtain realistic profiles. Moreover, a stretching mechanism is required to compensate for thermal expansion, even if the grids are operated in a "grid protection mode" at reduced duty cycle. Any kind of plating on the tungsten wires must be considered carefully because of possible melting and agglutination during irradiation.

SEM GRID DESIGN

The working principle of SEM grids is based on secondary electrons, which are released from the grid wires up on ion beam impact. The resulting current distribution

Content from this work may be used under the terms of the CC BY 4.0 licence (© 2022). Any distribution of this work must maintain attribution to the author(s), title of the work, publisher, and DOI

ISBN: 978-3-95450-241-7 ISSN: 2673-5350 doi:10.18429/JACoW-IBIC2022-WEP17

on an array of wires represents the beam profile in a given direction [7]. While grids cover both directions, harps cover only one coordinate axis. Due to the smaller size of the pLinac beam as compared to the UNILAC heavy ion beam, the traditional grid design of GSI only can be used for the LEBT section. The LEBT SEM grid is made of 64 wires with 2.0 mm spacing for each plane. It is designed in a classical way, consisting of a frame with spring holders for each wire.

The grids for the Linac section (SD-section, inflection and dump), designed by PROACTIVE R&D company in collaboration with GSI, have a smaller wire spacing of 0.5 mm. The active area is 32 × 32 mm^2 corresponding to 64 wires for each plane. At the inflection and in the rebuncher (SD) section a grid for both transverse directions mounted on a pneumatic drive. However, at the dump and additionally in the SD section separate harps for the horizontal and vertical profiles are mounted on two stepping motor drives to allow for transverse emittance measurements in connection with two upstream slits. Table 1 shows the relevant parameters.

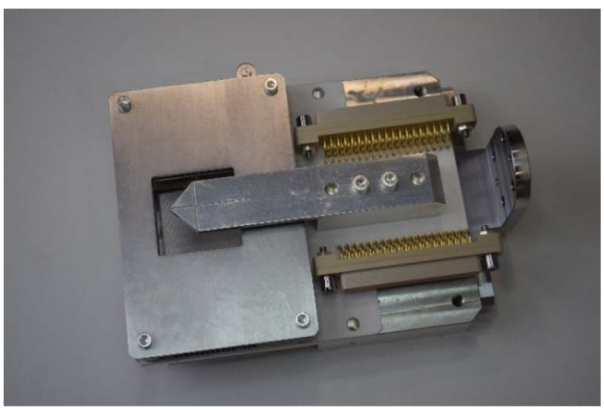


Figure 3: SEM harp by PROACTIVE R&D. The grid consists of two harps rotated by 90°, area 32 mm × 32 mm with diamond shaped cleaning electrode, 64 wires per harp, wire pitch 0.5 mm, thickness 100 µm.

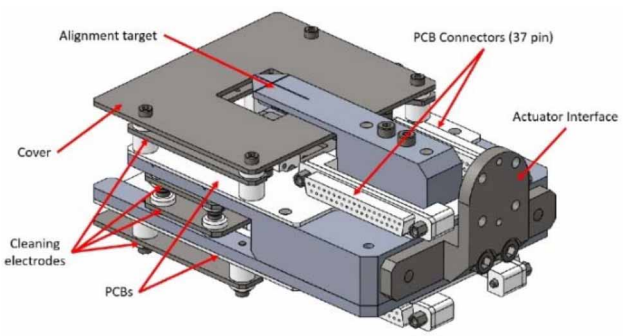


Figure 4: SEM grid design by PROACTIVE R&D.

The mechanical design of the grid can be seen in Figs. 3 and 4. The structure is based on a PCB to which the wires are soldered on one side. On the other side, a specially designed stretching system is used to keep wires under tension during irradiation.

Besides high resolution and a compact design, special care has been taken for the field distribution due to the cleaning electrodes. These electrodes are kept at a positive

Table 1: Parameters of pLinac and SEM Grids

No. of Grids / Harps	2 / 4
No. of wires Grid / Harp	2 × 64 / 1 × 64
Wire pitch / diameter	0.5 mm / 100 µm
Wire material	Tungsten (gold plated)
Detection area	32 × 32 mm^2
Vacuum requirement	$5 \cdot 10^{-9}$ mbar (no bakeout)
Max. beam current	70 mA
Pulse duration	10 – 100 µs
Repetition rate	1 – 4 Hz
Max. beam energy	68 MeV
Normal / max. grid temp.	2000 K / 3000 K

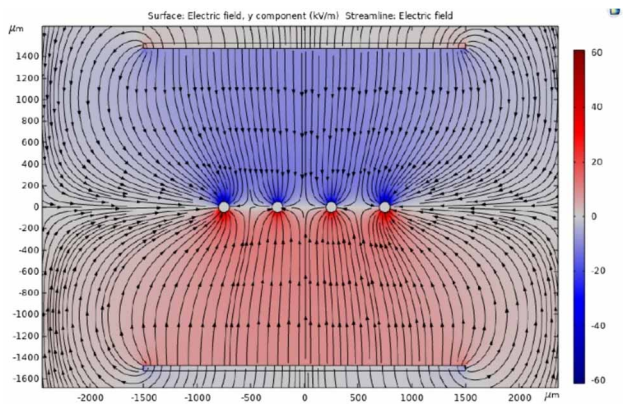


Figure 5: Field distribution calculated for co-planar wires. The diamond shaped cleaning electrodes are located at top and bottom respectively.

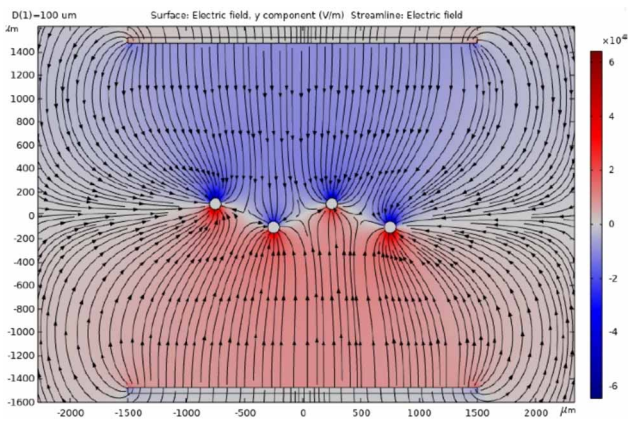


Figure 6: Field distribution with alternating wire positions. The diamond shaped cleaning electrodes are located at top and bottom respectively.

potential to extract the secondary electrons and thus prevent them from being captured by neighboring wires, which would deteriorate the measurement. The electric field distribution obtained with a parallel oriented diamond shaped electrode configuration is shown in Figs. 5 and 6. The potential required for the cleaning electrodes has been estimated to be ~200 V. As can be seen, the electric field vanishes in the plane where the four (representative) wires

Content from this work may be used under the terms of the CC BY 4.0 licence (© 2022). Any distribution of this work must maintain attribution to the author(s), title of the work, publisher, and DOI

ISBN: 978-3-95450-241-7 ISSN: 2673-5350 doi:10.18429/JACoW-IBIC2022-WEP17

Content from this work may be used under the terms of the CC BY 4.0 licence (© 2022). Any distribution of this work must maintain attribution to the author(s), title of the work, publisher, and DOI

are located. Consequently, a secondary electron generated at one of the wires and directed towards another one cannot be properly deterred from reaching it. This issue could generate unwanted crosstalk between the wires.

In order to solve this issue, a new, non-planar disposition of the wires has been studied. The electric field distribution of this new design is also shown in Figs. 5 and 6. As can be seen, with this new wire distribution the vanishing electric field plane is avoided, instead a rather sinusoidal shaped surface is observed on which the electric field vanishes. The electric field along a line joining two consecutive wires proves to be strongly repelling for electrons towards the ends of this line. A wire displacement of only 0.2 mm should provide a significant background reduction.

SEM GRID ACCEPTANCE TEST

The test of two prototype y-harps (gold coated / uncoated tungsten wires) was performed in two steps, in a first campaign a low intensity proton beam was used to prove the correct function of the harp in connection with the POLAND+ CSA electronics (proton beam parameters, see BPM section [8]). A second experimental campaign was performed with a high intensity Ar beam to check the wire stretching system, the upper limit of acceptable energy deposition and the actual heat load in comparison to simulations. The beamtime started with gold plated wires, later we switched to a harp with regular tungsten wires. We used an Ar_{10+} beam at 8.6 MeV/u, intensities 20 µA to 1.5 mA, pulse length 40 µs to 200 µs, repetition rate 1 Hz. In parallel to the measurements, simulations for wire heating were done with the pyTT code [9], predicting the wire temperature at the various measurements.

We checked the effect of the voltage on the diamond shaped cleaning electrode (extraction of secondary electrons to reduce wire cross-talk) while varying beam parameters. Figure 7 shows the voltage dependence of the integrated number of particles for two different spot sizes.

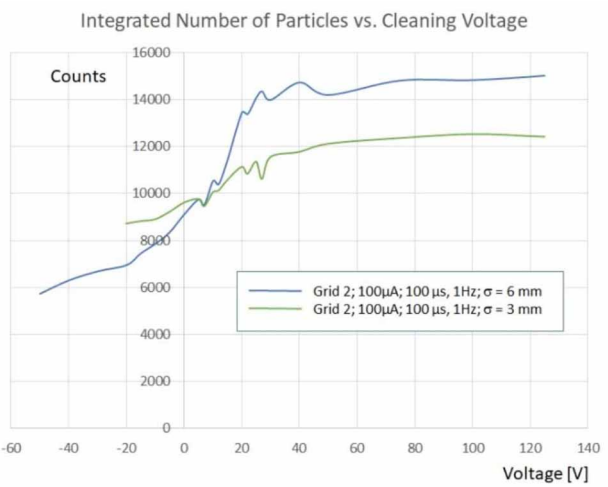


Figure 7: Number of particles, as a function of cleaning voltage. Sigma values indicate the beam size assuming Gaussian distribution in the calculations.

If the maximum current on the grid wires (maximum total counts) is taken as a criterion for optimum voltage, there is obviously not much effect from the cleaning electrode above ~40 V, which significantly reduces the effort for electrical connections. With proton beam, the saturation voltage was even smaller (<10 V). A comparison of the two curves in Fig. 5 shows that the number of counts is reduced most likely due to geometrical aspects at the smaller number of wires, while an effect on the slope of the curves cannot be observed (at given accuracy), which is a strong hint for a homogeneous field distribution as result of our electrode geometry optimization.

At inspection the gold plated grid showed no damage, even after heating to (theoretically) >2500 K. From this we concluded, that the wire temperature might have been overestimated in our calculations. Beam parameters (such as beam size, beam intensity, pulse length, etc.) and material properties (such as emissivity) are crucial for accurate thermal modeling. Big uncertainties on beam spot size and the emissivity of the material yielded too large uncertainties in the predicted temperatures. In an ideal case, temperature calibration measurements should be performed, which could not be done for several reasons. Thus, a systematic approach has been adopted to prove the suitability of the SEM grids. The harp was irradiated in the regular UNILAC 'grid protection mode', which at a spot size of σ = 3 mm an intensity of 500 µA and duration of 40 µs corresponds to a (calculated) temperature of ~2800 K. Starting from this point, the intensity and the pulse length were stepwise increased to 1.4 mA, 40 µs, which lead after a final step to 70 µs to destruction of some wires (T_{calc} = ~4200 K). The reasons for the strong increase of the current in Fig. 8, besides the position of the broken wires, is not clear. Several aspects contribute to the dynamic development of the profile, like time constant of the electronics and intensity variation during macro pulse.

To what extent thermionic emission plays a role has to be investigated. Analysis of the results and adjustment of our theoretical model is ongoing.

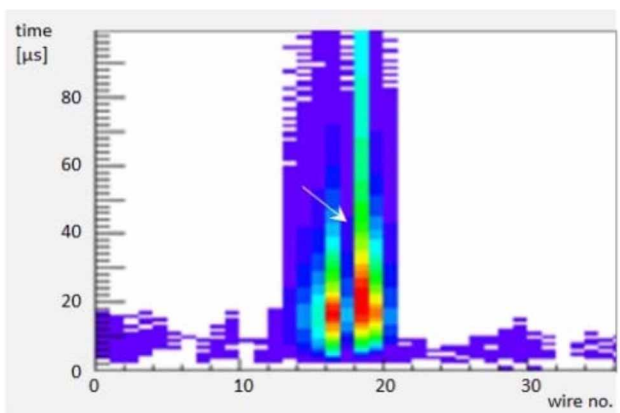


Figure 8: Development of the beam profile during one 70 µs macro pulse at destruction of one wire. Total span 100 µs, time slice 1 µs.

ISBN: 978-3-95450-241-7 ISSN: 2673-5350 doi:10.18429/JACoW-IBIC2022-WEP17

REFERENCES

[1] O. K. Kester, "Status of the FAIR Facility", in *Proc. IPAC'13*, Shanghai, China, May 2013, paper TUXB101, pp. 1085-1089.

[2] M. Miski-Oglu *et al.*, "Beam Commissioning of the Demonstrator Setup for the superconducting cw HMI/GSI Linac", *J. Phys.: Conf. Ser.*, vol. 1350, p. 012089, 2019. doi:10.1088/1742-6596/1350/1/012089

[3] L. Groening *et al.*, "Status of the FAIR 70 MeV Proton Linac", in *Proc. LINAC'12*, Tel Aviv, Israel, Sep. 2012, paper THPB034, pp. 927-929.

[4] R. M. Brodhage, A. Almomani, and U. Ratzinger, "Design Study of a High Frequency Proton Ladder RFQ", in *Proc. IPAC'13*, Shanghai, China, May 2013, paper THPWO014, pp. 3788-3790.

[5] G. Clemente *et al.*, "Development of room temperature crossbar-*H*-mode cavities", *Phys. Rev. ST Accel. Beams*, vol. 14, p. 110101, 2011. doi:10.1103/PhysRevSTAB.14.110101

[6] T. Sieber *et al.*, "Beam Diagnostics Layout for the FAIR Proton Linac", in *Proc. LINAC'14*, Geneva, Switzerland, Aug.-Sep. 2014, paper THPP063, pp. 998-1000.

[7] P. Forck, "Lecture Notes on Beam Instrumentation and Diagnostics", presented at Joint University Accelerator School (JUAS), Jan. 2011.

[8] M. Witthaus *et al.*, "SEM-GRID Prototype Electronics using Charge-Frequency-Converters", in *Proc. DIPAC'11*, Hamburg, Germany, May 2011, paper MOPD55, pp. 176-178.

[9] A. Navarro Fernandez, F. Roncarolo, and M. Sapinski, "Development of a Thermal Response Model for Wire Grid Profile Monitors and Benchmarking to CERN LINAC4 Experiments", in *Proc. IBIC'20*, Santos, Brazil, Sep. 2020, pp. 82-85. doi:10.18429/JACoW-IBIC2020-TUPP35

Content from this work may be used under the terms of the CC BY 4.0 licence (© 2022). Any distribution of this work must maintain attribution to the author(s), title of the work, publisher, and DOI

ISBN: 978-3-95450-241-7 ISSN: 2673-5350 doi:10.18429/JACoW-IBIC2022-WEP20

EMITTANCE DIAGNOSTICS AT PETRA IV

M. Marongiu*, G. Kube, M. Lantschner, A. Novokshonov, K. Wittenburg
Deutsches Elektronen-Synchrotron DESY, Germany

Abstract

The PETRA IV project will be a Diffraction Limited Light Source designed to be the successor of PETRA III, the 6 GeV 3rd generation hard X-Ray synchrotron light source at DESY in Hamburg. It will operate at a beam energy of 6 GeV with a design emittance of 20/4 pm rad. For a precise emittance online control, two dedicated diagnostics beamlines will be built up to image the beam profile with synchrotron radiation in the X-Ray region. With two beamlines, it will be possible to extract both the transverse beam emittances and the beam energy spread. Both beamlines will be equipped with two interchangeable X-Ray optical systems: a pinhole camera system to achieve high dynamic range and a Fresnel Diffractometry system for high resolution measurements in the range 1-18 µm. This paper describes the planned setup and deals with the possible limitations.

INTRODUCTION

The PETRA IV project [1] will be a Diffraction Limited Light Source designed to be the successor of PETRA III, the 6 GeV 3rd generation hard X-Ray synchrotron light source at DESY in Hamburg. It will operate at a beam energy of 6 GeV with a design emittance of 20/4 pm rad instead of the 1300/10 pm rad currently obtained in PETRA III. The machine will be installed in the same tunnel of the current operating one. Table 1 summarizes the main parameters of PETRA IV and PETRA III.

Table 1: Main Parameters of PETRA IV Compared with the Values Currently in Use at PETRA III

Parameters	PETRA IV	Petra III
Energy (GeV)	6	6
Circumference (m)	2304	2304
Current (mA)	80/200	100/120
Number bunches	80/1600	40/480
Emittance (pm rad)		
Horizontal	<20	1300
Vertical	<4	10
# Undulator beamlines	30	21 (26)

For a precise emittance online control, two dedicated diagnostics beamlines will be built up to image the beam profile with synchrotron radiation in the X-Ray region. With two beamlines in locations with different dispersion, it will be possible to extract both the transverse beam emittances and the beam energy spread. The emittance sensitivity required is 0.5 pm rad which translates in a beam size sensitivity requirement of 100 nm.

* marco.marongiu@desy.de

It will be also required to have a high dynamic range measurement; therefore, each beamline will be equipped also with an X-Ray pinhole camera system (XPC) to measure beam size above 15 µm. Figure 1 shows a sketch of the designed beamline. The overall beamline length of about 50 m derives from the requirement to place the detector part outside the accelerator tunnel.



Figure 1: Beamline sketch of the emittance measurement.

Different locations for the beamlines have been considered and, due to geometric constraints, it has been chosen a canted section using as a radiation source a 3 Pole Wiggler (3PW) with a peak magnetic field of around 0.8 T. Table 2 shows the main beam parameters at the beamline locations.

Table 2: Main beam parameters at the possible beamlines locations. The last column represents the relative dispersion contribution to the emittance. The 3 pole wiggler (3PW) considered has a peak magnetic field of around 0.8 T.

Rad. Source	β_x m	β_y m	σ_x µm	σ_y µm	D. %
3PW	4.6	4.6	9.6	4.3	0.04
3PW	2.6	2.6	8.1	3.3	10.3

X-RAY FRESNEL DIFFRACTOMETRY

In order to achieve a high resolution measurement, the X-Ray Fresnel diffractometry technique [2] (XFD) has been considered. Optimizing opportunely a single slit width (A), a double-lobed pattern emerges and the depth of its median dip is correlated to the source size (i.e. the dip becomes shallow with the increase of the source size). Figure 2 shows a sketch of the technique: the choices of the distance of the slit to the source point (L), the distance from the slit to the observation point (R) and the observing wavelength (λ) determine the slit width. The only requirement for the light

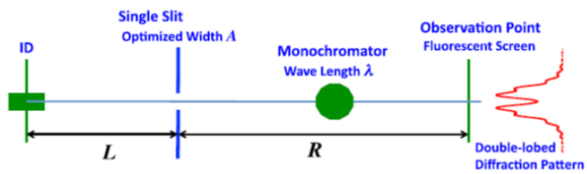


Figure 2: Sketch of the XFD measurement [2].

Content from this work may be used under the terms of the CC BY 4.0 licence (© 2022). Any distribution of this work must maintain attribution to the author(s), title of the work, publisher, and DOI

ISBN: 978-3-95450-241-7 ISSN: 2673-5350 doi:10.18429/JACoW-IBIC2022-WEP20

source is that the radiation should be a spherical wave with a flux distribution wider than the slit width.

Under these assumptions, the Point Spread Function (PSF) at the observation point can be expressed by Eq. (1).

$$I(y, y_e) \propto \left| \int_{-A/2}^{A/2} \sqrt{I_s(y_s - y_e)} \exp\left[j \frac{\pi}{\lambda} \frac{R+L}{RL} \left[(y_s - y_e) - \frac{L(y - y_e)}{L+R} \right]^2 \right] dy_s \right|^2, \quad (1)$$

where $I_s(y_s - y_e)$ is the flux intensity distribution of radiation at the slit, y_e is the electron position at the source point, y_s and y are the coordinates on the slit and the observation point, respectively.

Assuming an electron position at the source $y_e = 0$ and a constant flux distribution, Eq. (1) can be written as in Eq. (2).

$$\begin{aligned} N1 &= (R+L)A/2, \\ D &= \frac{\sqrt{RL\lambda(R+L)}}{(-1)^{1/4}\sqrt{\pi}}, \\ I(y) &\approx \left| \frac{(-1)^{3/4}\sqrt{\lambda RL}}{2\sqrt{R+L}} \left[Erfi\left(\frac{(-N1 - Ly)}{D} \right) \right. \right. \\ &\quad \left. \left. - Erfi\left(\frac{(N1 - Ly)}{D} \right) \right] \right|^2. \end{aligned} \quad (2)$$

The optimised aperture is obtained applying the condition of destructive interference of the light contributing to the center of the PSF ($y = 0$) and can be expressed as in Eq. (3).

$$A = \sqrt{7\lambda \frac{LR}{L+R}}. \quad (3)$$

The XFD scheme requires a monochromatic X-Ray: therefore, a Silicon (111) is considered to be used as a monochromator crystal since it generates a photon bandwidth narrow enough ($\approx 10^{-4}$).

The peak-to-valley intensity ratio is correlated to the beam source size: this correlation is particularly strong in a small interval of less than 20 µm (i.e. from 1 µm to 20 µm) where the sensibility to beam size variations reaches the sub-micron order. The precise values of sensitivities and dynamic range are related to the choice of the beamline parameters (λ, L, R).

For instance, Fig. 3 shows the sensitivity curves for different photon energies: it can be seen that lower energies correspond to higher dynamic range but also to lower sensitivity to small beam size changes. Indeed, the slope of the curves increases with the energy. Similar studies can be done varying the other beamline parameters: for instance, an increase of L or of R causes an increase of the dynamic range at the expense of the sensitivity.

For a quantitative estimation, one can evaluate the derivative of the sensitivity curves of Fig. 3 and observe in which

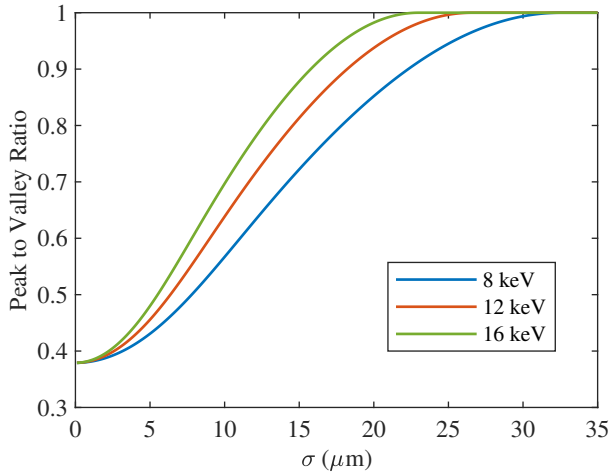


Figure 3: Sensitivity curves for three different observing photon energies. The curves are calculated considering $L = R = 20$ m and optimizing A for each energy according to Eq. (3).

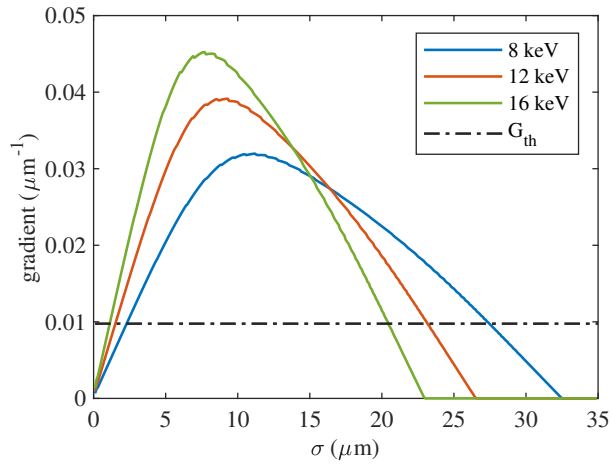


Figure 4: Derivatives of the sensitivity curves for three different observing photon energies. The sensitivity curves are calculated considering $L = R = 20$ m and optimizing A for each energy according to Eq. (3). The dash-dotted line represents the threshold value calculated for a sensitivity requirement of 100 nm and a camera sensor of 10 effective bits.

beam size range the derivatives are above a certain threshold. This threshold will be inversely proportional to the maximum sensitivity required and to the number of bits the camera sensor uses to digitize the intensity, as seen in Fig. 4. Hence, an increase of the number of bits of the sensor, or a more relaxed sensitivity requirement, allows a higher dynamic range.

Given the PETRA IV requirements, a possible solution is to place a slit at 30 m from the radiation source and the detector at 20 m from the slit selecting with a monochromator a photon energy of 16 keV; the optimized aperture value is 81 µm. This system is able to detect 100 nm beam size variation in a range between 1 µm and 18.9 µm assuming a camera sensor with 10 effective bits.

Content from this work may be used under the terms of the CC BY 4.0 licence (© 2022). Any distribution of this work must maintain attribution to the author(s), title of the work, publisher, and DOI

ISBN: 978-3-95450-241-7 ISSN: 2673-5350 doi:10.18429/JACoW-IBIC2022-WEP20

Content from this work may be used under the terms of the CC BY 4.0 licence (© 2022). Any distribution of this work must maintain attribution to the author(s), title of the work, publisher, and DOI

X-RAY PINHOLE CAMERA

In order to be able to measure with a higher dynamic range, also an X-Ray pinhole camera (XPC) will be implemented. The PSF is calculated in the image plane based on numerical near field calculations with the code SRW [3]. As a possible solution it is planned to place the pinhole at 10 m from the radiation source and, hence, at 40 m from the observation point; the pinhole aperture, optimized for a photon energy of 16 keV, is equal to 24 µm and the PSF rms size is 11 µm. Figure 5 shows the vertical profile of the PSF.

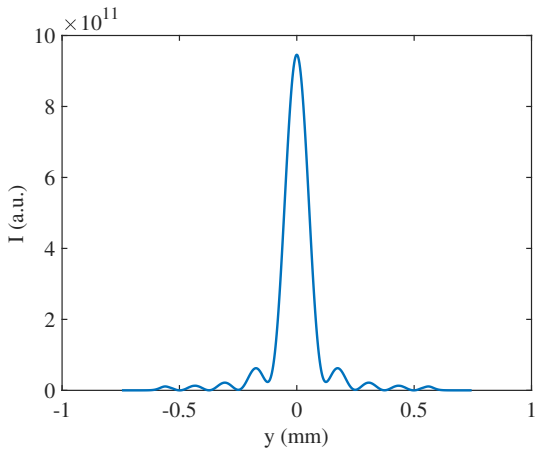


Figure 5: Vertical profile of the XPC PSF. The curve is calculated considering $L = 10$ m, $R = 40$ m, $E = 16$ keV and $A = 24$ µm.

One of the main issues regarding the XPC technique is the proper manufacturing of the pinhole target: indeed, in order to avoid the use of background subtraction techniques, the target must be thick enough (i.e. typically above 1 mm for radiation up to 60 keV) as shown in Fig. 6. Three materials have been considered: gold which was already tested at DIAMOND [4], the commonly used tungsten and tungsten carbide [5]. The transmission coefficient data, obtained with the simulation code SPECTRA [6], show that a 1 mm thickness could be sufficient in the case of gold and tungsten and a photon energy range below 60 keV; tungsten carbide requires instead a larger thickness (1.3 mm). The manufacture of a small aperture (about 25 µm) in a thick material (1 mm or more) is challenging: hence, different manufacturing techniques have been considered. At DIAMOND [4], a LIGA technique has been tested, however it is limited to about 250 µm thickness. Laser drilling results in a more suitable solution for thick material: a 20 µm hole in 1 mm gold target has been already produced successfully and will be tested in the near future. Studies for 2 mm thick material are ongoing.

Finally, it is fundamental to properly estimate the different contributions to the beam size measurement: indeed, the PSF of the pinhole, the PSF of the optical system and eventual misalignment contribute to the beam size measurement by adding in quadrature to the real rms beam size. A method to estimate all this contribution takes advantage of

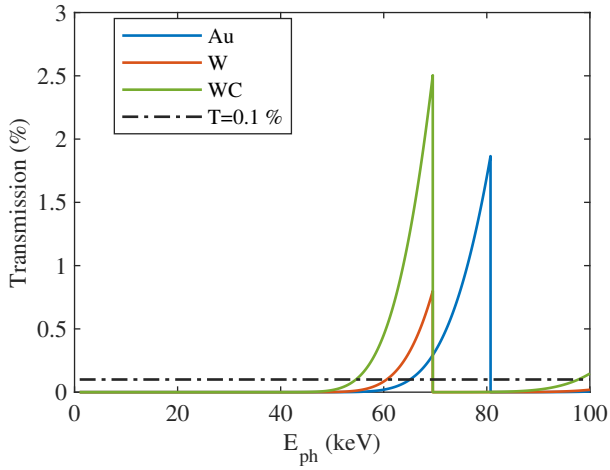


Figure 6: Transmission coefficient as a function of the photon energy for three different materials each one 1 mm thick. The blue curve represents gold, the red curve represents tungsten and the green one tungsten carbide. The dash-dotted curve represent the 0.1% threshold above which a background subtraction technique is required. Data calculated with the simulation code SPECTRA [6].

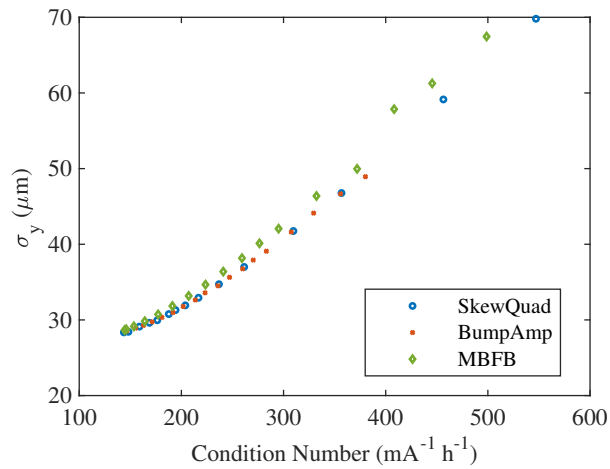


Figure 7: Measured rms vertical beam size as a function of the condition number. The blue circles represent the skew quadrupole case; the red dots represent the bump amplitude case and the green diamond the noise in the MBFB case.

the linear proportionality of the vertical beam size with the beam lifetime in Touschek dominated machine [4]. Three different sets of data have been taken at PETRA III to perform this evaluation: in the first one, the beam lifetime has been changed acting on the skew quadrupoles. In the second case, a localized symmetric dispersion bump in a damping wiggler has been used and in the last case, a white noise generator in the Multi Bunch Feedback (MBFB) has been used instead. Figure 7 shows a perfect overlapping of the first two data sets, while the third one shows a slightly different behaviour. However, the analysis of the full data is still ongoing.

ISBN: 978-3-95450-241-7 ISSN: 2673-5350 doi:10.18429/JACoW-IBIC2022-WEP20

CONCLUSION

The article summarizes the emittance diagnostic beamline setups that are currently planned for the PETRA IV machine. The possibility to observe beam size variation as small as 100 nm in a range between 1 µm and 18.9 µm is shown. To achieve a high dynamic range, a pinhole camera will be also installed. The article also deals with some possible limitations like the maximum aspect ratio achievable for the pinhole target with the currently available manufacturing techniques. Some prototypes are ready to be installed and tested in the PETRA III machine.

ACKNOWLEDGEMENT

The PETRA IV project team acknowledges funding of the technical design phase granted by the Behörde für Wissenschaft, Forschung, Gleichstellung und Bezirke (BWFGB) of the Freie und Hansestadt Hamburg, as well as by the Bundesministerium für Bildung und Forschung (BMBF) under the contract DES21TDR.

REFERENCES

[1] C. G. Schroer *et al.*, "PETRA IV: The ultralow-emittance source project at DESY," *J. Synchrotron Radiat.*, vol. 25, no. 5, pp. 1277–1290, 2018. doi:10.1107/S1600577518008858

[2] M. Masaki, S. Takano, M. Takao, and Y. Shimosaki, "X-Ray Fresnel diffractometry for ultralow emittance diagnostics of next generation synchrotron light sources," *Phys. Rev. Spec. Top. Accel Beams*, vol. 18, no. 4, p. 042 802, 2015. doi:10.1103/PhysRevSTAB.18.042802

[3] O. Chubar and P. Elleaume, "Accurate and Efficient Computation of Synchrotron Radiation in the Near Field Region," in *Proc. EPAC'98*, Stockholm, Sweden, Jun. 1998. https://jacow.org/e98/papers/THP01G.pdf

[4] L. M. Bobb and G. Rehm, "Beam Size Measurement Using High Aspect Ratio LIGA Apertures in an X-Ray Pinhole Camera," in *Proc. IPAC'17*, Copenhagen, Denmark, May 2017, pp. 445–447. doi:10.18429/JACoW-IPAC2017-MOPAB132

[5] F. Ewald, "Emittance measurement at ESRF-EBS with the X-Ray pinhole," presented at the Elettra 2.0 Workshop on Optical Diagnostics for Low-Emittance Storage Rings, 2022.

[6] T. Tanaka, "Major upgrade of the synchrotron radiation calculation code SPECTRA," *J. Synchrotron Radiat.*, vol. 28, no. 4, pp. 1267–1272, 2021. doi:10.1107/S1600577521004100

Content from this work may be used under the terms of the CC BY 4.0 licence (© 2022). Any distribution of this work must maintain attribution to the author(s), title of the work, publisher, and DOI

ISBN: 978-3-95450-241-7 ISSN: 2673-5350 doi:10.18429/JACoW-IBIC2022-WEP21

MERITS OF PULSE MODE OPERATION OF RESIDUAL GAS IONIZATION PROFILE MONITOR FOR J-PARC MAIN RING*

Kenichirou Satou†, Susumu Igarashi, and Yoichi Sato, J-PARC/KEK, Tokai, Japan

Abstract

The measurement accuracy of the ionization profile monitor (IPM) of J-PARC main ring (MR) depends on the flatness and stability of the gain of the position-sensitive microchannel plate (MCP). The flatness of the MCP deteriorates after long-term operation; the gain of the central area selectively decreases as the integrated output charge increases. The beam-based calibration, where the local bump shifts the beam and the reconstructing beam profiles determine the gain distribution, is used to calibrate the flatness. The immediate gain drop occurs when the output current from the MCP becomes comparable to the bias current is problematic. This gain drop depends on the bias voltage and the output current; thus, it is difficult to calibrate. A pulsed HV module of 30 kV, which collects ionized electrons and ions, was installed to solve these problems. The pulse mode operation can modulate the averaged output current from the MCP to improve gain stability. Profiles of the intense beam up to 3.3E13 particles per bunch were measured and compared with those measured by destructive profile monitors in beam transport lines 3–50 BT, and the Abort line. Estimated emittances were consistent at ±20%.

INTRODUCTION

The idea of detecting ionized electrons or ions generated by the interaction with residual gas to measure a beam profile was reported in the mid-1960s [1, 2]. The residual gas ionization profile monitor (IPM) has been widely used in proton and hadron synchrotrons because of its non-invasiveness to the beam since it does not insert solid material or gas into the beam. A small rate of nuclear collision with residual gas particles is preferable to a high-power proton synchrotron on its low beam power loss and thus lower induced remnant dose.

The first IPM system in KEK was used at KEK-PS [3], where the system collected positive ions using an external electric field (E_{ex}). These ions were detected using a microchannel plate (MCP). Similar monitors were designed for the J-PARC main ring (MR) and installed in 2008 [4-6]. These were operated in the ion collection using an intensive E_{ex} of 50 kV across 130 mm-size cage electrodes at the maximum. A horizontal type IPM (D2HIPM) and a vertical type IPM (D2VIPM) were installed in a straight line named Ins_B, where the horizontal dispersion function is zero. However, another horizontal type IPM (D3HIPM) is installed in the arc section, named Arc_C, where the horizontal dispersion function was non-zero. The Twiss parameters at these IPMs are (βx, βy, η_x) = (12.1 m, 27.3 m, 0 m), (13.1 m, 21.6 m, 0 m), and (8.4 m, 15.5 m, 2.0 m) for D2VIPM, D2HIPM, and D3HIPM, respectively. The MCPs are a two-stage type with 32 multi-strip anodes of 2.5 mm (in width), a glass tube with 15 μm in diameter, and an effective area of 30 mm × 80 mm. The resistances are 112 MΩ for D2HIPM and 120 MΩ for D2HIPM, respectively.

A fast data-taking system has realized the turn-by-turn (TxT) measurement. The TxT profiles are used widely in correction of dipole and quadrupole injection mismatches [7]. However, it was strenuous to measure beam emittance due to the strong beam space charge (E_{sc}) of MV/m level, signal purity contaminated with secondary electrons, and MCP's dynamic gain deterioration that occurred several msec after the electron multiplication occurred.

We modified the original DC type IPM to a gated IPM, where the pulsed E_{ex} is applied to switch the system in ~20 μs to solve the MCP's dynamic gain deterioration. The remaining sections describe this IPM system for J-PARC MR and the merits of pulse mode operation. Finally, the estimated accuracy of the system checked with the multi-ribbon profile monitors (MRPMs) in beam transport lines is presented.

IPM IMPROVEMENTS

At the initial stage of beam commissioning, where the beam intensity is 1/10 of the designed intensity of 4E13 ppb, three IPM systems were designed to collect positive ions with strong E_{ex} [4-6].

The dipole magnets were installed only in the D2HIPM to collect electrons against strong E_{sc} to measure an intense beam of several E13 particles per bunch (ppb) [8]. The guiding dipole field of B_g = 0.2 T was applied parallel to the vertical component E_{ext}, which was used to direct the electrons to the MCP. The B_g and the horizontal E_{sc} ($E_{sc\text{-}x}$) component produce an E × B drift motion, which converts the transversal kick by the $E_{sc\text{-}x}$ to the longitudinal drift motion.

Measuring only the ionized electrons, which are ~1000 electrons per bunch, is challenging. The contaminant of secondary electrons degenerates the signal purity and the measurement accuracy. To subdue the secondary electrons generated by the ion's impacts on the electrodes, we applied a simple idea of using a window on cage electrodes to collect the ions and demonstrated it first on IPM for the CERN PS [9]. This structure is called an ion trap. Applying the same idea subdues the secondaries onto the MCP detector and improves signal purity significantly [10].

It is necessary to check the difference in signal intensity between the ion and electron collection to check the signal purity; besides the detection efficiency of MCP, which is 10%–60% for electrons and 60%–85% for ions, in the case

* Work supported by Accelerator and Beamline Research and Technology Development for High-Power Neutrino Beams in the U.S.-Japan Science and Technology Cooperation Program in High Energy Physics.
† email address: kenichirou.satou@j-parc.jp

Content from this work may be used under the terms of the CC BY 4.0 licence (© 2022). Any distribution of this work must maintain attribution to the author(s), title of the work, publisher, and DOI

ISBN: 978-3-95450-241-7 ISSN: 2673-5350 doi:10.18429/JACoW-IBIC2022-WEP21

of the total kinetic energy of 2 ~ 50 keV, the signal intensities should be the same.

Finally, we used the pulse mode operation idea to improve our system. The pulse mode operation is realized at the Fermi National Accelerator Laboratory (FNAL) [11]. The system used the pulsed HV to accelerate the ionized particles onto the MCP detector. By using this system, we can modify operating duty by changing the gate width and operational frequency. A gated system was designed and installed in the D2HIPM [10]. The IPM operated with the system is called a gated IPM.

MERITS OF PULSE MODE OPERATION

By changing the gate width and timing, the gated IPM can modulate the duty of operation and monitor the signals at any time, for example, only 20 turn profiles after beam injection. The gated IPM has three merits.

The first is the extension of the MCP lifetime. Figure 1 shows an example of the measurement of gain flatness of the MCP, scanned with beams shifted horizontally by the local bump orbit. The initial gain of the MCP worsened as the integrated output charge increased in long-term usage. As shown in the Fig. 1 the gain at the center has decreased by approximately 40% since 2008. The lifetime of the MCP becomes much longer when the duty of the operation changes lower than 1%.

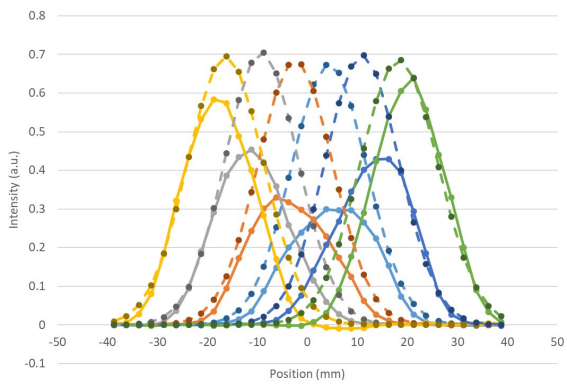


Figure 1: Gain balance measurement of MCP using a scanned beam shifted horizontally. Dashed lines are reconstructed profiles.

The second is to gain stability. Figure 2 shows the gain of a single-MCP glass tube (channel) modeled in [12] using a multi-dynodes model connected in parallel with the capacitor and resistor. Before the electron multiplication occurs, the capacitor is well charged. When a drain of a large current from a channel occurs, the stored charge in a capacitor decreases, and consequently, the local bias voltage. Thus, the local gain of the later stage of the dynodes decreases.

The output current limit should be 7% of the bias current of its channel (current channel) to maintain a flat gain. It also connects the channels in the in-plane direction. Fig. 3 shows that the sum of the signal from the MCP decreased immediately to 1/3 in 3 msec after the multiplication started. To measure profiles at, for example, 1 sec after the beam injection, fine-tuning of the bias voltage must ensure that the local output current from the beam center is less than 7% of the channel current.

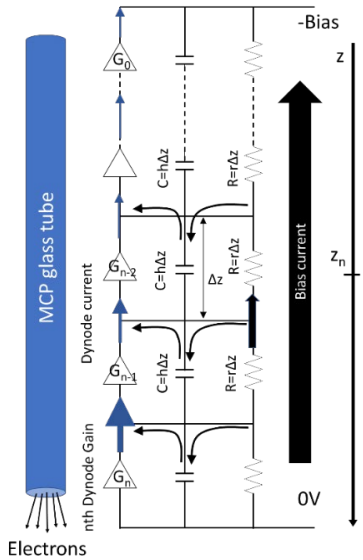


Figure 2: Multi-dynodes model of a single-MCP glass tune (channel).

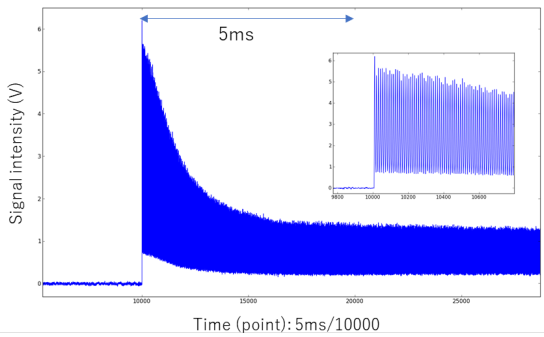


Figure 3: Total output current from the MCP, where the vertical scale factor is 1 V:10 µA. The output current is comparable to the bias current of MCP, 18 µA.

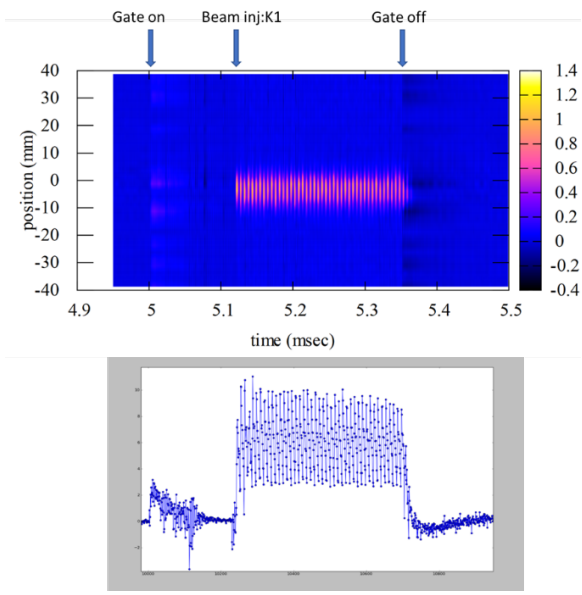


Figure 4: Signals from Gated IPM, just after the beam injection. The beam intensity was 2.4E13 ppb.

Content from this work may be used under the terms of the CC BY 4.0 licence (© 2022). Any distribution of this work must maintain attribution to the author(s), title of the work, publisher, and DOI

ISBN: 978-3-95450-241-7 ISSN: 2673-5350 doi:10.18429/JACoW-IBIC2022-WEP21

Content from this work may be used under the terms of the CC BY 4.0 licence (© 2022). Any distribution of this work must maintain attribution to the author(s), title of the work, publisher, and DOI

Under stable gain conditions, the gated IPM can select and measure beam profiles at any time. Figure 4 shows the cantor map and the sum signal of MCP, where the gate timing is selected for 20 turns after injection. The bias voltages were the same in both cases (Figs. 3 and 4).

The final is the stable gas pressure in the IPM chamber. The gated IPM, operated at 1% duty, did not change the gas pressure of 2.5E-7 Pa; the original IPM changed the gas pressure from 2E-7 Pa to 7E-7 Pa in about 10 sec. Stable gas pressure is preferable for checking the number of electrons detected from the output current.

DISCUSSION: PERFORMANCE CHECK WITH DESTRUCTIVE PROFILE MONITORS

We used the gated IPM to measure profiles for the beam whose intensity was between 2.4E12 ppb and 3.3E13 ppb (83% of the designed intensity), where only 3 GeV 1 bunch beams from the RCS were injected and accelerated to 30 GeV. The MRPM was used to measure the beam at the beam transport line from RCS to MR (3–50 BT) and at the Abort line to dump the beams. Furthermore, we extracted the beams at 3 GeV and 30 GeV to the Abort line. Figure 5 shows the locations of the IPMs and MRPMs.

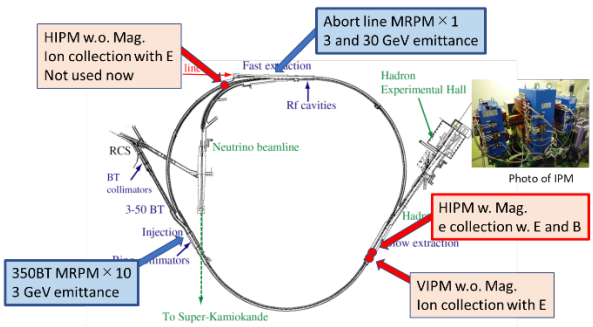


Figure 5: IPMs in MR and MRPMs in 3–50 BT and Abort line.

The HV and the B_g were set to −20 kV and 0.2 T, respectively. Similarly, the MCP's bias voltage was at 2.0 kV. Furthermore, we set the gate width and timing to measure only 20-turn profiles after the injection and before extraction. During the measurements, the gas pressure in the chamber was stable at 2.4E-7 Pa. Also, we repeated the measurement 20 times, and the signals were recorded and averaged to reduce the statistical error due to the small number of ionized electrons estimated to be 1.7E3 ppb for the 30 GeV beams with an intensity of 3.3E13 ppb.

The root mean square (RMS) emittance from the gated IPM was estimated as,

$$\varepsilon = ({\sigma_m}^2 - {\sigma_{anode}}^2 - {\sigma_{COD}}^2)/\beta_x \qquad (1)$$

where σ_m is the RMS width of a measured beam profile, σ_{anode} is the RMS width of the strip anode of the MCP, and σ_{COD} is the RMS of the deviation of the closed orbit distortion due to the ripple of the driving current to the bending magnets. The beam position monitors measured 0.7 mm σ_{COD} [13]. Also, the ripple currents to the quadruple magnet modulate the β_x. However, the estimated error was ±0.3% [13], which is negligible. The power supplies to the magnets are proposed to be replaced in 2022 [14] and the ripple will be improved to 1/10. Fig. 6 shows the profile measured at 3 GeV and 30 GeV, whose size is σ_m = 9.45 and 3.14 mm, respectively.

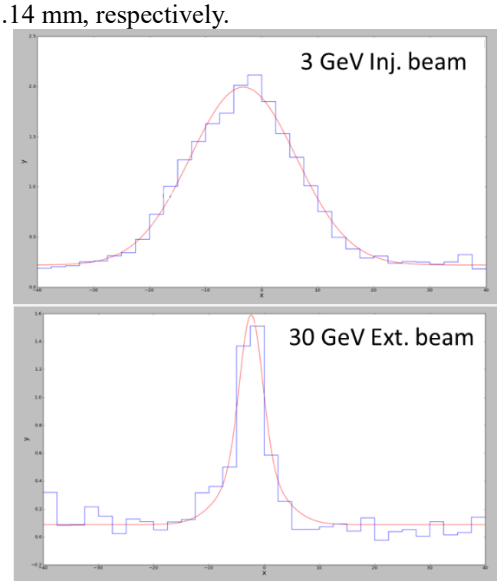


Figure 6: Profile measured by the gated IPM for the 3.3E13 ppb beam at injection and extraction energy. The blue lines are the measured profiles, and the red lines are the fitted results.

Figure 7 shows the beam parameters measured using the 10 MRPMs in 3–50 BT [15]. The beam intensity was 1.25E13 ppb. The solid lines represent the calculations using the optics parameters set to the 3–50 BT beam line. These calculations agree well with the measured data within an error of 4% in beam size.

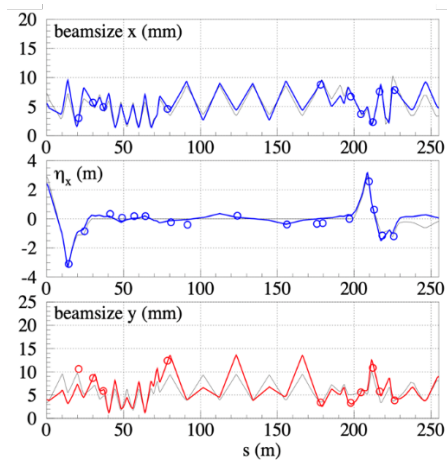


Figure 7: Beam parameters measured by the 10 MRPMs in 3–50 BT. Beam sizes for horizontal and vertical and dispersion function are shown with the calculation.

The beams whose intensity is 3.3E13 ppb, both the 3 GeV and 30 GeV cases, were also measured at the MRPM [16] in the Abort line. The Twiss parameters at the MRPM are (βx, βy, η_x) = (161 m, 15.2 m, −1.81 m) for 3 GeV and (147 m, 34.8 m, −1.78 m) for 30 GeV. The emittance was estimated as

ISBN: 978-3-95450-241-7 ISSN: 2673-5350 doi:10.18429/JACoW-IBIC2022-WEP21

$$\varepsilon = \frac{1}{\beta_x}\left\{{\sigma_m}^2 - {\sigma_{ribbon}}^2 - {\eta_x}^2\left({\Delta p}/{p}\right)^2\right\}, \qquad (2)$$

where σ_{ribbon} is the RMS size of the ribbon and ${\Delta p}/{p}$ denotes the momentum spread. The momentum spread is assumed to be 0.1% for both beams.

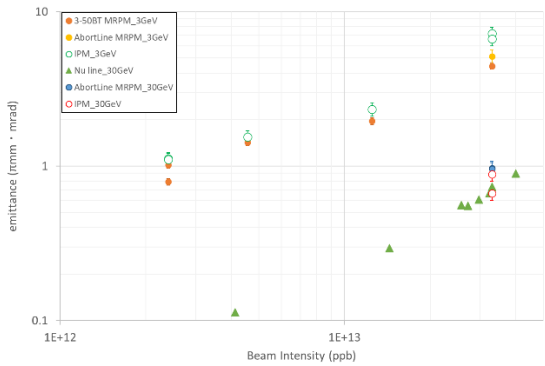


Figure 8: Emittance measured at the gated IPM and MRPMs. The open circles are from the gated IPM and the solid circles are from MRPMs. The solid triangle data were measured at the Neutrino beamline.

Figure 8 shows the estimated emittances. Also, we checked the estimated emittances using the data measured at the neutrino beamline [17, 18] at 30 GeV. The three datasets are consistent with each other by ±20%. The data from the gated IPM are 15% higher than that of the 3–50 BT MRPM measurement. A part of this would have originated from the optics mismatch of 3–50 BT to the MR because optics of the 3–50 BT were deliberately detuned to reduce beam loss after an injection.

SUMMARY

In this study, we improved the IPM system for J-PARC MR to measure electrons against strong E_{sp} and to eliminate secondary electrons. Furthermore, we upgraded it to a gated IPM system. Also, we have presented and elaborated on the three merits of the gated IPM. The beam emittance of intense beams up to 3.3E13 ppb was measured and compared with those from other profile monitors in the beam transport lines, 3–50 BT, Abort, and neutrino beamlines. The datasets used are consistent with each other by ±20%.

ACKNOWLEDGMENT

The author thanks Mr. J. R. Zagel and Dr. R. Thurman-Keup of the FNAL for their friendly and immense support received on the HV gate generator development and for several informative discussions on the gated IPM system.

REFERENCES

[1] V. Dudnikov, "The intense proton beam accumulation in storage ring by charge-exchange injection method", Ph.D. Thesis, INP, Novosibirsk, 1966: G. Budker, G. Dimov, and V. Dudnikov, in *Proc. Int. Symposium on Electron and Positron Storage Rings*, Saclay, France, 1966, Article No. VIII-6-1.

[2] F. Hornstra and W. H. Deluca, "Non-destructive beam profile detection systems for the ZGA", ANL internal report, 1967.

[3] T. Kawakubo, T. Ishida, E. Kadokura, Y Ajima, and T. Adachi, "Fast Data Acquisition System of a Non-Destructive Profile Monitor for a Synchrotron Beam by Using Micro Channel Plate with Multi-Anodes", *Nucl. Instrum. Methods Phys. Res., Sect. A*, vol. 302, pp. 397-405, 1991. doi:10.1016/0168-9002(91)90352-Q

[4] K. Satou *et al.*, "Beam Diagnostic System of the Main Ring Synchrotron of J-PARC", in *Proc. HB'08*, Nashville, TN, USA, Aug. 2008, paper WGF11, pp. 472-474.

[5] K. Satou *et al.*, "Development of IPM for J-PARC MR", in *Proc. 6th Accelerator Meeting in Japan*, Tokai, Aug. 2009, pp. 292-294.

[6] K. Satou, H. Harada, N. Hayashi, S. Lee, T. Toyama, and A. Ueno, "IPM Systems for J-PARC RCS and MR", in *Proc. HB'10*, Morschach, Switzerland, Sep.-Oct. 2010, paper WEO1C05, pp. 506-510.

[7] G. H. Wei *et al.*, "Beam Tuning of Injection and Fast Extraction of J-PARC MR", in *Proc. 6th Accelerator Meeting in Japan*, Tokai, Aug. 2009, pp. 307-309.

[8] K. Satou, H. Kuboki, and T. Toyama, "Profile Measurement by the Ionization Profile Monitor with 0.2T Magnet System in J-PARC MR", in *Proc. IBIC'16*, Barcelona, Spain, Sep. 2016, pp. 811-814. doi:10.18429/JACoW-IBIC2016-WEPG69

[9] K. Satou, J. W. Story, S. Levasseur, G. Schneider, D. Bodart, and M. Sapinski, "A Novel Field Cage Design for the CPS IPM and Systematic Errors in Beam Size and Emittance", *J. Phys. Conf. Ser.*, vol. 1067, 2018, p. 072008. doi:10.1088/1742-6596/1067/7/072008

[10] K. Satou, "Development of Gated IPM System for J-PARC MR", in *Proc. IBIC'19*, Malmö, Sweden, Sep. 8-12, 2019, pp. 343-346. doi:10.18429/JACoW-IBIC2019-TUPP020

[11] J. R. Zagel *et al.*, "Third Generation Residual Gas Ionization Profile Monitors at Fermilab", in *Proc. IBIC'14*, Monterey, CA, USA, Sep. 2014, paper TUPD04, pp. 408-411.

[12] L. Giudicotti, "Time-Dependent Model of Gain Saturation in Microchannel Plates and Channel Electron Multipliers", *Nucl. Instrum. Methods Phys. Res., Sect. A*, vol. 659, pp. 336-347, 2011. doi:10.1016/j.nima.2011.07.017

[13] T. Asami, private communication

[14] S. Igarashi *et al.*, "Accelerator Design for 1.3 MW Beam Power Operation of the J-PARC Main Ring", *Prog. Theor. Exp. Phys.*, vol. 2021, p. 033G01, 2021. doi:10.1093/ptep/ptab011

[15] Y. Hashimoto *et al.*, "Multi-ribbon Profile Monitor Using Carbon Graphite Foil for J-PARC", in *Proc. HB'10*, Morschach, Switzerland, Sep.-Oct. 2010, paper WEO2A01, pp 429-433.

[16] K. Sato, "Development of a Multi-Ribbon Prole Monitor in a beam dump line of J-PARC MR", MA theses, UTokyo, Tokyo, Japan, 2020.

[17] K. Sakashita, Preliminary data, Private communication.

[18] M. Friend, "Challenges in continuous beam profile monitoring for MW-power proton beams", in *Proc. IBIC'19*, Malmö, Sweden, Sep. 2019, pp. 253-256. doi:doi:10.18429/JACoW-IBIC2019-TUBO03

Content from this work may be used under the terms of the CC BY 4.0 licence (© 2022). Any distribution of this work must maintain attribution to the author(s), title of the work, publisher, and DOI

ISBN: 978-3-95450-241-7 ISSN: 2673-5350 doi:10.18429/JACoW-IBIC2022-WEP22

EXPERIMENTAL INVESTIGATION OF GOLD COATED TUNGSTEN WIRES EMISSIVITY FOR APPLICATIONS IN PARTICLE ACCELERATORS

A. Navarro*, M. Martin, F. Roncarolo, CERN, Geneva, Switzerland

Abstract

The operation of wire grids and wire scanners as beam profile monitors can be heavily affected, both in terms of measurement accuracy and wire integrity, by the thermal response of the wires to the energy deposited by the charged particles. Accurate measurements of material emissivity are crucial, as Radiative Cooling represent the most relevant cooling process. In this work, we present a method for emissivity measurements of gold-coated tungsten wires based on calorimetric techniques. The dedicated electrical setup allowed allowed transient and steady state measurements for temperatures up to 2000 K. A theoretical description of the measurement technique will be followed up by the electrical set up description and a detailed discussion about the measured results and uncertainties.

INTRODUCTION

Wire grids are examples of thin target detectors extensively used in particle accelerators for transverse beam profile measurements [1]. Depending on the the detector characteristics and beam parameters (intensity, energy, transverse and longitudinal beam size) the operation of the monitor can result in thermo-mechanical stresses, potentially perturbing the measurement accuracy and degrading the monitor integrity. To prevent these circumstances, a thorough understanding of the particle-detector interactions is of critical importance.

For simulating the particle-detector interaction and predict detector material heating and damage, a finite difference program has been implemented [2]. Uncertainties in the material properties such as melting (or sublimation) temperatures, heat capacity, thermal conductivity and/or emissivity, can induce large uncertainties in the simulation results. For published values in the scientific literature of the emissivity of tungsten wires (commonly used in particle accelerators), large uncertainties can be found. Figure 1 shows some examples of reported emissivity values as a function of the temperature.

To reduce the uncertainties of the thermal evolution models, we decided to experimentally measure the emissivity of gold-coated tungsten wires, widely used at CERN for wire grid detectors. Many techniques can be used for measuring the emissivity [3–5]. Each method has its own inherent advantages and drawbacks. The calorimetric method was used for the measurements reported in this paper. This methods gives information about the total hemispherical emissivity. The main advantage of this method is that it can measure small sample (~µm) sizes and it does not require expensive or sophisticated equipment. It is a direct absolute method, so no standard emissivity reference is necessary. Some disadvantages are: it is time consuming because it is typically performed in steady state; the sample needs to be placed under vacuum (typically 10^{-5} bar) to avoid convective losses; the measurement of the surface temperature is a big source of uncertainty.

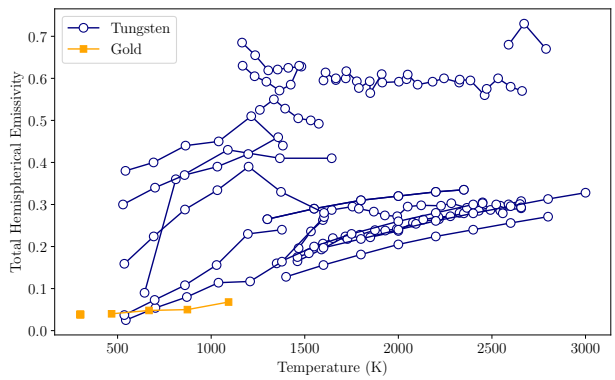


Figure 1: Examples of reported emissivity measurements for Gold and Tungsten. From Ref. [6].

SPECIFICS OF THE CALORIMETRIC METHOD

The calorimetric method is based on studying the energy balance of the sample material at a certain temperature, which is maintained via joule effect. For a temperature T, the resistance of a wire, with a wire length l(T), can be calculated by:

$$R(T) = \frac{\rho(T) l(T)}{S_f}, \quad (1)$$

where S_f is the section of the wire assumed to be constant over its length. $\rho(T)$ is the resistivity of the material and l(T) is the length of the sample, and they are both dependent on the material temperature. As a first approximation, l(T) can be modeled as a linear increase, $\Delta l(T) = l_0 \alpha_l (T - T_0)$, where α_l is the coefficient of thermal expansion. It is difficult to give a simple mathematical description of the variation of the resistivity with temperature, as it is very much material dependent. Tabulated values of the resistivity as a function of temperature can be found in literature.

Once thermal equilibrium is reached for a specific intensity, the average temperature of the sample can be determined by measuring the resistance and comparing it to the known values of R/R_0 for the material. The energy balance of the

* araceli.navarro.fernandez@cern.ch

Content from this work may be used under the terms of the CC BY 4.0 licence (© 2022). Any distribution of this work must maintain attribution to the author(s), title of the work, publisher, and DOI

ISBN: 978-3-95450-241-7 ISSN: 2673-5350 doi:10.18429/JACoW-IBIC2022-WEP22

system can be written as follows:

$$\left(\frac{\partial T}{\partial t}\right)_{tot} = \left(\frac{\partial T}{\partial t}\right)_{Ht} - \left(\frac{\partial T}{\partial t}\right)_{Rd} - \left(\frac{\partial T}{\partial t}\right)_{Con}, \quad (2)$$

where the term with the sub index Ht, represents heating, and it is accompanied by some cooling processes such as Radiative cooling (Rd) and Conduction cooling (Con). This term can be written as:

$$\left(\frac{\partial T}{\partial t}\right)_{Ht} = \frac{I^2 R(T)}{C_p(T)\rho_v V}. \quad (3)$$

Here I refers to the current applied to the wire sample and R is the resistance of that wire at a temperature T. C_p, ρ_v and V are the specific heat, the density and the volume of the wire. The heat power dissipated by radiation exchange between the surface (S) and the vacuum chamber at temperature T_0 is described by the Stefan-Boltzman law:

$$\left(\frac{\partial T}{\partial t}\right)_{Rd} = \frac{S\sigma_{SB}\epsilon(T)\left(T(x,t)^4 - T_0^4\right)}{C_p(T)\rho_v V}, \quad (4)$$

where σ_{SB} is the Stephan-Boltzmann constant and ϵ is the emissivity of the material. Finally, the thermal power loss due to thermal conduction can be described by Fourier's equation as follows:

$$\left(\frac{\partial T}{\partial t}\right)_{Con} = \alpha(T)\left(\frac{\partial^2 T}{\partial x^2}\right), \quad (5)$$

where $\alpha(T)$ is the so called thermal diffusivity of the medium (units of m^2/s).

In steady-state conditions ($\partial T/\partial t = 0$), Eq. (2) becomes a second order Boundary Value Problem (BVP) with Dirichlet boundary conditions (T(0) = T_{left} and T(L) = T_{right}). The solution of this equation can be calculated numerically. For that, the first step is to define a discrete set of nodes in the physical domain. Figure 2 shows an example of spatial discretization of an homogeneous wire. The parameter Δx indicates the local distance between the adjacent points in space.

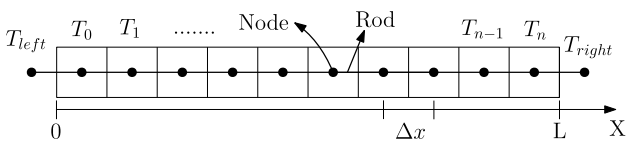


Figure 2: Space discretization of homogeneous rod.

Several numerical techniques exist to discretize the BVP [7]. For this study, a central difference (CD2) was considered for approximating the second order derivative. That is:

$$\left.\frac{d^2T}{dx^2}\right|_{x_i} = \frac{T_{i+1} - 2T_i + T_{i-1}}{2\delta_x^2} + O(\delta_x^2) \quad (6)$$

Note that with a little bit of algebra one can write the steady state equation as:

$$\begin{bmatrix} 1 & 0 & 0 & 0 & 0 & 0 \\ 1 & -2 & 1 & 0 & 0 & 0 \\ 0 & 1 & -2 & 1 & 0 & 0 \\ 0 & 0 & \ddots & \ddots & \ddots & 0 \\ 0 & 0 & 0 & 1 & -2 & 1 \\ 0 & 0 & 0 & 0 & 0 & 1 \end{bmatrix} \begin{bmatrix} T_0 \\ T1 \\ T2 \\ \vdots \\ T_N \\ T_{N+1} \end{bmatrix} = \begin{bmatrix} f_0 \\ f1 \\ f2 \\ \vdots \\ f_N \\ f_{N+1} \end{bmatrix},$$

where T_i are the unknowns of the BVP. $f_0 = T_{left}$ and $f_N = T_{right}$. While the rest can be written as:

$$f_i = \delta_x^2 \cdot \left(A + BT_i^4\right), \quad (7)$$

with $A = -\frac{1}{\alpha}\left(I^2R + S\epsilon\sigma_{SB}T_0^4\right)$ and $B = \frac{1}{\alpha}S\sigma_{SB}\epsilon$. Due to the T_i^4 term, this is nonlinear system of equations. For solving this system of equations Newton's method for non linear systems was used [7]. However, the objective of this study is to calculate the emissivity of the material, which is an extra unknown in our equation. For that, an iterative method with the following steps was used.

1. An initial guess of the emissivity is provided (ϵ_i^0, where the super-index indicates the iteration number).
2. With this value of the emissivity, the BVP is solved and then the average temperature along the wire is calculated (T_{sim}^n).
3. The numerically calculated average temperature is compared with the temperature measured experimentally (T_{meas}). The value of the emissivity is updated as follows:
$$\epsilon_j^{n+1} = \begin{cases} (\epsilon_j^n + 1)/2, & \text{if } e^n > 0 \\ (\epsilon_j^n)/2, & \text{if } e^n < 0 \end{cases}, \quad (8)$$
where $e^n = T_{sim}^n - T_{meas}$
4. This process is repeated until convergence.

EXPERIMENTAL DETAILS

A sketch of the experimental setup is shown in Fig. 3. The acquisition system consists of an assembly of two circuit boards: the measuring board and the acquisition board.

The measuring board has two main functionalities: holding the wire with both ends fixed on two turrets at a set distance, and measuring the current and the voltage drop in the wire. The current is measured by means of a shunt resistor, which was placed outside the vacuum to facilitate heat dissipation, and the voltage drop of the wire is measured directly at its mounting points, ensuring that only the voltage drop developed in the wire is taken into account. The board is located inside a vacuum vessel with a feed-through connector to transmit the signals across the vacuum barrier. The range of voltage (0 - 6 V) and intensity (0 - 2 A) applied to the wire cannot be directly measured by the Analogue-to-Digitcal Converters (ADC) and have to be processed beforehand by amplifiers with variable gain. The temperature at

Content from this work may be used under the terms of the CC BY 4.0 licence (© 2022). Any distribution of this work must maintain attribution to the author(s), title of the work, publisher, and DOI

ISBN: 978-3-95450-241-7 ISSN: 2673-5350 doi:10.18429/JACoW-IBIC2022-WEP22

Content from this work may be used under the terms of the CC BY 4.0 licence (© 2022). Any distribution of this work must maintain attribution to the author(s), title of the work, publisher, and DOI

the extremities of the wire (T_{left}, T_{right}) are measured by means of two temperature sensors mounted on the turrets.

The acquisition board captures and digitizes the measured signals, regulates the current flowing into the wire, and configures the measurement board for gain and common-mode offset. The measured current and voltage signals are digitized by the dual differential ADCs built into the microcontroller. The pulse conditioning block adapts the signal from the temperature sensors to the logic levels used by the microcontroller. The current, voltage and temperature signals are sent to a computer at a settable interval (minimum 100 µs) via a 1 Mbps USB serial connection.

The system is powered by a desktop power supply. Onboard DC-DC converters and linear regulators adapt the input voltage to the levels necessary to power the various analog parts of the circuit. The DAC, temperature sensor interface and the temperature sensors are powered by the USB connection from the computer. Four uncommitted amplifiers with BNC connectors are available to cross-check various signals with external equipment.

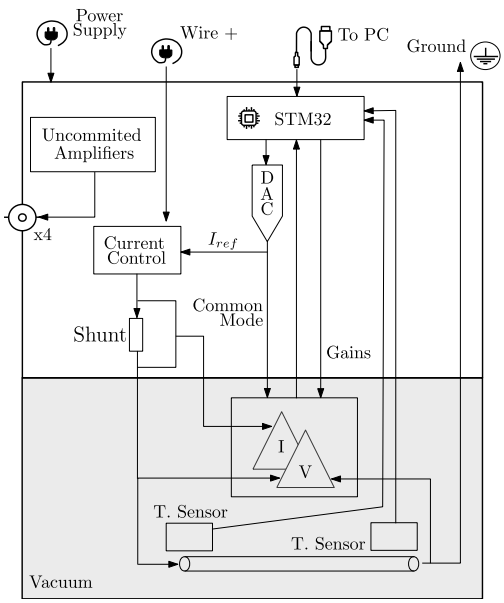


Figure 3: Schematic representation of electrical set-up.

RESULTS

For this analysis, Tungsten wires of two different diameters (20 µm and 40 µm) were measured, both with and without gold coating. Four samples of each wire type were measured to compile some statistics. Figure 4 shows the measured resistance (before calibration) as a function of time, for a 40 µm gold-coated Tungsten wire. In this case an intensity of 50 mA was provided. From this figure we can observe how the resistance increases until an equilibrium is reached. The steady-state (gray area) was considered to start when $dR/dt \lesssim 10^{-3}(\Omega/s)$. For each sample, the steady state resistance was computed for a variety of applied currents. A relationship between the average temperature and the applied intensity was calculated by comparing

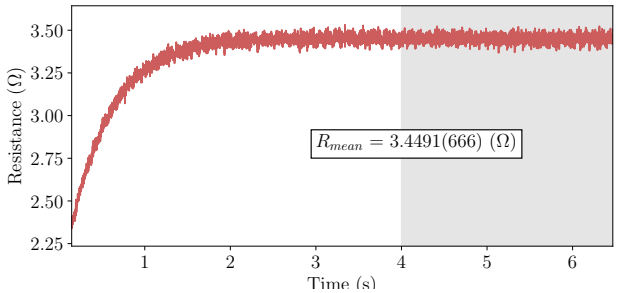


Figure 4: Raw data measurements (before calibration) of the resistance as a function of time. For a 40 µm gold-coated tungsten wire.

Table 1: Summary of R_0 Values for the Different Measured Cases

Composition	Diameter (µm)	R0 (ohm)
AuW	20	10.5(63)
AuW	40	1.438(76)
W	20	11.0(53)
W	40	1.562(58)

the measured resistance results with the tabulated values of R/R_0 [8]. To be able to compare our results to the tabulated ones, the value of R_0 was calculated using a parabolic model $R(I) = R_0 + AI^2$ and by extrapolating to zero. Only the low current ($I < 80$ mA) measurements were considered for determining R_0. Table 1 shows the values of the measured R_0 for the different samples. Note that the relative error when calculating R_0 for the 40 µm wires was smaller than 7%. However, the relative error for the 20 µm wires borders the 60%.

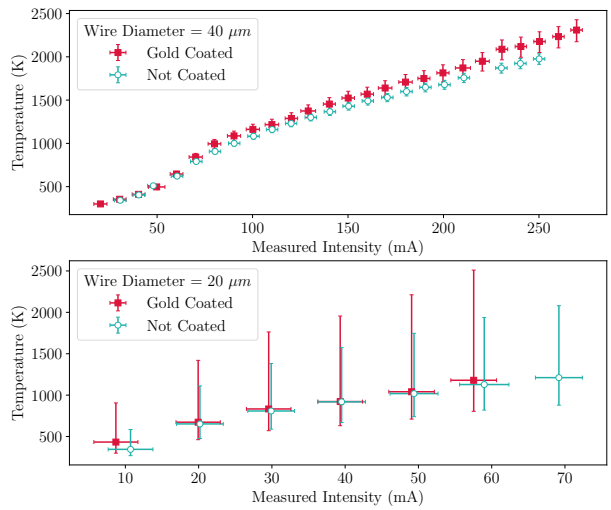


Figure 5: Mean temperature reached by the wires for different intensities. Top: 40 µm wires. Bottom: 20 µm wires.

The estimated values of the mean temperature as a function of the current are displayed in Fig. 5. A range of temperatures from 300 K to 2500 K was measured. The average temperature in the wires seemed to increase almost linearly

ISBN: 978-3-95450-241-7 ISSN: 2673-5350 doi:10.18429/JACoW-IBIC2022-WEP22

with the applied intensity. For the 20 µm wires, the uncertainties in the measurements of R_0 translated in big uncertainties in the determination of the wire temperature.

The boundary temperatures (T_{left} and T_{right}) increased quadratically with the applied current, always remaining below 350 K. Figure 6 shows the temperature (T_{left}) measured with the temperature sensors as a function of the applied intensity. For all the intensity range, $T_{left} \sim T_{right} \pm 1K$.

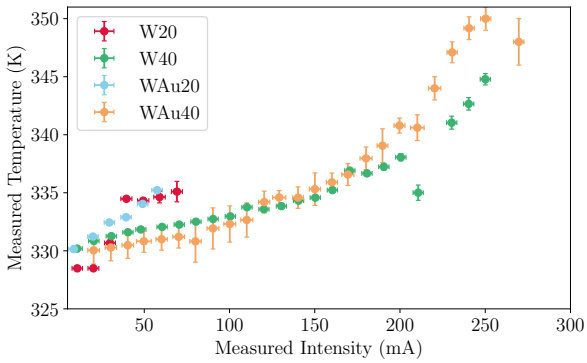


Figure 6: Summary of the boundary condition temperatures measured by the thermo-couple detectors at the extremes of the wires.

With increasing temperature, the temperature profile along the wire length becomes more constant. Figure 7 shows some examples of equilibrium thermal profiles computed for various currents. The numerical computation of the emissivity could be substantially simplified for high temperatures by assuming a constant profile. This is however not an accurate approximation at lower temperatures.

The emissivity of the material was calculated numerically for all the measured intensity range. It was not possible to determine the value of the emissivity for 20 µm wires due to the high uncertainties in the average temperature values. Figure 8 shows the computed values for the emissivity of the 40 µm wires. For both gold-coated and pure tungsten wires, the emissivity increased as the temperature increased. The emissivity of the pure tungsten wires was, in average, larger than the emissivity of the gold-coated tungsten wires, ranging from 0.087(12) up to 0.176(21). The emissivity values

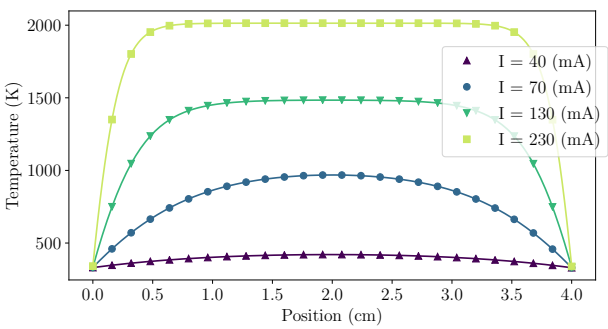


Figure 7: Steady state temperature profile calculated for different intensities.

for the gold-coated tungsten wires appear to be consistent with the reported values of the emissivity of gold. In the case of pure tungsten wires, both the slope of measured values agree with some published references. Particularly those reporting values of poor electromagnetic radiators. The average statistical relative error for the measured values (error bars in Fig. 8) was of 15.21% in the case of pure tungsten wires and 26.26% for gold-coated tungsten wires.

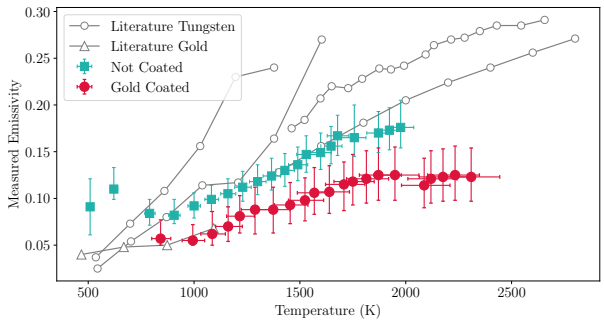


Figure 8: Emissivity of 40 µm. tungsten wires as a function of temperature.

CONCLUSIONS

In this article, a method to measure the emissivity of thin wires has been presented. Knowing accurately the value of the material is critical to properly simulate the thermal evolution of thin target detectors in particle accelerators. The measurement was done by means of the calorimetric methods. A dedicated set up, allowed for precise voltage and current measurements up to 2 A and 6 V respectively, which allowed for temperatures up to 2000 K to be measured. Due to the non-linearity of the BVP, numerical methods had to be used to determine the value of the emissivity. Several samples of tungsten wires (40 µm gold-coated and without coating) were measured. The values of the emissivity of the gold-coated wires appear to be consistent with the reported values of gold emissivity. The pure tungsten wires presented a systematically higher emissivity, however always smaller than 0.2. The average statistical error of the measured values was 15.21% for gold-coated wires and 26.26% for pure tungsten wires.

REFERENCES

[1] P. Forck, "Lecture notes on beam instrumentation and diagnostics", Joint Universities Accelerator School (JUAS 2010). http://www-bd.gsi.de

[2] A. Navarro Fernandez, F. Roncarolo and M. Sapinski, "Development of a Thermal Response Model for Wire Grid Profile Monitors and Benchmarking to CERN LINAC4 Experiments", in *Proc. IBIC'20*, Santos, Brazil, Sep. 2020, pp. 82–85. doi:10.18429/JACoW-IBIC2020-TUPP35

[3] A. El Bakali, R. Gilblas, T. Pottier, and Y. Le Maoult, "A fast and versatile method for spectral emissivity measurement at high temperatures", *Rev. Sci. Instrum.*, vol. 90, no. 11, p. 115116, 2019. doi:10.1063/1.5116425

[4] M. Honner and P. Honnerová, "Survey of emissivity measurement by radiometric methods", *Appl. Opt.*, vol. 54, no. 4, pp. 669-683, 2015. doi:10.1364/AO.54.000669

Content from this work may be used under the terms of the CC BY 4.0 licence (© 2022). Any distribution of this work must maintain attribution to the author(s), title of the work, publisher, and DOI

ISBN: 978-3-95450-241-7 ISSN: 2673-5350 doi:10.18429/JACoW-IBIC2022-WEP22

[5] C. Zhu, M. J. Hobbs and J. R. Willmott, "An accurate instrument for emissivity measurements by direct and indirect methods", *Meas. Sci. Technol.*, vol. 31, no. 4, p. 044007, 2020. doi:10.1088/1361-6501/ab5e9b

[6] Y. S. Touloukian, R. W. Powell, C. Y. Ho and P. G. Klemens, "Thermophysical properties of matter - the TPRC data series. Data book", United States, 1971.

[7] A. Meseguer, *Fundamentals of Numerical Mathematics for Physicists and Engineers*, Wiley, 2020.

[8] D. R. Lide, *CRC handbook of chemistry and physics*, vol. 85, CRC Press, 2004. doi:10.1201/9781315380476

Content from this work may be used under the terms of the CC BY 4.0 licence (© 2022). Any distribution of this work must maintain attribution to the author(s), title of the work, publisher, and DOI

ISBN: 978-3-95450-241-7 ISSN: 2673-5350 doi:10.18429/JACoW-IBIC2022-WEP23

ASSESSING THE PERFORMANCE OF THE NEW BEAM WIRE SCANNERS FOR THE CERN LHC INJECTORS

S. Di Carlo*, W. Andreazza, D. Belohrad, J. Emery, J.C. Esteban Felipe, A. Goldblatt, D. Gudkov, A. Guerrero, S. Jackson, G.O. Lacarrere, M. Martin Nieto, A.T. Rinaldi, F. Roncarolo, C. Schillinger, R. Veness
European Organization for Nuclear Research (CERN), Geneva, Switzerland

Abstract

Reliably measuring the transverse beam profile in the LHC injector chain is essential for the operation of the CERN accelerator complex. This report aims to assess the reliability, stability, and reproducibility of a new generation of beam wire scanners developed at CERN in the framework of the LHC Injectors Upgrade (LIU). The study includes data from over 60000 scans performed in 2021 and 2022, with a particular focus on reproducibility, investigation of optimal operational settings to ensure a large dynamic range, and evaluation of absolute accuracy through comparison with other instruments present in the injectors.

INTRODUCTION

The LHC Injectors Upgrade (LIU) [1] program started in 2010 with the purpose of improving the beam performance throughout the injector chain, in order to satisfy the specifications required by the High Luminosity LHC (HL-LHC) project, and was completed in 2021. In parallel to the improvement of the beam parameters, it was necessary to design various pieces of beam diagnostics instrumentation for the injectors: the LINAC4, the Proton Synchrotron Booster (PSB), the Proton Synchrotron (PS), and Super Proton Synchrotron (SPS). Following several years of design and testing of prototypes during the LHC Run2 (2015-2018) [2–6], the new beam instrumentation suite was installed during the second LHC Long Shutdown (LS2) in 2019 and 2020, while commissioning with beam started in 2021. This paper focuses on the description of the new LIU beam wire scanner (LIU BWS) design, giving a general overview followed by a more detailed evaluation of the performance at their particular location in each of LHC injectors involved: PSB, PS, and SPS.

THE LIU BEAM WIRE SCANNER

A BWS is an instrument designed to measure the transverse beam profile [7]. A thin wire passes through the beam producing a shower of secondary particles that are measured with a detection system. The rate of secondary particles is correlated with the position of the wire, allowing for the reconstruction of the 1-dimensional transverse profile of the beam, usually measured in the horizontal or vertical plane. Figure 1 shows a schematic of the LIU BWS working principle and architecture.

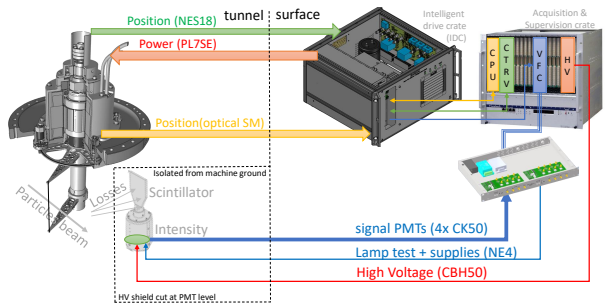


Figure 1: Schematic of the LIU BWS working principle and architecture [8]. The kinematic unit (the movable part of the scanner) and the detector measuring the secondary showers are placed in the accelerator's tunnel. These items are shown on the left side of the schematic. On the right side, we have the stand-alone control unit and the VME acquisition system, which are located in the service area on the surface. The CTRV is a CERN VME Timing Receiver board, while the VFC is the VME FMC Carrier board. The cables connecting tunnel and surface electronics are quite long, in some cases up to 150 m.

Upgrade Motivations

The design of a new LIU BWS was necessary in order to adequately measure the transverse profile of the new high intensity and brightness beams required by the HL-LHC project. The limitations of the present, old BWS are thoroughly discussed in previous works [9, 10] and here we briefly discuss some of the main shortcomings. The old wire scanners in the LHC injectors were either rotational (PSB, PS, SPS) or linear (SPS). The linear scanners in the SPS had strong limitations on beam intensity due to their low speed (1 m/s), leading to possible wire sublimation. For the rotational scanners the precision on the position of the wire was never better than 100 µm and was significantly degraded by electronic noise on the potentiometer reading, mechanical play, and vibrations [11]. From the operational point of view, the old wire scanners also required the operator to define the optimal working point for each measurement, which consisted of setting the detection parameters, i.e. the photo-multiplier tube (PMT) bias voltage and attenuation filter, before a beam profile could be measured. This often resulted in lengthy sessions of measurements. For the LIU BWS it was decided to design a unique standardised system, both, in terms of hardware and software, to satisfy the specifications of each of the LHC injectors. The LIU BWS is rotational, can be operated without need of selecting an op-

* salvatore.di.carlo@cern.ch

Content from this work may be used under the terms of the CC BY 4.0 licence (© 2022). Any distribution of this work must maintain attribution to the author(s), title of the work, publisher, and DOI

ISBN: 978-3-95450-241-7 ISSN: 2673-5350 doi:10.18429/JACoW-IBIC2022-WEP23

Content from this work may be used under the terms of the CC BY 4.0 licence (© 2022). Any distribution of this work must maintain attribution to the author(s), title of the work, publisher, and DOI

timal working point, and features higher speeds of the wire, up to 20 m/s in the PSB and 24 m/s in the PS and SPS. The LIU BWS is designed to improve reliability and availability, and in some cases increase the accuracy of the beam profile measurement.

Hardware Upgrades Overview

The LIU BWS features carbon wires with a 30 µm diameter. The kinematic unit has moving parts only in vacuum and uses magnetic and optical means to transfer power and signals to the outside. A solid rotor resolver and an optical encoder are used to measure the position of the shaft. The rotor resolver is used for trajectory control [12], while the optical encoder is used to precisely infer the fork and wire position during a scan [13]. The encoder was calibrated using a laser and exploiting the reflective and anti-reflective slits (40 µm pitch) engraved on the optical disc mounted on the shaft. The calibration allows to compensate for the uncertainties of the wire trajectory that are caused by the large acceleration to which the carbon wire is subjected [14]. The secondary shower is measured using one plastic scintillator (BC-408) coupled to four PMTs (Hamamatsu R9880U) and a related data acquisition system (DAQ). Neutral density filters of different optical density are used in front of each PMT to provide four different levels of attenuation. This scheme enables to cover the large dynamic range of signals coming from the secondary showers, with beams varying in energy (from 160 MeV to 450 GeV) and intensities (from about 10×10^{10} ppb to about 500×10^{10} ppb) across the LHC injectors [10]. Finally, the four output signals are digitized simultaneously by fast FMC ADCs with a sampling rate of 500 MS/s, which is sufficient to measure the profile of each bunch in the beam.

BWS PERFORMANCE ASSESSMENT

The first prototype LIU BWS was validated in 2017 and 2018 in all the injectors [15], and seventeen BWSs with the final design were installed during LS2. These are eight units in the PSB, five units in the PS, and four units in the SPS. The commissioning of the BWSs in the LHC injectors started in 2021, following the restart of the PSB in December 2020. The new BWSs have been extensively used in 2021 and 2022 to setup, tune, and characterize the new LIU beams, resulting in tens of thousand of scans, as shown in Figure 2. The only system failure reported in 2021 was a broken wire, due to an issue with carbon wire copper coating (used to facilitate the wire fixation), which was already known since the first LS2 tests.

Measurement Examples and Working Point Studies

Figure 3 shows an example LIU BWS beam profile measurement in the horizontal plane of a LHC25 beam in the PSB. Each measurement results in four estimations of the beam size, corresponding to the four PMTs with different attenuation. The best estimation of the beam size can be obtained by properly changing the high voltage and using

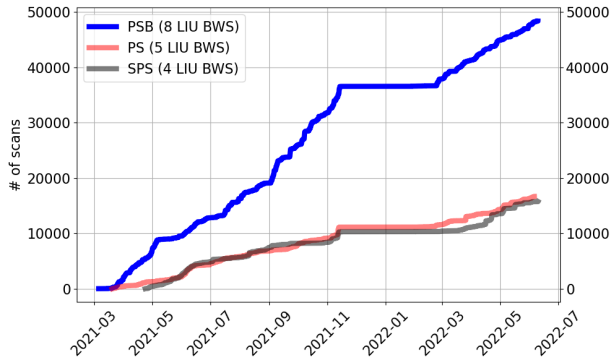


Figure 2: LIU BWS usage in 2021 and early 2022.

the appropriate PMT channel, with PMT channels with different attenuation agreeing within 3% in terms of beam size. The bias voltage for the PMTs must be chosen to ensure the signal is above the noise level, but at the same time does not saturate the digitizers or cause the PMTs to operate outside their linear regime. Both these effects may lead to an overestimation of the beam size. Currently, three high voltage bias levels can be selected by the operator to cope with the different beam types operated in the LHC injectors. Once the optimal high voltage has been selected, the BWS system has an algorithm to automatically select the best PMT read-out.

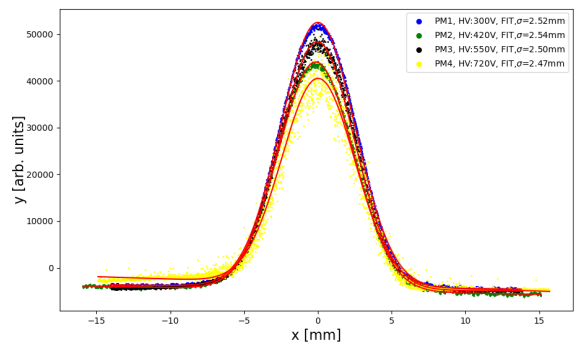


Figure 3: PSB horizontal profile of a LHC25 beam as measured by one of the LIU BWS.

Figure 4 shows one of the studies, performed to evaluate the selection of the optimal high voltage working point for the acquisition of a beam profile, in this case measuring the horizontal size of a LHCINDIV beam in the PSB. The high voltage was increased from 300 V to 1000 V in steps of 25 V and each time three scans were performed for statistical reasons. To select the best PMT for each measurement, we can either choose the one whose Gaussian fit to the beam profile corresponds to the minimum relative residual per point calculated as $\frac{1}{n}\sum_{i=1}^{n}\frac{|y-y_{fit}|}{y}$ where n is the number of points considered, or the one provided by the system's algorithm based on the ADC saturation detection. The upper plot of Figure 4 shows both histograms of beam sizes selected using either of these criteria. Both selections provide an average sigma of 2.21 mm, but the set of beam

ISBN: 978-3-95450-241-7 ISSN: 2673-5350 doi:10.18429/JACoW-IBIC2022-WEP23

sizes selected by the algorithm has a lower relative standard deviation (STD). The same study has been performed for other PSB beams with similar results. That proves that the algorithm is working properly and it is able to automatically provide the optimal PMT for each measurement. The lower plot of Figure 4 shows all the beam sizes obtained during the same high voltage scan, with each PMT plotted with a different color. Noticeable, each PMT provides a stable measurement, about 2.21 mm, within a certain range (indicated by vertical magenta lines), but it is degraded outside this range due to noise (lower voltages) or saturation (higher voltages). Similar studies have been performed at the PS and SPS.

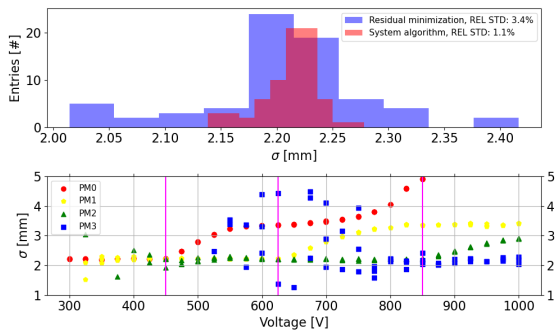


Figure 4: Top: comparison between residual minimization and algorithm methods to select optimal PMT. Bottom: voltage scan with vertical lines indicating optimal ranges for each PMT.

Figure 5 shows an example of LIU BWS measurement in the SPS for beams of type LHC25, with bunches separated by 25 ns. The upper plot shows the vertical profiles for each bunch in a batch of 72 bunches, and the lower plot the corresponding emittances. The emittance growth at the end of the batch is physical and it a result of electron cloud effects.

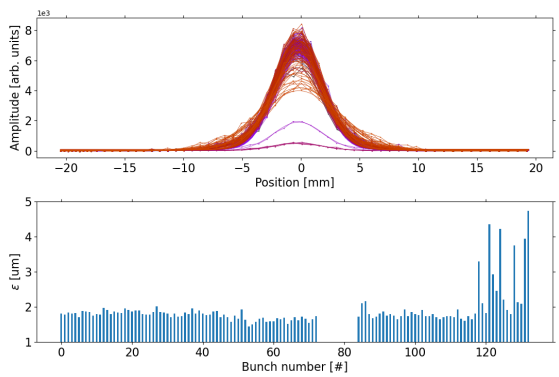


Figure 5: Top: SPS profiles of bunches separated by 25ns. Bottom: corresponding bunch-by-bunch emittances.

Preliminary Uncertainty Assessment

Since the LEGACY rotational BWSs were maintained in the PSB, we can directly compare them with the LIU BWSs. Figure 6 shows a comparison for the vertical emittance of different beams obtained with 30 measurements for each beam. We compare vertical emittances to minimize uncertainties arising from dispersion functions and momentum spread. The comparison indicates good agreement, demonstrating that the measurements provided by the LIU system are consistent. Mixing measurements from both systems and calculating the average RMS provides an upper limit estimation of the systematic uncertainty of 4%. The average statistical uncertainty is about 3% for the LEGACY system and 2% for the LIU system, and it was estimated from the RMS of the beams size distributions. Preliminary upper limit statistical uncertainty estimations on the beam size are 3% and 5% for the PS and SPS LIU BWSs, respectively.

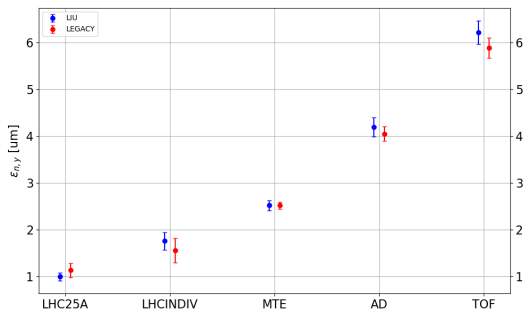


Figure 6: Comparison between LEGACY and LIU BWSs in the PSB for different beam types.

CONCLUSION AND OUTLOOK

The successful beam commissioning of the new LIU BWSs in the LHC injectors was presented, which demonstrated reliable and precise measurements with improved availability compared to the old BWSs. The next steps of the LIU BWS commissioning are the comparison between BWS and BGI in the PS, measurements at the SPS flat-top energy with reduced rotational speed, and further analysis where the uncertainty on the beam size measurement will have to be necessary decoupled from the bunch-by-bunch and shot-by-shot beam jitters, in order to provide a complete assessment of the LIU BWS absolute accuracy and resolution. Two new prototypes BWS have been designed for the LHC, in the context of an electro-mechanical consolidation, to cope with previous recurring operational system failures. The LHC prototypes are linear - in contrast with the rotational BWS installed in the LHC injectors in the context of the LIU upgrade - and mechanical modifications and new electronics have been designed. These prototypes will need to be extensively commissioned in expert mode, benefiting from the previous experience with the commissioning of the rotational BWS for the LHC injectors.

ACKNOWLEDGEMENTS

We gratefully acknowledge the help, during BWS measurement sessions, of Gian Piero Di Giovanni, James Ridewood, Hannes Bartosik, and Georges Trad.

Content from this work may be used under the terms of the CC BY 4.0 licence (© 2022). Any distribution of this work must maintain attribution to the author(s), title of the work, publisher, and DOI

ISBN: 978-3-95450-241-7 ISSN: 2673-5350 doi:10.18429/JACoW-IBIC2022-WEP23

Content from this work may be used under the terms of the CC BY 4.0 licence (© 2022). Any distribution of this work must maintain attribution to the author(s), title of the work, publisher, and DOI

REFERENCES

[1] M. Meddahi *et al.*, "LHC Injectors Upgrade Project: Towards New Territory Beam Parameters," in *Proc. 10th International Particle Accelerator Conf. (IPAC'19)*, Melbourne, Australia, 2019, pp. 3385–3390. doi:10.18429/JACoW-IPAC2019-THXPLM1

[2] M. Koujili *et al.*, "Fast and high accuracy wire scanner," in *Proc. 9th European Workshop on Beam Diagnostics and Instrumentation for Particle Accelerators (DIPAC'09)*, Basel, Switzerland, 2009, pp. 188–190.

[3] M. Koujili, Y. Ait-Amirat, B. Dehning, A. Djerdir, J. Emery, and J. H. Alvarez, "Design of an actuator for the fast and high accuracy wire scanner," in *2011 IEEE International Electric Machines Drives Conf. (IEMDC)*, 2011, pp. 1450–1455. doi:10.1109/IEMDC.2011.5994822

[4] R. Veness *et al.*, "Experience from the Construction of a New Fast Wire Scanner Prototype for the CERN- SPS and its Optimisation for Installation in the CERN-PS Booster," in *Proc. 4th International Beam Instrumentation Conf. (IBIC'15)*, Melbourne, Australia, 2016, pp. 479–482. doi:10.18429/JACoW-IBIC2015-TUPB061

[5] J. H. Alvarez, B. Dehning, and A. B. Condomines, "Minimisation of the wire position uncertainties of the new CERN vacuum wire scanner," Ph.D. dissertation, 2016. https://cds.cern.ch/record/2156989

[6] J. Emery *et al.*, "Design and validation methodology of the control system for a particle beam size measurement instrument at the CERN laboratory," in *2017 American Control Conf. (ACC)*, 2017, pp. 4221–4228. doi:10.23919/ACC.2017.7963604

[7] F. Roncarolo, "Accuracy of the transverse emittance measurements of the CERN large hadron collider," eng, Ph.D. dissertation, SB, 2006. doi:10.5075/epfl-thesis-3402

[8] J. Emery *et al.*, "Commissioning of the LHC Injectors BWS Upgrade," in *Proc. 10th International Beam Instrumentation Conf. (IBIC'21)*, Pohang, Rep. of Korea, 2021, pp. 239–243. doi:10.18429/JACoW-IBIC2021-TUPP18

[9] G. Baud *et al.*, "Performance Assessment of Wire-Scanners at CERN," 4 p, 2013. https://cds.cern.ch/record/1638354

[10] J. L. Sirvent Blasco, "Beam secondary shower acquisition design for the CERN high accuracy wire scanner," Presented 12 Dec 2018, 2018. https://cds.cern.ch/record/2640438

[11] A. E. Lokhovitskiy, A. Guerrero, and J. Koopman, "Fast wire scanner calibration system," in *Proc. 9th European Workshop on Beam Diagnostics and Instrumentation for Particle Accelerators (DIPAC'09)*, Basel, Switzerland, 2009, pp. 170–172.

[12] J. Emery, P. Andersson, F. Roncarolo, and Y. Thoma, "A low fluctuation control strategy for PMSM direct drive system targeting Particle Beam Instrumentation Application," in *Proc. 3rd IEEE Conf. on Control Technology and Applications (CCTA'19)*, Hong Kong, China, 2019. doi:10.1109/CCTA.2019.8920688

[13] J. L. Sirvent, J. Emery, and J. M. A. Poveda, "Design of an optical fibre based angular position sensor for wire scanners complying with ultra-high vacuum, high temperature and radiation conditions of the CERN's accelerators," Masters Thesis, Miguel Hernandez U., 2012. https://cds.cern.ch/record/1491608

[14] J. Emery *et al.*, "Laboratory and beam based studies for assessing the performance of the new fast wire scanners for the cern injector complex," in *Proc. 8th International Beam Instrumentation Conf. (IBIC'19)*, Malmö, Sweden, 2019, pp. 392–396. doi:10.18429/JACoW-IBIC2019-TUPP033

[15] J. Sirvent *et al.*, "Performance Assessment of Pre-Series Fast Beam Wire Scanner Prototypes for the Upgrade of the CERN LHC Injector Complex," in *Proc. 6th International Beam Instrumentation Conf. (IBIC'17)*, Grand Rapids, MI, USA, 2017, pp. 338–341. doi:10.18429/JACoW-IBIC2017-WEPCC03

ISBN: 978-3-95450-241-7 ISSN: 2673-5350 doi:10.18429/JACoW-IBIC2022-WEP24

MODELING AND EXPERIMENTAL EVALUATION OF A BUNCH ARRIVAL-TIME MONITOR WITH ROD-SHAPED PICKUPS AND A LOW-PI-VOLTAGE ULTRA-WIDEBAND TRAVELING WAVE ELECTRO-OPTIC MODULATOR FOR X-RAY FREE-ELECTRON LASERS*

A. Kuzmin†, E. Bründermann, C. Eschenbaum,C. Koos, A. Kotz, A.-S. Müller,
G. Niehues, A. Schwarzenberger, Karlsruhe Institute of Technology KIT, Karlsruhe, Germany
B. E. J. Scheible[1,‡], A. Penirschke, Technische Hochschule Mittelhessen, Friedberg, Germany
M. K. Czwalinna, H. Schlarb, Deutsches Elektronen-Synchrotron DESY, Hamburg, Germany
W. Ackermann, H. De Gersem, Technische Universität Darmstadt, Darmstadt, Germany
[1]also at Technische Universität Darmstadt, Darmstadt, Germany

Abstract

X-ray Free-Electron Laser (XFEL) facilities, such as the 3.4 km European XFEL, require long-range synchronization that necessitate the use all-optical links with electro-optic bunch arrival-time monitors (BAM). Current BAM systems achieve a resolution up to 3.5 fs for 250 pC bunches. Precise bunch arrival timing is essential for experiments, which study ultra-fast dynamical phenomena with highest temporal resolution. Future experiments will crucially rely on femtosecond pulses from bunch charges well below 20 pC. State-of-the-art BAMs are not allowing accurate timing for operation with such low bunch charges. Here, we report on the progress in the development of an advanced BAM based on rod-shaped pickups mounted on a printed circuit board and ultra-wideband travelling-wave electro-optic modulators with low operating voltages. We perform modeling and experimental evaluation for the fabricated pickups and electro-optic modulators and analytically estimate timing jitter for the advanced BAM system. Additionally, we discuss an experimental setup to demonstrate joint operation of new pickups and wideband EO modulators for low bunch charges less than 5 pC.

INTRODUCTION

X-ray Free-Electron Laser (XFEL) operation depends on a synchronization system with high timing stability and fs-precision [1]. Furthermore, precise bunch arrival timing between FEL and external laser pulses is essential for experiments, which study ultra-fast dynamical phenomena with highest temporal resolution [2]. For this reason, an all-optical synchronization system is implemented in several facilities, e.g. the 3.4 km long European XFEL [3].

This synchronization system is based on a pulsed optical reference, which is emitted by a commercial laser oscillator locked to the main oscillator for medium and long-term stability [1]. The reference laser pulses are distributed to different end-stations, e.g. electro-optic (EO) bunch arrival-time monitors (BAMs), via actively length-stabilized all-optical fiber links [1]. The BAM stations allow for precise arrival-time measurements by coupling to transient fields of every single bunch with cone-shaped pickups [1, 4, 5]. A bipolar radio-frequency (rf) pulse is fed to an electro-optic modulator (EOM) where the rf pulse is matched with the optical reference pulse [4]. The laser amplitude is modulated linearly to the arrival-time deviation, which can be determined afterwards in the data acquisition electronics [4].

The current BAMs achieve single bunch arrival-time measurements with a resolution of 3.5 fs for 250 pC bunches [6]. Experiments will crucially rely on fs pulses from bunch charges well below 20 pC. Therefore, an updated BAM for bunch charges lower than 5 pC is targeted. In this contribution the progress made in the two sub-projects is compiled and the overall improvement is estimated. Additionally, possibilities of the experimental demonstration are discussed.

NEW BAM DESIGN

In an ongoing project two components of the BAMs have been redesigned. The first objective was to update the pickups in order to increase the voltage signal by a factor of 10. The second objective was to develop and test a new electro-optical modulator which would allow further increase of timing resolution of a BAM. The new EOM has to be simultaneously broadband and has to feature low π-voltage.

Pickups

The state-of-the-art 40 GHz-pickups were shaped as a cone to reduce ringing and reflections by a constant line impedance [5]. In simulations they achieve 15 mV pC^{-1} ps^{-1} as normalized signal slew rate (SR), which is a decisive characteristic for the overall BAM sensitivity. The signal slope could be increased significantly by switching to an open-coax design with prolonged inner conductor, because of an increased active surface and reduced distance to the bunch [7]. Further improvement was found by implementation of these pickups in form of a rod mounted on a printed circuit board (PCB), their four signals are combined and fed to a common vacuum feedthrough [7]. This design surpassed the goal of 150 mV pC^{-1} ps^{-1} in simulations [7].

* Work supported by the German Federal Ministry of Education and Research (BMBF) under contract No. 05K19VKB and 05K19RO1.
† artem.kuzmin@kit.edu
‡ bernhard.scheible@iem.thm.de

Content from this work may be used under the terms of the CC BY 4.0 licence (© 2022). Any distribution of this work must maintain attribution to the author(s), title of the work, publisher, and DOI

ISBN: 978-3-95450-241-7 ISSN: 2673-5350 doi:10.18429/JACoW-IBIC2022-WEP24

Content from this work may be used under the terms of the CC BY 4.0 licence (© 2022). Any distribution of this work must maintain attribution to the author(s), title of the work, publisher, and DOI

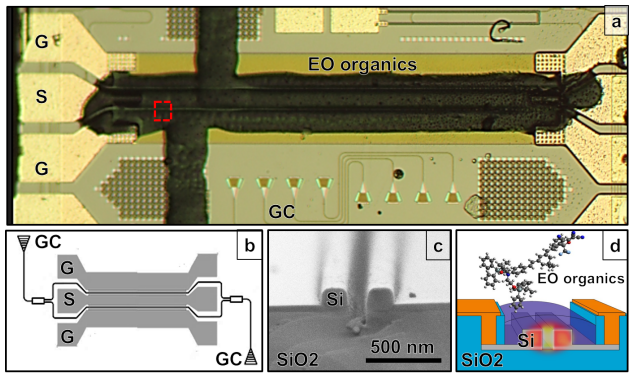


Figure 1: Silicon-Organic Hybrid MZM; **a:** optical image of 1-mm-long SOH-MZM with dispensed organic EO material; **b:** schematic representation of an MZM based on coplanar ground-signal-ground (GSG) electrodes, photonic waveguides and grating couplers (GC) for in/out -coupling of light; **c:** SEM image of a cross section of a Si slot-waveguide in one arm of MZM (region denoted with red square on **a**); **d:** schematic cross section of the SOH phase shifter.

EOMs

In the ongoing project we are developing Silicon-Organic Hybrid (SOH) traveling-wave Mach-Zehnder Modulators (MZM) with push-pull electrode configuration as shown in Fig. 1a. The schematic of an MZM with electrodes in ground-signal-ground (GSG) configuration forming a coplanar microwave waveguide is shown in Fig. 1b. The optical transmission, Tr, of an MZM with π-voltage, V_π, and optical insertion loss η_o, can be expressed as $\mathrm{Tr} = 1/2\eta_o\left[1+\cos\left(\phi+\pi V(t)/V_\pi\right)\right]$, where $V(t)$ is the signal voltage and ϕ is a dc optical phase shift between the arms, which defines the working point. The EO phase modulators in the two arms of the Mach-Zehnder interferometer are based on the integrated silicon slot-waveguides (see Fig. 1c, scanning electron microscope image of the waveguide cross section), formed by two parallel silicon rails with a typical width of 240 nm and height of 220 nm placed 140 nm apart. Such waveguides are fabricated by dry etching on the silicon-on-insulator platform (SOI). The optical mode is largely concentrated in the slot between rails. The slot is filled with an electro-optically active organic material, which is locally dispensed on the slot-waveguides (see Fig. 1d). The organic EO material is functionalized or "poled" in a vacuum chamber by heating the modulator chip up to the glass transition temperature of the EO material and applying a dc electric field between signal and ground in the same direction in both arms [8].

In the framework of this project, we considered two variations of SOH modulators that differ by the coupling approach of rf mode to the region with the optical mode. The *capacitively-coupled* (CC) SOH was in-house nano-fabricated and demonstrated an EO bandwidth of around 80 GHz, $V_\pi = 1.3$ V and the total optical loss, $\eta_o = 19$ dB [9], where 10 dB are attributed to the coupling loss through an on-chip grating couplers and can be eliminated using optical packaging with edge couplers, but due to fabrication complexity this is still an ongoing process. The *resistively-coupled* (RC) SOH employs highly-doped 70-nm-thin silicon slabs to connect electrodes with optical slot waveguide, which allows for lower π-voltages down to $V_\pi = 0.32$ V in 1-mm-long devices [8], but the bandwidth is limited by the RC-constant of slab-slot connection. The fabrication process of an RC-SOH is compatible with standard CMOS processes and was performed at an external foundry (Advanced Micro Foundaries, AMF, Singapore) in the framework of a multi-project wafer run based on our designs and modeling.

MODELING AND EXPERIMENTAL EVALUATION

The EO-Electrical (EO-E) response of the current generation of SOH was measured on the non-packaged RC-SOH chips using a 1550 nm cw-laser and the 110 GHz VectorStar Anritsu Vector Network Analyzer (VNA) with an ultra-fast Anritsu photodiode on a special probe-station developed in the ongoing project. The result is shown in Fig. 2 along with the modeled EO-E response based on optical and EM-simulations of a MZM in CST MWS and the analysis from Ref. [10]. The measured π-voltage is $V_\pi = 0.5$ V and the optical insertion loss is $\eta_o \approx 13$ dB.

The rms timing accuracy, σ_t, of a BAM system can be estimated using:

$$\sigma_t \approx \frac{\sigma_n}{\mathrm{SR}_{\mathrm{eff}}}, \tag{1}$$

where $\mathrm{SR}_{\mathrm{eff}}$ is the effective slew rate of the electrical pulse from the pickup structure modified by the response spectrum of the EOM, and σ_n is an equivalent input rms voltage noise of the modulator. This noise we model as a quadrature sum of independent noise sources added in the process of EO-E conversion and digitization of an incoming BAM pulse, $\sigma_n = \sqrt{\sigma_{\mathrm{RIN}}^2+\sigma_q^2+\sigma_{pd}^2+\sigma_{adc}^2+\ldots}$, where main contributions are from Relative Intensity Noise (RIN) of the laser, σ_{RIN}, optical quantum noise, σ_q, noise of a photodiode, σ_{pd}, characterized by its Noise Equivalent Power (NEP) and noise of an Analog-to-Digital Converter (ADC), σ_{adc}.

Here, we focus on the conventional direct detection scheme at the half-transmission point of MZM modulator and ignore noise from bunch charge fluctuations and pulsed laser jitter. To refer equivalent optical noises from the input of the photodiode to the input of the MZM, we use a small-signal transfer function of the MZM that can be derived from $\mathrm{Tr}(V)$-relation at the half-transmission point with $\phi = \pi/2$, with given π-voltage, V_π, and average input optical power P_o:

$$|\widetilde{H}_{\mathrm{mzm}}| = \frac{\partial \mathrm{Tr}}{\partial V} = \frac{\partial P_o/P_o}{\partial V} \approx \frac{\pi}{2\eta_o V_\pi}. \tag{2}$$

Additionally, we use the conversion gain of the photodiode, $|\widetilde{H}_{\mathrm{pd}}|$, to refer ADC noise to the MZM rf input. The contribution to the total equivalent rms voltage noise from rms optical power fluctuations σ_o: RIN, quantum noise and

ISBN: 978-3-95450-241-7 ISSN: 2673-5350 doi:10.18429/JACoW-IBIC2022-WEP24

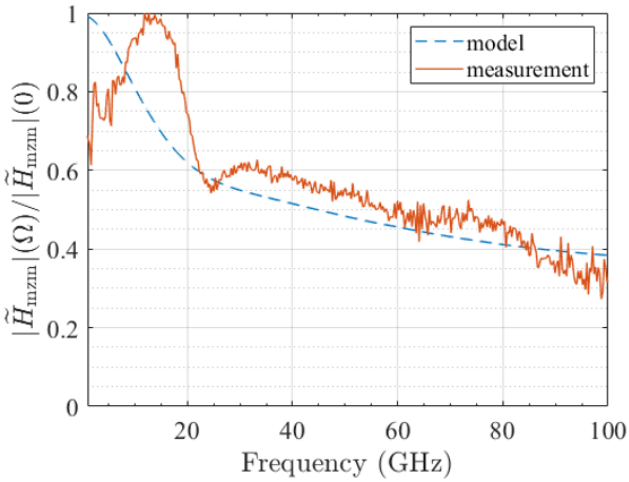


Figure 2: The normalized frequency dependence of the transfer function of RC-SOH MZM. The measured normalized transfer function at low frequency is lowered by the high output RF power provided by the VNA that caused over modulation.

NEP of the photodiode, denoted here as σ_{eoe}, then could be found as $\sigma_{\mathrm{eoe}} \approx |\widetilde{H}_{\mathrm{mzm}}|^{-1}(\sigma_{\mathrm{o}}/P_{\mathrm{o}})$:

$$\sigma_{\mathrm{eoe}} \approx \frac{2\eta_{\mathrm{o}} V_\pi}{\pi} \sqrt{\left(\frac{\delta P_{\mathrm{RIN}}}{P_{\mathrm{o}}}\right)^2 + \frac{2h\nu B}{P_{\mathrm{o}}} + \left(\frac{\mathrm{NEP}\sqrt{B}}{P_{\mathrm{o}}}\right)^2}, \quad (3)$$

where B is bandwidth of the ADC, δP_{RIN} is the rms RIN optical power fluctuations and $\nu \approx 193\,\mathrm{THz}$ is the optical frequency of the laser. The equivalent noise contribution from the ADC referred to the MZM rf input can be estimated using the known rms voltage noise, $\sigma_{v,\mathrm{adc}}$, of the ADC and the noise of a pre-amplifier, $\sigma_{v,\mathrm{amp}}$, with the gain G_{amp} :

$$\sigma_{\mathrm{adc}} \approx \frac{2\eta_{\mathrm{o}} V_\pi}{\pi P_{\mathrm{o}} |\widetilde{H}_{\mathrm{pd}}|} \sqrt{\sigma^2_{v,\mathrm{amp}} + \sigma^2_{v,\mathrm{adc}}/G_{\mathrm{amp}}}. \quad (4)$$

To calculate the effective slew rate, $\mathrm{SR}_{\mathrm{eff}}$ in Eq. (1), we use a simulated time trace of the BAM pulse ($\mathrm{SR}/q \approx 170\,\mathrm{mV\,pC^{-1}\,ps^{-1}}$ [7]) after attenuation in coaxial cables with normalized slew rate of $\mathrm{SR}/q \approx 130\,\mathrm{mV\,pC^{-1}\,ps^{-1}}$ and apply a filter that corresponds to the response spectrum of the EOM shown in Fig. 2. The resulting normalized slew rate, $\mathrm{SR}_{\mathrm{eff}}/q \approx 95\,\mathrm{mV\,pC^{-1}\,ps^{-1}}$, is about a factor of 1.5 smaller than the slew rate of the original pulse. For our jitter estimations we assume the average input laser power $P_{\mathrm{o}} \approx 5\,\mathrm{mW}$, relative intensity noise, $\delta P_{\mathrm{RIN}}/P_{\mathrm{o}} \approx 0.25\%$, the bandwidth of the ADC, $B = 200\,\mathrm{MHz}$ with typical SNR $\approx 70\,\mathrm{dBFS}$ and rms voltage noise $\sigma_{v,\mathrm{adc}} \approx 1\,\mathrm{mV}$ at 3 V full-scale, with a typical 200-MHz pre-amplifier rms-noise of $\sigma_{v,\mathrm{amp}} \approx 28\,\mu\mathrm{V}$, a gain of $G_{\mathrm{amp}} = 40\,\mathrm{dB}$, and a photodiode NEP $\approx 10\,\mathrm{pW}/\sqrt{\mathrm{Hz}}$ with conversion gain $|\widetilde{H}_{\mathrm{pd}}| \approx 400\,\mathrm{V\,W^{-1}}$. With the above specified parameters, π-voltage of the modulator, $V_\pi \approx 0.5\,\mathrm{V}$ and insertion loss $\eta_{\mathrm{o}} = 13\,\mathrm{dB}$ the estimated rms timing jitter (from Eq. (1)) amounts to $\sigma_t \approx 9\,\mathrm{fs}$ for a bunch charge of 1 pC. The contribution from RIN is about an order of magnitude larger than the contribution from quantum and photodiode noises, which are comparable. The contribution from the electronic noise of the back-end is insignificant.

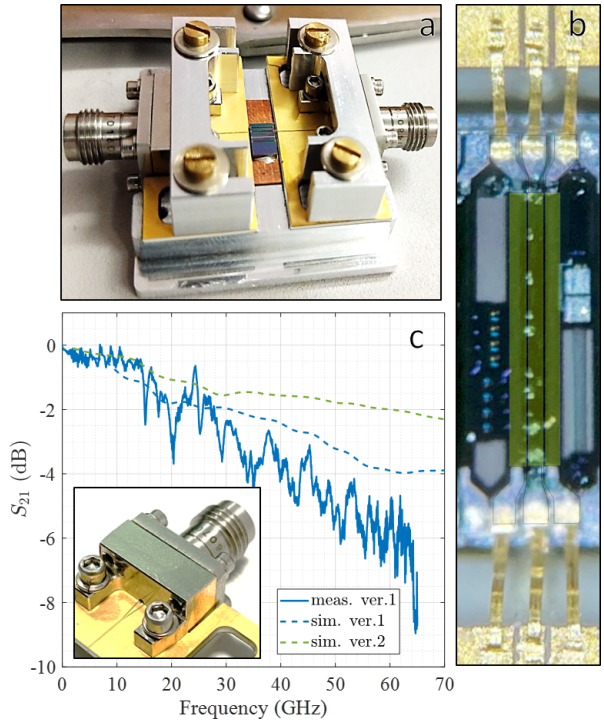


Figure 3: The prototype of the packaging solution for the SOH modulator; **a** the package with mounted rf-adapter PCBs from both sides of the chip. The openings from the sides are for the mounting the v-groove fiber arrays; **b** The optical microscope image of the SOH MZM connected to rf-adapter PCBs using golden ribbon bonds; **c** the measured and simulated rf transmission of the connectorized PCB; the green dashed curve demonstrates simulation of the second version of PCB with improved performance.

OUTLOOK

For the joint demonstration of a new BAM prototype, which employs the new pickups [7] and the EOMs presented here, we are developing microwave and optical packaging solution for SOH chips. The first version of the package is presented in Fig. 3a. The package is based on 1.85 mm-connectors ("V") and gold-plated alumina rf-adapter boards (inset in Fig. 3b). The rf-adapter boards are designed in a form of a tapered coplanar waveguide and laser-etched with a signal line width of 80 µm and a gap width of 25 µm. The chip is connected to the rf-adapter board using golden ribbon bonds (Fig. 3c). The graph in Fig. 3b shows the rf transmission measurements and EM-simulation of the first version of the assembly are shown in the inset. The simulation of the second version of the assembly is shown by the green dashed line. It features an improved transmission

Content from this work may be used under the terms of the CC BY 4.0 licence (© 2022). Any distribution of this work must maintain attribution to the author(s), title of the work, publisher, and DOI

ISBN: 978-3-95450-241-7 ISSN: 2673-5350 doi:10.18429/JACoW-IBIC2022-WEP24

Content from this work may be used under the terms of the CC BY 4.0 licence (© 2022). Any distribution of this work must maintain attribution to the author(s), title of the work, publisher, and DOI

and will be tested in the future. For the optical coupling, the v-groove optical fiber array will be aligned and glued to the edge couplers on the chip. The joint testing with non-hermetic pickup rod-shaped prototypes and a packaged SOH-EOM are planned at the test facility FLUTE at KIT with fs-short bunch charges as low as a few pC. The balanced photo-detection scheme with dual-output MZM will be tested to suppress a contribution from relative intensity noise [11, 12].

CONCLUSION

The new EOM prototypes for BAM were successfully fabricated and tested. The timing jitter of a BAM system is estimated based on the obtained slew rates from the new rod-shaped pickups and measured EO conversion efficiency and bandwidth of new silicon-organic hybrid (SOH) modulators. A jitter-charge product of $\sigma_t \times q \approx 9\,\mathrm{fs\,pC}$ is calculated for the normalized signal slew rate of $150\,\mathrm{mV\,pC^{-1}\,ps^{-1}}$ of the new pickups, a π-voltage of the EOM of $V_\pi = 0.5\,\mathrm{V}$ and its measured frequency response. The estimated timing resolution of a BAM is strongly dominated by the relative intensity noise, $\sigma_P/P \approx 0.25\%$, of the pulsed laser, which is about an order of magnitude larger than the contributions from quantum and photodiode noises. Using a balanced photo-detection scheme, and employing a dual-output SOH modulator with 180° phase difference between its outputs will enable at least 20 dB suppression of RIN noise. In this case the timing jitter of the BAM will be fundamentally limited only by the optical quantum noise and the available laser power.

REFERENCES

[1] S. Schulz *et al.*, "Femtosecond all-optical synchronization of an X-ray free-electron laser", *Nat. Commun.*, vol. 6, p. 5938, 2015. doi:/10.1038/ncomms6938

[2] E. J. Jaeschke, S. Khan, J. R. Schneider, and J. B. Hastings, *Synchrotron light sources and free-electron lasers: Accelerator physics, instrumentation and science applications*, 2nd Edition, Cham: Springer International Publishing, 2020. doi:10.1007/978-3-030-23201-6

[3] T. Lamb *et al.*, "Large-scale optical synchronization system of the European XFEL with femtosecond precision", in *Proc. IPAC'19*, Melbourne, Australia, May 2019, pp. 3835–3838. doi:10.18429/JACoW-IPAC2019-THPRB018

[4] F. Löhl *et al.*, "Electron bunch timing with femtosecond precision in a superconducting free-electron laser", *Phys. Rev. Lett.*, vol. 104, no. 14, p. 144801, Apr. 2010. doi:10.1103/PhysRevLett.104.144801

[5] A. Angelovski *et al.*, "Pickup signal improvement for high bandwidth BAMs for FLASH and European - XFEL", in *Proc. IBIC'13*, Oxford, UK, Sep. 2013, paper WEPC40, pp. 778–781.

[6] M. K. Czwalinna *et al.*, "Beam arrival stability at the European XFEL", in *Proc. IPAC'21*, Campinas, Brazil, May 2021, pp. 3714–3719. doi:10.18429/JACoW-IPAC2021-THXB02

[7] B. E. J. Scheible *et al.*, "Bunch arrival-time measurement with rod-shaped pickups on a printed circuit board for X-ray free-electron lasers", in *Proc. IBIC'21*, Pohang, Korea, Sep. 2021, pp. 417. doi:10.18429/JACoW-IBIC2021-WEPP19

[8] C. Kieninger *et al.*, "Ultra-high electro-optic activity demonstrated in a silicon-organic hybrid modulator", *Optica*, vol. 5, no. 6, p. 739, Jun. 2018. doi:10.1364/OPTICA.5.000739

[9] S. Ummethala *et al.*, "Hybrid electro-optic modulator combining silicon photonic slot waveguides with high-k radio-frequency slotlines", *Optica*, vol. 8, no. 4, p. 511, Apr. 2021. doi:10.1364/optica.411161

[10] H. Zwickel *et al.*, "Verified equivalent-circuit model for slot-waveguide modulators", *Opt. Express*, vol. 28, no. 9, p. 12951, Apr. 2020. doi:10.1364/oe.383120

[11] K. Kikuchi, "Fundamentals of coherent optical fiber communications", *J. Lightwave Technol.*, vol. 34, no. 1, p. 157–179, Jan. 2016. doi:10.1109/jlt.2015.2463719

[12] M. Endo, T. D. Shoji, and T. R. Schibli, "High-sensitivity optical to microwave comparison with dual-output Mach-Zehnder modulators", *Sci. Rep.*, vol. 8, no. 1, Mar. 2018. doi:10.1038/s41598-018-22621-1

ISBN: 978-3-95450-241-7 ISSN: 2673-5350 doi:10.18429/JACoW-IBIC2022-WEP25

INSTALLATION AND COMMISSIONING OF THE PULSED OPTICAL TIMING SYSTEM EXTENSION

F. Rossi*, M. Ferianis, Elettra Sincrotrone Trieste S.C.p.A., Trieste, Italy

Abstract

At the FERMI FEL user facility, a fully optical timing system has been operated, to synchronize it, since the start of machine commissioning, back in 2009. In the past years the system has been progressively extended to support more clients. The latest upgrade is focusing on the pulsed subsystem which provides the phase reference to remote lasers and the bunch arrival monitor diagnostic stations. In origin the pulsed subsystem had a capacity to feed simultaneously six stabilized fiber links. The upgrade to the original layout makes it possible to install up to eight new additional links. Here we will describe the new setup and the results achieved in terms of short- and long-term stability.

INTRODUCTION

FERMI [1] is a fourth generation light source, a seeded Free Electron Laser (FEL), operating as a user facility in Trieste, Italy. A state-of-art all optical timing and synchronization system [2] has been deployed implementing a hybrid architecture as a combination of pulsed and continuous wave techniques.

The pulsed optical timing subsystem generates and delivers with 10 femtosecond precision the reference to all phase critical FERMI clients, like lasers and longitudinal diagnostics. The installation started with two links in 2009 and, since then, has been progressively updated to the current configuration serving a total of six clients.

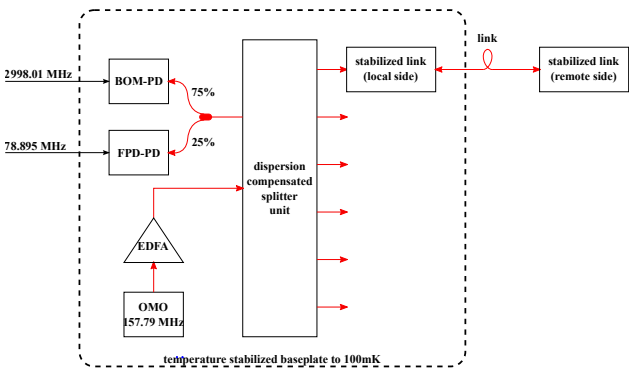


Figure 1: Block diagram of the original pulsed timing subsystem.

The block diagram of the subsystem originally installed is shown in Fig. 1. The optical master oscillator (OMO) is a soliton fiber laser working with a repetition rate of 157.79 MHz, i.e. one nineteenth of the 2998.01 MHz microwave frequency of the reference master oscillator (RMO). The OMO is phase locked to the RMO signal by a Balanced Optical Microwave Phase Detector (BOM-PD), while the ambiguity of the zero crossing selection is solved by using a Fast Photodiode Phase Detector (FPD-PD). The signal from the OMO, amplified by a single Erbium Doped Fiber Amplifier (EDFA), is delivered at the output ports of a splitter along a dispersion-compensated path. This one is entirely implemented in fiber and guarantees short pulses at the input of a stabilized link which is built around a balanced cross-correlator (BOCC). Six ports are dedicated to timing distribution purposes, other two are used to seed the phase detectors and, finally, one is reserved for the extension. Each splitter output port dedicated to the timing distribution provides pulses at 40 mW average power, while the full width at half maximum (FWHM) is about (165 ± 9) fs.

A progressive extension of the pulsed optical timing subsystem is expected in the coming years to feed new clients with the phase reference. To fulfil the installation requests of additional timing clients in FERMI (e.g. new bunch arrival monitor stations or a user laser oscillator) we have started working towards an upgrade of the original subsystem.

THE SLAVE SUBSYSTEM

The extension of the pulsed subsystem has been implemented by Cycle GmbH [3]. The design follows the same architecture of the original subsystem so the optical signal coming from a second port of the OMO is again amplified and split. The upgrade makes it possible to add up to eight new stabilized pulsed links to the timing system. The optical signal is mainly routed in fiber; along the path there is a minimal free-space section described below. One of the design requirements was to maintain mechanical and optical compatibility with the link stabilization units installed in the past.

The overall block diagram of the extended pulsed system is shown in Fig. 2. The part described in the previous section is called “master” while the new devices are hereafter indicated as “slave”. In fact the slave is locked to the master to remove residual timing drifts among the two splitters output ports. The key element of the tracking loop is a phase detector implemented by means of a BOCC. The error signal is used to drive an actuator – a combination of a fiber piezo stretcher and a motorized translation stage – to keep the pulses coming out from the outputs of the master and slave splitters synchronized. Part of the actuator block is also a manual free-space delay line used to align in time the pulses and set the zero-crossing of the BOCC in the dynamic range of the control loop.

There are two fiber interconnections between the master and slave subsystems at ports A and B. The former is included in the controlled path of the tracking system while

* fabio.rossi@elettra.eu

Content from this work may be used under the terms of the CC BY 4.0 licence (© 2022). Any distribution of this work must maintain attribution to the author(s), title of the work, publisher, and DOI

ISBN: 978-3-95450-241-7 ISSN: 2673-5350 doi:10.18429/JACoW-IBIC2022-WEP25

Content from this work may be used under the terms of the CC BY 4.0 licence (© 2022). Any distribution of this work must maintain attribution to the author(s), title of the work, publisher, and DOI

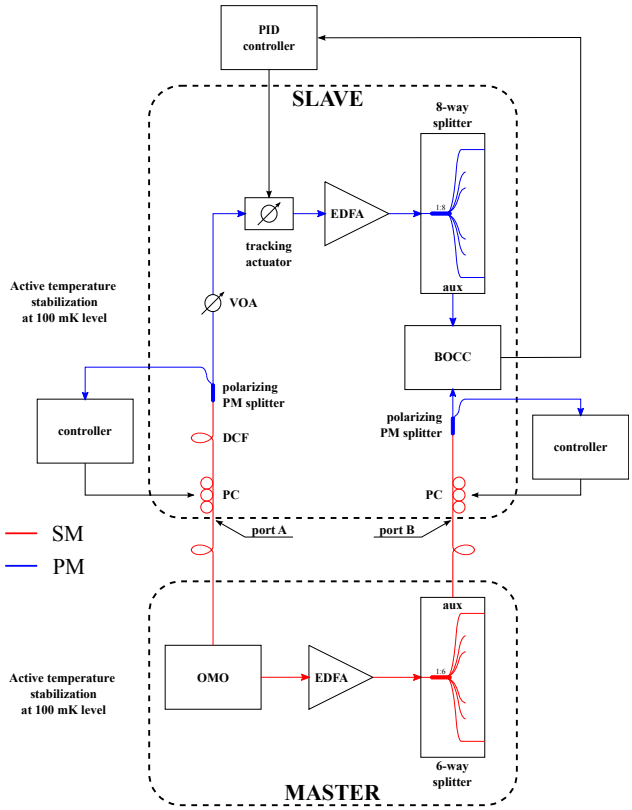


Figure 2: Simplified block diagram of the extended pulsed timing system. DCF: Dispersion Compensating Fiber, PC: Polarization Controller, PID: Proportional Integral Derivative, PM: Polarization Maintaining fiber, SM: Single Mode fiber, VOA: Variable Optical Attenuator.

the latter is the most critical from the point of view of the timing application. The fiber path at port B up to the BOCC must be as short as possible and temperature stabilized to avoid transferral of unwanted out-of-loop drifts that cannot be compensated.

The two subsystems mainly differ for the fiber type used which is polarization maintaining for the slave. For this reason, at the interface ports A and B there is a polarization controller used to set the proper state (linear along the slow axis) at the input of a polarizing fiber splitter. During the commissioning of the extension we have used the PCs in open loop mode though it is possible to control them for compensating polarization drifts of the signals arriving from the master subsystem. By using a PM design, the slave subsystem allows additional flexibility with regard to the choice of the new links. In case of more demanding requirements they might even be built with polarization maintaining technology.

The master and slave subsystems are sitting on the same optical table, in independent enclosures, each one using its own water-cooled baseplate. Moreover the aluminium baseplate of the slave is thermally insulated on the bottom face. The cooling systems of the two baseplates are also independent to avoid galvanic corrosion since they are made of different materials. The slave enclosure uses damping feet accurately chosen to attenuate mechanical vibrations. The side panels and the top lid integrate sheets of foam for the same purpose.

CHARACTERIZATION

During the commissioning of the extension we evaluated many aspects of the slave subsystem. Only the most relevant results will be reported here. A few characterizations have been done on a long-term timescale, described in the next section, in which cases the acquisition period lasted for a minimum of 24 hours.

Optical Signal Integrity

The shape of the optical pulses after the splitter has a direct impact on the fiber link stabilization units and in particular the behaviour of the femtosecond timing detector. The cross-correlation signal must show a unique zero-crossing point centered along a strictly monotonic transition - better with a constant slope - between maximum and minimum points. The design of the amplifier and the dispersion compensated path in the slave subsystem should therefore guarantee the integrity of the pulses. In order to achieve minimized distortion of their temporal profile, the autocorrelation taken at the splitter port should have a single central lobe and avoid as much as possible the presence of satellites.

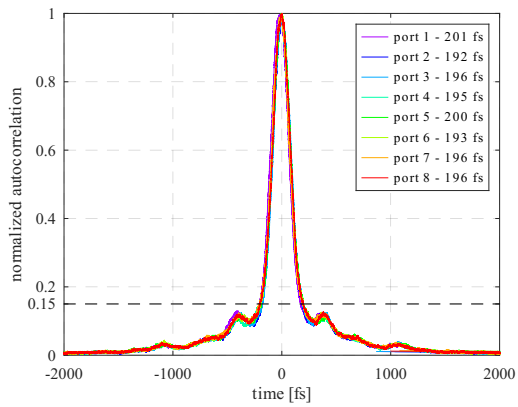


Figure 3: Autocorrelations after the slave splitter.

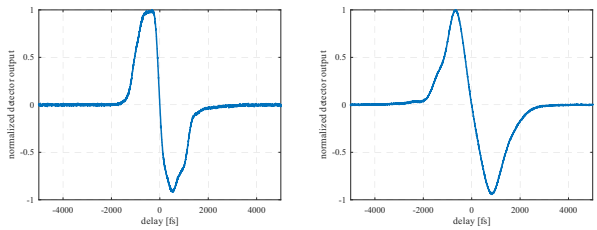
The working point of the slave subsystem must be accurately chosen by tuning the input power to the EDFA, by means of a VOA, and the gain value of the amplifier itself in order to match the specifications in terms of output pulse integrity, power and duration. The propagation along the fiber of the optical pulses from the OMO is affected by dispersion and non-linear effects due to the high power level between the amplifier output and the splitter. The average power available at each of the splitter output ports is more than 45 mW.

The dispersion compensated path has been designed to have a FWHM pulse duration less than 200 fs assuming a Gaussian shape. In Fig. 3 the measurements acquired with a FemtoChrome FR-103XL instrument are presented; the

ISBN: 978-3-95450-241-7 ISSN: 2673-5350 doi:10.18429/JACoW-IBIC2022-WEP25

result is (196 ± 5) fs FWHM. The autocorrelation of all the slave subsystem outputs shows a pedestal whose relative height has been optimized to be lower than 15% of the main central lobe.

The pedestal is due to residual uncompensated non-linear effects accumulated during the propagation in the fiber. Even if the autocorrelation is not optimal, we have verified that this result does not entail major issues with the downstream cross-correlations (e.g. for the link stabilization or remote client synchronization). In Fig. 4 we report examples of BOCC outputs used in the system characterization. In particular, the typical error signal used to lock the slave subsystem to the master is shown in Fig. 4a. A distortion is visible related to the signal integrity of the pulses but we consider it as a second order problem because the tracking loop works around the zero-crossing.



(a) (b)

Figure 4: Typical normalized cross-correlations: a) between the master and slave splitter outputs; b) between the OMO and one output of the slave splitter.

Relative Intensity Noise (RIN)

The optical signal at the output from the splitter is attenuated to operate the detection photodiode (battery powered EOTech ET-3500F) in the linear regime. Before entering a low noise baseband amplifier the electrical output from the detector is low-pass filtered. The voltage spectral density is then acquired by using the baseband input channel of a Keysight E5052B signal source analyzer (SSA). The relative intensity noise is calculated after a normalization of the acquired signal to the measured DC output from the amplifier.

The RIN performance depends on the EDFA working point; the best result we achieved is shown in Fig. 5. The orange trace (right axes) represents the partial integration from the given offset frequency to the amplifier bandwidth. The integrated RIN in the 10 Hz – 5 MHz bandwidth is 0.052% RMS compared to the 0.037% RMS value for the OMO measured with the same setup. The tracking loop status doesn't affect the result.

Additive Timing Jitter

The short-term stability achievable by the slave subsystem mostly depends on the EDFA in the chain between the OMO and the splitter output ports. For the characterization of this contribution we have measured the cross-correlation between the laser (it has a third output port not visible in Fig. 2)

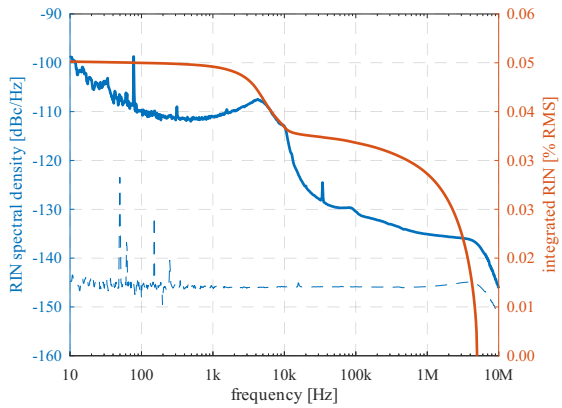


Figure 5: RIN measured after the slave splitter. The blue dashed trace represents the noise floor of the measurement setup. It is visible the cut-off frequency of the amplifier.

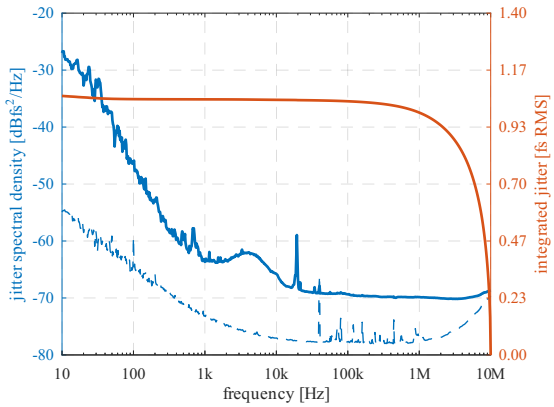


Figure 6: Additive jitter of the slave subsystem. The blue dashed trace represents the noise floor of the measurement setup.

and one of the ports of the slave splitter. The normalized signal used for the calibration is visible in Fig. 4b.

The jitter spectral density of the BOCC output in the zero-crossing acquired by the SSA is shown in Fig 6. The photodetector in the BOCC is the Thorlabs PDB450A with 1×10^4 transimpedance gain. In that configuration the detector supports the full analysis bandwidth 10 Hz – 10 MHz of the instrument, the integrated jitter is 1.1 fs RMS.

LONG-TERM MEASUREMENTS

Splitter Stability

The length mismatch of the splitter output pigtails was accurately evaluated by means of an external BOCC unit. We have compared a reference signal on one side and, sequentially, all the output ports of the splitter on the other side. The length difference was obtained by measuring the zero-crossing temporal shift of the cross-correlator output. The maximum difference measured among all the splitter ports is 1.16 mm. This result guarantees the interchangeability of the

Content from this work may be used under the terms of the CC BY 4.0 licence (© 2022). Any distribution of this work must maintain attribution to the author(s), title of the work, publisher, and DOI

ISBN: 978-3-95450-241-7 ISSN: 2673-5350 doi:10.18429/JACoW-IBIC2022-WEP25

Content from this work may be used under the terms of the CC BY 4.0 licence (© 2022). Any distribution of this work must maintain attribution to the author(s), title of the work, publisher, and DOI

splitter ports with a minimum acceptable phase difference if the relocation of a link stabilization unit is needed.

Even if the length equalization among the output ports described above is very good, a temperature control of the splitter box is mandatory to avoid residual drifts that cannot be compensated afterwards by the link stabilization units. The active temperature control allows to achieve a stabilization better than 10 mK over many days of operation.

The timing stability between two splitter ports was measured with an external BOCC unit installed in the slave enclosure. The result is shown in Fig. 7. The drift visible at the beginning relates to the initial transient (first three hours) needed for the stabilization of the setup. The peak to peak variation after the transitory is less than 6 fs over a 24-hour interval. We think it doesn't show the real performance but only a limit of the measurement setup itself.

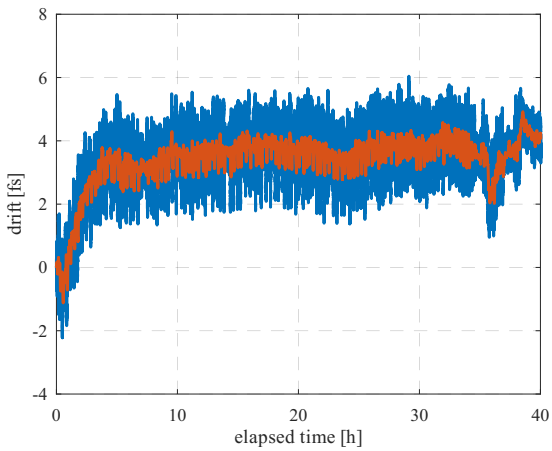


Figure 7: Long-term stability between two slave splitter ports.

Tracker Performance

The final and most demanding test was the characterization of the residual drift between the master and slave splitters with the tracker loop in operation. This measurement is quite challenging because the two subsystems are physically independent. Although they are on the same optical table each one is installed in its own enclosure. The typical result is shown in Fig. 8 where the residual drift is less than 20 fs peak to peak over a 24-hour interval.

The drift has been measured with an out-of-loop balanced cross-correlator installed inside the slave enclosure. The interconnection between the master and the BOCC adds an uncompensable drift to the result and limits the minimum value achievable with this setup. In our case it was implemented with a 2 m SMF fiber patch cord installed mostly inside the two splitter units which are temperature controlled with a peak to peak stability better than 10 mK. If we assume that the thermal coefficient of delay is typically in the order of a few tens of fs/m/K then the impact of the out-of-loop fiber on this measurement can be estimated in the order of a few femtoseconds.

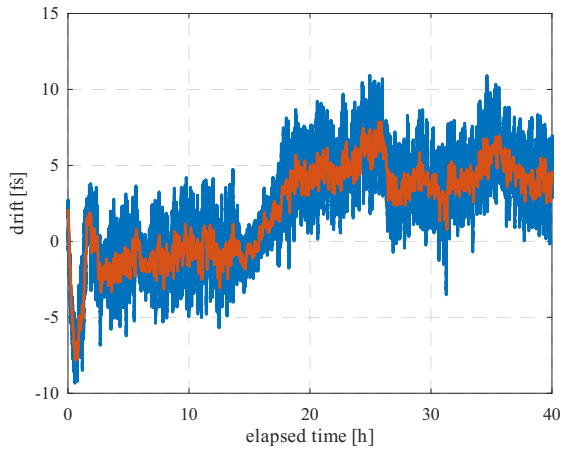


Figure 8: Long-term stability between master and slave subsystems with tracker loop active.

Even if the fibers of the master subsystem are temperature controlled, the polarization at ports A and B is slightly drifting, this has an impact on the behaviour of the tracking system and is probably limiting the long-term performance reported in this section.

CONCLUSIONS AND FUTURE WORK

We have validated the design and implementation of the pulsed timing subsystem extension. Before putting it in operation on a daily basis we will carry out monitoring for a longer period to evaluate its reliability. Furthermore an integration of the new hardware in the machine control system is mandatory.

In the future we will investigate about the issues regarding the polarization stability between the master and slave subsystems. We are also planning to install a testing stabilized short link in the laboratory between the two splitters or, alternatively, compare at the remote location the relative stability of two links connected to the master and slave subsystems, respectively.

ACKNOWLEDGEMENTS

The authors would like to thank Anan Dai, Marvin Edelmann, Franz Kaertner and Kemal Shafak from Cycle GmbH for the discussions and support during the in-house system commissioning.

REFERENCES

[1] E. Allaria *et al.*, "Highly coherent and stable pulses from the FERMI seeded free-electron laser in the extreme ultraviolet", *Nat. Photonics*, vol. 6, no. 9, 2012. doi:10.1038/nphoton.2012.233

[2] M. Ferianis, A. O. Borga, A. Bucconi, M. Predonzani, F. Rossi, and L. Pavlovic, "All-optical Femtosecond Timing System for the Fermi@Elettra FEL", in *Proc. FEL'11*, Shanghai, China, Aug. 2011, paper FROAI2, pp. 641–647.

[3] https://www.cyclelasers.com

ISBN: 978-3-95450-241-7 ISSN: 2673-5350 doi:10.18429/JACoW-IBIC2022-WEP26

STATUS OF A MONITOR DESIGN FOR SINGLE-SHOT ELECTRO-OPTICAL BUNCH PROFILE MEASUREMENTS AT FCC-ee

M. Reißig*, E. Bründermann, S. Funkner, B. Härer, G. Niehues, M. M. Patil, R. Ruprecht, C. Widmann, A.-S. Müller, Karlsruhe Institute of Technology, Karlsruhe, Germany

Abstract

At the KIT electron storage ring KARA (Karlsruhe Research Accelerator) an electro-optical (EO) near-field monitor is in operation performing single-shot, turn-by-turn measurements of the longitudinal bunch profile using electro-optical spectral decoding (EOSD). In context of the Future Circular Collider Innovation Study (FCCIS), a similar setup is investigated with the aim to monitor the longitudinal bunch profile of each bunch for dedicated top-up injection at the future electron-positron collider FCC-ee. This contribution presents the status of a monitor design adapted to cope with the high-current and high-energy lepton beams foreseen at FCC-ee.

INTRODUCTION

The future electron-positron collider FCC-ee is a planned high-energy, high-intensity accelerator located at CERN with approximately 100 km circumference and a beam energy up to 180 TeV [1]. To optimize luminosity, it will be operated with a top-up injection, which requires a detailed monitoring of the bunch profiles. In the frame of the Future Circular Innovation Study (FCCIS), a diagnostics tool for single-shot bunch-by-bunch measurements of the longitudinal bunch profile is under development at KIT. The design of this monitor is based on the electro-optical (EO) near-field monitor at the Karlsruhe Research Accelerator (KARA), which is able to perform turn-by-turn single-shot bunch profile measurements [2].

Bunch Profile Measurements at KARA

The EO near-field monitor at KARA offers turn-by-turn single-shot bunch profile measurements during an operation mode for short bunches. To resolve the bunch profile of single electron bunches with a length of 10 ps, a technique called electro-optical spectral decoding (EOSD) is used. Figure 1 shows the principle of an EOSD measurement at KARA in three consecutive steps.

In the first step, the electron bunch profile is encoded into the polarization of the chirped laser pulse. The electron's electric field changes the refractive index of the GaP (EO) crystal according to the Pockels effect. However, the change in refractive index in GaP depends on polarisation and propagation direction, because it is an anisotropic material. Therefore, the crystal becomes birefringent, which changes the polarization of the laser pulse from linear to elliptical in proportion to the electric field strength. The result is a modulation of the laser polarization that depends on the bunch charge density.

* micha.reissig@kit.edu

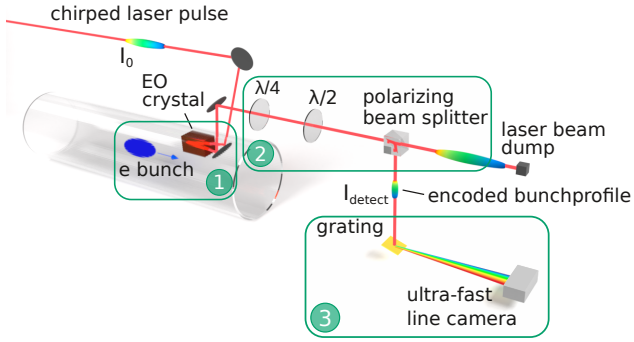


Figure 1: Scheme of the EO near-field setup at KARA. Adapted from [4].

In the second step, the bunch profile, which is now encoded in the laser polarization, is converted to an intensity modulation. This is achieved by a polarizing beam splitter (PBS), which only forwards light with a certain linear polarization to the spectrometer. A $\lambda/4$- and a $\lambda/2$-waveplate are set up in front of the PBS in a near-crossed configuration. This way, only very little light is transmitted if the laser pulse is not modulated and linearly polarized, but the transmitted intensity increases approximately linearly with the modulation of the polarisation.

In the third step, the intensity modulation of a single laser pulse is measured with a spectrometer containing the KIT-built, ultra-fast line camera KALYPSO [3]. In the spectrometer, the chirped laser pulse is refracted on a grating, which fans out the laser pulse according to the wavelength. The line camera then measures the laser intensity at different wavelengths, which corresponds to the longitudinal electron bunch profile.

Challenges for EO at FCC-ee

Simulations of the EO monitor at KARA for FCC-ee beam parameters showed, that there will be two major challenges that need to be tackled [5].

First, the operation mode for production of Z bosons at a collision energy of 90 GeV features a bunch length of $\sigma^{\mathrm{FCCee\,Z}} = 15.4$ mm, which is very large compared to the typical length during measurements at KARA of around $\sigma^{\mathrm{KARA}} \approx 3$ mm. The monitor at KARA is designed for short bunches. The laser pulse passes the crystal twice: first against the bunch direction (upstream) and after reflection at the back of the crystal, the laser pulse travels parallel to the bunch (downstream). Only the downstream modulation of the laser contributes to the bunch profile measurement, the upstream modulation is treated as a disturbance. For short bunches, the up- and downstream modulations do not

Content from this work may be used under the terms of the CC BY 4.0 licence (© 2022). Any distribution of this work must maintain attribution to the author(s), title of the work, publisher, and DOI

ISBN: 978-3-95450-241-7 ISSN: 2673-5350 doi:10.18429/JACoW-IBIC2022-WEP26

Content from this work may be used under the terms of the CC BY 4.0 licence (© 2022). Any distribution of this work must maintain attribution to the author(s), title of the work, publisher, and DOI

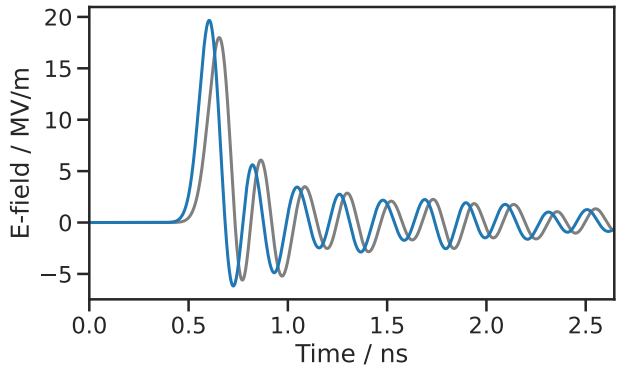


Figure 2: Simulation of the total E-field that the laser pulse experiences up- and downstream (grey and blue) with the KARA design, but with FCC-ee Z-mode beam parameters.

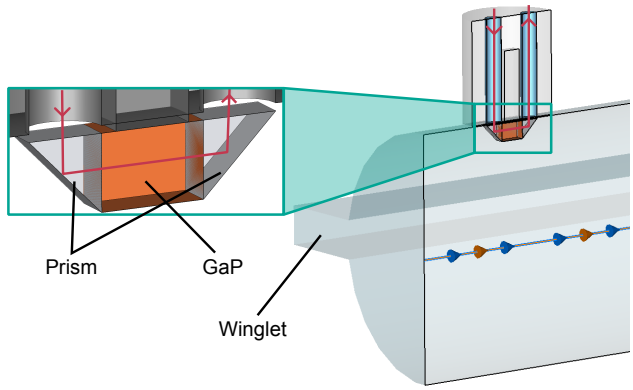


Figure 3: Concept design in CST [6] for the EO crystal holder for FCC-ee.

overlap, which allows a clean measurement of the bunch profile [5]. For long bunches however, the up- and downstream modulation do overlap, which is presented in Fig. 2 in a simulation of the KARA monitor under FCC-ee Z-mode beam conditions. Therefore, an EO monitor for FCC-ee should be designed to avoid the upstream signal.

The second major challenge is the large charge density, which causes a larger phase modulation of the laser pulse. According to simulations, the phase modulation at KARA is a few degrees, whereas it would be up to 100° for the same setup under FCC-ee Z-mode beam conditions [5]. This has the potential to provide a stronger signal, but the downside is that the relation of the bunch profile to the detected spectrum becomes non-linear. Additionally, it might cause distortions of the signal due to heat build-up in the crystal and its holder. For these reasons, the monitor should be designed in a way that phase modulation of the laser pulse is in a similar order of magnitude as in the monitor at KARA.

Besides these issues, the EO monitor for FCC-ee should introduce a small impedance in order to avoid disturbance of the beam and to reduce the wakefield. This is also important for the monitor itself, since the wakefield could overlap with the field of the next bunch and therefore disturb the bunch profile measurement.

CONCEPT IDEA FOR EO NEAR-FIELD AT FCC-ee

To address the mentioned issues, a first design concept has been developed and was tested in simulations.

In Fig. 3, a 3D model, created with CST [6], is presented with a vertically mounted EO crystal holder concept on top of the FCC-ee beam pipe. The principle is similar to the KARA setup, which is presented in Fig. 1, but the design of the crystal holder inside the beam pipe has been changed. Instead of the laser being reflected at the back of the crystal, it is now transmitted through it and therefore the unwanted upstream signal is avoided. The laser pulse is only propagating downstream through the crystal with the aim to get a cleaner signal without overlap of a disturbing signal. Instead of metal mirrors, prisms are used in this concept to guide the laser pulse through the crystal. With prisms, the goal is to reduce the impedance especially since one of the prisms is in front of the crystal, where a metal mirror would shield the crystal from the electric field of the electron bunch and therefore disturb the bunch profile measurement. The setup is mounted on the outer part of the beam pipe, with the crystal just sticking out of the inner pipe wall. This is to maximize the distance to the beam in order to reduce the electric field strength and therefore avoid a non-linear relation of the bunch profile and the measured EOSD signal. To reduce the field strength in the crystal further, it would also be possible to place the crystal and its holder horizontally into the winglet. But it should be on the winglet of the beam pipe on the inner side of the accelerator ring to avoid issues with synchrotron radiation.

Repetition Rate

The RF frequency of the cavities at FCC-ee during Z production is 400 MHz, which determines the maximum repetition rate of the electron bunches. The maximum repetition rate for EO near-field bunch profile measurements is limited by the length of the stretched laser pulse at the spectrometer and the decay of the wakefield, so that it does not overlap with the next bunch. A bottleneck will be the repetition rate of the line camera, which is already very fast at KARA, with the in-house developed KALYPSO at 2.7 MHz. The next version of KALYPSO, which is currently under development, will reach a repetition rate of up to 12 MHz [3] and might increase further by the time the FCC-ee will be build. At present, in order to reach 400 MHz, multiple setups will be necessary. On the one hand, multiple line cameras could be used at one EO monitor, where the laser pulse is split up and e.g. two line cameras are alternately taking measurements. On the other hand, multiple EO monitors can be set up around the ring to measure the bunch profile of different bunches. For example at a camera repetition rate of 10 MHz, a total of 40 EO monitors, each spaced about 2.5 km apart, around the ring would be able to track each bunch once per turn.

ISBN: 978-3-95450-241-7 ISSN: 2673-5350 doi:10.18429/JACoW-IBIC2022-WEP26

SIMULATION RESULTS

In order to evaluate the EO monitor concept, the laser path and its modulation by the electric field of the electron bunch has been simulated. For the simulation of the electric field, the numerical wakefield-solver by CST [6] has been used on a 3D model of beam pipe and crystal holder. The modulation of the laser pulse and the optics to convert the polarization modulation into an intensity modulation have been calculated analytically [5]. In the following subsections, the EO monitor concept is simulated using the most recent beam parameters of the 4 IP layout of the FCC-ee at the Z-pole energy [7] with a bunch length of $\sigma_z^Z = 15.4$ mm and a bunch charge of 38.93 nC.

Avoidance of the Upstream Signal

The primary change of the new monitor design compared to the KARA setup is that the laser is propagating through the crystal once, thus avoiding any disturbance by an upstream signal. The importance of avoiding the upstream signal has been shown in Fig. 2, where the up- and downstream signals overlap and therefore distort the bunch profile information. With the new concept, there is no upstream signal since the laser only propagates downstream through the crystal. This is presented in the simulation results for the phase modulation of the laser pulse in Fig. 4, where only the downstream signal contributes to the phase modulation, which helps to get a cleaner signal of the bunch profile.

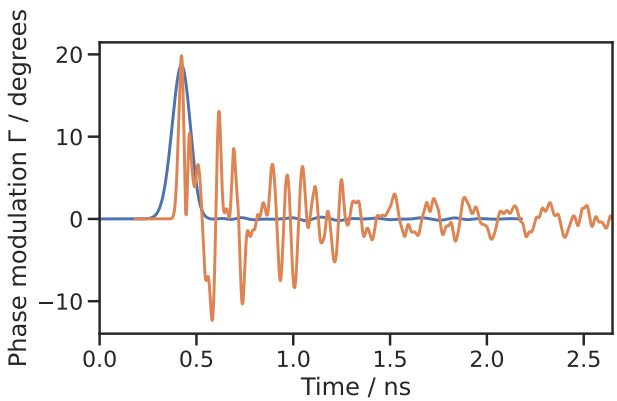


Figure 4: Comparison of the simulated phase modulation of the KARA monitor during low-alpha operation in orange and the new concept for FCC-ee during Z-mode in blue. The new concept manages to achieve a similar amplitude, even though the bunch length at FCC-ee for Z-operation $\sigma^{\text{FCCee Z}} = 15.4$ mm is longer then for KARA with $\sigma^{\text{KARA}} \approx 3$ mm and it has almost twenty times the bunch charge.

Reduction of the Impedance

By replacing the mirrors with prisms, the goal was to further reduce the impedance of the monitor and reduce disturbances of the signal caused by the wakefield. The phase modulation of the FCC-ee concept in Fig. 4 shows a pronounced first peak, whereas the following wakefield is very small in comparison. This will help the measurements, since the bunch profile is encoded in the first peak. A low amplitude of the wakefield is important, because at FCC-ee the bunch spacing might go down to 2.5 ns and the remaining wakefield could affect the next bunch. With a proper design of the in-vacuum EO arm, this can be overcome and the wakefields at 2 ns reduced for 500 MHz operation at KARA as shown in [8]. The distance of the crystal to the beam is an important factor as well, and due to the high E-fields at FCC-ee, the crystal is placed at 32 mm distance, whereas at KARA the crystal needs to be closer to around 14 mm distance to achieve a good signal amplitude. Fig. 4 shows that these measures lead to a strongly reduced wakefield at the FCC-ee concept in comparison to the KARA setup. Figure 5 presents the corresponding longitudinal impedance of the FCC-ee concept and the KARA monitor, which shows the same effect of a lower impedance for the FCC-ee concept due to the larger distance and updated design.

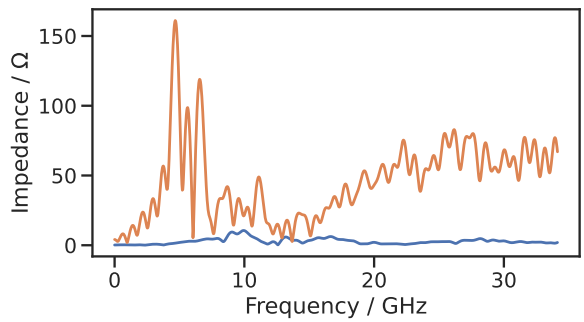


Figure 5: Comparison of the simulated longitudinal impedance of the KARA monitor during KARAs low-alpha mode in orange and the new concept for FCC-ee during Z-mode in blue. The new concept has a smaller impedance, which is caused by increasing the distance of the crystal to the beam and replacing the metal mirror by prisms.

Adjustments to High Bunch Charge

The strength of the electric field inside the crystal is an important factor for a successful bunch profile measurement and is dependent on the bunch charge density. If the electric field is weak, measurements are difficult, because the signal-to-noise ratio becomes small. If the E-field is strong, there is a risk of heating up the crystal and its holder, which can lead to misalignments of the laser and to mechanical stress on the crystal that changes the local birefringence. Additionally, strong fields lead to a larger modulation of the laser polarisation. For a larger modulation the impact of higher-order terms is stronger. The result is that the linear approximation of the relation between the bunch profile and the measured EOSD signal is not viable anymore.

In the simulations of the KARA monitor, the maximum field reaches 350 kV m^{-1} at a distance of the crystal to the beam of 14 mm. For the FCC-ee concept at operation for Z-

Content from this work may be used under the terms of the CC BY 4.0 licence (© 2022). Any distribution of this work must maintain attribution to the author(s), title of the work, publisher, and DOI

ISBN: 978-3-95450-241-7 ISSN: 2673-5350 doi:10.18429/JACoW-IBIC2022-WEP26

Content from this work may be used under the terms of the CC BY 4.0 licence (© 2022). Any distribution of this work must maintain attribution to the author(s), title of the work, publisher, and DOI

pole energy, the crystal is positioned at the edge of the beam pipe, 32 mm away from center, to maximize the distance to the beam. In this setting, the maximum E-field in the center of the crystal reaches 260 kV m^{-1}. As a result, the maximum field is weaker, but as shown in Fig. 4, the concept still achieves a maximum phase modulation of the laser pulse of around 20°, which is very similar to the modulation at the KARA monitor.

Simulated Bunch Profile Measurement

The usual procedure for an EOSD bunch profile measurement is to take the spectrum of one modulated laser pulse, subtract the background and divide the result by the spectrum of an unmodulated laser pulse. The background is measured by blocking the laser while taking a measurement with the line camera and the unmodulated signal is an EOSD measurement while no electron bunch is modulating the laser pulse. The result is a ratio of the modulated vs. the unmodulated laser intensity and is called modulation. Figure 6 presents the simulation of the modulation with the new monitor concept for FCC-ee during operation at Z-pole energy in comparison to a scaled Gaussian, which has the same width as the simulated bunch profile. This allows to compare the result of the simulated EOSD measurement with the shape of the initial bunch profile. It shows that the modulation is slightly asymmetric and the peak is more narrow than the initial bunch profile. This is caused by the electric field inside the crystal, which does not perfectly correspond to the bunch profile due to reflections and disturbances caused by the crystal edges and the prisms. However, the modulation is still very similar to the original bunch profile and since it is a systematic distortion, it can be taken into account during the analysis of the spectrum.

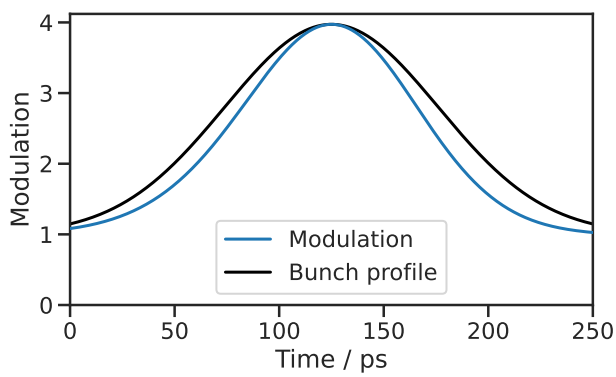


Figure 6: Simulated EOSD signal of the bunch profile with beam parameters of the FCC-ee at Z-pole energy in blue. The black line shows a scaled Gaussian with the same shape as the initial bunch profile. The simulated EOSD signal deviates slightly from the original bunch profile, which is caused by disturbances of the electric field in the EO crystal.

CONCLUSION AND OUTLOOK

FCC-ee is in need of a single-shot, bunch-by-bunch, bunch profile monitor and an EO near-field monitor as used at KARA is a promising candidate that is proposed as a baseline. The different beam properties, especially the longer bunches and higher charge density, require an adapted design for the crystal holder. Guiding the laser pulse through the crystal with prisms instead of metal mirrors allows a setup, where the beam propagates through the crystal only once and therefore avoids an unwanted upstream signal. This new design concept has been successfully tested in simulations under the conditions of FCC-ee during operation at Z-pole energy. The new design has a much lower impedance and therefore the wakefield is small enough to not interfere with the next electron bunch. Additionally, the new design achieves a similar amplitude of the laser modulation as the KARA design, despite the high bunch charge at FCC-ee. This is very important, since a smaller modulation reduces the signal-to-noise ratio and a larger modulation gives rise to non-linear effects that distort the bunch profile measurement. The simulated laser modulation is very similar to the initial bunch profile with only a small systematic deviation that can be taken into account during the analysis. The required repetition rate for bunch-by-bunch measurements at FCC-ee could be achieved by using a faster line camera and multiple EO monitors.

Since the suggested EO monitor concepts proves to be successful in the simulations for FCC-ee during operation at the Z-pole, future studies have to analyze the functionality for the three other operation modes as well. Especially the short bunches in combination with a high bunch charge during operation at the $t\bar{t}$ threshold will be challenging and might require adjustments to the crystal and / or its holder. For example to reduce the amplitude of the E-field, it might be beneficial to put the crystal into the winglet of the beampipe. In the next step, a proof-of-principle of the monitor design with prisms instead of mirrors should be tested, e.g. by adjusting the monitor at KARA and test it at an electron beam.

ACKNOWLEDGEMENTS

The Future Circular Collider Innovation Study (FCCIS) project has received funding from the European Union's Horizon 2020 research and innovation programme under grant No 951754. M. R. and M. M. P. acknowledges the support by the DFG-funded Doctoral School "Karlsruhe School of Elementary and Astroparticle Physics: Science and Technology". C. W. acknowledges funding by BMBF contract number 05K19VKD.

REFERENCES

[1] A. Abada *et al.*, "FCC-ee: The lepton collider", *Eur. Phys. J. Spec. Top.*, vol. 228, pp. 261–623, 2019. doi:10.1140/epjst/e2019-900045-4

[2] N. Hiller, "Electro-optical bunch length measurements at the ANKA storage ring", Ph.D. thesis, Karlsruher Institut für Tech-

ISBN: 978-3-95450-241-7 ISSN: 2673-5350 doi:10.18429/JACoW-IBIC2022-WEP26

nologie (KIT), Karlsruhe, Germany, 2013. doi:10.5445/IR/1000041159

[3] M. M. Patil *et al.*, "Ultra-Fast Line-Camera KALYPSO for fs-Laser-Based Electron Beam Diagnostics", in *Proc. IBIC'21*, Pohang, Korea, Sep. 2021, pp. 1–6. doi:10.18429/JACoW-IBIC2021-MOOB01

[4] S. Funkner *et al.*, "Revealing the Dynamics of Ultrarelativistic Non-Equilibrium Many-Electron Systems with Phase Space Tomography", 2019. doi:10.48550/arXiv.1912.01323

[5] M. Reißig *et al.*, "Development of an Electro-Optical Longitudinal Bunch Profile Monitor at KARA Towards a Beam Diagnostics Tool for FCC-ee", in *Proc. IPAC'22*, Bangkok, Thailand, 12-17 June 2022, pp. 296–299. doi:10.18429/JACoW-IPAC2022-MOPOPT025

[6] CST Studio Suite 2021, https://www.3ds.com/products-services/simulia/products/cst-studio-suite

[7] K. Oide, "$\beta_x^* = 10\,\mathrm{cm}$ optics for Z", 151st FCC-ee Optics Design Meeting, Mar. 2022, https://indico.cern.ch/event/1118299/.

[8] P. Schönfeldt *et al.*, "Towards Near-Field Electro-Optical Bunch Profile Monitoring in a Multi-Bunch Environment", in *Proc. IPAC'17*, Copenhagen, Denmark, May 2017, pp. 227–230. doi:10.18429/JACoW-IPAC2017-MOPAB055

Content from this work may be used under the terms of the CC BY 4.0 licence (© 2022). Any distribution of this work must maintain attribution to the author(s), title of the work, publisher, and DOI

ISBN: 978-3-95450-241-7 ISSN: 2673-5350 doi:10.18429/JACoW-IBIC2022-WEP28

STUDIES ON RADIALLY COUPLED FAST FARADAY CUPS TO MINIMIZE FIELD DILUTION AND SECONDARY ELECTRON EMISSION AT LOW INTENSITIES OF HEAVY IONS*

G. Rodrigues[1,†], K. Mal[1]. S. Kumar[1], R. Singh[2], C.P. Safvan[1], R. Mehta[1]
[1]Inter University Accelerator Centre, Aruna Asaf Ali Marg, New Delhi, India
[2]GSI Helmholtzzentrum fur Schwerionenforschung GmbH, Darmstadt, Germany

Abstract

Fast Faraday Cups (FFCs) are interceptive beam diagnostic devices used to measure fast signals from sub-nanosecond bunched beams and the operation of these devices is a well-established technique. However, for short bunch length measurements in non-relativistic regimes with ion beams, the measured profile is diluted due to field elongation and distortion by the emission of secondary electrons. Additionally, for short bunches with a low "signal to noise ratio" envisaged in the High Current Injector at the Inter University Accelerator Centre, the impedance matching of the EM structure puts severe design constraints. This work presents a detailed study on the modification of a radially-coupled coaxial FFC. The field dilution and secondary electron emission aspects are modelled through EM simulations and techniques to minimise these effects are explored.

INTRODUCTION

In the upcoming High Current Injector (HCI) Programme [1, 2] at New Delhi, India, there is an urgent need for developing diagnostics for longitudinal measurements which are critical for the successful operation of the High Current Injector. The operation of Faraday cups for intensity measurements is well established where the suppression of the emitted secondary electrons is carried out using a superimposed electric field, such that the emitted secondary electrons are retarded and recaptured [3]. For longitudinal charge profile measurements of short bunches (≤ 5 ns), it is critical to avoid impedance discontinuities in the Faraday cup structure until frequencies up to few GHz. Modified Faraday cup designs tailored to measure longitudinal charge distributions [3, 4] are called Fast Faraday Cups (FFC) [5]. Early FFC designs were tapered extension of coaxial cables allowing for full beam deposition on the central conductor while maintaining 50 Ω characteristic impedance [3, 6]. Following that, alternative FFC designs based on radial coupling in the central conductor [5] of a co-axial cable and microstrip based designs [4, 7] have been used in various accelerator laboratories. Recently [8], two FFC designs, one using a Radially-Coupled Coaxial Fast Faraday Cup (RCFFC) and a conventionally axially coupled FFC (ACFFC) were simulated with ion beams and compared with the measurements under similar beam conditions. A strong distortion in the longitudinal charge profile measurement due to secondary electrons is observed. External DC biasing of the central conductors minimises the distortion to a large extent. Most studies available in the literature are focused mainly on electromagnetic characteristics, i.e. targeting impedance mismatch aspects. However, there are additional challenges for short bunched beam measurements in non-relativistic regimes; a) the field elongation and b) distortion by the emission of secondary electrons. In this study, we will present a design modification of a Radially-Coupled Coaxial Fast Faraday Cup (RCFFC) considering the existing beam conditions at the High Current Injector Programme, which is presently under commissioning stages at the Inter-University Accelerator Center (IUAC), New Delhi. The primary drawback of the original design is the low "signal-to-noise" ratio due to the narrow beam limiting aperture of 0.8 mm along with the need for precise beam alignment with long averaging times for the measurement. The second challenge is the delayed signal induction due to emission of secondary electrons. The major modifications in our adapted design is to counter these challenges and are discussed in this contribution.

EM SIMULATIONS OF A MODIFIED RCFFC

The characteristic impedance (Z_{coax}) of a coaxial transmission line is defined with the following parameters [9], ε and μ as the permittivity and permeability of the material respectively, with r_1 and r_2 being the radii of the inner and outer conductor, respectively. The non-TEM mode with the lowest cut-off frequency (f_c) is TE_{11} and the cut-off frequency given by the standard known relation. Since the width of the co-axial line cannot be arbitrarily increased, a conical taper between a thin and a thick co-axial line was chosen. In order to minimise the reflection at the transition of coaxial and conical lines, it is necessary to design in such a way that the characteristic impedances of both the lines have the same impedance of 50 Ω. CST Microwave Studio [10] was used to design the RCFFC assembly with the interfacing option to the transmission line at the desired characteristic impedance of 50 Ω. Figure 1 shows the cross-sectional view of the model of the RCFFC, which consists of a metallic cube with two N-type connectors positioned concentrically. The collimating aperture of diameter 2 mm is chosen based on the relatively lower beam intensities of heavy ions available at the upcoming, High Current Injector Programme. A rod of diameter 6 mm was inserted between the central electrodes of the connectors and tapered down to 3 mm, being the diameter of the standard N-type connector pin.

* Work supported by VAJRA
† gerosro@gmail.com

Content from this work may be used under the terms of the CC BY 4.0 licence (© 2022). Any distribution of this work must maintain attribution to the author(s), title of the work, publisher, and DOI

ISBN: 978-3-95450-241-7 ISSN: 2673-5350 doi:10.18429/JACoW-IBIC2022-WEP28

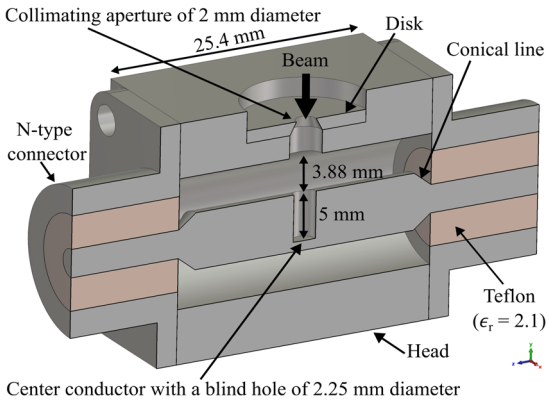


Figure 1: Model (cross-sectional view) of the RCFFC with the geometrical parameters

The rod acts as a collector as well as the transmission line's inner electrode. The diameter of the collector hole was chosen to be 2.25 mm to avoid hitting the beam directly. With these chosen dimensions, the first-order estimate of the RCFFC geometry parameters has been calculated using the analytical formula. For the chosen dimensions and the medium properties, the cut-off frequencies of the N-type connector and RCFFC head are 10.10 GHz and 9.64 GHz, respectively. In order to obtain the return loss (S_{11}) and insertion loss (S_{21}), a two-port analysis [11] was carried out by assigning two waveguide ports at the left and right N-type connectors; a Time Domain Reflection (TDR) [12] analysis was also performed to compute the distributed characteristic impedances along the coaxial and conical lines of the RCFFC.

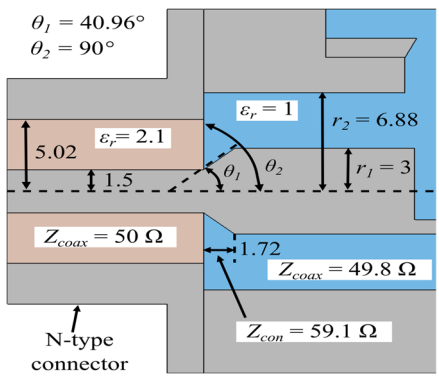


Figure 2: RCFFC geometry and its design parameters (unit: mm) for characteristic impedance of 50 Ω, with optimized design using CST-Microwave Studio.

The EM wave simulation was performed by considering only TEM mode at the waveguide ports with a frequency range up to 9 GHz to evaluate the performance. It was observed that the return loss of the RCFFC depicts two resonance peaks below the cut-off frequency (10.10 GHz) which are due to impedance mismatch at the conical lines and the center of the RCFFC, although, the insertion loss is not so large. Similarly, the characteristic impedance of the RCFFC is almost equal to theoretical impedance (50 Ω) but it also shows two capacitive peaks at the conical line and one inductive peak at the center of the RCFFC. The difference between the theoretical and simulated impedance at the conical line could possibly be due to the short length of the conical line. The inductive peak at the center of the RCFFC is due to the holes in the collector electrode and in the head of the RCFFC. To achieve uniform impedance and minimize the reflections at the junction between the conical and coaxial lines, the length of the conical line and inner radius of the outer conductor (r_2) were optimized. The optimized geometry parameters are shown in Fig. 2 where the length of the conical line is 1.72 mm and thus, the angle (θ_1) of the inner conductor of the conical line turns out to be 40.96°. The optimized inner radius (r_2) of the outer conductor is 6.88 mm to suppress the inductive peak at the center of the RCFFC. The theoretical characteristic impedance of the conical line and head of the RCFFC are 59.1 Ω and 49.8 Ω, respectively. The simulated return loss, insertion loss and characteristic impedance of the optimized geometry are shown in Fig. 3. and the return loss has been reduced from −30 dB to −55 dB. The insertion loss for the optimized geometry is also reduced. The impedance difference between the conical and coaxial lines was also significantly reduced and is almost equal to 50 Ω (see Fig. 3(b)). We can see that the insertion loss of the optimized RCFFC geometry attains a value of −0.005 dB at frequency 9 GHz. Using the well know relation between the bandwidth and the signal rise time, the rise time of the RCFFC geometry can be improved to a value better than 39 ps.

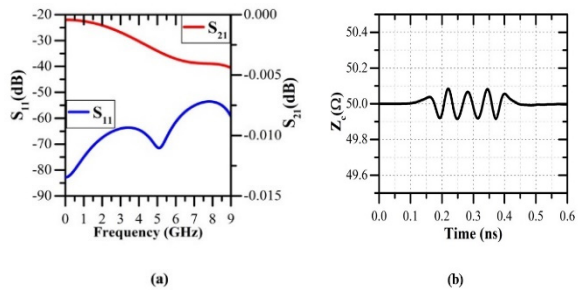


Figure 3: Simulated results of the optimized geometry, depicting (a) return loss at the input port, and insertion loss between two ports, (b) characteristic impedance (Z_c).

ROBUSTNESS OF THE DESIGN PARAMETERS

The effect of the manufacturing tolerances of the various parameters on the characteristic impedance of the RCFFC is further investigated. The diameter of the collector electrode ($d = 2r_1$), inner diameter of the outer conductor ($D = 2r_2$) and the transition length (L_{cone}) of coaxial to conical were increased by 0.1 mm individually about their optimized values (see Fig. 2). Figures 4(a) and 4(b) show the simulated reflection coefficient and the characteristic impedance of the RCFFC, respectively, when the diameter of the collector electrode (d), inner diameter of the outer conductor (D), and the transition length (L_{cone}) of the coaxial to conical line were increased by 0.1 mm.

For the sake of comparison, the reflection coefficient and the characteristic impedance for the optimal parameter values are also shown Fig. 4. It can be seen that a small change of 0.1 mm in the dimensions of the RCFFC causes significant changes in the reflection coefficient and characteristic

Content from this work may be used under the terms of the CC BY 4.0 licence (© 2022). Any distribution of this work must maintain attribution to the author(s), title of the work, publisher, and DOI

ISBN: 978-3-95450-241-7 ISSN: 2673-5350 doi:10.18429/JACoW-IBIC2022-WEP28

Content from this work may be used under the terms of the CC BY 4.0 licence (© 2022). Any distribution of this work must maintain attribution to the author(s), title of the work, publisher, and DOI

impedance, especially for the collector electrode. Therefore, these tolerances must be carefully considered during fabrication of the collector electrode.

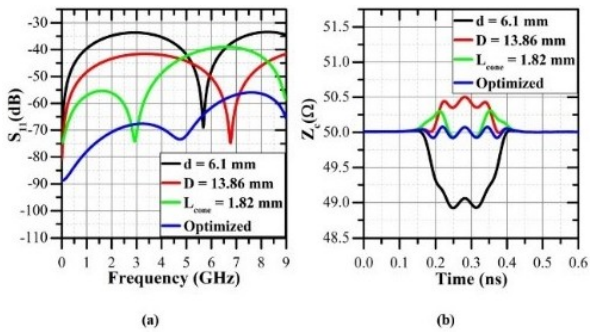


Figure 4: Simulated results showing the effect of individual tolerance on (a) Reflection coefficient and (b) Characteristic impedance of the RCFFC, when parameters are increased by 0.1 mm about their optimal values (d = 6 mm, D = 13.77 mm, and L_{cone} = 1.72 mm).

For the sake of comparison, the reflection coefficient and the characteristic impedance for the optimal parameter values are also shown Fig. 4. It can be seen that a small change of 0.1 mm in the dimensions of the RCFFC causes significant changes in the reflection coefficient and characteristic impedance, especially for the collector electrode. Therefore, these tolerances must be carefully considered during fabrication of the collector electrode.

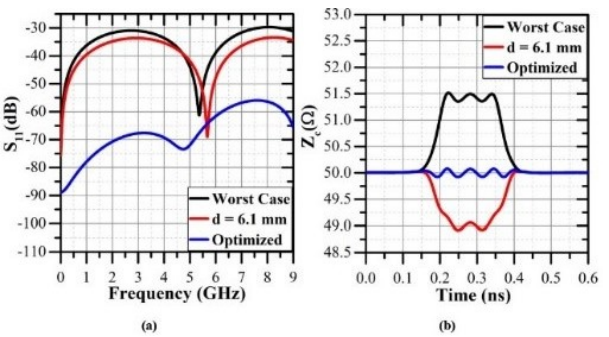


Figure 5: Simulated results showing the effect of tolerance on (a) Reflection coefficient and (b) Characteristic impedance of the RCFFC, for the worst case, for the case when d = 6.1 mm, and for the optimized parameters (d = 6 mm, D = 13.77 mm, and L_{cone} = 1.72 mm).

Let us consider the worst case, when all the dimensions of the RCFFC are off by 0.1 mm from their optimized values (d = 5.9 mm, D = 13.8 mm, and L_{cone} = 1.82 mm). Figure 5 shows the simulated reflection coefficient and characteristic impedance for the worst case, when the diameter of the collector electrode is only changed by 0.1 mm and for remaining optimal parameter values. From Fig. 5(a), a small change in the reflection coefficient is observed for the worst case compared to the case when the diameter of the collector electrode was changed by 0.1 mm alone. This further shows that how tight manufacturing tolerance is required for the collector electrode. Therefore, a margin of ± 0.1 mm is left to account for the manufacturing tolerances in order to obtain the reflection coefficient equal to −30 dB.

EMISSION OF SECONDARY ELECTRONS

Besides characteristic impedance, other properties need to be considered in design of the FFC for measuring bunch widths very accurately. In order to suppress all the SEs, electrostatic suppression is normally used in many conventional FCs [13–15] and FFCs [5, 16]. In our design, the electrostatic suppressor cannot be implemented in front of the collector electrode due to space constraints, therefore the blind hole structure in the collector itself , was modified. In order to minimise the losses of the SEs, their production mechanism, energy and angular distribution as well as the total yield (as a function of ion energy) are required. The energy distribution of the secondary electrons has a peak at few eV with a full width at half maximum (FWHM) of the same order of magnitude, thus about 80-95% of the ejected electrons are below 50 eV [17]. In order to stop the projectile ions of total energy 1.8 MeV/A, the thickness of the beam stopper should be much larger than the range of the projectiles. Copper material was chosen for the collector of the RCFFC because of its good electrical property and its excellent thermal conductivity. The range of ^{14}N ions of energy 25.2 MeV in copper has been calculated to be 8.2 µm using SRIM code [18] and similarly the range of ^{238}U of energy 428.4 MeV was found to be 12.7 µm. Thus, choosing a thickness of 1 mm is sufficient to stop all ions having energy of 1.8 MeV/A.

BUNCH LENGTH SIMULATIONS

The PIC solver of CST Microwave Studio calculates the EM fields and particle motion at discrete time samples. A Gaussian shaped longitudinal charge distribution with a beam bunch charge of 1 fC was used as the excitation source. signals at the N-type connectors, a short bunch length of σ = 13.5 ps with tails cut at 4σ and approximates 108 ps full width (8σ) was chosen to demonstrate the transient FFC signal induction process. For such a bunch travelling with velocity corresponding to β = 0.06, the full width of the bunch is approximately 2 mm which is less than the blind hole depth of (5 mm) in the collector electrode. The head of the RCFFC was maintained at ground potential and the inner conductor which acts as collector was at the floating potential. The beamlet formed by the aperture of diameter 2 mm in the collimation disk travels through a gap of length L = 3.88 mm between the grounded body and the collector electrode, and is absorbed within a blind hole situated inside the collector electrode. Figure 6(a) demonstrates the propagation of a Gaussian pulse, while Figs. 6(b) and 6(c) show respectively the induced surface current density and the induced voltage signal on one of the N-type connector. The time (x-axis) in Fig. 6(c) is translated by 94 ps to account for the wave traversal from center of the FFC to one of the N-type connectors. As it can be seen, the voltage signal starts to induce once the bunch starts to enter the gap and rises as the bunch approaches the

ISBN: 978-3-95450-241-7 ISSN: 2673-5350 doi:10.18429/JACoW-IBIC2022-WEP28

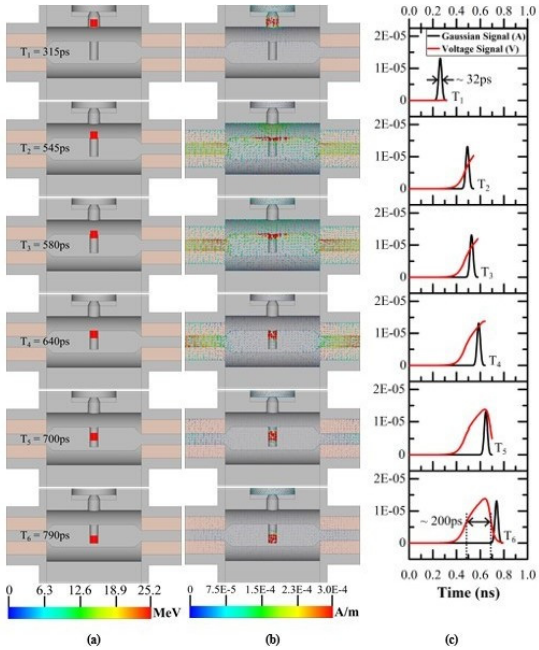


Figure 6: Simulation of a Gaussian pulse having bunch length $\sigma = 13.5$ ps with $\beta = 0.06$ through the RCFFC showing (a) Propagation of a Gaussian bunch; (b) induced surface current density; and (c) induced voltage signal on one of the N-type connectors and a Gaussian pulse.

collector electrode. The induced signal attains the highest value (at time $T_2 = 545$ ps), when the bunch is about to enter in the blind hole of the collector electrode. At this point ($T_2 = 545$ ps), the maximum density of the opposite charges (electrons) induces on the collector electrode (see Fig. 6(b) and the same density of the electrons travels with the bunch when bunch starts to enter into the blind hole. As a result, the signal starts to reduce and reaches zero at time $T_5 = 700$ ps (see Fig. 6(c) before absorbing the bunch into the collector electrode where negative charges are neutralised with the positive charges of the bunch. Also, from Fig. 6(b), after time $T_4 = 640$ ps, there is no flow of current from centre of the FFC to the N-types connectors except the earlier induced current. That means the induced signal should be reduced to zero once the bunch completely entered into the hole, while it had reduced to zero at time $T_5 = 700$ ps and the full width at half maximum (FWHM = $2.3548\,\sigma$) of the induced signal is approximately 200 ps. The modelling shows that the bunch length of the induced signal will be $\sigma_c = 85$ ps which is larger than the bunch length of the input beam ($\sigma_b = 13.5$ ps).

CONCLUSION

The radially coupled coaxial FFC (RCFFC) design for high intensity proton beams is modified for low intensity ion beams. The central conductor and the hole for the beamlet entry were widened while maintaining the characteristic impedance of the full structure close to 50 Ω. A transition method without curved structures was adopted for the transition from the N-type connector to the cup region to achieve uniform impedance and low reflection. Adaptations in the shape of the blind hole surface in the central conductor was made to reduce the number of secondary electrons exiting the blind hole. Signal induction procedure and its dependence on the FFC design parameters, like entry hole size and gap length was discussed in detail. The effect of secondary electron emission on the induced signal is studied and potential remedy is proposed.

ACKNOWLEDGEMENT

R. Singh and G. Rodrigues would like to acknowledge the help and support received from the Department of Science and Technology (DST) related to the VAJRA project (VJR/2018/000115).

REFERENCES

[1] A. Roy, "Accelerator development at the Nuclear Science Centre", *Current Science*, vol. 76, pp. 149–153, 1999. http://www.jstor.org/stable/24101229

[2] D. Kanjilal *et al.*, "High Current Injector at Nuclear Science Centre", in: *Proc. APAC'04*, Gyeongju, Korea, Mar. 2004, paper MOP10008, pp. 73-75. https://jacow.org/a04/papers/mop10008.pdf

[3] P. Strehl, *Beam Instrumentation and Diagnostics*, Springer Verlag, Berlin Heidelberg, 2006.

[4] W. R. Rawnsley *et al.*, "Bunch shape measurements using fast Faraday cups and an oscilloscope operated by LabVIEW over Ethernet", *AIP Conf. Proc.*, vol. 546, p. 547, 2000. doi:10.1063/1.1342629

[5] J.-P. Carniero *et al.*, "Longitudinal beam dynamics studies at the PIP-II injector test facility", *Int. J. Mod. Phys. A.*, vol. 34, no. 36, 2019. doi:10.1142/S0217751X19420132

[6] H. Chuaqui *et al.*, "Simple Faraday cup with subnanosecond response", *Rev. Sci. Instrum.* vol. 60, p. 141, 1989. doi:10.1063/1.1140572

[7] M. Bellato *et al.*, "Design and tests for the fast Faraday cup of the ALPI post-accelerator", *Nucl. Instrum. Methods Phys. Res., Sect. A,* vol. 382, p. 118, 1996. doi:10.1016/S0168-9002(96)00508-6

[8] R. Singh *et al.*, "Simulation and Measurements of the Fast Faraday Cups at GSI UNILAC", in Proc. IBIC'22, Krakow, Poland, 2022.

[9] D M. Pozar, *Microwave engineering*, 2nd Edition, 1998 John-Wiley & Sons.

[10] www.3ds.com/cst-studio-suite/

[11] S. Y. Liao, *Microwave Devices and Circuits*, Prentice Hall, New Jersey, USA, 1985.

[12] https://space.mit.edu/RDIO/CST_online/mergedProjects/3D

[13] J.D. Thomas *et al.*, "Performance enhancement study of an electrostatic Faraday cup detector", *Nucl. Instrum. Meth. Phys. Res., Sect. A,* vol. 536, pp. 11–23, 2005. doi:10.1016/J.NIMA.2004.07.211

[14] E. Ebrahimibasabi and S.Feghhi, "Design and construction of a secondary electron suppressed Faraday Cup for measurement of beam current in an electrostatics proton accelerator", *Int. J. Mass Spectrom.* vol. 386, pp. 1–5, 2015. doi:10.1016/j.ijms.2015.05.006

[15] Cantero *et al.*, "Design of a compact Faraday cup for low energy, low intensity ion beams", *Nucl. Instrum. Methods Phys. Res., Sect. A,* vol. 807, pp. 86–93. doi:10.1016/J.NIMA.2015.09.096

Content from this work may be used under the terms of the CC BY 4.0 licence (© 2022). Any distribution of this work must maintain attribution to the author(s), title of the work, publisher, and DOI

ISBN: 978-3-95450-241-7 ISSN: 2673-5350 doi:10.18429/JACoW-IBIC2022-WEP28

[16] J. V. Mathew and A. Bajaj, "An improved strip-line fast Faraday cup for beam bunch measurements", *Rev. Sci. Instrum*., vol. 91, p. 113305, 2020. doi:10.1063/5.0025457

[17] D. Hasselkamp, S. Hippler, and A. Scharmann, "Ion induced secondary electron spectra from clean metal surfaces", *Nucl. Instrum. Methods Phys. Res., Sect. B,* vol. 18, pp. 561-565, 1987. doi:10.1016/S0168-583X(86)80088-X

[18] SRIM - The Stopping and Range of Ions in Matter http://www.srim.org

Content from this work may be used under the terms of the CC BY 4.0 licence (© 2022). Any distribution of this work must maintain attribution to the author(s), title of the work, publisher, and DOI

ISBN: 978-3-95450-241-7 ISSN: 2673-5350 doi:10.18429/JACoW-IBIC2022-WEP29

OPTIMIZATION STUDY OF BEAM POSITION AND ANGULAR JITTER INDEPENDENT BUNCH LENGTH MONITOR FOR AWAKE RUN 2

C. Davut*,[1,2], G. Xia[1], University of Manchester, Manchester, UK
O. Apsimon[1], University of Liverpool, Merseyside, UK
P. Karataev, Royal Holloway, University of London, London, UK
S. Mazzoni, T. Lefevre, CERN, Geneva, Switzerland
[1]also at Cockcroft Institute, Daresbury, UK
[2]also at CERN, Geneva, Switzerland

Abstract

In this paper, a study using the Polarization Current Approach (PCA) model is performed to optimize the design of a short bunch length monitor using two dielectric radiators that produce coherent Cherenkov Diffraction Radiation (ChDR). The electromagnetic power emitted from each radiator is measuring a different part of the bunch spectrum using Schottky diodes. For various bunch lengths, the coherent ChDR spectrums are calculated to find the most suitable frequency bands for the detection system. ChDR intensities measured by each detector are estimated for different impact parameters to explore the dependence of bunch length monitor on beam position and angular jitter. It is found that, in the present configuration, the effects of beam position and angular jitter are negligibly small for bunch length measurement.

INTRODUCTION

In recent years, coherent Cherenkov Diffraction radiation (ChDR) has become a suitable candidate for non-invasive longitudinal bunch profile diagnostics with successful experimental validations [1, 2]. Although, the exact solutions of the electromagnetic problems are often not known, and detailed computer simulations require extensive time and resources, the properties of the radiation are often derived from simplified models, that assume specific assumptions on the radiator shape [3].

The emission characteristics of ChDR can be calculated by Polarization Current Approach (PCA) which describes simultaneously generated DR and ChDR as a solution to the "vacuum" set of macroscopic Maxwell's equations [4]. Among the other theoretical models, PCA introduces some limitations on the longitudinal size of the radiator when calculating of the spectral-angular distribution of ChDR that makes it a powerful tool to calculate expected radiation yield and directivity of ChDR cone [5].

Considering a relativistic charged particle with energy $\gamma = 1/\sqrt{1-\beta^2}$ moving rectilinearly at a distance b from a prismatic dielectric target, such as in Fig. 1, the particle field flattened into a plane perpendicular to its motion having a relation between its components $E_\perp \gg E_\parallel$ and $H \approx E$ for $\beta = v/c \sim 1$. The Fourier component of $E_\perp$ is spatially restricted in a circle with a radius which is called the effective field radius $l = \gamma\beta\lambda/2\pi$, where λ is the radiation wavelength. Hence, the following the condition should be satisfied :

$$l \gtrsim b. \tag{1}$$

In this case the dielectric medium will be polarised and the polarization radiation will be emitted [6].

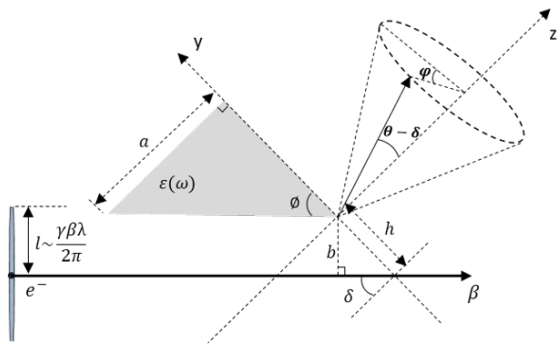


Figure 1: The geometry of ChDR emission by a relativistic charged particle moving rectilinearly at a distance b from the bottom surface of a prismatic dielectric target.

Therefore the spectral-angular distribution of ChDR can be calculated by Polarization Current Approach (PCA), as described in [4], in terms of its vertical and horizontal components with respect to particle trajectory and after the radiation is refracted out at the exit surface of the prism.

$$\frac{d^2W}{d\omega d\Omega} = S_e(\omega) = \frac{d^2W_\perp}{d\omega d\Omega} + \frac{d^2W_\parallel}{d\omega d\Omega}. \tag{2}$$

The total radiation intensity generated by an electron bunch can be described by

$$S(\omega) = S_e(\omega)\,[N + N(N-1)]\,F(\omega), \tag{3}$$

where $S(\omega)$ is the experimentally measured spectrum, $S_e(\omega)$ is the theoretically calculated single electron spectrum, N is the number of electrons within the bunch and $F(\omega)$ is the longitudinal bunch form factor [7]. As an important feature of the radiation spectrum, the domination of the longitudinal bunch form factor on the radiation spectrum indicates how far the radiation intensity extends in the frequency range. The amplitude of the longitudinal form factor

* can.davut@manchester.ac.uk

Content from this work may be used under the terms of the CC BY 4.0 licence (© 2022). Any distribution of this work must maintain attribution to the author(s), title of the work, publisher, and DOI

ISBN: 978-3-95450-241-7 ISSN: 2673-5350 doi:10.18429/JACoW-IBIC2022-WEP29

Content from this work may be used under the terms of the CC BY 4.0 licence (© 2022). Any distribution of this work must maintain attribution to the author(s), title of the work, publisher, and DOI

can be calculated as a modulus squared of a Fourier transform applied to the longitudinal charge distribution $\rho(z)$ within the bunch [8],

$$F(\omega) = \left| \int_0^\infty \rho(z) \exp\left(i\frac{\omega}{c}z\right) dz \right|^2 \quad (4)$$

and can be written in the following form for a bunch with Gaussian distribution,

$$F(\omega) = \exp\left(-\frac{\omega^2\sigma_z^2}{c^2}\right) = \exp(-k^2\sigma_z^2), \quad (5)$$

where $k = \omega/c = 2\pi/\lambda$ is the wave number. Finally, neglecting the contribution from incoherent emission, we can write

$$S(\omega) = N^2 S_e(\omega) F(\omega). \quad (6)$$

CALCULATION METHOD

The measurement concept of the longitudinal electron bunch length monitor consists of three Alumina radiators placed on only one side of the electron bunch (see Fig. 2).

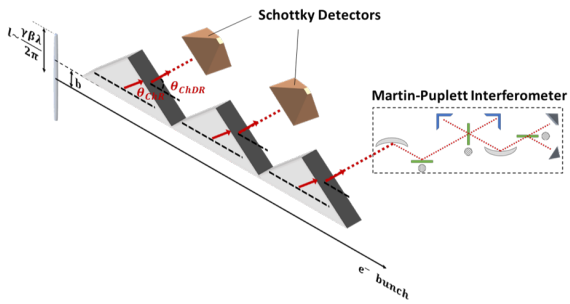


Figure 2: The geometry of ChDR emission by a relativistic charged particle moving rectilinearly at a distance b from the bottom surface of a prismatic dielectric target.

Two Schottky detectors having two different frequency ranges, is used to measure the ChDR from the first two radiators. Coherent ChDR spectral responses are measured by these two detectors and the longitudinal charge distribution of the bunch can be eliminated by by using a similar approach with [1].

$$\frac{S_1(\omega_1)}{S_2(\omega_2)} = \frac{S_{e1}(\omega_1)\, exp(-k_1^2\sigma_z^2)}{S_{e2}(\omega_2)\, exp(-k_2^2\sigma_z^2)}. \quad (7)$$

Thus, RMS bunch length can be calculated by,

$$\sigma_{z,rms} = \sqrt{\left| \frac{1}{k_2^2 - k_1^2} \ln\left(\frac{S_1(\omega_1) S_{e2}(\omega_2)}{S_2(\omega_2) S_{e1}(\omega_1)}\right)\right|}. \quad (8)$$

In order to calculate the ChDR radiation spectrum and intensity captured at the corresponding horn antenna aperture, the coordinate system in PCA equations is transformed into cartesian as depicted in Fig. 3. As ρ being the radius vector magnitude,

$$\begin{aligned} \sin\theta_x &= \frac{x}{\rho} = \sin\theta\sin\varphi \\ \sin\theta_y &= \frac{y}{\rho} = \sin\theta\cos\varphi. \end{aligned} \quad (9)$$

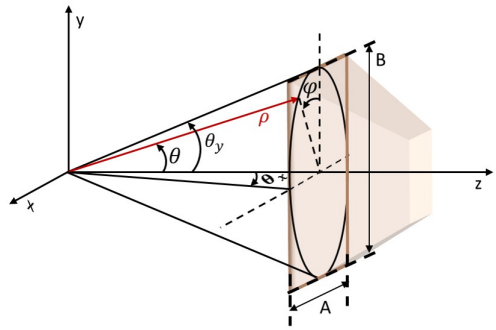


Figure 3: Transformation of coordinate system.

Thus, coherent ChDR spectrum can be calculated by

$$\frac{dW}{d\omega} = N^2\, exp(-k^2\sigma_z^2) \int_{\frac{-\Delta\theta_x}{2}}^{\frac{\Delta\theta_x}{2}} \int_{\theta_{ChDR}-\frac{\Delta\theta_y}{2}}^{\theta_{ChDR}+\frac{\Delta\theta_y}{2}} \frac{d^2W}{d\omega d\Omega} d\theta_x\, d\theta_y. \quad (10)$$

Hence ChDR intensity, $S(\omega)$, can be found by integrating Eq. (10) over each corresponding detector horn aperture with their frequency detection ranges.

PCA ANALYSIS

Since RMS bunch length is calculated by taking ChDR intensity ratios of detectors to be determined, it is important to find the most suitable frequency range of Schottky detectors operates in such a way that one should be used as normalization detector which measures nearly the same ChDR intensity independent from the bunch length while the other one should be sensitive to the bunch length. For that purpose, a variety of Schottky diode detectors and corresponding pyramidal and diagonal horn antennas available from Millitech [9] and Virginia Diodes [10] considered to determine the most suitable frequency bands of detectors to be used for this specific calculation method by using simulation parameters including the AWAKE Run 2 electron bunch parameters [11] in Table 1.

Table 1: Simulation Parameters

Parameter	Value
Bunch Energy, E	150 MeV
Bunch Length, σ_z	200 fs
Bunch Size, σ_r	5.25 m
Position Jitter	$< \sigma_r$
Impact Parameter, b	15 mm
Dielectric constant, $\varepsilon_{Alumina}$	9.5
Radiator Angle, ϕ	19
Radiator Length, a	16.28 mm

As coherent ChDR spectrum extend up to THz range for such a short electron bunch length, the diffraction effects dominate in lower frequencies while the domination of the bunch form factor begins at higher frequencies of the spectrum.These two effects lead us to have the advantage to choose the Schottky diodes to be used with different purposes considering the aim of the RMS bunch length calcula-

ISBN: 978-3-95450-241-7 ISSN: 2673-5350 doi:10.18429/JACoW-IBIC2022-WEP29

tion method. ChDR spectrum and intensity of each selected Schottky detector are shown in Fig. 4. According to the PCA simulations,the detectors which operate between 60-90 GHz and between 400-600 GHz are selected as normalization and sensitivity detector, respectively.

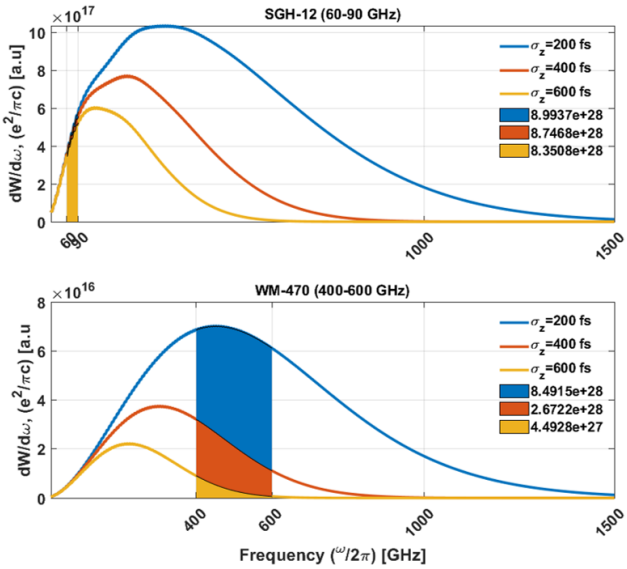


Figure 4: ChDR spectral responses calculated by using theoretical PCA model considering frequency ranges of each selected detector and its corresponding horn aperture.

Beam position and angular jitter is investigated with the selected Schottky detectors and results shown in Figs. 5 and 6, respectively. Although beam position jitter for AWAKE Run 2 is specified as less than σ_r, ChDR intensity captured by each detector is calculated for ± 1 mm to check the intensity ratio in wider range. It is found that the ± 1 mm beam position jitter causes 6% change in ChDR intensity ratio of the detectors while it is 0.03% in the range of $\pm\sigma_r$ as shown in Fig. 5.

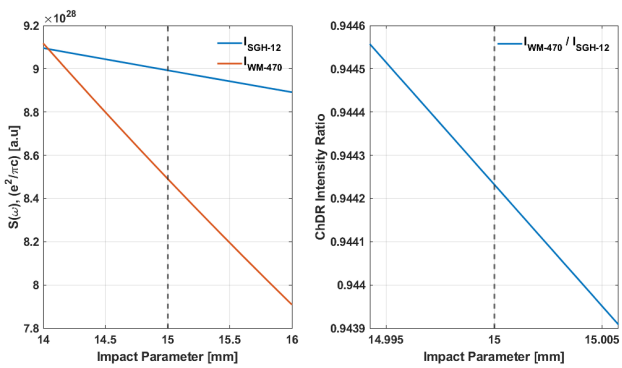


Figure 5: Impact parameter scan.

Following the same principle, angular jitter is also calculated in a wider range for a conventional accelerator, ± 1 mrad, and the change in the ChDR intensity ratio is found 0.9% as shown in Fig. 6.

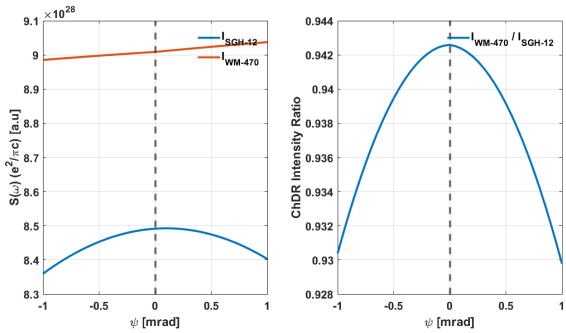


Figure 6: Angular jitter scan.

By having less than 1% sensitivity to beam position and angular jitter we can clearly say that the RMS bunch length calculation is independent from these effects.

The goal of RMS bunch length calculation method is not only being insensitive to the beam position and angular jitter but also being highly sensitive to any change in the bunch length simultaneously. Thus, bunch length sensitivity of the ChDR intensity ratio is calculated in the range of ± 10 fs. Figure 7 shows ChDR intensity for each selected detector and the intensity ratios in that range. It is found that ± 1 fs change in the bunch length causes 5% change in the ChDR intensity ratio.

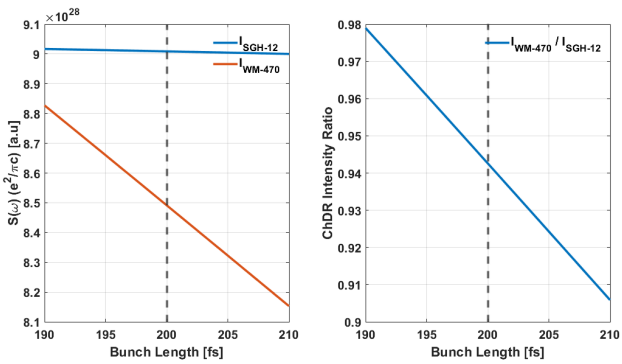


Figure 7: Bunch length sensitivity scan.

CONCLUSION AND FUTURE PLANS

The determination of the Schottky diodes and most suitable frequency ranges to be used for the detection of the ChDR was made by using PCA investigation of ChDR spectrum and intensity among a variety of Schottky diodes from Millitech and Virginia diodes. The dependence of ChDR intensity ratio to the beam position and angular jitter besides bunch length sensitivity of the calculation method was invenstigated. It was found that RMS bunch length calculation is independent of beam position and angular jitter by having $< 1\%$ change in the CHDR intensity ratio while having 5% for ± 1 fs bunch length change.

The commissioning of the bunch length monitor has been started and tests are on going in the CLEAR facility at CERN. Comprehensive analysis and the details will be published in a journal in the future.

Content from this work may be used under the terms of the CC BY 4.0 licence (© 2022). Any distribution of this work must maintain attribution to the author(s), title of the work, publisher, and DOI

ISBN: 978-3-95450-241-7 ISSN: 2673-5350 doi:10.18429/JACoW-IBIC2022-WEP29

Content from this work may be used under the terms of the CC BY 4.0 licence (© 2022). Any distribution of this work must maintain attribution to the author(s), title of the work, publisher, and DOI

ACKNOWLEDGEMENTS

C. Davut is supported by the Turkish Ministry of National Education, Republic of Turkey through the Postgraduate Study Abroad Program. The authors would like to acknowledge the support from the Cockcroft Institute Core Grant and the STFC AWAKE Run 2 Grant ST/T001917/1.

REFERENCES

[1] A. Curcio *et al.*, "Noninvasive bunch length measurements exploiting cherenkov diffraction radiation", *Phys. Rev. Accel. Beams*, vol. 23, no. 2, p. 022802, 2020. doi:10.1103/PhysRevAccelBeams.23.022802

[2] K. Fedorov *et al.*, "Development of longitudinal beam profile monitor based on coherent transition radiation effect for clara accelerator", *J. Instrum.*, vol. 15, no. 06, p. C06008, 2020. doi:10.1088/1748-0221/15/06/C06008

[3] K. Łasocha *et al.*, "Experimental Verification of Several Theoretical Models for ChDR Description", in *Proc. IPAC'22*, Bangkok, Thailand, Jun. 2022, pp. 2420–2423. doi:10.18429/JACoW-IPAC2022-THOYGD1

[4] M. V. Shevelev and A. S. Konkov, "Peculiarities of the generation of vavilov-cherenkov radiation induced by a charged particle moving past a dielectric target", *J. Exp. Theor. Phys.*, vol. 118, no. 4, pp. 501–511, 2014. doi:10.1134/S1063776114030182

[5] C. Davut, O. Apsimon, P. Karataev, T. Lefèvre, S. Mazzoni, and G. X. Xia, "Analytical and Numerical Characterization of Cherenkov Diffraction Radiation as a Longitudinal Electron Bunch Profile Monitor for AWAKE Run 2", in *Proc. IPAC'21*, Campinas, Brazil, May 2021, pp. 4355–4358. doi:10.18429/JACoW-IPAC2021-THPAB284

[6] M. L. Ter-Mikaelian, *High energy electromagnetic processes in condensed media*, Wiley-Interscience, 1972.

[7] J. S. Nodvick and D. S. Saxon, "Suppression of coherent radiation by electrons in a synchrotron", *Phys. Rev.*, vol. 96, no. 1, p. 180, 1954. doi:10.1103/PhysRev.96.180

[8] A. P. Potylitsyn, M. I. Ryazanov, M. N. Strikhanov, and A. A. Tishchenko, "Coherent radiation generated by bunches of charged particles", in *Diffraction Radiation from Relativistic Particles*, Berlin, Germany: Springer, 2010, pp. 197–220. doi:10.1007/978-3-642-12513-3_7

[9] Smiths Interconnect, https://www.smithsinterconnect.com

[10] Virginia Diodes, https://www.vadiodes.com/en/products/detectors

[11] P. Muggli and for the AWAKE Collaboration, "Physics to plan AWAKE Run 2", *J. Phys.: Conf. Ser.*, vol. 1596, p. 012008, 2020. doi:10.1088/1742-6596/1596/1/012008

ISBN: 978-3-95450-241-7 ISSN: 2673-5350 doi:10.18429/JACoW-IBIC2022-WEP30

CREATION OF THE FIRST HIGH-INDUCTANCE SENSOR OF THE NEW CCC-Sm SERIES*

V. Tympel[†,1], T. Stoehlker[1,2], Helmholtz Institute Jena, Jena, Germany
D. Haider, M. Schwickert, T. Sieber
GSI Helmholtz Centre for Heavy Ion Research, Darmstadt, Germany
L. Crescimbeni, F. Machalett, T. Schönau[3], F. Schmidl, P. Seidel
Institute of Solid State Physics (IFK) , Jena, Germany
M. Schmelz, R. Stolz, V. Zakosarenko[4], Leibniz-IPHT, Jena, Germany
[1]also at GSI Helmholtz Centre for Heavy Ion Research, Darmstadt, Germany
[2]also at Institute for Optics and Quantum Electronics, Jena, Germany
[3]also at Leibniz Institute of Photonic Technology, Leibniz-IPHT, Jena, Germany
[4]also at Supracon AG, Jena, Germany

Abstract

Cryogenic Current Comparators (CCC) for beamlines are presently used at CERN-AD and in the FAIR project at CRYRING with 100 mm and 150 mm beamline diameter, respectively, for non-destructive absolute measurement of beam currents in the amplitude range of below 10 μA_{pp} (current resolution 1 nA_{pp}). Both sensor versions (CERN-Nb-CCC and FAIR-Nb-CCC-XD) use niobium as a superconductor for the DC-transformer and magnetic shielding. The integrated flux concentrators have an inductance below 100 µH at 4.2 Kelvin. The new Sm-series (Smart & Small) is designed for a beamline diameter of 63 mm and is using lead (Pb) as superconductor. The first implemented sensor (IFK-Pb-DCCC-Sm-200) has two core-based pickup coils (2 x 100 µH at 4.2 K) and hence the option to use two SQUID units. During construction, some basic investigations such as on noise behaviour (fluctuation–dissipation theorem, white noise below 2 $pA_{rms}/\sqrt{Hz}$) and the magnetic shielding in terms of L_{core}-$C_{meander}$-resonance and additional mu-metal shielding were undertaken. These results are presented herein. Finally, a current resolution of 0.5 nA_{pp} was achieved without additional shielding measures in laboratory environment.

INTRODUCTION

Cryogenic Current Comparators (CCC) measure the azimuthal magnetic field of a charged particle beam non-destructively. By using superconducting components such as magnetic shielding, DC transformer, and SQUIDs, a current resolution in the nA range can be achieved [1]. After the development of large CCCs for the CERN Antiproton Decelerator (CERN-Nb-CCC) [2] and FAIR-project (FAIR-Nb-CCC-XD) [3], both with a current pulse resolution >1 nA, some new concepts are currently being tested on smaller size CCCs - the so-called Small & Smart series (CCC-Sm, <1 nA).

PICKUP COILS

To increase system availability and enable comparison experiments, the setup is carried out with two superconductive pickup coils (Dual-core CCC or DCCC). Standard Magnetec M-616 cores [4] were used for the first DCCC-Sm (see Fig. 1), which achieve an inductance of about 100 µH in a package of three cores per coil (see Fig. 2).

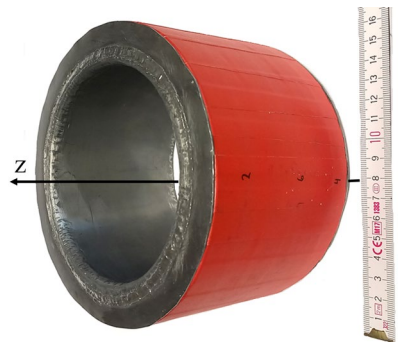


Figure 1: Pickup coil #1, one full-faced single-turn coil made of lead through three M-616 cores with z-axis as later beam direction.

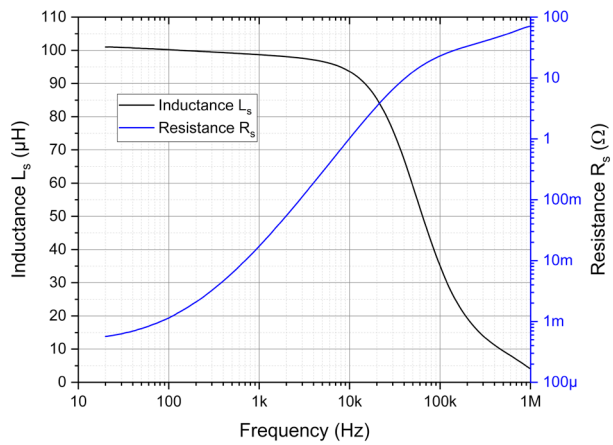


Figure 2: Pickup coil #1, serial inductance L_s and serial resistance R_s measured at 4.2 K.

* Work supported by the BMBF under contract No. 5P21SJRB
† volker.tympel@uni-jena.de

Content from this work may be used under the terms of the CC BY 4.0 licence (© 2022). Any distribution of this work must maintain attribution to the author(s), title of the work, publisher, and DOI

ISBN: 978-3-95450-241-7 ISSN: 2673-5350 doi:10.18429/JACoW-IBIC2022-WEP30

Content from this work may be used under the terms of the CC BY 4.0 licence (© 2022). Any distribution of this work must maintain attribution to the author(s), title of the work, publisher, and DOI

Fluctuation-Dissipation Theorem

Following the fluctuation-dissipation theorem (FDT), an expected value for the current noise density $i_{rms}/\sqrt{(\Delta f)}$ can be calculated by the serial inductance L_s and the serial resistance R_s of the pickup coil as functions of the frequency f, the fixed input coil inductance L_i (1 µH) of the SQUID, at a fixed temperature T (4.2 K) and a fixed frequency interval Δf, shown in Eq. (1) [5]:

$$\frac{{i_{rms}}^2}{\Delta f} = 4k_B T \cdot \frac{R_S(f)}{\left(2\pi f \cdot (L_i + L_S(f))\right)^2 + \left(R_S(f)\right)^2} \qquad (1)$$

Figure 3 shows the good agreement of the directly measured spectral current noise density with the calculation via the FDT in the white noise range > 1 kHz. The slight overestimation of the current noise density in the frequency range < 1 kHz (1/f noise) may be due to a systematic error in determining the resistance R_s (< 10 mΩ) for low frequencies.

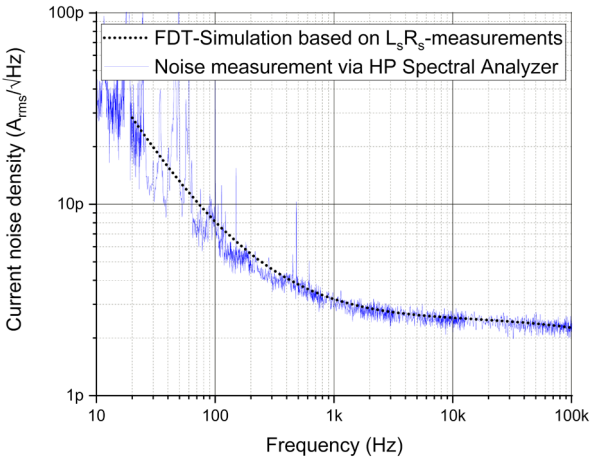


Figure 3: Pickup coil #1, spectral current noise density.

DUAL-CORE CCC

Two pickup coils then have been equipped with common superconducting shielding against magnetic interference signals (Fig. 4).

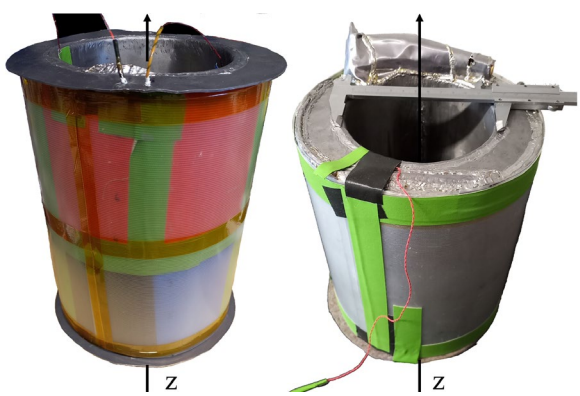


Figure 4: Left: Pickup coils #1 and #2 with inner loop of the shielding. Right: DCCC completed by the outer meander shielding, SQUID, and calibration coil.

Magnetic Shielding and LC-Resonances

Of course the magnetic shielding should not suppress the signal to be measured. Therefore, shielding consists of two superconductive coaxial tubes comprising the pickup coils connected to each other at one end. The longer the tube package, the better the suppression of interference signals [6]. Since long tubes would be impractical, the tubes are folded into a meander structure.

The opposite surfaces of the meander structure also form an electrical capacitance $C_{meander}$, which increases with increasing number of meanders or effective length of the tube package. The inner loop (see Fig. 4 left) creates an inductance L_{core}, which together with $C_{meander}$ forms a parallel LC-resonance circuit. It should be borne in mind that the inductance L_{core} is in fact caused by an additional winding through both pickup coils. Hence, the total inductance is the sum of L_{s1} and L_{s2} of about 200 µH.

Figure 5 shows the shift of the meander LC-resonance measured via the current noise density with 2, 6, and finally 12 full meander pairs (effective length of the shielding tube package: 240 cm). With increasing number of meanders, the parasitic capacitance is enlarged and thus the resonance frequency lowered which may negatively affect the stable work of the SQUID in flux locked loop mode.

The main part of the magnetic shielding is taken over by the superconducting meandering structure. As a first step, a shield with two full meander pairs (40 cm) was installed. As a result, an external, axially magnetic interference field B_z of 1 µT generated an apparent beam current of about 15 nA. This means even in the laboratory common 50 Hz magnetic fields the SQUID fully overrides in amplifier mode. An incomplete shielding with cryogenic mu-metal (4 mm thick, but 100 mm holes on both sides for the beamline) brought an improvement in shielding by a factor of 9.5 @ 1 Hz. More efficient is the use of further superconducting meanders. The final value of 12 full meander pairs (240 cm) leads to a damping below the currently existing detection limit in the laboratory of 5 pA/µT in z-direction.

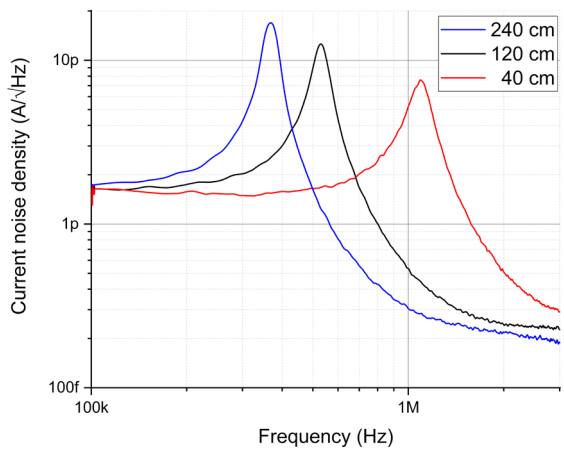


Figure 5: LC-resonance peaks of the DCCC at three processing stages with increasing number of full meander pairs or effective length of the shielding tube package.

ISBN: 978-3-95450-241-7 ISSN: 2673-5350 doi:10.18429/JACoW-IBIC2022-WEP30

Current Noise and Current Pulses

The current noise is a decisive parameter for the later achievable pulse current resolution. The noise measurements were carried out in the frequency range < 100 kHz with a HP 35670A and up to 5 MHz with a HP 89410A. An additional calibration coil and a certified multimeter Keithley 2002 were used for current calibration. Figure 6 shows the measured current noise density in the frequency range of 50 mHz to 5 MHz for the entire DCCC-Sm-200.

The high frequency range above 100 kHz is determined by the discussed meander LC-resonance and the frequency limitation of the core material. The medium frequency range (1 kHz to 100 kHz) has a close to constant noise behaviour (white noise). With < 2 $pA_{rms}/\sqrt{Hz}$ (min. 1.7 $pA_{rms}/\sqrt{Hz}$) the absolute values are $1/\sqrt{2}$ times smaller than values from the FDT studies, exactly as expected. A parallel connection of both pickup coils leads to an increase in noise, which is describable with the Pythagorean addition of the single independent noise sources. For two identical pickup coils, the noise increases by a factor of $\sqrt{2}$. At the same time, the current sensitivity doubles due to the simple addition of the two partial currents during calibration, so that ultimately a factor of $1/\sqrt{2}$ results.

The low frequency range < 1 kHz shows a significant increase in noise density, which ultimately (< 1 Hz) results in a $1/f^2$ behaviour, as it leads to Brownian noise (20 dB or current factor of 10 per decade). In addition, in the range between 3 Hz and 80 Hz, other interference signals become visible, most of which can be traced back to building vibrations.

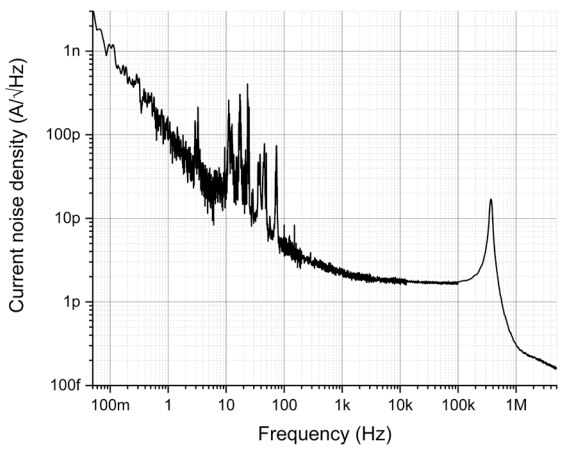


Figure 6: Total current noise density spectrum of the final DCCC-Sm-200, both pickup coils on one SQUID with input inductance of 1 µH.

The ultimate criterion for the application as a beam current meter is the achievable pulse current resolution. Measurements were performed by application of defined current pulses on the calibration coil (single wire through the DCCC). Figure 7 shows the 500 pA current pulses to be measured (dotted line) and the SQUID responses (blue line), smoothed with a 10 kHz low-pass filter and calibrated to current values. For similar measurements, the FAIR-Nb-CCC-XD required 1.6 nA current pulses.

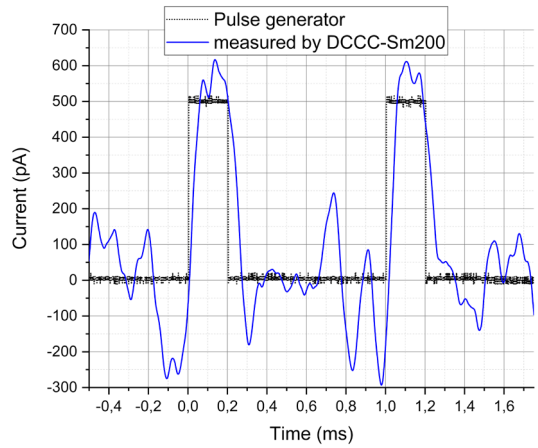


Figure 7: Pulse current resolution of the final DCCC-Sm-200, both pickup coils on one SQUID with input inductance of 1 µH.

CONCLUSION

It was shown that L_sR_s-measurements and the fluctuation-dissipation theorem are suitable for making predictions about the later current noise of CCCs. It was possible to create a lead foil-based Dual-core Cryogenic Current Comparator in smaller dimensions with a very high magnetic meander shielding factor below 5 pA/µT. This IFK-Pb-DCCC-Sm-200 with its 200 µH total inductor achieved a minimum current noise density of 1.7 $pA_{rms}/\sqrt{Hz}$, the smallest ever measured value for beamline CCCs at 4.2 K at the Cryo Detector Lab in Jena. This allowed for the first time the detection of a single current pulse below 1 nA with a CCC for beamlines.

OUTLOOK

In the meantime, Magnetec has produced special cores that geometrically have the dimensions of M-616, but use the core material developed for the FAIR-Nb-CCC-XD with improved low-temperature properties. Thus, it is possible to achieve 13% more inductance for the same geometry. With an additional core per pickup coil, the construction of the IFK-Pb-DCCC-Sm-300 could be started. It may have a total inductance 300 µH @ 4.2 K. The expected minimum white current noise density is accordingly 1.5 $pA_{rms}/\sqrt{Hz}$ – a similar R_s behaviour assumed. Because of the expected better performance, the full final SQUID setup (two SQUIDs with L_i = 1 µH to reduce Barkhausen noise and increase system availability, one SQUID for dynamic expansion with L_i = 27 nH) and the installation into a new beam-line cryostat will probably no longer take place with the Sm-200, but with the Sm-300.

REFERENCES

[1] W. Vodel, R. Geithner, and P. Seidel, "SQUID-Based Cryogenic Current Comparators", in *Applied Superconductivity Handbook on Devices and Applications Volume 2*, P. Seidel, Ed. Weinheim, Germany: Wiley-VCH, 2015, pp. 1096-1110.

Content from this work may be used under the terms of the CC BY 4.0 licence (© 2022). Any distribution of this work must maintain attribution to the author(s), title of the work, publisher, and DOI

ISBN: 978-3-95450-241-7 ISSN: 2673-5350 doi:10.18429/JACoW-IBIC2022-WEP30

[2] M. Fernandes, "SQUID-Based Cryogenic Current Comparator for Measuring Low-Intensity Antiproton Beams", Ph.D. thesis, University of Liverpool, UK, 2017.

[3] L. Crescimbeni *et al.*, "The Cryogenic Current Comparator at CRYRING@ESR", presented at IBIC'22, Krakow, Poland, Sept. 2022, paper TUP31, this conference.

[4] Magnetec, https://www.magnetec.de/wp-content/uploads/2018/11/m-616.pdf

[5] R. Geithner, "Optimierung eines kryogenen Stromkomparators für den Einsatz als Strahlmonitor", Ph.D. thesis, Phys. Dept., F. Schiller University Jena, Jena, Germany, 2013.

[6] N. Marsic *et al.*, "Numerical analysis of a folded superconducting coaxial shield for cryogenic current comparators", *Nucl. Instrum. Methods Phys. Res., Sect. A*, vol. 922, pp. 134-142, 2019. doi:10.1016/j.nima.2018.12.063

Content from this work may be used under the terms of the CC BY 4.0 licence (© 2022). Any distribution of this work must maintain attribution to the author(s), title of the work, publisher, and DOI

ISBN: 978-3-95450-241-7 ISSN: 2673-5350 doi:10.18429/JACoW-IBIC2022-WEP31

BOOSTER FILLPATTERN MONITOR

F. Falkenstern, J. Kuszynski, G. Rehm
Helmholtz-Zentrum Berlin, Germany

Abstract

The "Booster Fillpattern Monitor" is used to measure currents in each individual electron bunch in the booster of the BESSY II machine.

The booster with its circumference of 96 meters has space for max. 160 electron bunches. The distance between the electron bunches of 60 cm (96 m / 160) is determined by the RF Master Clock ~ 499,627 MHz. In practice, fill patterns of a one to five equally spaced bunches are in use.

The fill pattern monitor digitizes electrical pulses generated from a strip line using a broadband ADC. The sampling frequency is selected as an integer fraction of the bunching frequency, acquiring the full fill pattern over a number of turns.

Experiments performed at BESSY II demonstrate the performance of the setup and will be discussed.

INTRODUCTION

The BESSY II electron storage ring (SR) is a third-generation light source operating at an energy of 1.7 GeV with a stored current of 300 mA in the top-up mode [1]. The top-up injection in the SR allows almost constant synchrotron light for the users at the beamlines.

For injection into the BESSY II SR a full energy fast cycling booster synchrotron is used. Injection at full energy offers a lot of advantages for a high brilliance synchrotron radiation. It ensures a shot filling time, ion trapping etc. [2].

In the SR, electrons might be stored in any pattern consisting of up to 400 buckets (Fig 1).

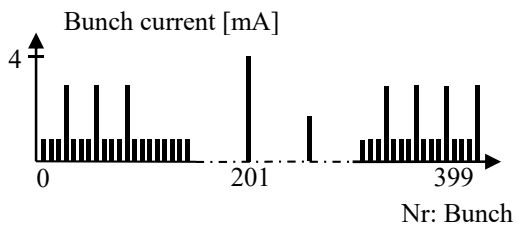


Figure 1: The typical fillpattern at storage ring BESSY II.

The injection of electrons in these buckets is managed from the TopUp engine [3]. It is possible to fill one to five buckets in the SR simultaneously. For this, the information from the fill pattern monitor (BunchView) in the SR is used [4].

The TopUp engine analyses this information and starts injection in the SR for filling the lost electrons in the emptiest bunches.

REQUIREMENTS

For the permanent optimization of the storage ring and the safe operation of the BESSYII machine, the reliably working injection into the storage ring is of great importance. In case of failure of injection system (Linac, Booster etc.), the beam in the storage ring is in decay mode. During the lifetime of about 8 hours, only half of the electrons remain in the storage ring after 8 hours. Most users at beamlines need constant synchrotron light (constant current in the SR) for their experiments. Therefore, the demands for diagnostics in this area have grown significantly. The booster fill pattern monitor was developed because of these increased demands on diagnostic capabilities.

REQUIREMENTS TO THE SYSTEM

The bunch resolved measurements have a large demand on the bandwidth of the RF signal, which makes acquisition and digitization difficult. Suppressing the signal noise with narrow analog filters is not possible. Improving the signal-to-noise ratio is then only possible by averaging of sampling data with digital processing. This requires many sample points from the analog (real) beam signals. For the bunch signals, which are repeated every turn, like the signals in the storage ring, it is mostly possible. In the booster, the circulated bunches are repeated during the booster period, but the induced bunch signal can vary a lot because of the acceleration of the electron buckets. Thus, averaging is not possible over many revolutions.

The second requirement is a sophisticated synchronization. The system needs a low jitter sample clock that is derived from the master clock (MC), revolution trigger and the start trigger of the booster. The measurement system can trigger internally (on the bunch signal) or externally on the start signal. While in operation it is mostly triggered by the external booster start trigger.

The third demand is the memory requirement of samples with high sample rate. It takes 35 ms to accelerate the electrons in the booster to the point of extraction. With the high sampling rate, it requires many megabytes of FIFO memory. As the FPGA card only allows a small FIFO memory, the external RAM memory would have to be declared as FIFO.

SETUP

The measuring system generates a current filling pattern in the booster every second. The external 1 Hz trigger starts recording data. The bunch signals (Fig. 2) are generated by a set of striplines (in the vacuum tube) and combined with the RF combiner (Fig 3).

Content from this work may be used under the terms of the CC BY 4.0 licence (© 2022). Any distribution of this work must maintain attribution to the author(s), title of the work, publisher, and DOI

ISBN: 978-3-95450-241-7 ISSN: 2673-5350 doi:10.18429/JACoW-IBIC2022-WEP31

Content from this work may be used under the terms of the CC BY 4.0 licence (© 2022). Any distribution of this work must maintain attribution to the author(s), title of the work, publisher, and DOI

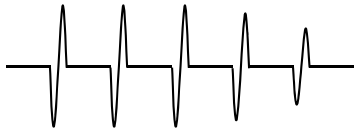


Figure 2: The five pulses induced from five bunches of electrons in the booster.

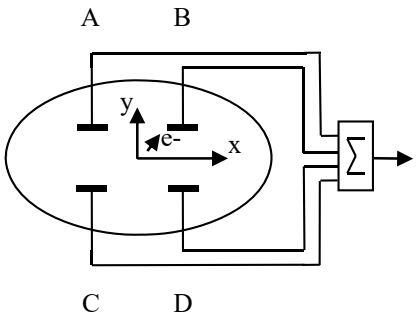


Figure 3: The bunch signals from the set of four striplines (A, B, C, D) in the booster are summed together.

The sum bunch signal (A+B+C+D) of this set of striplines is proportional to the bunch current in the booster. The signal is filtered, amplified, split and fed to two inputs of the fast broadband 14-bit ADC card.

The simplified block diagram (Fig. 4) shows the structure of the system.

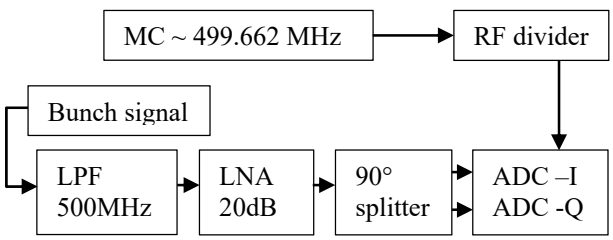


Figure 4: The block diagram with hardware of booster fillpattern monitors.

The digitization is synchronous to the integer fraction on the master clock (MC) of the BESSY machine of ~499.627 MHz.

The measurement of the bunch current is based on the IQ principle. The first ADC samples the I signal (amplitude) and the second converter samples the Q signal (phase) shifted by 90°. The sampling time of about 40 ms captures the whole time from the injection into the booster from the linac to the extraction from the booster into the storage ring. For averaging, the last sample values (100 turns) are taken just before the extraction. This improves the amplitude resolution of the acquired signals for each individual bunch. Calculating the vector amplitude as $A = \sqrt{I^2 + Q^2}$, can be simplified to A=I, for I>>Q. The information about the phase is used for testing purposes. The large changes in the phase can be an indication of booster or Linac instability.

The values of amplitude and phase obtained in this way are entered into the EPICS PVs (Fig. 5).

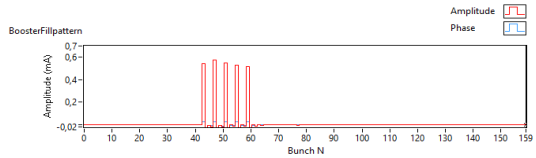


Figure 5: Fillpattern with five filled bunches in the booster ring of max 160 buckets.

CALIBRATION

For the normalization of the bunch current, it utilizes information from the beam current monitor in the booster [5]. The ADC signal noise of many empty bunches must be set to zero. The result, after one-time calibration, is shown in Fig. 6. The sum current of all bunches in the booster is then equal to the booster beam current.

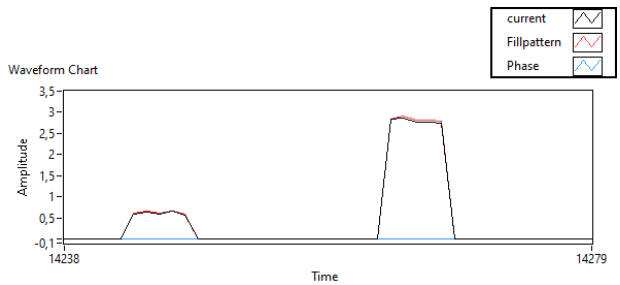


Figure 6: The correlation of current from one and five bunches in the booster (Fillpattern) to the current from the beam current monitor. The phase signal for the stable bunches in this time slot are then near zero.

The fill pattern during extraction (amplitude and phase) is stored in the individual PVs. The detection of the extraction is based on the comparison of the sampled data between two-time intervals in the 33 ms (14 ns * 2,300 M) and 38 ms (14 ns * 2,600 M) range. After extraction from the booster (35 ms) the bunch current (amplitude und phase) in the range of 38 ms is always zero. The sample frequency is about ~71.4 MHz (MC/7).

The larger sample data from ADCs are reduced by sampling every 1000th value and stored in PVs (Fig. 7).

ISBN: 978-3-95450-241-7 ISSN: 2673-5350 doi:10.18429/JACoW-IBIC2022-WEP31

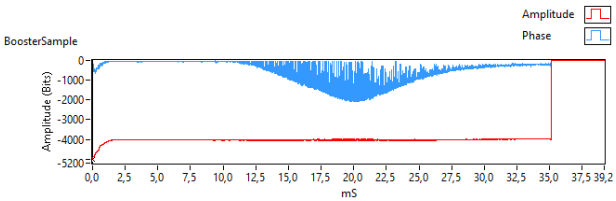


Figure 7: The data compressed of 2.8k for the amplitude and phase during accelerated and extracted electron buckets from the booster.

BUNCH NUMBERING

The bunch-number in the booster can be adapted to the number of bunches in the storage ring only within limits. The reason is, that the circumference of the storage ring is 2.5 times larger than that of the booster. Thus, the first 160 bunch-numbers in the storage ring will be equal to the number in the booster. The position of electron packets in the storage ring between 160 and 399 will be reachable after one or one and a half revolutions in the booster as shown in Fig. 8.

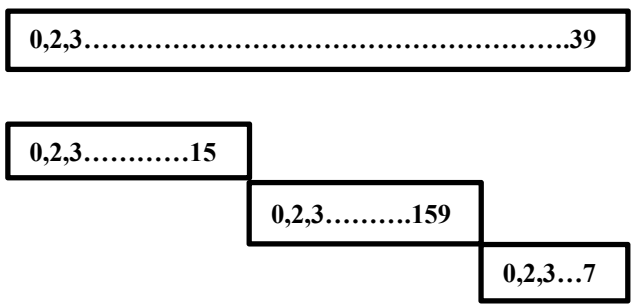


Figure 8: Number of electron bunches in the SR and the booster.

HARDWARE AND SOFTWARE

The hardware of the measurement system consists of a "Frontend Booster" module (RF amplifier and RF splitter) and a PXI crate with (RF divider1/7, PXIe controller, ADC/FPGA card). These plug-in units have found their place in the "RACK 6" (Fig. 9).

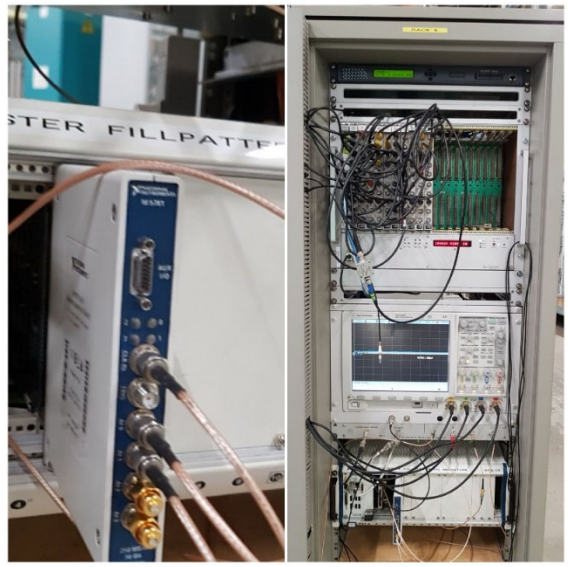


Figure 9: The Hardware of the booster fillpattern monitor is located under the scope in the RACK 6.

The PXIe controller with LabVIEW drives the ADC and FPGA card. The program calculates the all-bunch currents in the booster and update the corresponding EPICS data.

SUMMARY

The possibilities of advanced diagnostics like fill pattern monitor in the booster allows the improvement of injection at BESSYII. The system can be used for different physical studies.

The whole process of acceleration of electron bunches over time until extraction from the booster is stored for each individual bunch with the amplitude and phase. Thus, all deviations from normal acceleration processes are quickly detected and localized. The data can be arbitrarily compressed and stored in EPICS variables.

REFERENCES

[1] P. Kuske *et al.*, "Preparations of BESSY for Top Up Operation", in *Proc. EPAC'08*, Genoa, Italy, Jun. 2008, paper WEPC037, pp. 2067-2069.

[2] M. Abo-Bakr *et al.*, "The BESSY II* Booster Synchrotron", in *Proc. EPAC'96*, Sitges, Spain, paper TUP007G, pp. 527-529.

[3] T. Birke *et al.*, "Comprehensive Fill Pattern Control Engine: Key to Top-Up Operation Quality", in *Proc. ICALEPCS'15*, Melbourne, Australia, Oct. 2015, pp. 18-21. doi:10.18429/JACoW-ICALEPCS2015-MOC3O01

[4] F. Falkenstern *et al.*, "BunchView", in *Proc. DIPAC'09*, Basel, Switzerland, May 2009, paper MOPD40, pp. 128-130.

[5] J. Kuszynski *et al.*, Measuring beam intensity and lifetime in BESSY II", in *Proc. DIPAC'99*, Chester, UK, May 1999, paper PT03, pp. 159-161.

Content from this work may be used under the terms of the CC BY 4.0 licence (© 2022). Any distribution of this work must maintain attribution to the author(s), title of the work, publisher, and DOI

ISBN: 978-3-95450-241-7 ISSN: 2673-5350 doi:10.18429/JACoW-IBIC2022-WEP32

SECONDARY EMISSION MONITOR SIMULATION, MEASUREMENTS AND MACHINE LEARNING APPLICATION STUDIES FOR CERN FIXED TARGET BEAMLINES

L. Parsons França[1,2,3,*], F. Roncarolo[1], F. M. Velotti[1], M. Duraffourg[1], C.P. Welsch[2,3], H. D. Zhang[2,3], E. Kukstas[2,3]
[1]CERN, Geneva, Switzerland
[2]Cockcroft Institute, Daresbury, UK
[3]University of Liverpool, UK

Abstract

The CERN fixed target experimental areas have recently acquired new importance thanks to newly proposed experiments, such as those linked to Physics Beyond Colliders (PBC) activities. Secondary Emission Monitors (SEMs) are the instruments currently used for measuring beam current, position and size in these areas. Guaranteeing their reliability, resistance to radiation and measurement precision is challenging. This paper presents the studies being conducted to understand ageing effects on SEM devices, to calibrate and optimise the SEM design for future use in these beamlines. These include feasibility studies for the application of machine learning techniques, with the objective of expanding the range of tools available for data analysis.

INTRODUCTION

The TT20 beamline at CERN carries the 400 GeV/c beam from the SPS towards the fixed target experiments in the North Area (Fig. 1). The slow extracted beam is de-bunched[1], with total intensity ranging from a few 10^{11} (during machine setup and development) to a few 10^{13} protons (during physics), diluted along spills lasting between 1 to 5 seconds. The choice of instrumentation for beam position, size and intensity measurements is at the moment restricted to SEMs and scintillating screens [1].

SEM monitors generally consist of metallic wires or thin foils, intercepting the beam. As the beam passes through these surfaces some particles interact, transferring energy to the material [3]. If the electrons in the metal receive enough energy to escape the Fermi level, they are released, in a process known as Secondary Emission (SE), theoretically described by E. J. Sternglass [4].

The number of electrons emitted per incident proton is defined as the Secondary Emission Yield (SEY) and can be written as [5]:

$$SEY = 0.01 L_s \frac{dE}{dx}|_{el} \left[1 + \frac{1}{1 + (5.4 \cdot 10^{-6} E/A_p)} \right]. \quad (1)$$

It depends on the kinetic energy of the projectile (E), the electronic energy loss ($\frac{dE}{dx}|_{el}$), the mass of projectile (A_p) and the characteristic length of diffusion of low energy electrons (L_s), given by:

$$L_s = (3.68 \cdot 10^{-17} N Z^{1/2})^{-1}, \quad (2)$$

which varies according to the number of atoms per unit volume (N) and the atomic number (Z).

The signal measured by the SEM (N_{SEM}) is proportional to the number of protons (N_p), related via a calibration factor (C_f):

$$C_f = \frac{N_p}{N_{SEM}}. \quad (3)$$

This calibration factor is linked to the SEY and other properties, such as the electronics gain. More detailed information on this can be found in [6].

There are over 100 SEM monitors in the SPS complex, with varying *filling factors*, used for measuring different beam properties,: *single foils* (labelled as BSI) for beam intensity; *split foils* (BSP or BSM) for beam position; and *scanning single bands* (BBS) or *multiple band grids* (BSG) for both beam position and size. All of them are equipped with the same Data Acquisition System (DAQ), publishing the spill signals every 20 ms.

Given the nature of SE processes, like the SEY dependence on material properties (e.g. oxidation, vacuum conditioning, radiation damage, etc...) and the low particle fluxes to be

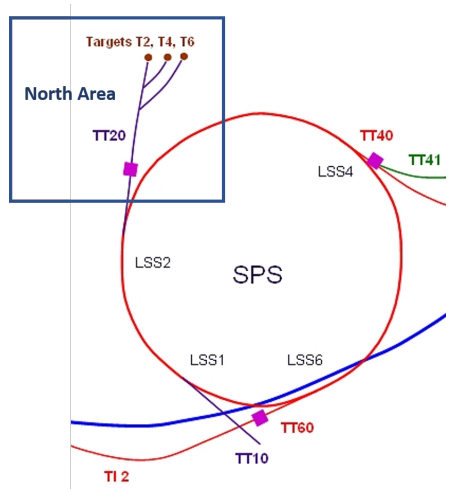


Figure 1: Schematic representation layout of SPS and North Area beamlines, sourced from [2].

* luana.parsons.franca@cern.ch
[1] The SPS RF is switched off at flat top, before extraction

Content from this work may be used under the terms of the CC BY 4.0 licence (© 2022). Any distribution of this work must maintain attribution to the author(s), title of the work, publisher, and DOI

ISBN: 978-3-95450-241-7 ISSN: 2673-5350 doi:10.18429/JACoW-IBIC2022-WEP32

monitored, absolute calibration and signal to noise are very challenging to control and optimize.

BEAM INTENSITY STUDIES

The SEY variation over time is particularly relevant for the BSI monitors, providing the experiments with accurate Proton On Target (POT) values.

Most of the SEMs in the TT20 area were installed in the late 1970s [7] and only refurbished when highly damaged. The presently used calibration factor, mainly composed by the SEY and the DAQ gain, is the result of dedicated studies in the 1990s [6].

Re-evaluation of the BSI absolute calibration was re-started in 2016. Due to the low extracted DC beam current in the slow extracted beam lines, determining the absolute calibration is not straightforward. Direct calibration with a BCT in the line during a fast extraction, as done in the CERN Proton Synchrotron (PS) to East Area beam line, is not currently possible at the SPS and there are no plans to implement it for the foreseeable future.

Figure 2 shows intensity measurements taken in 2017 by 2 BSI foils located inside the same tank in the TT20 beamline, correlated to the Beam Current Transformer (BCT) measurement in the SPS ring before de-bunching and extraction.

We would expect to see a linear relationship between BSI

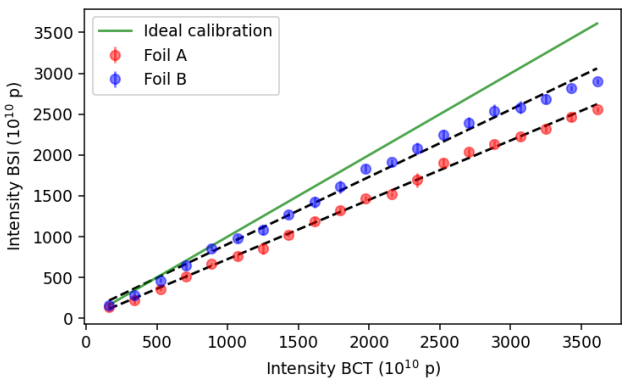


Figure 2: Intensity measured by BSI foils as a function of the intensity measured by BCT 2017.

and BCT, with slope equal to 1, in the ideal case of lossless extraction and perfect BSI calibration[2]. Non linearity could arise from SEY drift in time, DAQ dependence on signal level, or variation of losses with beam intensity.

A slope deviating from 1 could indicate systematic errors in the BSI calibration (e.g. SEY and DAQ gain), or the value for absolute extraction losses, which cannot be inferred by evaluating BCT and BSI values alone.

We also see non-linearity in Fig. 3, which shows how the ratio of intensities measured by the BSI[3] and BCT evolve over time. Interestingly the similarity in measurements between the two foils changes over time.

[2] BCT calibration is expected to be better than 1%

[3] The intensity of the BSI foils was calculated using the latest calibration available.

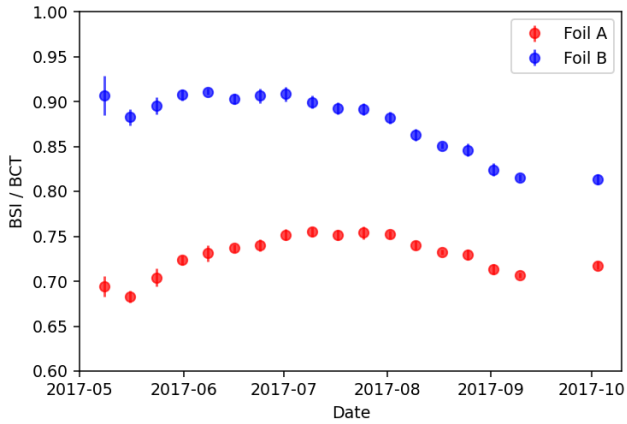


Figure 3: Intensity measured by BSI foils normalised by intensity of BCT as a function of time.

Therefore the examples in the figures clearly show the uncertainty on the single foil calibration and the *cross-talk* between foils (downstream foil also measures SE from charged particles generated by the first foil). These problems and other related issues are discussed in more detail in [7, 8].

A method for calibration, frequently used in the CERN Proton Synchroton (PS) experiment lines, is the activation method, described in [6, 9]. This method relies on measuring ^{24}Na activity of a thin foil (e.g. in Aluminum), exposed to the beam, located as close as possible to the BSI to be calibrated.

After exposure for a certain period of time, the foil is removed from the beamlines and the activation measured using a gamma spectrometer. From the activation one can infer the integrated number of protons that traversed the foil. This can be used to calibrate the BSI, by comparing the activation measured in the foil to the counts measured by the BSI during the exposure period. With this method the calibration accuracy is dominated by the error on the activation process cross section, normally known within 10%.

This method, although previously shown to be effective, is disruptive to beam operation: it requires stops to insert and remove the devices from the beamline, so needs to be planned in advance.

Despite this disadvantage, it is one of the only reliable options for determining the absolute calibration in the TT20 beamline and will be used in future calibration studies. In addition to this Montecarlo simulations of beam interactions with SEM monitors will be conducted, using Geant4, to investigate both the absolute calibration and changes to SEM monitor design. These simulations are currently under development.

MACHINE LEARNING STUDIES FOR BEAM PROFILE AND POSITION

BBSs (single bands that move to scan the beam) and BSGs (horizontal or vertical bands, normally 16 per plane, each

Content from this work may be used under the terms of the CC BY 4.0 licence (© 2022). Any distribution of this work must maintain attribution to the author(s), title of the work, publisher, and DOI

ISBN: 978-3-95450-241-7 ISSN: 2673-5350 doi:10.18429/JACoW-IBIC2022-WEP32

Content from this work may be used under the terms of the CC BY 4.0 licence (© 2022). Any distribution of this work must maintain attribution to the author(s), title of the work, publisher, and DOI

connected to a separate DAQ channel) are used for beam position and profile measurements.

Each band intercepts only a part of the total beam measured by the BSIs. In this case absolute calibration is no longer relevant, since it is still possible to measure the position and profile without precise knowledge of the absolute number of protons. The challenge is to distinguish the background generated by different particles from sources of electronic noise, and therefore maximise the signal to noise ratio.

Traditionally signal processing can be used to reduce the noise, but more recently there have been some applications that have used machine learning techniques for this purpose [10]. In this contribution we explore the possibility of reducing the noise in the signals of the BSGs using *autoencoders*.

An autoencoder is a deep neural network commonly used for image processing. As depicted in Fig. 4, it consists of two basic sections, the first part compresses the original image into a lower dimensional representation, via a series of layers. The second part mirrors the original layered structure, taking the compressed representation (also referred to as latent space) and trying to reconstruct the original image. Some resolution can be lost in this process. We aim to

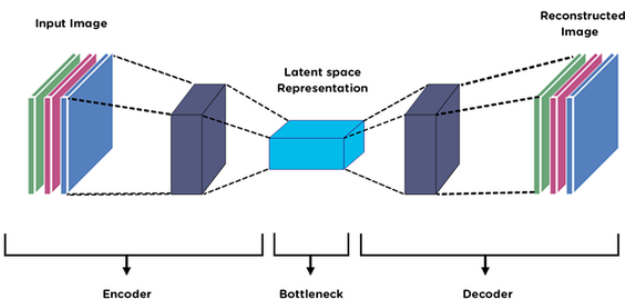


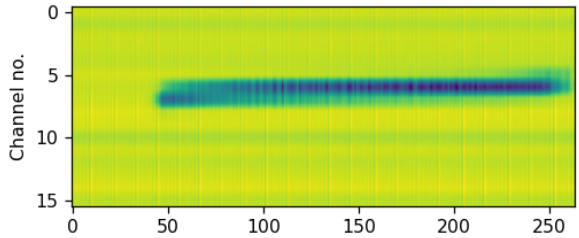
Figure 4: Graphic representation of Autoencoder sourced from [11].

exploit this resolution loss to our advantage: by creating a latent representation that is low enough,to create a smoothing effect, yet still able to retain the important features, needed for beam position and profile measurements.

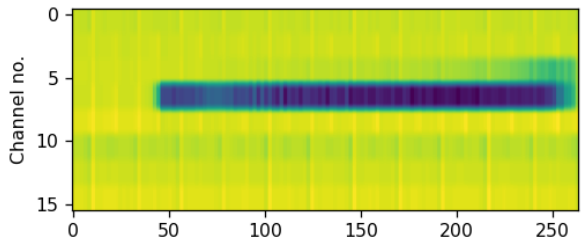
To test this application a combination of TensorFlow [12] and Keras [13] libraries were used to implement the following autoencoder architecture: encoder containing one 2D convolutional layer, one 2D max pooling layer; decoder: containing one 2D upsampling layer, one 2D convolutional layer.

The data that was fed to the autoencoder, consisted of a matrix containing the signal of each channel, corresponding to a wire of a BSG. The matrix was of dimensions 264 × 16. 264 corresponding to the number of data points in time in the spill (one every 20 ms) and 16 corresponding to the number of channels in the BSG.

This data was then pre-processed before being passed to the autoencoder. The pre-processing involved two steps: first of all adding padding to change the matrix dimensions from



(a) Original image.



(b) Autoencoder reconstruction.

Figure 5: Example of autoencoder reconstruction.

264 × 16 to 264 × 264, then scaling all the data points by subtracting the mean and dividing by the standard deviation. The pre-processed data for one BSG device was split into training and testing samples. 3117 training samples were then used to train the autoencoder. The training was carried out over 19 epochs, using a batch size of 240, the Adam optimiser, with a learning rate of 0.6×10^{-3} and the loss function was Binary Crossentropy.

Results

The trained model was first used to reconstruct the test data for the same BSG device (labeled as BSGH.211706). Subsequently the trained model was fed with data from 5 other BSG devices. Figure 5 pictures the original and the reconstructed image, with data samples from BSGV.210156. Comparing the original and the reconstructed image we can see that the profile is a bit broader in the reconstructed image and that it is overall a bit smoother.

Figure 6 shows the signal integral over all BSG channels as a function of time in the spill, for the original data and the data reconstructed by the autoencoder. In the original data set the larger error bars suggest a wider spread of data (ie:noise). The reconstructed data set, has smaller error bars, thus evidencing a reduction in the noise.

A plot to show the comparison of the effects of the autoencoder on the profile of the beam at a fixed point in time was also made (Fig. 7). Here we see a broadening of the profile peak in the reconstructed image, but also a smoother image, with noise reduced at the tails. This is beneficial in most of the operational cases, where beam position and size are inferred from the distribution mean and standard deviation.

Overall, the results obtained from the autoencoder reconstruction across the other BSGs, were similar to those presented in this paper, although there was some variation, depending on the instrument and the point in time where the profile was taken. It would be interesting to further in-

ISBN: 978-3-95450-241-7 ISSN: 2673-5350 doi:10.18429/JACoW-IBIC2022-WEP32

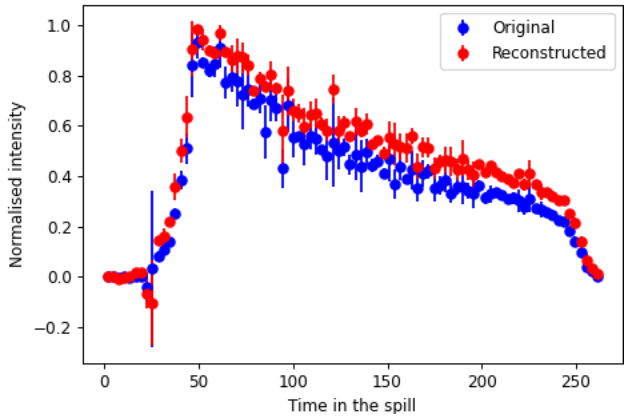


Figure 6: Comparison of normalised intensity as a function of time in the spill.

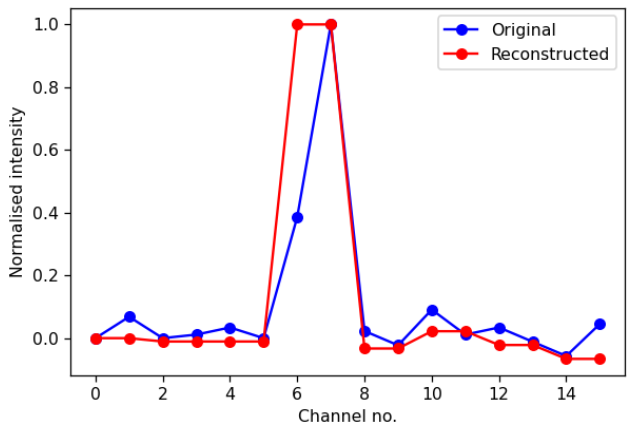


Figure 7: Comparison of normalised intensity as a function of channel number.

vestigate and quantify these variations and to include more devices in the analysis.

These initial results in noise reduction seem promising and could help improve the steering of the beam in the future, but still need to be validated for a conclusive evaluation.

CONCLUSION

Renewed interest in the fixed target experimental areas, has brought to attention the problems related to ageing SEM instrumentation present in these areas. This instrumentation requires upgrading and calibration in order to meet the needs of operators. In this contribution we have outlined the main challenges regarding these instruments, presenting the path currently being taken to solve these issues.

The first of these challenges is the absolute calibration of the BSI monitors in the TT20 beamline, which is limited by the absence of BCTs in the beamline. We are currently developing simulations to better understand the interaction between the beam and the instruments and we have plans to use the activation method as part of our absolute calibration studies.

The second major challenge affecting the profile and position measuring devices is the signal to noise ratio. In this contribution we have explored the use of autoencoders for noise reduction, presenting preliminary results. An autoencoder was trained on the data of one BSG device and the trained model was then tested on the data of 5 other devices.

The autoencoder was able to reconstruct the data successfully, reducing the noise, but also increasing the width of the profile. Not all results were consistent and in future we aim to quantify how consistently the autoencoder performs across different devices. We also aim to compare the moodified signal, with a reference signal for a more complete validation.

ACKNOWLEDGEMENTS

This work was supported by STFC Liverpool Centre for Doctoral Training on Data Intensive Science (LIV.DAT) under grant agreement ST/P006752/1 and CERN.

REFERENCES

[1] M. A. Fraser *et al.*, "Slow Extraction Efficiency Measurements at the CERN SPS," in *Proc. IPAC'18*, Vancouver, Canada, Apr.-May 2018, pp. 834–837. doi:10.18429/JACoW-IPAC2018-TUPAF054

[2] J. Wenninger, *SPS operation,* https://jwenning.web.cern.ch/SPS.html

[3] A. N. Fernandez, D. Belohrad, C. Bracco, E. Renner, F. Roncarolo, and J. Tassan-Viol, "PSB H0-H- Monitor Calibration and Commissioning," in *Proc. IBIC'21*, Pohang, Korea, Sep. 2021, p. 429. doi:10.18429/JACoW-IBIC2021-WEPP24

[4] E. J. Sternglass, "Theory of secondary electron emission by high-speed ions," *Phys. Rev.*, vol. 108, pp. 1–12, 1957. doi:10.1103/PhysRev.108.1

[5] D. Kramer, "Design and Implementation of a Detector for High Flux Mixed Radiation Fields," Ph.D. dissertation, Technical University of Liberec, Czechia, 2008. http://cds.cern.ch/record/1139227

[6] K. Bernier *et al.*, "Calibration of secondary emission monitors of absolute proton beam intensity in the CERN SPS North Area," CERN, Geneva, Switzerland, Tech. Rep., 1997. doi:10.5170/CERN-1997-007

[7] I. Ortega *et al.*, *North area beam instrumentation consolidation type: Na-cons groups: Be-bi & en-ea*, EDMS no. 2141518. https://indico.cern.ch/event/826747/contributions/3458702/attachments/1873506/3087270/NACONS_Request-BE-BI-V2.1.pdf

[8] M. Fraser and F. Velotti, *Upgraded beam instrumentation for slow extraction at sps*, EDMS no.2113420. https://indico.cern.ch/event/807016/contributions/3359176/attachments/1816894/2969841/FS-BI-SLAWG_-_2113420_v0.1.pdf

[9] A. Chapman-Hatchett *et al.*, "Calibration of the secondary emission monitors TBIU and TBID of the North Area targets stations T2, T4, and T6 in TCC2 for slow extracted protons of 400 GeV," CERN, Geneva, Switzerland, Tech. Rep., 1979. https://cds.cern.ch/record/2816600

Content from this work may be used under the terms of the CC BY 4.0 licence (© 2022). Any distribution of this work must maintain attribution to the author(s), title of the work, publisher, and DOI

ISBN: 978-3-95450-241-7 ISSN: 2673-5350 doi:10.18429/JACoW-IBIC2022-WEP32

[10] E. Almazrouei, G. Gianini, C. Mio, N. Almoosa, and E. Damiani, "Using autoencoders for radio signal denoising," in *Proc. 15th ACM Symposium on QoS and Security for Wireless and Mobile Networks*, 2019, pp. 11–17. doi:10.1145/3345837.3355949

[11] D. Birla, *Basics of autoencoders*, 2019, https://medium.com/@birla.deepak26/autoencoders-76bb49ae6a8f

[12] M. Abadi *et al.*, *TensorFlow: Large-scale machine learning on heterogeneous systems*, 2015, https://www.tensorflow.org

[13] F. Chollet *et al.*, *Keras*, 2015, https://keras.io

Content from this work may be used under the terms of the CC BY 4.0 licence (© 2022). Any distribution of this work must maintain attribution to the author(s), title of the work, publisher, and DOI

ISBN: 978-3-95450-241-7 ISSN: 2673-5350 doi:10.18429/JACoW-IBIC2022-WEP33

OPERATIONAL AND BEAM STUDY RESULTS OF MEASUREMENTS WITH THE TRANSVERSE FEEDBACK SYSTEM AT THE CANADIAN LIGHT SOURCE

S. Martens*, T. Batten†, D. Bertwistle, M. J. Boland‡,1
Canadian Light Source, Saskatoon, Canada
[1]also at University of Saskatchewan, Dept. of Phys. and Eng. Phys., Saskatoon, Canada

Abstract

A transverse bunch-by-bunch feedback system has been installed in the storage ring at the Canadian Light Source (CLS) to counteract beam instabilities. The 2.9 GeV electron storage ring is 171 m in circumference with 13 insertion devices currently installed, each contributing to the impedance of the ring and lowering the instability threshold. The new Transverse Feedback System (TFBS) provides improved bunch isolation, higher bandwidth amplification and diagnostics to study, understand and damp these instabilities. This paper will show and overview of the system setup, examples of operational performance and results of the diagnostic capabilities, including tune feedback, grow/damp measurements, and excite/damp measurements.

SYSTEM OVERVIEW

The Canadian Light Source storage ring is a third generation light source. Current standard operation uses 220 mA of stored electron current in the ring. The storage ring uses a compact lattice consisting of twelve double-bend achromat cells [1]. A table of storage ring parameters is listed in Table 1 [2]. Recent improvements have allowed the ring to transition from a fill-decay operation to a top-up operation, keeping the beam current consistent. The storage ring is subject to coupled bunch instabilities that arise via interaction between the vacuum chamber and the stored electron current. Changes over time to the configuration of the storage ring have impacted the growth of these instabilities. To improve diagnostics and stability for the beam, the existing Transverse Feedback System (TFBS) was upgraded to include Dimtel Equipment to identify and mitigate against coupled bunch instabilities.

Table 1: CLS Ring Parameters

Circumference	170.88 m
Beam Energy	2.9 GeV
Beam Current	220 mA
Periodicity	12 Cell
RF Frequency	500 MHz
Harmonic Number	285
Momentum Compaction	0.0038

* Stephen.Martens@lightsource.ca
† Tonia.Batten@lightsource.ca
‡ mark.boland@lightsource.ca

OPERATIONS

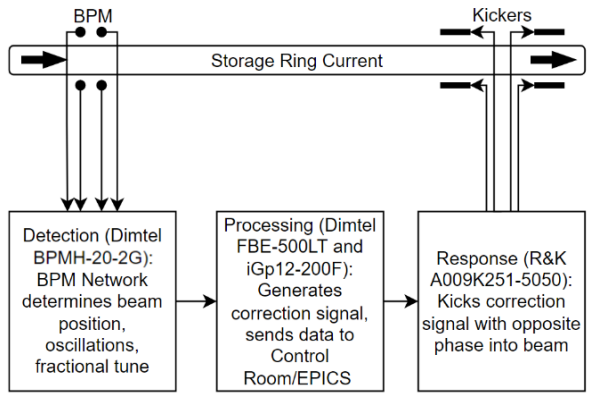


Figure 1: Transverse Feedback System Diagram and Hardware.

The Dimtel TFBS is currently in use in the storage ring to provide active damping against coupled bunch instabilities. In addition, it is used to provide bunch cleaning, tune measurements, tune feedback and diagnostics for beam instabilities in experiments.

TFBS Description

The TFBS uses three main elements depicted in Fig. 1. It uses a beam position monitor for detection, a network unit and processing system for analysis, and a kicker network for response. The four button BPM sends data to a hybrid RF-passive network unit which produces horizontal, vertical, and sum outputs. These signals are sent to the Bunch-By-Bunch Feedback front/back end unit and three 500 MHz processing units. The BPM signals are converted into a series of correction signals and sent to the response system which uses four broad-band RF power amplifiers and two kicker assemblies [3]. The 500 MHz RF signal is also input into the system to synchronise the timing [4]. The correction signal is applied to the beam to mitigate the instability identified by the processing system.

Tune Measurement and Feedback for Operations

The betatron tune of a synchrotron corresponds to the oscillation frequency of transverse motion within the ring. The number of complete oscillations within a single revolution of the ring is the integer tune, while the fractional oscillation corresponds to the fractional oscillation after a single turn [5]. The fractional tune can be measured by the

Content from this work may be used under the terms of the CC BY 4.0 licence (© 2022). Any distribution of this work must maintain attribution to the author(s), title of the work, publisher, and DOI

ISBN: 978-3-95450-241-7 ISSN: 2673-5350 doi:10.18429/JACoW-IBIC2022-WEP33

Content from this work may be used under the terms of the CC BY 4.0 licence (© 2022). Any distribution of this work must maintain attribution to the author(s), title of the work, publisher, and DOI

TFBS parasitically by tracking the beam motion spectrum. A "notch" appears at the betatron frequency - tracking the location of the notch allows for tracking of the tune [4], seen in Fig. 2. Previous systems were unable to measure the tune without causing unacceptable orbit perturbations.

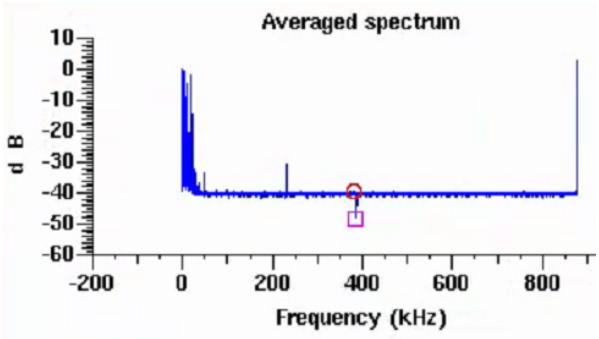


Figure 2: Transverse Feedback System displaying the averaged spectrum of the system. Note the "notch" in the spectrum identified with the square marker. This notch appears at the betatron frequency and tracking it allows for parasitic tune measurement.

The addition of the tune tracking provided by the TFBS also allows for a tune feedback system. Tune feedback collects fractional tune tracking measurements and identifies the difference from the set fractional tune. Quadrupoles in the storage ring lattice can be adjusted via a quadrupole feed-forward technique to correct tune shifts as they occur [6]. Tune feedback has successfully been implemented in October 2020 and is stabilizing the fractional tune during standard operation. The addition of tune feedback yields improved beam lifetime and injection efficiency [3].

DIAGNOSTICS FOR BEAM INSTABILITIES

The upgraded Dimtel TFBS allows for the measurement of coupled bunch instabilities across modes inside the storage ring. A ring with N bunches gives rise to N coupled bunch modes that can grow as a product of coupled bunch instabilities. Manipulation of the feedback network can allow these instabilities to grow intentionally, after which the growth and damping rates of modes along a single axis can be identified while varying storage ring conditions such as in-vacuum insertion device gaps.

Grow Damp Experiments

Early diagnostic experiments involved the use of grow damp measurements. The TFBS provides a "grow/damp enable" switch in software. A maximum of a 25.2 ms acquisition period is used to collect beam spot size data along one axis across all bunches. Some fraction of the acquisition period is dedicated to growth, and the remaining period is dedicated to damping. Upon enabling grow damps in software, the feedback network will be disabled across all bunches for the duration of the growth period. During this time, existing coupled bunch instabilities will cause the beam size to grow. At the end of the growth period, the feedback network is re-enabled and active damping against these instabilities resumes. Collected data is analysed using existing Dimtel MATLAB scripts which converts bunch data into modal data. An example can be seen in Figs. 3 and 4. Fitting exponentials to these modal growths can be done to find growth and damping rates and compared while varying storage ring parameters. Top-up of current is disabled throughout the experiment period as injection interfered with measurements. Results often showed large growths on the highest modes with little other structure present which is typically indicative of resistive wall instabilities [7, 8].

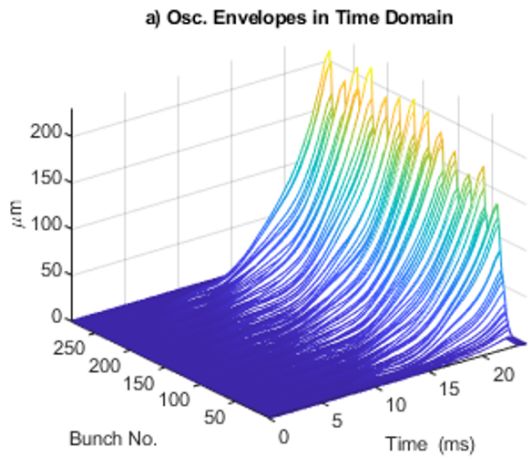


Figure 3: Example of Bunch Growth from a grow damp measurement. This measurement was taken while varying the gap width on the in-vacuum undulator (IVU) for the Brockhouse Beamline.

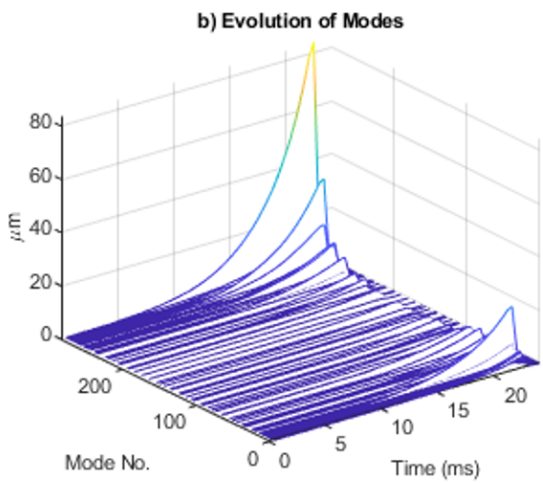


Figure 4: Example of Modal Growth from the same grow damp measurement as Fig. 3.

ISBN: 978-3-95450-241-7 ISSN: 2673-5350 doi:10.18429/JACoW-IBIC2022-WEP33

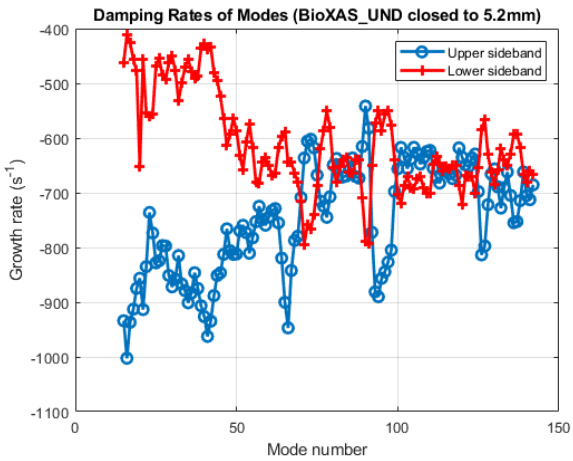


Figure 5: Example of modal damping rates from an excite damp experiment while varying the in-vacuum undulator gap width for the BioXAS beamline. The upper and lower sidebands are the sidebands of the revolution harmonic, and represent the first and second halves of the 285 modes in the CLS storage ring. The first and last 15 modes are removed.

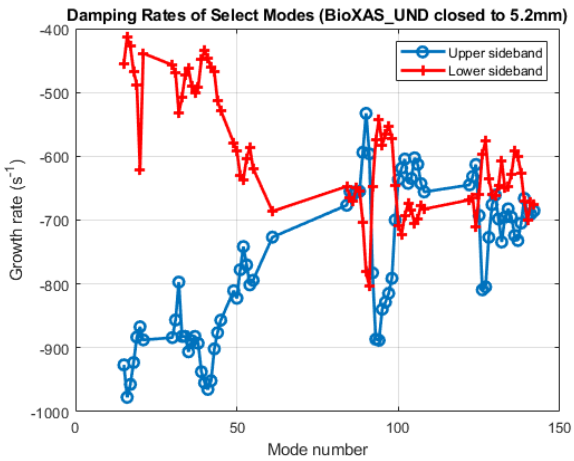


Figure 6: The same measurement as in Fig. 5, but a much smaller pre-defined selection of modes are scanned. Doing so significantly speeds up each scan.

Excite Damp Experiments

Later diagnostic experiments moved to using excite damp measurements. Grow damp measurements allow instabilities to grow passively by disabling the feedback network while excite damp measurements drive the feedback network to excite a specific mode deliberately. The iGp12 software was configured to have a gain of 0 during the growth period while an additional driving factor was prepared for every mode. Excitation would occur only on whichever modes were specified in Dimtel excite damp scripts. The damping acquisition period would occur over 10.0 ms with an additional 1.0 ms buffer [9].

Excite damp experiments were able to detect instabilities appearing on mid-range modes that could not be found with grow damps. Resistive wall effects that present on the highest modes make the stored beam too unstable too quickly during grow damp measurements for other modes to begin to show signs of unstable growth. Excite damp measurements can detect these instabilities due to their single-mode acquisition. Only the damping period of the acquisition is of interest as the growth period is largely driven by the intentional excitation by the feedback system rather than some property of the storage ring. The single-mode acquisition causes excite damp measurements to take significantly longer and require more storage space for raw data compared to grow damp measurements. These additional costs can be reduced by only scanning a pre-defined selection of modes rather than a full sweep. Examples of a sweep across all mid-range modes and of a pre-defined selection of modes can be seen in Figs. 5 and 6, respectively.

CONCLUSION

The Dimtel Transverse Feedback System has integrated into the existing storage ring control system. The feedback system has been used to successfully mitigate against instabilities that arise in the storage ring. Tune measurement and feedback is also enabled by new TFBS. The new system has also been used in multiple kinds of diagnostic experiments to detect and identify sources of coupled bunch instabilities in the machine.

ACKNOWLEDGEMENTS

Many thanks to Dmitry Teytelman of Dimtel Inc. for his instruction, discussions and training in the setup and experimentation using the Transverse Feedback System. Research at the CLS is funded by the Canada Foundation for Innovation (CFI), the National Research Council Canada (NRC), Natural Sciences and Engineering Research Council of Canada (NSERC), the Canadian Institutes of Health Research (CIHR), Western Economic Diversification Canada (WD), the Government of Saskatchewan, and the University of Saskatchewan.

REFERENCES

[1] J. Cutler, D. Chapman, and R. Lamb, "Brightest Light in Canada: The Canadian Light Source," *Synchrotron Radiat. News*, vol. 31, pp. 26–31, 2018. doi:10.1080/08940886.2018.1409557

[2] L. Dallin *et al.*, "Canadian Light Source Status and Commissioning Results," in *Proc. EPAC'04*, Lucerne, Switzerland, Jul. 2004. http://accelconf.web.cern.ch/e04/papers/THPKF007.pdf

[3] T. Batten and J. Vogt, "Upgrade of the Transverse Feedback System at the Canadian Light Source," presented at University of Saskatchewan, 2021, unpublished.

Content from this work may be used under the terms of the CC BY 4.0 licence (© 2022). Any distribution of this work must maintain attribution to the author(s), title of the work, publisher, and DOI

ISBN: 978-3-95450-241-7 ISSN: 2673-5350 doi:10.18429/JACoW-IBIC2022-WEP33

[4] D. Teytelman, *Bunch-by-bunch feedback and diagnostics in CLS*, 2018. https://wiki.dimtel.com/lib/exe/fetch.php?media=dim:cls_analysis_07feb18.pdf

[5] R. Steinhagen, *Tune and chromaticity diagnostics*, 2009. https://www.tandfonline.com/doi/full/10.1080/08940886.2018.1409557

[6] C. H. Kuo, J. Chen, P. C. Chiu, K. T. Hsu, and K. H. Hu, "Preliminary Tune Feedback Study in the Taiwan Light Source," in *Proc. DIPAC'11*, Hamburg, Germany, May 2011, pp. 491–493. https://jacow.org/DIPAC2011/papers/TUPD79.pdf

[7] S. Wang, M. G. Billing, S. Poprocki, D. L. Rubin, and D. Sagan, "Resistive Wall Instability and Impedance Studies of Narrow Undulator Chamber in CHESS-U," in *Proc. IPAC'17*, Copenhagen, Denmark, May 2017, pp. 3204–3207. doi:10.18429/JACoW-IPAC2017-WEPIK110

[8] A. Wolski, *Resistive Wall Instability in the NLC Main Damping Rings*, 2004, https://escholarship.org/uc/item/3xc585kj

[9] D. Teytelman, private communication about Excite Damp experiment, 2022.

Content from this work may be used under the terms of the CC BY 4.0 licence (© 2022). Any distribution of this work must maintain attribution to the author(s), title of the work, publisher, and DOI

ISBN: 978-3-95450-241-7 ISSN: 2673-5350 doi:10.18429/JACoW-IBIC2022-WEP34

ORBIT CORRECTION UPGRADE AT THE CANADIAN LIGHT SOURCE

T. Batten*, M. Bree†, J. M. Vogt‡, Canadian Light Source, Saskatoon, Canada

Abstract

The Canadian Light Source is a 3rd generation synchrotron that began user operations in 2005 and now supports 22 operational beamlines. The previous orbit correction system was experiencing an increasing number of failures associated with obsolete hardware. This system was upgraded to improve machine reliability and performance, as well as to support new diagnostic capabilities.

OVERVIEW

The orbit correction system is responsible for maintaining the orbit of the stored electron beam. It reads the beam positions at various points around the storage ring, computes the deviation of the beam from its ideal location, and then calculates and distributes new setpoints to the orbit corrector magnets. As the complexity of the machine increases with the addition of insertion devices, the speed and accuracy of this setpoint distribution becomes even more critical to quickly damp down perturbations in the stored beam so that a stable orbit is maintained.

OLD SYSTEM

The previous system used versa mezzanine eurocard (VME) based hardware to read beam positions and to distribute orbit correction magnet setpoints. The VME cards were obsolete and showing increasing signs of failure. The beam position readings were averaged onboard, which restricted the diagnostic capabilities, and the setpoints were not distributed in parallel, which limited the correction rate.

The software used to support this system had multiple layers, hosted on a variety of machines, in a number of different languages. Furthermore, the computer that hosted communication with the orbit correction hardware was running an obsolete operating system with a customized compile environment, on hardware that was becoming increasingly difficult to service or replace. As a result, implementing changes or diagnosing problems was challenging.

NEW SYSTEM

The upgrade eliminated all of the obsolete hardware and dramatically increased the diagnostic capabilities. The new orbit correction system exposes all of the raw data which is now used to analyze performance and identify potential issues.

Hardware

The new orbit correction system, shown in Fig. 1, incorporates D-tAcq analog to digital converters (ADC) [1,2] to read beam position monitor (BPM) positions and custom built nuclear instrument modules (NIM) that use PoLabs single board controllers (SBC) [3] to support parallel distribution of magnet power supply setpoints.

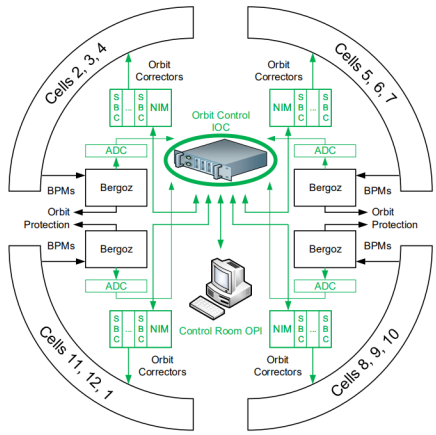


Figure 1: New orbit correction system architecture.

Software

The new software is running on more robust hardware, using a Scientific Linux 7 operating system, as shown in Fig. 2. This allows cores to be dedicated to specific tasks to ensure fast and predictable response times. In addition to simplifying the architecture, the new software is both dynamically configurable and easily extensible.

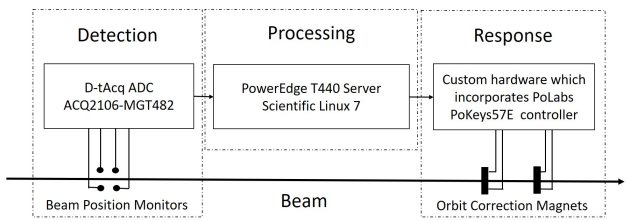


Figure 2: Orbit correction block diagram.

ENHANCEMENTS

The new diagnostic capabilities include:

Extensible Architecture

The architecture of the new software makes maintenance, support, and enhancement efforts more efficient. It supports dynamic saving and reloading of configuration and machine parameters for easy adjustment and machine recovery in the case of a hardware failure or a power outage.

* tonia.batten@lightsource.ca
† michael.bree@lightsource.ca
‡ johannes.vogt@lightsource.ca

Content from this work may be used under the terms of the CC BY 4.0 licence (© 2022). Any distribution of this work must maintain attribution to the author(s), title of the work, publisher, and DOI

ISBN: 978-3-95450-241-7 ISSN: 2673-5350 doi:10.18429/JACoW-IBIC2022-WEP34

Content from this work may be used under the terms of the CC BY 4.0 licence (© 2022). Any distribution of this work must maintain attribution to the author(s), title of the work, publisher, and DOI

Real-Time Logging

The beam position values and orbit corrector setpoints are exposed at a rate of up to 1000 Hz which allows correlation of this information with other machine parameters.

Figure 3 shows the effect of ramping the Biomedical Imaging and Therapy (BMIT) superconducting 4.3 Tesla wiggler from zero, and the associated response as the orbit correction system works to damp out this disturbance. The perturbations caused by this wiggler when ramping from 0 T, mean that this can only be done when the current in the ring is below the bad orbit threshold. The perturbation is not as significant at higher fields, however during normal operation additional compensation does occur to allow this wiggler to change field strength.

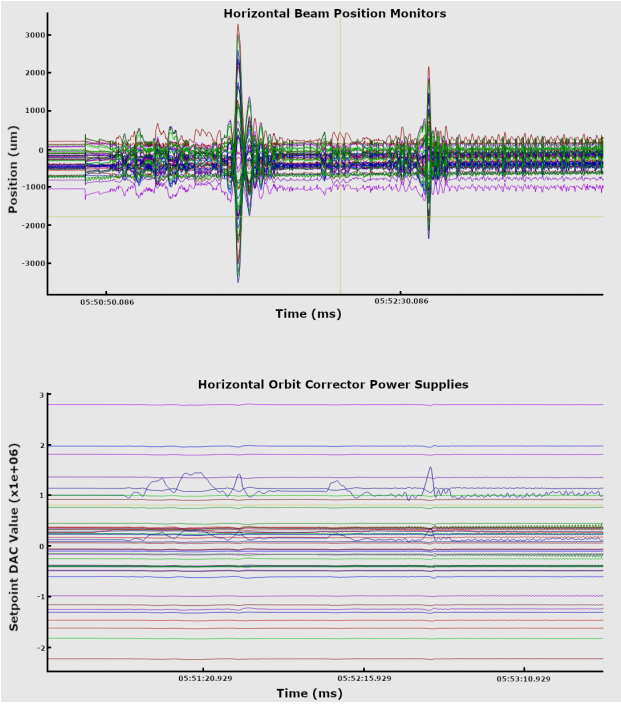


Figure 3: Logger showing horizontal beam position and orbit corrector setpoints during ramping of the BMIT super conducting wiggler.

Real-Time Analysis

Real-time root mean square and standard deviation values are calculated for individual and global beam position readings to support detection of noisy electronics.

Power spectral density and cumulative power spectral density data is calculated for all BPMs. This information quantifies noise in the stored beam as a function of frequency. The graphical user interface allows any combination of BPMs to be selected simultaneously. Figure 4 shows an example of this data from all of the horizontal beam position monitors.

Waveform Generation

Waveform signals can be sent to any combination of orbit correctors. This functionality has proven to be beneficial for

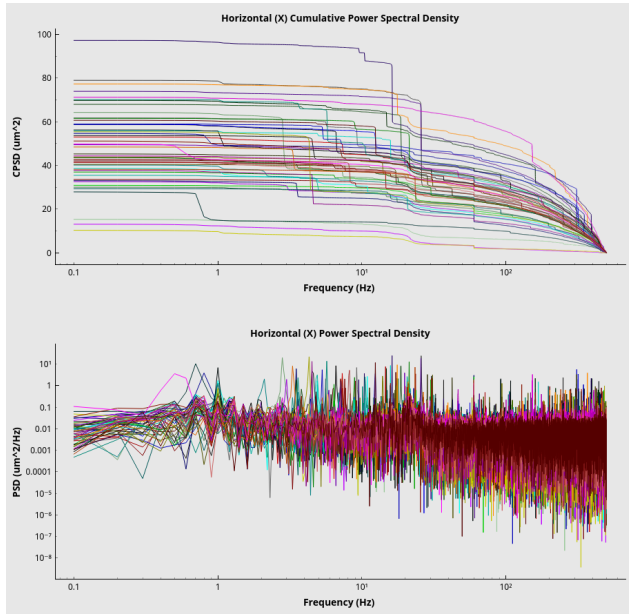


Figure 4: Horizontal beam position power spectral density and cumulative power spectral density.

both commissioning and as a diagnostic tool for analyzing noise issues. By introducing a sine or square wave with selectable frequency, amplitude and offset, the orbit correction system performance can be analyzed as it damps out the injected signal. This supports measurement of the closed loop bandwidth.

The sine wave generation, shown in Fig. 5, has also been used to diagnose noise issues reported by beamlines. This is done by moving the electron beam to determine whether the noise seen by the beamline is introduced by this beam motion.

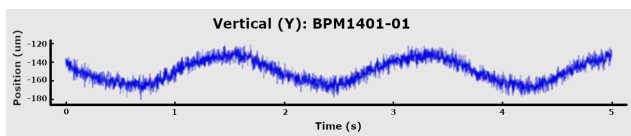


Figure 5: Beam motion resulting from a sine wave introduced on an orbit corrector.

The generation of a square wave, shown in Fig. 6, has been used to determine the step response of the system.

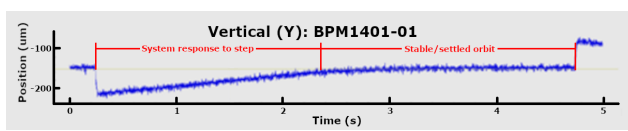


Figure 6: Introduction of a square wave to measure the response of the system.

Digital Filtering

Digital filtering is available on both beam position inputs and orbit corrector setpoints for future performance enhancements.

ISBN: 978-3-95450-241-7 ISSN: 2673-5350 doi:10.18429/JACoW-IBIC2022-WEP34

System Monitoring

A significant increase in the error handling ensures that a loss of communication with orbit correction hardware or a related external system is reported in real-time.

Hardware Verification

Verification of power supply components is automated. This automated testing is used to verify an individual, a subset of, or all orbit corrector power supplies. This allows quick and efficient testing and supports easy identification of issues.

PERFORMANCE LIMITATIONS

Magnet Bandwidth

It was initially believed that the bandwidth of the orbit correction magnets was on the order of 50 Hz. However, using the waveform generation functionality it has been determined that the bandwidths are between 15 and 30 Hz depending on the axis and type of magnet.

Noise on Beam Position Signals

There is noise on the beam position signals after the Bergoz electronics, used to convert the button signals to vertical and horizontal beam positions. To reduce this noise some averaging has had to be introduced, which impacts the bandwidth.

CONCLUSION

The new orbit correction system was commissioned in November 2021. This upgrade has improved reliability and maintainability, and has dramatically increased the diagnostic capabilities. The architecture supports easy integration of new functionality, providing the foundation for future enhancements.

ACKNOWLEDGEMENTS

Research at the CLS is funded by the Canada Foundation for Innovation, the Natural Sciences and Engineering Research Council of Canada, the National Research Council Canada, the Canadian Institutes of Health Research, the Government of Saskatchewan, Western Economic Diversification Canada, and the University of Saskatchewan.

REFERENCES

[1] D-tAcq ACQ435ELF 32 Channel Simultaneous Sampling Digitizer, https://www.d-tacq.com/acq435elf.shtml

[2] D-tAcq ACQ2106 6 Site ELF Carrier, https://www.d-tacq.com/acq2106.shtml

[3] PoLabs PoKeys57E Ethernet Computer Numerically Controlled Controller, https://www.poscope.com/product/pokeys57e/.

Content from this work may be used under the terms of the CC BY 4.0 licence (© 2022). Any distribution of this work must maintain attribution to the author(s), title of the work, publisher, and DOI

ISBN: 978-3-95450-241-7 ISSN: 2673-5350 doi:10.18429/JACoW-IBIC2022-WEP36

CONCEPTUAL DESIGN OF THE TRANSVERSE MULTI-BUNCH FEEDBACK FOR THE SYNCHROTRON RADIATION SOURCE PETRA IV

S. Jablonski, H.T. Duhme, B. Dursun, J. Klute, S. H. Mirza, S. Pfeiffer, H. Schlarb
Deutsches Elektronen Synchrotron (DESY), Hamburg, Germany

Abstract

PETRA IV will be a new, fourth-generation, high-brilliance synchrotron radiation source in the hard X-ray range. To keep the emittance low at high beam current an active feedback system to damp transverse multi-bunch instabilities is required. The particular challenge to the system is the very low-noise, while maintaining high bandwidth, which is defined by the 2 ns bunch spacing.

In this paper, we present the conceptual design of the transverse multi-bunch feedback (T-MBFB) system and technical challenges to fulfill the performance requirements. An overview is given on the hardware and the method for detecting and damping the coupled-bunch oscillations. Using modern high-speed ADCs enables direct sampling of pulses from beam pick-ups, which removes the necessity for down-converters. Powerful digital signal processing allows not only for the effective feedback implementation, but also for developing versatile tools for the machine diagnostics.

REQUIREMENTS FOR T-MBFB

The T-MBFB must be able to damp the coupled-bunch oscillations for two PETRA IV operation modes, i.e. brightness mode (maximum 3840 bunches, 2 ns bunch spacing, total current of 200 mA) and timing mode (80 bunches, 96 ns bunch spacing, total current of 80 mA). To suppress the possible oscillation modes, the feedback acts on each bunch (bunch-by-bunch, turn-by-turn system), which requires at least 500 MHz flat magnitude and linear phase detector electronics. The frequencies of the horizontal and vertical betatron oscillations are ~23.4 kHz and ~35.2 kHz, respectively [1].

PETRA IV is planned to have much lower horizontal electron beam emittance (< 20 pm rad in the brightness mode [2]) than PETRA III. The detector resolution must be finer than 1 µm to not degrade the beam emittance [1]. For ±1 mm expected transverse motion range, the required minimum SNR of the dectector is 60 dB. In a direct sampling detector scheme, the detector noise is dominated by the intrinsic noise of the ADCs, which is discussed later in the subsection on the RFSoC digitizer.

Another requirement is the feedback damping time τ of the multi-bunch instabilities, which was defined to be not worse than 20 turns in any operation mode and for the worst case, i.e. when the synchrotron chromaticity Q' is zero [1]. However, such a damping time is only required for a relatively small transverse oscillation amplitude at the pick-up, i.e. $A_p < 200$ µm.

Additionally, the bunch charge in the timing mode is considerably higher than in the brightness mode, therefore, the MBFB system must have a wide dynamic range and an overvoltage protection to ensure high performance and high reliability for both machine setups.

The T-MBFB requirements and some of the PETRA IV design parameters are summarized in Table 1.

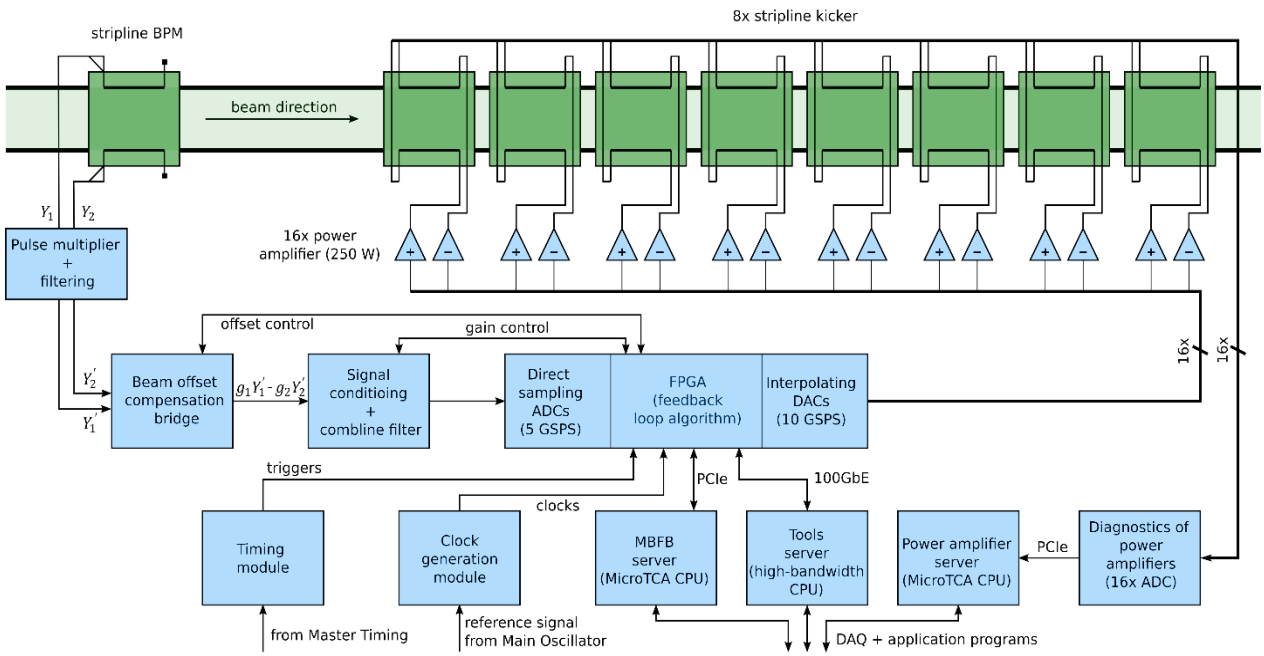


Figure 1: Simplified block diagram of the vertical transverse multi-bunch feedback (T-MBFB).

Content from this work may be used under the terms of the CC BY 4.0 licence (© 2022). Any distribution of this work must maintain attribution to the author(s), title of the work, publisher, and DOI

ISBN: 978-3-95450-241-7 ISSN: 2673-5350 doi:10.18429/JACoW-IBIC2022-WEP36

Table 1: PETRA IV Design Parameters in the Brightness (**B**) and Timing (**T**) Mode and the Requirements for the T-MBFB

Design Parameter	Value
Energy E	6 GeV
Revolution frequency f_{rev}	130.12 kHz
Emittance (ϵ_x / ϵ_y)	< 20 / 4 pm rad (**B**) / < 50 / 10 pm rad (**T**)
Total current I	200 mA (**B**), 80 mA (**T**)
Number of bunches M	max. 3840 (**B**), 80 (**T**)
Bunch current I_b	< 70 µA (**B**), 1 mA (**T**)
Bunch spacing T_{rep}	2 ns (**B**), 96 ns (**T**)
Bunch length σ_t	45.7 ps (**B**), 64.3 ps (**T**)
Betatron freq. (f_x / f_y)	23.4 kHz / 35.2 kHz
T-MBFB det. bandwidth	> 500 MHz
T-MBFB det. resolution	<1 µm at ±1 mm det. range
T-MBFB damping time τ	< 20 turns (A_p < 200 µm)

T-MBFB HARDWARE OVERVIEW

Figure 1 presents a simplified block diagram of the vertical T-MBFB. It is composed of a stripline BPM, a series of stripline kickers and a feedback controller electronics. In the following subsections, the particular components are treated in more detail.

Stripline BPM, Pulse Multiplier and Filtering

Stripline BPM is composed of four electrodes (stripline pick-ups) equally distributed around the beam pipe, i.e. every 90°, with a characteristic impedance Z_0 of 50 Ω. For the vertical beam position measurement, electrical pulses from the upper and lower pick-ups are combined together, creating signals Y_1 and Y_2 (Fig. 1), respectively. For the horizontal beam position measurement, the left and right pick-ups are combined.

The pick-up transfer function is mainly defined by the electrode length L and the electrode width α [3, 4]. The electrode length was selected to be 7.5 cm resulting in the maximum transfer function at 1 GHz and a relatively flat magnitude in the range from 750 MHz up to 1250 MHz, i.e. the frequency band used for the transverse oscillation modes detection. The electromagnetic simulations show that the electrode width α of about 34° is optimal regarding the coupled-out signal power and the characteristic impedance matching [5]. The vertical and horizontal BPMs are located at high beta $\beta_{p,ver}$ and $\beta_{p,hor}$ position in the ring, respectively, to improve the detector resolution.

Figure 2 shows the analog signal processing of a pulse after it is coupled out from the pick-up. Firstly, it is delivered to a pulse multiplier, i.e. a passive device composed with a 2-way power splitter, two coaxial cables differing in the electrical length by 1 ns and a 2-way power combiner. It improves the detector resolution by 3 dB, because twice more samples can be used for the pulse amplitude detection.

In the next step, the multiplied pulse is filtered with a 6-pole, lowpass, 2 GHz bandwidth, Bessel filter. Due to linear phase response of the filter, it does not produce any ringing overlapping the next bunch. After lowpass filtering, the signal is provided to the beam offset compensation bridge.

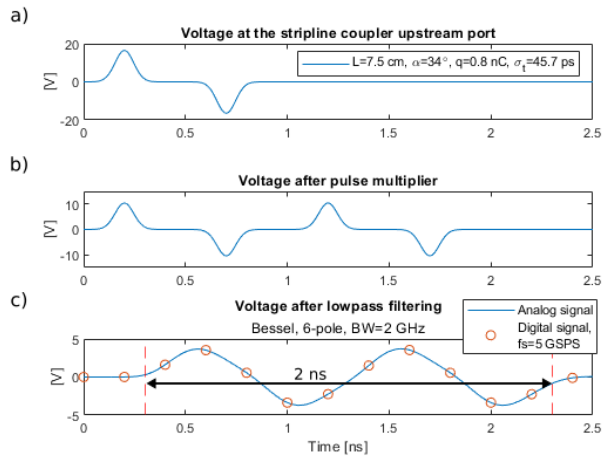


Figure 2: a) Voltage at the stripline coupler upstream port for the electrode length L=7.5 cm, electrode width α=34°, bunch charge of 0.8 nC and Gaussian bunch duration of 45.7 ps in the brightness mode, b) voltage after using the pulse multiplier, c) voltage after applying the 6-pole, lowpass, 2 GHz bandwidth, Bessel filter and a digital signal with a 5 GSPS RFSoC digitizer.

Beam Offset Compensation Bridge and Combline Filter

The in-phase signals Y_1' and Y_2' (Fig. 1) are conditioned to have the same amplitude using variable attenuators and further they are subtracted from each other using a wideband RF transformer. This circuitry is called beam offset compensation bridge (BOCB) and it is used to make the detector only sensitive to transverse beam oscillations, not to the absolute beam position in the vacuum chamber or to the uneven bunch filling.

In the frequency domain, the BOCB suppresses the bunch repetition harmonics and the revolution harmonics, which are associated to the set of frequencies [6]

$$f = pf_{rep} \pm mf_{rev}, \quad (1)$$

where p is the integer number ($-\infty < p < +\infty$), f_{rep} is the bunch repetition frequency, m = 0, 1, …, M-1 (M bunches equally spaced) and f_{rev} is the revolution frequency. The suppression of the above harmonics by more than 30 dB protects the electronics from saturation and increases the measurement resolution, because it allows to use almost full-scale of the ADCs for the betatron signal oscillation. The BOCB for the horizontal and vertical planes are implemented on a single MicroTCA module called DRTM-MBFB-CSI (Fig. 3).

Optionally, the harmonics suppression can be further increased by a combline filter connected in series with the BOCB. The filter is constructed using a delay line based on the fiber-optic technology.

Content from this work may be used under the terms of the CC BY 4.0 licence (© 2022). Any distribution of this work must maintain attribution to the author(s), title of the work, publisher, and DOI

ISBN: 978-3-95450-241-7 ISSN: 2673-5350 doi:10.18429/JACoW-IBIC2022-WEP36

Content from this work may be used under the terms of the CC BY 4.0 licence (© 2022). Any distribution of this work must maintain attribution to the author(s), title of the work, publisher, and DOI

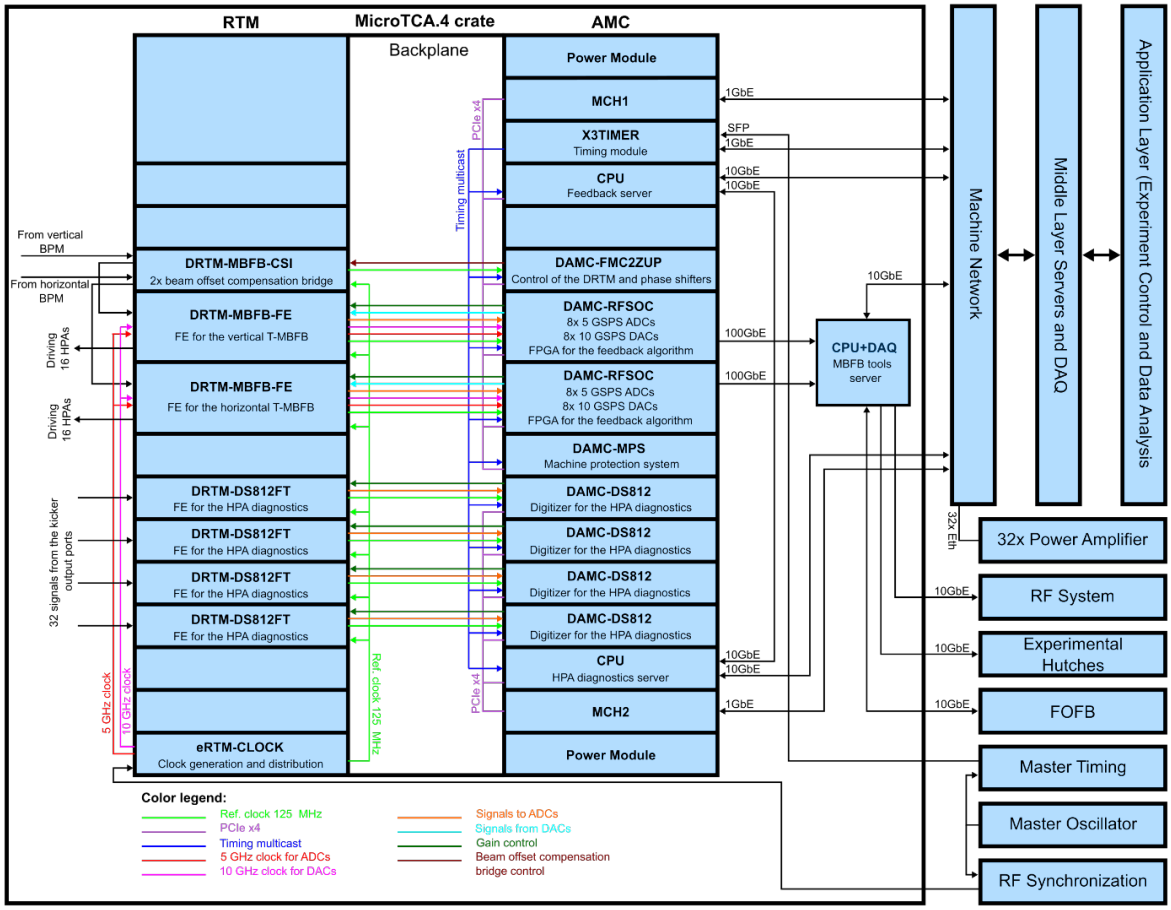


Figure 3: Implementation of the T-MBFB in the MicroTCA .4 form factor and interfaces to the control system, DAQ and various PETRA IV subsystems.

Zynq UltraScale+ RFSoC Integrating RF-ADCs, RF-DACs and FPGA

Advance in ADC technology allows for direct conversion of RF signals to the digital domain without using any analog down-converters. The signal from the BOCB (DRTM-MBFB-CSI) is fed to the ADC front-end module (DRTM-MBFB-FE), which includes a chain of RF amplifiers and variable attenuators to provide the high dynamic range required for the various machine operation modes. The conditioned signals are transmitted over Zone 3 connector to the AMC module DAMC-RFSOC. This module includes the Xillinx Zynq UltraScale+ RFSoC, a platform that integrates eight ADCs (14 bit, 5 GSPS), eight DACs (14 bit, 10 GSPS), processing resources (FPGA, APUs, RPUs) and various fast communication interfaces like 100GbE or PCIe. The MBFB system uses two DAMC-RFSOC modules, one for the horizonal and one for the vertical feedback (Fig. 3).

Resolution of the T-MBFB detector is limited by noise and spurs of the ADC. SNR of the ADC for a single pulse amplitude measurement with a 250 MHz bandwidth averaging filter is equal to about 62 dB, which is only a few dB more than specified in the PETRA IV requirements. However, it is improved by using the pulse multiplier (+3 dB in the brightness mode) and by simultaneous amplitude measurement with N parallel ADCs ($+10\log_{10}N$ dB). It is planned to use 4 ADCs for the feedback, which yielding a final detector SNR of about 71 dB.

After converting the analog pulses to the digital domain, the FPGA is used for the digital signal processing. The calculated kick values are streamed every 2 ns to eight, differential output DACs, which drive 16 high power amplifiers, i.e. one differential DAC is used for one stripline kicker (each electrode of the kicker is driven with the opposite polarization).

Stripline Kickers and Damping Time

The stripline kickers must reliably act upon every single bunch to damp the betatron oscillations. In a storage ring with 500 MHz bunch repetition rate (max. possible with given RF cavity frequency for PETRAIV), the decay time of the electromagnetic field inside the kicker has to be less than 2 ns in order to avoid the following bunch being affected. Additionally, the kicking strength, expressed as the shunt impedance R_s, should be maximized over the full spectrum from DC to 250 MHz.

Based on the formula for the ideal cylindrical stripline kicker given in the reference [7], the stripline length L was selected to be 30 cm, which provides relatively flat shunt impedance up to 250 MHz and zero shunt impedance at multiplies of 500 MHz what considerably reduces beam energy coupling out to the kicker load (see Fig. 4).

ISBN: 978-3-95450-241-7 ISSN: 2673-5350 doi:10.18429/JACoW-IBIC2022-WEP36

Figure 5 shows the damping time constant versus oscillation amplitude at the BPM calculated for the system with eight stripline kickers driven with the total electrical power P_t of 2.8 kW. The kicker shunt impedance was assumed to be 3.4 kΩ, which is the worst-case scenario, i.e. the fastest mode at 250 MHz. Damping time constant is lower than 20 turns for any operation mode and for $A_p < 258$ µm, which meets the T-MBFB requirements. The horizontal and vertical kickers are placed at high beta $\beta_{k,hor}$ and $\beta_{k,ver}$ locations.

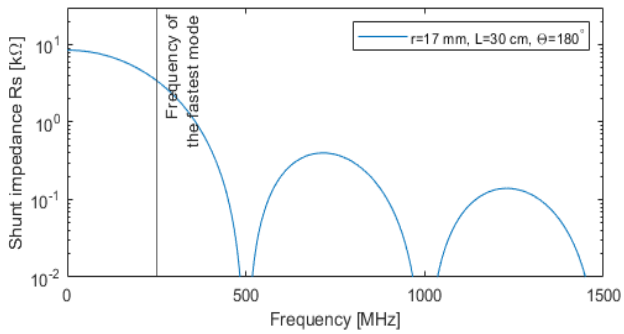


Figure 4: Shunt impedance of an ideal stripline kicker for the length L of 30 cm, the radius r of 17 mm and the opening angle of the striplines θ of 180°.

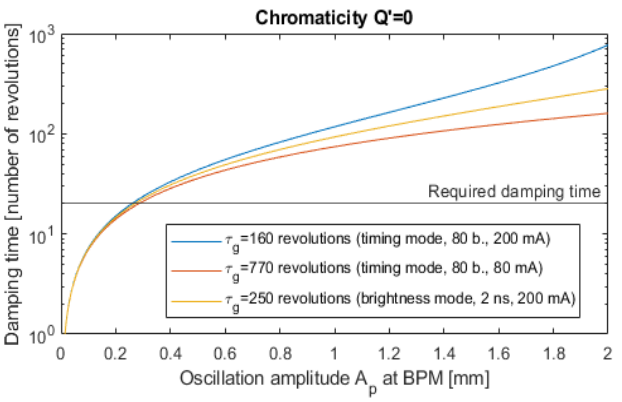


Figure 5: Damping time constant vs. oscillation amplitude A_p at BPM and for various growth rate time constants τ_g. The calculations are based on the following parameters: R_s=3.4 kΩ, P_t=2.8 kW, β_{BPM}=35 m, β_{kicker}=45 m.

Timing and System Clock

The main oscillator of ~500 MHz provides the reference signal to the master timing system and for RF synchronization. The RF synchronization distributes the reference signal to the eRTM-CLOCK, which generates low phase-noise 5 GHz and 10 GHz clocks for the feedback ADCs and DACs. The eRTM-CLOCK includes also a voltage-controlled phase shifter that compensates phase drifts of the RF synchronization in relation to the bunch phase.

The master timing multicasts data to the remote receivers (X3Timer) including a variety of information. The most critical are the revolution trigger and the absolute time with high resolution to time stamp various events. X3Timer distributes triggers and information data over AMC backplane to all AMC modules.

Redundancy

Mean time between failures (MTBF) of PETRA IV is a crucial parameter. In case of any component malfunction, the T-MBFB should be immediately brought back into operation. Therefore, the critical modules are made redundant so that the failures not lead to beam loss or in case of beam loss machine operators can restart the system promptly.

CONCLUSION

The concept of the T-MBFB hardware for the synchrotron radiation source PETRA IV has been developed. The envisioned design would fulfill the demanding performance requirements for detecting and damping high-bandwidth, coupled-bunch oscillations with enough resolution to not degrade the bunch emittance. RF-ADCs are used for the direct sampling of broadband pulses, which simplifies the analog design by omitting the down-conversion stage.

The feedback electronics is based on the MicroTCA.4 form factor that offers modularity, redundancy and availability of some commercial modules which reduces the development cost. The hardware structure gives flexibility for future upgrades and for the installation of additional modules in case any performance improvement is required.

In this paper, we have not reported any analysis of the MBFB algorithm, its implementation in the FPGA (firmware), diagnostic tools, DAQ and control system, which currently is in the design stage. The hardware provides powerful processing resources and high-speed communication interfaces, therefore, it can be flexibly used for various demanding firmware and software needs.

REFERENCES

[1] S. Antipov, C. Li, and Y.-C. Chae, "PETRA IV Multibunch Feedback Requirements", [Slides], Deutsches Elektronen-Synchrotron DESY, Hamburg, Oct. 2021.

[2] C. Schroer, I. Agapov, R. Roehlsberger, R. Wanzenberg, R. Brinkmann, E. Weckert, and W. Leemans, "PETRA IV: Upgrade of PETRA III to the Ultimate 3D X-ray Microscope", Conceptual Design Report, Deutsches Elektronen-Synchrotron DESY, Hamburg, 2019. https://bib-pubdb1.desy.de/record/426140

[3] M. Wendt, "BPM systems: A brief introduction to beam position monitoring", Contribution to CERN Accelerator School, 2020.

[4] R. E. Shafer, "Beam Position Monitoring", *AIP Conf. Proc.*, vol. 249, pp. 601–636, 1992. doi:10.1063/1.41980

[5] S. Strokov, "Stripline Monitor Simulation. S-Parameters, Signal Strength and Quality", [Slides], Deutsches Elektronen-Synchrotron DESY, Hamburg, Aug. 2022.

[6] M. Lonza and H. Schmickler, "Multi-bunch feedback systems", Contribution to the CERN Accelerator School: Advanced Accelerator Physics Course, Trondheim, Norway, Aug. 2013.

[7] M. Schedler, A. Roth, W.C.A. Hillert, and D. Heiliger, "A Broadband RF Stripline Kicker for Damping Transversal Multibunch Instabilities", in *Proc. IPAC'11*, San Sebastian, Spain, Sep. 2011, paper MOPO003, pp. 481-483.

Content from this work may be used under the terms of the CC BY 4.0 licence (© 2022). Any distribution of this work must maintain attribution to the author(s), title of the work, publisher, and DOI

ISBN: 978-3-95450-241-7 ISSN: 2673-5350 doi:10.18429/JACoW-IBIC2022-WEP37

MEASUREMENTS FOR EMITTANCE FEEDBACK BASED ON RESONANT EXCITATION AT DIAMOND LIGHT SOURCE

S. T. Preston*, T. Olsson, A. Morgan†, L. Bobb, Diamond Light Source, Oxfordshire, UK

Abstract

In the Diamond storage ring, the vertical emittance is kept at 8 pm rad by an emittance feedback which modifies the strengths of skew quadrupoles. A new feedback using a stripline kicker to control the vertical emittance by exciting the beam resonantly at a synchrotron sideband is planned to avoid modification of the optics. This is crucial for the anticipated Diamond-II upgrade of the storage ring, which will have a much smaller equilibrium emittance than the existing machine. A larger coupling is therefore needed to keep the vertical emittance at the same level, potentially reducing the off-axis injection efficiency and lifetime. Measurements of the beam oscillation and emittance have been performed at the existing storage ring to characterise the effects of chromaticity and impedance on the optimal excitation frequency, where the emittance is increased significantly while the beam oscillation is kept low. The implications for simulating the emittance feedback for the Diamond-II storage ring are also discussed.

INTRODUCTION

The vertical emittance of the Diamond Light Source storage ring is kept constant during user operation by a feedback system to maintain the source brightness, spot size and coherence as conditions in the machine change [1]. Before each machine run, the optics are corrected using LOCO [2], giving a vertical emittance on the order of a few pm rad. The emittance is then measured using two pinhole cameras and increased to 8 pm rad by changing the strengths of the skew quadrupoles in the ring [1]. This results in changes of the optics such as betatron coupling and vertical dispersion. Although not a concern for the existing ring, it could negatively affect the off-axis injection efficiency and lifetime for the planned Diamond-II storage ring, which will reduce the equilibrium emittance from 2.7 nm rad to 160 pm rad with open insertion devices and 120 pm rad with closed [3]. The required coupling to reach the same level of vertical emittance will then be considerably higher.

A new emittance feedback that does not affect the optics is therefore under development. Inspiration comes from the pulse picking by resonant excitation (PPRE) method operated at BESSY-II [4, 5], where the emittance of a single bunch is increased by driving the beam at a synchrotron sideband. The purpose is to extract single bunch light for timing users while operating with a multi-bunch fill pattern. At Diamond, the plan is to drive all the bunches and use a feedback system to adjust the excitation amplitude to keep the emittance constant.

* shaun.t.preston@gmail.com
† alun.morgan@diamond.ac.uk

Measurements at different excitation frequencies have been done at the existing Diamond storage ring. The optimal frequency and implications for predicting the behaviour of the Diamond-II storage ring are discussed. The new emittance feedback is also presented along with future plans.

THE DIAMOND MULTI-BUNCH FEEDBACK SYSTEM

The transverse multi-bunch feedback system (TMBF) for the Diamond storage ring is developed in-house. It uses a beam position monitor (BPM) to detect turn-by-turn bunch-by-bunch data and stripline kickers to apply excitation to the beam. More details about the hardware can be found in [6–8]. The system can apply multiple concurrent excitations to user defined groups of bunches, down to the level of a single bunch. In user operation, it is used both to damp coupled-bunch instabilities and for low gain frequency sweeps to measure the betatron and synchrotron tunes for tune feedback. During machine development, it is also used to drive the beam for instability studies.

FEEDBACK IMPLEMENTATION

The emittance feedback is implemented using the TMBF system for excitation and the existing pinhole cameras for measurement. An additional excitor is used to drive the beam at one of the synchrotron sidebands. In practice, this is realised by using a numerically controlled oscillator (NCO), whose amplitude and frequency can be adjusted as needed.

In order to implement the feedback, an additional control loop was added, which adjusts the amplitude of the NCO in order to maintain a target value of emittance. As in the existing emittance feedback system, the change in beam size is monitored by two pinhole cameras and the emittance calculated using this data.

To improve the effectiveness of the technique, tune tracking is also implemented. The purpose of tracking is to allow the excitation to follow the jitter in tune, which causes the excitation to stay on the peak of the desired sideband. This is achieved by using a phase-locked loop which monitors a single tracking bunch.

Interference can be reduced by turning off the TMBF system tune sweep for the tracking bunch and a few bunches either side and not applying an emittance excitation to them. These bunches only need a fraction of the charge of the others for sufficient lifetime without an emittance increase.

The feedback has run successfully in dedicated development time and is being integrated into the existing control system, which will allow switching between the existing skew quadrupole and sideband excitation methods for user operation.

Content from this work may be used under the terms of the CC BY 4.0 licence (© 2022). Any distribution of this work must maintain attribution to the author(s), title of the work, publisher, and DOI

ISBN: 978-3-95450-241-7 ISSN: 2673-5350 doi:10.18429/JACoW-IBIC2022-WEP37

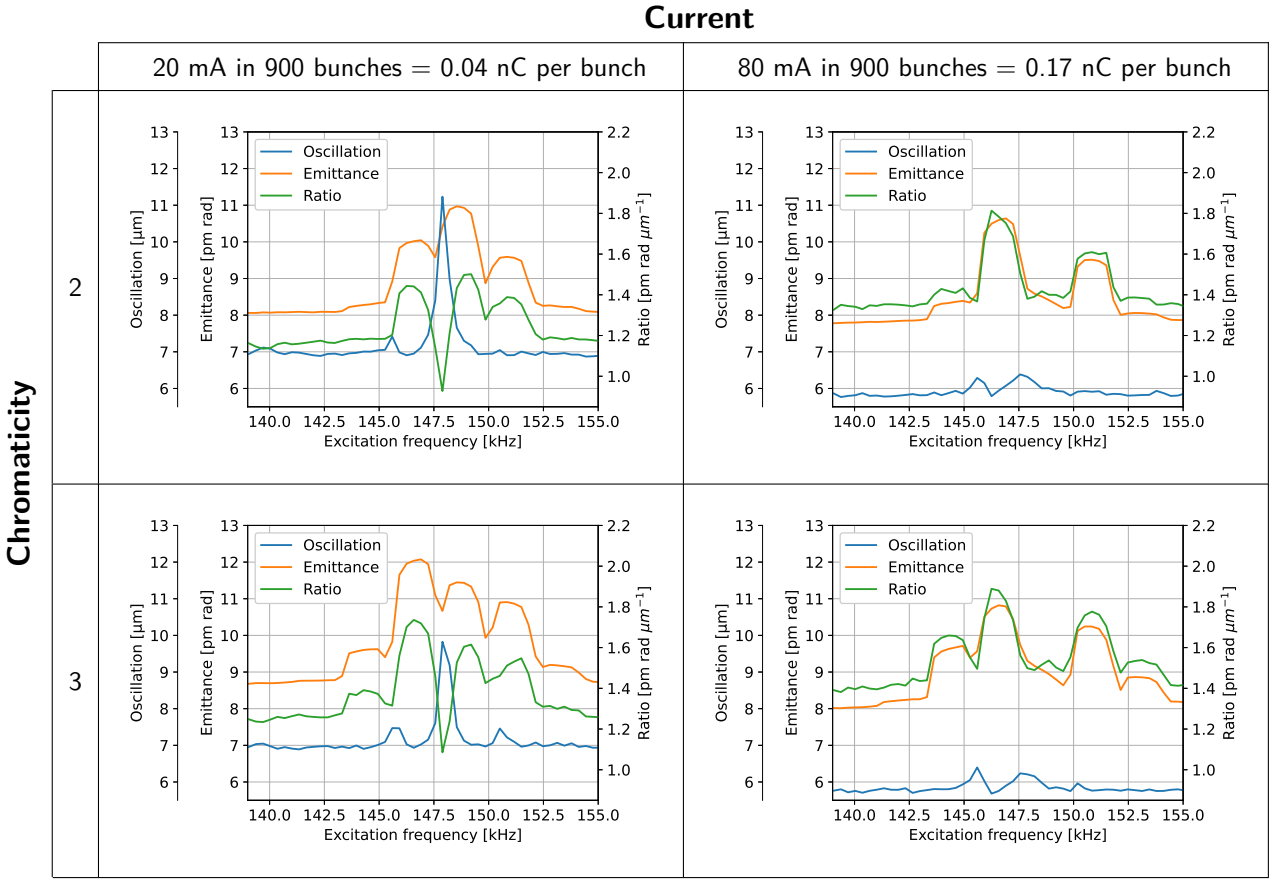


Figure 1: Measurements of beam RMS oscillation, vertical emittance and ratio of emittance to oscillation as a function of excitation frequency for different chromaticities (rows) and currents (columns). The ring was operated with a train of 900 bunches during the measurements. The gain of the excitation was set to −42 dB.

MEASUREMENTS OF EMITTANCE EXCITATION

The measurements were done using the TMBF system to excite the beam vertically over a frequency range including both the betatron tune and the first synchrotron sidebands. The oscillation of the beam was measured by extracting turn-by-turn data from the BPMs and calculating the RMS of the motion, whereas the emittance was extracted from the beam size measured by two pinhole cameras [9] at different positions in the ring. To get sufficient signal for the pinholes with low single bunch current, it was necessary to operate with a multi-bunch fill pattern in the machine. The measurements were therefore done using the normal fill pattern of 900 bunches. All of the insertion devices were open and the two superconducting wigglers turned off to give a lattice as close to bare as possible. Since the pinholes average over time, the measured beam size is a sum of the beam oscillation and emittance increase which has to be considered when comparing to simulations. Figure 1 shows the beam oscillation and vertical emittance for two different chromaticites and currents. Increasing the chromaticity makes additional sideband peaks appear and a strong current-dependent behaviour is observed, meaning the impedance is important. All of the measurements were taken using the same gain, but some at a higher current. This resulted in both smaller oscillation and emittance, so more gain is required at higher currents to get the same effect on the beam.

The ratio of the emittance to oscillation changes with current and chromaticity, which suggests that the optimal excitation frequency depends on the machine conditions. An empirical approach might be required where a good frequency is found during the setup of the machine by performing a frequency sweep. However, the measurements show that a good working point could be around the first lower synchrotron sideband, since the ratio is largest at this point for most of the measurements.

A complete impedance model does not currently exist for the Diamond storage ring, but previous measurements have been performed to fit a model consisting of broadband resonators, resistive-wall and an inductive component [10]. Using this model, simulations were run in `Elegant` [11, 12] to see if the behaviour observed in the measurements could be reproduced. The simulations were done using a single bunch and only broadband impedance as had previously been done for the Diamond-II storage ring, presented in more detail in [13]. The simulations showed similar behaviour with chromaticity as the measurements and the simulations

Content from this work may be used under the terms of the CC BY 4.0 licence (© 2022). Any distribution of this work must maintain attribution to the author(s), title of the work, publisher, and DOI

ISBN: 978-3-95450-241-7 ISSN: 2673-5350 doi:10.18429/JACoW-IBIC2022-WEP37

Content from this work may be used under the terms of the CC BY 4.0 licence (© 2022). Any distribution of this work must maintain attribution to the author(s), title of the work, publisher, and DOI

for Diamond-II, where additional synchrotron sidebands became visible with increasing chromaticity. It however proved difficult to achieve good agreement with the measurements at different currents. The addition of impedance broadened the peaks and made the lower and upper sidebands asymmetric as seen in the measurements, but the effect of the impedance was too weak. The current hypothesis is that the discrepancy comes from not including the effect of the long range wakefields in the model. The measurements were done around vertical coupled-bunch mode 0 out of a total 936 modes, but the TMBF system can also excite the beam around the other coupled-bunch modes given by the frequencies

$$f = \mu f_0 + \Delta f_\beta, \tag{1}$$

where μ is the coupled-bunch mode number (0-935), f_0 the revolution frequency and Δf_β the fractional part of the betatron tune converted to frequency [14].

During user operation, the TMBF system does a continuous frequency sweep with a very small gain to measure the tune. This is normally done around mode 80, but can be conducted around any mode. Figure 2 shows a comparison of the tune sweep around mode 0 and 80 for a case with a total current of 270 mA in the machine. The response of the beam changes with the coupled-bunch mode, which indicates that long range wakefields have a significant impact. This conclusion is also supported by a previous measurement of the coupled-bunch modes [15], where a tune sweep was performed around each mode and the mode damping times calculated from the Q factor when fitting a resonator to the tune peak. These fitted damping times showed good agreement with damping time extracted from drive-damp measurements. To predict the response of the beam from an excitation when operating with a multi-bunch fill pattern, it might therefore be necessary to include all the bunches and both short and long range wakefields in the simulation.

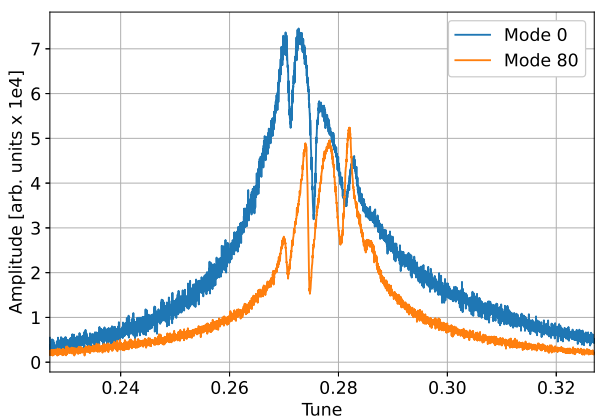


Figure 2: Comparison of vertical tune sweep around coupled-bunch mode 0 and 80 at 270 mA current.

DISCUSSION

A similar method to control the emittance is white noise excitation, which for example is used at ESRF [16]. In this method, the beam is excited at a broad range of frequencies instead of at a single frequency. The main advantage is that it is relatively simple to implement and that the method is insensitive to tune variations, which is useful for a machine without tune feedback. The disadvantage however is less separation between the emittance blow-up and betatron oscillations. Both tune and multi-bunch feedback is already implemented in the Diamond storage ring for other purposes, making emittance excitation using a single frequency easier to implement than white noise excitation. Using the multi-bunch feedback system for the excitation also has the advantage that the emittance of individual bunches can be manipulated, which might be of interest when operating with fill patterns, where a single bunch has been filled with higher charge for timing users. A larger excitation gain compared to the other bunches can then be given to the high-charge bunch to improve its lifetime while keeping the vertical emittance of the rest of the bunches at 8 pm rad. The new feedback also has the potential to control the horizontal emittance, which could be important for the Diamond-II storage ring, where the impact on the equilibrium emittance from the insertion devices is significant.

FUTURE WORK

The measurements highlighted some interesting areas that need to be studied further. Most important is the effect of coupled-bunch modes, which will require including both short and long range wakefields in the simulations. Also, to better understand the effect of the short range wakefields, additional measurements closer to operation with a single bunch in the ring could be done either by operating with a sparser fill pattern or by switching from measuring emittance to lifetime in case the signal is too weak for the pinholes.

Another interesting topic is the effect of the multi-bunch feedback on the beam oscillation. Since the feedback damps the dipole oscillations of the beam, it might counteract the oscillations driven by the excitation, and thus improve the ratio between the emittance blow-up and the beam oscillation.

For the Diamond-II storage ring, a detailed impedance model exists and simulations of emittance excitation for the case with a single bunch and short range wakefields have already been completed [13]. The measurements presented in this paper however indicate that the simulations for the new machine should be expanded to include the whole fill pattern and both short and long range wakefields to more accurately predict the behaviour and study how the optimal excitation frequency depends on the coupled-bunch modes.

The new storage ring will also include a harmonic cavity to increase the lifetime, reduce intra-beam scattering and mitigate instabilities by lengthening the electron bunches. This will drastically change the longitudinal dynamics of the beam, so the effect of the harmonic cavity on the emittance excitation must therefore be studied in more detail.

ISBN: 978-3-95450-241-7 ISSN: 2673-5350 doi:10.18429/JACoW-IBIC2022-WEP37

REFERENCES

[1] I. P. S. Martin, M. G. Abbott, M. Apollonio, D. Hickin, and R. Bartolini, "Operating the Diamond Storage Ring with reduced vertical emittance", in *Proc. IPAC'13*, Shanghai, China, May 2013, paper MOPEA071, pp. 249–251.

[2] J. Safranek, "Experimental determination of storage ring optics using orbit response measurements", *Nucl. Inst. Meth.*, vol. 388, pp. 27–36, 1997. doi:10.1016/S0168-9002(97)00309-4

[3] "Diamond-II Technical Design Report", Diamond Light Source, to be published, https://www.diamond.ac.uk/Home/About/Vision/Diamond-II.html

[4] K. Holldack *et al.*, "Single bunch x-ray pulses on demand from a multi-bunch synchrotron radiation source", *Nat. Commun.*, vol. 5, no. 4010, May 2014. doi:10.1038/ncomms5010

[5] J. G. Hwang, M. Koopmans, M. Ries, A. Schälicke, and R. Müller, "Analytical and numerical analysis of longitudinally coupled transverse dynamics of pulse picking by resonant excitation in storage rings serving timing and high-flux users simultaneously", *Nucl. Inst. Meth.*, vol. 940, pp. 387–392, 2019. doi:10.1016/j.nima.2019.06.053

[6] G. Rehm, M. G. Abbot, and A. F. D. Morgan, "New features and measurements using the upgraded transverse multibunch feedback at Diamond", in *Proc. IBIC'14*, Monterey, USA, Sep. 2014, paper WEPD24, pp. 696–699.

[7] M. G. Abbott, G. Rehm, and I. S. Uzun, "Architecture of transverse multi-bunch feedback processor at Diamond", in *Proc. ICALEPCS'15*, Melbourne, Australia, Oct. 2015, paper MOPGF097, pp. 298–301.

[8] M. G. Abbott, G. Rehm, and I. S. Uzun, "A new transverse and longitudinal bunch by bunch feedback processor", in *Proc. ICALEPCS'17*, Barcelona, Spain, Oct. 2017, pp. 1649–1654. doi:10.18429/JACoW-ICALEPCS2017-THPHA115

[9] C. Thomas, G. Rehm, and I. Martin, "X-ray pinhole camera resolution and emittance measurement", *Phys. Rev, Accel. Beams*, vol. 13, 2010. doi:10.1103/PhysRevSTAB.13.022805

[10] I. P. S Martin, M. Apollonio, R. T. Fielder, E. Koukovini-Platia, B. Singh and R. Bartolini, "Characterization of the double-double bench achromat lattice modification to the Diamond Light Source Storage Ring", *Phys. Rev. Accel. Beams*, vol. 21, 2018. doi:10.1103/PhysRevAccelBeams.21.060701

[11] M. Borland, "Elegant: A flexible SDDS-compliant code for accelerator simulation", Argonne National Lab., Illinois, USA, 2000.

[12] Y. Wang and M. Borland, "Pelegant: A parallel accelerator simulation code for electron generation and tracking", in *Proc. AIP'06*, vol. 877, pp. 241–247, 2006. doi:10.1063/1.2409141

[13] S. Preston, T. Olsson, and B. Singh, "Emittance feedback for the Diamond-II storage ring using resonant excitation", in *Proc. IPAC'22*, Bangkok, Thailand, Jun. 2022, pp. 1498–1501. doi:10.18429/JACoW-IPAC2022-TUPOMS035

[14] A. Chao, "Physics of collective beam instabilities in high energy accelerators", *Wiley series in beam physics and accelerator technology*, John Wiley & Sons, Inc., 1993.

[15] T. Olsson, "Collective effects in Diamond-II", in *27th European Synchrotron Light Source (ESLS) Workshop*, Barcelona, Spain, 2019, https://indico.cells.es/event/224/contributions/898/

[16] S. White, private communication.

Content from this work may be used under the terms of the CC BY 4.0 licence (© 2022). Any distribution of this work must maintain attribution to the author(s), title of the work, publisher, and DOI

ISBN: 978-3-95450-241-7 ISSN: 2673-5350 doi:10.18429/JACoW-IBIC2022-WEP38

CONTROL SYSTEM SUITE FOR BEAM POSITION MONITORS AT MAX IV

Áureo Freitas*, Carla Takahashi, Mirjam Lindberg, Robert Lindvall, Robin Svärd, Vincent Hardion
MAX IV Laboratory, Lund, Sweden

Abstract

MAX IV is a fourth generation synchrotron facility at Lund, Sweden. It is composed of a full energy linear accelerator and two storage rings with 1.5 GeV and 3 GeV, which requires hundreds of beam position monitors. In this context, Libera Single Pass E and Libera Brilliance+ are employed as BPM instruments. This paper will present an overview of the control system suite used in the facility, including the communication, data acquisition and storage pipelines, monitoring, configuration and software maintainability.

INTRODUCTION

MAX IV Laboratory [1] is a fourth generation light source located at Lund, Sweden. The accelerator complex consists of a 3 GeV, 250 m long full energy linac, two storage rings of 1.5 GeV and 3 GeV, and a Short Pulse Facility. During 2022 a total of sixteen beamlines are receiving light [2].

TANGO Controls is a toolkit for building distributed object based control systems. The distributed object in TANGO Controls is called a device and is created as an object in a container process called a device server. The device server implements the network communication and links to the configuration database and clients. TANGO device servers and clients can be written in Python, C++ or Java. TANGO comes with a full set of tools for developing, supervising, monitoring and archiving [3].

The TANGO Controls toolkit has been used to build the control systems for large and small physics experiments like synchrotrons, lasers, wind tunnels and radio telescopes, and it has been chosen as the Control System at MAX IV Laboratory.

CONTROL SYSTEM AT MAX IV

The control system at MAX IV Laboratory is distributed and consists of an estimated 370 servers, running 24,000 TANGO devices and providing 500,000 control points. The accelerator control system has a unique TANGO database and contains 200 servers. The servers are hosted in virtual machines running Linux operating systems and, for some applications, the TANGO servers are hosted in industrial computers and embedded systems. Figure 1 represents a small zoom of the control system complexity and interconnections.

Deploying and maintaining such big systems requires proper workflows and tools. MAX IV has been using Ansible [4] to manage and deploy its full control system, both software and infrastructure, for quite some time with great success. All required software (i.e. TANGO devices) is packaged as RPMs (Red Hat Package Manager) making deployment and dependency management easy [5].

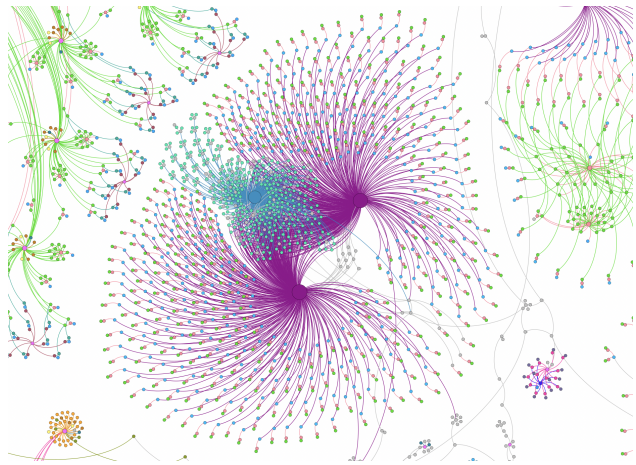


Figure 1: Zoom of the MAX IV 3 GeV storage ring control system. The two big pink stars represent the slow orbit feedback for the horizontal and vertical planes. The big blue star represents the Libera manager device.

BEAM POSITION MONITORS AT MAX IV

MAX IV uses a commercial solution for beam position monitors from I-Tech [6] with a custom firmware for internal needs. There are a total of 72 Libera Brilliance+ units in use in the storage rings, providing 236 beam position monitors (and an extra BPM for 3 GeV ring transfer line): 200 units in the 3 GeV ring and 36 units in the 1.5 GeV ring. For the linac, there are a total of 21 Libera Single Pass E units providing 48 beam position monitors.

Libera Brilliance+ features high precision position measurement of the electron beam in the booster or storage ring. Its digital signal processing supports programmable bandwidth and can facilitate all position measurements required in various regimes: pulsed, first turns, turn-by-turn and regular closed orbit. Acquisitions can be carried out simultaneously on all data paths: from raw ADC acquisition, turn-by-turn acquisition, slow acquisition to fast acquisition [7].

The instrument is based on the MTCA.0 modular technology and hosts up to 4 RAF (BPM) modules, one EVRX (timing) module and GDX (control) module in a single crate. The GDX module is used for the fast orbit feedback and to provide a continuous 10 kHz data streaming. This data is stored temporarily in a data storage cluster and is accessi-

* aureo.freitas@maxiv.lu.se

Content from this work may be used under the terms of the CC BY 4.0 licence (© 2022). Any distribution of this work must maintain attribution to the author(s), title of the work, publisher, and DOI

ISBN: 978-3-95450-241-7 ISSN: 2673-5350 doi:10.18429/JACoW-IBIC2022-WEP38

ble by multiple clients such as MATLAB and Python based applications.

Libera Single Pass E provides position measurement to resolve the bunch position from the very short signals produced by a bunch that is passing the beam position detector. It is a reliable and deterministic building block for fast-feedback building as well as for fast-forward loops, and thus enables attainment of high beam stability [8].

TANGO DEVICES FOR BPM

Figure 2 represents the TANGO devices for BPMs used in the storage rings at MAX IV. In total there are three layers and they are described in the following sections.



Figure 2: Control system schema for BPMs at the storage rings.

Figure 3 illustrates the amount of devices in production. Apart from those, there is one manager device per storage ring.

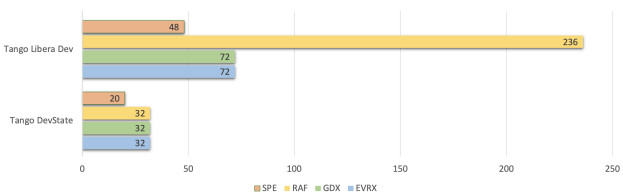


Figure 3: Representation of amount of TANGO devices for BPMs at MAX IV.

General Libera Device

This layer is based in the initial TANGO device class implemented by I-Tech, with internal modifications and developments made for MAX IV needs. This layer is responsible for exposing the different attributes and registers from Libera to TANGO. The device is written in C++ and runs embedded in the MTCA crate hosting an Ubuntu 14.04 operating system.

There are a total of four different devices classes, one per module, such as EVRX, RAF, GDX and SPE. For the RAF (BPM) module, there is one device per BPM. In general, the device loads a file that maps the internal registries and exposes them dynamically into TANGO as attributes. It is totally configurable and possible to have different attributes per crate, if needed.

DevState Device

The general Libera device only exposes the registries into TANGO and does not have any state management, meaning, that it is not possible to verify if actual state of each module (i.e. FAULT, ALARM) and this is the main goal of DevState device.

The idea of DevState device is to make an easy and configurable state machine representation of the BPMs subscribing to several registries exposed by general device class and compute the state machine. It is written in Python and runs in a virtual machine. A TANGO class property is used to map and generate the state machine / conditions using the registries exposed by the general device. Each state can have several status messages associated and propagated to the destination user.

The DevState device also contains another important feature which is the configuration of each individual registry, such as bit mask, interlock, among other attributes. It also verifies if the run-time configuration matches with the expected one and can serve a certain quantity of crates, usually. There is one DevState per storage ring achromat that serves three crates.

Manager Device

The principal of the manager device is to be a high level representation and a single point of configuration that reaches all BPMs. Like the DevState device, it is also written in Python and runs in a virtual machine. Basically it exposes several commands (i.e. Synchronize) that takes actions over the DevState devices and then distribute to each individual unit. There is a single manager device per storage ring.

MAINTAINABILITY

As mentioned above, Ansible is used at MAX IV to maintain software and firmware versions, repositories, general configuration, hostname, OS, file system, NTP, users, among other things like calibration.

Figure 4 shows a few of the Ansible AWX templates available for Liberas. AWX is an open source web-based user interface, REST API, and task engine built on top of Ansible [9].

The Liberas are organized by groups, one per storage ring and one for the linac and then, different firmware and/or software versions can be applied for individual groups.

The basic Ansible playbook starts configuring in sequence: hostname, users, repositories, software installation, firmware installation, system services, configuration, control system deployment and monitoring. Ansible opens the possibility to have a snapshot of the system and to retrieve the system to a certain state in the past with the versioning control, if

Content from this work may be used under the terms of the CC BY 4.0 licence (© 2022). Any distribution of this work must maintain attribution to the author(s), title of the work, publisher, and DOI

ISBN: 978-3-95450-241-7 ISSN: 2673-5350 doi:10.18429/JACoW-IBIC2022-WEP38

Content from this work may be used under the terms of the CC BY 4.0 licence (© 2022). Any distribution of this work must maintain attribution to the author(s), title of the work, publisher, and DOI

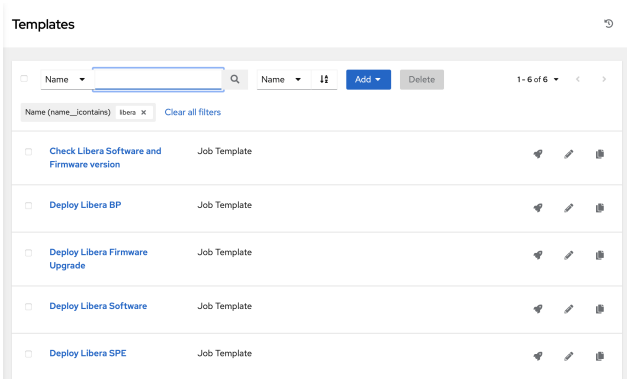


Figure 4: Example of Ansible AWX templates.

necessary. Also facilitate the maintainability since it can execute remote updates simultaneously for all units at MAX IV. TANGO devices and properties configuration are also maintained by Ansible.

There is a continuous integration and continuous deployment setup using GitLab CI/CD [10], that builds, tests, and publishes into the internal repository and triggers Ansible AWX templates if necessary.

MONITORING

MAX IV developed a Python Prometheus [11] exporter built into the Libera crate to export the required metrics to a Prometheus cluster and then stored by the Victoria metrics [12] into an internal Logging cluster.

The Libera Prometheus exporter is configurable and exposes hundred of metrics such as temperatures, fan speeds, voltages and currents.

Data visualization is done through Grafana dashboards [13]. Figure 5 illustrates a Grafana dashboard used for EVRX modules at 3 GeV ring. Several dashboards are available for daily monitoring and diagnostics. Dashboards are easy to make and anyone can create and share their own dashboards using the available metrics.



Figure 5: Grafana dashboard example for EVRX modules at 3 GeV ring.

There is also an alarm and notification system available which can be linked to group chats (bots), e-mail notifications, and other other functionalities.

APPLICATIONS

Several Python/PyQt [14] user interfaces are available for beam diagnostics in order to verify disturbances and actuation of feedback and/or feedforward systems. All the user interface applications follow the same procedure of continuous integration and deployment. The deployment and versioning control is managed by Ansible in the same way as the TANGO devices.

The storage ring slow orbit feedback (SOFB) loop uses a total of 200 BPMs in the large ring and 36 BPMs in the small ring for vertical and horizontal planes, resulting in 472 measurement points as inputs to the feedback system. The attributes push events thought TANGO at 10 Hz rate of the "slow" Libera data acquisition system. The events are synchronized in that all Libera Device Classes follow the same clock, so the position data from all BPMs are read and pushed every 0.1 s stamped with the same hardware time. The SOFB TANGO device subscribes to change events on all position attributes and will synchronize itself with the 10 Hz rate and write to the slow correctors. Figure 6 shows a user interface streaming 10 Hz data from BPMs and Figure 7 illustrates the differential value from measured orbit versus stored one [15].

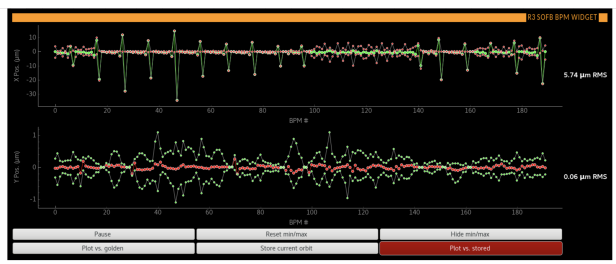


Figure 6: SOFB application displaying the beam position at 3 GeV ring, updated by SOFB iteration at 10 Hz. An alternative view in the application can show the kicks being applied to the corrector magnets.

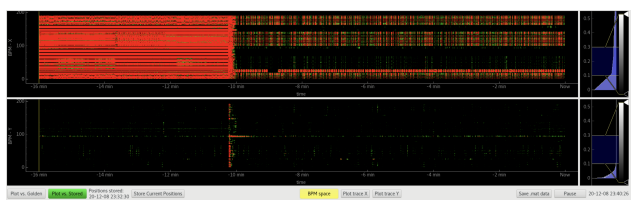


Figure 7: Example of BPMs differential trends versus stored orbit.

The fast orbit feedback (FOFB) makes use of the GDX fast (10 kHz) data stream from the same BPMs used as sensors in the SOFB. However, dedicated fast corrector magnets are used as actuators. The Libera Brilliance+ system is extended with custom SER modules having a RS485 interface to directly output the fast corrector set values. The feedback PI controller calculation is implemented in a FPGA running in the GDX module [16]. A TANGO device to interface to this system allows, for example, download of the response

ISBN: 978-3-95450-241-7 ISSN: 2673-5350 doi:10.18429/JACoW-IBIC2022-WEP38

matrix and the position reference values. Other control loops are also in place, such as a trajectory feedback for the linear accelerator.

FUTURE DEVELOPMENTS

X-ray beam position monitors (XBPM) at MAX IV are blade BPMs based on Alba Electrometer [17] for current measurement. They are not yet following the same control system stack as other beam position monitors (such as data acquisition and standard user interfaces). There is an idea to replicate the same control system structure as the RF BPMs to the XBPMs.

Currently, the XBPMs are located at the 3 GeV beamline frontends and it is an important diagnostic tool that is showing new, unprecedented information about the 3 GeV storage ring, its alignment, its stability and its insertion devices [18] and can be used in the future for control loop systems.

CONCLUSION

The control system suite for the beam position monitors at MAX IV Laboratory allows easy and quick maintainability, versioning control, snapshots and change-logs for troubleshooting, efficient continuous integration and deployment, and well proven efficiency for control loops at all accelerators with aim on beam stability.

All software developed by MAX IV is open source and available to everyone interested.

ACKNOWLEDGEMENTS

The authors would like to thanks the MAX IV Control and IT group, radio-frequency group, accelerator physicists and operators, without the collaboration of whom this work would not have been possible.

REFERENCES

[1] MAX IV Laboratory home page. http://maxiv.lu.se

[2] V. Hardion, P.J. Bell, M. Eguiraun, T. Eriksson, Á. Freitas, J.M. Klingberg, *et al.*, "Maturity of the MAX IV Laboratory in Operation and Phase II Development", in *Proc. ICALEPCS'21*, Shanghai, China, Oct. 2021, pp. 1–8. doi:10.18429/JACoW-ICALEPCS2021-MOAL01

[3] TANGO-Controls documentation. https://tango-controls.readthedocs.io

[4] Ansible, https://www.ansible.com

[5] B. Bertrand, Á. Freitas, and V. Hardion, "Control System Management and Deployment at MAX IV", in *Proc. ICALEPCS'21*, Shanghai, China, Oct. 2021, pp. 819–823. doi:10.18429/JACoW-ICALEPCS2021-THBL01

[6] I-Tech: Instrumentation Technologies. https://www.i-tech.si

[7] Libera Brilliance+. https://www.i-tech.si/products/libera-brilliance-3

[8] Libera Single Pass E. https://www.i-tech.si/products/libera-single-pass-e

[9] Ansible AWX. https://github.com/ansible/awx

[10] GitLab CI/CD. https://docs.gitlab.com/ee/ci

[11] Prometheus. https://prometheus.io

[12] Victoria metrics. https://victoriametrics.com

[13] Grafana. https://grafana.com

[14] PyQt. https://www.riverbankcomputing.com/software/pyqt

[15] P.J. Bell, V.H. Hardion, M. Lindberg, V. Martos, and M. Sjöström, "A General Multiple-Input Multiple-Output Feedback Device in Tango for the MAX IV Accelerators", in *Proc. ICALEPCS'19*, New York, NY, USA, Oct. 2019, pp. 1084–1088. doi:10.18429/JACoW-ICALEPCS2019-WEPHA012

[16] P. Leban, E. Janezic, and M. Sjöström, "Fast Orbit Feedback Application at MAX IV and SOLARIS Storage Rings", in *Proc. IPAC'14*, Dresden, Germany, June 2014, pp. 1748–1750. doi:10.18429/JACoW-IPAC2014-TUPRI078

[17] J.A. Avila-Abellan, M. Broseta, G. Cuní, O. Matilla, A. Milan-Otero, M. Rodriguez, *et al.*, "Em# Electrometer Comes to Light", in *Proc. ICALEPCS'17*, Barcelona, Spain, Oct. 2018, pp. 137-142. doi:10.18429/JACoW-ICALEPCS2017-TUAPL04

[18] A. Bartalesi, "The XBPM Project at MAX IV Frontends, Overview and First Results", in *Proc. MEDSI'18*, Paris, France, Jun 2018, pp. 340–342. doi:10.18429/JACoW-MEDSI2018-THPH03

Content from this work may be used under the terms of the CC BY 4.0 licence (© 2022). Any distribution of this work must maintain attribution to the author(s), title of the work, publisher, and DOI

ISBN: 978-3-95450-241-7 ISSN: 2673-5350 doi:10.18429/JACoW-IBIC2022-WEP40

A MODERN ETHERNET DATA ACQUISITION ARCHITECTURE FOR FERMILAB BEAM INSTRUMENTATION*

R. Santucci†, J. Diamond, N. Eddy, A. Semenov, D. Voy, Fermilab, Batavia, IL, USA

Abstract

The Fermilab Accelerator Division, Instrumentation Department is adopting an open-source framework to replace our embedded VME-based data acquisition systems. Utilizing an iterative methodology, we first moved to embedded Linux, removing the need for VxWorks. Next, we adopted Ethernet on each data acquisition module eliminating the need for the VME backplane in addition to communicating with a rack mount server. Development of DDCP (Distributed Data Communications Protocol), allowed for an abstraction between the firmware and software layers. Each data acquisition module was adapted to read out using 1 GbE and aggregated at a switch which up linked to a 10 GbE network. Current development includes scaling the system to aggregate more modules, to increase bandwidth to support multiple systems and to adopt MicroTCA as a crate technology. The architecture was utilized on various beamlines around the Fermilab complex including PIP2IT, FAST/IOTA and the Muon Delivery Ring. In summary, we were able to develop a data acquisition framework which incrementally replaces VxWorks & VME hardware as well as increases our total bandwidth to 10 Gbit/s using off the shelf Ethernet technology.

INTRODUCTION

The current framework of the Fermilab complex, regarding data acquisition, consists of three key areas: hardware platforms, embedded systems, and software. Of the large number of systems, many consist of a VME based platform with a variety of different VxWorks based crate controllers [1]. This architecture has proven extremely reliable; however, it has seen a technical debt build up. Aging crate hardware and stale software has led to rising maintenance costs as new requirements are needed to meet intensity goals and as new projects come online. To meet these new goals, each challenge was worked on iteratively, addressing each bottleneck in the full hardware/software life cycle. The primary hardware hurdle was removing the need of the VME back plane along with a VxWorks based crate controller. Moving to a Linux rack mount server and adopting a 10 GbE network, allowed us to increase bandwidth and decrease complexity in our systems. This was driven by the adoption of Ethernet on each digitizer. The Distributed Data Communication Protocol (DDCP) was developed to abstract an Ethernet field bus interface for the digitizers. This hardware abstraction layer, utilizing the POSIX socket API, allowed for easy adoption and network communication during development. Alongside aging hardware has been software stagnation. This stagnation, was largely driven by the complexity of individual systems with no common platforms. The move to Linux has allowed for the adoption of many new software technologies many of which utilize open-source communities. By transitioning to off the shelf Ethernet, we have been able to drastically increase our data throughput. Installations at the Fast/IOTA complex, the PIPII Test stand, as well as the current roll out to the Muon delivery ring have seen lower user complexity as a direct cause and effect from higher bandwidth. Future development will see the adoption of MicroTCA, standard socFPGA modules, and a common software suite to allow for easy adoption to more systems.

HARDWARE PLATFORMS

VME and VxWorks

Current Instrumentation front-ends utilize many different platforms, the primary being VME with a VxWorks RTOS. These systems have been in use ranging from 5 – 30 years. Although reliable, the cost to maintain these systems has become prohibitive. Crate controllers, (MVME500, MVME2400, MVME2401, MVME2434) have either seen drastic price increases or are no longer in production / available. Digitizer stockpiles are dwindling with no clear path to acquire more. Code bases have stagnated as it is prohibitive to update systems to modern compilers. The learning curve of VxWorks makes it difficult to train new developers on aging systems. In addition, data bandwidth requirements have shifted to need larger and larger amounts of data. Limited to a theoretical backplane speed of 40 MB/s (VMEbus IEEE-1014) adopting Ethernet was a less costly transition to increase bandwidth.

MicroTCA.4

Work is underway to transition from VME to the MTCA.4 platform for instrumentation [2]. In addition to modern crate standards, this platform provides Ethernet fabric on the backplane which is managed by the MTCA Carrier Hub (MCH) with a 10 Gbit uplink. The MTCA.4 standard also provides for a Rear Transition Module (RTM) which can be used to integrate analog signal conditioning which was typically done in an external crate for the VME systems.

Custom Digitizer

The hardware used to transition the DAQ from VME to Ethernet is a custom 8 channel 250 MS/s 16 bit digitizer board developed at Fermilab in 2016. A block diagram of the module is shown in Fig. 1. The board was originally targeted for VXS with Ethernet on the backplane. Unfortunately, this

* This manuscript has been authored by Fermi Research Alliance, LLC under Contract No. DE-AC02-07CH11359 with the U.S. Department of Energy, Office of Science, Office of High Energy Physics.
† rsantucc@fnal.gov

Content from this work may be used under the terms of the CC BY 4.0 licence (© 2022). Any distribution of this work must maintain attribution to the author(s), title of the work, publisher, and DOI

ISBN: 978-3-95450-241-7 ISSN: 2673-5350 doi:10.18429/JACoW-IBIC2022-WEP40

never came to fruition as the technology became obsolete and the VXS switches were no longer available. For flexibility, a front-panel Ethernet connection was also included on the design and has been the key to enabling the development of the Ethernet DAQ platform.

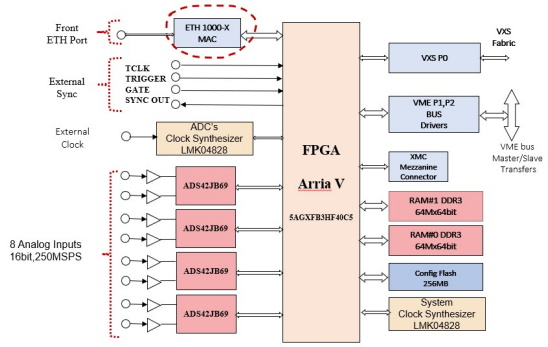


Figure 1: Block Diagram for the Fermilab 8 channel 250 MS/s VME/VXS digitizer. A key feature was the option to provide a Gigabit Ethernet interface from the FPGA to the front panel.

The first implementation of this digitizer was in the IOTA ring BPM system in 2018 [3]. The FAST/IOTA facility is a flexible complex focused on the development of new accelerator technologies. The initial BPM DAQ was a VMEbus system using an x86 slot controller running Linux instead of VxWorks. After initial commissioning, work began on modifying the system to use Ethernet instead of the VMEbus. In this configuration, the digitizers only use the VME crate for power and cooling. The DAQ upgrade occurred in two steps. The first step was to readout over Ethernet by the x86 slot controller. The second step was to replace the slot controller with a standard rack mount server which provided over an order of magnitude resource improvement at a fraction of the cost. The full server and switch configuration was used to readout two crates of digitizers for the PIP-II Injector Test BPM System [4].

The Distributed Data Communication Protocol (DDCP) interface was developed to facilitate the Ethernet interface between the FPGA and the front-end. To simplify the firmware designs, the UDP protocol was selected. The digitizer has an Altera Aria V with a NIOS softcore ARM processor implemented in HDL. The initial DDCP implementation was done in NIOS, but this proved to be a severe bottle neck for large data transfer with data rates <1 MB/s. A dedicated HDL interface was developed to handle high speed data readout. This implementation was able to operate at the full Gigabit Ethernet speed. By utilizing jumbo packets (9 kB) the system achieved real world data rates of 100 MB/s from a single card. This was a significant improvement from the measured rates of 8 MB/s for the same system through VMEbus.

SOFTWARE

Linux

From a software perspective, the biggest change has been adopting Linux on our embedded platforms. Moving away from VxWorks to the open-source community has seen easier adoption of new tools, a more gradual learning curve, and the ability to use plug and play off the shelf technologies. Real time applications can be developed using the RTAI framework or by dedicating specific cores to a FreeRTOS kernel.

DDCP

DDCP was developed as a Ethernet fieldbus protocol [5]. Relying on a request reply structure, data can be transmitted as scalars or structures. All nodes in a given system are given a unique ”slot” number. This has been expanded upon to be synonymous to the lower octet of the IP address. Data items, know as features, are accessed and manipulated with various defined operations with data being addressed as slot number, feature number, operation, index, and count. Devices can act as both a client or server on the network which allow for complex structures such as streams and interrupts. The typical architecture is one controller attached to many clients. DDCP can operate in both UDP and TCP mode, with UDP being advantageous when communicating with an FPGA where access to a TCP stack is limited.

Server

The software architecture can be broken into 2 categories, the server-based software, and the embedded node software. On the server, a Redis database is used to store live and aborted data as well as instrument configuration. Utilizing the different data types within Redis, we built a messaging system (pub/sub), a circular buffer(sets/gets), store configuration (Hash maps) as well as stream live data (Redis streams [6]) as shown in Fig. 2. Communication with embedded nodes is handled via DDCP or Redis TCP. When the systems are triggered, parallel reads can take advantage of the 10 Gbit network and process data asynchronously from the data acquisition once it hits the server. Each process on the server runs within its own container context. These include node monitors, data acquisition modules (bridging Redis and DDCP), multicast listeners, and buffer abort managers to name a few. Data access is handled via a memory API which allows for easy access from control systems (EPICS/ACNET), individual users, as well as system experts for diagnostics. This software suite has allowed for easy adoption of new systems as well as lowered overall

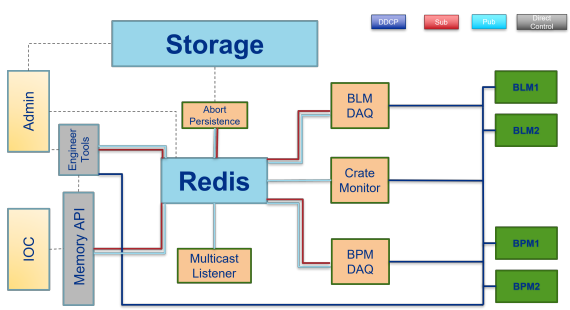


Figure 2: Block Diagram of the Redis system.

Content from this work may be used under the terms of the CC BY 4.0 licence (© 2022). Any distribution of this work must maintain attribution to the author(s), title of the work, publisher, and DOI

ISBN: 978-3-95450-241-7 ISSN: 2673-5350 doi:10.18429/JACoW-IBIC2022-WEP40

Content from this work may be used under the terms of the CC BY 4.0 licence (© 2022). Any distribution of this work must maintain attribution to the author(s), title of the work, publisher, and DOI

monolithic software complexity and has allowed for easier scaling. Future work includes direct streaming into a data lake storage layer as well as building out a dedicated EPICS to Redis driver. In addition, as a benefit to aggregating data in one place, new AI/ML models can be introduced to do server based learning before pushing data to the control system.

Each embedded node has the option of communicating via DDCP, a UDP protocol, or Redis, a TCP protocol. DDCP is utilized in embedded nodes which contain a standalone FPGA which has allowed easier communication between firmware and software. This requires a data acquisition module on the server cluster to bridge to Redis. If a socFPGA is used, the embedded node can communicate directly to Redis utilizing the Linux TCP stack.

NETWORK ARCHITECTURE

The data acquisition system has been designed to be highly modular. By moving away from the edge model, (data processing at each crate controller), we have been able to lower the complexity of our systems. The acquisition system utilizes either a single rack mount server or can be scaled to include multiple servers. These servers communicate to each system via a 10 Gbit network which is aggregated at house servers. Each house can aggregate any number of digitizers each of which communicates on a 1 Gbit network. Each digitizer acts as an independent client on the network. Each is individually addressable and does not inhibit any other. This model was an easy adoption as we already have Ethernet experience and is extremely cost friendly.

IOTA, PIP2IT, Muon Delivery Ring, Booster

The first iteration of the system was installed at the Fast/IOTA complex which aggregated 11 custom digitizers, reading out at a total of 2 MB of bursted data. A mirror of the IOTA system was also installed in the PIP2IT test stand. Work is currently being done to install the same system in the Muon Delivery Ring which will be scaled to 30 digitizers and a readout of 350 MB at 1 Hz (Fig. 3). Future work on the Booster BPM systems will see similar installations.

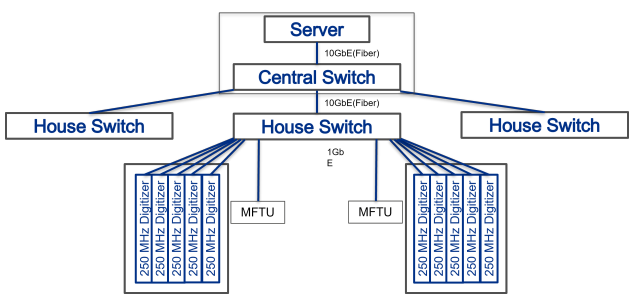


Figure 3: Muon Delivery Ring BPM System which utilizes an MFTU (Multi Function Timing Unit) for triggering and single house switches aggregating 2 VME crates with 5 digitizers at each house.

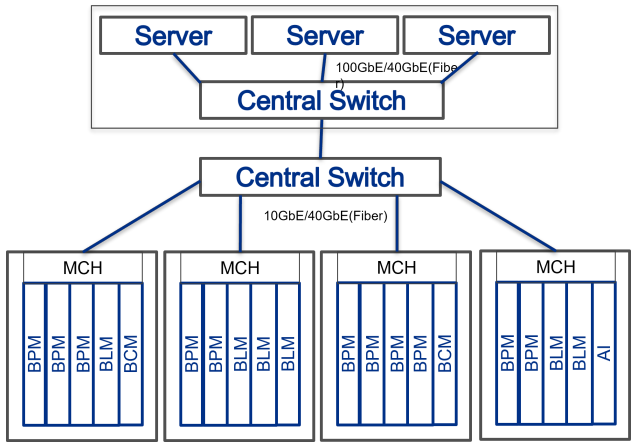


Figure 4: PIP2 Linac which will host multiple instrumentation devices within a crate, each addressable by IP address.

PIP2

Future work includes standardizing to a common hardware platform for the PIP2 Linac. The instrumentation department has decided to move to MicroTCA with one huge benefit being that it offers Ethernet on the backplane. This allows for the MCH crate handler to act as the 10 Gbit switch aiding in the network architecture (Fig. 4). Another benefit of the system is the ability to hot swap cards, dynamically allocate IP addresses based on slot numbers, as well as host multiple systems in one crate lowering cost. This work is in anticipation of the new PIP2 superconducting Linac in which all instrumentation devices will be front ended through the Ethernet architecture. By expanding to a 100 Gbit network, we anticipate reading out all 1500 instrumentation channels across 200 digitizers in parallel at 20 Hz. This equates to roughly 750 MB of data per second. By clustering multiple servers, load balancing and utilizing hot spares we can drastically improve up time of the system.

Future Work

With ambitious modernization goals, common platforms and cost saving techniques will be beneficial. By building out a highly modular Ethernet network, older systems can easily be upgraded to utilizing the system. By developing two IP protocols as drop in modules, new instruments and legacy systems can co exists side by side (Fig. 5).

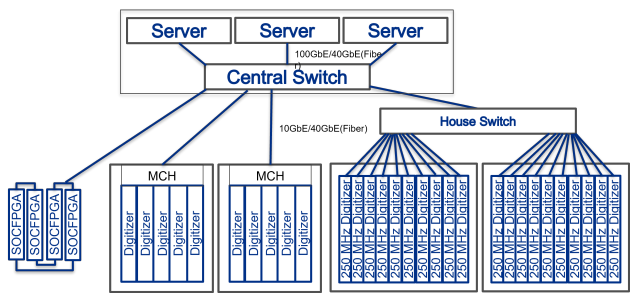


Figure 5: A hypothetical model showing the flexibility of Ethernet as a field bus talking with multiple systems.

ISBN: 978-3-95450-241-7 ISSN: 2673-5350 doi:10.18429/JACoW-IBIC2022-WEP40

CONCLUSION

The Fermilab Instrumentation department has been successful in its first pass to modernize its data acquisition framework. Systematically updating the complex to utilize off the shelf Ethernet technologies as well as building custom Ethernet modules has been a cost effective way to meet larger and faster data requirements. Initial installations at the IOTA ring and PIP2IT accelerator as well as current installations within the Muon delivery ring have allowed for the development of a software suite which can be used on future systems including the booster bpm system and PIP2 instrumentation system. By moving away from VME and VxWorks, costs and complexity are significantly lowered. This hardware and software standardization will modernize the acquisition system with hopes of easier maintainability and future upgrading.

ACKNOWLEDGEMENTS

This work was produced by Fermi Research Alliance, LLC under Contract No. DE-AC02-07CH11359 with the U.S. Department of Energy. Publisher acknowledges the U.S. Government license to provide public access under the DOE Public Access Plan

REFERENCES

[1] VMEBus, https://en.wikipedia.org/wiki/VMEbus

[2] MicroTCA, https://www.picmg.org/openstandards/microtca

[3] N. Eddy *et al.*, "Beam Instrumentation at the Fermilab IOTA Ring", in *Proc. IBIC'19*, Malmö, Sweden, Sep. 2019, pp. 22–28. doi:10.18429/JACoW-IBIC2019-MOBO02

[4] N. Eddy *et al.*, "BPM System for the PIP-II Injector Test Facility", in *Proc. IBIC'21*, Pohang, Korea, Sep. 2021, pp. 133–135. doi:10.18429/JACoW-IBIC2021-MOPP33

[5] AD Instrumentation DDCP (Direct Data Communication Protocol), AD Beams Document 9313-V2, https://beamdocs.fnal.gov/cgi-bin/sso/ShowDocument?docid=9313

[6] Redis, http://www.redis.io

Content from this work may be used under the terms of the CC BY 4.0 licence (© 2022). Any distribution of this work must maintain attribution to the author(s), title of the work, publisher, and DOI

ISBN: 978-3-95450-241-7 ISSN: 2673-5350 doi:10.18429/JACoW-IBIC2022-WEP41

ENeXAr: AN EPICS-BASED TOOL FOR USER-CONTROLLED DATA ARCHIVING

J. F. Esteban Müller*, European Spallation Source ERIC, Lund, Sweden

Abstract

ENeXAr is a data archival tool for EPICS-based systems. It is intended as a complement for traditional data archiving solutions, to cover use cases for which they are usually not designed: mainly for limited-duration high-data rates from a subset of signals. The service is particularly useful for activities related to machine commissioning, beam studies, and system integration testing. Data acquisition is controlled via PV Access RPC commands and the data is stored in standard HDF5-based NeXus files. The RPC commands allow users to define the acquisition parameters, the data structure, and the metadata. The usage of EPICS RPC commands means that the users are not required to install additional software. Also, acquisitions can be automatized directly from EPICS IOCs.

INTRODUCTION

Most accelerator facilities rely on data archiving services that continuously acquire and store data from all the signals that need to be monitored.

At ESS, our control system is based on EPICS [1] and we use the Archiver Appliance [2] for archiving data related to the machine operation.

There are use cases, however, when traditional data archivers are not optimal. For example, during system testing, machine commissioning activities, beam studies, or when troubleshooting issues with a particular device, users may require to acquire different signals than those regularly stored in the archiver. Often, these sets of signals contain long arrays (waveform records), which would be very costly to continuously archive for all systems, in terms of required network bandwidth and storage. However, acquiring only a subset of them for a limited period of time poses no issues.

Traditionally this is done using scripts, in which case the user needs to take care of acquiring the data using the EPICS libraries and storing the data. This results in different systems using a variety of file formats that make data analysis more complex.

The purpose of ENeXAr is to facilitate data acquisition and storage, by defining a set of commands that allow users to run an automatic data collection that saves the data in central storage, together with user-defined metadata. The only requirement for users is to have an EPICS base installation.

SOFTWARE ARCHITECTURE

ENeXAr is implemented in Python and it uses the pyepics [3] and p4p [4] packages for EPICS Channel Access and PV Access support, respectively.

Figure 1 shows a schematic view of its architecture. Clients send commands to the ENeXAr service via Remote Procedure Calls (RPC), using the PV Access protocol. There are also status PVs to monitor the service. ENeXAr processes the commands, some of which will trigger a data acquisition from EPICS IOCs. The connection to the IOCs can use either the PV Access (PVA) or Channel Access (CA) protocols.

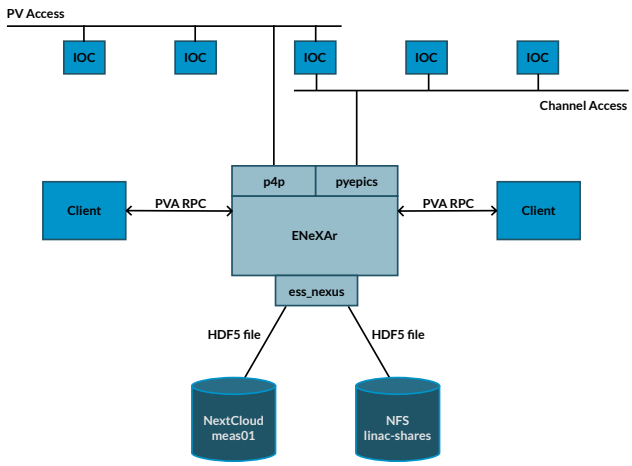


Figure 1: The architecture of the ENeXAr service. On the top, the IOCs produce data that is acquired by ENeXAr through EPICS using the pyepics and p4p epics modules. Clients send commands to the service using PV Access RPC calls. On the bottom, it is shown examples of storage backends that can be used.

The service runs on several processes using the Python multiprocessing library. The main limitation is that write operations to a single HDF5 file should always originate from the same process, since the h5py libraries do not allow for parallel write operations. As we will see later, that can be a performance bottleneck, although not very serious.

The acquisitions are then saved into the file storage backend. The data is formatted using the NeXus [5] convention and saved as HDF5 [6] files. Files are created using the ess-nexus Python package [7]. Files are not indexed and the directory structure inside the storage backend is completely managed by the users.

Multiple instances of ENeXAr can be deployed in the same network, provided that they use a different prefix for the PV names used for commands and status. That allows, for example, for each instance to use a different storage backend, or as a means for balance the load in the service.

USAGE

As stated above, the user controls the data acquisition via EPICS RPC calls, which can be generated by any EPICS7-

* JuanF.EstebanMuller@ess.eu

Content from this work may be used under the terms of the CC BY 4.0 licence (© 2022). Any distribution of this work must maintain attribution to the author(s), title of the work, publisher, and DOI

ISBN: 978-3-95450-241-7 ISSN: 2673-5350 doi:10.18429/JACoW-IBIC2022-WEP41

compatible client. One option is using the `pvcall` command from the command-line. The procedure names are formed by appending the command to the prefix that identifies the ENeXAr service. There is also a Python module available, called enexar-cli [8], which simplifies the usage of RPC calls from Python and also provides a JupyterLab graphical interface. Finally, calls can also be generated by other IOCs.

Below one can find the list of commands available, grouped by function, and with a short explanation.

Acquisition-Related Commands

To start and stop acquisitions, the following procedures are available:

- `ACQUIRE`: start the acquisition of a PV into a file. It could be a continuous measurement that is manually stopped later on, or only for a user-defined number of PV updates. The arguments to this call are the PV name, the file path, acquisition type, and optionally a set of metadata. It also supports EPICS filters for data reduction on the IOC side.
- `ACQUIRE_S`: synchronous version of the `ACQUIRE` command that will return only after the measurement is done. Only useful for short acquisitions.
- `STOP`: stop the acquisition of a given PV into a file. Other acquisitions to the same file will continue.

File-Related Commands

These are commands that determine the way ENeXAr deals with files. They don't correspond to the way files are managed by the operating system.

- `OPEN`: this command is required if the user wants to append data to an already existing (and closed) file. If the file does not exists, it is created, although in that case this command is not needed and the file can be created using the `ACQUIRE` command.
- `CLOSE`: closes a file and does not allow further acquisitions to be appended into the file, unless the `OPEN` command is used. If there is any acquisition running, they are stopped.
- `LS`: return the output of running the `ls` command on the path passed as a parameter.

Status-Related Commands

The following operations are available for users to check the status of the acquisitions and files managed by an ENeXAr instance:

- `STATUS`: prints all the acquisitions that are taking place.
- `IS_OPEN`: check if a file is open for appending data.
- `IS_ACQUIRING`: checks if a PV is being acquired into a given file.

INTEGRATION IN JUPYTER

At ESS, we use JupyterHub [9] to develop and run Python scripts that interface with the accelerator control system for commissioning and operations-related activities. This infrastructure also allows users to perform data analysis on the cloud.

In our configuration, the same storage backends that are used by ENeXAr to save data, are also mounted on JupyterHub to enable easy access to the users of the data.

The enexar-cli Python module delivers also a graphical user interface, which is built based on Jupyter Widgets [10]. The UI allows users to graphically start and stop acquisitions, as well as to check the service's status. Figure 2 shows a screenshot of the interface, which is based on another existing UI called "PV Saver" that was used to take data acquisitions directly into raw HDF5 files. This UI can be run using Voilà [11] to hide all Python code and make it more user-friendly.

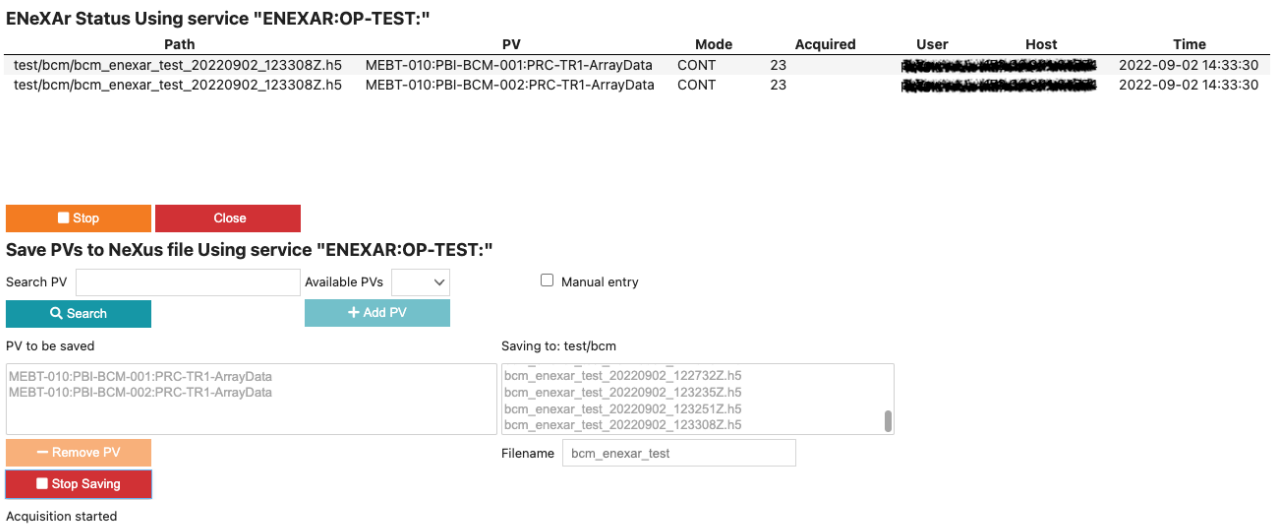


Figure 2: Screenshot of the Jupyter interface to ENeXAr, using Voilà [11] to render the UI. On the top, it shows the acquisitions that are currently taking place and on the bottom, the user can start new measurements.

Content from this work may be used under the terms of the CC BY 4.0 licence (© 2022). Any distribution of this work must maintain attribution to the author(s), title of the work, publisher, and DOI

ISBN: 978-3-95450-241-7 ISSN: 2673-5350 doi:10.18429/JACoW-IBIC2022-WEP41

Content from this work may be used under the terms of the CC BY 4.0 licence (© 2022). Any distribution of this work must maintain attribution to the author(s), title of the work, publisher, and DOI

WETEST INTEGRATION

One of the use cases of ENeXAr is to take acquisitions from IOCs while running system integration tests. These acquisitions can be used for calibration purposes or as part of the testing process.

At ESS, the Beam Diagnostics group relies on WeTest [12] for test automation. ENeXAr has been integrated in a forked version of WeTest to make possible this use case. An example of how to use it is shown in Fig. 3.

```
tests:
  - name: "Test 1"
    setter: "PV:set"
    commands:
    - name: "0"
      set_value: 0
      get_value: 0
    logger:
      - pv: "PV:TO:BE:ARCHIVED"
        server: "ENEXAR:PREFIX:"
        path: "measurements/test"
        acquisitions: 1
        metadata:
          file_user:
            name: "juan"
            affiliation: "ESS"
          file_entry:
            title: "Test"
            description: "Testing logger"
          instruments:
            INSTRUMENT_1:
              nxtype: "NXbeam_instrumentation"
              name: "Instrument name"
```

Figure 3: Snippet of a WeTest example test case using ENeXAr to perform an acquisiton.

BENCHMARK

The performance of ENeXAr was studied in a series of tests. Two virtual machines (VMs) were used for the tests, one to run a virtual soft-IOC, and another one running ENeXAR with the same storage backend as the one used in production. The status of the VMs and the virtualization cluster were monitored during the tests. In addition, we made sure that the two VMs were running on different hosts in the virtualization cluster, so that the data would be sent through the network.

The soft-IOC can be configured to generate a certain number of PVs, each of them with a given array length. During the tests, the number of PVs is varied, and the array length is adjusted to match the desired data rate. For our tests, the IOC was running at an update rate of 14 Hz, which is the pulse repetition rate of the ESS linac.

The first set of tests consisted of the acquisition of 1, 10, 20, and 50 PVs, storing each PV in a separate file, and sweeping the data rate from 100 Mbps to approximately 7.5 Gbps. Results are presented in Fig. 4, and they show that ENeXAr is able to cope with data rates of up to 2.5 Gbps, except for the case when only 1 long array is archived.

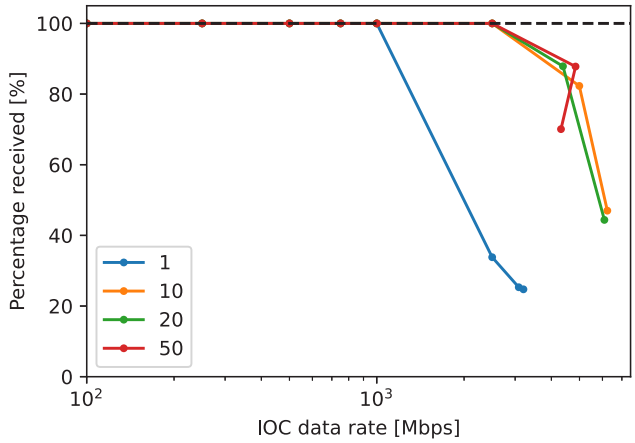


Figure 4: Storage success rate for different data rates produced by a single IOC and stored in one file per PV. The lines correspond to the number of PVs generated by the IOC, for which the array length is adjusted to match the desired data rate.

For the second test case, the same set of tests were run with the only difference that ENeXAr was configured to store all PVs in the same file. Figure 5 shows the results, which are slightly worse than in the previous case. For this configuration, the limit seems to be around 1 Gbps.

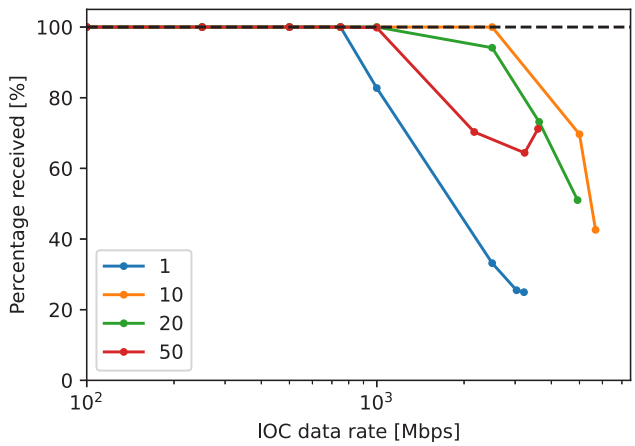


Figure 5: Storage success rate for different data rates produced by a single IOC and storing all PVs in the same file. The lines correspond to the number of PVs generated by the IOC, for which the array length is adjusted to match the desired data rate.

In the first case, each file is written to the storage backend from a different Python process. The results are compatible with the bottleneck being the storage backend. In the second case, all the data is written to a file from the same process, and the performance could be limited by the writing speed of the HDF5 libraries.

Finally, the same test cases were run using the PV Saver script, which is the tool that has been widely used at ESS for dedicated data acquisition. The results are presented in Fig. 6 and show a lower performance. Only 2 test cases achieve a 100% storage success rate, for the lowest data rate of 100 Mbps. This can be due to a combination of

ISBN: 978-3-95450-241-7 ISSN: 2673-5350 doi:10.18429/JACoW-IBIC2022-WEP41

two factors: PV Saver runs on a single process and it uses Jupyterhub's storage backend, which seems to be slower than the one used by ENeXAr.

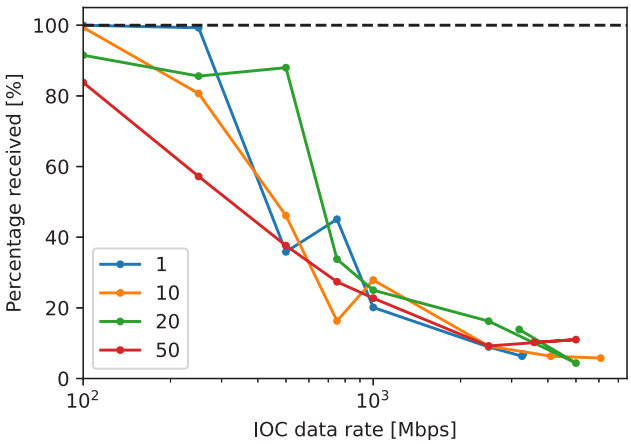


Figure 6: Storage success rate for different data rates produced by a single IOC, using the PV Saver script on JupyterHub. The lines correspond to the number of PVs generated by the IOC, for which the array length is adjusted to match the desired data rate.

SUMMARY

In this paper, the ENeXAr service was presented, which is an EPICS-based tool intended to simplify on-demand data acquisition from IOCs. Its architecture and usage were also described. Finally, results from performance tests were presented, showing a significantly better performance than the previously available alternatives.

The code publicly is available on `https://gitlab.esss.lu.se/ics-software/enexar` under the GPLv2 license.

ACKNOWLEDGEMENTS

Thanks to Emanuele Laface for the development of the "PV Saver" UI, which somehow triggered the development of ENeXAr and was used as a base for its Jupyter interface. Thanks also to Stephane Armanet and Alessi Curri for their support in setting up the test environment.

REFERENCES

[1] EPICS website, `https://epics-controls.org/`

[2] Archiver appliance website, `https://slacmshankar.github.io/epicsarchiver_docs`

[3] M. Newville, `https://pyepics.github.io/pyepics/`

[4] M. Davidsaver, `https://mdavidsaver.github.io/p4p/`

[5] NeXus data format website, `http://www.nexusformat.org/`

[6] HDF data format website, `https://www.hdfgroup.org/solutions/hdf5/`

[7] N. Milas and C. Derrez, *ESS NeXus repository*, `https://gitlab.esss.lu.se/ess-bp/ess_nexus`

[8] J. F. Esteban Müller, *ENeXAr-cli repository*, `https://gitlab.esss.lu.se/ics-software/enexar-cli`

[9] JupyterHub website, `https://jupyter.org/hubs`

[10] Jupyter Widgets website, `https://ipywidgets.readthedocs.io/`

[11] Voilà website, `https://voila.readthedocs.io/`

[12] WeTest repository, `https://github.com/epics-extensions/WeTest`

Content from this work may be used under the terms of the CC BY 4.0 licence (© 2022). Any distribution of this work must maintain attribution to the author(s), title of the work, publisher, and DOI

ISBN: 978-3-95450-241-7 ISSN: 2673-5350 doi:10.18429/JACoW-IBIC2022-WEP42

APPLICATION OF MACHINE LEARNING TOWARDS PARTICLE COUNTING AND IDENTIFICATION

S. Engel[1,*] R. Singh[2,†], P. Boutachkov[2]
[1] University of Essex, Colchester, England
[2] GSI Helmholtz Centre for Heavy Ion Research, Darmstadt, Germany

Abstract

An exploration into the application of three machine learning (ML) approaches to identify and separate events in the detectors used for particle counting at the GSI Helmholtz Centre for Heavy Ion Research was performed. A shape-based template matching algorithm (STMF), Peak Property-based Counting Algorithm (PPCA) and convolutional neural network (CNN) were tested for counting the number of particles accurately without domain-specific knowledge required to run the currently used algorithm. The three domain-agnostic ML algorithms are based on data from scintillation counters commonly used in beam instrumentation and represent proof-of-principle for an automated particle counting system. The algorithms were trained on a labelled set of over 150 000 experimental particle data. The results of the three classification approaches were compared to find a solution that best mitigates the effects of particle pile-ups. The two best-achieving algorithms were PPCA and CNN, achieving an accuracy of over 99%.

INTRODUCTION

As charged particle beams pass through a scintillation counter, it induces the excitations in the scintillation material which relaxed with emission of photons. These photons are amplified using photo multiplier tubes (PMT) which outputs a voltage pulse measured over time. The shortest pulse lengths are typically of the order of few ns given by the scintillation process itself. The transportation of these pulses from the radiation environment to the detection electronics is about 50-100 m, which further increases the pulse length due to cable dispersion. As the rate of particles arriving at the scintillator increases so does the probability for signal pile-ups, a overlap of sequential pulses. Due to complex slow extraction process from the particle accelerators and sub Poissonion particle distribution [1], non-negligible percentage of signal pile-ups occur at most particle arrival rates. These complex, hard-to-count, peak shapes change in a non-linear fashion. The interference causes difficulties in using conventional computing methods to accurately count particles, although strategies to mitigate them using hardware [2] and software solutions [3, 4] have been explored. Notably several ML approaches have been developed with some success by relying on domain-specific knowledge and feature engineering specific to the detector [3–5].

Other more general ML approaches rely on 2D data and/or data with multiple features [6], demonstrating domain-specific knowledge is not necessary to provide satisfactory results. Specifically, CNN's prove to be the ideal conventional ML solution because of their robustness and the ability to create a domain agnostic, end-to-end discriminating model which eliminates unnecessary domain-specific preprocessing [7].

* samuel-engel@outlook.com
† r.singh@gsi.de

DATA COLLECTION AND TRANSFORMATION

The major portion of the training and testing data consisted of high-resolution experimental data of 1.5×10^5 peaks collected at the SIS18 synchrotron at GSI with a sampling rate of 2.5 GSa/s. The data was labelled by fine-tuning the present particle counting algorithm. Therefore, only labeled data with a low extraction rate of up to 3×10^5 particles per second could be used.

Low-resolution data was generated by downsampling the high-resolution data collected at (2.5×10^9) samples per second as seen in Fig. 1. Data was downsampled by a factor of s to test the accuracy at various resolutions.

The high-resolution data was bootstrapped by combining an offset copy of a time series with the original to create more complex shapes representative of data with a higher rate of particles.

The validation data of 416 peaks was experimentally collected by firing a laser at the scintillation counter at precisely set intervals to selectively generate various pile-up shapes.

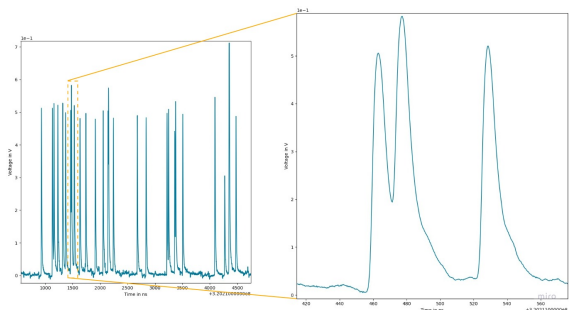


Figure 1: Graph showing a section of a time series with a close-up of a peak

TIME SERIES CLASSIFICATION USING SUPERVISED MACHINE LEARNING

1. Shape-based Template Matching Framework (STMF)
2. Peak Property-based Counting Algorithm (PPCA)
3. Convolutional neural network (CNN)

Content from this work may be used under the terms of the CC BY 4.0 licence (© 2022). Any distribution of this work must maintain attribution to the author(s), title of the work, publisher, and DOI

ISBN: 978-3-95450-241-7 ISSN: 2673-5350 doi:10.18429/JACoW-IBIC2022-WEP42

Shape-based Template Matching Framework

The shape-based template matching framework is an implementation based on a study exploring efficient matching of templates with sections of time series [8]. The training data time series is segmented into peak groups of $1, 2, 3 \ldots$ particles and a template is constructed for each one. A time series segment is classified by comparing it to every template to determine the best fit. The approach mimics the way humans approach the problem.

The templates were constructed using an averaging scheme which determines how each labelled peak group time series segment is combined. The cubic-spline dynamic time warping (CDTW) averaging function was iteratively applied to the two most similar time series. The averaged time series replaces the two original ones. Eventually, the result is a single time series representative of the peak group which became the template for that peak group.

An implementation of the dynamic time warping (DTW) algorithm was used to determine the similarity between a given peak group time series and every generated template. Dynamic time warping is a method of comparing two time series of unequal lengths and finding their similarity as demonstrated in Fig. 2. It warps the time series to match points regardless of shifts or distortions in time, creating a warping path [9]. A DTW warping path is a map matching each corresponding point in the two time series where the matching can be one-to-one, one-to-many or many-to-one due to the time series having unequal lengths [10].

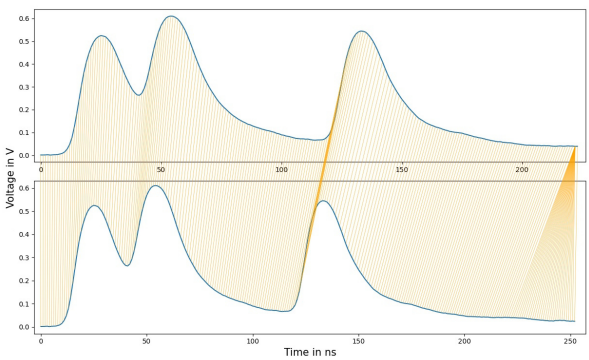


Figure 2: Graph showing a DTW mapping between two 3 peak time series segments.

Peak Property-based Counting Algorithm

The peak property based counting algorithm (PPCA) works on the principle of peaks having certain mathematical properties which define them, namely the peak width, height, prominence and the distance between peaks. The algorithm uses labelled data to find the optimal attribute ranges such that all peaks are counted correctly. Establishing the peak properties of the labelled peaks allows the algorithm to learn the mathematical property ranges which contain all the peaks being counted.

The algorithm works with segments of arbitrary length given every peak in the segment is present in its entirety in order to calculate all the properties. Prominence P is calculated as the vertical distance to the peak's lowest contour line PC_l. The peak's two contour lines are determined by the segment between the nearest peak on either side. The minimum point of each of the two segments are the peak bases. The highest peak base defines the lowest contour line PC_l. The height of a peak is the y value of the data point in the peak's centre. The peak width is determined at an evaluation height h_{eval} which is calculated first using $h_{\text{eval}} = h_{\text{peak}} - P \cdot 0.5$.

Half of the prominence P of a peak is subtracted from the height of the peak h_{peak} to find the height at which the width is measured. Half of the prominence is used to achieve the most accurate results across a variety of peak shapes. The width is calculated by getting an intersecting point with the data at the evaluation height on both sides. The distance between peaks is calculated as the horizontal distance between neighbouring peak centres. Lastly, a threshold is set to be just above the baseline in order to avoid any false positives arising from the noise in the baseline.

The training of the model weights relied on optimizing the parameters of the peak finding function. The labels of the training data contain the time at the centre of every peak. The first stage of the training involves extracting the properties of all labelled peaks which are visualized in Fig. 3.

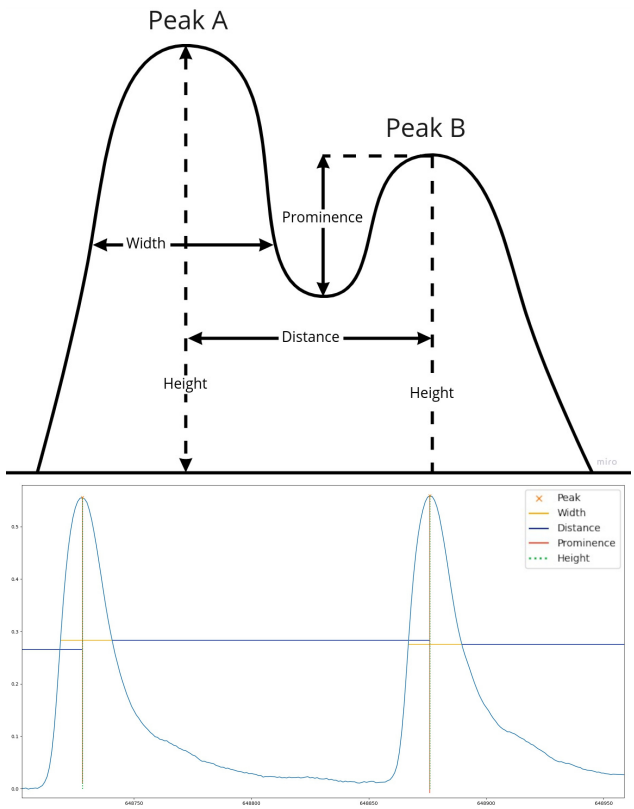


Figure 3: A visualization of the mathematical peak properties captured.

All the relevant peak data allows for several statistical methods to be applied to establish trends and find the most optimal combination of parameters for finding the peak's

Content from this work may be used under the terms of the CC BY 4.0 licence (© 2022). Any distribution of this work must maintain attribution to the author(s), title of the work, publisher, and DOI

ISBN: 978-3-95450-241-7 ISSN: 2673-5350 doi:10.18429/JACoW-IBIC2022-WEP42

Content from this work may be used under the terms of the CC BY 4.0 licence (© 2022). Any distribution of this work must maintain attribution to the author(s), title of the work, publisher, and DOI

lower and upper bound respectively. The number of standard deviations the minimum and maximum are from the mean is used as a measure to ensure an outlier is not causing distortions in order to get a clean set of weights representing peak property bounds. Finally the peak finding function is run on the test data set with the weights as the parameters. Comparing the results with the labels gives the loss function consisting of the sum of false positives and negatives. This step is repeated iteratively while progressively changing the weights, one at a time. The weights are optimized in an order of importance determined by the peak finding function. The optimization order starts with the peak height followed by the threshold, distance, prominence and lastly the width.

The algorithm uses the weights learned in the training step to identify distinct peaks representing particles. Each weight represents the lower or upper bound of one of the parameters. The resulting combination of lower and upper bounds defines ranges into which all particle peaks fall. The order in which the properties are evaluated is important in terms of performance. The goal is to eliminate the greatest number of particle peaks which fall outside of the bounds using the least computationally demanding property evaluation method. That way, the number of potential particle peaks is reduced and only a fraction has to be evaluated using the more computationally demanding property evaluation methods.

Convolutional Neural Network

The one-dimensional convolutional neural network (CNN) uses discriminative supervised learning to count particles. It learns features from raw time series data rather than through engineered features such as the peak shape or properties used for the previous two approaches. The input data is segmented into even-sized windows before the model is trained by learning the intrinsic features.

Every segment is labelled with the number of peak centres it contains meaning at least more than half of each peak's data points needs to be inside the window for it to be counted. Windows with only the baseline tend to vary very little from one another and their over-representation creates a redundancy which confuses the feature learning aspect of the CNN. A pruning technique had to be adapted to reduce redundant baseline data and decrease the time complexity of the algorithm. The technique settled on is based on separating windows labelled with 0 peaks into two categories. Baseline-only windows and windows with a fraction of a peak with less than 50% of the peak's data points. Just the baseline-only windows contain redundant information whereas the fractions of peaks are all different and contain key information. The baseline-only windows are reduced by a pruning factor which determines what proportion of baseline-only windows is kept.

The CNN model is developed using the Keras deep learning library which requires a 3-dimensional input for all its models. The design of the sequential model can be seen in Fig. 4. The input layer is fed data in the form of samples, time steps and features form the 3-dimensional input

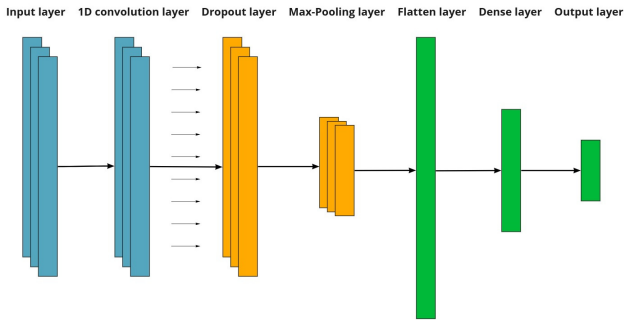


Figure 4: Diagram showing layers of the CNN model

required. The samples are the windows from the data segmentation step. Each sample or window has S time steps which is one of the hyper-parameters of the model. The last dimension is the features although in this case, the only feature available was the voltage. The lack of features was one of the main challenges with managing the deep learning approach and caused difficulties in increasing the model's accuracy without overfitting the data. The model starts with a pair of two 1D convolutional layers, the first one being the input layer. The dropout layer is used for regularization by ignoring some of the features of the two convolutional layers to limit overfitting.

The max-pooling layer reduces the size of the learned features by $\frac{1}{4}$ by summarizing the features to the most essential ones. All of the features are then flattened into a large 1d vector before it is passed to the fully-connected layer towards the end of the sequential Keras model. The fully connected layer is a dense layer which serves as a buffer to consolidate the learned features before prediction takes place. The last layer is the output layer which is also a dense layer. However, its job is to simply make a prediction based on the learned features passed down to it from the previous layers. A window can be fed directly into the model in a stream to enable real-time data classification. The model outputs a list of probabilities of the window containing 1 peak, 2 peaks etc. based on the learned features.

RESULTS & PERFORMANCE

The exploratory project is a proof-of-work showing machine learning can be used to successfully count particles. Such accuracy was achieved using a domain-agnostic approach which only takes into account the time series data and no specific information about the experiment or the instruments used. The comparison in terms of accuracy can be found in Table 1. However, assessing the accuracy of the 3 solutions solely based on the performance from the available data shows only one side of the picture. Considering the strengths and weaknesses of the three approaches allows predicting how the accuracy would change under different conditions. The PPCA not only has the highest accuracy out of the three algorithms but it is also strong in simplicity and observability. All of these qualities are highly desirable when it comes to conducting scientific analysis. However, the lack of complexity comes with a downside

ISBN: 978-3-95450-241-7 ISSN: 2673-5350 doi:10.18429/JACoW-IBIC2022-WEP42

of a lack of robustness. It is likely the PPCA is the least adaptable solution to varying conditions or new trends in the data. Specifically, a higher rate of particles producing more complex shapes could result in peaks that physically cannot be described using parameter limits. On the other hand, the CNN is specifically designed to learn intrinsic features in the data so as to allow it to adapt to different trends in the data. The CNN design is much more adaptable and has the fewest limits out of the 3 approaches in terms of how complex the peak shapes can be. The PPCA seems to be the most suitable approach for the data used in this contribution. However given that the difference in CNN performance compared to the PPCA is minimal, and with higher adaptability of CNN, we believe it could be a promising approach with wider variety of data. Lastly, the STMF suffers from the same weaknesses as the PPCA in terms of being limited by the complexity of the peak shapes. The more peaks there are in a segment, the less representative a template becomes meaning the number of segments without a match increases as well. Adapting the STMF to train multiple templates per peak label could address this issue but the increased complexity would not be worth the minimal improvement.

Table 1: Accuracy and Space Performance of the 3 Algorithms

	Accuracy (%)	Storage Requirements
PPCA	99.97	<1 kB
STMF	96.71	<20 kB
CNN	99.84	<1 MB

Table 2: Time Performance for Classification

	Average time in seconds	
	Classify 1 peak	Classify 1000 peaks
PPCA	0.00023	0.23
STMF	0.024	24.5
CNN	0.063	62.7

FUTURE WORK

The limitations of the labelled data restricted the algorithms to only be trained and tested at a low extraction rate up to 3×10^5 particles per second. Therefore, further development should focus on improving the chosen algorithm to enable classification at higher extraction rates without major losses in accuracy. The use of convolutional neural network has proven to be the best performing algorithm considering the combination of accuracy, adaptability and implementability. Therefore, a more in depth research into the application of a CNN for particle counting should be conducted. Exploring the ways in which the algorithm can be implemented as a part of the detector using an FPGA or a similar approach would also be a very productive area of future research.

ACKNOWLEDGEMENT

This project has received funding from the European Union's Horizon 2020 Research and Innovation programme under GA No 101004730.

REFERENCES

[1] R. Singh, P. Forck, and S. Sorge, "Reducing fluctuations in slow-extraction beam spill using transit-time-dependent tune modulation", *Phys. Rev. Applied*, vol. 13, p. 044 076, 4 2020. doi:10.1103/PhysRevApplied.13.044076

[2] W. H. Wong and H. Li, "A scintillation detector signal processing technique with active pileup prevention for extending scintillation count rates", *IEEE Transactions on Nuclear Science*, vol. 45, no. 3, pp. 838–842, 1998. doi:10.1109/23.682647

[3] P. J. Statham, "Pile-Up Correction for Improved Accuracy and Speed of X-Ray Analysis", *Microchimica Acta*, vol. 155, no. 1, pp. 289–294, 2006. doi:10.1007/s00604-006-0558-1

[4] D. J. R. Sevilla, "A Simple Pile-up Model for Time Series Analysis", vol. 843, no. 1, p. 44, 2017. doi:10.3847/1538-4357/aa72e8

[5] D. Bertolini, P. Harris, M. Low, and N. Tran, "Pileup Per Particle Identification", *Journal of High Energy Physics*, vol. 2014, no. 10, p. 59, 2014. doi:10.1007/JHEP10(2014)059

[6] P. Baldi, K. Bauer, C. Eng, P. Sadowski, and D. Whiteson, "Jet Substructure Classification in High-Energy Physics with Deep Neural Networks", *Physical Review D*, vol. 93, no. 9, p. 094 034, 27, 2016. doi:10.1103/PhysRevD.93.094034

[7] H. I. Fawaz, G. Forestier, J. Weber, L. Idoumghar, and P.-A. Muller, "Deep learning for time series classification: A review", 2018. doi:10.1007/s10618-019-00619-1

[8] V. Niennattrakul and C. A. Ratanamahatana, "Inaccuracies of Shape Averaging Method Using Dynamic Time Warping for Time Series Data", pp. 513–520, Proceedings of the 7th International Conference on Computational Science (ICCS'07).

[9] P. Senin, "Dynamic Time Warping Algorithm Review", pp. 1–23, 2008.

[10] C.-J. Hsu, K.-S. Huang, C.-B. Yang, and Y.-P. Guo, "Flexible Dynamic Time Warping for Time Series Classification", *Procedia Computer Science*, vol. 51, pp. 2838–2842, 1, 2015. doi:10.1016/j.procs.2015.05.444

Content from this work may be used under the terms of the CC BY 4.0 licence (© 2022). Any distribution of this work must maintain attribution to the author(s), title of the work, publisher, and DOI

ISBN: 978-3-95450-241-7 ISSN: 2673-5350 doi:10.18429/JACoW-IBIC2022-WEP43

CONTROL SYSTEMS OF DC ACCELERATORS AT KAHVELab

T. B. Ilhan*, A. Caglar, D. Halis, Yıldız Technical University, Istanbul, Turkey
A. Adiguzel, S. Oz, İstanbul University, İstanbul, Turkey
H. Cetinkaya, Dumlupınar University, Kutahya, Turkey
E. Elibollar, M. F. Er, A. Inanc, V. E. Ozcan, Boğaziçi University, İstanbul, Turkey
U. Kaya, İstinye University, İstanbul, Turkey
A. Ozbey, İstanbul University-Cerrahpaşa, Istanbul, Turkey
G. Turemen, TENMAK-NUKEN, Ankara, Turkey
N. G. Unel, University of California (UCI), California, USA

Abstract

KAHVE Laboratory has two functional particle sources: thermal electrons and ionized hydrogen. Each of these are followed by DC acceleration sections, for obtaining an electron beam to accelerate electrons MeV energy level and for providing protons to the radio frequency quadrupole accelerator which are being built. So far both systems have keV energy levels. Both systems employ LabVIEW based GUIs to interact with the user and to control and monitor the DC power supplies. The vacuum gauges, turbomolecular pumps, stepper motors and high voltage power supplies are all controlled with PLCs. The equipment under high voltage, are monitored and controlled via Arduino based wifi and bluetooth wireless communication protocols. The proton beamline has additional devices for beam diagnostics which are being commissioned like pepper pot plate, scintillator screen and faraday cup. Both systems are being standardize before MeV energy level for generalize to national labs which are working on detectors and accelerators. We believe such a setup could be a low budget control and readout example for modern small experiments and educational projects.

INTRODUCTION

The proton accelerator at KAHVELab utilizes a 20 kV high voltage power supply units (PSU), two low voltage PSUs, one four-channel low voltage PSU, two turbomolecular pumps, two vacuum gauges, three pneumatic cylinders with PLC and PC control combined all in one LabVIEW GUI as shown in Fig. 1. The system extracts 20 keV proton beam from microwave discharge ion source. Upgrade process of the ion source with permanent magnets and the addition of a 800 MHz RFQ is on going. After the RFQ, the beam energy will be 2 MeV.

The electron accelerator at KAHVELab uses 60 kV high voltage PSU, two four-channel low voltage PSUs, one low voltage PSU, two turbomolecular pumps, two vacuum gauges, two stepper motors, PLC and PC control combined, all in one LabVIEW GUI as shown in Fig. 2. It produces a 50keV electron beam using thoriated tungsten thermionic cathode. This project was supported by TUBITAK Project No: 117F462. Different cathode types, welding and hardening processes are successfully tested.

* taha.batuhan.ilhan@cern.ch, kahvelab@gmail.com

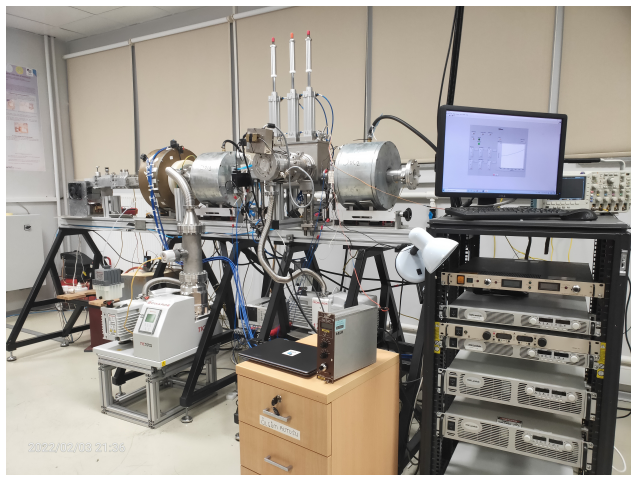


Figure 1: The Proton Accelerator at KAHVELab.

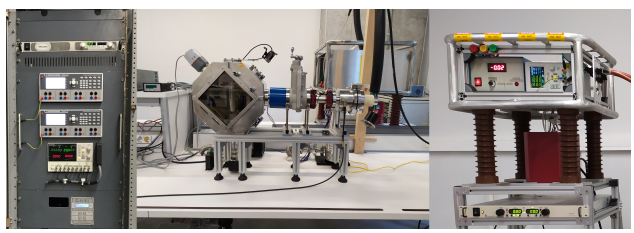


Figure 2: The Electron Accelerator at KAHVELab.

CONTROL SYSTEM DEVELOPMENT OF PROTON ACCELERATOR

The system [1] employs PLC and PC for controlling devices and automation at the moment. PC used for user interface and serial communication with devices which can not be controlled directly with PLC yet. Devices like vacuum gauges and pneumatic cylinders need digital and analogue signals for control. Also, PLC's have the ability to serial control of devices like turbomolecular pumps and power supplies. While developing a control system for these accelerators we found out LabVIEW is very easy for testing an instrument but not so much to build a stable control system. We therefore implemented a LabVIEW GUI controlled PLC system which is more stable than pure LabVIEW option. PLC's also has the benefit of providing digital and analogue signals. Unfortunately devices like PSUs or vacuum pumps do not have drivers for PLC's and we had to write one for each such device.

Content from this work may be used under the terms of the CC BY 4.0 licence (© 2022). Any distribution of this work must maintain attribution to the author(s), title of the work, publisher, and DOI

ISBN: 978-3-95450-241-7 ISSN: 2673-5350 doi:10.18429/JACoW-IBIC2022-WEP43

In Fig. 3 the automation panel of the proton beam line is shown. There are different types of PLC modules (Digital IO, Analog IO, Communication Modules etc.). In future we are planing to build different automation panels for each section of the beamline and develop main control system(like SCADA) to observe all beam parameters and accelerator status.



Figure 3: Automation Panel of the Proton Beamline

In Fig. 4, the proton beamline control GUI is shown. Recent system changes (Changing Ion Source from electromagnets to permanent magnets) forced us to make changes on the GUI. It is currently under development.

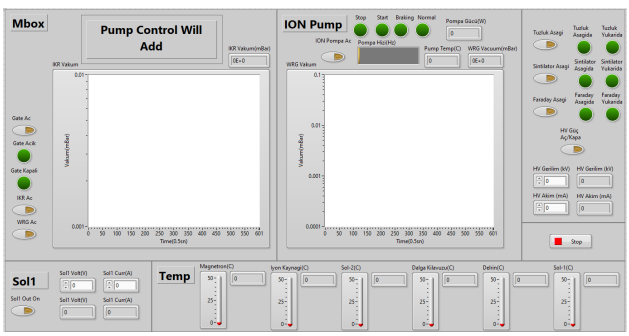


Figure 4: LabVIEW GUI of Proton Accelerator.

CONTROL SYSTEM DEVELOPMENT OF ELECTRON ACCELERATOR

The control system is similar to the Proton beamline with GUI and PLC-PC combined solution. In this system, fully control of an accelerator setup is archived [2]. All PSUs and controllers are fitted in a single rack as seen in Fig. 2. WiFi and Bluetooth wireless communication solutions are used for floating ground (HV) case. High Voltage Deck is upgraded with a safety case for avoiding electrical accidents. The target system was also upgraded to 2 axis (R-Z) motion for better target manipulation. Saving & Loading the beam configuration, data logging of vacuum measurements and beam parameters were added to GUI (see Fig. 5).

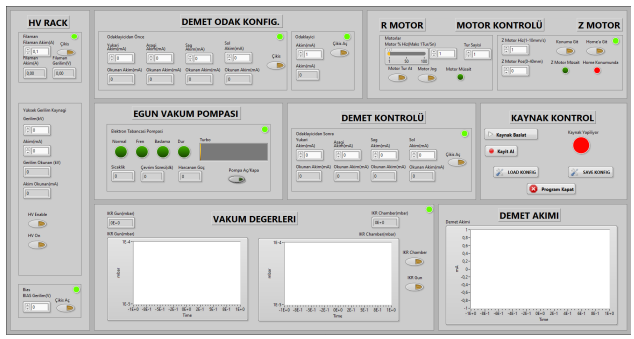


Figure 5: LabVIEW GUI of Electron Accelerator.

EXPERIMENTS

In the Fig. 6, focused 20 keV proton beam is shown. Once the 800 MHz RFQ production is completed, this beam will enter the RFQ to reach 2 MeV exit energy. Most of the devices on this beamline can be controlled with the LabVIEW GUI. Due to recent upgrades of some devices, the system development is still ongoing. In the next phase, all vacuum devices, beam production, measurement and cooling systems will be automatically controlled & monitored.

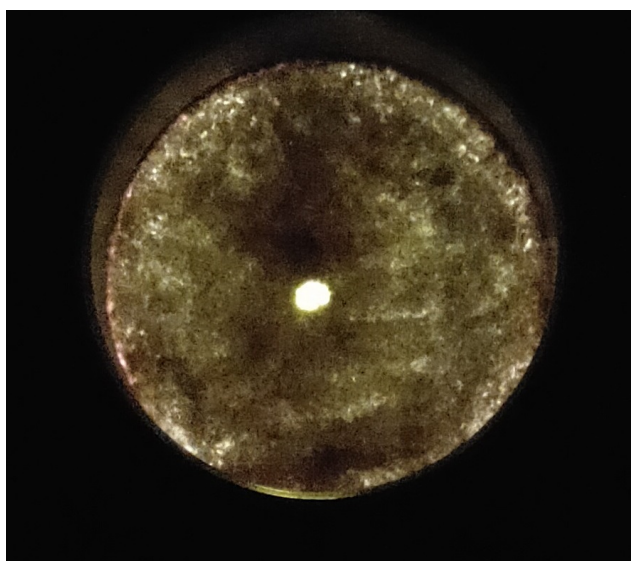


Figure 6: 20 keV Proton Beam [3].

Electron beam can be used for welding. In the Fig. 7, two stainless steel pipes with 0.4 mm thickness welded by an electron beam at 20 keV are shown. Such processes have been automated with a single weld button. In the background, PLC-PC combination with electrical signals, serial communication and wireless communication used together for this process. PID control for constant beam current will be added in future. After that this device can be used as an industrial Electron Beam Welding Machine or X-Ray generator.

Content from this work may be used under the terms of the CC BY 4.0 licence (© 2022). Any distribution of this work must maintain attribution to the author(s), title of the work, publisher, and DOI

ISBN: 978-3-95450-241-7 ISSN: 2673-5350 doi:10.18429/JACoW-IBIC2022-WEP43

Content from this work may be used under the terms of the CC BY 4.0 licence (© 2022). Any distribution of this work must maintain attribution to the author(s), title of the work, publisher, and DOI

In Fig. 7, rastering test with an electron beam is shown. With rastering of the electron beam one can build a scanning electron microscope. Beam optimization, calibration and automation of rastering is under further development.

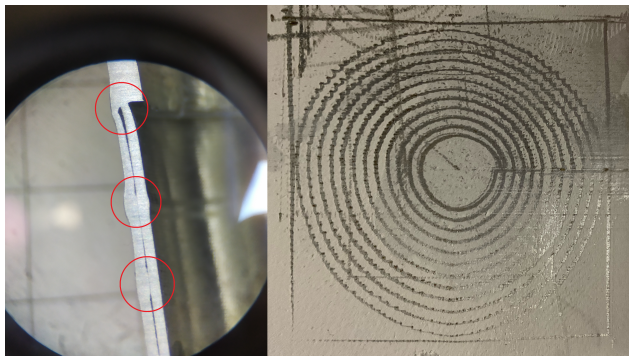


Figure 7: eBeam Welding and Rastering Tests.

WIRELESS SOLUTIONS

In Figs. 8 and 9, our WiFi and Bluetooth solutions are shown. Since some parts of accelerators should be on HV and sparks can damage most electrical devices we had to use wireless communication solutions. In Fig. 8's left side a WiFi controlled current meter is shown. This lab-made device can measure microampere and milliampere inputs from two different ports. In Fig. 8's right side, a Bluetooth controlled analogue output circuit with Arduino micro controller board is shown. This device can produce –10 to 10 V DC analogue output. In Fig. 9 our WiFi thermometer solution is shown. These devices are designed and assembled by our team. The external cases are made with a 3D printer when possible. These devices can be useful and cheap solutions for special cases. In the future we are planning to add temperature and humidity measurements in beam areas.

RESULT AND OUTLOOK

In the last three years, as KAHVELab, we managed to control different type devices (Turbomolecular pumps, vacuum gauges, low voltage PSUs, HV PSUs, pneumatic valves, sensors, motors) with different type of communications (TCP/IP, RS232, RS485, Analogue etc.). In the next three years, we are planning build systems which has multiple safety controls and can be controlled anyone who has a short training. We also plan to prepare control systems for these accelerators which will reach MeV energy level.

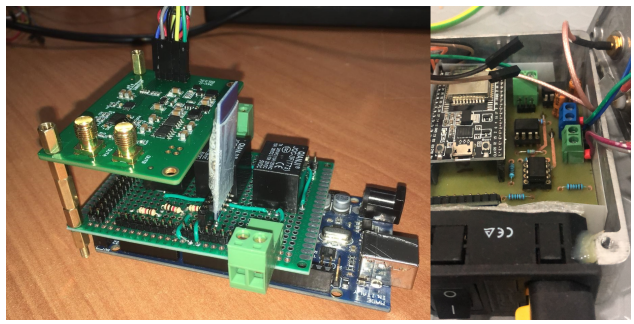


Figure 8: WiFi and Bluetooth Controllers.

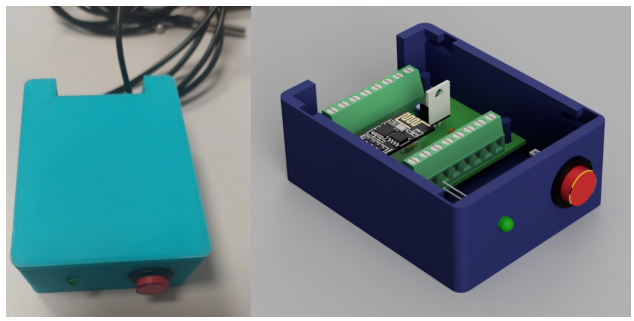


Figure 9: WiFi Thermometer Box.

REFERENCES

[1] A. Adıgüzel *et al.*, "Ion source and LEBT of KAHVELab proton beamline", doi:10.48550/arXiv.2208.00529, 2022.

[2] T.B. Ilhan, "Electron Beam Welding Device Control System Design", İstanbul University-Cerrahpasa, İstanbul, Turkey.

[3] D. Halis *et al.*, "Diagnostic Station of Proton Beam at KAHVELab (PTAK)", presented at IBIC'22, Kraków, Poland, Sep. 2022, paper WEP18, this conference.

ISBN: 978-3-95450-241-7 ISSN: 2673-5350 doi:10.18429/JACoW-IBIC2022-WE3I1

NOVEL FAST RADIATION-HARD SCINTILLATION DETECTOR FOR ION BEAM DIAGNOSTICS*

P. Boutachkov†, M. Saifulin[1], C. Trautmann[1], B. Walasek-Höhne
GSI Helmholtz Center for Heavy Ion Research, Darmstadt, Germany
E. Gorokhova, JSC S.I. Vavilov State Optical Institute, St. Petersburg, Russia
P. Rodnyi, I. Venevtsev, Peter the Great Polytechnic University, St. Petersburg, Russia
[1]also at Technical University Darmstadt, Darmstadt, Germany

Abstract

Novel radiation-hard scintillators were developed in the last years based on indium-doped zinc oxide ceramic with an extremely short decay time below a nanosecond. Fast counting detectors and fast screens were considered as potential beam diagnostic applications of this material. At the GSI/FAIR facility, scintillation detectors are commonly used for measuring the intensity and detailed time structure of relativistic heavy ion beams. The scintillating material is inserted directly into the beam path. Signals from individual ions are counted, providing systematic-error-free beam intensity information. Standard scintillators require frequent maintenance due to radiation damage. To address this limitation, a large area ZnO radiation-hard detector prototype was developed. The prototype detector operates at orders of magnitude higher irradiation levels, at higher counting rates and has better time resolution compared to a plastic scintillator. In addition, the novel detector material opens the possibilities for applications in other beam diagnostic systems, for example, scintillation screens for transverse profile measurements. Therefore, ZnO scintillation ceramics are of general interest for beam diagnostics.

INTRODUCTION

Scintillation detectors are used at the GSI/FAIR facility for intensity and micro-spill structure measurements. Ion beams from protons up to uranium with energies in the range of hundreds of MeV/u up to tens of GeV/u have to be characterized. The detectors utilize the interaction of the ion beam with a scintillator which generates photons. A photomultiplier tube (PMT) converts the light into an electrical signal.

The detector produces one pulse for each detected ion. Typical signal width measured from a BC400 or EJ212 plastic scintillator near the PMT location is of an order of 5 ns. The complex slow extraction process from the particle accelerators and the sub Poisson ion particle distribution [1] of the extracted particles lead to a non-negligible percentage of signal pile-ups at counting rates above a few times 10^6 particles per second. Higher counting rates are requested, hence scintillator materials with decay times of the order of nanosecond or shorter are desirable.

The typical dose at which a plastic scintillator has to be exchanged due to radiation damage is of the order of 50-100 kGy. This dose is regularly reached during micro-spill optimization. Therefore we investigated zinc oxide, an inorganic material which can substitute the plastic scintillator.

ZnO(In) RESPONSE TO HEAVY IONS

Fast luminescence from ZnO with indium or gallium doping was discovered in the sixties. A structureless band with a decay constant below a nanosecond located near the optical absorption edge was reported by W. Lehmann in Ref. [2]. The latter property limited the detector applications to cases where a few micrometers of scintillator material provide sufficient light output. In 2012, a breakthrough in ZnO scintillator production was reported by P. A. Rodnyi et al. [3]. Transparent ceramics from ZnO micro- and nano-powders were produced with a diameter of the order of 2 cm and thickness of 0.4 mm. The response of this material was tested at GSI with heavy ions. The results of these tests were reported in Ref. [4]. A photograph of the tested sample and an image with ion beam induced luminescence from 300 MeV/u ^{124}Xe ions is shown in Fig. 1.

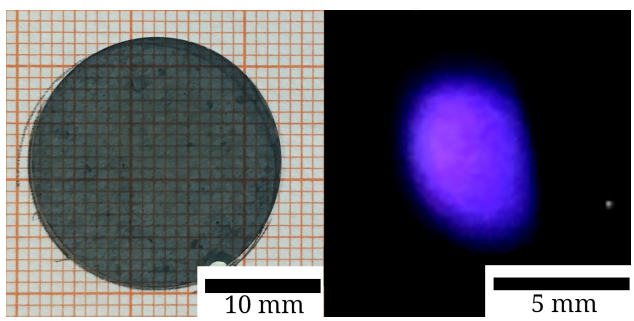


Figure 1: To the left, a ZnO(In) ceramic sample photograph. To the right, a color image of an ion beam induced luminescence by 300 MeV/u ^{124}Xe ions.

An international collaboration was formed under the ERA.Net RUS Plus Project RUS_ST2017-051 with the aim to develop ultra-fast ceramic detectors of ionizing radiation based on zinc oxide. Samples were produced and characterized at the Research Technological Institute of Optical Materials "Vavilov State Optical Institute" and Peter the Great St. Petersburg Polytechnic University. The ceramic microstructure was investigated at the Institute of Solid State Physics of the University of Latvia, while ionoluminescence

* This work was funded by DLR within the ERA.Net RUS Plus Project RUS_ST2017-051.
† P.Boutachkov@gsi.de (corresponding author)

Content from this work may be used under the terms of the CC BY 4.0 licence (© 2022). Any distribution of this work must maintain attribution to the author(s), title of the work, publisher, and DOI

ISBN: 978-3-95450-241-7 ISSN: 2673-5350 doi:10.18429/JACoW-IBIC2022-WE3I1

Content from this work may be used under the terms of the CC BY 4.0 licence (© 2022). Any distribution of this work must maintain attribution to the author(s), title of the work, publisher, and DOI

characterization and detector developments were performed at GSI.

Ionoluminescence properties of ZnO(In) and ZnO(Ga) samples were investigated at GSI with a variety of relativistic heavy ions, Ref. [4–7]. We discovered that:

Radiation Hardness of ZnO

The radiation hardness of ZnO is at least two orders of magnitude higher compared to plastic scintillators. Figure 2 shows the evolution of the ZnO(In) scintillation spectrum as a function of fluence. The ionoluminescence was induced from ^{197}Au ions with an energy of 4.8 MeV/u. In this experiment, the energy deposition per unit length by a gold ion is larger than that of ^{238}U ions at 250 MeV/u. The latter will deposit the highest energy density under the planned operation of ZnO-based detectors at GSI/FAIR. The data shows a single structureless band with a maximum intensity at ~390 nm. This is the fast near-band-edge (NBE) emission of ZnO(In). This study was presented at IBIC2022 by M. Saifulin et al. [5].

The response to radiation damage with 0.3 GeV/u Xe and U ions is reported in Ref. [4] and other heavy relativistic ions in Ref. [7]. In our investigation, apart from NBE, we did not observe new emission bands forming due to radiation damage.

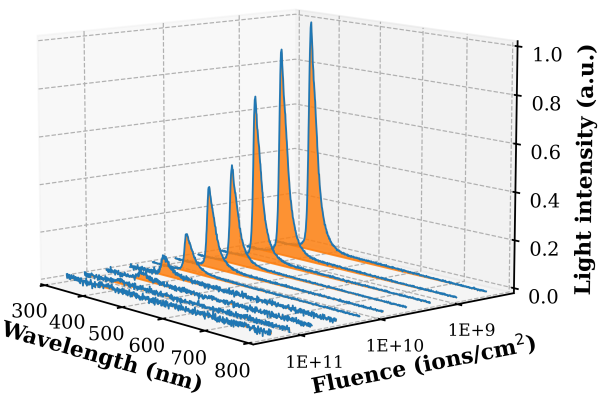


Figure 2: Ionoluminescence spectrum of ZnO doped with In, excited with ^{197}Au ions with energy of 4.8 MeV/u.

One of the samples irradiated with 0.3 GeV/u U ions was annealed in air at 500°C. Its radioluminescence properties before and after annealing were reported in Ref. [8]. The measurement shows that after annealing in air, the luminescent properties of the radiation-damaged material were improved relative to not damaged material. Further investigations performed at GSI with heavy ions confirmed that the luminescence properties of the bulk material are restored [7].

ZnO Light Output

The ZnO light output follows nearly the same trend versus deposited energy as BC400/Ej212 plastic scintillators. The light output of various ZnO samples as a function of deposited energy is discussed in Ref. [6, 7]. Figure 3 shows one of this data sets. The light output of all investigated samples as a function of deposited energy followed the same trend as the one of BC400/EJ212 plastic scintillators.

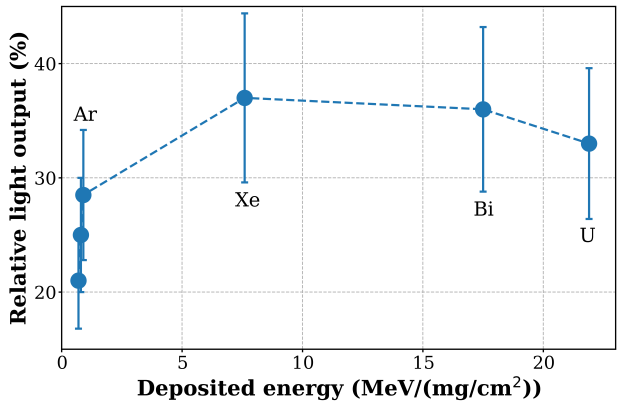


Figure 3: The light output of ZnO(In) as a function of deposited energy normalized to the light output of BC400/EJ212 plastic scintillators.

The research and development within the ERA.Net RUS Plus Project led to improvements in the production of the ZnO scintillating ceramics. A large number of samples with a variation of the light output of less than 5% were manufactured. These samples were used to build the multi-tile detector described below. In general, the light output of ZnO(In) ceramics obtained by using an optimized manufacturing process is of the order of 0.5 of the corresponding light output of the BC400 plastic scintillator.

ZnO Signal

The ZnO signal induced via ionoluminescence has a full-width at half-maximum below one nanosecond. Figure 4 shows a comparison of the signals from the ZnO(In) and the BC400 plastic scintillators acquired under the same conditions. The signals are convoluted with the PMT and the oscilloscope response. The PMT used for the measurement was Hamamatsu H13661, with a rise time of the order of 230 ps and full-width at half-maximum of the order of 430 ps. The 2 GHz oscilloscope which captured the signals was Tektronix MSO58. The signal width of bellow 1 ns resolves any pile-up limitations for the micro-spill structure measurements performed at GSI.

ZnO Radiation Damage

The reduction of the ZnO light output due to radiation damage follows the trend predicted by the Birks-black model. A fit with the Birks-Black model [9] of the experimental data from irradiation of a ZnO(In) sample with 4.8 MeV/u Au ions is shown in Fig. 5. The model has two parameters, the light output before irradiation and the critical fluence, this is the fluence at which the light output is reduced by a factor of two.

Figure 6 shows the data on the critical fluence, $\Phi_{1/2}$, versus deposited energy for ZnO(In) and BC400. The critical

ISBN: 978-3-95450-241-7 ISSN: 2673-5350 doi:10.18429/JACoW-IBIC2022-WE3I1

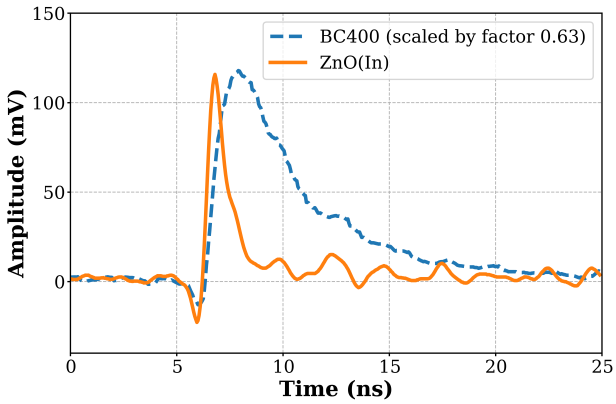


Figure 4: Comparison of the signals from ZnO(In) and BC400 plastic scintillator. The scintillators were bombarded with 300 MeV/u ^{238}U ions. The plastic scintillator data is scaled in order to match the ZnO(In) signal amplitude. The continuous orange line: ZnO(In) signal. Dashed blue line: BC400 signal.

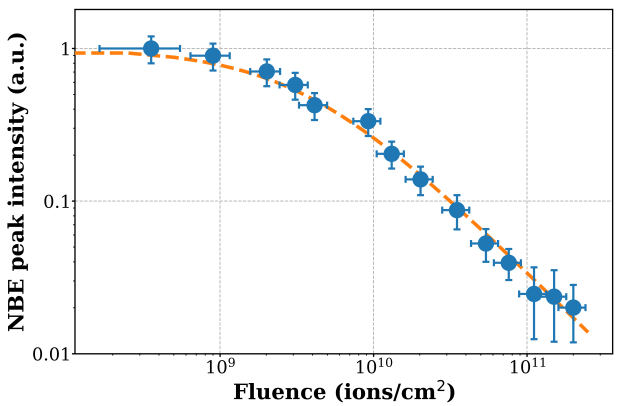


Figure 5: ZnO(In) light output as a function of fluence of ^{197}Au ions. The beam energy was 4.8 MeV/u. Blue dots represent experimental data. Dashed orange line represents a fit of the experimental data by the Birks-Black model.

fluence is determined from the damage mechanisms of the heavy ions interacting with the ZnO ceramics. The correlation between experimentally determined $\Phi_{1/2}$ and the calculated energy loss allows to predict the material longevity under operation conditions that were not investigated before.

Further data and details on this investigations are given in Ref. [10].

MULTI-TILE LARGE AREA DETECTOR

The production of the ceramic samples described in these studies is optimized for round samples with a diameter of the order of 2 cm. Square tiles with the size of 15×15 mm^2 were cut from the round samples. A detector prototype with an active area of 45×45 mm^2 was constructed by placing the scintillating ceramic tiles on a radiation-hard glass light guide. Photographs of part of the detector active area and the light guide are shown in Fig. 7. The detector was constructed

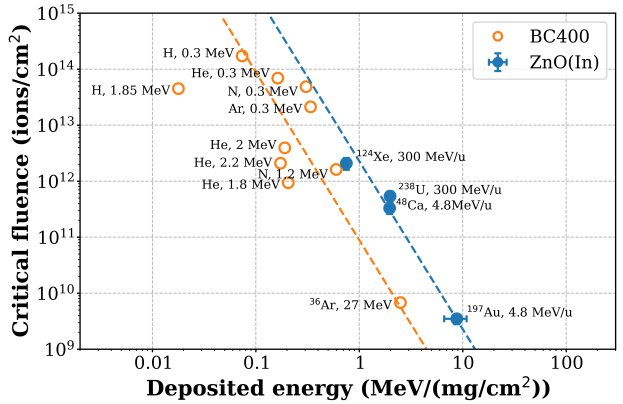


Figure 6: Critical fluence versus deposited energy for ZnO(In) and BC400. The dashed lines indicate the correlation between the material damage and the deposited energy.

from 18 tiles. Two layers of 3×3 tiles each were placed on each side of the radiation-hard light guide. The interfaces between the front and back tiles were shifted. Thus, if a particle passed between two front tiles, it was guaranteed to interact with a tile on the back of the detector.

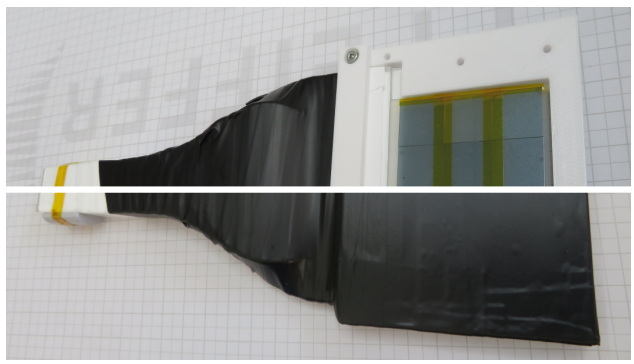


Figure 7: Photographs of the ZnO-based multi-tile scintillator detector. The upper photograph shows a part of the multi-tile assembly, while the bottom half is a photograph of the detector wrapped with PTFE and black tape.

The detector counting efficiency was validated relative to a 75×80 mm^2 BC400 plastic scintillator detector. All particles that passed the 45×45 mm^2 active area of the ZnO(In) multi-tile detector generated a clean easy-to-discriminate signal. Figure 8 illustrates the tile-detector concept and the experiment layout for this measurement. Further details on the detector construction, optimization and performance are given in M. Saifulin thesis [7].

It should be noted that there are no fundamental constraints for the production of larger samples. The tools and production technology can be scaled following a demand for larger ceramic pieces.

OUTLOOK

Zinc-oxide-based counting detector will be used at GSI/FAIR for micro-spill structure measurements.

Content from this work may be used under the terms of the CC BY 4.0 licence (© 2022). Any distribution of this work must maintain attribution to the author(s), title of the work, publisher, and DOI

ISBN: 978-3-95450-241-7 ISSN: 2673-5350 doi:10.18429/JACoW-IBIC2022-WE3I1

Content from this work may be used under the terms of the CC BY 4.0 licence (© 2022). Any distribution of this work must maintain attribution to the author(s), title of the work, publisher, and DOI

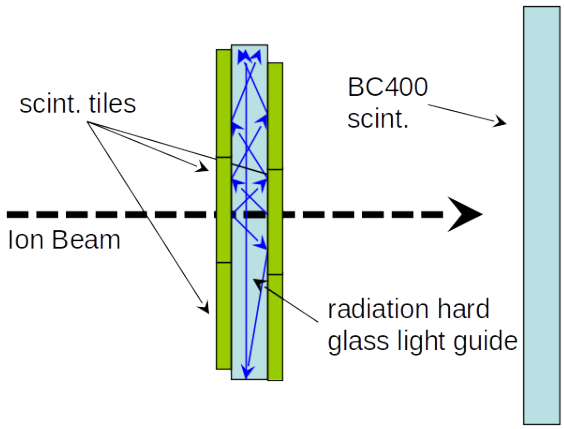


Figure 8: A conceptual drawing of the experiment in which the counting efficiency of the multi-tile detector was measured.

Currently, we are investigating ZnO as a scintillation screen material for transverse profile measurements at the future FAIR facility. Based on the measurements performed at XFEL [11] we expect that the CROMOX screens used at GSI will saturate when bombarded with 10^{10} fast-extracted U ions, focused to a 10 mm beam spot. ZnO has orders of magnitude shorter decay constant relative to CROMOX. The extraction time from SIS18/SIS100 is much longer than the decay time of ZnO, which makes it an excellent candidate for transverse profile measurements of the intense heavy ions beams at FAIR.

CONCLUSIONS

ZnO-based scintillating ceramics are promising materials to be used for heavy-ion particle detection applications. They are fast and radiation hard.

The response to relativistic heavy ions of ZnO scintillating ceramics with In and Ga doping was determined. It was discovered that the decrease of ionoluminescence as a function of ion fluence follows the Birks-Black model. The trend of the critical fluence as a function of deposited energy was established. Based on this data, the reduction of ionoluminescence due to radiation damage can be predicted for various operating conditions.

A multi-tile detector with a counting efficiency of 100% for relativistic heavy ions was constructed. With this achievement, it was demonstrated that there is no fundamental limit for the detector active area which can be reached with the current ZnO scintillating ceramic production technology.

REFERENCES

[1] R. Singh, P. Forck, and S. Sorge, "Reducing fluctuations in slow-extraction beam spill using transit-time-dependent tune modulation," *Phys. Rev. Applied*, vol. 13, no. 4, p. 044 076, 2020. doi:10.1103/PhysRevApplied.13.044076

[2] W. Lehmann, "Edge emission of *n*-type conducting ZnO and CdS," *Solid-State Electron.*, vol. 9, no. 11-12, pp. 1107–1110, 1966. doi:10.1016/0038-1101(66)90134-1

[3] P. Rodnyi, K. Chernenko, E. Gorokhova, S. Kozlovskii, V. Khanin, and I. Khodyuk, "Novel scintillation material–ZnO transparent ceramics," *IEEE Trans. Nucl. Sci.*, vol. 59, no. 5, pp. 2152–2155, 2012. doi:10.1109/TNS.2012.2189896

[4] P. Boutachkov *et al.*, "Radiation hardness investigation of zinc oxide fast scintillators with relativistic heavy ion beams," in *Proc. IBIC'19*, Malmö, Sweden, Sep. 2019, pp. 71–73. doi:10.18429/JACoW-IBIC2019-MOPP005

[5] M. Saifulin *et al.*, "ZnO(In) Scintillation Light Spectra Investigation for Heavy Ion Detector Application," presented at the 11th International Beam Instrumentation Conference (IBIC'22), Kraków, Poland, Sep. 2022, paper TUP29, this conference.

[6] M. Saifulin *et al.*, "Zinc Oxide-Based Fast Radiation-Hard Scintillation Ceramics for Heavy-Ion Beam Diagnostics," in *Proceedings of the 16th International Conference on Scintillating Materials and their Applications, Santa Fe, NM, USA*, 2022.

[7] M. Saifulin, to be submitted in 2023, Ph.D. dissertation, Technical University Darmstadt, Darmstadt, Germany.

[8] P. Rodnyi, I. Venevtsev, E. Gorokhova, S. Eron'ko, P. Boutachkov, and M. Saifulin, "Fast, efficient, and radiation hard ZnO:In ceramic scintillator," in *2019 IEEE International Conference on Electrical Engineering and Photonics (EExPolytech)*, IEEE, 2019, pp. 197–200. doi:10.1109/EExPolytech.2019.8906846

[9] J. Birks and F. Black, "Deterioration of anthracene under α-particle irradiation," *Proc. Phys. Soc. London, Sect. A*, vol. 64, no. 5, p. 511, 1951. doi:10.1088/0370-1298/64/5/112

[10] M. Saifulin *et al.*, "Ionoluminescence and optical transmission investigation of ZnO(In) fast ceramic scintillator irradiated with swift heavy ions," *J. Appl. Phys.*, 2022.

[11] G. Kube, S. Liu, A. Novokshonov, and M. Scholz, "Identification and Mitigation of Smoke-Ring Effects in Scintillator-Based Electron Beam Images at the European XFEL," in *Proc. FEL'19*, Hamburg, Germany, Aug. 2019, pp. 301–306. doi:10.18429/JACoW-FEL2019-WEB01

ISBN: 978-3-95450-241-7 ISSN: 2673-5350 doi:10.18429/JACoW-IBIC2022-WE3C2

TIME-RESOLVED PROTON BEAM DOSIMETRY FOR ULTRA-HIGH DOSE-RATE CANCER THERAPY (FLASH)

P. Casolaro*, G. Dellepiane, A. Gottstein, I. Mateu, P. Scampoli[1], S. Braccini
Albert Einstein Center for Fundamental Physics (AEC), Laboratory for High Energy Physics (LHEP), University of Bern, Bern, Switzerland
[1]also at Department of Physics "Ettore Pancini", University of Napoli Federico II, Complesso Universitario di Monte S. Angelo, Napoli, Italy

Abstract

A new radiotherapy modality, known as FLASH, is a potential breakthrough in cancer care as it features a reduced damage to healthy tissues, resulting in the enhancement of the clinical benefit. FLASH irradiations are characterized by ultra-high dose-rates (>40 Gy/s) delivered in fractions of a second. This represents a challenge in terms of beam diagnostics and dosimetry, as detectors used in conventional radiotherapy saturate or they are too slow for the FLASH regime. In view of the FLASH clinical translation, the development of new dosimeters is fundamental. Along this line, a research project is ongoing at the University of Bern aiming at setting-up new beam monitors and dosimeters for FLASH. The proposed detection system features millimeter scintillators coupled to optical fibers, transporting light pulses to a fast photodetector, readout by high bandwidth digitizers. First prototypes were exposed to the 18 MeV proton beam at the Bern medical cyclotron. The new detectors have been found to be linear in the range up to 780 Gy/s, with a maximum time resolution of 100 ns. These characteristics are promising for the development of a new class of detectors for FLASH radiotherapy.

INTRODUCTION

FLASH radiotherapy is a novel radiation delivery modality characterized by very fast irradiations (< 300 ms) and ultra-high dose rates (> 40 Gy/s). By comparison, conventional radiotherapy treatments are performed in a few minutes at dose rates of the order of 0.1 Gy/s. Since the first pioneering work by Favaudon et al. [1], many experiments have shown that FLASH irradiations drastically reduce normal tissue toxicity, while keeping the same effectiveness on the cancer cells as of the conventional radiotherapy [2]. This striking sparing effect on healthy tissue, also termed as FLASH effect, has been observed with more than one radiation type, including electrons, protons, photons, and carbon ions [3]. The dosimetry and beam monitoring of FLASH irradiations are challenging owing to the peculiar characteristics of FLASH beams. Ionization chambers are the gold standard for the dosimetry in conventional radiotherapy; however, these detectors feature relatively slow response and saturation at high dose rates [4]. Consequently they cannot be used for FLASH beams, without corrections. Along this line, a research project is ongoing at the University of Bern aiming at the proof-of-principle of a new detection system for dosimetry and beam monitoring in FLASH radiotherapy. The first dosimeter prototypes, based on plastic scintillators coupled to optical fibers, have been tested at the Bern cyclotron laboratory located at the Bern University Hospital (Inselspital).

* pierluigi.casolaro@lhep.unibe.ch

MATERIALS AND METHODS

This work reports on two measurements aimed at evaluating the feasibility of the proposed innovative system for ultra-high dose rate beams, namely: 1) the study of the detector response as a function of the average dose rate and 2) the time trend of the proton beam at high time resolution. This section describes the proposed innovative detection system and the specific dosimetry method tested at the Bern medical cyclotron.

The Innovative Detection System

The new detection system for ultra-high dose rate measurements is depicted in the schematic of Fig. 1.

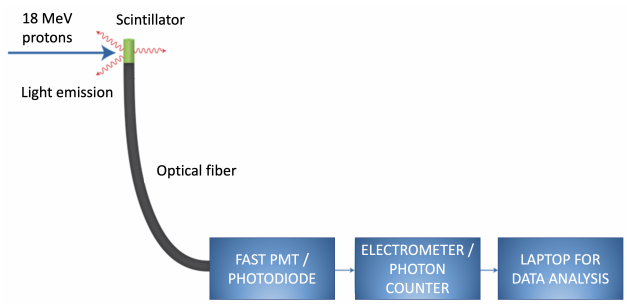


Figure 1: Schematic of the FLASH detection system.

Its main element is a scintillator of millimeter or submillimeter size coupled to an optical fiber. The light pulses are delivered to the data acquisition (DAQ) through the optical fiber. In this work, we used a (0.5×0.5×2) mm^3 polystyrene scintillator, and two different DAQs, one for the study of the linearity of the dose rate response and another for the beam monitoring at high time resolution. The former comprises a high speed response PhotoMultiplier Tube (PMT) and a Keysight B2985A electrometer; the latter comprises a single-photon detector module based on a silicon avalanche photodiode and a Ortec Multi-Channel Scaler (MCS). The MCS allows for measurements with 65536 chan-

Content from this work may be used under the terms of the CC BY 4.0 licence (© 2022). Any distribution of this work must maintain attribution to the author(s), title of the work, publisher, and DOI

ISBN: 978-3-95450-241-7 ISSN: 2673-5350 doi:10.18429/JACoW-IBIC2022-WE3C2

Content from this work may be used under the terms of the CC BY 4.0 licence (© 2022). Any distribution of this work must maintain attribution to the author(s), title of the work, publisher, and DOI

nels and a variable dwell time down to 100 ns. In this measurement, the dwell time was set to 50 µs.

The Bern Cyclotron Laboratory

The characterization of the detection system for ultra-high dose rates was performed with the IBA 18 MeV medical cyclotron located at the Bern University Hospital (Inselspital). The cyclotron is used overnight for the production of radioisotopes for nuclear medicine, in particular for the ^{18}F production for Positron Emission Tomography (PET) imaging. During the day, the cyclotron is used by the group of medical application of particle physics of the University of Bern for multidisciplinary research activities [5,6]. Part of these activities are possible thanks to a 6 meter long Beam Line Transfer (BTL), equipped with beam focusing, steering and diagnostic systems, which connect the cyclotron to a second bunker with independent access to the experimental area. The cyclotron allows for irradiations in a wide beam current range from a few pA to 10^2 µA. For the measurements reported in this work, we used an independent dosimetry system based on Faraday cup and collimators, which was recently validated for radiation damage studies [7]. The dosimetry on the scintillator position has been verified with radiochromic films [8, 9]. A picture of the experimental setup is shown in Fig. 2.

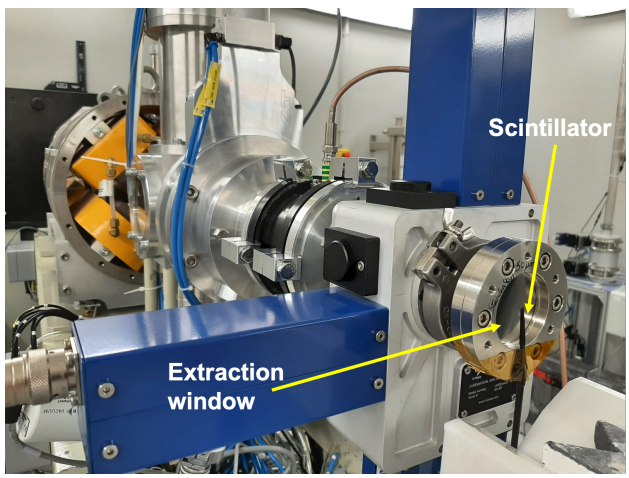


Figure 2: Beam Transfer Line of the Bern medical cyclotron. The optical fiber, with the scinitillator, is directly exposed to the proton beam, which is extracted in air.

The beam is extracted in air through a 50 µm stainless steel window. A 2-D beam monitor based on Ce-doped scintillation optical fibers [10] provides accurate measurements of the beam profile downstream the extraction window. The beam energy in the BTL, (18.3±0.3) MeV, was accurately measured in previous works [11–13]. The beam energy in the scintillator position was evaluated with energy loss calculations based on the SRIM/TRIM package [14]. It was found to be (17.5±0.3) MeV and the corresponding water stopping power S_W=2.9 $\frac{\text{keV}}{\mu\text{m}}$. A fast beam stopper positioned at the center of the cyclotrons, can provide proton beams of a few seconds.

RESULTS

The study of the response of the detection system as a function of the average dose rate has been performed with the high speed PMT and the electrometer, as discussed in the Methods section. Figure 3 shows the electrometer current I_{PMT} as a function of the proton beam average dose rate $\dot{D}$ in the range (30-780) Gy/s. The data are well fitted a straight line, with a coefficient of determination R^2=0.996. The values of the fitting parameter, namely the slope m and the intercept I_0, are reported in the inset of Fig. 3.

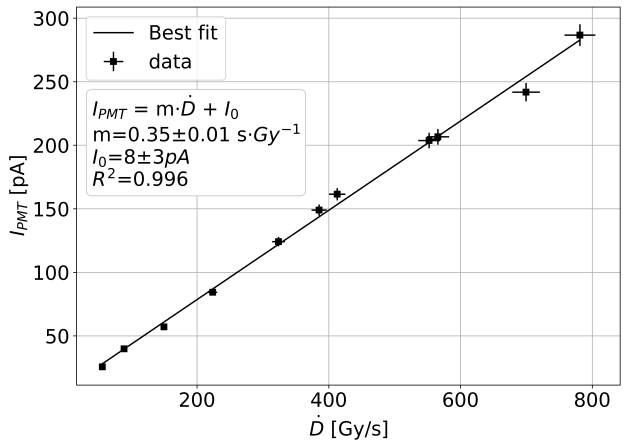


Figure 3: Photomultiplier current I_{PMT} as a function of the proton beam average dose rate $\dot{D}$. The inset reports the values of the fitting parameters and of the coefficient of determination R^2.

The time trend of the proton beam at high time resolution has been performed with a DAQ system comprising of the single-photon detector module and the MCS, as discussed in the Methods section. Figure 4 shows the photon counts with 50 µs dwell time as a function of the time for 1.5 seconds.

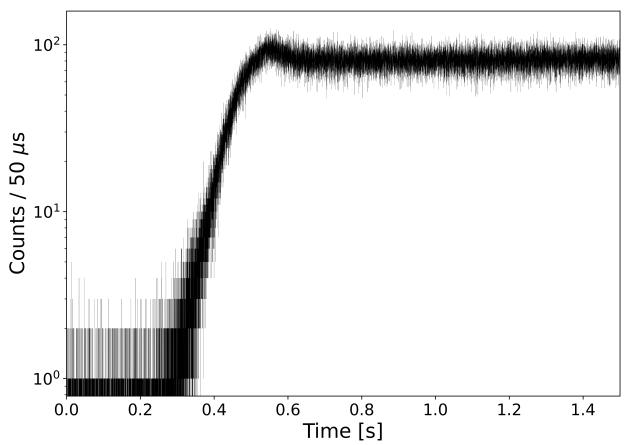


Figure 4: Time trend of the proton beam with 50 µs dwell time.

ISBN: 978-3-95450-241-7 ISSN: 2673-5350 doi:10.18429/JACoW-IBIC2022-WE3C2

The plot of Fig. 4 can be divided in three parts corresponding to the beam stopper position: 1) the beam is stopped during the first 200 ms, 2) the beam stopper is released and the counts detected by the single-photon detector module rapidly increase, 3) the beam is delivered to the scintillator and the counts reach a fixed average value. In order to evaluate the dark counts contribution, we measured the dark count rate in absence of beam. The dark count rate was found to be (5730±90) Hz.

CONCLUSION AND OUTLOOK

This work demonstrates the feasibility of a detection system based on fast scintillators and optical fibers for the ultra-high dose rate dosimetry for FLASH radiotherapy. In particular, we found that the response of a polystyrene scintillator is linear in the dose rate range (30-780) Gy/s. Furthermore, we successfully measured the proton beam for 1.5 seconds with a 50 µs dwell time. Even if such time resolution is enough for many clinical applications, higher time resolutions can be achieved by changing the dwell time. The Multi-Channel Scaler used in this work allows measurements down to 100 ns for a maximum of 655 ms. The spatial resolution is given by the scintillator size. In this first tests, we used a (0.5×0.5×2) mm^3 polystyrene scintillator. The findings reported in these work are very promising for the definition of a new class of detectors to be used in several applications for FLASH radiotherapy, including beam monitoring, quality control, and in-vivo dosimetry. Further steps of this project will be devoted to the test of scintillators featuring higher radiation resistance than polystyrene, and to study of the response of the system to pulsed electron beams.

ACKNOWLEDGEMENTS

The authors are thankful to the LHEP engineering staff, in particular Roger Hänni and Jan Christen, and the SWAN Isotopen AG team. The authors would like to thank Dominik Wermelinger for his dedication to this project who is carrying out within the framework of his Bachelor's thesis at the University of Bern. This project was partially funded by the Bern Center for Precision Medicine (BCPM) of the University of Bern, and by the Swiss National Science Foundation (SNSF) [Grant: CRSII5_180352].

REFERENCES

[1] V. Favaudon *et al.*, "Ultrahigh dose-rate FLASH irradiation increases the differential response between normal and tumor tissue in mice," *Sci. Transl. Med.*, vol. 6, no. 245, p. 245ra93, Jul. 2014. doi:10.1126/scitranslmed.3008973

[2] M.-C. Vozenin *et al.*, "The Advantage of FLASH Radiotherapy Confirmed in Mini-pig and Cat-cancer Patients," *Clin. Cancer Res.*, vol. 25, no. 1, pp. 35–42, Jun. 2018. doi:10.1158/1078-0432.ccr-17-3375

[3] B. Lin *et al.*, "FLASH Radiotherapy: History and Future," *Front. Oncol.*, vol. 11, May 2021. doi:10.3389/fonc.2021.644400

[4] F. Romano, C. Bailat, P. G. Jorge, M. L. F. Lerch, and A. Darafsheh, "Ultra-high dose rate dosimetry: Challenges and opportunities for FLASH radiation therapy," *Med. Phys.*, vol. 49, no. 7, pp. 4912–4932, May 2022. doi:10.1002/mp.15649

[5] S. Braccini, "The new bern PET cyclotron, its research beam line, and the development of an innovative beam monitor detector," *AIP Conf. Proc.*, vol. 1525, p. 144, 2013. doi:10.1063/1.4802308

[6] G. Dellepiane *et al.*, "Research on theranostic radioisotope production at the Bern medical cyclotron.", *Il nuovo cimento C*, vol. 44, no. 4-5, pp. 1–4, Sep. 2021. doi:10.1393/ncc/i2021-21130-6

[7] J. Anders *et al.*, "A facility for radiation hardness studies based on a medical cyclotron," *J. Instrum.*, vol. 17, p. P04021, Apr. 2022. doi:10.1088/1748-0221/17/04/p04021

[8] P. Casolaro, "Radiochromic Films for the Two-Dimensional Dose Distribution Assessment," *Appl. Sci.*, vol. 11, no. 5, p. 2132, Feb. 2021, doi:10.3390/app11052132

[9] P. Casolaro, L. Campajola, and F. D. Capua, "The physics of radiochromic process: one calibration equation for all film types," *J. Instrum.*, vol. 14, no. 08, p. P08006, Aug. 2019. doi:10.1088/1748-0221/14/08/p08006

[10] D. E. Potkins *et al.*, "A Low-cost Beam Profiler Based On Cerium-doped Silica Fibers," *Physics Procedia*, vol. 90, pp. 215–222, 2017. doi:10.1016/j.phpro.2017.09.061

[11] L. Campajola *et al.*, "Measurement of the proton beam energy of a medical cyclotron based on Rutherford Backscattering Analysis," *Nucl. Instrum. Methods Phys. Res., Sect. B*, vol. 440, pp. 114–117, Feb. 2019. doi:10.1016/j.nimb.2018.12.017

[12] P. Häffner, C. Belver Aguilar, S. Braccini, P. Scampoli, and P. A. Thonet, "Study of the Extracted Beam Energy as a Function of Operational Parameters of a Medical Cyclotron," *Instruments*, vol. 3, no. 4, p. 63, Dec. 2019. doi:10.3390/instruments3040063

[13] K. P. Nesteruk, M. Auger, S. Braccini, T. S. Carzaniga, A. Ereditato, and P. Scampoli, "A system for online beam emittance measurements and proton beam characterization," *J. Instrum.*, vol. 13, no. 01, p. P01011, Jan. 2018. doi:10.1088/1748-0221/13/01/p01011

[14] J. F. Ziegler, M. D. Ziegler, and J. P. Biersack, "SRIM – The stopping and range of ions in matter (2010)," *Nucl. Instrum. Methods Phys. Res., Sect. B*, vol. 268, pp. 1818–1823, Jun. 2010. doi:10.1016/j.nimb.2010.02.091

Content from this work may be used under the terms of the CC BY 4.0 licence (© 2022). Any distribution of this work must maintain attribution to the author(s), title of the work, publisher, and DOI

ISBN: 978-3-95450-241-7 ISSN: 2673-5350 doi:10.18429/JACoW-IBIC2022-WE3C3

FAST SPILL MONITOR STUDIES FOR THE SPS FIXED TARGET BEAMS

F. Roncarolo*, M. Bergamaschi, D. Belohrad, E. Calvo Giraldo, E. Effinger,
M. Martin Nieto, S. Mazzoni, I. Ortega Ruiz, J. Tan, C. Zamantzas,
P. A. Arrutia Sota, V. Kain, M. A. Fraser, F. M. Velotti, CERN, Geneva, Switzerland

Abstract

At the CERN Super Proton Synchrotron (SPS) the 400 GeV proton beam is supplied to the fixed target experiments in the North Area facility (NA) via a slow extraction process. The monitoring of the spill quality during the extraction, lasting 4.8 seconds with the present SPS setup, is of high interest for minimising beam losses and providing the users with uniform proton-on-target rates. The monitor development challenges include the need for detecting, sampling, processing and publishing the data at rates ranging from few hundred Hz to support the present operation to several hundreds of MHz to serve future experiments proposed within the Physics Beyond Collider (PBC) program. This paper gives an overview of the ongoing studies for optimizing the existing monitors performances and of the R&D dedicated to future developments. Different techniques are being explored, from Secondary Emission Monitors to Optical Transition Radiation (OTR), Gas Scintillation and Cherenkov detectors. Expected ultimate limitations from the various methods will be presented, together with 2022 experimental results, for example with a recently refurbished OTR detector.

SPS SLOW EXTRACTION

The main physics program at the CERN SPS relies on the delivery of 400 GeV protons to the NA fix target experiments. As illustrated in Fig. 1, this is achieved by a 4.8 s third integer slow extraction process [1] at the end of the SPS *fix target beam* cycle, lasting about 10 s from first injection to flat top. Among the parameters for assessing the spill quality, providing the experiments with a constant flux of protons on target during the spill is of paramount importance for the SPS physics program. For this purpose, the SPS 200 MHz RF system is disabled at the end of acceleration with the aim of extracting fully de-bunched beams.

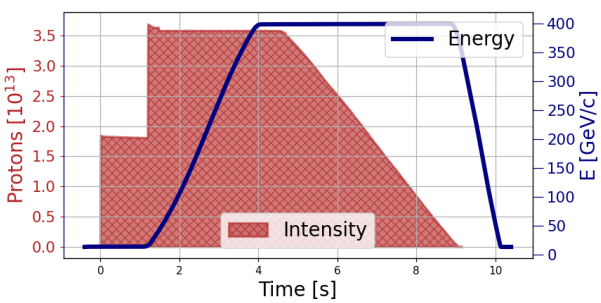


Figure 1: SPS Fix Target beams cycle.

Table 1: Key Parameters of Interest for the SPS Spill Monitors Requirements

Parameter	Value or Range	Comment
Spill Duration	4.8 s	present operation
	1 s	future, e.g. PBC
Beam Intensity	1 - 400 × 10^{11} p	
Spectrum Harmonics of Interest	50 Hz, 100 Hz	e.g. Noise, PC ripples
	43.86 kHz	SPS 1^{st} and 2^{nd} Harmonics*
	476 kHz	PS 1^{st} Harmonic**
	200 MHz	RF capture
	800 MHz	RF long. blow-up
	10 GHz	Future, e.g. PBC

* the SPS circulating beam structure includes 2×10 µs injections, the *abort gap* for the dump kickers rise
** the slow extracted beam can still contain a time structure from the PS (the SPS injector)

Therefore, measuring the beam current fluctuations at high frequencies during the spill in the transfer line from the SPS ring to the targets is of primary interest. Spill monitors can then provide signals for feed-back or feed-forward systems to equipment, such as RF cavities or magnet power converters, that are typically identified as possible sources of beam intensity fluctuations [2–4]. Table 1 summarises key parameters relevant for the spill monitors functional specifications.

SPS FAST SPILL MONITORS

From the parameters presented in Table 1, one can summarise the main challenges for spill monitoring as follows:

- monitoring beam currents ranging from few nA (1 × 10^{11} p in 4.8 s) to ≈1µA (4 × 10^{13} p in 1 s)
- by design the particles are un-bunched, standard electromagnetic beam position monitors and current transformers are not suitable
- to support the SPS slow extraction operation and optimisation, the overall monitor bandwidth must cover from very low frequencies to the several hundreds MHz, thus requiring *fast* spill monitors to identify the presence of (unwanted and normally relatively small) residual time structures from the SPS RF.

The SPS is now equipped with three *fast* spill monitors, based on independent measurement techniques and data

* federico.roncarolo@cern.ch

Content from this work may be used under the terms of the CC BY 4.0 licence (© 2022). Any distribution of this work must maintain attribution to the author(s), title of the work, publisher, and DOI

ISBN: 978-3-95450-241-7 ISSN: 2673-5350 doi:10.18429/JACoW-IBIC2022-WE3C3

acquisition systems, installed at different locations in TT20 beam line from the SPS to the targets.

Secondary Emission Monitor (SEM)

Apart for a limited number of beam imaging systems, all the diagnostics for beam position, transverse size and intensity in the NA primary lines is based on Secondary Emission Monitors (SEM)[1]. They consist of very thin (normally 12 µm) Titanium or Aluminium foils, or bands of different width and filling factor. The measurement relies on counting the secondary electrons generated by the primary protons traversing the foils/bands. The Secondary Emission Yield (SEY)[2] is few 10^{-2}.

One of the SEM monitors is equipped with a relatively fast amplifier (≈ 10 MHz BW). A low pass filtering (≈ 1 kHz) is necessary to minimise out-of-band noise and improve on signal-to-noise ratio. The amplifier output is digitised in the surface at a maximum rate of 200 kHz. This is the only *operational* system available so far in the SPS, and in the past it has been used as direct feedback to magnet power supplies, mainly to suppress 50 Hz magnet current ripples. At the moment, the monitor is exploited via SW in feed-forward mode to compensate for 50 and 100 Hz harmonics.

Diamond Beam Loss Monitors

For many years now, polycrystalline diamond detectors [6, 7] have been used as Beam Loss Monitors (dBLM) at CERN. They consist of synthetic diamond sensors, grown via a chemical vapour deposition (CVD) process, with a size of 10 × 10 mm and a thickness of 500 µm. They are normally placed few cm outside of the beam pipe, in strategic locations known to suffer from high beam losses, like beam injection and extraction regions. Assuming the losses time structure is the same as the slow extracted beam intensity, dBLMs can be very well exploited as fast spill monitors. In the past, they proved to be able resolving the 200 MHz structure of the SPS physics beam losses [8].

Recently, two dBLMs were installed in the first part of the TT20 beam line. The DAQ is based on analog 40 dB pre-amplifiers in the tunnel and 650 MHz ADCs in the service area. The analog BW has a lower limit at about 25 kHz (analog electronics cut-off) and a higher limit of 500 MHz (FMC ADC) [9]. Figure 2 shows how they were already successfully used to study the residual presence of the 200 MHz harmonic [10]. This was achieved by subtracting the power spectrum measured without beam to the one measured with beam. By moving the acquisition window of about 2 ms (which is at the moment the limit in amount of data that can be transferred per spill) along the 4.8 s, it was also possible to study the harmonic evolution along the spill[3].

[1] A recent, general, overview is included in [5]

[2] i.e. the probability of an electron to be emitted for a 400 GeV proton entering or exiting a Titanium or Aluminium surface

[3] A plot about this is included in the oral presentation associated to this contribution.

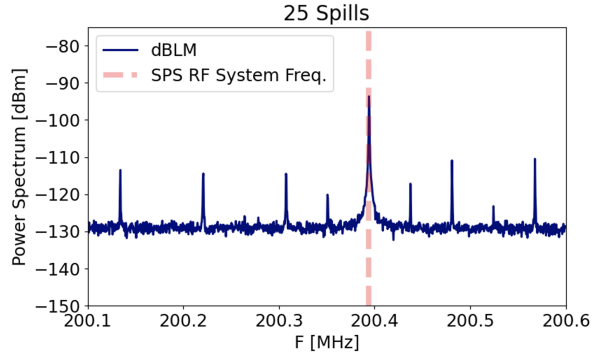


Figure 2: SPS beam power spectrum around the SPS 200 MHz nominal frequency, as measured by one of the TT20 dBLMs over a 2 ms chunk of the spill.

Optical Transition Radiation (OTR) - PMT System

The detection of OTR generated by charged particles traversing thin foils is very often implemented as an imaging system for transverse beam size measurements. When OTR was developed for the first time at the CERN SPS [11], OTR photons were measured by a Photo Multiplier Tube (PMT) and successfully served ed as *fast* spill monitor. Such a detector is intrinsically fast. The photon's emission can be considered as instantaneous, and the overall monitor BW would then be limited by the PMT rise and decay times and its readout electronics.

In 2021, an existing installation in the SPS TT20 line was refurbished with a new (movable) Titanium screen, a fast PMT [12] (anode with pulse rise time equal to 0.8 ns) and a wide BW (300 MHz) DC-coupled amplifier. The signal from the amplifier output in the tunnel is brought to the surface via 250 m CK50 cables, for which the specified attenuation is >7dB/100 m at 200 MHz. At the moment the signal digitisation is done via a fast oscilloscope (500 MHz analogue BW, 5 GS/s, 2 GS of memory). The detector layout overlaid on a picture of the present installation in TT20 is shown in Fig. 3.

Table 2 summarises a simulation performed to estimate the expected number of photons at the PMT photo-cathode. For a SPS physics beam of 3×10^{13} protons/spill, the calculations yield to about 15 photons/ns collected at the photo-cathode, which is considered suitable for monitoring at high rate (e.g. at 200 MHz as proposed.

The new system was successfully commissioned in 2022. From the beginning it was possible to reconstruct the spill intensity (see section below for comparison to the SEM detector) and monitor the beam power spectrum at least up to 200 MHz (see Fig. 4) even with the OTR screen in the retracted position. This suggests that the PMT detector, placed at ≈ 1 m from the beam axis, is sensitive to beam losses. Indeed, preliminary studies based on scanning the

Content from this work may be used under the terms of the CC BY 4.0 licence (© 2022). Any distribution of this work must maintain attribution to the author(s), title of the work, publisher, and DOI

ISBN: 978-3-95450-241-7 ISSN: 2673-5350 doi:10.18429/JACoW-IBIC2022-WE3C3

Content from this work may be used under the terms of the CC BY 4.0 licence (© 2022). Any distribution of this work must maintain attribution to the author(s), title of the work, publisher, and DOI

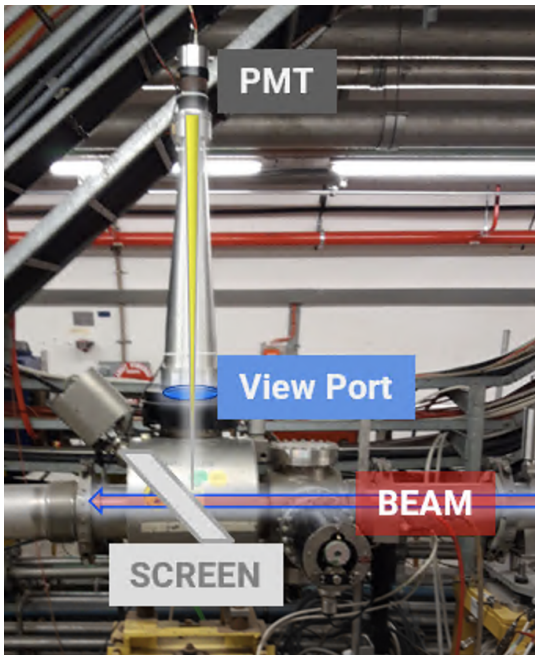


Figure 3: SPS OTR-PMT in the SPS TT20 beam line.

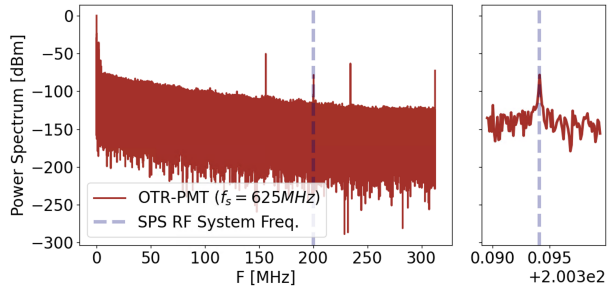
Table 2: Input parameters and main results of the simulation for the OTR-PMT optical system (see Fig. 3).

Input	
Protons Lorentz factor	$\gamma = 480$
OTR source ∅ (on foil)	5 mm
Source wavelength	550 nm
Foil - PMT distance	1 m
PMT photo-cathode acceptance (= top ∅ of the cone in Fig. 3)	40 mm
Output	
# of photons (500 nm≤ λ ≤600 nm)	3.78×10^{-3} ph/p
Photons collection at photo-cathode	61%

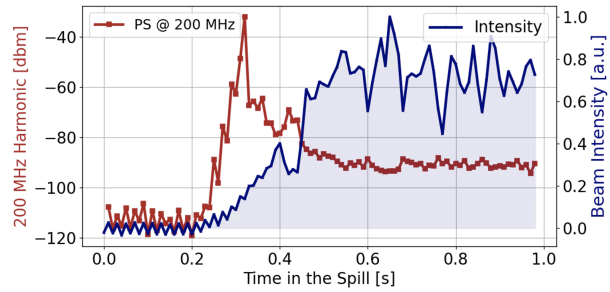
PMT voltage with the screen IN and OUT evidenced a signal gain with screen IN of only about 30 % to 40 %.

FAST SPILL MONITORS COMPARISON

The fast spill monitors based on Secondary Emission and OTR-PMT could be compared while measuring the same extracted beam, of $\approx 3 \times 10^{13}$ p/spill). A first example is shown in Fig. 5. While measuring the 4.8 s spill, the sampling frequency was set to 50 kHz. for the SEM and 1 MHz for the OTR-PMT. The data was then integrated off-line in bins of 1 ms for both monitors. The top plot demonstrates the excellent agreement in measuring the spill intensity envelope. The bottom plot highlights the capability for both instruments to identify low frequency harmonics, like the 50 and 100 Hz known to originate from noise in the magnets power supplies, and to affect the spill intensity. A second example, in Fig. 6, shows that the agreement between the two monitors is still excellent while looking at 50 kHz data.



(a) Left: Harmonics calculated over a 10 ms time window. Right: zoom around the SPS RF frequency at 200 MHz



(b) Evolution of the beam power measured at 200 MHz during the first part of the spill with the relative beam intensity extracted from the total PMT signal amplitude. Each point corresponds to a 10 ms integration time.

Figure 4: Example of SPS slow extracted beam power spectrum, measured with the OTR-PMT system.

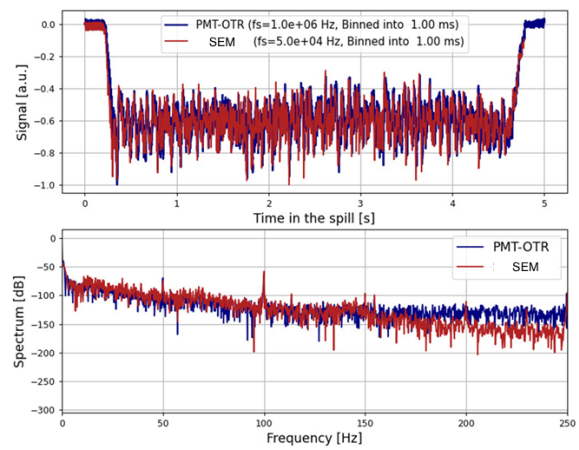


Figure 5: SEM and OTR-PMT detectors comparison in time and (low) frequency domain.

CONCLUSION AND OUTLOOK FOR FUTURE DEVELOPMENTS

Existing SPS Systems

Secondary Emission Monitor The SEM monitor at the beginning of TT20 is very robust and remains for the moment the only fully integrated spill monitor into the SPS control system and used operationally to minimise frequency ripple magnet power supplies. An upgrade of the in-vacuum parts of the monitor is foreseen, as this part is suspected to be a source of high noise in th system.. The DAQ will also

ISBN: 978-3-95450-241-7 ISSN: 2673-5350 doi:10.18429/JACoW-IBIC2022-WE3C3

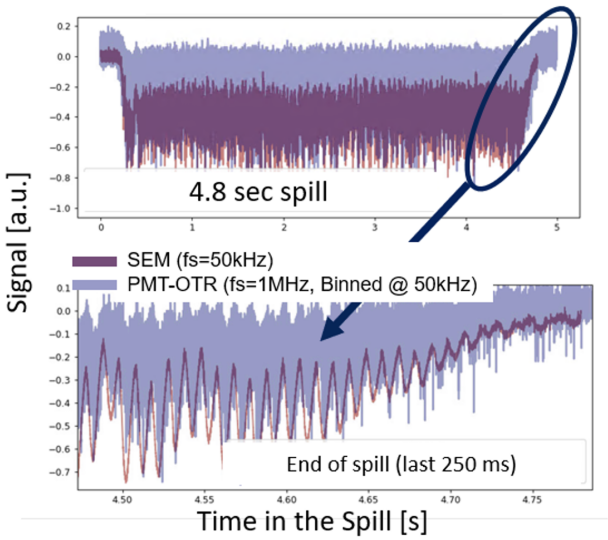


Figure 6: (top) SEM and OTR-PMT detectors comparison at 50 kHz acquisition rate, (bottom) zoom.

be upgraded to ensure higher analogue BW (~10 MHz max) and sampling rate.

Diamond BLM monitor dBLMs proved to work well, especially to study high frequency (up to 300 MHz) spill fluctuations. Their main limitations are signal-to-noise ratio and the management of the data acquired at 650 MS/s, for which only a portion of the spill (few ms) can be stored during each SPS cycle. Diamond BLMs will certainly continue to be exploited operationally as fast spill monitors and for cross calibration of other instruments.

OTR-PMT Monitor The prototype OTR-PMT detector was successfully commissioned with beam in 2022 and its performance were fully bench-marked with the SEM monitor up to 50 kHz. The dtectioon seet-up will be modified moving the PMT away from the beam line such that it will not be sensitive to beam losses. In that configuration, it is expected that the PMTs bias voltages can be increased to further improve on signal-to-noise ratio.

With the present DAQ architecture, the overall BW is limited to ≈500 MHz. In order to explore the GHz regime interesting for the CERN PBC program, we are studying the options of the signal digitisation in the SPS tunnel, and usage of optical link to transfer the data to the front-end computer.

New developments

Cherenkov proton Flux Monitor (CpFM) In 2016 - 2019, a new proton flux detector was developed by the UA9 collaboration [13] in the framework of the *crystal-assisted* slow extraction studies. The monitor (see Fig. 7) is based on a fused silica bar inserted on demand into the proton beam. The bar, acting as Cherenkov radiation source and light-guide, is coupled via a vacuum tight view port to an optical fibre bundle, bringing the light to a photo-multiplier detector. A second bar, installed in the retracted position, was used for systematic background subtraction. The system was validated in the SPS ring, and later in the TT20 line. At this location, it was optimised to work as a fast spill monitor [14]. In 2018 the CpFM was successfully tested with a 2 GS/s, 500 MHz BW digitiser. The measured data were processed to extract the 200 MHz harmonic component from the beam signal.

As Cherenkov radiation provides a larger flux of photons compared to OTR, that system could be one of the candidates for very fast monitoring (e.g. in the > 1 GHz regime) required for future PBC experiments. The CpFM will soon be put back in operation equipped with a CERN standard detection systems similar to the one used for the OTR-PMT detector.

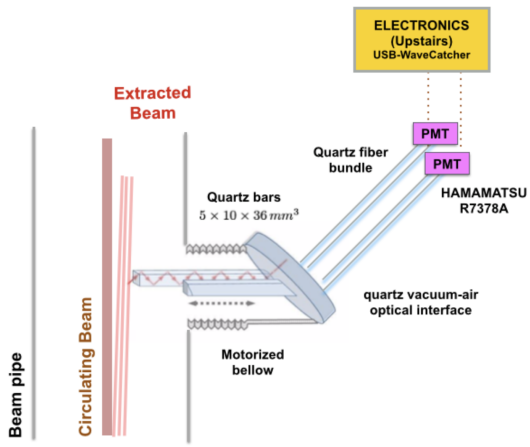


Figure 7: CpFM monitor layout (courtesy of F. Addesa).

Gas Scintillation detector For many years, the CERN Proton Synchrotron (PS) slow extracted beam to the East Area (EA) experimental lines is monitored by a gas scintillation detector. It is composed of a small chamber, separated from the upstream and downstream vacuum beam lines, fed with a constant flow of Nitrogen. The 24 GeV PS beam generates a gas scintillation (decay time ≈10 ns monitored by two PMTs (in coincidence to suppress background). The 10 ns analogue pulses are converted to NIM-standard (30 ns, −1 V) and sampled at 2 kHz. The suitability of this technique for the 400 GeV SPS beam is under investigation.

Timepix detector A novel fast spill detector technique could be based on the design of Timepix ionisation profile monitors [15] with the addition of focusing electrodes[4]. The detector response time (≤5 ns) and preliminary calculations on the expected ionized electrons yield makes this technique potentially exploitable for measurements at least up to 200 MHz.

REFERENCES

[1] Y. Baconnier, P. Faugeras, K. H. Kissler, B. de Raad, and W. Scandale, "Extraction from the cern sps," *IEEE Transactions on Nuclear Science*, vol. 24, no. 3, pp. 1434–1436, 1977. doi:10.1109/TNS.1977.4328969

[4] Inspired by the development described in [16]

Content from this work may be used under the terms of the CC BY 4.0 licence (© 2022). Any distribution of this work must maintain attribution to the author(s), title of the work, publisher, and DOI

ISBN: 978-3-95450-241-7 ISSN: 2673-5350 doi:10.18429/JACoW-IBIC2022-WE3C3

Content from this work may be used under the terms of the CC BY 4.0 licence (© 2022). Any distribution of this work must maintain attribution to the author(s), title of the work, publisher, and DOI

[2] F. M. Velotti *et al.*, "Characterisation of SPS Slow Extraction Spill Quality Degradation," in *Proc. IPAC'19*, Melbourne, Australia, May 2019, pp. 2403–2405. doi:10.18429/JACoW-IPAC2019-WEPMP034

[3] M. Pari, F. M. Velotti, M. A. Fraser, V. Kain, and O. Michels, "Characterization of the slow extraction frequency response," *Phys. Rev. Accel. Beams*, vol. 24, no. 8, p. 083 501, 2021. doi:10.1103/PhysRevAccelBeams.24.083501

[4] V. Kain *et al.*, "SPS Slow Extracted Spill Quality During the 2016 Run," in *Proc. IPAC'17*, Copenhagen, Denmark, May 2017, pp. 627–630. doi:10.18429/JACoW-IPAC2017-MOPIK049

[5] F. Roncarolo, "Status and plans for beam instrumentation for SX at CERN," presented at ICFA Mini-Workshop on Slow Extraction. https://conference-indico.kek.jp/event/163/contributions/3160/

[6] H. Frais-Kolbl, E. Griesmayer, H. Kagan, and H. Pernegger, "A fast low-noise charged-particle cvd diamond detector," *IEEE Trans. Nucl. Sci.*, vol. 51, no. 6, pp. 3833–3837, 2004. doi:10.1109/TNS.2004.839366

[7] E. Calvo Giraldo *et al.*, "The Diamond Beam Loss Monitoring System at CERN LHC and SPS," presented at IBIC'22, Kraków, Poland, Sep. 2022, paper TU2C2, this conference.

[8] B. Dehning, E. Effinger, H. Pernegger, D. Dobos, H. Frais-Kolbl, and E. Griesmayer, "Test of a Diamond Detector Using Unbunched Beam Halo Particles," CERN, Geneva, Switzerland, Tech. Rep., 2010. https://cds.cern.ch/record/1258407

[9] E. Effinger *et al.*, "A Prototype Readout System for the Diamond Beam Loss Monitors at LHC," in *Proc. IBIC'13*, Oxford, UK, Sep. 2013, pp. 182–185. https://jacow.org/IBIC2013/papers/MOPC45.pdf

[10] P. A. Arrutia Sota *et al.*, "dBLMs first results and MD planning," presented at CERN SLAWG meeting, 2022.

[11] J. Bosser, J. Mann, G. Ferioli, and L. Wartski, "Optical transition radiation proton beam profile monitor," *Nucl. Instrum. Methods Phys. Res., A*, vol. 238, 45–52. 23 p, 1984. doi:10.1016/0168-9002(85)91025-3

[12] Hamamatsu PMT R3377. https://www.hamamatsu.com/content/dam/hamamatsu-photonics/sites/documents/99_SALES_LIBRARY/etd/R2083_R3377_TPMH1227E.pdf

[13] UA9 Collaboration. https://home.cern/science/experiments/ua9

[14] F. M. Addesa, "In-vacuum Cherenkov light detectors for crystal-assisted beam manipulations," PhD thesis, Rome University, Rome, Italy, 2018. https://cds.cern.ch/record/2661725

[15] J. W. Storey *et al.*, "First Results From the Operation of a Rest Gas Ionisation Profile Monitor Based on a Hybrid Pixel Detector," in *Proc. IBIC'17*, Grand Rapids, MI, USA, Aug. 2017, pp. 318–322. doi:10.18429/JACoW-IBIC2017-WE2AB5

[16] The LHCb-RICH pixel hybrid photon detector. http://tilde-gys.web.cern.ch/~gys/LHCb/PixelHPDs.htm

ISBN: 978-3-95450-241-7 ISSN: 2673-5350 doi:10.18429/JACoW-IBIC2022-WE3C4

SIMULATED BEHAVIOR OF CNT WIRES IRRADIATED IN THE HiRadMat EXPERIMENTAL LINE AT CERN

A. Mariet*, B. Moser, R. Veness, CERN, Geneva, Switzerland
M. Devel, FEMTO-ST institute (UBFC, CNRS), ENSMM, Besançon, France
J.E. Groetz, Chrono Environnement (UFC, CNRS), Besançon, France
A. Mikhalchan, J. J. Vilatela, IMDEA Materials Institute, Madrid, Spain

Abstract

With the planned increase of luminosity at CERN for HL-LHC and FCC, instruments for beam quality control must meet new challenges. The current wires, made up of plain carbon fibers and gold-plated tungsten would be damaged due to their interactions with the higher luminosity beams. We are currently testing a new and innovative material, with improved performance: carbon nanotube fibers (CNTF). The HiRadMat (High Radiation for Material) experimental line at the output of the SPS is a user facility which can irradiate fix targets up to 440 GeV/c. CNTF with various diameters were irradiated in HiRadMat with different intensities, later imaged with a SEM microscope and tested for their mechanical properties. In addition, simulations have been carried out with the FLUKA particle physics Monte-Carlo code [1], in order to better understand the mechanisms and assess the energy deposition from protons at 440 GeV/c in those CNTF wires, depending mainly on their diameters and densities. This could lead to a good estimation of the CNTF temperature during irradiation. In this contribution, we first present the HiRadMat experimental setup and then we discuss the results of our FLUKA simulations.

INTRODUCTION

The search for performance in particle accelerators and in particular the increase in luminosity [2] pushes the engineering of beam instrumentation to be always at the cutting edge of technology. The precision of the quality control of the beams throughout their acceleration is paramount. Transverse profile monitoring is particularly challenging as it is often based on intercepting devices such as wire-scanners and SEM grids. Operational systems at CERN [3] typically use wire made out of carbon fiber and gold-plated tungsten. These materials in the form of wires are subjected to high mechanical and thermal stresses due to the energy deposited by the particles in the material. The physical properties of those materials have reached their limits for very high beam energies / intensities such as those obtained in the CERN Super Proton Synchrotron (SPS) and Large Hadron Collider (LHC) . The search for new and innovative materials that could be used in all beam conditions has therefore become a necessity. By their exceptional properties, carbon nanotubes, existing in the form of microscopic fibers, seem to be an ideal candidate. This paper presents, together with energy deposition simulations, the setup of an experiment performed at the HiRadMat beam line at CERN for the irradiation of carbon nanotube wires (CNT) with high intensity proton beams at 440 GeV/c [4, 5].

WIRE MANUFACTURING

CNT were produced at the IMDEA by floating catalyst chemical vapor deposition (FCCVD) in a reactor tube of mullite ceramic (SiO_2) heated to 1570 K with toluene (C_7H_8) and ferrocene ($Fe(C_5H_5)_2$) as carbon and iron source respectively. The carrier gas was hydrogen (H_2). The CNT obtained are mainly double or few multiwalls and some hundreds of µm long. The assembly of individual tubes to form a microscopic fiber (CNTF) occurred in the gas phase during growth. CNT entangle and form a dark aerogel which is drawn through and out of the reactor tube. This aerogel of CNT deposits on the winder to produce a fiber [6, 7] (Fig. 1-a and b). The diameter of the final fiber is controlled by varying the spinning rate of the winder, from 7 m/min for the thick diameters, to 28 m/min for the thin diameters.

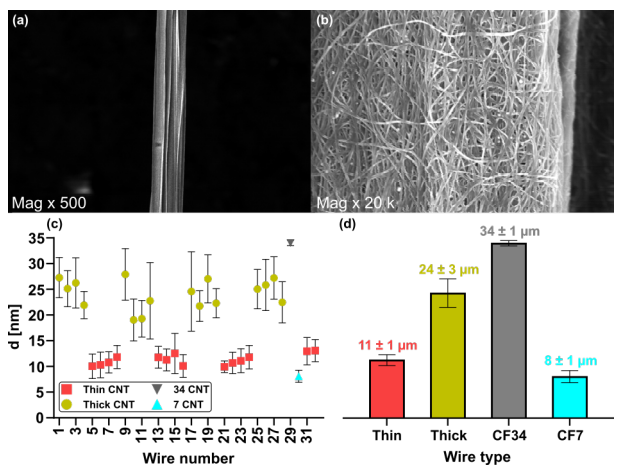


Figure 1: SEM pictures of an as-spun CNTF with a magnification of (a) x500 and (b) x20000; (c) Summary of the average diameters of each sample; (d) mean values in diameter for the thin and thick CNT fibers and average diameter for the 34 and 7 µm carbon fiber. CF stands for Carbon Fiber.

The diameter of the samples was estimated by 30 measurements all along the axis of the wires. Figure 1-d shows the average diameter of the 32 wires with the standard deviation. The red bar represents thin wires and shows an average diameter of 11 µm, the green bar the thick wires with 24 µm diameter and the grey and blue bars the 34 and 7 µm diam-

* alexandre.mariet@cern.ch

Content from this work may be used under the terms of the CC BY 4.0 licence (© 2022). Any distribution of this work must maintain attribution to the author(s), title of the work, publisher, and DOI

ISBN: 978-3-95450-241-7 ISSN: 2673-5350 doi:10.18429/JACoW-IBIC2022-WE3C4

Content from this work may be used under the terms of the CC BY 4.0 licence (© 2022). Any distribution of this work must maintain attribution to the author(s), title of the work, publisher, and DOI

eter carbon fiber respectively that are currently considered for wire-scanners.

EXPERIMENTAL SET-UP

Main Purpose

The HiRadMat beam line at CERN offers the possibility of testing and irradiating materials with protons extracted from the SPS. The facility can be tuned to provide a very wide range of beam parameters (momentum (p), beam size (σ_b), number of bunch (N_b), bunch intensity (I_b)) from low to high beam densities.

The purpose of the **CNT Yarn Characterization at High Irradiation** (CYCHI) is to irradiate carbon nanotube fibers and validate up to which extreme conditions they could replace the current carbon wire in Wire Scanners.

Two family of carbon fibers, with 7 and 34 µm were installed and tested using high momentum (440 GeV/c protons and an increasing intensity per beam up to $3.2{\cdot}10^{13}$ protons per beam. After irradiation, the fibers will be tested in tension.

CYCHI was conceived to re-use standard hardware components from the CERN beam instrumentation group (i.e. SEM grid and Beam TeleVision) that will be mounted on a custom vacuum tank closed by CF flanges and glassy carbon windows (Fig. 2).

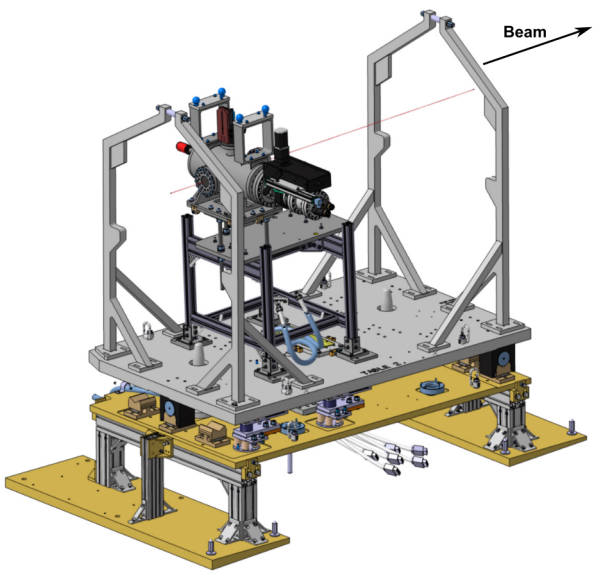


Figure 2: CYCHI experimental setup - (a) CAD model of CYCHI installed on the table B; (b) HiRadMat experimental line in the tunnel.

SEM Grid

Principle: The Secondary Electron Emission grid (SEM) is an instrument commonly used at CERN for measuring transverse beam profiles. The principle is to use a grid of wires spaced by a given distance. When the beam crosses the grid, the interaction between the particles and the wire creates secondary electron emission (SEM). As the diameter of the wires is the same, the number of secondary electrons emitted from each wire is proportional to the number of interacting particles such that a beam profile can be reconstructed by plotting the SEM current for each wire.

In CYCHI, a SEM grid is used as a support to irradiate different CNTFs. The distance between each CNTF is set to 4 mm, a distance large enough compared to the beam size in Hiradmat such that neighboring wires are not impacted during the irradiation test.

Wire support: The design of the grid was conceived not only as mechanical support but it also incorporates an electric circuit. Each wire was connected to a common ground via a 1 MΩ resistor with which it was possible to verify the state of the wire within the vacuum chamber. The support was made out of glass composite material and produced as a PCB (Fig. 3-a). In addition, two polarization plates in stainless steel, crossed by high voltage, are installed on both side of the grids to collect the secondary electrons (Fig. 3-b).

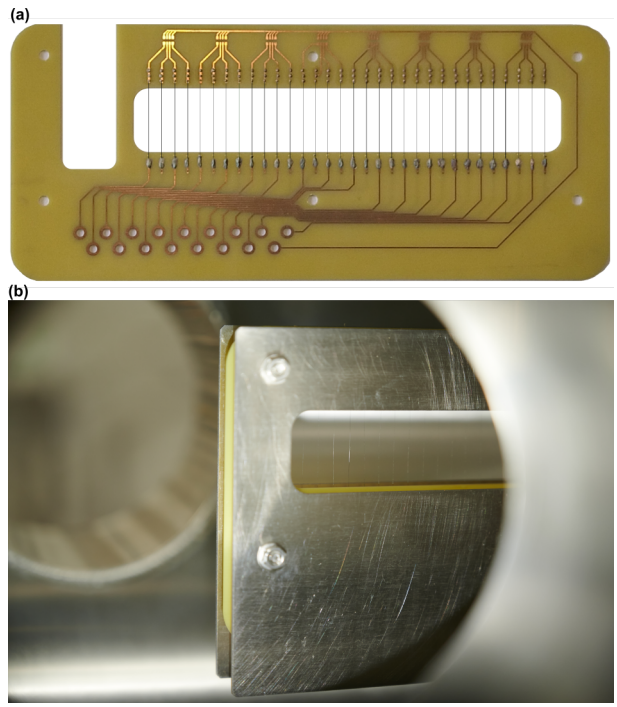


Figure 3: Experimental grid - (a) PCB and electronic outline of the support, tracks and resistors.; (b) Grid with polarisation plates mounted in the vacuum tank.

BTV

A Beam TeleVision (BTV) combines a fluorescent screen oriented at 45° from the beam axis with a camera placed on the top of the screen which captures the light produced by the interaction between the beam and the screen. The screen is composed of Chromox (99.5% of Al_2O_3) and 0.5% of Cr_2O_3), 500 µm thick, mounted on an aluminium support. Four small slits have been machined close to the edges of screen to monitor where its center is and provide a position

ISBN: 978-3-95450-241-7 ISSN: 2673-5350 doi:10.18429/JACoW-IBIC2022-WE3C4

reference for further measurements. By comparing the beam position measured on this screen and on another BTV placed downstream on the beam line, a precise positioning of the wires can be done, ensuring the protons cross the wires in its middle (Fig. 4).

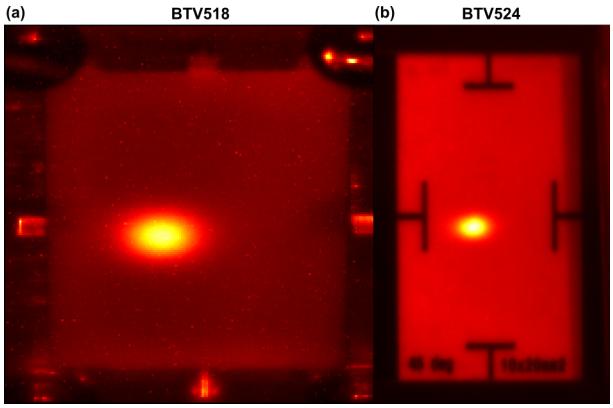


Figure 4: Beam image comparison for alignment - (a) raw BTV518 image; (b) image from reference BTV.

For each wire, the beam intensity was progressively increased from 1 to 10 pulses of 288 bunches, with a nominal number of protons per bunch of $1.1{\cdot}10^{11}$. The beam size on the wire was measured by the BTV. It was chosen to be $\sigma_h = \sigma_v = 0.25$ mm for the first part of the experiment and 0.50 mm for the second part.

Beam-Wire Interaction

This section is a theoretical estimation of the beam-CNTF interaction. Secondary electron emission is a surface phenomenon [8]. The signal measured by the SEM grid is directly function of the number of particles interacting with the wire. The fraction of the beam crossing the wire can be deduced from the horizontal relative alignment of the beam to the wire, the diameter of the wire, the horizontal beam size and the beam intensity. The intensity in the wire is expressed by

$$I_w = I_{beam}\frac{1}{2}\left[\mathrm{erf}\left(\frac{\frac{d_w}{2}-\mu}{\sigma_h\sqrt{2}}\right)+\mathrm{erf}\left(\frac{\frac{d_w}{2}+\mu}{\sigma_h\sqrt{2}}\right)\right], \quad (1)$$

where d_w is the diameter of the wire, μ the horizontal gaussian center of the beam, σ_h the horizontal beam size and *erf* the error function.

The real beam sizes were measured at 0.28 mm and 0.56 mm and the intensity of the beam between 2.66 and $3{\cdot}10^{13}$. Considering the measured values of beam size and intensity, the average numbers of protons crossing the wire I_w for nominal beam size of 0.25 mm are $4.28{\cdot}10^{11} \pm 3{\cdot}10^{10}$ and $8.68{\cdot}10^{11} \pm 1.20{\cdot}10^{11}$ for thin and thick wires respectively. The numbers for a nominal beam size of 0.50 mm are $2.21{\cdot}10^{11} \pm 2.69{\cdot}10^{10}$ and $4.62{\cdot}10^{11} \pm 4.35{\cdot}10^{10}$ for thin and thick wires respectively.

The number of interactions can be calculated by

$$N_{int} = I_w\left(1-\exp\left(-\frac{d_w\pi}{4}\frac{\rho\mathcal{N}_A\sigma_i}{M}\right)\right), \quad (2)$$

where ρ is the density of the material, $\mathcal{N}_A$ the Avogadro number, σ_i the inelastic collision cross section (σ_i = 209.8 mbarn) and M the molar mass of the fiber. For CNTF with 10% of iron as a weight fraction, the density was estimated at 1.42 g/cm^3, the molar mass at 13.03 g/mol and the effective Z at 6.47. The average number of interactions is summarized in Table 1.

Table 1: Number of Interactions Proton / Wire

d [µm]	Beam size [mm] 0.25	0.5
11	$5.21{\cdot}10^9$	$2.69{\cdot}10^9$
24	$2.29{\cdot}10^{10}$	$1.22{\cdot}10^{10}$

ENERGY DEPOSITION IN CNT

FLUKA Calculation

The assessment of energy deposited into the CNTF was performed with the FLUKA Monte-Carlo simulation code. Energy transfer from protons to the material wire at such a momentum (440 GeV/c) cannot be described only with the Bethe-Block formula, but needs to consider high energy secondary electrons, namely delta electrons. In the present case, the maximum energy for these secondaries could reach up to 149 GeV [9], meaning that they can be ejected from a very thin wire and do not contribute to the total energy loss into the material [10]. The threshold for delta ray consideration tracking was set to δ = 1 keV, a useful limit to consider also the influence between wires in a SEM grid configuration and the secondary emission yield (SEY). To illustrate the importance of this threshold, the energy deposition at δ = 1 keV was 4.15 keV, while with δ = 150 GeV the deposited energy was 6.41 keV, showing an increase of about 54%.

We consider a typical density of 1.3 g/cm^3 for this kind of full carbon CNTF. This is significantly lower compared to the one of carbon fiber (1.7 g/cm^3) currently used in wire-scanners. In both cases, the energy deposition is considerably reduced compared to a graphite wire from 7.64 keV (ρ = 2 g/cm^3) [11] to 4.15-4.50 keV.

The SEY was calculated using the following relation:

$$\mathrm{SEY} = 0.01L_s\frac{dE}{dx}\left[1+\frac{1}{1+5.4\cdot10^{-6}E/M_p}\right], \quad (3)$$

with $L_s = 3.68\cdot10^{-17}NZ^{1/3}$ the characteristic length describing the diffusion of low energy electrons, E and M_p the incident energy and mass of protons, N and Z are respectively the number of atoms per unit volume and the atomic number of the material. From the SEY, it is possible to assess the charge generation per incident proton Q(e/H) for a single CNTF, where Q(e/p) = 2SEY. This value multiplied by the real number of protons crossing the wire will be compared with the produced signal in the instrument. The deposited energy and the secondary emission yield obtained

Content from this work may be used under the terms of the CC BY 4.0 licence (© 2022). Any distribution of this work must maintain attribution to the author(s), title of the work, publisher, and DOI

ISBN: 978-3-95450-241-7 ISSN: 2673-5350 doi:10.18429/JACoW-IBIC2022-WE3C4

by the Fluka simulations for both diameters are summarized in the Table 2.

Table 2: Deposited Energy per Incident Proton into a CNT Wire and Secondary Emission Yield (SEY) for Two Compositions, Carbon and Carbon with 10% Fe as Weight Fraction

	Carbon (ρ = 1.30 g/cm^3)		Carbon + 10% Iron (ρ = 1.42 g/cm^3)	
d [µm]	**dE [eV/p]**	**SEY [/p/cm^2]**	**dE [eV/p]**	**SEY [/p/cm^2]**
11	1987	$4.15 \cdot 10^{-3}$	2151	$4.35 \cdot 10^{-3}$
24	4475	$4.28 \cdot 10^{-3}$	4850	$4.50 \cdot 10^{-3}$

Temperature Calculation

The Fluka simulations give a total deposited energy of 2150 eV with a peak at 1423 eV for a fiber of 11 µm and 4850 eV with a peak at 3514 eV for a fiber of 24 µm (Fig. 5). The maximum temperature, located at the center of the wire, can be conservatively estimated (no cooling consideration) by

$$T_{max} = T_{amb} + \frac{N_{int} E_{dep}}{\rho c_p d_w} \frac{1}{2\pi\sigma_x\sigma_y}, \quad (4)$$

with T_{amb} the ambient temperature setup at 300 K, $N_p = 3.2 \cdot 10^{13}$ the total number of protons and $c_p = 1.3$ J/g/K for pure carbon and $c_p = 0.5$ J/g/K for the CNT with iron (average value of the heat capacity between 300 and 1000 K for for both material).

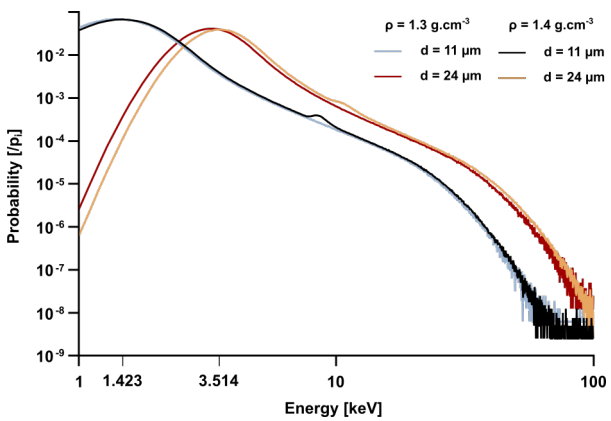


Figure 5: Energy deposition - Probability of a 440 GeV/c incident proton to deposit some energy in wires composed of pure carbon (ρ = 1.3 g/cm^3) in blue and red and composed of carbon and 10% in weight of iron (ρ = 1.42 g/cm^3) in black and orange of 11 and 24 µm in diameter.

The results on the maximum temperature calculated for a beam size of 0.25 mm show a significant impact of the material composition (Table 3). The presence of iron in the material allow a higher deposition of energy, but the main parameter responsible of the increase by a factor 2.2 is the lower heat capacity of iron. This indicates that the presence of few catalytic particles contributes to a massive risk of overheat compared with pure carbon. The comparison between the CNT and the carbon as structural difference is not possible with the fluka code. Thus, only the diameter and the density are variable parameters.

Table 3: Maximum Temperature of Various Samples in Diameter and Density for a Irradiation with a Beam Size of 0.25 mm

d [µm]	**Maximum temperature [K]** ρ = 1.30	ρ = 1.42	ρ = 1.70
11	1694	3813	-
24	1739	3933	-
7	-	-	1665
34	-	-	1756

All these results have to be considered carefully for many reasons : 1- the Monte Carlo simulations needs to have a high number of events to be statistically robust. The simulated deposited energy depends directly from that. 2- The specific heat capacity depends widely on the temperature (from 0.7 to 2.3 J/g/K for temperature between 300 and 4000 K). 3- The cooling mechanisms are complex and depends also on the temperature. 4- The thermal parameters (conductivity, emissivity) of the CNT fibers are incompletely known.

CONCLUSION

The use of carbon nanotubes for beam instrumentation is still in its infancy. The analysis of the physical and mechanical properties after irradiation as a function of the intensity at such energies has never been done. In order to predict the response in terms of secondary electrons produced for the SEM grid signal and the lifetime of the sample due to the increase in temperature, numerical simulations using a Fluka code were performed. It has been shown that the energy deposited in the wire decreases with wire diameter and increases with density. Secondary electron production also increases with increasing diameter and density. We therefore expect to observe a greater signal for thick wires than for thin wires. The simulated temperatures increase drastically for the CNTF with iron, mainly due to the lower heat capacity of iron. These temperatures should induce a change in the structure of the samples without destroying it by sublimation.

ACKNOWLEDGMENTS

The authors would like to thank all colleagues who contributed to the CYCHI project and to thank the HiRadMat team and SPS operation crew for their logistical and technical support.

REFERENCES

[1] G. Battistoni *et al.*, "The FLUKA code: description and benchmarking", *AIP Conf. Proc.*, vol. 896, pp.31–76, 2007. doi:10.1063/1.2720455

Content from this work may be used under the terms of the CC BY 4.0 licence (© 2022). Any distribution of this work must maintain attribution to the author(s), title of the work, publisher, and DOI

ISBN: 978-3-95450-241-7 ISSN: 2673-5350 doi:10.18429/JACoW-IBIC2022-WE3C4

[2] G. Apollinari *et al.*, "High luminosity large hadron collider HL-LHC", 2017. doi:10.48550/arXiv.1705.08830

[3] R. Veness *et al.*, "Experience From the Construction of a New Fast Wire Scanner Prototype for the CERN- SPS and its Optimisation for Installation in the CERN-PS Booster", in *Proc. IBIC'15*, Melbourne, Australia, Sep. 2015, pp. 479–482. doi:10.18429/JACoW-IBIC2015-TUPB061

[4] F. J. Harden, A. Bouvard, N. Charitonidis, and Y. Kadi, "HiRadMat: A Facility Beyond the Realms of Materials Testing", in *Proc. IPAC'19*, Melbourne, Australia, May 2019, pp. 4016–4019. doi:10.18429/JACoW-IPAC2019-THPRB085

[5] I. Efthymiopoulos *et al.*, "HiRadMat: A New Irradiation Facility for Material Testing at CERN", in *Proc. IPAC'11*, San Sebastian, Spain, Sep. 2011, paper TUPS058, pp. 1665–1667.

[6] A. Mikhalchan *et al.*, "Simultaneous improvements in conversion and properties of molecularly controlled CNT fibres", *Carbon*, vol. 179, pp. 417–424, 2021. doi:10.1016/j.carbon.2021.04.033

[7] B. Alemán *et al.*, "Strong Carbon Nanotube Fibers by Drawing Inspiration from Polymer Fiber Spinning", *ACS Nano*, vol. 9, pp. 7392–7398, 2015. doi:10.1021/acsnano.5b02408

[8] E. J. Sternglass, "Theory of Secondary Electron Emission by High-Speed Ions", *Phys. Rev.*, vol. 108, pp. 1–12, 1957. doi:10.1103/PhysRev.108.1

[9] K Nakamura and (Particle Data Group), "Review of Particle Physics", *J. Phys. G: Nucl. Part. Phys.*, vol. 37, p. 075021, 2010. doi:10.1088/0954-3899/37/7A/075021

[10] H. Bigland *et al.*, "Wire Materials for Scanners in the Large Hadron Collider: An Unusual Materials Selection Problem", *Adv. Eng. Mater.*, 2019. doi:10.1002/adem.201900927

[11] M. Sapinski, "Model of Carbon Wire Heating in Accelerator Beam", CERN, Geneva, Switzerland, Rep. CERN-AB-2008-030-BI, 2008.

Content from this work may be used under the terms of the CC BY 4.0 licence (© 2022). Any distribution of this work must maintain attribution to the author(s), title of the work, publisher, and DOI

ISBN: 978-3-95450-241-7 ISSN: 2673-5350 doi:10.18429/JACoW-IBIC2022-TH1I1

FIRST MEASUREMENT OF LONGITUDINAL PROFILE OF HIGH-POWER AND LOW-ENERGY H⁻ BEAM BY USING BUNCH SHAPE MONITOR WITH GRAPHITE TARGET

R. Kitamura* on behalf of J-PARC linac
JAEA/J-PARC, Tokai, Naka, Ibaraki, Japan

Abstract

A bunch-shape monitor (BSM) using the highly-oriented pyrolytic graphite (HOPG) target has been developed to measure the high-power and low-energy negative hydrogen ion beam at the front-end. The performance evaluation of the BSM using the HOPG target was conducted. The first measurement of longitudinal beam profiles at the front-end was demonstrated with the BSM. The measurement was consistent with the design simulation of the front-end. As a further application, the BSM using the HOPG target will be an attractive and powerful instrument to study the space-charge effect at the front-end.

INTRODUCTION

The Japan proton accelerator research complex (J-PARC) [1] linac supplies the 400-MeV negative hydrogen ion (H^-) beam to subsequent accelerators and experimental facilities. Recently, the user operation with a peak current of 50 mA was stable by the careful maintenance and beam tuning. Detailed beam studies are being conducted to reduce the beam loss towards higher power and the robustness of the stable operation. The medium-energy beam transport 1 (MEBT1) is important for the beam tuning of the linac. Figure 1 shows the configuration of the MEBT1. There are two functions of MEBT1 as follows. One is the beam matching between a 3-MeV radio-frequency quadrupole (RFQ) linac and a subsequent 50-MeV drift-tube linac. The other is the production of the bunch time structure for the injection into the rapid-cycle synchrotron. Since the parameters of the MEBT1 should be tuned to satisfy these requirements, the improvement of the longitudinal tuning in the MEBT1 is an interesting challenge to find a better solution for the high-power beam operation.

The bunch-shape monitor (BSM) [2,3] as the longitudinal beam profile monitor plays the important role to understand and improve the longitudinal beam dynamics in the MEBT1. However, the heat loading from the high-power and low-energy H^- beam in the MEBT1 caused the target failure of the BSM measurement which prevented the stable beam studies. We introduced the new graphite target for the BSM to mitigate the heat loading and successfully measured the longitudinal beam profiles in the MEBT1. In this report, the recent progress of the development of the BSM dedicated to the MEBT1 and its related studies are presented.

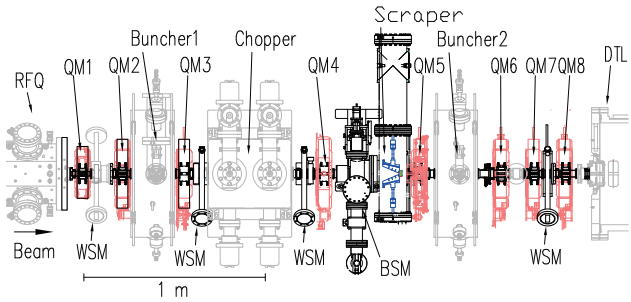


Figure 1: Configuration of the MEBT1.

NEW TARGETS FOR BSM

The BSM is a standard longitudinal beam profile monitor for the linac. Figure 2 shows the principle of the BSM. Secondary electrons are produced by the interaction between the H^- beam and the BSM target. The negative bias voltage is applied to the target to extract these secondary electrons into the deflector in the BSM. The electrons related to the longitudinal profile of the original H^- beam are modulated by the RF electric field in the deflector.

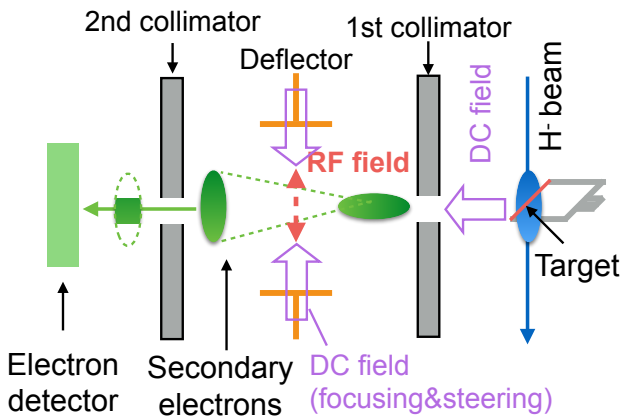


Figure 2: Principle of BSM.

The challenge of the BSM in the MEBT1 is to mitigate the heat loading from the high-power and the low-energy H^- beam. Therefore, we introduced a new strong target material for the BSM. There are three candidates for the BSM target as follows. One is the tungsten wire target, which is used as the standard target material for the usual BSM. However, the wire breaking frequently occurred due to heat loading in the MEBT1. Another candidate is a carbon nanotube (CNT)

* rkita@post.j-parc.jp

Content from this work may be used under the terms of the CC BY 4.0 licence (© 2022). Any distribution of this work must maintain attribution to the author(s), title of the work, publisher, and DOI

ISBN: 978-3-95450-241-7 ISSN: 2673-5350 doi:10.18429/JACoW-IBIC2022-TH1I1

wire [4, 5], which is used for the wire scanner monitor to measure the transverse profiles in the MEBT1. The advantage of the CNT is its low density. The effective heat loading to the target depends on the density of the target. The other candidate is the lamina graphite target. We used the highly-oriented pyrolytic graphite (HOPG) [6, 7] target, which is known as the candidate material of the beam scraper in the MEBT1. The advantage of the HOPG is its high thermal conductivity, which can reduce the thermal damage of the target.

Figure 3 shows the photographs of the CNT wire and the HOPG target mounted on the BSM target holder. Although the CNT is a good candidate for the BSM target, it is known as its electron emitter property. It is the disadvantage because the emission electrons cause the unexpected discharge of the bias voltage for the BSM target. Therefore, it should be confirmed whether the negative bias voltage is stably applied to the CNT wire. When the bias voltage was applied to the CNT wire, the luminescence from the insulator ceramics was observed. The spectrum peak due to emission electrons was detected by the spectroscopic measurement. As a result, the field electron emission from the CNT wire was inevitable and serious for the BSM operation.

On the other hand, the negative bias voltage was successfully applied to the HOPG target, which was a good characteristic as the BSM target. As described above, its high thermal conductivity is suitable to mitigate the heat loading from the high-power H^- beam. Therefore, we adopted the HOPG as the new target material of the BSM.

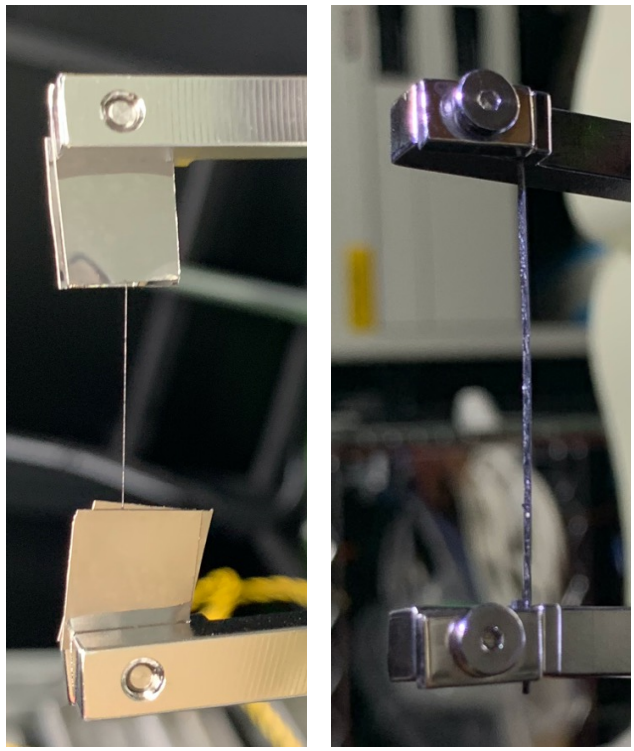


Figure 3: Photographs of the CNT wire (left) and HOPG (right) mounted on the BSM target holder. The diameter of the CNT wire is 0.1 mm and the size of the HOPG is a dimension of 0.2 mm(width)×1.0 mm(thickness)×48 mm(length).

STUDIES OF BSM USING GRAPHITE

The HOPG target is thicker than the original tungsten wire and the CNT wire. It should be confirmed whether the size of the HOPG target affects the measurement of the longitudinal profile. The test experiment was conducted at the test stand in the J-PARC linac building. The test stand consists of the 50-keV H^- ion source, the 3-MeV RFQ [8, 9], and the diagnostic beamline. The BSM was installed into the diagnostic beamline. Figure 4 shows the experimental setup of the test stand. The beam condition is as follows. The peak current, the energy, the pulse length, and repetition were 50 mA, 3 MeV, 50 μs, and 1 Hz, respectively, which was the almost same as the MEBT1.

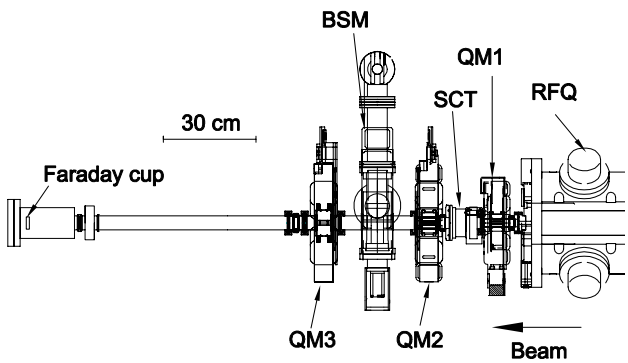


Figure 4: Configuration of the test stand.

Two types of HOPG targets were prepared, which were the small (0.2×1.0 mm^2) and the large (1.0×1.0 mm^2) targets. The minimum of the target size was determined by its cutting method (diamond wire sawing) [10]. The BSM target size affects the Time-of-Flight (ToF) of the extracted secondary electrons in the BSM. Therefore, it can be expected that the large target smears the longitudinal profile measured with the BSM. This ToF effect was estimated by the Geant4 simulation [11]. Figure 5 shows the comparison of longitudinal profiles measured with different sizes of HOPG targets. The profile corrected using the simulation was also shown in Fig. 5. Since the corrected profile with the target size of 0.2×1.0 mm^2 was consistent with the profile measured with that of 1.0×1.0 mm^2, we confirmed that the ToF effect could be evaluated with this procedure.

One advantage of the BSM using the HOPG target (HOPG-BSM) is to measure the longitudinal profile at any horizontal position. This implies the HOPG-BSM is not only the longitudinal profile monitor but also the both longitudinal and transverse profile monitor. In the first trial, we demonstrated the observation of the correlation between the longitudinal and transverse profiles under the space-charge effect. Figure 6 shows the longitudinal and horizontal profiles measured with the BSM when the quadrupole magnet was turned on and off. When the space-charge effect affects the beam profile, for example, it is expected that

Content from this work may be used under the terms of the CC BY 4.0 licence (© 2022). Any distribution of this work must maintain attribution to the author(s), title of the work, publisher, and DOI

ISBN: 978-3-95450-241-7 ISSN: 2673-5350 doi:10.18429/JACoW-IBIC2022-TH1I1

Content from this work may be used under the terms of the CC BY 4.0 licence (© 2022). Any distribution of this work must maintain attribution to the author(s), title of the work, publisher, and DOI

the transverse focusing affects longitudinal profile through space-charge force. From Fig. 6, we observed the correlation between the longitudinal phase and horizontal bunch profile. Although detailed studies are necessary, this result is attractive to understand the behavior of the high-power H^- beam at the front-end.

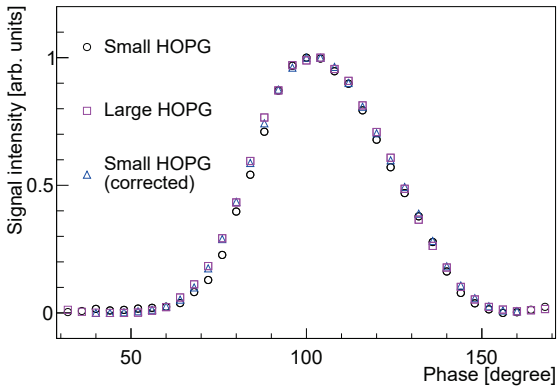


Figure 5: Comparison of longitudinal profiles measured with different size of HOPG targets.

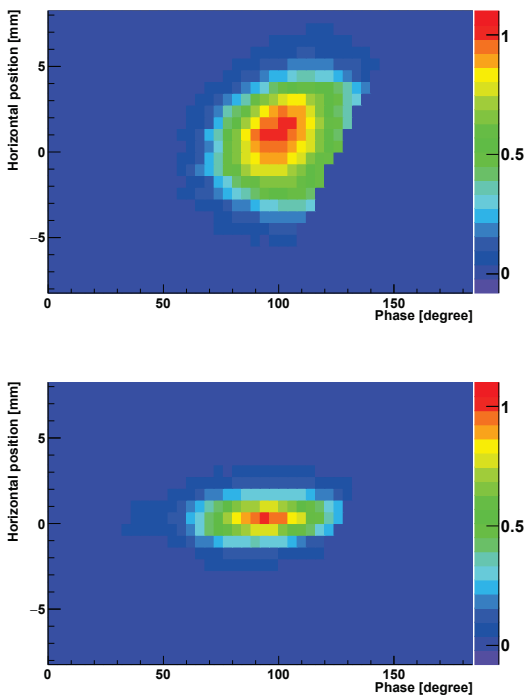


Figure 6: Longitudinal and horizontal profiles measured with the BSM. the top figure shows the profile tuning off the quadrupole magnet and the bottom figure shows that turning on the magnet.

FIRST LONGITUDINAL MEASUREMENT

The first measurement of the longitudinal beam profile in the MEBT1 was demonstrated with the HOPG-BSM. The peak current, the energy, the pulse length, and repetition in the measurement were 50 mA, 3 MeV, 100 µs, and 1 Hz, respectively. The longitudinal amplitude-scan method [12] with the buncher cavity was used to evaluate longitudinal beam parameters. The stable longitudinal measurement was realized thanks to the HOPG target. Figure 7 shows the typical waveform measured with the BSM. No target failure occurred during the measurement.

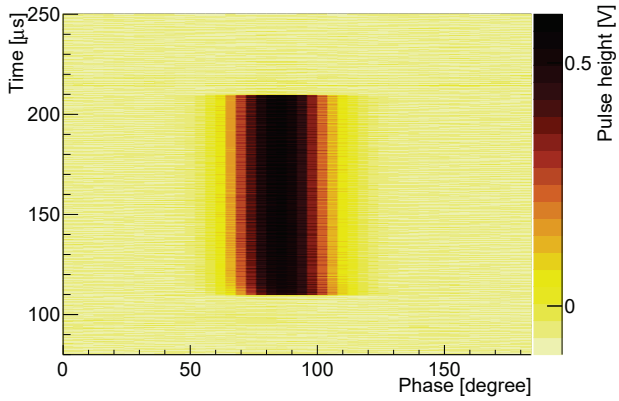


Figure 7: Measured waveform of the BSM.

Longitudinal beam parameters were evaluated using the IMPACT [13], which is the Particle-In-Cell code, to consider the space-charge effect in the MEBT1. Figure 8 shows the longitudinal bunch width measured with the BSM in terms of the buncher voltage. The data was used for the fitting of the IMPACT simulation. The fitting curve was consistent with the measurement for the amplitude scan.

Initial Twiss parameters at the RFQ exit evaluated with the data and the IMPACT were compared with the design simulation for the H^- ion source and the RFQ. Figure 9 shows longitudinal ellipses measured with the BSM and the design ellipse at the RFQ exit. The measurement using the BSM was consistent with the design simulation. This result shows our BSM and MEBT1 system were well understood in the high-power operation.

SUMMARY

The BSM using the HOPG target has been developed to measure the high-power H^- beam in the MEBT1. In this study, the performance evaluation of the HOPG-BSM was conducted. The first measurement of the longitudinal beam profile was demonstrated using the BSM in the MEBT1. The measurement was consistent with the design simulation of the MEBT1. Our HOPG-BSM is the attractive instrument and plays the important role to study the space-charge effect at the front-end.

ISBN: 978-3-95450-241-7 ISSN: 2673-5350 doi:10.18429/JACoW-IBIC2022-TH1I1

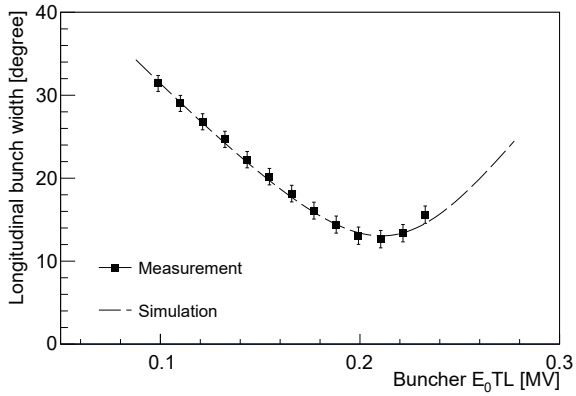


Figure 8: Longitudinal bunch width measured with the BSM in terms of the buncher voltage.

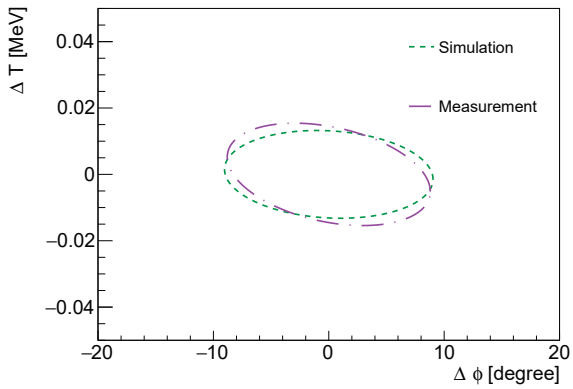


Figure 9: Longitudinal ellipses measured with the BSM and the design ellipse at the RFQ exit.

REFERENCES

[1] K. Hasegawa *et al.*, "Performance and Status of the J-PARC Accelerators", in *Proc. IPAC'18*, Vancouver, Canada, Apr.-May 2018, pp. 1038–1040. doi:10.18429/JACoW-IPAC2018-TUPAL017

[2] A. V. Feschenko, "Methods and Instrumentation for Bunch Shape Measurements (Invited)", in *Proc. PAC'01*, Chicago, IL, USA, Jun. 2001, paper ROAB002, pp.517–521.

[3] R. Kitamura *et al.*,"Bunch-Size Measurement of the High-Intensity H- Beam with 3 MeV by the Bunch Shape Monitor", *JPS Conf. Proc.*, vol. 33, p. 011012, 2021. doi:10.7566/JPSCP.33.011012

[4] A. Miura, T. Miyao, and K. Moriya, "Application of carbon nanotube wire for beam profile measurement of negative hydrogen ion beam", *J. Phys.: Conf. Ser.*, vol. 1067, p. 072020, 2018. doi:10.1088/1742-6596/1067/7/072020

[5] R. Kitamura *et al.*, "Development of the Bunch Shape Monitor Using the Carbon-Nano Tube Wire", in *Proc. IPAC'19*, Melbourne, Australia, May 2019, pp. 2543–2546. doi:10.18429/JACoW-IPAC2019-WEPGW033

[6] Y. Yamada, M. Yanase, D. Miura, and K. Chikuba, "Novel heatsink for power semiconductor module using high thermal conductivity graphite", *Microelectron. Reliab.*, vol. 64, pp. 484–488, 2016. doi:10.1016/j.microrel.2016.07.029

[7] L. Li, A. Fukui, and A. Wakejima, "Bonding GaN on high thermal conductivity graphite composite with adequate interfacial thermal conductance for high power electronics applications", *Appl. Phys. Lett.*, vol. 116, p. 142105, 2020. doi:10.1063/1.5144024

[8] Y. Kondo, T. Morishita, and R. A. Jameson, "Development of a radio frequency quadrupole linac implemented with the equipartitioning beam dynamics scheme", *Phys. Rev. Accel. Beams*, vol. 22, p. 120101, 2019. doi:10.1103/PhysRevAccelBeams.22.120101

[9] T. Morishita and Y. Kondo, "Electromagnetic design and tuning of the four-vane radio frequency quadrupole with nonuniform intervane voltage profile", *Phys. Rev. Accel. Beams*, vol. 23, p. 111003, 2020. doi:10.1103/PhysRevAccelBeams.23.111003

[10] A. Kumar and S. N. Melkote, "Diamond Wire Sawing of Solar Silicon Wafers: A Sustainable Manufacturing Alternative to Loose Abrasive Slurry Sawing", *Procedia Manuf.*, vol. 21, pp. 549–566, 2018. doi:10.1016/j.promfg.2018.02.156

[11] Geant4, http://geant4.cern.ch

[12] H. Wiedemann, *Particle Accelerator Physics 4th Edition*, Springer, 2015, pp.222–227.

[13] J. Qiang, R. D. Ryne, S. Habib, and V. Decyk, "An Object-Oriented Parallel Particle-in-Cell Code for Beam Dynamics Simulation in Linear Accelerators", *J. Comput. Phys.*, vol. 163, pp. 434–451, 2000. doi:10.1006/jcph.2000.6570

Content from this work may be used under the terms of the CC BY 4.0 licence (© 2022). Any distribution of this work must maintain attribution to the author(s), title of the work, publisher, and DOI

ISBN: 978-3-95450-241-7 ISSN: 2673-5350 doi:10.18429/JACoW-IBIC2022-TH1C3

SINGLE-SHOT ELECTRO-OPTIC DETECTION OF BUNCH SHAPES AND THZ PULSES: FUNDAMENTAL TEMPORAL RESOLUTION LIMITATIONS AND CURES USING THE DEOS STRATEGY*

Serge Bielawski, Clément Evain, Eléonore Roussel, Christophe Szwaj†
PhLAM, CNRS/Lille University, Lille, France
Christopher Gerth, Bernd Steffen, Deutsches Elektronen-Synchrotron DESY, Hamburg, Germany
Bahram Jalali, UCLA, Los Angeles, CA, USA

Abstract

We review a recent work aiming at improving the resolution of single-shot longitudinal diagnostics, that are based on electro-optic (EO) detection using a chirped laser pulse. This classical technique has indeed been known to present severe limitations in time resolution (and usable bandwidth), especially when long recording windows and/or short bunches are considered. We review recent results on a strategy designed for overcoming this limit, the DEOS technique (Diversity Electro-Optic Sampling). A special experimental design enables to reconstruct numerically the input electric signal with unprecedented temporal resolution. As a result, 200 fs temporal resolution over more than 10 ps recording length could be obtained at European XFEL - a performance that could not be realized using classical spectrally-decoded electro-optic detection. Although DEOS uses a radically novel conceptual approach, its implementation requires few hardware modifications of currently operating chirped pulse electro-optic detection systems.

INTRODUCTION: LIMITATION OF CLASSICAL CHIRPED PULSE ELECTRO-OPTIC DETECTION

Recording electric field evolutions in single-shot and with sub-picosecond resolution is required in electron bunch diagnostics, and THz applications. A popular strategy consists of transferring the unknown electric field onto a chirped laser pulse, which is eventually analyzed [1, 2] (see Fig. 1). The technique has been investigated and/or been used as routine diagnostics at FELIX, DESY, PSI, Eu-XFEL, KARA, SOLEIL, etc. However fundamental time-resolution limitations have been strongly limiting the potential of these methods. This limitation has been generally expressed as the shortest bunch duration τ_R (or THz pulse duration) that can be recorded without deformation [3]:

$$\tau_R = \sqrt{\tau_w \times \tau_L}, \qquad (1)$$

where τ_L is the compressed laser pulse duration, and τ_w is the stretched pulse duration, i.e., the duration of the recording window.

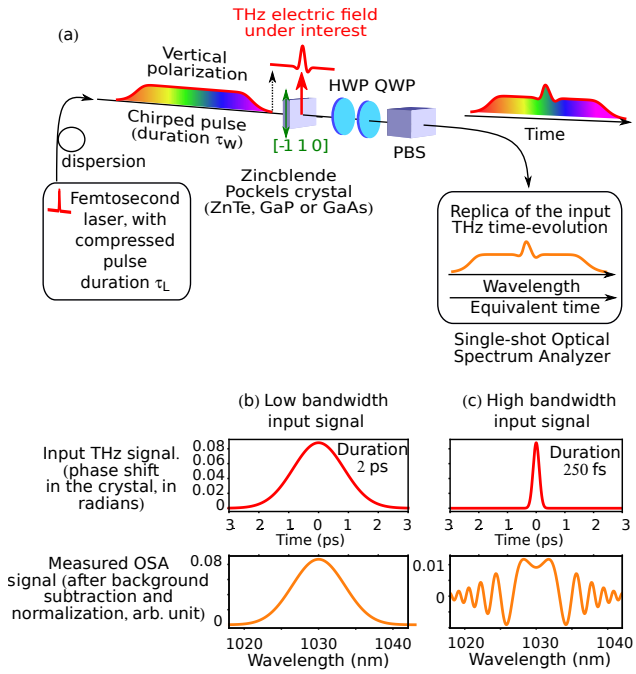


Figure 1: (a) Typical setup and limitations of classical single-output chirped pulse EO detection systems. The THz-bandwidth electric field is typically the Coulomb field created by an electron bunch, or a coherent THz pulse generated by coherent synchrotron radiation, coherent transition radiation, etc. The electric field modulates the intensity of a chirped laser pulse. The readout is performed (also in single-shot) using an optical spectrum analyser, usually composed of a grating and a camera. QWP and HWP: Quarter- and half-wave plates, PBS: Polarizing Beam-Splitter. As a main idea, one can expect the temporal laser modulation to be approximately replicated in the optical spectrum. Actually this works only for relatively low bandwidth THz pulses (b). For short (i.e., large bandwidth) THz pulses, strong deformations are observed (c). The DEOS technique presented here aims at solving this time resolution issue.

TRANSFER FUNCTION APPROACH

A main point of the DEOS approach consists of using the information contained at the two outputs of spectrally decoded EO systems. This involves two steps (see also Fig. 2):

* Work supported by: ULTRASYNC ANR-DFG project, CPER photonics for society, LABEX CEMPI, METEOR CNRS MOMENTUM grant, DESY/Helmholtz, MURI program on Optical Computing Award Number N00014-14-1-0505.
† christophe.szwaj@univ-lille.fr

Content from this work may be used under the terms of the CC BY 4.0 licence (© 2022). Any distribution of this work must maintain attribution to the author(s), title of the work, publisher, and DOI

ISBN: 978-3-95450-241-7 ISSN: 2673-5350 doi:10.18429/JACoW-IBIC2022-TH1C3

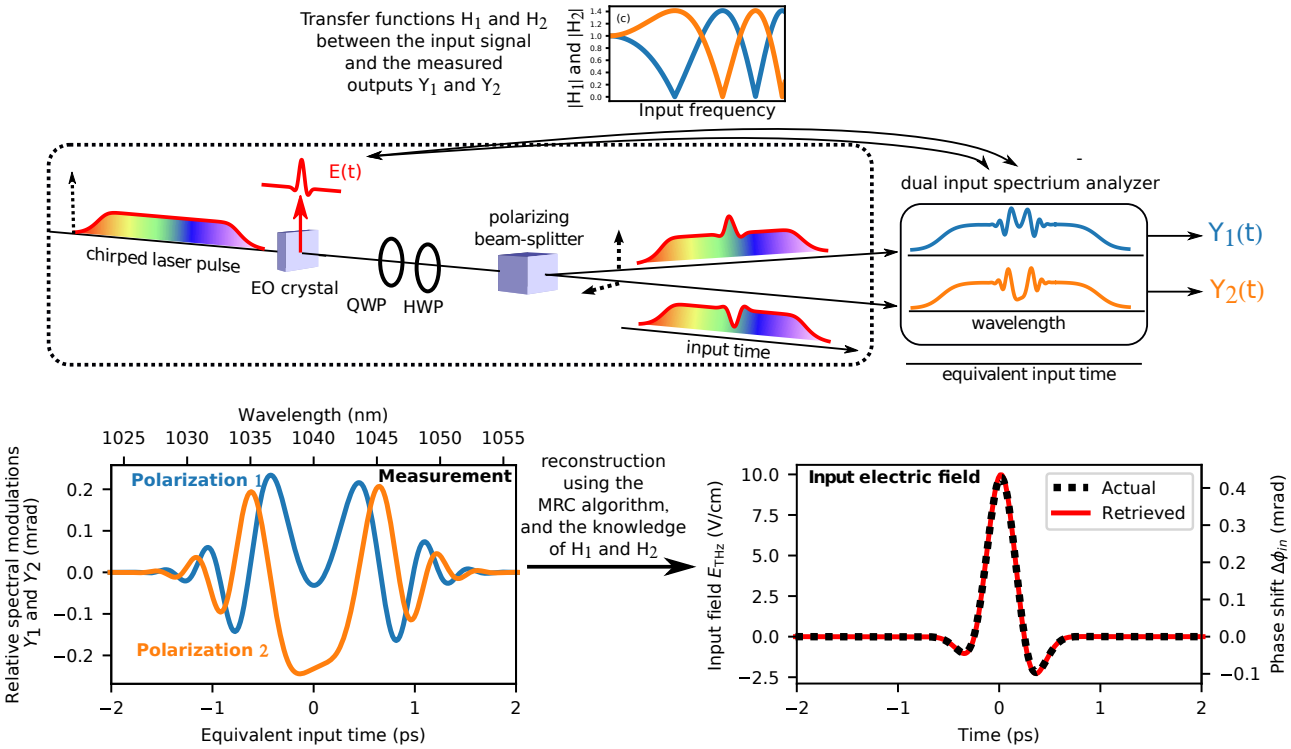


Figure 2: Principle of Diversity Electro-Optic Sampling (DEOS). Top: experimental setup. The key point consists of recording simultaneously the two output spectra exiting the polarizing beam-splitter, and choosing adequate waveplate orientations (see [4]). Bottom: reconstruction of the input field evolution, using the two recorded EO optical spectra (numerical simulation used for testing the strategy at the start of the project). Adapted from [4].

1. Finding the general relationship between the EO input and the measurements, using a Fourier-space approach.
2. Using this knowledge for "inverting the problem", i.e., retrieving the electric field to be measured, from the measurements. We will see that this will be possible (i.e., mathematically well-posed) by using the information contained in the **two outputs** of spectrally encoded EO systems.

Although this requires a non-trivial analytical work (see [4] for details), it can be shown that the input field is related to the output, through relatively simple transfer functions. If we note $\Delta\phi_{in}(t)$ the electric field-induced phase shift in the EO crystal, and $Y_1(t)$, $Y_2(t)$ the optical spectra at the two polarizing beam-splitter outputs, after background subtraction and normalization:

$$\tilde{Y}_1(\Omega) = H_1(\Omega)\Delta\tilde{\phi}_{in}(\Omega) \quad (2)$$

$$\tilde{Y}_2(\Omega) = H_2(\Omega)\Delta\tilde{\phi}_{in}(\Omega), \quad (3)$$

where the tildes denote the Fourier transform. The forms of the transfer functions $H_1(\Omega)$ and $H_2(\Omega)$ depend on the precise orientations of the laser polarization, EO crystal, and waveplates.

Classical Waveplate and Crystal Orientations

Before focusing on the new DEOS strategy, it is worth examining the transfer functions corresponding to the classical spectral decoding method. With the classical arrangement (see, e.g., [5,6]), it can be shown that [4]:

$$H_1(\Omega) = \cos\left(\frac{\Omega^2}{2C}\right) \quad (4)$$

$$H_2(\Omega) = -\cos\left(\frac{\Omega^2}{2C}\right), \quad (5)$$

where C is the chirp rate of the laser pulse ($C = d\omega/dt$, where ω is the laser optical frequency). Two conclusions may be drawn from this first study:

- Each transfer function vanishes at specific frequencies, the first zero being at $\Omega = \sqrt{C\pi}$. This implies that it is impossible to retrieve the input from the output, without prior knowledge, when the bandwidth exceeds $\sqrt{C\pi}$. For instance, the inversion formula:

$$\Delta\tilde{\phi}_{in}(\Omega) = \tilde{Y}_1(\Omega)/H_1(\Omega) \quad (6)$$

  is obviously mathematically ill-posed.

- The zeros of the two transfer functions occur at the same frequencies.

DEOS Waveplate and Crystal Orientations

As a main idea of DEOS, it is possible to adjust the optics (i.e., the laser polarization, and waveplate orientations)

Content from this work may be used under the terms of the CC BY 4.0 licence (© 2022). Any distribution of this work must maintain attribution to the author(s), title of the work, publisher, and DOI

ISBN: 978-3-95450-241-7 ISSN: 2673-5350 doi:10.18429/JACoW-IBIC2022-TH1C3

so that the zeros of the two transfer functions H_1 and H_2 are interleaved. Many laser polarization and waveplate arrangements are possible. We consider here the situation considered in [4]:

$$H_1(\Omega) = -\frac{1}{\sqrt{2}} \cos\left(\frac{\Omega^2}{2C} - \frac{\pi}{4}\right) \quad (7)$$

$$H_2(\Omega) = \frac{1}{\sqrt{2}} \cos\left(\frac{\Omega^2}{2C} + \frac{\pi}{4}\right). \quad (8)$$

The zeros of the two transfer functions occur at different frequencies. Therefore, the inversion problem (i.e., retrieving $\Delta\phi_{in}(t)$ from $Y_1(t)$ and $Y_2(t)$) is now mathematically well-posed. Several techniques are possible, and a classical one is the so-called Maximum Ratio Combining (MRC), that has been developed in the fifties for wireless communications [7], and for the photonic time-stretch ADC [8]. The input phase shift can be expressed as a function of the two measured outputs Y_1 and Y_2 as:

$$\Delta\tilde{\phi}_{in}^{retr}(\Omega) = \frac{H_1(\Omega)\tilde{Y}_1(\Omega) + H_2(\Omega)\tilde{Y}_2(\Omega)}{H_1^2(\Omega) + H_2^2(\Omega)}. \quad (9)$$

Then, the input signal $\Delta\phi_{in}^{retr}(t)$ is obtained from an inverse Fourier Transform of $\Delta\tilde{\phi}_{in}^{retr}(t)$.

Note on the Theoretical Limitation DEOS

In contrast to classical spectral decoding, the reconstruction formula Eq. (9) does not present the $\sqrt{\tau_L \tau_w}$ time resolution limitation. Hence the achievable time resolution is expected to be limited by the compressed laser pulse duration τ_L or the crystal bandwidth, whichever dominates. This is confirmed by numerical simulations [4].

EXPERIMENTAL RESULTS

Experimental Measurements at Eu-XFEL

After performing a series of tests using a table-top source [4], we realized a test at DESY, using a modification of the recently developed EO measurement setup [6] placed at the second bunch compressor. The bunch energy and RMS duration are of the order of 700 MeV and 200 fs respectively. A Gallium Phosphide (GaP) crystal is placed near the electron bunch, so that the bunch Coulomb field is along the [001] axis (note that DEOS crystal orientation differs from the classical EO case by 90 degrees). The setup and typical results are displayed in Fig. 3. As in the above numerical study, and table-top test, the raw spectrally decoded EO data present the typical oscillations, that are due to the non-flat nature of the transfer functions (see Fig. 3b). The DEOS reconstruction (see Fig. 3c) of the electric field presents a main peak, that corresponds to the electron bunch Coulomb field, and a small trailing component with opposite sign, that may be attributed to a reflection or wakefield in the vacuum chamber.

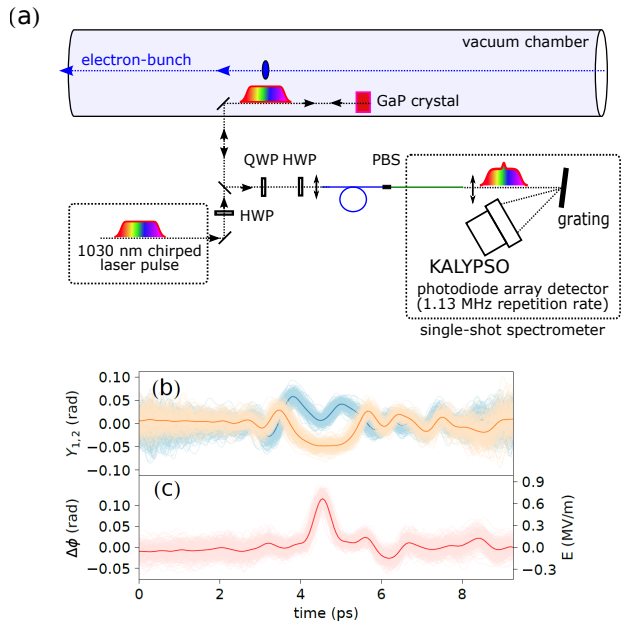


Figure 3: Typical longitudinal electron bunch shape measurements using DEOS at European XFEL. (a): experimental setup. (b): raw EO measurement on the two polarizations outputs. (c): retrieved Coulomb field of the electron bunch (From [4]).

CONCLUSION

We proposed a novel approach allowing electric field evolutions to be recorded in singe-shot. As a main advantage over previous spectrally encoded techniques, the time resolution is no more limited by the well-known limit $\tau_R = \sqrt{\tau_L \tau_w}$. The new recording bandwidth is found to be now limited by the compressed laser pulse duration τ_L or electro-optic crystal bandwidth, whichever come first. Theory and experimental tests are detailed in [4].

REFERENCES

[1] Z. Jiang and X.-C. Zhang, "Electro-optic measurement of THz field pulses with a chirped optical beam", *Appl. Phys. Lett.*, vol. 72, p. 1945, 1998. doi:10.1063/1.121231

[2] I. Wilke *et al.*, "Single-shot electron-beam bunch length measurements", *Phys. Rev. Lett.*, vol. 88, p. 124801, 2002. doi:10.1103/PhysRevLett.88.124801

[3] F. G. Sun, Z. Jiang, and X.-C. Zhang, "Analysis of terahertz pulse measurement with a chirped probe beam", *Appl. Phys. Lett.*, vol. 73, pp. 2233–2235, 1998. doi:10.1063/1.121685

[4] E. Roussel *et al.*, "Phase diversity electro-optic sampling: A new approach to single-shot terahertz waveform recording", *Light Sci. Appl.*, vol. 11, pp. 1–14, 2022. doi:10.1038/s41377-021-00696-2

[5] S. Casalbuoni *et al.*, "Numerical studies on the electro-optic detection of femtosecond electron bunches", *Phys. Rev. ST Accel. Beams*, vol. 11, p. 072802, 2008. doi:10.1103/PhysRevSTAB.11.072802

Content from this work may be used under the terms of the CC BY 4.0 licence (© 2022). Any distribution of this work must maintain attribution to the author(s), title of the work, publisher, and DOI

ISBN: 978-3-95450-241-7 ISSN: 2673-5350 doi:10.18429/JACoW-IBIC2022-TH1C3

[6] B. Steffen *et al.*, "Compact single-shot electro-optic detection system for THz pulses with femtosecond time resolution at MHz repetition rates", *Rev. Sci. Instrum.*, vol. 91, p. 045123, 2020. doi:10.1063/1.5142833

[7] L. R. Kahn, "Ratio squarer", in *Proc. of the Inst. Radio Eng.*, vol. 42, p. 1704, 1954.

[8] Y. Han, O. Boyraz, and B. Jalali, "Ultrawide-band photonic time-stretch A/D converter employing phase diversity", *IEEE Trans. Microwave Theory Tech.*, vol. 53, p. 1404, 2005. doi:10.1109/TMTT.2005.845757

Content from this work may be used under the terms of the CC BY 4.0 licence (© 2022). Any distribution of this work must maintain attribution to the author(s), title of the work, publisher, and DOI

ISBN: 978-3-95450-241-7 ISSN: 2673-5350 doi:10.18429/JACoW-IBIC2022-TH2C2

UPGRADED CMS FAST BEAM CONDITION MONITOR FOR LHC RUN 3 ONLINE LUMINOSITY AND BEAM INDUCED BACKGROUND MEASUREMENTS

Joanna Wańczyk*,[1]
on behalf of CMS Collaboration, CERN, Geneva, Switzerland
[1]also at Swiss Federal Institute of Technology Lausanne (EPFL), Lausanne, Switzerland

Abstract

The Fast Beam Condition Monitor (BCM1F) for the CMS experiment at the LHC was upgraded for precision luminosity measurement in the demanding conditions foreseen for LHC Run 3. BCM1F has been rebuilt with new silicon diodes, produced on the CMS Phase 2 outer tracker PS silicon wafers. The mechanical structure was adapted to include a three-dimensional printed titanium circuit for active cooling of the BCM1F sensors. The assembly and qualification of the detector quadrants were followed by the integration with the Pixel Luminosity Telescope (PLT) and Beam Conditions Monitor for Losses (BCML1) on a common carbon fibre carriage. This carriage was installed inside the Compact Muon Solenoid (CMS) behind the CMS pixel detector, at a distance of 1.9 m from the interaction point (IP). BCM1F will provide a real-time luminosity measurement as well as a measurement of the beam-induced background, by exploiting the arrival time information of the hits with a sub-bunch crossing precision. Moreover, regular beam overlap scans at CMS were introduced during Run 2, enabling an independent and nondestructive transverse profile measurement for LHC Operators. These proceedings describe the improved BCM1F detector design, its commissioning, and performance during the beginning of Run 3 operation.

INTRODUCTION

The Fast Beam Condition Monitor (BCM1F) is a dedicated, standalone luminometer, independent from all central CMS services. The sub-bunch crossing (BX) precision, enables the measurement of beam-induced background. The complete detector consists of four C-shapes (see Fig. 1), with a total of 48 channels. Each C-shape pair forms a ring around the beam pipe at an approximate radius of 7 cm, on either side of the interaction point (IP). In Run 2 good performance was achieved with mixed sensor types were used (sCVD, pCVD and Silicon). The Silicon sensors had much better signal-noise separation and response linearity [1].

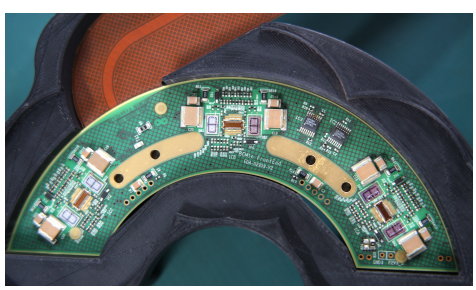


Figure 1: Picture of the Run 3 BCM1F C-shape.

DETECTOR DESCRIPTION

The full system diagram including both the front end and the two parallel back ends is shown in Fig. 2. The detector was completely rebuilt during Long Shutdown 2 (LS2), with radiation hard sensors made of acceptor-doped (p-type) silicon. To provide high performance operation throughout Run 3 period, a three-dimensional (3D) printed titanium active cooling loop was added.

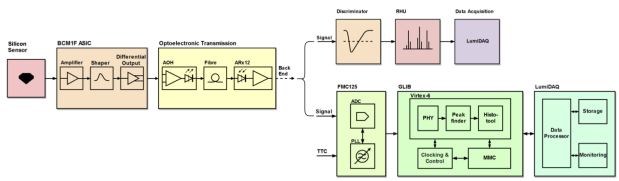


Figure 2: Diagram of the BCM1F detector architecture [2].

Front-End Electronics

Each C-shape is a single flex-rigid printed circuit board, which includes all front-end components: double silicon diodes, ASIC chips, and opto-electronic readout.

The new sensors were produced as a part of the CMS Phase 2 Outer Tracker sensor production [3]. The 300 µm thick wafers were prepared as double silicon sensors, each with dimensions of $1.7 \times 1.7\,\mathrm{mm}^2$. They are A/C-coupled to protect the amplifier from the leakage current, thus providing better signal-to-noise ratio (SNR). The signal is shaped with the fast asynchronous ASIC from the Run 2 design [4], implemented in IBM 130 nm. It provides a short peaking time (<10 ns), narrow pulses, as shown in Fig. 3, and sub-bunch timing resolution. The optical readout is placed at a larger distance from the IP, and uses analog-opto-hybrids (AOH), which convert the current into infrared light at a wavelength of 1310 nm.

The assembly and qualification of the detector quadrants were followed by integration with the Pixel Luminosity Telescope (PLT) and Beam Conditions Monitor for Losses (BCML1). Commissioning was done during the 2021 LHC pilot beam test at the injection energy of 450 GeV.

Back-End Electronics

The optical signal is converted into an 8 −bit-equivalent electric signal at the ARx12 optical receiver in the CMS service cavern (USC), shielded from the prompt radiation in the

* jwanczyk@cern.ch, joannawanczyk@epfl.ch

Content from this work may be used under the terms of the CC BY 4.0 licence (© 2022). Any distribution of this work must maintain attribution to the author(s), title of the work, publisher, and DOI

ISBN: 978-3-95450-241-7 ISSN: 2673-5350 doi:10.18429/JACoW-IBIC2022-TH2C2

experimental cavern. Subsequently, the signal is duplicated and propagated into two back end systems:

- VME system: a leading edge discriminator module (V895) is used with fixed threshold. It generates the logical output which is connected to the Real-Time Histogramming Unit (RHU) (see upper right in Fig. 2). An orbit occupancy histogram is formed with a 6.25 ns granularity (4 bins per BX). As the counts are based on the 5 ns discriminator pulses, the system is unable to differentiate the piled up pulses, causing some inefficiency.
- µTCA based system [5]: it consists of the FPGA Mezzanine Card (FMC) digitizer with a sampling frequency of 1.2024 GHz, AC coupling of the ADC inputs, and PLL to lock on the LHC bunch clock. Peak finding and histogramming is performed on the Xilinx Virtex-6 FPGA hosted by the Gigabit Link Interface Board (GLIB) (see bottom right in Fig. 2). As in the RHU, the orbit occupancy histogram is built based on the arrival time, but with enhanced resolution of 6 bins per BX. A derivative-based peak finder algorithm was implemented allowing for resolving double hits [2].

Data are acquired by the dedicated BRIL DAQ software, independent of the central CMS DAQ.

LABORATORY TESTS

The sensors were tested at DESY, and those with the best quality were chosen for the installation. The qualification was based on I-V and C-V characteristics, sensor pad and guard ring leakage current, guard ring breakthrough voltage, full depletion voltage around −260 V, capacitance after full depletion (see Fig. 4), and coupling capacitance. The

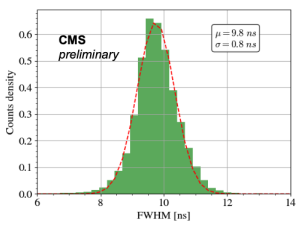


Figure 3: Distribution of the full width of radiation source pulses at half amplitude maximum.

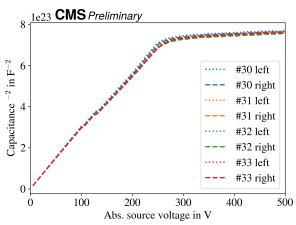


Figure 4: Sensor pad capacitance as a function of the applied high voltage bias.

C-shape PCBs were fabricated and the sensor bonding was performed at CERN. It was followed by detector-quadrant testing with internally generated test pulses as well as with a radiation source (Sr-90). The detector signal full width at half maximum (FWHM) timing distributions were in agreement with the design value: a mean around 10 ns for all channels was obtained (see Fig. 3), with the source hits amplitude spectra indicating good SNR. Prior to that, and during LS2, a test-beam was used to verify the new design with A/C coupling as well as the new cooling loop performance. The detector was finally assembled at CERN and installed in the CMS experimental cavern in July 2021.

RUN 3 COMMISSIONING

BCM1F has been operating since the beginning of LHC commissioning for the Run 3, measuring collision products at a center-of-mass energy of 13.6 TeV. During this time, the detector configuration was optimized with the per-channel timing alignment.

An example accumulated full orbit occupancy histogram is shown in Fig. 5: results from a single channel are shown using data collected over 6 hours and normalized over fixed time intervals (lumi-section, LS) of approximately 23.6 s each. In the very beginning of the orbit, occupancy corresponding to a bunch with a low occupancy signal is visible, which is caused by noncolliding bunches. It is followed by two sets of four bunch trains, which are also present later in the orbit. There are 2 individual colliding bunches present giving much narrower occupancy spikes around the bins 3000 and 10000. Afterglow tails are visible after each set of regular bunch trains, with an increased hit count observed due to the activated detector material. This signal contamination is corrected by applying an afterglow correction factor to each colliding bunch, see Fig. 6. The BCM1F uncalibrated data were fitted to an exponential function, aggregated over many orbits. The signal from the two well-separated (~µs) single colliding bunches was used, to account for the out of time hits in the following bunch crossings numbered with an identification number (BCIDs).

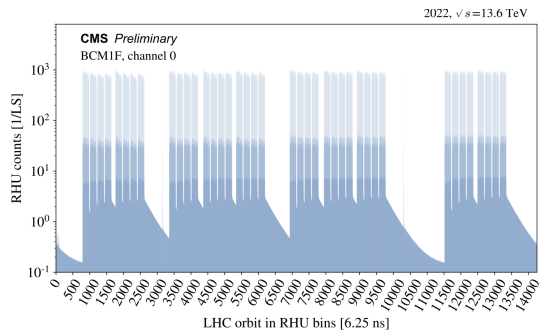


Figure 5: BCM1F measured LHC full orbit signal.

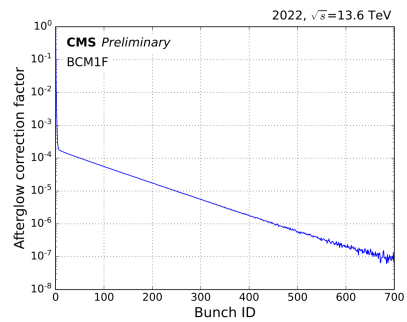


Figure 6: First Run 3 afterglow correction model based on the single colliding bunch response exponential tail.

Derivative Based Peak Finding Algorithm

The BCM1F µTCA back-end electronics was planned as an improvement to the baseline VME. The new peak finder

Content from this work may be used under the terms of the CC BY 4.0 licence (© 2022). Any distribution of this work must maintain attribution to the author(s), title of the work, publisher, and DOI

ISBN: 978-3-95450-241-7 ISSN: 2673-5350 doi:10.18429/JACoW-IBIC2022-TH2C2

Content from this work may be used under the terms of the CC BY 4.0 licence (© 2022). Any distribution of this work must maintain attribution to the author(s), title of the work, publisher, and DOI

algorithm uses a derivative based threshold, which is designed to differentiate the overlapping pulses to maintain the detection efficiency at high pileup. The derivative is calculated with a smooth noise-robust differentiator (SNRD, $N = 7$), and the peak detection is based on the derivative threshold level crossing, see Fig. 7. It was designed to provide noise suppression at high frequencies with efficient implementation into a digital system [2]. The electronics noise is also separated based on the low value of the maximum derivative, which is intrinsic to the channel performance, as well as by applying the amplitude cut off. The amplitude spectra for high energy collisions 13.6 TeV built using the new peak finder is shown in Fig. 8. The low amplitude Gaussian noise contribution was cut out with operational thresholds. The spectrum is a Landau distribution with the most probably value (MPV) corresponding to the energy loss of the minimum-ionizing particle. As the data were collected for 10 h, a higher charge deposition peaks are also observed, which correspond to the deposit of multiple MIP charges.

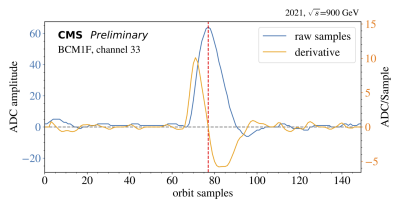


Figure 7: BCM1F µTCA sampled hit signal (blue), overlaid with the corresponding derivative (orange). The detected peak at derivative zero-crossing is marked with red line.

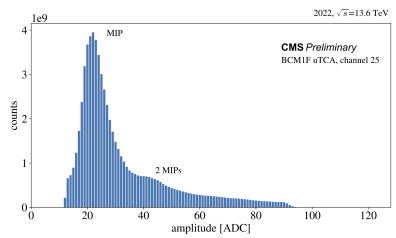


Figure 8: BCM1F µTCA per-channel amplitude spectrum.

BACKGROUND MEASUREMENT

The signals in the detector originating from beam-induced background particles are measured by different BCM1F channels, based on their location with respect to the CMS IP. Upstream beam channels are used to estimate the beam induced background. The time structure is shown in Fig. 9, where the contribution from both beams are shown at two periods within the LHC orbit. The beam direction can be defined by the time of arrival: beam 1 (B1) signal is visible in BCID 101 before beam 2 (B2), and the opposite for the second presented BCID. Based on the BCM1F measurements the beam conditions are assessed to guarantee safe operation for the other CMS subsystems. The beam-induced backgrounds measured using BCM1F are sent to the LHC as realtime feedback of the beam conditions prevalent close to the CMS experiment, see Fig. 10.

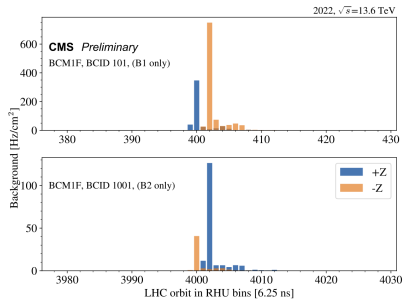


Figure 9: BCM1F average measured incoming and outgoing background for two individual nominal bunches.

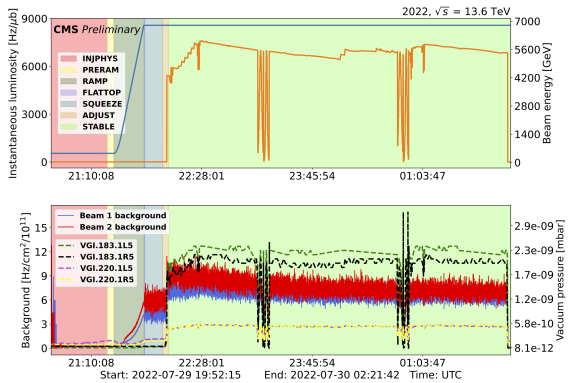


Figure 10: BCM1F measured B1 and B2 backgrounds over the LHC beam mode cycle.

LUMINOSITY MEASUREMENT

BCM1F has been the main online luminometer since the beginning of the Run 3. The luminosity measurement is based on the sum of counts within a colliding BCID. A zero counting algorithm is used, which allows for defining the average number of hits based on the zero-hit probability, and assuming that hits follow a Poissonian distribution [6].

During van der Meer (vdM) calibration [7, 8] the beam conditions are setup deliberately so that the instantaneous luminosity can be extracted from the bunch parameters, Eq. (1), using the number of colliding protons per beam $\{N_1, N_2\}$, the LHC frequency f, and the transverse convolved bunch sizes $\{\Sigma_x, \Sigma_y\}$.

$$L_{\text{inst}} = \frac{N_1 N_2 f}{2\pi \Sigma_x \Sigma_y}, \tag{1}$$

thus, the measured rate R can be used to define the visible cross section:

$$\sigma_{\text{vis}} = \frac{R}{L_{\text{inst}}}. \tag{2}$$

Subsequently, this calibration constant is used to measure the luminosity directly from the detector rate.

ISBN: 978-3-95450-241-7 ISSN: 2673-5350 doi:10.18429/JACoW-IBIC2022-TH2C2

Preliminary Calibration with Emittance Scans

As the main vdM program is planned only for the end of the year 2022, emittance scans are used to obtain preliminary detector calibration. These are short scans (10 s/step), usually performed over a narrow beam separation range (3.5 σ).

For the BCM1F μTCA each sensor is treated independently and a per channel calibration constant is extracted. The spread between good channels is within 15% from the average σ_{vis}. The stability of the online measurement can be observed with the calibration constant remeasured in subsequent scans. The BCM1F VME measurement in the early Run 3 period at nominal conditions is shown in Fig. 11, obtained as the average over all bunches per fill. The double-Gaussian fit function was used and BCM1F rate was corrected with the afterglow model and the beam induced background contribution based on the noncolliding bunch response as well as the prompt contribution just before the collision. The points were also color-coded depending on the single bunch instantaneous luminosity (SBIL). The root-mean-square (RMS) of the visible cross section in this period is 1.4%.

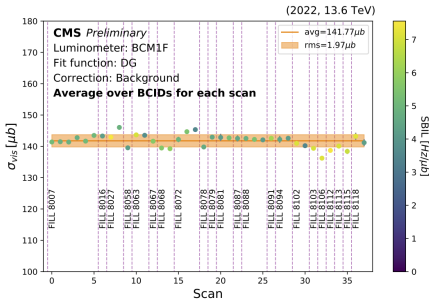


Figure 11: Calibration constant σ_{vis} over the early Run 3 period at nominal conditions.

Beam Overlap Measurement

The luminosity dependence over a separation scan includes the convolved bunch size, Eq. (1), therefore, the scans can be also used to study the bunch profile. During operation in the nominal conditions, a crossing angle ϕ is applied using the dipole corrector magnets to avoid long-range interactions. At CMS, it is applied in the horizontal plane $\{x\text{–}z\}$, hence the beam overlap includes the effect of this crossing angle:

$$\Sigma_x = \sqrt{(\sigma_{x_1}^2 + \sigma_{x_2}^2)\cos^2\frac{\phi}{2} + (\sigma_{z_1}^2 + \sigma_{z_2}^2)\sin^2\frac{\phi}{2}} \qquad \Sigma_y = \sqrt{\sigma_{y_1}^2 + \sigma_{y_2}^2}, \tag{3}$$

where σ are the bunch sizes in $\{x, y, z\}$ for B1 and B2. Figure 12 shows the bunch overlap evolution during a fill with β^* levelling in which the scans were performed after each β^* step, from 60 cm to 42 cm. The overlap width decreases along these steps.

The normalized emittance can be estimated for each plane after extracting the convolved width of the two colliding bunches σ_{eff}:

$$\epsilon = \frac{\sigma_{\text{eff}}^2}{\beta^*}\gamma\beta_{\text{rel}}, \quad \sigma_{\text{eff}} = \sqrt{\frac{\sigma_1^2 + \sigma_2^2}{2}}. \tag{4}$$

An example measurement is shown in Fig. 13, for a special fill which included bunches with wide range of normalized emittances: 3.95–7.25 μm in x and 1.79–5.59 μm in y.

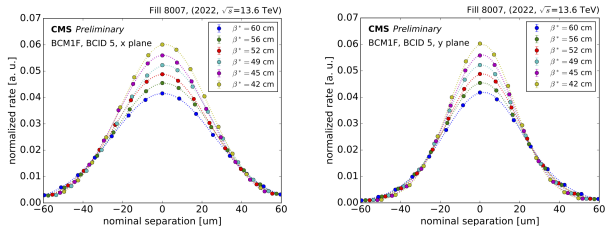


Figure 12: Evolution of beam overlap for various β^* steps during luminosity levelling. An example bunch is shown, for scans in both $\{x, y\}$ planes.

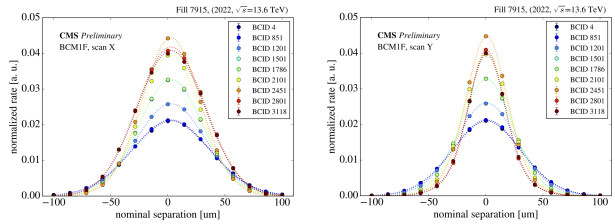


Figure 13: Beam overlap profile for 9 bunches with various emittances for both $\{x, y\}$ planes (left and right).

Orbit Displacement Measurement

The mean value is extracted from a Gaussian fit to the normalized rate over separation steps (see Figs. 12 and 13). It indicates the per-bunch orbit displacement, which is dependent on the number of parasitic collisions for a given filling pattern. An example of bunch train displacement structures measured by BCM1F for fill 8113 are shown in Fig. 14.

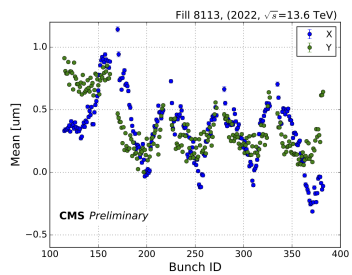


Figure 14: BCM1F measured per-bunch orbit displacement in both $\{x, y\}$ planes, zoomed into a set of bunch trains.

CONCLUSIONS

The commissioning of the upgraded BCM1F has been finalized. In the first months of the LHC Run 3, it has proven to be robust and reliable, providing CMS with online background and luminosity measurements. To achieve the best precision in luminosity, dedicated vdM calibration is necessary, planned for later in the year 2022.

Content from this work may be used under the terms of the CC BY 4.0 licence (© 2022). Any distribution of this work must maintain attribution to the author(s), title of the work, publisher, and DOI

ISBN: 978-3-95450-241-7 ISSN: 2673-5350 doi:10.18429/JACoW-IBIC2022-TH2C2

Content from this work may be used under the terms of the CC BY 4.0 licence (© 2022). Any distribution of this work must maintain attribution to the author(s), title of the work, publisher, and DOI

REFERENCES

[1] Moritz Guthoff, "The new Fast Beam Condition Monitor using poly-crystalline diamond sensors for luminosity measurement at CMS", *Nucl. Instrum. Methods Phys. Res., Sect. A*, vol. 936, pp. 717-718, 2019. doi:10.1016/j.nima.2018.11.071

[2] Alex Ruede, "New Peak Finding Algorithm for the BCM1F Detector of the CMS Experiment at CERN", Master Thesis, Ernst Abbe Hochschule Jena, 2018. https://cds.cern.ch/record/2310566/files/CERN-THESIS-2018-021.pdf

[3] Georg Auzinger, "Silicon Sensor Development for the CMS Tracker Upgrade", PhD thesis, Vienna University of Technology, 2013. https:/cds.cern.ch/record/1631093/files/CERN-THESIS-2013-211.pdf

[4] Jan Kaplon, Dominik Przyborowski, and Piotr Rymaszewski, "Design and Performance of the BCM1F Front End ASIC for the Beam Condition Monitoring System at the CMS Experiment", *IEEE Trans. Nucl. Sci.*, vol. 63, no. 4, Aug 2016. doi:10.1109/TNS.2016.2575781

[5] A. A. Zagozdzinska *et al.*, "Architecture of the upgraded BCM1F Backend Electronics for Beam Conditions and Luminosity measurement - hardware and firmware", *J. Instrum.*, vol. 10, p. C02020, 2015. doi:10.1088/1748-0221/10/02/c02020

[6] Olena Karacheban, "Luminosity measurement at CMS", PhD thesis, Brandenburg University of Technology Cottbus-Senftenberg, 2016. https://bib-pubdb1.desy.de/record/393347/files/Thesis.pdf&usg=AOvVaw3F8oI6Y0Vju1hd0XvaBUyM

[7] S. van der Meer, "Calibration of the effective beam height in the ISR", Technical Report CERN-ISR-PO-68-31, 1968. http://cds.cern.ch/record/296752/files/196800064.pdf

[8] CMS Collaboration, "Precision luminosity measurement in proton-proton collisions at $\sqrt{s}$ = 13 TeV in 2015 and 2016 at CMS", *Eur. Phys. J. C.*, vol. 81, p. 800, 2021. doi:10.1140/epjc/s10052-021-09538-2

ISBN: 978-3-95450-241-7 ISSN: 2673-5350

List of Authors

Bold papercodes indicate primary authors; ~~strike through/black~~ papercodes indicate **no submission received**

— A —

Abbott, M.G. MO3C2
Aboulbanine, Z. MOP28, TUP20, TUP21
Achenbach, P. ~~WE1I3~~
Ackermann, W. WEP24
Adelmann, A. ~~MO2C3~~
Adhikari, G.D. TUP20, TUP21
Adiguzel, A. ~~TUP22~~, ~~WEP18~~, WEP43
Ady, M. TUP17
Aftab, N. **MOP28**, TUP20, TUP21
Akhyani, M. TUP35, MO2C2
Alberdi-Esuain, B. **TUP18**
Alden, S.E. ~~WEP19~~
Aloev, A. TUP43
Alves, D. TUP30, TUP34
Alves, F. TUP09
Andreassen, O.Ø. TU3C3
Andreazza, W. MOP45, WEP23
Angal-Kalinin, D. MO1C3
Aoyagi, H. **MO3C3**
Apsimon, Ö. WEP29
Arnold, M. MOP26
Arrutia Sota, P.A. WE3C3
Arteche, A. TU1I1
Aryshev, A. MOP09
Atkinson, T. **MOP02**
Austin, M.R. TUP05

— B —

Baboi, N. **MO3C4**
Baeta Neves Diniz Santos, P.H. **WE2C4**
Bainbridge, A.R. MO1C3
Balci, E. MOP45
Balkova, Y. MOP22
Barboutis, A.B. MOP31
Bardorfer, A. TUP10, WEP08, WEP09
Baričevič, B. TUP10
Baron, R.A. MO2C2, MOP07, TUP35
Batten, T. WEP33, **WEP34**, ~~**THCI1**~~
Belohrad, D. MOP45, WEP23, WE3C3
Bence, A. TUP19
Benedetti, G. TUP40
Beni, N. MOP05
Benoist, N. MOP35
Bergamaschi, M. WE3C3
Berlioux, A. TUP19
Bernardi, L. MOP21
Bertwistle, D. WEP33
Bett, D.R. WEP12
Bielawski, S. TH1C3
Blokland, W. ~~**WEP05**~~
Blomley, E. MOP42
Bloomer, C. MOP15, **WEP15**
Bobb, L. MOP15, MOP18, MO3C2, WEP15, WEP37
Böhme, C. **MOP03**
Bogataj, L. WEP08, WEP09
Boland, M.J. WEP33
Boltz, T. MOP42
Boonpornprasert, P. MOP28, TUP20, TUP21
Boorman, G.E. TU3C3
Borland, M. TU2T1
Borowiec, P.B. MOP35
Bosco, A. TU3C3
Bosisio, L. TUP02
Boutachkov, P. TUP29, TUP36, WEP42, **WE3I1**
Braccini, S. WE3C2
Brajnik, G. **MOP13**, MOP14, TUP02
Brandenburg, S. MOP33
Brauch, A. **MOP26**
Bravin, E. MOP23, MOP45
Bree, M. WEP34
Breglio, G. MOP05
Breunlin, J. **WE2C2**
Brosi, M. MOP27
Broucquart, R. **TUP42**
Brown, G.W. TU2C3
Brown, K.A. TUP39
Bründermann, E. WEP24, WEP26
Bründermann, E. MOP42
Buontempo, S. MOP05
Buratin, E. **MOP34**, **MOP35**
Bustinduy, I. MOP07, TUP35, WEP17
Butti, D. **MOP23**, TUP16

— C —

Caglar, A. WEP43
Calvo Giraldo, E. **TU2C2**, WE3C3
Capitanio, B. TUP19
Cargnelutti, M. MOP13, WEP08, WEP09
Carmichael, L.R. TUP05
Carneiro, J.-P. TUP05
Carra, F. MOP05
Carrato, S. MOP14, TUP02
Caselle, M. MOP42
Casolaro, P. **WE3C2**
Castro Sequeiro, C. TUP17
Castro, L. ~~**WEP39**~~
Cauchon, G. TUP19
Cautero, G. TUP02
Cazorla, A.C. WEP16
Cerv, M. TUP10
Cetinkaya, H. ~~TUP22~~, ~~WEP18~~, WEP43
Cha, H.J. MOP27
Chin, E.P. TU2C3
Chritin, N.S. MOP45

Content from this work may be used under the terms of the CC BY 4.0 licence (© 2022). Any distribution of this work must maintain attribution to the author(s), title of the work, publisher, and DOI

ISBN: 978-3-95450-241-7 ISSN: 2673-5350

Content from this work may be used under the terms of the CC BY 4.0 licence (© 2022). Any distribution of this work must maintain attribution to the author(s), title of the work, publisher, and DOI

Chung, Y.S. ~~TUP14~~
Churchman, A.R. TUP17
Cirrone, G.A.P. ~~TU2I4~~
Clark, S.L. MOP43
Clarke, C.I. TU2C3
Cobau, W.G. TU2C3
Colja, M. **MOP14**
Condamoor, S. TUP01
Cook, G. MO3C2
Cook, N.M. TU2T1, TUP39
Corbett, W.J. MOP16, TUP01
Crescimbeni, L. **TUP31**, WEP30
Cristiano, A. **WEP10**
Curcio, A. TUP28, TU3C2
Czwalinna, M.K. WEP24

— D —

Da Silva, J. TUP19
Davut, C. **WEP29**
De Gersem, H. TUP31, WEP24
de Luis, D. TU3C2
De Maria, R. TUP15
De Monte, R. MOP13, MOP14
Degl'Innocenti, I. WEP12
Delagnes, É. MOP21
Delaviere, T. MOP33
Dellepiane, G. WE3C2
Denat, G. MOP35
Derrez, C.S. MO2C2, MOP07
Desch, K. MOP37, MOP38
Desmarchelier, G. ~~WEP13~~
Devel, M. WE3C4
Dewa, H. TUP32, WE2I3
Di Carlo, S. **WEP23**
Diamond, J.S. WEP40
Ditter, R. TUP12
Dölling, R. MOP19, **MOP24**
Donegani, E.M. MOP07, TUP35
Dooling, J.C. **TU2T1**
Dragonja, U. MOP13
Dritschler, T. MOP42
Duhme, H.T. MO3C4, TUP43, WEP14, WEP36
Duperrier, R.D. ~~WEP13~~
Dupuy, L. MOP33
Duraffourg, M. WEP32
Dursun, B. TUP43, WEP36

— E —

Eddy, N. WEP40
Edelen, J.P. **MOP10**, **TUP39**
Effinger, E. TU2C2, TUP03, WE3C3
Eichler, A. TUP43
Einstein-Curtis, J.A. MOP10, TUP39
El Ajjouri, M. **TUP09**
Elibollar, E. WEP43
Elsner, D. MOP37, MOP38
Emery, J. WEP04, WEP23
Enders, J. MOP26
Engel, S.E. **WEP42**
Er, M.F. WEP43
Eschenbaum, C. WEP24
Esen, S. ~~TUP22~~, ~~WEP18~~
Eshraqi, M. MO2C2, TUP35
Esteban Felipe, J.C. MOP45, WEP23
Esteban Müller, J.F. MOP40, **WEP41**
Evain, C. TH1C3

— F —

Falkenstern, F. **WEP31**
Fedel, G.S. TUP23
Feikes, J. MOP31, ~~TH1C4~~
Felcsuti, G. WE2C2
Ferianis, M. MOP07, WEP25
Fernández, F.F.B. TUP40
Fernández, J. ~~WEP13~~
Ferrand, G. ~~WEP13~~
Ferretti, C. TU3C4
Fienga, F. **MOP05**
Fisher, A.S. **TU2C3**
Forck, P. TUP17, TUP25, TUP36, WEP17
Fraser, M.A. WE3C3
Freitas, Á. TUP41, **WEP38**
Freund, W. WEP15
Friedman, P.S. TU3C4
Frommberger, F. MOP38
Frosio, T. TU2C3
Fujita, T. TU1C3, WE2I3, MO3C3
Fukami, K. TU1C3
Fukui, T. WE2I3
Funkner, S. WEP26

— G —

Gabrielli, A. TUP02
Galatyuk, T. MOP29
Galonska, M. MOP17
Gamelin, A. TUP09
Garcia Sosa, A. TUP35
Gąsior, M. **WEP06**
Gassner, D.M. MOP43
Gastaldi, F. MOP21
Gatti, G. TU3C2
Gebreyohannes, F.T. MOP21
Geerebaert, Y. MOP21
Gehrke, T. MOP17
Geloni, G. TUP16
Georgiev, G.Z. MOP28, TUP20, TUP21
Gerth, C. TH1C3
Gevin, O. MOP21
Gibson, S.M. MOP23, **TU1I1**, TUP15, TU3C3, ~~**WEP19**~~
Gil, P. ~~**WEP13**~~
Ginter, T.N. TU3C4
Giordano, F. MOP05
Giuressi, D. TUP02
Gloor, M. TUP12
Goethem, M.J. MOP33

ISBN: 978-3-95450-241-7 ISSN: 2673-5350

Goldblatt, A. **TU3C3**, WEP23
Gonzalez Berges, M. TU2C2
Good, J. MOP28, TUP21
Gorokhova, E.I. TUP29, WE3I1
Gorzawski, A.A. TUP23
Gottstein, A. WE3C2
Grannan, A.M. TU2T1
Graziani, C.J. TU2T1
Grünert, J. WEP15
Grespan, F. TUP35
Grishin, V. MOP07
Groetz, J.E. WE3C4
GroSS, M. MOP28, TUP20, TUP21
Gudkov, D. WEP12, WEP23
Guerin, H. **TUP15**
Guerrero, A. WEP23
Guillaumat, R. MOP21
Gula, K. ~~WEP35~~

— H —

Haase, A.A. TUP11
Haberer, Th. MOP17
Haddad, F. MOP21
Härer, B. WEP26
Haider, D.M. TUP31, WEP30
Halama, A.J. MOP03
Halis, D. ~~**WEP18**~~, WEP43
Hall, C.C. MOP10
Hanna, B.M. TUP05
Hardion, V. TUP41, WEP38
Harms, E.R. TUP05
Hassanzadegan, H. MOP07, TUP35
Henares, J.L. TU3C2
Henderson, J. MO1C3
Henderson, M.J. MOP10
Hermann, R.L. **MOP17**
Herranz, J. **WEP17**
Hill, R. WEP10
Hillert, W. MOP28, MOP37
Hiraiwa, T. TU1C3
Hoehl, A. ~~TH1C4~~
Hoffmann, A. MOP28, TUP20
Hofmann, T. TU3C3
Holz, M. TUP41
Holz, M. MOP12, TUP13
Houghton, C.E. **MOP15**
Hubert, N. TUP09, TUP19, TUP42
Hudson, L. MO3C2
Hulsart, R.L. MOP43
Hwang, J.-G. MOP02, TUP18

— I —

Ibrahim, M.A. TUP05
Igarashi, S. WEP21
Ilhan, T.B. ~~WEP18~~, **WEP43**
Ilinski, P. **MOP44**
Imanol Apiñaniz, J. TU3C2
Inagaki, T. TUP32
Inanc, A. WEP43
Irace, A. MOP05
Iriso, U. TUP16, TUP40, **WEP16**
Ischebeck, R. MOP01

— J —

Jabłoński, S. TUP43, **WEP36**
Jackson, S. WEP23
Jacob, J. MOP35
Jacobson, B.T. TU2C3
Jalali, B. TH1C3
Jamróz, J.J. TUP23
Jarvis, J.D. ~~**TH2I3**~~
Jin, Y. TUP02
Jones, B. TUP35
Jones, J.K. MO1C3
Joshi, N.Y. MO1C3
Jürgensen, L.E. MOP26

— K —

Kadyrov, R.A. TU2C3
Kain, V. WE3C3
Kaipainen, A. TU3C4
Kamerdzhiev, V. MOP03
Kamps, T. TUP18
Karataev, P. WEP29
Kaya, U. WEP43
Kedych, V. **MOP29**
Keil, B. **TUP12**, WE2C4
Kersevan, R. TUP15
Kim, E.-S. ~~TUP14~~
Kim, G.D. ~~TUP14~~, ~~WEP11~~
Kim, J. MOP16
Kitamura, R. **TH1I1**
Kittelmann, I. MOP07
Klag, P. ~~**WE1I3**~~
Klaproth, S. TUP25
Klein, R. MOP31, ~~TH1C4~~
Klute, J. TUP43, WEP36
Kobayashi, K. MO3C3
Kocevar, H. MOP07
Koehler, A. **TU3I1**
Kolbinger, B. TUP15
Koos, C. WEP24
Kopmann, A. MOP42
Koschitzki, C. TUP21
Kotz, A. WEP24
Koumeir, C. MOP21
Kowalski, G.W. ~~**WEP35**~~
Kowalski, S.K. MOP22
Kral, J. TU2C2
Krasilnikov, M. MOP28, TUP20, TUP21
Krawczyk, P. ~~MO1I2~~
Krejcik, P. TUP11
Kronenberg, S. MOP38
Krouptchenkov, I. WEP14
Kruchinin, K.O. MOP09
Krüger, W. MOP29

Content from this work may be used under the terms of the CC BY 4.0 licence (© 2022). Any distribution of this work must maintain attribution to the author(s), title of the work, publisher, and DOI

ISBN: 978-3-95450-241-7 ISSN: 2673-5350

Krupa, M. WEP10, **WEP12**
Kruschinski, A. ~~**TH1C4**~~
Kube, G. TUP13, TUP21, **WEP08**, WEP09, WEP20
Kubota, K. WE2I3
Kukstas, E. WEP32
Kumar, S. WEP28
Kurfürst, C. TUP10
Kuszynski, J. WEP31
Kuzmin, K. **WEP24**
Kwiatkowski, R. **TUP04**
Kwon, J.W. ~~TUP14~~, ~~**WEP11**~~

— L —

Labat, M. **TUP19**
Lacarrere, G.O. WEP23
Lanceri, L. TUP02
Lannoy, C. **TUP34**
Lantschner, M. WEP20
Łasocha, K. TUP28, TUP34
Last, A. MOP18
Leban, P. MOP13, WEP08, **WEP09**
Lee, D.W. TU2T1
Lee, Y. TU2T1
Lefèvre, T. MOP45, TU1I1, TUP15, TUP16, WEP29
Lensch, T. WEP14
Levens, T.E. TU1I1, WEP06
Leverington, B. MOP17
Levin, D.S. **TU3C4**
Levinsen, Y. MO2C2, **TUP35**
Li, J. MOP31
Li, S. ~~**MO2C3**~~
Li, X. TUP21
Li, X.-K. MOP28, TUP20
Lidia, S.M. ~~**MO2I1**~~
Lim, E.H. ~~**TUP14**~~, ~~WEP11~~
Lindberg, M. TUP41, WEP38
Lindberg, R.R. TU2T1
Lindvall, R. WEP38
Linev, S. MOP29
Lipka, D. **MOP12**, TUP13, WEP14
Lishilin, O. TUP21
Liu, F. ~~WEP05~~
Liu, J. WEP15
Liu, Z. ~~TUP06~~
Lobach, I. **MO2I4**
Lorbeer, B. MO3C4, **WEP14**
Lovric, G. WE1C2
Ludwig, F. TUP43
Lueangaramwong, A. MOP28, TUP20, TUP21
Luo, Z.Q. ~~**TUP06**~~
Lyapin, A. **MOP08**, **MOP09**, MOP39

— M —

Machalett, F. WEP30
Maesaka, H. TU1C3, **TUP32**, WE2I3
Magniette, F. MOP21
Maier, S. **MOP27**
Mal, K. WEP28
Manigot, P. MOP21
Marcellini, F. MOP24
Marich, M. **TUP02**
Mariet, A. **WE3C4**
Marinkovic, G. TUP12, WE2C4
Marongiu, M. **WEP20**
Marqversen, O. **TUP30**
Marrazzo, V.R. MOP05
Marsic, N. TUP31
Martínez Samblas, J. TU2C2
Martens, S.J. **WEP33**
Martí, Z. TUP40
Martin Nieto, M. MOP45, WEP22, WEP23, WE3C3
Martins, J.P.S. MOP40, TUP23
Masaki, M. TU1C3, **WE2I3**
Mases Solé, I. WEP16
Mateu, I. WE3C2
Mathisen, S.L. MO1C3, **MOP32**
Mazzoni, S. **MOP45**, TUP16, TUP17, WEP29, WE3C3
McCallum, M.S. MOP09, **MOP39**
Mehta, R. WEP28
Melkumyan, D. TUP21
Michel, J. MOP29
Mikhalchan, A. WE3C4
Milas, N. **MO2C2**, MOP07, **TUP23**, TUP35
Milosic, T. TUP36
Miniskar, N.R. ~~WEP05~~
Mirza, S.H. **TUP43**, WEP36
Miyamoto, R. MO2C2, TUP35
Mochihashi, A. MOP27, MOP42
Mock, J.A. TU2C3
Moldes, J. TUP40
Morales Vigo, S. TU2C2
Morgan, A.F.D. MO3C2, WEP37
Moser, B. WE3C4
Mounet, N. TUP34
Müller, A.-S. MOP27, MOP42, WEP24, WEP26
Mueller, F. TUP21
Müller, M. MOP31
Müller, W.F.O. TUP31
Muyan, G. TUP10
Myalski, S. TUP10

— N —

Nagaitsev, S. MO2I4
Nantista, C.D. **TUP11**
Nasse, M.J. MOP27
Navarro Fernandez, A. WEP17, **WEP22**
Navrotski, G. TU2T1
Neswold, R. TUP05
Nevay, L.J. ~~WEP19~~
Newton, M.E. WEP15
Niedermayer, P.J. **MOP36**
Niehues, G. WEP24, WEP26

Content from this work may be used under the terms of the CC BY 4.0 licence (© 2022). Any distribution of this work must maintain attribution to the author(s), title of the work, publisher, and DOI

ISBN: 978-3-95450-241-7 ISSN: 2673-5350

Niemczyk, R. MOP28, TUP20
Nietubyc, R. ~~MO1I1~~, **~~MO1I2~~**, TUP04
Noll, D. MO2C2, MOP07, TUP35
Nosych, A.A. TUP16, WEP16
Novokshonov, A.I. **TUP21**, **~~WE1I1~~**, WEP20

— O —

Oblak, M.O. WEP08, WEP09
Oeftiger, A. **TU1I2**
Ogur, S. ~~TUP22~~, ~~WEP18~~
Olsson, T. WEP37
Oppelt, A. MOP28, TUP21
Ortega Ruiz, I. WE3C3
Osawa, H. MO3C3
Overton, T.J. MO1C3
Oz, S. ~~WEP18~~, WEP43
Ozbey, A. WEP43
Ozcan, E.V. ~~TUP22~~, ~~WEP18~~, WEP43
Ozkan Loch, C. **MOP01**, WE1C2

— P —

Pacey, T.H. **MO1C3**, MOP32
Paglovec, P. MOP13, TUP10, WEP08, WEP09
Palm, M. MOP45
Panaś, R. **TUP28**, ~~WEP35~~
Paniccia, M.C. **MOP43**
Papaevangelou, T. MOP07
Park, J. TU2C3
Paroli, B. TUP16
Parry, N.L. TUP01
Parsons França, L. **WEP32**
Patil, M.M. WEP26
Pédeau, D. TUP19
Penirschke, A. WEP24
Perez Juarez, E.P.J. MO3C2
Pérez-Hernández, J.A.P. TU3C2
Petenev, Y. **MOP31**
Peters, A. MOP17
Petringa, G. **~~TU2I4~~**
Pfeiffer, S. TUP43, WEP36
Pichoff, N. ~~WEP13~~
Piekarski, M. **TUP38**
Pieloni, T. TUP34
Pietralla, N. MOP26
Pietraszko, J. MOP29
Poirier, F. MOP21
Pollard, A.E. MO1C3
Potenza, M.A.C. TUP16
Pozenel, A. TUP10
Preston, S. **WEP37**
Proft, D. **MOP38**
Prost, L.R. TUP05
Puławski, S. MOP22
Puls, J. ~~TH1C4~~
Purtschert, J. TUP12

— Q —

Qian, H.J. MOP28, TUP20, TUP21

— R —

Rajput, K. ~~WEP05~~
Ramos Garcia, M.T. TUP15
Ramuhalli, P. ~~WEP05~~
Reader, A.J. MOP28
Rehm, G. MOP02, MOP18, **~~MO3I1~~**, TUP43, WEP31
Reichert, T. TUP25
ReiSSig, M. **WEP26**
Reiter, A. TUP25, TUP31
Repič, B. MOP13, WEP08, WEP09
Repovž, M. **TUP10**
Richard, C.J. MOP28, **TUP20**
Ries, M. MOP02
Rinaldi, A.T. WEP23
Ristow, N.A. TU3C4
Rivera, R.A. TUP05
Rodnyi, P. TUP29, WE3I1
Rodrigues, G.O. TUP25, **WEP28**
Rodríguez Páramo, Á. WEP17
Rodriguez, E. TU2C3
Rohrer, M. MOP19
Romanov, A.L. MO2I4, MOP10, **~~TH2I1~~**
Roncarolo, F. TU3C3, WEP22, WEP23, WEP32, **WE3C3**
Rose, A.J. MO3C2
Rossi, F. **WEP25**
Rost, A. MOP29
Roussel, E. TH1C3
Roy, P.K. TU2C3
Ruprecht, R. WEP26
Rupsch, G.R. MOP03

— S —

Saccani, M. **TUP03**, WEP04
Safranek, J.A. MOP16, TUP01
Safvan, C.P. WEP28
Saifulin, M. **TUP29**, WE3I1
Salgado-López, C. **TU3C2**
Salvachúa, B. TU2C2
Salvant, B. MOP05, TUP15
Samadi, N. MOP01, **WE1C2**
Sameed, M. TUP17
Santamaria Garcia, A. MOP42
Santana-Leitner, M. TU2C3
Santucci, R.R. **WEP40**
Sapinski, M. **MOP19**, MOP24
Sato, Y. WEP21
Satou, K. **WEP21**
Saveliev, Y.M. MO1C3
Scampoli, P. WE3C2
Scheible, B.E.J. WEP24
Scheidt, K.B. MOP34, MOP35
Schillinger, C. WEP23

Content from this work may be used under the terms of the CC BY 4.0 licence (© 2022). Any distribution of this work must maintain attribution to the author(s), title of the work, publisher, and DOI

ISBN: 978-3-95450-241-7 ISSN: 2673-5350

Content from this work may be used under the terms of the CC BY 4.0 licence (© 2022). Any distribution of this work must maintain attribution to the author(s), title of the work, publisher, and DOI

Schiwietz, G. MOP02
Schlarb, H. TUP43, WEP24, WEP36
Schmelz, M. TUP31, WEP30
Schmidl, F. TUP31, WEP30
Schmidt, C.J. MOP29
Schmidt-Föhre, F. WEP08, WEP09
Schmitzer, C. TUP10
Schneider, G. TUP15, TUP17, WEP12
Schoefer, V. TUP39
Schönau, T. WEP30
Schram, M. ~~WEP05~~
Schreiber, P. MOP27, MOP42
Schwarz, M. MOP27
Schwarzenberger, A. WEP24
Schwickert, M. TUP31, WEP30
Scomparin, L. **MOP42**
Sebek, J.J. TUP01
Sedláček, O. **TUP17**
Seguí, L. MOP07
Seidel, P. WEP30
Semenov, A. WEP40
Serin, M. ~~WEP18~~
Servagent, N. MOP21
Shea, T.J. **MOP07**
Shemyakin, A.V. MO2I4, TUP05
Shi, X. WE1C2
Shields, W. MOP08
Siano, M. **TUP16**
Sidorowski, K. TUP17
Sieber, T. TUP31, WEP17, WEP30
Silva, H.A. MOP07
Simon, C. ~~WEP13~~
Singh, R. MOP36, TU1I2, **TUP25**, TUP36, WEP28, WEP42
Sito, L. MOP05
Sjöström, M. TUP41
Škabar, M. TUP10
Smith, R.J. MOP32
Snedden, E.W. MO1C3
Snuverink, J. ~~MO2C3~~
Sorge, S. TUP36
Sosnowski, J. **WEP07**
Soutome, K. TU1C3, WE2I3
Spreitzer, A. MOP38
Stampfli, A.M.M. MOP01
Stancari, G. MO2I4
Stant, L.T. **MO3C2**
Steffen, B. TH1C3
Steinmann, J.L. MOP42
Stephan, F. MOP28, TUP20, TUP21
Stöhlker, T. TUP31, WEP30
Stolz, R. TUP31, WEP30
Storey, J.W. TUP15
Stringer, O. TUP17
Strokov, S. **TUP13**, TUP21
Stulle, F. MOP33
Sugimoto, T. WE2I3
Svärd, R. WEP38
Svintozelskyi, V. MOP29
Swain, C. MO1C3
Switka, M.T. **MOP37**, MOP38
Szczepanski, B. TUP43
Szewiński, J. TUP04
Szillasi, Z. MOP05
Szlachetko, J. ~~**MO1I1**~~
Szwaj, C. **TH1C3**

— **T** —

Tagg, J. TU3C3
Takahashi, C. **TUP41**, WEP38
Takahashi, S. MO3C3
Takano, S. **TU1C3**, WE2I3
Takao, M. TU1C3
Takeuchi, M.T. WE2I3
Tan, J. WE3C3
Tanaka, H. TU1C3, WE2I3
Taoutaou, F. MOP35
Tarawneh, H. TUP41
Tarkeshian, R. MO2C2, MOP07
Thiebaux, C. **MOP21**
Thieberger, P. MOP43
Thomas, C.A. MOP07
Thomasset, M. TUP19
Tian, K. **MOP16**, **TUP01**
Tipper, A. MO3C2
Titmarsh, R. **MOP40**
Tollervey, C. MO1C3
Torino, L. TUP16, **TUP40**
Toufexis, F. TUP01
Trad, G. MOP23, TUP16
Träger, M. MOP29
Trautmann, C. TUP29, WE3I1
Traxler, M. MOP29
Türemen, G. WEP43
Tympel, V. TUP31, **WEP30**

— **U** —

Udrea, S. TUP17
Ueshima, K. TU1C3, TUP32
Ulrich-Pur, F. MOP29
Unel, G. ~~**TUP22**~~, ~~WEP18~~, WEP43
Urbaniak, M.U. **MOP22**

— **V** —

Vashchenko, G. MOP28, TUP20, TUP21
Velotti, F.M. WEP32, WE3C3
Veness, R. TUP17, WEP23, WE3C4
Venevtsev, I.D. TUP29, WE3I1
Verderi, M. MOP21
Vigali, A. MOP13
Viganò, W. TUP03, **WEP04**
Vila Comamala, J. MOP01
Vilatela, J.J. WE3C4
Vilcins, S. MOP12, TUP13, WEP14

ISBN: 978-3-95450-241-7 ISSN: 2673-5350

Vitale, L. TUP02
Vitoratou, N. **MOP18**
Vogt, J.M. WEP34
Vojskovic, I. MO2C2, TUP35
Volpe, L. TU3C2
Voy, D.C. WEP40

— W —

Walasek-Höhne, B. TUP29, WE3I1
Walsh, D.A. MO1C3
Wańczyk, J.M. **TH2C2**
Wang, G.M. ~~**WE2T1**~~
Wang, HS. ~~**TUP26**~~
Warner, A. **TUP05**
Watanabe, T. TU1C3, WE2I3
Wawrzyniak, A.I. ~~**MOOI1**~~, ~~MO1I1~~, TUP04, ~~WEP35~~, ~~**THCI2**~~
Wójcik, K.W. MOP22
Weber, M. MOP42
Weih, S. MOP26
Weilbach, T. TUP20, TUP21
Welch, J.J. TU2C3
Welsch, C.P. TUP17, WEP32
Werner, M. WEP14
Widmann, C. WEP26
Wiechecki, J.J. ~~WEP35~~
Wiese, S. MOP02
Wittenburg, K. WEP08, WEP09, WEP20
Wolf, M. TUP10
Wolfenden, J. MO1C3
Wu, J.Y. TUP05

— X —

Xia, G.X. WEP29
Xiao, M. **MOP33**

— Y —

Yanagida, K. TUP32
Yang, J. **TUP36**
Yépez, D. TUP40
Young, A.R. ~~WEP05~~
Yucesan, Y.A. ~~WEP05~~

— Z —

Zakosarenko, V. TUP31, WEP30
Zaloga, D.R. TUP04
Zamantzas, C. TU2C2, TUP03, WE3C3
Zeng, R.H. MO2C2, TUP35
Zeus, M. WEP16
Zhang, H.D. TUP17, WEP32
Zhou, Y.M. ~~**TH1I2**~~
Zhukov, A.P. ~~WEP05~~

Content from this work may be used under the terms of the CC BY 4.0 licence (© 2022). Any distribution of this work must maintain attribution to the author(s), title of the work, publisher, and DOI

ISBN: 978-3-95450-241-7 ISSN: 2673-5350

ISBN: 978-3-95450-241-7 ISSN: 2673-5350

Institutes List

7S
Peligros (Granada), Spain
- Fernández, J.
- Gil, P.

AEC
Bern, Switzerland
- Braccini, S.
- Casolaro, P.
- Dellepiane, G.
- Gottstein, A.
- Mateu, I.
- Scampoli, P.

ALBA-CELLS
Cerdanyola del Vallès, Spain
- Benedetti, G.
- Fernández, F.F.B.
- Iriso, U.
- Martí, Z.
- Moldes, J.
- Nosych, A.A.
- Torino, L.
- Yépez, D.
- Zeus, M.

ANL
Lemont, Illinois, USA
- Borland, M.
- Dooling, J.C.
- Grannan, A.M.
- Graziani, C.J.
- Lee, Y.
- Lindberg, R.R.
- Lobach, I.
- Navrotski, G.
- Shi, X.

Atomki
Debrecen, Hungary
- Beni, N.
- Szillasi, Z.

BERGOZ Instrumentation
Saint Genis Pouilly, France
- Delaviere, T.
- Dupuy, L.
- Stulle, F.

BNL
Upton, New York, USA
- Brown, K.A.
- Clark, S.L.
- Gassner, D.M.
- Hulsart, R.L.
- Paniccia, M.C.
- Schoefer, V.
- Thieberger, P.
- Wang, G.M.

Boğaziçi University
Bebek / İstanbul, Turkey
- Elibollar, E.
- Er, M.F.
- Inanc, A.
- Ozcan, E.V.

Boğaziçi University, Kandilli Accelerator
İstanbul, Turkey
- Ilhan, T.B.

CEA-DRF-IRFU
France
- Desmarchelier, G.
- Duperrier, R.D.

CEA-IRFU
Gif-sur-Yvette, France
- Delagnes, É.
- Ferrand, G.
- Gebreyohannes, F.T.
- Gevin, O.
- Papaevangelou, T.
- Pichoff, N.
- Seguí, L.
- Simon, C.

CERN
Meyrin, Switzerland
- Ady, M.
- Alves, D.
- Andreassen, O.Ø.
- Andreazza, W.
- Arrutia Sota, P.A.
- Balci, E.
- Belohrad, D.
- Beni, N.
- Bravin, E.
- Breglio, G.
- Buontempo, S.
- Butti, D.
- Calvo Giraldo, E.
- Carra, F.
- Castro Sequeiro, C.
- Chritin, N.S.
- Churchman, A.R.
- Cristiano, A.
- De Maria, R.
- Degl'Innocenti, I.
- Di Carlo, S.
- Duraffourg, M.
- Effinger, E.
- Emery, J.
- Esteban Felipe, J.C.
- Fienga, F.
- Fraser, M.A.
- Gąsior, M.
- Giordano, F.
- Goldblatt, A.
- Gonzalez Berges, M.

Content from this work may be used under the terms of the CC BY 4.0 licence (© 2022). Any distribution of this work must maintain attribution to the author(s), title of the work, publisher, and DOI

ISBN: 978-3-95450-241-7 ISSN: 2673-5350

Content from this work may be used under the terms of the CC BY 4.0 licence (© 2022). Any distribution of this work must maintain attribution to the author(s), title of the work, publisher, and DOI

- Gudkov, D.
- Guerin, H.
- Guerrero, A.
- Hofmann, T.
- Jackson, S.
- Kain, V.
- Kersevan, R.
- Kolbinger, B.
- Krupa, M.
- Lacarrere, G.O.
- Lannoy, C.
- Lefèvre, T.
- Levens, T.E.
- Mariet, A.
- Marqversen, O.
- Marrazzo, V.R.
- Martin Nieto, M.
- Martínez Samblas, J.
- Mases Solé, I.
- Mazzoni, S.
- Morales Vigo, S.
- Moser, B.
- Mounet, N.
- Navarro Fernandez, A.
- Ogur, S.
- Ortega Ruiz, I.
- Palm, M.
- Parsons França, L.
- Ramos Garcia, M.T.
- Rinaldi, A.T.
- Roncarolo, F.
- Saccani, M.
- Salvachúa, B.
- Salvant, B.
- Schillinger, C.
- Schneider, G.
- Sedláček, O.
- Sidorowski, K.
- Sito, L.
- Storey, J.W.
- Szillasi, Z.
- Tagg, J.
- Tan, J.
- Trad, G.
- Velotti, F.M.
- Veness, R.
- Viganò, W.
- Wańczyk, J.M.
- Zamantzas, C.

CLPU
Villamayor, Spain
- Curcio, A.
- de Luis, D.
- Gatti, G.
- Henares, J.L.
- Imanol Apiñaniz, J.
- Pérez-Hernández, J.A.P.
- Salgado-López, C.
- Volpe, L.

CLS
Saskatoon, Saskatchewan, Canada
- Batten, T.
- Bertwistle, D.
- Boland, M.J.
- Bree, M.
- Vogt, J.M.

Cockcroft Institute
Warrington, Cheshire, United Kingdom
- Angal-Kalinin, D.
- Bainbridge, A.R.
- Jones, J.K.
- Overton, T.J.
- Saveliev, Y.M.
- Sedláček, O.
- Stringer, O.
- Swain, C.
- Welsch, C.P.
- Wolfenden, J.
- Zhang, H.D.

Cockcroft Institute, Lancaster University
Lancaster, United Kingdom
- Henderson, J.

CTUP/FNSPE
Prague, Czech Republic
- Kral, J.

Cyclotron ARRONAX
Saint-Herblain, France
- Haddad, F.
- Koumeir, C.
- Poirier, F.

DESY
Hamburg, Germany
- Aloev, A.
- Baboi, N.
- Czwalinna, M.K.
- Duhme, H.T.
- Dursun, B.
- Eichler, A.
- Gerth, C.
- Holz, M.
- Jabłoński, S.
- Klute, J.
- Krouptchenkov, I.
- Kube, G.
- Lantschner, M.
- Lensch, T.
- Lipka, D.
- Lorbeer, B.
- Ludwig, F.
- Marongiu, M.
- Mirza, S.H.
- Novokshonov, A.I.
- Pfeiffer, S.
- Schlarb, H.
- Schmidt-Föhre, F.
- Steffen, B.

ISBN: 978-3-95450-241-7 ISSN: 2673-5350

- Strokov, S.
- Szczepanski, B.
- Vilcins, S.
- Werner, M.
- Wittenburg, K.

DESY Zeuthen
Zeuthen, Germany
- Aboulbanine, Z.
- Adhikari, G.D.
- Aftab, N.
- Boonpornprasert, P.
- Georgiev, G.Z.
- Good, J.
- GroSS, M.
- Hoffmann, A.
- Koschitzki, C.
- Krasilnikov, M.
- Li, X.-K.
- Li, X.
- Lishilin, O.
- Lueangaramwong, A.
- Melkumyan, D.
- Mueller, F.
- Niemczyk, R.
- Oppelt, A.
- Qian, H.J.
- Richard, C.J.
- Stephan, F.
- Vashchenko, G.
- Weilbach, T.

DLR
Berlin, Germany
- Koehler, A.

DLS
Oxfordshire, United Kingdom
- Abbott, M.G.
- Bloomer, C.
- Bobb, L.
- Cook, G.
- Houghton, C.E.
- Hudson, L.
- Morgan, A.F.D.
- Olsson, T.
- Perez Juarez, E.P.J.
- Preston, S.
- Rose, A.J.
- Stant, L.T.
- Tipper, A.
- Vitoratou, N.

Dumlupnar University, Faculty of Science and Arts
Kutahya, Turkey
- Cetinkaya, H.

EBG MedAustron
Wr. Neustadt, Austria
- Cerv, M.
- Kurfürst, C.
- Muyan, G.
- Myalski, S.
- Pozenel, A.
- Repovž, M.
- Schmitzer, C.
- Wolf, M.

Elettra-Sincrotrone Trieste S.C.p.A.
Basovizza, Italy
- Brajnik, G.
- Cautero, G.
- De Monte, R.
- Ferianis, M.
- Giuressi, D.
- Rossi, F.

ELSA
Bonn, Germany
- Desch, K.
- Elsner, D.
- Frommberger, F.
- Kronenberg, S.
- Proft, D.
- Spreitzer, A.
- Switka, M.T.

EPFL
Lausanne, Switzerland
- Akhyani, M.
- Lannoy, C.
- Pieloni, T.

ESRF
Grenoble, France
- Benoist, N.
- Borowiec, P.B.
- Buratin, E.
- Denat, G.
- Jacob, J.
- Scheidt, K.B.
- Taoutaou, F.

ESS
Lund, Sweden
- Akhyani, M.
- Baron, R.A.
- Derrez, C.S.
- Donegani, E.M.
- Eshraqi, M.
- Esteban Müller, J.F.
- Fedel, G.S.
- Garcia Sosa, A.
- Gorzawski, A.A.
- Grishin, V.
- Hassanzadegan, H.
- Jamróz, J.J.
- Jones, B.
- Kittelmann, I.
- Kocevar, H.
- Levinsen, Y.
- Martins, J.P.S.
- Milas, N.
- Miyamoto, R.

Content from this work may be used under the terms of the CC BY 4.0 licence (© 2022). Any distribution of this work must maintain attribution to the author(s), title of the work, publisher, and DOI

ISBN: 978-3-95450-241-7 ISSN: 2673-5350

Content from this work may be used under the terms of the CC BY 4.0 licence (© 2022). Any distribution of this work must maintain attribution to the author(s), title of the work, publisher, and DOI

- Noll, D.
- Shea, T.J.
- Silva, H.A.
- Tarkeshian, R.
- Thomas, C.A.
- Vojskovic, I.
- Zeng, R.H.

ESS Bilbao
Zamudio, Spain
- Bustinduy, I.
- Rodríguez Páramo, Á.

European Organization for Nuclear Research (CERN)
Geneva, Switzerland
- Sameed, M.

EuXFEL
Schenefeld, Germany
- Freund, W.
- Geloni, G.
- Grünert, J.
- Liu, J.

FAIR
Darmstadt, Germany
- Rost, A.

Fermilab
Batavia, Illinois, USA
- Austin, M.R.
- Carmichael, L.R.
- Carneiro, J.-P.
- Diamond, J.S.
- Eddy, N.
- Hanna, B.M.
- Harms, E.R.
- Ibrahim, M.A.
- Jarvis, J.D.
- Nagaitsev, S.
- Neswold, R.
- Prost, L.R.
- Rivera, R.A.
- Romanov, A.L.
- Santucci, R.R.
- Semenov, A.
- Shemyakin, A.V.
- Stancari, G.
- Voy, D.C.
- Warner, A.
- Wu, J.Y.

FRIB
East Lansing, Michigan, USA
- Lidia, S.M.

FSU Jena
Jena, Germany
- Schmidl, F.
- Schönau, T.
- Seidel, P.

FZJ
Jülich, Germany
- Böhme, C.

German Cancer Research Center (DKFZ)
Heidelberg, Germany
- Gehrke, T.

Goethe Universität Frankfurt
Frankfurt am Main, Germany
- Michel, J.

GOI
St Petersburg, Russia
- Gorokhova, E.I.

GSI
Darmstadt, Germany
- Boutachkov, P.
- Crescimbeni, L.
- Forck, P.
- Galatyuk, T.
- Haider, D.M.
- Halama, A.J.
- Kamerdzhiev, V.
- Linev, S.
- Milosic, T.
- Niedermayer, P.J.
- Oeftiger, A.
- Pietraszko, J.
- Reichert, T.
- Reiter, A.
- Rupsch, G.R.
- Saifulin, M.
- Schmidt, C.J.
- Schwickert, M.
- Sieber, T.
- Singh, R.
- Sorge, S.
- Stöhlker, T.
- Träger, M.
- Trautmann, C.
- Traxler, M.
- Udrea, S.
- Ulrich-Pur, F.
- Walasek-Höhne, B.
- Yang, J.

HIJ
Jena, Germany
- Stöhlker, T.
- Tympel, V.

HIT
Heidelberg, Germany
- Galonska, M.
- Haberer, Th.
- Hermann, R.L.
- Peters, A.

HU Berlin
Berlin, Germany
- Kamps, T.

ISBN: 978-3-95450-241-7 ISSN: 2673-5350

HUST
Wuhan, People's Republic of China
- Liu, Z.
- Luo, Z.Q.

HZB
Berlin, Germany
- Alberdi-Esuain, B.
- Atkinson, T.
- Falkenstern, F.
- Feikes, J.
- Hwang, J.-G.
- Kamps, T.
- Kruschinski, A.
- Kuszynski, J.
- Li, J.
- Petenev, Y.
- Rehm, G.
- Ries, M.
- Schiwietz, G.
- Wiese, S.

I-Tech
Solkan, Slovenia
- Bardorfer, A.
- Baričevič, B.
- Bogataj, L.
- Cargnelutti, M.
- Dragonja, U.
- Leban, P.
- Oblak, M.O.
- Paglovec, P.
- Repič, B.
- Škabar, M.
- Vigali, A.

IBS
Daejeon, Republic of Korea
- Chung, Y.S.
- Kim, G.D.
- Kwon, J.W.

ICMAB
Bellatera, Spain
- Cazorla, A.C.

IMDEA
Madrid, Spain
- Mikhalchan, A.
- Vilatela, J.J.

INFN-Napoli
Napoli, Italy
- Buontempo, S.

INFN-Trieste
Trieste, Italy
- Bosisio, L.
- Gabrielli, A.
- Jin, Y.
- Lanceri, L.

INFN/LNL
Legnaro (PD), Italy
- Grespan, F.

INFN/LNS
Catania, Italy
- Cirrone, G.A.P.
- Petringa, G.

Integrated Sensors, LLC
Ottawa Hills, Ohio, USA
- Friedman, P.S.

IOQ
Jena, Germany
- Machalett, F.
- Stöhlker, T.

IPHT
Jena, Germany
- Schmelz, M.
- Schönau, T.
- Stolz, R.
- Zakosarenko, V.

IPQ KIT
Karlsruhe, Germany
- Eschenbaum, C.
- Koos, C.
- Kotz, A.
- Schwarzenberger, A.

İstanbul University
İstanbul, Turkey
- Adiguzel, A.
- Esen, S.
- Oz, S.

İstinye University, Institute of Sciences
İstanbul, Turkey
- Kaya, U.

IUAC
New Delhi, India
- Kumar, S.
- Mal, K.
- Mehta, R.
- Rodrigues, G.O.
- Safvan, C.P.

IUC
İstanbul, Turkey
- Ozbey, A.

J-PARC, KEK & JAEA
Ibaraki-ken, Japan
- Sato, Y.
- Satou, K.

JAEA/J-PARC
Tokai-Mura, Naka-Gun, Ibaraki-Ken, Japan
- Kitamura, R.

Jagiellonian University
Kraków, Poland
- Łasocha, K.

Content from this work may be used under the terms of the CC BY 4.0 licence (© 2022). Any distribution of this work must maintain attribution to the author(s), title of the work, publisher, and DOI

ISBN: 978-3-95450-241-7 ISSN: 2673-5350

Content from this work may be used under the terms of the CC BY 4.0 licence (© 2022). Any distribution of this work must maintain attribution to the author(s), title of the work, publisher, and DOI

JAI
Egham, Surrey, United Kingdom
- Alden, S.E.
- Bett, D.R.
- Lyapin, A.
- McCallum, M.S.
- Shields, W.

JASRI
Hyogo, Japan
- Dewa, H.
- Fujita, T.
- Fukami, K.
- Inagaki, T.
- Maesaka, H.
- Masaki, M.
- Soutome, K.
- Sugimoto, T.
- Takano, S.
- Takao, M.
- Takeuchi, M.T.
- Watanabe, T.
- Yanagida, K.

JASRI/SPring-8
Hyogo, Japan
- Aoyagi, H.
- Fujita, T.
- Kobayashi, K.
- Osawa, H.
- Takahashi, S.

JLab
Newport News, Virginia, USA
- Rajput, K.
- Schram, M.

KCL
London, United Kingdom
- Reader, A.J.

KEK
Ibaraki, Japan
- Aryshev, A.
- Igarashi, S.
- Kruchinin, K.O.

KIT
Eggenstein-Leopoldshafen, Germany
- Blomley, E.
- Brosi, M.
- Bründermann, E.
- Bründermann, E.
- Caselle, M.
- Cha, H.J.
- Dritschler, T.
- Funkner, S.
- Härer, B.
- Kopmann, A.
- Kuzmin, K.
- Last, A.
- Maier, S.
- Mochihashi, A.
- Müller, A.-S.
- Nasse, M.J.
- Niehues, G.
- Patil, M.M.
- ReiSSig, M.
- Ruprecht, R.
- Santamaria Garcia, A.
- Schreiber, P.
- Schwarz, M.
- Scomparin, L.
- Steinmann, J.L.
- Weber, M.
- Widmann, C.

Korea University Sejong Campus
Sejong, Republic of Korea
- Lim, E.H.

KPH
Mainz, Germany
- Achenbach, P.
- Klag, P.

KUS
Sejong, Republic of Korea
- Kim, E.-S.

LLR
Palaiseau, France
- Bernardi, L.
- Gastaldi, F.
- Geerebaert, Y.
- Guillaumat, R.
- Magniette, F.
- Manigot, P.
- Thiebaux, C.
- Verderi, M.

MAX IV Laboratory, Lund University
Lund, Sweden
- Breunlin, J.
- Felcsuti, G.
- Freitas, Á.
- Hardion, V.
- Holz, M.
- Ilinski, P.
- Lindberg, M.
- Lindvall, R.
- Sjöström, M.
- Svärd, R.
- Takahashi, C.
- Tarawneh, H.

MPI-P
München, Germany
- Bergamaschi, M.

Naples University Federico II
Napoli, Italy
- Scampoli, P.

ISBN: 978-3-95450-241-7 ISSN: 2673-5350

NCBJ
Świerk/Otwock, Poland
- Krawczyk, P.
- Kwiatkowski, R.
- Nietubyc, R.
- Sosnowski, J.
- Szewiński, J.
- Zaloga, D.R.

NSCL
East Lansing, Michigan, USA
- Ginter, T.N.

NSRC SOLARIS
Kraków, Poland
- Gula, K.
- Kowalski, G.W.
- Panaś, R.
- Piekarski, M.
- Szlachetko, J.
- Wawrzyniak, A.I.
- Wiechecki, J.J.

ORNL
Oak Ridge, Tennessee, USA
- Blokland, W.
- Liu, F.
- Miniskar, N.R.
- Ramuhalli, P.
- Young, A.R.
- Zhukov, A.P.

ORNL RAD
Oak Ridge, Tennessee, USA
- Yucesan, Y.A.

PARTREC
Groningen, The Netherlands
- Brandenburg, S.
- Goethem, M.J.

PhLAM/CERLA
Villeneuve d'Ascq, France
- Bielawski, S.
- Evain, C.
- Roussel, E.
- Szwaj, C.

Proactive Research and Development
Sabadell, Spain
- Herranz, J.

PSI
Villigen PSI, Switzerland
- Adelmann, A.
- Baeta Neves Diniz Santos, P.H.
- Ditter, R.
- Dölling, R.
- Gloor, M.
- Ischebeck, R.
- Keil, B.
- Li, S.
- Lovric, G.
- Marcellini, F.
- Marinkovic, G.
- Ozkan Loch, C.
- Purtschert, J.
- Rohrer, M.
- Samadi, N.
- Sapinski, M.
- Snuverink, J.
- Stampfli, A.M.M.
- Vila Comamala, J.

PTB
Berlin, Germany
- Barboutis, A.B.
- Hoehl, A.
- Klein, R.
- Müller, M.
- Puls, J.

QST
Sendai, Miyagi, Japan
- Ueshima, K.

RadiaSoft LLC
Boulder, Colorado, USA
- Cook, N.M.
- Edelen, J.P.
- Einstein-Curtis, J.A.
- Hall, C.C.
- Henderson, M.J.

RIKEN SPring-8 Center
Hyogo, Japan
- Fukami, K.
- Hiraiwa, T.
- Inagaki, T.
- Maesaka, H.
- Soutome, K.
- Sugimoto, T.
- Takano, S.
- Tanaka, H.
- Watanabe, T.

RIKEN SPring-8 Center, Innovative Light Sources Division
Hyogo, Japan
- Fukui, T.
- Maesaka, H.

Royal Holloway, University of London
Surrey, United Kingdom
- Arteche, A.
- Boorman, G.E.
- Bosco, A.
- Gibson, S.M.
- Guerin, H.
- Karataev, P.
- Nevay, L.J.

SARI-CAS
Pudong, Shanghai, People's Republic of China
- Zhou, Y.M.

SES
Hyogo-pref., Japan
- Kubota, K.

Content from this work may be used under the terms of the CC BY 4.0 licence (© 2022). Any distribution of this work must maintain attribution to the author(s), title of the work, publisher, and DOI

ISBN: 978-3-95450-241-7 ISSN: 2673-5350

Content from this work may be used under the terms of the CC BY 4.0 licence (© 2022). Any distribution of this work must maintain attribution to the author(s), title of the work, publisher, and DOI

SLAC
Menlo Park, California, USA
- Boltz, T.
- Brown, G.W.
- Chin, E.P.
- Clarke, C.I.
- Cobau, W.G.
- Condamoor, S.
- Corbett, W.J.
- Fisher, A.S.
- Frosio, T.
- Haase, A.A.
- Jacobson, B.T.
- Kadyrov, R.A.
- Kim, J.
- Krejcik, P.
- Mock, J.A.
- Nantista, C.D.
- Park, J.
- Parry, N.L.
- Rodriguez, E.
- Roy, P.K.
- Safranek, J.A.
- Santana-Leitner, M.
- Sebek, J.J.
- Tian, K.
- Toufexis, F.
- Welch, J.J.

SOLEIL
Gif-sur-Yvette, France
- Alves, F.
- Bence, A.
- Berlioux, A.
- Broucquart, R.
- Capitanio, B.
- Cauchon, G.
- Da Silva, J.
- El Ajjouri, M.
- Gamelin, A.
- Hubert, N.
- Labat, M.
- Pédeau, D.
- Thomasset, M.

SPbPU
St. Petersburg, Russia
- Rodnyi, P.
- Venevtsev, I.D.

SSRF
Shanghai, People's Republic of China
- Wang, HS.
- Zhou, Y.M.

STFC/DL/ASTeC
Daresbury, Warrington, Cheshire, United Kingdom
- Angal-Kalinin, D.
- Bainbridge, A.R.
- Henderson, J.
- Jones, J.K.
- Joshi, N.Y.
- Mathisen, S.L.
- Pacey, T.H.
- Pollard, A.E.
- Saveliev, Y.M.
- Smith, R.J.
- Snedden, E.W.
- Tollervey, C.
- Walsh, D.A.

STFC/RAL/ISIS
Chilton, Didcot, Oxon, United Kingdom
- Titmarsh, R.

SUBATECH
Nantes, France
- Haddad, F.
- Servagent, N.

Supracon AG
Jena, Germany
- Zakosarenko, V.

Taras Shevchenko National University of Kyiv
Kyiv, Ukraine
- Svintozelskyi, V.

TEMF, TU Darmstadt
Darmstadt, Germany
- Ackermann, W.
- De Gersem, H.
- Marsic, N.
- Müller, W.F.O.

TENMAK-NUKEN
Ankara, Turkey
- Türemen, G.

The University of Liverpool
Liverpool, United Kingdom
- Apsimon, Ö.
- Kukstas, E.
- Sedláček, O.
- Stringer, O.
- Swain, C.
- Welsch, C.P.
- Wolfenden, J.
- Zhang, H.D.

The University of Manchester
Manchester, United Kingdom
- Davut, C.
- Overton, T.J.

THM
Friedberg, Germany
- Klaproth, S.
- Penirschke, A.
- Scheible, B.E.J.

TU Darmstadt
Darmstadt, Germany
- Arnold, M.
- Brauch, A.
- Enders, J.
- Galatyuk, T.
- Jürgensen, L.E.

ISBN: 978-3-95450-241-7 ISSN: 2673-5350

- Kedych, V.
- Krüger, W.
- Pietralla, N.
- Saifulin, M.
- Trautmann, C.
- Weih, S.

UCI
Irvine, California, USA
- Unel, G.

UCLA
Los Angeles, California, USA
- Jalali, B.

UCSC
Santa Cruz, California, USA
- Lee, D.W.

UFC
Besançon, France
- Devel, M.
- Groetz, J.E.

UMAN
Manchester, United Kingdom
- Joshi, N.Y.
- Xia, G.X.

UMCG
Groningen, The Netherlands
- Xiao, M.

Universita' degli Studi di Milano & INFN
Milano, Italy
- Paroli, B.
- Potenza, M.A.C.

Universität Heidelberg
Heidelberg, Germany
- Leverington, B.

University of Essex, Physics Centre
Colchester, United Kingdom
- Engel, S.E.

University of Hamburg, Institut für Experimentalphysik
Hamburg, Germany
- Hillert, W.

University of Huddersfield
Huddersfield, United Kingdom
- Hill, R.

University of Michigan
Ann Arbor, Michigan, USA
- Ferretti, C.
- Kaipainen, A.
- Levin, D.S.
- Ristow, N.A.

University of Napoli Federico II
Napoli, Italy
- Breglio, G.
- Fienga, F.
- Irace, A.
- Marrazzo, V.R.
- Sito, L.

University of Saskatchewan
Saskatoon, Canada
- Martens, S.J.

University of Silesia in Katowice
Katowice, Poland
- Balkova, Y.
- Kowalski, S.K.
- Puławski, S.
- Urbaniak, M.U.
- Wójcik, K.W.

University of Trieste
Trieste, Italy
- Carrato, S.
- Colja, M.
- Marich, M.

University of Warwick
Coventry, United Kingdom
- Newton, M.E.

Università degli Studi di Milano
Milano, Italy
- Siano, M.

Università degli Studi di Trieste
Trieste, Italy
- Vitale, L.

Université Paris Science et Lettres
Paris 6ème, France
- Castro, L.

Université Paris-Saclay, CNRS/IN2P3, IJCLab
Orsay, France
- Ogur, S.

YTU
İstanbul, Turkey
- Caglar, A.
- Halis, D.
- Ilhan, T.B.
- Serin, M.

Content from this work may be used under the terms of the CC BY 4.0 licence (© 2022). Any distribution of this work must maintain attribution to the author(s), title of the work, publisher, and DOI